Determination of the bremsstrahlung spectra by unfolding technique based on ^{209}Bi(γ, xn) reactions

Nikola Jovančević [a,1], David Knežević [b,*,1], Miodrag Krmar [a,1], Dimitrije Maletić [b,1], Alexey Zhemchugov [c,1], Milomir Milaković [a,1]

[a] *Department of Physics, Faculty of Science, University of Novi Sad, Trg Dositeja Obradovica 3, Novi Sad, 21000, Serbia*
[b] *Institute of Physics Belgrade, Pregrevica 118, Zemun, 11080, Serbia*
[c] *Joint Institute for Nuclear Research, Dubna, 141980, Moscow Region, Russia*

ARTICLE INFO

ABSTRACT

This work explores and describes the possibility of assessment of high energy bremsstrahlung spectrum, through the use of photonuclear reactions. Experimentally obtained values of saturation activities of various Bi isotopes, created by ^{209}Bi(γ, xn) reactions in the 100 MeV bremsstrahlung beam were used in calculations. The photon spectrum is obtained by utilizing the unfolding techniques and cross sections data calculated by the TALYS 1.96 code. The experimental results were compared with the results obtained by Geant4 Monte Carlo simulation.

1. Introduction

High energy photon radiation produced by the powerful electron accelerators, has found a wide range of applications in science, technology or medicine (Kawano et al., 2020; Zilges et al., 2022). Photon-induced nuclear reactions represent a very interesting and challenging field of nuclear physics. Considering that the character of photonuclear reactions is purely electromagnetic, they can also be applied to probe various nuclear structure parameters in order to understand some of the nuclear properties.

Photons required for these reactions are usually produced as bremsstrahlung radiation using an electron accelerator. In order to correctly interpret the results obtained by photonuclear reactions, it is very important to know the shape of bremsstrahlung spectrum. The intensities and energies of the photons in the beam are usually so high that no direct measurement of the energy spectrum of the bremsstrahlung is possible. The extremely high photon flux of x-ray beams causes signal pile-up, and saturation-induced dead times in the commonly used spectroscopy systems. The energy deposit of high-energy photons in common detector materials is small, so the probability of detecting the full energy of the photon is very low. Since the probabilities of the interactions of the incident electrons are well known, it is possible to estimate the most important parameters of the bremsstrahlung beam by numerical simulations such as those that can be obtained in Geant4 (Agostinelli et al., 2003).

Experimentally, the energy spectrum of photon radiation can be obtained from the results of some selected photonuclear reactions for which the energy differential cross sections are well known. If the energy of photons in the beam is high enough, various particles can be created, (protons, neutrons, alpha particles, etc.) as a result of photonuclear reactions. In this paper, the focus is set on the (γ, xn) reactions. Considering that there is no Coulomb barrier for neutrons, these reactions have a much higher probability than the reactions emitting charged particles. Cross sections for (γ, n) reactions on a large number of stable nuclei are already well known in the Giant Dipole Resonance energy region (up to 30 MeV). In this energy region, the energy spectrum of the used photons can be reconstructed numerically, using the measured activities of the products of several nuclear reactions having well known cross sections. The results of the cross section measurements for emission of one or more neutrons in higher energy regions are not very abundant in literature (Soppera et al., 2014; Otuka et al., 2014). Due to a very poor set of experimental data, most of the needed information is currently acquired through theoretical calculations. In this paper, TALYS 1.96 code was used for the calculations (Koning and Rochman, 2012).

In the recently published paper (Medic et al., 2021), it was shown that cross section of one photonuclear reaction can be reconstructed in some desired energy region using a set of activation data and standard unfolding procedure, developed primary for neutron induced reactions. In this experiment, SAND-II (McElroy et al., 1967) and GRAVEL (Matzke, 1994) unfolding codes were used to extract unknown cross section. It was considered that the function describing the energy spectrum of incident photons is satisfactorily known. In this study, we

---

* Corresponding author.
E-mail addresses: nikola.jovancevic@df.uns.ac.rs (N. Jovančević), davidk@ipb.ac.rs (D. Knežević).
[1] These authors contributed equally to this work.

are dealing with a slightly different problem: reconstructing the shape of the function describing energy spectra of bremsstrahlung radiation using a set of activation data. Similar approach can be found in previous work (Knežević et al., 2016). To solve this problem, it is necessary to know the cross sections of photonuclear reactions creating the products whose activity was measured in the experiment. Natural monoisotope ^{209}Bi was chosen to be activated in this experiment, using 100 MeV bremsstrahlung beam. Up to nine neutrons could be emitted in (γ, xn) reactions. Data for cross sections for (γ, n) and (γ, 2n) reactions performed on ^{209}Bi can be found in the literature (Harvey et al., 1964; Forkman and Petersson, 1987). For higher neutron multiplicity, there are several papers presenting the analysis of the outputs of ^{209}Bi(γ, xn) reaction (Soppera et al., 2014; Naik et al., 2009, 2011; Otuka et al., 2014; Belyshev et al., 2015; Ermakov et al., 2010), however without measured cross sections. In the paper (Gheorghe et al., 2017, 2019) cross sections for (γ, n), (γ, 2n), (γ, 3n) and (γ, 4n) were measured, but only up to 40 MeV, with contributions of the reactions that, beside the emission of neutrons, also emit protons. The most important goal of this study is to check whether it is possible to reconstruct the shape of the high-energy bremsstrahlung spectra using a couple of existing unfolding codes. In order to achieve this, it is necessary to measure the activities of the products of several photonuclear reactions obtained by exposing the Bi target to a beam of high-energy photons, but it is also necessary to have energy differential cross sections for these reactions. This study tests the possibility of using results of TALYS 1.96 calculations as a source of reliable cross-section data in the unfolding procedure. Additionally, obtained results of the bremsstrahlung energy spectra are then compared with the results of Geant4 calculation.

2. The method

Saturation activity of the product of a photonuclear reaction performed in bremsstrahlung beam depends on the cross-section $\sigma(E)$ and the flux of incident particles $\Phi(E)$:

$$A = \int_{E_T}^{E_{max}} \sigma(E)\Phi(E)dE \tag{1}$$

where E_T is the energy threshold for nuclear reaction and E_{max} is endpoint energy (energy of incident electrons).

If several different products of nuclear reactions are obtained during the exposure of the selected target, it is sometimes more convenient to use normalized saturation activity:

$$A_n = \frac{A_k}{A_{nor}} = \frac{\int_{E_{T,k}}^{E_{max}} \sigma_k(E)\Phi(E)dE}{\int_{E_{T,nor}}^{E_{max}} \sigma_{nor}(E)\Phi(E)dE} \tag{2}$$

where subscripts k and nor denote quantities related to observed product of some photonuclear reaction and quantities related to product chosen to be the normalization one, respectively.

If the values of normalized saturation activities for several products of photonuclear reactions in the photon beam of the selected energy are experimentally determined, Eqs. (1) and (2) can be taken as the basis for the unfolding procedure. The solution of the integral in Eq. (1) should provide the values of the bremsstrahlung spectrum striking the target. In order to utilize the unfolding method, it is necessary to transform the integral equations into a system of discrete equations:

$$A_k = \sum_i^c \Phi_i \cdot \sigma_{ik} \cdot \Delta E_i; \quad k = 1, 2, \dots, m \tag{3}$$

where A_k is the measured saturation activity of each isotope k produced by irradiation, with m isotopes in total, which equals 7 in this case. The cross section for a certain energy bin, E_i, and for creation of an isotope k, is described by σ_{ik}. ΔE_i represents the width of the energy bin i, with c total energy bins, while Φ_i represents the photon flux that needs to be determined. Since the number of bins, c, is much larger than the number of isotopes, m, this set of equations is under-determined. This

means that, without any assumptions about the shape of the photon flux spectrum, there is an infinite number of spectra that satisfies the equations. The unfolding procedure overcomes this issue by starting with a guess, or default, a priori photon spectrum function.

2.1. A priori photon spectrum

Default spectrum contains the available a priori information about the shape of the spectrum, such as theoretical predictions about the shape of the spectrum. In previous work with the unfolding methods, this spectrum was constructed based on a theoretical prediction (Knežević et al., 2016) and also by averaging the experimental spectrum values within a number of energy intervals (Ilić et al., 2020). The robustness of the numerical procedure was checked using a combination of an increasing linear function (at low energies) and a decreasing one (in the high-energy part) and obtained spectra were comparable to the GEANT simulation. For the purposes of this study, it was decided that the theoretical thin target Schiff function (Schiff, 1951) can be used in the capacity of the default spectrum.

2.2. Cross sections data

In this work, TALYS 1.96 code was used to determine the cross sections. Detailed description of TALYS 1.96 can be found in Koning and Rochman (2012). Cross section data that were used for (γ,2n) to (γ,8n) reactions were calculated with default TALYS 1.96 parameters, except for level density and photon strength function. There are several other important parameters, but the analysis of their influence on the output of TALYS 1.96 calculation exceeds the scope of this pilot study and will be the subject of subsequent research. Six level density and nine photon strength function models were used (Koning and Delaroche, 2003; Hauser and Feshbach, 1952; Kalbach, 1986; Gilbert and Cameron, 1965; Dilg et al., 1973; Zubov et al., 2009; Ignatyuk et al., 1993; Goriely et al., 2001, 2008; Hilaire et al., 2012; Brink, 1957; Axel, 1962; Kopecky and Uhl, 1990; Kopecky et al., 1993; Goriely and Khan, 2002; Goriely et al., 2004; Goriely, 1998; Daoutidis and Goriely, 2012; Goriely et al., 2018; Plujko et al., 2008):

Level density models

1. LD model 1. — the constant temperature Fermi-Gas model,
2. LD model 2. — the back-shifted Fermi gas model,
3. LD model 3. — the generalized super-fluid model,
4. LD model 4. — the microscopic level densities based on the Goriely's tables,
5. LD model 5. — Hilaire's combinatorial tables and
6. LD model 6. — the temperature dependent Hartree–Fock-Bogoliubov model, Gogny force.

Photon strength function models

1. Strength 1. — Kopecky–Uhl generalized Lorentzian,
2. Strength 2. — Brink–Axel Lorentzian,
3. Strength 3. — Hartree–Fock BCS tables,
4. Strength 4. — Hartree–Fock–Bogoliubov tables,
5. Strength 5. — Goriely's hybrid model,
6. Strength 6. — Goriely T-dependent HFB,
7. Strength 7. — T-dependent RMF,
8. Strength 8. — Gogny D1M HFB+QRPA and
9. Strength 9. — SMLO.

In a recently published paper (Deiev et al., 2022), on the example of photonuclear reactions on ^{181}Ta, it was concluded that TALYS 1.96 results are not always in good agreement with experimental values of average cross sections and that it is not possible to choose only one optimal model that would satisfactorily describe all (γ,xn) reactions.

However, the results of Naik et al. (2011), Belyshev et al. (2015) show that TALYS 1.96 cross sections employed to estimate average cross sections and reaction yields show a good agreement with experimental results obtained in bismuth photoactivation. It should be noted that TALYS 1.96 cross sections for several ^{209}Bi(γ,xn) reactions agree reasonably well with results of measurements (Gheorghe et al., 2017, 2019). This was a solid basis for assuming that TALYS 1.96 cross sections could be used in this study. It was decided that cross sections obtained by all six level density and nine photon strength function models should be used as response functions for unfolding algorithm and results obtained by all of them are presented further.

2.3. Unfolding procedure

In order to calculate the final spectrum starting from the a priori one, cross section values and experimentally obtained activities, SAND-II (McElroy et al., 1967) and GRAVEL (Matzke, 1994) algorithms were used in the unfolding method. GRAVEL algorithm is a modified SAND-II algorithm, and both are iterative algorithms that take the initial assumption about the spectrum shape and, through a number of iterative steps, arrive to the final shape of the spectrum. From the Jth iteration step of the neutron fluence rate (Φ_i^J, for the energy bin E_i), the next iteration, Φ_i^{J+1}, is calculated by:

$$\Phi_i^{J+1} = \Phi_i^J \cdot f(A_k, \epsilon_k, \sigma_{ki}, \Phi_i^J) \tag{4}$$

The function f is defined as:

$$f = exp\left(\frac{\sum_{ik} W_{ik}^J \log\left(\frac{A_k}{\sum_i \sigma_{ki} \Phi_i^J}\right)}{\sum_k W_{ik}^J}\right) \tag{5}$$

The difference between the SAND-II and GRAVEL algorithms is in the definition of the W_{ik}^J. In the SAND-II algorithm, it is defined as:

$$W_{ik}^J = \frac{\sigma_{ki} \Phi_i^J}{\sum_i \sigma_{ki} \Phi_i^J}, \tag{6}$$

while in GRAVEL it is defined as:

$$W_{ik}^J = \frac{\sigma_{ki} \Phi_i^J A_k^2}{\sum_i \sigma_{ki} \Phi_i^J \epsilon_k^2} \tag{7}$$

where W_{ik}^J is the weight factor, A_k is the measured activity, ϵ_k is the measurement uncertainty, and the σ_{ki} is the cross section for production of the kth Bi isotope in the energy bin E_i.

3. Measurement and results

^{209}Bi was chosen because it is a natural mono isotope and has a number of neutron deficient isotopes with half-lives sufficiently long for off-line analysis. Since these isotopes also have a significant number of strong gamma transition, activity of all the isotopes created can be determined using gamma-spectroscopy. For irradiation in 100 MeV bremsstrahlung beam, a 1.5 g grain of high purity bismuth was used. The bismuth grain had the shape of a flattened drop with a maximum thickness of 1 mm.

As previously mentioned, ^{209}Bi in interaction with 100 MeV bremsstrahlung beam can emit up to 9 neutrons in (γ, xn) reactions.

3.1. Irradiation

Irradiation was performed at the LINAC 200, located at the Laboratory of Nuclear Problems, JINR, Dubna (Nozdrin et al., 2021). Irradiation of natural bismuth target by bremsstrahlung created in tungsten target irradiated by 100 MeV electron beam was performed. The scheme of the experimental setup is presented in Fig. 1. Practically mono-energetic 100 MeV electron beam with frequency of 25 Hz and
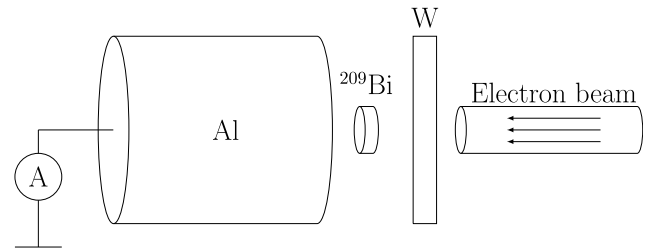

Fig. 1. Scheme of the experimental setup (not to scale).

pulse duration of 2 µs was focused into 5.65 mm thickness tungsten target to generate bremsstrahlung for ^{209}Bi activation. A ^{209}Bi sample was located behind the tungsten target and exposed to photons. The Al cylinder (Faraday cup) was connected to ammeter Keithley 6485 to monitor the beam current. The exposure time was 15 min and the beam current varied between $1 \cdot 10^{-7}$ A and $3 \cdot 10^{-7}$ A. Short-term instabilities in the intensity of the electron beam were not taken into account when calculating the saturation activity, mainly due to the much longer half-lives of the observed isotopes.

The bismuth target had much smaller dimensions than the used tungsten Bremsstrahlung converter, and a significantly smaller number of electrons with reduced energy, which penetrated Al cylinder, fell on it. For this reason, it can be expected that the production of bremsstrahlung in bismuth and associated activation is significantly lower.

3.2. Gamma spectroscopy measurement and normalized saturation activities

After the irradiation, the Bi sample was transferred to the HPGe detector in order to measure induced gamma activity. The length of the irradiation was 900 s. Time difference between the end of irradiation and the start of gamma measurement was 10 min. Two spectra were recorded: the first lasting up to 3600 s, and the next right after the first, lasting 16,200 s. The first spectrum was used to determine the saturation activities of short-lived Bi isotopes, starting with ^{202}Bi and lighter. In the second spectrum, gamma peaks of long-lived isotopes with a sufficiently small statistical uncertainty of their intensities were obtained. The estimation of the saturation activity was performed using the intensities of characteristic gamma lines from the products of the nuclear reaction. Some parts of collected gamma spectra are presented in Fig. 2.

The saturation activity can be calculated as:

$$A = \frac{N_\gamma \cdot M \cdot \lambda}{m \cdot N_A \cdot \epsilon \cdot \eta \cdot p_\gamma \cdot e^{-\lambda \Delta t}}$$
$$\cdot \frac{1}{(1 - e^{\lambda t_{irr}}) \cdot (1 - e^{\lambda t_m})} \tag{8}$$

where N_γ is a number of detected γ photons of selected energy, λ is the decay constant, M and m are the mass number and the mass of the irradiated target, N_A is the Avogadro constant, ϵ is the total efficiency of the detector at the observed energy, η is the natural abundance of the activated isotope, p_γ is the quantum yield of detected photons, Δt, t_{irr} and t_m represent the cooling, irradiation and measurement time, respectively.

The ratio of the calculated saturation activities was determined as:

$$A_n = \frac{A_k}{A_{nor}} = \frac{N_{\gamma k} \cdot \lambda_k \cdot \epsilon_{nor} \cdot p_{\gamma nor} \cdot e^{-\lambda_{nor} \Delta t}}{N_{\gamma nor} \cdot \lambda_{nor} \cdot \epsilon_k \cdot p_{\gamma k} \cdot e^{-\lambda_k \Delta t}}$$
$$\cdot \frac{(1 - e^{\lambda_{nor} t_{irr}}) \cdot (1 - e^{\lambda_{nor} t_m})}{(1 - e^{\lambda_k t_{irr}}) \cdot (1 - e^{\lambda_k t_m})} \tag{9}$$

where subscript *nor* represents values related to the product of reaction used for normalization and subscript k denotes all quantities related to other Bi isotopes obtained in photonuclear reactions.
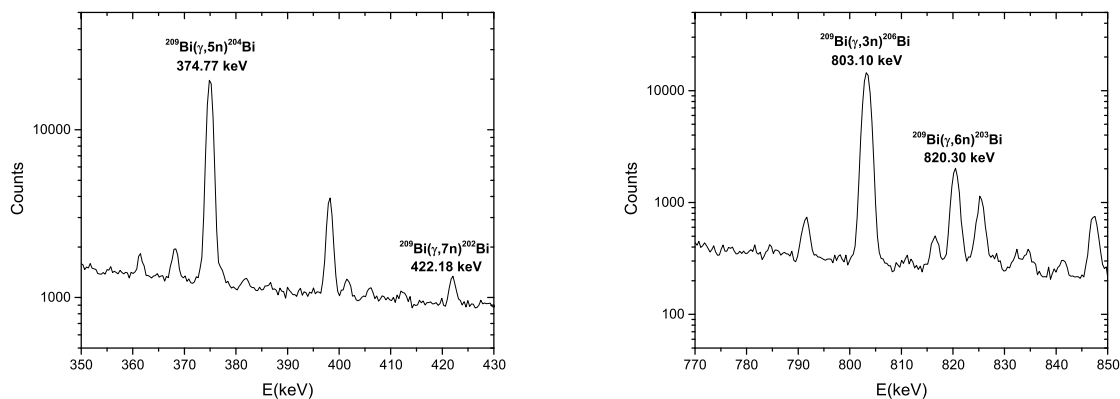
Fig. 2. Part of the γ-ray spectrum collected after irradiation of ^{209}Bi with some of the lines used for the calculation of saturation activities labeled.

The use of ratios of saturation activities, has the advantage because it is not necessary to know the absolute efficiency of the detector for the energies of the gamma transition analyzed, only the relative one. The best isotope for the normalization is ^{206}Bi, because its half-life is long enough to allow off-line gamma spectroscopy measurements (6.243 days). Additionally, ^{206}Bi has a number of intensive gamma lines in recorded spectra.

The relative efficiency of the detector was determined using 15 single gamma lines of ^{206}Bi, in the energy interval from 183.98 keV to 1878.65 keV. A combination of an exponential function and a third-order polynomial was used to describe the relative efficiency. It was estimated that in this way in the mentioned energy interval the relative efficiency can be obtained with an uncertainty of up to 3%. Possible effects of self-absorption of gamma radiation in the target itself (although its thickness in the middle was about 1 mm) are reduced by the use of relative efficiency to the ratio of attenuation of radiation of different energies that pass an identical path through the absorption medium. It is estimated that the biggest difference can be expected in the case of ^{207}Bi, whose saturation activity calculated with the lowest energy of 569.7 keV (Table 1). It can be expected that the difference in self-absorption at this energy and self-absorption at 803.1 keV (^{206}Bi gamma radiation used for normalization) amounts to several percent.

Normalized saturation activities of Bi isotopes were measured for seven isotopes originating from $(\gamma, 2n)$ reaction up to $(\gamma, 8n)$ reaction. The choice of gamma lines for each individual isotope was made very carefully and not in all cases the most intense gamma transitions were chosen. It was significant that there are no close gamma lines of other isotopes and no separable doublets. In addition, it was important that all used gamma lines were energetically close to the selected gamma line of ^{206}Bi, which served as a normalization isotope. In this way, the potential uncertainty that would arise from relative efficiency or different self-absorption in bismuth itself is minimized. Obtained values of normalized activities, as well as measurement uncertainties, are presented in Table 1. Uncertainties of the saturation activities, listed in Table 1, originate exclusively from the statistical uncertainties of the integrals of the selected gamma lines, as well as the uncertainty with which the relative efficiency was calculated. Although the cross section for the ^{209}Bi (γ, n) reaction is the largest one, the ^{208}Bi gamma line of 2614.5 keV was not used in the analysis. The half-life of this bismuth isotope is $3.63 \cdot 10^4$ years. In addition, the same gamma line, but from the decay of ^{208}Tl, is very intense in the background spectra, and unfortunately our detector could not provide the conditions to completely eliminate the surrounding background of natural radiation.

It was noted in a recent publication (Belyshev et al., 2015) that the contribution of $(\gamma, p\,5n)$ reactions can have significant output compared to $(\gamma, 6n)$ one. In this study, activities of bismuth isotopes were measured, including ^{203}Bi. Lead isotope ^{203}Pb, as daughter nucleus of ^{203}Bi decay, can also be formed in reactions with the emission of protons in addition to neutrons. In this situation, it can be formed in

Table 1

Saturation activities, R_{A_s}, of activated Bi isotopes. The activities are calculated relative to the ^{206}Bi isotope. Gamma-ray transitions used to determine the activity of the isotopes of interest are presented in the fourth column (Demichev, 2022). E_γ - gamma-ray energy and p_γ - gamma-ray intensity.

Source: Relevant data was taken from NNDC (2023).

Reaction	Radionuclide	$T_{1/2}$	E_γ [keV]	R_{A_s}	p_γ
^{209}Bi$(\gamma, 2n)$	^{207}Bi	31.55 y	569.7 keV	6.7 (3)	0.9775
^{209}Bi$(\gamma, 3n)$	^{206}Bi	6.243 d	803.1 keV	1.00 (3)	0.990
^{209}Bi$(\gamma, 4n)$	^{205}Bi	15.31 d	703.44 keV	0.45 (2)	0.3108
^{209}Bi$(\gamma, 5n)$	^{204}Bi	11.22 h	899.15 keV	0.177 (5)	0.99
^{209}Bi$(\gamma, 6n)$	^{203}Bi	11.76 h	820.3 keV	0.097 (4)	0.297
^{209}Bi$(\gamma, 7n)$	^{202}Bi	1.71 h	960.67 keV	0.046 (2)	0.99283
^{209}Bi$(\gamma, 8n)$	^{201}Bi	103 min	786.4 keV	0.020 (1)	0.098

excited states and in the prompt transitions transferred to the ground state. These prompt transitions do not interfere with gamma transitions originating from the decay of ^{203}Bi, which were detected in the off-line measurement.

3.3. Cross sections functions

As stated in Section 2.2, the cross sections for (γ, xn) nuclear reactions were calculated using the TALYS 1.96 code. Different estimates of the density of the excited state of the observed nucleus and different estimates of photon strength function were used. The values of cross section functions for different level density functions and same photon strength function have very similar shape. This is not the case when photon strength functions vary for fixed level density. The example of this is presented in Fig. 3. Evident differences in general shape of the cross section function, their amplitudes, thresholds, etc. appear when different models are used in calculations.

3.4. Unfolding determination of photon spectra

For each of the observed photonuclear reactions, 54 different estimates for cross sections were obtained, as a combination of all models taken for the density of excited states and photon strength functions. The unfolding procedure was performed separately for each of them.

The identical procedure was repeated using both codes GRAVEL as well as for SAND-II and for each of the 54 different cross section estimates in order to obtain the shape of the photon spectrum.

The unfolding was done for 343 energy bins covering fixed width energy regions from 14.5 MeV, which is slightly below the threshold for the (n, 2n) reaction, up to the 100 MeV, the maximal energy of accelerated electrons. Obtained unfolding results for different level density and photon strength options in TALYS 1.96 for GRAVEL and SAND-II are shown in Figs. 4 and 5, respectively. For easier overview of the results, all results obtained for different level density models with the same photon strength function model are presented with the same color.
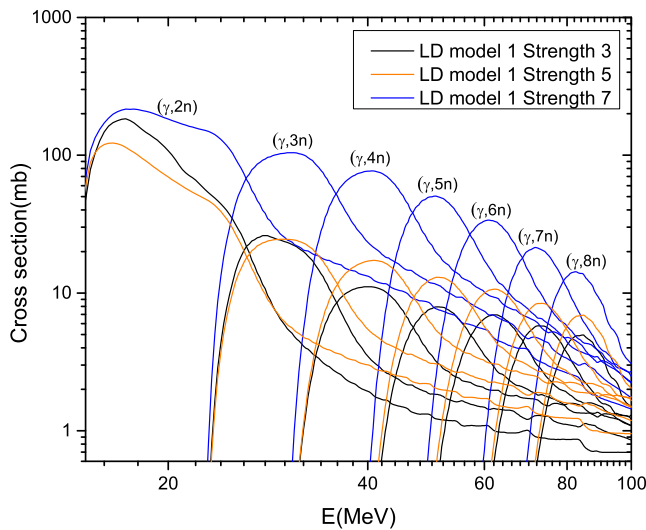
Fig. 3. Part of the cross sections for the used γ,xn reactions derived from different TALYS 1.96 photon strength function models (3, 5 and 7) and fixed level density model (1).
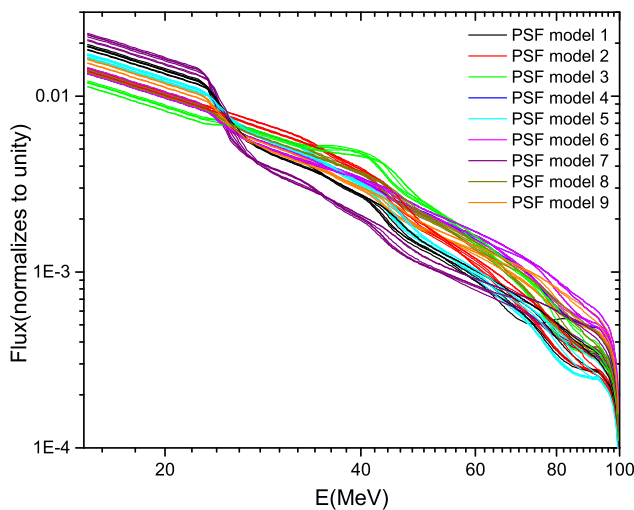

Fig. 4. Unfolding results obtained with GRAVEL algorithm for different cross sections obtained by varying level density and photon strength function models in TALYS 1.96.
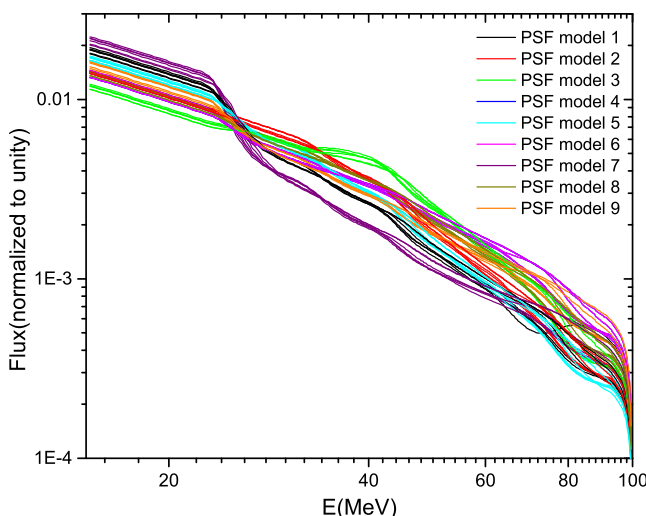

Fig. 5. Unfolding results obtained with SAND-II algorithm for different cross sections obtained by varying level density and photon strength function models in TALYS 1.96.

3.5. Geant4 simulation of bremsstrahlung spectrum

The only way to check the energy spectrum obtained by unfolding procedure is to compare it with the simulation results. The theoretical expression for the shape of the energy spectrum of bremsstrahlung, which was used as the starting point of unfolding, was obtained using Schiff's function for a thin target. A thick target is used in the experiment and it can be expected that the shape of the bremsstrahlung spectrum differs significantly from the theoretical estimate. In this case, the estimation of the shape of the photon spectrum obtained by simulation is the only possibility to check the validity of the unfolding results.

To get the MC simulated bremsstrahlung spectrum at the place of the Bi sample, the incident electron beam hitting the 5.65 mm thick W target was simulated and the photons, 1 cm away from W target were tracked. The simulation was done using Geant4 version 4.10.05.p01. We simulated incident electron beam with particle energy of gaussian random of $E_k = (100.0 \pm 0.1)$ MeV, and position with gaussian random spread in x and y having sigma of 0.1 mm, but without any directional spread. The physics list used was QBBC, which uses Standard EM option. As output from G4 simulation, the energy and position of gammas on a wide area at 1 cm distance from W target was recorded. This allowed us to create different gamma beams by selecting only gammas hitting specific parts of the wider area, without the need to repeat the G4 simulation from the start. This way, firstly, the gamma spectra could be obtained with sufficient statistics because of the rotational symmetry around the incident electron beam axis. Secondly, we can select the specific area where Bi sample could be positioned, and finally, the Bi sample could have specific distances from the incident electron beam axis. The obtained gamma spectra could then be compared with unfolding results.

4. Discussion

It can be observed that the spectra obtained by different unfolding codes do not differ significantly in the entire energy region of interest. Figs. 4 and 5 show that the estimates of the photon spectrum, obtained using different level density models and the same photon strength function, do not differ significantly in energy region up to the 60 MeV. Significant differences, within some photon strength function models, appear in the high-energy part of the spectrum. On the other hand, it can be seen that the different photon strength function models produce significantly different estimates of the photon spectrum.

Since the SAND-II and GRAVEL algorithms have no routine for standard sensitivity analysis and uncertainty propagation, it is necessary to analyze all the possible sources of uncertainty.

4.1. Uncertainty analysis

The uncertainty of the ratios of the saturated activities were calculated by including uncertainties of all the contributing elements from Eq. (9). Main source of uncertainty comes from the statistical error of measured gamma ray intensity (Gilmore, 2008) and from determination of relative efficiency, to a much lesser extent. However, the exact influence of these uncertainties on final results cannot be determined in unfolding algorithm, although they do influence final results. This item will be a subject of some future analysis.

Cross sections were calculated using TALYS 1.96, and there is no cross section uncertainty estimation that can be introduced in the error propagation. However, Figs. 4 and 5 show that the unfolding procedure using different level density and photon strength function models for cross section calculation results in different photon spectra.

In order to obtain estimate of the range in which the photon flux values could be found for each of the observed energies, it was decided that: (i) after the unfolding procedure using GRAVEL and SAND-II algorithms, all unfolding results should be averaged, and (ii) the highest
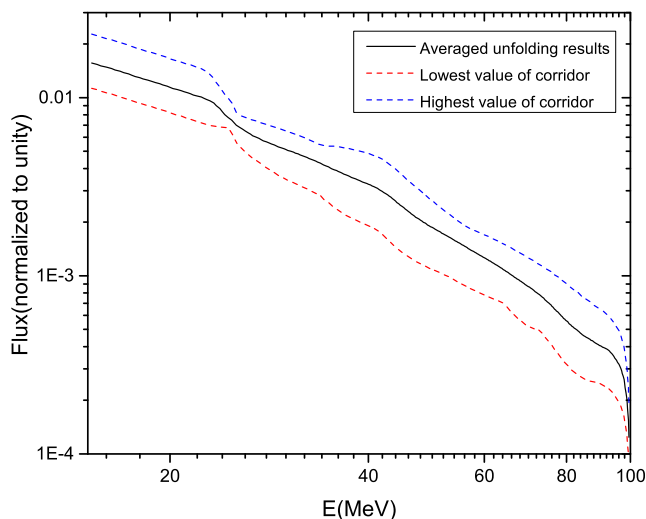
Fig. 6. Averaged unfolding results from SAND-II and GRAVEL algorithms for different cross sections obtained by varying level density model in TALYS 1.96. Lowest and highest corridor values were determined by the lowest and highest values among all of the unfolded bremsstrahlung spectra for each energy bin.

Table 2
The χ^2 values for each of the level density and photon strength function models used. Values are presented for default function (before unfolding) and after the unfolding by SAND-II and GRAVEL algorithm.

1. Default function

			χ^2			
Reaction	LD 1	LD 2	LD 3	LD 4	LD 5	LD 6
PSF 1	98.840	144.492	150.392	126.904	99.221	107.962
PSF 2	175.870	178.358	182.959	156.132	130.626	145.326
PSF 3	153.864	154.139	157.580	136.262	106.275	121.961
PSF 4	67.959	67.720	70.156	54.210	34.774	44.064
PSF 5	178.722	178.785	184.124	158.852	130.908	142.910
PSF 6	67.811	67.521	70.000	54.148	34.773	44.053
PSF 7	90.969	87.762	94.238	73.478	54.979	57.426
PSF 8	124.311	124.522	127.719	107.513	80.816	94.095
PSF 9	75.911	74.635	78.344	60.491	40.599	47.698

2. SAND-II results

			χ^2			
Reaction	LD 1	LD 2	LD 3	LD 4	LD 5	LD 6
PSF 1	0.719	0.494	0.598	0.596	0.253	0.447
PSF 2	0.913	0.635	0.660	0.755	0.426	0.739
PSF 3	0.419	0.229	0.345	0.838	0.702	0.950
PSF 4	0.779	0.515	0.583	0.677	0.315	0.588
PSF 5	0.908	0.575	0.672	0.681	0.339	0.589
PSF 6	0.776	0.514	0.569	0.674	0.315	0.588
PSF 7	0.428	0.258	0.286	0.735	0.289	0.418
PSF 8	0.964	0.654	0.779	0.765	0.358	0.645
PSF 9	0.585	0.346	0.386	0.634	0.874	0.417

3. GRAVEL results

			χ^2			
Reaction	LD 1	LD 2	LD 3	LD 4	LD 5	LD 6
PSF 1	0.858	0.264	0.421	0.786	0.437	0.724
PSF 2	0.478	0.259	0.416	0.716	0.191	0.438
PSF 3	0.893	0.544	0.743	0.794	0.480	0.677
PSF 4	0.490	0.959	0.364	0.914	0.532	0.916
PSF 5	0.530	0.268	0.461	0.967	0.797	0.366
PSF 6	0.488	0.955	0.998	0.909	0.532	0.916
PSF 7	0.434	0.245	0.380	0.695	0.086	0.249
PSF 8	0.600	0.334	0.490	0.692	0.834	0.423
PSF 9	0.855	0.558	0.649	0.791	0.238	0.555

and the lowest value for photon flux, chosen between all 108 obtained spectra, for a particular energy, will be used to construct an uncertainty corridor.

The result of averaging and selection of the maximal and minimal estimated flux values, are depicted in Fig. 6. So, each point in Fig. 6, forming a solid line, has an average value of all of the unfolding results (108 of them, for both unfolding methods). The dashed lines are determined by the minimum and maximum values selected in the 108 estimated spectra representing the uncertainty corridor in this case.

There is another way to validate the obtained results. When there are 54 estimations for cross sections for all observed photonuclear reactions and corresponding photon spectra obtained by unfolding procedure, it is possible to calculate saturation activities for each cross-section photon spectra pair. The very same procedure can be repeated for both unfolding algorithms. These values can be compared with the experimentally established results, shown in Table 2. Comparison of calculated ratio of saturation activity R_{A_c} to the experimentally obtained values R_{A_s}, taking into account the errors of the experimental values, ϵ_{A_s}, can be done through parameter χ^2, value of which can be calculated as:

$$\chi^2 = \frac{1}{n} \sum_{i=1}^{n} \frac{\left(R_{A_{ci}} - R_{A_{si}} \right)^2}{\epsilon_{A_{si}}^2} \tag{10}$$

where subscript i refers to individual reactions observed, and n represents the number of reactions used for the unfolding, seven in this case.

This value can be used as a measure of quality of unfolding procedure for an individual set of level density and photon strength function models. Table 2 shows the χ^2 for all combinations of models used. First set of data named "Default function" represents χ^2 obtained when experimental saturation activities were compared with calculated ones obtained using default spectrum (Schiff function). Next two sets of presented χ^2 values are obtained using both GRAVEL and SAND-II algorithms.

4.2. Comparison with Geant4 simulation

The results of the unfolding, compared with the default spectrum and also with the Geant4 Monte Carlo simulation are presented in

Fig. 7. It can be seen that the unfolding procedure significantly modified the default Schiff's function. Good agreement was obtained between the Geant4 Monte Carlo simulation and the unfolding results. Geant4 Monte Carlo simulation was done for the approximate dimensions of the Bi target (1 mm diameter circle). Fig. 7 also shows that the simulated photon spectrum differs significantly from Schiff's estimate after Geant4 has taken into account the effects of the thick target. As could be expected (Wood, 2018), the thick target emits more photons than predicted by Schiff's expression at low energies, while in the high-energy part it is the opposite. The photon spectrum obtained by unfolding predicts slightly larger values compared to the Geant4 estimate of the thick target spectrum, in the energy range up to 26 MeV. From this energy up to 44 MeV it agrees relatively well with the Geant4 estimate, after which it predicts lower values for the most part of the spectrum up to 100 MeV.

In the search for a possible explanation, the assumption was made that the Bi target may not have been positioned in the very center of the photon beam. It is known that the angular distribution of high energy bremsstrahlung is a very sharp forward-directed function (in the direction of incident electrons). Because of this, simulation was done for several different positions of the Bi sample: on the beam axis, 1 mm off the beam axis, and 2 mm off the beam axis. The distance of the Bi target from tungsten was 1 cm.

In both off-axis geometries, the Geant4 simulation agrees quite well with the result of unfolding in the low-energy half of the spectrum. It is also evident that there is still a difference in the high-energy half of the spectrum, but it is smaller than in the case in which the Bi sample was
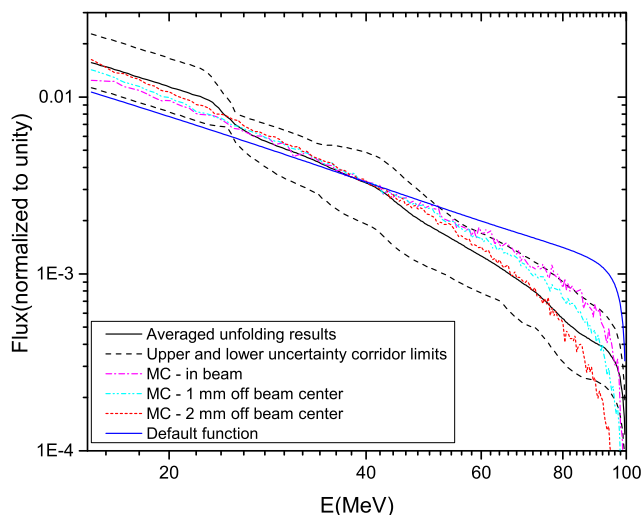
Fig. 7. Comparison of default function, simulation and unfolding spectrum. The unfolding results were averaged from the results for different LD models used in TALYS 1.96, and lowest and highest values of corridor were calculated. Simulation was done for a circular target with 1 mm radius 1 cm away from tungsten in 3 different positions from the main beam axis: in the beam, 1 mm off beam, and 2 mm off beam.

Fig. 8. Comparison of simulation and unfolding spectra obtained with averaging unfolding results for all level densities within PSF model 4 and PSF model 8, with lowest and highest values of corridor calculated. Simulation was done for a circular target with 1 mm radius 1 cm away from tungsten in 3 different positions from the main beam axis: in the beam, 1 mm off beam, and 2 mm off beam.

supposedly on the beam axis. Better agreement between the simulation and the unfolding result for off-axis position of the Bi sample, suggests that the target was not centered properly.

In order to extract additional information from the unfolding procedure, for each photon strength function model, all unfolding results for different models of density of levels were averaged, and highest and lowest values corridor was constructed. The results averaged in this way were then compared with the Geant4 Monte Carlo simulations. Photon strength function models 4 and 8 showed the best agreement with the Geant4 Monte Carlo simulations, and these results are presented in Fig. 8.

5. Conclusion

This paper describes an attempt to determine the shape of the 100 MeV bremsstrahlung energy spectrum using existing unfolding codes. From the experimental data, it was necessary for these studies to have saturation activities for several Bi isotopes produced by (γ, xn) nuclear reaction. Activation measurements of the Bi sample in a 100 MeV bremsstrahlung photon beam were performed. Based on the measured gamma spectra, normalized saturation activities were determined. They served as input for unfolding calculations. Two codes developed for application in the field of neutron activation, GRAVEL and SAND II were available. Besides the activation data, differential energy cross sections are also required for the observed photonuclear reactions. The results obtained using the TALYS 1.96 code were used, in the absence of experimental data. A Geant4 spectrum simulation was made for the selected geometry of bremsstrahlung production, and the unfolding spectra were compared with it.

The unfolding results agree with the shape of the bremsstrahlung spectrum obtained by the simulation, with some differences in the high-energy part of the spectrum. This is a good indicator that the existing unfolding codes, combined with the cross sections calculated using the TALYS 1.96 code, can also be used in the field of photonuclear reactions.

It should be mentioned that in one of the already established methods (Schwengner et al., 2005), the authors reconstructed the shape of the spectrum of high-energy bremsstrahlung radiation by measuring proton energies after photo disintegration of deuterium. A positive
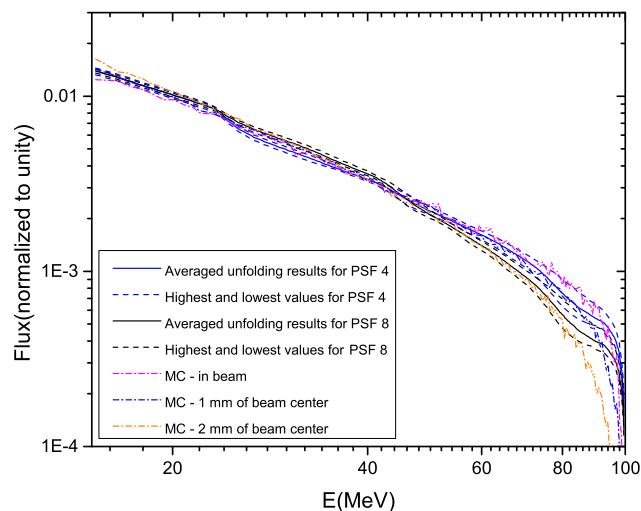
motivation for the development of the method described in this paper could be found in the fact that it requires much simpler measuring equipment than the case described in Schwengner et al. (2005).

The described preliminary measurements and calculations are encouraging enough to continue in the same direction. The first possibilities to improve the methodology are recognized in the more carefully performed experiment, where the positioning of the activated sample itself is primarily preferred. The half-lives of the obtained products of photonuclear reactions are in a very wide range, as can be seen from Table 1, so there is room for optimization of the timing of gamma spectroscopic measurements. The TALYS 1.96 code itself provides many more possibilities for estimating the cross-section of photonuclear reactions than was done in this study. Probably, in addition to the density of excited states and photon strength functions, some other effects could be included to obtain a more realistic cross-section estimate.

And finally, let us look at what possibilities the results of this study open up. The described method could be used for calibrations of high-energy photon beams, in combination with simulation results. One possibility is particularly interesting here. If the energy spectrum of the photon beam is accurately determined, it is possible to obtain an energy differential cross section for one chosen photonuclear reaction using the same technique of photoactivation measurements and unfolding. In Fig. 3 it can be seen that the results of the TALYS 1.96 calculation can differ so that experimental verification would be very welcome.

Declaration of competing interest

The authors declare that they have no known competing financial interests or personal relationships that could have appeared to influence the work reported in this paper.

Data availability

Data will be made available on request.

Acknowledgement

References

Agostinelli, S., Allison, J., Amako, K.a., Apostolakis, J., Araujo, H., Arce, P., Asai, M., Axen, D., Banerjee, S., Barrand, G., et al., 2003. GEANT4—A simulation toolkit. Nucl. Instrum. Methods Phys. Res. Sec. A 506 (3), 250–303.

Axel, P., 1962. Electric dipole ground-state transition width strength function and 7-MeV photon interactions. Phys. Rev. 126 (2), 671.

Belyshev, S., Filipescu, D., Gheoghe, I., Ishkhanov, B., Khankin, V., Kurilik, A., Kuznetsov, A., Orlin, V., Peskov, N., Stopani, K., et al., 2015. Multinucleon photonuclear reactions on ^{209}Bi: Experiment and evaluation. Eur. Phys. J. A 51 (6), 1–9.

Brink, D., 1957. Individual particle and collective aspects of the nuclear photoeffect. Nucl. Phys. 4, 215–220.

Daoutidis, I., Goriely, S., 2012. Large-scale continuum random-phase approximation predictions of dipole strength for astrophysical applications. Phys. Rev. C 86 (3), 034328.

Deiev, O., Timchenko, I., Olejnik, S., Kushnir, V., Mytrochenko, V., Perezhogin, S., 2022. Cross sections of photoneutron reactions on ta 181 at $E_{\gamma max}$ up to 95 MeV. Phys. Rev. C 106 (2), 024617.

Demichev, M., 2022. Study of ^{209}Bi(γ,xn) reactions in energy region up to 100 MeV. In: LXXII International Conference "Nucleus-2022: Fundamental Problems and Applications" Book of Abstracts.

Dilg, W., Schantl, W., Vonach, H., Uhl, M., 1973. Level density parameters for the back-shifted fermi gas model in the mass range 40<A< 250. Nuclear Phys. A 217 (2), 269–298.

Ermakov, A., Ishkhanov, B., Kapitonov, I., Makarenko, I., Orlin, V., 2010. Photodisintegration of heavy nuclei in the energy region above the giant dipole resonance. Phys. Atom. Nuclei 73 (5), 737–745.

Forkman, B., Petersson, R., 1987. Photonuclear cross-sections. In: Handbook on Nuclear Activation Data.

Gheorghe, I., Utsunomiya, H., Katayama, S., Filipescu, D., Belyshev, S., Stopani, K., Orlin, V., Varlamov, V., Shima, T., Amano, S., et al., 2017. Photoneutron cross-section measurements in the Bi 209 (γ, x n) reaction with a new method of direct neutron-multiplicity sorting. Phys. Rev. C 96 (4), 044604.

Gheorghe, I., Utsunomiya, H., Katayama, S., Filipescu, D., Belyshev, S., Stopani, K., Orlin, V., Varlamov, V., Shima, T., Amano, S., et al., 2019. Erratum: Photoneutron cross-section measurements in the Bi 209 (γ, x n) reaction with a new method of direct neutron-multiplicity sorting [Phys. Rev. C 96, 044604 (2017)]. Phys. Rev. C 99 (5), 059901.

Gilbert, A., Cameron, A., 1965. A composite nuclear-level density formula with shell corrections. Can. J. Phys. 43 (8), 1446–1496.

Gilmore, G., 2008. Practical Gamma-Ray Spectroscopy. John Wiley & Sons.

Goriely, S., 1998. Radiative neutron captures by neutron-rich nuclei and the r-process nucleosynthesis. Phys. Lett. B 436 (1–2), 10–18.

Goriely, S., Hilaire, S., Koning, A.J., 2008. Improved microscopic nuclear level densities within the Hartree-Fock-Bogoliubov plus combinatorial method. Phys. Rev. C 78 (6), 064307.

Goriely, S., Hilaire, S., Péru, S., Sieja, K., 2018. Gogny-HFB+ QRPA dipole strength function and its application to radiative nucleon capture cross section. Phys. Rev. C 98 (1), 014327.

Goriely, S., Khan, E., 2002. Large-scale QRPA calculation of E1-strength and its impact on the neutron capture cross section. Nuclear Phys. A 706 (1–2), 217–232.

Goriely, S., Khan, E., Samyn, M., 2004. Microscopic HFB+ QRPA predictions of dipole strength for astrophysics applications. Nuclear Phys. A 739 (3–4), 331–352.

Goriely, S., Tondeur, F., Pearson, J., 2001. A Hartree–Fock nuclear mass table. At. Data Nucl. Data Tables 77 (2), 311–381.

Harvey, R., Caldwell, J., Bramblett, R., Fultz, S., 1964. Photoneutron cross sections of Pb 206, Pb 207, Pb 208, and Bi 209. Phys. Rev. 136 (1B), B126.

Hauser, W., Feshbach, H., 1952. The inelastic scattering of neutrons. Phys. Rev. 87 (2), 366.

Hilaire, S., Girod, M., Goriely, S., Koning, A.J., 2012. Temperature-dependent combinatorial level densities with the D1M Gogny force. Phys. Rev. C 86 (6), 064317.

Ignatyuk, A., Weil, J., Raman, S., Kahane, S., 1993. Density of discrete levels in sn 116. Phys. Rev. C 47 (4), 1504.

Ilić, S., Jovančević, N., Daraban, L., Stroh, H., Oberstedt, S., Hult, M., Bonaldi, C., Geerts, W., Hambsch, F.-J., Lutter, G., et al., 2020. The cross-sections for the ^{187}Re(n,p)^{187}W and ^{185}Re(n,3n)^{183}Re reactions in the energy range between 13.08 MeV and 19.50 MeV. Eur. Phys. J. A 56 (8), 1–11.

Kalbach, C., 1986. Two-component exciton model: Basic formalism away from shell closures. Phys. Rev. C 33 (3), 818.

Kawano, T., Cho, Y., Dimitriou, P., Filipescu, D., Iwamoto, N., Plujko, V., Tao, X., Utsunomiya, H., Varlamov, V., Xu, R., Capote, R., Gheorghe, I., Gorbachenko, O., Jin, Y., Renstrøm, T., Sin, M., Stopani, K., Tian, Y., Tveten, G., Wang, J., Belgya, T., Firestone, R., Goriely, S., Kopecky, J., Krtička, M., Schwengner, R., Siem, S., Wiedeking, M., 2020. IAEA photonuclear data library 2019. Nucl. Data Sheets 163, 109–162. http://dx.doi.org/10.1016/j.nds.2019.12.002, URL https://www.sciencedirect.com/science/article/pii/S0090375219300699.

Knežević, D., Jovančević, N., Krmar, M., Petrović, J., 2016. Modeling of neutron spectrum in the gamma spectroscopy measurements with Ge-detectors. Nucl. Instrum. Methods Phys. Res. A 833, 23–26.

Koning, A., Delaroche, J., 2003. Local and global nucleon optical models from 1 keV to 200 MeV. Nuclear Phys. A 713 (3–4), 231–310.

Koning, A., Rochman, D., 2012. Modern nuclear data evaluation with the TALYS code system. Nucl. Data Sheets 113 (12), 2841–2934. http://dx.doi.org/10.1016/j.nds.2012.11.002, Special Issue on Nuclear Reaction Data. URL https://www.sciencedirect.com/science/article/pii/S0090375212000889.

Kopecky, J., Uhl, M., 1990. Test of gamma-ray strength functions in nuclear reaction model calculations. Phys. Rev. C 41 (5), 1941.

Kopecky, J., Uhl, M., Chrien, R., 1993. Radiative strength in the compound nucleus Gd 157. Phys. Rev. C 47 (1), 312.

Matzke, M., 1994. Report PTB-N-19. Phys.-Tech. Bundesanstalt, Braunschweig.

McElroy, W., Berg, S., Crockett, T., Hawkins, R., 1967. SAND-II, a computer-automated iterative method for neutron flux spectra determination by foil activation. In: Report AFWL-TR-67-41. US Air Force Weapons Laboratory.

Medic, Z., Jovancevic, N., Maletic, D., Teterev, Y., Mitrofanov, S., Belov, A., Krmar, M., Hult, M., Oberstedt, S., 2021. The application of the unfolding technique for determination of photo-nuclear reaction cross-section with an example on the ^{115}In(γ,γ')^{115m}In reaction. Eur. Phys. J. A 57 (8), 1–14.

Naik, H., Singh, S., Goswami, A., Manchanda, V.K., Kim, G., Kim, K.S., Lee, M.W., Rahman, M.S., Raj, D., Ganesan, S., et al., 2011. Measurement of photo-neutron cross-sections in ^{208}Pb and ^{209}Bi with 50–70 MeV bremsstrahlung. Nucl. Instrum. Methods Phys. Res. B 269 (12), 1417–1424.

Naik, H., Singh, S., Reddy, A., Manchanda, V., Ganesan, S., Raj, D., Rahman, S., Kim, K., Lee, M., Kim, G., et al., 2009. Measurement of photo-fission yields and photo-neutron cross-sections in ^{209}bi with 50 and 65 MeV Bremsstrahlung. Eur. Phys. J. A 41 (3), 323–330.

NNDC, 20.07.2023. https://www.nndc.bnl.gov/ensdf/.

Nozdrin, M., Gostkin, M., Kobets, V., Samofalova, Y., Shirkov, G., Trifonov, A., Yunenko, K., Zhemchugov, A., et al., 2021. Linac-200: A new electron test beam facility at JINR.

Otuka, N., Dupont, E., Semkova, V., Pritychenko, B., Blokhin, A., Aikawa, M., Babykina, S., Bossant, M., Chen, G., Dunaeva, S., Forrest, R., Fukahori, T., Furutachi, N., Ganesan, S., Ge, Z., Gritzay, O., Herman, M., Hlavač, B., Katō, K., Lalremruata, B., Lee, Y., Makinaga, A., Matsumoto, K., Mikhaylyukova, M., Pikulina, G., Pronyaev, V., Saxena, A., Schwerer, O., Simakov, S., Soppera, N., Suzuki, R., Takács, S., Tao, X., Taova, S., Tárkányi, F., Varlamov, V., Wang, J., Yang, S., Zerkin, V., Zhuang, Y., 2014. Towards a more complete and accurate experimental nuclear reaction data library (EXFOR): International collaboration between nuclear reaction data centres (NRDC). Nucl. Data Sheets 120, 272–276. http://dx.doi.org/10.1016/j.nds.2014.07.065, URL https://www.sciencedirect.com/science/article/pii/S0090375214005171.

Plujko, V., Kadenko, I., Gorbachenko, O., Kulich, E., 2008. The simplified description of dipole radiative strength function. Internat. J. Modern Phys. E 17 (01), 240–244.

Schiff, L., 1951. Energy-angle distribution of thin target Bremsstrahlung. Phys. Rev. 83 (2), 252.

Schwengner, R., Beyer, R., Dönau, F., Grosse, E., Hartmann, A., Junghans, A., Mallion, S., Rusev, G., Schilling, K., Schulze, W., et al., 2005. The photon-scattering facility at the superconducting electron accelerator ELBE. Nucl. Instrum. Methods Phys. Res. A 555 (1–2), 211–219.

Soppera, N., Bossant, M., Dupont, E., 2014. JANIS 4: An improved version of the NEA Java-based nuclear data information system. Nucl. Data Sheets 120, 294–296. http://dx.doi.org/10.1016/j.nds.2014.07.071, URL https://www.sciencedirect.com/science/article/pii/S0090375214005237.

Wood, W.M., 2018. Shot-by-shot spectrum model for rod-pinch, pulsed radiography machines. AIP Adv. 8 (2), 025105.

Zilges, A., Balabanski, D., Isaak, J., Pietralla, N., 2022. Photonuclear reactions—From basic research to applications. Prog. Part. Nucl. Phys. 122, 103903.

Zubov, A., Adamian, G., Antonenko, N., 2009. Application of statistical methods for analysis of heavy-ion reactions in the framework of a dinuclear system model. Phys. Part. Nuclei 40 (6), 847–889.

Article

Transverse emittance reduction in muon beams by ionization cooling

The MICE Collaboration*

Accelerated muon beams have been considered for the next-generation studies of high-energy lepton–antilepton collisions and neutrino oscillations. However, high-brightness muon beams have not yet been produced. The main challenge for muon acceleration and storage stems from the large phase-space volume occupied by the beam, derived from the production mechanism of muons through the decay of pions. The phase-space volume of the muon beam can be decreased through ionization cooling. Here we show that ionization cooling leads to a reduction in the transverse emittance of muon beams that traverse lithium hydride or liquid hydrogen absorbers in the Muon Ionization Cooling Experiment. Our results represent a substantial advance towards the realization of muon-based facilities that could operate at the energy and intensity frontiers.

Muon accelerators are considered to be potential enablers of fundamental particle physics studies at the energy and intensity frontiers. Such machines have great potential to provide multi-TeV lepton–antilepton collisions at a muon collider[1–3] or act as sources of intense neutrino beams with well-characterized fluxes and energy spectra at a neutrino factory[4–6].

The benefit of using muons in circular storage rings arises from their fundamental nature and their mass, which is 207 times that of electrons. As elementary particles, colliding muons offer the entire centre-of-mass energy to the production of short-distance reactions. This is an advantage over proton–proton colliders, such as the Large Hadron Collider[7], where each colliding proton constituent carries only a fraction of the proton energy. Compared with the electron, the larger muon mass leads to a dramatic reduction in synchrotron radiation losses, which scale as $1/m^4$. In addition, the spread in the effective centre-of-mass energy induced by beamstrahlung[8], the emission of radiation resulting from the interaction of a charged particle beam with the electric field produced by an incoming beam, is substantially lower for muons. Thus, a muon collider could achieve multi-TeV and precise centre-of-mass energies with a considerably smaller facility than an electron–positron collider such as the proposed electron–positron variant of the Future Circular Collider[9], the Circular Electron Positron Collider[10], the International Linear Collider[11] or the Compact Linear Collider[12].

The primary challenges in building a muon collider facility stem from the difficulty of producing intense muon bunches with a small phase-space volume, as well as the short muon lifetime (2.2 μs at rest). A proton-driver scheme is currently the most attractive option due to its potential to generate intense muon beams. An alternative, positron-driven muon source has been proposed and is under conceptual study[13]. In the proton-driver scheme, an intense proton beam impinges on a target to produce a secondary beam primarily composed of pions and kaons. The pions and kaons decay into muons to create a tertiary muon beam. The resulting muon beam occupies a large phase-space volume, which must be reduced (cooled) to allow efficient acceleration and sufficient flux and luminosity. The muon capture, cooling and acceleration must be executed on a timescale comparable with the muon lifetime.

Traditional cooling techniques such as stochastic cooling[14], electron cooling[15] or synchrotron radiation cooling[16] are impractical as the amount of time required to adequately cool the beam greatly exceeds the muon lifetime. Alternative muon cooling techniques are currently under development. A scheme developed at the Paul Scherrer Institute, whereby a surface muon beam is moderated to $\mathcal{O}(\text{eV})$ kinetic energies in cryogenic helium gas and has its beam spot decreased using strong electric and magnetic fields, has demonstrated promising phase-space compression[17]. Another demonstrated technology is the production of ultracold muons through resonant laser ionization of muonium atoms[18]. This technique for cooling positive muons has been proposed for an e⁻μ⁺ collider[19].

This paper describes the measurement of ionization cooling, the proposed technique by which the phase-space volume of the muon

*A list of authors and their affiliations appears at the end of the paper. ✉e-mail: paul.jurj13@imperial.ac.uk

beam can be sufficiently compressed before substantial decay losses occur[20,21]. Ionization cooling occurs when a muon beam passes through a material, known as the absorber, and loses both transverse and longitudinal momenta by ionizing atoms. The longitudinal momentum can be restored using radio-frequency accelerating cavities. The process can be repeated to achieve sufficient cooling within a suitable time frame[22].

The Muon Ionization Cooling Experiment (MICE; http://mice.iit.edu) was designed to provide the first demonstration of ionization cooling by measuring a reduction in the transverse emittance of the muon beam after the beam has passed through an absorber. A first analysis conducted by the MICE collaboration has demonstrated an unambiguous cooling signal by observing an increase in the phase-space density in the core of the beam on passage through an absorber[23]. Here we present the quantification of the ionization cooling signal by measuring the change in the beam's normalized transverse emittance, which is a central figure of merit in accelerator physics. A beam-sampling procedure is employed to improve the measurement of the cooling performance by selecting muon subsamples with optimal beam optics properties in the experimental apparatus. This beam sampling enables the probing of the cooling signal in beams with lower input emittances than those studied in the first MICE analysis[23] and facilitates a comparison between the measurement and theoretical model of ionization cooling.

Ionization cooling

The normalized root-mean-square (r.m.s.) emittance is a measure of the volume occupied by the beam in phase space. It is a commonly used quantity in accelerator physics that describes the spatial and dynamical extent of the beam, and it is a constant of motion under linear beam optics. This work focuses on the four-dimensional phase space transverse to the beam propagation axis. The MICE coordinate system is defined such that the beam travels along the z axis, and the state vector of a particle in the transverse phase space is given by $\mathbf{u} = (x, p_x, y, p_y)$. Here x and y are the position coordinates and p_x and p_y are the momentum coordinates. The normalized transverse r.m.s. emittance is defined as[24]

$$\varepsilon_\perp = \frac{1}{m_\mu c} |\mathbf{\Sigma}_\perp|^{\frac{1}{4}}, \tag{1}$$

where m_μ is the muon mass and $|\mathbf{\Sigma}_\perp|$ is the determinant of the beam covariance matrix. The covariance matrix elements are calculated as $\mathbf{\Sigma}_{\perp,ij} = \langle u_i u_j \rangle - \langle u_i \rangle \langle u_j \rangle$.

The impact of ionization cooling on a beam crossing an absorber is best described through the rate of change of the normalized transverse r.m.s. emittance, which is approximately equal to[21,25,26]

$$\frac{d\varepsilon_\perp}{dz} \simeq -\frac{\varepsilon_\perp}{\beta^2 E_\mu} \left| \frac{dE_\mu}{dz} \right| + \frac{\beta_\perp (13.6 \, \text{MeV} c^{-1})^2}{2\beta^3 E_\mu m_\mu X_0}, \tag{2}$$

where βc is the muon velocity, E_μ is the muon energy, $|dE_\mu/dz|$ is the average rate of energy loss per unit path length, X_0 is the radiation length of the absorber material and $\beta_\perp$ is the beam transverse betatron function at the absorber defined as $\beta_\perp = \frac{\langle x^2 \rangle + \langle y^2 \rangle}{2 m_\mu c \varepsilon_\perp} \langle p_z \rangle$. The emittance reduction (cooling) due to ionization energy loss is expressed through the first term. The second term represents emittance growth (heating) due to multiple Coulomb scattering by the atomic nuclei, which increases the angular spread of the beam. MICE recently measured scattering in lithium hydride (LiH) and observed good agreement with the GEANT4 model[27].

The cooling is influenced by both beam properties and absorber material. Heating is weaker for beams with lower transverse betatron function at the absorber. This can be achieved by using superconducting solenoids that provide strong symmetrical focusing in the

transverse plane. The absorber material affects both terms in the equation, and optimal cooling can be realized by using materials with a low atomic number for which the product $X_0|dE_\mu/dz|$ is maximized. The performance of a cooling cell can be characterized through equilibrium emittance, which is obtained by setting $d\varepsilon_\perp/dz = 0$ and is given by

$$\varepsilon_\perp^{\text{eqm}} \simeq \frac{\beta_\perp (13.6 \, \text{MeV} c^{-1})^2}{2\beta m_\mu X_0} \left| \frac{dE_\mu}{dz} \right|^{-1}. \tag{3}$$

Beams having emittances below equilibrium are heated, whereas those having emittances above are cooled.

Experimental apparatus

The main component of the experiment was the MICE channel, a magnetic lattice of 12 strong-focusing superconducting coils symmetrically placed upstream and downstream of the absorber module. The schematic of the MICE channel and instrumentation is shown in Fig. 1.

Muons were produced by protons from the ISIS synchrotron[28] impinging on a titanium target[29] and were delivered to the cooling channel via a transfer line[30,31]. Tuning the fields of two bending magnets in the transfer line enabled the selection of a beam with average momentum in the range of 140–240 MeV c^{-1}. A variable-thickness brass and tungsten diffuser mounted at the entrance of the channel allowed the generation of beams with input emittance in the range of 3–10 mm.

The superconducting coils were grouped in three modules: two identical spectrometer solenoids situated upstream and downstream of the focus-coil module that housed the absorber. Each spectrometer solenoid contained three coils that provided a uniform magnetic field of up to 4 T in the tracking region, and two coils used to match the beam into or out of the focus-coil module. The focus-coil module contained a pair of coils designed to tightly focus the beam at the absorber. The large angular divergence (small $\beta_\perp$) of the focused beam reduced the emittance growth caused by multiple scattering in the absorber and increased the cooling performance. The two focus coils could be operated with identical or opposing magnetic polarities. For this study, the focus coils and the spectrometer solenoids were powered with opposite-polarity currents, thereby producing a field that flipped polarity at the centre of the absorber. This magnetic-field configuration was used to prevent the growth of the beam canonical angular momentum. The field within the tracking regions was monitored using calibrated Hall probes. A soft-iron partial return yoke was installed around the magnetic lattice to contain the field.

Due to a magnet power lead failure during the commissioning phase, one of the matching coils in the downstream spectrometer solenoid was rendered inoperable. The built-in flexibility of the magnetic lattice allowed a compromise between the cooling performance and transmission that ensured the realization of an unambiguous ionization cooling signal.

As discussed above, absorber materials with low atomic numbers are preferred for ionization cooling lattices. Lithium hydride and liquid hydrogen (LH$_2$) were the materials of choice in MICE. The LiH absorber was a disc with a thickness of 65.37 ± 0.02 mm and a density of 0.6957 ± 0.0006 g cm^{-3} (all uncertainties represent the standard error)[23]. The lithium used to produce the absorber had an isotopic composition of 95.52% ^{6}Li and 4.48% ^{7}Li.

The liquid hydrogen was contained within a 22-litre aluminium vessel: a 300-mm-diameter cylinder with a pair of dome-shaped containment windows at its ends[32]. An additional pair of aluminium windows were mounted for safety purposes. The on-axis thickness of the LH$_2$ volume was 349.6 ± 0.2 mm. The density of LH$_2$ was measured to be 0.07053 ± 0.00008 g cm^{-3} at 20.51 K (ref. 33). The cumulative on-axis thickness of the aluminium windows was 0.79 ± 0.01 mm.

A comprehensive set of detectors were used to measure the particle species, position and momentum upstream and downstream of
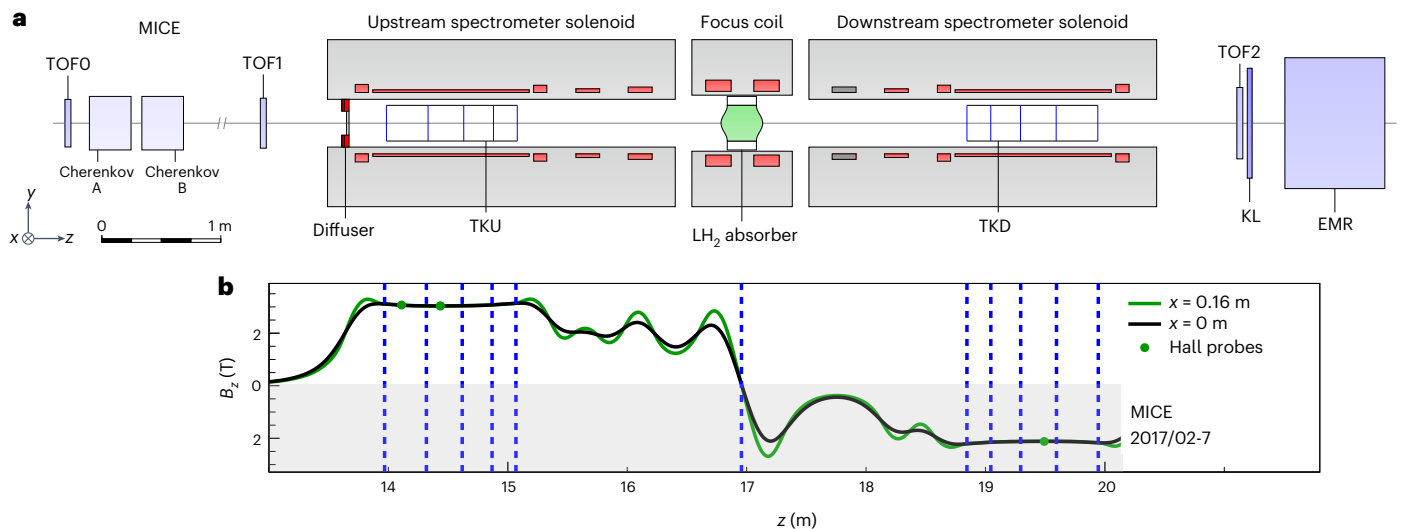
Fig. 1 | Schematic layout of the MICE experimental setup and the modelled magnetic field. a, Powered magnet coils are shown in red, absorber in green and detectors are individually labelled (see the main text for descriptions). TOF0, TOF1 and TOF2 are TOF hodoscopes; KL is a lead–scintillator pre-shower calorimeter; EMR is the electron–muon ranger. **b**, Modelled longitudinal magnetic field B_z is shown along the length of the MICE channel on axis (black line) and at 160 mm from the beam axis (green line) in the horizontal plane. The measurements of Hall probes situated at 160 mm from the axis are also shown (green circles). The vertical dashed lines indicate the positions of the tracker stations and the absorber.

the absorber[33,34]. The rate of muons delivered to the experiment was sufficiently low to allow the individual measurement of each incident particle. The data collected in cycles of several hours were aggregated offline and the phase space occupied by the beam before and after the absorber was reconstructed.

Upstream of the cooling channel, a velocity measurement provided by a pair of time-of-flight (TOF) detectors[35] was used for electron and pion rejection. A pair of threshold Cherenkov counters[36] were used to validate the TOF measurement. Downstream, a further TOF detector (TOF2)[37], a pre-shower sampling calorimeter and a fully active tracking calorimeter, namely, the electron–muon ranger[38,39], were employed to identify electrons from muon decays that occurred within the channel as well as to validate the particle measurement and identification by the upstream instrumentation. Particle position and momentum measurements upstream and downstream of the absorber were provided by two identical scintillating fibre trackers[40] immersed in the uniform magnetic fields of the spectrometer solenoids.

Each tracker (named TKU and TKD for upstream and downstream, respectively) consisted of five detector stations with a circular active area of 150 mm radius. Each station comprised three planes of 350-μm-diameter scintillating fibres, each rotated 120° with respect to its neighbour. In each station, the particle position was inferred from a coincidence of fibre signals. The particle momentum was reconstructed by fitting a helical trajectory to the reconstructed positions and accounting for multiple scattering and energy loss in the five stations[41]. For particles with a helix radius comparable with the spatial kick induced by multiple scattering, the momentum resolution was improved by combining the tracker momentum measurement with the velocity measurement provided by the upstream TOF detectors. The measurements recorded by the tracker reference planes, at the stations closest to the absorber, were used to estimate the beam emittance.

Observation of emittance reduction

The data studied here were collected using beams that passed through a lithium hydride or liquid hydrogen absorber. Scenarios with no absorber present or the empty LH_2 vessel were also studied for comparison. For each absorber setting, three beam-line configurations were used to deliver muon beams with nominal emittances of 4, 6 and

10 mm and a central momentum of approximately 140 MeV c^{-1} in the upstream tracker. For each beam-line/absorber configuration, the final sample contained particles that were identified as muons by the upstream TOF detectors and tracker and had one valid reconstructed trajectory in each tracker. The kinematic, fiducial and quality selection criteria for the reconstructed tracks are listed in Methods. A Monte Carlo simulation of the whole experiment was used to estimate the expected cooling performance and to study the performance of the individual detectors[42].

The beam matching into the channel slightly differed from the design beam optics due to inadequate focusing in the final section of the transfer line. This mismatch resulted in an oscillatory behaviour of the transverse betatron function in the TKU region and an increased, sub-optimal $\beta_\perp$ at the absorber, which degraded the cooling performance. An algorithm based on rejection sampling was developed to select beams with a constant betatron function in the TKU, in agreement with the design beam optics. The selection was performed on the beam ensemble measured in the TKU and was enabled by the unique MICE capability to measure the muon beams particle by particle. An example comparison between the betatron function of an unmatched parent beam and that of a matched subsample is shown in Fig. 2. The $\beta_\perp$ value of the subsample is approximately constant in the TKU, and consequently, its value at the absorber centre is ~28% smaller than the corresponding value of the parent beam.

The sampling algorithm enabled the selection of subsamples with specific emittances. This feature was exploited to study the dependence of the cooling effect on input emittance. For each absorber setting, each of the three parent beams were split into two distinct samples and six statistically independent beams with matched betatron functions ($\beta_\perp = 311$ mm, $d\beta_\perp/dz = 0$) and emittances of 1.5, 2.5, 3.5, 4.5, 5.5 and 6.5 mm at the TKU were sampled. The numbers of muons in each sample are listed in Extended Data Table 1. The two-dimensional projections of the phase space of the sampled beams on the transverse position and momentum planes are shown in Extended Data Figs. 1 and 2, respectively.

Figure 3 shows the emittance change induced by the lithium hydride and liquid hydrogen absorbers, as well as the corresponding empty cases, for each emittance subsample. The measurement uncertainty (Fig. 3, coloured bands) is dominated by systematic
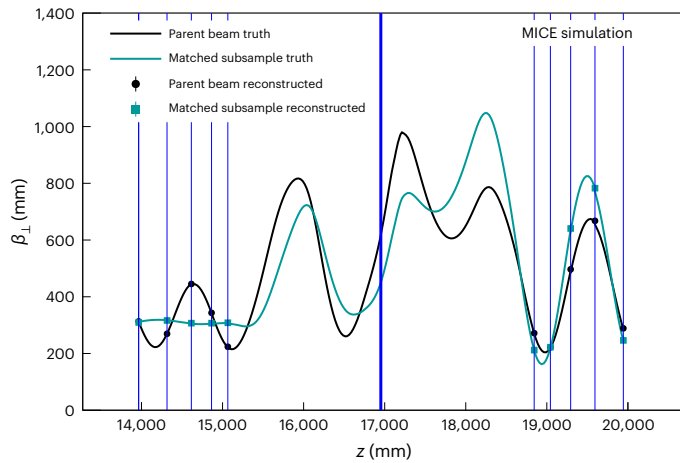
Fig. 2 | Simulated MICE muon beam betatron function. Evolution of the simulated transverse betatron function $\beta_\perp$ through the cooling channel containing the full LH_2 vessel for the parent beam (black) and matched subsample (dark cyan). The corresponding lines represent the simulation truth, whereas the circles and squares at the tracker stations (vertical blue lines) represent the reconstructed simulation. The thick vertical blue line marks the central position of the absorber. The error bars show the statistical standard error and are smaller than the markers for all the points.

uncertainties, which are listed in Extended Data Table 3 and described in detail in Methods. A correction was made to account for detector effects and for the inclusion only of events that reached the TKD. Good agreement between data and simulation is observed in all the configurations. The reconstructed data agree well with the model prediction. The model includes the heating effect in aluminium windows (Methods). The properties of the absorber and window materials used for the model calculation are listed in Extended Data Table 2.

The empty absorber cases show no cooling effects. In the empty channel case (No absorber), slight heating occurs due to optical aberrations and scattering in the aluminium windows of the two spectrometer solenoids. Additional heating caused by scattering in the windows of the LH_2 vessel is observed in the Empty LH_2 case. The LiH and Full LH_2 absorbers demonstrate emittance reduction for beams with emittances larger than ~2.5 mm. This is a clear signal of ionization cooling, a direct consequence of the presence of absorber material in the path of the beam.

For beams with 140 MeV c^{-1} momentum and $\beta_\perp = 450$ mm at the absorber centre, the theoretical equilibrium emittances of the MICE LiH and LH_2 absorbers, including the contributions from the corresponding set of aluminium windows, are ~2.5 mm in both cases. By performing a linear fit to the measured cooling trends (Fig. 3), the effective equilibrium emittances of the absorber modules are estimated to be 2.6 ± 0.4 mm for LiH and 2.4 ± 0.4 mm for LH_2. The parameters of the linear fits to the four emittance change trends are shown in Table 1. Our null hypothesis was that for each set of six input-beam settings, the slopes of the emittance change trends in the presence and absence of an absorber are compatible. A Student's t-test found that the probabilities of observing the effects measured here are lower than 10^{-5} for both the LiH–No absorber and Full LH_2–Empty LH_2 pairs; hence, the null hypotheses were rejected.

There is no significant improvement in cooling in this measurement when using liquid hydrogen compared with lithium hydride. Scattering in the absorber windows degraded the performance of LH_2 and rendered it similar to that of LiH. MICE was based on an early stage cooling-channel concept, requiring a large-bore absorber to accommodate the beam. In lower-emittance cooling systems with smaller-bore beam pipes, the relative window thickness may be reduced, leading to a better performance of hydrogen absorbers.

Towards a muon collider

The measurement reported here demonstrates the viability of this beam cooling technique as a means of producing low-emittance muon beams for a muon collider or a neutrino factory. The muon collider targets a transverse emittance of $\mathcal{O}(10^{-2}$ mm) and a longitudinal emittance of $\mathcal{O}(10^2$ mm). To achieve these targets, substantial longitudinal and transverse emittance reduction is required, which must be demonstrated. The muon beam must traverse multiple cooling cells that produce magnetic fields stronger than those achieved by MICE and which contain high-gradient radio-frequency cavities to restore the beam longitudinal momentum[22]. Design studies for a muon cooling demonstrator facility are currently in progress[43–45].

Our measurement is an important development towards the muon cooling demonstrator, a key intermediary step in the pursuit of a muon collider. The demonstration of ionization cooling by the MICE collaboration constitutes a substantial and encouraging breakthrough in the
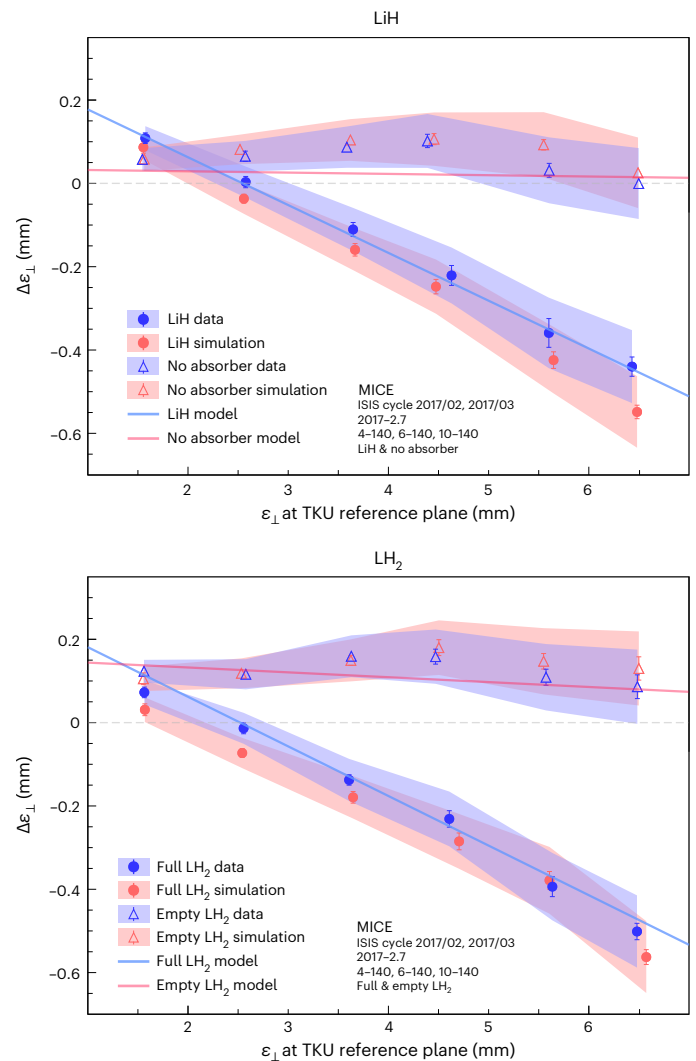

Fig. 3 | Transverse emittance change measured by MICE. Emittance change between the TKU and TKD reference planes, $\Delta\varepsilon_\perp$, as a function of emittance at TKU for 140 MeV c^{-1} beams crossing the LiH (top) and LH_2 (bottom) MICE absorbers. Results for the empty cases, namely, No absorber and Empty LH_2, are also shown. The measured effect is shown in blue, whereas the simulation is shown in red. The corresponding semitransparent bands represent the estimated total standard error. The error bars indicate the statistical error and for some of the points, they are smaller than the markers. The solid lines represent the approximate theoretical model defined by equation (10) (Methods) for the absorber (light blue) and empty (light pink) cases. The dashed grey horizontal lines indicate a scenario where no emittance change occurs.

Table 1 | Best-fit parameters of the measured emittance change trends

Absorber configuration	Intercept (mm)	Slope
No absorber	0.102±0.007	−0.011±0.012
LiH	0.297±0.006	−0.115±0.013
Empty LH$_2$	0.150±0.005	−0.006±0.013
Full LH$_2$	0.279±0.007	−0.118±0.013

Parameters of the linear fits performed on the measured emittance change trends corresponding to the four absorber configurations. Uncertainties represent the total standard error.

research and development efforts to deliver high-brightness muon beams suitable for high-intensity muon-based facilities.

Online content

Any methods, additional references, Nature Portfolio reporting summaries, source data, extended data, supplementary information, acknowledgements, peer review information; details of author contributions and competing interests; and statements of data and code availability are available at https://doi.org/10.1038/s41567-024-02547-4.

References

1. Neuffer, D. V. & Palmer, R. B. Progress toward a high-energy, high-luminosity µ⁺-µ⁻ collider. *AIP Conf. Proc.* **356**, 344–358 (1996).
2. Ankenbrandt, C. M. et al. Status of muon collider research and development and future plans. *Phys. Rev. ST Accel. Beams* **2**, 081001 (1999).
3. Palmer, R. Muon colliders. *Rev. Accel. Sci. Tech.* **7**, 137–159 (2014).
4. Geer, S. Neutrino beams from muon storage rings: characteristics and physics potential. *Phys. Rev. D* **57**, 6989–6997 (1998).
5. De Rújula, A., Gavela, M. & Hernández, P. Neutrino oscillation physics with a neutrino factory. *Nucl. Phys. B* **547**, 21–38 (1999).
6. Bogomilov, M. et al. Neutrino factory. *Phys. Rev. ST Accel. Beams* **17**, 121002 (2014).
7. Evans, L. The Large Hadron Collider. *New J. Phys.* **9**, 335 (2007).
8. Noble, R. J. Beamstrahlung from colliding electron-positron beams with negligible disruption. *Nucl. Instrum. Methods Phys. Res. A* **256**, 427–433 (1987).
9. Abada, A. et al. FCC-ee: the lepton collider. *Eur. Phys. J. Spec. Top.* **228**, 261–623 (2019).
10. CEPC Study Group et al. CEPC conceptual design report: volume 1—accelerator. Preprint at https://arxiv.org/abs/1809.00285 (2018).
11. Behnke, T. et al. The International Linear Collider technical design report—volume 1: executive summary. Preprint at https://arxiv.org/abs/1306.6327 (2013).
12. Charles, T. K. et al. The Compact Linear Collider (CLIC)—2018 summary report. Preprint at https://arxiv.org/abs/1812.06018 (2018).
13. Antonelli, M., Boscolo, M., Di Nardo, R. & Raimondi, P. Novel proposal for a low emittance muon beam using positron beam on target. *Nucl. Instrum. Methods Phys. Res. A* **807**, 101–107 (2016).
14. Möhl, D., Petrucci, G., Thorndahl, L. & Van Der Meer, S. Physics and technique of stochastic cooling. *Phys. Rep.* **58**, 73–102 (1980).
15. Parkhomchuk, V. V. & Skrinskii, A. N. Electron cooling: 35 years of development. *Phys. Uspekhi* **43**, 433–452 (2000).
16. Kolomenski, A. A. & Lebedev, A. N. The effect of radiation on the motion of relativistic electrons in a synchrotron. In *CERN Symposium on High Energy Accelerators and Pion Physics* 447–455 (CERN, 1956).
17. Antognini, A. et al. Demonstration of muon-beam transverse phase-space compression. *Phys. Rev. Lett.* **125**, 164802 (2020).
18. Bakule, P. et al. Slow muon experiment by laser resonant ionization method at RIKEN-RAL muon facility. *Spectrochim. Acta Part B* **58**, 1019–1030 (2003).
19. Hamada, Y., Kitano, R., Matsudo, R., Takaura, H. & Yoshida, M. µTRISTAN. *Prog. Theor. Exp. Phys.* **2022**, 053B02 (2022).
20. Skrinskii, A. N. & Parkhomchuk, V. V. Methods of cooling beams of charged particles. *Sov. J. Part. Nucl.* **12**, 223–247 (1981).
21. Neuffer, D. Principles and applications of muon cooling. *Part. Accel.* **14**, 75–90 (1983).
22. Stratakis, D. & Palmer, R. B. Rectilinear six-dimensional ionization cooling channel for a muon collider: a theoretical and numerical study. *Phys. Rev. ST Accel. Beams* **18**, 031003 (2015).
23. Bogomilov, M. et al. Demonstration of cooling by the muon ionization cooling experiment. *Nature* **578**, 53–59 (2020).
24. Wiedemann, H. *Particle Accelerator Physics* 4th edn (Springer Nature, 2015).
25. Penn, G. & Wurtele, J. S. Beam envelope equations for cooling of muons in solenoid fields. *Phys. Rev. Lett.* **85**, 764–767 (2000).
26. Jurj, P. B. *Normalised Transverse Emittance Reduction via Ionisation Cooling in MICE 'Flip Mode'*. PhD thesis, Imperial College London (2022).
27. Bogomilov, M. et al. Multiple Coulomb scattering of muons in lithium hydride. *Phys. Rev. D* **106**, 092003 (2022).
28. Thomason, J. The ISIS Spallation Neutron and Muon Source—the first thirty-three years. *Nucl. Instrum. Methods Phys. Res. A* **917**, 61–67 (2019).
29. Booth, C. N. et al. The design, construction and performance of the MICE target. *J. Instrum.* **8**, P03006 (2013).
30. Bogomilov, M. et al. The MICE muon beam on ISIS and the beam-line instrumentation of the Muon Ionization Cooling Experiment. *J. Instrum.* **7**, P05009 (2012).
31. Adams, D. et al. Pion contamination in the MICE muon beam. *J. Instrum.* **11**, P03001 (2016).
32. Bayliss, V. et al. The liquid-hydrogen absorber for MICE. *J. Instrum.* **13**, T09008 (2018).
33. Bogomilov, M. et al. Performance of the MICE diagnostic system. *J. Instrum.* **16**, P08046 (2021).
34. Bogomilov, M. et al. The MICE particle identification system. *Nucl. Phys. B* **215**, 316–318 (2011).
35. Bertoni, R. et al. The design and commissioning of the MICE upstream time-of-flight system. *Nucl. Instrum. Methods Phys. Res. A* **615**, 14–26 (2010).
36. Cremaldi, L., Sanders, D. A., Sonnek, P., Summers, D. J. & Reidy, J. A Cherenkov radiation detector with high density aerogels. *IEEE Trans. Nucl. Sci.* **56**, 1475–1478 (2009).
37. Bertoni, R. et al. *The Construction of the MICE TOF2 Detector* Tech. Report No. MICE-NOTE-DET-286 (MICE Collaboration, 2010).
38. Asfandiyarov, R. et al. A totally active scintillator calorimeter for the Muon Ionization Cooling Experiment (MICE). Design and construction. *Nucl. Instrum. Methods Phys. Res. A* **732**, 451–456 (2013).
39. Adams, D. et al. Electron-muon ranger: performance in the MICE muon beam. *J. Instrum.* **10**, P12012 (2015).
40. Ellis, M. et al. The design, construction and performance of the MICE scintillating fibre trackers. *Nucl. Instrum. Methods Phys. Res. A* **659**, 136–153 (2011).
41. Dobbs, A. et al. The reconstruction software for the MICE scintillating fibre trackers. *J. Instrum.* **11**, T12001 (2016).
42. Asfandiyarov, R. et al. MAUS: the MICE analysis user software. *J. Instrum.* **14**, T04005 (2019).
43. Rogers, C. A demonstrator for muon ionisation cooling. *Phys. Sci. Forum* **8**, 37 (2023).
44. Accettura, C. et al. Towards a muon collider. *Eur. Phys. J. C* **83**, 864 (2023).
45. The International Muon Collider Collaboration; https://muoncollider.web.cern.ch

The MICE Collaboration

M. Bogomilov[1], R. Tsenov[1], G. Vankova-Kirilova[1], Y. P. Song[2], J. Y. Tang[2], Z. H. Li[3], R. Bertoni[4], M. Bonesini[4], F. Chignoli[4], R. Mazza[4], A. de Bari[5], D. Orestano[6], L. Tortora[6], Y. Kuno[7], H. Sakamoto[7,33], A. Sato[7], S. Ishimoto[8], M. Chung[9], C. K. Sung[9], F. Filthaut[10,11], M. Fedorov[11], D. Jokovic[12], D. Maletic[12], M. Savic[12], N. Jovancevic[13], J. Nikolov[13], M. Vretenar[14], S. Ramberger[14], R. Asfandiyarov[15], A. Blondel[15], F. Drielsma[15,34], Y. Karadzhov[15], S. Boyd[16], J. R. Greis[16,35], T. Lord[16,36], C. Pidcott[16,37], I. Taylor[16,38], G. Charnley[17], N. Collomb[17], K. Dumbell[17], A. Gallagher[17], A. Grant[17], S. Griffiths[17], T. Hartnett[17], B. Martlew[17], A. Moss[17], A. Muir[17], I. Mullacrane[17], A. Oates[17], P. Owens[17], G. Stokes[17], P. Warburton[17], C. White[17], D. Adams[18], V. Bayliss[18], J. Boehm[18], T. W. Bradshaw[18], C. Brown[18,26], M. Courthold[18], J. Govans[18], T. Hayler[18], M. Hills[18], J. B. Lagrange[18], C. Macwaters[18], A. Nichols[18], R. Preece[18], S. Ricciardi[18], C. Rogers[18], T. Stanley[18], J. Tarrant[18], M. Tucker[18], S. Watson[18,39], A. Wilson[18], R. Bayes[19,40], J. C. Nugent[19], F. J. P. Soler[19], G. T. Chatzitheodoridis[19,20,21], A. J. Dick[20,21], K. Ronald[20,21], C. G. Whyte[20,21], A. R. Young[20,21], R. Gamet[22], P. Cooke[22], V. J. Blackmore[23], D. Colling[23], A. Dobbs[23,41], P. Dornan[23], P. Franchini[23,42], C. Hunt[23], P. B. Jurj[23✉], A. Kurup[23], K. Long[23], J. Martyniak[23], S. Middleton[23,43], J. Pasternak[23], M. A. Uchida[23,44], J. H. Cobb[24], C. N. Booth[25], P. Hodgson[25], J. Langlands[25], E. Overton[25,45], V. Pec[25], P. J. Smith[25], S. Wilbur[25], M. Ellis[26,46], R. B. S. Gardener[26], P. Kyberd[26], J. J. Nebrensky[26,47], A. DeMello[27], S. Gourlay[27], A. Lambert[27], D. Li[27], T. Luo[27], S. Prestemon[27], S. Virostek[27], M. Palmer[28], H. Witte[28], D. Adey[29,48], A. D. Bross[29], D. Bowring[29], A. Liu[29,49], D. Neuffer[29], M. Popovic[29], P. Rubinov[29], B. Freemire[30,49], P. Hanlet[30,50], D. M. Kaplan[30], T. A. Mohayai[30,51], D. Rajaram[30,52], P. Snopok[30], Y. Torun[30], L. M. Cremaldi[31], D. A. Sanders[31], L. R. Coney[32,53], G. G. Hanson[32] & C. Heidt[32,54]

[1]Department of Atomic Physics, St Kliment Ohridski University of Sofia, Sofia, Bulgaria. [2]Institute of High Energy Physics, Chinese Academy of Sciences, Beijing, China. [3]Sichuan University, Chengdu, China. [4]Sezione INFN Milano Bicocca, Dipartimento di Fisica G. Occhialini, Milano, Italy. [5]Sezione INFN Pavia and Dipartimento di Fisica, Università di Pavia, Pavia, Italy. [6]INFN Sezione di Roma Tre and Dipartimento di Matematica e Fisica, Università Roma Tre, Roma, Italy. [7]Department of Physics, Graduate School of Science, Osaka University, Toyonaka, Japan. [8]High Energy Accelerator Research Organization (KEK), Institute of Particle and Nuclear Studies, Tsukuba, Japan. [9]Pohang University of Science & Technology, Pohang, Korea. [10]Nikhef, Amsterdam, The Netherlands. [11]Radboud University, Nijmegen, The Netherlands. [12]Institute of Physics, University of Belgrade, Belgrade, Serbia. [13]Faculty of Sciences, University of Novi Sad, Novi Sad, Serbia. [14]CERN, Geneva, Switzerland. [15]DNPC, Section de Physique, Université de Genève, Geneva, Switzerland. [16]Department of Physics, University of Warwick, Coventry, UK. [17]STFC Daresbury Laboratory, Daresbury, UK. [18]STFC Rutherford Appleton Laboratory, Harwell Oxford, Didcot, UK. [19]School of Physics and Astronomy, University of Glasgow, Glasgow, UK. [20]SUPA and the Department of Physics, University of Strathclyde, Glasgow, UK. [21]Cockcroft Institute, Daresbury Laboratory, Daresbury, UK. [22]Department of Physics, University of Liverpool, Liverpool, UK. [23]Department of Physics, Blackett Laboratory, Imperial College London, London, UK. [24]Department of Physics, University of Oxford, Oxford, UK. [25]Department of Physics and Astronomy, University of Sheffield, Sheffield, UK. [26]College of Engineering, Design and Physical Sciences, Brunel University, Uxbridge, UK. [27]Lawrence Berkeley National Laboratory, Berkeley, CA, USA. [28]Brookhaven National Laboratory, Upton, NY, USA. [29]Fermilab, Batavia, IL, USA. [30]Illinois Institute of Technology, Chicago, IL, USA. [31]University of Mississippi, Oxford, MS, USA. [32]University of California, Riverside, CA, USA. [33]Present address: RIKEN 2-1 Horosawa, Wako, Japan. [34]Present address: SLAC National Accelerator Laboratory, Menlo Park, CA, USA. [35]Present address: TNG Technology Consulting, Unterföhring, Germany. [36]Present address: Dimensional Fund Advisors, London, UK. [37]Present address: Department of Physics and Astronomy, University of Sheffield, Sheffield, UK. [38]Present address: Defence Science and Technology Laboratory, Salisbury, UK. [39]Present address: ATC, Royal Observatory Edinburgh, Edinburgh, UK. [40]Present address: Laurentian University, Sudbury, Ontario, Canada. [41]Present address: OPERA Simulation Software, Kidlington, UK. [42]Present address: Department of Physics, Royal Holloway, University of London, Egham, UK. [43]Present address: The Division of Physics, Mathematics and Astronomy, Caltech, Pasadena, CA, USA. [44]Present address: Rutherford Building, Cavendish Laboratory, University of Cambridge, Cambridge, UK. [45]Present address: Arm, Sheffield, UK. [46]Present address: Macquarie Group, Sydney, New South Wales, Australia. [47]Present address: United Kingdom Atomic Energy Authority (UKAEA), Culham Science Centre, Abingdon, UK. [48]Present address: Institute of High Energy Physics, Chinese Academy of Sciences, Beijing, China. [49]Present address: Euclid Techlabs, Bolingbrook, IL, USA. [50]Present address: Fermilab, Batavia, IL, USA. [51]Present address: Department of Physics, Indiana University Bloomington, Bloomington, IN, USA. [52]Present address: KLA, Ann Arbor, MI, USA. [53]Present address: European Spallation Source ERIC, Lund, Sweden. [54]Present address: Swish Analytics, Oakland, CA, USA. ✉e-mail: paul.jurj13@imperial.ac.uk

Methods

Event reconstruction

Each TOF hodoscope was composed of two planes of scintillator slabs oriented along the x and y directions. Photomultiplier tubes (PMTs) at both ends of each slab were used to collect and amplify the signal produced by a charged particle traversing the slab. A coincidence of signals from the PMTs of a slab was recorded as a slab hit. A pair of orthogonal slab hits formed a space point. The information collected by the four corresponding PMTs was used to reconstruct the position and the time at which the particle passed through the detector. A detailed description of the TOF time calibration is provided elsewhere[46]. The MICE data acquisition system readout was triggered by a coincidence of signals from the PMTs of a single slab of the TOF1 detector. All the data collected by the detector system after each TOF1 trigger were aggregated, forming a particle event.

For each tracker, signals from the scintillating fibres in the five stations were combined to reconstruct the helical trajectories of the traversing charged particles. The quality of each fitted track was indicated by the χ^2 per degree of freedom as

$$\chi^2_{\text{dof}} = \frac{1}{n-5} \sum_{i=1}^{n} \frac{\delta x_i^2}{\sigma_i^2}, \qquad (4)$$

where n is the number of tracker planes that contributed to the reconstruction, δx_i is the distance between the measured position in the ith tracker plane and the fitted track and σ_i is the position measurement resolution in the tracker planes. A more detailed description of the reconstruction procedure and its performance can be found in other MICE work[33,41].

Sample selection

The measurements taken by the detector system were used to select the final sample. The following selection criteria ensured that a pure muon beam, with a narrow momentum spread, and fully transmitted through the channel, was selected for analysis:

- One reconstructed space point found in TOF0 and TOF1, and one reconstructed track found in TKU and TKD
- Time-of-flight between TOF0 and TOF1 consistent with that of a muon
- Momentum measured in TKU consistent with that of a muon, given the TOF0–TOF1 time-of-flight
- In each tracker, a reconstructed track contained within the cylindrical fiducial volume defined by a radius of 150 mm and with $\chi^2_{\text{dof}} < 8$
- Momentum measured in TKU in the 135–145 MeV c^{-1} range
- Momentum measured in TKD in the 120–170 MeV c^{-1} range for the empty absorber configurations and 90–170 MeV c^{-1} range for the LiH and LH$_2$ absorbers
- At the diffuser, a track radial excursion contained within the diffuser aperture radius by at least 10 mm

The same set of selection criteria was applied to the simulated beams.

Beam sampling

The sampling procedure developed to obtain beams matched to the upstream tracker is based on a rejection sampling algorithm[47,48]. It was designed to carve out a beam subsample that followed a four-dimensional Gaussian distribution described by a specific (target) covariance matrix from an input-beam ensemble (parent).

The custom algorithm required an estimate of the probability density function underlying the beam ensemble. Since the MICE beams were only approximately Gaussian and approximately cylindrically symmetric, the kernel density estimation technique was used to evaluate the parent-beam density in a non-parametric fashion[49,50]. In the kernel density estimation, each data point is assigned a smooth weight

function, also known as the kernel, and the contributions from all the data points in the dataset are summed. The multivariate kernel density estimator at an arbitrary point $\mathbf{u}$ in d-dimensional space is given by

$$\hat{f}(\mathbf{u}) = \frac{1}{nh^d} \sum_{i=1}^{n} K\left(\frac{\mathbf{u} - \mathbf{u}_i}{h}\right), \qquad (5)$$

where K is the kernel, n is the sample size, h is the width of the kernel and $\mathbf{u}_i$ represents the coordinate of the ith data point in the sample. In this analysis, Gaussian kernels of the following form were used:

$$K\left(\frac{\mathbf{u} - \mathbf{u}_i}{h}\right) = \frac{1}{\sqrt{(2\pi)^d |\mathbf{\Sigma}_\perp|}} \exp\left[-\frac{1}{2} \frac{(\mathbf{u} - \mathbf{u}_i)^\mathsf{T} \mathbf{\Sigma}_\perp^{-1} (\mathbf{u} - \mathbf{u}_i)}{h^2}\right], \qquad (6)$$

where $\mathbf{\Sigma}_\perp$ is the covariance matrix of the dataset. The width of the kernel is chosen to minimize the mean integrated squared error, which measures the accuracy of the estimator[51]. Scott's rule of thumb was followed in this work, where the kernel width was determined from the sample size n and the number of dimensions d through $h = n^{-1/(d+4)}$ (ref. 50).

The kernel density estimation form described in equations (5) and (6) was used to estimate the transverse phase-space density of the initial, unmatched beams, with the estimated underlying density denoted by Parent($\mathbf{u}$). The target distribution Target($\mathbf{u}$) is a four-dimensional Gaussian defined by a covariance matrix parameterized through the transverse emittance ($\varepsilon_\perp$), transverse betatron function ($\beta_\perp$), mean longitudinal momentum and mean kinetic angular momentum[25].

The sampling was performed on the beam ensemble measured at the TKU station closest to the absorber. For each particle in the parent beam, with four-dimensional phase-space vector $\mathbf{u}_i$, the sampling algorithm worked as follows:

1. Compute the selection probability as

$$P_{\text{select}}(\mathbf{u}_i) = \mathcal{C} \times \frac{\text{Target}(\mathbf{u}_i)}{\text{Parent}(\mathbf{u}_i)}, \qquad (7)$$

where the normalization constant $\mathcal{C}$ ensures that the selection probability $P_{\text{select}}(\mathbf{u}_i) \leq 1$;
2. Generate a number ξ_i from the uniform distribution $\mathcal{U}([0,1])$;
3. If $P_{\text{select}}(\mathbf{u}_i) > \xi_i$, then accept the particle. Otherwise, reject it.

The normalization constant $\mathcal{C}$ was calculated before the sampling iteration presented in steps 1–3 above. It required an iteration through the parent ensemble (of size n) and it was calculated as

$$\mathcal{C} = \min_{i \in \{1,\dots,n\}} \frac{\text{Parent}(\mathbf{u}_i)}{\text{Target}(\mathbf{u}_i)}. \qquad (8)$$

The target parameters of interest were $\varepsilon_\perp$, $\beta_\perp$ and $\alpha_\perp = -\frac{1}{2}\mathrm{d}\beta_\perp/\mathrm{d}z$. For beams with central momentum of 140 MeV c^{-1} and a solenoidal magnetic field of 3 T, the matching conditions in the TKU were $(\beta_\perp, \alpha_\perp) = (311\,\text{mm}, 0)$. The target mean kinetic angular momentum was kept at the value measured in the parent beam for which the sampling efficiency was at a maximum.

Emittance change calculation and model

The emittance change measured by the pair of MICE scintillating fibre trackers is defined as

$$\Delta\varepsilon_\perp = \varepsilon_\perp^{\text{d}} - \varepsilon_\perp^{\text{u}}, \qquad (9)$$

where $\varepsilon_\perp^{\text{d}}$ is the emittance measured in the downstream tracker and $\varepsilon_\perp^{\text{u}}$ is the emittance measured in the upstream tracker. In each tracker, the measurement is performed at the station closest to the absorber.

Starting from the cooling equation shown in equation (2), the emittance change induced by an absorber material of thickness z can be expressed as a function of the input emittance $\varepsilon_\perp^u$ as follows:

$$\Delta\varepsilon_\perp(\varepsilon_\perp^u) \approx (\varepsilon_\perp^{eqm} - \varepsilon_\perp^u)\left[1 - \exp\left(-\frac{|dE_\mu/dz|}{\beta^2 E_\mu}z\right)\right], \qquad (10)$$

where $\varepsilon_\perp^{eqm}$ is the equilibrium emittance and the mean energy loss rate $|dE_\mu/dz|$ is described by the Bethe–Bloch formula[52].

The expected emittance change depends on the type and amount of material that the beam traverses between the two measurement locations. Aside from the absorber material under study and absorber-module windows, the beam crossed an additional pair of aluminium windows, one downstream of TKU and the other upstream of TKD. All the windows were made from Al 6061-T651 alloy. Equation (10) was used to estimate the theoretical cooling performance, including the effect of aluminium windows. The properties of the absorber and window materials required for the calculation are shown in Extended Data Table 2. For each absorber configuration, the beam properties required for the model ($\beta, \beta_\perp, E_\mu$) were obtained from the simulation of the 3.5 mm beam.

Systematic uncertainties

The emittance change measurement assumes a specific arrangement of detector and magnetic fields. As this arrangement is known with limited accuracy, it is a source of systematic uncertainty in the $\Delta\varepsilon_\perp$ measurement. To assess this uncertainty, the experimental geometry was parameterized and these parameters were varied one by one in the simulation of the experiment. For each parameter considered, the resulting shift in the simulated emittance change was assigned as its associated systematic uncertainty. The following contributions to the systematic uncertainty were considered in this analysis.

Uncertainties in the tracker alignment affect the reconstructed beam phase space. A tracker displacement along an axis perpendicular to the beam line by ±3 mm and a tracker rotation about an axis perpendicular to the beam line by ±3 mrad were investigated. These variations are conservative estimates determined from the MICE tracker alignment surveys. The cylindrical symmetry of the tracker measurement was validated by performing translations and rotations along and about different axes perpendicular to the beam line.

A significant systematic uncertainty arises due to the limited knowledge of the magnetic-field strength in the tracking region, which directly impacts the momentum measurement. The three coils that produced the magnetic field in the tracking region were labelled as End 1, Centre and End 2, with the End 1 coil closest to the absorber. The effect associated with the uncertainty in the magnetic field was studied by varying the Centre coil current by ±1% and the currents in the End coils by ±5%. A conservative approach was taken when investigating the End coils, as the effect of the soft-iron partial return yoke was not included in the magnetic-field model used for track reconstruction.

The amount of energy loss and multiple scattering in each tracker station depends on the materials used. A variation of ±50% in the density of the glue used to fix the scintillating fibres was investigated. This alteration was used to account for uncertainty in the amount of silica beads added to the glue mixture.

All the sources of uncertainty presented so far were studied in both spectrometer solenoids. Additionally, as the TOF01 time measurement was used to assist the momentum reconstruction of muons with low transverse momentum, a variation corresponding to the 60 ps uncertainty on the TOF measurement was studied. The uncertainties associated with the individual parameter alterations are shown in Extended Data Table 3, for beams with input emittances in the [1.5, 2.5...6.5] mm range. For each input emittance, the total systematic uncertainty was obtained by adding all the individual contributions in quadrature.

References

46. Karadzhov, Y., Bonesini, M., Graulich, J. S. & Tzenov, R. *TOF Detectors Time Calibration* Tech. Report No. 251 (2009).
47. von Neumann, J. Various techniques used in connection with random digits. *J. Res. Natl Bureau Stand. Appl. Math. Series* **12**, 36–38 (1951).
48. Wells, M. T., Casella, G. & Robert, C. P. Generalized accept-reject sampling schemes. *Lect. Notes Monogr. Series* **45**, 342–348 (2004).
49. Silverman, B. W. *Density Estimation for Statistics and Data Analysis* 1st edn (Routledge, 1998).
50. Scott, D. W. *Multivariate Density Estimation: Theory, Practice, and Visualization* (John Wiley & Sons, 2015).
51. Marron, J. S. & Wand, M. P. Exact mean integrated squared error. *Ann. Stat.* **20**, 712–736 (1992).
52. Leroy, C. & Rancoita, P. G. *Principles of Radiation Interaction in Matter and Detection* (World Scientific, 2011).
53. Bogomilov, M. et al. MICE raw data. *figshare* https://doi.org/10.17633/rd.brunel.3179644.v1 (2016).
54. Bogomilov, M. et al. MICE reconstructed data. *figshare* https://doi.org/10.17633/rd.brunel.5955850.v1 (2018).
55. Bogomilov, M. et al. Source code of MAUS—the MICE analysis user software. *figshare* https://doi.org/10.17633/rd.brunel.8337542.v2 (2019).
56. Zyla, P. A. et al. Review of particle physics. *Progr. Theor. Exp. Phys.* **2020**, 083C01 (2020).

Author contributions

All authors contributed considerably to the design or construction of the apparatus or to the data taking or analysis described in this Article.

Extended Data Fig. 1 | Beam transverse profiles in the (top) upstream and (bottom) downstream trackers (TKU and TKD). Measured transverse beam profiles for each absorber configuration (rows) and input emittance (columns). In each histogram, the number of events in each bin is normalized to the number of events contained by the bin with most entries. The beams that pass through an absorber present a smaller transverse size in the downstream tracker than the beams that traverse an empty absorber module. This effect is caused by a change in focusing due to energy loss.
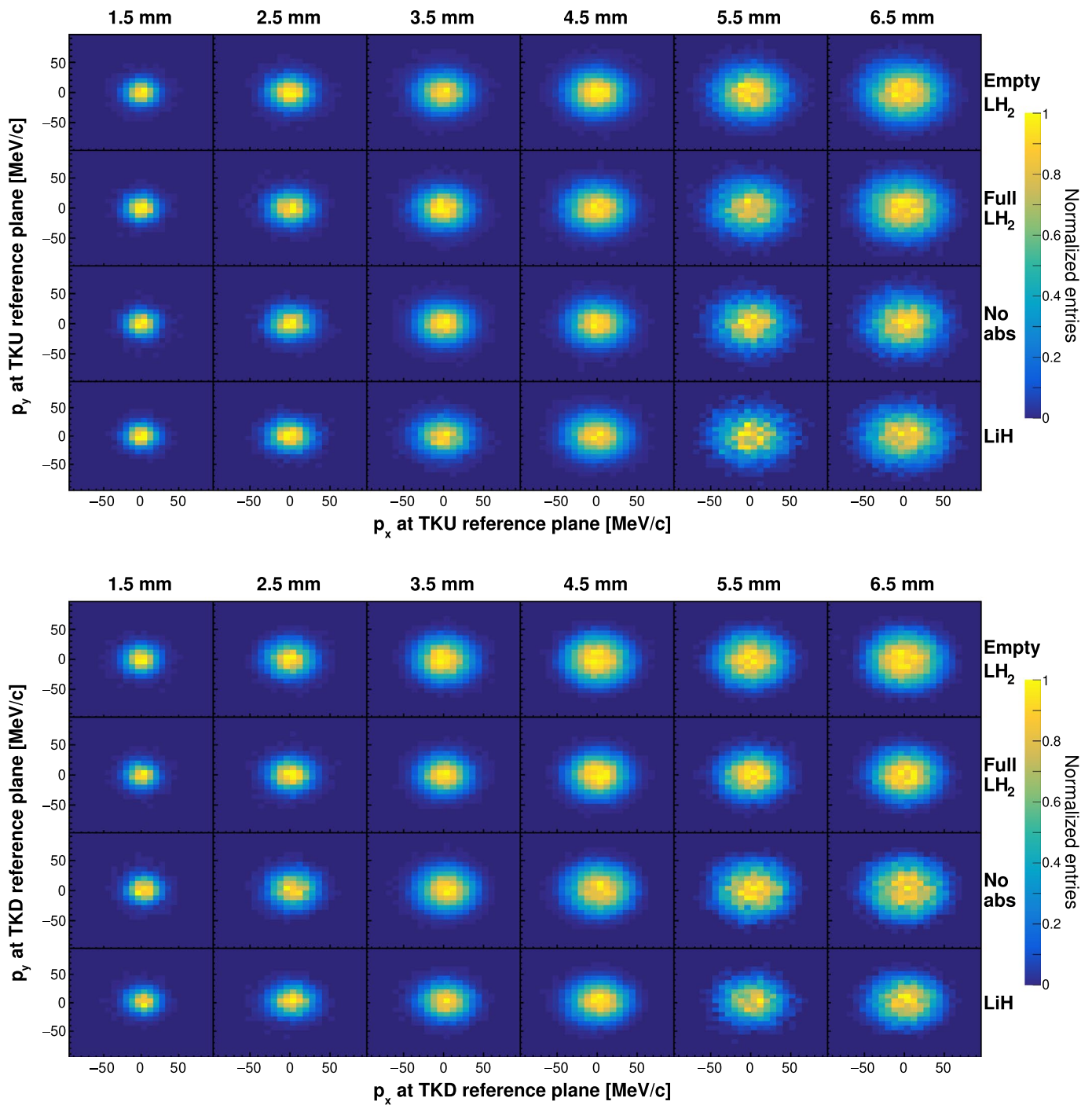
Extended Data Fig. 2 | Beam transverse momentum in the (top) upstream and (bottom) downstream trackers (TKU and TKD). Measured x and y components of the beam transverse momentum, p_x and p_y, for each absorber configuration (rows) and input emittance (columns). In each histogram, the number of events in each bin is normalized to the number of events contained by the bin with most entries. The beams that pass through an absorber present a smaller transverse momentum in the downstream tracker than the beams that traverse an empty absorber module.

Extended Data Table 1 | The sample size of the MICE matched beams

Absorber \\ Input $\varepsilon_\perp$ [mm]	1.5	2.5	3.5	4.5	5.5	6.5
Empty LH_2	8141	10162	19525	29896	13196	22080
Full LH_2	5199	8541	16757	20836	9063	15326
No absorber	4496	4792	32836	17659	5324	8573
LiH	4549	4372	9150	21071	3927	7618

The number of muons in each final sample is listed for each absorber configuration and target input transverse emittance $\varepsilon_\perp$.

Extended Data Table 2 | Material properties of the MICE absorbers and aluminium alloy windows

Material \ Property	MICE LiH	Liquid H_2	Al 6061-T651
Density, ρ [g/cm^3]	0.6957	0.07053	2.727
$\langle Z/A \rangle$	0.56716	0.99212	0.48145
I [eV]	36.5	21.8	166
X_0 [cm]	102.04	866	8.68

Z and A are the atomic and mass numbers of the material, respectively, I is the mean excitation energy of the atoms in the material, and X_0 is the radiation length of the material[56].

Extended Data Table 3 | Systematic uncertainties affecting the measurement of emittance change $\Delta\varepsilon_\perp$

Input $\varepsilon_\perp$ [mm] / Parameter alteration	Systematic uncertainty [mm]					
	1.5	2.5	3.5	4.5	5.5	6.5
TKU translation	0.003	0.002	0.001	0.005	0.003	0.002
TKU rotation	0.003	0.003	0.002	0.005	< 0.001	0.003
TKU glue density	0.003	0.001	0.003	0.003	0.004	0.002
Upstream End 1 coil current	0.009	0.011	0.016	0.018	0.024	0.023
Upstream Centre coil current	0.018	0.021	0.028	0.034	0.042	0.050
Upstream End 2 coil current	0.007	0.006	0.006	0.005	0.010	0.015
TKD translation	0.003	0.003	0.001	0.001	0.004	< 0.001
TKD rotation	0.001	0.002	0.001	0.005	< 0.001	0.001
TKD glue density	0.005	< 0.001	0.001	0.004	0.003	0.002
Downstream End 1 coil current	0.003	0.010	0.014	0.018	0.024	0.027
Downstream Centre coil current	0.013	0.021	0.032	0.044	0.053	0.054
Downstream End 2 coil current	0.001	0.005	0.009	0.007	0.008	0.012
TOF01 time	0.001	< 0.001	0.004	0.006	0.007	0.007
Total systematic uncertainty	0.026	0.035	0.048	0.063	0.077	0.084

The systematic uncertainties associated with parameter alterations in the upstream tracker (TKU), downstream tracker (TKD), upstream and downstream coils, and time-of-flight measurement (TOF01) are listed for each input transverse emittance $\varepsilon_\perp$.

Article

Demonstration of cooling by the Muon Ionization Cooling Experiment

MICE collaboration*

The use of accelerated beams of electrons, protons or ions has furthered the development of nearly every scientific discipline. However, high-energy muon beams of equivalent quality have not yet been delivered. Muon beams can be created through the decay of pions produced by the interaction of a proton beam with a target. Such 'tertiary' beams have much lower brightness than those created by accelerating electrons, protons or ions. High-brightness muon beams comparable to those produced by state-of-the-art electron, proton and ion accelerators could facilitate the study of lepton–antilepton collisions at extremely high energies and provide well characterized neutrino beams[1–6]. Such muon beams could be realized using ionization cooling, which has been proposed to increase muon-beam brightness[7,8]. Here we report the realization of ionization cooling, which was confirmed by the observation of an increased number of low-amplitude muons after passage of the muon beam through an absorber, as well as an increase in the corresponding phase-space density. The simulated performance of the ionization cooling system is consistent with the measured data, validating designs of the ionization cooling channel in which the cooling process is repeated to produce a substantial cooling effect[9–11]. The results presented here are an important step towards achieving the muon-beam quality required to search for phenomena at energy scales beyond the reach of the Large Hadron Collider at a facility of equivalent or reduced footprint[6].

High-quality muon beams

Fundamental insights into the structure of matter and the nature of its elementary constituents have been obtained using beams of charged particles. The use of time-varying electromagnetic fields to produce sustained acceleration was pioneered in the 1930s[12–14]. Since then, high-energy and high-brightness particle accelerators have delivered electron, proton and ion beams for applications ranging from the search for new phenomena in the interactions of quarks and leptons to the study of nuclear physics, materials science and biology.

Muon beams can be created using a proton beam striking a target to produce a secondary beam comprising many particle species including pions, kaons and muons. The pions and kaons decay to produce additional muons, which are captured by electromagnetic beamline elements to produce a tertiary muon beam. Capture must be realized on a timescale compatible with the muon lifetime at rest, 2.2 μs. Without acceleration, the energy and intensity of the muon beam is limited by the energy and intensity of the primary proton beam and the efficiency with which muons are captured.

Accelerated high-brightness muon beams have been proposed as a source of neutrinos at neutrino factories and for the delivery of multi-TeV lepton–antilepton collisions at muon colliders[1–6]. Muons have attractive properties for the delivery of high-energy collisions. The muon is a fundamental particle with mass 207 times that of the electron. This high mass results in suppression of synchrotron radiation, potentially enabling collisions between beams of muons and antimuons at energies far in excess of those that can be achieved in an electron–positron collider, such as the proposed International Linear Collider[15], the Compact Linear Collider[16], the Circular Electron–Positron Collider[17] and the electron–positron option of the Future Circular Collider[18]. The virtual absence of synchrotron radiation makes it possible to build a substantially smaller facility with the same or greater physics reach.

The energy available in collisions between the constituent gluons and quarks in proton–proton collisions is considerably less than the energy of the proton beam because the colliding quarks and gluons each carry only a fraction of the proton's momentum. Muons carry the full energy of the beam, making muon colliders attractive for the study of particle physics beyond the energy reach of facilities such as the Large Hadron Collider[19].

Most of the proposals for accelerated muon beams exploit the proton-driven muon-beam production scheme outlined above and use beam cooling to increase the brightness of the tertiary muon beam before acceleration and storage to ensure sufficient luminosity or beam current. Four cooling techniques are in use at particle accelerators: synchrotron radiation cooling[20], laser cooling[21], stochastic cooling[22] and electron cooling[23]. In each case, the time required to cool the beam is long compared to the muon lifetime. Frictional cooling of muons, in which muons are electrostatically accelerated through an energy-absorbing medium at energies significantly below 1 MeV, has been demonstrated but with low efficiency[24–26].

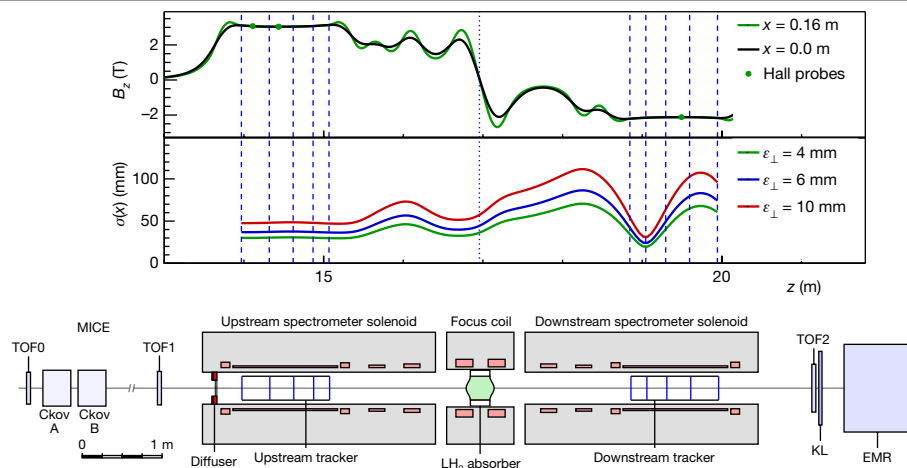*A list of participants and their affiliations appears at the end of the paper.

Article

Fig. 1 | The MICE apparatus, the calculated magnetic field and the nominal horizontal width of the beam. The modelled field, B_z, is shown on the beam axis (black line) and at 160 mm from the axis (green line) in the horizontal plane. The readings of Hall probes situated at 160 mm from the beam axis are also shown. Vertical lines indicate the positions of the tracker stations (dashed lines) and the absorber (dotted line). The nominal r.m.s. beam width, $\sigma(x)$, is calculated assuming a nominal input beam and using linear beam transport equations. See text for the description of the MICE apparatus. TOF0, TOF1 and TOF2 are time-of-flight detector stations; KL is a lead–scintillator pre-shower detector; EMR is the Electron–Muon Ranger.

The technique demonstrated in this study, ionization cooling[7,8], is based on a suitably prepared beam passing through an appropriate material (the absorber) and losing momentum through ionization. Radio-frequency cavities restore momentum only along the beam direction. Passing the muon beam through a repeating lattice of material and accelerators causes the ionization cooling effect to build up in a time much shorter than the muon lifetime[9–11]. Acceleration of a muon beam in a radio-frequency accelerator has recently been demonstrated[27], and reduced beam heating, damped by the ionization cooling effect, has been observed[28]. Ionization cooling has not been demonstrated so far. Experimental validation of the technique is important for the development of muon accelerators. The international Muon Ionization Cooling Experiment (MICE; http://mice.iit.edu) was designed to demonstrate transverse ionization cooling, the realization of which is presented here.

The brightness of a particle beam can be characterized by the number of particles in the beam and the volume occupied by the beam in position–momentum phase space. The phase-space volume occupied by the beam and the phase-space density of the beam are conserved quantities in a conventional accelerator without cooling. The phase space considered here is the position and momentum transverse to the direction of travel of the beam, $\mathbf{u} = (x, p_x, y, p_y)$, where x and y are coordinates perpendicular to the beam line, and p_x and p_y are the corresponding components of the momentum. The z axis is the nominal beam axis.

The normalized root-mean-square (r.m.s.) emittance is conventionally used as an indicator of the phase-space volume occupied by the beam[29], but this quantity is not conserved when scraping or optical aberrations affect the edge of the beam. The distribution of amplitudes[30,31] is used here to study effects in the core of the beam. The amplitude of a particle is the distance of the particle from the beam centroid in normalized phase space, and is a conserved quantity in a conventional accelerator without cooling. The phase-space density of the beam is also directly studied using a k-nearest-neighbour technique[32].

MICE cooling apparatus

The MICE collaboration has built a tightly focusing solenoid lattice, absorbers and instrumentation to demonstrate the ionization cooling of muons. A schematic of the apparatus is shown in Fig. 1.

A transfer line[33–35] brought a beam, composed mostly of muons, from a target[36] in the ISIS synchrotron[37] to the cooling apparatus. The central momentum of the muons could be tuned between 140 MeV c^{-1} and 240 MeV c^{-1} (c, speed of light in vacuum). A variable-thickness brass and tungsten diffuser allowed the emittance of the incident beam to be varied between 4 mm and 10 mm.

The tight focusing (low β function) and large acceptance required by the cooling section was achieved using 12 superconducting solenoids. The solenoids were contained in three warm-bore modules cooled by closed-cycle cryocoolers. The upstream and downstream modules (spectrometer solenoids) were identical, each containing three coils to provide a uniform field region of up to 4 T within the 400-mm-diameter warm bore for momentum measurement, as well as two 'matching' coils to match the beam to the central pair of closely spaced 'focus' coils, which focus the beam onto the absorber. The focus coils were designed to enable peak on-axis fields of up to 3.5 T within one module with a 500-mm-diameter warm bore containing the absorbers.

For the experiment reported here the focus coils were operated in 'flip' mode with a field reversal at the centre. Because the magnetic lattice was tightly coupled, the cold mass-suspension systems of the modules were designed to withstand longitudinal cold-to-warm forces of several hundred kN, which could arise during an unbalanced quench of the system. At maximum field, the inter-coil force on the focus coil cold mass was of the order of 2 MN. The total energy stored in the magnetic system was of the order of 5 MJ and the system was protected by both active and passive quench-protection systems. The normal charging and discharging time of the solenoids was several hours. The entire magnetic channel was partially enclosed by a 150-mm-thick soft-iron return yoke for external magnetic shielding. The magnetic fields in the tracking volumes were monitored during operation using calibrated Hall probes.

One of the matching coils in the downstream spectrometer solenoid was not operable owing to a failure of a superconducting lead. Although this necessitated a compromise in the lattice optics and acceptance, the flexibility of the magnetic lattice was exploited to ensure a clear cooling measurement.

The amplitude acceptance of approximately 30 mm, above which particles scrape, was large compared to that of a typical accelerator. Even so, considerable scraping was expected and observed for the highest-emittance beams. Ionization cooling cells with even larger acceptances, producing less scraping, have been designed[9–11].
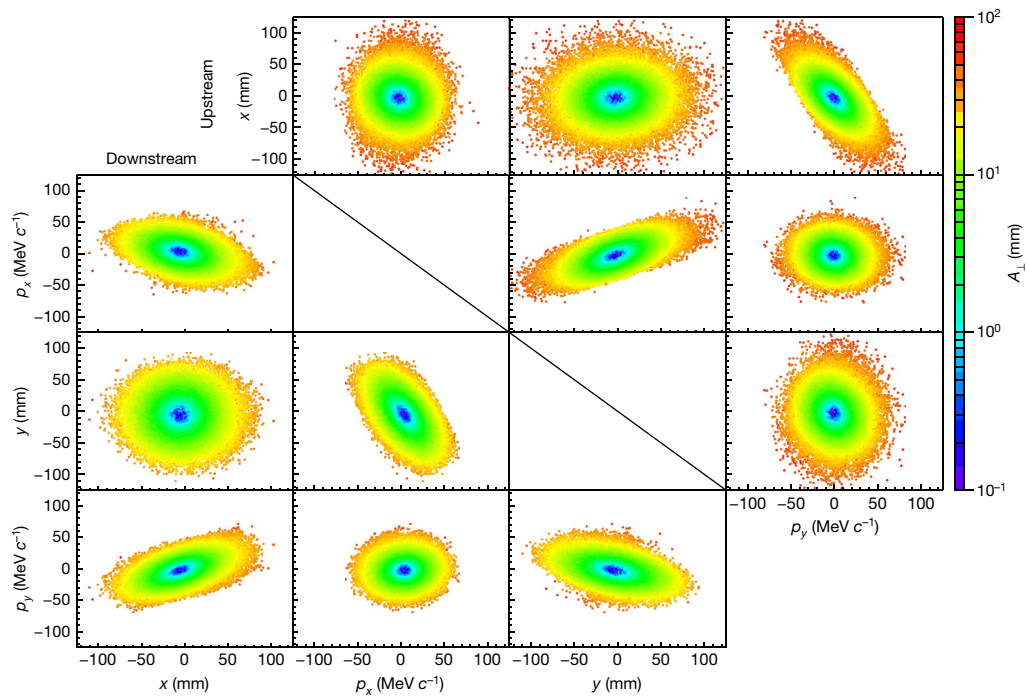
Fig. 2 | Beam distribution in phase space for the 6–140 Full LH2 setting of MICE. Measured beam distribution in the upstream tracker (above the diagonal) and in the downstream tracker (below the diagonal). The measured coordinates of the particles are coloured according to the amplitude $A_\perp$ of the particle.

The magnetic lattice of MICE, shown in Fig. 1, was tuned so that the focus of the beam was near the absorber, resulting in a small beam width and large angular divergence. The tight focusing, corresponding to a nominal transverse β function of around 430 mm at the centre of the absorber, yielded an optimal cooling performance.

Materials with low atomic number, such as lithium and hydrogen, have a long radiation length relative to the rate of energy loss, and consequently better cooling performance, making them ideal absorber materials. Therefore, cooling by both liquid-hydrogen and lithium hydride absorbers was studied.

The liquid hydrogen was contained within a 22-l vessel[38] in the warm bore of the focus coil. Hydrogen was liquefied by a cryocooler and piped through the focus coil module into the absorber body. When filled, the absorber presented 349.6 ± 0.2 mm of liquid hydrogen along the beam axis with a density of 0.07053 ± 0.00008 g cm^{-3} (all uncertainties represent the standard error). The liquid hydrogen was contained between a pair of aluminium windows covered by multi-layer insulation. A second pair of windows provided a secondary barrier to protect against failure of the primary containment windows. These windows were designed to be as thin as possible so that any scattering in them would not cause substantial heating. The total thickness of all four windows on the beam axis was 0.79 ± 0.01 mm.

The lithium hydride absorber was a disk of thickness 65.37 ± 0.02 mm with a density of 0.6957 ± 0.0006 g cm^{-3}. The isotopic composition of the lithium used to produce the absorber was 95% ^{6}Li and 5% ^{7}Li. The cylinder had a thin coating of parylene to prevent ingress of water or oxygen. Configurations with the empty liquid-hydrogen containment vessel and with no absorber were also studied.

MICE beam instrumentation

Detectors placed upstream and downstream of the apparatus measured the momentum, position and species of each particle entering and leaving the cooling channel in order to reconstruct the full four-dimensional phase space, including the angular momentum introduced by the solenoids. Particles were recorded by the apparatus one at a time, which enabled high-precision instrumentation to be used and particles other than muons to be excluded from the analysis. Each ensemble of muons was accumulated over a number of hours. This is acceptable because space-charge effects are not expected at a neutrino factory and in a muon collider they become important only at very low longitudinal emittance[39]. Data-taking periods for each absorber were separated by a period of weeks owing to operational practicalities. The phase-space distribution of the resulting ensemble was reconstructed using the upstream and downstream detectors. The emittance reconstruction in the upstream detector system is described in ref. [40].

Upstream of the cooling apparatus, two time-of-flight (TOF) detectors[41] measured the particle velocity. A complementary velocity measurement was made upstream by the threshold Cherenkov counters Ckov A and Ckov B[42]. Scintillating fibre trackers, positioned in the uniform-field region of each of the two spectrometer solenoids, measured the particle position and momentum upstream and downstream of the absorber[43,44]. Downstream, an additional TOF detector[45], a mixed lead–scintillator pre-shower detector and a totally active scintillator calorimeter, the Electron–Muon Ranger[46,47], identified electrons produced by muon decay and allowed cross-validation of the measurements made by the upstream detectors and the trackers.

Each tracker consisted of five planar scintillating-fibre stations. Each station comprised three views; each view was composed of two layers of 350-μm-diameter scintillating fibres positioned at an angle of 120° with respect to the other views. The fibres were read out by cryogenic visible-light photon counters[48]. The position of a particle crossing the tracker was inferred from the coincidence of signals from the fibres, and the momentum was calculated by fitting a helical trajectory to the signal positions, with appropriate consideration for energy loss and scattering in the fibres.

Each TOF detector was constructed from two orthogonal planes of scintillator slabs. Photomultiplier tubes at each end of every TOF detector slab were used to determine the time at which a muon passed through the apparatus with a 60-ps resolution[41]. The momentum resolution of particles with a small helix radius in the tracker was improved
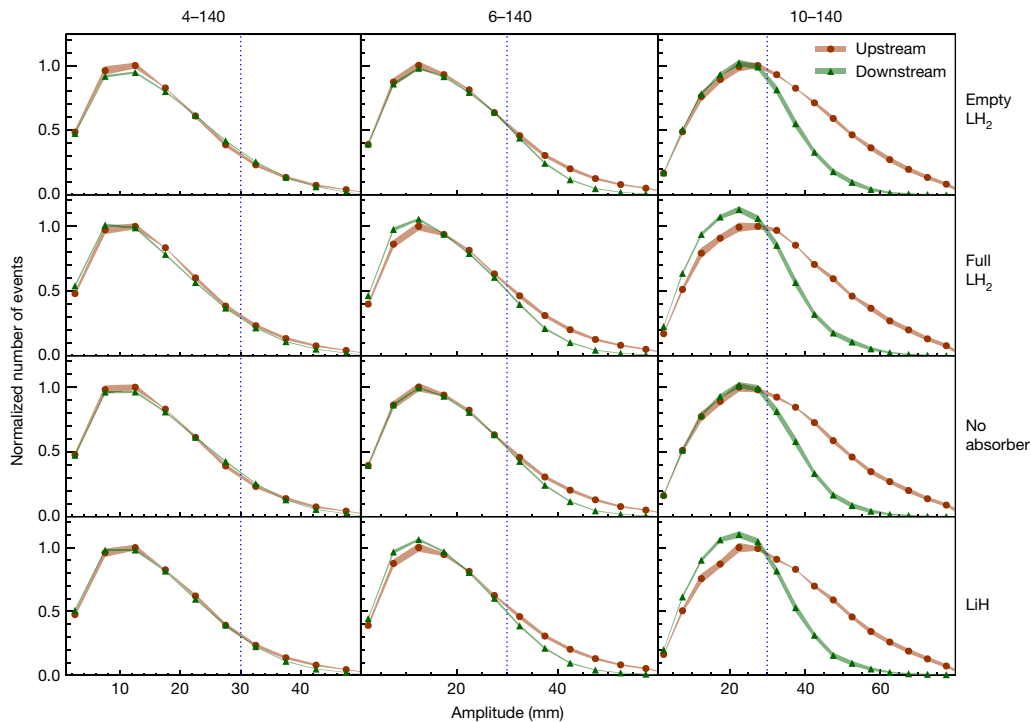
Fig. 3 | Muon amplitudes measured by MICE. The measured upstream distributions are shown by red circles while the downstream distributions are shown by green triangles. Both upstream and downstream distributions are normalized to the bin with the most entries in the upstream distribution (see text). Coloured bands show the estimated standard error, which is dominated by systematic uncertainties. Vertical lines indicate the approximate channel acceptance above which scraping occurs. The number of events in each sample is listed in Extended Data Table 2. Data for each experimental configuration were accumulated in a single discrete period.

by combining the TOF measurement of velocity with the measurement of momentum in the tracker.

A detailed Monte Carlo simulation of the experiment was performed to study the resolution and efficiency of the instrumentation and to determine the expected performance of the cooling apparatus[49,50]. The simulation was found to give a good description of the data[40].

Demonstration of cooling

The data presented here were taken using beams with a nominal momentum of 140 MeV c^{-1} and a nominal normalized r.m.s. emittance in the upstream tracking volume of 4 mm, 6 mm and 10 mm; these settings are denoted as '4–140', '6–140' and '10–140', respectively. Beams with a higher emittance have more muons at high amplitudes and occupy a larger region in phase space. For each beam setting, two samples were considered for the analysis. The 'upstream sample' contained particles identified as muons by the upstream TOF detectors and tracker, for which the muon trajectory reconstructed in the upstream tracker was fully contained in the fiducial volume and for which the reconstructed momentum fell within the range 135 MeV c^{-1} to 145 MeV c^{-1} (which is considerably higher than the momentum resolution of the tracker, 2 MeV c^{-1}). The 'downstream sample' was the subset of the upstream sample for which the reconstructed muons were fully contained in the fiducial volume of the downstream tracker. Each of the samples had between 30,000 and 170,000 events. Examples of the phase-space distributions of the particles in the two samples are shown in Fig. 2. The strong correlations between y and p_x and between x and p_y are due to the angular momentum introduced by the solenoidal field. The shorter tails along the semi-minor axis compared to the semi-major axis in these projections arise from scraping in the diffuser.

The distributions of amplitudes in the upstream and downstream samples for each of the 4–140, 6–140 and 10–140 datasets are shown in Fig. 3. The nominal acceptance of the magnetic channel is also indicated. A correction has been made to account for the migration of events between amplitude bins due to the detector resolution and to account for inefficiency in the downstream detector system (see Methods). Distributions are shown for the measurements with an empty liquid-hydrogen vessel ('Empty LH$_2$'), with a filled liquid-hydrogen vessel ('Full LH$_2$'), with no absorber ('No absorber') and with the lithium hydride absorber ('LiH'). The distributions were normalized to allow a comparison of the shape of the distribution between different absorbers. Each pair of upstream and downstream amplitude distributions is scaled by $1/N^u_{max}$, where N^u_{max} is the number of events in the most populated bin in the upstream sample.

The behaviour of the beam at low amplitude is the key result of this study. For the 'No absorber' and 'Empty LH$_2$' configurations, the number of events with low amplitude in the downstream sample is similar to that observed in the upstream sample. For the 6–140 and 10–140 configurations for both the 'Full LH$_2$' and the 'LiH' samples, the number of events with low amplitude is considerably larger in the downstream sample than in the upstream sample. This indicates an increase in the number of particles in the beam core when an absorber is installed, which is expected if ionization cooling takes place. This effect can occur only because energy loss is a non-conservative process.

A reduction in the number of muons at high amplitude is also observed, especially for the 10–140 setting. Whereas part of this effect arises owing to migration of muons into the beam core, a substantial number of high-amplitude particles outside the beam acceptance intersected the beam pipe or fell outside the fiducial volume of the downstream tracker. The beam pipe was made of materials with higher atomic number than those of the absorber materials, so interactions in the beam pipe tended to be dominated by multiple Coulomb scattering, leading to beam loss.

A χ^2 test was performed to determine the confidence with which the null hypothesis that for the same input beam setting, the amplitude distributions in the downstream samples of the 'Full LH$_2$' and 'Empty LH$_2$'
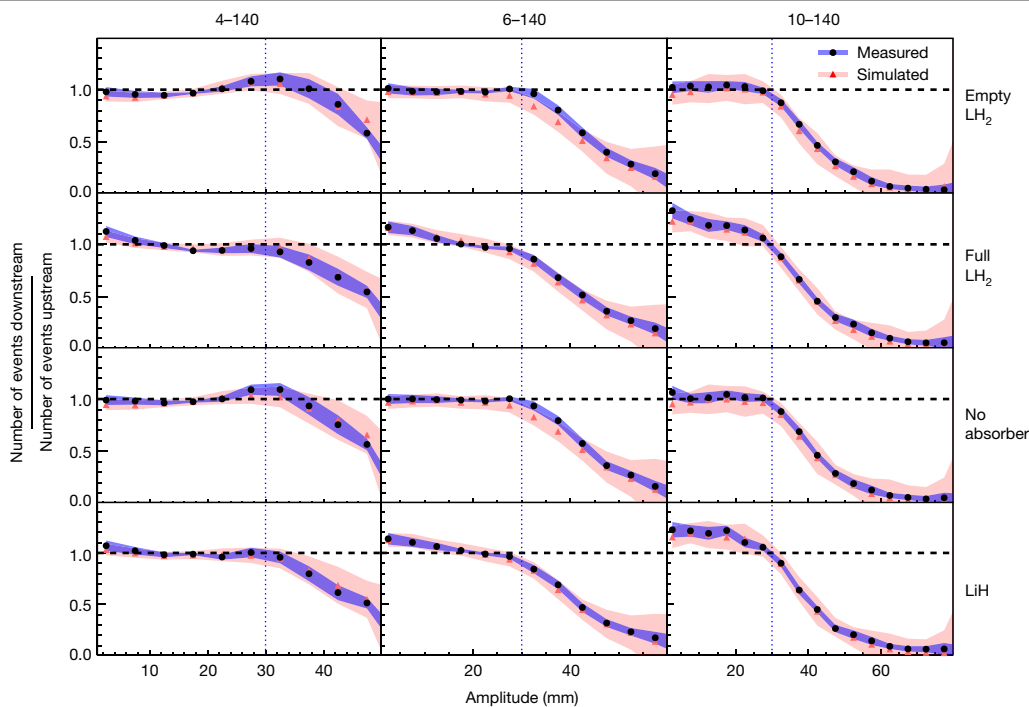
Fig. 4 | Downstream-to-upstream ratio of number of events in MICE. A ratio greater than unity in the beam core, which is evidence of ionization cooling, is observed in the data obtained with the 6–140 and 10–140 beams with both the full LH$_2$ absorber and the LiH absorber. The effect predicted from the simulation is shown in red and that measured is shown in black. The corresponding shading shows the estimated standard error, which is dominated by systematic uncertainty. Vertical lines indicate the channel acceptance above which scraping occurs. The number of events in each sample is listed in Extended Data Table 2. Data for each experimental configuration were accumulated in a single discrete period.

configurations are compatible, and the amplitude distributions in the downstream samples of the 'LiH' and 'No absorber' configurations are compatible. The test was performed on the uncorrected distributions using only statistical uncertainties. Systematic effects are the same for the pairs of distributions tested, and cancel. Assuming that this null hypothesis is correct, the probability of observing the effect seen in the data is considerably lower than 10^{-5} for each beam setting and for each 'Full LH$_2$'–'Empty LH$_2$' and 'LiH'–'No absorber' pair; therefore, the null hypothesis was rejected.

The fractional increase in the number of particles with low amplitude is most pronounced for the 10–140 beams. High-amplitude beams have high transverse emittance, $\varepsilon_\perp$, and a larger transverse momentum relative to the stochastic increase in transverse momentum due to scattering, so they undergo more cooling. For the magnet settings and beams studied here, heating due to multiple Coulomb scattering becomes dominant over ionization cooling at an emittance of around 4 mm. As a result, only modest cooling is observed for the 4–140 setting in both the 'Full LH$_2$' and 'LiH' configurations.

The ratios of the downstream to the upstream amplitude distributions are shown in Fig. 4. In the 'No absorber' and 'Empty absorber' configurations, the ratios are consistent with 1 for amplitudes of less than 30 mm, confirming the conservation of amplitude in this region, irrespective of the incident beam. Above 30 mm the ratios drop below unity, indicating that at high amplitude there are fewer muons downstream than upstream, as outlined above. The presence of the absorber windows does not strongly affect the amplitude distribution. For the 6–140 and 10–140 datasets, the addition of liquid-hydrogen or lithium hydride absorber material causes the ratios to rise above unity for the low-amplitude particles that correspond to the beam core. This indicates an increase in the number of particles in the beam core and demonstrates ionization cooling.

The density in phase space is an invariant of a symplectic system; therefore, an increase in phase-space density is also an unequivocal demonstration of cooling. Figure 5 shows the normalized density of the upstream and downstream samples, $\rho_i(\mathbf{u}_i)/\rho_0$, as a function of α, the fraction of the upstream sample that has a density greater than or equal to ρ_i. This is known as the quantile distribution. To enable comparison between different beam configurations, the densities for each configuration have been normalized to the peak density in the upstream tracker, ρ_0. To enable comparison between the upstream and downstream distributions, the fraction of the sample is always relative to the total number of events in the upstream sample. The transmission is the fraction of the beam for which the density in the downstream tracker reaches zero. For the 'No absorber' and 'Empty LH$_2$' cases, the downstream density in the highest-density regions is indistinguishable from the upstream density. A small amount of scraping is observed for the 4–140 and 6–140 beams. More substantial scraping is observed for the 10–140 beam. In all cases, for 'Full LH$_2$' and 'LiH' the phase-space density increases, and the increase is greater for higher-emittance beams. These observations demonstrate the ionization cooling of the beam when an absorber is installed. In the presence of an absorber, beams with larger nominal emittance show a greater increase in density than those with a lower nominal emittance.

Conclusions

Ionization cooling has been unequivocally demonstrated. We have built and operated a section of a solenoidal cooling channel and demonstrated the ionization cooling of muons using both liquid hydrogen and lithium hydride absorbers. The effect has been observed through the measurement of both an increase in the number of small-amplitude particles (Figs. 3, 4) and an increase in the phase-space density of the beam (Fig. 5). The results are well described by simulations (Fig. 4). This demonstration of ionization cooling is an important advance in the development of high-brightness muon beams. The seminal results presented in this paper encourage further development of high-brightness
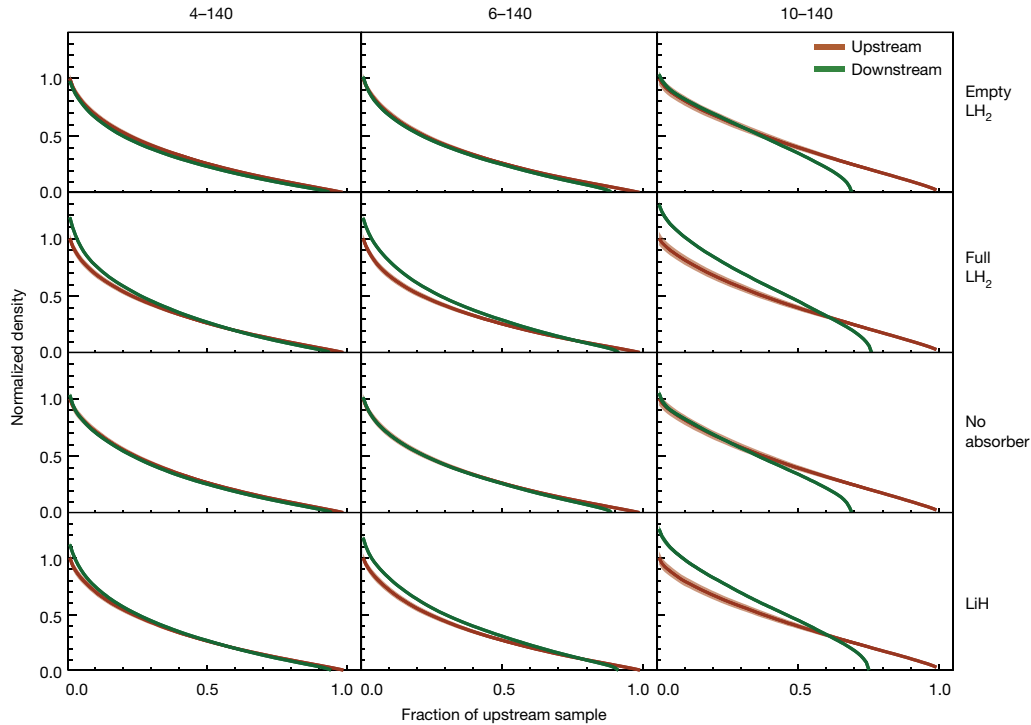
Fig. 5 | Normalized quantile distribution of the beam density in MICE.
Upstream and downstream quantiles are indicated by orange and green lines, respectively, as a function of the fraction of the upstream sample. For each configuration, the density is normalized to the highest-density region in the upstream sample. The estimated standard error is indicated by the thickness of the coloured bands and is dominated by systematic uncertainty. The number of events in each sample is listed in Extended Data Table 2. Data for each experimental configuration were accumulated in a single discrete period.

muon beams as a tool for the investigation of the fundamental properties of matter.

Online content

Any methods, additional references, Nature Research reporting summaries, source data, extended data, supplementary information, acknowledgements, peer review information; details of author contributions and competing interests; and statements of data and code availability are available at https://doi.org/10.1038/s41586-020-1958-9.

1. Neuffer, D. V. & Palmer, R. B. A high-energy high-luminosity μ^+–μ^- collider. *AIP Conf. Proc.* **356** 344–358 (1996).
2. Geer, S. Neutrino beams from muon storage rings: characteristics and physics potential. *Phys. Rev. D* **57**, 6989–6997 (1998).
3. Alsharo'a, M. M. et al. Recent progress in neutrino factory and muon collider research within the Muon Collaboration. *Phys. Rev. Accel. Beams* **6**, 081001 (2003).
4. Palmer, R. B. Muon colliders. *Rev. Accel. Sci. Tech.* **7**, 137–159 (2014).
5. Boscolo, M. et al. Low emittance muon accelerator studies with production from positrons on target. *Phys. Rev. Accel. Beams* **21**, 061005 (2018).
6. Neuffer, D. & Shiltsev, V. On the feasibility of a pulsed 14 TeV c.m.e. muon collider in the LHC tunnel. *J. Instrum.* **13** T10003 (2018).
7. Skrinsky, A. N. & Parkhomchuk, V. V. Cooling methods for beams of charged particles. *Sov. J. Part. Nucl.* **12**, 223–247 (1981).
8. Neuffer, D. Principles and applications of muon cooling. *Part. Accel.* **14**, 75–90 (1983).
9. Rogers, C. T. et al. Muon front end for the neutrino factory. *Phys. Rev. Accel. Beams* **16**, 040104 (2013).
10. Stratakis, D. & Palmer, R. B. Rectilinear six-dimensional ionization cooling channel for a muon collider: a theoretical and numerical study. *Phys. Rev. Accel. Beams* **18**, 031003 (2015).
11. Neuffer, D. et al. Final cooling for a high-energy high-luminosity lepton collider. *J. Instrum.* **12**, T07003 (2017).
12. Lawrence, E. O. & Livingston, M. S. The production of high speed protons without the use of high voltages. *Phys. Rev.* **38**, 834 (1931).
13. Lewis, G. N., Livingston, M. S. & Lawrence, E. O. The emission of alpha-particles from various targets bombarded by deutons of high speed. *Phys. Rev.* **44**, 55–56 (1933).
14. R. Wideröe. Das Betatron. *Z. Angew. Phys.* **5**, 187–200 (1953).
15. Behnke, T. et al. *The International Linear Collider Technical Design Report – Volume 1: Executive Summary* (ILC, 2013).
16. Burrows, P. N. et al. (eds) *The Compact Linear Collider (CLIC): 2018 Summary Report* (CERN, 2018).
17. CEPC Study Group. *CEPC Conceptual Design Report: Volume 1 – Accelerator*. (IHEP, 2018).
18. Abada, A. et al. FCC-ee: the lepton collider. *Eur. Phys. J. Spec. Top.* **228**, 261–623 (2019).
19. Myers, S. The Large Hadron Collider 2008–2013. *Int. J. Mod. Phys. A* **28**, 1330035 (2013).
20. Lee, S. Y. *Accelerator Physics* 3rd edn (World Scientific, 2012).
21. Schröder, S. et al. First laser cooling of relativistic ions in a storage ring. *Phys. Rev. Lett.* **64**, 2901–2904 (1990).
22. Möhl, D., Petrucci, G., Thorndahl, L., & van der Meer, S. Physics and technique of stochastic cooling. *Phys. Rep.* **58**, 73–119 (1980).
23. Parkhomchuk, V. V. & Skrinsky, A. N. Electron cooling: 35 years of development. *Phys. Uspekhi* **43**, 433–452 (2000).
24. Mühlbauer, M. et al. Frictional cooling: experimental results. *Hyperfine Interact.* **119**, 305–310 (1999).
25. Abramowicz, H. et al. A muon collider scheme based on frictional cooling. *Nucl. Instrum. Methods Phys. Res. A* **546**, 356–375 (2005).
26. Taqqu, D. Compression and extraction of stopped muons. *Phys. Rev. Lett.* **97**, 194801 (2006).
27. Bae, S. et al. First muon acceleration using a radio frequency accelerator. *Phys. Rev. Accel. Beams* **21**, 050101 (2018).
28. Mori, Y. et al. Neutron source with emittance recovery internal target. In *Proc. of the 23rd Particle Accelerator Conference* (JACoW, 2009); http://accelconf.web.cern.ch/AccelConf/PAC2009/papers/th4gac04.pdf.
29. Penn, G. & Wurtele, J. S. Beam envelope equations for cooling of muons in solenoid fields. *Phys. Rev. Lett.* **85**, 764–767 (2000).
30. Holzer, E. B. Figure of merit for muon cooling – an algorithm for particle counting in coupled phase planes. *Nucl. Instrum. Methods Phys. Res. A* **532**, 270–274 (2004).
31. Rogers, C. *Beam Dynamics in an Ionisation Cooling Channel*. PhD thesis, Imperial College London (2008).
32. Drielsma, F. *Measurement of the Increase in Phase Space Density of a Muon Beam through Ionization Cooling*. PhD thesis, Univ. Geneva (2018).
33. Bogomilov, M. et al. The MICE muon beam on ISIS and the beam-line instrumentation of the Muon Ionization Cooling Experiment. *J. Instrum.* **7**, P05009 (2012).
34. Adams, D. et al. Characterisation of the muon beams for the Muon Ionisation Cooling Experiment. *Eur. Phys. J. C* **73**, 2582 (2013).
35. Bogomilov, M. et al. Pion contamination in the MICE muon beam. *J. Instrum.* **11**, P03001 (2016).
36. Booth, C. N. et al. The design and performance of an improved target for MICE. *J. Instrum.* **11**, P05006 (2016).
37. Thomason, J. W. G. The ISIS Spallation Neutron and Muon Source – the first thirty-three years. *Nucl. Instrum. Methods Phys. Res. A* **917**, 61–67 (2019).
38. Bayliss, V. et al. The liquid-hydrogen absorber for MICE. *J. Instrum.* **13**, T09008 (2018).
39. Stratakis, D., Palmer, R. B. & Grote, D. P. Influence of space-charge fields on the cooling process of muon beams. *Phys. Rev. Accel. Beams* **18**, 044201 (2015).

40. Blackmore, V. et al. First particle-by-particle measurement of emittance in the Muon Ionization Cooling Experiment. *Eur. Phys. J. C* **79**, 257 (2019).
41. Bertoni, R. et al. The design and commissioning of the MICE upstream time-of-flight system. *Nucl. Instrum. Methods Phys. Res. A* **615**, 14–26 (2010).
42. Cremaldi, L. et al. A Cherenkov radiation detector with high density aerogels. *IEEE Trans. Nucl. Sci.* **56**, 1475–1478 (2009).
43. Ellis, M. et al. The design, construction and performance of the MICE scintillating fibre trackers. *Nucl. Instrum. Methods Phys. Res. A* **659**, 136–153 (2011).
44. Dobbs, A. et al. The reconstruction software for the MICE scintillating fibre trackers. *J. Instrum.* **11**, T12001 (2016).
45. Bertoni, R. et al. *The Construction of the MICE TOF2 Detector*. MICE Technical Note 254 (2010); http://mice.iit.edu/micenotes/public/pdf/MICE0286/MICE0286.pdf.
46. Adams, D. et al. Electron–Muon Ranger: performance in the MICE Muon Beam. *J. Instrum.* **10**, P12012 (2015).
47. Asfandiyarov, R. et al. The design and construction of the MICE Electron–Muon Ranger. *J. Instrum.* **11**, T10007 (2016).
48. Petroff, M. D. & Stapelbroek, M. G. Photon-counting solid-state photomultiplier. *IEEE Trans. Nucl. Sci.* **36**, 158–162 (1989).
49. Agostinelli, S. et al. GEANT4: a simulation toolkit. *Nucl. Instrum. Methods Phys. Res. A* **506**, 250–303 (2003).
50. Asfandiyarov, R. et al. MAUS: the MICE Analysis User Software. *J. Instrum.* **14**, T04005 (2019).

MICE collaboration

M. Bogomilov[1], R. Tsenov[1], G. Vankova-Kirilova[1], Y. P. Song[2], J. Y. Tang[2], Z. H. Li[3], R. Bertoni[4], M. Bonesini[4], F. Chignoli[4], R. Mazza[4], V. Palladino[5], A. de Bari[6], D. Orestano[7], L. Tortora[7], Y. Kuno[8], H. Sakamoto[8,34], A. Sato[8], S. Ishimoto[9], M. Chung[10], C. K. Sung[10], F. Filthaut[11,12], D. Jokovic[13], D. Maletic[13], M. Savic[13], N. Jovancevic[14], J. Nikolov[14], M. Vretenar[15], S. Ramberger[15], R. Asfandiyarov[16], A. Blondel[16], F. Drielsma[16], Y. Karadzhov[16], S. Boyd[17], J. R. Greis[17], T. Lord[17], C. Pidcott[17,35], I. Taylor[17,36], G. Charnley[18], N. Collomb[18], K. Dumbell[18], A. Gallagher[18], A. Grant[18], S. Griffiths[18], T. Hartnett[18], B. Martlew[18], A. Moss[18], A. Muir[18], I. Mullacrane[18], A. Oates[18], P. Owens[18], G. Stokes[18], P. Warburton[18], C. White[18], D. Adams[19], V. Bayliss[19], J. Boehm[19], T. W. Bradshaw[19], C. Brown[19,20], M. Courthold[19], J. Govans[19], M. Hills[19], J.-B. Lagrange[19], C. Macwaters[19], A. Nichols[19], R. Preece[19], S. Ricciardi[19], C. Rogers[19]*, T. Stanley[19], J. Tarrant[19], M. Tucker[19], S. Watson[19,37], A. Wilson[19], R. Bayes[21,38], J. C. Nugent[21], F. J. P. Soler[21], G. T. Chatzitheodoridis[21,22,23], A. J. Dick[22,23], K. Ronald[22,23], C. G. Whyte[22,23], A. R. Young[22,23], R. Gamet[24], P. Cooke[24], V. J. Blackmore[25], D. Colling[25], A. Dobbs[25,39], P. Dornan[25], P. Franchini[25], C. Hunt[25,40], P. B. Jurj[25], A. Kurup[25], K. Long[25], J. Martyniak[25], S. Middleton[25,41], J. Pasternak[25], M. A. Uchida[25,42], J. H. Cobb[26], C. N. Booth[27], P. Hodgson[27], J. Langlands[27], E. Overton[27,43], V. Pec[27], P. J. Smith[27], S. Wilbur[27], M. Ellis[20,44], R. B. S. Gardener[20], P. Kyberd[20], J. J. Nebrensky[20], A. DeMello[28], S. Gourlay[28], A. Lambert[28], D. Li[28], T. Luo[28], S. Prestemon[28], S. Virostek[28], M. Palmer[29], H. Witte[29], D. Adey[30,45], A. D. Bross[30], D. Bowring[30], A. Liu[30,46], D. Neuffer[30], M. Popovic[30], P. Rubinov[30], B. Freemire[31,46], P. Hanlet[31,47], D. M. Kaplan[31], T. A. Mohayai[31,47], D. Rajaram[31], P. Snopok[31], Y. Torun[31], L. M. Cremaldi[32], D. A. Sanders[32], D. J. Summers[32], L. R. Coney[33,48], G. G. Hanson[33] & C. Heidt[33]

[1]Department of Atomic Physics, St Kliment Ohridski University of Sofia, Sofia, Bulgaria. [2]Institute of High Energy Physics, Chinese Academy of Sciences, Beijing, China. [3]Sichuan University, Chengdu, China. [4]Sezione INFN Milano Bicocca, Dipartimento di Fisica G. Occhialini, Milan, Italy. [5]Sezione INFN Napoli and Dipartimento di Fisica, Università Federico II, Complesso Universitario di Monte S. Angelo, Naples, Italy. [6]Sezione INFN Pavia and Dipartimento di Fisica, Pavia, Italy. [7]INFN Sezione di Roma Tre and Dipartimento di Matematica e Fisica, Università Roma Tre, Rome, Italy. [8]Osaka University, Graduate School of Science, Department of Physics, Toyonaka, Japan. [9]High Energy Accelerator Research Organization (KEK), Institute of Particle and Nuclear Studies, Tsukuba, Japan. [10]UNIST, Ulsan, South Korea. [11]Nikhef, Amsterdam, The Netherlands. [12]Radboud University, Nijmegen, The Netherlands. [13]Institute of Physics, University of Belgrade, Belgrade, Serbia. [14]Faculty of Sciences, University of Novi Sad, Novi Sad, Serbia. [15]CERN, Geneva, Switzerland. [16]DPNC, Section de Physique, Université de Genève, Geneva, Switzerland. [17]Department of Physics, University of Warwick, Coventry, UK. [18]STFC Daresbury Laboratory, Daresbury, Cheshire, UK. [19]STFC Rutherford Appleton Laboratory, Harwell Oxford, Didcot, UK. [20]Brunel University, Uxbridge, UK. [21]School of Physics and Astronomy, The University of Glasgow, Glasgow, UK. [22]SUPA and Department of Physics, University of Strathclyde, Glasgow, UK. [23]Cockcroft Institute, Daresbury Laboratory, Daresbury, UK. [24]Department of Physics, University of Liverpool, Liverpool, UK. [25]Department of Physics, Blackett Laboratory, Imperial College London, London, UK. [26]Department of Physics, University of Oxford, Oxford, UK. [27]Department of Physics and Astronomy, University of Sheffield, Sheffield, UK. [28]Lawrence Berkeley National Laboratory, Berkeley, CA, USA. [29]Brookhaven National Laboratory, Upton, NY, USA. [30]Fermilab, Batavia, IL, USA. [31]Illinois Institute of Technology, Chicago, IL, USA. [32]University of Mississippi, Oxford, MS, USA. [33]University of California, Riverside, CA, USA. [34]Present address: RIKEN 2-1 Horosawa, Wako, Japan. [35]Present address: Department of Physics and Astronomy, University of Sheffield, Sheffield, UK. [36]Present address: Defence Science and Technology Laboratory, Salisbury, UK. [37]Present address: ATC, Royal Observatory Edinburgh, Edinburgh, UK. [38]Present address: Laurentian University, Sudbury, Ontario, Canada. [39]Present address: OPERA Simulation Software, Kidlington, UK. [40]Present address: CERN, Geneva, Switzerland. [41]Present address: School of Physics and Astronomy, University of Manchester, Manchester, UK. [42]Present address: Cavendish Laboratory, Cambridge, UK. [43]Present address: Arm, Sheffield, UK. [44]Present address: Westpac Group, Sydney, New South Wales, Australia. [45]Present address: Institute of High Energy Physics, Chinese Academy of Sciences, Bejing, China. [46]Present address: Euclid Techlabs, Bolingbrook, IL, USA. [47]Present address: Fermilab, Batavia, IL, USA. [48]Present address: European Spallation Source ERIC, Lund, Sweden. *e-mail: chris.rogers@stfc.ac.uk

Article

Methods

Characterization of beam brightness

In particle accelerators, the average beam brightness $\bar{B}$ is defined as the beam current, I, passing through a transverse phase-space volume $\mathcal{V}_4$ (ref. [51])

$$\bar{B} = \frac{I}{\mathcal{V}_4} \qquad (1)$$

The normalized r.m.s. emittance is often used as an indicator of the phase-space volume occupied by the beam and is given by[29]

$$\varepsilon_\perp = \frac{\sqrt[4]{|V|}}{m_\mu c} \qquad (2)$$

where m_μ is the muon mass and $|V|$ is the determinant of the covariance matrix of the beam in the transverse phase space $\mathbf{u} = (x, p_x, y, p_y)$. The covariance matrix has elements $v_{ij} = \langle u_i u_j \rangle - \langle u_i \rangle \langle u_j \rangle$. The distribution of individual particle amplitudes also describes the volume of the beam in phase space.

The amplitude is defined by[30]

$$A_\perp = \varepsilon_\perp R^2(\mathbf{u}, \langle \mathbf{u} \rangle) \qquad (3)$$

where $R^2(\mathbf{u}, \mathbf{v})$ is the square of the distance between two points, $\mathbf{u}$ and $\mathbf{v}$, in the phase space, normalized to the covariance matrix:

$$R^2(\mathbf{u}, \mathbf{v}) = (\mathbf{u} - \mathbf{v})^{\mathrm{T}} V^{-1} (\mathbf{u} - \mathbf{v}) \qquad (4)$$

The normalized r.m.s. emittance is proportional to the mean of the particle amplitude distribution. In the approximation that particles travel near the beam axis, and in the absence of cooling, the particle amplitudes and the normalized r.m.s. emittance are conserved quantities. If the beam is well described by a multivariate Gaussian distribution, then R^2 is distributed according to a χ^2 distribution with four degrees of freedom, so the amplitudes are distributed according to

$$f(A_\perp) = \frac{A_\perp}{4\varepsilon_\perp^2} \exp\left(\frac{-A_\perp}{2\varepsilon_\perp}\right) \qquad (5)$$

The rate of change of the normalized transverse emittance as the beam passes through an absorber is given approximately by[8,29,31]

$$\frac{d\varepsilon_\perp}{dz} \approx -\frac{\varepsilon_\perp}{\beta^2 E_\mu} \left| \frac{dE_\mu}{dz} \right| + \frac{\beta_\perp (13.6\ \mathrm{MeV}\ c^{-1})^2}{2\beta^3 E_\mu m_\mu X_0} \qquad (6)$$

where βc is the muon velocity, E_μ is the muon energy, $|dE_\mu/dz|$ is the mean energy loss per unit path length, X_0 is the radiation length of the absorber and $\beta_\perp$ is the transverse betatron function at the absorber[29]. The first term of this equation describes 'cooling' by ionization energy loss and the second term describes 'heating' by multiple Coulomb scattering. Equation (6) implies that there is an equilibrium emittance for which the emittance change is zero.

If the beam is well described by a multivariate Gaussian distribution both before and after cooling, then the downstream and upstream amplitude distributions $f^{\mathrm{d}}(A_\perp)$ and $f^{\mathrm{u}}(A_\perp)$ are related to the downstream and upstream emittances $\varepsilon_\perp^{\mathrm{d}}$ and $\varepsilon_\perp^{\mathrm{u}}$ by

$$\frac{f^{\mathrm{d}}(A_\perp)}{f^{\mathrm{u}}(A_\perp)} = \left(\frac{\varepsilon_\perp^{\mathrm{u}}}{\varepsilon_\perp^{\mathrm{d}}}\right)^2 \exp\left[-\frac{A_\perp}{2}\left(\frac{1}{\varepsilon_\perp^{\mathrm{d}}} - \frac{1}{\varepsilon_\perp^{\mathrm{u}}}\right)\right] \qquad (7)$$

In the experiment described in this paper, many particles do not travel near the beam axis. These particles experience effects from optical aberrations, as well as geometrical effects such as scraping, in which high-amplitude particles outside the experiment's aperture are removed from the beam. Scraping reduces the emittance of the ensemble and selectively removes those particles that scatter more than the rest of the ensemble. Optical aberrations and scraping introduce a bias in the change in r.m.s. emittance that occurs because of ionization cooling. In this work the distribution of amplitudes is studied. To expose the behaviour in the beam core, independently of aberrations affecting the beam tail, V and $\varepsilon_\perp$ are recalculated for each amplitude bin, including particles that are in lower-amplitude bins and excluding particles that are in higher-amplitude bins. This results in a distribution that, in the core of the beam, is independent of scraping effects and spherical aberrations.

The change in phase-space density provides a direct measurement of the cooling effect. The k-nearest-neighbour algorithm provides a robust non-parametric estimator of the phase-space density of the muon ensemble[32,34,52]. The separation of pairs of muons is characterized by the normalized squared distance, $R_{ij}^2(\mathbf{u}_i, \mathbf{u}_j)$, between muons with positions $\mathbf{u}_i$ and $\mathbf{u}_j$. A volume $\mathcal{V}_{ik}$ is associated with each particle, which corresponds to the hypersphere that is centred on $\mathbf{u}_i$ and intersects the kth nearest particle (that is, the particle that has the kth smallest R_{ij}). The density, ρ_i, associated with the ith particle is estimated by

$$\rho_i(\mathbf{u}_i) = \frac{k}{n} \frac{1}{|V|^{1/2}} \frac{1}{\mathcal{V}_{ik}} = \frac{2k}{n\pi^2} \frac{1}{|V|^{1/2}} \frac{1}{R_{ik}^4} \qquad (8)$$

where n is the number of particles in the ensemble. An optimal value for k is used, $k = n^{4/(4+d)} = \sqrt{n}$, with phase-space dimension $d = 4$ (ref. [32]).

Data taking and reconstruction

Data were buffered in the front-end electronics and read out after each target actuation. Data storage was triggered by a coincidence of signals in the photomultiplier tubes (PMTs) serving a single scintillator slab in the upstream TOF station closest to the cooling channel (TOF1). The data recorded in response to a particular trigger are referred to as a 'particle event'.

Each TOF station was composed of a number of scintillator slabs that were read out using a pair of PMTs, one mounted at each end of each slab. The reconstruction of the data began with the search for coincidences in the signals from the two PMTs serving any one slab in a TOF plane. Such coincidences are referred to as 'slab hits'. 'Space points' were then formed from the intersection of slab hits in the x and y projections of each TOF station separately. The position and time at which a particle giving rise to the space point crossed the TOF station were then calculated using the slab position and the times measured in each of the PMTs. The relative timing of the two upstream TOF stations (TOF0 and TOF1) was calibrated relative to the measured time taken for electrons to pass between the two TOF detectors, on the assumption that they travelled at the speed of light.

Signals in the tracker readout were collected to reconstruct the helical trajectories ('tracks') of charged particles in the upstream and downstream trackers (TKU and TKD, respectively). Multiple Coulomb scattering introduced significant uncertainties in the reconstruction of the helical trajectory of tracks with a bending radius of less than 5 mm. For this class of track, the momentum was deduced by combining the tracker measurement with the measurements from nearby detectors. The track-fitting quality was characterized by the χ^2 per degree of freedom

$$\chi_{\mathrm{df}}^2 = \frac{1}{n} \sum_i \frac{\delta x_i^2}{\sigma_i^2} \qquad (9)$$

where δx_i is the distance between the fitted track and the measured signal in the ith tracker plane, σ_i is the resolution of the position measurement in the tracker planes and n is the number of planes that had

a signal used in the track reconstruction. Further details of the reconstruction and simulation may be found in ref. [50].

Beam selection

Measurements made in the instrumentation upstream of the absorber were used to select the input beam. The input beam (the upstream sample) was composed of events that satisfied the following criteria:

• Exactly one space point was found in TOF0 and TOF1 and exactly one track in TKU.

• The track in TKU had $\chi^2_{df} < 8$ and was contained within the 150-mm fiducial radius over the full length of TKU.

• The track in TKU had a reconstructed momentum in the range 135–145 MeV c^{-1}, corresponding to the momentum acceptance of the cooling cell.

• The time-of-flight between TOF0 and TOF1 was consistent with that of a muon, given the momentum measured in TKU.

• The radius at which the track in TKU passed through the diffuser was smaller than the diffuser aperture.

The beam emerging from the cooling cell (the downstream sample) was characterized using the subset of the upstream sample that satisfied the following criteria:

• Exactly one track was found in TKD.

• The track in TKD had $\chi^2_{df} < 8$ and was contained within the 150-mm fiducial radius of TKD over the full length of the tracker.

The same sample-selection criteria were used to select events from the simulation of the experiment, which included a reconstruction of the electronics signals expected for the simulated particles.

Calculation of amplitudes

The amplitude distributions obtained from the upstream and downstream samples were corrected for the effects of the detector efficiency and resolution and for the migration of events between amplitude bins. The corrected number of events in a bin, N_i^{corr}, was calculated from the raw number of events, N_j^{raw}, using

$$N_i^{corr} = E_i \sum_j S_{ij} N_j^{raw} \tag{10}$$

where E_i is the efficiency correction factor and S_{ij} accounts for the detector resolution and event migration. E_i and S_{ij} were estimated from the simulation of the experiment. The uncorrected and corrected amplitude distributions for a particular configuration are shown in Extended Data Fig. 1. The correction is small relative to the ionization cooling effect, which is clear even in the uncorrected distributions.

It can be seen from equation (7) that in the limit of small amplitudes, and in the approximation that the beam is normally distributed in the phase-space variables, the ratio of the number of muons is equal to the ratio of the square of the emittances,

$$\lim_{A_\perp \to 0} \frac{f^d(A_\perp)}{f^u(A_\perp)} = \left(\frac{\varepsilon_\perp^u}{\varepsilon_\perp^d} \right)^2 \tag{11}$$

The ratio of f^d to f^u in the lowest-amplitude bin of Fig. 3, which is an approximation to this ratio, is listed in Extended Data Table 1.

Data availability

The unprocessed and reconstructed data that support the findings of this study are publicly available on the GridPP computing Grid at https://doi.org/10.17633/rd.brunel.3179644 (MICE unprocessed data) and https://doi.org/10.17633/rd.brunel.5955850 (MICE reconstructed data). Source data for Figs. 3–5 and Extended Data Fig. 1 are provided with the paper.

Publications using MICE data must contain the following statement: "We gratefully acknowledge the MICE collaboration for allowing us access to their data. Third-party results are not endorsed by the MICE collaboration."

Code availability

The MAUS software[50] that was used to reconstruct and analyse the MICE data is available at https://doi.org/10.17633/rd.brunel.8337542. The analysis presented here used MAUS version 3.3.2.

51. Reiser, M. in *Theory and Design of Charged Particle Beams* 51–103 (John Wiley & Sons, 2008).
52. Mack, Y. P. & Rosenblatt, M. Multivariate k-nearest neighbor density estimates. *J. Multiv. Anal.* **9**, 1–15 (1979).

Extended Data Fig. 1 | Corrected and uncorrected amplitude distributions for the 10–140 'LH2 full' configuration. The uncorrected data are shown by open points and the corrected data by filled points. Orange circles correspond to the upstream distribution and green triangles to the downstream distribution. Shading represents the estimated total standard error. Error bars show the statistical error and for most points are smaller than the markers.

Extended Data Table 1 | Ratio of number of muons downstream to number of muons upstream having an amplitude of less than 5 mm

	4-140	6-140	10-140
LH2 empty	$0.98 \pm 0.005 \pm 0.05$	$1.01 \pm 0.006 \pm 0.05$	$1.02 \pm 0.02 \pm 0.05$
LH2 full	$1.12 \pm 0.009 \pm 0.05$	$1.16 \pm 0.009 \pm 0.05$	$1.32 \pm 0.02 \pm 0.07$
None	$0.99 \pm 0.006 \pm 0.05$	$1.00 \pm 0.005 \pm 0.05$	$1.06 \pm 0.02 \pm 0.06$
LiH	$1.07 \pm 0.008 \pm 0.05$	$1.14 \pm 0.01 \pm 0.05$	$1.23 \pm 0.03 \pm 0.07$

Uncertainties denote standard error; statistical uncertainty is followed by the total uncertainty.

Article

Extended Data Table 2 | Number of events in the samples shown in Fig. 3–5

	4-140		6-140		10-140	
	Upstream	Downstream	Upstream	Downstream	Upstream	Downstream
LH2 empty	163508	153813	158520	140981	123067	85082
LH2 full	71823	67640	117383	107329	82371	62660
None	91804	86877	172606	153809	54195	37436
LiH	87514	82682	98443	89875	43423	32715

Forecasting of VOC emissions from traffic and industry using classification and regression multivariate methods

Andreja Stojić [a,*], Dimitrije Maletić [a], Svetlana Stanišić Stojić [b], Zoran Mijić [a], Andrej Šoštarić [c]

[a] Institute of Physics Belgrade, University of Belgrade, Pregrevica 118, 11080 Belgrade, Serbia
[b] Singidunum University, Danijelova 32, 11010 Belgrade, Serbia
[c] Institute of Public Health Belgrade, Bulevar Despota Stefana 54, 11000 Belgrade, Serbia

HIGHLIGHTS

- Receptor models were applied for the purpose of VOC source apportionment.
- MVA methods were used for forecasting contributions from traffic and industry.
- Forecast was based on inorganic pollutant concentrations and meteorological data.
- Predicted values were consistent with the results of receptor modeling.
- The highest forecast accuracy was achieved with relative error of only 6%.

ARTICLE INFO

ABSTRACT

In this study, advanced multivariate methods were applied for VOC source apportionment and subsequent short-term forecast of industrial- and vehicle exhaust-related contributions in Belgrade urban area (Serbia). The VOC concentrations were measured using PTR-MS, together with inorganic gaseous pollutants (NO_x, NO, NO_2, SO_2, and CO), PM_{10}, and meteorological parameters. US EPA Positive Matrix Factorization and Unmix receptor models were applied to the obtained dataset both resolving six source profiles. For the purpose of forecasting industrial- and vehicle exhaust-related source contributions, different multivariate methods were employed in two separate cases, relying on meteorological data, and on meteorological data and concentrations of inorganic gaseous pollutants, respectively. The results indicate that Boosted Decision Trees and Multi-Layer Perceptrons were the best performing methods. According to the results, forecasting accuracy was high (lowest relative error of only 6%), in particular when the forecast was based on both meteorological parameters and concentrations of inorganic gaseous pollutants.

© 2015 Published by Elsevier B.V.

1. Introduction

Volatile organic compounds (VOC) comprise a diverse group of species which are of concern due to their potentially detrimental impact on human health and the environment. Under sufficiently conducive meteorological conditions, they are important precursors in the formation of ozone, the abundant and reactive gaseous pollutant, capable of inducing oxidative damage to living cells (Kampa and Castanas, 2008). In addition, several VOC species such as styrene and benzene have been identified as toxic or mutagenic, while epidemiological evidence indicates that repetitive daily or intermittent exposure is associated with numerous adverse health effects, mainly respiratory and hearth disorders (Musselman and Korfmacher, 2014; Hsieh and Tsai, 2003). As regards environmental issues, the significant impact of VOC on climate change is observed in spite of their low concentrations in ambient air, and arises from their ability to form secondary aerosol and their properties as greenhouse gases (Chin and Batterman, 2012).

The ubiquity of VOC results from both biogenic and anthropogenic emissions, whereas the latter often dominate in heavily populated areas and are associated with vehicle transport, industrial activities, fossil fuel refining and distribution, biomass burning, solvent usage, *etc.* (Lee et al., 2002; Na et al., 2004). The abundance and spatial distribution of gaseous pollutants originating from remote emission sources mostly depend on their atmospheric lifetimes (Jobson et al., 1999), whereas, in the case of locally generated pollution, this relationship is no longer sustained, and VOC levels and variability are mainly controlled by emission rates and meteorological factors (Liu et al., 2012).

* Corresponding author at: Pregrevica 118, 11080 Belgrade, Serbia.
E-mail addresses: andreja.stojic@ipb.ac.rs (A. Stojić), dimitrije.maletic@ipb.ac.rs (D. Maletić), sstanisic@singidunum.ac.rs (S. Stanišić Stojić), zoran.mijic@ipb.ac.rs (Z. Mijić), andrej.sostaric@zdravlje.org.rs (A. Šoštarić).

Apart from being an important regional traffic hub with a population of 1.6 million residents, the capital of Serbia, Belgrade, and its suburban area is home to network of coal-fired power plants and different industrial facilities, such as the petrochemical complex, chemical plant, and oil refinery. In such complex urban environments with the prevalence of local emission sources, meteorological conditions play a significant role in the VOC mixing and distribution. The methods which simulate the variations of VOC emissions with sufficient reliability, based solely on meteorological data, can be used to forecast temporal distribution of VOC species, which is essential for development of efficient abatement strategies (Liu et al., 2012).

In this study several multivariate (MVA) methods were employed to assess the impact of traffic- and industry-related sources on VOC levels in Belgrade urban area, and predict their contribution dynamics. The petrochemical/chemical industry (PC) and vehicle exhaust emissions (VE) present one of the most significant emission sources. Their contributions were estimated using widely applied receptor models, Positive Matrix Factorization (PMF) and Unmix, based on the assumption that, in a complex VOC mixture, species emitted from the same source are statistically interrelated (Song et al., 2008). Subsequently, classification and regression MVA methods were applied in order to predict the source contribution dynamics on the basis of meteorological dataset and concentrations of inorganic gaseous pollutants (IG) — NO_x, NO, NO_2, SO_2 and CO. The supervised learning algorithms for classification and regression analyses were specifically designed within Toolkit for Multivariate Analysis (TMVA) (Hoecker et al., 2007) within the ROOT framework (Brun and Rademakers, 1997), for extensive data processing in high-energy physics, but their applications are not restricted to these requirements (Maletić et al., 2014). The best performing MVA methods were Boosted Decision Trees (BDT and BDTG), designed for the purpose of MiniBooNE neutrino experiment (Yang et al., 2005), and based on complex method of cuts, and Multi-Layer Perceptrons (MLP), based on artificial neural networks (ANN) (Rojas, 1996).

Nowadays, the forecasting of air pollutant concentrations is an essential issue in environmental research due to a wide range of potential benefits. Besides providing information for early public warnings to the susceptible populations, as well as assistance in the assessment of regulation policies, the accurate and reliable forecast could be useful for development of preventive approaches and considerable reduction in the number of measurement sites over the area. This study reveals that presented MVA methods can be successfully used for forecasting the contributions of different emission sources in the investigated area.

2. Materials and methods

The measurement site is located at the Institute of Public Health in Belgrade (44°49′ N, 20°28′ E), in the urban canyon street with heavy and slow traffic. Proton Transfer Reaction Mass Spectrometer (Standard PTR-quad-MS, Ionicon Analytik, GmbH, Austria) was used for on-line measurements of concentrations of 36 VOC-related masses in the period from January 22nd to March 24th 2014. A detailed description of the method is given elsewhere (Lindinger et al., 1998; de Gouw and Warneke, 2007). The inlet of the instrument, 3 m heated (70 °C) silcosteel line inner diameter 3 mm, was placed 3 m above ground. VOC data, with 0.5 s dwell time, and five control parameters (m/z 21, m/z 25, m/z 30, m/z 32, and m/z 37) were obtained in 24 s cycles.

Drift tube parameters included: pressure, ranging from 2.08 to 2.11 mbar; temperature, 60 °C; voltage, 600 V; E/N parameter, 145 Td providing reaction time of 90 μs. The count rate of $H_3O^+H_2O$ was 1 to 7% of the $5.1 \cdot 10^6$ counts s^{-1} count rate of primary H_3O^+ ions. The calibration was done according to Taipale et al. (2008). For this purpose, TO-15 Supelco gas mixture (m/z 57, m/z 79, m/z 93, m/z 107, and m/z 121) was diluted with ASGU 370-p HORIBA system zero air to five concentrations in the range from 0.5 to 100 ppb. Normalized sensitivities were in the range from 6.2 to 14.3 npcs ppb^{-1}. Detection limit of 1-h

averaged VOC concentrations was less than 0.5 ppb, except for methanol (2.0 ppb) and acetone (1.1 ppb). Key m/z-signals in the dataset, identified using a method developed by Galbally et al. (2008), were observed for 29 out of 36 masses, and used for further analysis.

The concentrations of IG, PM_{10}, and meteorological data (atmospheric pressure, temperature, humidity, precipitation, wind speed and direction) were obtained from the automatic monitoring station at the measurement site (Institute of Public Health Belgrade).

US EPA Unmix 6.0 (USEPA, 2007) and Positive Matrix Factorization (Version 3.0) (USEPA, 2008) receptor models were applied to the 1169 observations of 1-hour-averaged concentrations of 29 species in order to identify emission sources (Table 1). The usages of these models as well as the theoretical background are detailed in literature (Henry, 2003). Briefly, Unmix is based on an eigenvalue analysis and does not allow down weighting of individual data points (Henry, 1997), while PMF decomposes a matrix of ambient data into two matrices representing source contribution and source profile (Paatero and Tapper, 1994). A value equal to the half of the method detection limit (DL) for each variable was used for concentrations below the DL. The number of pollutants selected as Unmix and PMF input variables was chosen using a combination of trial and error with the general goal of maximizing the number of input variables that produced feasible and physically interpretable solutions and following additional fit diagnostics criteria (Chan et al., 2011). After selecting the base run, 100 bootstrap runs with R^2-value of 0.6 were performed to evaluate the uncertainty of the PMF resolved profiles. In addition, PMF was run with different Fpeak values to explore the rotational freedom and reported results were for its value adjusted to 0.2.

Statistical analyses, including bivariate polar plot and bivariate cluster (k-means clustering, grouping similar conditions together) analysis, were performed with the statistical software environment R (Team, 2012), using the Openair package (Carslaw and Ropkins, 2012). The

Table 1

Basic statistics for measured parameters: VOC related masses [ppb], NO_x, NO_2, NO, SO_2 [μg m^{-3}], and CO [mg m^{-3}] concentrations.

Parameter	Mean	Median	Min	Max	10th	90th	St. dev.
NO_x	149.69	121.01	11.24	912.42	37.14	301.52	116.19
NO_2	62.94	54.96	8.86	239.09	21.36	115.61	38.17
NO	86.76	58.67	1.19	673.33	11.12	205.61	88.32
CO	0.68	0.59	0.16	3.42	0.36	1.10	0.38
SO_2	21.54	17.43	3.85	236.46	7.74	39.94	16.70
Ethylbenzene	2.31	1.76	<DL	36.93	0.37	4.63	2.41
mp-Xylene	8.99	6.86	<DL	124.62	1.41	17.25	9.52
o-Xylene	1.88	1.46	<DL	18.52	0.28	3.79	1.72
m/z 41 (propylene)	1.89	1.66	0.34	19.88	0.80	2.94	1.43
m/z 43	4.87	4.42	1.27	28.40	2.32	7.84	2.52
m/z 45 (acetaldehyde)	5.04	4.29	1.31	38.85	2.28	7.92	3.53
m/z 47 (ethanol)	7.81	3.02	<DL	177.33	<DL	17.39	15.55
m/z 57 (MTBE)	1.94	1.63	0.26	28.82	0.75	2.92	1.93
m/z 59 (acetone)	7.16	5.67	<DL	30.79	1.61	15.57	5.42
m/z 61 (acetic acid)	4.85	4.48	1.36	25.98	2.58	7.24	2.36
m/z 71	0.63	0.58	0.11	5.32	0.29	0.94	0.39
m/z 73	0.87	0.78	0.17	7.89	0.46	1.32	0.52
m/z 75	1.28	0.97	0.26	45.29	0.54	1.80	2.09
m/z 79 (benzene)	1.35	1.10	0.05	6.95	0.50	2.44	0.90
m/z 81	0.81	0.68	0.07	9.88	0.25	1.33	0.78
m/z 83	14.4	10.16	0.37	92.44	3.05	31.65	11.99
m/z 85	9.43	6.73	0.17	65.12	1.96	20.52	7.85
m/z 87	2.53	2.20	0.49	12.36	1.03	4.55	1.48
m/z 93 (toluene)	3.36	2.63	0.19	29.66	1.15	6.11	2.62
m/z 99	0.49	0.43	<DL	2.32	0.17	0.91	0.31
m/z 101	1.25	1.05	0.37	5.34	0.58	2.33	0.71
m/z 105 (styrene)	0.53	0.43	0.11	16.39	0.22	0.76	0.81
m/z 121 (C9 aromatics)	4.32	3.13	0.28	24.96	1.19	8.59	3.88
m/z 137 (monoterpenes)	0.89	0.65	<DL	8.50	0.19	1.67	0.90

DL — detection limit.

results were used for analysis of source contribution dynamics, the impact of potential emission sources, as well as wind speed and direction, on the air quality at the measurement site.

The impact of planetary boundary layer (PBL) height on VOC source contribution dynamics was also taken into consideration. PBL height was obtained combining Raman Lidar system case study observations (Banks et al., 2014) performed within the framework of EARLINET network (Belgrade station), and calculations using MeteoInfo software (Wang, 2014) and GDAS1 (Global Data Assimilation System) data.

Subsequently, MVA methods were used for forecasting of PC and VE source contribution dynamics in two separate cases: they either used meteorological values as inputs, or meteorological values and IG concentrations, while the VOC distributions and evaluated VOC values were not used as inputs. In addition to this, all MVA methods training and testing were conducted once more with the additional input variable *i.e.*, previously predicted source contribution values. The results obtained this way have "Prev" suffix. All MVA methods were used both for classification, which served to differentiate between pollution indicators of high and low significance for the source contribution dynamics, and regression methods, which were used to obtain mapped functional behavior of dependency of the source contribution on the examined variables. A sample of events, each consisting of source contribution value and input (meteorological, or meteorological and IG concentration) data, was used to train and test methods. The MVA methods used in the analysis were: Boosted Decision Trees (BDT, BDTG), Artificial Neural Network Multilayer Perceptron (MLP), MLP with Bayesian Extension (MLPBNN), Support Vector Machine (SVM), Linear Discriminant (LD), Fisher Discriminant (Fisher), Multidimensional Probability Density Estimator Range Search Method (PDERS), Function Discrimination Analysis with Genetic Algorithm Converger (FDA_GA), Likelihood Method and Function Discriminant Analysis (FDA).

3. Results and discussion

Both receptor models, PMF and Unmix resolved six-profile solution including 29 compounds, and for the purpose of this study, the profiles which correspond to VE and PC were analyzed and compared (Fig. 1). In depth analysis of all Unmix- and PMF-resolved profiles is presented in our previous study (Stojić et al., 2015). In the expanded seven-source solution, Unmix resolved two VE profiles instead of one, with total contribution of 31.2%, whereas one of them did not include majority of IG. Similarly, expansion of PMF model to seven profiles resulted in further division and three VE profiles, all comprising dominant portions of different species associated with vehicle emissions. The attempts to obtain five-profile solutions also failed to provide reasonable results.

The Unmix resolved source which can be attributed to VE (VE_{Unmix}) exhibits very high correlations with related PMF resolved profiles (both VE_{PMF1} and VE_{PMF2}, as separated, and VE_{PMF} in total, summed as in Hopke et al., 2006), 0.83, 0.88, and 0.89, respectively (Fig. 2). The significant share of benzene, toluene, o-xylene, mp-xylene and ethylbenzene is apportioned to these profiles, together with IG suggesting the relationship with combustion processes. Unlike gasoline, diesel emissions are associated with 15 times less CO, seven times more NO_x and 10–14 times less BTEX (Thornhill et al., 2010). The shares of CO and NO_x are in the same range, which together with considerable portions of benzene, toluene, and extremely high portions of o-xylene, mp-xylene and ethylbenzene indicates that the observed pollutants mainly originate from gasoline combustion, at least in the surrounding of the measurement site. Toluene to benzene (T/B) ratio for the analyzed profiles ranges from 2.16 to 2.49, which complies with the results from previous studies on VE emissions in winter season (from 2 to 5) (Lough et al., 2005).

The estimated average contribution of VE_{Unmix} to total observed concentrations (27.6%) significantly exceeds the total contribution of two PMF resolved profiles, VE_{PMF1} and VE_{PMF2} (20.31%). This is probably due to the fact that significant shares of certain VOC species included

in Unmix solution, such as gasoline additive, methyl tertiary butyl ether (MTBE) and C9 aromatics, which are known to be tracers of mobile or gasoline evaporative emissions, were apportioned between PC and the profile assigned to gasoline evaporation in the PMF model solution.

Similarly, the compounds detected at m/z 71 (methyl vinyl ketone, methacrolein, isoprene oxidation products) and m/z 73 (methyl ethyl ketone, butanal) with moderate contributions to VE_{Unmix}, 29.8 and 26.0%, respectively, are not included in PMF profiles assigned to VE, while their dominant shares are apportioned to PC. Since both of the species are positively correlated with propylene, MTBE, benzene, toluene, and styrene (from 0.64 to 0.89), as well as with monoterpenes and isoprene (from 0.47 to 0.91), their origin can be recognized as anthropogenic in VE profiles, or biogenic in profiles related to PC, which contain certain amount of biogenic tracers. Finally, in Unmix resolved profiles, the dominant shares of benzene, toluene, and styrene are apportioned to VE source, whereas in PMF model solution these species mainly contribute to PC. Therefore, the estimated contribution of industrial emissions also differs, and is 7% higher for PMF than for Unmix resolved profile.

The contributions of all VE profiles exhibited a regular diurnal pattern, characterized by prominent morning and late afternoon peak (6:00–09:00 AM, 6:00–10:00 PM), which is consistent with the expected rush hour and accumulation of pollutants in the shallow boundary layer (Fig. 2) (Bon et al., 2011). The decrease in traffic intensity and expansion of daytime boundary layer result in lowest values of profile contributions in the afternoon (12:00–5:00 PM). The traffic load is significantly decreased on weekends, thus being compliant with the expected tendency in city's central zone.

The prevailing wind direction changed from NE in January to W, SW and E in March which was followed by gradual increase in contribution of VE profiles, since the western sectors belong to central traffic-congested area. It should also be noted that the registered episode of extreme wind, blowing up to 20.6 m s^{-1} from NE direction (from January, 30th to February, 2nd) had a significant impact on profile contributions, which suggests that the dominant share arises from local sources distributed around the measurement site, as expected. According to the results of bivariate cluster analysis between 55.0 and 64.4% of vehicle emissions are mainly related to locally generated pollution concentrated in the stagnant zone across the canyon street (Fig. 2).

As regards the PC, the significant decrease in contribution of all related profiles was observed in March, with the change in wind direction, since the major local source of petrochemical evaporation is Petrohemija, located in the industrial zone of Pančevo, about 13 km of air distance in the NE direction. It is one of the largest chemical industrial complexes in Southeastern Europe with annual production of more than six hundred thousand tons of propylene, 1,3-butadiene, MTBE, plastic and rubber polymers, and other petrochemicals. In compliance with this, the results of bivariate cluster analysis show that the contributions of industrial profiles are mainly associated with moderate wind blowing from the N/E sector (from 72.7 to 81.5%) (Fig. 2). The contribution of regional transport is estimated to be around 25%, as determined by using air back trajectory sector analysis (TSA) (Zhu et al., 2011) and PBL height (Stojić et al., 2015).

The PC profiles resolved by Unmix (PC_{Unmix}) and PMF (PC_{PMF}) exhibit relatively good correlation, particularly in domain of source contributions less than 1 (Fig. 2). They are distinguished mainly by significant portions of propylene, MTBE, benzene, toluene, styrene, and propionic acid (m/z 75) produced by the ethylene hydrocarboxylation. The presence of acetic acid, its fragments detected at m/z 43, and its intermediate precursor, acetaldehyde, can be associated with the emissions from a large Methanol and Acetic Acid Complex, Kikinda, located in the N/NE sector, about 100 km of air distance from the measurement site. Since the pollutants mainly originate from evaporative processes, gaseous oxides do not contribute to these profiles, excluding moderate share of CO apportioned to PC_{PMF}.
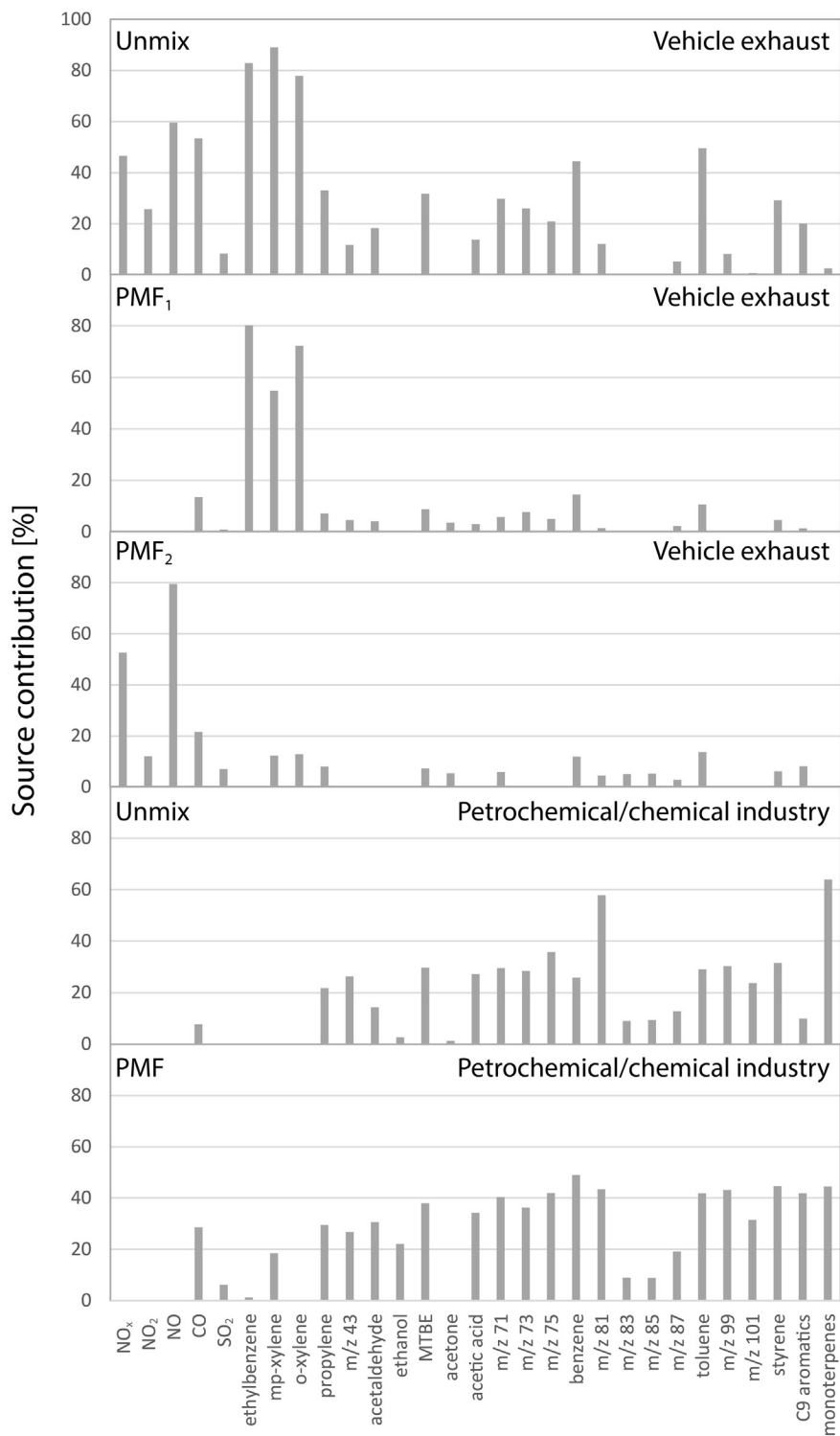
Fig. 1. Unmix- and PMF-resolved VE and PC source profiles [%].

Unlike traffic-related emissions, diurnal patterns of PC profiles exhibit a gradual increase during working hours (9:00 AM–6:00 PM) on weekdays and Saturdays, whereas on Sundays their contributions are decreased to minimum, as expected for industrial activities (Fig. 2).

Eventually, no model solution resolved profile which can be assigned exclusively to biogenic emissions, which clearly reflects the negligible significance of biosphere, particularly in urban areas and winter season. Nevertheless, significant shares of monoterpenes, monoterpene oxidation products (m/z 81), and other species identified of probable biogenic origin (m/z 71, m/z 73, m/z 99, and m/z 101) are apportioned to industrial profiles. The reason for this is probably Botanical garden, a large area of vegetation located about 150 m from the measurement site, on the pathway of air masses coming from the NE and encompassing chemical and petrochemical industrial complexes.
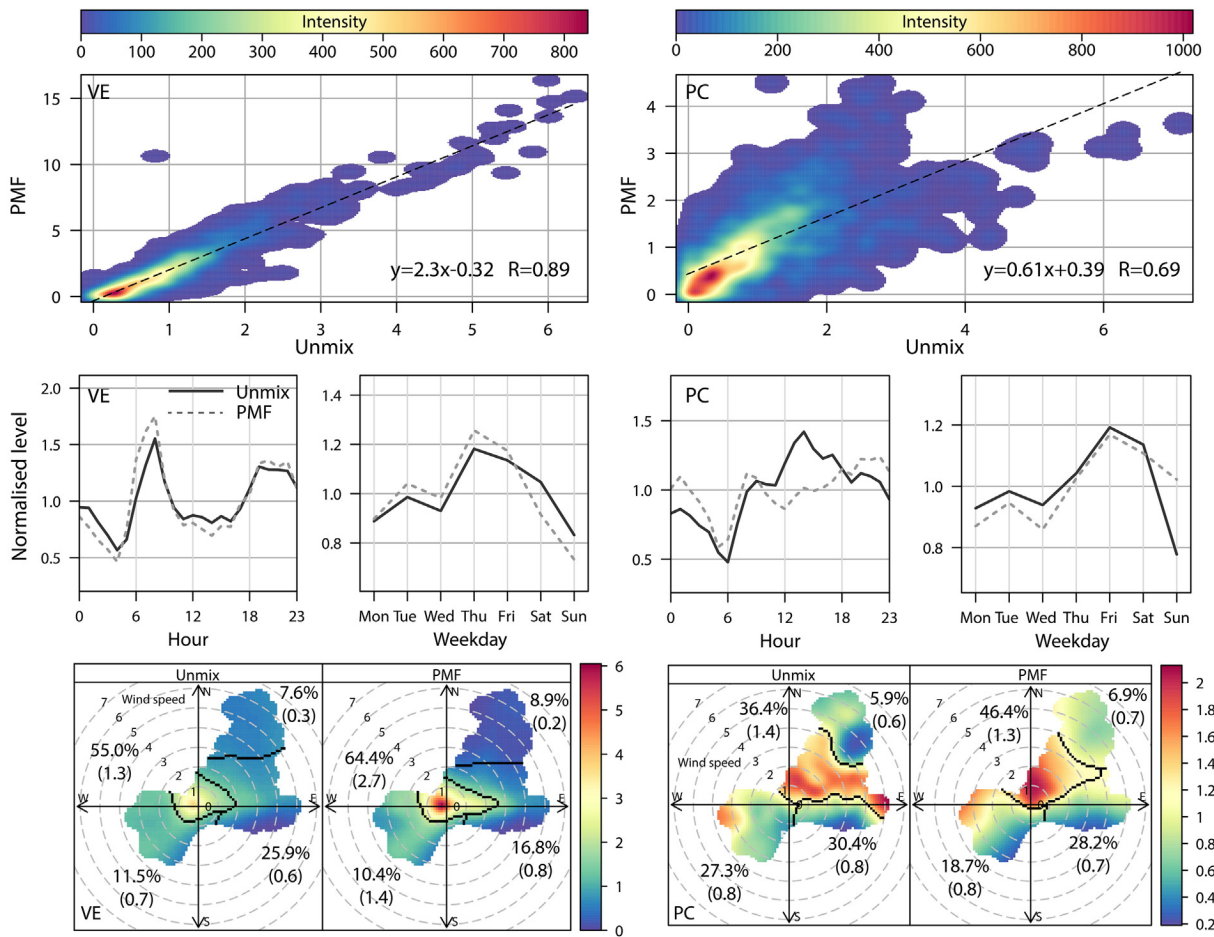
Fig. 2. Characteristics of PMF- and Unmix-resolved VE and PC normalized source contributions: intensity plot and linear fit (above); daily, weekly variations (middle), and bivariate and cluster plot (below).

3.1. Classification MVA methods

All MVA methods were applied for forecast of both industrial- (PMF and Unmix) and traffic-related (PMF$_2$ and Unmix) source contributions and prediction of potentially health-damaging events. For the purpose of this study the forecasting of both VE$_{PMF1}$ and VE$_{PMF2}$, and VE$_{PMF}$ in total, was conducted, and herein presented results are related to VE$_{PMF2}$ only, to demonstrate how accurate forecasts can be produced.

The necessity to urge caution was estimated on the basis of the predicted source contributions, as follows: the values above 60% are considered to require the increased level of caution, whereas those exceeding 75% are considered as extremely high-alarm triggering values. Both values were chosen as arbitrary limits. Prior to method trainings and analyses of their performances, the input variables that did not exhibit significant linear correlations with source contributions were excluded. Also, one input variable was excluded for every two that were observed to be highly correlated. Therefore, the number of meteorological variables having significant impact on profile contributions is reduced to two per source. For both vehicle exhaust profiles, wind speed is ranked first, followed by temperature. For industrial profiles, the first and second ranked were temperature and wind speed (PC$_{PMF}$), and pressure and temperature (PC$_{Unmix}$), respectively.
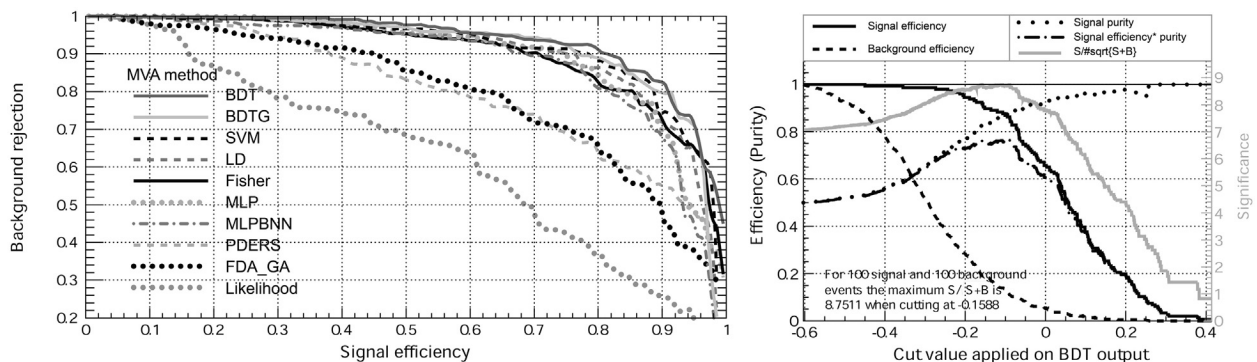

Fig. 3. ROC curve for various MVA methods used as VE$_{PMF}$ (25%) classifiers (left), and cut efficiencies and optimum cut value for BDT method evaluating (right) on the basis of meteorological data only.

Table 2
The best performing MVA methods for alarm triggering value (25%) and level of caution (40%) forecasting (10% of background inhibition in signal).

Sources	M–IG–Prev[a]		M–IG		M–Prev		M	
	Method	Sig. eff.	Met.	Sig. eff.	Met.	Sig. eff.	Method	Sig. eff.
VE_{PMF2} (25%)	MLPBNN	0.997 (04)	BDT	0.999 (01)	BDT	0.814 (32)	BDT	0.813 (32)
	BDT	0.989 (08)	LD	0.986 (09)	SVM	0.783 (34)	BDTG	0.755 (35)
VE_{Unmix} (25%)	LD	0.890 (25)	BDT	0.853 (29)	BDT	0.743 (36)	BDT	0.686 (38)
	BDT	0.885 (26)	SVM	0.845 (29)	SVM	0.743 (36)	BDTG	0.656 (39)
PC_{PMF} (25%)	BDT	0.859 (29)	BDT	0.769 (35)	BDT	0.832 (31)	BDT	0.621 (41)
	LD	0.894 (26)	MLPBNN	0.730 (37)	LD	0.861 (29)	BDTG	0.642 (40)
PC_{Unmix} (25%)	BDT	0.841 (30)	MLPBNN	0.855 (29)	BDT	0.801 (33)	BDT	0.661 (39)
	LD	0.875 (27)	BDT	0.787 (33)	LD	0.831 (31)	BDTG	0.707 (37)
VE_{PMF2} (40%)	MLPBNN	0.988 (07)	MLPBNN	0.999 (01)	BDT	0.700 (29)	BDT	0.677 (30)
	BDTG	0.975 (10)	BDT	0.977 (09)	BDTG	0.683 (30)	BDTG	0.623 (31)
VE_{Unmix} (40%)	BDT	0.797 (26)	BDT	0.787 (26)	BDT	0.650 (31)	BDTG	0.540 (32)
	SVM	0.795 (26)	MLPBNN	0.825 (24)	SVM	0.600 (32)	BDT	0.575 (32)
PC_{PMF} (40%)	BDT	0.866 (22)	BDT	0.760 (27)	BDT	0.847 (23)	BDT	0.650 (31)
	LD	0.855 (23)	BDTG	0.757 (28)	Fisher	0.833 (24)	MLPBNN	0.593 (32)
PC_{Unmix} (40%)	BDT	0.852 (23)	BDT	0.757 (28)	BDT	0.826 (24)	BDTG	0.691 (30)
	SVM	0.830 (24)	BDTG	0.727 (29)	SVM	0.803 (26)	BDT	0.626 (31)

[a] Input variables: M — meteorological parameters, IG — inorganic gaseous pollutants, Prev — MVA method had information of forecast for previous hours.

The estimation of classification method performances was done using the Receiver Operating Characteristic (ROC) curve (Fig. 3, left). The method with the largest integral is considered the best performing method, provided that signal efficiency is high (close to 1), and the highest possible background rejection (the significant distinction between background levels and predicted source contributions) is achieved. In general, better performance was observed when both meteorological and IG concentrations were used (Table 2). As regards VE_{PMF2}, the predicted contributions and background were almost completely separated when using both input variables, whereas BDT method based on meteorological data only, exhibited the best performance for prediction of higher values (Fig. 4). In comparison to this, somewhat poorer method predictions were obtained for VE_{Unmix}, PC_{PMF} and PC_{Unmix}. This could suggest that certain variables which were not used as input data would assist to improve the predictive method performances.

As shown in Fig. 3 (right), the optimum cut value was determined on the basis of the value of significance. The comparison of method performance is conducted by evaluating signal efficiencies (Table 2). Thereby, more accurate predictions are obtained in cases where hysteresis-like curves, formed by source contribution and background efficiency curves, cover large area.

If only 10% of signal background inhibition is allowed for predictions based on meteorology and IG concentrations, all episodes of high VE_{PMF2} contribution would be properly identified as alarm triggering values (Table 2). However, if only meteorological data were used, the percentage of the accurately identified alarm triggering values decrease to 81%.

The prediction of industry-related pollution episodes was efficient for both resolved profiles, PC_{PMF} and PC_{Unmix}, although the negligibly better solution was obtained for PC_{Unmix} predicted on the basis of meteorological data only.

Table 2 shows that certain MVA methods are capable of forecasting the source contribution values which are considered to require the increased level of caution. The overall performance was satisfying, while the methods using meteorological and IG concentration data provided more accurate predictions.

According to the results, the forecast of vehicle exhaust-related pollution was more precise when using PMF-derived source contributions for classification. As regards industry-related pollution, the results are not straightforward to interpret. In case that MVA method had information of forecast for previous hours, most accurate prediction was mainly obtained for PMF source contributions, whereas in the case of forecast relying on input data exclusively, most accurate prediction was predominantly obtained for Unmix source contributions.

3.2. Regression MVA methods

Regression MVA methods were applied to interpret the dependency of the source contributions on the examined meteorological data, and both meteorological data and IG concentrations. As described in previous section, the statistical relationships were examined and certain number of variables was excluded from the input dataset.

Median and standard deviations were calculated respectively to be: 1.05 and 1.30 for VE_{PMF2}, 1.03 and 0.94 for VE_{Unmix}, 1.02 and 0.86 for
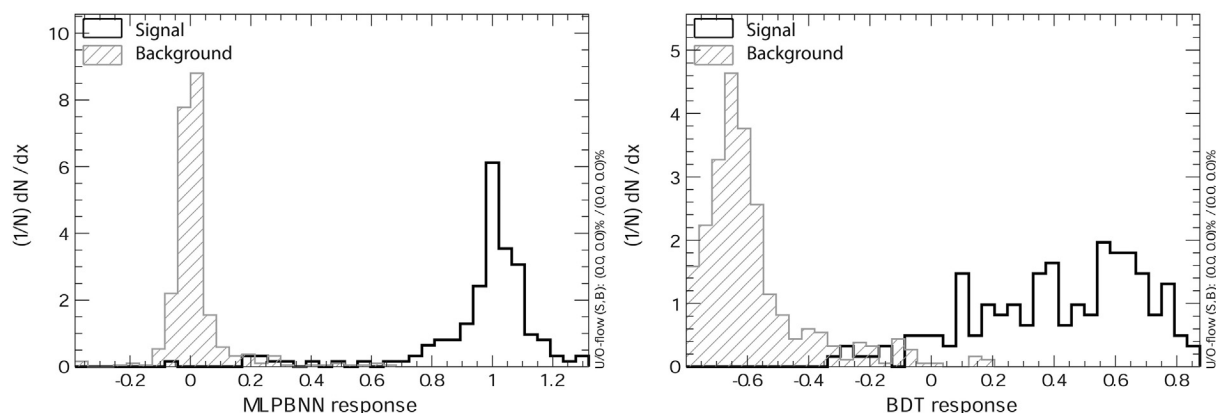

Fig. 4. VE_{PMF2} TMVA response for classifiers: MLPBNN (left) and BDT (right). Meteorological parameters and inorganic gaseous pollutant concentrations were used as input data.

Table 3
Absolute errors of best performing regression methods.

Target	M–IG–Prev		M–IG		M–Prev		M	
	Value	Method	Value	Method	Value	Method	Value	Method
VE_{PMF2}	0.07	BDTG	0.06	MLP	0.25	BDT	0.35	BDT
VE_{PMF2}	0.08	c_LD	0.07	c_LD	0.35	c_BDTG	0.48	c_BDTG
VE_{Unmix}	0.22	BDT	0.22	c_BDTG	0.24	c_BDT	0.29	BDTG
VE_{Unmix}	0.22	c_MLP	0.25	LD	0.29	BDTG	0.41	BDT
PC_{Unmix}	0.18	LD	0.32	c_BDTG	0.24	LD	0.35	c_BDTG
PC_{Unmix}	0.23	c_BDT	0.37	BDT	0.26	MLP	0.44	BDT
PC_{PMF}	0.26	LD	0.34	BDT	0.31	LD	0.43	BDT
PC_{PMF}	0.31	c_BDT	0.42	c_MLP	0.33	c_BDTG	0.45	c_BDTG

PC_{PMF}, and 1.02 and 0.95 for PC_{Unmix}. Low absolute errors obtained for the best performing regression methods (Table 3) indicate that source contributions were successfully evaluated, particularly when both meteorological and IG were used as input data. The same conclusion can be drawn from Fig. 5, in which PC_{Unmix} and VE_{PMF2}-derived source contributions and variations predicted using regression methods produce almost identical time-series plot. In contrast to this, VE_{Unmix} appears to be more robust to changes in input variables, which suggests that it is less dependent on meteorological data. Similar to classification methods, most successful regression methods are the BDT and MLP based. In some MVA methods, corrections were done to adjust linear regression coefficients between source contributions and evaluated
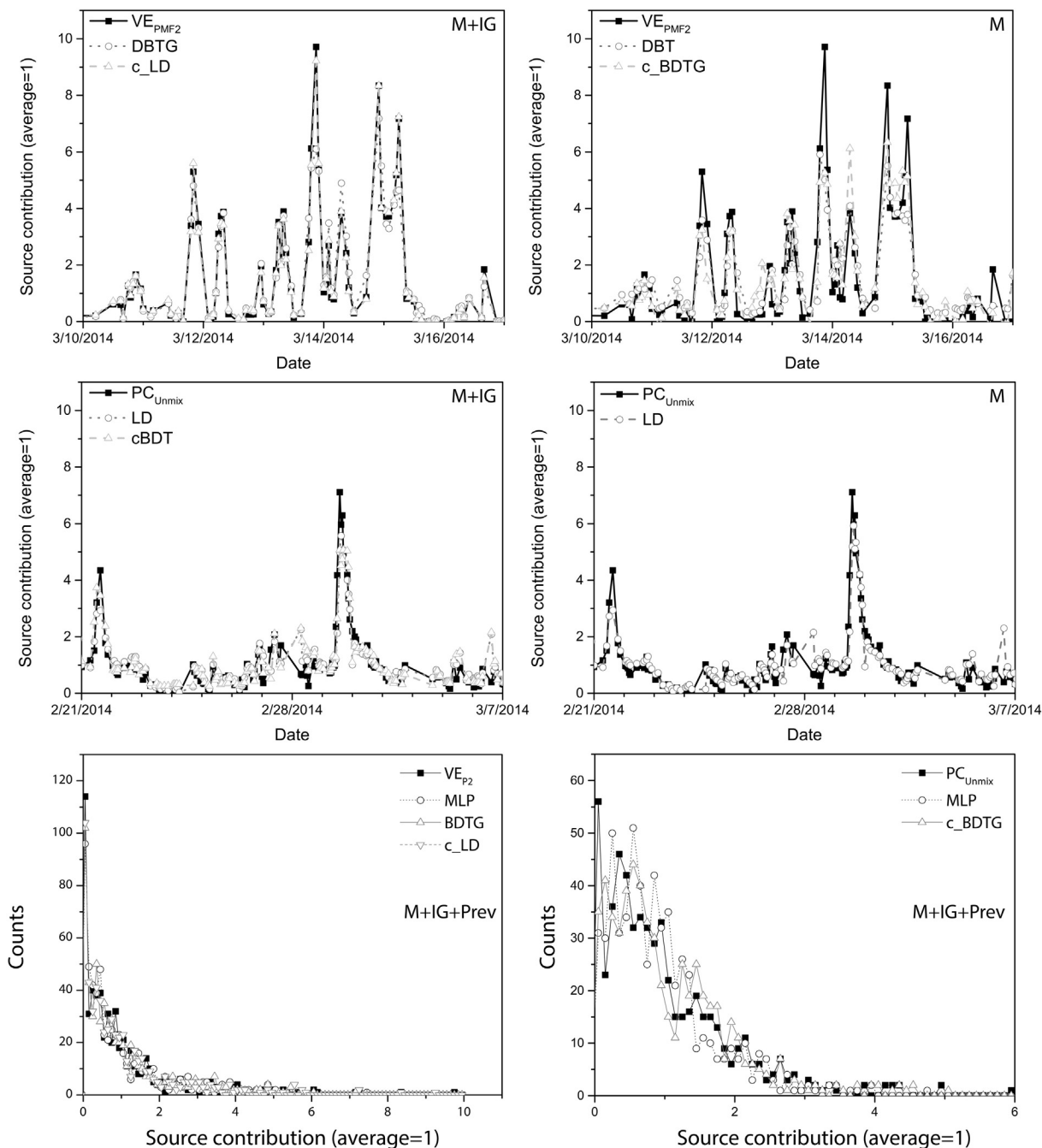

Fig. 5. The comparison of receptor model-derived normalized source contributions and contributions obtained by the use of the best performing MVA methods. Meteorological parameters and inorganic gaseous pollutant concentrations (M + IG), meteorological parameters (M) and previously predicted source contribution values (Prev) are used as input data.

values to be closer to 1, using test samples only. If corrections are done using training sample, evaluated values can be considered as extension of training process. The MVA methods corrected this way are presented with prefix "c_".

As previously mentioned, the predictions based on meteorological data exclusively were less accurate, although still satisfying. In this case, minor differences in time-series plots of source contributions and regression method predictions as well as higher absolute errors were observed, particularly for PC_{PMF}. In general, forecasting of industry-related contributions is more accurate when both meteorological data and IG concentrations were used (Fig. 5, middle).

In addition to previously mentioned indicators, the similarity of source contribution and evaluated values confirms that presented methods may become an efficient tool for forecasting of source contributions (Fig. 5, below).

Finally, it should be emphasized that the results are promising in both cases, for forecasting contributions of local origin as in the case of vehicle exhaust, as well as for forecasting contributions which are to certain extent (25%) associated with regional transport as in the case of industry-related source. Related to this, it can be assumed that slightly lower performance of MVA methods in the case of industry-related contribution forecast is probably associated with the impact of transported pollution.

4. Conclusion

Given the fact that timely information on occurrence of dangerous air pollutant levels is very important for prevention of human health damage, particularly for the protection of vulnerable categories of people, design and implementation of early warning systems is an issue of high relevance in environmental science. The multivariate methods herein presented are capable of identifying emission sources, estimating their contributions and providing reliable prediction of source contribution dynamics which is the most important. In this study, two receptor models, Unmix and PMF, are used for the purpose of VOC source apportionment in Belgrade urban area, and the profiles identified as vehicle exhaust and industrial emissions with contributions ranging from 18 to 28%, are analyzed and compared. Subsequently, classification and regression MVA methods were used for prediction of the source contribution dynamics using registered meteorological parameters and IG as input data. According to the results, all examined methods show satisfying forecast capabilities, in the case of local source contributions as well as of contributions which are to certain extent (25%) associated with regional transport. Thereby, the best regression methods are considered to provide the most accurate prediction of hourly source contributions, closest possible to the receptor model-derived values with relative errors starting from 6%. The use of advanced MVA methods for forecasting of episodes of dangerous pollutant concentrations may support air quality management on a day-to-day basis, although it should be emphasized that, in this case, the reliable public warning highly depends on accurate meteorological forecast.

References

Banks, R.F., Tiana-Alsina, J., Baldasano, J.M., Rocadenbosch, F., 2014. Retrieval of boundary layer height from lidar using extended Kalman filter approach, classic methods, and backtrajectory cluster analysis. SPIE Remote Sensing. International Society for Optics and Photonics (92420 F-92420 F, October).

Bon, D.M., Ulbrich, I.M., de Gouw, J.A., Warneke, C., Kuster, W.C., Alexander, M.L., Vargas, O., 2011. Measurements of volatile organic compounds at a suburban ground site (T1) in Mexico City during the MILAGRO 2006 campaign: measurement comparison, emission ratios, and source attribution. Atmos. Chem. Phys. 11 (6), 2399–2421.

Brun, R., Rademakers, F., 1997. ROOT—an object oriented data analysis framework. Nucl. Instrum. Methods Phys. Res., Sect. A 389, 81–86.

Carslaw, D.C., Ropkins, K., 2012. openair—an R package for air quality data analysis. Environ. Model Softw. 27, 52–61.

Chan, Y.C., Hawas, O., Hawker, D., Vowles, P., Cohen, D.D., Stelcer, E., Simpson, R., Golding, G., Christensen, E., 2011. Using multiple type composition data and wind data in PMF analysis to apportion and locate sources of air pollutants. Atmos. Environ. 45, 439–449.

Chin, J.Y., Batterman, S.A., 2012. VOC composition of current motor vehicle fuels and vapors, and collinearity analyses for receptor modeling. Chemosphere 86, 951–958.

de Gouw, J., Warneke, C., 2007. Measurements of volatile organic compounds in the earth's atmosphere using proton-transfer-reaction mass spectrometry. Mass Spectrom. Rev. 26, 223–257.

Galbally, I.E., Hibberd, M.F., Lawson, S.J., Bentley, S.T., Cheng, M., Weeks, I.A., Gillett, R.W., Selleck, P.W., 2008. A study of VOCs during winter 2006 at Wagerup, Western Australia. Report to Alcoa World Alumina Australia. CSIRO, Aspendale.

Henry, R.C., 1997. History and fundamentals of multivariate air quality receptor models. Chemom. Intell. Lab. Syst. 37, 37–42.

Henry, R.C., 2003. Multivariate receptor modeling by N-dimensional edge detection. Chemom. Intell. Lab. Syst. 65, 179–189.

Hoecker, A., Speckmayer, P., Stelzer, J., Therhaag, J., Von Toerne, E., Voss, H., Backes, M., Carli, T., Cohen, O., Christov, A., Dannheim, D., Danilowski, K., Henrot-Versille, S., Jachowski, M., Kraszewski, K., Krasznahorkay, A., Kruk, M., Mahalalel, Y., Ospanov, R., Prudent, X., Robert, A., Schouten, D., Tegenfeldt, F., Voigt, A., Voss, K., Wolter, M., Zemla, A., 2007. TMVA Users Guide — Toolkit for Multivariate Data Analysis, PoSACAT 040. http://arxiv.org/abs/physics/0703039.

Hopke, P.K., Ito, K., Mar, T., Christensen, W.F., Eatough, D.J., Henry, R.C., Kim, E., Laden, F., Lall, R., Larson, T.V., Liu, H., Neas, L., Pinto, J., Stolzel, M., Suh, H., Paatero, P., Thurston, G.D., 2006. PM source apportionment and health effects: 1. Intercomparison of source apportionment results. J. Expo. Sci. Environ. Epidemiol. 16 (3), 275–286.

Hsieh, C.C., Tsai, J.H., 2003. VOC concentration characteristics in Southern Taiwan. Chemosphere 50, 545–556.

Institute of Public Health in Belgrade, d. http://www.beoeko.com/?page_id=595&stanica=1 (Accessed: 29th August, 2014).

Jobson, B.T., McKeen, S.A., Parrish, D.D., Fehsenfeld, F.C., Blake, D.R., Goldstein, A.H., Schauffler, S.M., Elkins, J.W., 1999. Trace gas mixing ratio variability versus lifetime in the troposphere and stratosphere: observations. J. Geophys. Res. Atmos. 104 (D13), 16091–16113.

Kampa, M., Castanas, E., 2008. Human health effects of air pollution. Environ. Pollut. 151, 362–367.

Lee, S.C., Chiu, M.Y., Ho, K.F., Zou, S.C., Wang, X., 2002. Volatile organic compounds (VOCs) in urban atmosphere of Hong Kong. Chemosphere 48, 375–382.

Lindinger, W., Hansel, A., Jordan, A., 1998. On-line monitoring of volatile organic compounds at pptv levels by means of proton-transfer-reaction mass spectrometry (PTR-MS) medical applications, food control and environmental research. Int. J. Mass Spectrom. Ion Process. 173, 191–241.

Liu, W.T., Hsieh, H.C., Chen, S.P., Chang, J.S., Lin, N.H., Chang, C.C., Wang, J.L., 2012. Diagnosis of air quality through observation and modeling of volatile organic compounds (VOCs) as pollution tracers. Atmos. Environ. 55, 56–63.

Lough, G.C., Schauer, J.J., Lonneman, W.A., Allen, M.K., 2005. Summer and winter nonmethane hydrocarbon emissions from on-road motor vehicles in the Midwestern United States. J. Air Waste Manage. Assoc. 55, 629–646.

Maletić, D.M., Udovičić, V.I., Banjanac, R.M., Joković, D.R., Dragić, A.L., Veselinović, N.B., Filipović, J.Z., 2014. Comparison of multivariate classification and regression methods for the indoor radon measurements. Nucl. Technol. Radiat. Prot. 29, 17–23.

Musselman, R.C., Korfmacher, J.L., 2014. Ozone in remote areas of the Southern Rocky Mountains. Atmos. Environ. 82, 383–390.

Na, K., Kim, Y.P., Moon, I., Moon, K.C., 2004. Chemical composition of major VOC emission sources in the Seoul atmosphere. Chemosphere 55, 585–594.

Paatero, P., Tapper, U., 1994. Positive matrix factorization: a non-negative factor model with optimal utilization of error estimates of data values. Environmetrics 5, 111–126.

Rojas, R., 1996. Neural Networks. Springer-Verlag, Berlin.

Song, Y., Dai, W., Shao, M., Liu, Y., Lu, S., Kuster, W., Goldan, P., 2008. Comparison of receptor models for source apportionment of volatile organic compounds in Beijing, China. Environ. Pollut. 156, 174–183.

Stojić, A., Stojić, S.S., Mijić, Z., Šoštarić, A., Rajšić, S., 2015. Spatio-temporal distribution of VOC emissions in urban area based on receptor modeling. Atmos. Environ. 106, 71–79.

Taipale, R., Ruuskanen, T.M., Rinne, J., Kajos, M.K., Hakola, H., Pohja, T., Kulmala, M., 2008. Technical note: quantitative long-term measurements of VOC concentrations by PTR-MS—measurement, calibration, and volume mixing ratio calculation methods. Atmos. Chem. Phys. 8, 6681–6698.

Team, R.C., 2012. R: a language and environment for statistical computing. http://cran.case.edu/web/packages/dplR/vignettes/timeseries-dplR.pdf (Accessed: 4th April, 2014).

Thornhill, D.A., Williams, A.E., Onasch, T.B., Wood, E., Herndon, S.C., Kolb, C.E., Marr, L.C., 2010. Application of positive matrix factorization to on-road measurements for source apportionment of diesel-and gasoline-powered vehicle emissions in Mexico City. Atmos. Chem. Phys. 10 (8), 3629–3644.

USEPA, 2007. EPA Unmix 6.0 Fundamentals and User guide. USEPA Office of Research and Development.

USEPA, 2008. EPA Positive Matrix Factorization (PMF) 3.0 Fundamentals and User guide. USEPA Office of Research and Development.

Wang, Y.Q., 2014. MeteoInfo: GIS software for meteorological data visualization and analysis. Meteorol. Appl. 21, 360–368.

Yang, H.J., Roe, B.P., Zhu, J., 2005. Studies of boosted decision trees for MiniBooNE particle identification. Nucl. Instrum. Methods Phys. Res., Sect. A 555, 370–385.

Zhu, L., Huang, X., Shi, H., Cai, X., Song, Y., 2011. Transport pathways and potential sources of PM_{10} in Beijing. Atmos. Environ. 45, 594–604.

PHOTO ACTIVATION OF 391.69 keV ISOMER STATE OF ^{113m}In BY $(\gamma, 2n)$ REACTION

Z. Medic^2, M. Krmar^1, N. Jovancevic^1, D. Maletic^2, Y. Teterev^3, S. Mitrofanov^3

^{1}*Physics Department, Faculty of Sciences,*
University of Novi Sad, Novi Sad, Serbia
^{2} *Institute of Physics, Belgrade, Serbia*
^{3} *Flerov Laboratory of Nuclear Reactions,*
Joint Institute for Nuclear Research, Dubna, Russia

Natural indium targets were exposed to high energy bremsstrahlung radiation, from 9 MeV to 23 MeV. Using the measured gamma spectra, the yield ratio of ^{113m}In and ^{115m}In was determined. It was checked to what extent the measured values of the yield ratio can be reproduced using the existing experimental data of cross-sections of relevant photonuclear reactions, as well as cross-sections obtained by TALYS calculations. The measured reaction yield ratio was used to reconstruct the energy differential cross section of $^{115}In(\gamma, 2n)^{113m}In$ using the unfolding procedure.

PACS numbers: 25.20.âĽŠx, 24.10.âĽŠi,07.85.Nc, 27.60.+j

I. INTRODUCTION

Photonuclear reactions are appealing phenomena that occur when external radiation interacts with the nucleus through electromagnetic forces, without involving the nuclear force. The theoretical understanding of this phenomenon, particularly the Giant Dipole Resonance (GDR), has been relatively successful [1]. As experimental techniques advanced, systematic data collection was initiated, primarily focusing on (γ, n) nuclear reactions. In these reactions, the nucleus releases excitation energy by emitting one neutron after interacting with electromagnetic radiation. A comprehensive systematic dataset [2] exists in the form of energy differential cross sections for these reactions. However, there is a scarcity of experimental data for $(\gamma, 2n)$ reactions, and for (γ, xn) reactions involving more than two emitted neutrons. Energy differential cross sections are only available through theoretical estimation. Numerical codes, such as TALYS 1.9 [3], have been developed to estimate cross sections for various nuclear reactions based on theoretical assumptions.

Indium photoactivation, involving (γ, n) as well as (γ, γ') reactions, has been a subject of extensive research. Despite this, uncertainties persist regarding the photoexcitation of the ^{115m}In isomeric state, leading to variations in measured cross sections among different authors. To date, only one set of experimental measurements for the energy differential cross section of the $^{115}In(\gamma, 2n)^{113m}In$ reaction has been published, dating back over 60 years [4]. Cross section estimates for this reaction obtained using the TALYS 1.9 code differ slightly depending on the choice of functions describing the level density and radiation strength function.

This paper aims to compare the relative yields of the $^{115}In(\gamma, 2n)^{113m}In$ reaction measured at several energies with calculated ones. Available cross-sectional data, both experimental and estimated using TALYS 1.9 were used. Furthermore, we will attempt to reconstruct the energy differential cross section for this reaction based on unfolding technique.

II. THE METHOD

Natural indium consists of two isotopes, ^{115}In (95.7%) and ^{113}In (4.3%). In high-energy photon beams with energies below 16.3 MeV, the only method to excite ^{113}In to its long-lived excited state at 391.69 keV is through the $^{113}In(\gamma, \gamma')^{113m}In$ reaction. However, when the photon energy exceeds 16.3 MeV, the $^{115}In(\gamma, 2n)^{113m}In$ nuclear reaction becomes dominant. Consequently, the formation of ^{113m}In can occur via two distinct reactions, and the total activity produced during irradiation is a result of the combined contribution of both of them. The probabilities of these mentioned reactions are determined by cross sections, denoted as $\sigma_{\gamma,2n}^{115}$ for $^{115}In(\gamma, 2n)^{113m}In$ and $\sigma_{\gamma,\gamma'}^{113}$ for $In(\gamma, \gamma')^{113m}In$, where the atomic number of the parent nuclei is indicated as a superscript. The yield of ^{113m}In can be expressed as follows:

$$Y(^{113m}In) = \frac{m_t}{M}N_{av}(0.957\int_{E_t^{\gamma,2n}}^{E_{max}}\sigma_{\gamma,2n}^{115}(E)\Phi(E)dE+$$
$$+0.043\int_{E_t^{\gamma,\gamma}}^{E_{max}}\sigma_{\gamma,\gamma}^{113}(E)\Phi(E)dE)$$

$$(1)$$

where the mass of the exposed target is denoted by m_t, M is the mass number and N_{av} is Avogadro's number. $E_t^{\gamma,2n}$ and $E_t^{\gamma,\gamma}$ are energy thresholds for the $^{115}In(\gamma, 2n)^{113m}In$ and $^{113}In(\gamma, \gamma')^{113m}In$ reactions respectively. The maximum energy of photons is denoted by E_{max}, and the flux of incident photons is $\Phi(E)$. The

integrals in Equation 1 are commonly referred to as "saturation activity."

After irradiation, the gamma spectra of the indium target should be recorded. The yield of ^{113m}In can then be calculated by analyzing the intensity of the 391.69 keV gamma line:

$$Y(^{113m}In) =$$
$$= \frac{N_\gamma(391)\lambda_{113}}{\epsilon(391)p_\gamma^{391}e^{-\lambda_{113}\Delta t}(1 - e^{-\lambda_{113}t_{irr}})(1 - e^{-\lambda_{113}t_m})} \quad (2)$$

where N_γ is detected number of 391.69 keV gamma photons, λ_{113} is decay constant of ^{113m}In, ϵ is the detector's efficiency at the observed energy. The quantum yield of the 391.69 keV transition is denoted by p_γ^{391}, and Δt, t_{irr}, and t_m represent the cooling, irradiation, and measurement times, respectively.

The processing of the data obtained in the experiment can be significantly simplified by observing the relative yield of ^{113m}In. The optimal procedure involves normalizing the yield of ^{113m}In with the yield of some other isotope obtained from the same target and measured at the same time. The most suitable candidate for normalization is ^{115m}In, which forms through the photoactivation of the isomer state at 336.24 keV. The yield ratio of ^{113m}In and ^{115m}In can be expressed as follows:

$$\frac{Y(^{113m}In)}{Y(^{115m}In)} = \frac{\int_{E_{th}^{\gamma,2n}}^{E_{max}} \sigma_{\gamma,2n}^{115}(E)\Phi(E)dE}{\int_{E_{th}^{\gamma,\gamma}}^{E_{max}} \sigma_{\gamma,\gamma}^{115}(E)\Phi(E)dE} +$$
$$+ \frac{0.043 \int_{E_{th}^{\gamma,\gamma}}^{E_{max}} \sigma_{\gamma,\gamma}^{113}(E)\Phi(E)dE}{0.957 \int_{E_{th}^{\gamma,\gamma}}^{E_{max}} \sigma_{\gamma,\gamma}^{115}(E)\Phi(E)dE} \quad (3)$$

The cross-section for the $^{115}In(\gamma,\gamma')^{115m}In$ reaction is denoted as $\sigma_{\gamma,\gamma'}^{115}$. Experimental data for this cross-section, which are not always consistent, can be found in databases [5], along with the cross-section for the $^{113}In(\gamma,\gamma')^{113m}In$ reaction.

The advantage of this approach is that no absolute photon flux is necessary. For the numerical procedure, only the shape of the photon spectra is required. It can be derived by simulation for a known geometry of bremsstrahlung production.

The experimentally obtained yield ratio of ^{113m}In to ^{115m}In can be expressed as follows:

$$\frac{Y(^{113m}In)}{Y(^{115m}In)} = \frac{N_\gamma(391)}{N_\gamma(336)} \frac{\lambda^{113}}{\lambda_{115}} \frac{\epsilon(336)}{\epsilon(391)} \frac{p_\gamma^{336}}{p_\gamma^{391}} \cdot$$
$$\cdot \frac{e^{-\lambda_{115}\Delta t}(1 - e^{-\lambda_{115}t_{irr}})(1 - e^{-\lambda_{115}t_m})}{e^{-\lambda_{113}\Delta t}(1 - e^{-\lambda_{113}t_{irr}})(1 - e^{-\lambda_{113}t_m})} \quad (4)$$

All quantities in Equation (4) with the "336" index or "115" subscript have the same meaning as explained in Equation 2, describing the decay of ^{115m}In. Importantly, this approach does not require the absolute value of the detector efficiency; instead, relative efficiency can be used.

Using the measured intensities of the corresponding gamma lines in collected gamma spectra, the experimental values of the $Y(^{113m}In)/Y(^{115m}In)$ yield ratio can be determined (Eq. 4). With the estimated shape of the photon bremsstrahlung spectra $\Phi(E)$, the same $Y(^{113m}In)/Y(^{115m}In)$ yield ratio can be obtained from Equation 3, using theoretical or available experimental cross sections for observed photonuclear reactions. There are two ways in which Equation 3 and Equation 4 can be applied in the context of studying the photoactivation of ^{113}In:

1. For several selected energies of the photon beam (denoted as E_{max}), which are higher than the threshold for the $(\gamma, 2n)$ reaction, the yield ratios of $Y(^{113m}In)/Y(^{115m}In)$ can be determined using the obtained gamma spectra. Numerical codes like TALYS 1.9 can provide estimates of the cross sections for all three reactions in Equation 3. Using the known experiment geometry, the shape of the photon flux $\Phi(E)$ can be obtained by simulation, as well as the integrals (saturation activities) appearing in Equation 3. Based on calculated $Y(^{113m}In)/Y(^{115m}In)$ yield ratios, conclusions can be drawn regarding the model assumptions' capacity (level density and radiation strength function) to reproduce the experimental yields.

2. Cross sections corresponding to the three saturation activities in Equation 3 can be found in databases. It can be used to estimate the yield ratio and compare it with the obtained measurement results, providing an additional assessment of the relevance of the existing experimental values of the observed reactions' cross sections. It should be noted that for $^{115}In(\gamma,\gamma')$ and $^{113}In(\gamma,\gamma')$, measurements of cross sections were not conducted in the entire energy region covered by this experiment.

3. If the yield ratio of $Y(^{113m}In)/Y(^{115m}In)$ is determined for several different energies above the 16.3 MeV threshold, the cross section for the $^{115}In(\gamma,2n)^{113m}In$ reaction can be determined using a suitable unfolding algorithm. It is noteworthy that only one available result of the $^{115}In(\gamma,2n)^{113m}In$ cross section measurement dates back more than sixty years ago [4].

III. MEASUREMENTS

A. Irradiation

The irradiation was carried out using MT25 Microtron [6] located in Flerow Laboratory of Nuclear reactions, JINR, Dubna. Technical details concerning used device

and irradiation procedure are described in couple of previous publications [7].

Indium disks were exposed to bremsstrahlung with endpoint energies from 9 MeV to 23 MeV in steps of 1 MeV. For the photon production a 1 mm thick tungsten radiator was used. The distance between the the tungsten radiator and an indium disk was 136 cm. The scheme of the experimental setup is presented in the Figure 1.
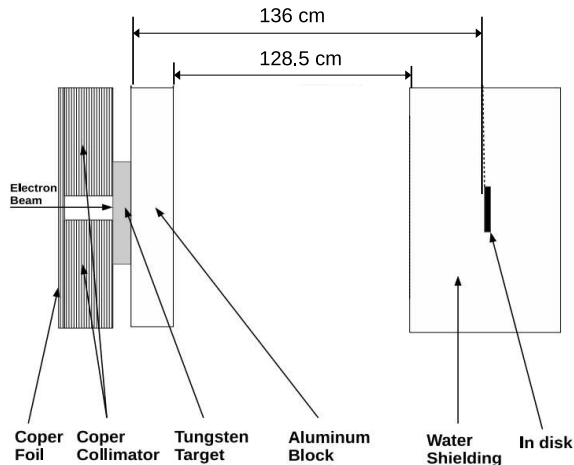

FIG. 1: Geometry of experimental setup (not in scale).

When high-energy photons interact with a tungsten target, fast neutrons are inevitably produced. The number of neutrons created is highly dependent on the maximum bremsstrahlung energy. It was observed that the saturation activity of ^{116m}In, produced by neutron capture, was about 130 times higher at a photon energy of 23 MeV than at the endpoint energy of 10 MeV. The influence of ^{115m}In production by inelastic neutron scattering, ^{115}In(n,nâĂŹ)^{115m}In, especially at high photon energies was minimized by placing the indium disks at the center of a water container with a diameter of 15 cm. In this manner, fast neutrons resulting from photo-nuclear reactions in tungsten were thermalized. The necessity for this action was confirmed by noting a noticeable difference in ^{115m}In activity between exposures with and without water surrounding the indium disk. A 15% higher saturation activity of ^{115m}In was observed when the disk was exposed outside the water container at a maximum photon energy of 23 MeV, compared to the saturation activity when the disk was positioned inside the water container.

The irradiation times and intensities of bremsstrahlung beams (the integral numbers of accelerated electrons striking tungsten target Q) are presented in Table I.

TABLE I: Irradiation characteristics for each indium disk: m- mass of disk, E_{max}- bremsstrahlung endpoint energy, Q - integral number of electrons striking tungsten target, t_{irr} - time of irradiation

Disk No.	m[g]	E_{max} [MeV]	Q [mAs]	t_{irr} [s]
1	0.7711	9.00(5)	7000	1800.0(5)
2	0.6317	10.00(5)	6000	1800.0(5)
3	0.6813	11.00(5)	6000	1800.0(5)
4	0.6545	12.00(5)	6000	1800.0(5)
5	0.6533	13.00(5)	2700	1800.0(5)
6	0.6317	14.00(5)	2767	1800.0(5)
7	0.6685	15.00(5)	4000	1800.0(5)
8	0.6685	16.00(5)	4000	1800.0(5)
9	0.6813	17.00(5)	2700	1680.0(5)
10	0.6531	18.00(5)	2700	960.0(5)
11	0.6758	19.00(5)	2700	2100.0(5)
12	0.7233	20.00(5)	2700	1600.0(5)
13	0.7194	21.00(5)	3200	1600.0(5)
14	0.6778	22.00(5)	4000	1600.0(5)
15	0.7202	23.00(5)	3500	1600.0(5)

B. Gamma spectroscopy measurements

After the exposition, the Indium coins were measured using an HPGe detector with a relative efficiency of 25% and shielded by 5 cm of lead. The irradiated Indium samples were placed directly on the vertical dipstick of the detector. The time between the end of irradiation and the start of measurement varied from 34 minutes to 221 minutes, depending on the activity of the exposed Indium coins and the availability of the detector.

The cooling time for the samples irradiated at high energies was longer because the activity of ^{116m}In, resulting from an increasing number of neutrons in the vicinity of the Microtron, significantly exceeded the activity of ^{115m}In and ^{113m}In. Considering that the half-life of ^{116m}In ($T_{1/2}$ = 54.41 minutes) is shorter than the half-lives of ^{115m}In ($T_{1/2}$ = 4.468 hours) and ^{113m}In ($T_{1/2}$ = 1.658 hours), measurements were taken after the activity of ^{116m}In had decreased to ensure low levels of dead time (up to 2%). Each Indium sample was measured for a duration of 30 minutes.

In all recorded spectra, a prominent 336.24 keV gamma line, produced by the de-excitation of the isomer state of ^{115m}In, was observed. However, the gamma line of ^{113m}In (391.69 keV) was very weak at low endpoint energies of the photon beam, and in some spectra, it exhibited a statistical uncertainty of up to 45%. Above 17 MeV energies, there was a rapid increase in the intensity of the 391.69 keV gamma line as the ^{115}In$(\gamma, 2n)^{113m}$In reaction began to take place.

Furthermore, several strong gamma lines emitted after the decay of ^{116m}In, produced by neutron capture of ^{115}In, were visible in all recorded spectra. These gamma lines were used to calculate the relative detection efficiency for the applied counting geometry. The relative efficiency was obtained using a combination of exponen-
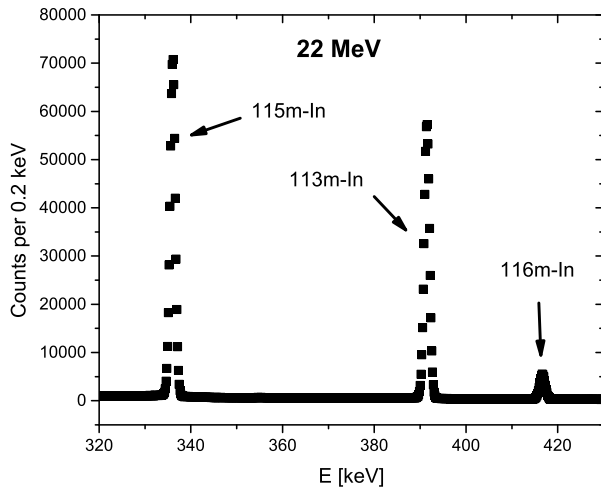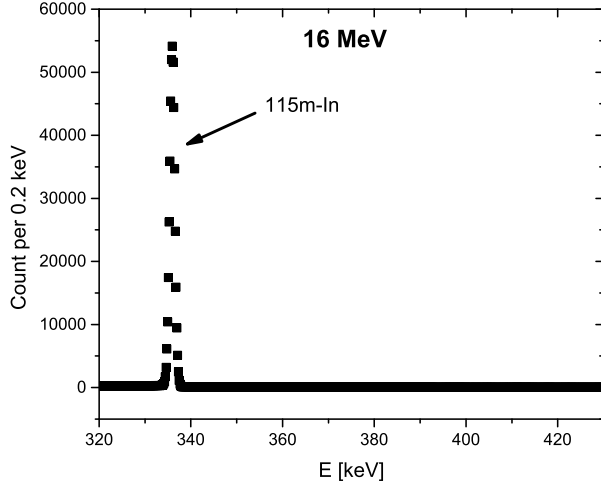
FIG. 3: Experimentally obtained relative yields $\frac{Y(^{113m}In)}{Y(^{115m}In)}$.

FIG. 2: Part of the γ-ray spectra collected after irradiation with 16 MeV and 22 MeV beams. The γ lines of interested are labelled. Energy width of one channel is 0.2 keV.

tial and second-order polynomial functions. The GENIE 2000 software was employed to extract the intensities of the observed gamma lines. Parts of detected of gamma spectra are presented in Figure 2.

C.   Determination of relative yield

The intensities of the 336.24 keV and 391.69 keV gamma lines were determined in all the recorded spectra. To obtain relative yields for all the used photon energies, Equation 4 was applied. The results obtained from this analysis are presented in Figure 3.
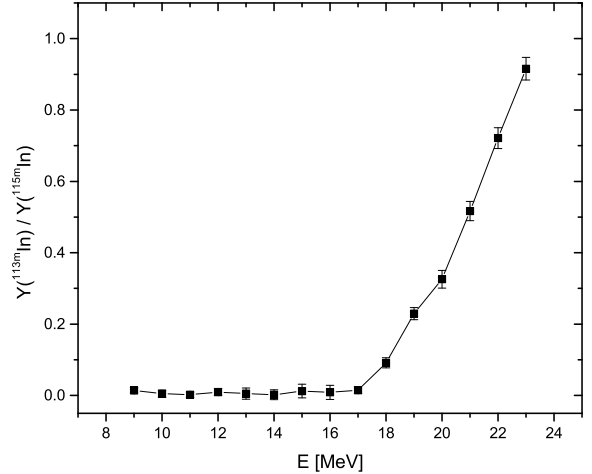
Based on the data depicted in Figure 3, it is evident that the relative yield, as defined by Equation 3, remains approximately constant over a wide range of energies, up to the threshold for the $^{115}In(\gamma, 2n)^{113m}In$ reaction. However, beyond this energy threshold, the yield ratio starts to increase rapidly.

In the lower energy region, up to 17 MeV, the activity of ^{113m}In is solely attributed to the photo activation of the isomeric state $(^{113}In(\gamma, \gamma')^{113m}In$ reaction), as described by the second term in Equation 3. The mean value of the relative yield in the energy range from 9 MeV to 16 MeV was found to be 0.039(4).

To investigate whether this trend of the yield ratio between the photo activation of ^{113}In and ^{115}In isomeric states persists at higher energies, TALYS 1.9 estimations of cross sections for the $^{113}In(\gamma, \gamma)^{113m}In$ and $^{115}In(\gamma, \gamma)^{115m}In$ reactions were calculated. The values of the second term in Equation 3 were then determined for the energy range from 18 MeV to 23 MeV. Multiple models of level density were used for this test, and remarkably consistent results were obtained. For instance, with the TALYS 1.9 levle density model 1 (constant temperature Fermi-gas model) and GLO (Kopecky-Uhl-generalized Lorentzian) model for the strength function, the second term in Equation 3 varied between 0.0386 and 0.0388 in the mentioned energy range. Consequently, it can be inferred that the contribution of the second term in Equation 3 remains constant throughout the entire energy interval depicted in Figure 3, with the mean value of 0.039(4) serving as a reliable estimation.

The $Y(^{113m}In)/Y(^{115m}In)$ ratio was adjusted using this value, and subsequently, the analysis focused on the first term in Equation 3. In this simplified form, the corrected yield ratio reduces to the ratios of the saturation activities of the $^{115}In(\gamma, 2n)^{113m}In$ and

$^{115}In(\gamma,\gamma`)^{115m}In$ reactions.

D. Determination of photon flux

The calculation of relative yield Eq. 1 require knowing of bremsstrahlung photon spectra. For that purpose it was used Monte Carlo (MC) simulations.

To estimate the flux of incident photons $\Phi(E)$ for the six used energies we employed Geant4 (G4) version 10.05.p01 [8] with the experimental Physics list QBBC. QBBC uses the standard G4 electromagnetic physics option without optical photon simulations and, the hadronic part of this physics list consists of elastic, inelastic, and capture processes. Each hadronic process is built from a set of cross sections and interaction models, which provide the detailed physics implementation. The simulated photon spectra are depicted in Fig. 3.
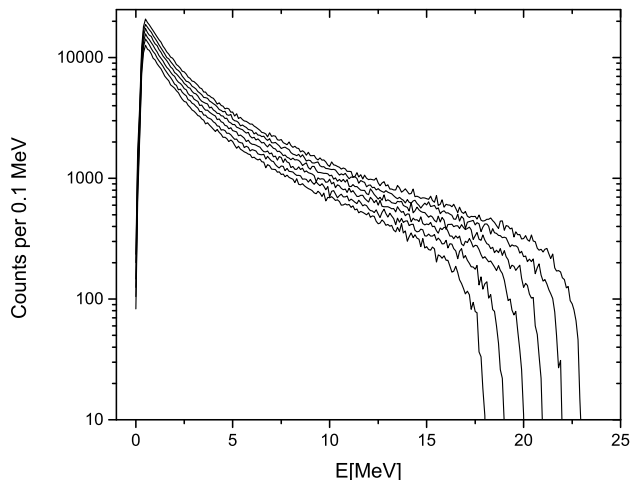

FIG. 4: Spectra of photon flux on the indium disks for electrons energies between 18 MeV and 23 MeV incident on the tungsten radiator. The electron energy corresponds to the end-point energy of the respective photon-flux spectrum (E_{max} in the table I.)

IV. RESULTS AND DISCUSSION

As it was mentioned in The Method section, the set of obtained experimental data gives us two possibilities: A) to check whether the theoretical and experimental cross-section values of the observed photonuclear reactions can reproduce the obtained results of measurement and B) to reconstruct the cross-section for $^{115}In(\gamma,2n)^{113m}In$ reaction.

A. Comparison of measured yield ratios with calculated ones

In the analysis of equation 3, we had the advantage of utilizing multiple data sets:

1. Results obtained from TALYS 1.9 calculations for $\sigma_{\gamma,\gamma}^{115}$ and $\sigma_{\gamma,2n}^{115}$.

2. Experimentally derived cross section for the $^{115}In(\gamma,2n)^{113m}In$ reaction.

3. Several measured cross sections for the photo activation of ^{115m}In.

1. $\sigma_{\gamma,\gamma}^{115}$ and $\sigma_{\gamma,2n}^{115}$ estimated by TALYS 1.9

For the first check, TALYS 1.9 estimates of the cross sections of the observed reactions were chosen to be used. There were employed two different strength function models, and for each of them, cross sections for all six models describing the level density available in TALYS 1.9 were calculated. Available level density models in the TALYS 1.9 are [9–17]:

- LD model 1. - the constant temperature Fermi-Gas model;

- LD model 2. - the back-shifted Fermi gas model;

- LD model 3. - the generalised super-fluid model;

- LD model 4. - the microscopic level densities based on the Goriely'âĂŸs tables;

- LD model 5. - Hilaire'âĂŸs combinatorial tables;

- LD model 6. - the temperature dependent Hartree-Fock-Bogoliubov model, Gogny force.

The first cross-section estimation was performed using the GLO model for the radiation strength function, just as recommended in reference [18]. The reliability of the obtained results was checked by comparing the TALYS 1.9 results with the experimentally derived cross-section of the $^{115}In(\gamma,\gamma')^{115m}In$ reaction. In this way, different models of the level density yield small differences in the cross-section, but for all of them, it is common that the maximum value of the cross-section is at 9.2 MeV, while the maximum value in the peak ranges from 0.865 mbarn to 1.14 mbarn. In most of the experimental results, the value of the cross-section in the peak is around 1 mbarn. However, in the reference [18], after careful measurements and calculation, it is obtained that the maximum value of the cross-section could exceed 3 mbarn if some other model for the radiation strength function was chosen. For this reason, the decision was made to perform the calculations with cross sections obtained using another model of the strength function, which gives cross sections with a maximum value of around 3 mbarn. The Brink-Axel Lorentzian strength function (BAL) was used. In

this case, the maximum cross-section value is at 9.2 MeV, and six different models of level density give peak values in the range from 2.96 mbarn to 3.66 mbarn. Six cross sections obtained using the GLO model and six cross sections obtained using the BAL model for the strength function are presented in Figure 5.
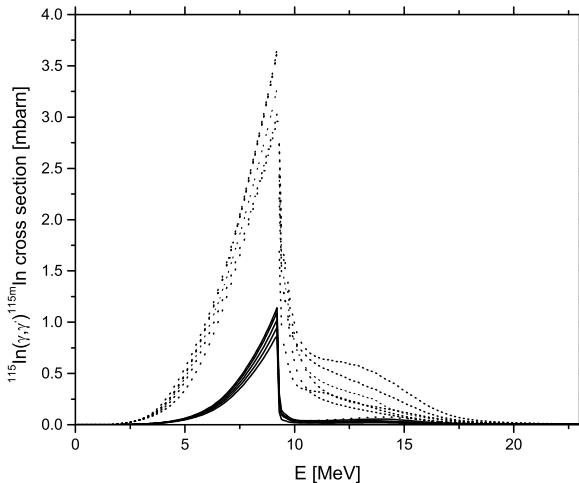

FIG. 5: TALYS 1.9 calculation of cross sections for $^{115}In(\gamma,\gamma)^{115m}In$ reaction obtained using the GLO (solid line) and BAL (dotted line) models for radiation strength function and six models for level density.
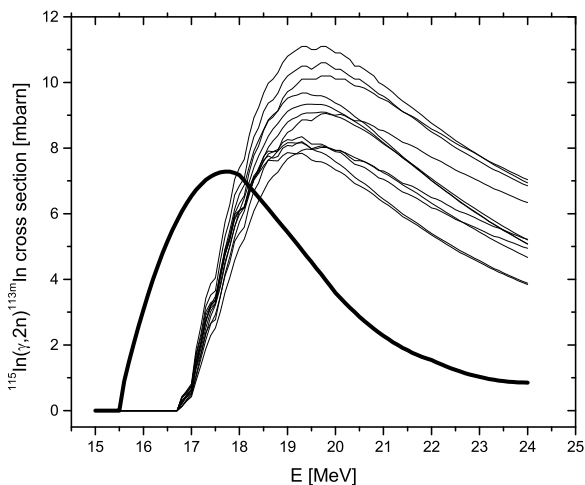

FIG. 6: Tine line - TALYS 1.9 calculation of cross sections for $^{115}In(\gamma,2n)^{113m}In$ reaction obtained using the GLO and BAL models for radiation strength function and six models for level density; the thick line - experimental data from ref. [4]
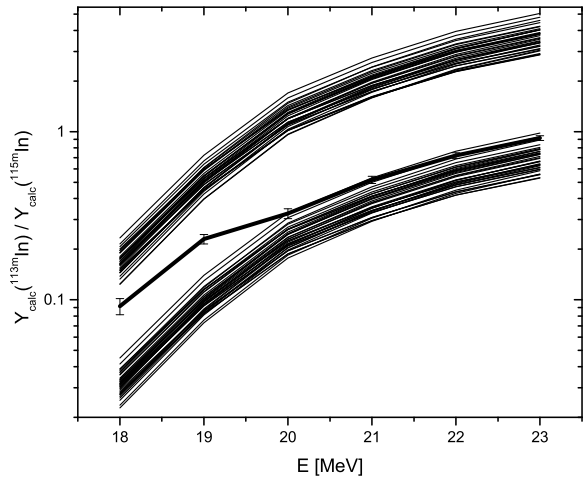

FIG. 7: Comparison of calculated yields $Y(^{113m}In)/Y(^{115m}In)$ using Talys 1.9 results with measured ones presented by thick solid line. The upper band consisting of 36 values of the $Y(^{113m}In)/Y(^{115m}In)$ yield ratio was obtained with the GLO model, while the lower band contains yield values calculated using the BAL model.

The procedure was completely repeated for the $^{115}In(\gamma,2n)^{113m}In$ reaction. Both the GLO and BAL strength function models were chosen, and for each of them, the cross sections with all six level density models were calculated. The results obtained are presented in Figure 6.

From the graphical representation of the TALYS 1.9 cross-section, it can be observed that there is a certain scatter in the shape of the function. However, unlike the case of the $^{115}In(\gamma,\gamma')^{115m}In$ reaction, no distinct separation into two clearly separated groups can be seen. The only existing measured cross section for this reaction [4] is depicted by the thick solid line in the figure 6. A notable observation is that the measured cross-section values significantly differ from the cross sections obtained by TALYS 1.9 calculation.

The integrals (saturation activities) in the first term of Equation 3 were calculated for several endpoint energies ranging from 18 MeV to 23 MeV using the obtained cross sections and G4 photon flux simulations. For each observed energy, six estimates for cross sections (and consequently, six values of saturation activities) were obtained for both the $(\gamma,2n)$ and (γ,γ') reactions using one chosen model of the strength function.

Each saturation activity value obtained using one strength function model, for the $(\gamma,2n)$ reaction was combined with each value for the (γ,γ') reaction, resulting in 36 estimates for one observed energy. The same procedure was repeated for a second model of the strength function, leading to another 36 combinations of satura-

tion activity ratios. The outcomes of these calculations are presented in Figure 7. At first glance, it can be seen that the obtained results of $Y(^{113m}In)/Y(^{115m}In)$ yield ratio are grouped into two bands, each obtained using one strength function. The upper band is obtained using GLO strength function model, while BAL model gives the lower cluster.

It is important to note that the lines in Figure 7, are provided solely as visual aids and do not result from a fit. The experimental results are represented by points and a thick line.

2. TALYS estimate for $\sigma_{\gamma,\gamma}^{115}(E)$ and experimentally determined $\sigma_{\gamma,2n}^{115}(E)$

Available data for the $^{115}In(\gamma,2n)^{113m}In$ reaction cross section $\sigma_{\gamma,2n}^{115}(E)$ can be found in reference [4]. The saturation activities of this reaction were calculated for several endpoint energies from 18 MeV to 23 MeV of the using these cross section and reconstructed photon spectra $\Phi(E)$. Calculations of $\sigma_{\gamma,\gamma}^{115}(E)$ were performed using two different models of strength function, and all six models for level densities. For both groups of six cross section estimates, saturation activities were calculated, in the range between 18 MeV and 23 MeV. Ratios of saturation activities were calculated and obtained values are compared with experimentally derived in Figure 8. Thick solid line connects experimentally derived values $Y(^{113m}In)/Y(^{115m}In)$ ratios of reaction yields. Thin solid lines are obtained using GLO model of strength function, while thin dotted lines represents ratios of saturation activities calculated using cross sections estimated using BAL strength function model. Considering that two groups of cross sections for $\sigma_{\gamma,\gamma}^{115}(E)$ reactions differ significantly in amplitude depending on chosem model of strength function, as can be seen from Figure 5, calculated ratios of reaction yields $Y(^{113m}In)/Y(^{115m}In)$ are grouped in two separated clusters.

3. Experimentally determined both $\sigma_{\gamma,\gamma}^{115}(E)$ and $\sigma_{\gamma,2n}^{115}(E)$

Although there are several published results of measurements of the cross section for the $^{115}In(\gamma,\gamma')^{115m}In$ reaction, none of them fully satisfy the requirements of this study. The primary reason is that the cross sections for the mentioned reaction were not measured across a sufficiently wide energy range. The only paper presenting cross section results at high energies [4] was rejected due to unrealistically high values of the cross section in the 20 MeV region. Consequently, the decision was made to utilize the cross sections published in the reference [19], which demonstrate a reasonable agreement with the TALYS 1.9 estimates.

However, it should be noted that the main limitation of this data set is that the cross sections are only determined up to a maximum energy of 12 MeV. To accommodate
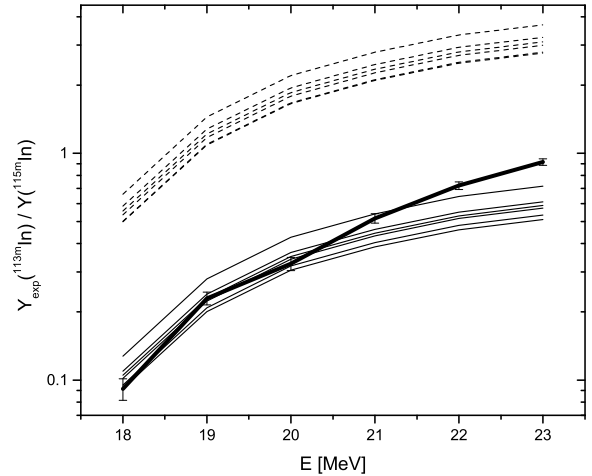

FIG. 8: Comparison of calculated yield ratios $Y(^{113m}In)/Y(^{115m}In)$ using Talys 1.9 results available experimental data [4] with measured ones. Upper band is obtained using GLO model while the lower one is calcilated using BAL model

the analysis, it is assumed that the cross section values in the energy interval from 12 MeV to 23 MeV are not significantly large. Under this assumption, the absence of data in the high-energy region would not have a substantial impact on the value of the saturation activity. Figure 5 reveals that GLO model used for calculating the TALYS 1.9 cross section predicts a very small value of the cross section in the high-energy area.

Similarly, the saturation activity for the $^{115}In(\gamma,2n)^{113m}In$ reaction was calculated using the experimental cross-sectional values published in reference [4]. The calculated values of the yield ratio are then compared with the experimental data in Figure 9.

B. Cross section of $^{115}In(\gamma,2n)^{113m}In$ reaction obtained by unfolding procedure

In this study, we applied the unfolding technique to obtain a more suitable cross section for the $^{115}In(\gamma,2n)^{113m}In$ reaction in the energy range from the reaction threshold up to 23 MeV.

To derive the unfolding values of the phase cross section, the Equation 3 was transformed as follows:

$$A_k = \frac{Y(^{113m}In)}{Y(^{115m}In)} \cdot \int_{E_{th}^{\gamma,\gamma}}^{E_{max_k}} \sigma_{\gamma,\gamma}^{115}(E)\Phi(E)_k dE =$$
$$= \int_{E_{th}^{\gamma,2n}}^{Emax_k} \sigma_{\gamma,2n}^{115}(E)\Phi(E)_k dE \quad (5)$$
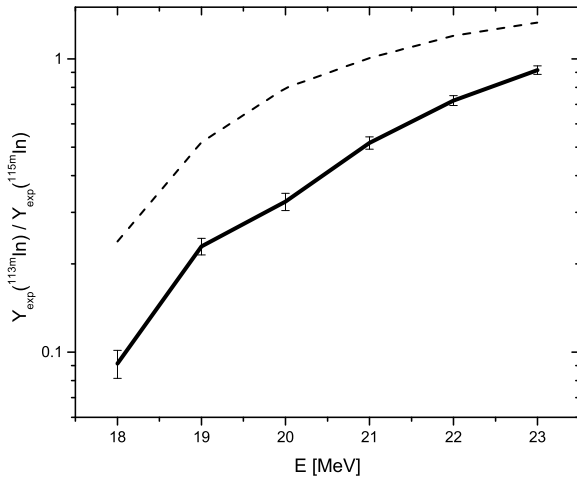
where the index k indicates the number of the irradiated

FIG. 9: Comparison of calculated yield ratios $Y(^{113m}In)/Y(^{115m}In)$ using available experimental data for the $^{115}In(\gamma,\gamma`)^{115m}In$ reaction [19] and $^{115}In(\gamma,2n)^{113m}In$ reaction [4] with measured ones. Results of calculations are connected by dashed line

FIG. 10: Unfolded results for the $^{115}In(\gamma,2n)^{115m}In$ cross-section (line with a corridor of uncertainty) in comparison with default TALYS 1.9 function.

disk and in this case it goes from 1 to 6 for 6 activated energy.

For the unfolding process, the input quantities included $A_k = Y_k(^{113m}In)/Y_k(^{115m}In)$. $\int_{E_{th}^{\gamma,\gamma}}^{E_{max_k}} \sigma_{\gamma,\gamma}^{115}(E)\Phi(E)_k dE$ (saturation activity of $^{115}In(\gamma,\gamma')^{115m}In$ multiplied by experimentally determined reaction yields). In Equation 5, A_k was calculated using the values of the cross section function for the $^{115}In(\gamma,\gamma')^{115m}In$ reaction obtained by TALYS 1.9 calculations using Model 6 for level density and BAL model for radiation strength function. This specific model combination was selected as it demonstrated the best agreement with experimentally determined yields (Fig. 7).

Similarly, in the unfolding procedure for the $^{115}In(\gamma,2n)^{113m}In$ reaction, the starting default function utilized TALYS 1.9 calculations with Model 3 for level density and BAL for radiation strength function, as this combination also provided the best agreement with experimental results (Fig. 7).

The unfolding procedure employed the MAXED algorithm [20], which utilizes input data of measured induced specific saturated activity A_k to derive a function $\sigma(E)$ maximizing the relative entropy S, defined as follows:

$$S = -\int \left(\sigma(E) \ln \left(\frac{\sigma(E)}{\sigma_{def}(E)} \right) + \sigma_{def}(E) - \sigma(E) \right) dE \tag{6}$$

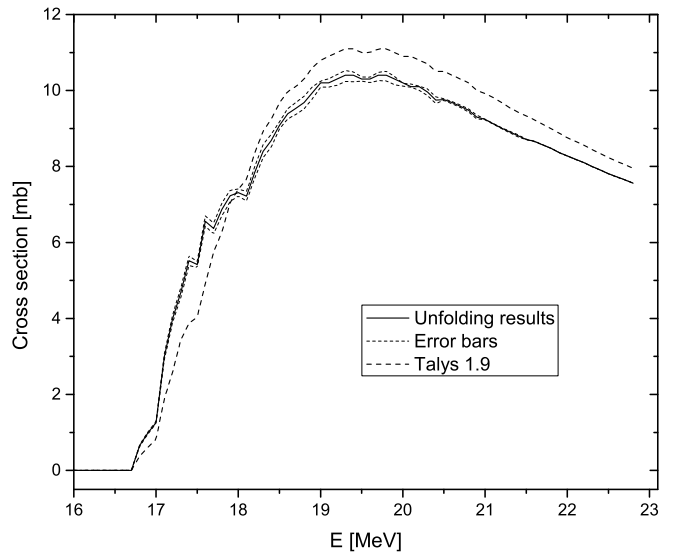Here, $\sigma_{def}(E)$ represents the default cross-section function.

Unfolding procedures were conducted within the energy range of 16 MeV to 22.8 MeV, which was divided into 71 bins. The result obtained by employing the MAXED algorithm is depicted in Figure 10. Corridor of uncertainty was calculated by MAXED algorithm and included influence of uncertainty of A to final cross section values.

To validate the unfolding results, an induced activity $(A_{kc} = \sum \sigma(E_i) \cdot \Phi(E_i) \cdot \Delta E)$ was calculated and then compared with the measured data. This comparison was performed for default cross-section functions and the MAXED results and the sum of the squared of relative deviation σ is calculated as:

$$S = \frac{1}{(k-1)} \sum_1^k \sigma^2 = \frac{1}{(k-1)} \sum_1^k \left(\frac{A_{kc} - A_{ke}}{A_{ke}} \right)^2 \tag{7}$$

The obtained values are $S = 0.13$ for the default spectrum and $S = 0.08$ for the unfolding results. This indicates that the unfolding outcomes provide a better description of the measured experimental data compared to the TALYS 1.9 calculations.

V. DISCUSSION

The first check was conducted by utilizing the cross section values obtained by the TALYS 1.9 code for both reactions, $^{115}In(\gamma,2n)^{113m}In$ and $^{115}In(\gamma,\gamma)^{115m}In$. Each estimate for the $^{115}In(\gamma,2n)^{113m}In$ reaction was combined with each estimate obtained for the $^{115}In(\gamma,\gamma)^{115m}In$ reaction, resulting in 36 distinct values for the saturation activity ratios for a specific strength function choice.

It is evident that the 36 combinations of saturation activity ratios are grouped into two clusters. The lower cluster was obtained using the BAL radiation strength function, which provides higher cross section values for the $^{115}In(\gamma,\gamma')^{115m}In$ reaction, approximately around 3 mbarn. Notably, at energies of 20 MeV and above, the highest estimated ratios of saturation activities align closely with the experimental results. However, at energies below 20 MeV, the experimental values slightly exceed the values obtained based on TALYS 1.9 sections.

On the other hand, the upper cluster comprises 36 combinations of saturation activity ratios obtained using the GLO model for the radiation strength function. It is evident that lower estimations of cross sections for the $^{115}In(\gamma,\gamma')^{115m}In$ reaction, around 1 mbarn, lead to overestimated values of the yield ratio.

In summary, the analysis of these saturation activity ratios obtained through different radiation strength function models indicates that the BAL model tends to yield better agreement with experimental data at higher energies, while the GLO model tends to overestimate the yield ratio due to lower estimations of the cross sections for the $^{115}In(\gamma,\gamma')^{115m}In$ reaction. If we focus on the energy region higher than 20 MeV, it can be observed that of the 36 TALYS combinations there are some that show good agreement with the experiment. It can be observed that the best agreement with the experiment is given by the combination in which the cross section for $^{115}In(\gamma,2n)^{113m}In$ reaction is calculated using LD model 3 (the generalised super-fluid model) and cross section of $^{115}In(\gamma,\gamma')^{115m}In$ reaction is estimated using LD model 6 (the temperature dependent Hartree-Fock-Bogoliubov model, Gogny force).

In the second scenario, where one experimentaly established cross-section was available in the databases for the $^{115}In(\gamma,2n)^{113m}In$ reaction, the comparison with the experimental results yielded similar outcomes. Notably, the cross-section for the $^{115}In(\gamma,\gamma')^{115m}In$ reaction, calculated using the GLO radiation strength function in all six subvariants obtained by choosing the level density function, exhibited significantly higher values of the saturation activity ratio compared to the measured values. The estimated ratios of saturation activities were found to be larger than the experimental ones when using cross sections for the $^{115}In(\gamma,2n)^{113m}In$ reaction, which have maximum values around 1 mbarn.

Of particular interest was the comparison of the experimental values of the $Y(^{113m}In)/Y(^{115m}In)$ yield ratio with the calculated values when employing the BAL radiation strength function to estimate the cross section of the $^{115}In(\gamma,\gamma')^{115m}In$ reaction. Remarkably, a much better agreement with the experimental data was achieved in this case. Figure 6 clearly illustrates that the experimental value of the cross section for the $^{115}In(\gamma,2n)^{113m}In$ reaction has a lower threshold compared to the prediction from TALYS 1.9 calculations. Consequently, the saturation activity calculated using this cross section increases more rapidly with increasing energy than the saturation activities obtained using the TALYS 1.9 cross sections for the same reaction in energy region up to 20 MeV. For this reason, it can be seen in Figure 8 that the measured and calculated values of $Y(^{113m}In)/Y(^{115m}In)$ yield ratio coincide at lower energies, while the difference is observed at energies higher than 20 MeV. However, as the experimental cross-section decreases significantly faster in high energy region, compared to the TALYS 1.9 cross-section, the ratio of saturation activities shows a slower increase with increasing energy. This effect is evident in Figure 8, where the experimental values of the ratio of saturation activities at energies above 20 MeV are higher than the calculated ones.

In Figure 9, it is evident that when calculating the ratio of saturation activities using experimentally established cross sections for both reactions, the obtained values significantly exceed the values measured in this experiment. This outcome was anticipated, as the cross section utilized for the $^{115}In(\gamma,\gamma')^{115m}In$ reaction has values similar to those obtained using the GLO model for the radiation strength function.

It was shown that, based on the measured $Y(^{113m}In)/Y(^{115m}In)$ yield ratio values, the unfolding technique can be used to estimate the energy differential cross section for the $^{115}In(\gamma,2n)^{113m}In$ nuclear reaction. The resulting estimate is shown in Figure 10. This result is significantly different from the cross section shown in reference [4], however shows good agreement with the results of TALYS1.9 calculations. Slight deviations from the smooth flow of the curve in the energy region around 18 MeV originate from some numerical effects in the unfolding procedure itself, the most probable source of which is insufficient number and accuracy of the measured data.

VI. CONCLUSIONS

In this work, the $Y(^{113m}In)/Y(^{115m}In)$ yield ratio were measured in the energy interval from 18 MeV to 23 MeV, in order to verify the capacity of the existing methods for evaluating the cross-section of relevant photonuclear reactions to reproduce the obtained experimental results. It was also checked whether it is possible to obtain agreement with the measured $Y(^{113m}In)/Y(^{115m}In)$ yield ratios with the available cross sections of the observed photonuclear reactions.

Comparisons of experimental values of $Y(^{113m}In)/Y(^{115m}In)$ yield ratio with the results of calculations based on TALYS1.9 evaluated cross sections, showed that the best agreement is obtained if the cross section of $^{115}In(\gamma,\gamma')^{115}In$ reactions is calculated in the way suggested in reference [18]. This raises the need to carefully check the cross-section for $^{115}In(\gamma,\gamma')^{115}In$ reaction, since most of the so far known measurements give lower values of the cross-section than suggested in [18]. However, it was shown

in this experiment that those lower cross section values for the $^{115}In(\gamma,\gamma')^{115}In$ reaction, good agreement with the measured $Y(^{113m}In)/Y(^{115m}In)$ yield ratios is not obtained.

Based on cross sections for a given reaction, estimated using TALYS 1.9, $Y(^{113m}In)/Y(^{115m}In)$ yield ratios were and compared with measured ones. This study shows that the best agreement with the experimental data is obtained when the cross sections for the $^{115}In(\gamma,2n)^{113m}In$ reaction is estimated using generalised super-fluid model for the level density calculation, and temperature dependent Hartree-Fock-Bogoliubov model, Gogny force model for $^{115}In(\gamma,\gamma')^{115}In$ reaction. In both cases the BAL model of the radiation strength function is recommended. However, these re-

sults should only be conditionally accepted since there is a certain deviation between the experimental and calculated $Y(^{113m}In)/Y(^{115m}In)$ yield ratio values at lower energies.

Also in this paper, the estimation of cross sections for $^{115}In(\gamma,2n)^{113m}In$ reaction was performed using the unfolding method. The first results are encouraging and in much better agreement with the cross sections obtained by TALYS1.9 calculations than the only cross section for this reaction that can be found in the literature. There is room to better determine this cross section in repeated measurements where the saturation activities would be determined for a larger number of energies in the energy interval of interest.

[1] A. Zilges, D. Balabanski, J. Isaak, and N. Pietralla, Progress in Particle and Nuclear Physics **122**, 103903 (2022).

[2] T. Kawano, Y. Cho, P. Dimitriou, D. Filipescu, N. Iwamoto, V. Plujko, X. Tao, H. Utsunomiya, V. Varlamov, R. Xu, R. Capote, I. Gheorghe, O. Gorbachenko, Y. Jin, T. Renstrãÿm, M. Sin, K. Stopani, Y. Tian, G. Tveten, J. Wang, T. Belgya, R. Firestone, S. Goriely, J. Kopecky, M. KrtiÄĐka, R. Schwengner, S. Siem, and M. Wiedeking, Nuclear Data Sheets **163**, 109 (2020).

[3] A. Koning and D. Rochman, Nuclear Data Sheets **113**, 2841 (2012), special Issue on Nuclear Reaction Data.

[4] O. Bogdankevich, L. Lazareva, and F. Nikolaev, Journal of Experimental and Theoretical Physics **4**, 320 (1957).

[5] "Janis nuclear data," https://www.oecd-nea.org/jcms/pl_39910/janis.

[6] "25-microtron," http://flerovlab.jinr.ru/mt-25-microtron/.

[7] M. Krmar, Y. Teterev, A. Belov, and S. Mitrofanov, Nuclear Instruments and Methods in Physics Research Section A: Accelerators, Spectrometers, Detectors and Associated Equipment **901**, 133 (2018).

[8] S. Agostinelli, J. Allison, K. Amako, J. Apostolakis, H. Araujo, P. Arce, M. Asai, D. Axen, S. Banerjee, G. Barrand, F. Behner, L. Bellagamba, J. Boudreau, L. Broglia, A. Brunengo, H. Burkhardt, S. Chauvie, J. Chuma, R. Chytracek, G. Cooperman, G. Cosmo, P. Degtyarenko, A. Dell'Acqua, G. Depaola, D. Dietrich, R. Enami, A. Feliciello, C. Ferguson, H. Fesefeldt, G. Folger, F. Foppiano, A. Forti, S. Garelli, S. Giani, R. Giannitrapani, D. Gibin, J. GÃşmez Cadenas, I. GonzÃąlez, G. Gracia Abril, G. Greeniaus, W. Greiner, V. Grichine, A. Grossheim, S. Guatelli, P. Gumplinger, R. Hamatsu, K. Hashimoto, H. Hasui, A. Heikkinen, A. Howard, V. Ivanchenko, A. Johnson, F. Jones, J. Kallenbach, N. Kanaya, M. Kawabata, Y. Kawabata, M. Kawaguti, S. Kelner, P. Kent, A. Kimura, T. Kodama, R. Kokoulin, M. Kossov, H. Kurashige, E. Lamanna, T. LampÃľn, V. Lara, V. Lefebure, F. Lei, M. Liendl, W. Lockman, F. Longo, S. Magni, M. Maire, E. Medernach, K. Minamimoto, P. Mora de Freitas, Y. Morita, K. Murakami, M. Nagamatu, R. Nartallo, P. Nieminen, T. Nishimura, K. Ohtsubo, M. Okamura, S. O'Neale, Y. Oohata, K. Paech, J. Perl, A. Pfeiffer, M. Pia, F. Ranjard, A. Rybin, S. Sadilov, E. Di Salvo, G. Santin, T. Sasaki, N. Savvas, Y. Sawada, S. Scherer, S. Sei, V. Sirotenko, D. Smith, N. Starkov, H. Stoecker, J. Sulkimo, M. Takahata, S. Tanaka, E. Tcherniaev, E. Safai Tehrani, M. Tropeano, P. Truscott, H. Uno, L. Urban, P. Urban, M. Verderi, A. Walkden, W. Wander, H. Weber, J. Wellisch, T. Wenaus, D. Williams, D. Wright, T. Yamada, H. Yoshida, and D. Zschiesche, Nuclear Instruments and Methods in Physics Research Section A: Accelerators, Spectrometers, Detectors and Associated Equipment **506**, 250 (2003).

[9] A. Koning and J. Delaroche, Nuclear Physics A **713**, 231 (2003).

[10] W. Hauser and H. Feshbach, Physical review **87**, 366 (1952).

[11] C. Kalbach, Physical Review C **33**, 818 (1986).

[12] A. Gilbert and A. Cameron, Canadian Journal of Physics **43**, 1446 (1965).

[13] W. Dilg, Nuclear Physic A **217**, 269 (1973).

[14] A. Zubov, G. Adamian, and N. Antonenko, Physics of Particles and Nuclei **40**, 847 (2009).

[15] A. Ignatyuk, J. Weil, S. Raman, and S. Kahane, Physical Review C **47**, 1504 (1993).

[16] S. Goriely, S. Hilaire, and A. J. Koning, Physical Review C **78**, 064307 (2008).

[17] S. Hilaire, M. Girod, S. Goriely, and A. J. Koning, Physical Review C **86**, 064317 (2012).

[18] M. Versteegen, D. Denis-Petit, V. Méot, T. Bonnet, M. Comet, F. Gobet, F. Hannachi, M. Tarisien, P. Morel, M. Martini, and S. Péru, Phys. Rev. C **94**, 044325 (2016).

[19] V. Mazur, I. Sokolyuk, Z. Bigan, and I. Kobal, Physics of Atomic Nuclei **56**, 10 (1993).

[20] M. Reginatto and P. Goldhagen, Health physics **77**, 579 (1999).

ELSEVIER
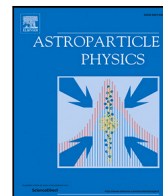
Detection of high energy X-ray radiation following muon captures on Pb

S. Ilić [c], M. Krmar [a], D. Knežević [b], D. Maletić [b], N. Jovančević [a],*

[a] *Department of Physics, Faculty of Science, University of Novi Sad, Trg Dositeja Obradovića 4, 21000 Novi Sad, Serbia*
[b] *Institute of Physics University of Belgrade, Pregrevica 118, 11080 Belgrade, Serbia*
[c] *Faculty of Technical Sciences, University of Novi Sad, Trg Dositeja Obradovića 6, 21000 Novi Sad, Serbia*

ARTICLE INFO

ABSTRACT

Low background HPGe detector, shielded by lead, was used to collect background gamma spectra for more than 180 days. Three lines, originating from transitions of muons captured in orbitals of lead atoms were for the first time recognized in background spectra. Relative intensities of detected transitions were calculated and compared with the theoretical prediction.

1. Introduction

Gamma spectrometry using high-purity HPGe detectors is a widely used method in many fields, from particle physics to environmental sciences. One of the main tasks in gamma spectrometry is to reduce the background [1–3].

Different components contribute to the background. Most important is gamma radiation originating from naturally occurring radionuclides. This component can be reduced by passive shielding. In underground laboratories, neutrons emitted from the spontaneous fission of Th and U as well as in different (α, n) reactions can elevate a level of background radiation [4,5]. Cosmic radiation, especially muons can be a significant contributor to the background in detector systems at shallow depths [6,7]. They deposit energy in different parts of detector systems through various processes: ionization, photonuclear reactions, cascades of hadrons induced by muons, muon-induced spallation, and muon captures by nuclei. Neutrons produced in muon capture can be captured by the surrounding nucleus and binding energy is released by the emission of gamma radiation [4,8–11]. Spectra obtained from muon captures on different atoms can be found [12].

In interactions, muons behave like heavy electrons and they can be captured by atoms, usually into high atomic orbits. During the transition of a muon from higher orbits to lower ones, electromagnetic radiation is emitted. This radiation has a significantly higher energy than the radiation generated during the transition of electrons between its stationary states. Muon transition energies are of the order of hundreds of keV, comparable with the energies of nuclear excitation and if detected, they can be expected next to the lines of the gamma spectrum.

It is very important to mention that there is a view that so far no muon transitions have been observed in the analysis of background
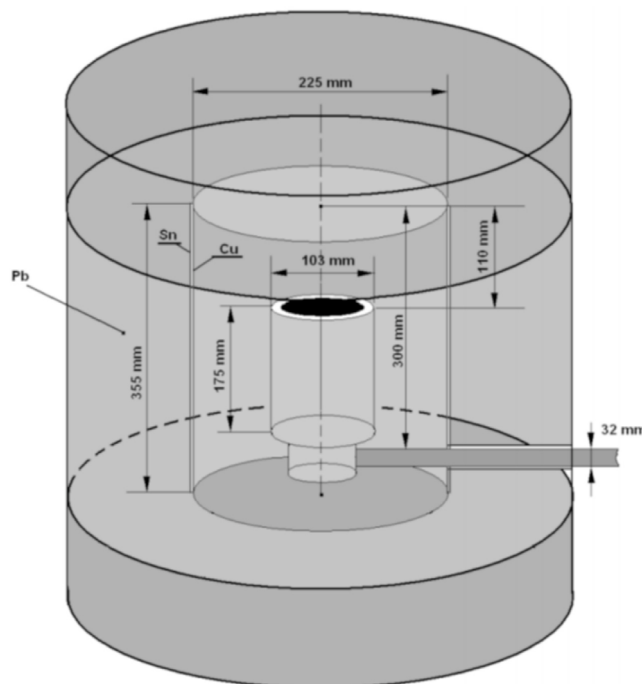

Fig. 1. Schematic view of the HPGe detector with lead shielding.

spectra of HPGe detectors [13]. In a study [14], it is even explicitly stated that X radiations of high energies originating from muon transi-

---

* Corresponding author.

E-mail address: nikola.jovancevic@df.uns.ac.rs (N. Jovančević).

Table 1
Intensities of detected X-ray following muon captures on Pb.

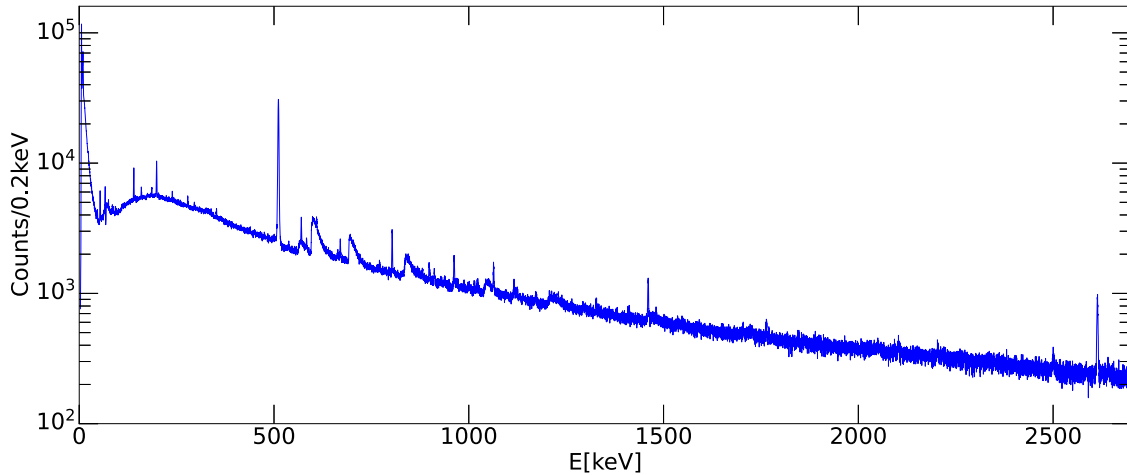| E [keV]	Efficiency [10^{-3}]	Intensity [10^{-3}]	Relative intensity (this work) [%]	Relative intensity from Ref. [13][%]
938	2.40(2)	5.23(42)	65.0(79)	84.9
972	2.08(2)	5.12(49)	63.6(95)	60.38
2501	0.945(8)	8.05(59)	100.0(73)	100

Fig. 2. Total background spectrum.

tions that follow muon capture on detector or shielding material were not observed in background spectra up to now. However, in one of the most detailed recorded background gamma spectra [15] energies of the peaks corresponding to muon cascade between lead orbitals are listed, but they were not identified. As the background spectrum was collected during the long measurement time and as the interaction of muons with germanium detectors is part of the standard research at the Department of Physics in Novi Sad, this was the motivation for studying these processes in this work.

This paper presents the results of the analysis of the background gamma spectrum, recorded for 180 days, in which the existence of three transitions with energies 938 keV, 972 keV, and 2501 keV originating from muon transitions is clearly visible. Calculations of the efficiency of the detector system are performed by simulation and obtained relative intensities of three observed peaks were compared with results of theoretical estimations [13].

2. Experimental setup

Measurements were performed in the low background laboratory at the Department of Physics in Novi Sad at 80 m above sea level [17]. The germanium detector used in the experiment was a coaxial (closed-end) HPGe n-type detector made by Canberra (GX10021) having $380\,cm^3$ of active volume. The relative efficiency of the detector is 100%. The detector shield was made of bulk lead labeled Canberra 777B. The total mass of the shield, presented in Fig. 1 is 1633 kg. The thickness of the shield is 15 cm. Outer 125 mm is made from regular low background lead while the inner 25 mm is made of low-background lead of about 20 Bq/kg. The shield contains a layer of tin with a thickness of 1 mm and high-purity copper with a thickness of 1.5 mm as lining materials. Nitrogen gas evaporating from the dewar vessel was used to flush the interior of the detector from background radon.

The efficiency of the detector system was obtained by simulation using the Geant4 program package 10.5.1 [18]. It was supposed that muons were being captured by atoms uniformly in the volume of the lead shield. Muon cascades in lead atoms produce X-rays radiation. In the Geant4 simulation, electromagnetic radiation is initialized inside
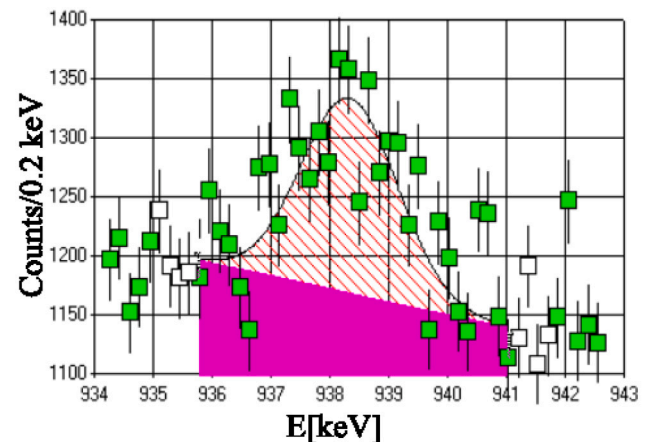

Fig. 3. The part of the spectrum with 938 keV peak with experimental points and fitting data. The dashed area is calculated net peak area, solid colored is a continuum. Green-marked counts per channel are considered by a Genie2000 in the calculations.

the whole volume of lead shielding. The energy of this radiation corresponds to energies emitted in muon transitions from higher to lower orbits in the lead atoms. Radiation is generated to be emitted in random directions from the whole volume of the lead shield. Interactions of photons were followed and efficiency was calculated as a ratio of the number of fully detected photons and created ones. Table 1 shows values of the efficiency for energies of interest (938 keV, 972 keV, and 2501 keV).

Several measurements of the background were made. The final spectrum represents the sum of all background spectra collected by the Genie 2000 program package. The total measurement time was 15836560 s (183.3 days). The full spectrum is depicted in Fig. 2. The detected peaks and their intensities are summarized in Table 2.

Table 2

List of detected peaks in a total background spectrum. The peaks whose origins were not determined are marked with a question mark. Single and double escape peaks are labeled with SEP and DEP. Line energies are compared with energies taken from the ENSDF database [16].

E [keV]	cps [10^{-3}]	Uncertainty[%]	Origin of the peak
23.4	0.093	67.4	^{70}Ge(n,γ)
46.5	0.270	5.2	^{210}Pb
53.6	1.193	1.3	^{73m}Ge,^{234}U,^{214}Pb
66.4	1.187	1.4	^{73m}Ge
70.5	0.434	3.5	^{73}Ge
75.0	0.198	7.8	PbKa2
77.3	0.066	18.0	BiKa1
84.9	0.297	5.1	PbKb1
87.5	0.188	7.8	PbKb2
93.1	0.230	6.5	^{234}Th
110.2	0.112	13.6	^{235}U
140.1	1.913	1.1	^{74}Ge(n,γ)
143.9	0.101	16.7	^{235}U
155.4	0.060	28.2	^{223}Ra
159.6	0.554	3.3	^{77m}Ge
175.1	0.127	13.7	^{70}Ge(n,γ)
186.3	0.451	4.0	^{226}Ra,^{235}U,^{66}Cu
198.6	2.482	0.9	^{71m}Ge
203.4	0.126	14.0	^{235}U
238.9	0.381	4.7	^{212}Pb
254.0	0.049	34.3	^{74}Ge(n,γ)
278.6	0.477	3.6	^{64}Cu,^{208}Tl,^{228}Ac
295.2	0.209	7.9	^{214}Pb
326.4	0.155	10.4	^{228}Th,^{70,72}Ge$(n,n\}\gamma)$
331.5	0.135	11.8	^{228}Ac.
344.3	0.069	22.1	^{228}Ac?
352.2	0.354	4.5	^{214}Pb,^{211}Bi
438.9	0.126	10.9	^{40}KDEP
453.6	0.003	79.3	^{212}Bi
465.1	0.037	6.3	^{214}Pb
487.9	0.054	10.0	^{214}Pb
500.3	0.080	16.0	^{70}Ge(n,γ)
511.0	29.426	0.2	Annihilation
537.7	0.190	6.5	?
565.9	0.380	3.4	^{206}Pb
569.9	1.294	1.2	^{76}Ge,^{207}Pb
575.3	0.296	4.5	^{74}Ge(n,γ)
583.5	0.369	3.5	^{208}Tl,^{208}Pb,^{74}Ge,^{73}Ge
595.8	0.807	1.8	^{74}Ge$(n,n\}\gamma),^{207}$Pb,^{73}Ge(n,γ)
609.1	0.438	3.5	^{214}Bi
663.9	0.111	10.4	^{206}Pb(n,n}γ),^{137}Cs
670.1	0.525	2.4	^{63}Cu,^{70}Ge$(n,n\}\gamma)$
693.2	0.500	2.0	^{72}Ge$(n,n\}e^-)$
703.7	0.052	24.5	^{214}Bi
708.6	0.064	19.3	^{70}Ge(n,γ)
728.3	0.038	28.3	^{212}Bi
770.8	0.135	8.9	^{65}Cu,^{228}Ac?
787.1	0.061	17.0	^{212g}Bi,^{214}Pb,^{214}Bi
794.9	0.042	22.0	^{228}Ac?
803.3	1.120	1.2	^{206}Pb$(n,n\}\gamma)$
825.4	0.035	27.2	?
839.1	0.419	2.7	^{214}Pb,^{228}Ac
844.1	0.070	16.5	^{27}Al
846.8	0.090	12.7	^{56}Fe,^{76}Ge$(n,n\}\gamma)$
861.4	0.013	53.0	^{208}Pb$(n,n\}\gamma)$
868.4	0.103	10.0	^{73}Ge(n,γ)
881.3	0.129	7.9	^{206}Pb$(n,n\}\gamma)$
898.4	0.368	1.6	^{207}Pb$(n,n\}\gamma)$
905.6	0.024	39.0	^{228}Ac,^{214}Bi
911.5	0.189	5.0	^{228}Ac
938.2	0.125	7.7	Pb $4f_{7/2} - 3d_{5/2}$
949.1	0.045	20.0	^{40}KSEP,^{228}Ac
962.3	0.663	1.7	^{63}Cu
969.3	0.092	10.0	^{228}Ac
972.3	0.106	7.6	Pb $4f_{5/2} - 3d_{3/2}$
981.3	0.038	21.7	^{206}Pb$(n,n\}\gamma),^{208}$Pb$(n,n\}\gamma)$

(*continued on next page*)

Table 2 (*continued*).

| E [keV]	cps [10^{-3}]	Uncertainty[%]	Origin of the peak
987.8	0.093	10.0	^{228}Ac
1014.5	0.111	8.3	^{27}Al$(n,n\}\gamma)$
1021.6	0.167	5.6	Annihilation peaks summing
1043.5	0.068	14.0	^{70}Ge
1063.8	0.459	2.3	^{207}Pb,^{74}Ge$(n,n\}\gamma)$
1116.1	0.252	3.8	^{65}Cu
1120.5	0.093	9.4	^{214}Bi
1124.6	0.105	8.3	^{228}Ac?
1131.6	0.040	21.3	^{73}Ge(n,γ)
1172.7	0.107	7.9	^{60}Co
1229.9	0.078	4.5	^{74}Ge$(n,n\}\gamma)$
1238.4	0.013	25.8	^{56}Fe,^{214}Bi
1326.9	0.180	4.6	^{63}Cu
1332.1	0.066	11.7	^{60}Co
1407.8	0.029	24.1	^{214}Bi
1412.1	0.083	9.0	^{65}Cu
1433.6	0.048	6.3	^{206}Pb$(n,n\}\gamma)$
1460.5	0.563	1.7	^{40}K
1481.2	0.048	15.2	^{65}Cu
1591.9	0.037	18.2	^{208}Tl,^{208}PbDEP
1635.5	0.023	27.0	^{76}Ge(n,γ)
1704.2	0.050	27.4	^{206}Pb$(n,n\}\gamma)$
1764.2	0.131	5.3	^{214}Bi
1770.3	0.055	11.8	^{207}Pb
1844.2	0.041	15.1	^{206}Pb$(n,n\}\gamma)$
1847.2	0.046	14.0	^{214}Bi
2103.2	0.068	8.7	^{208}Tl,^{208}Pb(SEP)
2203.4	0.042	13.4	^{214}Bi
2223.1	0.045	12.1	$p(n,\gamma)d$
2447.3	0.025	20.4	?
2501.0	0.076	7.1	Pb $3d_{5/2} - 2p_{3/2}$
2614.5	0.777	1.1	^{208}Tl,^{208}Pb$(n,n\}\gamma)$
2640.6	0.028	17.5	?
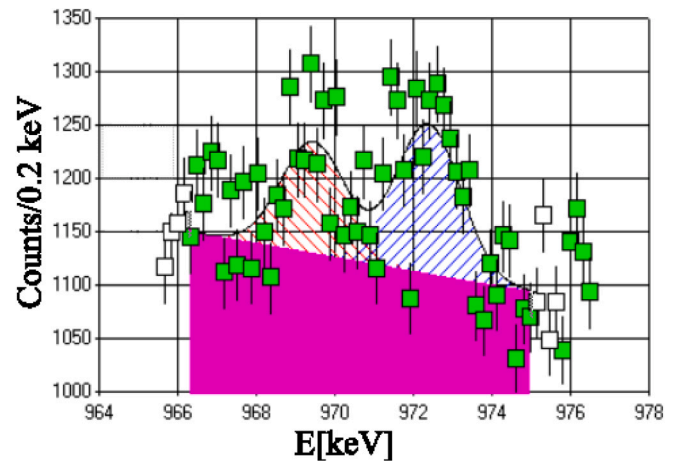
Fig. 4. The part of the spectrum with 972 keV peak with experimental points and fitting data.

3. Results

The obtained gamma spectrum was analyzed using the Genie 2000 program package. Three peaks, that can originate from muon orbital transitions in lead were found at energies: 938 keV, 972 keV, and 2501 keV. The results of the processing (fitting) procedure are shown in Figs. 3–5. The intensities (counts per second) of the analyzed peaks are presented in Table 1.

The next step was the normalization of intensities to the most intense peak. It can be seen in Table 1 that the largest number of detected events is registered under the peak at the energy of 2501 keV. Obtained relative intensities can be compared with the results of the theoretical calculations presented in [13]. Relative intensities experimentally obtained in this work are shown in Table 1.
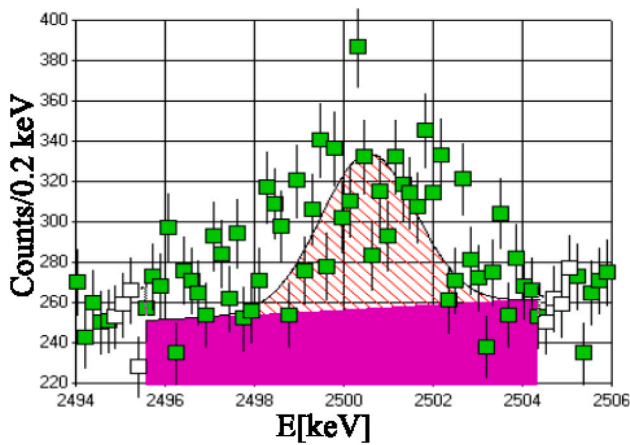
Fig. 5. The part of the spectrum with 2501 keV peak with experimental points and fitting data.

4. Discussion and conclusion

High energy X-ray radiation following muon capture on lead nuclei was recognized for the first time in background spectra. Comparing theoretical and experimentally obtained relative intensities for three observed transitions, some level of agreement can be seen. The highest intensity peak in both sets of data is at the energy of 2501 keV. Relative intensities of experimental and theoretical values of 972 keV transition agree in the frame of experimental uncertainty. Some differences can be noticed for the peak at the energy of 938 keV.

The poor counting statistics of such a low-probability event are probably the root cause of the obtained differences. There is little room to improve this by enriching the background spectrum with new measurements. A more detailed evaluation of the efficiency of the detector system could be helpful, and possible progress in theoretical evaluations of the intensity of muon transitions in lead atoms would also be useful.

Declaration of competing interest

The authors declare that they have no known competing financial interests or personal relationships that could have appeared to influence the work reported in this paper.

Data availability

Data will be made available on request.

References

[1] P. Povinec, Underground low-level counting, in: Proceedings of the 3rd International Conference on Low-Level Measurements of Radioactivity in the Environment, World Scientific. P, Singapore, 1994, pp. 113–139.
[2] P.P. Povinec, Developments in analytical technologies for marine radionuclide studies, in: Radioactivity in the Environment, vol. 6, Elsevier, 2005, pp. 237–294.
[3] I. Bikit, I. Aničin, J. Slivka, M. Krmar, J. Puzović, L. Čonkić, Population of the 283 keV level of 137 Ba by the β decay of 137 Cs, Phys. Rev. C 54 (6) (1996) 3270–3272.
[4] Y. Feige, B. Oltman, J. Kastner, Production rates of neutrons in soils due to natural radioactivity, J. Geophys. Res. 73 (10) (1968) 3135–3142.
[5] G. Heusser, Low-radioactivity background techniques, Annu. Rev. Nucl. Part. Sci. 45 (1) (1995) 543–590.
[6] T.K. Gaisser, R. Engel, E. Resconi, Cosmic Rays and Particle Physics, Cambridge University Press, 2016.
[7] NCRP, Exposure of the Population in the United States and Canada from Natural Background Radiation, NCRP Report No. 94, 1987.
[8] A. Da Silva, B. Pritychenko, B. Dougherty, M. Gray, A. Lu, A. Smith, D. Akerib, D. Bauer, B. Cabrera, D. Caldwell, et al., Neutron background for a dark matter experiment at a shallow depth site, Nucl. Instrum. Methods Phys. Res. A 354 (2–3) (1995) 553–559.
[9] V. Kudryavtsev, N. Spooner, J. McMillan, Simulations of muon-induced neutron flux at large depths underground, Nucl. Instrum. Methods Phys. Res. A 505 (3) (2003) 688–698.
[10] S. Croft, L.C. Bourva, The specific total and coincidence cosmic-ray-induced neutron production rates in materials, Nucl. Instrum. Methods Phys. Res. A 505 (1–2) (2003) 536–539.
[11] R. Arthur, J. Reeves, H. Miley, Use of low-background germanium detectors to preselect high-radiopurity materials intended for constructing advanced ultralow-level detectors, IEEE Trans. Nucl. Sci. 35 (1) (1988) 582–585.
[12] D. Zinatulina, C. Briançon, V. Brudanin, V. Egorov, L. Perevoshchikov, M. Shirchenko, I. Yutlandov, C. Petitjean, Electronic catalogue of muonic X-rays, in: EPJ Web of Conferences, vol. 177, EDP Sciences, 2018, p. 03006.
[13] D.F. Measday, The nuclear physics of muon capture, Phys. Rep. 354 (4–5) (2001) 243–409.
[14] P.P. Povinec, P. Vojtyla, J.-F. Comanducci, Monte Carlo simulation of background characteristics of gamma-ray spectrometers—a comparison with experiment, Radioact. Environ. 11 (2008) 163–208.
[15] P. Bossew, A very long-term HPGe-background gamma spectrum, Appl. Radiat. Isot. 62 (4) (2005) 635–644.
[16] NNDC, et al., Evaluated Nuclear Structure Data File (ENSDF), http://dx.doi.org/10.18139/nndc.ensdf/1845010.
[17] N. Jovančević, M. Krmar, D. Mrda, J. Slivka, I. Bikit, Neutron induced background gamma activity in low-level Ge-spectroscopy systems, Nucl. Instrum. Methods Phys. Res. A 612 (2) (2010) 303–308.
[18] S. Agostinelli, J. Allison, K.a. Amako, J. Apostolakis, H. Araujo, P. Arce, M. Asai, D. Axen, S. Banerjee, G. Barrand, et al., GEANT4—a simulation toolkit, Nucl. Instrum. Methods Phys. Res. A 506 (3) (2003) 250–303.

New insights from cross-correlation studies between solar activity indices and cosmic-ray flux during Forbush decrease events

Mihailo Savić, Nikola Veselinović [*], Aleksandar Dragić, Dimitrije Maletić, Dejan Joković, Vladimir Udovičić, Radomir Banjanac, David Knežević

Institute of Physics Belgrade, University of Belgrade, Pregrevica 118, 11080 Belgrade, Serbia

Abstract

Observed galactic cosmic ray intensity can be subjected to a transient decrease. These so-called Forbush decreases are driven by coronal mass ejection induced shockwaves in the heliosphere. By combining in situ measurements by space borne instruments with ground-based cosmic ray observations, we investigate the relationship between solar energetic particle flux, various solar activity indices, and intensity measurements of cosmic rays during such an event. We present cross-correlation study done using proton flux data from the SOHO/ERNE instrument, as well as data collected during some of the strongest Forbush decreases over the last two completed solar cycles by the network of neutron monitor detectors and different solar observatories. We have demonstrated connection between the shape of solar energetic particles fluence spectra and selected coronal mass ejection and Forbush decrease parameters, indicating that power exponents used to model these fluence spectra could be valuable new parameters in similar analysis of mentioned phenomena. They appear to be better predictor variables of Forbush decrease magnitude in interplanetary magnetic field than coronal mass ejection velocities.

1. Introduction

Cosmic rays (CRs) are high-energy charged particles that arrive at Earth from space, mainly originating from outside of our Solar system. CRs are modulated in the heliosphere (Heber et al., 2006) due to interaction with the interplanetary magnetic field (IMF) frozen in a constant stream of charged particles from Sun - the solar wind (SW). Transients in the heliosphere additionally modulate CRs. One type of transients are interplanetary coronal mass ejections (ICMEs), closely related to coronal mass ejections (CMEs).

ICMEs interact with SW, and as the speed of particles in ICME is different than the speed of SW particles, a bow shock can be created, affecting the CR flux (Belov et al., 2014). This interaction between ICMEs and residual solar wind can be one of the causes of short-term depression in CR flux, detectable at Earth (Subramanian et al., 2009). Such transient decrease in observed flux is known as a Forbush decrease (FD), a type of CR flux modulation that has been studied extensively since its initial discovery in the 1930s (Gopalswamy (2016) and references therein). There are two clearly distinguishable classes of Forbush decreases: recurrent and non-recurrent. Non-recurrent FDs, typically caused by ICMEs (Dumbovic et al., 2012), are mostly characterized by a sudden offset, which lasts about a day, followed by a gradual recovery phase within several days (Cane, 2000). Due to ICME sub-structures

---

* Corresponding author.
  E-mail address: veselinovic@ipb.ac.rs (N. Veselinović).

(the sheath and the associated shock and magnetic cloud) FD can have one or two-step profile, which depends on transit of one or both structures to the observer (Richardson and Cane, 2011). Recurrent FDs have different profile, with gradual onset and decrease and symmetrical recovery caused by high-speed streams from coronal holes (Melkumyan et al., 2019). In this paper we will focus on non-recurrent ICME induced FDs.

Apart from FD profile, one of the main parameters that is used to describe a Forbush decrease is its magnitude. The effect is not the same for all CR particles, as it depends on their rigidity. Rigidity is defined as $R \equiv B\rho = p/q$, where ρ is gyroradius of the particle due to magnetic field B, p is particle momentum, and q is its charge. The higher the rigidity of a particle, the less it is affected by heliospheric inhomogeneities, hence the reduction in flux is less pronounced.

Another phenomenon that can accompany violent events on the Sun is emission of fast-moving particles, commonly known as solar energetic particles (SEP). The occurrence of such particles is typically related to eruptions on the surface of the Sun, which can be characterized by bursts of X-rays - solar flares (SF), and/or emission of coronal plasma - already mentioned CMEs. When excess of these solar energetic particles with high energy penetrates the geomagnetic field, it can cause a sudden and brief increase in measured CR flux at Earth - a ground level enhancement (GLE). Because GLEs can be harmful to human infrastructures (potentially damaging power lines, satellites in orbit, etc.), they have been studied in detail for decades.

Variations of CR flux have been monitored at Earth for decades using ground and underground-based detectors, primarily neutron monitors (NM) (Belov et al., 2000; Koldobskiy et al., 2019) and muon detectors (Mendonça et al., 2016; Veselinović et al., 2015). Different types of ground-based detectors complement each other in terms of their CR energy domain (Veselinovic et al., 2017), muon detectors being sensitive to energies higher than those detectable by NMs. In addition, CR flux is also (especially in the last couple of decades) directly measured in space using space-borne instruments (Dumbovic et al., 2020; von Forstner et al., 2020). In the MeV energy range most space probe particle detectors are sensitive to, enhancement of SEP flux can enshroud CR flux, thus making a task of establishing decoupled event-integrated energy spectra (or spectral fluences) for SEP and CRs a laborious task (Koldobskiy et al., 2021; Bruno and Richardson, 2021).

Many authors have studied the connection between SFs, CMEs/ICMEs and SEP, consequential effects on the geomagnetic field and compound effect of the IMF and geomagnetic field disturbances on CRs. Most relevant for our analysis is work that studied connection between different FD and ICME parameters (Belov et al. (2000), Belov (2008), Papaioannou et al. (2020) and references therein), which has among other, shown significant correlation between CME speeds and FD magnitudes. More precisely, CME speeds have been established as the best predictor

variables of FD magnitudes for primary CR particles with 10 GV rigidity detected at Earth. Also of interest is the work that studied the connection between the disturbance of geomagnetic field and CR flux measured at Earth (Alhassan et al., 2021; Badruddin et al., 2019), where a significant correlation between FD magnitude and different geomagnetic parameters due to common solar or interplanetary origin has been established.

SF, CME/ICME, SEP and FD events are very often related processes that occur either simultaneously or in succession, in which case can be thought of as different components of one more complex event. CMEs (along with their interplanetary counterparts ICMEs) have been recognized as the main driver of FDs, while on the other hand there has been plenty of evidence for the relationship between CMEs with SEP. Namely, there are two different known mechanism for SEP acceleration: acceleration during magnetic-reconnection events usually resulting in solar flares (which produce short impulsive SEP events), and acceleration caused by CME induced shock waves (which result in gradual SEP events) (Reames, 1999). For this study the second class is of interest. Another type of closely related events that are important for this analysis are energetic storm particle (ESP) events, which represent particles accelerated locally by interplanetary shocks driven by fast CMEs (Desai and Giacalone, 2016). Even though details of the mechanism and the precise role of CME induced shock in the evolution of SEP events are not fully understood (Anastasiadis et al., 2019), we believe that analysis of how SEP/ESP events relate to CME, geomagnetic and FD events could provide some valuable new insight. We are especially interested in, and will concentrate the most on, the possibility of the last of these connections. To do so, we have decided to look into the shape of SEP/ESP fluence spectra and analyze how it relates to different CME, geomagnetic and especially FD parameters.

It should be noted that different mentioned types of events, even when related, do not need to occur at the same place nor at the same time. This is due to the fact that SEP travel along magnetic field lines, while CME/ICME shocks travel mostly directly away from the Sun. Furthermore, modulation of primary CR, detected as FD upon their arrival at Earth, can happen anywhere in the heliosphere. Hence, in general case, detection of these events should not necessarily be simultaneous. However, we believe that for the class of events selected for this analysis we can assume that they occur and are detected within a certain time window. We will elaborate more on this in Section 2.3.

The article is structured as follows: first we list various sources of data and justify the selection of solar cycle 23 and 24 FD events to be used in the analysis; then we describe parametrization of SEP events (involving calculation and parametrization of SEP fluence spectra); finally we perform correlative analysis between established SEP parameters and various CME, FD and geomagnetic indices and discuss the observed dependencies.

2. Data

Sources of SEP proton flux, various solar and space weather parameters, as well as ground CR measurements and different FD parameters used in this study are listed below. Different criteria for FD event selection are also described.

2.1. Solar energetic particle flux data

The source for SEP flux data was the ERNE instrument (Torsti et al., 1995) onboard the Solar and Heliospheric Observatory (SOHO). Instrument consists of two separate particle detectors. The Low-Energy Detector (LED) and the High-Energy Detector (HED). Former covers ion fluxes and count rates in the $1.3 - 13$ MeV/nucleon energy range, and latter ion fluxes and count rates in the $13 - 130$ MeV/nucleon energy range. Both ranges are separated in ten energy channels. SOHO has been making in situ observation from Lagrangian point L1 for the last three solar cycles (data available at https://omniweb.gsfc.nasa.gov/ftpbrowser/flux_spectr_m.html). ERNE data for solar cycles 23, 24 and current cycle 25 allows the study of variations of proton fluences in SEP events during this period (Paassilta et al., 2017; Belov et al., 2021). Higher channels are more correlated with measured CR flux (Veselinovic et al., 2021) and it appears as if flux in these channels is a mixture of CR and energetic proton fluxes of particles with the same energy. Important feature of HED detector is that, due to rather large geometric factor, during large intensity proton events SOHO/ERNE data have been subject to saturation effects in higher energy channels (Valtonen and Lehtinen, 2009; Miteva et al., 2020).

2.2. IZMIRAN directory of Forbush decreases

IZMIRAN database is an online repository developed at the Institute of Terrestrial Magnetism, Ionosphere and Radiowave Propagation (IZMIRAN) at Moscow Troitsk, Russia. It contains an extensive list of Forbush decreases and various parameters from solar, space weather, cosmic ray and geomagnetic measurements, spanning from the late 1950s (http://spaceweather.izmiran.ru/eng/dbs.html). Database has been compiled from a number of sources, such as measurements by ground-based detectors, instruments mounted on various satellites, as well as public data provided by different agencies specializing in monitoring solar, space and atmospheric weather and geomagnetism. Extensive list of sources and data repositories used to compile this database are referenced in a number of publications listed on the IZMIRAN internet site (IZMIRAN Space Weather Prediction Center, 2016).

We have decided to use IZMIRAN database as our primary source of data for Forbush decrease parameters as well as for selected variables, parameters and indices that describe associated space weather and geomagnetic

phenomena. Selection of parameters pertinent to our analysis was mostly based on previous work by other authors (i.e. Belov (2008), Lingri et al. (2016)), where they established which quantities are most relevant in these types of studies.

Chosen parameters fall into three categories (abbreviations to be used throughout the text are given in parentheses). First category are FD related parameters - Forbush decrease magnitude for 10 GV rigidity primary particles (M) and Forbush decrease magnitude for 10 GV rigidity primary particles corrected for magnetospheric effect using Dst index (M_M). These magnitudes are determined using global survey method (GSM). GSM combines measurements from a world-wide network of neutron monitors (NMs), takes into account different anisotropies, disturbances of atmospheric and geomagnetic origin, as well as apparatus-specific features, and produces an estimated hourly variation of CR flux outside Earth's atmosphere and magnetosphere (Belov et al., 2018). Specifically, correction for magnetospheric effect takes into account the fact that geomagnetic disturbances affect the effective cutoff threshold rigidities and effective asymptotic directions of primary particles for different NM stations (Belov et al., 2005).

Second group of parameters used from IZMIRAN database are CME and SW related parameters - the average CME velocity between the Sun and the Earth, calculated using the time of the beginning of the associated X-ray flare (V_{mean}), the average CME velocity between the Sun and the Earth, calculated using the time of the beginning of the associated CME observations (V_{meanC}) and maximal hourly solar wind speed in the event (V_{max}). Izmiran DB authors have matched detected FD events with associated CMEs using a SOHO LASCO CME catalog (Belov et al., 2014). Catalog includes a comprehensive list of CME events along with some of most relevant parameters, i.e. speeds calculated by tracking CME leading edge (as described in Yashiro et al. (2004), further sources available at https://cdaw.gsfc.nasa.gov/CME_list/catalog_description.htm).

Final group of parameters from IZMIRAN database used in this analysis are related to geomagnetic field - maximal Kp index in the event (Kp_{max} - based on data from NOAA Space Weather Prediction Center, https://www.swpc.noaa.gov/products/planetary-k-index), maximal 3-h Ap index in the event (Ap_{max} - defined as the mean value of the variations of the terrestrial magnetic field, derived from Kp index) and minimal Dst index in the event (Dst_{min} - calculated using data provided by World Data Center for Geomagnetism, Kyoto, http://wdc.kugi.kyoto-u.ac.jp/dstdir/index.html).

2.3. Selection of FD events

Time interval used for this analysis was dictated by the period of operation of SOHO/ERNE device, which was commissioned in December 1995 (data available from June 1996) and is still operational. That coincides with the

beginning of solar cycle 23 and lasts through cycle 24, so we considered all FD events that occurred in this period, concentrating on events with magnitudes for 10 GV particles larger 4% in the analysis. There are several reason for such magnitude cut, primary reason being that even though we often reference neutron monitor data in the analysis, CR related research in our laboratory is mainly based on muons detectors, which are generally less sensitive to FDs of smaller magnitude and GLE events. Additionally, it is known that all larger FDs (i.e. with magnitudes greater than 5%) are caused by CMEs (Belov, 2008). Since we use CME speed as a reference parameter in the analysis, introducing such cut made event selection simpler, as practically all considered FD events would have an associated CME. Finally, CME speed is less reliably determined in the case of weaker CME events (Yashiro et al., 2004).

One important step in the event selection procedure is to make sure that for each global event both proton flux increase detected by SOHO/ERNE and FD are related to the same CME. As mentioned in the introduction, detection of these separate events is not necessarily simultaneous. However, we have checked the direction of CMEs/ICMEs for all events for which such information was available, and in all these cases they moved directly toward Earth. This would imply that detection of the increase of energetic particles, Forbush decrease and geomagnetic storm associated with a given CME should be detectable within a relatively small time window. To illustrate this, on Fig. 1 we have shown time series for proton flux (in

one selected energy channel), CR flux and *Dst* index for one such event. Furthermore, because of large magnitudes of FDs selected for the analysis, we believe it to be the case for all events.

Another important point is that we cannot say with certainty what is the exact origin of detected proton flux solely based on SOHO/ERNE data. They could be of solar origin (SEP), particles accelerated locally at shock in interplanetary space (ESP), or combination of both. For the sake of simplicity we have decided to use the somewhat more general term SEP for these energetic particles, having mentioned limitation of its use in mind.

As determination of SEP fluence is not a straightforward procedure (as explained in more detail in Section 3.1), from the initial set of events we discarded all for which fluence value was difficult to determine or had a large uncertainty due to overlap and unclear separation of proton flux time series of successive events. That set was then further reduced based on the quality of FD identification flag assigned to each event in the IZMIRAN database, taking into account only events where identification was confident or reliable enough. Applying mentioned selection criteria resulted in the final set of 21 events, presented in Table 1 with some of the parameters of interest.

3. Parametrization of SEP fluence energy spectra

Parametrization procedure for any of the selected FD events can be broken down into two steps: 1 - calculation
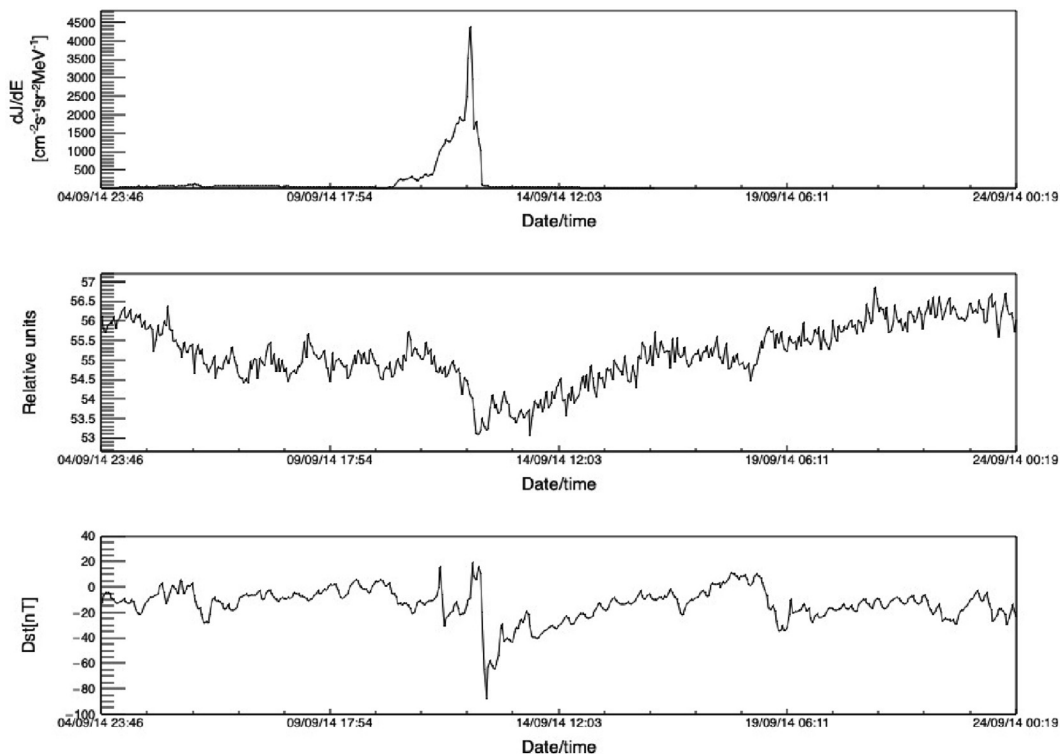

Fig. 1. Time series of hourly data for the same time interval around FD event of 12 Septemeber 2014: proton flux in the $1.3 - 1.6$MeV channel (top), Athens neutron monitor count rate (middle), and Dst index (bottom).

Table 1
Forbush decrease events from solar cycles 23 and 24 selected for the analysis, along with some of the FD, CME and geomagnetic field parameters of interest.

Date/Time	M [%]	M_M [%]	X flare	V_{mean} [km s^{-1}]	V_{meanC} [km s^{-1}]	V_{max} [km s^{-1}]	Kp_{max}	Ap_{max}	Dst_{min} [nT]
2001.09.29 09:40:00	4.3	4.4	M 1.0/	852.0	831	694.0	5.33	56.0	−56.0
2001.10.11 17:01:00	7.0	6.9	M 1.4/2F	766.0	769	572.0	6.0	80.0	−71.0
2001.10.21 16:48:00	5.4	7.3	X 1.6/2B	855.0	858	677.0	7.67	179.0	−187.0
2001.11.24 05:56:00	9.2	9.8	M 9.9/	1323.0	1366	1024.0	8.33	236.0	−221.0
2002.04.17 11:07:00	6.2	7.0	M 1.2/SF	742.0	745	611.0	7.33	154.0	−127.0
2002.09.07 16:36:00	4.6	5.1	C 5.2/SF	860.0	863	550.0	7.33	154.0	−181.0
2003.10.30 16:19:00	14.3	9.4	X10.0/2B	2109.0	2140	1876.0	9.0	400.0	−383.0
2003.11.20 08:03:00	4.7	6.8	M 3.2/2N	854.0	872	703.0	8.67	300.0	−422.0
2004.07.26 22:49:00	13.5	14.4	M 1.1/1F	1279.0	1290	1053.0	8.67	300.0	−197.0
2004.09.13 20:03:00	5.0	5.3	M 4.8/SX	945.0	948	613.0	5.33	56.0	−50.0
2005.05.15 02:38:00	9.5	12.2	M 8.0/SX	1207.0	1231	987.0	8.33	236.0	−263.0
2006.12.14 14:14:00	8.6	9.6	X3.4/4B	1154.0	1165	955.0	8.33	236.0	−146.0
2011.02.18 01:30:00	5.2	4.7	X2.2/	579.0	579	691.0	5.0	48.0	−30.0
2011.08.05 17:51:00	4.3	4.8	M 9.3/	1089.0	1104	611.0	7.67	179.0	−115.0
2011.10.24 18:31:00	4.9	6.5	-	-	633	516.0	7.33	154.0	−147.0
2012.03.08 11:03:00	11.7	11.2	X5.4/	1187.0	1188	737.0	8.0	207.0	−143.0
2012.07.14 18:09:00	6.4	7.6	X 1.4/	822.0	834	667.0	7.0	132.0	−127.0
2013.06.23 04:26:00	5.9	5.3	M 2.9/	832.0	844	697.0	4.33	32.0	−49.0
2014.09.12 15:53:00	8.5	5.9	X1.6/2B	893.0	897	730.0	6.33	94.0	−75.0
2015.06.22 18:33:00	8.4	9.1	M2.6/	1027.0	1040	742.0	8.33	236.0	−204.0
2017.09.07 23:00:00	6.9	7.7	X9.3/	-	1190	817.0	8.33	236.0	−124.0

of SEP fluence in different energy channels and 2 - determination of power exponents for SEP fluence spectra.

3.1. SEP fluence calculation

SEP fluence is calculated by integrating SOHO/ERNE proton flux time series in separate energy channels over time period associated with a given FD event. First step in this procedure is to determine this time period (and hence integration boundaries) as precisely as possible. Most more energetic events we considered for this analysis have a strong SF associated with them. This may lead to a complex picture, as FD event of interest often occurs in the middle of a turbulent period where additional FDs (sometimes associated with other CMEs) precede or follow it. As a consequence, clear separation of successive events and determination of optimal integration boundaries may not be simple nor straightforward. To make this procedure more reliable, we have used IZMIRAN database and neutron monitor data (courtesy of the Neutron Monitor Database (Neutron Monitor Database, 2022)) in parallel with SOHO/ERNE proton time series, trying to identify prominent features in all three sources, so we could separate events of interest in all energy channels as clearly as possible.

Baseline for integration was determined based on a data interval of at least one (but preferably several) days, where proton flux was negligibly different from zero relative to the flux during the event. If possible, time interval before the event was taken for the calculation of baseline unless there was a preceding disturbance, in which case quiet interval following the event was taken instead. Integration of fluence for several selected SOHO/ERNE energy channels

for the event of 12 September 2014 is shown on Fig. 2. Integration interval is indicated with vertical dashed lines and baseline value with a horizontal dashed line.

One interesting feature that can be observed in SOHO/ERNE data time series is that in some cases proton flux in the highest energy channels can dip below the baseline after the initial increase. For a number of events such behavior is even more pronounced, where in extreme cases it can happen that no flux increase is observed, but rather just the decrease. We believe this indicates that the highest energy channels have non-negligible contribution of low-energy cosmic rays, which can increase uncertainty for fluence calculation. We will refer to this again when discussing fluence spectra in Section 3.2.

To make fluence calculation procedure more reliable we have assigned a quality flag to each event, based on our estimate of the uncertainty of integration, and decided on a quality cut we deemed acceptable for further analysis. As mentioned in Section 2.3, 21 events have passed this criterium. Even then, for a number of events calculated fluence proved to be sensitive to small variations of integration boundaries, which makes it especially difficult to give a reliable estimate of the error for the integration procedure and should be kept in mind when discussing the results.

3.2. Determination of SEP fluence spectra power exponents

Fluence energy spectra for all selected events were formed using values for different energy channels, calculated as explained in the previous section. The choice of parameters to be used to describe their shape and characteristics depends on the analytic expression used to model
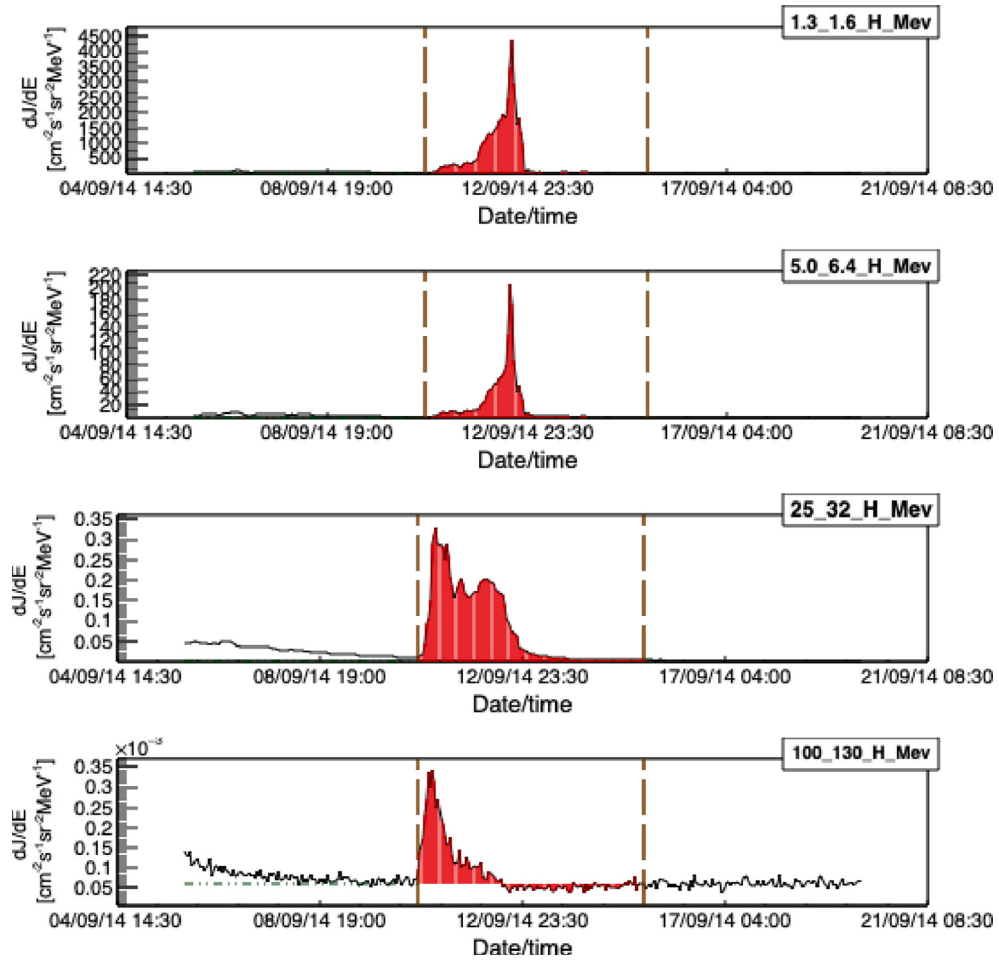
Fig. 2. Solar proton flux for four selected energy channels during FD event of 12 September 2014. Vertical dashed lines indicate integration interval, horizontal dashed line indicates the baseline value, while areas shaded red correspond to result of the integration used to calculate the SEP fluence.
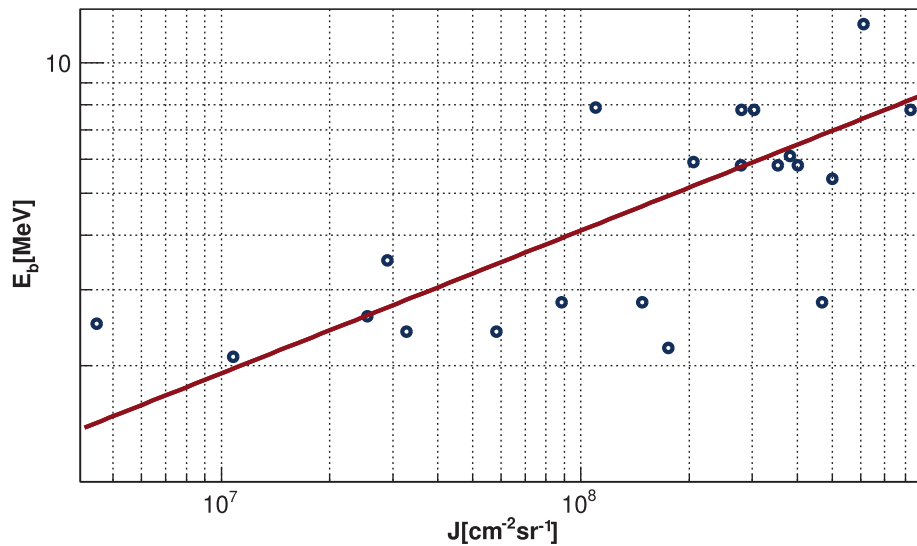

Fig. 3. "Knee" energy dependence on SEP fluence (integrated over full energy range) for selected events. Power function fit is indicated by the red line.

the spectrum. In general, during a SEP event spectra exhibit a characteristic "bend" or a "knee", which is not so straightforward to describe theoretically. Various expressions were proposed to model this observed feature (Ellison and Ramaty, 1985; Mottl et al., 2001), out of which we have decided to use the following double power law one (Band et al., 1993; Zhao et al., 2016), as we feel it is well suited for our analysis:

$$\frac{dJ}{dE} = \begin{cases} E^{-\alpha} \exp\left(-\frac{E}{E_b}\right) & E \leqslant (\beta - \alpha)E_b, \\ E^{-\beta}[(\beta - \alpha)E_b]^{\beta-\alpha} \exp(\alpha - \beta) & E > (\beta - \alpha)E_b, \end{cases}$$

(1)

where E_b is knee energy at which the break occurs, while α and β are power-law exponents that describe energy ranges below and above the break respectively, and consequently are variables we chose to parametrize the SEP event.

These power-law exponents obtained by fitting fluence spectra with Expression 1 can be very sensitive to variation of knee energy, so some care needs to be taken in order to determine E_b as accurately as possible.

Determination of knee energy using "by eye" method proved to be uncertain enough for us to decide on using a more quantitative approach, which is based on the fact that knee energy generally depends on the integral fluence of the event (as described in Nymmik (2013) and Miroshnichenko and Nymmik (2014)). In accordance with this, we firstly determined the knee energy "by eye", plotted it against integral fluence and then fitted this dependence with a power function in the form of $E_b = aJ^b$ (Fig. 3), where E_b is the knee energy, J integral fluence, and a and b are fit parameters. We then used these fit parameteres to determine E_b for each event. In several cases where there has been some overlap of proton flux time series profiles associated with different successive events, small correction for integral fluence was introduced, which also affected the knee energy value.

Fluence spectra were then fitted with expression given in Eq. 1, using thusly calculated knee energy. On Fig. 4 we can see two characteristic examples that illustrate how well this expression actually models the fluence spectrum during a SEP event. In case of 11 October 2001 event (Fig. 4a) we see that the theoretical model fits the experimental data reasonably well, except for some small disagreement in the highest energy channels (feature we believe can be explained by our assumption that there is a non-negligible contribution of low-energy CR in this energy range). On the other hand, for a number of events with greater SEP flux higher energy channels tend to get saturated (as mentioned in Section 2.1). This in turn leads to an underestimated fluence and consequently poorer fit in this energy range, as can be seen for the 24 November 2001 event shown on Fig. 4b. Contribution of flux in these high-energy channels to integral fluence is very small, so this underestimated value does not significantly affect the value of knee energy or uncertainty of the exponent α. However,
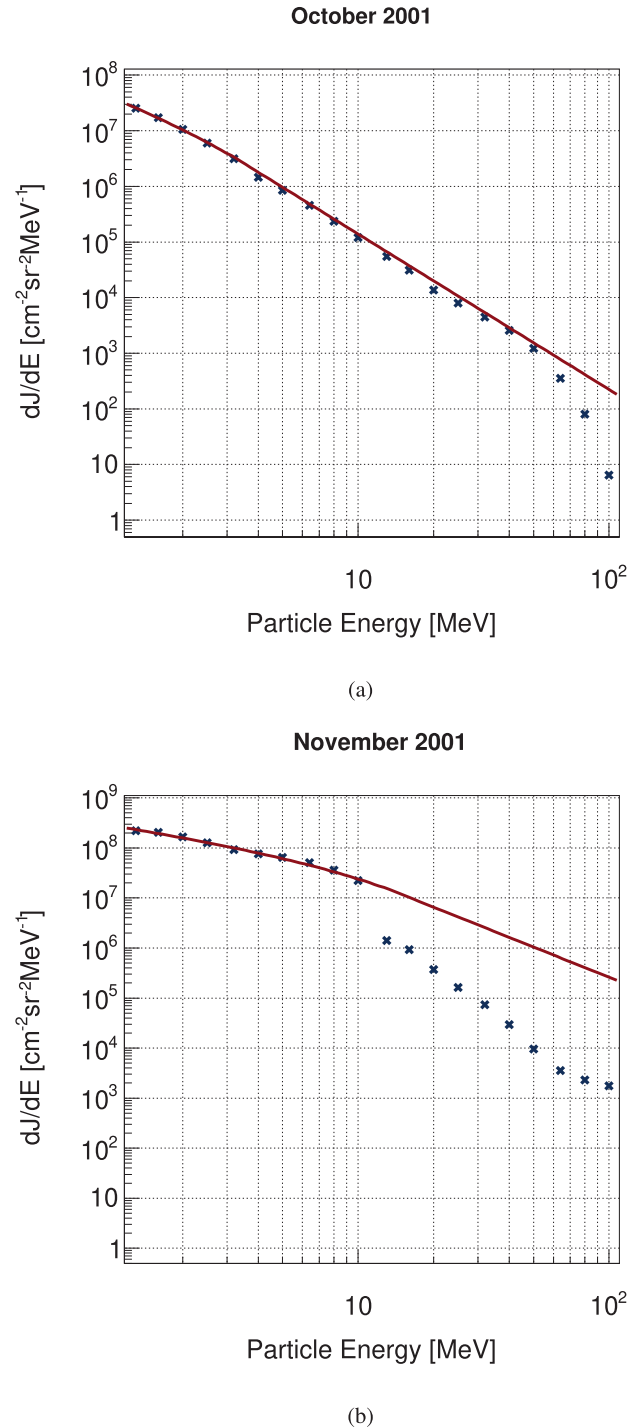

October 2001

November 2001

Fig. 4. SEP fluence energy spectra for the: (a) 11 October 2001 event, (b) 24 November 2001 event. Red lines indicate the double power law fit.

the uncertainty of exponent β is more significantly affected and for this reason in further analysis we will rely on exponent α more for the parametrization of fluence spectra.

4. Correlative analysis

We have performed correlative analysis between power exponents chosen to parametrize SEP fluence and selected

Table 2
Correlation coefficients (r) between SEP fluence spectra power exponents and selected FD, CME and geomagnetic field indices.

|	α	β	M	M_M	V_{meanC}	V_{mean}	V_{max}	Kp_{max}	Ap_{max}	Dst_{min}
α	1.00	0.96	0.67	0.64	0.77	0.75	0.66	0.40	0.53	−0.40
β	0.96	1.00	0.67	0.67	0.72	0.70	0.60	0.44	0.50	−0.38
M	0.67	0.67	1.00	0.84	0.79	0.79	0.79	0.53	0.65	−0.41
M_M	0.64	0.67	0.84	1.00	0.57	0.57	0.53	0.69	0.69	−0.46
V_{meanC}	0.77	0.72	0.79	0.57	1.00	1.00	0.92	0.61	0.77	−0.58
V_{mean}	0.75	0.70	0.79	0.57	1.00	1.00	0.92	0.62	0.78	−0.60
V_{max}	0.66	0.60	0.79	0.53	0.92	0.92	1.00	0.49	0.71	−0.58
Kp_{max}	0.40	0.44	0.53	0.69	0.61	0.62	0.49	1.00	0.94	−0.78
Ap_{max}	0.53	0.50	0.65	0.69	0.77	0.78	0.71	0.94	1.00	−0.87
Dst_{min}	−0.40	−0.38	−0.41	−0.46	−0.58	−0.60	−0.58	−0.78	−0.87	1.00
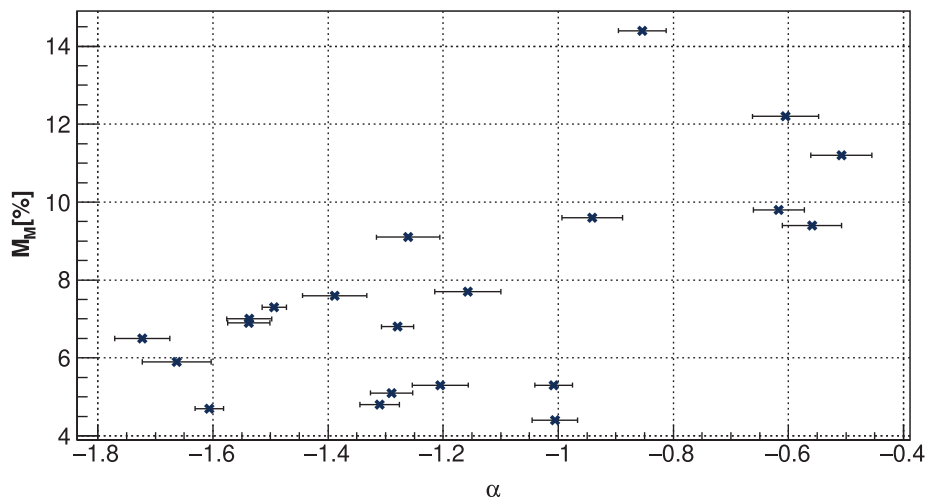
Fig. 5. Dependence of FD magnitude for particles with 10 GV rigidity corrected for magnetospheric effects (M_M) on power exponent α.

parameters from Izmiran database. The results are presented in Table 2. Worth noting is the slightly lower statistics for V_{mean} due to exclusion of two events for which this parameter was not available.

Strong correlation between FD magnitude for particles with 10 GV rigidity (M) and mean CME (V_{meanC}, V_{mean}) and maximum SW (V_{max}) velocities illustrates the important role these parameters have in driving FD events, as has been discussed in detail by several authors (i.e. Belov et al. (2014)). On the other hand, correlation between these velocities and parameter M_M is noticeably smaller. M_M is FD magnitude for particles with 10 GV rigidity corrected for magnetospheric effect (using Dst index), so we could approximate it as an estimated measure of the FD magnitude in interplanetary magnetic field.

If we now look at how SEP fluence spectra power exponents relate to other parameters in Table 2, we observe the best correlation with mean CME velocities, while it is somewhat smaller with maximum SW velocity. Correlation with FD magnitude (M) is smaller than for CME velocities, however interestingly the correlation with the corrected FD magnitude (M_M) appears larger than in the case of CME velocities. One possible explanation for this could be that the shape of SEP fluence spectrum is more related to CR disturbance induced in interplanetary magnetic and less

to one induced in geomagnetic field. What could support this assumption further is the fact that we observe smaller correlation between α and β exponents and geomagnetic indices Kp_{max}, Ap_{max} and Dst_{min} than between these indices and CME velocities.

It should be said that even though SEP fluence spectra power exponents are not directly measured independent variables, the procedure to calculate them is relatively simple, while procedure used to calculate FD magnitudes (using GSM approach) is somewhat less straightforward and accessible. Hence, these exponents could be used to give a first estimate of Forbush decrease magnitudes outside atmosphere and magnetosphere. Having this in mind, we could conclude that SEP fluence power exponents could be better predictor variables (in the sense described above) of FD magnitude in interplanetary space than CME velocities are, while they are less reliable predictor variables of FD magnitude observed at Earth. If true, this could possibly lead us a small step closer to empirically decoupling the effects of IMF and geomagnetic fields on CR.

To further examine how FD magnitude corrected for magnetospheric effects is related to the shape of SEP fluence spectra, we have analyzed their dependence, which is plotted on Fig. 5. Both power exponents exhibit similar dependence, but only plot for α is shown, as it has consid-

Table 3

Correlation coefficients (r) between FD magnitudes for particles with 10 GV rigidity (uncorrected M and corrected for magnetospheric effect M_M) and SEP fluence spectra power exponents, selected FD, CME and geomagnetic field indices for particles with $M_M \geqslant 6\%$ (left) and particles with $M_M < 6\%$ (right).

	$M_M \geqslant 6\%$					$M_M < 6\%$				
	α	β	V_{meanC}	V_{mean}	V_{max}	α	β	V_{meanC}	V_{mean}	V_{max}
M	0.82	0.76	0.84	0.85	0.78	−0.55	−0.25	−0.08	−0.10	0.62
M_M	0.77	0.76	0.52	0.49	0.55	−0.38	0.01	0.23	0.19	0.17

erably smaller uncertainty (as mentioned in Section 3.2) and we believe it to be a more reliable parameter. We can see that the graph is fairly linear, as could be expected based on the correlation coefficients, but on closer inspection it appears as if there are two separate classes of events with somewhat different behavior. If we loosely divide all FD events into low-magnitude set (with M_M less than 6%) and high-magnitude set (with M_M greater or equal to 6%), we can observe much weaker dependence of corrected FD magnitude on power exponent α for the first class than for the second one.

To check if this observation is well founded, we look into the correlation coefficients for these two separate classes, which are shown in Table 3.

We can see that correlation coefficients for these two sets are indeed very different. While in case of FDs with M_M equal or greater than 6% we observe an even larger correlation than before between power exponents α and β and both FD magnitude and corrected FD magnitude (approaching the values of correlation coefficients for CME velocities), coefficients for FDs with M_M less than 6% have very different values, correlation even being negative. Although statistics for this second set of events is rather small (and hence the uncertainty for correlation coefficients might be large), it appears that the assumption about two classes of events does stand. What is more, we observe a similarly drastic difference in correlation coefficients between FD magnitudes and mean CME velocities (with little to none correlation for events with $M_M < 6\%$), also pointing to the existence of two separate classes of events. This could need to be further confirmed using larger statistics, i.e. by including FD events with magnitudes smaller than 4%.

5. Conclusions

We analyzed the connection between CME, SEP and FD events, investigating how the shape of SEP fluence spectra during the global disturbance relates to different CME and FD parameters typically used in such analysis. We fitted SEP fluence spectra with double power law and used power exponents (α and β) from these fits to parametrize the shape of SEP fluence spectra.

By the means of correlative analysis we investigated the connection between SEP fluence spectra power exponents and selected CME and SW parameters (mean CME and maximum SW velocities), as well as selected FD parameters (magnitude for 10 GV particles and magnitude for 10 GV particles corrected for magnetospheric effect) and various parameters of geomagnetic activity (Kp, Ap and Dst indices).

We observed largest correlation between power exponents and CME velocities. The correlation between power exponents and FD magnitude (M) is significant yet smaller than in case of mean CME velocities (V_{meanC}, V_{mean}) and FD magnitude. On the other hand, the correlation between FD magnitude corrected for magnetospheric effects (M_M) and power exponents is larger than between these magnitudes and mean CME velocities.

The dependence of corrected FD magnitude on power exponent α possibly indicates two separate classes of events in terms of corrected magnitude value, rough boundary being corrected FD magnitude value of 6%. Events with corrected FD magnitude larger than 6% show increased correlation with power exponent α, while for the set of events with this magnitude smaller than 6% correlation even has opposite sign. Similarly considerable difference between two classes of events can be observed in correlations of mean CME velocities and corrected FD magnitude. Even taking into account smaller number of events used in the analysis, this could be an indication of these two groups of events exhibiting different behavior.

With everything considered, we believe we have demonstrated an important connection of the shape of SEP fluence spectra with CME and FD events, and that power exponents α and β can be valuable new parameters to be used in the future study of mentioned phenomena. They seem to be better predictor variables of FD magnitude (and hence CR disturbance) in interplanetary magnetic field than CME velocities, especially in the case of events where FD magnitude corrected for magnetospheric effect is larger than 6%.

Declaration of Competing Interest

The authors declare that they have no known competing financial interests or personal relationships that could have appeared to influence the work reported in this paper.

Acknowledgments

References

Alhassan, J.A., Okike, O., Chukwude, A.E., 2021. Testing the effect of solar wind parameters and geomagnetic storm indices on galactic cosmic ray flux variation with automatically-selected forbush decreases. Res. Astron. Astrophys. 21 (9), 234. https://doi.org/10.1088/1674-4527/21/9/234.

Anastasiadis, A., Lario, D., Papaioannou, A., et al., 2019. Solar energetic particles in the inner heliosphere: status and open questions. Philosoph. Trans. Roy. Soc. A: Mathe. Phys. Eng. Sci. 377 (2148), 20180100. https://doi.org/10.1098/rsta.2018.0100, URL: https://royalsocietypublishing.org/doi/abs/10.1098/rsta.2018.0100.

Badruddin, B., Aslam, O.P. M., Derouich, M. et al., 2019. Forbush decreases and geomagnetic storms during a highly disturbed solar and interplanetary period, 4–10 september 2017. Space Weather, 17(3), 487–496. URL: https://agupubs.onlinelibrary.wiley.com/doi/abs/10.1029/2018SW001941. https://doi.org/10.1029/2018SW001941.

Band, D., Matteson, J., Ford, L., et al., 1993. BATSE Observations of Gamma-Ray Burst Spectra. I. Spectral Diversity. Astrophys. J. 413, 281–292. https://doi.org/10.1086/172995.

Belov, A., 2008. Forbush effects and their connection with solar, interplanetary and geomagnetic phenomena. Proc. Int. Astron. Union 4 (S257), 439–450. https://doi.org/10.1017/S1743921309029676.

Belov, A., Abunin, A., Abunina, M., et al., 2014. Coronal mass ejections and non-recurrent forbush decreases. Sol. Phys. 289, 3949–3960. https://doi.org/10.1007/s11207-014-0534-6.

Belov, A., Baisultanova, L., Eroshenko, E., et al., 2005. Magnetospheric effects in cosmic rays during the unique magnetic storm on november 2003. J. Geophys. Res.: Space Phys. 110 (A09S20). https://doi.org/10.1029/2005JA011067.

Belov, A., Eroshenko, E., Oleneva, V., et al., 2000. What determines the magnitude of forbush decreases? Adv. Space Res. 27 (3), 625–630. https://doi.org/10.1016/S0273-1177(01)00095-3, URL: https://www.sciencedirect.com/science/article/pii/S0273117701000953.

Belov, A., Eroshenko, E., Yanke, V., et al., 2018. The Global Survey Method Applied to Ground-level Cosmic Ray Measurements. Sol. Phys. 293 (4), 68. https://doi.org/10.1007/s11207-018-1277-6.

Belov, A., Papaioannou, A., Abunina, M., et al., 2021. On the rigidity spectrum of cosmic-ray variations within propagating interplanetary disturbances: Neutron monitor and SOHO/EPHIN observations at ∼1–10 GV. Astrophys. J. 908 (1), 5. https://doi.org/10.3847/1538-4357/abd724.

Bruno, A., Richardson, I.G., 2021. Empirical model of 10–130 mev solar energetic particle spectra at 1 au based on coronal mass ejection speed and direction. Sol. Phys. 296 (36). https://doi.org/10.1007/s11207-021-01779-4.

Cane, H., 2000. Coronal mass ejections and forbush decreases. Space Sci. Rev. 93 (1), 55–77. https://doi.org/10.1023/A:1026532125747.

Desai, M., Giacalone, J., 2016. Large gradual solar energetic particle events. Living Rev. Sol. Phys. 13 (3). https://doi.org/10.1007/s41116-016-0002-5.

Dumbovic, M., Vršnak, B., Calogovic, J., et al., 2012. Cosmic ray modulation by different types of solar wind disturbances. A&A 538, A28. https://doi.org/10.1051/0004-6361/201117710.

Dumbovic, M., Vrsnak, B., Guo, J., et al., 2020. Evolution of coronal mass ejections and the corresponding forbush decreases: Modeling vs. multi-spacecraft observations. Sol. Phys. 295 (104). https://doi.org/10.1007/s11207-020-01671-7.

Ellison, D.C., Ramaty, R., 1985. Shock acceleration of electrons and ions in solar flares. Astrophys. J. 298, 400–408. https://doi.org/10.1086/163623.

Freiherr von Forstner, J.L., Guo, J., Wimmer-Schweingruber, R.F., et al., 2020. Comparing the properties of icme-induced forbush decreases at earth and mars. J. Geophys. Res.: Space Phys. 125(3), e2019JA027662. URL: https://agupubs.onlinelibrary.wiley.com/doi/abs/10.1029/2019JA027662. https://doi.org/10.1029/2019JA027662. E2019JA027662 10.1029/2019JA027662.

Gopalswamy, N., 2016. History and development of coronal mass ejections as a key player in solar terrestrial relationship. Geosci. Lett. 3 (8), 18. https://doi.org/10.1186/s40562-016-0039-2.

Heber, B., Fichtner, H., Scherer, K., 2006. Solar and heliospheric modulation of galactic cosmic rays. Space Sci. Rev. 125 (1), 81–91. https://doi.org/10.1007/s11214-006-9048-3.

IZMIRAN Space Weather Prediction Center, 2016. Izmiran space weather prediction center. URL: http://spaceweather.izmiran.ru/eng/about.html [Online; accessed 29-January-2022].

Koldobskiy, S.A., Bindi, V., Corti, C., et al., 2019. Validation of the neutron monitor yield function using data from ams-02 experiment, 2011–2017. J. Geophys. Res.: Space Phys. 124 (4), 2367–2379. https://doi.org/10.1029/2018JA026340, URL: https://agupubs.onlinelibrary.wiley.com/doi/abs/10.1029/2018JA026340.

Koldobskiy, S., Raukunen, O., Vainio, R., et al., 2021. New reconstruction of event-integrated spectra (spectral fluences) for major solar energetic particle events. Astron. Astrophys. 647, A132. https://doi.org/10.1051/0004-6361/202040058.

Lingri, D., Mavromichalaki, H., Belov, A., et al., 2016. Solar activity parameters and associated forbush decreases during the minimum between cycles 23 and 24 and the ascending phase of cycle 24. Sol. Phys. 291, 1025–1041. https://doi.org/10.1007/s11207-016-0863-8.

Melkumyan, A., Belov, A., Abunina, M., et al., 2019. On recurrent Forbush Decreases. In: Lagutin, A., Moskalenko, I., Panasyuk, M. (Eds.), Journal of Physics Conference Series, IOP Publishing, Bristol, United Kingdom volume 1181 of Journal of Physics Conference Series. p. 012009, https://doi.org/10.1088/1742-6596/1181/1/012009.

de Mendonça, R.R. S., Braga, C.R., Echer, E., et al., 2016. The temperature effect in secondary cosmic rays (Muons) observed at the ground: analysis of the global muon detector network data. Astrophys. J. 830(2), 88. https://doi.org/10.3847/0004-637x/830/2/88.

Miroshnichenko, L., Nymmik, R., 2014. Extreme fluxes in solar energetic particle events: Methodological and physical limitations. Radiation Measur. 61, 6–15. https://doi.org/10.1016/j.radmeas.2013.11.010, URL: https://www.sciencedirect.com/science/article/pii/S1350448713003806.

Miteva, R., Samwel, S.W., Zabunov, S., et al., 2020. On the flux saturation of SOHO/ERNE proton events. Bulgarian Astron. J. 33, 99.

Mottl, D.A., Nymmik, R. A., Sladkova, A.I., 2001. Energy spectra of high-energy SEP event protons derived from statistical analysis of experimental data on a large set of events. In: El-Genk, M.S., Bragg, M.J. (Eds.), Space Technology and Applications International Forum - 2001, AIP Publishing LLC., New York volume 552 of American Institute of Physics Conference Series, pp. 1191–1196, https://doi.org/10.1063/1.1358071.

Neutron Monitor Database, 2022. Neutron Monitor Database. URL: https://www.nmdb.eu/.

Nymmik, R., 2013. Charge states of heavy ions, as determined from the parameters of solar energetic particle spectra. Bull. Russian Acad. Sci.: Phys. 77, 490–492. https://doi.org/10.3103/S1062873813050419.

Paassilta, Miikka, Raukunen, Osku, Vainio, Rami, et al., 2017. Catalogue of 55–80 mev solar proton events extending through solar cycles 23 and 24. J. Space Weather Space Clim. 7, A14. https://doi.org/10.1051/swsc/2017013.

Papaioannou, A., Belov, A., Abunina, M., et al., 2020. Interplanetary coronal mass ejections as the driver of non-recurrent forbush decreases. Astrophys. J. 890 (2), 101. https://doi.org/10.3847/1538-4357/ab6bd1.

Reames, D.V., 1999. Particle acceleration at the sun and in the heliosphere. Space Sci. Rev. 90 (3), 413–491. https://doi.org/10.1023/A:1005105831781.

Richardson, I.G., Cane, H.V., 2011. Galactic Cosmic Ray Intensity Response to Interplanetary Coronal Mass Ejections/Magnetic Clouds in 1995–2009. Sol. Phys. 270 (2), 609–627. https://doi.org/10.1007/s11207-011-9774-x.

Subramanian, P., Antia, H.M., Dugad, S.R., et al., 2009. Forbush decreases and turbulence levels at coronal mass ejection fronts. A&A 494 (3), 1107–1118. https://doi.org/10.1051/0004-6361:200809551.

Torsti, J., Valtonen, E., Lumme, M., et al., 1995. Energetic particle experiment erne. Sol. Phys. 162 (1–2), 505–531. https://doi.org/10.1007/BF00733438.

Valtonen, E., Lehtinen, I.-V., 2009. Solar energetic particle fluences from soho/erne. Acta Geophys. 57, 116–124. https://doi.org/10.2478/s11600-008-0056-4.

Veselinovic, N., Dragic, A., Savic, M., et al., 2017. An underground laboratory as a facility for studies of cosmic-ray solar modulation. Nucl. Instrum. Methods Phys. Res. Section A: Accelerat. Spectromet. Detectors Assoc. Equip. 875, 10–15. URL: https://www.sciencedirect.com/science/article/pii/S0168900217309634. https://doi.org/10.1016/j.nima.2017.09.008.

Veselinovic, Nikola, Savic, Mihailo, Dragic, Aleksandar, et al., 2021. Correlation analysis of solar energetic particles and secondary cosmic ray flux. Eur. Phys. J. D 75 (6), 173. https://doi.org/10.1140/epjd/s10053-021-00172-x.

Veselinović, N., Dragić, A., Maletić, D., et al., 2015. Cosmic rays muon flux measurements at Belgrade shallow underground laboratory. In: Trache, L., Chesneanu, D., Alexandru Ur, C. (Eds.), Exotic Nuclei and Nuclear/Particle Astrophysics (V) From Nuclei to Stars: Carpathian Summer School of Physics 2014, AIP Publishing LLC., New York volume 1645 of American Institute of Physics Conference Series, pp. 421–425. https://doi.org/10.1063/1.4909614.

Yashiro, S., Gopalswamy, N., Michalek, G., et al., 2004. A catalog of white light coronal mass ejections observed by the soho spacecraft. J. Geophys. Res.: Space Phys. 109 (A7). https://doi.org/10.1029/2003JA010282.

Zhao, L., Zhang, M., Rassoul, H.K., 2016. Double power laws in the event-integrated solar energetic particle spectrum. Astrophys. J. 821 (1), 62. https://doi.org/10.3847/0004-637x/821/1/62.

Multiple Coulomb scattering of muons in lithium hydride

M. Bogomilov,[1] R. Tsenov,[1] G. Vankova-Kirilova,[1] Y. P. Song,[2] J. Y. Tang,[2] Z. H. Li,[3] R. Bertoni,[4] M. Bonesini,[4] F. Chignoli,[4] R. Mazza,[4] V. Palladino,[5] A. de Bari,[6] D. Orestano,[7] L. Tortora,[7] Y. Kuno,[8] H. Sakamoto,[8] A. Sato,[8] S. Ishimoto,[9] M. Chung,[10] C. K. Sung,[10] F. Filthaut,[11] M. Fedorov,[12] D. Jokovic,[13] D. Maletic,[13] M. Savic,[13] N. Jovancevic,[14] J. Nikolov,[14] M. Vretenar,[15] S. Ramberger,[15] R. Asfandiyarov,[16] A. Blondel,[16] F. Drielsma,[16] Y. Karadzhov,[16] G. Charnley,[17] N. Collomb,[17] K. Dumbell,[17] A. Gallagher,[17] A. Grant,[17] S. Griffiths,[17] T. Hartnett,[17] B. Martlew,[17] A. Moss,[17] A. Muir,[17] I. Mullacrane,[17] A. Oates,[17] P. Owens,[17] G. Stokes,[17] P. Warburton,[17] C. White,[17] D. Adams,[18] V. Bayliss,[18] J. Boehm,[18] T. W. Bradshaw,[18] C. Brown,[18] M. Courthold,[18] J. Govans,[18] M. Hills,[18] J.-B. Lagrange,[18] C. Macwaters,[18] A. Nichols,[18] R. Preece,[18] S. Ricciardi,[18] C. Rogers,[18] T. Stanley,[18] J. Tarrant,[18] M. Tucker,[18] S. Watson,[18] A. Wilson,[18] R. Bayes,[19] J. C. Nugent ⊙,[19] F. J. P. Soler,[19] R. Gamet,[20] P. Cooke,[20] V. J. Blackmore,[21] D. Colling,[21] A. Dobbs,[21] P. Dornan,[21] P. Franchini,[21] C. Hunt,[21] P. B. Jurj,[21] A. Kurup,[21] K. Long,[21] J. Martyniak,[21] S. Middleton,[21] J. Pasternak,[21] M. A. Uchida,[21] J. H. Cobb,[22] C. N. Booth,[23] P. Hodgson,[23] J. Langlands,[23] E. Overton,[23] V. Pec,[23] P. J. Smith,[23] S. Wilbur,[23] G. T. Chatzitheodoridis,[24] A. J. Dick,[24] K. Ronald,[24] C. G. Whyte,[24] A. R. Young,[24] S. Boyd,[25] J. R. Greis,[25] T. Lord,[25] C. Pidcott,[25] I. Taylor,[25] M. Ellis,[26] R. B. S. Gardener,[26] P. Kyberd,[26] J. J. Nebrensky,[26] M. Palmer,[27] H. Witte,[27] D. Adey,[28] A. D. Bross,[28] D. Bowring,[28] P. Hanlet,[28] A. Liu,[28] D. Neuffer,[28] M. Popovic,[28] P. Rubinov,[28] A. DeMello,[29] S. Gourlay,[29] A. Lambert,[29] D. Li,[29] T. Luo,[29] S. Prestemon,[29] S. Virostek,[29] B. Freemire,[30] D. M. Kaplan,[30] T. A. Mohayai,[30] D. Rajaram,[30] P. Snopok,[30] Y. Torun,[30] L. M. Cremaldi,[31] D. A. Sanders,[31] D. J. Summers,[31] L. R. Coney,[32] G. G. Hanson,[32] and C. Heidt[32]

(MICE Collaboration)

[1]*Department of Atomic Physics, St. Kliment Ohridski University of Sofia, 5 James Bourchier Blvd, Sofia, Bulgaria*
[2]*Institute of High Energy Physics, Chinese Academy of Sciences, 19 Yuquan Rd, Shijingshan District, Beijing, China*
[3]*Sichuan University, 252 Shuncheng St, Chengdu, China*
[4]*Sezione INFN Milano Bicocca and Dipartimento di Fisica G. Occhialini, Piazza della Scienza 3, Milano, Italy*
[5]*Sezione INFN Napoli and Dipartimento di Fisica, Università Federico II, Complesso Universitario di Monte S. Angelo, via Cintia, Napoli, Italy*
[6]*Sezione INFN Pavia and Dipartimento di Fisica, Università di Pavia, Via Agostino Bassi 6, Pavia, Italy*
[7]*Sezione INFN Roma Tre and Dipartimento di Matematica e Fisica, Università Roma Tre, Via della Vasca Navale 84, Roma, Italy*
[8]*Osaka University, Graduate School of Science, Department of Physics, 1-1 Machikaneyamacho, Toyonaka, Osaka, Japan*
[9]*High Energy Accelerator Research Organization (KEK), Institute of Particle and Nuclear Studies, Tsukuba, Ibaraki, Japan*
[10]*Department of Physics, UNIST, 50 UNIST-gil, Ulsan, South Korea*
[11]*NIKHEF, Science Park 105, Amsterdam, Netherlands*
[12]*Radboud University, Houtlaan 4, Nijmegen, Netherlands*
[13]*Institute of Physics, University of Belgrade, Serbia*
[14]*Faculty of Sciences, University of Novi Sad, Trg Dositeja Obradovića 3, Novi Sad, Serbia*
[15]*CERN, Esplanade des Particules 1, Geneva, Switzerland*
[16]*DPNC, Section de Physique, Université de Genève, 24 Quai Ernest-Ansermet, Geneva, Switzerland*
[17]*STFC Daresbury Laboratory, Keckwick Ln, Daresbury, Cheshire, United Kingdom*
[18]*STFC Rutherford Appleton Laboratory, Harwell Campus, Didcot, United Kingdom*
[19]*School of Physics and Astronomy, Kelvin Building, University of Glasgow, Glasgow, United Kingdom*
[20]*Department of Physics, University of Liverpool, Oxford St, Liverpool, United Kingdom*
[21]*Department of Physics, Blackett Laboratory, Imperial College London, Exhibition Road, London, United Kingdom*
[22]*Department of Physics, University of Oxford, Denys Wilkinson Building, Keble Rd, Oxford, United Kingdom*
[23]*Department of Physics and Astronomy, University of Sheffield, Hounsfield Rd, Sheffield, United Kingdom*
[24]*SUPA and the Department of Physics, University of Strathclyde, 107 Rottenrow, Glasgow, United Kingdom*

[25]*Department of Physics, University of Warwick, Gibbet Hill Road, Coventry, United Kingdom*
[26]*College of Engineering, Design and Physical Sciences, Brunel University,*
Kingston Lane, Uxbridge, United Kingdom
[27]*Brookhaven National Laboratory, 98 Rochester Street, Upton, New York, USA*
[28]*Fermilab, Kirk Rd and Pine Street, Batavia, Illinois, USA*
[29]*Lawrence Berkeley National Laboratory, 1 Cyclotron Road, Berkeley, California, USA*
[30]*Illinois Institute of Technology, 10 West 35th Street, Chicago, Illinois, USA*
[31]*University of Mississippi, University Avenue, Oxford, Mississippi, USA*
[32]*University of California, 900 University Avenue, Riverside, California, USA*

Multiple Coulomb scattering (MCS) is a well-known phenomenon occurring when charged particles traverse materials. Measurements of muons traversing low Z materials made in the MuScat experiment showed that theoretical models and simulation codes, such as GEANT4 (v7.0), over-estimated the scattering. The Muon Ionization Cooling Experiment (MICE) measured the cooling of a muon beam traversing a liquid hydrogen or lithium hydride (LiH) energy absorber as part of a programme to develop muon accelerator facilities, such as a neutrino factory or a muon collider. The energy loss and MCS that occur in the absorber material are competing effects that alter the performance of the cooling channel. Therefore measurements of MCS are required in order to validate the simulations used to predict the cooling performance in future accelerator facilities. We report measurements made in the MICE apparatus of MCS using a LiH absorber and muons within the momentum range 160 to 245 MeV/c. The measured RMS scattering width is about 9% smaller than that predicted by the approximate formula proposed by the Particle Data Group, but within the latter's stated uncertainty. Data at 172, 200 and 240 MeV/c are compared to the GEANT4 (v9.6) default scattering model. These measurements show agreement with this more recent GEANT4 (v9.6) version over the range of incident muon momenta.

I. INTRODUCTION

Multiple Coulomb scattering (MCS) describes the multiple interactions of charged particles in the Coulomb field of the nuclei and electrons of a material. Rossi and Greisen derived a simple expression for the root-mean-square (RMS) scattering angle in the small angle approximation [1] by integrating the Rutherford cross section [2]. The mean square scattering angle $\langle \theta^2 \rangle$ after multiple collisions traversing a thickness dz of material can be expressed as a function of radiation length X_0

$$\frac{d\langle \theta^2 \rangle}{dz} = \frac{E_s^2}{p^2 \beta^2} \frac{1}{X_0}, \qquad (1)$$

where $E_s = 21.2$ MeV/c, p is the momentum of the charged particle and β its speed in units of the speed of light, c. The projection of the scattering angle onto a plane containing the incident track gives the RMS projected scattering angle $\theta_0 = \sqrt{\langle \theta^2/2 \rangle}$ [3]

$$\theta_0 = \frac{14.85 \text{ MeV/c}}{p\beta} \sqrt{\frac{\Delta z}{X_0}}. \qquad (2)$$

Molière [4,5] developed a theory of MCS based on the scattering of fast charged particles from atomic nuclei that showed good agreement with data. Bethe [6] improved the treatment by taking into account interactions with electrons within the atom. The theory was subsequently improved by Fano [7] to account for elastic and inelastic scattering.

Most of the models of MCS mentioned above reproduce data very well [8] for small angle scatters and when the atomic number, Z, of the target nuclei is large. Highland [9] compared the Molière theory with the simple formula by Rossi and Greisen Eq. (1), and found a distinct Z dependence of the value of E_s. As a consequence, Highland recommended that a logarithmic term be added to the Rossi-Greisen formula to improve the agreement with Molière's theory, especially at low Z such as for liquid hydrogen or lithium hydride. The formula for θ_0, the RMS width of the Gaussian approximation for the central 98% of the projected scattering angle distribution on a plane, was reviewed by Lynch and Dahl [10] and is now recommended by the Particle Data Group [3] as

$$\theta_0 = \frac{13.6 \text{ MeV/c}}{p\beta} \sqrt{\frac{\Delta z}{X_0}} \left(1 + 0.038 \ln \frac{\Delta z}{X_0 \beta^2} \right), \quad (3)$$

claimed to be accurate to 11% over the full range of values of Z.

Multiple scattering has not been well modeled for low Z materials in standard simulations. Data collected by the MuScat experiment [8] indicate that GEANT4 v7.0 [11] and the Molière model overestimate MCS for these materials. However, a simple Monte Carlo method, which samples the Wentzel scattering cross section [12] to generate the MCS distributions, was shown by Carlisle and Cobb in [13] to agree very well with muon scattering data from the MuScat experiment. Since the time of MuScat, GEANT4 has evolved through several versions and the comparison to data made in this analysis uses GEANT4 v9.6.

Emittance is a measure of the average spread of particle coordinates in position and momentum phase space and has dimensions of length times angle, e.g., mm · radians, usually written as just mm. The Muon Ionization Cooling Experiment (MICE) made measurements of emittance reduction in low Z absorbers, i.e., those materials that can be used to reduce muon-beam emittance via ionization cooling [14], thus providing the first observation of the ionization cooling process [15] that can be used to cool beams of muons for a neutrino factory [16] or a muon collider [17–20]. The normalized transverse emittance of the MICE muon beam [21] is reduced due to energy loss and increased by the scattering in the absorber material. The rate of change in the normalized emittance, ϵ_n, [14] is given by

$$\frac{d\epsilon_n}{dz} \approx -\frac{\epsilon_n}{p_\mu \beta}\left\langle \frac{dE_\mu}{dz}\right\rangle + \frac{\beta_\perp p_\mu}{2m_\mu}\frac{d\theta_0^2}{dz}, \qquad (4)$$

where $\frac{dE_\mu}{dz}$ is the energy loss of muons per unit distance, m_μ the muon mass, p_μ the muon momentum and $\beta_\perp$ the betatron function.

To make accurate predictions of the emittance in the absorber materials, the model in the simulation must be validated. This is particularly important for the prediction of the equilibrium emittance, the case when $d\epsilon_n/dz = 0$ and

$$\epsilon_n = \frac{\beta_\perp p_\mu^2 \beta}{2m_\mu}\frac{d\theta_0^2}{dz}\left\langle \frac{dE_\mu}{dz}\right\rangle^{-1}. \qquad (5)$$

This provides the minimum emittance for which cooling is effective and is lowest for low Z absorbers. There is thus great interest in performing a detailed measurement of MCS of muons traversing low Z absorbers, such as liquid hydrogen or lithium hydride (LiH). Here, we report the first measurement of MCS of muons in lithium hydride in the muon momentum range 160 to 245 MeV/c, using the MICE apparatus. Accurate MCS modeling will ensure design studies for future facilities are as informative as possible [22]. This paper is divided as follows: Sec. II outlines the MICE experiment, describes the analysis method and defines the relevant measurement angles, Sec. III describes the data collected and the event selection and Sec. IV describes the data deconvolution method and the multiple scattering results, with a final short conclusion in Sec. V.

II. METHOD

The MICE configuration for the MCS measurements presented here consisted of two scintillating fiber trackers, one upstream (US) and one downstream (DS) of a lithium hydride absorber. Each tracker contained five stations, each composed of three planes of scintillating fiber employing 120° stereo views, immersed in helium gas [23]. Thin aluminum windows separated the helium volume from the vacuum containing the absorber. The tracker position resolution was determined to be 470 µm [24]. The solenoid magnets surrounding the trackers were turned off for these measurements to allow straight-track reconstruction of the muons before and after the absorber.

The muon beam was generated by protons with a kinetic energy of 700 MeV at the STFC Rutherford Appleton Laboratory ISIS synchrotron facility [21,25] impinging on a titanium target [26,27]. The beam line is described in [21].

A schematic diagram of the MICE cooling channel and detectors is shown in Fig. 1. A time of flight (TOF) system, consisting of three detectors (TOF0 and TOF1 upstream and TOF2 downstream of the apparatus), was used to measure the momentum of reconstructed muons [28]. The Cherenkov detector, preshower system (KL) and electron-muon ranger (EMR) were used to confirm the TOF's particle identification performance [21,29,30]. The MICE coordinate system is defined with $+z$ pointing along the
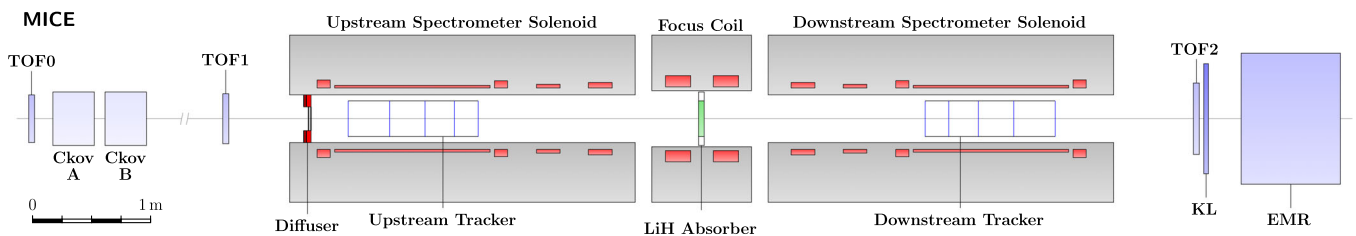

FIG. 1. Schematic of the MICE cooling channel. The spectrometer solenoids and focus coils were not powered during the measurements described here. A variable thickness diffuser upstream of the trackers was fully retracted during the measurements. Acronyms are defined in the text.

beam direction toward the downstream region, $+y$ pointing upward and $+x$ defined to be consistent with a right-handed coordinate system.

The MICE LiH absorber was a disk, 65.37 ± 0.02 mm thick (along the z-axis) and 550 mm in diameter. The absorber was coated with a thin parylene layer to prevent the ingress of water or oxygen. The composition of the LiH disk by weight was 81% ^{6}Li, 4% ^{7}Li and 14% ^{1}H with some trace amounts of carbon, oxygen and calcium. The density of the disk was measured to be 0.6957 ± 0.0006 g/cm^3, and the radiation length was calculated to be 70.38 g/cm^2.

Multiple scattering is characterized using either the three-dimensional (3D) angle between the initial and final momentum vectors, θ_{Scatt}, or the 2D projected angle of scattering. The projected angles between the track vectors in the x-z (θ_Y) and y-z (θ_X) planes of the experimental coordinate system can be used, but these are only the true projected angles if the incident muon has no component of momentum in a direction perpendicular to these planes, i.e., the y or x direction respectively. To obtain the correct projected angle, a plane of projection must be defined for each incoming muon. The rotation calculated about an axis in the plane defined for each incoming muon is, to a very good approximation, the rotation around the specified axis. The precise definitions of θ_X and θ_Y are given in the Appendix.

Table I shows the expected RMS projected scattering angles, θ_0, obtained using Eq. (3), for the LiH absorber and the material in each of the trackers. The number of radiation lengths traversed by a muon as it passes through the absorber was larger than that which it traversed as it passed through the trackers hence the majority of the scattering occurs in the absorber. Nevertheless the scattering in the trackers is significant and must be corrected for.

III. DATA SELECTION AND RECONSTRUCTION

A coincidence of two PMTs firing in TOF1 was used to trigger readout of the detector system including the trackers. The muon rate was such that only a single incident particle was observed in the apparatus per readout. Data reconstruction and simulation were carried out using MAUS

(MICE Analysis and User Software) v3.3.2 [31] (which uses GEANT4 v9.6.p02). Position and angle reconstruction was performed using data from the MICE trackers while momentum reconstruction was performed using data from the TOF detectors.

A. Position and angle reconstruction

Space points were created from the signals generated in the three scintillating fiber planes contained in a tracker station. Multiple space points that formed a straight line through the tracker were associated together. Space points that did not match a possible track were rejected. A Kalman filter [32] was used to provide an improved estimate of the track position and angle in each tracker at the plane nearest to the absorber.

An upstream track was required for the event to be considered for analysis, with a minimum of three space points among the five stations of the upstream tracker. No requirement was made on the presence of a downstream track. All scattering distributions were normalized to the number of upstream tracks selected in the analysis. The efficiency of the trackers has been shown to be very close to 100% [33].

A residual misalignment between the upstream and downstream trackers was corrected by rotating all upstream tracks by a fixed angle in the range 1–7 mrad. The final uncertainty in the rotation angles following the alignment procedure was 0.07 mrad.

B. Momentum reconstruction

Time of flight was used to measure the momentum of the muon at the absorber. Two time of flight measurements were used, designated as TOF01, the time of flight between TOF0 and TOF1, and TOF12, the time of flight between TOF1 and TOF2. The average momentum between time of flight detectors was calculated by evaluating

$$p = \frac{m_\mu c}{\sqrt{\frac{t_\mu^2}{t_e^2} - 1}} - \Delta p_{BB} - p_{MC}, \qquad (6)$$

TABLE I. Material budget affecting particles passing through the MICE LiH absorber. The material thickness normalized by the radiation length is given with the RMS width of the scattering distribution calculated from the full PDG formula [3] in Eq. (3). Note that the thickness shown for the tracker materials (He, Al windows, and scintillating fibers) includes both trackers.

Material	z (cm)	z/X_0	ρ (g cm^{-3})	θ_0 (mrad) 172 MeV/c	200 MeV/c	240 MeV/c
Tracker He	226	0.00030	1.663×10^{-4}	1.09	0.91	0.73
Al Window	0.032	0.0036	2.699	4.31	3.58	2.89
Scintillating Fibers	1.48	0.036	1.06	14.9	12.4	10.0
Total Tracker		0.038		15.8	13.2	10.6
LiH	6.5	0.0641	0.6957	21.3	17.7	14.3
Total with LiH		0.1058		29.9	24.8	20.0

which assumes the mass of the electron to be ≈ 0 and where t_μ is the time of flight of the muon and t_e is the average time of flight of positrons ($t_e = 25.40$ ns for TOF01 and 27.38 ns for TOF12). Δp_{BB} was an additional term which accounted for the Bethe-Bloch most probable energy loss [34] of the muon as it passes through matter and was chosen to yield an optimal reconstructed momentum at the center of the absorber. When measuring the momentum using TOF01, accounting for the material upstream of the LiH absorber, Δp_{BB} was of order ~ 25 MeV/c (the correction varied as a function of muon momentum and was calculated separately for each selected sample of muons). p_{MC} accounted for the bias between the reconstructed and true momentum observed in the Monte Carlo (MC) simulation; this arises primarily due to the simplifying assumptions intrinsic to Eq. (6), e.g., that the path length between the TOF detectors can be approximated to the straight line on-axis distance between the two detectors when in fact the particle's trajectory may have curved through various magnetic fields or scattered in material. p_{MC} was used when calculating the momentum with both TOF01 and TOF12 and the correction, p_{MC}, was ~ 2–6 MeV/c. After correction, the reconstructed data were well described by the MC as shown in Fig. 2.

For muons reaching the end of the channel, the momentum measurement was made using TOF1 and TOF2. In this case the absorber sits near the midpoint between the detectors and the distance between them was larger than the distance between TOF0 and TOF1 which results in a slightly smaller uncertainty. In the selected samples, $\sim 90\%$ of muons reach TOF2. If no hit was recorded in TOF2, the momentum measurement was made using TOF0 and TOF1. The TOF01 distribution is shown in Fig. 3.

Characteristics of the time-of-flight samples selected using TOF01 are shown in Table II. The resolution of the TOF system was ≈ 70 ps which corresponds to ~ 4–10 MeV/c depending on the momentum setting. The agreement between the reconstructed momentum and the simulated true muon momentum at the center of the absorber is shown in Fig. 2(a) and a residual plot ($p_{\mathrm{Reconstructed}} - p_{\mathrm{Truth}}$) is shown in Fig. 2(b).

C. Data collection

Six datasets were collected during the ISIS user cycle 2015/04 using muon beams with a nominal 3 mm emittance, at three nominal momenta (172, 200 and 240 MeV/c). The three datasets collected with the LiH absorber in place are referred to as 'LiH' data while the three datasets with no absorber in place are referred to as "no absorber" data. The beams typically had RMS widths of 30–36 mm and divergences of 9.0–9.4 mrad, after the selection described in Sec. III D. The no absorber datasets were used to determine the scattering attributable to the tracking detectors and thus to extract the true MCS distribution due to the LiH absorber. Two methods,
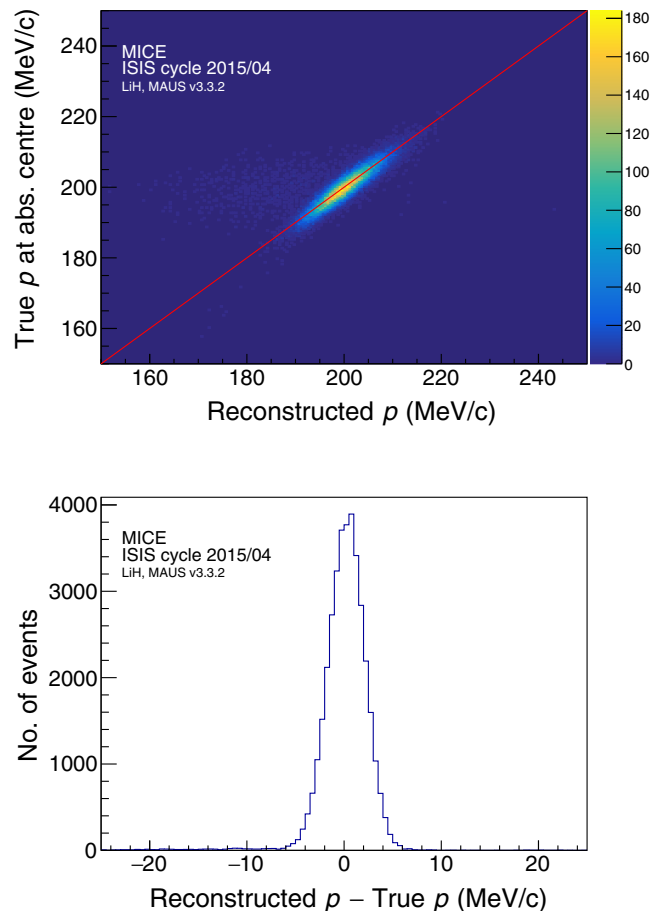

FIG. 2. Top: comparison of the reconstructed and true momentum for the MC sample, for the bin with average momentum 200 MeV/c. Bottom: residual between reconstructed and true momentum for the MC sample. The systematic error associated with the momentum reconstruction is discussed in Sec. IV D.
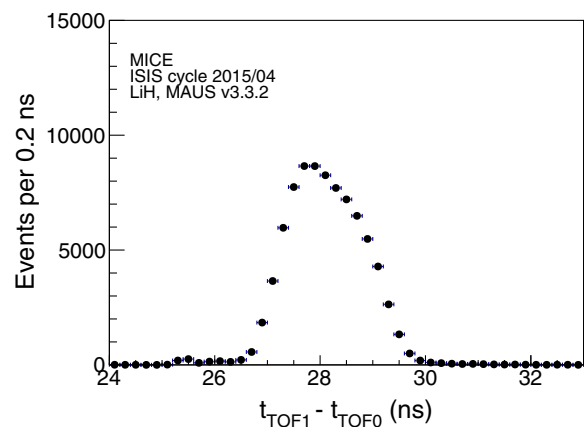

FIG. 3. Combined time-of-flight between TOF0 and TOF1 distribution of LiH data for all beam line settings after all selection cuts.

TABLE II.   Characteristics of the samples selected for model comparison; the standard deviation of the reconstructed momenta are compared with the spread of true momenta of equivalent samples selected from the simulation.

Desired momentum (MeV/c)	Lower TOF limit (ns)	Upper TOF limit (ns)	Measured $\langle p \rangle$ (MeV/c)	Standard deviation (MeV/c)	True MC momentum spread (MeV/c)
172	28.60	28.80	171.55 ± 0.06	4.37 ± 0.06	4.82
200	27.89	28.09	199.93 ± 0.07	5.92 ± 0.05	5.97
240	27.16	27.36	239.76 ± 0.13	8.95 ± 0.09	8.21

TABLE III.   Particle selection criteria and survival rates for the muon sample with a LiH absorber.

Selection	Description	Fraction events surviving each cut
Upstream track selection	Exactly one TOF0 space point, exactly one TOF1 space point and one upstream track.	100.0%
Diffuser cut	Upstream tracks were projected to the diffuser position. Any track outside the radius of the diffuser aperture was rejected.	81.7%
Fiducial selection	Upstream tracks, when projected to the far end of the downstream tracker, have a projected distance from axis less than 90 mm.	3.7%

described in Sec. IV, were used. Positively charged muon beams were used to minimize pion contamination, which was measured to be less than 1.4% [29]. Positron contamination was identified and rejected using the time-of-flight system.

D. Event selection

The data from the three nominal muon beams were merged into one sample and all muons in the sample were treated identically. Unbiased scattering distributions were selected from the data samples using the cuts listed in Table III. The fraction of events selected by each cut is also shown. Events that produced one space point in TOF0 and one space point in TOF1 were selected. A beam diffuser, otherwise used to increase the beam emittance, was fully retracted for all of the runs used in this analysis. A fraction of the muon beam traversed the diffuser ring in its retracted position, adding additional energy loss. Any upstream tracks that traversed the outer ring of the diffuser were removed.

A fiducial selection to ensure that the unscattered downstream track was likely to have been within the volume of the downstream tracker was also applied. If the upstream track, when projected to the downstream end of the downstream tracker, passed outside of the fiducial radius $r_0 = 90$ mm the track was rejected.

Finally, particles with a time of flight between stations TOF0 and TOF1 compatible with the passage of a muon (above 26 ns) were selected. The data were then binned in 200 ps Δt_{01} bins (Fig. 3) to yield eleven quasi-monochromatic samples. Most positrons, which had a TOF between 25 and 26 ns, were excluded by this binning. Three of these samples, with mean momentum of 172, 200

TABLE IV.   Sample size after selection.

Absorber	p (MeV/c)	No. of events US	No. of events DS
LiH	172	6479	5906
	200	8589	8112
	240	5612	5445
No Absorber	172	1500	1469
	200	2025	1995
	240	1394	1378

and 240 MeV/c and containing 0.19, 0.25 and 0.19% of the total number of events respectively, were compared to the GEANT4 and Molière models. The sample at 172 MeV/c enabled comparison with MuScat while samples at 200 and 240 MeV/c were of interest for the MICE experiment. The selected sample sizes are shown in Table IV.

E. Acceptance correction

The simulated geometric acceptance of the downstream tracker as a function of the projected scattering angles θ_X and θ_Y is shown in Fig. 4. The acceptance depends on the scattering angle so the scattering angle distributions must be corrected by the acceptance determined from simulation. The acceptance data were fitted by a seventh order polynomial,

$$\epsilon = a + b\theta_i^2 + c\theta_i^4 + d\theta_i^6 + e\theta_i^7,$$

where i is the bin number and a, b, c, d and e are fit parameters. This smoothed fluctuations in the tails of the acceptance function.
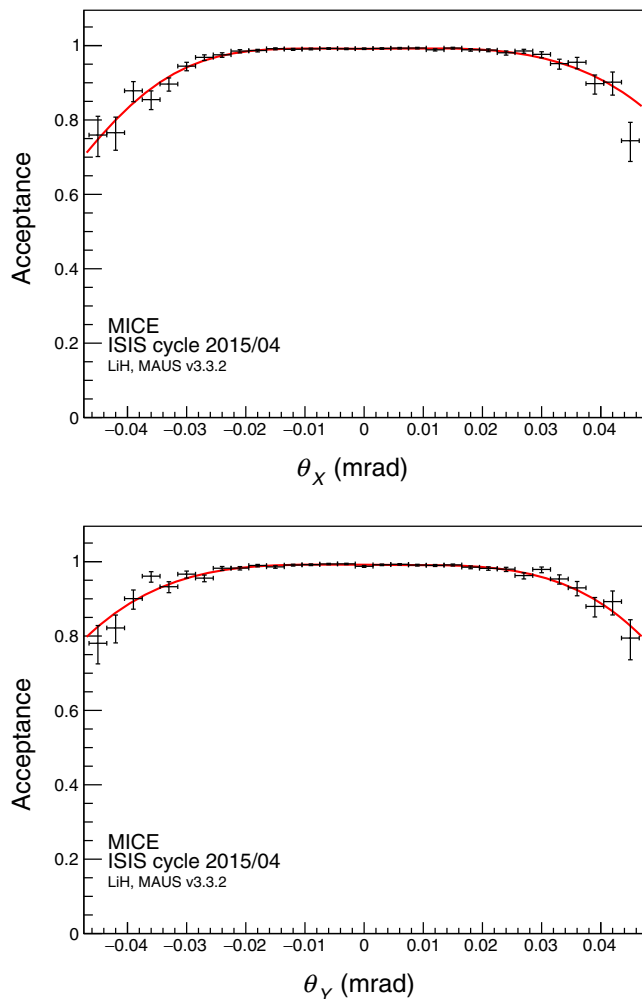
FIG. 4. The simulated fraction of events reconstructed by the trackers as a function of scattering angle after event selection. The red curve is an asymmetric seventh order polynomial fitted to the points and used for the acceptance correction.

F. Comparison to simulation

The MICE MC simulation models particles arising from protons incident on the target. G4beamline [35] was used to simulate particles from immediately after the target to just upstream of TOF0. The remainder of MICE, including the downstream portion of the beam line and cooling channel, was simulated using MAUS [31]. The simulation is handled in this way to reduce the computing resources required, as only a small subset of particles at the target is transported to the end of the cooling channel.

A comparison between the momentum distributions for reconstructed MC and data for the selected samples at three momenta (172, 200 and 240 MeV/c) is shown in Fig. 5. The measured distributions of x and y positions and slopes for the selected upstream muon samples are well described by the GEANT4 (v9.6) MC, as illustrated in Fig. 6. All MC scattering distributions include both statistical and systematic errors.

IV. RESULTS

A. Raw data MC comparison

The θ_X and θ_Y distributions from the LiH and no absorber data are compared to GEANT4 (v9.6) simulations in Figs. 7–9 and the θ^2_{Scatt} distribution in Fig. 10, at three momenta: 172, 200 and 240 MeV/c. The simulation gives an adequate description of the data; a summary of the comparison given in Table V. The integrals of these distributions are between 88% and 96% demonstrating that the selection criteria ensure high transmission for the selected sample. In this analysis GEANT4 (v9.6) is used with the QGSP_BERT (v4.0) physics list. In this configuration, multiple Coulomb scattering is modelled by the G4WentzelVI model [36,37]. The G4WentzelVI model is a mixed algorithm simulating both the hard collisions one by one and using a multiple scattering theory to treat the effects of the soft collisions at the end of a given step; this prevents the number of steps in the simulation from becoming too large and also reduces the dependence on the step length. This model is expected to provide results similar in accuracy to single scattering but in a computationally efficient manner. Single scattering is based on the assumption that the effect of multiple scattering can be modeled as if the hard scatters are the sum of many individual scatters while soft scatters are sampled from a distribution. "Hard" scatters are inelastic and result in large-angle deflections and large energy transfers. "Soft" scatters

TABLE V. Distribution widths of multiple scattering in lithium hydride and the χ^2 comparisons between data and the GEANT4 simulation. The χ^2/NDF were calculated using the number of bins as the number of degrees of freedom. Statistical and systematic uncertainties are given for the data distributions. Only statistical uncertainties are given for the model.

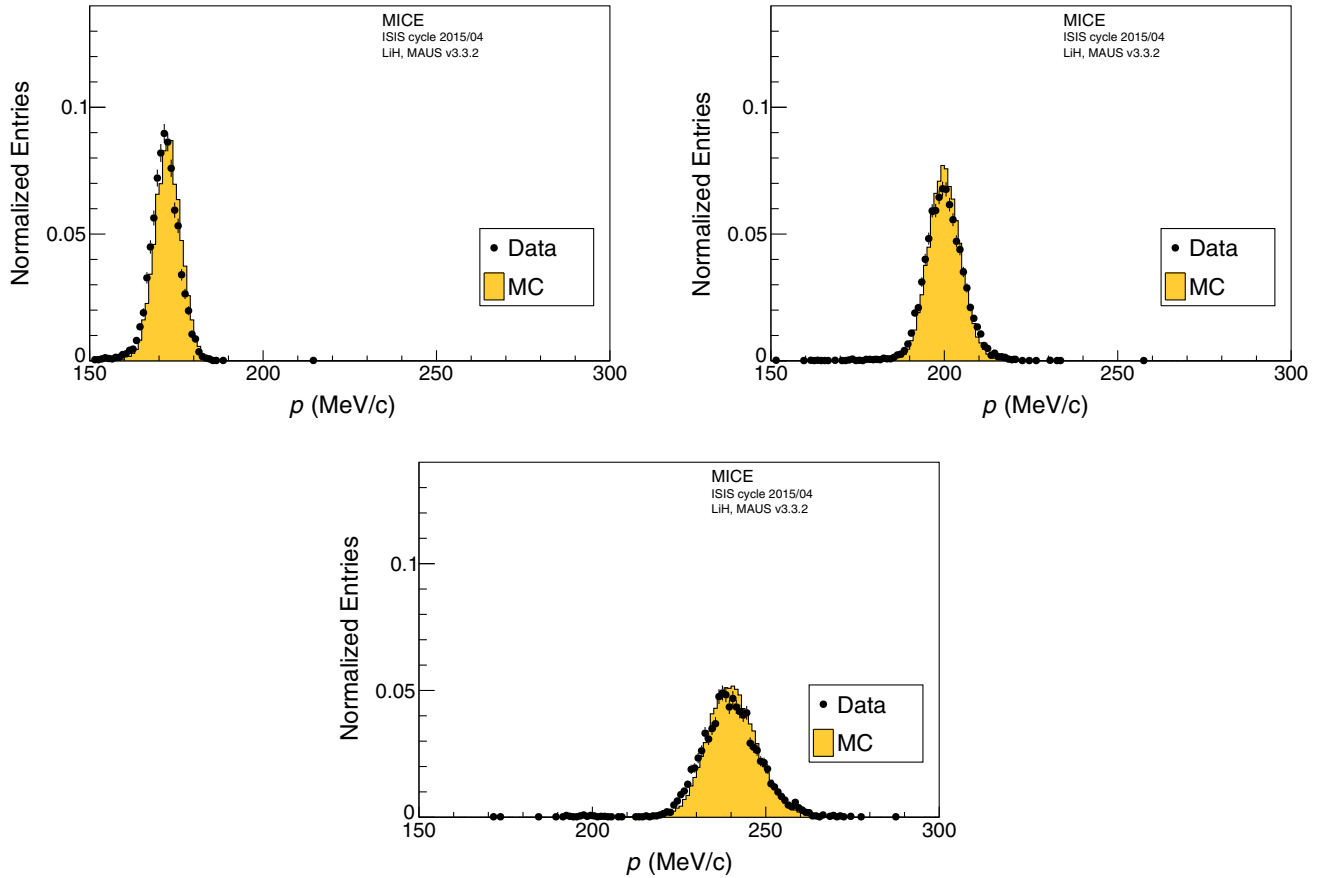| p (MeV/c)	Angle	θ_{Data} (mrad)	θ_{G4} (mrad)	χ^2/NDF	P-value
171.55	θ_X	$21.16 \pm 0.28 \pm 0.48$	21.87 ± 0.25	23.67/31	0.79
171.55	θ_Y	$20.97 \pm 0.27 \pm 0.48$	21.51 ± 0.25	37.86/31	0.15
199.93	θ_X	$18.38 \pm 0.18 \pm 0.33$	18.76 ± 0.09	17.75/31	0.96
199.93	θ_Y	$18.35 \pm 0.18 \pm 0.33$	18.89 ± 0.09	27.93/31	0.57
239.76	θ_X	$15.05 \pm 0.17 \pm 0.21$	15.69 ± 0.06	8.07/31	1.00
239.76	θ_Y	$15.03 \pm 0.16 \pm 0.21$	15.55 ± 0.06	8.23/31	1.00

FIG. 5. Comparison of reconstructed muon momentum at the center of the absorber for the 172, 200 and 240 MeV/c samples for data and simulation.

are elastic and result in small-angle deflections with small energy transfers.

B. Convolution with scattering models

The data collected with the absorber were compared to GEANT4 and the Molière scattering models by performing a convolution of the scattering model with no absorber data. The convolution,

$$n_{\text{conv}}(\theta) = n_{\text{NA}}(\theta) * n_{\text{model}}(\theta), \qquad (7)$$

where $n_{\text{conv}}(\theta)$ is the forward convolved distribution, $n_{\text{NA}}(\theta)$ is the scattering distribution measured with the no absorber data and $n_{\text{model}}(\theta)$ is the scattering distribution predicted by the model, is performed by adding an angle sampled from the predicted scattering distribution in the absorber for a given model (GEANT4 or Molière) to the angle determined from a given trajectory selected from the no absorber data. This takes into account scattering in the measurement system. The trajectories described by the sum of angles are extrapolated to the downstream tracker and if the track would not have been contained within the downstream tracker then it is not shown in the scattering distribution but the event is still counted in the

normalization. The net effect is a distribution, $n_{\text{conv}}(\theta)$, that is the convolution of the raw scattering model $n_{\text{model}}(\theta)$ with the detector effects given by the no absorber distribution $n_{\text{NA}}(\theta)$. Plots of the lithium hydride absorber data and the no absorber data convolved with either the GEANT4 simulation or the Molière model are shown in Fig. 11, with the residuals shown in Fig. 12, and the results are summarized in Table VI.

The Molière distributions for the lithium hydride absorber were calculated using the procedure described by Gottschalk [38] for mixtures and compounds. Pure ^{6}LiH with a thickness of 4.498 g cm^{-2} was assumed. Distributions were calculated for monoenergetic muons of 172, 200 and 240 MeV/c. Because the muon energy loss is small—about 11 MeV—the muon momentum was taken to be constant through the absorber.

Fano's correction to the Molière distribution was used to account for the scattering by atomic electrons. The values of the parameter U_{in}, which appears in the correction, were $-U_{\text{in}} = 3.6$ for hydrogen, as calculated exactly by Fano, and $-U_{\text{in}} = 5.0$ for lithium as suggested by Gottschalk for other materials.

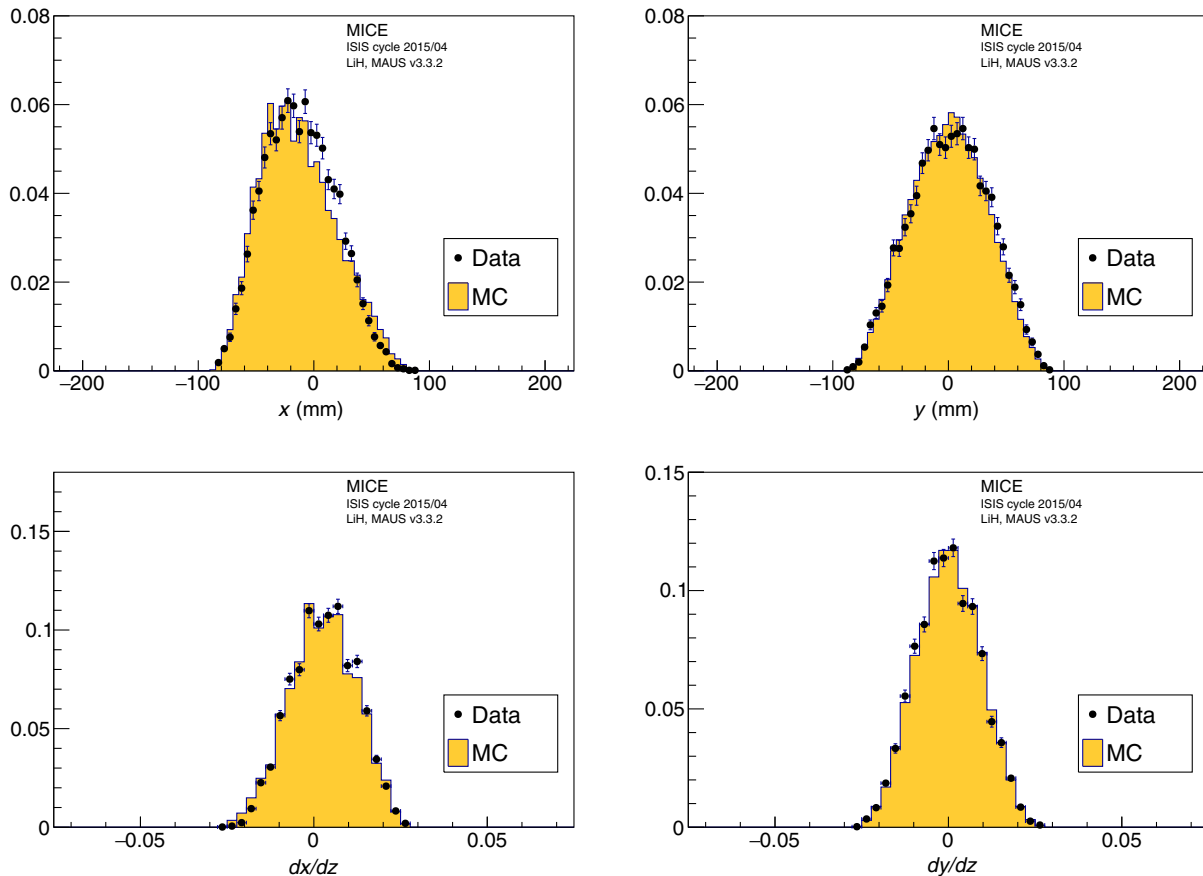A cubic spline was used to interpolate between the tabulated points of the functions given by Molière and

FIG. 6.   Comparison between Monte Carlo simulations and data for muons in the 200 MeV/c sample with the LiH absorber installed. All distributions are for the selected muons at the upstream reference plane. Top left: x distribution, top right: y distribution, bottom left: dx/dz distribution and bottom right: dy/dz distribution.

TABLE VI.   Distribution widths of multiple scattering in lithium hydride data compared to no absorber data convolved with two different models of scattering (GEANT4 and Molière). The χ^2/NDF were calculated using the number of bins as the number of degrees of freedom. Statistical and systematic uncertainties are given for the data distributions.

p (MeV/c)	Angle	θ_{Data} (mrad)	θ_{G4} (mrad)	χ^2/NDF	P-value	θ_{Mol} (mrad)	χ^2/NDF	P-value
171.55	θ_X	$21.16 \pm 0.28 \pm 0.48$	21.36 ± 0.05	30.29/31	0.45	22.64 ± 0.06	34.72/31	0.25
171.55	θ_Y	$20.97 \pm 0.27 \pm 0.48$	21.32 ± 0.05	29.10/31	0.51	22.58 ± 0.06	41.14/31	0.08
199.93	θ_X	$18.38 \pm 0.18 \pm 0.33$	18.09 ± 0.03	21.78/31	0.86	19.00 ± 0.04	28.04/31	0.57
199.93	θ_Y	$18.35 \pm 0.18 \pm 0.33$	18.02 ± 0.03	26.98/31	0.62	18.98 ± 0.04	35.41/31	0.23
239.76	θ_X	$15.05 \pm 0.17 \pm 0.21$	15.07 ± 0.02	4.08/31	1.00	15.62 ± 0.02	9.48/31	1.00
239.76	θ_Y	$15.03 \pm 0.16 \pm 0.21$	15.11 ± 0.02	3.44/31	1.00	15.70 ± 0.02	8.62/31	1.00

Bethe. Systematic errors in the calculation arising from, for example, the description of the absorber as pure ^{6}LiH were estimated to be of the order of one percent.

The calculated widths, θ_m, of the central Gaussian term of the projected Molière distributions are given in Table VII. If scattering by electrons is not included, i.e., Fano's electron correction is set to zero, the distributions are approximately twenty percent narrower. We note that Bethe's *ansatz* $Z^2 \to Z(Z+1)$ [6] to describe

the electron contribution is inappropriate here because the maximum kinematically allowed scattering angle of a 200 MeV/c muon by an electron is of the order of 4 milliradians, much less than the width of the scattering distribution. The Molière predictions shown in Table VII differ from those shown in Table VI as these are the predictions solely from the Molière calculation not the Molière prediction convolved with MICE no absorber scattering data.
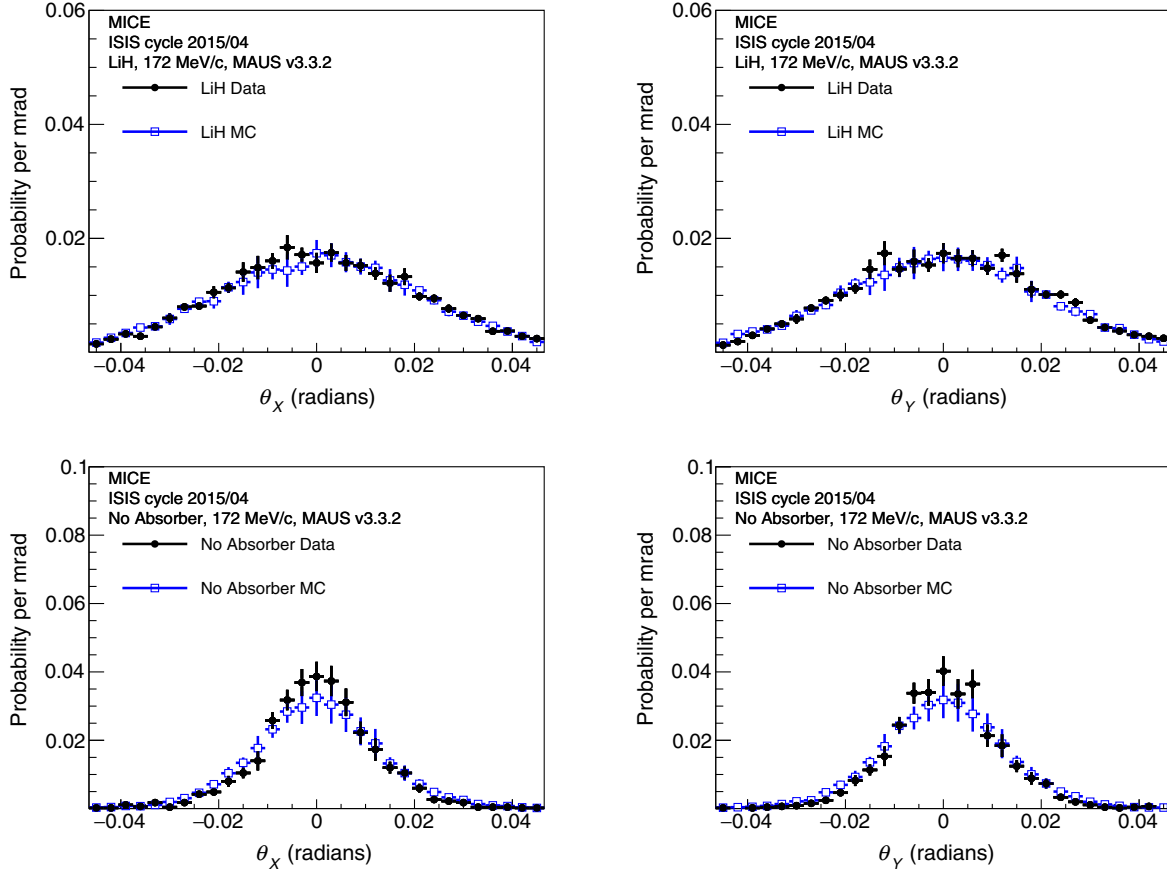
FIG. 7.   Scattering probability functions θ_X and θ_Y reconstructed from the 172 MeV/c muon beam with (top) and without (bottom) the LiH absorber in place compared to reconstructed MC scattering distributions. The black points are the real data and the blue open squares are the simulated data.

TABLE VII.   Calculated widths, θ_m, of the central Gaussian term of the projected Molière distribution for the lithium hydride absorber at each selected muon momentum.

Momentum MeV/c	θ_m milliradians
172	20.03
200	16.87
240	13.60

C. Deconvolution

To determine the underlying scattering distribution in the absorber, the effects of scattering in nonabsorber materials and the detector resolution must be deconvolved from the measured scattering distribution. The measured scattering distribution with the absorber in the MICE channel can be written

$$s'(i) = A(i) \sum_{k=0}^{k=31} s(k)(h(i-k)/A(i-k)), \qquad (8)$$

where $s'(i)$ is the number of events measured in the ith bin with the absorber in the channel, $s(k)$ is the scattering

distribution due only to the absorber material without the detector, $h(i-k)$ is the no absorber scattering distribution which includes the detector resolution and $A(i)$ is the acceptance function at bin (i). This system of linear equations can be written in matrix form as

$$\vec{s'} = \mathbf{H}\vec{s} \qquad (9)$$

where $\vec{s'}$ is the a vector where each entry is the number of events in a bin of the scattering distribution of all material in the channel. Similarly for $\vec{s}$ but for a scattering distribution of only the absorber and $\mathbf{H}$ is a matrix which transforms one to the other. The unfolding step employs Gold's [39] deconvolution algorithm to extract the true scattering distribution (s) solely due to the absorber material, as described in [40] and implemented in the ROOT [41] TSpectrum class. The advantages of using the Gold deconvolution algorithm are that it does not rely on simulated data or scattering models and is a purely data-driven technique making use of all of the data collected. The output of the deconvolution is compared to the GEANT4 and Molière prediction in Fig. 13.
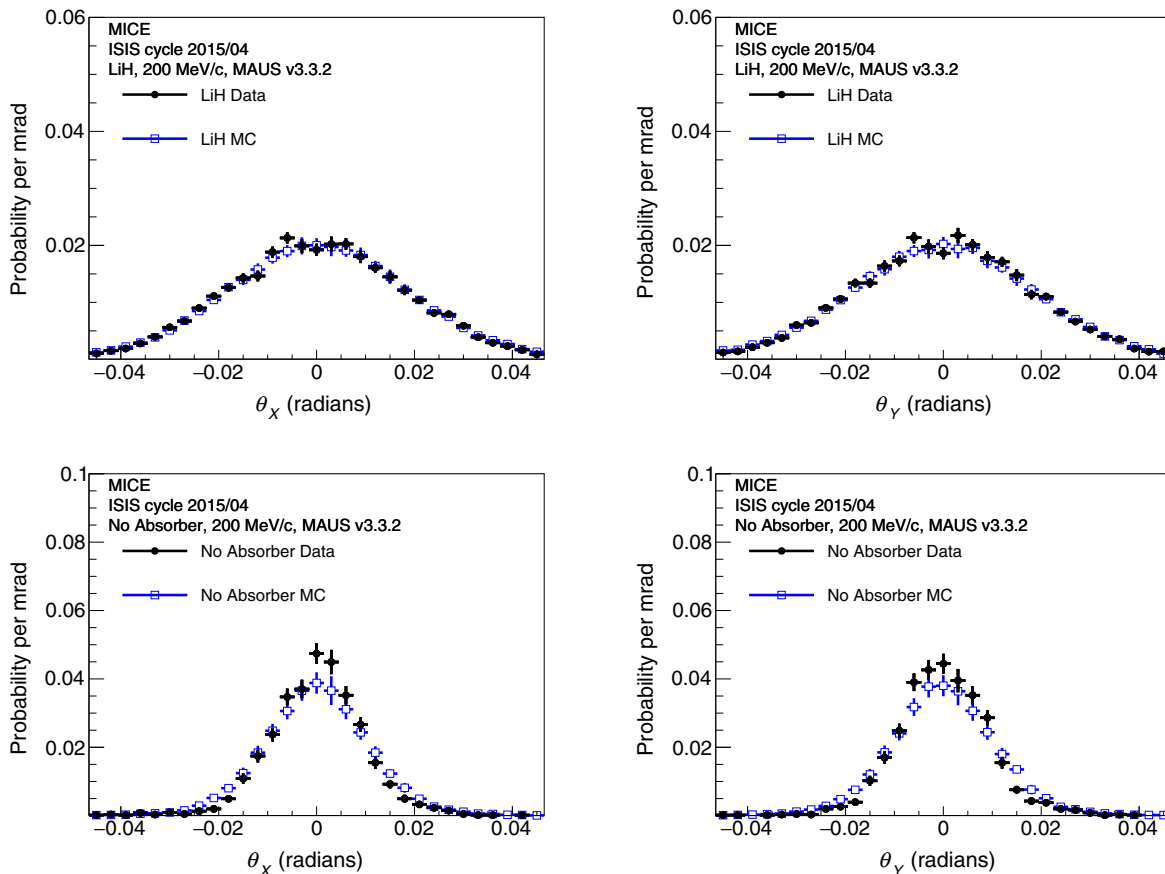
FIG. 8.   Scattering probability functions θ_X and θ_Y reconstructed from the 200 MeV/c muon beam with (top) and without (bottom) the LiH absorber in place compared to reconstructed MC scattering distributions. The black points are the real data and the blue open squares are the simulated data.

D. Systematic uncertainties

Six contributions to the systematic uncertainty in the scattering distributions are considered here; uncertainties in the time of flight; measured alignment; fiducial radius; choice of plane in which to measure scattering; effect of pion contamination; and in the deconvolution procedure. To calculate the systematic uncertainty for the individual bins of the scattering plots shown in Figs. 7–10 and 13 the numerical derivative is calculated with the expression

$$\sigma_{\text{sys},i} = \frac{dn_i}{d\alpha}\sigma_\alpha \approx \frac{\Delta n_i}{\Delta\alpha}\sigma_\alpha, \qquad (10)$$

where Δn_i is the change in the number of entries in a bin that results from altering a parameter α with a known uncertainty σ_α in the analysis or simulation by an amount $\Delta\alpha$. The uncertainty in the measured width of the distribution is calculated in a similar way using

$$\sigma_{\text{sys}} \approx \frac{\Delta\theta_0}{\Delta\alpha}\sigma_\alpha, \qquad (11)$$

where $\Delta\theta_0$ is the change in the width of the scattering distribution when measured in either the x or y projection. The systematic uncertainties are reported for the RMS width of the θ_X distribution ($\theta_{0,X}$) and the width of the θ_Y distribution ($\theta_{0,Y}$) separately.

A significant systematic uncertainty is due to the TOF selection criteria which directly impact the momentum range of the particles used in the scattering measurement. The scale is set using the measured 70 ps uncertainty on the time-of-flight measurement. The effect of particles incorrectly appearing inside or outside of the 200 ps bin selection window is determined by offsetting the no absorber data by 200 ps and the change in the measured scattering width is treated as the systematic uncertainty.

Uncertainties in the alignment have a direct effect on the angles measured by the tracker. The alignment of the MICE trackers is characterized by offsets parallel to x and y, with an uncertainty of 0.2 mm, and angles of rotation about the x and y axes, with an uncertainty of 0.07 mrad. The uncertainties in the width of the scattering distributions were extracted from a number of pseudo-experiments, where the alignment parameters were varied in each iteration.
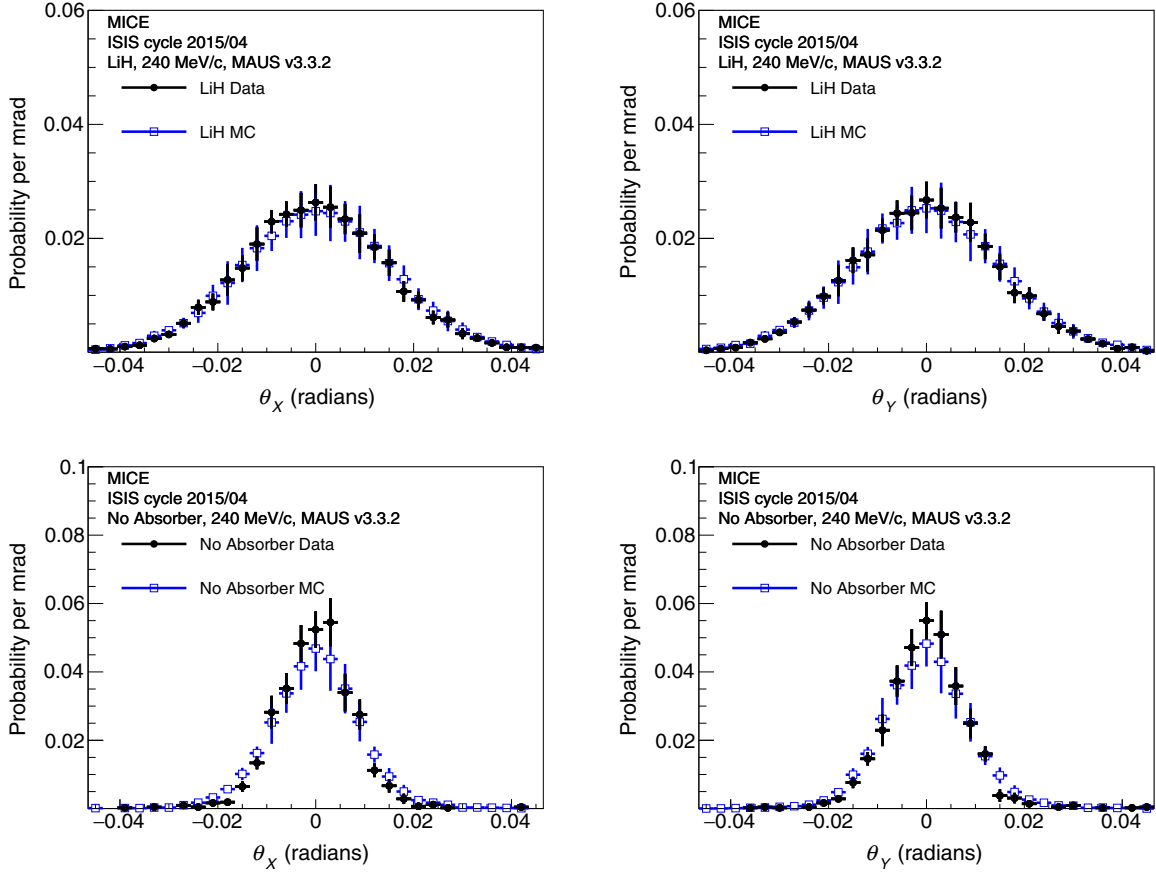
FIG. 9.   Scattering probability functions θ_X and θ_Y reconstructed from the 240 MeV/c muon beam with (top) and without (bottom) the LiH absorber in place compared to reconstructed MC scattering distributions. The black points are the real data and the blue open squares are the simulated data.

The choice of the fiducial region may systematically affect the results. A scan over the possible values of the fiducial radius was completed and the variation in the width of the scattering distributions for samples adjacent to the selected value of 90 mm was used to set the uncertainty.

The definitions of the scattering angles are given in Sec. II and the Appendix. In the definition of the projected scattering angles, θ_x and θ_y, $\hat{\mathbf{v}}$ is the unit vector mutually orthogonal to the y direction and the momentum vector and $\hat{\mathbf{u}}$ is the unit vector parallel to the upstream momentum vector. They are related via the formula

$$\hat{\mathbf{v}} = \hat{\mathbf{s}} \times \hat{\mathbf{u}}, \qquad (12)$$

where $\hat{\mathbf{s}}$ is arbitrarily defined as $\hat{\mathbf{s}} = (0, -1, 0)$. This expression defines a direction perpendicular to a plane containing the upstream track. There are an infinite number of planes that contain this track, so we consider the uncertainty introduced by the definition of $\hat{\mathbf{s}}$ by rotating it between 0° and 180°, in increments of 1°, around the x-axis, with the analysis repeated after each increment. The

resulting maximum change in measured scattering angle is included in the systematic uncertainties in Table VIII.

The MICE muon beam has pion contamination with an upper limit $f_\pi < 1.4\%$ at 90% C.L. [29]. To measure the effect of this contamination on the scattering measurement for muons, a Monte Carlo study was performed. The measurement was simulated with the MICE beam, including simulated impurities, and a pure muon sample, with the systematic error being the difference between the two results.

The difference between the deconvolved result and the true scattering distribution from a GEANT4 simulation was taken to be an additional source of systematic error. This accounts for any bias introduced by the Gold deconvolution procedure. The systematic uncertainties for the deconvolution procedure showed significant variation from bin to bin so a parabolic smoothing function was used to assign the systematic uncertainty to each bin.

All systematic uncertainties, and their quadratic combination, for the three selected momenta of 172, 200 and 240 MeV/c are included in Table VIII. The dominant systematic uncertainties are those in the momentum scale of the TOF system and the deconvolution procedure.
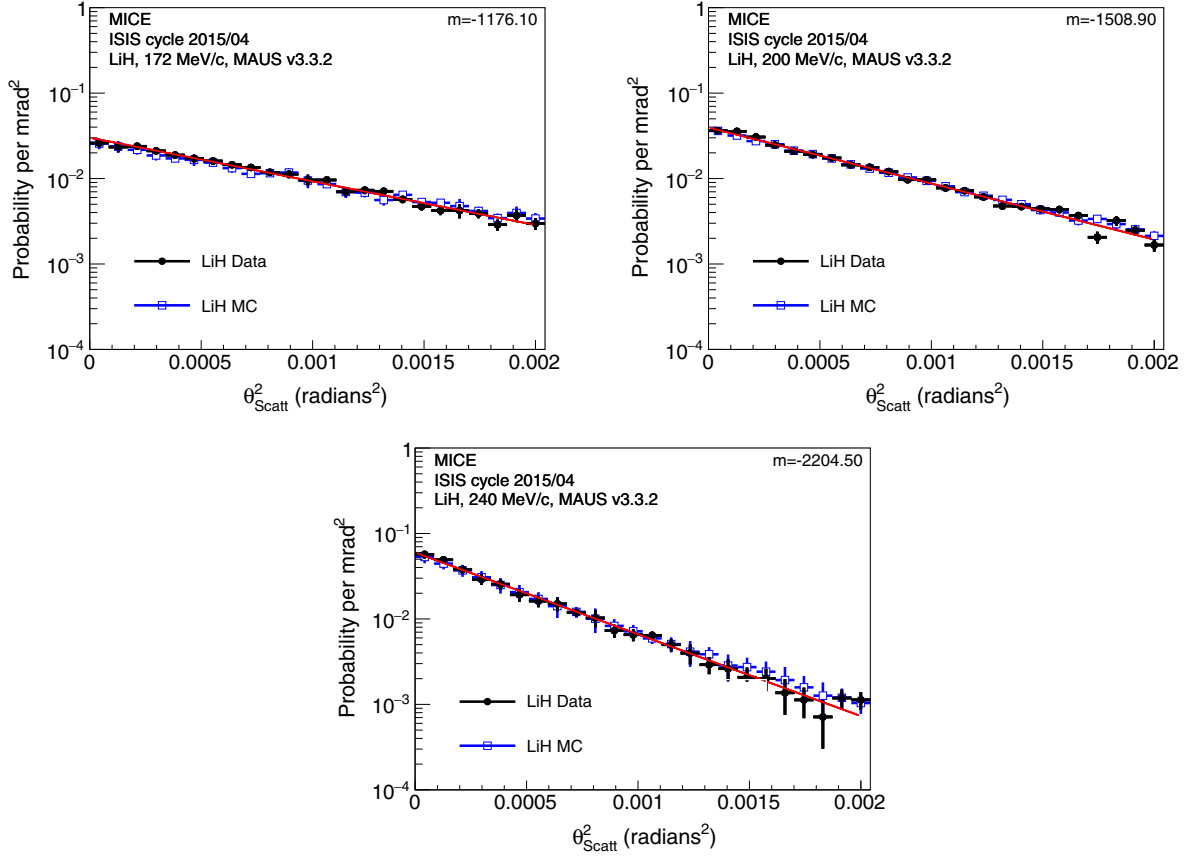
FIG. 10. θ_{Scatt}^2 distributions reconstructed from the 172, 200 and 240 MeV/c muon samples. The LiH absorber was in the beamline in these samples. The black points are the real data and the blue open squares are the reconstructed simulated data. A function $Ae^{-m\theta_{\text{Scatt}}^2}$ was fitted to the data distribution and is shown by the red line with m displayed on the plot.

E. Model comparisons

The residual between the scattering distribution in data and that predicted by the models is used to quantify the level of agreement between data and simulation. The normalized residual is defined as

$$\text{residual} = \frac{p_{\text{data}}(\theta_i) - p_{\text{simulation}}(\theta_i)}{\sqrt{\sigma_{\text{stat}}^2 + \sum \sigma_{\text{sys},i}^2}} \qquad (13)$$

where $p_{\text{data}}(\theta_i)$ is the probability of scattering at angle θ_i measured with the MICE data and $p_{\text{simulation}}(\theta_i)$ is the probability of scattering predicted by the corresponding model. The systematic uncertainties $\sigma_{\text{sys},i}^2$, discussed in Sec. IV D, are calculated and summed in quadrature on a bin by bin level. The χ^2 derived from these residuals appears in Table V. The χ^2 between the scattering distribution from the data and that predicted by the model is calculated using

$$\chi^2 = \sum_{i=0}^{N} \frac{(p_{\text{data}}(\theta_i) - p_{\text{simulation}}(\theta_i))^2}{\sigma_{\text{stat}}^2 + \sum_{\text{sys}} \sigma_{\text{sys},i}^2} \qquad (14)$$

where N is the number of bins and sys is the number of systematic errors. The χ^2 was calculated using 31 data points and demonstrates good agreement between data and MC. The χ^2 calculation in Eq. (14) was repeated for both the forward convolution comparison to real data and for the comparison between the deconvolved data and the GEANT4 and Molière models. The systematic uncertainties are added on a bin by bin basis in the calculation of the χ^2 in Eq. (14).

There is very little difference between the GEANT4 simulation, the Molière calculations and the deconvolved data. The deconvolved θ_X and θ_Y multiple scattering distributions on lithium hydride for the 172, 200 and 240 MeV/c muon samples are shown in Fig. 13, and these are compared with a GEANT4 LiH simulation and the Molière calculation.

The distributions of the projections in θ_X and θ_Y were characterized using a Gaussian fit within a ± 45 mrad range, with the results shown in Table IX for deconvolved data using the Gold deconvolution algorithm and the true distributions extracted from the GEANT4 simulation and the Molière model calculation. The table shows that the deconvolved θ_X and θ_Y projections of the scattering
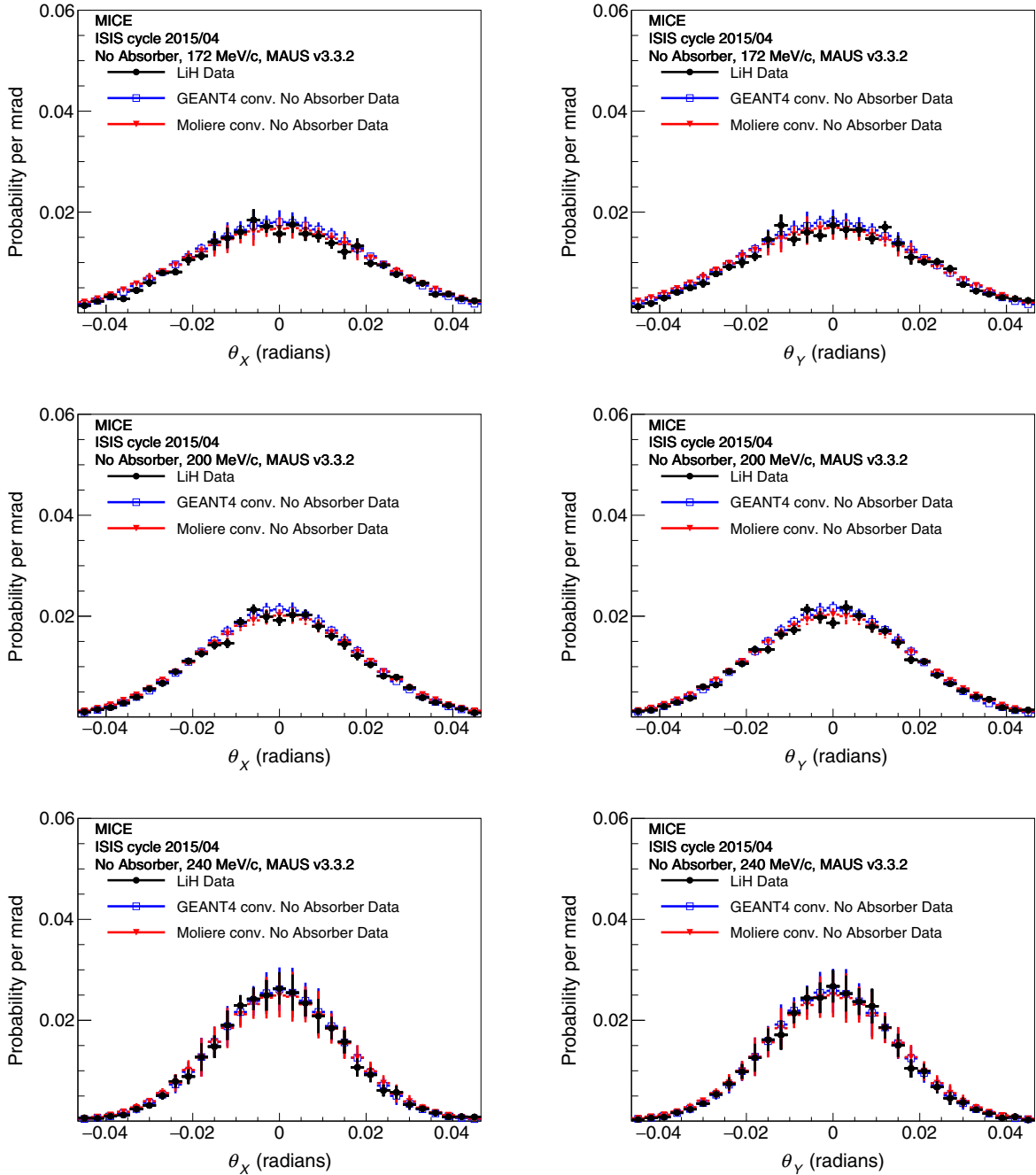
FIG. 11.   Scattering probability functions reconstructed from the 172, 200 and 240 MeV/c muon beams with the LiH absorber in place (black dots) compared to the GEANT4 scattering model (blue dots) and the Molière model (red dots) in LiH convolved with the no absorber distribution.

distributions are approximately consistent with the GEANT4 and Molière distributions, but the Molière distribution is systematically wider than the rest and significantly wider than that given by GEANT4.

F. Momentum-dependent measurements

The selected samples are plotted as a function of mean momentum for each sample, to confirm the dependence of

the widths of the scattering distributions on momentum. The number of events contained in each TOF bin is between 3500 and 9000 events. The deconvolved scattering widths as a function of momentum are shown in Fig. 14. The widths, θ_0, are fitted to

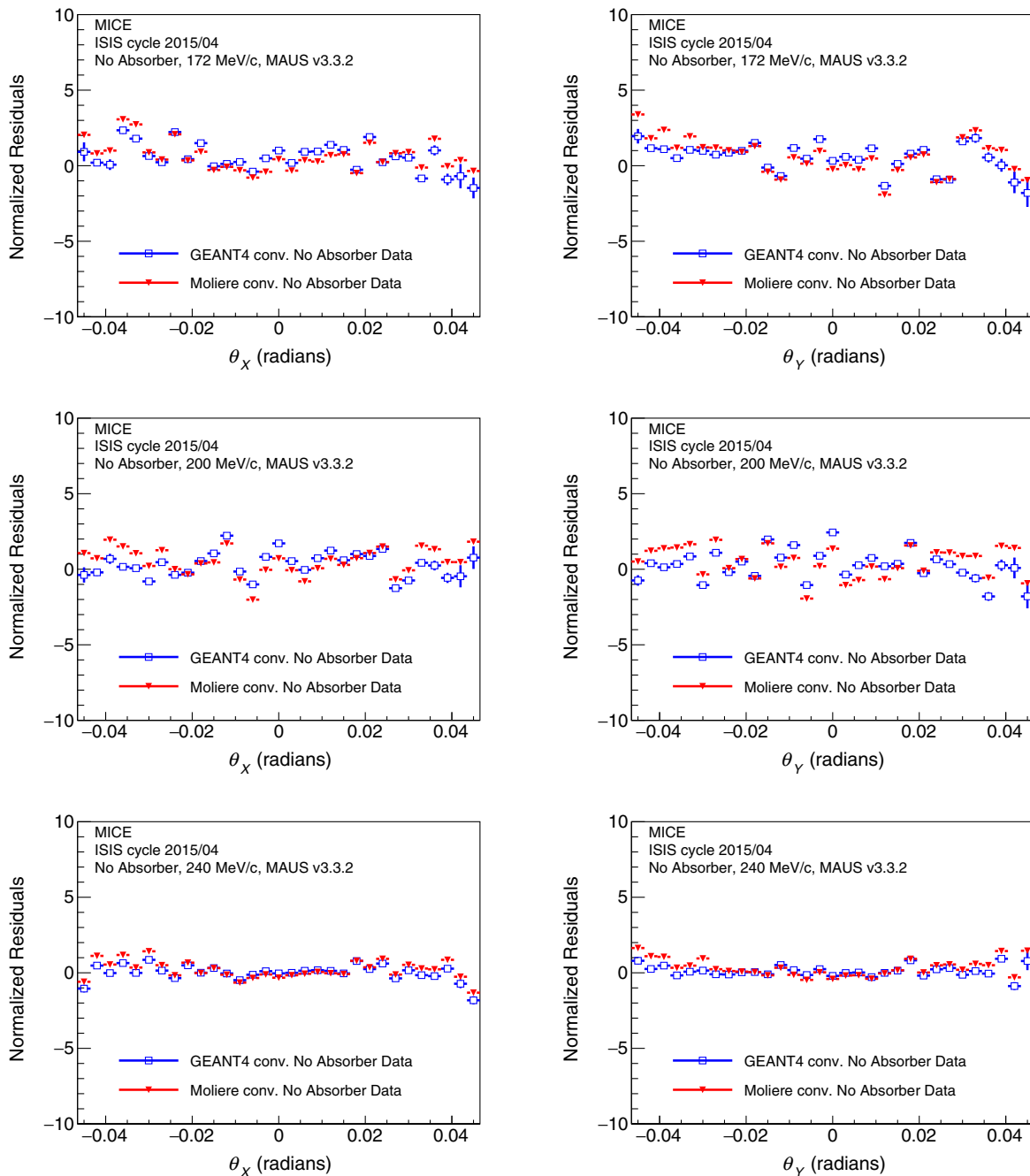$$\theta_0 = \frac{13.6 \ [\text{MeV}/c]a}{p\beta}, \tag{15}$$

FIG. 12.   Scattering residuals between data with the LiH absorber and no absorber data convolved with either GEANT4 or the Molière scattering models in LiH for the 172, 200 and 240 MeV/c samples. The residuals are normalized to the estimated uncertainty in the data in each bin. The agreement improves at higher momentum where the scattering distributions are narrower.

where a is a fit coefficient, motivated by Eq. (3), where the β dependence of the log term is negligible, changing the calculated value by less than 1%.

The coefficient, a, is compared with the prediction from the PDG formula in Eq. (3). The values of the coefficients, a, determined from the fits to the $\theta_{0,X}$ and $\theta_{0,Y}$ distributions are shown in Table X. The numerical derivative of the

momentum with respect to TOF of the sample was calculated and used to assess the systematic uncertainty associated with the measurement.

Measurements using the projected angles are systematically smaller than the PDG prediction. The average of the two fits to the $\theta_{0,X}$ and $\theta_{0,Y}$ muon scattering widths as a function of momentum yields $a = 208.1 \pm 1.5$ mrad,
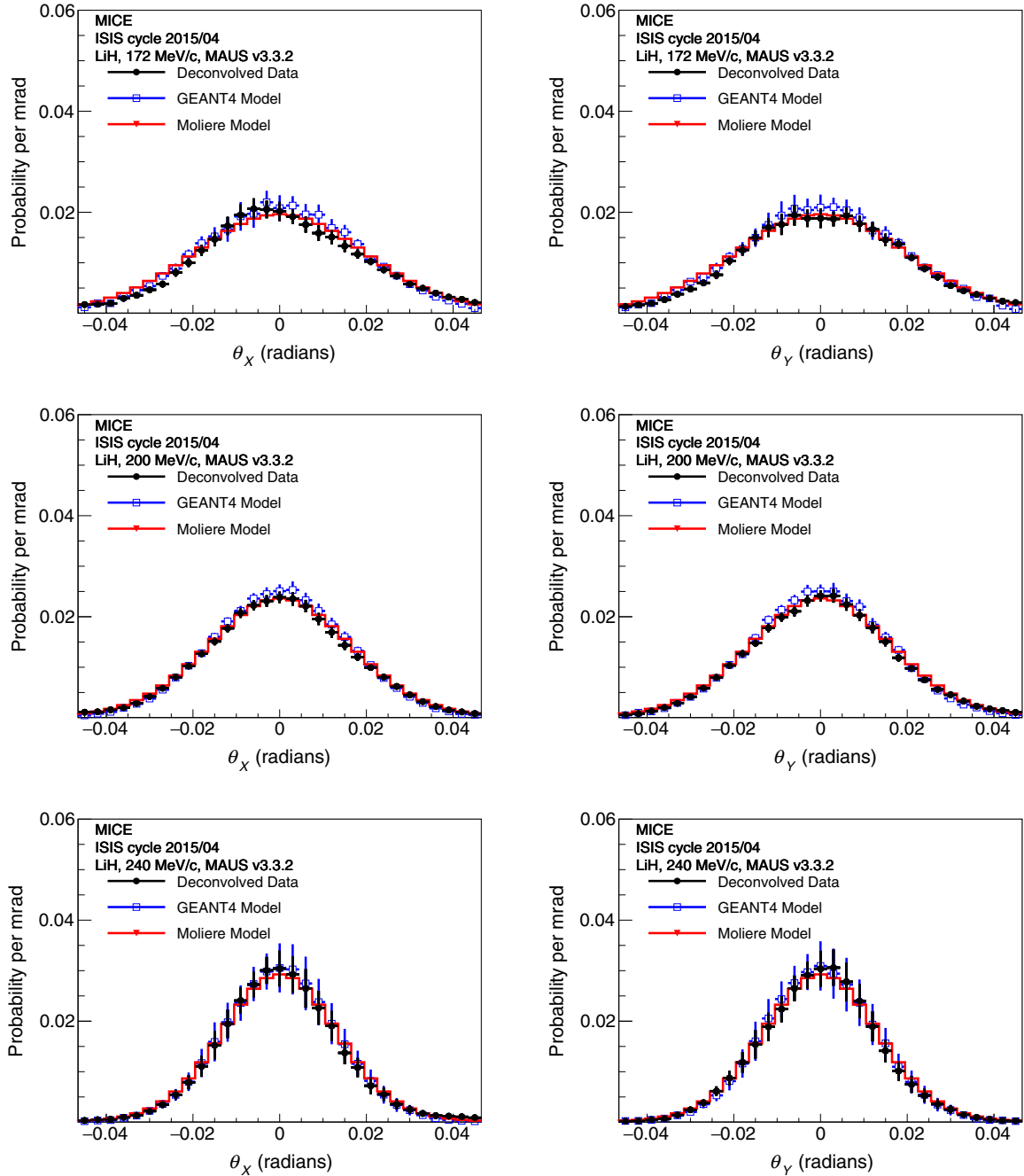
FIG. 13.   Projected θ_X and θ_Y multiple scattering probability functions at 172, 200 and 240 MeV/c after deconvolution. The GEANT4 and Molière scattering distributions in LiH are provided for comparison.

which is 9% smaller than the value proposed by the PDG formula, $a = 226.7$ mrad, but still within the uncertainties of that approximate formula, Eq. (3), which is quoted as accurate to 11%.

V. CONCLUSIONS

Presented here is an analysis of the LiH multiple Coulomb scattering data taken during ISIS user run 2015/04 using MICE. These data were compared to the GEANT4 (v9.6) default scattering model [11] and the full Molière calculation [4,5]. A χ^2 statistic was used to make quantitative statements about the validity of the proposed models. Three approaches are taken; the measured LiH and no absorber scattering distributions were compared to GEANT4, the forward convolution using the no absorber data was compared to both GEANT4 and the Molière model and the deconvolution of the LiH scattering data using the

TABLE VIII. Systematic uncertainties associated with the width of the scattering distributions of $\theta_{0,X}$ and $\theta_{0,Y}$ in three representative momentum bins.

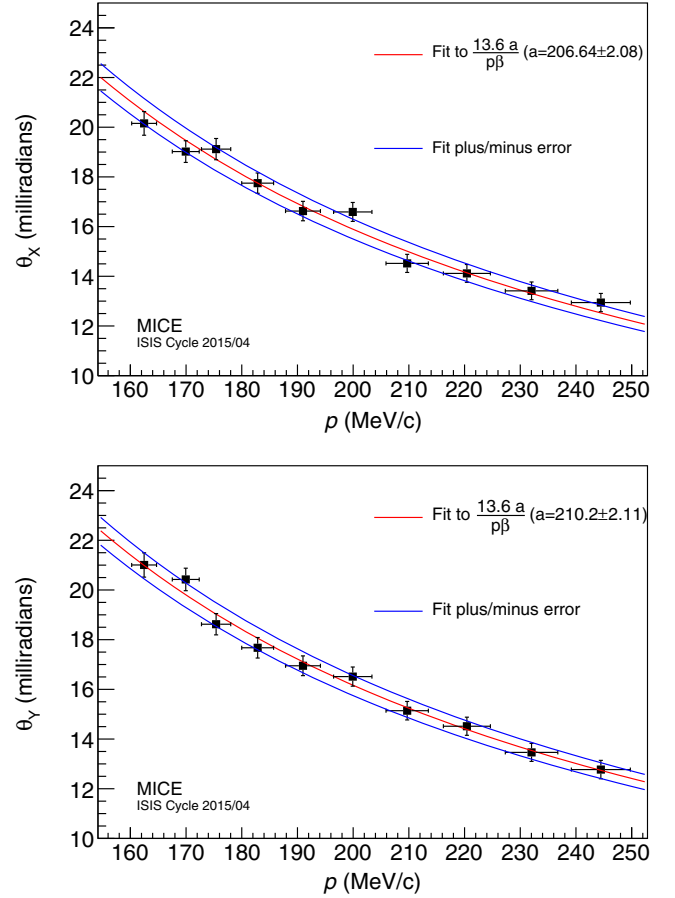| p (MeV/c)	Type	$\Delta\theta_{0,X}$ (mrad)	$\Delta\theta_{0,Y}$ (mrad)
171.55	TOF selection	0.64	0.64
	Alignment	< 0.01	0.01
	Fiducial radius	< 0.01	< 0.01
	θ angle definition	< 0.01	< 0.01
	π contamination	< 0.01	< 0.01
	Deconvolution	1.25	1.19
	Total sys.	1.39	1.35
199.93	TOF selection	0.29	0.29
	Alignment	0.02	< 0.01
	Fiducial radius	0.01	0.01
	θ definition	< 0.01	< 0.01
	π contamination	< 0.01	< 0.01
	Deconvolution	0.70	0.47
	Total sys.	0.73	0.54
239.76	TOF selection	0.27	0.27
	Alignment	< 0.01	< 0.01
	Fiducial radius	0.01	0.01
	θ definition	< 0.01	< 0.01
	π contamination	0.01	0.01
	Deconvolution	0.27	0.41
	Total sys.	0.36	0.49

FIG. 14. The results of the scattering analysis using data in a number of momentum bins. Scattering widths are reported after application of the Gold deconvolution.

no absorber data was compared to both GEANT4 and the Molière model. In all cases the GEANT4 scattering widths agreed with the measured data at each of the nominal momenta, but the Molière model produces systematically wider distributions.

The momentum dependence of scattering was examined by selecting 200 ps time of flight samples from the muon beam data. The momentum dependence from 160 to 245 MeV/c was compared to the dependence in Eq. (3), from the PDG [3], and it was found that the measured RMS scattering width is about 9% smaller than the approximate PDG estimation, but within the latter's stated uncertainty.

TABLE X. Results of the fit to the scattering widths as a function of momentum, given by Eq. (15). The value predicted by the PDG is also shown.

Angle	a (mrad)
$\theta_{0,X}$	206.6 ± 2.1
$\theta_{0,Y}$	210.2 ± 2.1
PDG	226.7

TABLE IX. Widths of best fit Gaussian fitted to central ± 45 mrad of scattering distributions after deconvolution compared to GEANT4 and Molière models. Statistical and systematic uncertainties are given for the data distributions. Only statistical uncertainties are given for the GEANT4 model.

p (MeV/c)	Angle	$\theta_{\text{Gold}}^{\text{meas}}$ (mrad)	$\theta_{G4}^{\text{true}}$ (mrad)	$\theta_{\text{Molière}}^{\text{true}}$ (mrad)
171.55	θ_X	$19.03 \pm 0.26 \pm 1.39$	18.62 ± 0.13	20.03
171.55	θ_Y	$18.95 \pm 0.24 \pm 1.35$	18.59 ± 0.12	20.03
199.93	θ_X	$16.59 \pm 0.17 \pm 0.73$	15.82 ± 0.05	16.87
199.93	θ_Y	$16.36 \pm 0.17 \pm 0.55$	15.82 ± 0.05	16.87
239.76	θ_X	$13.29 \pm 0.17 \pm 0.37$	13.16 ± 0.04	13.60
239.76	θ_Y	$13.21 \pm 0.16 \pm 0.49$	13.10 ± 0.04	13.60

APPENDIX: DEFINITION OF SCATTERING ANGLES

The projections of the scattering angle onto the *y*-*z* or *x*-*z* plane, angles θ_X and θ_Y, are defined by considering the inner product of the downstream momentum $\mathbf{p}_{DS}$ with the component of the upstream momentum vector $\mathbf{p}_{US}$, perpendicular to the projection plane. The scattering projection into the plane defined by the momentum vector and the *y*-axis is

$$\theta_Y = \arctan\left(\frac{\mathbf{p}_{DS} \cdot \hat{\mathbf{v}}}{\mathbf{p}_{DS} \cdot \hat{\mathbf{u}}}\right) = \arctan\left(\frac{\mathbf{p}_{DS} \cdot (\hat{\mathbf{y}} \times \mathbf{p}_{US})|\mathbf{p}_{US}|}{(\mathbf{p}_{DS} \cdot \mathbf{p}_{US})|\hat{\mathbf{y}} \times \mathbf{p}_{US}|}\right),$$
(A1)

where $\hat{\mathbf{y}}$ is the unit vector in the *y* direction, $\hat{\mathbf{v}} = \hat{\mathbf{y}} \times \mathbf{p}_{US}/|\hat{\mathbf{y}} \times \mathbf{p}_{US}|$ is the unit vector mutually orthogonal to the *y* direction and the momentum vector and $\hat{\mathbf{u}} = \mathbf{p}_{US}/|\mathbf{p}_{US}|$ is the unit vector parallel to the upstream momentum vector. A scattering angle in the perpendicular plane must then be defined as

$$\theta_X = \arctan\left(|\mathbf{p}_{US}|\frac{\mathbf{p}_{DS} \cdot (\mathbf{p}_{US} \times (\hat{\mathbf{y}} \times \mathbf{p}_{US}))}{|\mathbf{p}_{US} \times (\hat{\mathbf{y}} \times \mathbf{p}_{US})|\mathbf{p}_{DS} \cdot \mathbf{p}_{US}}\right),$$
(A2)

where the downstream vector is now projected onto the unit vector $\hat{\mathbf{v}} = \mathbf{p}_{US} \times (\hat{\mathbf{y}} \times \mathbf{p}_{US})/|\mathbf{p}_{US} \times (\hat{\mathbf{y}} \times \mathbf{p}_{US})|$. These two expressions can be expressed in terms of the gradients of the muon tracks before and after the scatters,

$$\theta_Y = \arctan\left\{\frac{\sqrt{1 + (\frac{dx}{dz})_{US}^2 + (\frac{dy}{dz})_{US}^2}}{\sqrt{1 + (\frac{dx}{dz})_{US}^2}}\right.$$
$$\left.\times\left(\frac{(\frac{dx}{dz})_{DS} - (\frac{dx}{dz})_{US}}{1 + (\frac{dx}{dz})_{US}(\frac{dx}{dz})_{DS} + (\frac{dy}{dz})_{US}(\frac{dy}{dz})_{DS}}\right)\right\},$$
(A3)

$$\theta_X = \arctan\left\{\sqrt{\frac{1 + (\frac{dx}{dz})_{US}^2 + (\frac{dy}{dz})_{US}^2}{(1 + (\frac{dx}{dz})_{US}^2 + (\frac{dy}{dz})_{US}^2)(1 + (\frac{dx}{dz})_{US}^2)}}\right.$$
$$\left.\times\left(\frac{(\frac{dy}{dz})_{DS}(1 + (\frac{dx}{dz})_{US}^2) + ((\frac{dx}{dz})_{DS}(\frac{dx}{dz})_{US} - 1)(\frac{dy}{dz})_{US}}{1 + (\frac{dx}{dz})_{US}(\frac{dx}{dz})_{DS} + (\frac{dy}{dz})_{US}(\frac{dy}{dz})_{DS}}\right)\right\}.$$
(A4)

In the approximation of small angles (i.e., $\frac{dx}{dz} \approx \frac{dy}{dz} \ll 1$) these produce the more familiar forms

$$\theta_X = \left(\frac{dy}{dz}\right)_{DS} - \left(\frac{dy}{dz}\right)_{US}$$
(A5)

for scattering about the *x*-axis or

$$\theta_Y = \left(\frac{dx}{dz}\right)_{DS} - \left(\frac{dx}{dz}\right)_{US}$$
(A6)

for scattering about the *y*-axis. The more exact expressions, Eqs. (A3) and (A4), are used throughout for this analysis.

[1] B. Rossi and K. Greisen, Cosmic-ray theory, Rev. Mod. Phys. **13**, 240 (1941).

[2] E. Rutherford, LXXIX. The scattering of α and β particles by matter and the structure of the atom, Philos. Mag. Ser. 6 **21**, 669 (1911).

[3] P. Zyla *et al.* (Particle Data Group), Review of particle physics, Prog. Theor. Exp. Phys. **2020**, 083C01 (2020).

[4] G. Molière, Theorie der Streuung schneller geladener Teilchen I. Einzelstreuung am abgeschirmten Coulomb-Feld, Z. Naturforsch. **A2**, 133 (1947).

[5] G. Molière, Theory of the scattering of fast charged particles. 2. Repeated and multiple scattering, Z. Naturforsch. **A3**, 78 (1948).

[6] H. A. Bethe, Molière's theory of multiple scattering, Phys. Rev. **89**, 1256 (1953).

[7] U. Fano, Inelastic collisions and the Molière theory of multiple scattering, Phys. Rev. **93,** 117 (1954).

[8] D. Attwood *et al.*, The scattering of muons in low Z materials, Nucl. Instrum. Methods Phys. Res., Sect. B **251,** 41 (2006).

[9] V. L. Highland, Some practical remarks on multiple scattering, Nucl. Instrum. Methods **129,** 497 (1975).

[10] G. R. Lynch and O. I. Dahl, Approximations to multiple Coulomb scattering, Nucl. Instrum. Methods Phys. Res., Sect. B **58,** 6 (1991).

[11] S. Agostinelli *et al.* (GEANT4 Collaboration), GEANT4: A Simulation toolkit, Nucl. Instrum. Methods Phys. Res., Sect. A **506,** 250 (2003).

[12] G. Wentzel, Zwei Bemerkungen über die Zerstreuung korpuskularer Strahlen als Beugungserscheinung, Z. Phys. **40,** 590 (1926).

[13] T. Carlisle, Step IV of the Muon Ionization Cooling Experiment (MICE) and the multiple scattering of muons, Ph.D. thesis, Oxford U., 2013.

[14] D. Neuffer, Principles and applications of muon cooling, Part. Accel. **14,** 75 (1983).

[15] M. Bogomilov *et al.* (MICE Collaboration), Demonstration of cooling by the muon ionization cooling experiment, Nature (London) **578,** 53 (2020).

[16] M. Bogomilov *et al.*, Neutrino factory, Phys. Rev. ST Accel. Beams **17,** 121002 (2014).

[17] D. Neuffer, P. Snopok, and Y. Alexahin, Front end for a neutrino factory or muon collider, J. Instrum. **12,** T11007 (2017).

[18] C. T. Rogers, D. Stratakis, G. Prior, S. Gilardoni, D. Neuffer, P. Snopok, A. Alekou, and J. Pasternak, Muon front end for the neutrino factory, Phys. Rev. ST Accel. Beams **16,** 040104 (2013).

[19] D. Stratakis and R. B. Palmer, Rectilinear six-dimensional ionization cooling channel for a muon collider: A theoretical and numerical study, Phys. Rev. ST Accel. Beams **18,** 031003 (2015).

[20] D. Neuffer, H. Sayed, J. Acosta, T. Hart, and D. Summers, Final cooling for a high-energy high-luminosity lepton collider, J. Instrum. **12,** T07003 (2017).

[21] M. Bogomilov *et al.* (MICE Collaboration), The MICE Muon Beam on ISIS and the beam-line instrumentation of the Muon Ionization Cooling Experiment, J. Instrum. **7,** P05009 (2012).

[22] K. Long, D. Lucchesi, M. Palmer, N. Pastrone, D. Schulte, and V. Shiltsev, Muon colliders to expand frontiers of particle physics, Nat. Phys. **17,** 289 (2021).

[23] M. Ellis *et al.*, The design, construction and performance of the MICE scintillating fibre trackers, Nucl. Instrum. Methods Phys. Res., Sect. A **659,** 136 (2011),

[24] M. Bogomilov *et al.* (MICE Collaboration), Performance of the MICE diagnostic system, J. Instrum. **16,** P08046 (2021).

[25] D. Adams *et al.* (MICE Collaboration), Characterisation of the muon beams for the Muon Ionisation Cooling Experiment, Eur. Phys. J. C **73,** 2582 (2013).

[26] C. N. Booth *et al.*, The design, construction and performance of the MICE target, J. Instrum. **8,** P03006 (2012).

[27] C. N. Booth *et al.*, The design and performance of an improved target for MICE, J. Instrum. **11,** P05006 (2016).

[28] R. Bertoni, A. Blondel, M. Bonesini, G. Cecchet, A. de Bari, J. Graulich, Y. Karadzhov, M. Rayner, I. Rusinov, R. Tsenov, S. Terzo, and V. Verguilov, The design and commissioning of the mice upstream time-of-flight system, Nucl. Instrum. Methods Phys. Res., Sect. A **615,** 14 (2010).

[29] M. Bogomilov *et al.* (MICE Collaboration), Pion contamination in the MICE muon beam, J. Instrum. **11,** P03001 (2015).

[30] D. Adams *et al.* (MICE Collaboration), Electron-Muon Ranger: Performance in the MICE Muon Beam, J. Instrum. **10,** P12012 (2015).

[31] R. Asfandiyarov *et al.*, MAUS: The MICE analysis user software, J. Instrum. **14,** T04005 (2018).

[32] R. Kalman, A new approach to linear filtering and prediction problems., J. Basic Eng. **82,** 35 (1960).

[33] A. Dobbs, C. Hunt, K. Long, E. Santos, M. A. Uchida, P. Kyberd, C. Heidt, S. Blot, and E. Overton, The reconstruction software for the MICE scintillating fibre trackers, J. Instrum. **11,** T12001 (2016).

[34] H. Bichsel, Shell corrections in stopping powers, Phys. Rev. A **65,** 052709 (2002).

[35] T. J. Roberts, K. B. Beard, D. Huang, S. Ahmed, D. M. Kaplan, and L. K. Spentzouris, G4Beamline particle tracking in matter-dominated beam lines, Conf. Proc. C **0806233,** WEPP120 (2008).

[36] J. Allison *et al.*, Recent developments in GEANT4, Nucl. Instrum. Methods Phys. Res., Sect. A **835,** 186 (2016).

[37] V. N. Ivanchenko, O. Kadri, M. Maire, and L. Urban, GEANT4 models for simulation of multiple scattering, J. Phys. Conf. Ser. **219,** 032045 (2010).

[38] B. Gottschalk, A. M. Koehler, R. J. Schneider, J. M. Sisterson, and M. S. Wagner, Multiple Coulomb scattering of 160 MeV protons, Nucl. Instrum. Methods Phys. Res., Sect. B **74,** 467 (1993).

[39] R. Gold, An iterative unfolding method for response matrices, Technical Report No. ANL-6984.

[40] M. Morháč, J. Kliman, V. Matoušek, M. Veselský, and I. Turzo, Efficient one- and two-dimensional Gold deconvolution and its application to γ-ray spectra decomposition, Nucl. Instrum. Methods Phys. Res., Sect. A **401,** 385 (1997).

[41] R. Brun and F. Rademakers, ROOT: An object oriented data analysis framework, Nucl. Instrum. Methods Phys. Res., Sect. A **389,** 81 (1997).

[42] http://www.gridpp.ac.uk/.

Modeling Meteorological Effects on Cosmic Ray Muons Utilizing Multivariate Analysis

M. Savić[1] , D. Maletić[1], A. Dragić[1], N. Veselinović[1], D. Joković[1], R. Banjanac[1], V. Udovičić[1], and D. Knežević[1]

[1]Institute of Physics Belgrade, University of Belgrade, Belgrade, Serbia

Abstract Correction of meteorological effects on muon component of secondary cosmic rays significantly extends the usability of muon monitors. We propose a new data driven empirical method for correction of meteorological effects on muon component of secondary cosmic rays, based on multivariate analysis. Several multivariate algorithms implemented in Toolkit for Multivariate Data Analysis with ROOT framework are trained and then applied to correct muon count rate for barometric and temperature effects. The effect of corrections on periodic and aperiodic cosmic ray variations is analyzed and compared with integral correction method, as well as with neutron monitor data. The best results are achieved by the application of linear discriminant method, which increases sensitivity of our muon detector to cosmic ray variations beyond other commonly used methods.

Plain Language Summary Primary cosmic rays are energetic particles that arrive at Earth from space. On their journey toward Earth they are affected by the solar wind (a stream of charged particles emanating from the sun), which has information about various solar processes embedded in it. In top layers of the atmosphere primary cosmic rays interact with nuclei of air molecules and produce large number of secondary particles that propagate toward Earth's surface. These secondary particles preserve information about variations of primary cosmic rays, which allows for the study of solar processes using Earth based detectors. One type of secondary particles that can be detected on the ground are muons. However, muons are affected by the conditions in the atmosphere, which can disturb the information about variations of primary cosmic rays. That is why it is important to model these atmospheric effects on cosmic ray muons as well as possible so they can be corrected for. In this study, we present a new method for modeling and correction of atmospheric effects on cosmic ray muons, that is based on multivariate analysis utilizing machine learning algorithms. This method increases sensitivity of our muon detector to cosmic ray variations beyond other commonly used methods.

1. Introduction

Meteorological effects on muon component of secondary cosmic rays have been known and studied for almost a century. A number of meteorological parameters contribute to variation of muon flux in the atmosphere, but two are the most significant: atmospheric pressure and atmospheric temperature.

Aperiodic fluctuations of intensity, discovered in the very early cosmic ray measurements, were eventually attributed to the variation of atmospheric pressure by Myssowsky & Tuwim (1926) (associated effect dubbed *barometric*), while *temperature effect* has been discovered more than a decade later and has two components: *negative* (first quantitively described by Blackett, 1938) and *positive* (suggested by Forró, 1947). Barometric effect represents variation of muon flux due to variation of the mass of the absorber (air column) above the detector. Negative temperature effect is a consequence of dependence of effective height of muon generation level on the atmospheric temperature, resulting in longer muon path and increased probability of decay with higher temperature. Positive temperature effect has to do with positive correlation between atmospheric temperature and air density, decreasing the probability of nuclear interactions and increasing the probability of decay of muon-generating pions with the increase of temperature.

In order to study variations of primary cosmic rays (CR) using Earth based muon detectors, it is of the utmost importance to describe these meteorological effects as precisely as possible so they can be corrected for. A precise correction for meteorological effects significantly increases sensitivity of muon detectors to CR variations, making them a more usable counterpart to neutron monitors (the other widely used type of

ground based cosmic ray detectors), as muon detectors are normally responsive to higher energy primary cosmic rays. Additionally, muon monitors have a unique application in diagnostics of the atmosphere, allowing for prediction of atmospheric temperatures provided a good model of meteorological effects is available (Belov et al., 1987; Kohno et al., 1981).

Several empirical and theoretical models of meteorological effects have been proposed over the years, based on which corrections can be performed. Even though full set of meteorological effects is larger, in this analysis we will concentrate on the correction of temperature and barometric effect only, so results can be more easily compared to other methods.

Some of the most commonly used methods for temperature correction are: method of effective level of generation, introduced by Duperier (1949), integral method, developed by Feinberg (1946), Dorman (1954), and others (Maeda & Wada, 1954; Wada, 1962), method of mass-averaged temperature developed by Dvornikov et al. (1976), and method of effective temperature (mostly applicable to underground detectors) (Barrett et al., 1952).

Each of these methods have their own advantages, but in this study, we have decided to use the integral method as a reference against which to compare the results of our analysis. Main reason being is that it is derived from the theory of meteorological effects, which involves the most detailed analysis, as well as it being the least approximative. According to this approach, relative variation of muon count rate due to the temperature effect can be expressed as:

$$\left(\frac{\delta I}{I}\right)_{temp} = \int_{0}^{h_0} \alpha(h) \cdot \delta T(h) \cdot dh, \tag{1}$$

where α is temperature coefficient density function, δT is temperature variation and h_0 is atmospheric depth of the observation level expressed in g/cm^2. Temperature coefficient density function is calculated theoretically, while temperature variation is calculated relative to some reference temperature for the period, usually mean temperature. In practical application, integration in Equation 1 is substituted with a sum, taking into account some finite number of isobaric levels.

Analysis of barometric effect is also included in the theory of meteorological effects, but barometric coefficient is rarely calculated theoretically. Most commonly it is determined using linear regression, assuming linear dependence between atmospheric pressure and muon flux:

$$\left(\frac{\delta I}{I}\right)_{pres} = \beta \cdot \delta P, \tag{2}$$

where β is barometric coefficient, and δP represents atmospheric pressure variation.

Each of the mentioned methods is at least in some part approximative, so the idea behind this work is to introduce a new empirical method for correction of meteorological effects that would be data driven, assuming as little as possible upfront. Other advantages of such approach are that it does not depend on the design of the detector, location of the site or topology of the surrounding terrain (as these would ideally be factored in by the model), and that it can be applied in near-real time. Additionally, proposed method can be used in the analysis and potential correction of temperature effect of neutron component of cosmic rays, as part of detected neutrons can originate from cosmic ray muons captured in the nuclei of the shielding of a neutron monitor detector (Dorman, 2004). Finally, in principle it can easily be generalized to take wider set of meteorological parameters into account.

As the presented problem is multidimensional, involving a relatively large number of correlated variables, we have decided to employ multivariate analysis, relying on machine learning techniques. In some recent work (Morozova et al., 2017; Savic et al., 2019) decorrelation of atmospheric variables and numerical modeling has been successfully applied to the study of interaction of cosmic rays with Earth's atmosphere, so utilizing adaptive and flexible machine learning methods could possibly yield further improvement, potentially revealing additional dependencies and taking higher order effects into account. This approach involves application of a number of multivariate algorithms, more or less rooted in statistical machine learning, to our problem and comparing their consistency and effectiveness with selected reference results.

Large part of variations observed in continuous cosmic ray measurements can be attributed to different space weather phenomena, due to modulation of primary cosmic rays in the heliosphere. In terms of temporal properties, they can be classified as periodic or aperiodic. We will test how newly introduced methods for correction of meteorological effects affect the sensitivity for detection of both periodic as well as aperiodic variations of muon flux of nonterrestrial origin, and how it ultimately compares to the sensitivity of neutron monitors.

2. Data

For the analysis of meteorological effects both muon flux and meteorological data are needed. Muon flux was measured experimentally in the Low Background Laboratory at the Institute of Physics Belgrade, while meteorological data is a combination of modeled atmospheric temperature profiles, and atmospheric pressure and ground level temperature measured locally.

2.1. CR Muon Data

Low Background Laboratory (LBL) is located on the grounds of the Institute of Physics Belgrade. Geographical coordinates for the laboratory are 44°51′N and 20°23′E, with elevation of 75 m and geomagnetic cutoff rigidity of 5.3 GV. Detector system is comprised of a $100 \times 100 \times 5$ cm plastic scintillator with accompanying read-out electronics. Median energy for the detector system is (59 ± 2) GeV (Veselinović et al., 2017), with muon flux of $(1.37 \pm 0.06) \times 10^{-2}$ per cm^2 s. Electron contamination determined for a previously used experimental setup was ~24% (Dragić et al., 2008), and is assumed to be comparable for the current one (Joković, 2011). More detailed description of the laboratory and the experimental setup can be found elsewhere (Dragic et al., 2011). Native muon count rate data has time resolution of 5 min, but hour sums are also frequently used in analysis.

Continuous cosmic ray muon flux measurements have been ongoing in LBL since 2002, current setup being utilized since 2009. Data are available to public via an online interface on the Belgrade Cosmic Ray Station internet site (Low Background Laboratory for Nuclear Physics, 2020).

As with any long-term measurement, some shorter interruptions and inconsistencies are unavoidable, hence when choosing the interval to be used for the analysis we decided to use a one-year period from June 1, 2010 to May 31, 2011, where measurements had the most continuity and consistency. Additionally, using a one-year period should remove any potential bias, primarily due to annual temperature variation.

2.2. Meteorological Data

Meteorological parameters needed for the analysis come from two sources: Atmospheric temperature profile data are produced by an atmospheric numerical model, while atmospheric pressure and ground temperature data come from local measurements.

Meteorological balloon soundings above Belgrade done by Republic Hydro-meteorological Service of Serbia (RHMZ, 2020) are not frequent enough for the purposes of this analysis, so modeled data for atmospheric temperature profile are used instead. Several numerical atmospheric models can provide such data. In this work, we have chosen Global Forecast System (GFS) produced by National Centers for Environmental Prediction (GFS, 2020), which has been found to be in best agreement with ballon soundings done above Belgrade. Comparison was done where soundings data were available, as described in our previous study (Savic et al., 2019). GFS provides a large number of modeled atmospheric parameters among which are atmospheric temperatures for different isobaric levels. Modeled data sets are being produced four times per day (at hours 00:00, 06:00, 12:00, and 18:00). In addition, analysis data are also available, reprocessed *post festum* and taking into account real data measured by world network of meteorological services. In this analysis, we have been using such reprocessed atmospheric temperatures for the following isobaric levels: 10, 20, 30, 50, 70, 100, 150, 200, 250, 300, 350, 400, 450, 500, 550, 600, 650, 700, 750, 800, 850, 900, 925, and 975 mb. Data are available with spatial resolution of 0.5° of geographical longitude/latitude, so coordinates closest to the laboratory coordinates were chosen. Data were then interpolated with cubic spline, similar as in Berkova et al. (2012), and sampled in finer time resolution needed for the analysis.

Atmospheric pressure and ground temperature data are compiled from different meteorological stations in and around Belgrade, and then interpolated as described in more detail elsewhere (Savic et al., 2016). Finally, unique time series of combined modeled and measured meteorological data, with finest time resolution of 5 min, is assembled to be used in the analysis.

3. Methodology

The use of machine learning has seen an unprecedented expansion in the last decade. The main strength of such approach being that it does not assume any a priori model, but is data driven and thus able to potentially discover hidden dependencies. This is especially true when applied to large data sets with many correlated variables. In this study, we want to establish whether such approach would yield any improvements when applied to the problem of meteorological effect on cosmic ray muons.

To test this, we have decided to use toolkit for multivariate analysis (TMVA) package which provides a ROOT-integrated environment for application of multivariate classification and regression techniques (Hoecker et al., 2007). The package has been developed for the use in high-energy physics and contains implementation of a number of supervised learning algorithms, which utilize training and testing procedures on a sample data set to determine the mapping function. Mapping function maps the input parameters to output target value, trying to model the actual functional dependence ("target" function) as accurately as possible. The structure of the mapping function is algorithm specific, and can be a single global function or a set of local models. Trained algorithm is then applied to the full data set and provides either a signal/background separation (in case of classification) or prediction of target value (in case of regression).

For us, the later application is especially interesting. The idea is to train the mapping function, using meteorological parameters as input variables, and muon count rate as the regression target, and use trained function to produce the predicted target output for a larger data set. In principle, implementation of this procedure is specific for different analysis frameworks. TMVA provides template code for the training and application of multivariate methods, where optimal parameters obtained in the training/testing phase are stored in "weight" files to be used in the application phase. Thusly predicted muon count rate would ideally contain only variations related to meteorological effects, while the residual difference between modeled and measured muon count rate would contain variations of non-meteorological origin. We would apply this procedure for a number of algorithms implemented in TMVA, compare their performance and efficiency based on several criteria, and finally suggest the methods best suited for the modeling, and ultimately the correction, of meteorological effects.

Corrected muon count rate would be calculated according to the following equation:

$$N_\mu^{(corr)} = \Delta N_\mu + \langle N_\mu \rangle, \tag{3}$$

where

$$\Delta N_\mu = N_\mu^{(mod)} - N_\mu \tag{4}$$

is the difference between the modeled and measured muon count rate.

Not all machine learning methods are equally suited for all types of problems and selection of the optimal method for a particular application is rarely straightforward. The efficiency of different algorithms depends on a number of factors: Whether they are used for classification or regression, is correlation between parameters linear or nonlinear, what is the general complexity of the problem and required level of optimization, and so on. One can only assume the efficiency of any given algorithm upfront but there is no clear general rule which one will perform best in a particular situation. Often, several algorithms with specific strengths and weaknesses can be applied to the same problem and only through analysis of the final result the optimal one can be determined. For this reason, in our analysis we have decided to indiscriminately include the largest number of algorithm classes available in TMVA, and only after extensive parallel testing narrow the selection down to the optimal one.

We will briefly describe different classes of multivariate methods available in TMVA, as well as list specific algorithms that were chosen as representative for each class. First class are methods based on probability

density estimation (PDE) techniques, where actual probability density function is estimated based on the available data. Here we have selected to test two specific multidimensional implementations, somewhat similar in nature: PDE range-search (PDE-RS) and k-nearest neighbor (KNN) algorithms. Examples of use of this approach for multivariate regression are scarce, but the success with which PDERS was applied in classification problems in high-energy physics (Carli & Koblitz, 2003) motivated its use here. Second class are methods based on function discriminant analysis. These methods are widely used for dimensionality reduction and classification. Here, we selected the linear discriminant (LD) algorithm which shares some similarities in the approach with principal component analysis (PCA), in that it maps a space of potentially correlated input variables onto a smaller space of uncorrelated variables, but in addition to PCA it also maximizes the separation between output classes, making it a natural choice for application to our problem. Algorithms that employ higher order functions were also tested, but as could be expected performed more poorly. Application of artificial neural networks (ANN) to multivariate regression problems has seen expansion in recent years, where ANN methods often perform better than more straightforward regression techniques, especially if some degree of nonlinearity is present. Even though the dependence of cosmic ray muon flux on atmospheric temperatures is linear, we felt it is certainly worth investigating how ANN methods would perform when applied to this problem, and if any additional hidden dependence would be revealed. We have chosen to apply the MLP, as it is the fastest and most flexible available ANN algorithm in TMVA. Finally, method of boosted regression trees (BDT) employs a larger number (*forest*) of binary decision trees, which split the phase space of input variables based on a yes/no decision to a series of sequential cuts applied, so to predict a specific value of the output variable. They have been very successfully applied to classification problems in high-energy physics (Lalchand, 2020), but can also be used for multivariate regression with the similar rationale as for the ANN. We have selected two representative algorithms for testing: boosted decision tree (BDT) and gradient boosted decision tree (BDTG).

In this analysis, the procedure is applied to correction of barometric and temperature effect but it is easy to see how it can be extended to include more atmospheric variables, especially as such data is readily available from atmospheric numerical models.

3.1. Training Procedure

For the training/testing data subset we have selected data for the 10 geomagnetically quietest days of each month (list provided by GFZ German Research Center for Geosciences, GFZ Potsdam, 2020), as we expect variations due to meteorological effects to be more pronounced here. This subset was then further split into training and testing data set, where 70% of randomly selected data was used for training while remaining 30% was used for testing. Data time resolution used was 5 min as it gave us a larger statistics for training.

There is a number of settings that can be manipulated for each of the multivariate algorithms used. They vary from some basic parameters, to selection of different subalgorithms or various options that can be turned on or off. For each algorithm, we have selected the optimal set of parameters. The criterium for optimal performance was minimizing the average quadratic deviation of the modeled output versus the target value. Also, where allowed by the algorithm, input variables were decorrelated prior to further processing.

Table 1 shows the values of average quadratic deviation for the modeled output (modeled muon count rate) versus the target value (measured muon count rate) for different algorithms. First two columns refer to the training data subset while second two columns refer to the testing data subset. First and third column represent average quadratic deviation defined as $(\Sigma(f_{MVA} - f_{target})^2)^{1/2}$ (where f_{MVA} and f_{target} represent modeled and measured count rates, respectively), while second and fourth columns represent truncated average quadratic deviation which takes into account 90% of data with least deviation. As previously mentioned, the criterium for selection of optimal parameters for every algorithm is the minimal value of average quadratic deviation for the test data subset.

3.2. Algorithm Performance Analysis

All presented multivariate algorithms have no built in knowledge about the studied effect, so in addition to quantitative test mentioned in the section above, we introduce some qualitative analysis designed to estimate the integrity of modeled data. Prime concern here would be to test whether the suggested procedure

Table 1
Average Quadratic Deviation for Selected Multivariate Methods

Method	Training		Testing	
	Average deviation (counts/5 min)	Truncated deviation (counts/5 min)	Average deviation (counts/5 min)	Truncated average (counts/5 min)
PDERS	234	185	258	201
KNN	224	177	233	185
LD	286	225	284	223
MLP	228	180	234	186
BDT	219	182	237	188
BDTG	223	174	236	187

Abbreviations: BDT, boosted decision tree; BDTG, gradient boosted decision tree; KNN, k-nearest neighbor; LD, linear discriminant.

for the correction of barometric and temperature effect (PT correction) removes these meteorological effects only, while leaving all other features nonperturbed. To this end, we will analyze several distributions of modeled data, compare them with raw and reference PT corrected data (obtained using the integral method) and look for possible anomalous features.

First, we will look into structure of distributions of difference between modeled and measured muon count rate as a function of measured count. We want to make comparison between these distributions in the training phase (for the test data subset) and after the trained algorithm was applied to the full data set. We would expect these distributions to be consistent, and appearance of some new structures or strong trends would point to some perturbation in the application phase. We have selected two examples to illustrate the difference in consistency of application of trained algorithms—BDTG and PDERS, their distributions shown in Figure 1.

We can see that distributions for BDTG algorithm for test data subset (Figure 1a) and full data set (Figure 1b) are fairly similar, and any structures and trends in the test distributions are mostly well replicated in the full data set distributions (different statistics taken into account). This is the case for most applied algorithms except for PDERS, where some dependence of the count rate, negligible for the test data distribution (Figure 1c), exists for the full data set distribution (Figure 1d).

Another, more important feature, is that for some algorithms distributions we analyzed in the previous paragraph are not smooth, but rather display some structures. To get further insight into these structures, for all featured methods we plotted distributions of modeled muon count rate along with the distribution of raw count rate on the same graph, as shown in Figure 2.

In order to better understand shapes of distributions and any structures observed in plots in Figure 2, it would be helpful to compare them to equivalent plots for muon count rates corrected for pressure and temperature effects using a well-established reference method. However, before we take a look at these distributions, we will first briefly describe procedures used to obtain reference PT correction.

Temperature and barometric effect are typically corrected for independently, where one of several methods mentioned in Section 1 is used for temperature correction, and barometric coefficient for pressure correction is determined empirically. Integral method for correction of temperature effect is widely accepted as the most accurate one. It is based on the theory of meteorological effects and takes complete atmospheric temperature profile and relevant processes into account. Most thorough description of the theory of meteorological effects is given by Dorman (2004), where temperature coefficient density function $\alpha(h)$ in Equation 1 is given in its integral form. In order to be applied, this function is then calculated through integration, substituting parameters specific to the location of the experiment. Temperature coefficient density functions for the location of Low Background Laboratory for Nuclear Physics were calculated using Monte Carlo integration technique. In order to determine barometric coefficient, temperature corrected muon data were plotted as a function of atmospheric pressure (using entries for 10 geomagnetically quietest days
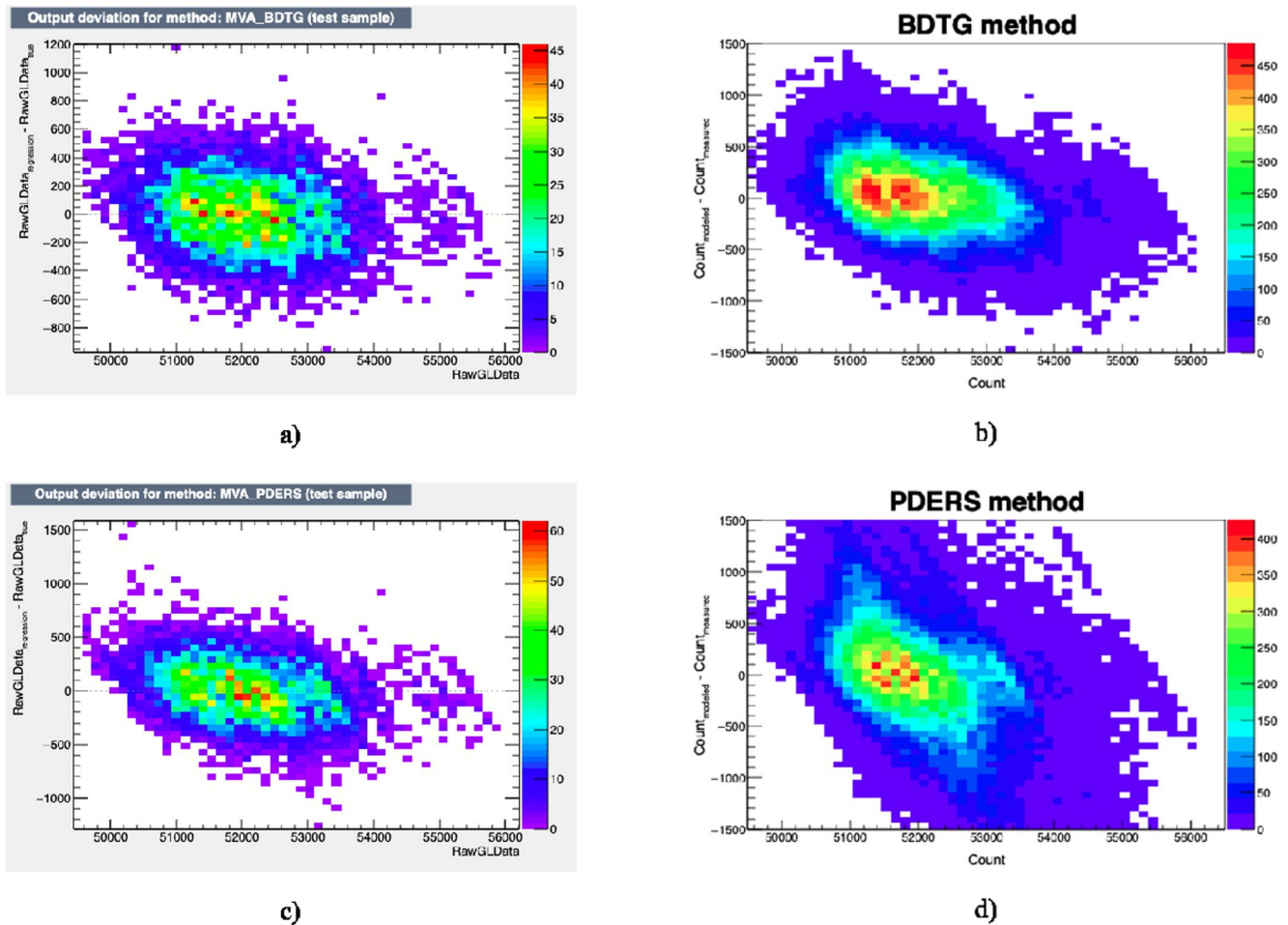
Figure 1. Distribution of difference between modeled (regression) and measured (true) muon count rate as a function of measured muon count rate for: (a) gradient Boosted decision tree (BDTG)—test data set, (b) BDTG—full data set, (c) PDERS—test data set, and (d) PDERS—full data set.

of each month only), coefficient determined via linear regression separately for each calendar year. Both procedures are presented in greater detail in our previous work (Savic et al., 2016).

Distributions equivalent to ones shown in Figures 1 and 2 were plotted for reference pressure and temperature corrected data, as shown in Figure 3. The analog for the modeled muon count rate is calculated from the variation due to pressure and temperature effects calculated based on the integral method. It is worth pointing out that distributions for reference PT corrected data are noticeably less smooth, which can be mostly attributed to lower statistics used as only hour summed data was available for this correction.

Based on these plots, we can conclude that we should not expect a significant deviation between raw and corrected data and that corresponding distributions should not have any characteristic structures. Most plots in Figure 2 are consistent with this expectation, however, some structures can be observed in KNN plots, and to a degree in BDT plots, while distribution plotted for PDERS algorithm does not have these structures but appears to somewhat deviate from raw data distribution.

Another insight into performance and consistency of different multivariate algorithms when applied to the modeling of meteorological parameters can be gathered by the way of spectral analysis of PT corrected data. Pressure and temperature corrected muon count rate was determined for all selected algorithms using modeled data, as described in Section 3. Since some gaps exist in our muon data, Lomb-Scargle algorithm was used to obtain the power spectra, as it is less sensitive to uneven data sampling (Press et al., 2007). Figure 4 shows power spectra for raw and muon count rates corrected for pressure and temperature effects using integral and two illustrative examples of multivariate methods. Full spectrum as well as selected interval
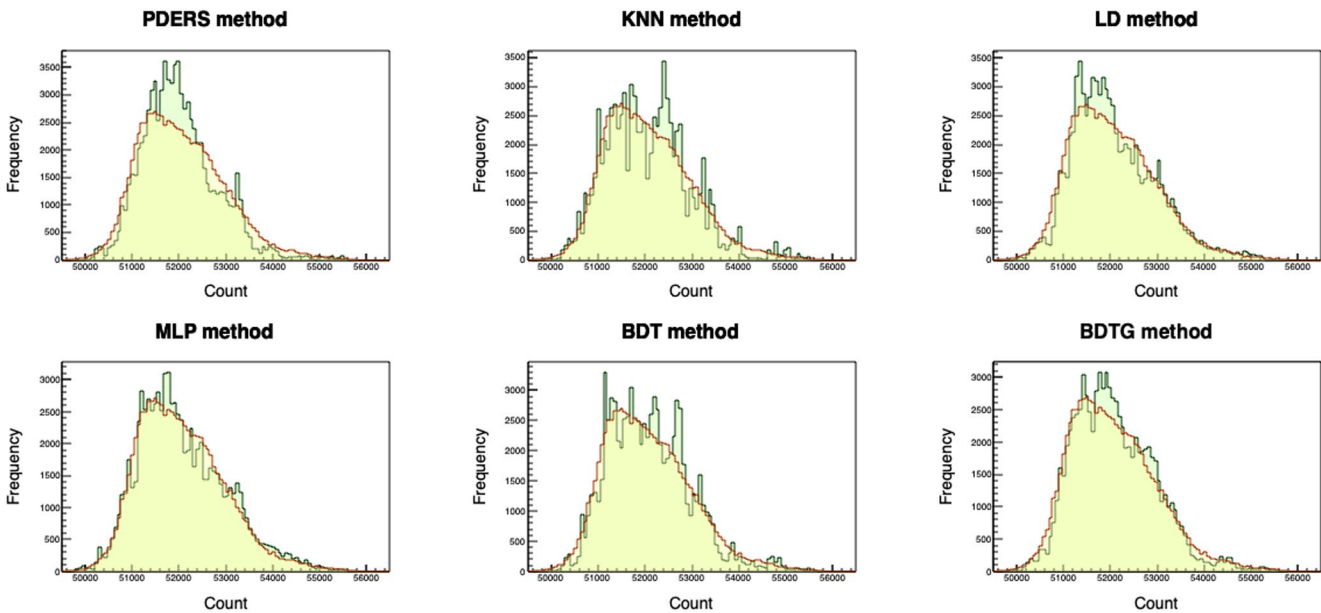
Figure 2. Comparison between distributions of raw (yellow) and muon count rate modeled by selected multivariate methods (green).

of frequencies around the periodicity of one day are shown, red dashed line indicating significance level of 0.01.

If integral method is again used as a reference, we can see that thus obtained PT correction does not remove daily variation, but rather makes it more pronounced. This should not come as a surprise, as only smaller part of the diurnal variation can be attributed to meteorological effects (Quenby & Thambyahpillai, 1960), while larger part is of nonmeteorological origin. Hence, removing variation due to atmospheric pressure would make daily variation more prominent. LD, and to a degree BDT/BDTG methods, have an effect on daily variation similar to the integral method, but for BDT method (bottom right in Figure 4) we observe emergence of some frequencies with significant power that cannot be associated with any known periodicity of cosmic rays, and probably have artificial origin. Such features are even more pronounced for the remaining multivariate algorithms, where in addition an over-reduction of power frequency corresponding to diurnal variation to can be observed. Over-reduction of daily variation coupled with introduction of artificial variations with significant powers points to possible inadequateness or overtraining of some of the multivariate methods.
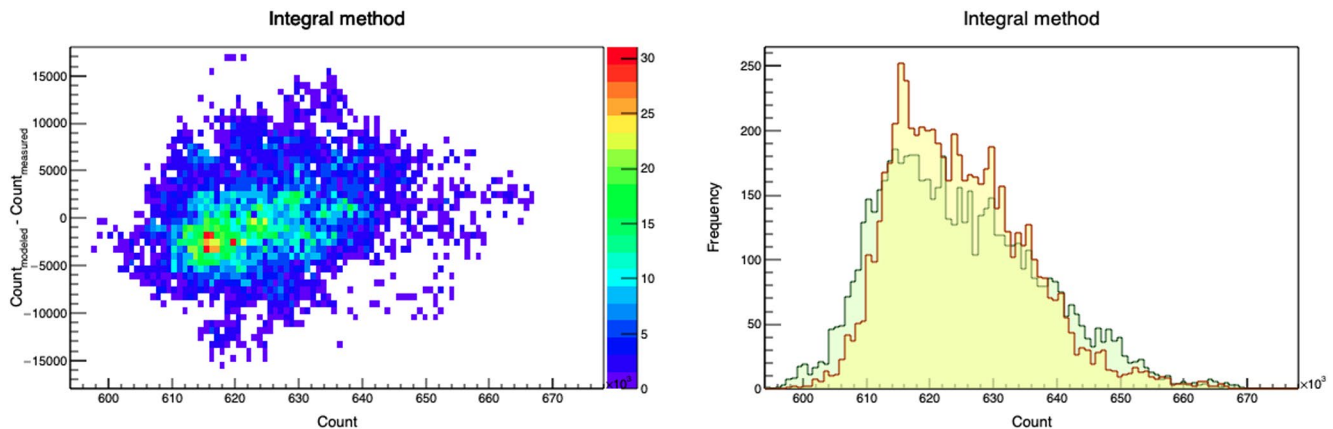

Figure 3. Distribution of difference between muon count rate calculated from the variation due to pressure and temperature effect using integral method and measured muon count rate as a function of measured muon count rate (left), and comparison between distributions of raw (yellow) and calculated muon count rate (green) shown on the right.
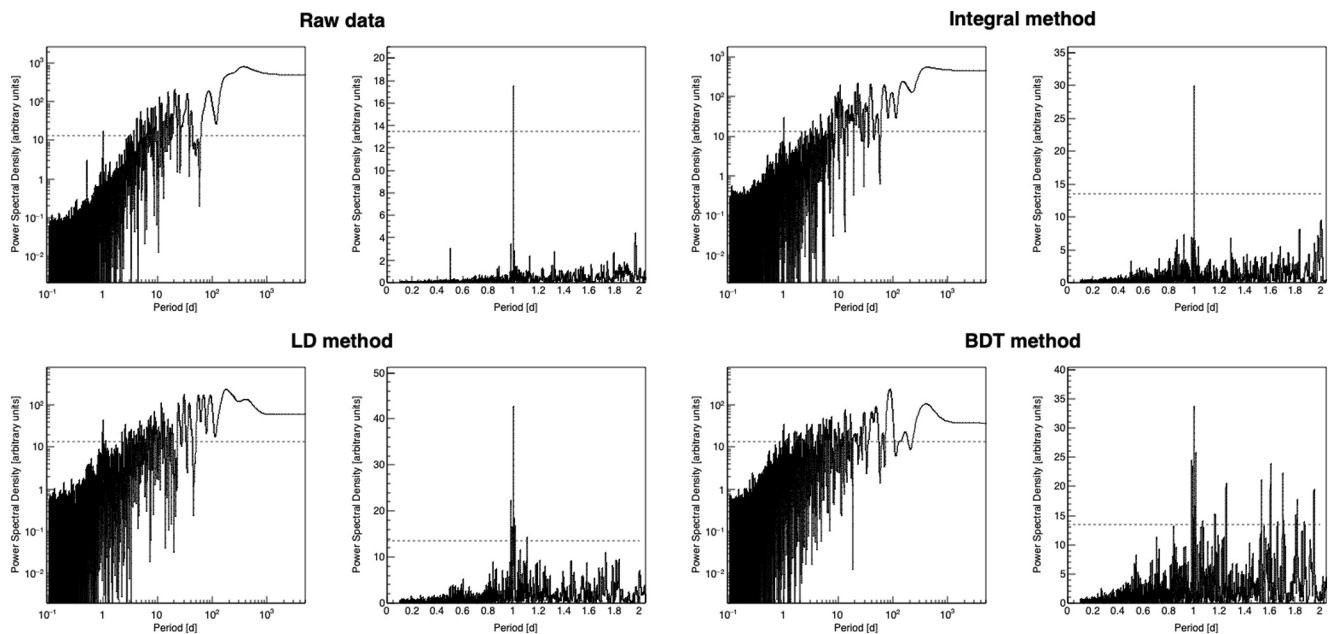
Figure 4. Power spectra for raw data (top left), PT corrected data using integral method (top right), and PT corrected data using selected multivariate methods (second row). For each method, both full spectrum and a range of frequencies around periodicity of one day are shown. Significance level of 0.01 is indicated by the red dashed line.

The effect on annual variation is difficult to determine based on the spectral analysis as period of only one year is analyzed, but we will introduce some quantitative tests in the next section that will help us with this estimate.

4. Results

We will use two criteria to estimate the efficiency of newly introduced methods for PT corrections. One will rely on the effectiveness with which the multivariate algorithms remove the annual variation and reduce variance, while the other will be based on the effect the correction has on detection sensitivity for aperiodic events, such as Forbush decreases (Forbush, 1937). In both cases, we will compare the results with the ones obtained by the integral method.

4.1. Effects of PT Correction on Periodic CR Variations

Significant part of the annual variation of cosmic ray muon flux can be attributed to the variation of atmospheric temperature (Hess, 1940). As mentioned before, the effectiveness with which this effect is corrected for will affect the detector sensitivity to variations of primary cosmic rays of non-atmospheric origin.

We will examine time series for pressure and temperature corrected data and compare them with raw and pressure corrected time series, especially taking note of how PT correction affects the annual variation. In order to estimate this effect, we fit the time series (except for raw data) with sine function with a period of one year. The amplitude of pressure corrected data determined from such fit will be used as an estimate of the annual muon flux variation, and serve as a reference against which to compare the effect of PT correction by different methods. In Figure 5 time series for raw, pressure corrected and pressure and temperature corrected data are shown. For the sake of simplicity, not all time series for data PT corrected using multivariate algorithms are shown, but rather only characteristic ones. Table 2 shows values for the annual variation amplitude for pressure and PT corrected time series, as well as possibly more informative reduction of annual variation calculated relative to the amplitude of the pressure corrected muon flux.

While, time series in Figure 5 for data PT corrected using integral, LD and BDTG methods do not seem to have some unexpected fluctuations, that is not the case for MLP method, where one can observe some
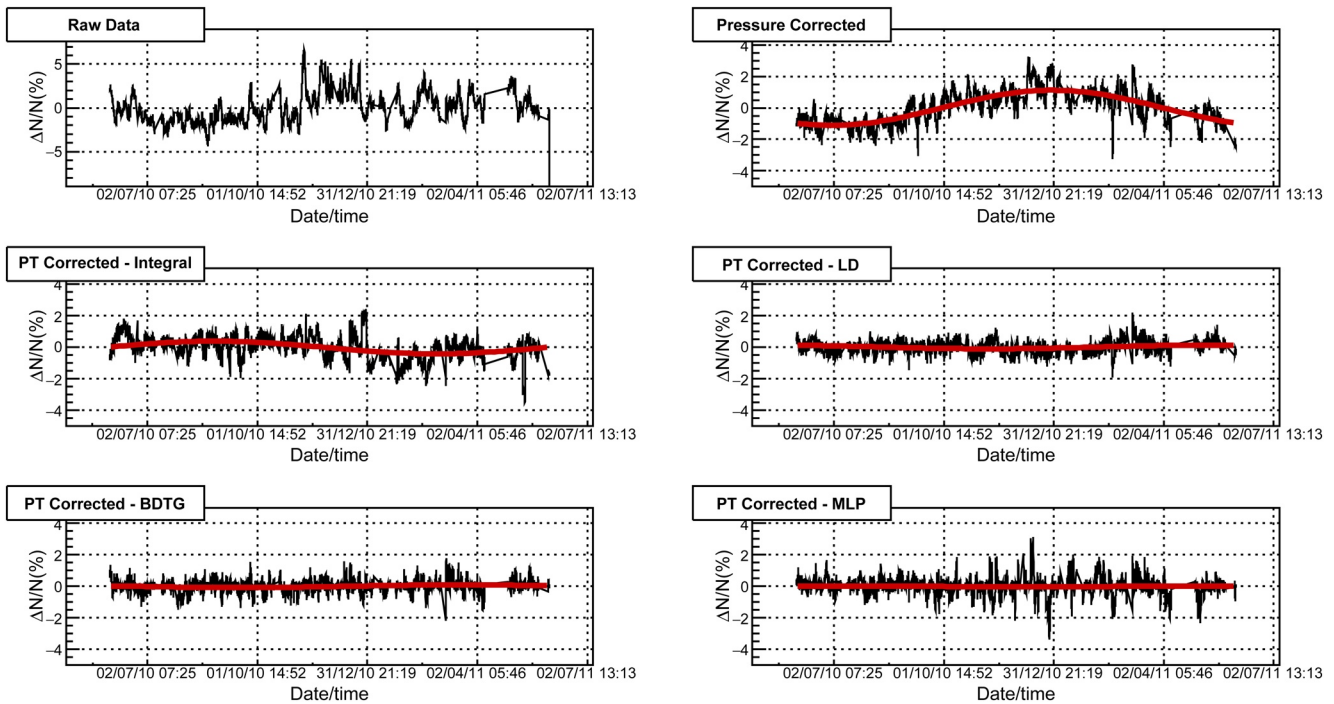
Figure 5. Muon count rate time series for the period from June 1, 2010 to May 31, 2011: raw data (top left), pressure corrected data (top right), PT corrected data using integral method (second row left) and data PT corrected using selected multivariate methods.

data that appears to deviate from the mean more significantly than what would be intuitively expected. For remaining multivariate algorithms this is even more the case. In order to try and quantify this visual comparison, we will analyze the effect corrections have on standard deviation of the data. If calculated relative to the mean muon flux for the whole period, standard deviation would be sensitive to the residual annual variation. To make standard deviation independent of the seasonal variation, we used a moving ten-day window to determine the mean value and then calculated the standard deviation relative to it.

Figure 6 shows distributions of relative variation of muon flux in respect to the moving window mean value for raw data and PT corrected data using integral, LD and MLP methods. It is based on these distributions that standard deviation was determined and results are presented in Table 3. Comparing standard deviations for PT corrected muon flux obtained by multivariate methods with the one obtained by the integral method, we can see that for LD, BDT, and BDTG algorithms they have comparable values. The difference is somewhat larger in the case of MLP, which is in accordance with features observed in Figure 6, while it is significantly larger for the remaining algorithms. This indicates that PT correction performed using KNN and PDERS (and possibly MLP) algorithms probably introduces some artificial features into PT corrected muon flux data.

One way to evaluate the effectiveness of different algorithms in reduction of the seasonal variation even better, would be to compare the PT corrected muon data to pressure corrected time series for selected neutron monitor detectors. The reasoning is based on a well-known fact that meteorological effects on the neutron component of secondary cosmic rays are dominated by the barometric effect. Temperature effect does exist for the secondary cosmic ray neutrons, but whether calculated theoretically (Dorman, 2004) or determined experimentally (Kaminer et al., 1965), it is still an order of magnitude smaller than for the muon component and typically not corrected for in neutron monitor data. Based on this, we

Table 2
Amplitude and Reduction of the Amplitude of Annual Variation Relative to Pressure Corrected Data (P Corrected) for PT Corrected Data (Using Integral and Selected Multivariate Methods)

Method	Amplitude (%)	Relative reduction (% of P corrected)
P corrected	1.11 ± 0.09	/
Integral	0.40 ± 0.03	64 ± 6
PDERS	0.09 ± 0.02	92 ± 3
KNN	0.24 ± 0.04	79 ± 5
LD	0.11 ± 0.03	90 ± 4
MLP	0.03 ± 0.01	98 ± 2
BDT	0.12 ± 0.03	89 ± 4
BDTG	0.086 ± 0.009	92 ± 2

Abbreviations: BDT, boosted decision tree; BDTG, gradient boosted decision tree; KNN, k-nearest neighbor; LD, linear discriminant.
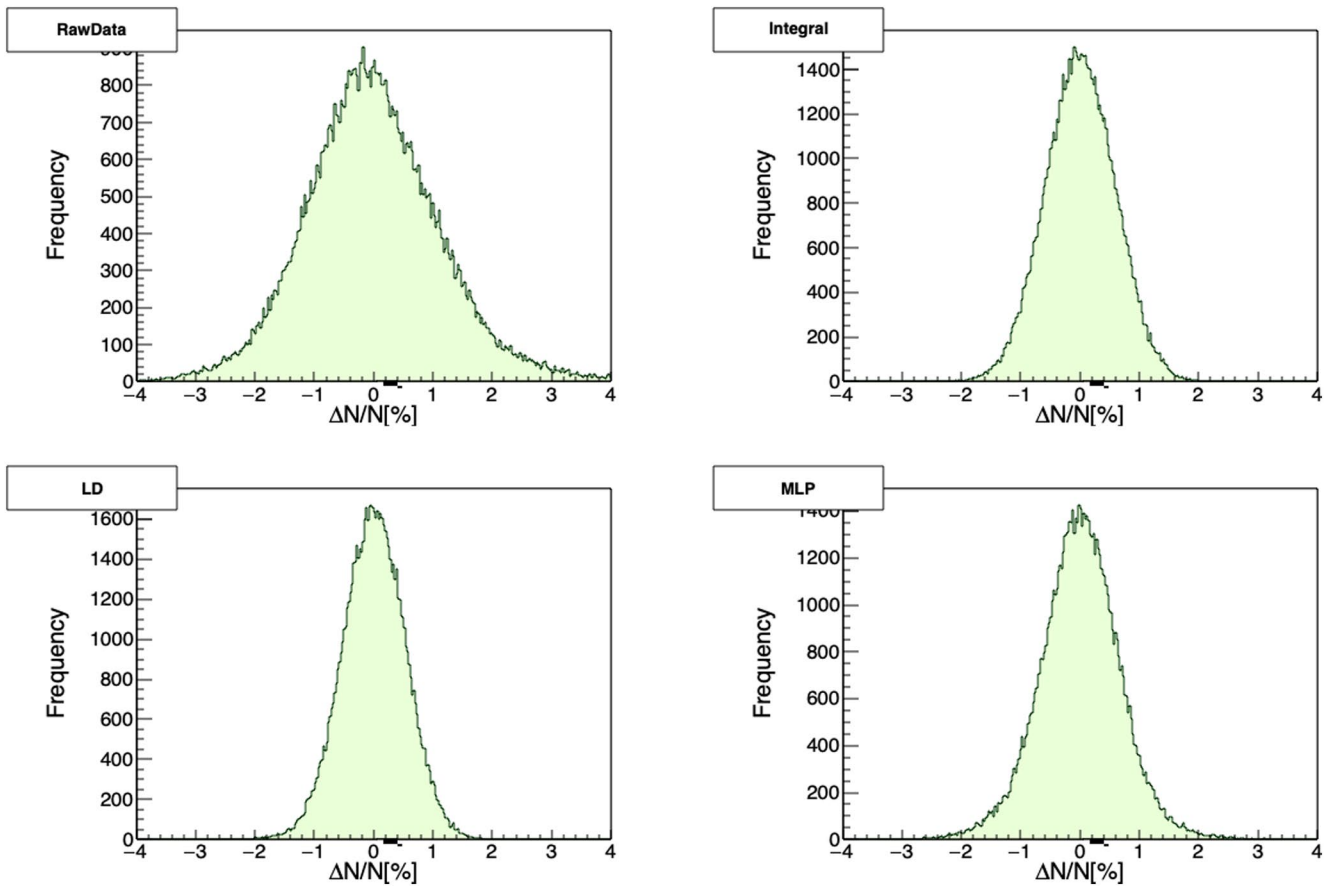
Figure 6. Relative variation of muon count rate calculated in respect to mean count in the ten-day moving window, for raw data (top left), PT corrected using integral method (top right), and data PT corrected using selected multivariate methods (second row).

believe pressure corrected neutron monitor data to be (in the first approximation) independent from meteorological effects, and hence a good reference for the evaluation of effectiveness of different methods for PT corrections of muon flux data.

For this comparison, we have chosen neutron monitors located in Athens and Rome, as they had the most consistent operation in the period we use for the analysis. Respective geomagnetic cutoff rigidities for these neutron monitors are 8.53 and 6.27 GV. Pressure and efficiency corrected relative neutron count rate was acquired via Neutron Monitor Database (NEST, 2020), presented for the said period in Figure 7. As for the muon flux data, relative neutron count rate time series were fitted with sinusoidal function, with a period of one year, to obtain the amplitude used as an estimate of the annual variation. Neutron monitors are more sensitive to lower energy secondaries than muon detectors so their time series can exhibit larger variations, which in turn can affect the fitting algorithm. However, in this case the fits seem to be dominantly affected by the relatively stable period between June and November 2010, hence we believe them to be a reliable estimate of the seasonal variation amplitude. Thus acquired annual variation amplitude for Rome neutron monitor is $(0.29 \pm 0.01)\%$, while for the Athens neutron monitor it is $(0.17 \pm 0.05)\%$.

Table 3
Standard Deviation of Relative Variation of Muon Count Rate for Raw and Data Corrected for Pressure and Temperature Effect (Using Integral and Selected Multivariate Methods)

Method	Raw	Integral	PDERS	KNN	LD	MLP	BDT	BDTG
Relative deviation (%)	1.117	0.592	0.990	0.785	0.533	0.687	0.607	0.551

Abbreviations: BDT, boosted decision tree; BDTG, gradient boosted decision tree; KNN, k-nearest neighbor; LD, linear discriminant.
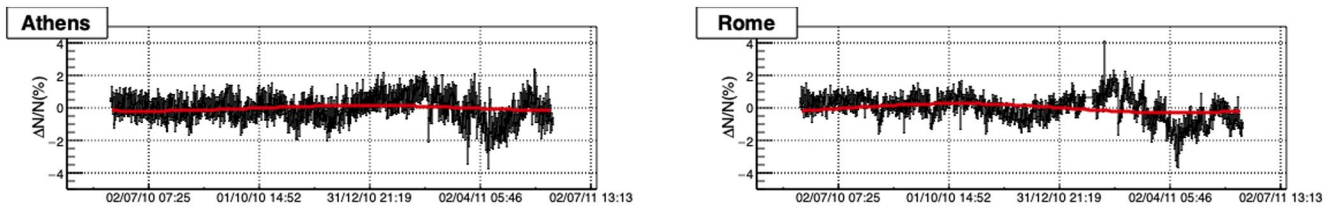
Figure 7. Relative neutron count rate time series for the period from June 1, 2010 to May 31, 2011 for Athens (left) and Rome (right) neutron monitors.

Comparing these values with the ones in Table 2, we see that methods KNN, LD, and BDT yield the most similar results. PDERS and MLP seem to underestimate the annual variation, while the integral method estimates a somewhat larger value.

Observed overall poor performance of KNN and PDERS algorithms could possibly be explained by the fact that these algorithms perform best when applied to problems involving strong nonlinear correlations, and are less efficient when dependencies between variables are dominantly linear (Hoecker et al., 2007). Additionally, these algorithms typically need a large training sample, so possibly statistics in our analysis was inadequate. However, artificial neural networks (such as MLP) should in principle be well suited for multivariate linear regression, and perform better than observed results suggest. Most likely, using minimization of the average quadratic deviation as a sole criterium for the selection of optimal parameters in the training phase may lead to overtraining (Montgomery et al., 2006), and additional qualitative criteria (i.e., ones introduced here) and more careful parameter control should also be used. BDT and BDTG algorithms performed reasonably well even though they are not optimized for treatment of linear multivariate problems, however, spectral analysis indicates a further improvement can be made. Additionally, all algorithms would probably benefit from a longer data interval of several years being used.

4.2. Effects of PT Correction on Aperiodic CR Variations

As mentioned before, apart from increasing sensitivity of muon detectors to periodic variations of primary cosmic rays, correcting raw muon flux data for meteorological parameters also affects detector sensitivity to aperiodic events which occur due to heliospheric modulation of primary cosmic rays. Here, we will analyze the effect PT correction, performed by application of different multivariate algorithms, has on detection of Forbush decrease events. We have chosen to concentrate on Forbush decreases as our muon detector is much less sensitive to other aperiodic events, such as ground level enhancements (GLE).

Forbush decrease (FD) events are typically characterized by their amplitude, so it could be a natural choice for a parameter to be used as a measure of detection sensitivity. However, another requirement for definition of sensitivity could be that detected signal significantly deviates from random fluctuations. That is, why we have decided to use the ratio of the amplitude to the standard deviation of muon flux, or relative amplitude, as an estimate of sensitivity to aperiodic events, rather than the actual amplitude. As we primarily focus on the magnitude of Forbush decreases, when we mention an FD event in the following text it mainly refers to the decrease phase and not the recovery phase.

To determine the amplitude, we have used a method proposed by Barbashina et al. (2009). The idea is to make the result independent from different trends leading up to, and following the actual FD. To do this, two intervals are defined: one i days before the onset of the FD, where i can have value $(1,…,n)$ days, and the other p days after the end of the decrease, where p can have value $(1,…,m)$ days. These intervals are then detrended using fit parameters obtained from linear regression. Mean count is determined for the detrended time series before the onset of FD for j days (where $j = 1,…,i$), and for the detrended time series during recovery stage for q days (where $q = 1,…,p$). Thus, in total we obtain $n!$ values for mean detrended count before the onset of FD, and $m!$ for mean detrended count for the recovery stage. FD amplitude estimate is then calculated for each combination of "before" and "after" values according to the following formula:

$$A_{ij}^{pq} = \frac{\langle I_{before}^{(i,j)} \rangle - \langle I_{after}^{(p,q)} \rangle}{\langle I_{before}^{(i,j)} \rangle} \times 100\%, \tag{5}$$
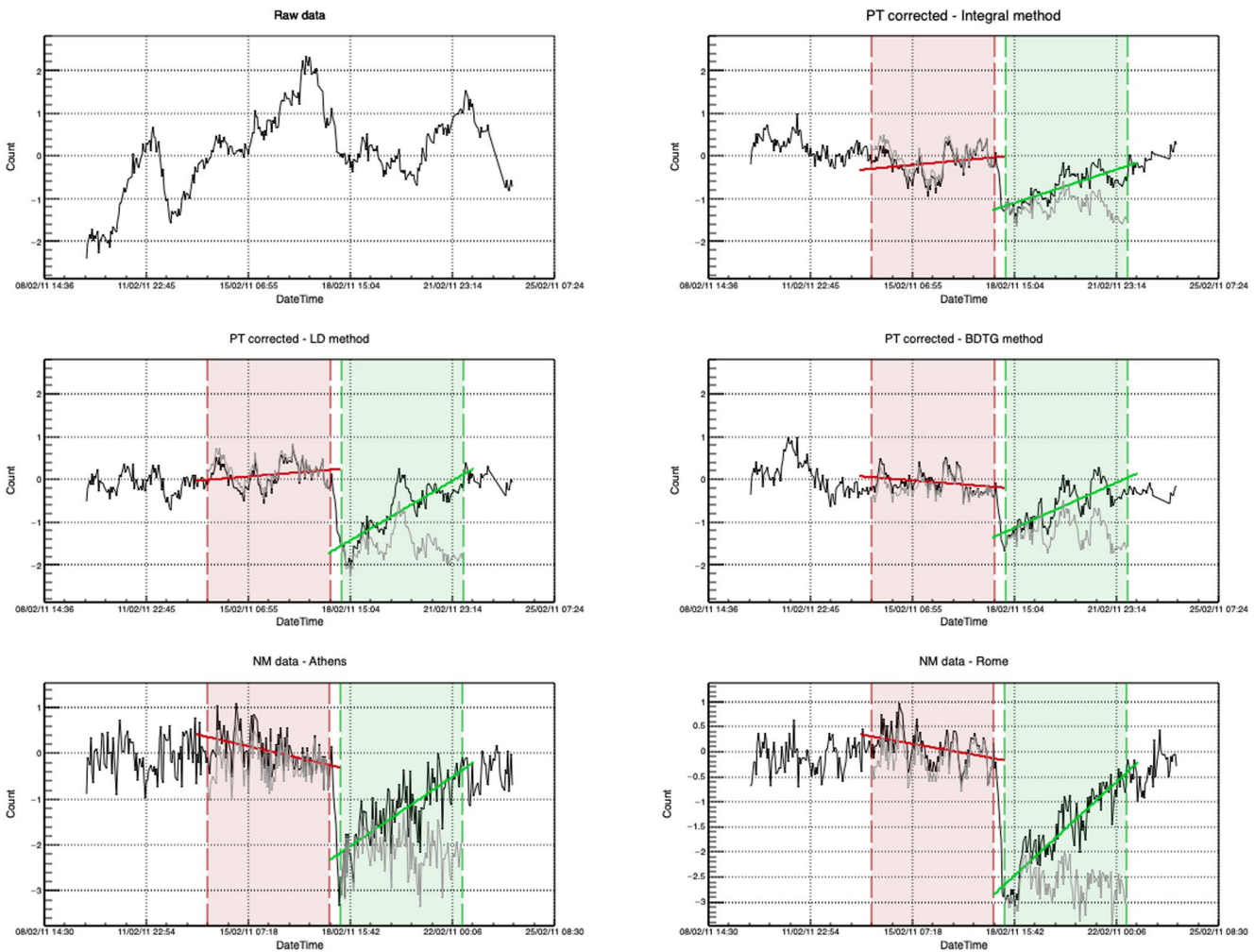
Figure 8. Time series for the interval around Forbush decrease of February 18, 2011: raw muon data (top left), PT corrected muon data using integral (top right), linear discriminant (center left) and gradient boosted decision tree (center right) methods, and neutron monitor data for Athens (bottom left) and Rome (bottom right) neutron monitors. Interval leading into (red) and following the Forbush decrease (FD) (green) are highlighted, as well as detrended intervals used to determine FD amplitude (gray).

where I_{before} and I_{after} are respective values for mean detrended count for intervals before the onset and after the end of the Forbush decrease. Finally, FD amplitude is calculated as the average of individual A_{ij}^{pq} values, rms deviation from the mean of the distribution used as an error estimate.

During the one-year period we used for the analysis there was a large number of Forbush events, but most of them had rather small amplitudes. We have analyzed several, however, here we will focus on the one with the largest magnitude as the results are most easily interpreted. The event is a Forbush decrease that occurred on February 18, 2011 in relation to X2.2 solar flare, and according to IZMIRAN space weather database (IZMIRAN, 2020) had 10 GV rigidity particle variation magnitude of 5.4. In Figure 8, we have shown plots that represent procedure described in the previous paragraph, applied to PT corrected datasets using integral method and selected multivariate algorithms. Procedure is also applied to pressure and efficiency corrected data for Athens and Rome neutron monitors, raw data also presented for reference. On the plots, interval leading to the onset of FD is indicated by red dashed lines, while recovery interval after the decrease is indicated by green dashed lines. We have chosen the lengths of both intervals to be four days ($n = m = 4$). Linear fits are represented by solid red and green lines, respectively, while detrended intervals are plotted using gray lines. Amplitudes and relative amplitudes calculated from the differences of means of detrended intervals are shown in Table 4.

Table 4
Amplitudes and Relative Amplitudes for the Forbush Decrease of February 18, 2011 for PT Corrected Muon Data and Selected Neutron Monitors

Method/NM monitor	Integral	LD	BDTG	Athens	Rome
FD amplitude (%)	1.38 ± 0.14	1.96 ± 0.18	1.10 ± 0.13	1.97 ± 0.15	2.68 ± 0.15
Relative FD amplitude	4.31 ± 0.44	7.09 ± 0.65	4.78 ± 0.56	5.30 ± 0.40	8.65 ± 0.48

Abbreviations: BDTG, gradient boosted decision tree; FD, Forbush decrease; LD, linear discriminant.

We see that relative amplitudes for this Forbush decrease, calculated based on data corrected for pressure and temperature using LD and BDTG algorithms, have sensitivity that is comparable or better than the sensitivity of integral method, even approaching the sensitivity of reference neutron monitors in the case of LD algorithm. However, when LD algorithm is concerned, such result can be at least in part explained by the fact that the calculated absolute FD amplitude is larger than expected for a muon detector. We would expect this value to be comparable to the value calculated based on the integral method. The reason for this discrepancy could be systematic, but also could be somewhat related to features of the studied FD event. Ideally, we should extend this analysis to more events, but selected time period was relatively calm in terms of solar activity, and February 2011 event was the only significant one with magnitude for 10 GV rigidity particles larger than five. Preliminary analysis done on Forbush decrease events of larger magnitude, that are outside the period used for analysis in this work, does show somewhat smaller effect for LD method, so that could be one of the focuses in the continuation of this work. We have excluded plots for the remaining multivariate algorithms as the results were either poorer (in the case of BDT and MLP) or inconsistent (in the case of PDERS and KNN).

5. Conclusions

We have selected a number of multivariate algorithms included in the TMVA package to apply for the correction of barometric and temperature effect on cosmic ray muons. Optimal parameters were determined for each algorithm based on the average quadratic deviation of modeled from measured data. Different distributions of modeled data for training phase and after the application of trained methods were compared to estimate the performance of selected algorithms. Pressure and temperature correction was done and spectral analysis performed to further test the algorithm consistency. The effect of the correction was analyzed for long-term (annual) and short-term (Forbush decrease) cosmic ray variations. In both cases, the efficiency of multivariate algorithms was compared to integral method and pressure corrected neutron monitor data.

Multidimensional probability density estimator algorithms (PDERS and KNN) appear not to be well suited for the modeling of pressure and temperature effect, most likely due to highly linear correlations between variables. MLP seems to have underperformed, while methods based on boosted decision trees (particularly BDTG) proved to be more successful, especially when effect on aperiodic variations was concerned. It should be expected that both MLP and BDT(G) methods can be improved if a longer period is used for analysis and parameters beyond average quadratic deviation of modeled data are used for algorithm optimization during training phase. Out of presented algorithms, LD proved to be the most consistent and effective in removing the pressure and temperature effects. In terms of the effect of PT correction on annual and aperiodic variations, this method matched or outperformed the integral method, while the effect it had on aperiodic effects was somewhat overestimative. This could give us grounds to assume at least part of the temperature effect is not taken into account by the integral method, and that there could be room for further improvement in modeling of meteorological effects beyond what theory currently provides.

Data Availability Statement

Raw muon count rate data set used in this study are publicly available online on the Belgrade Cosmic Ray Station site (http://www.cosmic.ipb.ac.rs/). Modeled atmospheric temperature data are available online on the NOAA GFS page (https://www.ncdc.noaa.gov/data-access/model-data/model-datasets/global-forcast-

system-gfs). Latest atmospheric pressure and ground temperature data are available online on the site of Republic Hydro-meteorological Service of Serbia (http://www.hidmet.gov.rs/). List of international geomagnetically quiet days can be downloaded from the GFZ site (https://www.gfz-potsdam.de/en/kp-index/). Neutron monitor data can be accessed online via NEST browser interface (http://www01.nmdb.eu/nest/).

References

Barbashina, N., Dmitrieva, A., Kompaniets, K., Petrukhin, A., Timashkov, D., Shutenko, V., et al. (2009). Specific features of studying Forbush decreases in the muon flux. *Bulletin of the Russian Academy of Sciences: Physics*, *73*, 343–346. https://doi.org/10.3103/S1062873809030198

Barrett, P. H., Bollinger, L. M., Cocconi, G., Eisenberg, Y., & Greisen, K. (1952). Interpretation of cosmic-ray measurements far underground. *Reviews of Modern Physics*, *24*, 133–178. https://doi.org/10.1103/RevModPhys.24.133

Belov, A., Blokh, Y., Dorman, L., & Rogovaya, S. (1987). The temperature diagnostics of the atmosphere allowing for the temperature of the near-surface layer. *International Cosmic Ray Conference*, *4*, 263.

Berkova, M., Belov, A., Eroshenko, E., & Yanke, V. (2012). Temperature effect of muon component and practical questions of how to take into account in real time. *Astrophysics and Space Sciences Transactions*, *8*, 41–44. https://doi.org/10.5194/astra-8-41-2012

Blackett, P. M. S. (1938). On the instability of the Barytron and the temperature effect of cosmic rays. *Physical Review*, *54*, 973–974. https://doi.org/10.1103/PhysRev.54.973

Carli, T., & Koblitz, B. (2003). A multi-variate discrimination technique based on range-searching. *Nuclear Instruments and Methods in Physics Research Section A: Accelerators, Spectrometers, Detectors and Associated Equipment*, *501*, 576–588. https://doi.org/10.1016/S0168-9002(03)00376-0

Dorman, L. I. (1954). On the temperature effect of the hard component of cosmic rays. *Reports of Academy of Sciences of USSR (DAN SSSR)*, *95*, 49–52.

Dorman, L. I. (2004). *Cosmic rays in the Earth's atmosphere and underground*. Springer. Retrieved from https://books.google.rs/books?id=mKLv68WBu5kC

Dragić, A., Joković, D., Banjanac, R., Udovičić, V., Panić, B., Puzović, J., & Aničin, I. (2008). Measurement of cosmic ray muon flux in the Belgrade ground level and underground laboratories. *Nuclear Instruments and Methods in Physics Research Section A: Accelerators, Spectrometers, Detectors and Associated Equipment*, *591*(3), 470–475.

Dragic, A. L., Udovicic, V. I., Banjanac, R., Jokovic, D. R., Maletic, D. M., Veselinovic, N. B., et al. (2011). The new set-up in the Belgrade low-level and cosmic-ray laboratory. *Nuclear Technology & Radiation Protection*, *26*(3), 181–192. https://doi.org/10.2298/NTRP1103181D

Duperier, A. (1949). The meson intensity at the surface of the Earth and the temperature at the production level. *Proceedings of the Physical Society Section A*, *62*(11), 684–696. https://doi.org/10.1088/0370-1298/62/11/302

Dvornikov, V. M., Krestyannikov, Y. Y., & Sergeev, A. (1976). Determination of the mass-average temperature on the cosmic ray intensity data. *Geomagnetism and Aeronomy*, *16*, 923–925.

Feinberg, E. L. (1946). On the nature of cosmic ray barometric and temperature effects. *Reports of Academy of Sciences of USSR (DAN SSSR)*, *53*, 421–424. https://doi.org/10.1038/157421a0

Forbush, S. E. (1937). On the effects in cosmic-ray intensity observed during the recent magnetic storm. *Physical Review*, *51*, 1108–1109. https://doi.org/10.1103/PhysRev.51.1108.3

Forró, M. (1947). Temperature effect of cosmic radiation at 1000-m water equivalent depth. *Physical Review*, *72*, 868–869. https://doi.org/10.1103/PhysRev.72.868

GFS. (2020). Retrieved from https://www.ncdc.noaa.gov/data-access/model-data/model-datasets/global-forcast-system-gfs

GFZ Potsdam. (2020). Retrieved from https://www.gfz-potsdam.de/en/kp-index/

Hess, V. F. (1940). On the seasonal and the atmospheric temperature effect in cosmic radiation. *Physical Review*, *57*, 781–785. https://doi.org/10.1103/PhysRev.57.781

Hoecker, A., Speckmayer, P., Stelzer, J., Therhaag, J., von Toerne, E., Voss, H., & Zemla, A. (2007). *Tmva—Toolkit for multivariate data analysis*. Ithaca, NY: Cornell University.

IZMIRAN. (2020). Retrieved from http://spaceweather.izmiran.ru/eng/dbs.html

Joković, D. (2011). *Detekcija i spektroskopija miona iz kosmičkog zračenja plastičnim scintilacionim detektorima (Detection and spectroscopy of cosmic ray muons with plastic scintillation detectors) (Doctoral dissertation)*. Faculty of Physics, University of Belgrade. Retrieved from http://www.cosmic.ipb.ac.rs/documents/jokovic-thesis.pdf

Kaminer, N. S., Ilgatch, S. F., & Khadakhanova, T. S. (1965). Temperature effect of the cosmic ray neutron component. In *Proceedings of the 9th International Cosmic Ray Conference* (Vol. 1, p. 486).

Kohno, T., Imai, K., Inue, A., Kodama, M., & Wada, M. (1981). Estimation of the vertical profile of atmospheric temperature from cosmic-ray components. In *Proceedings of the 17th International Cosmic Ray Conference* (Vol. 10, p. 289).

Lalchand, V. (2020). Extracting more from boosted decision trees: A high energy physics case study. In *33rd Annual Conference on Neural Information Processing Systems* (Vol. 1).

Low Background Laboratory for Nuclear Physics. (2020). Retrieved from http://www.cosmic.ipb.ac.rs/

Maeda, K., & Wada, M. (1954). Atmospheric temperature effect upon the cosmic ray intensity at sea level. *Journal of the Scientific Research Institute*, *48*, 71–79.

Montgomery, D. C., Peck, E. A., & Vining, G. G. (2006). *Introduction to linear regression analysis* (4th ed.). Hoboken, NJ: Wiley & Sons.

Morozova, A. L., Blanco, J. J., & Ribeiro, P. (2017). Modes of temperature and pressure variability in midlatitude troposphere and lower stratosphere in relation to cosmic ray variations. *Space Weather*, *15*(5), 673–690. https://doi.org/10.1002/2016SW001582

Myssowsky, L., & Tuwim, L. (1926). Unregelmäßige intensitätsschwankungen der höhenstrahlung in geringer seehöhe. *Zeitschrift für Physik*, *39*, 146–150. https://doi.org/10.1007/BF01321981

NEST. (2020). Retrieved from http://www01.nmdb.eu/nest/

Press, W. H., Teukolsky, S. A., Vetterling, W. T., & Flannery, B. P. (2007). *Numerical recipes 3rd edition: The art of scientific computing* (3rd ed.). New York: Cambridge University Press.

Quenby, J. J., & Thambyahpillai, T. (1960). Atmospheric temperature effects on the solar daily variation of cosmic ray intensity. *The Philosophical Magazine: A Journal of Theoretical Experimental and Applied Physics*, *5*(54), 585–600. https://doi.org/10.1080/14786436008241210

RHMZ. (2020). Retrieved from http://www.hidmet.gov.rs/index-eng.php

Savic, M., Dragic, A., Veselinovic, N., Udovicic, V., Banjanac, R., Jokovic, D., & Maletic, D. (2016). Effect of pressure and temperature corrections on muon flux variability at ground level and underground. In *25th European cosmic ray Symposium*.

Savic, M. R., Dragic, A. L., Maletic, D. M., Veselinovic, N. B., Banjanac, R. M., Jokovic, D. R., & Udovicic, V. I. (2019). A novel method for atmospheric correction of cosmic-ray data based on principal component analysis. *Astroparticle Physics*, *109*, 1–11. https://doi.org/10.1016/j.astropartphys.2019.01.006

Veselinović, N., Dragić, A., Savić, M., Maletić, D., Joković, D., Banjanac, R., & Udovičić, V. (2017). An underground laboratory as a facility for studies of cosmic-ray solar modulation. *Nuclear Instruments and Methods in Physics Research Section A: Accelerators, Spectrometers, Detectors and Associated Equipment*, *875*, 10–15. https://doi.org/10.1016/j.nima.2017.09.008

Wada, M. (1962). Atmospheric effects on the cosmic-ray meson intensity. *Journal of the Physical Society of Japan Supplement*, *17*, 508. https://doi.org/10.1143/jpsj.17.1805

Results of the first national indoor radon survey performed in Serbia

Maja Eremić Savković[1], Vladimir Udovičić[2], Dimitrije Maletić[2], Gordana Pantelić[3], Predrag Ujić[3], Igor Čeliković[3], Sofija Forkapić[4], Vladimir Marković[5], Vesna Arsić[6], Jovana Ilić[6], Branko Markoski[7]

[1] Serbian Radiation and Nuclear Safety and Security Directorate, Belgrade, Serbia
[2] Institute of Physics Belgrade, University of Belgrade, Serbia
[3] Vinča Institute of Nuclear Sciences, University of Belgrade, Serbia
[4] Department of Physics, Faculty of Science, University of Novi Sad, Serbia
[5] Faculty of Science, University of Kragujevac, Serbia
[6] Serbian Institute of Occupational Health "Dr Dragomir Karajovic", Serbia
[7] Technical Faculty "Mihajlo Pupin", University of Novi Sad, Serbia

Abstract

The first step in every systematic approach to investigating population exposure to radon on a national level is to perform a comprehensive indoor radon survey. Based on the general knowledge of the radon levels in Serbia and corresponding doses, the results obtained from a national indoor radon survey would allow policy-makers to decide if it is necessary to establish a national radon programme. For this reason, Serbia initiated work on a national radon action plan (RAP) in 2014 when it was decided to carry out the first national indoor radon survey. The responsibility for establishing the RAP in Serbia is that of the national regulatory body in the field of radiation protection – the Serbian Radiation and Nuclear Safety and Security Directorate (SRBATOM), formerly known as the Serbian Radiation Protection and Nuclear Safety Agency (SRPNA). The first national indoor radon survey was supported by the International Atomic Energy Agency (IAEA) through a Technical Cooperation Programme. Thanks to the IAEA, we received 6,000 passive radon devices based on track-etched detectors. In addition, in order to ensure technical support for the project, SRBATOM formed a task force made up of expert radon representatives from national research institutions. This paper presents a thorough description of the sampling design of the first Serbian indoor radon survey. It also presents the results of the national indoor radon survey, including descriptive statistics and testing of the distribution of the obtained results for log-normality. Based on GPS coordinates, indoor radon data were projected onto a map of 10x10 km grid cells. Two values were calculated for each cell to create two distinct maps. One map shows the arithmetic mean value of indoor radon concentration per grid cell, and the other map shows the number of radon detectors per grid cell used for the calculation of mean values.

Keywords: radon mapping, radon action plan

1. Introduction

According to recent epidemiological studies, an increase in the risk of lung cancer is positively related to an increase in indoor ^{222}Rn concentration (Darby et al., 2005). As a result, international regulations and recommendations (EURATOM, 2013; IAEA, 2014; WHO, 2009), as well as comprehensive national radon programmes have been set up in many countries with the aim of reducing population exposure to indoor radon and the corresponding risks. The representative national indoor radon survey is one of the first steps in a national radon programme aimed at identifying existing exposure situations in the country and radon priority areas (RPA), with a focus on reducing individual risks in these areas.

Radon levels in dwellings have been extensively investigated and monitored worldwide over the last 30 years. On the basis of experiences from abroad, guidelines for performing indoor radon surveys have recently been published (IAEA, 2013; Da Silva et al., 2014; Font, 2009; UNSCEAR, 2008). In the last decade, national and regional indoor radon surveys were carried out in almost all countries of southeast Europe (Radolić et al., 2006; Vukotić et al., 2019; Kunovska et al., 2018; Stojanovska et al., 2012; Cosma et al., 2013).

At the European level, the Radiation Environmental Monitoring (REM) group of the Joint Research Centre (JRC) of the European Commission initiated a project in 2006 to develop a European Atlas of Natural Radiation. One of the maps in this Atlas is the European Indoor Radon Map (EIRM). The aim of the project, among other activities, was to provide information about the levels of environmental radiation by collecting and evaluating the data and harmonizing procedures (Dubois et al., 2010; Bossew et al., 2015). A digital version of the European Atlas of Natural Radiation was completed and published (Cinelli et al., 2019). Additionally, a qualitative overview of the indoor radon surveys in Europe was presented in a review article (Pantelić et al., 2019).

Based on the acquired knowledge from research on radon, a group of radon professionals in Serbia organized a Radon Forum in 2014 and decided to start work on a national radon action plan (RAP). One of the conclusions of the meeting was that the focal point in Serbia for all national radon activities is the regulatory body in the field of radiation protection, the Serbian Radiation and Nuclear Safety and Security Directorate (SRBATOM), formerly known as the Serbian Radiation Protection and Nuclear Safety Agency (SRPNA). SRBATOM formed a "radon working group" composed of representatives from institutes and universities with radon-related research experience. The short- and long-term plans of the RAP were described in a paper by Udovičić et al., 2016. The first national indoor radon survey was conducted in 2015-2016 as the first step in establishing a RAP in Serbia. The project was supported by the IAEA through the national project: SRB9003 – Enhancing the Regulatory Infrastructure and Legislative System, with two components:

– An expert mission on "National Radon Trial Survey and Raising Awareness of Key Stakeholders" held on 2 February 2015 in SRBATOM, Belgrade. The objectives of the IAEA expert mission were to find the best and the most appropriate sampling design of the first national indoor radon survey in Serbia. We targeted two key stakeholders in the project: the Ministry of Environmental Protection and the Ministry of Education, Science and Technological Development;

– Equipment: provision of 6,000 track-etched radon detectors; distribution of the detectors across Serbian territory was the responsibility of SRBATOM.

The paper details the sampling design of the first national indoor radon survey. The results of the first national indoor radon survey, together with descriptive statistics are given as well. For the purpose of presenting the data, a map of 10x10 km grid cells, was created. The result was the creation of two distinct maps: one showing the annual average indoor radon concentrations per grid cell, and the other showing the number of radon detectors per cell used to calculate mean values.

2. Materials and methods

It is well known that there are two types of indoor radon surveys:

- population-weighted surveys where indoor radon levels are measured in randomly selected dwellings (to estimate the distribution of public exposure to radon), and

- geographically based surveys where dwellings are randomly selected to obtain a minimum number of measurements per chosen area unit, e.g. a grid square, an administrative unit, etc. (to identify radon priority areas or to create a radon map).

In the case of Serbia, some of the relevant data from the last census held in 2011 include: a total population of around 7,200,000 (ca. 4,270,000 living in urban and ca. 2,910,000 living in rural areas) with a mean population density of 95 km^{-2}, total area of ca. 88,000 km^2, total housing units of ca. 3,200,000. When carefully designed, surveys can in principle meet the requirements and objectives

of both types of survey. We opted for a stratified sampling design (a sampling design in which the target is partitioned into separate groups – STRATA). We defined STRATA according to the administrative division of Serbia into districts; the number of districts is 25.

A good communication strategy during the realization of the national programme for indoor radon measurement was applied. The radon-risk communication plan consisted of several elements: general information about radon and a leaflet with detailed guidelines regarding the placing of the detector that was given to each volunteer; the internet sites for radon professionals (radon forum) and the public; public relations and education (presentations in schools); communication with key stakeholders and public media (newspapers, TV, radio stations, etc.).

Each institution within the radon working group was responsible for a given set of administrative regions (districts). The number of detectors meant to be deployed per district was set according to the size of the population in each district. Majority of detectors was given to physics teachers in high schools and the rest to environmental protection officers in municipalities of these districts. After we gave a lecture on radon and national campaign in each selected school, we asked pupils to participate in the campaign by exposing detectors in their homes. Physics teachers were responsible for collection of detectors and sending them back to SRPNA. Environmental protection officers have distributed the rest of the detectors to volunteers that got information regarding the survey over public media. There were no preselection of volunteers, but everybody who expressed their wish to participate, could participate. The only limitation was number of available detectors.

Each participant completed a predefined questionnaire, which, in terms of building characteristics, included information about the type of building (if a dwelling was a family house or a flat in an apartment building), on which floor the dwelling was, the year of construction, existence of a cellar, wall material, type of heating, existence of hydro-isolation and window design. In total, 6,000 passive radon devices based on a CR-39 detector (Radtrak², Radonova) were distributed during October 2015 and left in houses and apartments for six months (till April 2016). One detector was deployed in each dwelling, except for 100 randomly-selected dwellings (covering typical dwellings all over Serbia according to the monography by Jovanović Popović et al., 2013), where an additional detector was deployed for twelve months in order to gain a proper estimation of the annual indoor radon concentration. Afterwards, the detectors were collected and sent to the authorized laboratory (Radonova) to be processed, and we subsequently received data from the first national indoor radon survey in Serbia. Finally, each participant in the project received a report with the result of the radon measurement and recommendations for further action.

3. Results and Discussion

The first important fact about the national indoor radon survey performed in Serbia was the relatively high return rate of detectors (88%), i.e. that the number of collected detectors was 5,300. Since distribution of detectors was on voluntary basis, this could create bias in the survey as it was reported in some other national surveys (Burke et al., 2011). Since participants in the projects were mainly high school students and volunteers, there could be a tendency for participation in such studies to be biased towards people who are more highly educated, which can further be correlated with their level of wealth and consequently on their housing. In addition, survey could be biased toward more urban than rural areas and younger than old households. The potential social bias can be expected and this is going to subject of profound analysis.

During the project preparation phase, we obtained 63 of the 100 deployed pairs of detectors with results aimed at estimating a seasonal correction factor, which is determined as the arithmetic mean (AM) of the ratio of radon concentrations obtained from detectors exposed in certain dwellings for 12 months – R(12) and 6 months – R(6). Descriptive statistics that include the arithmetic mean (AM), standard deviation (SD), minimum, maximum and median used to deduce the seasonal correction factor are presented in Table 1. The obtained seasonal correction factor of 0.79 is almost

152 the same as the previously reported value (Daraktchieva et al., 2018) of 0.82 applied for the same
153 exposure time of six months starting from October.

154

155 **Table 1.**
156 Descriptive statistics of the dataset used to estimate the seasonal correction factor. Rn(12) and Rn(6)
157 denote the radon concentrations measured by detectors exposed for 12 and 6 months, respectively.
158 AM(SD) – arithmetic mean and standard deviation.
159

	AM(SD)	Minimum	Maximum	Median
Rn(12)/Rn(6)	0.79(0.17)	0.52	1.39	0.76

160
161
162 The descriptive statistics of the dataset from the national indoor radon survey in Serbia, with applied
163 seasonal correction factors, are presented in Table 2. GM – geometric mean; GSD – geometric
164 standard deviation.
165

166 **Table 2.**
167 Descriptive statistics of the dataset from the national indoor radon survey in Serbia with applied
168 seasonal correction factors.
169

AM(SD) Bq/m^3	Minimum Bq/m^3	Maximum Bq/m^3	Median Bq/m^3	GM(GSD) Bq/m^3
105(150)	3	4335	60	60(3)

170
171
172 The frequency table and exceedance probabilities with respect to national radon action levels are
173 presented in Table 3. The current legislation in Serbia regarding radon prescribes action levels for
174 chronic exposure to radon in homes of 200 Bq/m^3 for newly built structures, and 400 Bq/m^3 for
175 existing buildings.

176

177 **Table 3.**
178 Distribution of the data on national radon legislation.
179

0-200 Bq/m^3	200-400 Bq/m^3	> 400 Bq/m^3	> 1000 Bq/m^3
4137 (87%)	479 (10%)	158 (3%)	14 (0.3%)

180
181 As a part of the standard analysis of the data obtained from the indoor radon surveys, empirical
182 distribution was tested for log-normality (IAEA, 2013). The log-normal distribution of the seasonally
183 corrected annual average indoor radon concentrations obtained from the national indoor radon survey
184 in Serbia is shown in Fig. 1, while a quantile-quantile plot of the log-transformed data for indoor
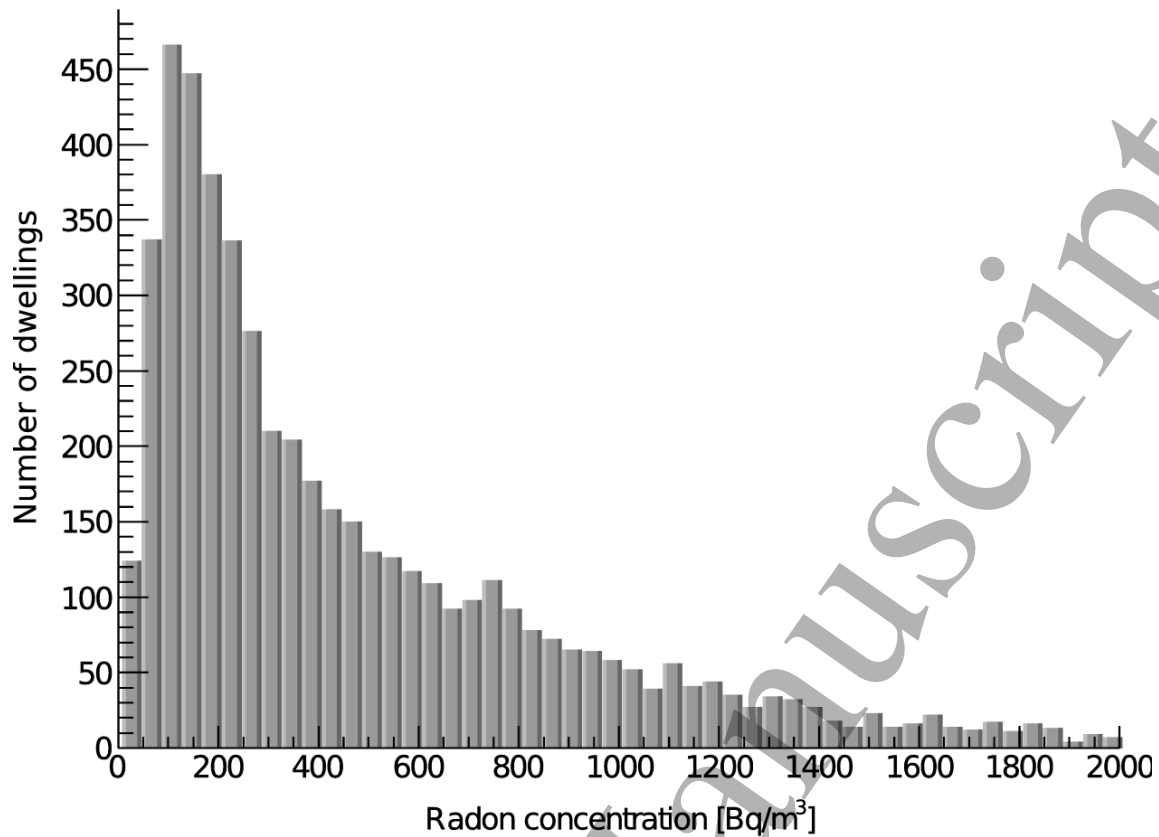185 radon concentrations is given in Fig. 2.

Fig. 1. Log-normal distribution of the seasonally corrected annual average indoor radon concentrations measured during the national indoor radon survey in Serbia.
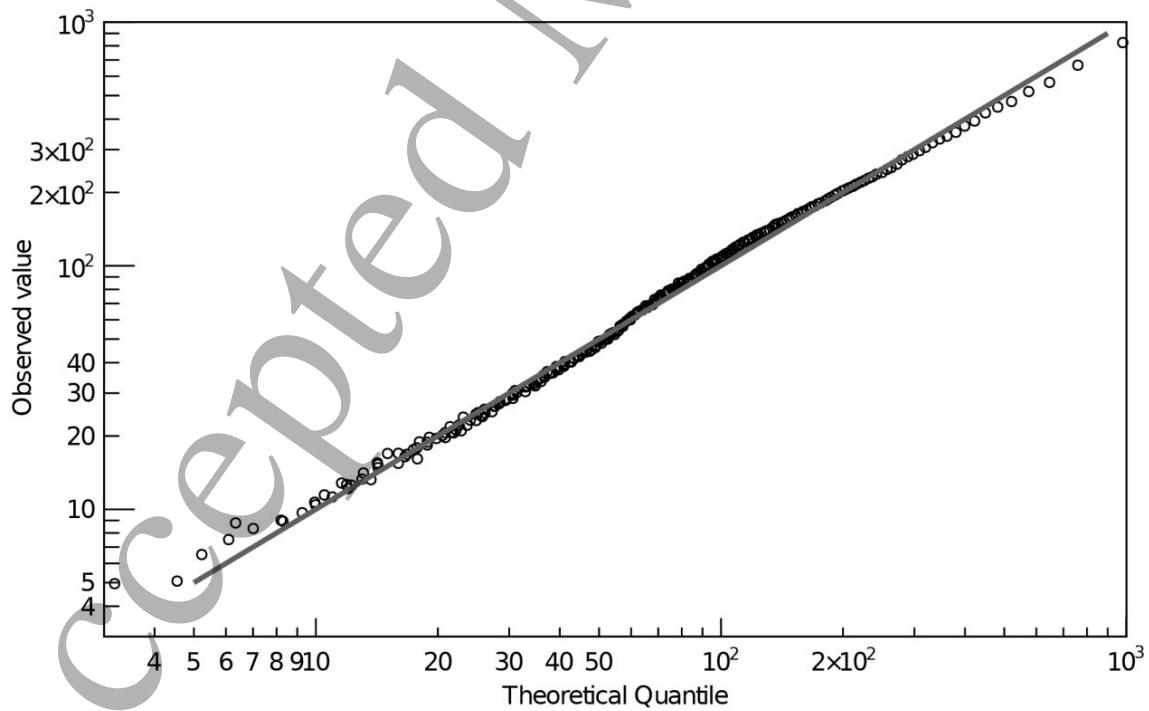

Fig. 2. The quantile-quantile plot of the log-transformed data for indoor radon concentrations.

Since we chose a stratified sampling design, we have presented the results per district. The distribution of the number of returned detectors with results, the average radon concentration and the number and percentage of houses with radon levels exceeding 400 Bq/m^3 by district are shown in Table 4. Based on the numbers of collected, as well as distributed detectors, the national indoor radon survey is population-weighted. The number of collected detectors from the Belgrade district was five times greater than the average number of collected detectors from other districts. This ratio is in good agreement with data from the last census regarding the size of the populations in districts in Serbia.

Table 4.

Distribution of the population (based on data from the last census in 2011), number of returned detectors, arithmetic mean (AM) with standard deviation (SD) and geometric mean (GM) with geometric standard deviation (GSD) of the indoor radon concentration, number and percentage of dwellings with radon levels exceeding 400 Bq/m^3 by district.

| District	Population (Census 2011)	N	AM(SD) (Bq/m^3)	GM(GSD) (Bq/m^3)	Number of dwellings with radon levels exceeding 400 Bq/m^3	Percentage of dwellings with radon levels exceeding 400 Bq/m^3
Central Banat	186,851	37	159(96)	135(2)	1	2.7
Podunavlje	198,184	245	155(206)	92(3)	22	9
Braničevo	180,480	269	144(198)	93(3)	20	7.4
Srem	311,053	199	136(148)	85(3)	11	5.5
West Bačka	187,581	125	135(119)	91(3)	4	3.2
Mačva	297,778	20	129(110)	84(3)	0	0
Nišava	373,404	332	125(332)	68(3)	12	3.6
Pčinja	158,717	10	124(120)	77(3)	1	10
Zlatibor	284,929	330	119(159)	65(3)	20	6.1
North Banat	146,690	54	119(64)	99(2)	0	0
Pomoravlje	212,839	108	114(134)	73(2)	5	4.6
Zaječar	118,295	174	107(105)	71(3)	3	1.7
North Bačka	185,552	88	104(89)	72(3)	1	1.1
Moravica	212,149	173	103(149)	60(3)	9	5.2
South Banat	291,327	126	93(96)	55(3)	1	0.8
Toplica	90,600	31	91(87)	70(3)	1	3.2
Bor	123,848	128	90(114)	47(3)	4	3.1
South Bačka	607,835	523	87(92)	50(3)	7	1.3
Jablanica	215,463	62	86(77)	70(2)	1	1.6
Rasina	240,463	125	84(85)	56(3)	1	0.8
Belgrade	1,639,121	1040	79(115)	41(3)	28	2.7
Raška	300,102	226	78(89)	54(2)	2	0.9
Kolubara	174,228	158	77(99)	47(3)	3	1.9
Pirot	92,277	109	70(73)	60(2)	0	0
Šumadija	290,900	258	70(74)	46(3)	3	1.2

211 According to Article 103 of the EU-BSS, Member States are obliged to identify areas where the
212 annual average radon concentration in a significant number of buildings is expected to exceed the
213 respective national reference level. The question of delineation of radon priority areas (RPA) is very
214 sensitive and left to each country to decide on its own operable definition. Consequently, there are
215 numerous definitions of RPA across the EU (Bossew, 2019). The obtained distribution of radon
216 concentration per district and the percentage of houses with an annual average radon concentration
217 exceeding a certain level will serve as a guideline for the Serbian authority first to define RPA and
218 then to delineate RPA.
219 Also, the results presented in Table 4 show the limitations of the survey in the low number of results
220 obtained from some districts (Pčinja, Mačva, Toplica and central Banat). Improving this will be the
221 task of future national indoor radon measurement campaigns.
222 Indoor radon data based on GPS coordinates were projected onto a map of 10x10 km grid cells and
223 are shown in Fig. 3.
224
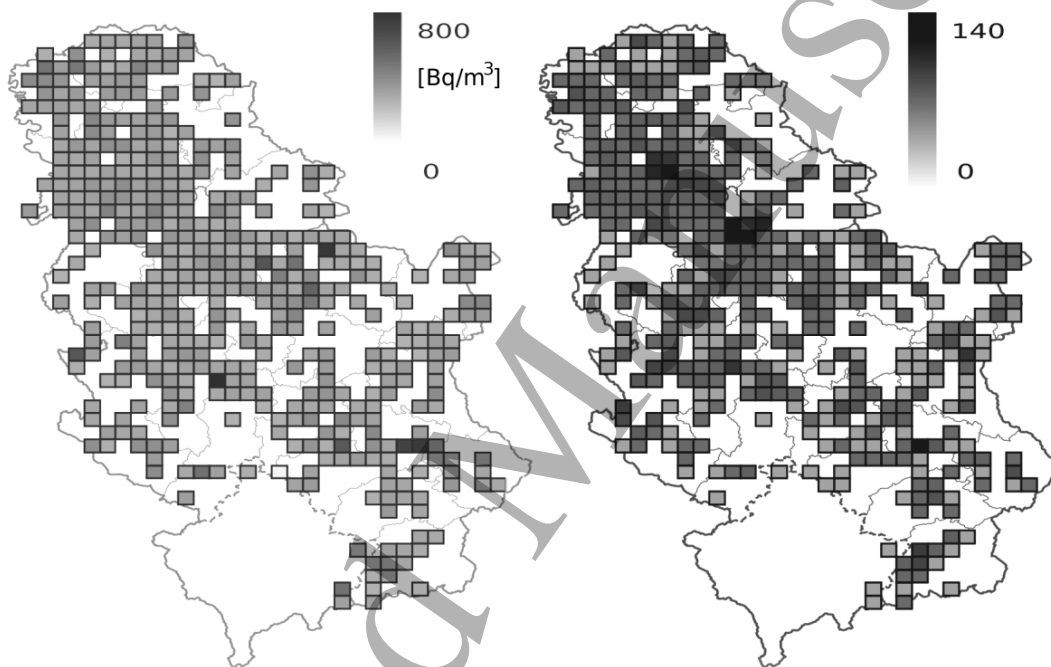
225
226 Fig. 3. Indoor radon map of the Republic of Serbia (left) and the distribution of the number of
227 measurements over 10x10 km grid cells of seasonally corrected annual average indoor radon
228 concentrations (right).
229

230 The second map shows the distribution of the number of measurements of annual indoor radon
231 concentrations in 10x10 km grid cells (Fig. 3). The total number of non-empty cells is 429, with a
232 minimum 1 to a maximum 146 detectors per cell. Since the total area of the Republic of Serbia is ca.
233 88,000 km^2 and the number of empty cells is 450, this means that within this survey we covered 50%
234 of the territory.
235

4. Conclusions

237

238 The first national indoor radon survey in Serbia was performed between October 2015 to April 2016.
239 The survey was population-weighted. From the obtained results, the estimated annual arithmetic
240 mean radon level is 105 Bqm^{-3}. Based on our results and the fact that 3% of all measurements
241 exceeded the currently defined action level of 400 Bqm^{-3}, we conclude that Serbia has a radon

242 problem. The results of the national radon survey serve to evaluate the existing exposure situation
243 and give the good basis for the next steps in establishing and developing a RAP in Serbia with the
244 main goal of reducing population exposure to indoor radon and the corresponding risks to public
245 health. The indoor radon data based on GPS coordinates were projected onto a map with 10x10 km
246 grid cells. The obtained distribution of radon concentration per district and the percentage of
247 dwellings with an annual average radon concentration exceeding a certain level will serve as a
248 guideline for the Serbian authority to establish a definition of RPA, to provide additional
249 measurements in districts where necessary, and finally, to use all these data to delineate RPA.

250

Acknowledgements

252

256

References

258 Bossew P, Tollefsen T, Cinelli G, Gruber V and De Cort M 2015 Status of the European Atlas of
259   Natural Radiation *Radiation Protection Dosimetry* 167(1-3) 29-36.
260 Burke Ó, Murphy P 2011 The use of volunteer radon measurements for radon mapping purposes: an
261   examination of sampling bias issues *Journal of Radiological Protection* 31 319–328.
262 Daraktchieva Z, Howarth C B, Gooding T D, Bradley E J and Hutt N 2018 Validation Scheme for
263   Organisations Making Measurements of Radon in UK Buildings: 2018 Revision, PHE-CRCE-
264   040.
265 Darby S *et al*. 2005 Radon in homes and risk of lung cancer: collaborative analysis of individual data
266   from 13 European case-control studies *Brit. Med. J.* 330 223-227.
267 Da Silva N C and Bossew P 2014 The Planned Brazilian Indoor Radon Survey—Concepts and
268   Particular Challenges *Radiation Protection Dosimetry* 162(1-2) 105-109.
269 Dubois G, Bossew P, Tollefsen T and De Cort M 2010 First steps towards a European atlas of
270   natural radiation: status of the European indoor radon map *Journal of Environmental*
271   *Radioactivity* 101 786-798.
272 Cinelli G, Tollefsen T, Bossew P, Gruber V, Bogucarskis K, De Felice L and De Cort M 2019
273   Digital version of the European Atlas of natural radiation *Journal of Environmental Radioactivity*
274   196 240-252.
275 Cosma C, Cucos A and Dicu T 2013 Preliminary Results Regarding the First Map of Residential
276   Radon in Some Regions in Romania *Radiation Protection Dosimetry* 155(3) 343-350.
277 EURATOM, 2013. Council Directive 2013/59/EURATOM of 5 December 2013 Laying Down Basic
278   Safety Standards for Protection against the Dangers Arising from Exposure to Ionising Radiation,
279   and Repealing Directives 89/618/Euratom, 90/ 641/Euratom, 96/29/Euratom, 97/43/Euratom and
280   2003/122/Euratom, Article 74 Indoor Exposure to Radon. http://eur-
281   lex.europa.eu/LexUriServ/LexUriServ. do?uri¼OJ: L:2014:013:0001:0073:EN: PDF.
282 Font Ll 2009 On radon surveys: Design and data interpretation *Radiation Measurements* 44, 964-
283   968.
284 IAEA, 2013. In: National and regional surveys of radon concentration in dwellings; review of
285   methodology and measurement techniques. IAEA Analytical Quality in Nuclear Application
286   Series No. 33, Report IAEA/AQ/33. Available on www-
287   pub.iaea.org/MTCD/Publications/PDF/IAEA-AQ-33_web.pdf.

288 IAEA, 2014. In: EUROPEAN COMMISSION, FOOD AND AGRICULTURE ORGANIZATION
289   OF THE UNITED NATIONS, INTERNATIONAL ATOMIC ENERGY AGENCY,
290   INTERNATIONAL LABOUR ORGANIZATION, OECD NUCLEAR ENERGY
291   AGENCY,PAN AMERICAN HEALTH ORGANIZATION, UNITED NATIONS
292   ENVIRONMENT PROGRAMME, WORLD HEALTH ORGANIZATION, Radiation Protection
293   and Safety of Radiation Sources: International Basic Safety Standards, IAEA Safety Standards
294   Series No. GSR Part 3, IAEA, Vienna.
295 Jovanović Popović M, Ignjatović D, Radivojević A, Rajčić A, Ćuković Ignjatović N, Đukanović Lj,
296   Nedić M 2013. National Typology of Residential Buildings in Serbia, Faculty of Architecture
297   University of Belgrade, Belgrade, ISBN 978-86-7924-102-3.
298 Kunovska B, Ivanova K, Badulin V, Cenova M and Angelova A 2018 Assessment of Residential
299   Radon Exposure in Bulgaria *Radiation Protection Dosimetry* 181(1), 34-37.
300 Pantelić G, Čeliković I, Živanović M, Vukanac I, Krneta Nikolić J, Cinelli G, Gruber V 2019.
301   Qualitative overview of indoor radon surveys in Europe. Journal of Environmental Radioactivity
302   204, 163-174.
303 Radolić V, Vuković B, Stanić D, Katić M, Faj Z, Šuveljak B, Lukačević I, Faj D, Lukić M, Planinić
304   J 2006 National survey of indoor radon levels in Croatia *Journal of Radioanalytical and Nuclear
305   Chemistry* 269(1), 87–90.
306 Stojanovska Z, Januseski J, Boev B and Ristova M 2012 Indoor Exposure of Population to Radon in
307   the FYR of Macedonia *Radiation Protection Dosimetry* 148(2), 162-167.
308 Udovičić V, Maletić D, Eremić Savković M, Pantelić G, Ujić P, Čeliković I, Forkapić S, Nikezić D,
309   Marković V, Arsić V and Ilić J 2016 First steps towards national radon action plan in Serbia
310   *Nukleonika* 61(3) 361-365.
311 UNSCEAR (United Nation Scientific Committee on the Effects of Atomic Radiation Report), 2008.
312   Sources and Effects of Ionizing Radiation, Report to the General Assembly. United Nations, New
313   York.
314 Vukotić P, Antovic N, Djurovic A, Zekic R, Svrkota N, Andjelic T, Svrkota R, Mrdak R, Bjelica N,
315   Djurovic T, Dlabac A and Bogicevic M 2019 Radon Survey in Montenegro – A Base to Set
316   National Radon Reference and "Urgent Action" Level *Journal of Environmental Radioactivity*
317   196, 232-239.
318 WHO, 2009. In: Handbook on Indoor Radon e a Public Health Perspective.
319   www.who.int/ionizing_radiation/env/radon/en/imdex1.html.
320

THE EUROPEAN
PHYSICAL JOURNAL C

First particle-by-particle measurement of emittance in the Muon Ionization Cooling Experiment

MICE Collaboration

D. Adams[15], D. Adey[25,34], R. Asfandiyarov[13], G. Barber[18], A. de Bari[6], R. Bayes[16], V. Bayliss[15], R. Bertoni[4], V. Blackmore[18,a], A. Blondel[13], J. Boehm[15], M. Bogomilov[1], M. Bonesini[4], C. N. Booth[20], D. Bowring[25], S. Boyd[22], T. W. Bradshaw[15], A. D. Bross[25], C. Brown[15,23], G. Charnley[14], G. T. Chatzitheodoridis[16,21], F. Chignoli[4], M. Chung[10], D. Cline[30], J. H. Cobb[19], D. Colling[18], N. Collomb[14], P. Cooke[17], M. Courthold[15], L. M. Cremaldi[28], A. DeMello[26], A. J. Dick[21], A. Dobbs[18], P. Dornan[18], F. Drielsma[13], K. Dumbell[14], M. Ellis[23], F. Filthaut[11,32], P. Franchini[22], B. Freemire[27], A. Gallagher[14], R. Gamet[17], R. B. S. Gardener[23], S. Gourlay[26], A. Grant[14], J. R. Greis[22], S. Griffiths[14], P. Hanlet[27], G. G. Hanson[29], T. Hartnett[14], C. Heidt[29], P. Hodgson[20], C. Hunt[18], S. Ishimoto[9], D. Jokovic[12], P. B. Jurj[18], D. M. Kaplan[27], Y. Karadzhov[13], A. Klier[29], Y. Kuno[8], A. Kurup[18], P. Kyberd[23], J-B. Lagrange[18], J. Langlands[20], W. Lau[19], D. Li[26], Z. Li[3], A. Liu[25], K. Long[18], T. Lord[22], C. Macwaters[15], D. Maletic[12], B. Martlew[14], J. Martyniak[18], R. Mazza[4], S. Middleton[18], T. A. Mohayai[27], A. Moss[14], A. Muir[14], I. Mullacrane[14], J. J. Nebrensky[23], D. Neuffer[25], A. Nichols[15], J. C. Nugent[16], A. Oates[14], D. Orestano[7], E. Overton[20], P. Owens[14], V. Palladino[5], M. Palmer[24], J. Pasternak[18], V. Pec[20], C. Pidcott[22,33], M. Popovic[25], R. Preece[15], S. Prestemon[26], D. Rajaram[27], S. Ricciardi[15], M. Robinson[20], C. Rogers[15], K. Ronald[21], P. Rubinov[25], H. Sakamoto[8,31], D. A. Sanders[28], A. Sato[8], M. Savic[12], P. Snopok[27], P. J. Smith[20], F. J. P. Soler[16], Y. Song[2], T. Stanley[15], G. Stokes[14], V. Suezaki[27], D. J. Summers[28], C. K. Sung[10], J. Tang[2], J. Tarrant[15], I. Taylor[22], L. Tortora[7], Y. Torun[27], R. Tsenov[1], M. Tucker[14], M. A. Uchida[18], S. Virostek[26], G. Vankova-Kirilova[1], P. Warburton[14], S. Wilbur[20], A. Wilson[15], H. Witte[24], C. White[14], C. G. Whyte[21], X. Yang[30], A. R. Young[21], M. Zisman[26]

[1] Department of Atomic Physics, St. Kliment Ohridski University of Sofia, Sofia, Bulgaria
[2] Institute of High Energy Physics, Chinese Academy of Sciences, Beijing, China
[3] Sichuan University, Chengdu, China
[4] Dipartimento di Fisica G. Occhialini, Sezione INFN Milano Bicocca, Milan, Italy
[5] Sezione INFN Napoli and Dipartimento di Fisica, Università Federico II, Complesso Universitario di Monte S. Angelo, Naples, Italy
[6] Sezione INFN Pavia and Dipartimento di Fisica, Pavia, Italy
[7] INFN Sezione di Roma Tre and Dipartimento di Matematica e Fisica, Università Roma Tre, Rome, Italy
[8] Department of Physics, Graduate School of Science, Osaka University, Toyonaka, Osaka, Japan
[9] High Energy Accelerator Research Organization (KEK), Institute of Particle and Nuclear Studies, Tsukuba, Ibaraki, Japan
[10] UNIST, Ulsan, Korea
[11] Nikhef, Amsterdam, The Netherlands
[12] Institute of Physics, University of Belgrade, Belgrade, Serbia
[13] DPNC, Section de Physique, Université de Genève, Geneva, Switzerland
[14] STFC Daresbury Laboratory, Daresbury, Cheshire, UK
[15] STFC Rutherford Appleton Laboratory, Harwell Oxford, Didcot, UK
[16] School of Physics and Astronomy, The University of Glasgow, Kelvin Building, Glasgow, UK
[17] Department of Physics, University of Liverpool, Liverpool, UK
[18] Blackett Laboratory, Department of Physics, Imperial College London, London, UK
[19] Department of Physics, University of Oxford, Denys Wilkinson Building, Oxford, UK
[20] Department of Physics and Astronomy, University of Sheffield, Sheffield, UK
[21] SUPA and the Department of Physics, University of Strathclyde, Glasgow, UK
[22] Department of Physics, University of Warwick, Coventry, UK
[23] Brunel University, Uxbridge, UK
[24] Brookhaven National Laboratory, Upton, NY, USA
[25] Fermilab, Batavia, IL, USA
[26] Lawrence Berkeley National Laboratory, Berkeley, CA, USA
[27] Illinois Institute of Technology, Chicago, IL, USA
[28] University of Mississippi, Oxford, MS, USA
[29] University of California, Riverside, CA, USA

Springer

[30] University of California, Los Angeles, CA, USA
[31] *Current address:* RIKEN, Wako, Japan
[32] *Also at* Radboud University, Nijmegen, The Netherlands
[33] *Current address:* Department of Physics and Astronomy, University of Sheffield, Sheffield, UK
[34] *Current address:* Institute of High Energy Physics, Chinese Academy of Sciences, Bejing, China

Abstract The Muon Ionization Cooling Experiment (MICE) collaboration seeks to demonstrate the feasibility of ionization cooling, the technique by which it is proposed to cool the muon beam at a future neutrino factory or muon collider. The emittance is measured from an ensemble of muons assembled from those that pass through the experiment. A pure muon ensemble is selected using a particle-identification system that can reject efficiently both pions and electrons. The position and momentum of each muon are measured using a high-precision scintillating-fibre tracker in a 4 T solenoidal magnetic field. This paper presents the techniques used to reconstruct the phase-space distributions in the upstream tracking detector and reports the first particle-by-particle measurement of the emittance of the MICE Muon Beam as a function of muon-beam momentum.

1 Introduction

Stored muon beams have been proposed as the source of neutrinos at a neutrino factory [1,2] and as the means to deliver multi-TeV lepton-antilepton collisions at a muon collider [3,4]. In such facilities the muon beam is produced from the decay of pions generated by a high-power proton beam striking a target. The tertiary muon beam occupies a large volume in phase space. To optimise the muon yield for a neutrino factory, and luminosity for a muon collider, while maintaining a suitably small aperture in the muon-acceleration system requires that the muon beam be 'cooled' (i.e., its phase-space volume reduced) prior to acceleration. An alternative approach to the production of low-emittance muon beams through the capture of $\mu^+\mu^-$ pairs close to threshold in electron–positron annihilation has recently been proposed [5]. To realise the luminosity required for a muon collider using this scheme requires the substantial challenges presented by the accumulation and acceleration of the intense positron beam, the high-power muon-production target, and the muon-capture system to be addressed.

D. Cline, M. Zisman: Deceased.

[a] e-mail: v.blackmore@imperial.ac.uk

A muon is short-lived, with a lifetime of $2.2\,\mu$s in its rest frame. Beam manipulation at low energy (≤ 1 GeV) must be carried out rapidly. Four cooling techniques are in use at particle accelerators: synchrotron-radiation cooling [6]; laser cooling [7–9]; stochastic cooling [10]; and electron cooling [11]. In each case, the time taken to cool the beam is long compared to the muon lifetime. In contrast, ionization cooling is a process that occurs on a short timescale. A muon beam passes through a material (the absorber), loses energy, and is then re-accelerated. This cools the beam efficiently with modest decay losses. Ionization cooling is therefore the technique by which it is proposed to increase the number of particles within the downstream acceptance for a neutrino factory, and the phase-space density for a muon collider [12–14]. This technique has never been demonstrated experimentally and such a demonstration is essential for the development of future high-brightness muon accelerators or intense muon facilities.

The international Muon Ionization Cooling Experiment (MICE) has been designed [15] to perform a full demonstration of transverse ionization cooling. Intensity effects are negligible for most of the cooling channels conceived for the neutrino factory or muon collider [16]. This allows the MICE experiment to record muon trajectories one particle at a time. The MICE collaboration has constructed two solenoidal spectrometers, one placed upstream, the other downstream, of the cooling cell. An ensemble of muon trajectories is assembled offline, selecting an initial distribution based on quantities measured in the upstream particle-identification detectors and upstream spectrometer. This paper describes the techniques used to reconstruct the phase-space distributions in the spectrometers. It presents the first measurement of the emittance of momentum-selected muon ensembles in the upstream spectrometer.

2 Calculation of emittance

Emittance is a key parameter in assessing the overall performance of an accelerator [17]. The luminosity achieved by a collider is inversely proportional to the emittance of the colliding beams, and therefore beams with small emittance are required.

A beam travelling through a portion of an accelerator may be described as an ensemble of particles. Consider a beam that propagates in the positive z direction of a right-handed Cartesian coordinate system, (x, y, z). The position of the ith particle in the ensemble is $\mathbf{r}_i = (x_i, y_i)$ and its transverse momentum is $\mathbf{p}_{Ti} = (p_{xi}, p_{yi})$; $\mathbf{r}_i$ and $\mathbf{p}_{Ti}$ define the coordinates of the particle in transverse phase space. The normalised transverse emittance, ε_N, of the ensemble approximates the volume occupied by the particles in four-dimensional phase space and is given by

$$\varepsilon_N = \frac{1}{m_\mu} \sqrt[4]{\det \mathcal{C}}, \tag{1}$$

where m_μ is the rest mass of the muon, $\mathcal{C}$ is the four-dimensional covariance matrix,

$$\mathcal{C} = \begin{pmatrix} \sigma_{xx} & \sigma_{xp_x} & \sigma_{xy} & \sigma_{xp_y} \\ \sigma_{xp_x} & \sigma_{p_x p_x} & \sigma_{yp_x} & \sigma_{p_x p_y} \\ \sigma_{xy} & \sigma_{yp_x} & \sigma_{yy} & \sigma_{yp_y} \\ \sigma_{xp_y} & \sigma_{p_x p_y} & \sigma_{yp_y} & \sigma_{p_y p_y} \end{pmatrix}, \tag{2}$$

and $\sigma_{\alpha\beta}$, where $\alpha, \beta = x, y, p_x, p_y$, is given by

$$\sigma_{\alpha\beta} = \frac{1}{N-1} \left(\Sigma_i^N \alpha_i \beta_i - \frac{\left(\Sigma_i^N \alpha_i\right)\left(\Sigma_i^N \beta_i\right)}{N} \right), \tag{3}$$

and N is the number of muons in the ensemble.

The MICE experiment was operated such that muons passed through the experiment one at a time. The phase-space coordinates of each muon were measured. An ensemble of muons that was representative of the muon beam was assembled using the measured coordinates. The normalised transverse emittance of the ensemble was then calculated by evaluating the sums necessary to construct the covariance matrix, $\mathcal{C}$, and using Eq. 1.

3 The Muon Ionization Cooling Experiment

The muons for MICE came from the decay of pions produced by an internal target dipping directly into the circulating proton beam of the ISIS synchrotron at the Rutherford Appleton Laboratory (RAL) [18,19]. The burst of particles resulting from one target dip is referred to as a 'spill'. A transfer line of nine quadrupoles, two dipoles and a superconducting 'decay solenoid' selected a momentum bite and transported the beam into the experiment [20]. The small fraction of pions that remained in the beam were rejected during analysis using the time-of-flight hodoscopes, TOF0 and TOF1, and Cherenkov counters that were installed in the MICE Muon Beam line upstream of the cooling experiment [21,22]. A 'diffuser' was installed at the upstream end of the experiment to vary the initial emittance of the beam by introducing a changeable amount of tungsten and brass, which are high-Z materials, into the beam path [20].

A schematic diagram of the experiment is shown in Fig. 1. It contained an absorber/focus-coil module sandwiched between two spectrometer-solenoid modules that provided a uniform magnetic field for momentum measurement. The focus-coil module had two separate windings that were operated with the same, or opposed, polarities. A lithium-hydride or liquid-hydrogen absorber was placed at the centre of the focus-coil module. An iron Partial Return Yoke (PRY) was installed around the experiment to contain the field produced by the solenoidal spectrometers (not shown in Fig. 1). The PRY was installed at a distance from the beam axis such that its effect on the trajectories of particles travelling through the experiment was negligible.

The emittance was measured upstream and downstream of the absorber and focus-coil module using scintillating-fibre tracking detectors [26] immersed in the solenoidal field provided by three superconducting coils E1, C, and E2. The
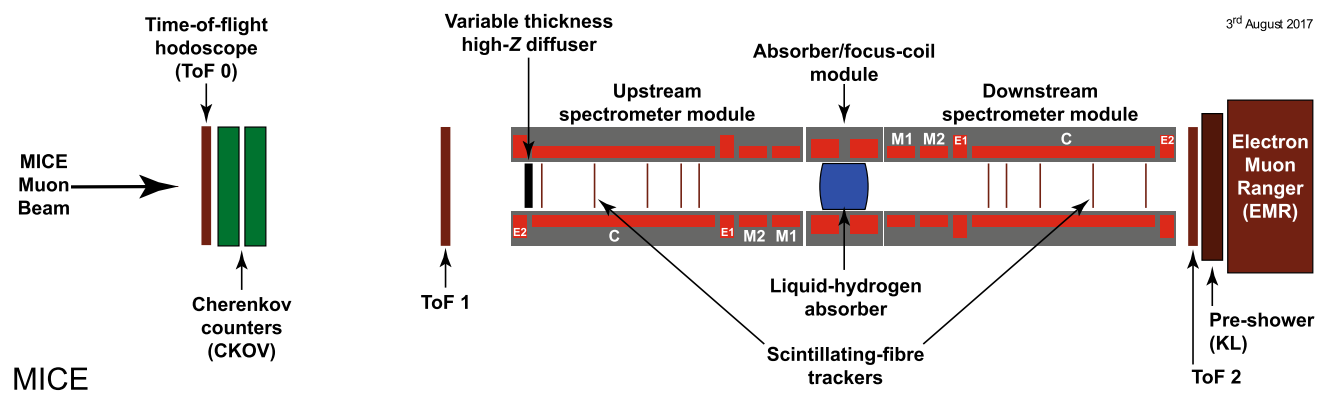
Fig. 1 Schematic diagram of the MICE experiment. The red rectangles represent the coils of the spectrometer solenoids and focus-coil module. The individual coils of the spectrometer solenoids are labelled E1, C, E2, M1 and M2. The various detectors (time-of-flight hodoscopes (TOF0, TOF1) [23,24], Cherenkov counters [25], scintillating-fibre trackers [26], KLOE-Light (KL) calorimeter [20,27], and Electron Muon Ranger (EMR) [28,29]) are also represented. The Partial Return Yoke (PRY) is not shown

Fig. 2 **a** Top and **b** side views of the MICE Muon Beam line, its instrumentation, and the experimental configuration. A titanium target dipped into the ISIS proton 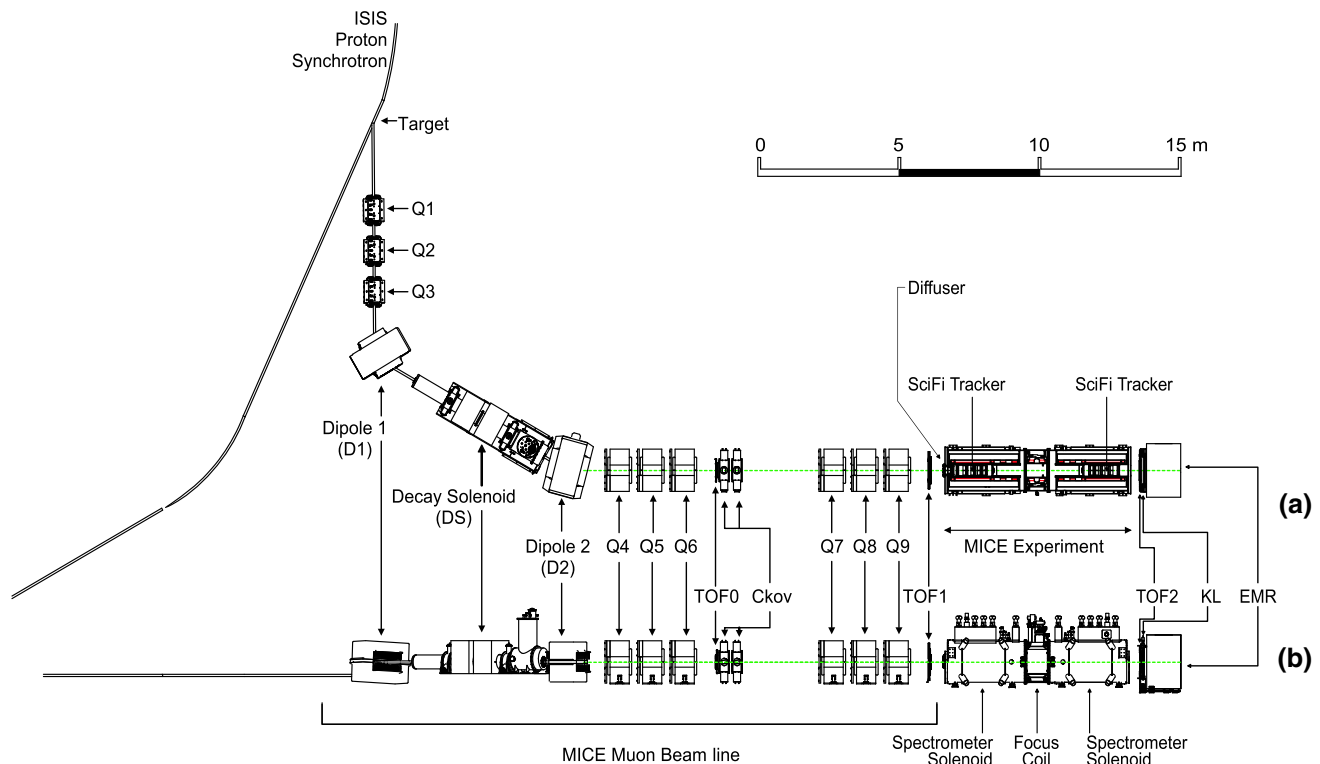synchrotron and the resultant spill of particles was captured with a quadrupole triplet (Q1–3) and transported through momentum-selecting dipoles (D1, D2). The quadrupole triplets (Q4–6, Q7–9) transported particles to the upstream spectrometer module. The time-of-flight of particles, measured between TOF0 and TOF1, was used for particle identification

trackers were used to reconstruct the trajectories of individual muons at the entrance and exit of the absorber. The trackers were each constructed from five planar stations of scintillating fibres, each with an active radius of 150 mm. The track parameters were reported at the nominal reference plane: the surface of the scintillating-fibre plane closest to the absorber [30]. Hall probes were installed on the tracker to measure the magnetic-field strength in situ. The instrumentation up- and downstream of the spectrometer modules was used to select a pure sample of muons. The reconstructed tracks of the selected muons were then used to measure the muon-beam emittance at the upstream and downstream tracker reference planes. The spectrometer-solenoid modules also contained two superconducting 'matching' coils (M1, M2) that were used to match the optics between the uniform-field region and the neighbouring focus-coil module. The MICE coordinate system is such that the z axis is coincident with the beam direction, the y axis points vertically upward, and the x axis completes a right-handed co-ordinate system. This paper discusses the measurement of emittance using only the tracker and beam-line instrumentation upstream of the absorber. The diffuser was fully retracted for the data presented here, i.e. no extra material was introduced into the centre of the beam line, so that the incident particle distribution could be assessed.

4 MICE Muon beam line

The MICE Muon Beam line is shown schematically in Fig. 2. It was capable of delivering beams with normalised transverse emittance in the range $3 \lesssim \varepsilon_N \lesssim 10$ mm and mean momentum in the range $140 \lesssim p_\mu \lesssim 240$ MeV/c with a root-mean-squared (RMS) momentum spread of $\sim$ 20 MeV/c [20] after the diffuser (Fig. 1).

Pions produced by the momentary insertion of a titanium target [18,19] into the ISIS proton beam were captured using a quadrupole triplet (Q1–3) and transported to a first dipole magnet (D1), which selected particles of a desired momentum bite into the 5 T decay solenoid (DS). Muons produced in pion decay in the DS were momentum-selected using a second dipole magnet (D2) and focused onto the diffuser by a quadrupole channel (Q4–6 and Q7–9). In positive-beam running, a borated polyethylene absorber of variable thickness was inserted into the beam just downstream of the decay solenoid to suppress the high rate of protons that were produced at the target [31].

The composition and momentum spectra of the beams delivered to MICE were determined by the interplay between the two bending magnets D1 and D2. In 'muon mode', D2 was set to half the current of D1, selecting backward-going

muons in the pion rest frame. This produced an almost pure muon beam.

Data were taken in October 2015 in muon mode at a nominal momentum of $200\,\mathrm{MeV}/c$, with ISIS in operation at 700 MeV. These data [32] are used here to characterise the properties of the beam accepted by the upstream solenoid with all diffuser irises withdrawn from the beam. The upstream E1-C-E2 coils in the spectrometer module were energised and produced a field of 4 T, effectively uniform across the tracking region, while all other coils were unpowered. Positively charged particles were selected due to their higher production rate in 700 MeV proton-nucleus collisions.

5 Simulation

Monte Carlo simulations were used to determine the accuracy of the kinematic reconstruction, to evaluate the efficiency of the response of the scintillating-fibre tracker, and to study systematic uncertainties. A sufficient number of events were generated to ensure that statistical uncertainties from the simulations were negligible in comparison to those of the data.

The beam impinging on TOF0 was modelled using G4beamline [33]. Particles were produced at the target using a parameterised particle-production model. These particles were tracked through the MICE Muon Beam line taking into account all material in and surrounding the beam line and using realistic models of the fields and apertures of the various magnets. The G4beamline simulation was tuned to reproduce the observed particle distributions at TOF0.

The MICE Analysis User Software (MAUS) [34] package was used to simulate the passage of particles from TOF0 through the remainder of the MICE Muon Beam line and through the solenoidal lattice. This simulation includes the response of the instrumentation and used the input distribution produced using G4beamline. MAUS was also used for offline reconstruction and to provide fast real-time detector reconstruction and data visualisation during MICE running. MAUS uses GEANT4 [35,36] for beam propagation and the simulation of detector response. ROOT [37] was used for data visualisation and for data storage. The particles generated were subjected to the same trigger requirements as the data and processed by the same reconstruction programs.

6 Beam selection

Data were buffered in the front-end electronics and read out at the end of each spill [20]. For the reconstructed data presented here, the digitisation of analogue signals received from the detectors was triggered by a coincidence of signals in the PMTs serving a single scintillator slab in TOF1. Any slab in TOF1 could generate a trigger.

The following cuts were used to select muons passing through the upstream tracker:

– *One reconstructed space-point in TOF0 and TOF1* Each TOF hodoscope was composed of two perpendicular planes of scintillator slabs arranged to measure the x and y coordinates. A space-point was formed from the intersection of hits in the x and y projections. Figure 3a, b show the hit multiplicity in TOF0 plotted against the hit multiplicity in TOF1 for reconstructed data and reconstructed Monte Carlo respectively. The sample is dominated by events with one space-point in both TOF0 and TOF1. This cut removes events in which two particles enter the experiment within the trigger window.

– *Relative time-of-flight between TOF0 and TOF1, t_{rel}, in the range $1 \leq t_{\mathrm{rel}} \leq 6\,ns$* The time of flight between TOF0 and TOF1, t_{01}, was measured relative to the mean positron time of flight, t_e. Figure 3c shows the relative time-of-flight distribution in data (black, circles) and simulation (filled histogram). All cuts other than the relative time-of-flight cut have been applied in this figure. The time-of-flight of particles relative to the mean positron time-of-flight is calculated as

$$t_{\mathrm{rel}} = t_{01} - (t_e + \delta t_e) \, ,$$

where δt_e accounts for the difference in transit time, or path length travelled, between electrons and muons in the field of the quadrupole triplets [21]. This cut removes electrons from the selected ensemble as well as a small number of pions. The data has a longer tail compared to the simulation, which is related to the imperfect simulation of the longitudinal momentum of particles in the beam (see Sect. 7.1).

– *A single track reconstructed in the upstream tracker with a track-fit χ^2 satisfying $\frac{\chi^2}{N_{\mathrm{DOF}}} \leq 4$* N_{DOF} is the number of degrees of freedom. The distribution of $\frac{\chi^2}{N_{\mathrm{DOF}}}$ is shown in Fig. 3d. This cut removes events with poorly reconstructed tracks. Multi-track events, in which more than one particle passes through the same pixel in TOF0 and TOF1 during the trigger window, are rare and are also removed by this cut. The distribution of $\frac{\chi^2}{N_{\mathrm{DOF}}}$ is broader and peaked at slightly larger values in the data than in the simulation.

– *Track contained within the fiducial volume of the tracker* The radius of the track measured by the tracker, R_{track}, is required to satisfy $R_{\mathrm{track}} < 150\,\mathrm{mm}$ to ensure the track does not leave and then re-enter the fiducial volume. The track radius is evaluated at 1 mm intervals between the stations. If the track radius exceeds 150 mm at any of these positions, the event is rejected.
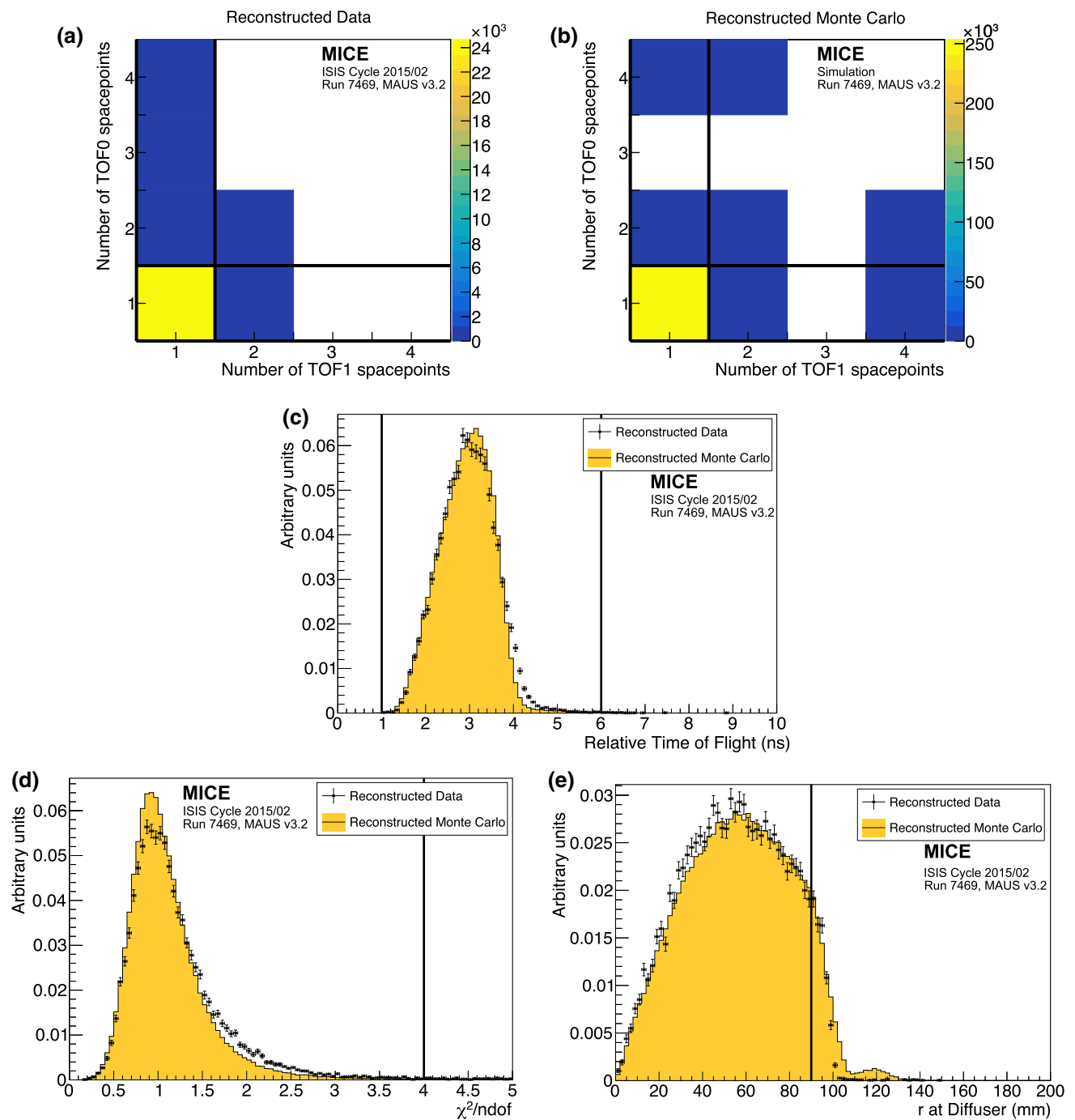
Fig. 3 Distribution of the quantities that were used to select the sample used to reconstruct the emittance of the beam: **a** the number of space-points in TOF0 plotted against the number of space-points in TOF1 for reconstructed data, and **b** reconstructed simulation; **c** distribution of the relative time-of-flight, t_{rel}; **d** distribution of $\frac{\chi^2}{N_{\mathrm{DOF}}}$; and **e** distribution of R_{diff}. The 1D distributions show reconstructed data as solid (black) circles and reconstructed MAUS simulation as the solid (yellow) histogram. The solid (black) lines indicate the position of the cuts made on these quantities. Events enter these plots if all cuts other than the cut under examination are passed

– *Extrapolated track radius at the diffuser, $R_{\mathrm{diff}} \leq 90\,mm$* Muons that pass through the annulus of the diffuser, which includes the retracted irises, lose a substantial amount of energy. Such muons may re-enter the track-

ing volume and be reconstructed but have properties that are no longer characteristic of the incident muon beam. The aperture radius of the diffuser mechanism (100 mm) defines the transverse acceptance of the beam injected
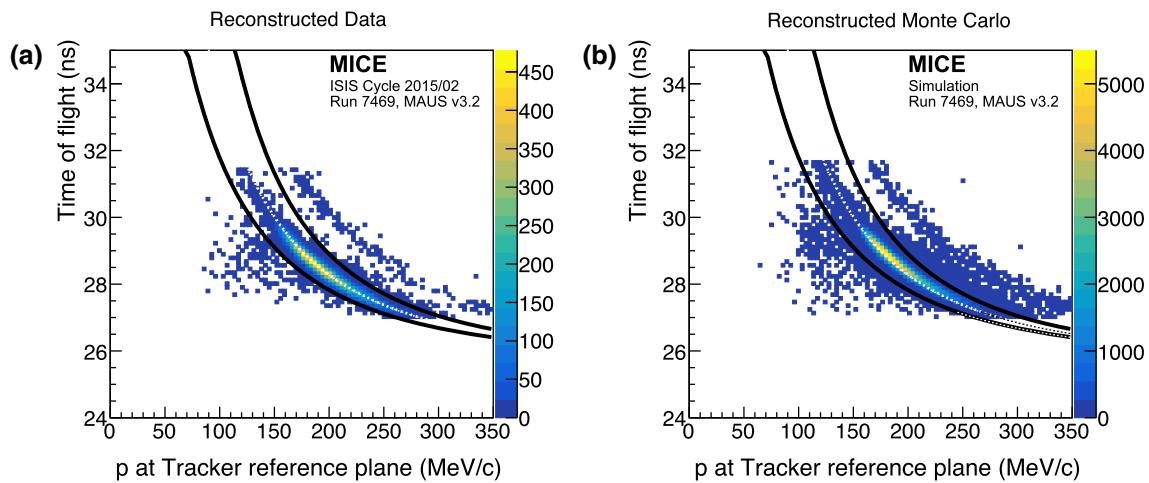
Fig. 4 Time of flight between TOF0 and TOF1 (t_{01}) plotted as a function of the muon momentum, p, measured in the upstream tracker. All cuts other than the muon hypothesis have been applied. Particles within the black lines are selected. The white dotted line is the trajectory of a muon that loses the most probable momentum (20 MeV/c) between TOF1 and the tracker in **a** reconstructed data, and **b** reconstructed Monte Carlo

Table 1 The number of particles that pass each selection criterion. A total of 24,660 particles pass all of the cuts

Cut	No. surviving particles	Cumulative surviving particles
None	53 276	53 276
One space-point in TOF0 and TOF1	37 619	37 619
Relative time of flight in range 1–6 ns	37 093	36 658
Single reconstructed track with $\frac{\chi^2}{N_{\mathrm{DOF}}} \leq 4$	40 110	30 132
Track within fiducial volume of tracker	52 039	29 714
Extrapolated track radius at diffuser $\leq$ 90 mm	42 592	25 310
Muon hypothesis	34 121	24 660
All	24 660	24 660

into the experiment. Back-extrapolation of tracks to the exit of the diffuser yields a measurement of R_{diff} with a resolution of $\sigma_{R_{\mathrm{diff}}} = 1.7$ mm. Figure 3e shows the distribution of R_{diff}, where the difference between data and simulation lies above the accepted radius. These differences are due to approximations in modelling the outer material of the diffuser. The cut on R_{diff} accepts particles that passed at least $5.9\sigma_{R_{\mathrm{diff}}}$ inside the aperture limit of the diffuser.

– *Particle consistent with muon hypothesis* Figure 4 shows t_{01}, the time-of-flight between TOF0 and TOF1, plotted as a function of p, the momentum reconstructed by the upstream tracking detector. Momentum is lost between TOF1 and the reference plane of the tracker in the material of the detectors. A muon that loses the most probable momentum, $\Delta p \simeq 20$ MeV/c, is shown as the dotted (white) line. Particles that are poorly reconstructed, or have passed through support material upstream of the tracker and have lost significant momentum, are excluded by the lower bound. The population of events above the upper bound are ascribed to the passage of pions, or mis-reconstructed muons, and are also removed from the analysis.

A total of 24,660 events pass the cuts listed above. Table 1 shows the number of particles that survive each individual cut. Data distributions are compared to the distributions obtained using the MAUS simulation in Figs. 3 and 4. Despite minor disagreements, the agreement between the simulation and data is sufficiently good to give confidence that a clean sample of muons has been selected.

The expected pion contamination of the unselected ensemble of particles has been measured to be $\leq 0.4\%$[22]. Table 2 shows the number of positrons, muons, and pions in the MAUS simulation that pass all selection criteria. The criteria used to select the muon sample for the analysis presented here efficiently reject electrons and pions from the Monte Carlo sample.

Table 2 The number of reconstructed electrons, muons, and pions at the upstream tracker that survive each cut in the Monte Carlo simulation. Application of all cuts removes almost all positrons and pions in the reconstructed Monte Carlo sample. In the Monte Carlo simulation, a total of 253,504 particles pass all of the cuts described in the text

Cut	e	μ	π	Total
None	14, 912	432,294	1610	463,451
One space-point in TOF0 and TOF1	11, 222	353,613	1213	376,528
Relative Time of flight in range 1–6 ns	757	369,337	1217	379,761
Single reconstructed track with $\frac{\chi^2}{N_{\mathrm{DOF}}} \leq 4$	10, 519	407,276	1380	419,208
Track within fiducial volume of tracker	14, 527	412,857	1427	443,431
Tracked radius at diffuser $\leq$ 90 mm	11, 753	311,076	856	334,216
Muon hypothesis (above lower limit)	3225	362,606	411	367,340
Muon hypothesis (below upper limit)	12, 464	411,283	379	424,203
Muon hypothesis (overall)	2724	358,427	371	361,576
All	22	253,475	5	253,504

7 Results

7.1 Phase-space projections

The distributions of $x, y, p_x, p_y, p_z,$ and $p = \sqrt{p_x^2 + p_y^2 + p_z^2}$ are shown in Fig. 5. The total momentum of the muons that make up the beam lie within the range $140 \lesssim |p| \lesssim 260$ MeV/c. The results of the MAUS simulation, which are also shown in Fig. 5, give a reasonable description of the data. In the case of the longitudinal component of momentum, p_z, the data are peaked to slightly larger values than the simulation. The difference is small and is reflected in the distribution of the total momentum, p. As the simulation began with particle production from the titanium target, any difference between the simulated and observed particle distributions would be apparent in the measured longitudinal and total momentum distributions. The scale of the observed disagreement is small, and as such the simulation adequately describes the experiment. The distributions of the components of the transverse phase space (x, p_x, y, p_y) are well described by the simulation. Normalised transverse emittance is calculated with respect to the means of the distributions (Eq. 2), and so is unaffected by this discrepancy.

The phase space occupied by the selected beam is shown in Fig. 6. The distributions are plotted at the reference surface of the upstream tracker. The beam is moderately well centred in the (x, y) plane. Correlations are apparent that couple the position and momentum components in the transverse plane. The transverse position and momentum coordinates are also seen to be correlated with total momentum. The correlation in the (x, p_y) and (y, p_x) plane is due to the solenoidal field, and is of the expected order. The dispersion and chromaticity of the beam are discussed further in Sect. 7.2.

7.2 Effect of dispersion, chromaticity, and binning in longitudinal momentum

Momentum selection at D2 introduces a correlation, dispersion, between the position and momentum of particles. Figure 7 shows the transverse position and momentum with respect to the total momentum, p, as measured at the upstream-tracker reference plane. Correlations exist between all four transverse phase-space co-ordinates and the total momentum.

Emittance is calculated in 10 MeV/c bins of total momentum in the range $185 \leq p \leq 255$ MeV/c. This bin size was chosen as it is commensurate with the detector resolution. Calculating the emittance in momentum increments makes the effect of the optical mismatch, or chromaticity, small compared to the statistical uncertainty. The range of $185 \leq p \leq 255$ MeV/c was chosen to maximise the number of particles in each bin that are not scraped by the aperture of the diffuser.

7.3 Uncertainties on emittance measurement

7.3.1 Statistical uncertainties

The statistical uncertainty on the emittance in each momentum bin is calculated as $\sigma_\varepsilon = \frac{\varepsilon}{\sqrt{2N}}$ [38–40], where ε is the emittance of the ensemble of muons in the specified momentum range and N is the number of muons in that ensemble. The number of events per bin varies from ~ 4000 for $p \sim 190$ MeV/c to ~ 700 for $p \sim 250$ MeV/c.

7.4 Systematic uncertainties

7.4.1 Uncorrelated systematic uncertainties

Systematic uncertainties related to the beam selection were estimated by varying the cut values by an amount correspond-
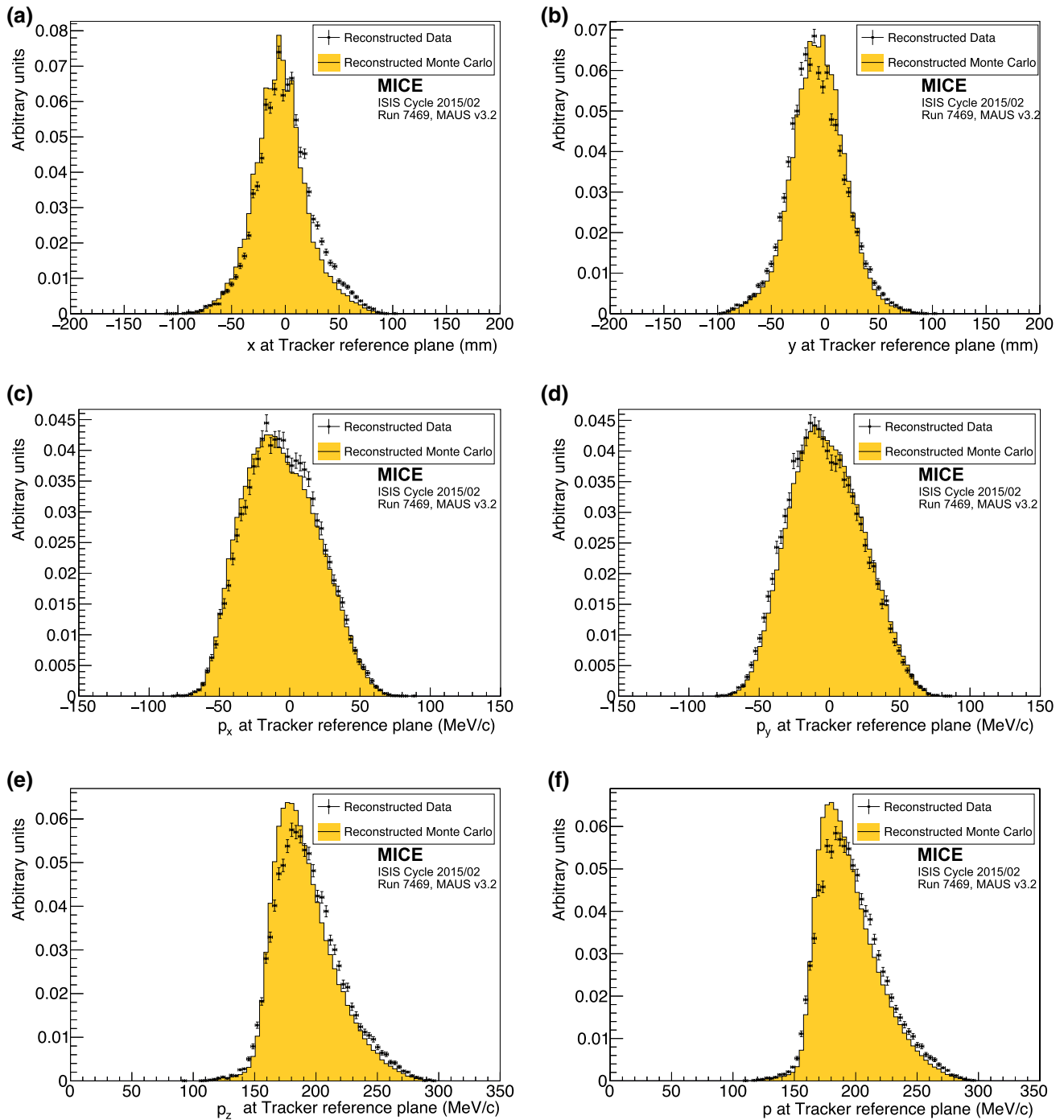
Fig. 5 Position and momentum distributions of muons reconstructed at the reference surface of the upstream tracker: **a** x, **b** y, **c** p_x, **d** p_y, **e** p_z, and **f** p, the total momentum. The data are shown as the solid circles while the results of the MAUS simulation are shown as the yellow histogram

ing to the RMS resolution of the quantity in question. The emittance of the ensembles selected with the changed cut values were calculated and compared to the emittance calculated using the nominal cut values and the difference taken as the uncertainty due to changing the cut boundaries. The overall uncertainty due to beam selection is summarised in Table 3. The dominant beam-selection uncertainty is in the

selection of particles that successfully pass within the inner 90 mm of the diffuser aperture.

Systematic uncertainties related to possible biases in calibration constants were evaluated by varying each calibration constant by its resolution. Systematic uncertainties related to the reconstruction algorithms were evaluated using the MAUS simulation. The positive and negative deviations
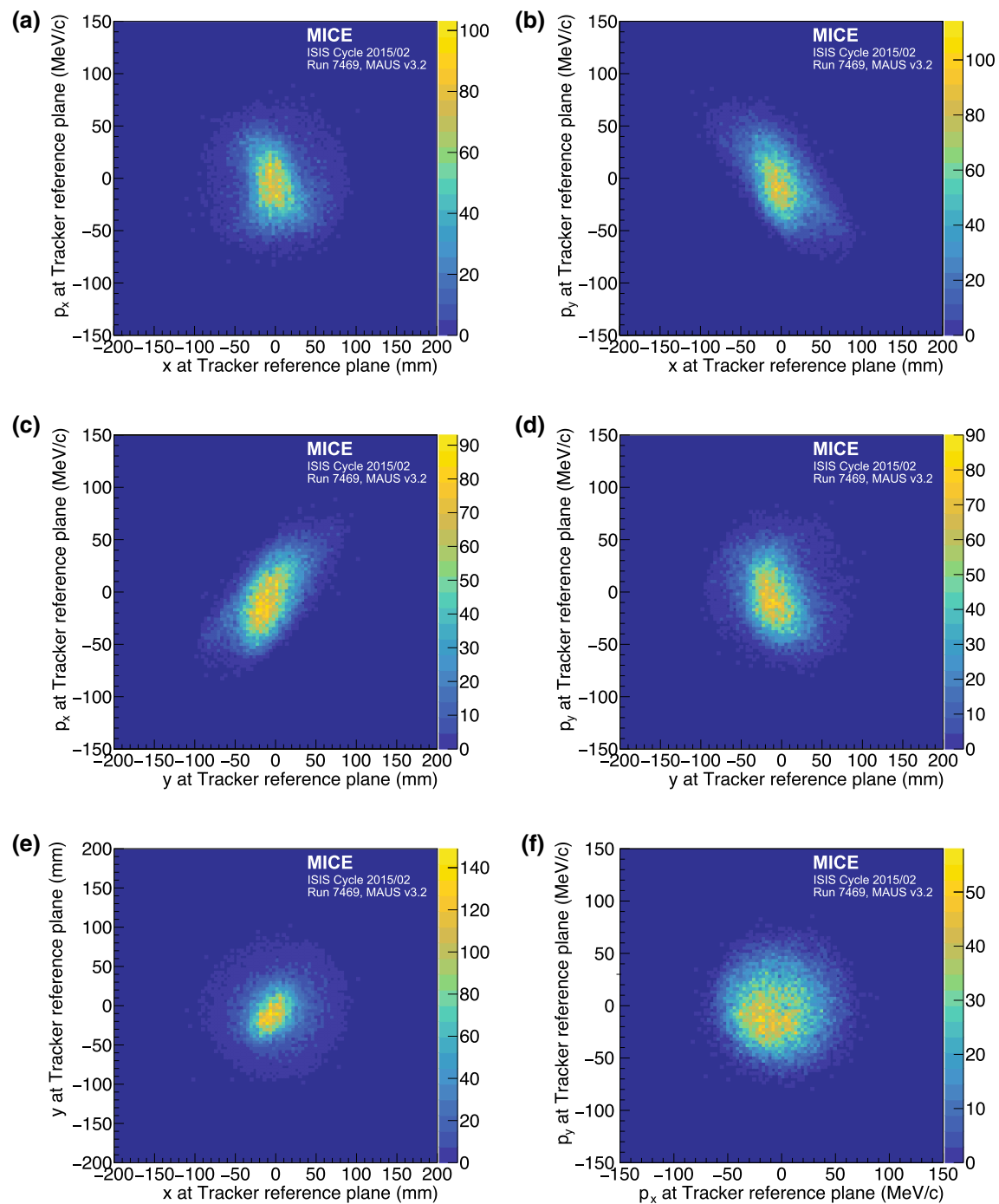
Fig. 6 Transverse phase space occupied by selected muons transported through the MICE Muon Beam line to the reference plane of the upstream tracker. **a** (x, p_x), **b** (x, p_y). **c** (y, p_x), **d** (y, p_y). **e** (x, y), and **f** (p_x, p_y)

from the nominal emittance were added in quadrature separately to obtain the total positive and negative systematic uncertainty. Sources of correlated uncertainties are discussed below.

7.4.2 Correlated systematic uncertainties

Some systematic uncertainties are correlated with the total momentum, p. For example, the measured value of p dictates the momentum bin to which a muon is assigned for the emittance calculation. The uncertainty on the emittance reconstructed in each bin has been evaluated by allowing the
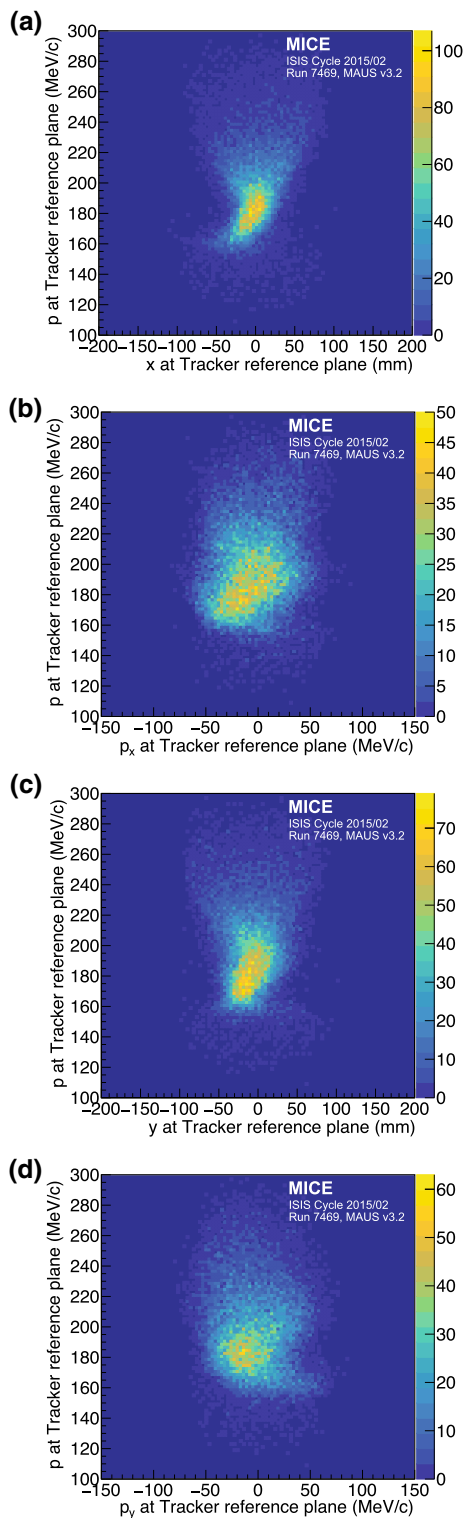
Fig. 7 The effect of dispersion, the dependence of the components of transverse phase space on the momentum, p, is shown at the reference surface of the upstream tracker: **a)** (x, p); **b** (p_x, p); **c** (y, p); **d** (p_y, p)

momentum of each muon to fluctuate around its measured value according to a Gaussian distribution of width equal to

the measurement uncertainty on p. In Table 3 this uncertainty is listed as 'Binning in p'.

A second uncertainty that is correlated with total momentum is the uncertainty on the reconstructed x, p_x, y, and p_y. The effect on the emittance was evaluated with the same procedure used to evaluate the uncertainty due to binning in total momentum. This is listed as 'Tracker resolution' in Table 3.

Systematic uncertainties correlated with p are primarily due to the differences between the model of the apparatus used in the reconstruction and the hardware actually used in the experiment. The most significant contribution arises from the magnetic field within the tracking volume. Particle tracks are reconstructed assuming a uniform solenoidal field, with no fringe-field effects. Small non-uniformities in the magnetic field in the tracking volume will result in a disagreement between the true parameters and the reconstructed values. To quantify this effect, six field models (one optimal and five additional models) were used to estimate the deviation in reconstructed emittance from the true value under realistic conditions. Three families of field model were investigated, corresponding to the three key field descriptors: field scale, field alignment, and field uniformity. The values of these descriptors that best describe the Hall-probe measurements were used to define the optimal model and the uncertainty in the descriptor values were used to determine the 1σ variations.

7.4.3 Field scale

Hall-probes located on the tracker provided measurements of the magnetic field strength within the tracking volume at known positions. An optimal field model was produced with a scale factor of 0.49% that reproduced the Hall-probe measurements. Two additional field models were produced which used scale factors that were one standard deviation, $\pm 0.03\%$, above and below the nominal value.

7.4.4 Field alignment

A field-alignment algorithm was developed based on the determination of the orientation of the field with respect to the mechanical axis of the tracker using coaxial tracks with $p_T \approx 0$ [41]. The field was rotated with respect to the tracker by 1.4 ± 0.1 mrad about the x axis and 0.3 ± 0.1 mrad about the y axis. The optimal field model was created such that the simulated alignment is in agreement with the measurements. Two additional models that vary the alignment by one standard deviation were also produced.

7.4.5 Field uniformity

A COMSOL [42] model of the field was used to generate the optimal model which includes the field generated by each coil

Table 3 Emittance together with the statistical and systematic uncertainties and biases as a function of mean total momentum, $\langle p \rangle$

| Source	$\langle p \rangle$ (MeV/c)						
	190	200	210	220	230	240	250
Measured emittance (mm rad)	3.40	3.65	3.69	3.65	3.69	3.62	3.31
Statistical uncertainty	$\pm 3.8 \times 10^{-2}$	$\pm 4.4 \times 10^{-2}$	$\pm 5.0 \times 10^{-2}$	$\pm 5.8 \times 10^{-2}$	$\pm 7.0 \times 10^{-2}$	$\pm 8.4 \times 10^{-2}$	$\pm 9.2 \times 10^{-2}$
Beam selection:							
Diffuser aperture	4.9×10^{-2}	5.3×10^{-2}	4.9×10^{-2}	4.7×10^{-2}	4.2×10^{-2}	11.0×10^{-2}	4.4×10^{-2}
	-3.5×10^{-2}	-5.1×10^{-2}	-5.7×10^{-2}	-5.0×10^{-2}	-3.5×10^{-2}	-5.0×10^{-2}	-9.6×10^{-2}
$\frac{\chi^2}{N_{\mathrm{DOF}}} \leq 4$	5.1×10^{-3}	2.0×10^{-3}	1.0×10^{-2}	4.1×10^{-3}	1.2×10^{-3}	5.5×10^{-3}	7.9×10^{-3}
	-4.8×10^{-3}	-1.3×10^{-3}	-1.8×10^{-3}	-3.3×10^{-3}	-2.8×10^{-4}	-6.5×10^{-3}	-4.7×10^{-4}
Muon hypothesis	4.5×10^{-3}	2.2×10^{-4}	6.4×10^{-3}	3.1×10^{-3}	1.4×10^{-3}	2.6×10^{-3}	1.3×10^{-3}
	-3.2×10^{-3}	-6.8×10^{-3}	-8.8×10^{-4}	-4.7×10^{-3}	-1.1×10^{-2}	-6.7×10^{-2}	-4.1×10^{-3}
Beam selection (Overall)	4.9×10^{-2}	5.3×10^{-2}	5.0×10^{-2}	4.7×10^{-2}	4.2×10^{-2}	1.1×10^{-1}	4.5×10^{-2}
	-3.6×10^{-2}	-5.2×10^{-2}	-5.8×10^{-2}	-5.0×10^{-2}	-3.9×10^{-2}	-8.4×10^{-2}	-9.6×10^{-2}
Binning in p	$\pm 1.8 \times 10^{-2}$	$\pm 2.1 \times 10^{-2}$	$\pm 2.3 \times 10^{-2}$	$\pm 2.9 \times 10^{-2}$	$\pm 3.5 \times 10^{-2}$	$\pm 4.3 \times 10^{-2}$	$\pm 5.2 \times 10^{-2}$
Magnetic field misalignment and scale:							
Bias	-1.3×10^{-2}	-1.4×10^{-2}	-1.5×10^{-2}	-1.6×10^{-2}	-1.6×10^{-2}	-1.7×10^{-2}	-1.6×10^{-2}
Uncertainty	$\pm 2.0 \times 10^{-4}$	$\pm 2.9 \times 10^{-4}$	$\pm 8.0 \times 10^{-4}$	$\pm 4.8 \times 10^{-4}$	$\pm 5.5 \times 10^{-4}$	$\pm 4.8 \times 10^{-4}$	$\pm 4.9 \times 10^{-4}$
Tracker resolution	$\pm 1.6 \times 10^{-3}$	$\pm 2.1 \times 10^{-3}$	$\pm 2.8 \times 10^{-3}$	$\pm 3.8 \times 10^{-3}$	$\pm 5.3 \times 10^{-3}$	$\pm 7.0 \times 10^{-3}$	$\pm 9.5 \times 10^{-3}$
Total systematic uncertainty	5.2×10^{-2}	5.7×10^{-2}	5.5×10^{-2}	5.6×10^{-2}	5.5×10^{-2}	11.7×10^{-2}	6.9×10^{-2}
	-4.0×10^{-2}	-5.6×10^{-2}	-6.2×10^{-2}	-5.8×10^{-2}	-5.2×10^{-2}	-9.5×10^{-2}	-11.0×10^{-2}
Corrected emittance (mm rad)	3.41	3.66	3.71	3.67	3.71	3.65	3.34
Total uncertainty	± 0.06	± 0.07	$+0.07$	± 0.08	± 0.09	$+0.14$	$+0.12$
			-0.08			-0.13	-0.14
Total uncertainty (%)	$+1.90$	$+1.96$	$+2.01$	$+2.19$	$+2.40$	$+3.97$	$+3.47$
	-1.63	-1.94	-2.15	-2.34	-2.37	-3.49	-4.30
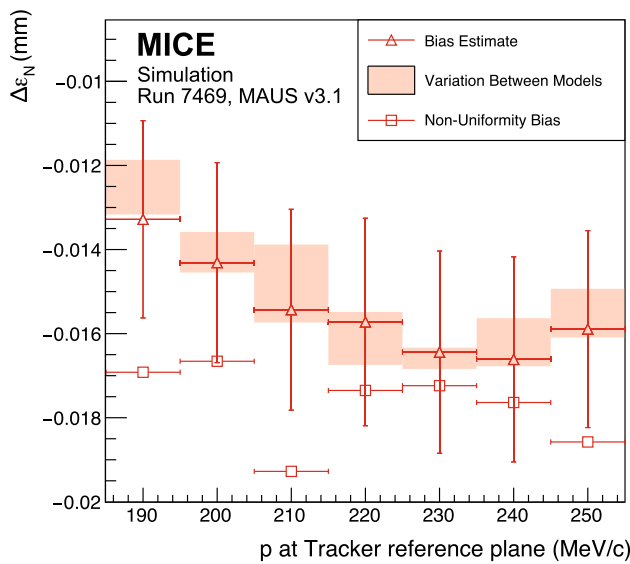
Fig. 8 The systematic bias and uncertainty on the reconstructed emittance under different magnetic field model assumptions. The bias estimate (open triangles) includes the non-uniformity bias (open squares). The variation between the models (see text) is indicated by the shaded bands

using the 'as-built' parameters and the partial return yoke. A simple field model was created using only the individual coil geometries to provide additional information on the effect of field uniformity on the reconstruction. The values for the simple field model were normalised to the Hall-probe measurements as for the other field models. This represents a significant deviation from the COMSOL model, but demonstrates the stability of the reconstruction with respect to changes in field uniformity, as the variation in emittance between all field models is small (less than 0.002 mm).

For each of the 5 field models, multiple 2000-muon ensembles were generated for each momentum bin. The deviation of the calculated emittance from the true emittance was found for each ensemble. The distribution of the difference between the ensemble emittance and the true emittance was assumed to be Gaussian with mean ε and variance $s^2 = \sigma^2 + \theta^2$, where σ is the statistical uncertainty and θ is an additional systematic uncertainty. The systematic bias for each momentum bin was then calculated as [43]

$$\Delta\varepsilon_N = \langle\varepsilon\rangle - \varepsilon_{\text{true}} \, , \tag{4}$$

where $\varepsilon_{\text{true}}$ is the true beam emittance in that momentum bin and $\langle\varepsilon\rangle$ is the mean emittance from the N ensembles. The systematic uncertainty was calculated assuming that the distribution of residuals of ε_i from the mean, $\langle\varepsilon\rangle$, satisfies a χ^2 distribution with $N-1$ degrees of freedom,

$$\chi^2_{N-1} = \sum_i^N \frac{(\varepsilon_i - \langle\varepsilon\rangle)^2}{\sigma^2 + \theta^2} \, , \tag{5}$$
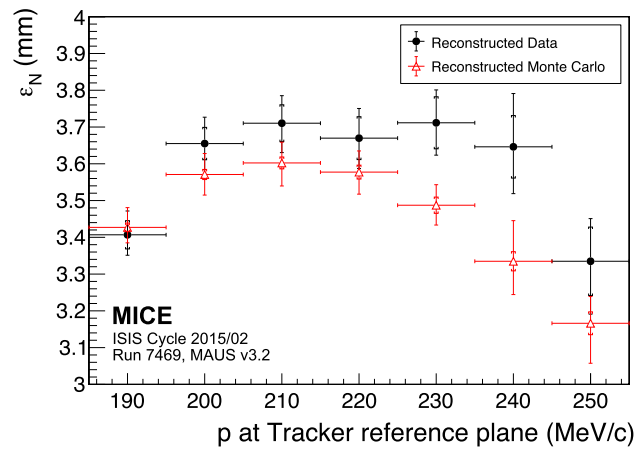

Fig. 9 Normalised transverse emittance as a function of total momentum, p, for data (black, filled circle) and reconstructed Monte Carlo (red, open triangle). The inner error bars show the statistical uncertainty. The outer error bars show the quadratic sum of the statistical and systematic uncertainties

and θ was estimated by minimising the expression ($\chi^2_{N-1} - (N-1))^2$ [43].

The uncertainty, θ, was consistent with zero in all momentum bins, whereas the bias, $\Delta\varepsilon_N$, was found to be momentum dependent as shown in Fig. 8. The bias was estimated from the mean difference between the reconstructed and true emittance values using the optimal field model. The variation in the bias was calculated from the range of values reconstructed for each of the additional field models. The model representing the effects of non-uniformities in the field was considered separately due to the significance of the deviation from the optimal model.

The results show a consistent systematic bias in the reconstructed emittance of ≈ -0.015 mm that is a function of momentum (see Table 3). The absolute variation in the mean values between the models that were used was smaller than the expected statistical fluctuations, demonstrating the stability of the reconstruction across the expected variations in field alignment and scale. The effect of the non-uniformity model was larger but still demonstrates consistent reconstruction. The biases calculated from the optimal field model were used to correct the emittance values in the final calculation (Sect. 7.5).

7.5 Emittance

The normalised transverse emittance as a function of p is shown in Fig. 9. The emittance has been corrected for the systematic bias shown in Table 3. The uncertainties plotted are those summarised in Table 3, where the inner bars represent the statistical uncertainty and outer bars the total uncertainty. The emittance of the measured muon ensembles (black, filled circle) is approximately flat in the range

$195 \leq p \leq 245\,\mathrm{MeV}/c$, corresponding to the design momentum of the experiment. The mean emittance in this region is $\approx 3.7\,\mathrm{mm}$. The emittance of the reconstructed Monte Carlo is consistently lower than that of the data, and therefore gives only an approximate simulation of the beam.

8 Conclusions

A first particle-by-particle measurement of the emittance of the MICE Muon Beam was made using the upstream scintillating-fibre tracking detector in a 4 T solenoidal field. A total of 24,660 muons survive the selection criteria. The position and momentum of these muons were measured at the reference plane of the upstream tracking detector. The muon sample was divided into 10 MeV/c bins of total momentum, p, from 185–255 MeV/c to account for dispersion, chromaticity, and scraping in apertures upstream of the tracking detector. The emittance of the measured muon ensembles is approximately flat from $195 \leq p \leq 245\,\mathrm{MeV}/c$ with a mean value of $\approx 3.7\,\mathrm{mm}$ across this region.

The total uncertainty on this measurement ranged from $^{+1.9}_{-1.6}\%$ to $^{+3.5}_{-4.3}\%$, increasing with total momentum, p. As p increases, the number of muons in the reported ensemble decreases, increasing the statistical uncertainty. At the extremes of the momentum range, a larger proportion of the input beam distribution is scraped on the aperture of the diffuser. This contributes to an increase in systematic uncertainty at the limits of the reported momentum range. The systematic uncertainty introduced by the diffuser aperture highlights the need to study ensembles where the total momentum, p, is close to the design momentum of the beam line. The total systematic uncertainty on the measured emittance is larger than that on a future measurement of the ratio of emittance before and after an absorber. The measurement is sufficiently precise to demonstrate muon ionization cooling.

The technique presented here represents the first precise measurement of normalised transverse emittance on a particle-by-particle basis. This technique will be applied to muon ensembles up- and downstream of a low-Z absorber, such as liquid hydrogen or lithium hydride, to measure emittance change across the absorber and thereby to study ionization cooling.

Data Availability Statement This manuscript has associated data in a data repository. [Authors' comment: The data that support the findings of this study are publicly available on the GridPP computing Grid via the data DOIs (the MICE unprocessed data: 10.17633/rd.brunel.3179644; the MICE reconstructed data: 10.17633/rd.brunel.5955850). Publications using the MICE data must contain the following statement: "We gratefully acknowledge the MICE collaboration for allowing us access to their data. Third-party results are not endorsed by the MICE collaboration and the MICE collaboration does not accept responsibility for any errors in the third-party's understanding of the MICE data."]

References

1. S. Geer, Phys. Rev. D **57**, 6989 (1998). https://doi.org/10.1103/PhysRevD.57.6989
2. M. Apollonio, et al., Oscillation physics with a neutrino factory (2002). arXiv:hep-ph/0210192
3. D.V. Neuffer, R.B. Palmer, Conf. Proc. C **940627**, 52 (1995)
4. R.B. Palmer, Rev. Accel. Sci. Tech. **7**, 137 (2014). https://doi.org/10.1142/S1793626814300072
5. M. Boscolo, M. Antonelli, O.R. Blanco-Garcia, S. Guiducci, S. Liuzzo, P. Raimondi, F. Collamati, Low emittance muon accelerator studies with production from positrons on target (2018). https://doi.org/10.1103/PhysRevAccelBeams.21.061005. arXiv:1803.06696 [physics.acc-ph]
6. S.Y. Lee, *Accelerator Physics*, 3rd edn. (World Scientific Publishing Co, Singapore, 2012). https://doi.org/10.1142/8335
7. S. Schröder, R. Klein, N. Boos, M. Gerhard, R. Grieser, G. Huber, A. Karafillidis, M. Krieg, N. Schmidt, T. Kühl, R. Neumann, V. Balykin, M. Grieser, D. Habs, E. Jaeschke, D. Krämer, M. Kristensen, M. Music, W. Petrich, D. Schwalm, P. Sigray, M. Steck, B. Wanner, A. Wolf, Phys. Rev. Lett. **64**, 2901 (1990). https://doi.org/10.1103/PhysRevLett.64.2901
8. J.S. Hangst, M. Kristensen, J.S. Nielsen, O. Poulsen, J.P. Schiffer, P. Shi, Phys. Rev. Lett. **67**, 1238 (1991). https://doi.org/10.1103/PhysRevLett.67.1238
9. P.J. Channell, J. Appl. Phys. **52**(6), 3791 (1981). https://doi.org/10.1063/1.329218
10. J. Marriner, Nucl. Instrum. Methods A **532**, 11 (2004). https://doi.org/10.1016/j.nima.2004.06.025
11. V.V. Parkhomchuk, A.N. Skrinsky, Physics-Uspekhi **43**(5), 433 (2000)
12. A.N. Skrinsky, V.V. Parkhomchuk, Sov. J. Part. Nucl. **12**, 223 (1981) [**Fiz. Elem. Chast. Atom. Yadra 12,557 (1981)**]
13. D. Neuffer, Conf. Proc. C **830811**, 481 (1983)
14. D. Neuffer, Part. Accel. **14**, 75 (1983)
15. The MICE collaboration, International MUON Ionization Cooling Experiment. http://mice.iit.edu. Accessed 4 Mar 2019
16. M. Apollonio et al., JINST **4**, P07001 (2009). https://doi.org/10.1088/1748-0221/4/07/P07001
17. J.B. Rosenzweig, *Fundamentals of Beam Physics* (Oxford University Press, Oxford, 2003)

18. C.N. Booth et al., JINST **8**, P03006 (2013). https://doi.org/10.1088/1748-0221/8/03/P03006
19. C.N. Booth et al., JINST **11**(05), P05006 (2016). https://doi.org/10.1088/1748-0221/11/05/P05006
20. M. Bogomilov et al., JINST **7**, P05009 (2012). https://doi.org/10.1088/1748-0221/7/05/P05009
21. D. Adams et al., Eur. Phys. J. C **73**(10), 2582 (2013). https://doi.org/10.1140/epjc/s10052-013-2582-8
22. M. Bogomilov et al., JINST **11**(03), P03001 (2016). https://doi.org/10.1088/1748-0221/11/03/P03001
23. R. Bertoni, Nucl. Instrum. Methods A **615**, 14 (2010). https://doi.org/10.1016/j.nima.2009.12.065
24. R. Bertoni, M. Bonesini, A. de Bari, G. Cecchet, Y. Karadzhov, R. Mazza, The construction of the MICE TOF2 detector (2010). http://mice.iit.edu/micenotes/public/pdf/MICE0286/MICE0286.pdf. Accessed 4 Mar 2019
25. L. Cremaldi, D.A. Sanders, P. Sonnek, D.J. Summers, J. Reidy Jr., I.E.E.E. Trans, Nucl. Sci. **56**, 1475 (2009). https://doi.org/10.1109/TNS.2009.2021266
26. M. Ellis, Nucl. Instrum. Methods A **659**, 136 (2011). https://doi.org/10.1016/j.nima.2011.04.041
27. F. Ambrosino, Nucl. Instrum. Methods A **598**, 239 (2009). https://doi.org/10.1016/j.nima.2008.08.097
28. R. Asfandiyarov et al., JINST **11**(10), T10007 (2016). https://doi.org/10.1088/1748-0221/11/10/T10007
29. D. Adams et al., JINST **10**(12), P12012 (2015). https://doi.org/10.1088/1748-0221/10/12/P12012
30. A. Dobbs, C. Hunt, K. Long, E. Santos, M.A. Uchida, P. Kyberd, C. Heidt, S. Blot, E. Overton, JINST **11**(12), T12001 (2016). https://doi.org/10.1088/1748-0221/11/12/T12001
31. S. Blot, *Proceedings 2nd International Particle Accelerator Conference (IPAC 11) 4–9 September 2011* (San Sebastian, 2011) https://accelconf.web.cern.ch/accelconf/IPAC2011/papers/mopz034.pdf. Accessed 4 Mar 2019
32. The MICE Collaboration, The MICE RAW Data. https://doi.org/10.17633/rd.brunel.3179644 (**MICE/Step4/07000/07469.tar**)
33. T. Roberts, et al., G4beamline; a "Swiss Army Knife" for Geant4, optimized for simulating beamlines. http://public.muonsinc.com/Projects/G4beamline.aspx. Accessed 17 Sept 2018
34. D. Rajaram, C. Rogers, The mice offline computing capabilities (2014). http://mice.iit.edu/micenotes/public/pdf/MICE0439/MICE0439.pdf (**MICE Note 439**)
35. S. Agostinelli, Nucl. Instrum. Methods Phys. Res. A **506**, 250 (2003)
36. J. Allison et al., IEEE Trans. Nucl. Sci. **53**, 270 (2006). https://doi.org/10.1109/TNS.2006.869826
37. R. Brun, F. Rademakers, Nucl. Instrum. Methods A **389**, 81 (1997). https://doi.org/10.1016/S0168-9002(97)00048-X
38. J. Cobb, Statistical errors on emittance measurements (2009). http://mice.iit.edu/micenotes/public/pdf/MICE341/MICE268.pdf. Accessed 4 Mar 2019
39. J. Cobb, Statistical errors on emittance and optical functions (2011). http://mice.iit.edu/micenotes/public/pdf/MICE341/MICE341.pdf. Accessed 4 Mar 2019
40. J.H. Cobb, Statistical Errors on Emittance (2015, Private communication)
41. C. Hunt, Private communication Publication-in-progress
42. COMSOL Multiphysics software Webpage: https://www.comsol.com. Accessed 4 Mar 2019
43. L. Lyons, J. Phys. A Math. Gen. **25**(7), 1967 (1992). http://stacks.iop.org/0305-4470/25/i=7/a=035

Rigidity dependence of Forbush decreases in the energy region exceeding the sensitivity of neutron monitors

M. Savić, N. Veselinović *, A. Dragić, D. Maletić, D. Joković, R. Banjanac, V. Udovičić

Institute of Physics, University of Belgrade, Pregrevica 118, 11080 Zemun, Serbia

Abstract

Applicability of our present setup for solar modulation studies in a shallow underground laboratory is tested on four prominent examples of Forbush decrease during solar cycle 24. Forbush decreases are of interest in space weather application and study of energy-dependent solar modulation, and they have been studied extensively. The characteristics of these events, as recorded by various neutron monitors and our detectors, were compared, and rigidity spectrum was found. Linear regression was performed to find power indices that correspond to each event. As expected, a steeper spectrum during more intense extreme solar events with strong X-flares shows a greater modulation of galactic cosmic rays. Presented comparative analysis illustrates the applicability of our setup for studies of solar modulation in the energy region exceeding the sensitivity of neutron monitors.
© 2018 COSPAR. Published by Elsevier Ltd. All rights reserved.

1. Introduction

Galactic cosmic rays (GCRs) traverse the heliosphere; this leads to variation in the cosmic ray (CR) flux due to solar activity. The influence of solar and heliospheric modulation is pronounced for primary CR particles with low rigidity or momentum over unit charge. CRs interact, upon arrival, with Earth's atmosphere causing electromagnetic and hadronic showers. A network of ground-based CR detectors, neutron monitors (NMs), and muon detectors, located at various locations around the globe, as well as airborne balloons and satellites, provide valuable data to study the effect of these modulations on the integrated CR flux with time. Energies of the primary particles in NMs are sensitive to the state of solar activity and reach up to 40 GeV. Muon detectors have a significant response from 10 GeV up to several hundred GeV for surface, and

one order of magnitude greater for underground detectors, depending on the depth (Duldig, 2000). This energy interval allows muon detectors to monitor not only modulation effects on lower-energy CRs but also galactic effects on primary CRs with high energies where solar modulation is negligible. Because of the sensitivity to different energies of the primary particle flux, observations of muon detectors complement those of NMs in studies of long-term CR variations, CR anisotropy, and gradients or rigidity spectrum of Forbush decreases (FDs).

FDs (Forbush, 1954) represent decreases of the observed GCR intensity under the influence of coronal mass ejections (CMEs) and interplanetary counterparts of coronal mass ejections (ICMEs) and/or high-speed streams of solar wind (HSS) from the coronal holes (Belov, 2008). FDs belong to two types depending on the drivers: non-recurrent and recurrent decreases. This work addresses several non-recurrent FDs.

These sporadic FDs are caused by ICMEs. As the matter with its magnetic field moves through the solar system,

it suppresses the CR intensity. FDs of this kind have an asymmetric profile, and the intensity of GCRs has a sudden onset and recovers gradually. Sometimes an early phase of FD prior to the dip (precursor of FD) shows an increase in CR intensity. These precursors of FDs are caused by GCR acceleration at the front of the advancing disturbance on the outer boundary of the ICME, as the primary CR particles are being reflected from the approaching shock (Papailiou et al., 2013). The FD profile depends on the area, velocity, and intensity of CME magnetic field produced in extreme events that originate at the Sun (Chauhan et al., 2008).

Data from observed modulation of GCR intensity contain information regarding the transport of GCRs through the interplanetary environment. GCR transport parameters are connected with the interplanetary magnetic field (IMF) in the heliosphere. It is empirically established that the radial diffusion coefficient is proportional to the rigidity of CR (Ahluwalia, 2005). In this article, we present an analysis of the amplitude of FD during four events, which were recorded by plastic scintillator muon detectors, located at the Belgrade muon station, as well as by a network of NMs.

2. Belgrade CR station

The Low-Background Laboratory for Nuclear Physics (LBLNP) is a part of the Institute of Physics, University of Belgrade. It is composed of two separate laboratory facilities, ground-level laboratory (GLL) and underground laboratory (UL), dug into a cliff. The overburden of the UL is approximately 12 m of loess soil, which is equivalent to 25 m of water (m.w.e). Laboratory is dedicated to measurements of low radiation activities and studies of muon and electromagnetic components of CRs at ground and shallow underground levels. The geographic position of the laboratory is at 75 m a.s.l., at 44°51′N latitude and 20°23′E longitude; geomagnetic vertical rigidity cutoff is 5.3 GV at the surface. The equipment was upgraded in 2008, and now, it consists of two identical sets of detectors and accompanying data processing electronics: one is situated in GLL and the other in UL. Detectors are a pair of plastic scintillator detectors, with dimensions of 100 cm × 100 cm × 5 cm and four PMTs that are directly coupled to the corners. Signals from two opposite PMTs on a single detector are summed, and the coincidence of the two diagonals is found. Fig. 1 presents the coincident sum spectra of two diagonals of large scintillator detectors.

Summing over diagonals suppresses the acquisition of electromagnetic component of the secondary CR shower and collects mainly the muon component of secondary CRs. A well-defined peak in the energy spectra corresponds to a muon energy loss of ∼11 MeV. The average muon flux measured in the laboratory is 137(6) muons/m²s for GLL and 45(2) muons/m²s for UL. For more detailed description, see Dragić et al. (2011). Integral of this distribution, without low energy part, is used to form time series of this
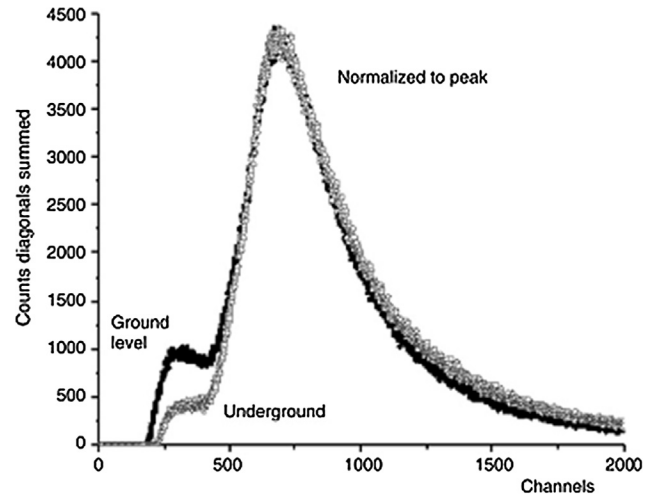

Fig. 1. The coincident spectra of two diagonals of large plastic detectors in UL and GLL normalized for comparison.

CR muons spectrum integrated over different time intervals. This time series is then corrected for efficiency, atmospheric pressure, and temperature (Savić et al., 2015).

The CR flux measured at the ground level varies because of changes in atmospheric conditions. Effects of the atmospheric pressure can be easily accounted for, similar like for NMs, but the temperature effect is somewhat more difficult to treat. The difficulties arise from the interplay of positive and negative temperature effects. With temperature increase, the atmospheric density decreases; hence, less pions interact and more muons are created from decay. The result is a positive effect of more muons at the ground level. On the other hand, the altitude of muon production level is high due to the expansion of the atmosphere when the temperature is high, muon path length is long, and decay probability of muons is high before they reach the ground level. Negative effect is dominant for low-energy muons (mostly detected in GLL) and positive for high-energy muons. A proper treatment of the temperature effect requires knowledge of the entire temperature profile of the atmosphere. This meteorological variation must be corrected to study CR variations originating outside the atmosphere.

For ground (and underground)-based CR detectors, the response function, i.e., the relation between particles of GCR spectra at the top of the atmosphere and recorded secondary particles at the surface level, should be accurately known. The total detector count rate can be expressed as follows (Caballero-Lopez and Moraal, 2012):

$$N(R_0, h, t) = \sum_i \int_{R_0}^{\infty} (S_i|(R, h)j_i(R, t))dR$$
$$= \int_{R_0}^{\infty} W(R, h, t)dR \tag{1}$$

where $N(R_0, h, t)$ is the detector counting rate, R_0 is the geomagnetic cutoff rigidity, h is the atmospheric depth, and t represents time. $S_i(R, h)$ represents the detector yield

function for primary particles of type i and $j_i(R,t)$ represents the primary particle rigidity spectrum of type i at time t. The total response function $W(R,h,t)$ is the sum of $S_i(R,h)$ and $j_i(R,t)$. The maximum value of this function is in the range of 4–7 GV at sea level, depending on the solar modulation epoch at time t (Clem and Dorman, 2000). One of the methods to find this response function is to use the numerical simulation of propagation of CRs through the atmosphere. CORSIKA simulation package (Heck et al., 1998) was to simulate CR transport through the atmosphere and GEANT4 (Agostinelli et al., 2003) to simulate the propagation of secondary CRs through overburden and response of the detectors to find the relationship between the count rate at our site and the flux of primary particles on top of the atmosphere.

The excellent agreement of the simulated and measured flux (Fig. 2) allows us to establish that the cutoff energy for primary CR protons for showers detected in GLL is caused by its geomagnetic rigidity, and the median energy is ~60 GeV. For UL, the cutoff energy due to earth overburden is 12 GeV, and the median energy is ~120 GeV. These values give us opportunity to study solar modulation at energies exceeding energies detected with a NM. Observation of the solar activity and related magnetic disturbances in the heliosphere that create transient CR intensity variation at several different energies can provide an energy-dependent description of these phenomena.

3. Data analysis

The new setup in the LBLNP, presented by Dragić et al. (2011) coincides with the start of the 24th solar cycle, thus allowing us to observe the increase and decrease in solar activity and the effect of solar modulation at energies higher than ones studied using NMs.
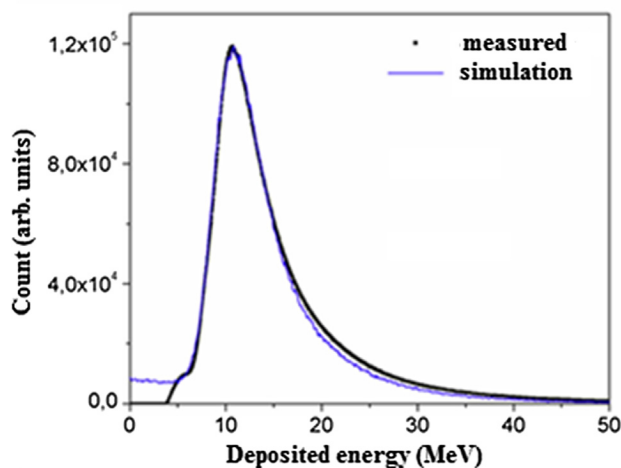

Fig. 2. Simulated (blue line) and measured spectra (black line) for muon detectors in UL. (For interpretation of the references to colour in this figure legend, the reader is referred to the web version of this article.)

Muon time series was searched for days where the average muon flux was significantly lower than the background level. The background level is determined from the moving averages of hourly count rates 10 days before the event. These decreases in the count rate, in GLL and UL, are then compared with space weather events of solar cycle 24. Data collected in UG and GLL are compared with four NM stations from the neutron monitor database [http://www.nmdb.eu/]. Three of these NMs (Athens, Rome, and Jungfraujoch) have cutoff rigidity and geographic proximity similar to the Belgrade CR station.

A high correlation is found between the count rates measured by the NMs in the LBLNP in March 2012 (Table 1), but for GLL and UL, as the cutoff energy of the primary flux increases, the correlation slightly decreases.

3.1. Selected Forbush decreases

The Belgrade CR station has detected, both in GLL and UL, several significant structures connected to some extreme solar effects. Several, more prominent, Forbush decreases occurred in March 2012, September 2014, June 2015, and most recently in September 2017.

The FD that occurred on March 8, 2012 was recorded at the Belgrade CR station as well as at other stations (Fig. 3). This FD was separated into two following two CMEs. These CMEs produced an intense disturbance in the interplanetary space and caused a severe geomagnetic storm when the shockwave reached Earth on March 8, 2012. During this event, a very complex combination of modulation occurs (Lingri et al., 2016). Two CMEs from the same active region as the September 10 (X1.6) flare produced FD on September 12, 2014. There was a relatively fast partial halo CME and a larger and rapidly moving halo CME trailing behind the first one on September 10. These two gave rise to the FD that was first detected by NMs on September 12, 2014. This FD was not a classical two-step FD as expected, probably due to the interaction of slower and faster CMEs. The FD profile (Fig. 3) showed a small second step several hours after the first, similar to the FD that occurred in February 2011 (Papaioannou et al., 2013). In June 2015, a large activity occurred in the Sun from powerful AR 2371 that produced several CMEs from the Sun. These CMEs induced a complex modulation of GCRs that led to an FD occurrence on June 22, 2015 with an unusual structure (Samara et al., 2018).

A sudden burst of activity from the Sun early in September 2017, after a prolonged period of low solar activity, produced several flares, including the largest solar flare seen from Earth since 2006, an X9.3 flare. This activity produced several Earth-directed CMEs. Throughout this time, Earth experienced a series of geomagnetic storms, which started promptly after the first CME. This unusual activity produced an FD, which was recorded with detectors in terms of ground level enhancement (GLE) on Earth and Mars (Guo et al., 2018).

Table 1
Correlation matrix of the linear correlation coefficient (in%) for recorded hourly flux at the Belgrade CR station with its temperature- and pressure-corrected underground and ground-level detectors (UL_tpc and GLL_tpc), only pressure-corrected detectors (UL_pc, GLL_pc), and raw data detectors (UL_raw and GLL_raw) and recordings at Rome, Oulu, Jungfraujoch (Jung.) and Athens NMs for March 2012.

|	Athens	Rome	Jung.	Oulu	GLL_raw	GLL_pc	GLL_tpc	UL_raw	UL_pc	UL_tpc
UL_tpc	75	81	80	81	76	73	78	86	97	100
UL_pc	77	83	83	83	73	78	72	84	100	97
UL_raw	57	71	70	74	94	49	51	100	84	86
GLL_tpc	86	86	84	83	59	90	100	51	72	78
GLL_pc	90	92	90	89	56	100	90	49	78	73
GLL_raw	63	79	78	81	100	56	59	94	73	76
Oulu	90	98	98	100	81	89	83	74	83	81
Jung.	91	98	100	98	78	92	84	70	83	80
Rome	91	100	98	98	79	92	86	71	83	81
Athens	100	91	91	90	63	90	86	57	77	75
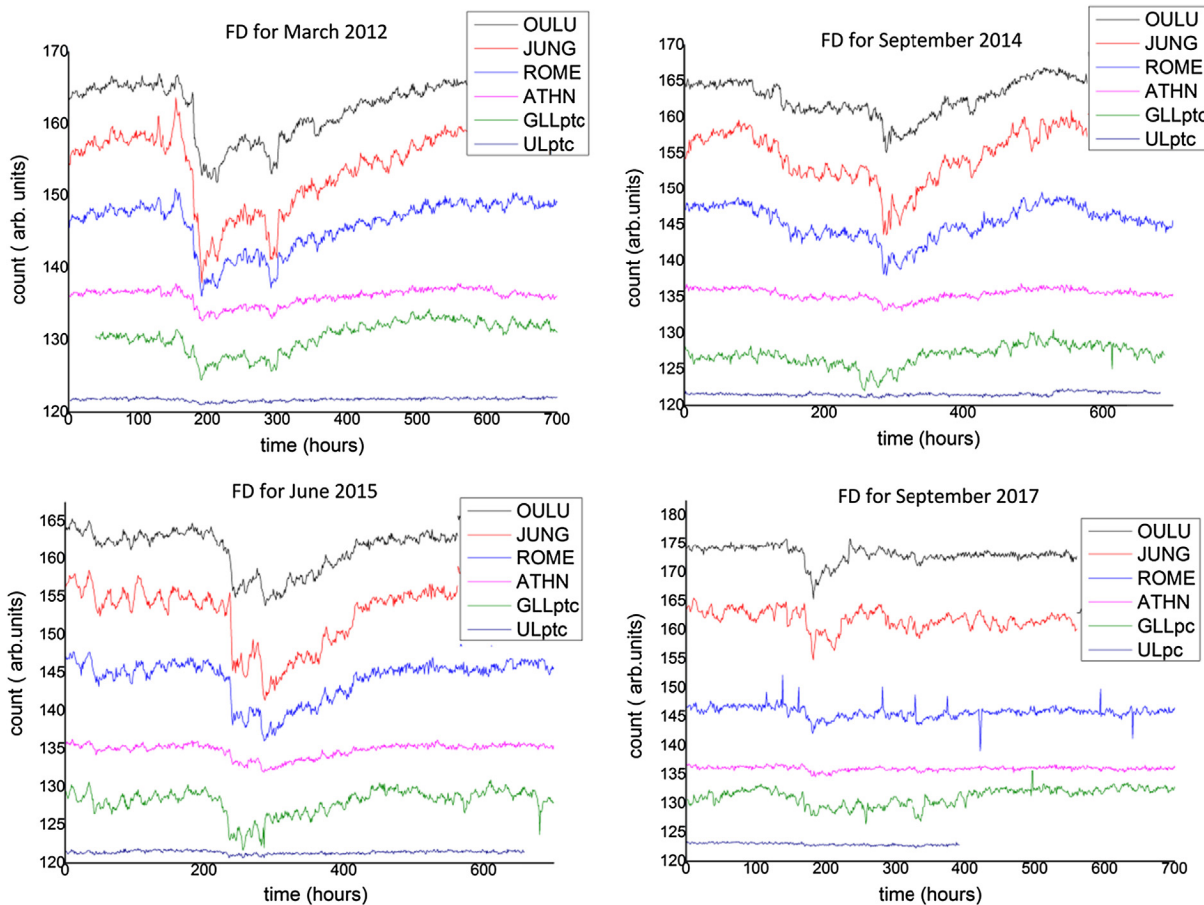
Fig. 3. Comparison of hourly time series over a one month period for pressure- and temperature-corrected count rates of the Belgrade muon monitor station (GLL$_{ptc}$ and UL$_{ptc}$) and NMs at Athens (ATHN), Rome (ROME), Jungfraujoch (JUNG), and Oulu (OULU) for extreme solar events in March 2012, September 2014, and June 2015. Count rates are shifted for comparison. For extreme solar event in September 2017, for GLL and UL, the count rate is pressure-corrected only.

4. FD and median rigidity

For each event, we study the energy dependence of FD amplitude. The energy dependence of FD amplitude is expected to follow the power law: $\Delta N/N \sim R^{-\gamma}$ (Cane, 2000). To obtain reliable values of amplitudes, we defined amplitude as a relative decrease in the hourly count rate of the minimum compared with the average of seven days'

Table 2
Median and cutoff rigidity for several stations.

Stations	Median rigidity R_m (GV)	Min. rigidity R_0 (GV)
Athens	25.1	8.53
Mexico	25.1	8.28
Almaty	15.8	6.69
Lomnicky stit	12.6	3.84
Moscow	15.8	2.43
Kiel	15.8	2.36
Yakutsk	12.6	1.65
Apatity	12.6	0.65
Inuvik	12.6	0.3
Mc Murdo	12.6	0.3
Thule	12.6	0,3
South Pole	10	0.1
UL	122	12.3
GLL	63	5.3

Table 3
Power indices of the median rigidity dependence of the dip of the FD. Power indices are obtained for NMs only, NMs and the Belgrade muon station, and Belgrade station only.

γ	NM only	NM + Belgrade	Belgrade station only
March 2012	0.82 ± 0.08	0.78 ± 0.03	0.715
Sept. 2014	0.79 ± 0.16	0.67 ± 0.06	0.744
June 2015	0.57 ± 0.05	0.58 ± 0.02	0.764
Sept. 2017	1.27 ± 0.16	0.86 ± 0.07	0.739

count rate before FDs (not including possible precursory increases). Such a long base period was used because of the higher activity of the Sun prior to registered FDs and sensitivity of the muon detectors.

Amplitudes are determined for two of our detectors and for 12 NMs. To investigate the rigidity spectrum of mentioned FDs, the median rigidity R_m is defined. R_m is the rigidity of the response of the detector to GCR spectrum where 50% of the detector counting rate lies below R_m (Ahluwalia and Fikani, 2007). For this study, we used a list of R_m for 12 NM stations given by Minamino et al. (2014). For an NM, the median rigidity can be computed from the detector response function derived from surveys for particulate station, usually around the minima of solar activity; this is because the intensity of lowest rigidity GCRs is maximum at that time.

For the Belgrade muon station, R_m was found using the response function acquired by the Monte Carlo method of
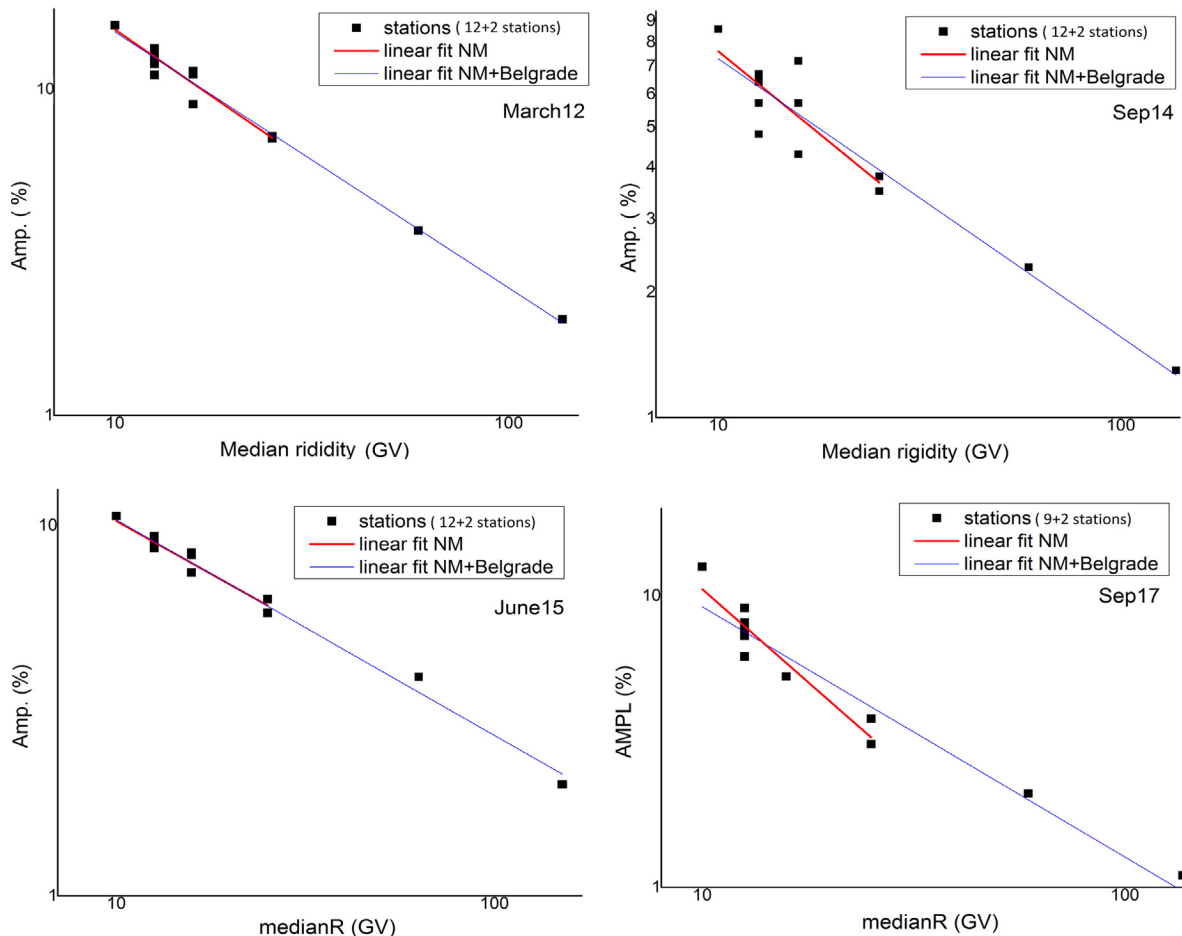

Fig. 4. Rigidity spectrum of FD from March 8, 2012, September 12, 2014, June 22, 2015, and September 8, 2017. Points represent the amplitude of the event as seen by NMs and the Belgrade CR station.

CR transport. Approximate values of R_m for the detectors used in this study are provided in Table 2.

For every selected event, a scatter plot is drawn (Fig. 4). All plots show, plotted in log-log scale, a clear median rigidity dependence of the amplitude of FD decrease.

Linear regression was performed to find power indices corresponding to each event. Power indices are given in Table 3.

Higher power indices can be due to more complex variations in GCRs. This more complex variation is a result of a series of CMEs during this event that leads to large compound ICME structure with multiple shocks and transient flow (Zhao and Zhang, 2016). Results obtained from the power law are generally consistent with those obtained in previous studies (Ahluwalia and Fikani, 2007, Lingri et al., 2016, Klyueva et al., 2017) conducted for NMs only.

A more significant difference observed for indices during the 2017 event was because we used only pressure-corrected data for the muon flux recorded at the Belgrade station. For all other events and data, we performed both pressure and temperature correction. Without temperature corrections, variation in the count rate in muon detectors is higher and it can affect the results.

We expect that when the newly improved, internally developed technique for temperature correction of the CR flux is implemented, the amplitude of the FD measured at the Belgrade muon station will be more consistent with other events and measurements. More data points on the graphs are needed to understand indices better, particularly in an energy region between NM and our laboratory. Similar work (Braun et al., 2009) discussed the extension up to 15 and 33 GeV, but there are no data available for FDs during cycle 24 and cannot be incorporated into this work. As for other operating muon telescopes, there is an agreement between the data obtained at our stations data and the URAGAN data for FD in June 2015 (Barbashina et al., 2016), but we have no data on other FDs and/or median energies of other stations. Our new experimental setup described elsewhere (Veselinović et al. 2017) will provide two additional median energies (121 and 157 GeV) to monitor variations in the CR flux.

5. Conclusion

The Belgrade CR station, with both ground level and underground setups, monitors the effect of solar modulation on the CR flux since 2008. Extreme solar events, like Forbush decreases, were detected during solar cycle 24 at the site, suggesting that these phenomena can be studied at energies higher than typical ones detected with NMs. GLL and UL data, as well as data from several NM stations, were used to analyze four intense FDs. The magnitude of FDs is energy (rigidity) dependent and follows the power law. Data used to find the rigidity dependence of these transient solar modulation of GCR were obtained over much higher range of rigidities than region NMs are

sensitive in, thus allowing more extensive studies of CR solar modulation processes.

References

Agostinelli, S., et al., GEANT4—A Simulation Toolkit, 2003. Nuclear Instruments and Methods in Physics Research Section A 506, pp. 250–303. https://doi.org/10.1016/S0168-9002(03)01368-8.

Ahluwalia, H.S., 2005. Cycle 20 solar wind modulation of galactic cosmic rays: understanding the challenge. J. Geophys. Res. 110, A10106. https://doi.org/10.1029/2005JA011106.

Ahluwalia, H.S., Fikani, M.M., 2007. Cosmic ray detector response to transient solar modulation: Forbush decreases. J. Geophys. Res. 112 (A8), A08105. https://doi.org/10.1029/2006JA011958.

Barbashina, N.S., Ampilogov, N.V., Astapov, I.I., Borog, V.V., Dmitrieva, A.N., Petrukhin, A.A., Sitko, O.A., Shutenko, V.V., Yakovleva, E.I., 2016. Characteristics of the Forbush decrease of 22 June 2015 measured by means of the muon hodoscope URAGAN. J. Phys.: Conf. Ser. 675 (3). https://doi.org/10.1088/1742-6596/675/3/032038, article id. 032038.

Belov, A.V., 2008. Forbush effects and their connection with solar, interplanetary and geomagnetic phenomena. In: Proceedings of the International Astronomical Union 4.S257, pp. 439–450. https://doi.org/10.1017/S1743921309029676.

Braun, I., Engler, J., Hörandela, J.R., Milke, J., 2009. Forbush decreases and solar events seen in the 10–20 GeV energy range by the Karlsruhe Muon Telescope. Adv. Space Res. 43 (4), 480–488. https://doi.org/10.1016/j.asr.2008.07.012.

Caballero-Lopez, R.A., Moraal, H., 2012. Cosmic-ray yield and response functions in the atmosphere. J. Geophys. Res. Space Phys. 117 (A12), 7461–7469. https://doi.org/10.1029/2012JA017794.

Cane, H.V., 2000. Coronal mass ejections and Forbush decreases. Space Sci. Rev. 93 (1–2), 55–77. https://doi.org/10.1023/1026532125747.

Chauhan, M.L., Jain Manjula, S.K., Shrivastava, S.K., 2008. Study of two major Forbush decrease events of 2005. In: Proceedings of the 30th International Cosmic Ray Conference, Mexico City, vol. 1 (SH), pp. 307–310. https://doi.org/10.7529/ICRC2011/V10/0097.

Clem, J.M., Dorman, L.I., 2000. Neutron monitor response functions, cosmic rays and earth. Space Sci. Rev. 93 (1/2), 335–359. https://doi.org/10.1023/A:1026515722112.

Dragić, A., Udovičić, V., Banjanac, R., Joković, D., Maletić, D., Veselinović, N., Savić, M., Puzović, J., Aničin, I.V., 2011. The new setup in the Belgrade low-level and cosmic-ray laboratory. Nucl.

Technol. Radiat. Protect. 26 (3), 181–192. https://doi.org/10.2298/NTRP1101064N.

Duldig, M.L., 2000. Muon observations. In: Bieber, J.W., Eroshenko, E., Evenson, P., Flückiger, E.O., Kallenbach, R. (Eds.), Cosmic Rays and Earth. Space Sciences Series of ISSI. Springer, Dordrecht, pp. 207–226. https://doi.org/10.1007/978-94-017-1187-6_1.

Forbush, S.E., 1954. World-wide cosmic ray variations, 1937–1952. J. Geophys. Res. 59 (4), 525–542. https://doi.org/10.1029/JZ059i004p00525.

Guo, J., Dumbović, M., Wimmer-Schweingruber, R.F., Temmer, M., Lohf, H., Wang, Y., Veronig, A., Hassler, D.M., Leila, M., Mays, L. M., Zeitlin, C., Ehresmann, B., Witasse, O., Freiherr von Forstner, J. L., Heber, B., Holmström, M., Posner, A., 2018. Modeling the evolution and propagation of the 2017 September 9th and 10th CMEs and SEPs arriving at Mars constrained by remote-sensing and in-situ measurement. Also Available at: arXiv preprint arXiv:1803.00461.

Heck, D., Knapp, J., Capdevielle, J.N., Schatz, G., Thouw, T., 1998. CORSIKA: a Monte Carlo code to simulate extensive air showers. Forschungszentrum Karlsruhe GmbH, p. V +90, TIB Hannover, D-30167 Hannover.

Klyueva, A.I., Belov, A.V., Eroshenko, E.A., 2017. Specific features of the rigidity spectrum of Forbush effects. Geomag. Aeron. 57 (2), 177–189. https://doi.org/10.1134/S0016793217020050.

Lingri, D., Mavromichalaki, H., Belov, A., Eroshenko, E., Yanke, V., Abunin, A., Abunina, M., 2016. Solar activity parameters and associated Forbush decreases during the minimum between cycles 23 and 24 and the ascending phase of cycle 24. Sol. Phys. 291 (3), 1025–1041. https://doi.org/10.1007/s11207-016-0863-8.

Minamino, Mohanty, Morishita, et al. for the GRAPES-3 Collaboration, 2014. Rigidity Dependence of Forbush Decreases, Poster #654. In: Proceedings of the 33rd International Cosmic Ray Conference, Rio de Janeiro, Brazil, pp. 3612–3615.

Papailiou, M., Mavromichalaki, H., Abunina, M., Belov, A., Eroshenko, E., Yanke, V., Kryakunova, O., 2013. Forbush decreases associated with western solar sources and geomagnetic storms: a study on precursors. Sol. Phys. 283 (2), 557–563. https://doi.org/10.1007/s11207-013-0231-x.

Papaioannou, A., Belov, A.A., Mavromichalaki, H., Eroshenko, E., Yanke, V., Asvestari, E., Abunin, A., Abunina, M., 2013. The first Forbush decrease of solar cycle 24. J. Phys. Conf. Ser. 409 (1). https://doi.org/10.1088/1742-6596/409/1/012202.

Samara, E., Smponias, I.A., Lytrosyngounis, I., Lingri, D., Mavromichalaki, H., Sgouropoulos, C., 2018. Unusual cosmic ray variations during the Forbush decreases of June 2015. Sol. Phys. 293 (67). https://doi.org/10.1007/S11207-018-1290-9.

Savić, M., Maletić, D., Joković, D., Veselinović, N., Banjanac, R., Udovičić, V., Dragić, V., 2015. Pressure and temperature effect corrections of atmospheric muon data in the Belgrade cosmic-ray station. J. Phys. Conf. Ser. 632 (1). https://doi.org/10.1088/1742-6596/632/1/012059, article id. 012059.

Veselinović, N., Dragić, A., Savić, M., Maletić, D., Joković, D., Banjanac, R., Udovičić, V., 2017. An underground laboratory as a facility for studies of cosmic-ray solar modulation. Nucl. Instrum. Meth. A875, 10–15. https://doi.org/10.1016/j.nima.2017.09.008.

Zhao, L.-L., Zhang, H., 2016. Transient galactic cosmic-ray modulation during solar cycle 24: a comparative study of two prominent forbush decrease events. Astrophys. J. 827 (1). https://doi.org/10.3847/0004-637X.

CrossMark

An underground laboratory as a facility for studies of cosmic-ray solar modulation

N. Veselinović, A. Dragić *, M. Savić, D. Maletić, D. Joković, R. Banjanac, V. Udovičić

Institute of Physics, University of Belgrade, Pregrevica 118, 11080 Zemun, Serbia

A B S T R A C T

The possibility of utilizing a shallow underground laboratory for the study of energy dependent solar modulation process is investigated. The laboratory is equipped with muon detectors at ground level and underground (25mwe), and with an underground asymmetric muon telescope to have a single site detection system sensitive to different median energies of primary cosmic-ray particles. The detector response functions to galactic cosmic rays are determined from Monte Carlo simulation of muon generation and propagation through the atmosphere and soil, based on CORSIKA and GEANT4 simulation packages. The present setup is suitable for studies of energy dependence of Forbush decreases and other transient or quasi-periodic cosmic-ray variations.

© 2017 Elsevier B.V. All rights reserved.

1. Introduction

Galactic cosmic rays (GCR) arriving at Earth after propagating through the heliosphere interact with nuclei in the atmosphere. These interactions of primary CRs lead to production of a cascade (shower) of secondary particles: hadrons, electrons, photons, muons, neutrinos. Ground based CR detectors are designed to detect some species of secondary cosmic radiation. Widely in use are neutron monitors [1,2], muon telescopes [3,4], various types of air shower arrays [5], γ-ray air Cherenkov detectors [6], air fluorescence detectors [7] etc.

The flux and energy spectra of GCR are modulated by the solar magnetic field, convected by the solar wind. Particularly affected are GCR at the low energy side of the spectrum (up to ~100 GeV). Therefore, secondary CRs generated in the atmosphere can be used for studying solar and heliospheric processes. Among the best known effects of the solar modulation are CR flux variations with 11 year period of the solar cycle, 22 year magnetic cycle, diurnal variation and Forbush decrease. The so called corotation with the solar magnetic field results in the flux variation with the 27-day period of solar rotation.

Modulation effects have been studied extensively by neutron monitors (NM) [8,9], sensitive up to several tens of GeV, depending on their geomagnetic location and atmospheric depth. Muon detectors at ground level are sensitive to primary particles of higher energies than NMs. Underground muon detectors correspond to even higher energy primaries. For this reason muon observations complement NM observations in studies of long-term CR variations, CR anisotropy and gradients

or rigidity spectrum of Forbush decreases. However, muon observations suffer from difficulties to disentangle variations of atmospheric origin. While the effect of atmospheric pressure is similar to NMs and easy to account for, the temperature effect is more complicated. The entire temperature profile of the atmosphere is contributing, with different net temperature effect on muon flux at different atmospheric layers, as a result of interplay of positive and negative temperature effects. The positive temperature effect is a consequence of reduced atmospheric density with the temperature increase, resulting in less pion interactions and more decays into muons [10]. The negative temperature effect comes from the increased altitude of muon production at the periods of high temperature, with the longer muon path length and the higher decay probability before reaching the ground level [11]. Both effects are accounted for by the integral method of Dorman [12]. The negative temperature effect is dominant for low energy muons (detected at ground level) and the positive for high energy muons (detected deep underground). At shallow depth of several tens of meters of water equivalent both temperature effects contribute to the overall temperature effect. Several detector systems with different sensitivity to primaries at the same location have the advantage of sharing common atmospheric and geomagnetic conditions.

Belgrade CR station is equipped with muon detectors at ground level and at the depth of 25 m.w.e. Underground laboratory is reached only by muons exceeding energy threshold of 12 GeV. The existing detectors are recently amended by additional setup in an attempt to fully exploit laboratory's possibilities to study solar modulation at different

---

median rigidities. In the present paper the detector systems at the Belgrade CR station are described. Response functions of muon detectors to galactic cosmic rays are calculated. The detector system represents useful extension of modulation studies with neutron monitors to higher energies, as it is demonstrated in the case of a recent Forbush event.

2. Description of Belgrade CR station

The Belgrade cosmic-ray station, situated at the Low Background Laboratory for Nuclear Physics at Institute of Physics, is located at near-sea level at the altitude of 78 m a.s.l. Its geographic position is: latitude 44°51′N and longitude 20°23′E, with vertical cut-off rigidity 5.3 GV. It consists of the ground level lab (GLL) and the underground lab (UL) which has useful area of 45 m^2, dug at a depth of 12 m. The soil overburden consists of loess with an average density 2.0 ± 0.1 g/cm^3. Together with the 30 cm layer of reinforced concrete the laboratory depth is equivalent to 25 m.w.e. At this depth, practically only the muonic component of the atmospheric shower is present [13].

2.1. Old setup

The experimental setup [14] consists of two identical sets of detectors and read out electronics, one situated in the GLL and the other in the UL. Each setup utilizes a plastic scintillation detector with dimensions 100 cm × 100 cm × 5 cm equipped with 4 PMTs optically attached to beveled corners of a detector. Preamplifier output of two diagonally opposing PMTs are summed and fed to a digitizer input (CAEN FADC, type N1728B). FADC operates at 100 MHz frequency with 14 bit resolution. The events generating enough scintillation light to produce simultaneous signals in both inputs exceeding the given threshold are identified as muon events. The simulated total energy deposit spectrum is presented on the left panel of Fig. 1. After the appropriate threshold conditions are imposed on the signals from two diagonals, the spectrum is reduced to the one represented on the right panel of the same figure. Contribution from different CR components are indicated on both graphs and experimentally recorded spectrum is plotted as well.

Particle identification is verified by a two-step Monte Carlo simulation. In the first step development of CR showers in the atmosphere is traced, starting from the primary particles at the top of the atmosphere by CORSIKA simulation package. CORSIKA output contains information on generated particles (muons, electrons, photons, etc.) and their momenta at given observation level. More details on CORSIKA simulation will be given in Section 3. This output serves as an input for the second step in simulation, based on GEANT4. In the later step energy deposit by CR particles in the plastic scintillator detector are determined, together with the light collection at PMTs. Contributions from different CR components to recorded spectrum are also shown in Fig. 1.

According to the simulation, 87.5% of events in the coincident spectrum originate from muons. To account for the contribution from other particles to the experimental spectrum not all the events in the spectrum are counted when muon time series are constructed. Muon events are defined by setting the threshold corresponding to muon fraction of recorded spectrum. Threshold is set in terms of "constant fraction" of the spectrum maximum, which also reduces count rate fluctuations due to inevitable shifts of the spectrum during long-term measurements.

2.2. Upgrade of the detector system

Existing detectors enable monitoring of CR variations at two different median energies. An update is contemplated that would provide more differentiated response. Two ideas are considered. First one was to extend the sensitivity to higher energies with detection of multi-muon events underground. An array of horizontally oriented muon detectors ought to be placed in the UL. Simultaneous triggering of more than

one detector is an indication of a multi-muon event. The idea was exploited in the EMMA underground array [15], located at the deeper underground laboratory in Pyhasalmi mine, Finland, with the intention to reach energies in the so called knee region. For a shallow underground laboratory, exceeding the energy region of solar modulation would open the possibility to study CR flux variations originating outside the heliosphere. Second idea is an asymmetric muon telescope separating muons with respect to zenith angle. Later idea is much less expensive to be put into practice.

Both ideas will be explained in detail and response function to GCR for existing and contemplated detectors calculated in the next section.

3. Calculation of response functions

Nature of variations of primary cosmic radiation can be deduced from the record of ground based cosmic ray detectors provided relation between the spectra of primary and secondary particles at surface level are known with sufficient accuracy. Relation can be expressed in terms of rigidity or kinetic energy.

Total detector count rate can be expressed as:

$$N(E_{th}, h, t) = \sum_i \int_{E_{th}}^{\infty} Y_i(E, h) \cdot J_i(E, t) dE \tag{1}$$

where E is primary particle energy, i is type of primary particle (we take into account protons and α particles), $J_i(E, t)$ is energy spectrum of primary particles, h is atmospheric depth and $Y_i(E, h)$ is the so called yield function. E_{th} is the threshold energy of primary particles. It depends on location (geomagnetic latitude and atmospheric altitude) and detector construction details. At a given location on Earth, only particles with rigidity above vertical rigidity cut-off contribute to the count rate. Also, detector construction often prevents detection of low energy particles. For instance, muon detectors are sometimes covered with a layer of lead. In present configuration our detectors are lead free.

Historically, yield functions were calculated empirically, often exploiting the latitude variations of neutron and muonic CR component [16–18]. With the advancement of computing power and modern transport simulation codes it became possible to calculate yield functions from the interaction processes in the atmosphere [19,20]. The yield function for muons is calculated as:

$$Y_i(E, h) = \int_{E_{th}}^{\infty} \int S_i(\theta, \phi) \cdot \Phi_{i,\mu}(E_i, h, E, \theta, \phi) dE d\Omega \tag{2}$$

where $S(\theta, \phi)$ is the effective detector area and integration is performed over upper hemisphere. $\Phi_{i,\mu}(E_i, h, E, \theta, \phi)$ is the differential muon flux per primary particle of the type i with the energy E_i.

Total differential response function:

$$W(E, h, t) = \sum_i Y_i(E, h) \cdot J_i(E, t) \tag{3}$$

when normalized to the total count rate gives the fraction of count rate originating from the primary particles with the energy in the infinitesimal interval around E. Integration of differential response function gives the cumulative response function.

The response functions of our CR detectors are calculated using Monte Carlo simulation of CR transport through the atmosphere with CORSIKA simulation package. Simulation was performed with protons and α-particles as primary particles. They make ∼94% (79% + 14.7%) of all primaries [21]. Implemented hadron interaction models were FLUKA for energies below 80 GeV, and QGSJET II-04 for higher energies. If the old version of QGSJET is used, a small discontinuity in response function is noticed at the boundary energy between two models. Geomagnetic field corresponds to the location of Belgrade $B_x = 22.61$ μT, $B_z = 42.27$ μT. Power law form of differential energy spectrum of galactic cosmic rays $J_p(E) \sim E^{-2.7}$ is assumed. Energy range of primary particles is between 1 GeV and $2 \cdot 10^7$ GeV. Interval of zenith angles is $0° < \theta < 70°$. Low energy thresholds for secondary particles are: 150 MeV for hadrons and muons and 15 MeV for electrons
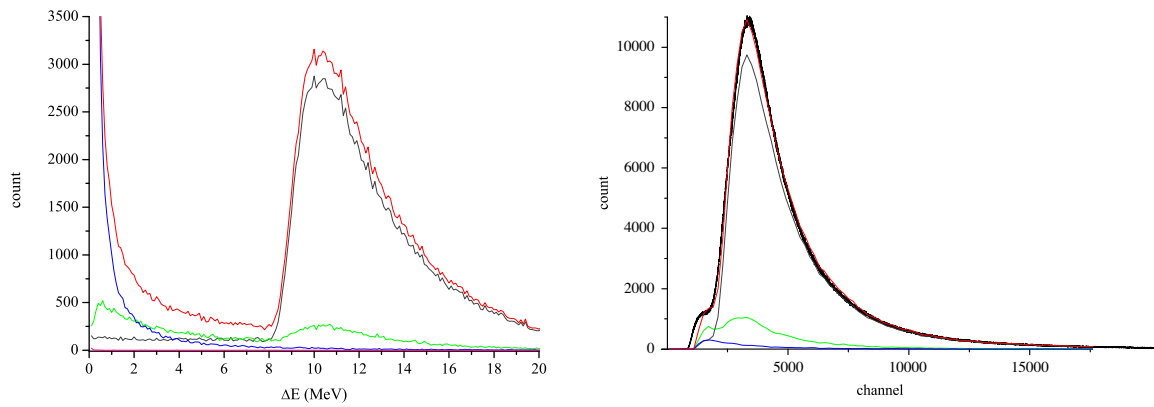
Fig. 1. Left — ΔE spectrum in the plastic scintillator detector, derived from GEANT simulation; right — the same, but for the events exceeding threshold on both diagonals. Contribution of different CR components to the total energy deposit in the detector: muons-gray line, photons-blue line, electrons-green line and sum of all contributions — red line. The black curve on the right panel is the experimental spectrum. (For interpretation of the references to color in this figure legend, the reader is referred to the web version of this article.)
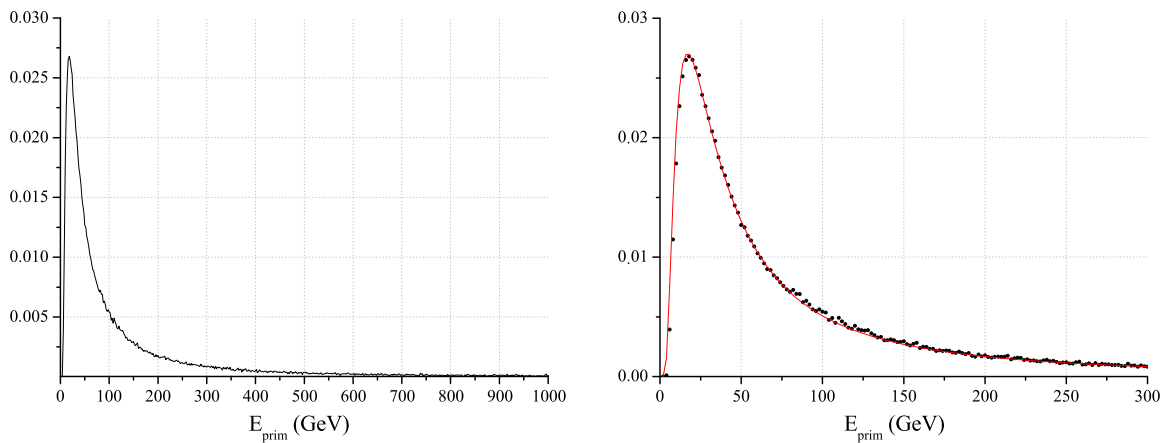

Fig. 2. Left: normalized total response function of ground level muon detector to galactic cosmic rays; right: same as left, fitted with Dorman function (red line). (For interpretation of the references to color in this figure legend, the reader is referred to the web version of this article.)
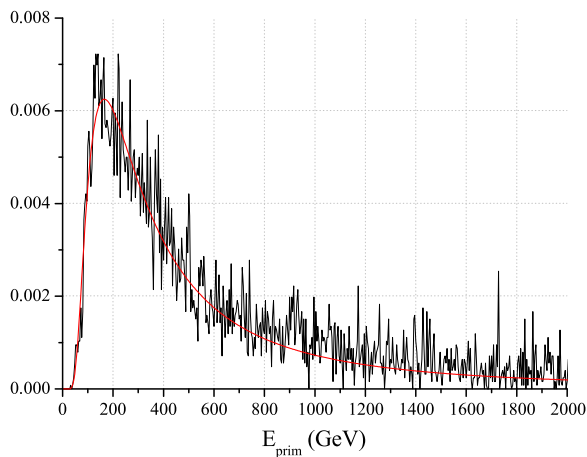

Fig. 3. Response function for multi-muon events in UL to galactic cosmic rays.

and photons. Selected atmospheric model is AT511 (Central European atmosphere for May 11 1993). Observational level is at 78m a.s.l.

For calculation of response functions for underground detectors, simulation of particle propagation through the soil overburden is performed using the code based on GEANT4 package. For precise calculation of energy loss, chemical composition of the soil needs to be known. The

composition used in our work is taken from a geochemical study of neighboring loess sections of Batajnica and Stari Slankamen [22]. Most abundant constituents are quartz (SiO_2) 70%, alumina (Al_2O_3) 15% and quicklime (CaO) 10%, while others include Fe_2O_3, MgO, TiO_2, K_2O,.... Inaccuracy of our knowledge of the soil chemical composition should not strongly affect our results since, at relevant energies, dominant energy loss mechanism for muons is ionization which, according to Bethe–Bloch formula depends mostly on $\langle Z\rangle/\langle A\rangle$. Soil density profile is probed during laboratory construction. It varies slowly with depth and average density is found to be (2.0 ± 0.1) g/cm^3.

In the simulation, the effective area and angular acceptance of different modes of asymmetric muon telescope (single, coincident and anticoincident) are taken into account.

According to Dorman [12], response function can be parametrized as:

$$W(E) = \begin{cases} 0, & \text{if } E < E_{th}; \\ \dfrac{a \cdot k \cdot \exp(-aE^{-k})}{E^{(k+1)}(1 - aE_{th}^{-k})}, & \text{otherwise}; \end{cases} \tag{4}$$

with the high energy asymptotics: $W(E) \approx a \cdot k \cdot E^{-(k+1)}$.

3.1. Ground level

Calculated response function for ground level muon detector is presented on Fig. 2, together with fitted Dorman function (4).
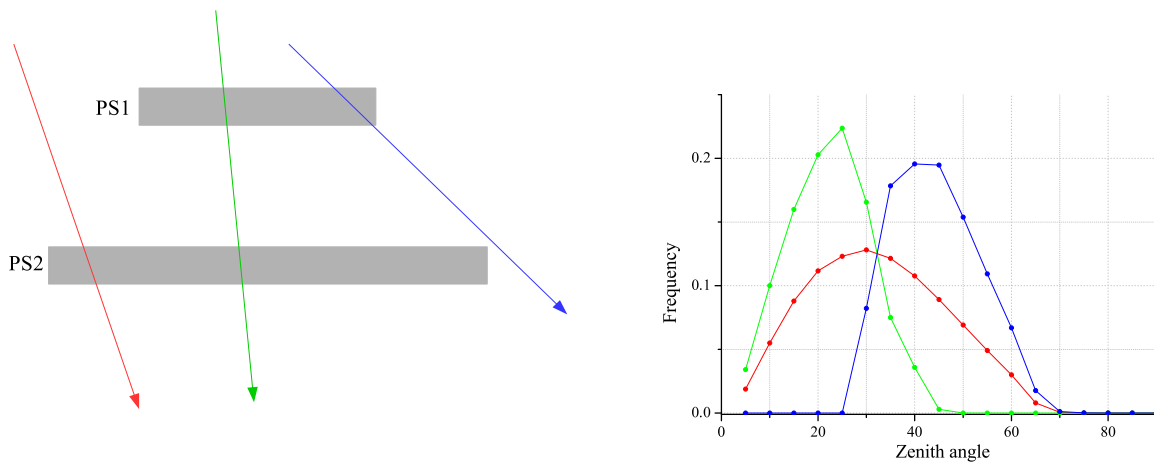
Fig. 4. Left: Schematic view of the asymmetric muon telescope; PS1 — plastic scintillator detector 1, PS2 — plastic scintillator detector 2. Right: angular distribution of detected muons in single mode (red), coincident mode (green) and anticoincident mode (blue), normalized to number of counts in each mode. (For interpretation of the references to color in this figure legend, the reader is referred to the web version of this article.)
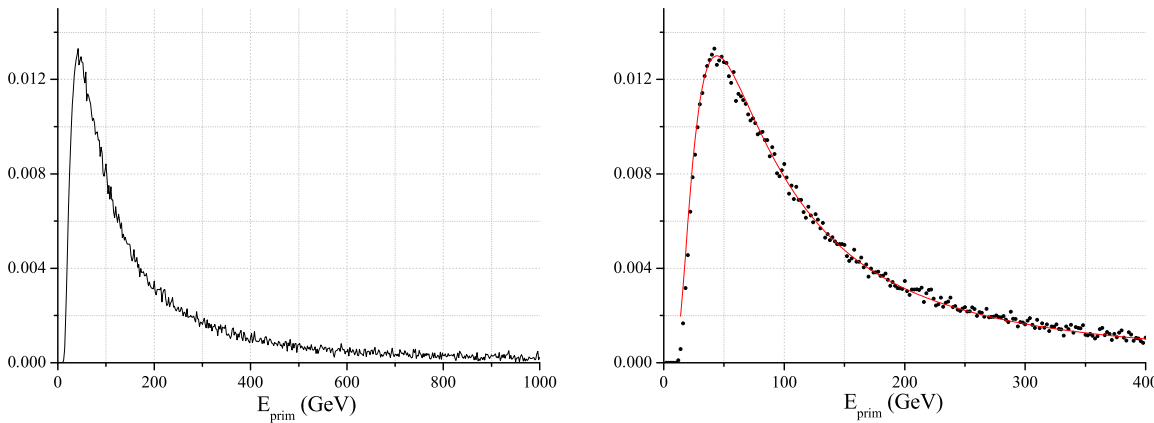
Fig. 5. Response function of single mode of ASYMUT in the UL to galactic cosmic rays. On the right panel the energy interval of interest is enlarged and Dorman function fit is plotted (red line). (For interpretation of the references to color in this figure legend, the reader is referred to the web version of this article.)
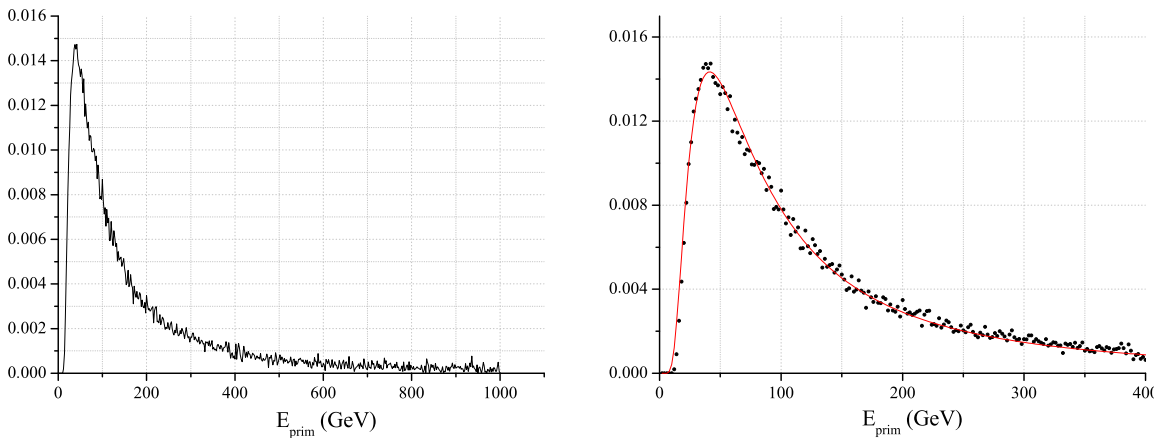
Fig. 6. Response function of coincident mode of asymmetric muon telescope in the UL to galactic cosmic rays. On the right panel the interesting energy interval is enlarged and Dorman function fit is plotted (red line). (For interpretation of the references to color in this figure legend, the reader is referred to the web version of this article.)

3.2. Underground

3.2.1. Multi-muon events

Count rate of multi-muon events underground turned out to be too low for the above mentioned array detector experiment to be feasible in our laboratory. To collect enough events for construction of the response function (Fig. 3), allowed muon separation is 200 m, fairly

exceeding laboratory dimensions. Under these conditions calculated median energy is 270 GeV.

3.2.2. ASYmmetric MUon Telescope (ASYMUT)

Asymmetric muon telescope is an inexpensive detector, constructed from components already available in the laboratory. It consists of two plastic scintillators of unequal dimensions. The lower is identical to the

Fig. 7. Response function of anticoincident mode of asymmetric muon telescope in the UL to galactic cosmic rays. On the right panel the interesting energy interval is enlarged and Dorman function fit is plotted (red line). (For interpretation of the references to color in this figure legend, the reader is referred to the web version of this article.)
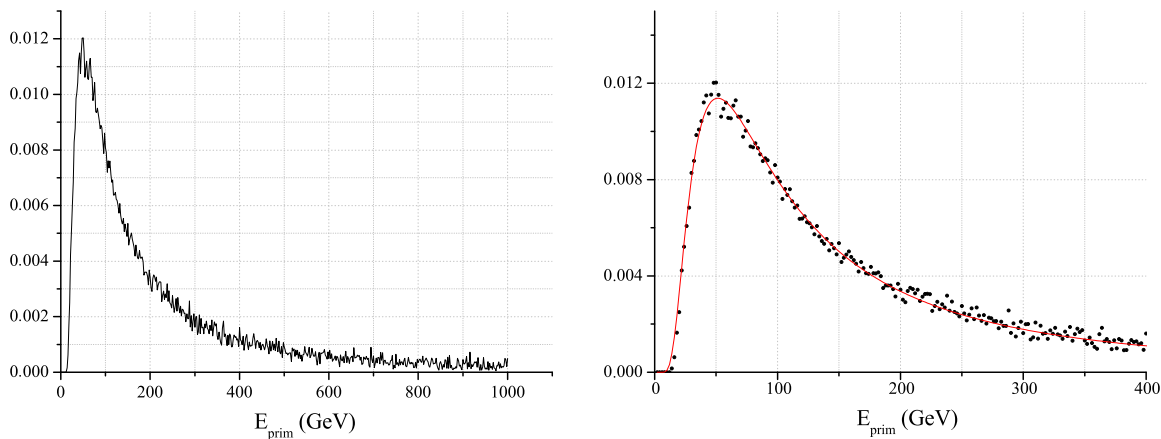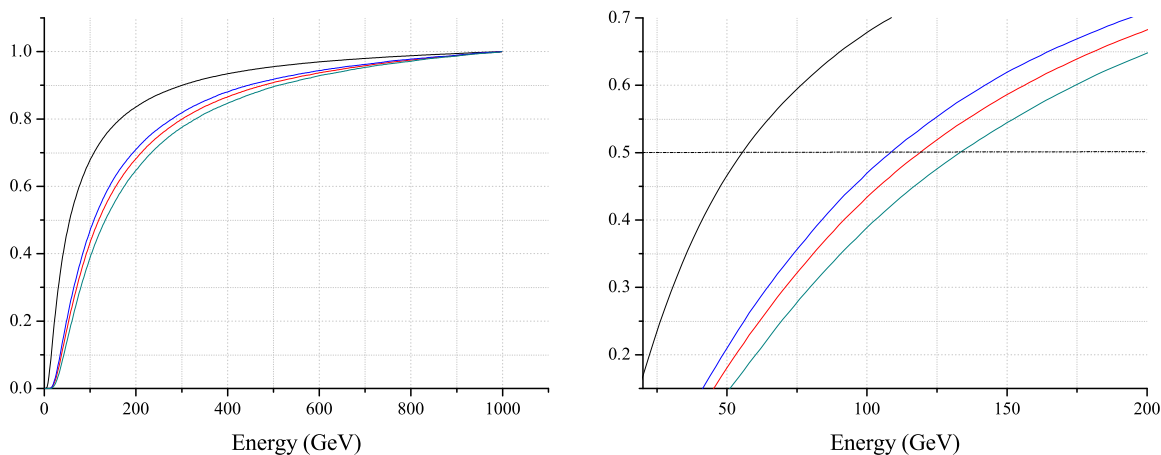

Fig. 8. Cumulative response function to galactic cosmic rays of different muon detectors in the Belgrade CR station: black curve — GLL; red curve — single UL; green curve — CC mode and blue curve — ANTI CC mode of asymmetric muon telescope. The 0.5 level corresponds to median energy. Cumulative response function with enlarged region around this level is shown in the right picture. (For interpretation of the references to color in this figure legend, the reader is referred to the web version of this article.)

one located in the GLL ($100 \times 100 \times 5$ cm) and upper one is $50 \times 46 \times 5$ cm. Detectors are separated vertically by 78 cm, as depicted in Fig. 4, to have roughly the same count rate in the coincident and anticoincident mode. Lower detector in single mode operates in the same manner as the one in the GLL, with wide angular acceptance. The coincident mode is composed of the events registered in both upper and lower detector. In the anticoincident mode, muons passing through the upper but not the lower detector are counted. Therefore, the later mode favors inclined muon paths. Different angular distribution means different path length of muons registered in three modes of ASYMUT (right part of Fig. 4) and also different energy distribution of parental primary particles.

The response functions to GCR of three modes of ASYMUT are shown on Figs. 5–7 and respective cumulative response functions are shown on Fig. 8.

Important parameters describing shapes of response functions are summarized in Table 1. The most often used characteristics of a detector system is its median energy E_{med}. Primary particles with the energy below E_{med} give 50% contribution to detector count rate. The energy interval (($E_{0.05}, E_{0.95}$) is responsible for 90% of registered events. Fitted value of the parameter k from Dorman function (Eq. (4)) is also presented. The parameters $E_{0.05}$ and E_{med} are determined with 1 GeV accuracy, while the uncertainty of $E_{0.95}$ is much higher due to small number of very high energy events and is conservatively estimated as 10%.

Table 1
Sensitivity of Belgrade CR detectors (GLL — ground level; UL — underground based ASY-MUT single mode; CC — ASYMUT coincident mode; ANTI — ASYMUT anticoincident mode) to GCR primary particles. Primaries with the energy below $E_{0.05}$ (and above $E_{0.95}$) contribute with 5% to the count rate of a corresponding detector. E_{med} is median energy, E_{th} threshold energy and k is Dorman parameter.

det	E_{th} (GeV)	$E_{0.05}$ (GeV)	E_{med} (GeV)	$E_{0.95}$ (GeV)	k
GLL	5	11	59	915	0.894(1)
UL	12	31	137	1811	0.971(4)
CC	12	27	121	1585	1.015(3)
ANTI	14	35	157	2031	0.992(4)

3.3. Conclusions

Usefulness of our setup for solar modulation studies is tested on the example of investigation of a Forbush decrease of 8 March 2012. In the first half of March 2012 several M and X class solar flares erupted from the active region 1429 on the Sun. The strongest were two X class flares that bursted on March 7. The first one is the X5.4 class flare (peaked at 00:24 UT) and the second one is the X1.3 class flare (peaked at 01:14 UT). The two flares were accompanied by two fast CMEs, one of which was Earth-directed [23]. Several magnetic storms were also registered on Earth, and a series of Forbush decreases is registered. The most pronounced one was registered on March 8. Characteristics of this event as recorded by various neutron monitors and our detectors are compared.
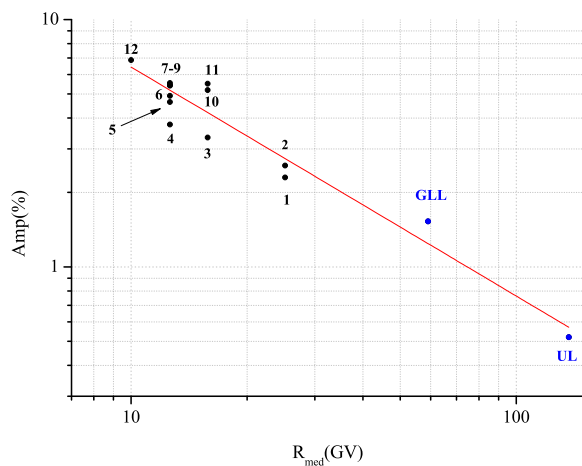
Fig. 9. Rigidity spectrum of FD from 12 March 2012. Black points represent the amplitude of the event as seen by twelve NMs: 1 — Athens, 2 — Mexico City; 3 — Almaty, 4 — Lomnicky stit; 5 — Moscow; 6 — Kiel; 7 — Yakutsk; 8 — Apatity; 9 — Inuvik; 10 — McMurdo; 11 — Thul; 12 — South Pole. Blue points are from Belgrade CR station: GLL — ground level and UL — underground. (For interpretation of the references to color in this figure legend, the reader is referred to the web version of this article.)

Amplitude of a Forbush decrease is one of its main characteristics. Dependence of FD amplitude on median rigidity (or energy) is expected to follow the power law: $\Delta N / N \sim R^{-\gamma}$ [12].

For investigation of rigidity spectrum of mentioned FD data from 12 NMs are combined with the data from our two detectors (GLL and UL) that were operational at the time of the event. Neutron monitor data in the period between 1 March 2012 and 1 April 2012 are taken from the NMDB database (www.nmdb.eu) [24]. The exponent of the rigidity spectrum of this FD γ is obtained by the least-square fitting of the data with the power function (Fig. 9) and found to be $\gamma = 0.92 \pm 0.18$. Presented analysis illustrates applicability of our setup for studies of consequences of CR solar modulation process in the energy region exceeding sensitivity of neutron monitors.

Acknowledgments

References

[1] J.A. Simpson, The cosmic ray nucleonic component: The invention and scientific uses of the neutron monitor, Cosmic Rays Earth (2000) 11–32.

[2] J.W. Bieber, Neutron monitoring: Past, present, future, in: Jonathan F.O. (Ed.) AIP Conference Proceedings, vol. 1516, No. 1, 2013.

[3] M.L. Duldig, Muon observations, in: Cosmic Rays and Earth, Springer, Netherlands, 2000, pp. 207–226.

[4] S. Cecchini, M. Spurio, Atmospheric muons: experimental aspects, Geosci. Instrum. Methods Data Syst. Discuss. 2 (2012) 603–641.

[5] K.-H. Kampert, A.A. Watson, Extensive air showers and ultra high-energy cosmic rays: a historical review, Eur. Phys. J. H 37 (3) (2012) 359–412.

[6] A. de Angelis, O. Mansutti, M. Persic, Very-high energy gamma astrophysics, Riv. Nuovo Cimento 31 (4) (2008) 187–246. http://dx.doi.org/10.1393/ncr/i2008-10032-2.

[7] F. Arqueros, J.R. Hörandel, B. Keilhauer, Air fluorescence relevant for cosmic-ray detection — review of pioneering measurements, Nucl. Instrum. Methods A 597 (2008) 23–31. http://dx.doi.org/10.1016/j.nima.2008.08.055.

[8] J.A. Lockwood, W.R. Webber, The 11 year solar modulation of cosmic rays as deduced from neutron monitor variations and direct measurements at low energies, J. Geophys. Res. 72 (23) (1967) 5977–5989.

[9] I.G. Usoskin, G.A. Bazilevskaya, G.A. Kovaltsov, Solar modulation parameter for cosmic rays since 1936 reconstructed from ground-based neutron monitors and ionization chambers, J. Geophys. Res. 116 (2011) A02104. http://dx.doi.org/10.1029/2010JA016105.

[10] A. Duperier, The meson intensity at the surface of the earth and the temperature at the production level, Proc. Phys. Soc. A 62 (11) (1949) 684.

[11] P.M. Blackett, On the instability of the barytron and the temperature effect of cosmic rays, Phys. Rev. 54 (11) (1938) 973.

[12] L. Dorman, Cosmic Rays in the Earth's Atmosphere and Underground, Springer Science + Business Media, LLC., New York, 2004.

[13] G. Hausser, Cosmic ray-induced background in ge-spectrometry, Nucl. Instrum. Methods B 83 (1–2) (1993) 223–228.

[14] A. Dragić, V. Udovičić, R. Banjanac, D. Joković, D. Maletić, N. Veselinović, M. Savić, J. Puzović, I.V. Aničin, The new setup in the Belgrade low-level and cosmic-ray laboratory, Nucl. Technol. Radiat. Prot. 26 (3) (2011) 181–192. http://dx.doi.org/10.2298/NTRP1101064N.

[15] T. Kalliokoski, L. Bezrukov, T. Enqvist, H. Fynbo, L. Inzhechik, P. Jones, J. Joutsenvaara, J. Karjalainen, P. Kuusiniemi, K. Loo, B. Lubsandorzhiev, V. Petkov, T. Rih, J. Sarkamo, M. Slupecki, W. Trzaska, A. Virkajrvi, Can EMMA solve the puzzle of the knee? Prog. Part. Nucl. Phys. 66 (2011) 468–472.

[16] W.H. Fonger, Cosmic radiation intensity-time variations and their origin. II. Energy dependence of 27-day variations, Phys. Rev. 91 (2) (1953) 351.

[17] E.E. Brown, Neutron yield functions for the nucleonic component of cosmic radiation, Il Nuovo Cimento (1955–1965) 6 (4) (1957) 956–962.

[18] L. Dorman, Cosmic Ray Variations, State Publishing House for Technical and Theoretical Literature, 1957.

[19] E.O. Fluckiger, et al., A parameterized neutron monitor yield function for space weather applications, in: Proceedings of the 30th International Cosmic Ray Conference, Mexico City, Mexico, vol. 1 (SH), 2008, pp. 289–292.

[20] M. Zazyan, A. Chilingarian, Calculations of the sensitivity of the particle detectors of ASEC and SEVAN networks to galactic and solar cosmic rays, Astropart. Phys. 32 (2009) 185–192.

[21] K. Nakamura, et al., 24. Cosmic rays, J. Phys. G 37 (2010) 075021.

[22] B. Buggle, B. Glaser, L. Zoller, U. Hambach, S. Markovic, I. Glaser, N. Gerasimenko, Geochemical characterization and origin of Southeastern and Eastern European loesses (Serbia, Romania, Ukraine), Quat. Sci. Rev. 27 (2008) 1058–1075.

[23] NASA Goddard Space Weather Research Center, Summary of the space weather event associated with the X5.4 and X1.3 flare on March 7.

[24] H. Mavromichalaki, et al., Applications and usage of the real-time Neutron Monitor Database, Adv. Space Res. 47 (12) (2011) 2210–2222.

25-Dec-2024
EPJA-107911.R2
SOME RESULTS OF 209Bi PHOTOACTIVATION EXPERIMENT

Dear Professor Krmar:

It is a pleasure to accept your manuscript entitled "SOME RESULTS OF 209Bi PHOTOACTIVATION EXPERIMENT" in its current form for publication in the European Physical Journal A - "Hadrons and Nuclei".
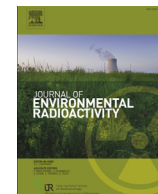
Thank you for your fine contribution. On behalf of the Editors of the European Physical Journal A, we look forward to your continued contributions to the Journal.

Sincerely yours,

Professor Maria Borge
Editor-in-Chief
European Physical Journal A - "Hadrons and Nuclei"

Correlation analysis of the natural radionuclides in soil and indoor radon in Vojvodina, Province of Serbia

S. Forkapic [a, *], D. Maletić [b], J. Vasin [c], K. Bikit [a], D. Mrdja [a], I. Bikit [a], V. Udovičić [b], R. Banjanac [b]

[a] University of Novi Sad, Faculty of Sciences, Department of Physics, Laboratory for Radioactivity and Dose Measurements, 21000 Novi Sad, Serbia
[b] Institute of Physics Belgrade, University of Belgrade, Belgrade, Serbia
[c] Institute of Field and Vegetable Crops, 21000 Novi Sad, Serbia

ABSTRACT

The most dominant source of indoor radon is the underlying soil, so the enhanced levels of radon are usually expected in mountain regions and geology units with high radium and uranium content in surface soils. Laboratory for radioactivity and dose measurement, Faculty of Sciences, University of Novi Sad has rich databases of natural radionuclides concentrations in Vojvodina soil and also of indoor radon concentrations for the region of Vojvodina, Northern Province of Serbia. In this paper we present the results of correlative and multivariate analysis of these results and soil characteristics in order to estimate the geogenic radon potential. The correlative and multivariate analysis were done using Toolkit for Multivariate Analysis software package TMVA package, within ROOT analysis framework, which uses several comparable multivariate methods for our analysis. The evaluation ranking results based on the best signal efficiency and purity, show that the Boosted Decision Trees (BDT) and Multi Layer Preceptor (MLP), based on Artificial Neural Network (ANN), are multivariate methods which give the best results in the analysis. The BDTG multivariate method shows that variables with the highest importance are radionuclides activity on 30 cm depth. Moreover, the multivariate regression methods give a good approximation of indoor radon activity using full set of input variables. On several locations in the city of Novi Sad the results of indoor radon concentrations, radon emanation from soil, gamma spectrometry measurements of underlying soil and geology characteristics of soil were analyzed in detail in order to verify previously obtained correlations for Vojvodina soil.

© 2016 Elsevier Ltd. All rights reserved.

1. Introduction

It is well known that radon and their short lived progenies have the most impact to the population effective dose from radioactive sources (UNSCEAR, 2008). Recent epidemiological studies show that the radiation risk due to radon exists on concentrations that were considered negligible (WHO, 2009). In most European countries radon mapping has been carried out and the results are summing in the publications of Joint Research Centre of European Commission (JRC EC) which coordinates of the project of European Natural Radioactivity Atlas (De Cort et al., 2011). Therefore, all member states (including candidate countries) must propose the reference level of radon in dwellings and working places and identify radon priority areas with high radon potential according to EU directive (EURATOM, 2013). There are two different concepts in definition of radon potential: the first one relative to number of houses with indoor radon concentrations above the reference value (depends of construction types, living habits and meteorology) and the other one geogenic radon potential relative to local geophysical parameters (radon concentration in soil and the permeability of soil) (Gruber et al., 2013). Geogenic radon emanates from radium and uranium rich minerals into the soil pore space and it migrates through the soil by diffusion and convection due to the gradient in concentrations. Geogenic radon potential (GRP) therefore describes radon in the subsurface soil as the main contributor to radon buildup in houses and in contrast to indoor radon potential (IRP) it is independent on human influence and temporally constant over a geological timescale. In the lack of soil gas radon and soil gas permeability measurements, our first steps toward the geogenic

radon map are to find correlations between available radio-geochemical data and indoor radon concentration measurements in order to predict radon prone areas and validate geogenic prognosis.

In Serbian Northern Province Vojvodina several indoor radon surveys were performed in the period of four years from 2002 to 2005 by Laboratory for radioactivity and dose measurement, Faculty of Sciences, University of Novi Sad (Forkapić et al., 2007). The same laboratory during this period carried out radioactivity monitoring of soil on 50 different locations in Vojvodina region (Bikit et al., 2005) in cooperation with the Institute of Field and Vegetable Crops who determined the geochemical soil characteristics, mechanical composition and content of total N, $CaCO_3$ and available phosphorus P_2O_5 and potassium K_2O. The locations were

selected in a way to proportionally represent all geomorphological units (Košćal et al., 2005): two mountains, four loess plateaus, three loess terraces, four alluvial plains, two sandstone terrains and all soil types (IUSS, 2014): Chernozem, Vertisol, Fluvisol, Cambisol, Planosol, Solonchak and Solonetz. The influence of clay and humus content and humidity of soil on radon adsorption to the soil grains were discussed and analyzed using correlative and multivariate analysis with indoor radon concentrations.

The demand for detailed analyses of large amount of data in high-energy physics resulted in wide and intense development and usage of multivariate methods. Many of multivariate methods and algorithms for classification and regression are already integrated into the analysis framework ROOT (Brun and Rademakers, 1997), more specifically, into the Toolkit for Multivariate analysis (TMVA)
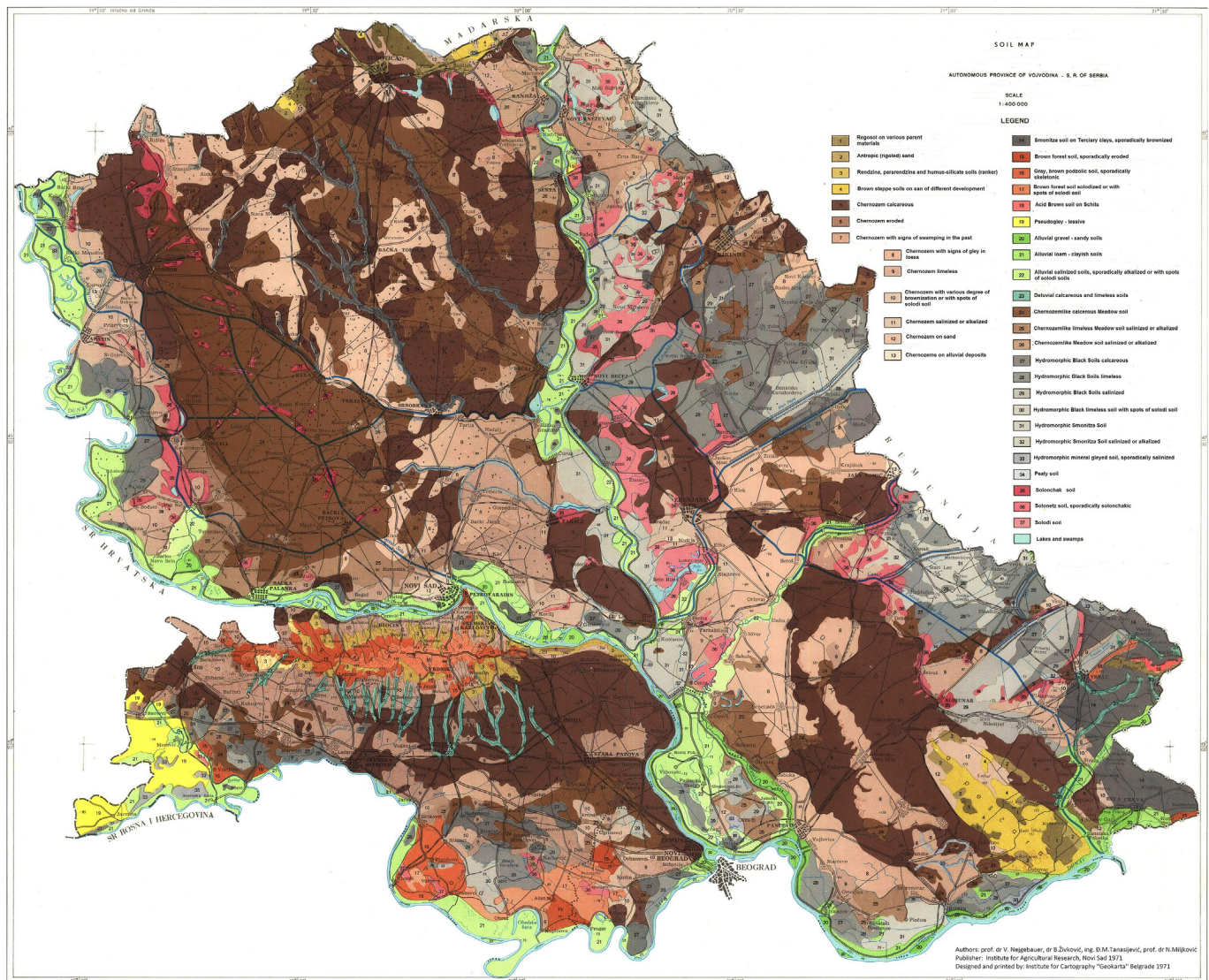
Fig. 1. Soil map of Vojvodina Province (Nejgebauer et al., 1971): 1 — Regosol on various parent materials; 2 — Antropic (rigoled) sand; 3 — Rendzina, pararendzina and humus-silicate soils (ranker), 4 — Brown steppe soils on sand of different development; 5 — Chernozem calcareous; 6 — Chernozem eroded; 7 — Chernozem with signs of swamping in the past; 8 — Chernozem with signs of glay in loess; 9 — Chernozem limeless; 10 — Chernozems with various degree of brownization or with spots of solodi soil; 11 — Chernozem salinized or alkalized; 12 — Chernozem on sand; 13 — Chernozems on alluvial deposits; 14 — Smonitza soil on Terciary clays, sporadically brownized; 15 — Brown Forest soil, sporadically eroded; 16 — Gray, brown podzolic soil sporadically skeletonic; 17 — Brown Forest soil solodized or with spots of solodi soil; 18 — Acid Brown Soil on Schits; 19 — Pseudogley — lessive; 20 — Alluvial gravel — sandy soils; 21 — Alluvial loam — clayish soils; 22 — Alluvial salinized soils, sporadically alkalized or with spots of solodi soils; 23 — Deluvial calcerous and limeless soils; 24 — Chernozemlike calcerous Meadow Soil; 25 — Chernozemlike limeless Meadow Soil salinized or alkalized; 26 — Chernozemlike Meadow soil salinized or alkalized; 27 — Hydromorphic Black Soils calcareous; 28 — Hydromorphic Black Soils limeless; 29 — Hydromorphic Black Soils salinized; 30 — Hydromorphic Black limeless soil with spots of solodi soil; 31 — Hydromorphic Smonitza Soil; 32 — Hydromorphic Smonitza Soil salinized or alkalized; 33 — Hydromorphic mineral gleyed soil, sporadically salinized; 34 — Peaty Soil; 35 — Solonchak Soil; 36 — Solonetz soil, sporadically solonchakic; 37 — Solodi Soil.

(Hoecker et al., 2007). Institute of Physics Belgrade used these multivariate methods to create, test and apply all available classifiers and regression methods implemented in the TMVA in order to find the method that would be the most appropriate and yield maximum information on the dependence of radon concentrations on the multitude of input variables.

The first step is to calculate and rank the correlation coefficients between all the variables involved, what will help in setting up and testing the framework for running the various multivariate methods contained in the TMVA. Although these correlation rankings will later be superseded by method-specific variable rankings, they are useful at the beginning of the analysis.

The next step is to use and compare the multivariate methods in order to find out which one is best suited for classification (division) of indoor radon concentrations into what would be considered acceptable and what would be considered increased concentration.

In order to be able to use the multivariate classification, the set of input events used, have to be split into those the correspond to the signal (the indoor radon concentrations that are considered increased) and to the background (consisting of indoor radon concentrations that are declared acceptable). This splitting of the set of input events is for the purposes of this preliminary analysis performed at the limiting value of 120 Bq/m^3. This value is used for classification analyses, and is selected because this splitting ensures maximum employment of multivariate comparison methods, and this particular value reflects the fact that in our test case the statistics on higher radon concentration values are lower. The method of multivariate regression, however, does not require preliminary splitting of input events, and is therefore a more general one. Main aim is to find out which method can, if any, on the basis of input variables only, give an output that would satisfactorily close match the observed variations of indoor radon concentrations.

In this paper we proposed and analyzed the application of multivariate techniques developed at CERN for experiments with particle physics for correlation analysis of experimental indoor radon data and soil characteristics. Obtained results were verified

Table 1
Classification of soil types for 50 locations of sampling.

No	Locality	Soil type (national classification) (Škorić et al., 1985)	Soil group (FAO-WRB) (IUSS, 2014)
1	Horgoš	Arenosol	Protic ARENOSOL (Calcaric, Aridic)
2	Palić	Solonchak	Haplic SOLONCHAK (Siltic)
3	Žednik	Chernozem	Calcic CHERNOZEM (Loamic, Pachic)
4	Aleksa Šantić	Chernozem	Haplic CHERNOZEM (Loamic, Pachic)
5	Tornjoš	Chernozem	Gleyic CHERNOZEM (Loamic, Pachic)
6	Gakovo	Chernozem	Haplic CHERNOZEM (Loamic, Pachic)
7	Kula	Chernozem	Calcic, Gleyic CHERNOZEM (Loamic, Pachic)
8	Bečej	Humoglej	Mollic Oxigleyic GLEYSOL (Clayic)
9	Srbobran	Chernozem	Calcic, Gleyic CHERNOZEM (Loamic, Pachic)
10	Srpski Miletić	Chernozem	Gleyic CHERNOZEM (Loamic, Pachic)
11	Bogojevo	Humogley — marsh swamp soil	Mollic Oxigleyic GLEYSOL (Loamic)
12	Nadalj	Chernozem	Gleyic CHERNOZEM (Loamic, Pachic)
13	Ruski Krstur	Chernozem	Gleyic CHERNOZEM (Loamic, Pachic)
14	Parage	Chernozem	Gleyic CHERNOZEM (Loamic, Pachic)
15	Rimski Šančevi	Chernozem	Haplic CHERNOZEM (Clayic, Pachic)
16	Žabalj	Chernozem	Gleyic CHERNOZEM (Loamic, Pachic)
17	Maglić	Chernozem	Gleyic CHERNOZEM (Loamic, Pachic)
18	Kać	Fluvisol	Gleyic FLUVISOL (Loamic, Salic)
19	Bačko Novo Selo	Fluvisol	Gleyic FLUVISOL (Loamic)
20	Banatsko Aranđelovo	Humogley — marsh swamp soil	Mollic Oxigleyic GLEYSOL (Clayic)
21	Sanad	Fluvisol	Stagnic FLUVISOL (Clayic)
22	Crna Bara — Čoka	Chernozem	Gleyic CHERNOZEM (Clayic, Pachic)
23	Kikinda	Chernozem	Haplic CHERNOZEM (Clayic, Pachic)
24	Rusko Selo	Humogley — marsh swamp soil	Mollic Oxigleyic GLEYSOL (Clayic)
25	Torda	Humogley — marsh swamp soil	Mollic Oxigleyic GLEYSOL (Clayic)
26	Kumane	Solonetz	Gleiyc, Salic SOLONETZ (Clayic)
27	Begejci	Chernozem	Gleyic CHERNOZEM (Clayic, Pachic)
28	Zrenjanin	Chernozem	Calcic CHERNOZEM (Clayic, Pachic)
29	Boka	Solonetz	Haplic SOLONETZ (Clayic)
30	Orlovat	Chernozem	Gleyic CHERNOZEM (Loamic, Pachic)
31	Vršački Ritovi	Humogley — marsh swamp soil	Mollic Oxigleyic GLEYSOL (Clayic)
32	Kozjak	Chernozem	Gleyic CHERNOZEM (Loamic, Pachic)
33	Ilandža	Humogley — marsh swamp soil	Mollic Oxigleyic GLEYSOL (Clayic)
34	Idvor	Chernozem	Gleyic CHERNOZEM (Clayic, Pachic)
35	Padina	Chernozem	Haplic CHERNOZEM (Loamic, Pachic)
36	Vršac	Eutric Cambisol	Eutric CAMBISOL (Clayic)
37	Crepaja	Chernozem	Haplic CHERNOZEM (Loamic, Pachic)
38	Deliblato	Chernozem	Haplic CHERNOZEM (Arenic, Pachic)
39	Bavanište	Chernozem	Haplic CHERNOZEM (Loamic, Pachic)
40	Petrovaradin	Eutric Cambisol	Eutric CAMBISOL (Clayic)
41	Šid	Chernozem	Haplic CHERNOZEM (Loamic, Pachic, Stagnic)
42	Rivica	Chernozem	Haplic CHERNOZEM (Clayic, Pachic)
43	Ruma	Chernozem	Haplic CHERNOZEM (Loamic, Pachic)
44	Inđija	Chernozem	Haplic CHERNOZEM (Loamic, Pachic)
45	Morović	Pseudogley	Gleyic, Fluvic, Luvic PLANOSOL (Loamic)
46	Višnjićevo	Pseudogley	Gleyic, Fluvic, Luvic PLANOSOL (Loamic)
47	Sremska Mitrovica	Chernozem	Haplic CHERNOZEM (Clayic, Pachic)
48	Popinci	Chernozem	Gleyic CHERNOZEM (Clayic, Pachic)
49	Donji Tovarnik	Humogley — marsh swamp soil	Mollic Oxigleyic GLEYSOL (Clayic)
50	Kupinovo	Fluvisol	Haplic FLUVISOL (Loamic)

Fig. 2. The RAD7 complete for soil gas measurements (Durridge, 2014).

Fig. 3. Receiver operating characteristic (ROC) for all Multivariate methods used for classification of indoor radon concentration using climate variables. It shows that BDT and MLP methods are the best ones for radon.

Table 2
Correlation coefficients between indoor radon concentration and input variables.

Number	Parameter	Correlation coefficient
1	Elevation	+0.11
2	pH	0
3	CaCO₃	−0.03
4	Humus	+0.15
5	Total N	+0.13
6	P₂O₅	−0.01
7	K₂O	+0.01
8	Coarse sand	−0.08
9	Fine sand	−0.19
10	Powder	+0.16
11	Clay	+0.17
12	Ra-226 30 cm	+0.27
13	U-238 30 cm	+0.17
14	Th-232 30 cm	+0.22
15	K-40 30 cm	+0.10
16	U-238 surface	−0.17
17	Ra-226 surface	+0.04
18	Th-232 surface	0
19	K-40 surface	+0.02
20	Cs-137 surface	−0.17

and discussed on measured soil gas data for Novi Sad districts.

2. Study area

Vojvodina region is located in the Pannonian Basin of Central Europe. The choice of sampling locations was made on the basis of the presence of certain soil types (Škorić et al., 1985) on the Pedological Map of Vojvodina (Nejgebauer et al., 1971) which is shown on Fig. 1. The observed soil types were classified in Table 1 according to the FAO-WRB classification (IUSS, 2014). The dominant soil type at the examined area is Chernozem. Parent material (geological substrate) for this type of soil, and for the largest part of the surface of Vojvodina, is loess — loose sedimentary rock deposited by wind-accumulation in the Pleistocene (during inter-glacial periods).

3. Materials and methods

Indoor radon mapping of Vojvodina Province was performed using the etched track detectors CR39 on about 3000 locations in ground floor rooms during three years from 2002 to 2005. The time of exposure was 90 day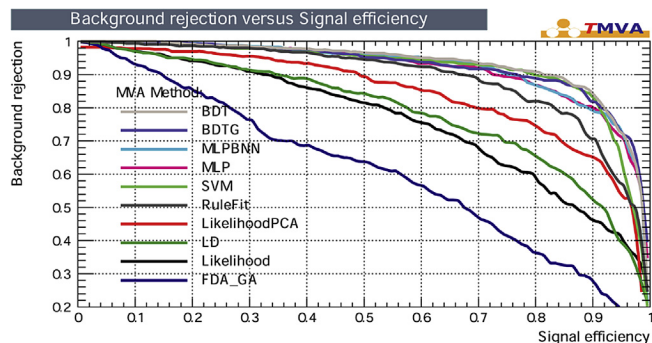s during the winter seasons, from December to March. The etching and counting of tracks were performed by Radosys Company. For this study the average indoor radon concentrations in the nearest village or city to locations of soil sampling were calculated and used in correlation analysis. The results of intercomparison of radon CR-39 detector systems conducted in CLOR's accredited calibration laboratory and quality control data of commercially available Hungarian RadoSys systems are presented and discussed in (Mamont-Ciesla et al., 2010).

For radioactivity measurements from each location of an approximately area 10 × 10 m, 10 subsamples of soil were collected, mixed and homogenized. The soil was sampled from the surface layer (0–10 cm). For chemical analysis soil was sampled by agro-chemical probe to a depth of 30 cm. Soil samples were dried at 105 °C to constant mass. After that all mechanical contaminants, mainly small stone peaces and plant material were removed. Dried soil samples were homogenized as fine powder and measured in cylindrical geometry 62 mm × 67 mm on the cap of HPGe detector. Typical mass of samples was 200 g-300 g and measurement time was 80 ks. Activity concentrations of radionuclides gamma emitters were determined by the method of low-level gamma spectrometry on actively and passively shielded germanium detectors with maximal background reduction. Detector calibrations and quality control measurements were done with certified reference material in cylindrical geometry type CBSS2 supplied by Czech Metrology Institute. Every year laboratory participates with accepted results in world-wide open proficiency tests for gamma spectrometry organized by IAEA Reference Materials Group, Terrestrial Environment Laboratory. The gamma spectra were acquired and analyzed using the Canberra Genie 2000 software. The program calculates the activity concentration of an isotope from all prominent gamma lines after peaked background subtraction. All measurement uncertainties are presented at 95% confidence level. A special procedure developed in the Novi Sad laboratory was used for the determination of the ^{238}U activity concentration from gamma-lines of the first progeny of this radionuclide, ^{234}Th (Bikit et al., 2003).

pH-value was measured in the suspension of soil with water (10 g: 25 cm3) by pH meter PHM62 standard- Radiometar Copenhagen. Content of humus was determined according to method of Tjurin. The total nitrogen content was determined by Kjldahl on the system for digestion and titration Tacator. The available phosphorus and potassium were measured using the extraction with ammonium lactate. For soil characterization purposes, removal of organic matter by H_2O_2 and of carbonates by HCl was carried out. Then, the sample is shaken with a dispersing agent and sand is separated from clay and powder with a 63 μm sieve. The sand is fractionated by dry sieving, and by the pipette method the clay and powder fractions are determined (IUSS, 2014). Particle size in the soil

Table 3
Evaluation results ranked by best signal efficiency and purity (area) It shows that BDT and MLP methods are the best ones for radon. @B is part of Background events classified as Signal events.

MVA method	Signal efficiency at bkg eff.(error):				Separation	Significance
	@B = 0.01	@B = 0.10	@B = 0.30	ROC-integ		
BDT	0.212(16)	0.814(16)	0.959(08)	0.932	0.609	1.614
BDTG	0.243(17)	0.767(17)	0.966(07)	0.927	0.611	1.676
MLPBNN	0.224(17	0.754(17)	0.957(08)	0.922	0.600	1.579
MLP	0.228(17)	0.728(18)	0.955(08)	0.919	0.577	1.540
SVM	0.211(16)	0.797(16)	0.938(09)	0.918	0.587	1.611
RuleFit	0.162(15)	0.671(19)	0.906(12)	0.891	0.482	1.263
LikelihoodPCA	0.000(00)	0.491(20)	0.845(14)	0.843	0.404	1.099
LD	0.047(08)	0.348(19)	0.744(18)	0.789	0.271	0.806
Likelihood	0.031(07)	0.328(19)	0.674(19)	0.764	0.208	0.589
FDA_GA	0.031(07)	0.147(14)	0.363(19)	0.611	0.093	0.353
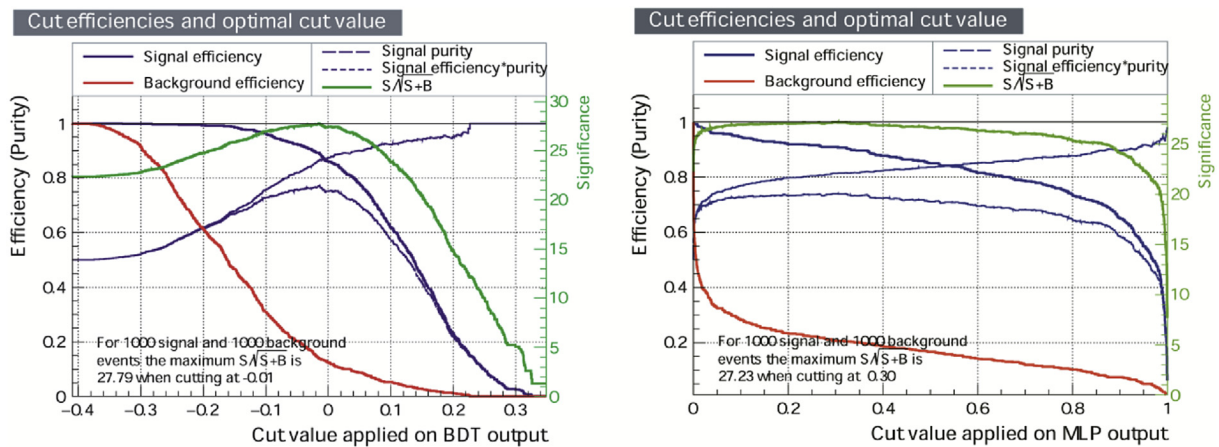
Fig. 4. Cut efficiency and optimal cut value of BDT (left) and MLP (right) classification MVA method for indoor radon concentration.
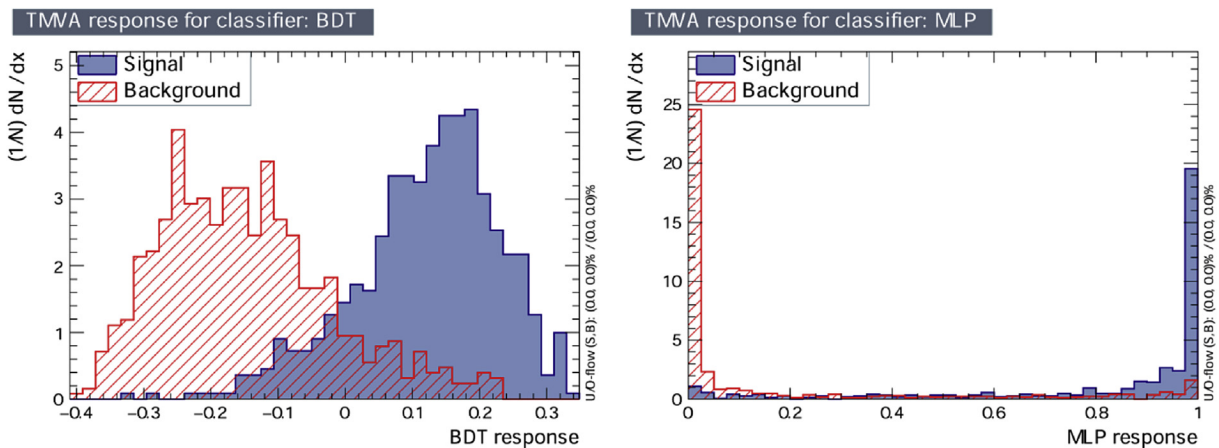
Fig. 5. Distribution of BDT and ANN MLP classification method outputs for input signal and background events.

samples was determined by the pipette method with sodium pyrophosphate as peptizing agent. Based on particle size analysis the following fractions were determined according to IUSS classification: coarse sand (0.2−2 mm), fine sand (0.02−0.2 mm), powder (0.002−0.02 mm) and clay (<0.002 mm).

Soil gas radon activity concentration was measured in situ by RAD7 alpha-spectrometer (DURRIDGE Company) with stainless soil gas probe using grab protocol (Fig. 2). While pumping, the air flow rate is about 0.7 l/min and therefore 3.5 l of soil gas is extracted from the soil at the depth of 70 cm. The last calibration of used

device was performed in radon chamber at the accredited trial metrological Lab. SUJCHBO Kamenna, Czech Republic. Calibration laboratory is traceable to PTB Braunschweig, Germany. After that callibration laboratory participated with RAD7 device in the 2015 NRPI Intercomparison of Radon gas Measurement Instruments with satisfactory results (|zeta score|< 2 − Report number NRPI REG 01-2016, January 2016).

The Toolkit for Multivariate Analysis (TMVA) provides a ROOT-integrated environment for the processing, parallel evaluation and application of multivariate classification and multivariate

Table 4
Variable importance for BDTG MVA method for indoor radon.

BDTG rank	Variable	Variable importance $\times 10^{-2}$
1	Total N	6.490
2	U-238 30 cm	6.425
3	K-40 30 cm	6.040
4	Th-232 30 cm	5.495
5	Humus	5.490
6	K_2O	5.406
7	Clay	5.360
8	U-238 surface	5.218
9	Fine	5.116
10	$CaCO_3$	5.081
11	P_2O_5	5.003
12	Cs-137 surface	4.715
13	Ra-226 30 cm	4.656
14	Elevation	4.595
15	K-40 surface	4.509
16	pH	4.435
17	Ra-226 surface	4.188
18	Powder	4.082
19	Th-232 surface	4.026
20	Coarse	3.671
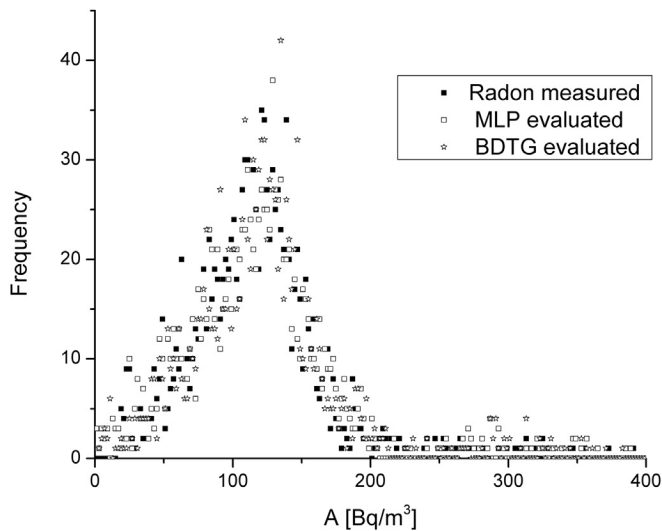
Fig. 6. Distribution of indoor radon concentrations and outputs from MLP Multivariate regression method's evaluation for of indoor radon concentration.

regression methods. All multivariate methods in TMVA belong to the family of "supervised learning" algorithms. They make use of training events, for which the desired output is known, to determine the mapping function that either describes a decision boundary (classification) or an approximation of the underlying functional behavior defining the target value (regression). The two most important Multivariate methods for our purposes are "Boosted Decision Trees" (BDT) and "Artificial Neural Networks" (ANN).

Boosted Decision Trees (BDT) have been successfully used in High Energy Physics analysis for example by the MiniBooNE experiment (Hai-Jun et al., 2005). In BDT, the selection is done on a majority vote on the result of several decision trees. However, the advantage of the straightforward interpretation of the decision tree is lost.

An Artificial Neural Network (ANN) (Rojas, 1996) is most generally speaking any simulated collection of interconnected neurons, with each neuron producing a certain response at a given set of input signals. ANNs in TMVA belong to the class of Multilayer Perceptrons (MLP), which are feed-forward neural networks.
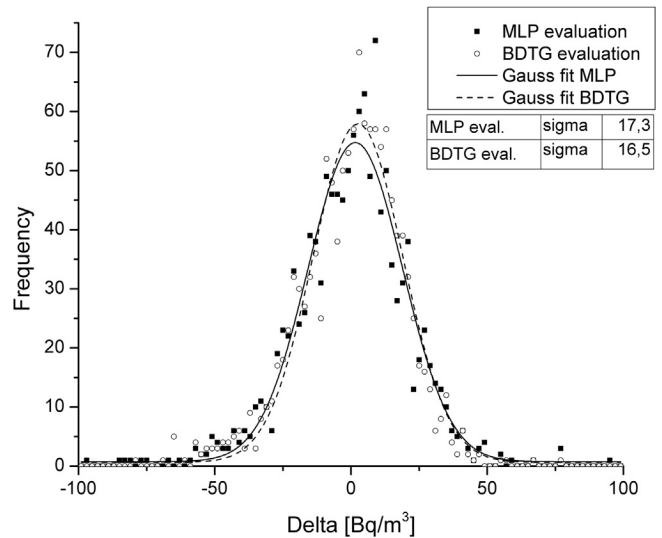
Fig. 7. Distributions of differences of outputs from MLP Multivariate regression method and measured indoor radon concentrations.

4. Results and discussion

Table 2 shows linear correlation coefficients, which tells us how big is the correlation of input variable and indoor radon concentration. We can notice that radon is more correlated to radioisotopes at depth of 30 cm.

In order to use MVA methods, the sample has to have significant statistics. Since set intended to be used in this analysis does not have enough statistics, we artificially increased the sample by introducing of copy of same sample events, but with modified values of input and measured radon concentrations multiplying initial value with 1 + random Gaussian values with sigma 1/10. We are using the input events (set of soil sample properties and radionuclides activity in 30 cm depth and on surface) to train, test and evaluate the 12 multivariate methods implemented in TMVA. The graph presenting the "Receiver operating characteristic" (ROC) for each multivariate method (Fig. 3) may be considered as the most indicative in comparing the different methods used for classification of radon concentrations using climate variables. On this graph one can read the dependence of background rejection on signal efficiency. The best method is the one that holds maximum value of background rejection for highest Signal efficiency (Table 3), i.e. the best method has ROC curve closest to the upper right corner on the graph presented in Fig. 3. It turns out that the method best suited for our purpose is the Boosted Decision Trees (BDT) method. This means that BDT gives most efficient classification of input events. This is seen in Fig. 4, which shows the distribution of BDT classification method outputs for input signal and background events. The second best method is the implementation of ANN Multilayer Perceptrons (MLP).

In Fig. 4, one can see the values of signal and background efficiency and significance. Significance, calculated as N(Signal)/sqrt(N(Signal)+N(Background)), can be used as the value for comparison of various multivariative methods, and also for comparison of method efficiencies for different sets of input variables.

Fig. 5 shows the distribution of BDT classification method outputs for input signal and background events. These figures again demonstrate that classification methods work well i.e. that the separation of signal and background works very good. Also, the significance value for BDT is higher for higher cut values for splitting of input events. Interestingly, it appears that other multivariate
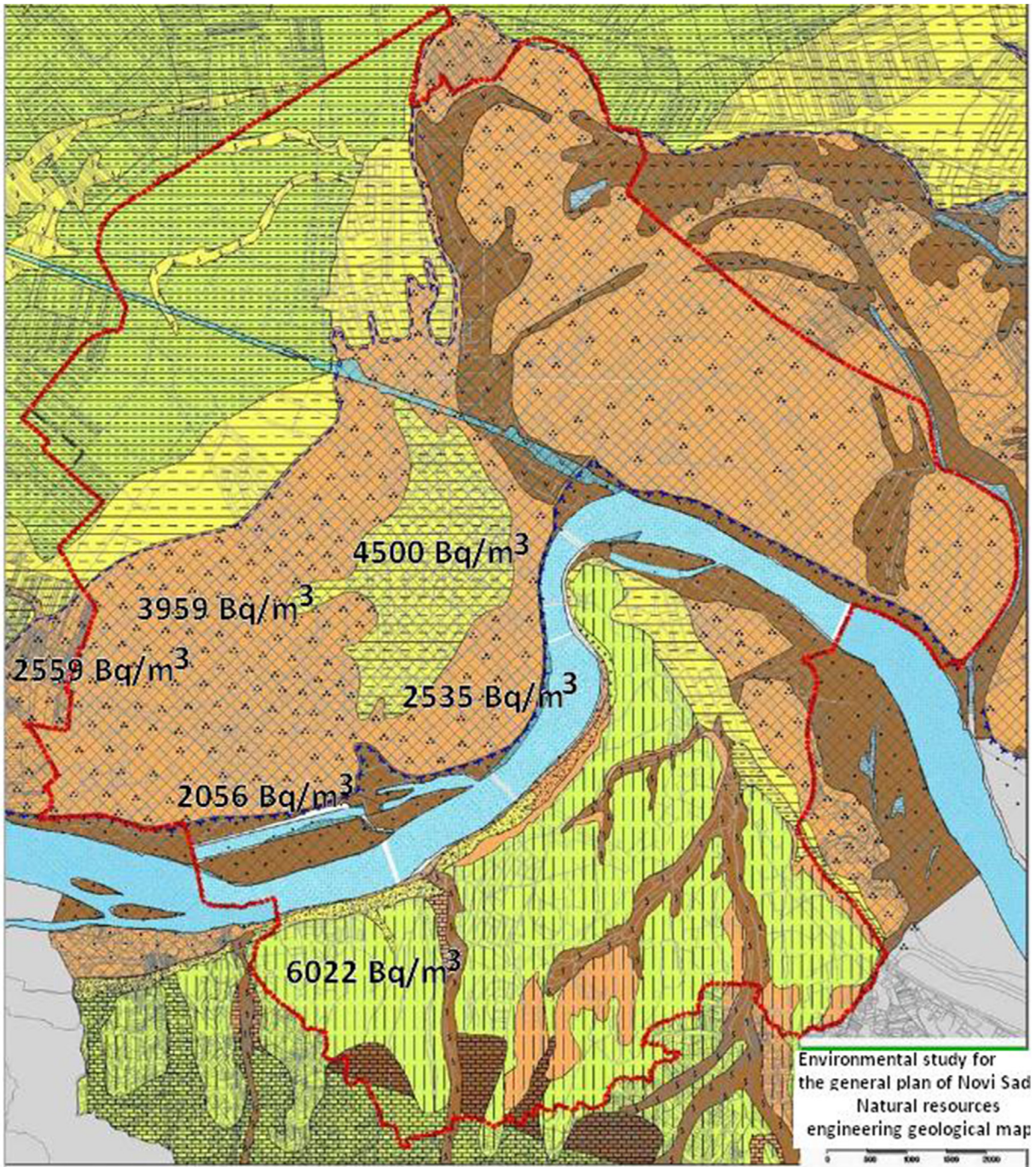
Lithological classification

- contemporary riverbanks fine sandy
- older riverbanks sandy clay
- sediments old lakes and swamps rich in organic matter
- sediments of new swamps
- sediments of loess valley
- redeposited loess
- loess clay
- unchanged loess
- Delluvial gravel-sandy clay
- Tertiary (clay, marl, conglomerates, clays, sands)
- Mesozoic flysch
- Eruptive rocks

Fig. 8. Lithological map of Novi Sad city (Obrknežev et al., 2009) with maximal soil gas radon activity concentrations measured in six parts of the city.
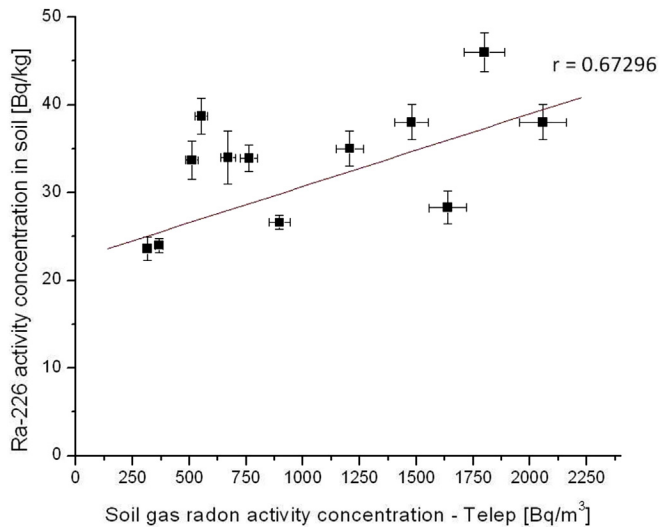
Fig. 9. Correlation between radium activity concentrations in the soil and soil gas activity concentrations for Telep district.
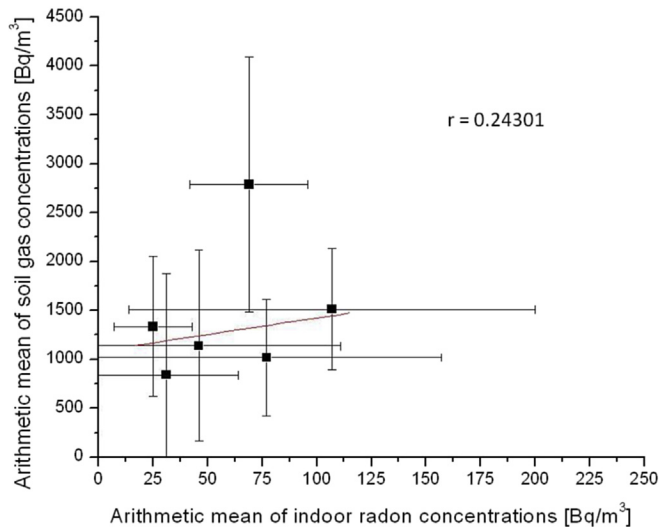

Fig. 10. Correlations between arithmetic means of soil gas concentrations and indoor radon activity concentrations with standard deviations (error bars) for six districts of Novi Sad city.

methods also give better results under these new conditions.

Ranking of the BDTG input variables (Table 4) is derived by counting how often the variables are used to split decision tree nodes, and by weighting each split occurrence by the separation it has achieved and by the number of events in the node. As seen from Table 4, besides Total N, radionuclides on 30 cm depth appears to be the most important variables for indoor radon.

Regression is the approximation of the underlying functional behavior defining the target value. We tried to find the best regression method that will give output values (predicted indoor radon concentration) closest to the actual concentrations that corresponds to specific input variables. The best multivariate regression method is found to be BDT, and the second one is MLP, same as in case of multivariate classifiers. Fig. 6 presents the distribution of indoor radon concentrations and outputs from the MPL multivariate regression method evaluation of radon concentration using all input variables.

To best way to estimate the quality of the method is to look at the differences between the output values from MLP multivariate regression method and the values of measured indoor radon concentrations (Fig. 7). The figure indicates the good predictive power of multivariate regression methods as applied for prediction of variations of indoor radon concentrations based on full set of input variables.

In the city of Novi Sad Laboratory for dose and radioactivity measurements performed soil gas measurements by active device RAD7 coupled with soil gas probe on about 100 locations divided in 6 districts of the city. In order to verify previously obtained correlations we analyzed in detail all available parameters: radionuclide contents of the soil, average indoor radon concentrations in each district, maximal and average soil gas concentrations for each district and geomorphologic units. Results are shown on Figs. 8–10 and in Table 5. Indoor radon concentrations were measured by gamma spectrometry method using charcoal canisters for radon adsorption. The MDA for this technique of indoor radon measurement is about 2 Bq/m³ and the measurement uncertainty depends on count rates in post radon gamma lines, detector efficiency and charcoal water gain.

The effects of radium activity concentrations in deep layers of examined soil to indoor radon concentrations were analyzed through linear correlations and the results are shown on Figs. 9 and 10. We used Pearson correlation coefficient based on a comparison of the actual impact of observed variables to one another in relation to the maximum potential impact of the two variables (1) and obtained almost high positive correlation between radium activity concentrations in soil and soil gas concentrations (r = 0.67296) and low positive correlation between arithmetic means of soil gas concentrations and indoor radon activity concentrations (r = 0.24301).

$$r = \frac{\sum_i x_i y_i - \frac{1}{n}\sum_i x_i \sum_i y_i}{\sqrt{\left[\sum_i y_i^2 - \left(\frac{1}{n}\right)\left(\sum_i y_i\right)^2\right]\left[\sum_i x_i^2 - \left(\frac{1}{n}\right)\left(\sum_i x_i\right)^2\right]}} \quad (1)$$

5. Conclusion

In the paper the possibility of multivariate analysis application for radon potential estimation is described in detailed. The most appropriate multivariate method of analysis of indoor radon measurements is selected from a wide spectrum of multivariate methods developed for data analysis in high-energy physics and implemented in the Toolkit for Multivariate Analysis software package. The evaluation ranking results based on the best signal efficiency and purity, show that the Boosted Decision Trees (BDT) and Multi Layer Perceptron (MLP), based on Artificial Neural Network (ANN), are multivariate methods which give the best results in the analysis. Further multivariate analysis results give insight into the dependence of indoor radon concentrations with other radionuclides activity both 30 cm underground and on surface during the time of measurements, as well as soil properties variables. The BDTG multivariate method shows that variables with the highest importance are radionuclides activity in deep layers compared with the activity of surface layer, but also the humus and clay content (Table 4). Moreover, the multivariate regression methods give a good approximation of indoor radon activity using full set of input variables.

This study showed that radiogeochemical data are useful to generate maps of radon priority areas. We confirmed the assumption that the soil types which contain the highest content of clay

Table 5
Comparison of available data for each analyzed district of Novi Sad city with the description of geomorphologic unit and the number of samples that were considered. Numbers in brackets are the standard deviations for the average values and the measurement uncertainties for measured values in the range column.

City district (Geomorphologic unit)	Average of soil gas concentrations [Bq/m³]	Range of soil gas concentrations [Bq/m³]	Average of indoor radon concentrations [Bq/m³]	Range of indoor radon concentrations [Bq/m³]	Average of Ra-226 concentrations in soil [Bq/kg]	Range of Ra-226 concentrations in soil [Bq/kg]
Telep (Contemporary riverbanks, fine sandy) 13 samples	1020(596)	315(16)−2056(105)	77(80)	4(2)−313(8)	33(7)	23,6(13)−46,0(22)
Detelinara (Loess clay) 29 samples	1138(976)	312(17)−4500(220)	46(65)	4(2)−345(14)	30(7)	14,1(14)−45(2)
Liman (Older riverbanks, sandy clay) 17 samples	1334(715)	230(12)−2535(130)	25(18)	6(2)−74(5)	27(7)	14,9(14)−40,5(21)
Veternik (Older riverbanks, sandy clay) 16 samples	1512(616)	104(7)−2559(132)	107(93)	34(4)−276(8)	32(5)	22,3(14)−41(2)
Novo Naselje (Older riverbanks, sandy clay) 19 samples	840(1033)	122(8)−3959(198)	31(33)	4(2)−92(6)	31(6)	19(2)−44(2)
Sremska Kamenica (Unchanged loess) 14 samples	2787(1306)	1582(80)−6022(302)	69(27)	38(4)−110(6)	36(7)	19,9(16)−43,5(17)

and humus best adsorb and retain radon which is reflected in elevated soil gas radon concentrations and higher geogenic radon potential. This conclusion could be used for selection of locations for planning radon permeability measurements. The best correlation of radon concentrations with total nitrogen amount in the soil is very interested result and it will be studied in next research.

The results of detailed analysis of databases for radon and soil radioactivity measurements for the city of Novi Sad validated geogenic prognosis that soil gas radon concentrations mostly depend on geomorphologic units and litologic distribution in study area. Good agreement of radium content in soil samples and radon soil gas activity concentrations obtained.

The multivariate regression methods used gives as a result a "mapped" functional behavior of indoor radon and input variables. Using this "mapped" function, the search for radon priority areas is straightforward. The best performing multivariate methods identified most important variables, and help with simplification of "mapped" function which then requires smaller number of input variables. Further analysis of "mapped" function can point to which are the most important mechanisms for increase of indoor radon concentrations.

So the multivariate methods can be used in identifying the most significant variables, help identify radon priority areas, and help with physics analysis of processes of radon emanation.

Acknowledgements

References

Bikit, I., et al., 2003. Simple method for depleted uranium determination. Jpn. J. Appl. Phys. 42, 5269−5273.

Bikit, I., et al., 2005. Radioactivity of the soil in Vojvodina (northern province of Serbia and Montenegro). J. Environ. Radioact. 78, 11−19.

Brun, R., Rademakers, F., 1997. Root − an object oriented data analysis framework. Nucl. Inst. Meth. Phys. Res. A 389, 81.

De Cort, M., et al., 2011. Towards a European atlas of natural radiation: goal, status and future perspectives. Radioprotection 46, 737−743.

Durridge, 2014. RAD7 Radon Detector User Manual, Revision 7.26. DURRIDGE Company. http://www.durridge.com/documentation/RAD7Manual.pdf.

EURATOM, 2013. Council Directive 2013/59/EURATOM of 5 December 2013 Laying Down Basic Safety Standards for Protection against the Dangers Arising from Exposure to Ionising Radiation, and Repealing Directives 89/618/Euratom, 90/641/Euratom, 96/29/Euratom, 97/43/Euratom and 2003/122/Euratom, Article 74 Indoor Exposure to Radon. http://eur-lex.europa.eu/LexUriServ/LexUriServ.do?uri=OJ: L:2014:013:0001:0073:EN: PDF.

Forkapić, S., et al., 2007. Indoor radon in rural dwellings of the south-Pannonian region. Radiat. Prot. Dosim. 123, 378−383.

Gruber, V., et al., 2013. The European map of geogenic radon potential. J. Radiol. Prot. 33, 51−60.

Hai-Jun, Y., et al., 2005. Studies of boosted decision trees for MiniBooNE particle identification. Nucl. Instrum. Meth. A555, 370−385. http://arxiv.org/abs/physics/0508045.

Hoecker, A., et al., 2007. TMVA − Toolkit for Multivariate Data Analysis. PoS ACAT 040, arXiv:physics/070303.

IUSS Working Group WRB, 2014. World reference base for soil resources 2014. In: International Soil Classification System for Naming Soils and Creating Legends for Soil Maps. World Soil, 106. FAO, Rome.

Košćal, M., et al., 2005. Geomorphological Map of Vojvodina with Legends. Geo-zavod − Gemini, Beograd.

Mamont-Cieśla, K., et al., 2010. Intercomparison of radon CR-39 detector systems conducted in CLOR's calibration chamber. Nukleonika 55 (4), 598−593.

Nejgebauer, V., et al., 1971. The Pedological Map of Vojvodina (R 1 : 50.000). Institute for Agricultural Research, Novi Sad.

Obrknežev, R., et al., 2009. The Study of Environmental Protection in the City of Novi Sad, Public Enterprise "Urbanizam". Department of Urban Planning, Novi Sad.

Rojas, R., 1996. Neural Networks. Springer-Verlag, Berlin.

Škorić, A., et al., 1985. Classification of soils in Yugoslavia, academy of Sciences and arts of Bosnia and Herzegovina special editions, book LXXVIII, Sarajevo.

UNSCEAR, 2008. Ionizing Radiation: Sources and Effects, UNSCEAR 2008 REPORT, VOLUME II. United Nations, New York. http://www.unscear.org/unscear/en/publications/2008_1.html.

WHO, 2009. In: Handbook on Indoor Radon − a Public Health Perspective. www.who.int/ionizing_radiation/env/radon/en/imdex1.html.

Production of ^{117m}Sn and ^{119m}Sn by photonuclear reactions on natural antimony

M. Krmar[1], N. Jovančević[1], Ž. Medić[2], D. Maletić[2], Yu. Teterev[3], S. Mitrofanov[3], K. D. Timoshenko[3], S. I. Alexeev[3], H. Marukyan[4], I. Kerobyan[4], R. Avetisyan[4], R. Dallakyan[4], A. Hakobyan[4], L. Vahradyan[4], H. Mkrtchyan[4], A. Petrosyan[4], H. Torosyan[4]

[1]Physics Department, Faculty of Science, University Novi Sad, Serbia

[2]Institute of Physics, Belgrade, Serbia

[3] Flerov Laboratory of Nuclear Reactions, Joint Institute for Nuclear Research, Dubna, Russia

[4]A.Alikhanyan National Science Laboratory (Yerevan Physics Institute), Yerevan, Armenia

Abstract

Natural antimony targets were irradiated in a 60 MeV bremsstrahlung beam and gamma spectrometric measurements were performed. The goal was to establish the yield of ^{117m}Sn, a radionuclide with great potential for application in medicine. Considering that ^{117m}Sn is predominantly produced through a photonuclear reaction in which an charged particle is emitted (^{121}Sb(γ,p3n)), the yield of this tin isotope is much lower than the yields of several antimony isotopes produced in (γ,xn) reactions. It has been estimated that photonuclear reactions on natural antimony could produce ^{117m}Sn activities needed for therapeutic applications, with accelerators having electron currents of the order of mA. For the used bremsstrahlung energy of 60 MeV, it was estimated how much ^{119m}Sn activity can be expected when exposing the antimony target.

Key words: photonuclear reactions, ^{117m}Sn production, 60 MeV bremsstrahlung

1. INTRODUCTION

Photonuclear reactions represent a very interesting field in which the nucleus, as a system determined by a strong interaction, is subjected to electromagnetic forces. This reactions are conducted by the interaction of high-energy electromagnetic radiation (10 MeV and more) with nuclei of the selected target. The process of the highest probability is emission of one neutron. If the energy of the electromagnetic radiation is high enough, the excited nucleus can emit two of more neutrons, with lower probability. Protons and other charged particles can leave the nucleus, but with a much lower probability due to the effect of the Coulomb barrier.

Electromagnetic nature of interaction makes photonuclear reactions a suitable method for studies of the nucleus and some of its properties. Photonuclear reactions have become a convenient method in number of basic research (Zilges et al., 2022; Pietralla et al., 2019). Besides that, they could be quite acceptable way for production of radionuclides. The need for the production of radionuclides used in medicine is particularly important (Qaim, 2017). In currently established practice, certain number of neutron-deficient radionuclides and positron sources, usually are produced by proton cyclotrons (IAEA, 2021). However, some of them can be obtained through photonuclear reactions.

The main objective of this work is to check feasibility of ^{117m}Sn producing in photon beams of high energies, up to several tens of MeV. Tin isotope ^{117m}Sn has shown extremely promising properties in the process of theranostics (Lewington, 2005). The 158.562 keV gamma radiation (Blachot, 2002), emitted after de-excitation of the isomeric state is almost ideal for SPECT diagnostic purposes, while the large number of conversion electrons (113% emission probability) can provide a high local dose at some specific location where the radiopharmaceutical labeled with this isotope would be accumulated.

In order to obtain high specific activities of ^{117m}Sn, several different nuclear reactions using charged particles were taken in consideration (Stevenson et al., 2015). Two most important directions were using proton beams (Ermolaev et al.,2009) and alpha particles (Aslam et al., 2018; Aikava et al., 2018; Ditrói et al., 2016; Duchemin et al., 2016; Maslov et al., 2011). Photonuclear reactions for production of ^{117m}Sn were not frequently studied. Couple attempts was made to get ^{117m}Sn by (γ,γ`) reaction on enriched ^{117}Sn target (Aksenov et al., 1992; Gerbish et al., 2006). In present paper, the possibility of producing ^{117m}Sn by photonuclear reactions on a target made of natural antimony in 60 MeV bremsstrahlung beam was analyzed. Natural antimony contains two isotopes, ^{121}Sb and ^{123}Sb. For the purposes of this study, the reactions ^{121}Sb(γ,p3n) and ^{123}Sb(γ,p5n) are considered. Photonuclear reactions in which no charged particles are emitted, ^{121}Sb(γ,4n) and ^{123}Sb(γ,6n), have significantly higher cross sections, but unfortunately they do not lead to the creation of ^{117m}Sn after beta decay (EC) of produced ^{117}Sb.

Several isotopes of the target element are usually obtained through (γ,xn) nuclear reactions. In this case, several neutron deficient active isotopes of Sb can be obtained, depending on endpoint

2

energy of used bremsstrahlung beam. All of them, after EC create Sn daughter nuclei. It is particularly interesting to see to what extent the produced ^{117m}Sn would be contaminated by the activity of other products of possible photonuclear reactions. In this work, special attention is paid to ^{119m}Sn, which would be created through two photonuclear reactions.

1. MATERIALS AND METHODS

1.1 Expected nuclear reactions

Natural antimony consists of two isotopes: ^{121}Sb (57.36%) and ^{123}Sb (42.64%). Relevant part of the isotope chart is presented in Figure 1. During exposure of a natural antimony target to a flux of high-energy photons, several types of nuclear reactions occur.

a) (γ,n) and (γ,xn) reactions

Several antimony isotopes, (depending on the endpoint energy of the bremsstrahlung beam used in experiment) could be produced in reactions with emission of one or more neutrons. Both ground state and Sb isomers are created. Besides ^{122}Sb, which decays mostly (97.6%) to ^{122}Te through the emission of a beta particle, all other Sb isotopes decay through electron capture. It can be seen (Figure 1) that in this way stable tin nuclei will be formed. Two of the stable tin isotopes have isomers ^{117m}Sn and ^{119m}Sb, however decays of ^{117}Sb and ^{119}Sb do not populate their metastable states. This means that no Sn activity should be expected after decay of antimony isotopes created in (γ,n) and (γ,xn) reactions. If Sn fraction is chemically extracted from the irradiated antimony target, the output of (γ,n) and (γ,xn) reactions can estimate how much non-active Sn would be obtained together with ^{117m}Sn, produced in some other reactions.

Sb116	Sb117	Sb118	Sb119	Sb120	Sb121	Sb122	Sb123
15.8 m	2.80 h	3.6 m	38.19 h	15.89 m	Stable	2.7238 d	Stable
3^+	$5/2^+$	1^+	$5/2^+$	1^+	$5/2^+$	2^-	$7/2^+$
EC	EC	EC	EC	EC	57.36 %	EC, β$^-$	42.64 %
Sn115	**Sn116**	**Sn117**	**Sn118**	**Sn119**	**Sn120**	**Sn121**	**Sn115**
Stable	Stable	Stable	Stable	Stable	Stable	27.06 h	Stable
$1/2^+$	0^+	$1/2^+$	0^+	$1/2^+$	0^+	$3/2^+$	$1/2^+$
0.34 %	14.53 %	7.68 %	24.23 %	8.59 %	32.59 %	β$^-$	0.34 %
In114	**In115**	**In116**	**In117**	**In118**	**In119**	**In120**	**In121**
71.9 s	4.41E+14y	14.10 s	43.2 m	5.0 s	2.4 m	3.08 s	23.1 s
1^+	$9/2^+$	1^+	$9/2^+$	1^+	$9/2^+$	1^+	$9/2^+$
EC, β$^-$	β$^-$, 95.7 %	EC, β$^-$	β$^-$	β$^-$	β$^-$	β$^-$	β$^-$

Figure 1. Part of the isotope chart presenting Sb, Sn and In isotopes of interest

3

b) (γ,p) and (γ,pxn) reactions

If one proton (with or without neutrons) is emitted during the irradiation of the Sb target, tin isotopes will be formed. All of Sn isotopes created in this way are stable, with exception of ^{121}Sn. This isotope is formed in ^{123}Sb(γ,pn) reaction in the ground state, but also as an isomer. After decay of the ground state of ^{121}Sn, beta radiation of relatively low energy (Q value: 390.1 keV) is emitted without the emission of gamma radiation. The ^{121m}Sn has a half-life of 55 years and low activity would be created in photon beam. Additionally, it could be expected that ^{119m}Sn and ^{117m}Sn isomers will be created (half lifes 293.1 days and 13.6 days, respectively). Sn-119m can be formed in ^{121}Sb(γ,pn) and ^{123}Sb(γ,p3n) reactions. Another isomer, ^{117m}Sn can be produced in ^{121}Sb(γ,p3n) and ^{123}Sb(γ,p5n) reactions, if the endpoint energy of bremsstrahlung is high enough.

Sn-117m has very suitable characteristics for use in medicine. The scheme of de-excitation of the metastable state is shown in Figure 2. The gamma radiation energy emitted is almost ideal for diagnostic procedures. The transitions of 314.3 keV and 156.2 keV are almost entirely realized by the emission of conversion electrons. It was estimated that 1.13 conversion electrons are emitted per one decay of ^{117m}Sn. Due to the low penetrating power, these electrons in the tissues deposit their energy in a small space around the location where the radiopharmaceutical labeled with ^{117m}Sn accumulates. In this way, a therapeutic dose can be deposited in a controlled area.
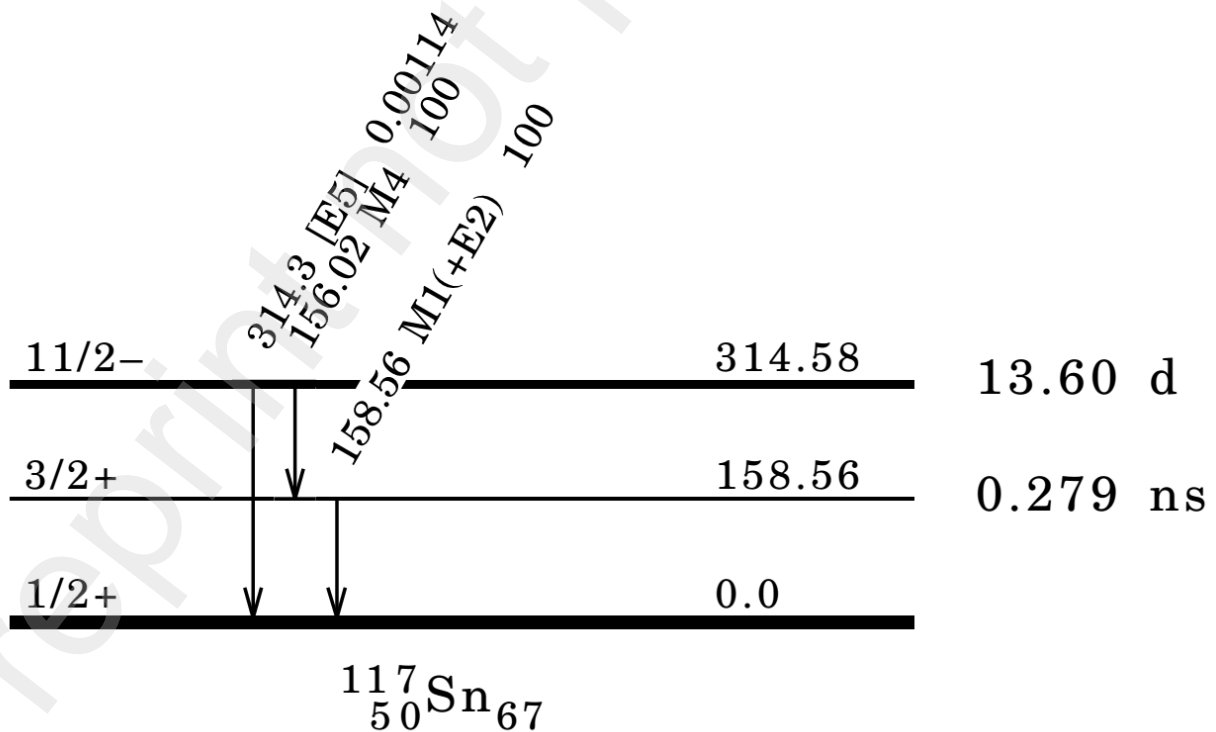
Figure 2. Decay scheme of ^{117m}Sn. For absolute intensities of transitions, multiply by 0.864

The decay scheme of ^{119m}Sn is shown in Figure 3. During the de-excitation of the metastable state of 89.53 keV, gamma radiation of energy 23.87 keV is emitted. It is determined that 0.161 photons are emitted per decay. Such low energy photon radiation has very little chance of leaving the patient's body, so it cannot be used for diagnostic purposes in nuclear medicine. It was measured that the transitions shown in Figure 3 are realized to the greatest extent by the emission of conversion electrons. It is estimated that 1.83 conversion electrons are emitted per ^{119m}Sn decay. These electrons could also play a significant role in radionuclide therapy.
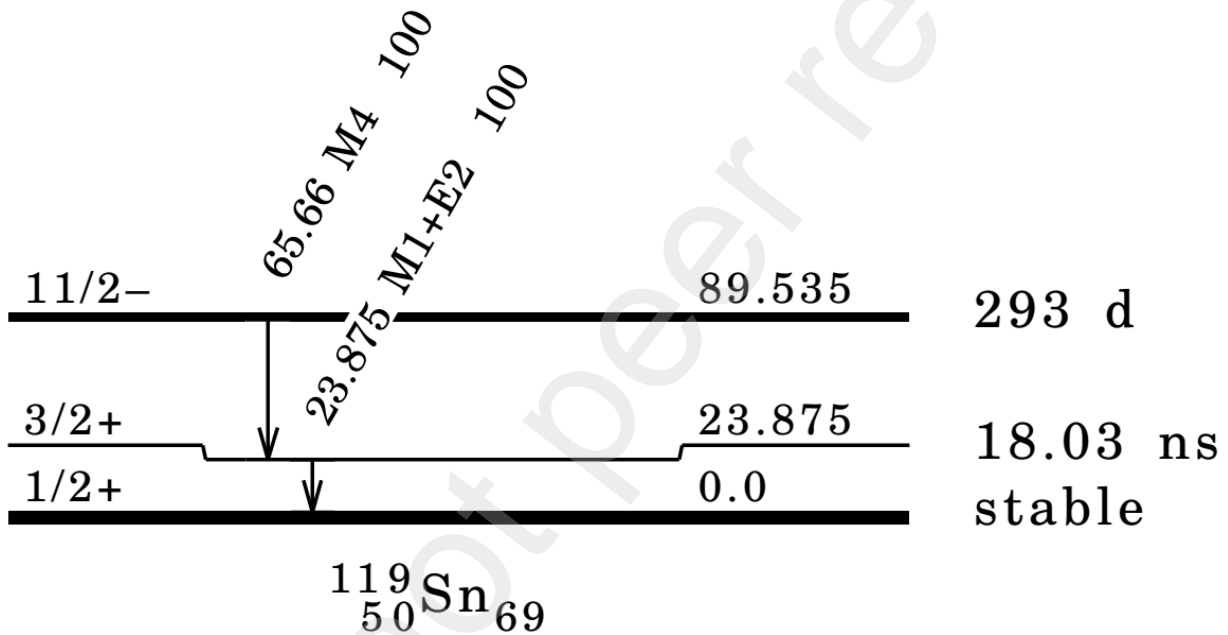
Figure 3. Decay scheme of ^{119m}Sn.

c) (γ,α), $(\gamma,\alpha n)$ and $(\gamma,\alpha xn)$ reactions

Additional interesting possibility, which could be expected during exposition of antimony target in high energy photon beams, is emission of alpha particle, with or without neutrons. Reactions (γ,α), $(\gamma,\alpha n)$, $(\gamma,\alpha 2n)$, etc. will produce indium isotopes. In the simplest case, when just an alpha particle is emitted after interaction of high energy photons with ^{123}Sb, isotope of indium ^{119}In would be created. It is the heaviest isotope of indium that can be formed in this way. Considering that the half-life of ^{119}In is 2.4 min, it is unlikely that it will be identified in an off-line gamma radiation measurement. The same is with ^{118}In, which has a half-life of 5 sec. Just ^{117}In and lighter isotopes could be detected in some standard off-line gamma spectroscopy measurements.

The decay of the ground state of ^{117}In populates the isomeric state ^{117m}Sn to a very small extent (0.344%), while the decay of the isomer ^{117m}In completely bypasses it.

It should be emphasized that after the decay of ^{117}Sb, as well as the decay of both the ground and isomer states of ^{117}In, the emission of photon radiation of 158.56 keV occurs. This is also the only gamma radiation emitted after de-excitation of the 314.58 keV isomeric state of ^{117m}Sb, which complicates the interpretation of gamma spectra recorded immediately after the irradiation of the antimony target. The half-life of ^{117}Sn is 2.8 days, while ^{117}In and ^{117m}In have half-life of 43.2 min and 116.2 min, respectively, which is significantly shorter than the half-life of ^{117m}Sn. In repeated measurements after a sufficiently long time interval, the presence of ^{117m}Sn in the irradiated sample can be determined.

d) (n,γ) reactions

The production of bremsstrahlung radiation with endpoint energies higher than the binding energy of neutrons in the nuclei of irradiated materials leads to the emission of neutrons. The sources of neutrons are usually a bremsstrahlung converter, collimators, filters and all other materials affected by the photon beam. These neutrons can be captured by the nuclei of the target material. It is most likely that ^{122}Sb and ^{124}Sb are formed in the interactions of neutrons and Sb target nuclei. The easiest way to assess the presence of neutrons at the location of the irradiated target is to identify the gamma lines of ^{124}Sb. The half-life of this radionuclide is 60.20 days, so for its identification purposes, the spectrum recorded three days after irradiation was used. Only two gamma lines of 602.73 keV (97.8%) and 1690.98 keV (47.3%) were observed in the spectrum. The intensity of these gamma lines in the measured spectrum is four orders of magnitude lower than the ^{120m}Sb gamma lines, which have a similar quantum yield. In addition, in the spectrum of the gold foil exposed together with the Sb target, a gamma line of 411.8 keV can be observed. This gamma transition originates from ^{198}Au produced by the capture of neutrons on ^{197}Au. Based on these three very weak lines, it was estimated that the neutron capture does not give activities that can be compared with the activities obtained through photonuclear reactions and that the contribution of (n,γ) reactions can be neglected.

1.2 Reaction yields

Considering that antimony consist of two isotopes, ^{121}Sb (57.36%) and ^{123}Sb (42.64%), in some cases, one product of photonuclear reaction can be formed in two different ways. Total activity of observed product can be result of two reactions, whose probabilities are defined by the cross sections $\sigma_i^{121}(E)$ and $\sigma_i^{123}(E)$ for observed i-th reaction. Atomic number of parent nuclei is denoted in superscript. The yield of some isotope, identified in gamma spectrum of antimony target, in some general case can be expressed as:

6

$$\frac{m_t}{M} N_{av} \left(0.5726 \int_{E_t^i}^{E_{max}} \sigma_i^{121}(E) \cdot \Phi(E) \cdot dE + 0.4264 \int_{E_t^i}^{E_{max}} \sigma_i^{123}(E) \cdot \Phi(E) \cdot dE \right)$$

$$= \frac{N_\gamma \lambda}{\varepsilon \, p_\gamma e^{-\lambda \Delta t} \left(1 - e^{-\lambda t_{irr}} \right)(1 - e^{-\lambda t_m})} \qquad (1)$$

where m_t and M are the mass of the exposed target used in experiment and the atomic mass number, N_{Av} is Avogadro number, E_t^i is the energy threshold for observed nuclear reaction and E_{max} is the maximal energy of photons, $\Phi(E)$ is flux of photons, N_γ is the number of detected gamma photons of chosen energy, λ is the decay constant, ε is absolute peak efficiency of the detector at the chosen energy, p_γ is the quantum yield of detected photons, Δt, t_{irr} and t_m are cooling, irradiation and measurement time respectively.

For brevity, the above equation can be represented as:

$$\frac{m_t}{M} N_{av} \left(0.5726 \, R_i^{121} + 0.4264 \, R_i^{123} \right) = \frac{N_\gamma \lambda}{\varepsilon \, p_\gamma e^{-\lambda \Delta t} \left(1 - e^{-\lambda t_{irr}} \right)(1 - e^{-\lambda t_m})} \qquad (2)$$

Integrals denoted by symbol R are called saturation activities. A common way is to divide Equation (1) or Equation (2) by the term $\frac{m_t}{M} N_{av}$. In this way, the right-hand side of the equation yields the total saturation activity that can be determined from gamma spectroscopic measurements. In our case, it would be the sum of two saturation activities weighted by the abundances of isotopes ^{121}Sb and ^{123}Sb in the natural element.

Immediately after irradiation of the antimony target, several gamma spectra should be recorded, to identify short-living products of photonuclear reactions. It is very important to record gamma spectra of antimony target several days after irradiation, to get evidence about long-living radionuclides. The next step would be to determine the intensities of the characteristic gamma lines in the spectrum, in order to determine the experimental values of the yields (or saturation activity) of the identified products based on the right side of the Equation (1).

In this way, the output of all those photonuclear reactions that produce an unstable nucleus that emits gamma radiation of sufficiently high energy and intensity can be determined. There are several photonuclear reaction products whose yields cannot be determined from measured gamma spectra. Such is, for example, the isomer ^{119m}Sn reaching the ground state by the emission of low-energy gamma radiation of 23.87 keV, which could not be measured with the available detector.

In similar cases, the yield of the nuclear reaction was estimated computationally, as shown in the left side of Equation (1). For the purposes of this evaluation, it is necessary to have the differential cross sections $\sigma_i^{121}(E)$ and $\sigma_i^{123}(E)$ of the reaction that produces the observed nucleus as a product, as well as the value of the photon flux $\Phi(E)$. Differential cross sections for

photonuclear reactions in which multiple particles are emitted can be rarely found in the literature, so theoretical estimates obtained with TALYS or a similar code should be used. The function describing the photon flux can be obtained by simulation, if the geometry of the bremsstrahlung production is well known. The normalization of the obtained photon flux function can be performed by activating some material having the differential cross section for some photonuclear reaction well known. In this experiment, a gold foil and a well-known cross section for a $^{197}Au(\gamma,n)^{196}Au$ nuclear reaction was used to calibrate the photon beam.

1.3 Ratio of ^{117m}Sb and ^{119m}Sb activities

The aim of this work is to check the possibility of producing ^{117m}Sb through photonuclear reactions. Based on Section 1.1, it can be expected that in the case of complete chemical separation of the tin fraction from the irradiated Sb target, the activity of ^{117m}Sn and the gamma line at 158.56 keV would remain. This certainly does not mean that ^{117m}Sn is the only active isotope of tin that can be expected in this experiment. During the exposure of the antimony target, ^{119}Sb is formed as a product of $^{121}Sb(\gamma,2n)$ and $^{123}Sb(\gamma,4n)$ reactions. The half-life of this antimony isotope is 38.19 h. It decays through an electron capture and populates ^{119}Sn excited state of 23.87 keV. The gamma radiation emitted by the de-excitation of this state is not noticeable in the measured spectra due to the low efficiency of the available detector in the low-energy region. The ^{119}Sn nucleus has a metastable state of 89.53 keV, but it is not populated by the decay of ^{119}Sb.

There is a possibility that the creation of ^{119m}Sn also occurs through $^{121}Sb(\gamma,pn)$ and $^{123}Sb(\gamma,p3n)$ reactions. Considering that the cross section for photonuclear reactions decreases very sharp with the number of emitted particles, it can be considered that the probability of creation of ^{119m}Sn is higher than the probability of creation of ^{117m}Sn.

The low energy of photon radiation ^{119m}Sn did not provide the possibility to determine the yield of this isomer in this current experiment. The only possibility is to determine the activity ratio of the isotopes ^{117m}Sn and ^{119m}Sn with the help of theoretical estimates of the cross sections for the relevant nuclear reactions.

Equation (2) for the example of production ^{117m}Sn can be written in a slightly different form:

$$\frac{m_t}{M}N_{av}\left(1 - e^{-\lambda_{117}t_{irr}}\right)\left(0.5726\,R_{\gamma,p3n}^{121} + 0.4264\,R_{\gamma,p5n}^{123}\right) = \frac{N_\gamma\,\lambda_{117}}{\varepsilon p_\gamma e^{-\lambda_{117}\Delta t}(1 - e^{-\lambda_{117}t_m})} \quad (3)$$

where subscript of saturation activity R denotes nuclear reaction producing observed radionuclide. Both the left and right sides of the Equation (3) give the activity of ^{117m}Sn at the

end of the irradiation. The left-hand side of Equation (3) provides a way to estimate the activity from known cross-section and photon flux values, while the right-hand side of Equation (3) allows the activity to be calculated using data obtained from the gamma spectrum.

An analogous equation can be written for the production of ^{119m}Sn. The activity ratio of ^{117m}Sn and ^{119m}Sn can be represented as:

$$\frac{A_{119}}{A_{117}} = \frac{\lambda_{119}}{\lambda_{117}} \frac{0.5726 \, R_{\gamma,pn}^{121} + 0.4264 \, R_{\gamma,p3n}^{123}}{0.5726 \, R_{\gamma,p3n}^{121} + 0.4264 \, R_{\gamma,p5n}^{123}} \tag{4}$$

The above Equation (4) was written assuming that the sample irradiation time t_{irr} is significantly shorter than the half-life of the observed photonuclear reaction products. Regarding that we are talking about long-lived radionuclides, this assumption is quite realistic.

In order to obtain an estimate of the activity ratio, it is necessary to calculate the saturation integrals of the relevant nuclear reactions. For the bremsstrahlung production geometry used in this experiment, the photon flux is obtained by GEANT4 simulation. Considering that it is necessary to determine the ratio of ^{119m}Sb and ^{117m}Sn activities, it is quite sufficient to know only the shape of the photon spectrum. The shape of the photon spectrum $\Phi(E)$ is obtained by using GEANT4 software package [13], version v11.1.0, with standard G4 electromagnetic physics option selected. The simulation starts with creating 30M of 60 MeV electrons in the beam, with a Gaussian spread in energy of 0.01 MeV. The photon spectrum is obtained at the place of irradiated sample based on the geometry used in this experiment.

There are no experimental values of the differential cross section for the observed nuclear reactions, so the only possibility is to use theoretical estimates, which can be obtained with the TALYS code.

2. MEASUREMENTS AND RESULTS

A pure antimony target was exposed to a beam of bremsstrahlung radiation with a maximum energy of 60 MeV. The experiment was carried out using the linear electron accelerator LUE-75 located at A. Alikhanyn National Science Laboratory in Yerevan, Armenia. Accelerated electrons, after passing through a cylindrical collimator (length of 20 mm, diameter of 15 mm) strike a pure tungsten convertor. The thickness of the convertor was 2 mm. A 30 mm long aluminum cylinder was placed directly behind it. The function of the aluminum was to stop the electrons that penetrated the tungsten. At a distance of 60 mm from the tungsten plate, a coin-shaped antimony target (diameter of 1 cm and a mass of 0.5772 g) was placed. Duration of exposition was 30 min. The current of accelerated electrons was 1.2 µA.

Exposed Sb coin was placed 8.6 cm from the end cap of HPGe detector. The spectrum used in this work was recorded for 53599 s, and 12000 s passed between the end of the irradiation and the beginning of the measurement. In the measured spectra, gamma lines from several Sb isotopes were identified, as well as several gamma lines of indium isotopes.

The relative efficiency of the detector was determined using the [206]Bi gamma lines. For the purposes of the experiment, simultaneously with the antimony target, a cylindrical bismuth sample of the same dimensions, weighing 1.1 g, was exposed in the photon beam. The photonuclear reaction [209]Bi(γ,3n)[206]Bi gave sufficient activity to obtain a satisfactory number of very intense gamma lines in the spectrum recorded the next day for 24526 s. The absolute photo-peak efficiency curve was obtained by normalizing the relative efficiency with the help of the measurement of the ^{137}Cs calibration source.

Three days (264960 s) after the first measurement, the second one was performed for a 65125 s. The time between the first and second measurements was long enough for [117]Sb, [117]In and [117m]In to completely decay. In that case, all photons of energy 158.56 keV originate from the decay of [117m]Sn only. Part of the spectra containing this line is depicted in Figure 4.
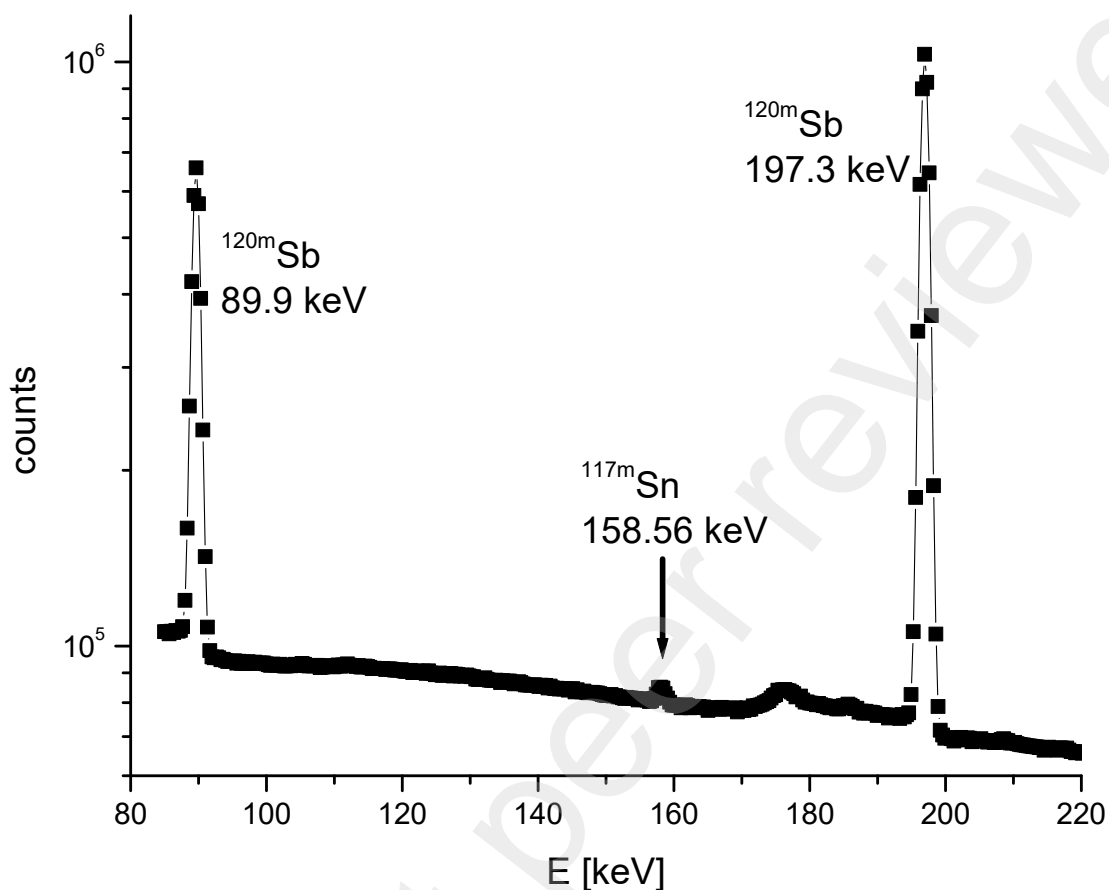
Figure 4. Part of the gamma spectra recorded three days after irradiation of Sb target

The intensities of selected gamma lines were determined using the GENIE 2000 software package. The yields of identified radionuclides were calculated as shown on the right side of Equation (1). Obtained results are depicted in Table 1.

Table 1. Yields and sum of saturation activities of identified products of photonuclear reactions

radionuclide	Half-life	Possible ways of production	Yield $\cdot 10^6$ [s^{-1}]	Sat. Act. $\cdot 10^{-15}$ [s^{-1}]
^{122}Sb	2.70 d	^{123}Sb(γ,n) $(+^{121}$Sb$(n, \gamma))$	75.9	26.6
^{120m}Sb	5.76 d	^{121}Sb$(\gamma,n) + ^{123}$Sb$(\gamma,3n)$	6.05	2.12
^{118m}Sb	5.00 h	^{121}Sb$(\gamma,3n) + ^{123}$Sb$(\gamma,5n)$	0.456	0.160
^{117}Sb	2.80 h	^{121}Sb$(\gamma,4n) + ^{123}$Sb$(\gamma,6n)$	1.26	0.441
^{116m}Sb	60.3 min	^{121}Sb$(\gamma,5n) + ^{123}$Sb$(\gamma,7n)$	0.026	0.0091

11

[116mln]	54.41 min	[121]Sb(γ,αn)	0.0027	0.00095
[117mSn]	13.60 d	[121]Sb(γ,p3n) + [123]Sb(γ,p5n)	0.092	0.0322

As could be expected, the highest yield among Sb isotopes has reaction products formed after the emission of the smallest number of neutrons. Table 1 shows that [122]Sb and [120m]Sb have the highest yield. With the increasing number of emitted particles, the probability of a photonuclear reaction drops sharply, so the yield of lighter antimony isotopes is also lower.

The [116m]In yield was determined based on the obtained gamma line intensity of 1097.33 keV. Considering that both [116m]In and [116m]Sb populate the same excited states of [116]Sn, 1293.56 keV gamma photons are emitted after the decay of both of these radionuclides. The yield of [116m]Sb was determined based on the intensity of the gamma line of 1293.56 keV, but the contribution of [116m]In was subtracted.

The yields of [117]Sb and [117m]Sn were determined based on the intensity of the gamma line of 158.56 keV. In the first measurement, started 3 hours and 20 min after the end of the irradiation, the largest contribution to this gamma line is from [117]Sb. After three days, this radionuclide completely disappeared and all detected photons of this energy can be attributed to [117m]Sn. Based on the intensity of the gamma line of 158.56 keV from the second spectrum, a yield of [117m]Sn was determined. This intensity was used to estimate the contribution of [117m]Sn to the observed gamma line in the first spectrum. Based on the intensity of the corrected 158.56 keV gamma line, the yield of [117]Sb shown in Table 2 was determined.

The ratio of [119m]Sn and [117m]Sn activities was determined as shown in Equation (4). It is not necessary to know the absolute value of the photon flux. Only the shape of the photon spectrum obtained by GEANT4 simulation for a given geometry of bremsstrahlung production is necesary.

Cross sections for observed reactions were estimated using the TALYS code. It was decided to use SMLO model for a strength function. It could be expected that the choice of the strength function model has an impact on the estimation of the cross section, but this analysis is beyond the scope of this paper. Six different models of level density were employed in calculations. Cross sections were calculated using phenomenological ((1) The Fermi Gas Model + Constant Temperature Model, (2) The Back-shifted Fermi gas Model, (3) The Generalized Superfluid Model) and microscopic ((4) Skyrme-Hartree-Fock-Bogoluybov, (5) Gogny-Hartree-Fock-Bogoluybov and (6) Temperature-dependent Gogny-Hartree-Fock-Bogoluybov models) of level density. Different models for the densities of states give estimates of cross sections that can differ significantly from each other. In Figure 5 and Figure 6 are depicted the energy differential cross sections for the two reactions at [121]Sb which give [119m]Sn and [117m]Sn as a result.

The estimation of the activity ratio of [119m]Sn and [117m]Sn at the end of the irradiation was made using all six cross sections obtained by the TALYS code. The smallest value of 0.124 is obtained

12

when the model of Fermi Gas + Constant Temperature Model is chosen for the density of states, while The Generalized Superfluid Model gives the highest ratio estimate of 0.268.
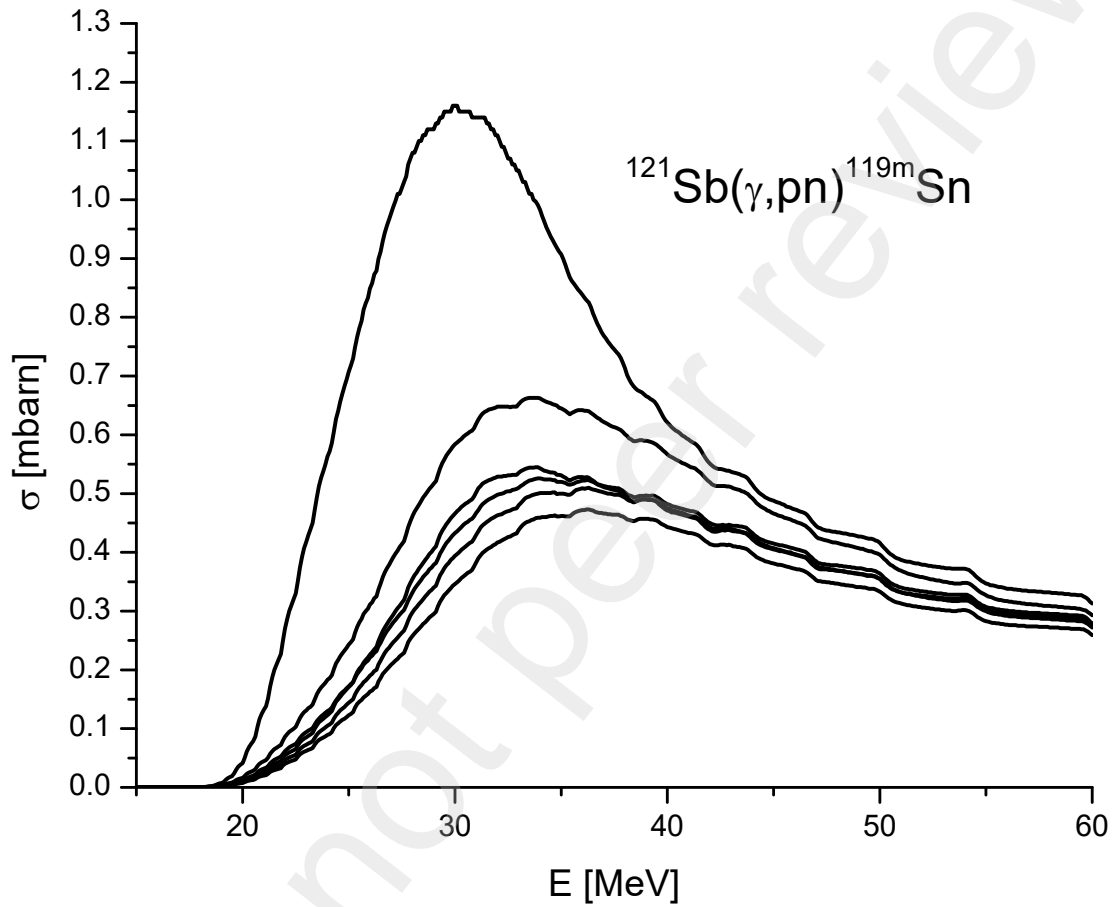
Figure 5. Cross sections for $^{121}Sb(\gamma,pn)^{119m}Sn$ reaction estimated using TALYS code. The order of the models that gave the shown sections, according to increasing amplitudes, is 1, 2, 4, 5, 3 and 6

13
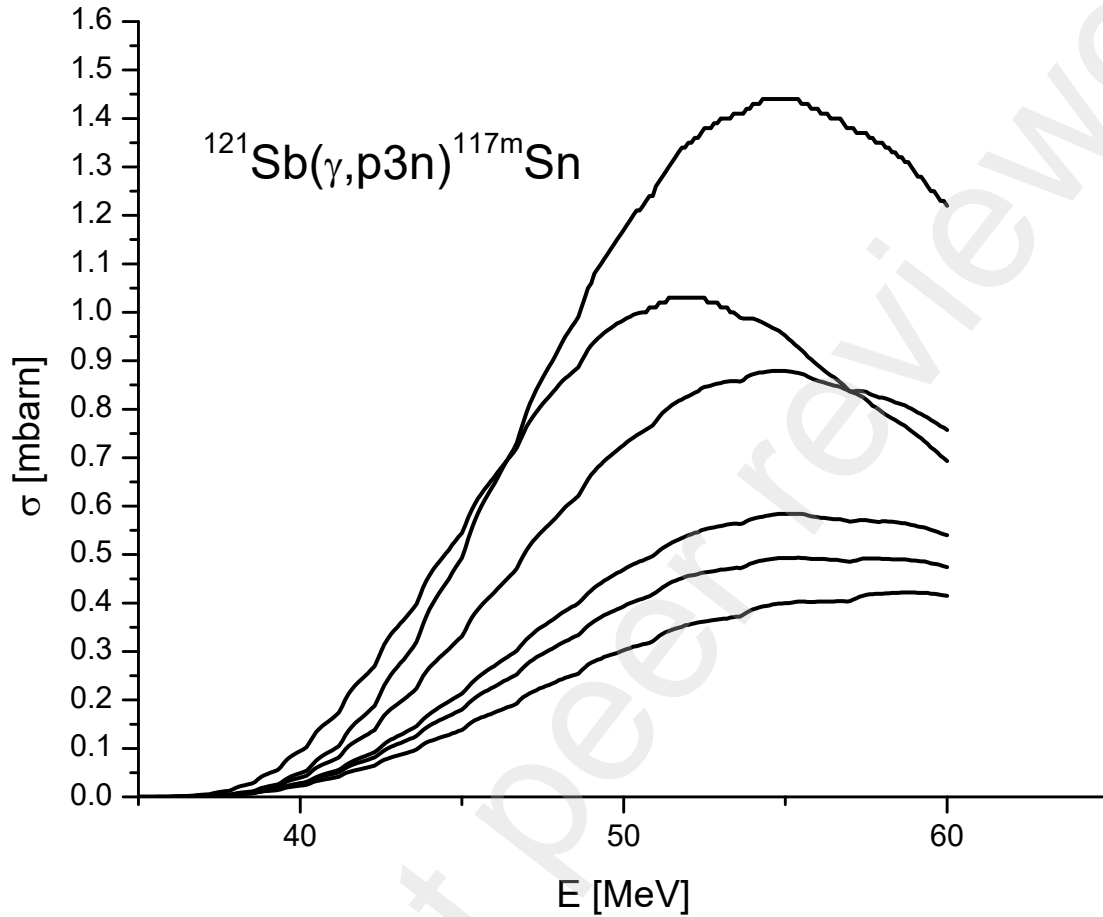
Figure 6. Cross sections for ^{121}Sb(γ,p3n)^{117m}Sn reactions estimated using TALYS code. The order of the models that gave the shown sections, according to increasing amplitudes, is 1, 2, 4, 5, 3 and 6

3. DISCUSSIONS

Based on the results shown in Table 1, it can be seen that ^{121}Sb(γ,p3n) and ^{123}Sb(γ,p5n) nuclear reactions, give a low yield of ^{117m}Sn comparing to the activities of the produced antimony isotopes. If the right side of Equation (4) is used to calculate the activities of radionuclides identified in the measured spectra, it is obtained that, at the moment when the irradiation was finished, the activity of ^{122}Sb was 3.85·10^5 Bq, the activity of ^{120m}Sn was 1.53·10^4 Bq, while the activity of ^{117}Sb was 1.47·10^5 Bq. During the irradiation of the antimony target, an activity of ^{117m}Sn of about 100 Bq was obtained. This is three orders of magnitude less than the activity of

14

Sb isotopes that have been identified. Considering that the formation of ^{117m}Sn occurs with the emission of charged particles, so low level of activity could be expected.

The method currently considered the most promising is the production of ^{117m}Sn by interactions of accelerated alpha particles with cadmium or indium targets (Aslam et al., 2018; Aikava et al., 2018; Ditrói et al., 2016; Duchemin et al., 2016; Maslov et al., 2011). Since the range of alpha particles in these materials is very small, order of microns, the most common way to show the output of reaction is through the integral yield or Thick Target production Yield (TTY), as it is called by some authors. This quantity is expressed in units of kBq/µAh. For example, on enriched targets of ^{116}Cd, an integral yield of 410 kBq/µAh was recorded in a (α,3n) nuclear reaction (Maslov et al., 2011; Ditrói et al., 2016) . The mechanism of photon interaction with metal targets is significantly different and they take place throughout the entire depth of the target and reaction yield depends on the target mass and thickness. However, from the estimated activity of ^{117m}Sn, a numerical value can be obtained that could somehow be equivalent to TTY, at least for the geometry used in experiment. With the experimental parameters listed in Section 2, it can be estimated that the production of ^{117m}Sn in photonuclear reaction is 0.17 kBq/(µA h).

Such an assessment could be expected taking into consideration the large difference in the values of the cross section for ^{116}Cd(α,3n)^{117m}Sn and ^{121}Sb(γ,p3n)^{117m}Sn reactions. The maximum cross-section for the ^{116}Cd(α,3n)^{117m}Sn reaction is about 1 barn in the region of 35 MeV (Montgomery and Porile, 1969; Rebeles et al., 2008; Ditrói et al., 2016; Duchemin et al., 2016]. From Figure 6 it can be seen that the theory for the ^{121}Sb(γ,p3n)^{117m}Sn reaction predicts a cross section of less than 1 mbarn.

The experiment showed that with an antimony target weighing slightly more than half a gram, in a photon beam produced with an electron current of 1.2 µA during 30 minutes of exposure, a very low activity of ^{117m}Sn is obtained, order of magnitude 0.1 kBq. For the purposes of medical application of this radionuclide, significantly greater activities are required. Standard therapy dose of ^{117m}Sn is usually 1 GBq for 70 kg patient (Srivastava et al., 1998). More ^{117m}Sn activity can be obtained by increasing: target mass, irradiation time and electron current. The obtained activity depends linearly on the mass and electron current and in this case also on the irradiation time, since the half-life of ^{117m}Sn is 13.6 days. It can be expected that an increase in the maximum bremsstrahlung energy can give a growth of the obtained activity of the product of the photonuclear reaction as well. In any case, there is room for increasing the yield of ^{117m}Sn, which still needs to be investigated.

According to the estimates based on Equation (4), it can be expected that the activity of the long-lived ^{119m}Sn will be even lower and that in the bremsstrahlung beam of maximum energy of 60 MeV it will be up to 26% of the activity of ^{117m}Sb. This ratio can be expected to be smaller at higher bremsstrahlung energies. It can be seen in Figure 6, that some significant cross section component at energies higher than 60 MeV for the reaction (γ,p3n) exist. Considering that the

15

dominant way of production of ^{117m}Sn is through this reaction, a higher yield of this radionuclide can be expected at higher energies.

If there is an effective method to chemically separate the tin fraction from the antimony target, the activity of the ^{117m}Sn and ^{119m}Sn isotopes would be present in the obtained material only. This can be a very convenient way to produce two radionuclides of high specific activity (activity per unit mass), since a source of radiation without a carrier would be obtained. In photonuclear reactions on natural antimony, several isotopes of Sb are created. All of them, after decay give Sn nuclei as product. In this way, stable isotopes of tin with two active isomers ^{119m}Sn and ^{117m}Sn are created.

Based on the measured activity of antimony isotopes, it is possible to estimate the number of tin nuclei that would form in a characteristic interval of time. The measured activities of ^{122}Sb, ^{120m}Sb, ^{118m}Sb, ^{117}Sb and ^{116m}Sb were used for the approximate estimation of the amount of tin that is created from the decay of Sb isotopes. This estimation do not include all the ways of creating tin from the decay of antimony isotopes, but only those whose activity could be determined based on the measured gamma spectra. However, it can be enough to estimate the order of magnitude of the number of Sn nuclei created and the mass of tin.

In a completely arbitrarily chosen case where the decay of the created antimony isotopes lasted 24 hours after irradiation, it was found that the total mass of tin that was created was of the order of 10^{-13} grams. This means that by photonuclear reactions on natural antimony, very high specific activities of ^{117m}Sn can be obtained, order of magnitude up to 10^9 MBq/g.

4. CONCLUSIONS

In the experiment described in this paper, photoactivation of a target made of natural antimony was performed in a bremsstralung beam with a maximum energy of 60 MeV, followed by gamma spectrometric measurements. As could be expected, the highest activity in the activated target was registered by neutron-deficient isotopes of antimony, obtained in (γ,xn) reactions.

These isotopes of antimony decay mainly through electron capture and give stable isotopes of tin as a product. The only tin activity detected in the experiment came from ^{117m}Sn. In the experiment ^{119m}Sn was produced also, but the available detector could not detect it due to low-energy of emitted gamma radiation.

In the gamma spectroscopic measurement, which was performed after a few days, when all sources of interference disappeared, the activity of ^{117m}Sn, which was created in the irradiation of the target, was determined. In the described experiment, the yield of ^{117m}Sn that was obtained is about 2500 times lower than the yield of the same isotope obtained by (α,3n) reaction on enriched ^{116}Cd.

Such a large difference in yield can be explained by the fact that the cross section for the $^{116}Cd(\alpha,3n)^{117m}Sn$ reaction is significantly higher than the cross sections of $^{123}Sb(\gamma,p5n)^{117m}Sn$ and $^{121}Sb(\gamma,p3n)^{117m}Sn$ of photonuclear reactions. However, this still does not mean that photonuclear reactions on antimony should be left out of consideration as a possible commercial source of ^{117m}Sn. There is still significant room to increase the yield of these photonuclear reactions. The yield can be significantly increased in photon accelerator beams that have higher electron currents.

In addition to ^{117m}Sn, some amount of ^{119m}Sn is also obtained in photonuclear reactions. Some of its characteristics, such as a large number of conversion electrons can contribute to the therapeutic effect. It was estimated that in the bremsstrahlung photon beam with a maximum energy of 60 MeV, the activity of ^{119m}Sn is obtained, which would less than 27% of the activity of ^{117m}Sn.

Acknowledgments

5. REFERENCES

Aikawa M., Saito M., Ukon N., Komori Y., Haba H., 2018. Activation cross sections of alpha-induced reactions on ^{nat}In for ^{117m}Sn production. Nuclear Inst. and Methods in Physics Research B 426, 18-21

Aslam M.N., Zubia K., Qaim S.M. 2018. Nuclear model analysis of excitation functions of α-particle induced reactions on In and Cd up to 60 MeV with relevance to the production of high specific activity ^{117m}Sn. Applied Radiation and Isotopes 132, 181-188

IAEA radioisotopes and radiofarmaceuticals reports No.4, 2021. Alternative radionuclide production with a cyclotron. IAEA, Viena

Blachot j., 2002. Nuclear data Sheets for A = 117, Nuclear Data Sheets 95, 679-836

Ditrói F., TakácsS., Haba H., Komori Y., Aikawa M., 2016. Cross section measurement of alpha particle induced nuclear reactions on natural cadmium up to 52 MeV. Applied Radiation and Isotopes 118, 266-276

17

Duchemin C., Essayan M., Guertin A., Haddad F., Michel N., Métivier V., 2016. How to produce high specific activity tin-117 m using alpha particle beam. Applied Radiation and Isotopes 115, 113-124

Ermolaev S.V., Zhuikov B.L., Kokhanyuk V.M., Abramov A.A., Togaeva N.R., Khamianov S.V., Srivastava S.C., 2009. Production of no-carrier-added ^{117m}Sn from proton irradiated antimony. Journal of Radioanalytical and Nuclear Chemistry 280, No.2. 319–324

Lewington V.J. 2005. Bone-seeking radionuclides for therapy, The Journal of Nuclear Medicine 46, No. 1 (Suppl), 38S-47S

Maslov O.D., Starodub G.Ya., Vostokin G.K., Gustova M.V., Dimitriev S.N., Shvetsov V.N., Szucs Z., Jansen D., Zeevaart J.R., 2011. Production of ^{117m}Sn with high specific activity by cyclotron, Applied Radiation and Isotopes 69, 965-968

Montgomery, D.M., Porile, N.T., 1969. Reactions of ^{116}Cd with intermediate energy ^{3}He and ^{4}He ions. Nucl. Phys. A 130, 65–76.

Pietralla N., Isaak J. and Wernerc V., 2019. Photonuclear reactions: Achievements and perspectives. Eur. Phys. J. A **55**, 237

Qaim S.M., 2017. Nuclear data for production and medical application of radionuclides: Present status and future needs. Nuclear Medicine and Biology 44, 31-59

Rebeles, R.A., Hermanne, A., Van den Winkel, P., Tárkányi, F., Takács, S., Daraban, L., 2008. Alpha induced reactions on 114Cd and 116Cd: an experimental study of excitation functions. Nucl. Instrum. Methods B 266 (21), 4731–4737.

Srivastava S.C., H.L., Krishnamurthy G.T., I Zanzi I., Silberstein E.B., Meinken G., Mausner L.F., Swailem F., D'Alessandro T., Cabahug C.J., Lau Y., Park T., Madajewicz S., 1998. Treatment of metastatic bone pain with tin-117m Stannic diethylenetriaminepentaacetic acid: a phase I/II clinical study, Clinical Cancer Research . Jan;4(1):61-8.

Stevenson N.R., George G.St., Simón J., Srivastava S.C., Mueller D.W., Gonzales G.R., Rogers J.A., Frank R.K., Horn I.M., 2015. Methods of producing high specific activity Sn-117m with commercial cyclotrons. Journal of Radioanalyitical Nuclear Chemistry 305, 99–108

Zilges A., Balabanski D.L., Isaak J., Pietralla N., 2022. Photonuclear reactions - From basic research to applications. Progress in Particle and Nuclear Physics 122, 103903

18

19

THE EUROPEAN
PHYSICAL JOURNAL A

Search for the evidence of ^{209}Bi(γ,p5n)^{203}Pb reaction in 60 MeV bremsstrahlung beams

M. Krmar[1,a], **N. Jovančević**[1], **D. Maletić**[2], **Ž. Medić**[2], **D. Knežević**[2], **M. Savić**[2], **Yu. Teterev**[3], **S. Mitrofanov**[3], **K. D. Timoshenko**[3], **S. I. Alexeev**[3], **H. Marukyan**[4], **I. Kerobyan**[4], **R. Avetisyan**[4], **L. Poghosyan**[4], **R. Dallakyan**[4], **A. Hakobyan**[4], **L. Vahradyan**[4], **H. Mkrtchyan**[4], **A. Petrosyan**[4]

[1] Physics Department, Faculty of Science, University Novi Sad, Novi Sad, Serbia
[2] Institute of Physics, Belgrade, Serbia
[3] Flerov Laboratory of Nuclear Reactions, Joint Institute for Nuclear Research, Dubna, Russia
[4] A. Alikhanyan National Science Laboratory (Yerevan Physics Institute), Yerevan, Armenia

Communicated by Jose Benlliure

Abstract Samples made from natural bismuth were exposed in 60 MeV end-point bremsstrahlung beam. In this paper, a simple model for determination the share of two ways of ^{203}Pb formation: by the decay of ^{203}Bi, produced in ^{209}Bi(γ,6n)^{203}Bi reaction and by ^{209}Bi(γ,p 5n)^{203}Pb reaction is described. The method employs the ratio of ^{203}Pb and ^{203}Bi nuclei numbers and activities at the end of the exposure as the input value. This ratio was estimated from gamma spectra measured after irradiation of natural Bi sample. It was found that the rate of production of ^{203}Pb by ^{209}Bi(γ,p 5n)^{203}Pb reaction is about 6% of the ^{203}Bi production rate in the ^{209}Bi(γ,6n)^{203}Bi reaction. Obtained result is compared with TALYS based estimation.

1 Introduction

The simplest photonuclear reaction (γ,n) usually takes place through the well-known mechanism of giant dipole resonance. For a large number of stable nuclei, the energy differential cross section of this reaction has been successfully measured [1, 2]. Data on photonuclear reactions can be found in available databases [3] also. The experimental evidence for the (γ,2n) reaction is much poorer, while for reactions when three or more neutrons are emitted (usually denoted by (γ,xn)), the reaction cross sections can be obtained by mainly by theoretical calculations [4]. For reactions in which a charged particle, such as proton in the simplest case, is emitted (single or in addition to one or more neutrons) there is a much poorer experimental evidence. In the interactions of

high energy photons with nuclei, the probability of emission of a charged particle is significantly lower than the emission of neutrons due to the existence of the Coulomb barrier. It is a reason why experimental data concerning (γ,p xn) are insufficient in literature.

Cross sections for photonuclear reactions on natural bismuth (monoisotope ^{209}Bi) with emission of one and two neutrons can be found in the reference [5]. In several recently published papers [6–11], photonuclear reactions with Bi target exposed in bremsstrahlung photon beams having endpoint energies up to 70 MeV were studied. Irradiation of such a heavy element by the high energy photons can give several products of (γ,xn) reactions. In these publications, the relative yield of photonucleated reactions on ^{209}Bi was analyzed, while in reference [12] the cross section results for reactions (γ,n), (γ,2n), (γ,3n) and (γ,4n) were presented. The authors of reference [12] used natural bismuth target and quasimonochromatic laser Compton-scattering γ-ray beams with energies up to 40 MeV. In reference [11], reaction channel (γ,pxn) with emission of one proton along with several neutrons is accounted for.

In this paper, an attempt was made to establish experimental evidence for ^{209}Bi(γ,p 5n)^{203}Pb nuclear reaction by comparison of intensities of gamma lines following EC decay of ^{203}Bi and ^{203}Pb. Lead-203 can be formed by (γ,p 5n) nuclear reaction, but it is certainly created after decay of ^{203}Bi, obtained in ^{209}Bi(γ,6n)^{203}Bi reaction. After activation of the target made from natural bismuth by 60 MeV endpoint energy bremsstrahlung beam, several gamma spectra were successively measured. Gamma lines from the measured spectra were selected in order to estimate the ratio of created nuclei numbers of ^{203}Bi and ^{203}Pb in the moment

Springer

Fig. 1 Part of the chart containing relevant nuclides

Bi202	Bi203	Bi204	Bi205	Bi206	Bi207	Bi208	Bi209
1.72 h	11.76 h	11.22 h	15.31 d	6.243 d	31.55 y	3.68E5 y	Stable
5+	9/2-	6+	9/2-	6(+)	9/2+	(5)+	9/2-
EC,α	EC,α	EC	EC	EC	EC	EC	100%
Pb201	**Pb202**	**Pb203**	**Pb204**	**Pb205**	**Pb206**	**Pb207**	**Pb208**
9.33 h	5.24E4 y	51.873 h	1.4E17 y	1.53E7 y	Stable	Stable	Stable
5/2-	0+	5/2-	0+	5/2-	0+	1/2-	0+
EC	EC	EC	1.4%	EC	24.1%	24.1%	52.4%

when irradiation was stopped. Probability ratio for the occurrence of (γ,6n) and (γ,p 5n) nuclear reactions can be obtained from these data.

For the purposes of this paper, the cross sections for the observed nuclear reactions were extracted using the TALYS code. These cross-sections were used to estimate the ratio of probabilities of nuclear reactions of interest in order to compare them with the values obtained by measurements.

2 Materials and methods

Considering that lead isotopes ^{206}Pb, ^{207}Pb and ^{208}Pb are stable (Fig. 1), ^{209}Bi(γ,p3n)^{205}Pb is the very first photonuclear reaction on ^{209}Bi which can give active lead as a product. However, half life of ^{205}Pb is $1.57 \cdot 10^7$ y and small amount of produced ^{205}Pb, would be very difficult to detect. Moreover, this isotope does not emit gamma radiation.

The next candidate which can be used to verify if (γ,pxn) on natural bismuth can yield measurable amounts of reaction products is ^{204m}Pb. Half life of ^{204m}Pb is 67.2 min and de-excitation of isomer state takes place through several gamma transitions having high quantum yield. However, ^{204m}Pb can be created by decay of ^{204}Bi, produced in (γ,5n) photonuclear reaction. This means that de-excitation of the isomeric state of ^{204m}Pb created in (γ,p 4n) results in gamma transitions that are almost the same as those occurred after the ^{204}Bi decay. It is very difficult to estimate how ^{204}Bi decay and ^{204m}Pb de-excitation contribute to the total intensity of some of measured gamma lines.

Another possibility to check if irradiation of ^{209}Bi by high-energy photons results in proton emission together with several neutrons is lead isotope ^{203}Pb. This isotope can be created by (γ,p 5n) reaction. Half-life of ^{203}Pb is 51.873 h and after decay two intensive lines in gamma spectra can be observed. A study of gamma photons originating from the decay of ^{203}Pb could be a good way to determine if (γ,p 5n) reaction can give measurable amount of ^{203}Pb during irradiation of the natural bismuth target by high energy photons. But in order to do that, it is necessary to estimate, in some way, how much of the ^{203}Pb activity comes from decay of ^{203}Bi.

2.1 Irradiation

In interactions of ^{209}Bi nuclei with high energy photons, several bismuth isotopes can be created through (γ,xn) reactions. Suppose that a bismuth isotope ^{203}Bi, we have chosen to analyze, is formed at a constant rate q in a photon beam. The change of the number of nuclei of observed bismuth isotope can then be described by the following differential equation:

$$\frac{dN_{Bi}}{dt} = q - \lambda_{Bi} N_{Bi} \tag{1}$$

λ_{Bi} is decay constant of ^{203}Bi, created in (γ,6n) photonuclear reaction. The number of created ^{203}Bi nuclides after irradiation time t_{irr} is:

$$N_{Bi} = \frac{q}{\lambda_{Bi}}(1 - \exp(-\lambda_{Bi} t_{irr})) \tag{2}$$

The dynamics of the number of ^{203}Pb nuclei created exclusively by the decay of ^{203}Bi can be expressed as:

$$\frac{dN_{Pb}}{dt} = \lambda_{Bi} N_{Bi} - \lambda_{Pb} N_{Pb} \tag{3}$$

The very same ^{203}Pb isotope can additionally be produced through the (γ,p 5n) nuclear reaction. In the case when the production of ^{203}Pb occurs, process can be described by the following equation:

$$\frac{dN_{Pb}}{dt} = \lambda_{Bi} N_{Bi} + p - \lambda_{Pb} N_{Pb} \tag{4}$$

where p denotes a constant rate of ^{203}Pb production through the (γ,p 5n) nuclear reaction. It can be considered that at the very beginning ($t = 0$), there were no ^{203}Pb nuclei. The solutions of differential Eqs. 3 and 4 describing time evolution of the number of ^{203}Pb isotopes are:

$$N_{Pb} = q\left[\frac{1}{\lambda_{Pb}}(1 - \exp(-\lambda_{Pb} t_{irr}))\right.$$
$$\left. + \frac{1}{\lambda_{Pb} - \lambda_{Bi}}(\exp(-\lambda_{Pb} t_{irr}) - \exp(-\lambda_{Bi} t_{irr}))\right] \tag{5}$$

in the case when ^{203}Pb originates from the decay of ^{203}Bi, and

$$N_{Pb} = q \left[\frac{1 + \frac{p}{q}}{\lambda_{Pb}} (1 - \exp(-\lambda_{Pb} t_{irr})) \right.$$
$$\left. + \frac{1}{\lambda_{Pb} - \lambda_{Bi}} (\exp(-\lambda_{Pb} t_{irr}) - \exp(-\lambda_{Bi} t_{irr})) \right] \quad (6)$$

when production of ^{203}Pb through (γ,p 5n) can not be neglected.

Using Eqs. 2 and 5 ratio $N_{Pb}(t_{irr})/N_{Bi}(t_{irr})$ of produced numbers of ^{203}Pb and ^{203}Bi nuclei, in the case when ^{203}Pb is produced only by the ^{203}Bi decay, can be determined as:

$$\frac{N_{Pb}(t_{irr})}{N_{Bi}(t_{irr})} = \frac{\frac{\lambda_{Bi}}{\lambda_{Pb}}(1 - \exp(-\lambda_{Pb} t_{irr})) + \frac{\lambda_{Bi}}{\lambda_{Pb} - \lambda_{Bi}}(\exp(-\lambda_{Pb} t_{irr}) - \exp(-\lambda_{Bi} t_{irr}))}{1 - \exp(-\lambda_{Bi} t_{irr})} \quad (7)$$

It can be seen from Eq. 7 that the ratio of ^{203}Pb and ^{203}Bi nuclei numbers does not depend on the rate q at which Bi is generated in photonuclear reaction.

In a similar way, using Eqs. 2 and 6, it can be determined the ^{203}Pb/^{203}Bi nuclei number ratio for the case when the ^{203}Pb isotope is formed by decay of ^{203}Bi and the direct ^{209}Bi(γ,p 5n) reaction as well.

$$\frac{N_{Pb}(t_{irr})}{N_{Bi}(t_{irr})} = \frac{(1 + \frac{p}{q})\frac{\lambda_{Bi}}{\lambda_{Pb}}(1 - \exp(-\lambda_{Pb} t_{irr})) + \frac{\lambda_{Bi}}{\lambda_{Pb} - \lambda_{Bi}}(\exp(-\lambda_{Pb} t_{irr}) - \exp(-\lambda_{Bi} t_{irr}))}{1 - \exp(-\lambda_{Bi} t_{irr})} \quad (8)$$

From the above Eq. 8, we can see that the ratio p/q, ie. the production rate of ^{203}Bi by the emission of six neutrons and the rate of production of ^{203}Pb by (γ,p 5n) nuclear reaction affects ratio of these two isobars. It can be seen that, if there is no proton emission, ie. if $p = 0$, Eq. 8 turns into Eq. 7.

All the above equations, as well as those that will follow in which the ratios of the nuclei of the observed two isotopes N_{Pb}/N_{Bi} can be written in the form where the ratios of their activities A_{Pb}/A_{Bi} appear.

2.2 Decay measurement

At the moment when the irradiation is completed, there will be some number of both radionuclides in the bismuth sample: $N_{Pb}(t_{irr})$ and $N_{Bi}(t_{irr})$. After the end of the irradiation, it is possible to register gamma spectra of irradiated sample and $N_{Pb}(t_{irr})$ and $N_{Bi}(t_{irr})$ can be considered as the initial numbers of ^{203}Bi and ^{203}Pb. Let's denote them as N_{Bi}^0 and N_{Pb}^0. Starting from the end of irradiation, activity of ^{203}Bi

will decrease according to a well-known exponential law

$$N_{Bi}(t) = N_{Bi}^0 \exp(-\lambda_{Bi} t) \quad (9)$$

while the dynamics of the time change of ^{203}Pb activity will be determined by the rate of its simultaneous decay and creation from ^{203}Bi. It is well known that a number of daughter nuclei in the case of simultaneous decay can be described as:

$$N_{Pb}(t) = \frac{\lambda_{Bi}}{\lambda_{Pb} - \lambda_{Bi}} N_{Bi}^0 (\exp(-\lambda_{Bi} t) - \exp(-\lambda_{Pb} t)) + N_{Pb}^0 \exp(-\lambda_{Pb} t) \quad (10)$$

Let's assume that the recording of the gamma spectrum started at the moment t_1 after the end of the irradiation, and that the measurement was stopped at the moment t_2. In that time interval, the number of decayed ^{203}Bi nuclei is:

$$N_{Bi}^D = N_{Bi}^0 (\exp(-\lambda_{Bi} t_1) - \exp(-\lambda_{Bi} t_2)) \quad (11)$$

By integrating the function that describes the temporal change of ^{203}Pb activity within the same time limits, it is obtained that the total number of ^{203}Pb nuclei that decayed is:

$$N_{Pb}^D = \frac{\lambda_{Bi}}{\lambda_{Bi} - \lambda_{Pb}} N_{Bi}^0 (\exp(-\lambda_{Pb} t_1) - \exp(-\lambda_{Pb} t_2))$$
$$- \frac{\lambda_{Pb}}{\lambda_{Bi} - \lambda_{Pb}} N_{Bi}^0 (\exp(-\lambda_{Bi} t_1) - \exp(-\lambda_{Bi} t_2))$$
$$+ N_{Pb}^0 (\exp(-\lambda_{Pb} t_1) - \exp(-\lambda_{Pb} t_2)) \quad (12)$$

From Eqs. 11 and 12 the values of N_{Bi}^0 and N_{Pb}^0 can be estimated, but in some cases it is more convenient to analyze the ratio of the number of decays of the observed two nuclides:

$$\frac{N_{Pb}^D}{N_{Bi}^D} = \frac{\lambda_{Bi}}{\lambda_{Bi} - \lambda_{Pb}} \frac{\exp(-\lambda_{Pb}t_1) - \exp(-\lambda_{Pb}t_2)}{\exp(-\lambda_{Bi}t_1) - \exp(-\lambda_{Bi}t_2)}$$
$$- \frac{\lambda_{Pb}}{\lambda_{Bi} - \lambda_{Pb}} + \frac{N_{Pb}^0}{N_{Bi}^0} \frac{\exp(-\lambda_{Pb}t_1) - \exp(-\lambda_{Pb}t_2)}{\exp(-\lambda_{Bi}t_1) - \exp(-\lambda_{Bi}t_2)}$$
$$(13)$$

As can be seen from Eq. 13, if the ratio of the decay numbers of ^{203}Pb and ^{203}Bi is known, it is possible to estimate the ratio of the initial numbers of these two nuclides N_{Pb}^0/N_{Bi}^0.

In order to determine the ratio of the number of decays N_{Pb}^D/N_{Bi}^D in a selected time interval, two gamma lines, one from ^{203}Pb and another from ^{203}Bi should be selected their intensities should be determined. Let's denote registered intensities with N_{Bi}^R and N_{Pb}^R. Ratio N_{Pb}^D/N_{Bi}^D can be determined as:

$$\frac{N_{Pb}^D}{N_{Bi}^D} = \frac{N_{Pb}^R}{N_{Bi}^R} \frac{\varepsilon_{Bi} p_\gamma^{Bi}}{\varepsilon_{Pb} p_\gamma^{Pb}} \tag{14}$$

The quantum yields of the observed gamma transitions of ^{203}Bi and ^{203}Pb are denoted by p_γ^{Bi} and p_γ^{Pb} while ε_{Bi} and ε_{Pb} are the absolute detection efficiency at the selected energies. From Eq. 14 it can be seen that it is sufficient to know the relative efficiency of the detector system for the used geometry.

2.3 Procedure of the results extraction

And finally, let's summarize the procedure that can be used to prove whether a measurable contribution of (γ,p 5n) reaction could be expected:

(a) the ratio of ^{203}Pb and ^{203}Bi nuclei numbers, expected at the end of irradiation, without contribution of (γ,p 5n) reaction, could be calculated using Eq. 7;
(b) intensities of selected gamma lines should be obtained. The N_{Pb}^D/N_{Bi}^D ratio can be calculated using Eq. 14;
(c) Equation 13 should be used to obtain the ratio of initial nuclei numbers N_{Pb}^0/N_{Bi}^0, created during exposition in the photon beam;
(d) obtained N_{Pb}^0/N_{Bi}^0 ratio can be compared with the result derived from Eq. 7. If the obtained values coincide within the interval of experimental error, it can be concluded that the reaction (γ,p 5n) does not give a measurable contribution to the activity of ^{203}Pb. However, if the contribution of the reaction (γ,p 5n) to the total number of ^{203}Pb cannot be neglected, the N_{Pb}^0/N_{Bi}^0 ratio obtained by Eq. 13 should be greater than the ratio acquired from Eq. 7
e) and finally, if the ratios N_{Pb}^0/N_{Bi}^0 differ, it is possible to find the value of the parameter p/q in Eq. 8 which gives the N_{Pb}^0/N_{Bi}^0 ratio experimentally established.
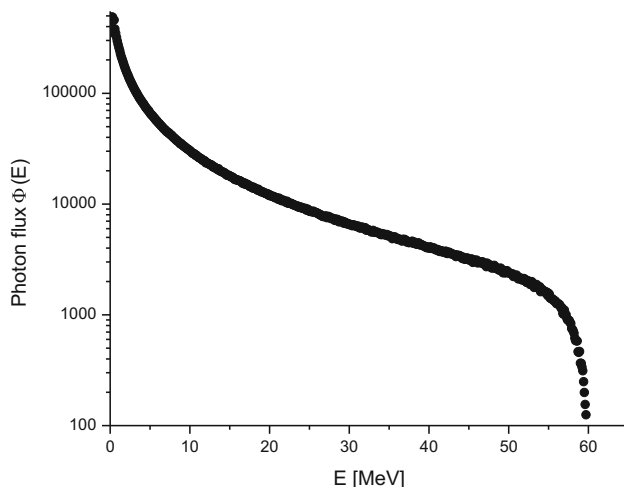
Fig. 2 The shape of the photon spectrum $\Phi(E)$ obtained for 30 M incident electrons

The described procedure can give confirmation about contribution of the (γ,p 5n) reaction to the total activity of ^{203}Pb and to estimate the value p/q.

2.4 Theoretical calculations

The rate of some nuclear reaction at the selected target is directly proportional to the product of the cross section and the number of incident particles. This means that the quantities p and q would be proportional to the saturation activities of observed reactions:

$$q \sim \int_{E_t}^{E_{max}} \sigma_{6n}(E)\Phi(E)dE \tag{15}$$

$$p \sim \int_{E_t}^{E_{max}} \sigma_{p,5n}(E)\Phi(E)dE \tag{16}$$

where $\Phi(E)$ is photon fluency, E_t is energy threshold for observed nuclear reaction and E_{max} is end-point energy of the photon spectra (in our case 60 MeV). By $\sigma_{6n}(E)$ and $\sigma_{p,5n}(E)$ cross-sections for (γ,6n) and (γ,p 5n) nuclear reactions are denoted respectively.

The simplest way to check the obtained result for the p/q ratio would be to calculate the saturation activities for these two reactions using Eqs. 15 and 16 and compare them with the experimental result.

The shape of the photon spectrum $\Phi(E)$ is obtained by using Geant4 software package [13], version v11.1.0, with standard G4 electromagnetic physics option selected. The simulation starts with creating 30 M of 60 MeV electrons in the beam, with very small Gaussian spread in energy of 0.01 MeV. The photon spectrum, obtained at the place of irradiated sample based on the geometry described in the next section is presented in Fig. 2.

There is no experimental evidence of the cross sections of ^{209}Bi (γ,6n) and ^{209}Bi (γ,p 5n) nuclear reactions in literature. Related information can be obtained using some numerical code for evaluation of the cross sections for nuclear reactions. In this experiment, TALYS 1.9 code was used to estimate cross sections for ^{209}Bi(γ,p 5n)^{203}Pb and ^{209}Bi(γ,6n)^{203}Bi reactions. It was decided to use SMLO model for a strength function. It can be expected that the choice of the strength function model has an impact on the estimation of the cross section, but that analysis is beyond the scope of this paper. Six different models of level density were employed in calculations. Cross sections were calculated using phenomenological (1. The Fermi Gas Model + Constant Temperature Model, 2. The Back-shifted Fermi gas Model, 3. The Generalized Superfluid Model) and microscopic (4. Skyrme-Hartree–Fock-Bogoluybov, 5. Gogny-Hartree–Fock-Bogoluybov and temperature-dependent 6. Gogny-Hartree–Fock-Bogoluybov models) of level density [14].

3 Measurements

One coin-shaped sample of natural bismuth (high purity 99.999%), 1 cm diameter and mass of 1.1 g, was exposed in bremsstrahlung photon beam having maximal energy of 60 MeV. The source of the photon beams was the linear electron accelerator LUE-75 located at A. Alikhanyan National Science Laboratory in Yerevan, Armenia. Accelerated electrons, after passing through a cylindrical collimator (length of 20 mm and a diameter of 15 mm) strike a pure tungsten converter. The thickness of the converter was 2 mm, and a 30 mm long aluminum cylinder was placed directly behind it. The function of the aluminum was to stop the electrons that passed through the tungsten. At a distance of 60 mm from the tungsten plate, a Bi coin was placed. Duration of exposition was 30 min.

After 22 min., exposed Bi coin was placed 86 mm from the end cap of HPGe detector. Measurement setup is presented in Fig. 3. Activity of measured samples was high enough and no detector shielding was used. Sample was fixed by tape to the holder ring above detector. First 5400 s spectrum was measured and second one was collected during 79,463 s. In the measured spectra, gamma lines from several Bi isotopes were identified. The lightest one was ^{202}Bi. Gamma line intensities were determined using the GENIE software package.

The most intense ^{203}Pb gamma transition of 279.2 keV (quantum yield 81%) was selected for calculation procedure. In both collected spectra, a prominent single 279.2 keV gamma line appeared. For example, in the first spectrum, intensity of this line was 5.87(28)$\cdot10^3$ counts. In the second spectrum, intensity of this line was 3.71(2)$\cdot10^5$ detected

Fig. 3 Measurement setup

counts. Several strong gamma lines of ^{203}Bi were identified in spectra, however almost all of them are parts of doublets or even multiplets. In order to avoid errors caused during the numerical procedure in separation of the intensity of individual lines in doublets, several gamma transitions of ^{203}Bi were chosen for calculation. Ratio of decayed nuclei N_{Pb}^D/N_{Bi}^D was calculated using Eq. 14 and intensities of 264.2 keV, 816.2 keV and 1033.8 keV gamma lines of ^{203}Bi and mean average was calculated. For example, in the first spectrum intensity of 264.2 keV gamma line was 3.63(7)$\cdot10^4$ detected counts. Considering that activity of ^{203}Bi decreased all the time, while the activity of ^{203}Pb increased, intensity 264.2 keV gamma line was smaller than 279.2 keV gamma line of ^{203}Pb in second spectra. Intensity of 264.2 keV gamma line was 1.015(15)$\cdot10^4$ counts. Two segments of measured gamma spectra are depicted in Fig. 4.

It can be seen from the Eq. 14 that the N_{Pb}^D/N_{Bi}^D ratio can be obtained using the relative efficiency of the detection system. The best way to get relative efficiency is to use gamma lines of ^{206}Bi. Half-life of this isotope is 6.243 days and there are many intensive gamma transitions from 183.98 to 2 MeV. The longer spectrum was used and 16 gamma lines of ^{206}Bi, starting from 183.98 keV to 1878.65 keV were selected to get relative efficiency. Combination of an exponential function and a second order polynomial was used in fit procedure.

Fig. 4 Two parts of gamma spectra: **a**) low energy part containing ^{203}Pb gamma line (279.2 keV) and ^{203}Bi/^{206}Bi doublet; **b**) multiplet containing three ^{203}Bi lines
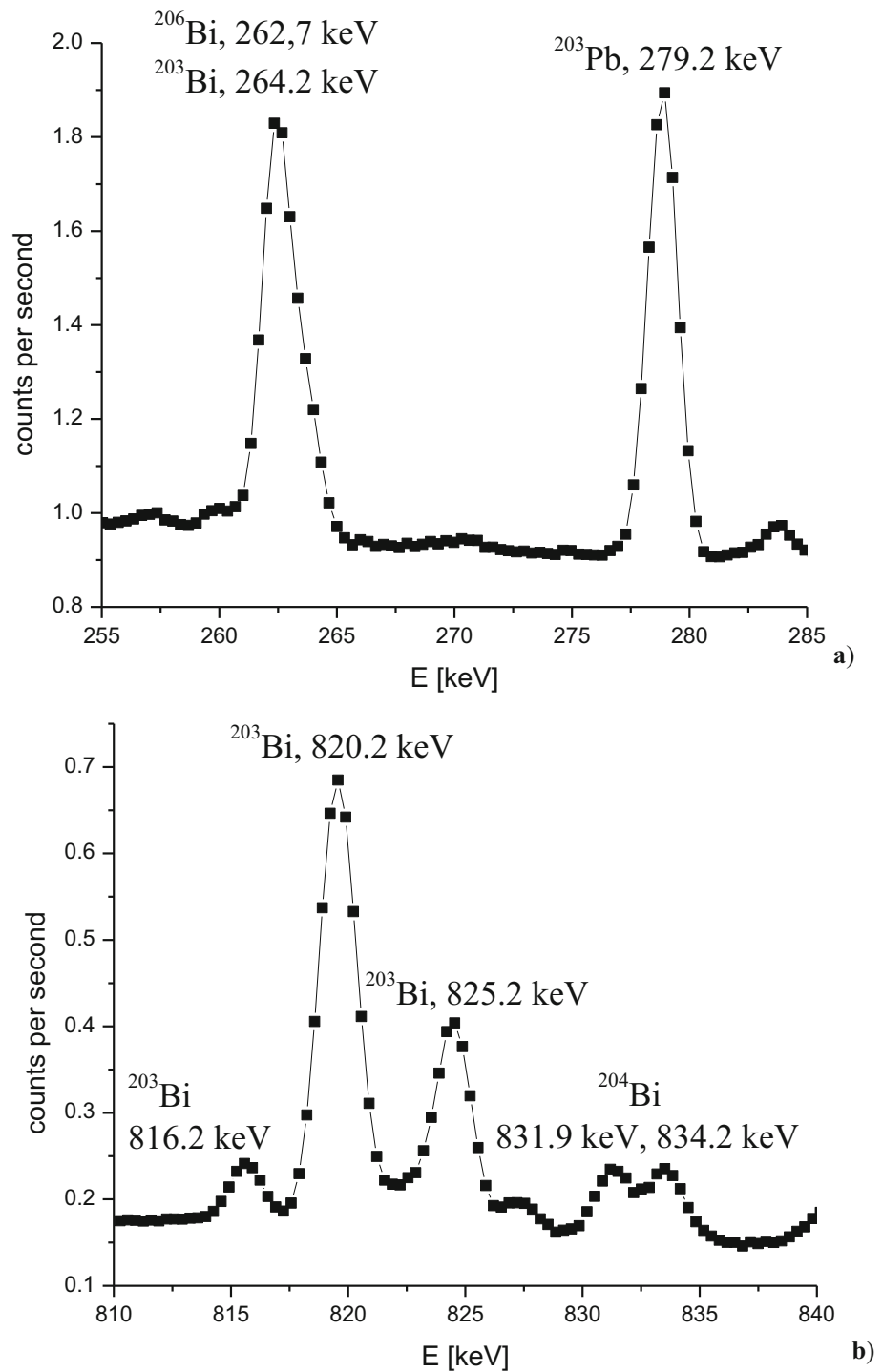
4 Results and discussion

4.1 Experiment

The estimation of the $N_{Pb}(t_{irr})/N_{Bi}(t_{irr})$ ratio at the moment when irradiation was stopped can be obtained from the Eq. 7.

This equation describes output of the (γ,6n) reaction, without proton emission. It was obtained that the ratio of created ^{203}Pb and ^{203}Bi nuclei is $N_{Pb}(t_{irr})/N_{Bi}(t_{irr}) = 0.0148$. If no ($\gamma$,p 5n) reaction occurs, it could be expected that number of ^{203}Pb created nuclei is 1.48% of the number of ^{203}Bi nuclei, after 30 min of irradiation. Ratio of activities of two

Table 1 ^{203}Pb/^{203}Bi activity ratio at the end of irradiation

	$N_{Pb}(t_{irr})/N_{Bi}(t_{irr})$	$A_{Pb}(t_{irr})/A_{Bi}(t_{irr})$
Without proton emission ((γ,6n) only), Eq. 7	0.0148	0.00335
Experimental based values, Eq. 13	0.0758(8)	0.0172(2)

mentioned nuclei after irradiation is $A_{Pb}(t_{irr})/A_{Bi}(t_{irr}) = 0.00335$.

The intensities of the selected gamma lines were determined in both measured spectra. Relative efficiency of detection was calculated using gamma lines of ^{206}Bi. Ratio of ^{203}Pb and ^{203}Bi nuclei that decayed in the observed time interval was evaluated as shown in Eq. 14. Obtained N_{Pb}^{D}/N_{Bi}^{D} ratio was used to calculate value of N_{Pb}^{0}/N_{Bi}^{0} ratios by Eq. 13. The ratio of activities at the moment when irradiation was stopped was calculated as well. Both registered spectra gave ratio results that agreed within experimental error. In the continuation of the paper, the results obtained from gamma lines measured in a longer spectrum will be presented, due to better counting statistics. The calculated and experimental values are presented in Table 1.

It can be seen from the data presented in Table 1 that the ratio of the numbers of created ^{203}Pb and ^{203}Bi nuclei, as well as their activity ratio, at the end of irradiation, extracted from the measured spectra, differs significantly from the estimation based on the assumption that no proton is emitted in photonuclear reaction. This leads us to the conclusion that the production of ^{203}Pb by some other process, probably (γ,p 5n), in addition to the decay of ^{203}Bi can have a significant contribution.

After the experimental confirmation of the possibility that (γ,p 5n) nuclear reaction can make a measurable contribution to total ^{203}Pb activity, the very next step is to estimate p/q ratio. Equation 8 gives such a possibility. If the irradiation time was 30 min and experimentally obtained ratio of ^{203}Pb and ^{203}Bi nuclei is 0.0758(8), it was estimated using Eq. 8, that p/q factor is 0.060(1). This means that the rate of production of ^{203}Pb by ^{209}Bi(γ,p 5n) reaction is 6% of the rate of ^{209}Bi(γ,6n) ^{203}Bi (Fig. 5).
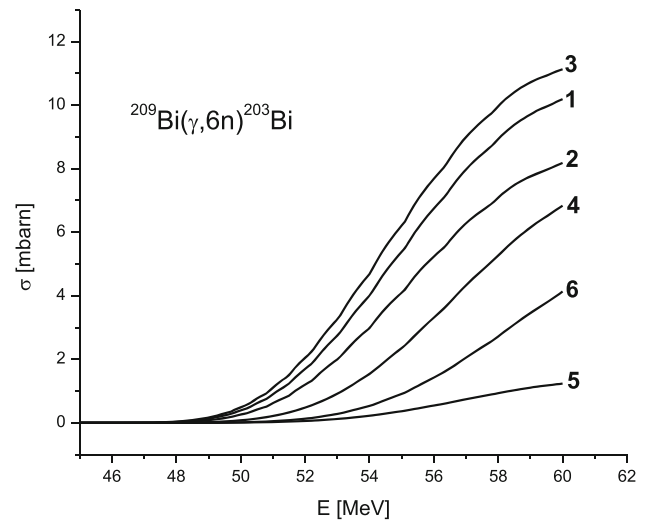
Fig. 5 TALYS estimations for cross section of ^{209}Bi(γ,6n)^{203}Bi reaction. The numbers indicate the level density model as numbered in Sect. 2.4
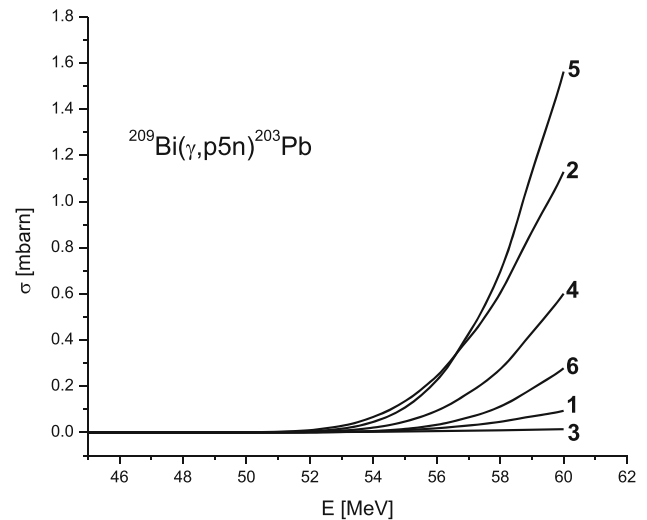
Fig. 6 TALYS estimations for cross section of ^{209}Bi(γ,p 5n)^{203}Pb reaction. The numbers indicate the level density model as numbered in Sect. 2.4

4.2 Calculated ratio of ^{209}Bi(γ,p 5n) and ^{209}Bi(γ,6n) reaction probabilities

And finally, in order to estimate ratio of probabilities of ^{209}Bi(γ,p 5n) and ^{209}Bi(γ,6n) reactions, denoted as p and q, it is necessary to calculate the energy differential cross section for both reactions using the TALYS code. The obtained results, for all six models of level densities are shown in Figs. 5 and 6. As might be expected, the cross section for a reaction without emission of positive charged particle is significantly larger than cross section for emission of one proton in addition to five neutrons. It should also be noted that the

Table 2 Ratio p/q obtained using measured activities and simulation performed with six different models of level densities (in the same order as stated in Sect. 2.4)

	p/q ratio
Estimated using TALYS cross sections	0.00278
	0.0472
	0.000698
	0.0329
	0.5077
	0.0295
Estimated from Eq. 8	0.060(1)

estimated cross sections for both observed reactions can be very different from each other, depending on which density of states model is chosen.

With the obtained values of cross section and chosen bremsstrahlung function it is possible to calculate p/q ratio using both Eqs. 15 and 16. The result of TALYS estimations are depicted in Table 2, together with results of calculations based on measured data.

It is referred that the results obtained in the photo-activation experiments on ^{208}Pb and ^{209}Bi [7, 8] are in good agreement with the calculations performed using the TALYS code. Some examples can be found in the literature [15, 16] that the results of TALYS calculations do not completely match the results of measurements. For the purpose of analyzing the obtained results, it is particularly important to emphasize that one of the conclusions presented in reference [11] is that the shares of ^{209}Bi$(\gamma,$p 4n$)$ and ^{209}Bi$(\gamma,$p 5n$)$ reaction are not negligible. The authors estimated that the yield of the ^{209}Bi$(\gamma,$p 4n$)$ reaction obtained experimentally at 55.6 MeV bremsstrahlung beam was almost 15 times higher than the yield estimated using the TALYS code. In the case of ^{209}Bi$(\gamma,$p 5n$)$ reaction, this difference is even greater.

Here, it is particularly important to point out that, based on the results presented in reference [11], it can be concluded that the yield of ^{209}Bi$(\gamma,$p 5n$)^{203}$Pb reaction is about 9.4 times higher than the yield of reaction ^{209}Bi$(\gamma,$6n$)^{203}$Bi. As can be seen from Table 2, in this paper it is estimated that the yield of ^{209}Bi$(\gamma,$6n$)^{203}$Bi reaction is over 16 times higher than the yield of ^{209}Bi$(\gamma,$p 5n$)^{203}$Pb reaction. It is most likely that the Coulomb barrier significantly reduces the probability of reactions in which a charged particle is emitted.

According to the data presented in Table 2, it is difficult to get general conclusion concerning agreement between TALYS estimation and experimental results. As can be seen, TALYS estimations can be almost two orders of magnitude smaller than the experimentally obtained p/q value, as well as one order of magnitude higher.

5 Conclusions

In this study, an attempt was made to check if ^{203}Pb is formed in photonuclear reactions on ^{209}Bi exclusively from the decay of ^{203}Bi formed in $(\gamma,$6n$)$ reaction or $(\gamma,$p 5n$)$ reaction also plays a part in it, as indicated in reference [11]. It has been shown that this estimation can be made if the ratio of ^{203}Pb and ^{203}Bi nuclei numbers, at the moment when the exposure of the Bi target in the photon beam is completed, is known.

Irradiation of the target from natural bismuth was performed at 60 MeV bremsstrahlung beam. Induced activity was measured in standard off-beam experiment. Registered spectra were used to extract numbers of created ^{203}Bi and ^{203}Pb nuclei. The obtained ratio of nuclei numbers indicates that ^{203}Pb is formed in some other way, other than from the decay of ^{203}Bi. The most likely mechanism is the $(\gamma,$p 5n$)$ reaction. Based on the experimentally estimated ^{203}Pb/^{203}Bi nuclei number (or activity) ratio at the moment when the irradiation was stopped, it is possible to estimate how much of the ^{203}Pb activity originates from $(\gamma,$p 5n$)$ reaction. It was obtained that the number of produced ^{203}Pb nuclei is about 7.6% of the number of ^{203}Bi nuclei. Based on this value, it was established that the rate of production of ^{203}Pb through $(\gamma,$p 5n$)$ reactions is about 6% of the rate of production of ^{203}Bi by $(\gamma,$6n$)$ reaction. This is significantly less than presented in reference [11].

In order to verify the obtained results, a TALYS simulation of cross-sections for $(\gamma,$p 5n$)$ and $(\gamma,$6n$)$ reaction was performed. According to the obtained cross-sections, ratio of reaction rates of both reactions was calculated using one model of strength function and six models of level density function. Due to large scatter of TALYS cross sections for both reactions obtained results of ratios of reaction rates differ significantly.

This approach neither verified nor contradicted certain indications [11] that TALYS code underestimates the probability of photonuclear events in which a proton is realized in addition to neutrons. A new experiment that primarily makes advantage of wider range of energies, preferably higher than 60 MeV and a more detailed analysis of theoretical results and TALYS simulations may eliminate this doubt. The new measurements will also help to resolve the dilemma of whether the yield of ^{209}Bi$(\gamma,$p 5n$)^{203}$Pb reaction is significantly higher than the yield of the ^{209}Bi$(\gamma,$6n$)^{203}$Bi reaction, as stated in reference [11], or whether this ratio is significantly lower, as obtained in the measurements described in this paper. The method described in this study is not limited to the case of ^{209}Bi, and can be applied to other targets and products of photonuclear reactions.

References

1. Handbook on Nuclear Activation Data, Technical Report Series 273, IAEA Vienna (1987)
2. Handbook of photonuclear data for applications: Cross sections and spectra, IAEA TECDOC 1178, IAEA Vienna (2000)
3. Experimental Nuclear Reaction Data (EXFOR) https://www-nds.iaea.org/exfor/
4. A.J. Koning, D. Rochman, Nucl. Data Sheets **113**(12), 2841–2934 (2012)
5. R.R. Harvey, J.T. Caldwell, R.L. Bramblett, S.C. Fultz, Phys. Rev. **136**(1B), 126–131 (1964)
6. H. Naik, A.V.R. Reddy, S. Ganesan, D. Raj, K. Kim, G. Kim, Y.D. Oh, D.K. Pham, M.H. Cho, I.S. Ko, W. Namkung, J. Korean Phys. Soc. **52**(3), 934–939 (2008)
7. H. Naik, S. Singh, A.V.R. Reddy, V.K. Manchanda, S. Ganesan, D. Raj, M.S. Rahman, K.S. Kim, G. Kim, Y.D. Oh, H.-S. Lee, M.-H. Cho, I.S. Ko, W. Namkung, Eur. Phys. J. A **41**, 323–334 (2009)
8. H. Naik, S. Singh, A. Goswami, V.K. Manchanda, G. Kim, K.S. Kim, M.-W. Lee, M.S. Rahman, D. Raj, S. Ganesan, S. Suryanarayana, M.-H. Cho, W. Namkung, Nucl. Instrum. Methods Phys. Res. B **269**, 1417–1424 (2011)
9. A.N. Ermakov, B.S. Ishkhanov, I.M. Kapitonov, I.V. Makarenko, V.N. Orlin, Phys. At. Nucl. **73**(5), 737–745 (2010)
10. S.S. Belyshev, A.N. Ermakov, B.S. Ishkhanov, V.V. Khankin, A.S. Kurilik, A.A. Kuznetsov, V.I. Shvedunov, K.A. Stopani, Nucl. Instrum. Methods Phys. Res. A **745**, 133–137 (2014)
11. S.S. Belyshev, D.M. Filipescu, I. Gheoghe, B.S. Ishkhanov, V.V. Khankin, A.S. Kurilik, A.A. Kuznetsov, V.N. Orlin, N.N. Peskov, K.A. Stopani, O. Tesileanu, V.V. Varlamov, Eur. Phys. J. A **51**, 67 (2015)
12. I. Gheorghe, H. Utsunomiya, S. Katayama, D. Filipescu, S. Belyshev, K. Stopani, V. Orlin, V. Varlamov, T. Shima, S. Amano, S. Miyamoto, Y.-W. Lui, T. Kawano, S. Goriely, Phys. Rev. C 96, 044604 (1917) Erratum Physical Review C 99, 059901 (2019)
13. S. Agostinelli et al., Geant4—a simulation toolkit. Nucl. Instrum. Meth. A **506**, 250–303 (2003)
14. A. Koning, S. Hilaire, S. Goriely, Simulation of nuclear reactions, TALYS-1.96/2.0, https://www-nds.iaea.org/talys/tutorials/talys_v1.96.pdf
15. O.S. Deiev, I.S. Timoshenko, S.N. Olejnik, V.A. Kushnir, V.V. Mytrochenko, S.A. Perezhogin, Phys. Rev. C **106**, 024617 (2022)
16. A.N. Vodin, O.S. Deiev, I.S. Timoshenko, S.N. Olejnik, M.I. Ayzatskiy, V.A. Kushnir, V.V. Mytrochenko, S.A. Perezhogin, Eur. Phys. J. A **57**, 208 (2021)

Regular Article

Application of Geant4 simulation in measurement of cosmic-ray muon flux and studies of muon-induced background

Dejan Joković[a] , Dimitrije Maletić, Aleksandar Dragić, Nikola Veselinović, Mihailo Savić, Vladimir Udovičić, Radomir Banjanac, David Knežević

Institute of Physics, University of Belgrade, Pregrevica 118, Belgrade 11080, Serbia

Abstract The low-level underground laboratory at the Institute of Physics Belgrade is a facility for gamma-ray spectroscopy measurements and for measurements of cosmic-ray muon intensity. Related to the two research subjects, studies of cosmic-ray muon-induced background in gamma spectroscopy are of particular interest. Continuous measurements of cosmic muon intensity at the ground level and underground sites have been carried out by means of plastic scintillation detectors. The detector response, interpretation of the experimental spectra and their calibration were obtained and verified using a Geant4-based simulation. The results of the simulation were used in measurement of muon flux at the surface and shallow underground (25 m w e)—the measured fluxes are (170 ± 6) m^{-2} s^{-1} and (44 ± 1) m^{-2} s^{-1}, respectively. An underground muon detector can operate in coincidence with a high-purity germanium gamma-ray detector, which allows investigations of muon-induced processes in germanium spectrometers. In low-level gamma spectroscopy, neutrons produced by muons in the lead shielding of a germanium detector contribute to the detector background. Simulation of prompt muon-induced background as well as simulation of neutron production by cosmic muons in lead were carried out. Estimated neutron yield in lead is $(3.1 \pm 0.4) \times 10^{-5}$ neutrons per g/cm^2, per tagged muon. Also the average neutron multiplicity is calculated.

1 Introduction

The low-background underground laboratory at the Institute of Physics Belgrade has been designed as a multi-purpose facility for gamma-ray spectroscopy measurements of low activities, as well as for measurements of cosmic-ray intensity. The two main research objectives intersect in studies of cosmic-ray muon-induced background in gamma spectroscopy measurements. The laboratory is located at near-sea level, at the altitude of 78 m. It consists of two separate parts—the ground level and the underground; the shallow underground part is dug at the depth of about 12 m beneath the surface. The earth above the underground site consists of four layers of loess with average density of (2.0 ± 0.1) g/cm^3. With the 30 cm thick concrete ceiling, the overburden is approximately equal to 25 m of water equivalent (m w e; 1 m w e gives an interaction depth of 1 hg/cm^2). It provides a good environment for gamma spectroscopy—the overburden soil layer absorbs almost all nucleonic component of cosmic rays and reduces muon flux by about four times. Radon concentration is kept low by preventing diffusion from the soil and by maintaining constant overpressure in the room. One shielded high-purity germanium (HPGe) spectrometer is dedicated for low-level gamma measurements in the underground laboratory. It can operate in coincidence with a muon scintillation detector, which enables investigations of muon-induced events in the germanium detector. More details on the laboratory can be found in [1].

Cosmic-ray muon intensity has been continuously measured at both the ground level and underground sites since 2002. The current experimental set-up, described in the next section, was upgraded and commissioned in 2008. Measurements of muon intensity and its temporal variations can give some information on primary cosmic radiation, interaction processes in the atmosphere and solar modulation. Low-energy primary cosmic rays are under large influence of interplanetary magnetic field, whose structure varies because of solar activity, which has various periodic and aperiodic features. Therefore, temporal variations of cosmic muon flux are expected to be a good indicator of solar activity. These measurements yielded some results on muon flux and its variations [2–5]. In shallow and deep underground laboratories cosmic muons represent an important source of background, either directly or by generating high-energy neutrons in interactions in rock or detector and its surroundings [6–8]. Results of a preliminary study on muon-induced neutron production rate were published in [9].

Today applications of various Monte Carlo simulation methods make an essential part of experimental research. These simulation methods are found to be very useful for modeling detector response, accurate interpretation of experimental data, particularly

experimental spectra and their features, as well as for detector calibration. There is a handful of Monte Carlo toolkits used in nuclear and particle physics studies, one of the most commonly used is Geant4 (Geometry aNd Tracking), which has been developed and maintained at CERN [10–12]. Geant4 is a framework for accurate Monte Carlo simulations of particle transport through matter. It contains a complete set of routines for modeling particle trajectories and interactions: detector geometry and materials, physics processes, event generation, detector response and analysis and visualization. Versatility and flexibility of Geant4 allow users to build customized simulation programmes that fit their specific needs. Another advantage of the toolkit is that a built simulation can be easily modified, so as to be suitable for different detector configurations. Increase in computational power enabled Geant4 simulations to be no longer time demanding in order to achieve good statistical uncertainties, due to use of parallel computing, multithreading, etc. Uses of Geant4 span from high energy, nuclear and accelerator physics to medical and space science.

In experiments carried out in the Belgrade underground laboratory, Geant4-based simulations have been developed in order to obtain detector response for various detector configurations, as well as for interpretation of the experimental spectra and their calibration. They include simulations of response of the plastic scintillation detectors for cosmic-ray muon studies and simulations of the germanium detector for gamma spectroscopy. Here we present an overview of applications of Geant4 simulations in measurement of cosmic-ray muon fluxes at the ground level and underground sites and for estimation of muon-induced background in the lead shield of the HPGe detector.

2 Experimental set-up

Measurements of cosmic-ray muon intensity have been performed by means of plastic scintillation detectors, situated in both the ground level and underground parts of the laboratory. Each detector configuration consists of one large scintillator with an accompanying data acquisition system. The two experimental set-ups are identical but they operate independently, each detector has its dedicated data acquisition module. A sketch of the detector set-up is displayed in Fig. 1.

The polystyrene-based scintillator (similar to NE102) has a rectangular shape with base area 100 cm × 100 cm and thickness 5 cm, housed in 1 mm thick aluminum. It lies horizontally on its largest side. At each corner of the scintillator a 2-inch photomultiplier tube (PMT) is attached, pointing at the detector's diagonal. Individual signals from the photomultiplier tubes looking at the same diagonal, i.e., two opposite photomultipliers, are summed in one output signal. Hence two output signals from the two detector's diagonals are recorded and stored on tape. The data acquisition system is based on a fast 4-channel analog-to-digital converter (ADC), model CAEN N1728B, which has 100 MHz sampling frequency (time resolution 10 ns). Two input ADC channels are used for the summed signals from the two diagonals of the scintillator, respectively, there are two signals per scintillator, each feeding one ADC channel. The third and/or fourth ADC channels are reserved for other detectors, such as germanium detector. Information about each event (input channel, time tag, amplitude) whose amplitude is above threshold is stored in an event list, which allows offline analyses of single and coincidence events between different channels within a chosen time window. Time and amplitude spectra are formed by histogramming data from the event list, for single ADC channels or for two or more coinciding channels.

Single spectra of the plastic scintillators result from the summed signals from the PMTs on the same diagonal, which are fed to two ADC channels separately; hence two single spectra are produced for each detector. The typical experimental spectra, for both the surface and underground detectors, are presented in Fig. 2. They are mainly composed of energy deposit spectra of cosmic rays that pass through the scintillator and of Compton scattered environmental gamma radiation, as a dominant source of background. The main feature in the spectra is a peak that should correspond to muon and electron energy loss in the 5 cm thick scintillator. However, this energy loss peak, and subsequently cosmic events, cannot be separated from the background, which is quite significant because of the detector's large size and its four PMTs (Fig. 2).

Fig. 1 Experimental set-up for cosmic-ray intensity measurements: plastic scintillation detector (1), photomultiplier tubes (2), analog-to-digital converter (3)
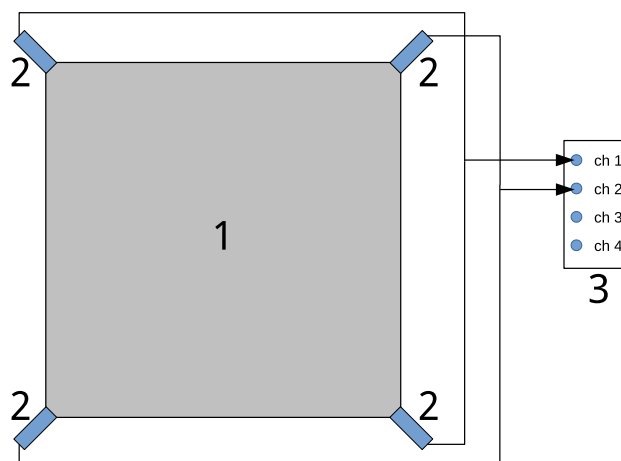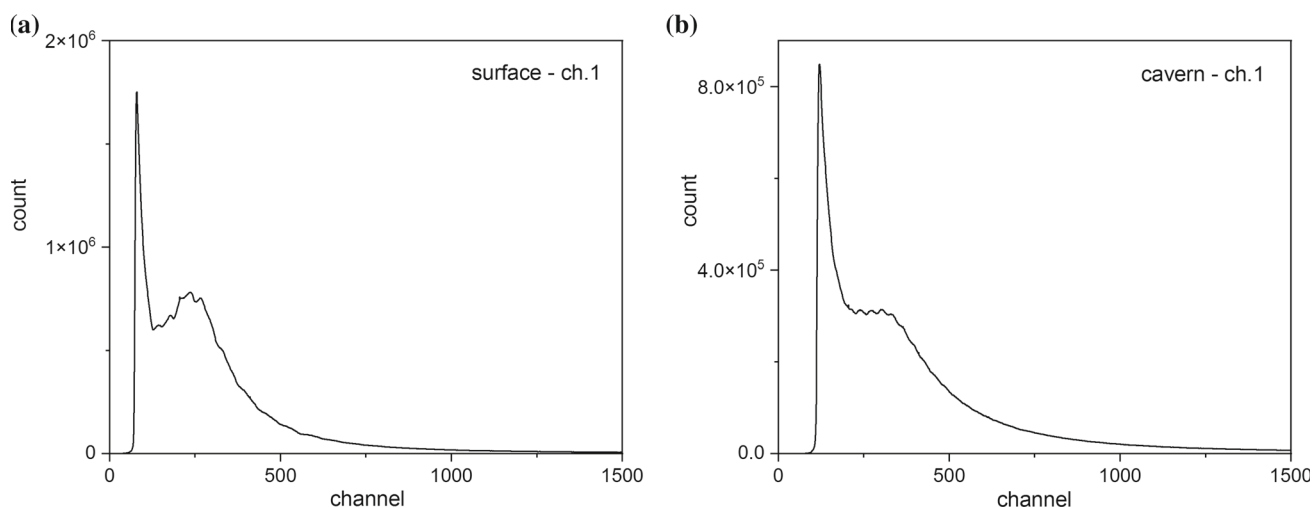
Fig. 2 Typical single spectra of the surface (left) and underground (right) scintillation detectors, produced by the summed signals from the PMTs looking at the same detector's diagonal. They are composed of energy deposit spectra of cosmic rays and of environmental gamma radiation

Fig. 3 Normalized coincidence spectra of the surface and underground detectors. The spectra are considered as solely energy deposit spectra of cosmic-ray charged particles. Both spectra exhibit a peak that corresponds to charged particle energy loss in the 5 cm thick plastic scintillator
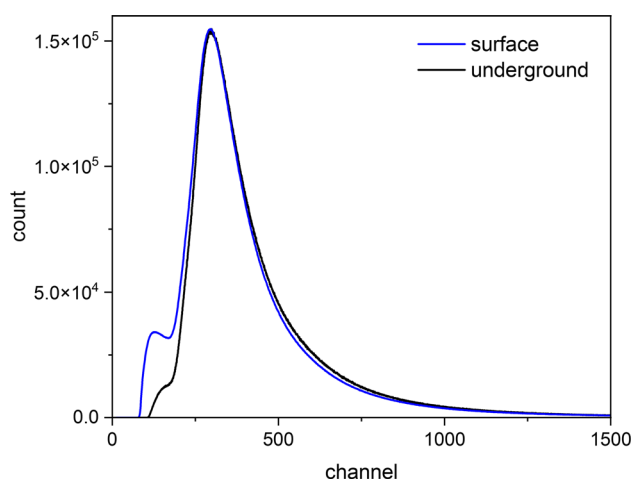
Investigation of responses of the single PMTs have shown that cosmic events can be selected by coinciding events that promptly trigger all four PMTs, i.e., both detector's diagonals. Time interval spectra of coincidences between the ADC channels that are fed by the two diagonals, have a sharp peaked distribution that is 40 ns wide and stretches up to ±50 ns upon the peak (given the 10 ns time resolution of the ADCs). Prompt coincidences selected within a time window of 100 ns are associated to cosmic rays. This procedure virtually removes background, as environmental gamma rays cannot trigger both diagonals. The coincidence spectra are considered as solely due to energy losses by charged particles in the scintillator. These interpretations of the experimental spectra have been supported by Geant4 simulations. The individual coincidence spectra per the diagonal are then summed into one energy deposit spectrum, per the detector; the coincidence spectra for both the surface and underground detectors are presented in Fig. 3.

The coincidence spectra of the scintillators show a well-defined peak of the charged particle energy losses, while the low-energy background present in the single spectra vanishes (Figs. 2, 3). Since the specific energy loss for muons is ~ 2 MeV per g/cm^2, the spectral peak should be at the energy ~ 11 MeV, for the 5 cm thick plastic scintillator. Comparing the spectra of the detectors at the surface and in the underground laboratory one can notice the difference in their shape at lower energies. This difference points to the contribution of electromagnetic component of cosmic rays (electrons, positrons and photons), whose flux is significant at the surface. It is absent underground, where practically only muon component is present. Hence, it is plausible to assume that events recorded by the underground detector are only muon events, while for the surface detector they include electromagnetic component. Moreover, due to edge effects there are some cosmic events that fall below the instrumental cuts. The amount of these lost events can be found by comparing experimental results with simulations (Sect. 3).

3 Measurement of cosmic-ray muon flux

3.1 Simulation

With the aim of corroborating the aforementioned statements and interpretations, a Geant4-based application for modeling detector response of the scintillation detectors has been developed. It can be also used for calibration of spectra. The simulation has been done along the same lines as in the previous works [2, 13]. Latest Geant4 version used for this work is 11.0. In Geant4, an event is generated by defining primary particle, its initial position, momentum direction and energy. In the simulation of the underground detector, primary particles were muons, since it can be assumed that only muons are present at the depth of 25 m w e. Muons were gunned from the horizontal and vertical sides of the detector. Particle positions and momentum directions were generated in accordance with the muon directional intensity, which depends on zenith angle: $I(\theta) = I(0)\cos^n\theta$, where n has a value 1.85 at sea level and 1.55 at the 25 m w e depth [14, 15]. Integrated intensity of muons that pass through the horizontal surface is

$$J_h = \int_\Omega I(\theta)\cos\theta\sin\theta \mathrm{d}\theta \mathrm{d}\phi = 2\pi I(0)\int_0^{\pi/2}\cos^{(n+1)}\theta\sin\theta \mathrm{d}\theta = 2\pi I(0)\frac{1}{n+2}, \tag{1}$$

while integrated intensity of muons that pass through the vertical surface is

$$J_v = \int_\Omega I(\theta)\sin^2\theta\cos\phi \mathrm{d}\theta \mathrm{d}\phi = I(0)\int_\Omega \cos^n\theta\sin^2\cos\phi \mathrm{d}\theta \mathrm{d}\phi, \tag{2}$$

latter integrated over a quarter of the sphere. From the ratio J_h/J_v it follows that muons have higher probability to hit the horizontal than the vertical surface—for $n = 1.55$, $J_h/J_v = 3.64$ per unit area, and for $n = 1.85$, $J_h/J_v = 3.88$. These probabilities were taken into account when primary positions on the horizontal and vertical detector's sides were generated.

The particle energy was calculated in two steps. First, energy at the surface was sampled from the Gaisser's formula for muon energy spectrum at sea level [16]:

$$\frac{\mathrm{d}j_\mu(E)}{\mathrm{d}E} = 0.14 E^{-2.7}\left(\frac{1}{1 + 1.1\frac{E\cos\theta}{115\,\text{GeV}}} + \frac{0.054}{1 + 1.1\frac{E\cos\theta}{850\,\text{GeV}}}\right), \tag{3}$$

where E is the muon energy in GeV, and $\cos\theta$ is sampled from the $\cos^{1.85}\theta$ distribution. The formula does not describe well experimental data at lower energies and larger zenith angles, so it was modified according to [17]. Muon energy loss in the earth layer was calculated from the practical equation for total energy loss of muons in standard rock, in units of MeV [18]:

$$-\left(\frac{\mathrm{d}E}{\mathrm{d}x}\right) = 1.84 + 4.65\cdot 10^{-6}E + 0.076\ln\left(\frac{E'}{m_\mu c^2}\right)\left[\text{MeV}/(\text{g}/\text{cm}^2)\right], \tag{4}$$

where E' is the maximum transferable energy $E' = E^2/(E + m_\mu^2 c^2/2m_e)$, m_μ is the mass of the muon, and m_e is the mass of the electron. The muon path length, i.e., layer thickness, dx was calculated as $25/\cos\theta$ hg/cm². The energy loss was then subtracted from the value sampled from Eq. 3, and the deducted value was taken for the initial muon energy in the simulation. The muon energy spectrum underground is thus hardened because low-energy muons are removed.

Muons were tracked through the scintillator as a sensitive detector. When a muon passes through a material, it interacts with matter—in these interactions it deposits a portion of its energy, which adds to the overall energy deposit spectrum. Physics processes were applied through the Geant4 physics list QGSP_BERT_HP, which include all interactions leading to production of secondaries, as well as for calculation of energy losses in the detector. For the purpose of simulation of the plastic scintillators electromagnetic interactions of muons, electrons and gammas are relevant (constructor G4EmStandardPhysics_option4 was activated).

The normalized simulated and experimental spectra agree very well, thus verifying interpretation of the detector response and the experimental results (Fig. 4). Furthermore, by comparing the two spectra one can find the percentage of muon events that are not recorded due to instrumental cuts. It is equal to the ratio of counts in the two spectra, here it is approx. 6%. This correction was applied in calculation of the muon flux underground. Relative arbitrariness in estimation of the fraction of lost events contributes to the uncertainty of the measured muon flux to a large degree.

When the same simulation was applied for the surface detector, there was a large discrepancy between the simulation and experimental results. This led to a conclusion that besides muonic, electromagnetic component of cosmic rays also had to be taken into account. Therefore, the model was further extended, so as to include all secondary cosmic-ray particles at the surface. Particle fluxes at the surface were obtained using CORSIKA (COsmic Ray SImulations for KAscade) programme [19, 20]. It is a Monte Carlo code for simulation of extensive air showers generated by primary cosmic rays in their interactions with air nuclei at the top of the atmosphere. It produces spectra of secondary cosmic rays at a chosen observation level (altitude) above the surface. The output is in a form of a list that keeps information about each particle—its type, momentum, energy and time of arrival. Geant4 provides an interface that can read output files from external event generators and use information to generate primary particles (type, momentum and energy). Hence, CORSIKA served as a primary event generator, while the detector response was modeled by the Geant4 simulation. Details on the CORSIKA simulation—primary cosmic-ray spectrum, hadron interaction models, geomagnetic field, atmospheric model, observation level—can be found in [3].
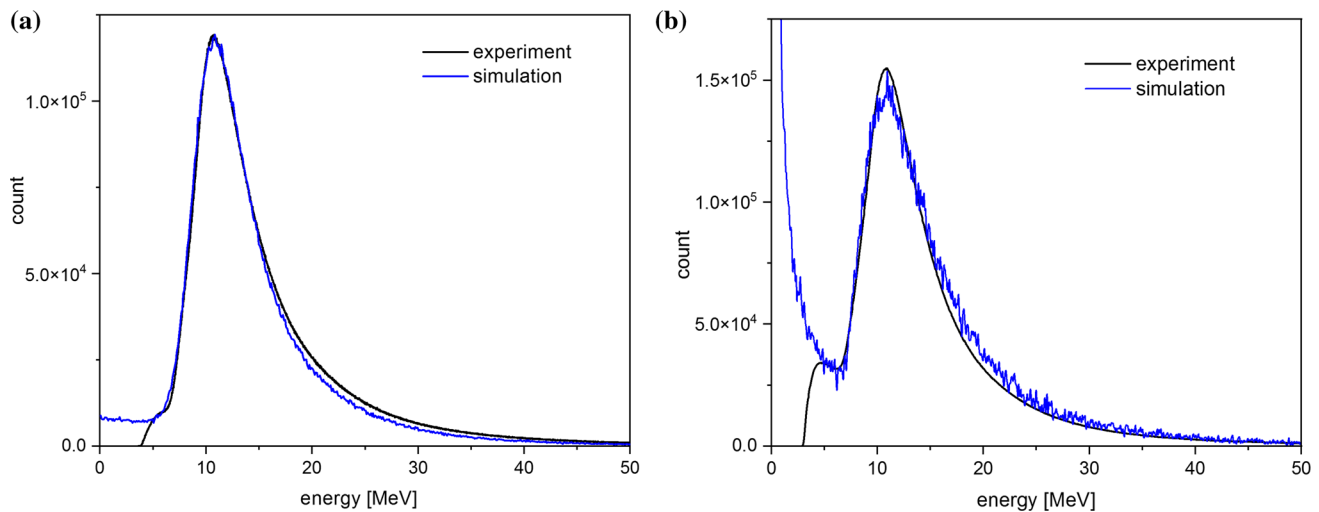
Fig. 4 Normalized experimental (black line) and simulated (blue line) energy deposit spectra of the scintillation detectors in the underground laboratory (left) and at the surface (right). Peak of charged particle energy losses in the spectra is at energy about 11 MeV, approx. equal to muon energy loss in the 5 cm thick plastic scintillator

Primary particles for the simulation of the surface detector, muons, electrons and gammas were, respectively, selected from the CORSIKA output. The energy deposit spectra were then obtained separately for the three types of particles. These individual spectra exhibit some different features, the main difference is that the muon spectrum is virtually the same as for the underground detector, while the gamma ray spectrum is mostly at lower energies [3]. The sum of the individual energy deposit spectra gives the resultant simulated spectrum, which is in good agreement with the experimental one (Fig. 4). It is clearly separated into two parts at ~ 6 MeV, which nearly corresponds to the threshold set by instrumental cuts. At energies exceeding the threshold muon events are dominant, however there is a small but non-negligible contribution of electrons and gammas. The fraction of muons in the simulated spectrum above the instrumental cut is equal to the ratio of muon counts to the total counts—muons make about 87% of the total number of events above the 6 MeV threshold.

3.2 Results

The cosmic muon flux is calculated from the equation $\Phi = N_\mu/(S\,t)$, where N_μ is number of muons, S surface area and t measurement time. The average muon flux underground was calculated from data recorded during 289 days of measurement ($t = 2.497 \times 10^7$ s). The detection efficiency to muons for this type of detector is close to 100% [21]; the simulation confirms this assumption, but it contributes to uncertainty of the measured flux to a smaller extent. The number of muon events was corrected for events below the instrumental cuts, which was equal to the ratio of normalized counts in the simulated and experimental spectra. About 6% of muon events falls below the cuts. After correction for lost events, the total number of muons is 1.149×10^9. The horizontal area of the detector is 1 m^2, however muons also hit vertical sides. On the other hand, muons have higher probability to hit the horizontal than the vertical surface, due to $cos^n\theta$ directional distribution – 3.64 times higher for the underground detector. The effective detector area is thus 1.055 m^2. Finally, the muon flux underground, at the 25 m w e depth, is $\Phi = (44 \pm 1)$ m^{-2} s^{-1}. Statistical uncertainties are much smaller than systematic ones, which are partially associated to experimental data treatment, such as the selection of time window for coinciding the single detector spectra and estimation of the fraction of lost muon events below instrumental cuts. Uncertainty of the simulation is roughly estimated by varying parameters of simulation, particularly angular distribution of muons (exponent n in $cos^n\theta$), thickness of the overburden and calculation of muon energy loss (Eq. 4).

At the surface, the total cosmic-ray flux is the sum of muon and electromagnetic fluxes. First the total flux above the instrumental cut was calculated from the experimental data. Then the percentage of muons above the cut was found from the simulated data—approx. 87% of the total number of events. The flux was also corrected for muon events below the cuts (+ 6%). The effects of seasonal variations are mostly removed due to long measurement time. The total number of cosmic events is 4.079×10^9. After all corrections applied ($N_\mu = N_{tot} \times 0.87 \times 1.06$), the number of muon events is 3.762×10^9. The time of measurement is 244 days (2.108×10^7 s), and the effective detector area is 1.0515 m^2. Finally, muon flux at the surface is $\Phi = (170 \pm 6)$ m^{-2} s^{-1}. The uncertainty was evaluated in a similar way as for the calculation of the muon flux underground. There is also a contribution to the uncertainty that comes from the correction for the fraction of muons in the total flux, which was calculated from the simulation data.

The measured fluxes underground and at the surface are consistent with the previous work, though the muon flux at the surface gives 24% higher value [2]. Integrated muon intensity at sea level is often referred as about 1 cm^{-2} min^{-1} [22], the calculated flux at the surface is in accord with this value. The underground flux adds to the list of muon data in underground laboratories [23]. The integral flux of electromagnetic component at the surface is very approximately estimated to 30% of the total flux.

4 Simulation of muon-induced background

4.1 Muon-induced background in the germanium detector

The muon detector in the underground laboratory can operate in coincidence with a coaxial high-purity germanium detector (ORTEC GEM30). The detector is based on a cylindrical p-type crystal, with the diameter 58.5 mm and the length 56.4 mm, and the active volume 149 cm^3. The relative efficiency is 35%, with respect to the efficiency of a 3×3 inch NaI detector. The detector is placed inside a 12 cm thick lead castle made of lead with low content of ^{210}Pb (specific activity 25 Bq/kg). Due to the 12 m overburden and thick lead shielding, it is suitable for gamma spectroscopy of low-activities. The muon detector is placed directly above the lead castle at the distance 44 cm, and can serve as a veto for additional background suppression. Signals from the HPGe detector are fed into an input channel of the same ADC that is used by the muon detector. The acquisition system allows up to four different inputs; here two inputs are used for signals from the muon detector and one for the HPGe detector. Events recorded by both detectors are stored in one list with information about each event (input channel, trigger time and amplitude). This allows analyses of coincidence or anticoincidence between different channels, by selecting proper time window. In the coincidence mode muon-induced events in the germanium detector can be studied. In the anticoincidence mode the scintillator can serve as an anti-cosmic veto detector.

Geant4 simulations have found wide-ranging applications in gamma spectroscopy with germanium detectors. One of the main subjects that have been studied is evaluation of muon-induced background in germanium detectors, operating at the surface and underground [24–28]. The simulation that combines the underground scintillator and the HPGe detector was performed with a goal to obtain coincidence response of the two-detector system to cosmic muons. It was used to estimate prompt muon-induced background, which originates from direct muon interaction with the germanium crystal or from electrons ionized by muons in the detector and surroundings. It can also give a prediction of background reduction by the anti-cosmic veto [13].

Configuration of an HPGe detector is more complex than a simple scintillator box, which is why the detailed knowledge of the detector geometry is an essential precondition for an accurate modeling. In this simulation the detector was constructed utilizing the detector parameters provided by the manufacturer. The geometry was tested by varying these parameters and looking at how the changes affect the detector response. This method can be also used for uncertainty estimation. Small changes of the parameters may give rise to large deviations between simulated and experimental results. In order to overcome these difficulties an optimization procedure is often performed, by tuning the detector parameters so as to achieve the best possible agreement with experimental values [29]. For use in gamma spectroscopy Geant4 provides low-energy electromagnetic packages that best model interactions of low-energy gamma rays. Here the G4EmStandardPhysics_option4 constructor class, which combines electromagnetic models for simulations with high accuracy, was activated.

First, the simulation of the germanium background generated by prompt muon interactions in the lead shield was performed. Primary muons were generated on the surface of the lead castle, the top and side surfaces. Energy and angular distributions of muons are the same as used in the simulation of muons underground, described in Sect. 3.1. Per event, initial position and momentum direction were sampled from $\cos^n\theta$ distribution ($n = 1.55$), while energy was sampled from the modified Gaisser's formula and subtracted for the muon energy loss (Eq. 3, 4). Here the germanium crystal is a sensitive detector for calculation of energy deposit. The energy deposit spectrum is in high-energy part due to muons that traverse through the germanium crystal, which has a broad peak at about 43 MeV [13]. For gamma spectroscopy measurements the range up to 3 MeV is mostly of interest. This part of the spectrum is due to secondary particles produced by muons in the detector's surroundings, mainly in the lead castle. The prominent annihilation peak builds upon the continuous spectrum.

Then the simulation of the scintillator and the HPGe detector working in coincidence was carried out, with primary muons now generated on the scintillator's surface, in the same way as described in Sect. 3.1. A sketch of the visualized Geant4 geometry and a muon event is displayed in Fig. 5. The coincidences were selected with a simple condition that a muon has to deposit energy in both detectors. The simulated coincidence spectrum of the germanium detector up to 3 MeV, together with the background spectrum, is shown in Fig. 6. The prominent annihilation peak builds upon the continuous spectrum. Integral of this spectrum gives the number of vetoed background events in the range of 0–3 MeV.

Relative background reduction by the anti-cosmic veto was found as a ratio of counts in the two spectra. For the given configuration the veto halves the prompt muon background in the lead shield. However, the total background of the HPGe detector would be diminished by only 15%. The new set-up has the muon detector half the distance closer to the lead castle, which should to some extent improve background reduction. A common anti-cosmic veto system consists of detectors that are placed above and to the sides of a lead castle, so that the veto is triggered by any arriving muon. This type of set-up would provide background reduction as good as possible for the HPGe detector. However, at the moment it is not planned to add more veto detectors.

4.2 Neutron production by muons in lead

Neutrons produced in interactions of cosmic-ray muons with the detector and its surroundings contribute to background, especially in sensitive experiments in deep underground laboratories searching for rare events. In interactions with the detector neutrons produce signals that may mimic signals from the events searched for. Therefore investigation of neutron-induced background is of great importance for low-background measurements. For lead-shielded germanium detectors neutrons produced by cosmic muons in lead

Fig. 5 Visualization of the Geant4 geometry of the scintillator and HPGe detector, and a coincidence muon event. Particle tracks are: blue—muon, green—photon, red—electron
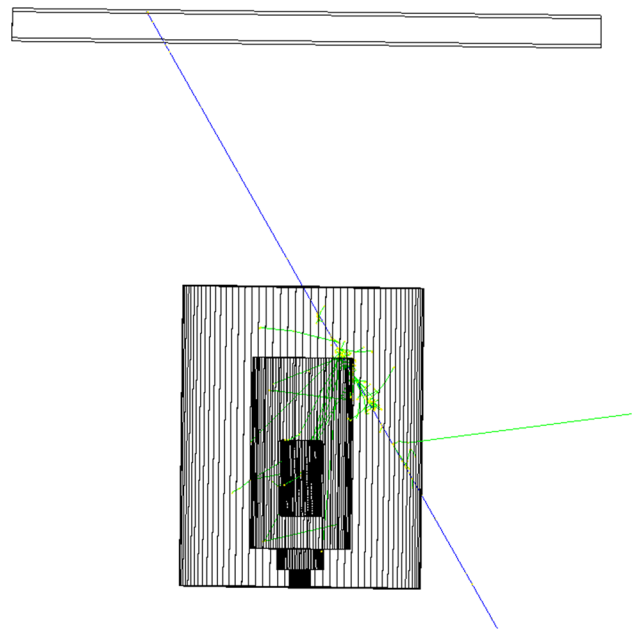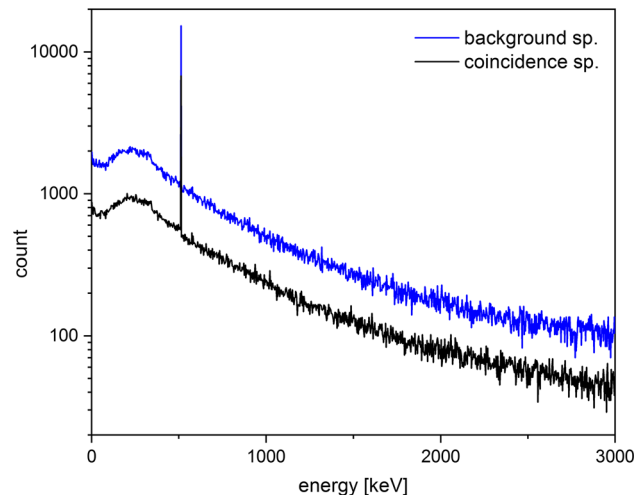
Fig. 6 Normalized background spectrum (blue line) and coincidence spectrum of the HPGe detector (black line) induced by prompt muon interactions in lead, and estimated anti-cosmic veto suppression [13]

are an unavoidable source of background. As it was already pointed out, the experimental set-up in the underground laboratory enables studies of muon-induced events in the HPGe detector, when it works in coincidence with the muon detector. Preliminary results on flux of fast neutrons produced by muons in the lead shielding of the HPGe detector were reported in [9]. Data were collected during over 400 days of measurement. Neutrons were identified from the 692 keV line in the coincidence spectrum, which arises from neutron inelastic scattering on Ge-72 isotope. Neutron production rate can be determined from count rate in the 692 keV line in the spectrum [30]. The muon-induced neutron flux, within the volume of the lead shielding, is $(3.1 \pm 0.5) \times 10^{-4}$ cm^{-2} s^{-1}.

A variety of Geant4 simulation methods have been utilized in studies of production of neutrons by cosmic muons in lead at the surface and underground [31–33]. Here we present the first results of the simulation of muon-induced neutron production in the lead shielding of the HPGe detector. It was done in the same manner as the previous simulations. Primary muons were generated on the top and side surfaces of the lead castle. Muon energy and directional distributions followed the same procedure described in Sect. 3. Hadronic interactions were included through the Geant4 QGSP_BERT_HP physics list. It uses high precision neutron models and cross sections for low-energy neutron interactions. For electromagnetic part the G4EmStandardPhysics_option4 constructor was activated. The simulation was then repeated with the physics lists FTFP_BERT_HP and Shielding, latter is recommended for neutron transport. All three physics models invoke the same classes for neutron interactions. There was no significant difference in the results. Because energy thresholds for production of secondary particles were set at low values, large number of particles was produced. Hence all secondaries but muons and neutrons were killed, and only muons and neutrons were tracked through the lead volume.

Fig. 7 Multiplicity distribution of neutrons produced by muons in lead at the 25 m w e depth
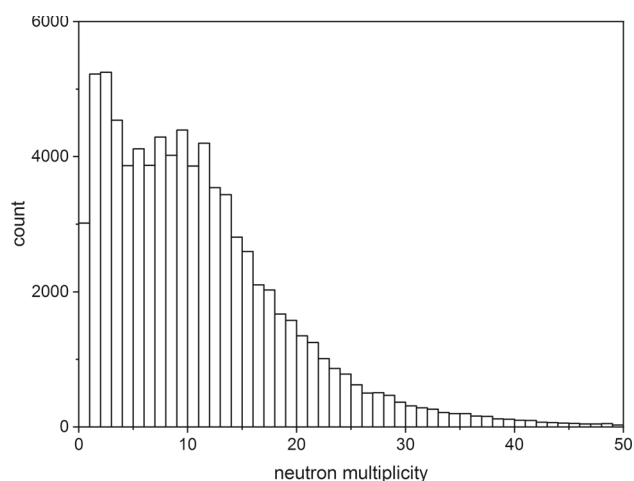
Neutron yield in lead can be determined from the equation $Y_n = N_n/(N_\mu l_\mu \rho)$, where N_n is number of neutrons produced, N_μ is number of muons, l_μ is the mean path length of muons and ρ is density. In total 10^8 muon histories were generated, and 9.34×10^5 neutrons were produced. The mean path length that muons travel through the lead castle, obtained from the simulation, is 26.6 cm. Finally, the neutron yield in the lead volume is $(3.1 \pm 0.4) \times 10^{-5}$ neutrons per gcm^{-2} per muon. It was also looked at how many of these neutrons reach the HPGe detector inside the lead castle—it was approx. 2.4% of all neutrons, though statistics was rather poor for precise studies of neutron-induced processes in the germanium detector. Additionally, neutron multiplicity for each event was found, as number of neutrons per tagged muon. Its distribution is shown in Fig. 7, while the average multiplicity is 11.5.

5 Conclusion

The Geant4-based simulations have been extensively used in experiments carried out in the low-background underground laboratory at the Institute of Physics Belgrade. Here presented overview describes applications of Geant4 simulations in measurements of cosmic-ray muon intensity and in gamma spectroscopy studies of events which have origin in cosmic muons. Detector responses of the plastic scintillation detectors and the germanium detector were obtained in order to evaluate experimental results. In simulations of the surface scintillator primary particles were generated by CORSIKA programme, so as to include electromagnetic component, which is absent underground. Simulated energy deposit spectra showed good agreement with experimental ones. Comparing these spectra precise calculations of muon integral intensity could be calculated. The measured muon fluxes at the surface and underground are (170 ± 6) m^{-2} s^{-1} and (44 ± 1) m^{-2} s^{-1}, respectively. The results are consistent with our previous work and available muon data.

Simulation studies of cosmic muon interactions with lead were performed with a goal to estimate muon-induced background in the germanium detector. Muons can cause two types of background: the first one is due to prompt interactions of muons and secondary particles produced by muons and the second one is due to delayed decays of Ge nuclei produced in neutron inelastic collisions. The prompt muon-induced background was estimated with a simulation of the scintillator and the HPGe detector in coincidence, for the given detector configuration. The two detectors can operate in coincidence or anticoincidence provided the correct selection criteria between recorded events. When they work in anticoincidence the scintillator serves as an anti-cosmic veto. Simulated prompt muon background is also an estimation of the reduction of cosmic background by the veto, which in this case is by one half. The new experimental set-up has the muon detector close to the lead castle, which should improve the background reduction. Another task that was carried out was the simulation of neutron production by cosmic muons in lead. The estimated yield in the lead volume is $(3.1 \pm 0.4) \times 10^{-5}$ neutrons per gcm^{-2} per muon. Also neutron multiplicity per tagged muon is obtained. The results make a good basis for further studies of cosmic muon-induced processes in the vicinity of germanium detectors, including production of neutrons and other particles in the overburden rocks.

Data Availability Statement This manuscript has associated data in a data repository. [Authors' comment: Data sets generated during the current study are available from the corresponding author. Time series of muon flux data are available at http://cosmic.ipb.ac.rs/muon_station/index.html. The simulation code used in this work is publicly available at the zenodo.org data repository, https://doi.org/10.5281/zenodo.10005170.]

Declarations

Conflict of interest The authors have no competing interests to declare that are relevant to the content of this article.

References

1. A. Dragić et al., Nucl. Technol. Radiat. Prot. **26**, 181 (2011)
2. A. Dragić et al., Nucl. Instrum. Methods Phys. Res. A **591**, 470 (2008)
3. N. Veselinović et al., Nucl. Instrum. Methods Phys. Res. A **875**, 10 (2017)
4. M. Savić et al., Astropart. Phys. **109**, 1 (2019)
5. N. Veselinović et al., Eur. Phys. J. D **75**, 173 (2021)
6. V.A. Kudryavtsev, L. Pandola, V. Tomasello, Eur. Phys. J. A **36**, 171 (2008)
7. D. Barker, D.-M. Mei, C. Zhang, Phys. Rev. D **86**, 054001 (2012)
8. H.W. Bae, E.J. Jeon, Y.D. Kim, S.W. Lee, Astropart. Phys. **114**, 60 (2020)
9. A. Dragić et al., J. Phys. Conf. Ser. **409**, 012054 (2013)
10. Geant4, https://geant4.web.cern.ch/
11. S. Agostinelli et al., Nucl. Instrum. Methods Phys. Res. A **506**, 250 (2003)
12. J. Allison et al., Nucl. Instrum. Methods Phys. Res. A **835**, 186 (2016)
13. D.R. Joković et al., Appl. Radiat. Isot. **67**, 719 (2009)
14. P.K.F. Grieder, *Cosmic Rays at Earth* (Elsevier, Amsterdam, 2001), p.372
15. P.K.F. Grieder, *Cosmic Rays at Earth* (Elsevier, Amsterdam, 2001), p.498
16. T.K. Gaisser, *Cosmic Rays and Particle Physics* (Cambridge University Press, Cambridge, 1990), p.71
17. M. Guan et al., *Muon Simulation at the Daya Bay Site* (Lawrence Berkeley National Laboratory, 2010)
18. P.K.F. Grieder, *Cosmic Rays at Earth* (Elsevier, Amsterdam, 2001), p.467
19. CORSIKA, https://www.iap.kit.edu/corsika/
20. D. Heck et al., CORSIKA: a Monte Carlo code to simulate extensive air showers, Report FZKA 6019. (Forschungszentrum Karlsruhe, 1998)
21. T. Enquist et al., Nucl. Instrum. Methods Phys. Res. A **554**, 286 (2005)
22. P.A. Zyla et al., Prog. Theor. Exp. Phys. **2020**, 083C01 (2020)
23. B. Mitrica et al., Adv. High Energy Phys. **2013**, 256230 (2013)
24. N. Jovančević et al., Nucl. Instrum. Methods Phys. Res. A **612**, 303 (2010)
25. N.Q. Hung, V.H. Hai, M. Nomachi, Appl. Radiat. Isot. **121**, 87 (2017)
26. R. Breier, M. Laubenstein, P.P. Povinec, Appl. Radiat. Isot. **126**, 188 (2017)
27. M. Baginova, P. Vojtyla, P.P. Povinec, Astropart. Phys. **143**, 102756 (2022)
28. J. Knezevic et al., Nucl. Instrum. Methods Phys. Res. A **1032**, 166624 (2022)
29. M. Travar et al., J. Radioanal. Nucl. Chem. **332**, 817 (2023)
30. G. Škoro et al., Nucl. Instrum. Methods Phys. Res. A **316**, 333 (1992)
31. L. Reichhart et al., Astropart. Phys. **47**, 67 (2013)
32. Q. Du et al., Astropart. Phys. **102**, 12 (2018)
33. R. Kneiβl et al., Astropart. Phys. **111**, 87 (2019)

The application of the unfolding technique for determination of photo-nuclear reaction cross-section with an example on the ^{115}In(γ,γ')^{115m}In reaction

Z. Medic[1], N. Jovancevic[1], D. Maletic[2], Y. Teterev[3], S. Mitrofanov[3], A. Belov[3], M. Krmar[1], M.Hult[4], S. Oberstedt[4]

[1]*Physics Department, Faculty of Sciences,*
University of Novi Sad, Novi Sad, Serbia
[2] *Institute of Physics, Belgrade, Serbia*
[3] *Flerov Laboratory of Nuclear Reactions,*
Joint Institute for Nuclear Research, Dubna, Russia
[4] *European Commission,*
Joint Research Centre (JRC), Geel, Belgium

The cross-section function for the ^{115}In(γ,γ')^{115m}In reaction was determined in the energy range up to $E_\gamma = 9.6$ MeV using the bremsstrahlung facility at the MT25 Microtron, JINR, Dubna. Natural indium disks were irradiated with bremsstrahlung, each disk with a beam of different endpoint energy. To the measured saturation activity built up in the wide-energy photon beam we applied the unfolding technique, developed recently at the JRC-Geel with the primary purpose of being used in neutron activation. The results were compared with TALYS 1.9 calculations and existing experimental data. Our results suggest that the application of existing unfolding technique allow determining unknown excitation functions of photon-induced reactions.

PACS numbers: 25.20.x, 24.10.i,07.85.Nc, 27.60.+j

I. INTRODUCTION

Experimental data obtained in nuclear reactions induced by photons on various materials are important for a number of different applications. High-energy photons are used to produce radionuclides for medicine and other applications. They are used in radiotherapy, industry, activation analysis and play significant roles in astrophysical processes and in the dynamics of nuclear reactors [1]. Therefore, cross-sections of photo-nuclear reactions are often studied in a wide energy region. The rich amount of experimental results obtained, can be found in several databases such as Refs. [2–8].

The aim of this paper is to apply the NAXSUN technique (Neutron Activation X-Section determined using UNfolding) to determine the differential cross section for the excitation of the 336.2 keV isomer in ^{115}In as a function of the photon energy, using photons from bremsstrahlung beams of several different endpoint energies. The NAXSUN technique was developed at the JRC-GEEL and utilized to obtain neutron-induced reaction cross sections as a function of incident neutron energy [9–13]. For the photo-activation measurements we adapted the NAXSUN technique and examined its applicability in photon-induced reactions.

There are several reasons why the excitation of ^{115}In isomer state was chosen to test the possibility of extending the NAXSUN technique to the field of photo-nuclear reactions. Natural indium is a mixture of two isotopes ^{113}In (4.3%) and ^{115}In (95.7 %) [14]. It is a soft metal that is easy to shape in the desired irradiation and detection geometry. It can be used in several different ways as an activation detector for neutrons or photons. The high thermal neutron cross section of 160 b [15] has made ^{115}In a frequently used nuclide for neutron monitoring. The excitation of the 336.2 keV [14] isomeric state by non-elastic neutron scattering, ^{115}In(n,n')^{115m}In, is recognized as one of the most common reactions for detection and monitoring of fast neutrons. Moreover, detection of photons having energies higher than 9 MeV (produced by LINAC-s used in radiotherapy, for example), which is the threshold energy for the photo-nuclear reaction ^{115}In(γ,n)^{114}In, is possible by using activation foils made of natural indium. And finally, high-energy photons may excite the isomeric state via the reaction ^{115}In(γ,γ')^{115m}In.

All these reactions make indium the material of choice in experimental circumstances, when it is necessary to register the presence of neutrons and photons at the same location. For neutron reactions on ^{115}In cross sections are well known, and reliable data on the differential cross section for the ^{115}In(γ,n)^{114}In reaction are available, too. There are several experimental data sets [16–20], included in database [8], for photo-excitation of the ^{115m}In isomeric state. The cross-section values of the ^{115}In(γ,γ')^{115m}In reaction and the shape of the cross-section function in those several sources differ somewhat (datasets are shown in Fig. 12). Furthermore, data available in literature [8], show discrepancy with TALYS 1.9 [21, 22] calculations, as can be seen in Figure 11 and Figure 12, below in this text. Additional objective of this paper is to report on a new measurement of the ^{115}In(γ,γ')^{115m}In cross section.

Possible applicability of NAXSUN techniques in photnuclear reactions can open a broad research field. Dif-

ferential cross sections for (γ,n) reactions are well documented with reliable experimental material. However, at higher photon energies, when two or more neutrons are emitted, the results of measuring the flux-weighted averaged cross section and measurements with quasi-monoenergetic photon beam can be found in the literature [2, 3, 8]. For a specific channel of (γ,xn) nuclear reactions, energy differential cross-sections can be obtained using theoretical calculations only. The introduction of the NAXSUN techniques could make it possible to measure energy differential cross-sections for these nuclear reactions as well.

II. THE METHOD

The NAXSUN technique is based on irradiation of several identical metal disks in different, but overlapping, neutron fields. It is followed by gamma-spectrometric measurements and unfolding procedures. This method has solely been used for measuring cross section curves for neutron-induced reactions [11–13].

The yield of activation products from some nuclear reactions, here the photo-excitation of the first excited and meta-stable state in ^{115}In in a bremsstrahlung beam, can be quantified by its saturation activity (maximum equilibrium activity when the rate of production of reaction product equals the rate of decay) A:

$$A = \int_{E_{th}}^{E_{max}} \sigma(E) \cdot \Phi(E) \cdot dE \qquad (1)$$

where $\sigma(E)$ is the cross section for the studied nuclear reaction, $\Phi(E)$ is the flux spectrum of incident photons and E is the photon energy. E_{th} is the energy threshold for the nuclear reaction and, E_{max} is the endpoint energy of the bremsstrahlung beam. After exposure to the photon beam, the induced activity of ^{115m}In is measured by a high energy resolving γ-spectrometer.

One indium disk at the time was exposed in a bremsstrahlung beam of particular endpoint energy. The endpoint energies ranged from 5 MeV to 10 MeV. In this way disks were exposed to different but overlapping photon fields, similar to the measurements performed in our previous work, where broad-energy neutrons fields were applied [11–13]. After irradiation the saturation activity of each of the six disks is determined by γ-spectromety.

If the photon flux-spectrum, $\Phi(E)$ can be estimated, as shown in Section III D. in this paper, the general task comes down to the solution of six integral equations (Eq. 1) for each irradiated sample, and the determination of the unknown function $\sigma(E)$, which describes the cross section of the photo-nuclear reaction. Having six known values of saturation activity, A, the problem can be transformed into a system of discretized equations:

$$A_k = \sum_i^c \Phi_{ik} \cdot \sigma_i \cdot \Delta E_i; \quad k = 1, 2, ...m \qquad (2)$$

where A_k is the measured saturation activity of each irradiated disk, k, with m activated disks, k running from 1 to 6 . The photon flux for a certain energy bin, E_i and disk k is described by Φ_{ik}. ΔE_i is the width of energy bin i, and c is the number of energy bins. σ_i represents the sought cross section function. Since c is larger than m the system of equations is under-determined and an unfolding procedure needs to be applied. In this work, we used three unfolding algorithms, SANDII, GRAVEL and MAXED [23–27], to take into account corresponding systematic uncertainties.

III. MEASUREMENTS

A. Material

Six identical metal disks of indium with natural isotopic abundances were used. The material has a high level of purity with 99.9% of natural indium. Disks had an identical shape with a diameter of 20.0(1) mm and and an average thickness of 0.210(1) g cm^{-1}. Two more indium discs were used to check influence of neutrons on excitation of ^{115}In isomer state. Sources of neutrons are described in next section.

B. Irradiation

All experimental activities were performed at the Flerov Laboratory of Nuclear Reactions of the JINR, Dubna. The MT25 Microtron [28] was used to produce the bremsstrahlung beams for irradiation of the indium disks. A more detailed description of the Microtron and the experimental setup can be found in ref. [29]. Indium disks were exposed to bremsstrahlung with endpoint energies from 5 MeV to 10 MeV in steps of 1 MeV (Table I). For the photon production we used a 1mm thick tungsten radiator. The distance between the the radiator and an indium disk was 60 cm.

An 8 mm thick beryllium plate was placed in front of the In sample, 52.5 cm far from the tungsten radiator, to serve in another study [29]. The influence of the beryllium plate on the photon flux was corrected by Monte Carlo simulation as described below. The scheme of the experimental set up is presented in the Figure 2.

Energy thresholds for photo-disintegration of ^{9}Be (followed by emission of neutron) and ^{183}W(γ,n)^{182}W are 1.7 MeV and 6.2 MeV respectively [30]. In order to minimize the influence of inelastic neutron scattering, ^{115}In(n,n')^{115m}In reaction, the indium disks were placed in the center of a water container with a diameter of 15 cm. In this way, fast neutrons created in photo-nuclear reactions in beryllium and tungsten are thermalized. The need for such an action was confirmed by a noticeable difference in ^{115m}In activity, after exposure with and without water around the indium disk. At a maximum photon energy of 23 MeV the saturation activity of ^{115m}In in the

TABLE I: Irradiation characteristics for each indium disk: E_{max} - bremsstrahlung endpoint energy, Q - integral number of electrons striking tungsten target, t_{irr} - time of irradiation

Disk No.	E_{max} [MeV]	Q [mAs]	t_{irr} [s]
1	5.00(5)	12	5880.0(5)
2	6.00(5)	10	1320.0(5)
3	7.00(5)	12	1740.0(5)
4	8.20(5)	3.5	1680.0(5)
5	9.00(5)	7	1020.0(5)
6	10.00(5)	6	840.0(5)

disk exposed outside the water container was 15% higher than the saturation activity of ^{115m}In, when the disk was located inside the water container. Furthermore, we may expect significantly lower parasitic neutron production at lower energies. We observed too that the saturation activity of ^{116}In produced by neutron capture is about 130 times lower at a photon-energy of 10 MeV than at endpoint energy of 23 MeV. This means that there is an insignificant influence of non-elastic scattering of high-energy neutrons on the excitation of the isomeric state in ^{115}In with samples placed in the water container.

The irradiation time was longer for lower photon-energies and ranged from 14 minutes at 10 MeV to 98 minutes at 5 MeV. The Microtron electron current varied from 2 μA to 7 μA. The integral number of electrons striking the tungsten radiator (Q) is summarized in the Table I.
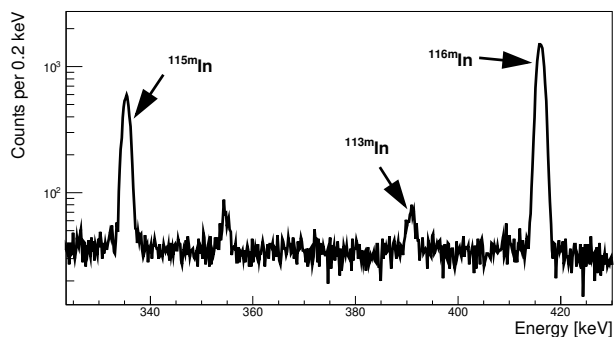
C. Gamma spectroscopy measurements

FIG. 1: Part of the γ-ray spectrum collected after irradiation of indium disk No. 6. The γ lines of interested are labelled. Energy width of one channel is 0.2 keV

After exposure, the decay spectra of the indium disks were measured using an HPGe detector. The relative efficiency of the detector was 25% and, it was passively shielded by 5 cm of lead. The irradiated indium disks were located directly on the vertical end-cap of the detector. The elapsed time between the end of the irradiation and the start of each measurement was between 6 min and 2 h depending on detector availability. Considering that the half life of ^{115m}In is $T_{1/2} = 4.468$ h [14], in the worst case, more than 73% of initial activity remained. The measurement time for each activated disk was 30 min that was sufficient to obtain good counting statistics. For example, in the spectrum of that indium disk exposed to the 7 MeV bremsstrahlung beam the statistical uncertainty of the ^{115m}In gamma line was about 3% at 1 σ.

The recorded spectra have very simple structure (part of the γ-ray spectrum collected after irradiation of indium disk No. 6. is presented in figure 1). In all of them the prominent 336.2 keV gamma line from the de-excitation of the isomeric level in ^{115m}In is observed. The gamma line of the isomeric state of ^{113m}In, $E_\gamma = 391.7$ keV [14], is noticeable in some of measured spectra, especially in the spectrum from the indium disk exposed at 10 MeV endpoint energy as depicted in Fig. 1. In the γ-ray spectrum of the disk exposed to the 5 MeV bremsstrahlung, the 391.7 keV gamma line is not observed at all. The reason is the low abundance of ^{113}In in natural indium, i.e. 4.3 % in combination with the small flux at 5 MeV. Several other gamma lines (416.9 keV, 1097.3 keV and 1293.5 keV [14]) emitted after the decay of ^{116m}In, produced by neutron capture of ^{115}In, appeared only in spectra of those indium disks exposed at higher endpoint energies.

The saturation activity of ^{115m}In can be determined from the peak area of the 336.2 keV gamma line according to:

$$A_k = \frac{N_\gamma \cdot M\lambda}{m \cdot N_A \cdot \epsilon \cdot \eta \cdot p_\gamma \cdot e^{-\lambda\Delta t} \cdot (1 - e^{-\lambda t_{irr}}) \cdot (1 - e^{-\lambda t_m})} \tag{3}$$

where N_γ is the number of detected γ rays with $E_\gamma = 336.2$ keV, λ is the decay constant, M and m are the mass number and the mass of the In disk used, N_A is Avogadro constant , ϵ is the total efficiency of the detector at 336.2 keV, η is the natural abundance of ^{115}In, p_γ is a gamma emission probability, Δt, t_{irr} and t_m are cooling, irradiation and measurement time, respectively. Total efficiency was determined using calibration sources and LabSOCS software. Since indium is a soft metal, our samples were designed to match existing detector calibrations.

We notice that the saturation activity for $E_{max} = 5$ MeV is almost 150 times lower than the one at $E_{max} = 10$ MeV. All saturation activities, A_k, are summarized in table III. The statistical uncertainty at 5 MeV and at 6 MeV is about 10 % and, above 7 MeV the statistical uncertainty is up to 4 %.

D. Determination of photon flux

1. Monte Carlo simulation

The application of unfolding procedures to our problem requires information about the Φ_{ik} from eqn. 1, i.e. shape and intensity of the bremsstrahlung photon spectra. This was obtained using Monte Carlo (MC) simulations and the measured values of the integral number of electrons striking the tungsten radiator.

To estimate the flux of incident photons $\Phi(E)$ for the six used energies we employed Geant4 (G4) version 10.05.p01 [31] with the experimental Physics list QBBC. QBBC uses the standard G4 electromagnetic physics option without optical photon simulations and, the hadronic part of this physics list consists of elastic, inelastic, and capture processes. Each hadronic process is built from a set of cross sections and interaction models, which provide the detailed physics implementation.

Figure 2 depicts the setup geometry as entered to the Geant4 simulations. Elements of simulations are starting from the electron beam, shown to the left of the figure, going to the indium disk placed in the water container on the right. In the G4 simulations electron beam starting position is 10 cm before Cu foil.

The geometry of the Geant4 simulations consists of an electron beam of six energies, assuming a $\pm 1\%$ uncertainty (k=1) for all energies. Then, on the beam path comes first a 70 μm thick copper foil followed by a copper cylindrical collimator with a 12 mm-wide circular hole. Next comes a 1 mm thick tungsten radiator followed by a 2 cm thick aluminium block. The distance between the tungsten radiator and the indium disk is 60 cm. In front of the indium disk we placed an 8 mm thick beryllium sheet and the water shielding. We simulated about 2×10^8 electrons for six different electron beam energies. From the simulation we obtained the integral number of photons, spectrum shape and the distribution of photons on the surface of an indium disk for each energy. To get approximation of integral number of gammas, which hit the indium sample, the number of photons from the simulation were scaled, having in mind that the number of electrons per mAs is 6.242×10^{15} and that each beam energy had a different number of electrons per second. The estimated integral number of photons hitting an indium disk at the particular endpoint energy is shown in the last column of table II. The simulated photon spectra are depicted in Fig. 3.

In Figure 4 the simulated areal distribution of the photon flux on the indium disks is shown for the 10 MeV endpoint energy. The distribution is flat across the entire disk. Corresponding results were obtained for the other endpoint energies.
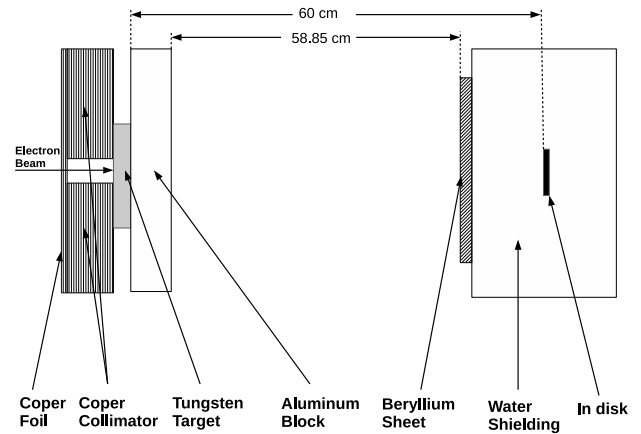
FIG. 2: Geometry of experimental setup (not in scale).
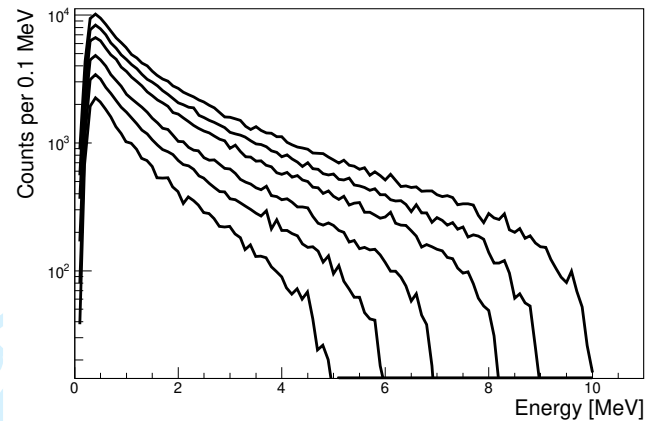
FIG. 3: Spectra of photon flux on the indium disks for all electrons energies incident on the tungsten radiator. The electron energy corresponds to the end-point energy of the respective photon-flux spectrum (E_{max} in the table I.)

2. Normalization of photon flux

To obtain absolute cross section values, it is necessary to have accurate values of the photon flux at the place of the exposed indium disks. In our experimental setup, the total number of electrons striking the tungsten radiator, expressed in mAs in Table I, could only serve as a relative measure. For the absolute calibration of the Monte-Carlo simulated photon spectra, it was necessary to use another nuclide with well-known photo-activation cross section. In the absence of some well-accepted standard, it was decided to use the photo-activation of ^{113}In for spectrum normalisation. As can be seen in Figure 1, the characteristic gamma line of ^{113m}In is present in
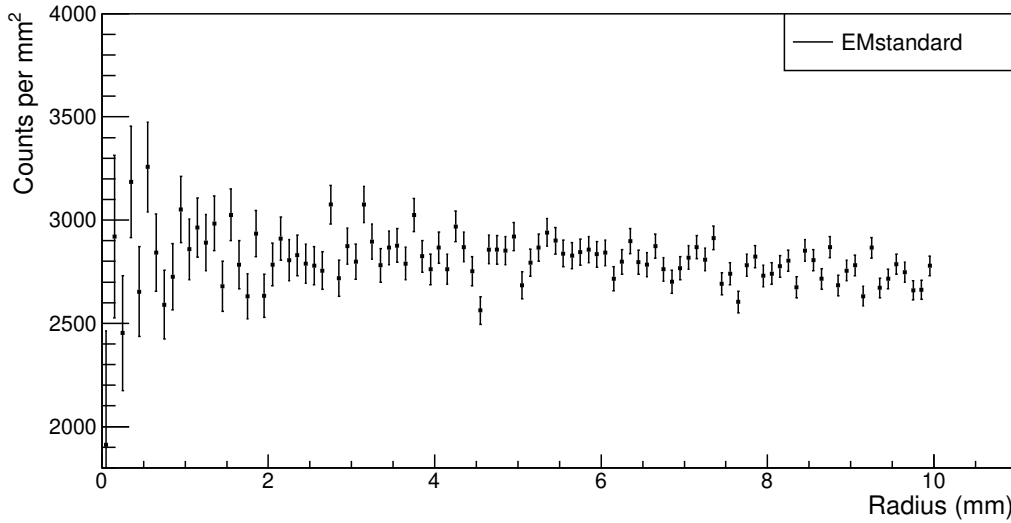
FIG. 4: The photon distribution on the surface of an indium disk, simulated for the endpoint energy 10 MeV.

TABLE II: Irradiation characteristics of the indium disks: E_{max}- endpoint energy; $N_{e,S}$ - simulated number of electrons; $N_{\gamma,S}$ - simulated number of photons; S - scaling factor; $N_{\gamma Scaled}$ - scaled number of photons.

E [MeV]	$N_{e,S}$ [10^6]	$N_{\gamma,S}$	S [10^7]	$N_{\gamma Scaled}$ [10^{12}]
5.00(5)	200	25312	3.12	9.48
6.00(5)	199	43163	3.14	13.54
7.00(5)	194	65120	3.22	25.14
8.20(5)	192	99595	3.25	11.33
9.00(5)	192	129258	3.25	29.42
10.00(5)	187	165313	3.34	33.11

TABLE III: Saturation activity, A_k, for a given endpoint energy, E_{max} calculated according to eqn. 3

Disk No.	Energy [MeV]	A_k[10^{-18} Bq/atom]
1	5.00(5)	0.0090(9)
2	6.00(5)	0.044(5)
3	7.00(5)	0.161(7)
4	8.20(5)	0.191(5)
5	9.00(5)	0.87(3)
6	10.00(5)	1.33(3)
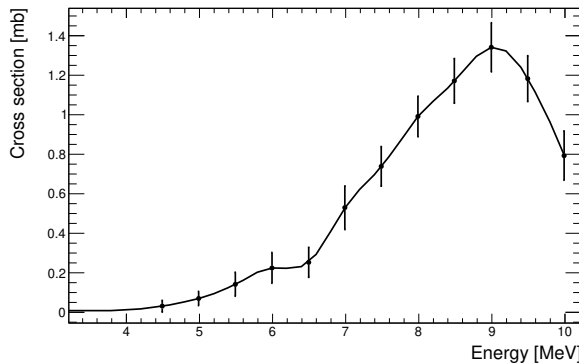
FIG. 5: Cross section for $^{113}In(\gamma,\gamma')^{113m}In$ reaction (points - measured data [32], line - spline interpolation).

the spectrum after irradiation of the indium samples at higher energies. The cross section function for the reaction ^{113}In$(\gamma, \gamma')^{113m}$In was taken from Ref.[32] as de-

picted in Fig. 5. In this study, samples of natural indium were irradiated in the range of 4 MeV to 12 MeV with 0.5 MeV increments. The cross section was calculated using Penfold-Leis method [33]. Photon flux was determined using an absolutely calibrated ionization chamber with a build-up cap of appropriate thickness.

Saturation activity for ^{113}In$(\gamma,\gamma')^{113m}$In reaction at some chosen energy, A_c, can be calculated based on the equation 2. Photon flux spectra were calculated using Monte-Carlo simulation with a number of incident electrons specified in Tab. II. Simulated spectra were corrected by Microtron electron current Q, as a relative measure, taken from Tab. I. Interpolated values of the cross-section from Fig. 5 were taken to calculate the saturation activity A_c for the 10 MeV photon beam. The measured values of the saturation activities for the A_m obtained using the intensity of the 391.7 keV gamma line detected for 10 MeV was $1.10(18) \times 10^{-18}$ Bq/atom. Based on that, a normalization factor of $r = A_m/A_c = 6.2(11)$ was obtained and used to normalise photon spectra, which were used in unfolding procedures.

IV. EXPERIMENTAL RESULTS

A. Default functions for unfolding procedures

Cross-section unfolding procedures require an initial guess of the sought function, the so-called default function, to proceed further with the unfolding calculation. This function should be a reasonably good guess of the real cross-section function. In this work we used the TALYS 1.9 code [22] for determining this default functions.

TALYS 1.9 is a computer code for the simulation of nuclear reactions. A detailed description of TALYS 1.9 can be found in Ref. [22]. By this code it is possible to calculate various physical quantities for all possible outgoing reaction channels using different physical models in the calculations. In this work we calculated the cross section for the ^{115}In$(\gamma, \gamma')^{115m}$In reaction, for incident photon energies ranging from 0 to 10 MeV. All parameters of calculations were code-default values except level density parameters. Available level density models in the TALYS 1.9 are [34–42]:

- LD model 1. - the constant temperature Fermi-Gas model;

- LD model 2. - the back-shifted Fermi gas model;

- LD model 3. - the generalised super-fluid model;

- LD model 4. - the microscopic level densities based on the Goriely's tables;

- LD model 5. - Hilaire's combinatorial tables;

- LD model 6. - the temperature dependent Hartree-Fock-Bogoliubov model, Gogny force.

Six different excitation functions for the ^{115}In$(\gamma, \gamma')^{115m}$In reaction were obtained (see Fig. 6) and used as default functions for the unfolding procedures.

Other parameters such as photon strength functions (PSF) can also have a significant impact on cross-section values. However, detailed theoretical analysis was not part of this study and those parameters are not change from the default values given by the TALYS 1.9., which are for example the standard Lorentzian (Brink-Axel model) for PSF.

B. Unfolding results

Three unfolding algorithms were used in this work and their results were compared. The first one was the SANDII iterative algorithm [27], the second was the GRAVEL algorithm, which is an improved version of SANDII [26] and, the third one was the MAXED algorithm that uses the maximum entropy principle to calculate the unfolded function [23].
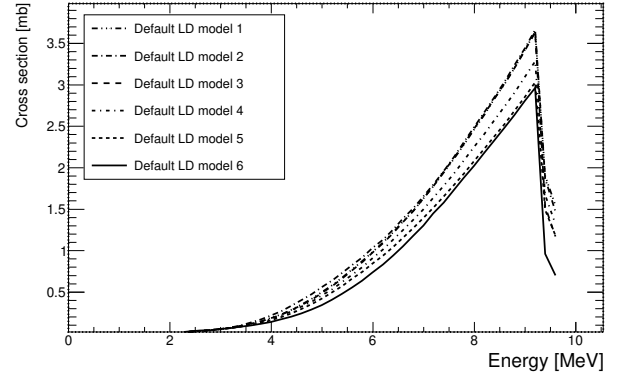
FIG. 6: Default functions for the ^{115}In$(\gamma, \gamma')^{115m}$In cross-section obtained by TALYS 1.9 for six different level density models (for details see text).
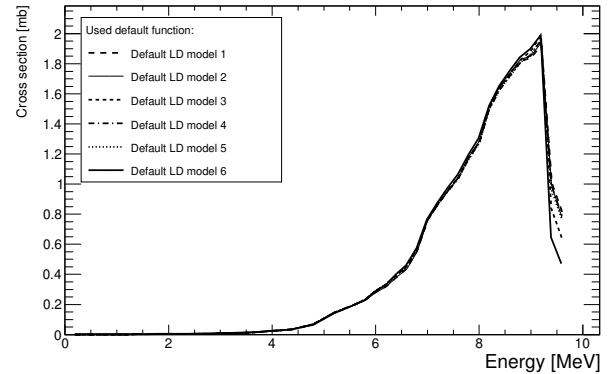
FIG. 7: Unfolded ^{115}In$(\gamma, \gamma')^{115m}$In cross-section for each default function, produced using the SANDII unfolding algorithm.

The SANDII and GRAVEL algorithm give the solution:

$$\sigma_i^{J+1} = \sigma_i^J f(A_k \epsilon_k \Phi_{ki} \sigma_i^J)$$

$$f = \exp\left(\frac{\sum_{k=1}^m W_{ik}^J \ln\left(\frac{A_k}{\sum_{i=1}^n W_{ik}^J \sigma_i^J} \right)}{\sum_{k=1}^m W_{ik}^J} \right), i = 1, 2...n$$

(4)

where in the case of the SANDII W_{ik}^J is:

$$W_{ik}^J = \frac{\Phi_{ki}\sigma_i^J}{\sum_{i=1}^n \Phi_{ki}^J}.$$

(5)

and in the case of the GRAVEL W_{ik}^J is:

$$W_{ik}^J = \frac{\Phi_{ki}\sigma_i^J}{\sum_{i=1}^n \Phi_{ki}^J} \frac{A_k^2}{\epsilon_k^2}.$$

(6)
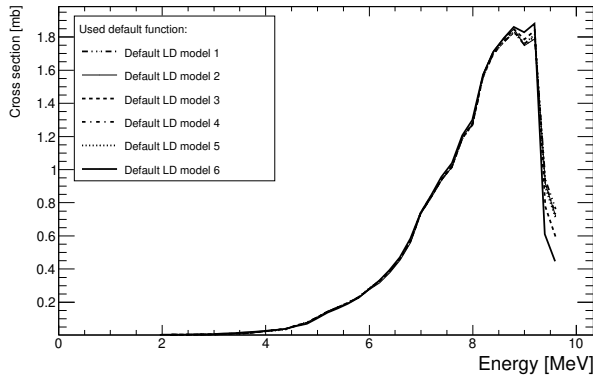
FIG. 8: Unfolded ^{115}In$(\gamma, \gamma')^{115m}$In cross-section for each default function, produced using the GRAVEL unfolding algorithm.
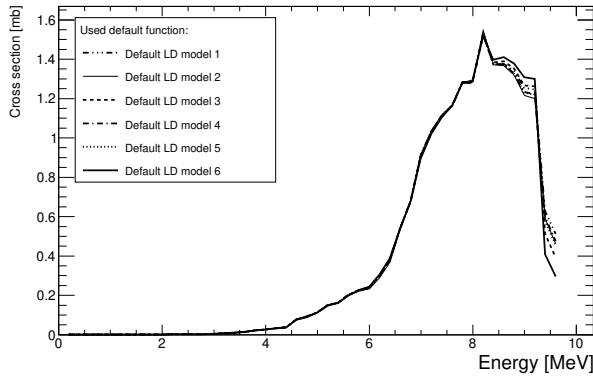
FIG. 9: Unfolded ^{115}In$(\gamma, \gamma')^{115m}$In cross-section for each default function, produced using the MAXED unfolding algorithm.

A_k is measured saturated activity, ϵ_k is measured uncertainty, cross-section for energy bin E_i is σ_i and photon flux is Φ_{ki} when irradiating k disk at energy bin E_i, J is number of the iteration step, m is number of activated discs and n is number of energy bins.

The MAXED algorithm provides by the fitting input data (measured induced specific saturated activity A_k), a function $\sigma(E)$ that maximizes the relative entropy:

$$S = -\int \left(\sigma(E) \ln\left(\frac{\sigma(E)}{\sigma_{def}(E)} \right) + \sigma_{def}(E) - \sigma(E) \right) dE \tag{7}$$

where $\sigma_{def}(E)$ is the default cross section function.

Unfolding procedures were performed in the energy range between 0 MeV and 9.6 MeV grouped into 48 bins. The results obtained by the SANDII, GRAVEL and MAXED algorithms for all used default functions are presented in Figures 7, 8 and 9.

C. Analysis of uncertainties

We will analyse here following sources of uncertainties that could have affect the final results: the measurement of saturated gamma activity, determination of normalisation factor, Monte Carlo calculation of photon spectra and unfolding procedures.

1. Gamma activation measurement

The uncertainty values of saturated gamma activity were determinated by taking into account contribution of uncertainties of all parameters from equation 3, and obtained values are presented in table III. Those uncertainties are dominated by statistical error of measurement of gamma peak intensity. Uncertainties of gamma activation measurement are affected the final results. However, only the MAXED algorithm gives the possibility to estimate the error of the cross section values depending on the error of the measured activity, while for the other two algorithms such an error analysis is not possible [43]. Cross section uncertainty of the MAXED code due to saturated gamma activity measurement uncertainty is presented in the first column of Table V in the case of the LD model 6 used as default function. Similar results were obtained for other 5 default functions. The influence of the measured gamma activity uncertainty on the error of the final results using other algorithms requires additional analyses that are not part of this study.

2. Normalisation factor

The cross section values for the ^{113}In$(\gamma, \gamma')^{113m}$In reaction taken from Ref. [32] were determined with uncertainty that varied form 50 % at low energy to 10% at higher energy. That lead to uncertainty of 17% for normalisation factor which introduced additional uncertainty of the final results obtained in this study. This problem can be solved by introducing precise measurement of photon flux as a part of this technique or by selecting another reaction (with well-known efficient cross-sections) as the standard for normalization.

3. Monte Carlo calculation of photon spectra

In this study, the QBBC model which is recommended for medical and space physics simulations was used [44, 45]. Analysis of possible systematic uncertainty introduced by the choice of the model in the Geant4 simulation was done by comparing results from other available models.

EM standard option model used in the QBBC physics list, as well as previously studied models [46], EM standard option3, Livermore and Penelope, predict the correct absolute scale and are able to reproduce the
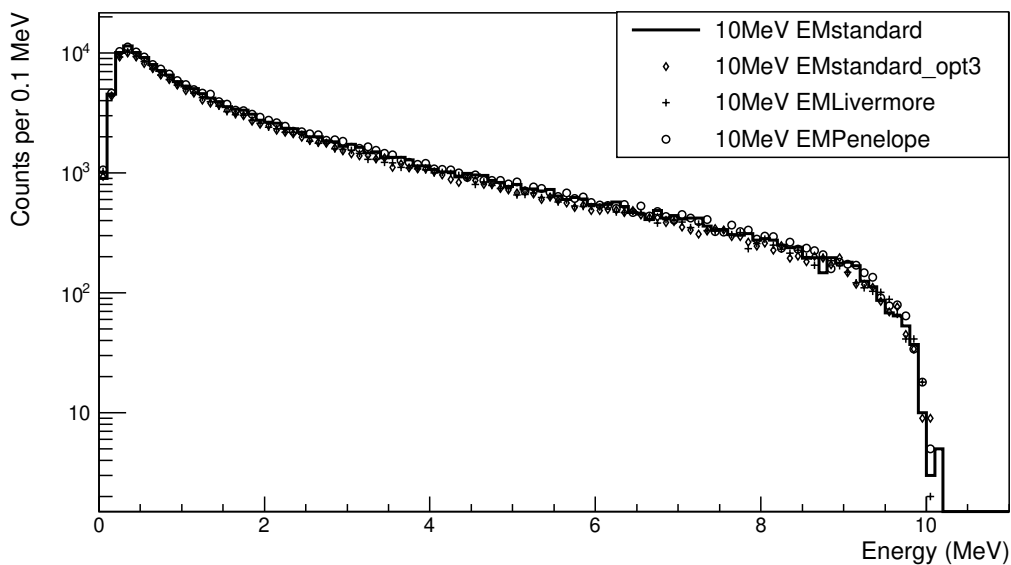
FIG. 10: Spectra of photon flux on the indium disks for 10 MeV endpoint energy obtained by different models: EMstandard, EM standard_opt3, EMLivermore and EMPenelope.
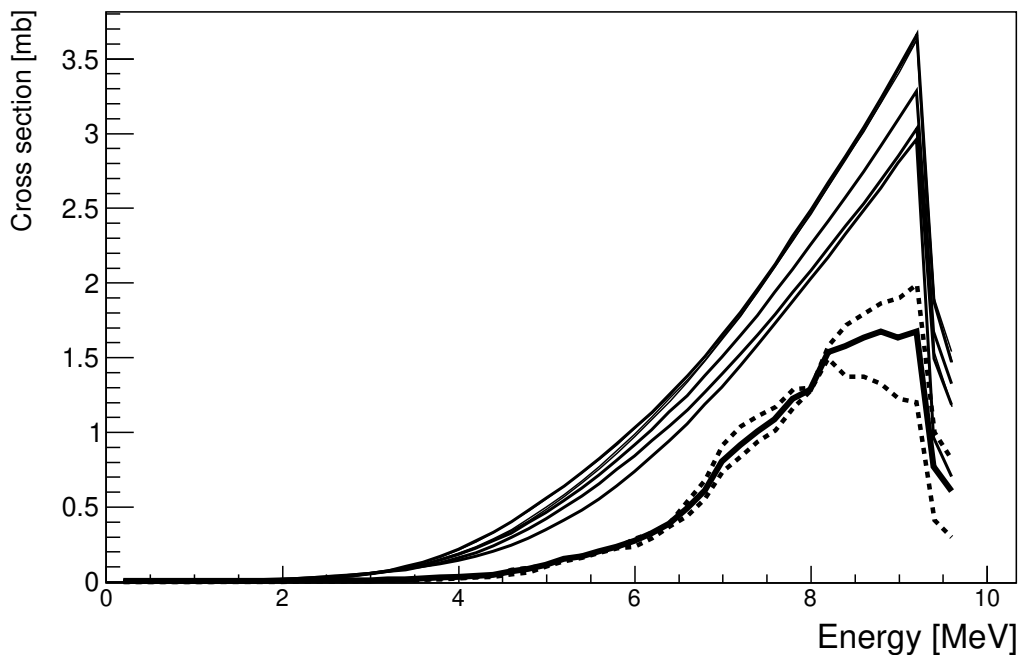
FIG. 11: Unfolded results for the ^{115}In$(\gamma, \gamma')^{115m}$In cross-section (line with a corridor of uncertainty) in comparison with default TALYS 1.9 functions (Fig. 6).

shape of the energy spectra at forward emission angles, which make the leading contribution to the total radiated energy. Nevertheless, all models over-estimate the bremsstrahlung emission in the backward hemisphere and predict a harder energy distribution than measured [46], which is not the case here, where all bremsstrahlung
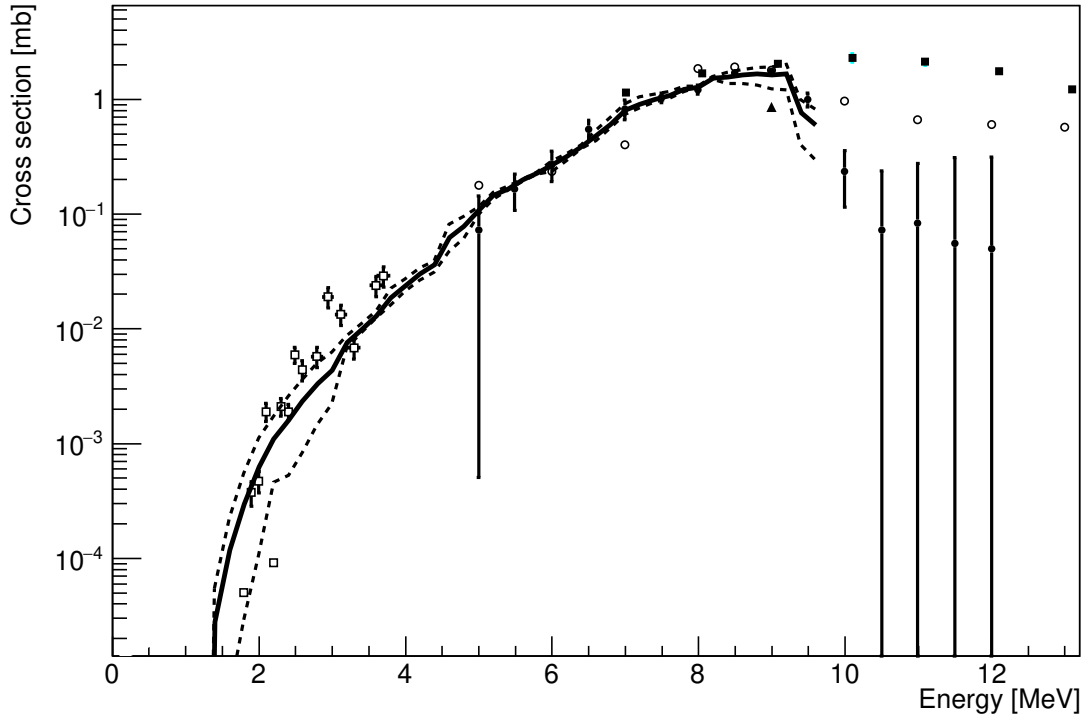
FIG. 12: Comparison of the ^{115}In$(\gamma, \gamma')^{115m}$In cross-section obtained in this work (line with uncertainty bars) with existing experimental data ($\circ$ -[16], $\blacksquare$ - [17], , $\bullet$ - [18], $\blacktriangle$-[19], $\square$ - [20]).

emission are in the narrow forward region. Obtained results by comparing different models are presented in the Fig 10. Based on those results we consider that the uncertainty introduced by the choice of the model in the Geant4 simulation is negligible.

4. Unfolding procedures

The validation of the unfolding results was done by calculating an induced activity $(A_c = \sum \sigma(E_i) \cdot \Phi(E_i) \cdot \Delta E)$ and subsequent comparison with the measured data $(A_k$, table III). This was done for all default cross-section functions and for all three algorithms, SANDII, GRAVEL and MAXED. In table IV, the χ^2 values are presented:

$$\chi^2 = \frac{(A_c - A_k)^2}{\sigma_{A_k}^2} \qquad (8)$$

These results suggested that unfolding results can reproduce the measured values of A_k much more accurately than the default functions.

For all three unfolding algorithms averaged cross sections for all variants of default function were calculated. The standard deviations from average values for algorithms are presented in table V. The objective of this

study was not to judge which of the three unfolding algorithms would give most realistic results. Therefore, we treated all obtained cross sections with equal weights in the following. The final result, depicted in Fig. 11, represents the cross section averaged over all 18 variants, i.e. three unfolding codes and six default functions.

The solid line represents the averaged cross section. Dashed lines depict the maximum and minimum values of the cross sections representing uncertainty corridor obtained directly from the spectrum unfolding which is also presented in table V (σ_U and σ_D).

It turns out that the LD model 2 of the MAXED code gives the lowest estimation of the cross section. The maximum amplitude of the unfolded cross section is obtained with SANDII code using the LD model 4. In this way the region of the most probable values for the ^{115}In$(\gamma, \gamma')^{115m}$In reaction cross section, i.e. the uncertainty, was estimated.

In this way, the direct contributions to the uncertainty of the final result from the the measured gamma activity and the normalization factor were not taken into account and that will be part of a future study during the development of this technique.

TABLE IV: The χ^2 values 8 for: 1. Default functions before unfolding procedures, 2. SANDII results, 3. GRAVEL results and 4. MAXED results.

1. Default functions

| | χ^2 | | | | | |
Energy [MeV]	Ld model 1	Ld model 2	Ld model 3	Ld model 4	Ld model 5	Ld model 6
5.00(5)	253.03	280.01	252.84	272.95	282.51	297.59
6.00(5)	33.40	39.41	32.73	34.67	34.81	30.09
7.00(5)	107.44	116.33	105.32	107.33	106.26	87.90
8.20(5)	0.03	0.31	0.02	0.14	0.21	0.38
9.00(5)	112.89	132.55	110.05	120.70	123.58	112.17
10.00(5)	120.07	144.36	119.75	130.04	133.45	117.23

2. SANDII results

| | χ^2 | | | | | |
Energy [MeV]	Ld model 1	Ld model 2	Ld model 3	Ld model 4	Ld model 5	Ld model 6
5.00(5)	0.16	0.14	0.28	0.30	0.32	0.54
6.00(5)	0.58	0.51	0.62	0.64	0.66	0.90
7.00(5)	2.56	2.53	2.69	2.75	2.72	1.90
8.20(5)	0.08	0.04	0.06	0.06	0.07	0.11
9.00(5)	6.55	6.72	7.27	7.77	7.62	5.62
10.00(5)	0.76	0.79	0.34	0.39	0.38	0.50

3. GRAVEL results

| | χ^2 | | | | | |
Energy [MeV]	Ld model 1	Ld model 2	Ld model 3	Ld model 4	Ld model 5	Ld model 6
5.00(5)	0.77	0.52	0.80	0.93	1.00	2.57
6.00(5)	0.24	0.21	0.27	0.25	0.26	0.32
7.00(5)	4.80	4.46	4.45	4.70	4.61	3.59
8.20(5)	0.31	0.21	0.30	0.31	0.31	0.26
9.00(5)	4.47	4.25	4.14	4.44	4.40	3.95
10.00(5)	1.01	1.15	0.91	0.97	0.96	0.79

4. MAXED results

| | χ^2 | | | | | |
Energy [MeV]	Ld model 1	Ld model 2	Ld model 3	Ld model 4	Ld model 5	Ld model 6
5.00(5)	0.06	0.05	0.06	0.07	0.07	0.10
6.00(5)	0.35	0.28	0.35	0.34	0.35	0.41
7.00(5)	2.73	2.62	2.72	2.64	2.60	2.76
8.20(5)	3.64	3.72	3.64	3.76	3.76	3.56
9.00(5)	3.06	2.85	2.88	2.87	2.84	2.85
10.00(5)	2.16	2.50	2.33	2.32	2.40	2.33

V. DISCUSSION

According to the TALYS 1.9 calculations, the cross section for a selected nuclear reaction channel can be calculated using different nuclear level density models. In Figure 6 all TALYS 1.9 calculations of the $^{115}\text{In}(\gamma, \gamma')^{115m}\text{In}$ differential cross-section have a very similar shape. The only difference may be observed in the amplitude of the functions. It is evident, all TALYS 1.9 calculated cross sections show an exponential growth with increasing energy. When the process of neutron emission starts to compete with the process of de-excitation through electromagnetic transition, the cross section for the $^{115}\text{In}(\gamma, \gamma')^{115m}\text{In}$ reaction drops sharply. According to TALYS 1.9, this happens at around 9 MeV.

Results obtained with three different unfolding algorithms are depicted individually in figures 7, 8 and 9. One can see a very interesting trend on them. Differ-

ences in the calculated cross sections, presented in Figure 6, which are not large but still visible, do not produce a significant scatter in the values of the cross section obtained by one single code. For example, different default functions, when used as an input for the SANDII unfolding procedure, give very similar functions describing the cross section (Fig. 7). The same can be seen with the other two codes (Fig. 8 and Fig. 9). Comparison of the results of three different algorithms, shows that SANDII and GRAVEL give functions of a very similar shape, with a small difference just at maximum energy. Results obtained by the MAXED code predicts slightly different form of the energy differential cross section for the $^{115}\text{In}(\gamma, \gamma')^{115m}\text{In}$ reaction. The maximum of the MAXED function is shifted towards 8 MeV, while SANDII predicts that the maximum cross-section value could be at 9 MeV, very similar to the TALYS 1.9 calculations.

Sharp peaks and small discontinuities can be noticed

TABLE V: Analysis of uncertainties. $\sigma_{MAXEDAc}$ - Cross section uncertainty of MAXED code due to measurement uncertainty; σ_{SANDII} - Standard deviation of average SANDII results; σ_{GRAVEL} - Standard deviation of average GRAVEL results; σ_{MAXED} - Standard deviation of average MAXED results; σ_U - Upper limit of final results; σ_D - Down limit of final results.

Energy [MeV]	$\sigma_{MAXEDAc}$ [%]	σ_{SANDII} [%]	σ_{GRAVEL} [%]	σ_{MAXED} [%]	σ_U [%]	σ_D [%]
0.2	8568.00	10.94	14.21	25.59	100.49	99.99
0.4	3561.00	10.79	14.45	45.28	105.83	100.00
0.6	341.20	10.98	14.17	35.66	105.17	100.00
0.8	227.50	11.11	14.32	25.27	101.48	99.99
1	171.70	11.03	14.04	19.87	98.56	99.78
1.2	149.10	10.96	14.32	16.56	96.92	99.56
1.4	123.20	11.13	14.16	13.57	95.09	98.14
1.6	85.50	11.12	14.00	12.44	86.72	94.71
1.8	81.27	10.98	14.15	10.82	85.21	90.20
2	52.99	11.10	13.98	12.17	74.33	83.02
2.2	55.47	10.89	13.68	8.35	56.57	58.67
2.4	47.59	10.92	13.71	10.13	61.19	66.70
2.6	44.83	10.51	12.97	10.26	56.38	63.56
2.8	31.66	9.47	12.17	10.88	48.19	57.08
3	36.10	7.68	10.34	8.25	40.95	49.71
3.2	20.04	5.59	7.92	4.86	14.57	11.22
3.4	17.51	3.23	5.60	3.03	11.16	6.88
3.6	13.32	1.44	3.54	1.58	8.85	5.50
3.8	10.30	1.42	1.72	1.07	20.42	13.81
4	7.42	2.59	1.54	1.30	12.16	12.01
4.2	7.73	3.68	2.26	1.60	10.48	13.41
4.4	8.01	4.36	2.67	2.28	8.58	13.76
4.6	15.53	4.03	3.26	2.58	29.84	24.26
4.8	13.53	3.86	3.20	2.08	21.77	20.88
5	16.38	2.84	2.88	0.85	6.23	8.65
5.2	12.87	2.17	2.73	0.89	4.87	8.13
5.4	9.82	1.57	2.03	0.47	4.20	4.11
5.6	7.14	0.89	1.47	0.38	1.26	4.09
5.8	9.05	0.75	0.94	0.64	1.74	2.63
6	11.47	1.07	0.61	1.26	7.86	12.82
6.2	11.67	1.72	1.09	1.32	4.67	8.03
6.4	8.48	1.61	1.03	1.38	2.64	4.03
6.6	6.55	1.53	0.86	0.14	11.59	9.67
6.8	4.47	1.35	1.03	0.33	12.83	8.67
7	7.04	0.21	0.21	0.81	14.30	8.32
7.2	6.02	0.46	0.53	0.63	13.90	8.67
7.4	4.55	0.64	0.62	0.34	11.14	6.61
7.6	3.69	0.78	0.74	0.19	8.43	5.87
7.8	5.62	0.81	0.62	0.23	5.81	4.21
8	3.46	0.77	0.66	0.34	1.45	0.81
8.2	7.03	0.67	0.53	0.61	3.01	2.64
8.4	5.60	0.67	0.43	0.58	9.07	12.84
8.6	5.19	0.70	0.60	1.06	9.94	16.22
8.8	5.06	0.62	0.59	1.48	11.44	20.89
9	6.35	1.05	1.51	2.39	16.41	25.35
9.2	5.12	1.18	1.65	2.65	18.73	28.26
9.4	3.83	14.44	13.97	13.30	31.07	46.82
9.6	3.79	17.09	16.59	16.29	36.01	50.74

in the results obtained by applying the GRAVEL and the MAXED codes in high energy region above 6 MeV. With a reasonable assumption that the cross section of the ^{115}In$(\gamma, \gamma')^{115m}$In reaction should be smooth in the region where a giant dipole resonance is dominant mechanism of excitation of nuclei, it may be concluded that these peaks originate from some numerical phenomena related to the algorithm itself. The number and amplitude of these peaks increase in cases, where the reconstruction of the cross section is performed with a larger number of bins.

It can be seen in Figure 11 that in the energy inter-

val up to 8 MeV there is a very nice agreement between average, smallest and largest estimation of the cross section, leaving us with a very small systematic uncertainty introduced by the different unfolding algorithms. The differences appear in the region between 8 and 10 MeV. The same figure shows all six results from TALYS 1.9 calculations used as default functions. It can be seen that, without special adjustments, TALYS 1.9 gives significantly higher predictions for the cross-section than that obtained from the unfolding of our data. For this reason, there is a large difference between the saturation activities measured and calculated using the cross section estimated on the basis of the TALYS 1.9 calculations, as shown by χ^2 in Table IV.

The obtained average function was compared with existing experimental data from literature, which are unfortunately not very abundant. Figure 12 depicts the comparison of our results (full line) with data from different authors [16–20], presented by symbols. Most of the data generally shows the same trend, i.e. a growth up to 9 MeV, after which the cross section sharply decrease. In the low-energy region, up to about 4 MeV, our results show the same trend as the data from Ref. [20]. This data is scattered around the line representing our data, obtained by the unfolding technique. The biggest difference between our data and the one from Ref. [20] is around 3 MeV, where our estimation is five times smaller. There is still some room for improvements by using for irradiation photon spectra with endpoint energy less then 5 MeV. It should be noted here that in low-energy region, up to 3 MeV where the excitation of individual levels is possible, some structural effects in the cross section curve should be expected. It is probably a reason of the scatter of the measurements published in reference [20]. Initial TALYS 1.9 function did not take into account the structural effects at low energies.

In the energy region between 5 MeV and 10 MeV the agreement between unfolding results and previous measurements is much better. For example, cross-sections obtained in this project and values published in Ref. [18], presented by closed circles on Figure 12, are consistent within experimental uncertainties declared by the authors in Ref. [18] and our corridor defined by highest and lowest estimation as presented in Figure 11. A distinct difference appears at 9 MeV only, where our estimation of the cross-section is 30 % lower. The point at 5 MeV in reference [18] was determined with very large uncertainty. Cross-section values published in reference [17], presented by black squares at Figure 12 differ from our results up to 35 %. In energy region above 6.5 MeV our values are systematically lower, however, it is interesting to note that in measurements referred in this reference, there is no sharp drop of the cross-section after neutron emission threshold energy at all.The maximum of cross section function presented in this publication is at 10 MeV and minimum of the cross section peak is in energy region between 15 MeV and 18 MeV. Authors used $^{63}Cu(\gamma,n)^{62}Cu$ and absolute ionisation chamber gor

calibration and control of bremsstrahlung beam. Authors used [33] algorithm for calculation. The results published in the reference [16] show maximum of cross section peak at 9 MeV, with the drop at energies higher than the binding energy of neutrons, although not so sharp as presented in reference [18]. Values presented in this reference (◦ - in Figure 12) are scattered around our results with a maximum deviation of 50 %. Authors of publication [16] used NaI detectors for gamma spectra measurements and ionisation chamber with 7.5 cm thick aluminium walls for reconstruction of photon flux spectra. No information related to calculation cross section function were not presented.

To reveal possible factors, which could affect the cross-section values obtained in this study, we can start from the function describing the flux of the bremsstrahlung photons in eqns. 1 and 2. This function was obtained by simulation with a reasonable number of incident electrons, from the point of view of the duration of a typical GEANT4 simulation. The amplitude of this function was calculated by normalization based on the measured intensity of ^{113m}In gamma line of $E_\gamma = 391.7$ keV in obtained spectra. This was the only way to determine the flux of photons striking the target and, probably, some new method should be developed in a subsequent measurement campaign. Best candidates for new normalisation procedure could be the (γ,γ') reaction on ^{11}B or the $^{115}In(\gamma,n)^{114m}In$ reaction.

VI. CONCLUSIONS

The results presented in this work demonstrates the successful application of the NAXSUN technique also in the field of photonuclear reactions. We suggest that this method has potential in reconstructing energy differential cross sections using activation data from photonuclear reactions. The method was tested in the low-energy region, up to an endpoint energy of 10 MeV, on the example of photoactivation of the ^{115}In isomeric state, where it was sufficient to monitor the intensity of only one nicely isolated gamma line in the spectrum. If additional checks confirm the potential of this method, one of the possible applications could be in determining the cross section functions of (γ,xn) photonuclear reactions with the emission of more than one neutron, for a number of irradiated nuclei and reaction products (having sufficiently long half-life). For now, only average cross-sections can be found in literature for these nuclear reactions [2, 3, 47, 48], and there are no experimentally established energy differential cross-sections for photonuclear reactions with multiple neutron emission at all.

In this paper, TALYS 1.9 calculations are used to construct the default functions, and the question remains for future work, whether it is possible to expand the method of determining the default function using mean values of efficient cross section as in the case of neutron induced nuclear reactions presented in our previous work

[11]. This might be an interesting attempt, although the results of this work shows that the impact of a different choice of a default function obtained by only one selected code on the final result is not crucial.

In our analysis, different results were observed by three different algorithms. Differences are the most significant between the MAXED and the other two of the algorithms (Figs. 7,8, 9). The obtained results are encouraging enough, but they also open the necessity of subsequent experimental activities in which it will be possible to check, which of the used unfolding codes gives the most

reliable approximation to the real cross-section value.

Although the differential cross-section of ^{115}In$(\gamma,\gamma')^{115m}$In was not of primary interest in this project, it is worth to notice that good agreement with previously published results was obtained. Some of the existing measurement results are quite different, especially at energies higher than 10 MeV [16–18], but it has been observed that they show quite good agreement in the energy range from 5 MeV to 10 MeV. In the same area, our results are fully consistent with literature data.

[1] T. Kawano, Y. Cho, P. Dimitriou, D. Filipescu, N. Iwamoto, V. Plujko, X. Tao, H. Utsunomiya, V. Varlamov, R. Xu, R. Capote, I. Gheorghe, O. Gorbachenko, Y. Jin, T. Renstrøm, M. Sin, K. Stopani, Y. Tian, G. Tveten, J. Wang, T. Belgya, R. Firestone, S. Goriely, J. Kopecky, M. Krtička, R. Schwengner, S. Siem, and M. Wiedeking, Nuclear Data Sheets **163**, 109 (2020).

[2] "Experimental nuclear reaction data (exfor)," https://www-nds.iaea.org/exfor/exfor.htm.

[3] N. Otuka, E. Dupont, V. Semkova, B. Pritychenko, A. Blokhin, M. Aikawa, S. Babykina, M. Bossant, G. Chen, S. Dunaeva, R. Forrest, T. Fukahori, N. Furutachi, S. Ganesan, Z. Ge, O. Gritzay, M. Herman, S. Hlavač, K. Katō, B. Lalremruata, Y. Lee, A. Makinaga, K. Matsumoto, M. Mikhaylyukova, G. Pikulina, V. Pronyaev, A. Saxena, O. Schwerer, S. Simakov, N. Soppera, R. Suzuki, S. Takács, X. Tao, S. Taova, F. Tárkányi, V. Varlamov, J. Wang, S. Yang, V. Zerkin, and Y. Zhuang, Nuclear Data Sheets **120**, 272 (2014).

[4] "The endf, evaluated nuclear data file," https://www-nds.iaea.org/exfor/endf.htm.

[5] D. Brown, M. Chadwick, R. Capote, A. Kahler, A. Trkov, M. Herman, A. Sonzogni, Y. Danon, A. Carlson, M. Dunn, D. Smith, G. Hale, G. Arbanas, R. Arcilla, C. Bates, B. Beck, B. Becker, F. Brown, R. Casperson, J. Conlin, D. Cullen, M.-A. Descalle, R. Firestone, T. Gaines, K. Guber, A. Hawari, J. Holmes, T. Johnson, T. Kawano, B. Kiedrowski, A. Koning, S. Kopecky, L. Leal, J. Lestone, C. Lubitz, J. M. Damián, C. Mattoon, E. McCutchan, S. Mughabghab, P. Navratil, D. Neudecker, G. Nobre, G. Noguere, M. Paris, M. Pigni, A. Plompen, B. Pritychenko, V. Pronyaev, D. Roubtsov, D. Rochman, P. Romano, P. Schillebeeckx, S. Simakov, M. Sin, I. Sirakov, B. Sleaford, V. Sobes, E. Soukhovitskii, I. Stetcu, P. Talou, I. Thompson, S. V. D. Marck, L. Welser-Sherrill, D. Wiarda, M. White, J. Wormald, R. Wright, M. Zerkle, G. Žerovnik, and Y. Zhu, Nucl. Data Sheets **148**, 1 (2018).

[6] "Iaea photonuclear data," https://www-nds.iaea.org/photonuclear/pdfilelist.html.

[7] T. Kawano, Y. Cho, P. Dimitriou, D. Filipescu, N. Iwamoto, V. Plujko, X. Tao, H. Utsunomiya, V. Varlamov, R. Xu, R. Capote, I. Gheorghe, O. Gorbachenko, Y. Jin, T. Renstrøm, M. Sin, K. Stopani, Y. Tian, G. Tveten, J. Wang, T. Belgya, R. Firestone, S. Goriely, J. Kopecky, M. Krtička, R. Schwengner, S. Siem, and M. Wiedeking, Nuclear Data Sheets **163**, 109 (2020).

[8] "Janis nuclear data," https://www.oecd-nea.org/jcms/pl_39910/janis.

[9] G. Lövestam, M. Hult, A. Fessler, T. Gamboni, J. Gasparro, W. Geerts, R. Jaime, P. Lindahl, S. Oberstedt, and H. Tagziria, Nuclear Instruments and Methods in Physics Research Section A: Accelerators, Spectrometers, Detectors and Associated Equipment **580**, 1400 (2007).

[10] L. Daraban, N. Jovančević, S. Oberstedt, and F.-J. Hambsch, Physics Procedia **59**, 138 (2014).

[11] N. Jovancevic, L. Daraban, and S. Oberstedt, Nuclear Instruments and Methods in Physics Research Section A: Accelerators, Spectrometers, Detectors and Associated Equipment **739**, 68 (2014).

[12] N. Jovančević, L. Daraban, H. Stroh, S. Oberstedt, M. Hult, C. Bonaldi, W. Geerts, F.-J. Hambsch, G. Lutter, G. Marissens, *et al.*, The European Physical Journal A **52**, 148 (2016).

[13] S. Ilić, N. Jovančević, L. Daraban, H. Stroh, S. Oberstedt, M. Hult, C. Bonaldi, W. Geerts, F.-J. Hambsch, G. Lutter, G. Marissens, M. Vidali, and D. Knežević, The European Physical Journal A **56**, 202 (2020).

[14] E. Browne and R. Firestone, *Table of Radioactive Isotopes* (John Wiley and Sons, 1986).

[15] J. Kopecky, J. Sublet, J. Simpson, R. Forrest, and D. Nierop, *Atlas of neutron capture cross sections* (International Atomic Energy Agency (IAEA), INDC(NDS)–362, 1997).

[16] O. Bogdankevich, L. Lazareva, and F. Nikolaev, Journal of Experimental and Theoretical Physics **4**, 320 (1957).

[17] V. Bokhinyuk, A.I.Guthy, A.M.Parlag, M.T.Sabolchy, I.V.Sokolyuk, and I.V.Khimich, Ukrainian Journal of Physics **51**, 657 (2006).

[18] V. Mazur, I. Sokolyuk, Z. Bigan, and I. Kobal, Physics of Atomic Nuclei **56**, 10 (1993).

[19] N. Demekhina, A. Danagulyan, and G. Karapetyan, Physics of Atomic Nuclei **64**, 1796 (2001).

[20] W. Tornow, M. Bhike, S. Finch, Krishichayan, and A. Tonchev, Physical Review C **98**, 064305 (2018).

[21] "Talys nuclear code," https://tendl.web.psi.ch/tendl_2019/talys.html.

[22] A. Koning and D. Rochman, Nuclear Data Sheets **113**, 2841 (2012), special Issue on Nuclear Reaction Data.

[23] M. Reginatto and P. Goldhagen, Health physics **77**, 579 (1999).

[24] W. L. Goffe, Studies in Nonlinear Dynamics & Econometrics **1** (1996).

[25] R. Behrens, Journal of Instrumentation **4**, P03027 (2009).

[26] M. Matzke, Report PTB-N-19 **I-IV** (1994).

[27] W. N. McElroy, S.Berg, and T. Crockett, Los Alamos National Laboratory report, AFWL-TR-67-41 **I-IV** (1967).

[28] "25-microtron," http://flerovlab.jinr.ru/mt-25-microtron/.

[29] M. Krmar, Y. Teterev, A. Belov, and S. Mitrofanov, Nuclear Instruments and Methods in Physics Research Section A: Accelerators, Spectrometers, Detectors and Associated Equipment **901**, 133 (2018).

[30] B. Forkman and R. Petersson, *Photonuclear cross-sections in Handbook on Nuclear Activation data* (Technical Reports Series No. 273, IAEA, Viena, 1987).

[31] S. Agostinelli, J. Allison, K. Amako, J. Apostolakis, H. Araujo, P. Arce, M. Asai, D. Axen, S. Banerjee, G. Barrand, F. Behner, L. Bellagamba, J. Boudreau, L. Broglia, A. Brunengo, H. Burkhardt, S. Chauvie, J. Chuma, R. Chytracek, G. Cooperman, G. Cosmo, P. Degtyarenko, A. Dell'Acqua, G. Depaola, D. Dietrich, R. Enami, A. Feliciello, C. Ferguson, H. Fesefeldt, G. Folger, F. Foppiano, A. Forti, S. Garelli, S. Giani, R. Giannitrapani, D. Gibin, J. Gómez Cadenas, I. González, G. Gracia Abril, G. Greeniaus, W. Greiner, V. Grichine, A. Grossheim, S. Guatelli, P. Gumplinger, R. Hamatsu, K. Hashimoto, H. Hasui, A. Heikkinen, A. Howard, V. Ivanchenko, A. Johnson, F. Jones, J. Kallenbach, N. Kanaya, M. Kawabata, Y. Kawabata, M. Kawaguti, S. Kelner, P. Kent, A. Kimura, T. Kodama, R. Kokoulin, M. Kossov, H. Kurashige, E. Lamanna, T. Lampén, V. Lara, V. Lefebure, F. Lei, M. Liendl, W. Lockman, F. Longo, S. Magni, M. Maire, E. Medernach, K. Minamimoto, P. Mora de Freitas, Y. Morita, K. Murakami, M. Nagamatu, R. Nartallo, P. Nieminen, T. Nishimura, K. Ohtsubo, M. Okamura, S. O'Neale, Y. Oohata, K. Paech, J. Perl, A. Pfeiffer, M. Pia, F. Ranjard, A. Rybin, S. Sadilov, E. Di Salvo, G. Santin, T. Sasaki, N. Savvas, Y. Sawada, S. Scherer, S. Sei, V. Sirotenko, D. Smith, N. Starkov, H. Stoecker, J. Sulkimo, M. Takahata, S. Tanaka, E. Tcherniaev, E. Safai Tehrani, M. Tropeano, P. Truscott, H. Uno, L. Urban, P. Urban, M. Verderi, A. Walkden, W. Wander, H. Weber, J. Wellisch, T. Wenaus, D. Williams, D. Wright, T. Yamada, H. Yoshida, and D. Zschiesche, Nuclear Instruments and Methods in Physics Research Section A: Accelerators, Spectrometers, Detectors and Associated Equipment **506**, 250 (2003).

[32] Z. Bigan, V. Zheltonozhsky, V. Kirishchuk, a. D. S. V.M. Mazur, and P. Trifonov, Bulletin Russian Academy of Sciences - Physics **70**, 292 (2006).

[33] A. Penfold and J. Leiss, Physical Review **114**, 1332 (1959).

[34] A. Koning and J. Delaroche, Nuclear Physics A **713**, 231 (2003).

[35] W. Hauser and H. Feshbach, Physical review **87**, 366 (1952).

[36] C. Kalbach, Physical Review C **33**, 818 (1986).

[37] A. Gilbert and A. Cameron, Canadian Journal of Physics **43**, 1446 (1965).

[38] W. Dilg, Nuclear Physic A **217**, 269 (1973).

[39] A. Zubov, G. Adamian, and N. Antonenko, Physics of Particles and Nuclei **40**, 847 (2009).

[40] A. Ignatyuk, J. Weil, S. Raman, and S. Kahane, Physical Review C **47**, 1504 (1993).

[41] S. Goriely, S. Hilaire, and A. J. Koning, Physical Review C **78**, 064307 (2008).

[42] S. Hilaire, M. Girod, S. Goriely, and A. J. Koning, Physical Review C **86**, 064317 (2012).

[43] M. Reginatto, P. Goldhagen, and S. Neumann, Nuclear Instruments and Methods in Physics Research Section B: Beam Interactions with Materials and Atoms **476**, 242–246 (2002).

[44] A. V. Ivantchenko, V. N. Ivanchenko, J.-M. Q. Molina, and S. L. Incerti, International Journal of Radiation Biology **88(1-2)**, 171–175 (2011).

[45] "Geant4-userdoc," https://geant4-userdoc.web.cern.ch/UsersGuides/PhysicsListGuide/BackupVersions/V10.6c/html/reference_PL/QBBC.html.

[46] L. Pandola, C. Andenna, and B. Caccia, Nuclear Instruments and Methods in Physics Research Section B: Beam Interactions with Materials and Atoms **350**, 41 (2015).

[47] H. Naik, G. Kim, K. Kim, M. Zaman, A. Goswami, M. W. Lee, S.-C. Yang, Y.-O. Lee, S.-G. Shin, and M.-H. Cho, Nuclear Physics A **948**, 28 (2016).

[48] M. Zaman, G. Kim, H. Naik, K. Kim, Y.-S. Cho, Y.-O. Lee, S.-G. Shin, M.-H. Cho, Y.-R. Kang, and M.-W. Lee, Nuclear Physics A **960**, 22 (2017).

Study of gamma ray transitions and level scheme of $^{56}_{25}$Mn using the $^{55}_{25}$Mn(n_{th},2γ) reaction

David Knezevic [a,b,*], Nikola Jovancevic [b], Anatoly M. Sukhovoj [c],
Aleksandar Dragic [a], Liudmila V. Mitsyna [c], Zsolt Revay [d],
Christian Stieghorst [d], Stephan Oberstedt [e], Miodrag Krmar [b],
Ilija Arsenic [f], Dimitrije Maletic [a], Dejan Jokovic [a]

[a] University of Belgrade, Institute of Physics Belgrade, Pregrevica 118, 11080 Zemun, Serbia
[b] University of Novi Sad, Faculty of Science, Department of Physics, Trg Dositeja Obradovica 3, 21000 Novi Sad, Serbia
[c] Joint Institute for Nuclear Research, 141980 Moscow region, Dubna, Russia
[d] Technische Universität München, Heinz Maier-Leibnitz Zentrum (MLZ), Lichtenbergstr. 1, D-85747 Garching, Germany
[e] European Commission, Joint Research Centre, Directorate G – Nuclear Safety and Security, Unit G.2, Retieseweg 111, B-2440 Geel, Belgium
[f] University of Novi Sad, Faculty of Agriculture, Trg Dositeja Obradovica 8, 21000 Novi Sad, Serbia

Abstract

This work provides new data about the level scheme of $^{56}_{25}$Mn studied by the $^{55}_{25}$Mn(n_{th},2γ) reaction. The spectroscopic information were collected using the gamma-gamma coincidence spectrometer at the Technische Universität München, Heinz Maier-Leibnitz Zentrum (MLZ), Garching, Germany. The intensities, energies of primary and secondary transitions of 71 energy-resolved cascades, as well as intermediate cascade levels were determined. The updated level scheme of $^{56}_{25}$Mn was obtained from analyzing the intensity spectra of the strongest cascades. The comparison with the existing data in the ENSDF database shows that 23 primary transitions, 24 intermediate cascades levels as well as 32 secondary transitions determinated in this work can be recommended as new nuclear data.

2019 Published by Elsevier B.V.

* Corresponding author at: University of Belgrade, Institute of Physics Belgrade, Pregrevica 118, 11080 Zemun, Serbia.
E-mail addresses: davidk@ipb.ac.rs (D. Knezevic), nikola.jovancevic@df.uns.ac.rs (N. Jovancevic).

1. Introduction

Accurate data about the nuclear level scheme play an important role in the understanding of the nuclear properties. They are necessary for studying nuclear reactions as well as for determining nuclear structure parameters. In this work we chose to study the level scheme of the $^{56}_{25}$Mn. For that purpose, we used the two-step gamma-cascade method based on measurements of coincident prompt gamma rays following thermal neutron capture [1–4]. An advantage of this technique is a low Compton background in collected spectra owing to the use of the background-subtraction algorithm [1].

The properties of $^{56}_{25}$Mn nucleus have been studied by means of thermal and resonance neutron capture [5–24] but also by other methods, such as the ^{56}Cr β^- decay [25], ^{48}Ca(^{11}B,3nγ) [26], ^{54}Cr(^{3}He,p) [27], ^{54}Cr(α,d) [28], ^{55}Mn(d,p) [29–32], ^{56}Fe(μ^-, $\nu\gamma$) [33], ^{56}Fe(t,^{3}He) [34], ^{56}Fe(^{12}C,^{12}N) [35,36], ^{58}Fe(d,α) [37]. The overview of excitation data shows the need for collecting new accurate spectroscopic data on $^{56}_{25}$Mn.

In this work, we present new information on the $^{56}_{25}$Mn nucleus (levels, gamma ray transition energies and their intensities per capture). The obtained results were compared with the existing ENSDF data [38]. As it is an odd-odd nucleus, the $^{56}_{25}$Mn can also be interesting from a theoretical point of view, such as studying the level density and the radiative strength function. Since the two-step gamma ray-cascades method provides the possibility to estimate simultaneously the level density and radiative strength functions, in a future work, these nuclear parameters may be obtained for this nuclei as well, as it was done in [39–44] for other investigated nuclei.

2. Experimental setup and measurement

The objective of this experiment was the detection of two-step gamma ray cascades in $^{56}_{25}$Mn following thermal neutron capture on $^{55}_{25}$Mn, $^{55}_{25}$Mn(n_{th},2γ)$^{56}_{25}$Mn. The measurement was carried out at the PGAA station of Technische Universität München, Heinz Maier-Leibnitz Zentrum (MLZ), Garching, Germany [45,46].

The experimental setup consisted of two HPGe detectors with relative efficiencies of 60% and 30%. The distance between detectors was 22.5 cm (this distance is the distance between the detector cap of the 60% detector and the point on the axis of the 30% detector that lies on the line determined by the detector cap of the 60% detector and the position of the sample). Target was placed at 9 cm from the detector with a 30% efficiency (distance measured on the above mentioned line) as shown in Fig. 1. The other detector was surrounded by an active anti-Compton suppression made of bismuth germanate (BGO). The shielding against scattered neutrons consisted of a 1 mm thick boron-containing plastic tube that was built around the detectors. The detector was also surrounded by 10 cm of lead shielding to reduce background gamma ray radiation. The necessary experimental data for the analysis (energy of both detected coincident photons and time difference between their detection) were collected by a N1728B CAEN ADC digitizer. For the mono-isotopic manganese ($^{55}_{25}$Mn) the preparation of a high-purity target for the experiment is considerably easier compared to nuclei of more complex isotopic composition. The target was high-purity (99.9%) natural manganese powder with the mass of 50 mg. The relative efficiency of the detectors was determined from single gamma ray spectra accumulated using a PVC tar-
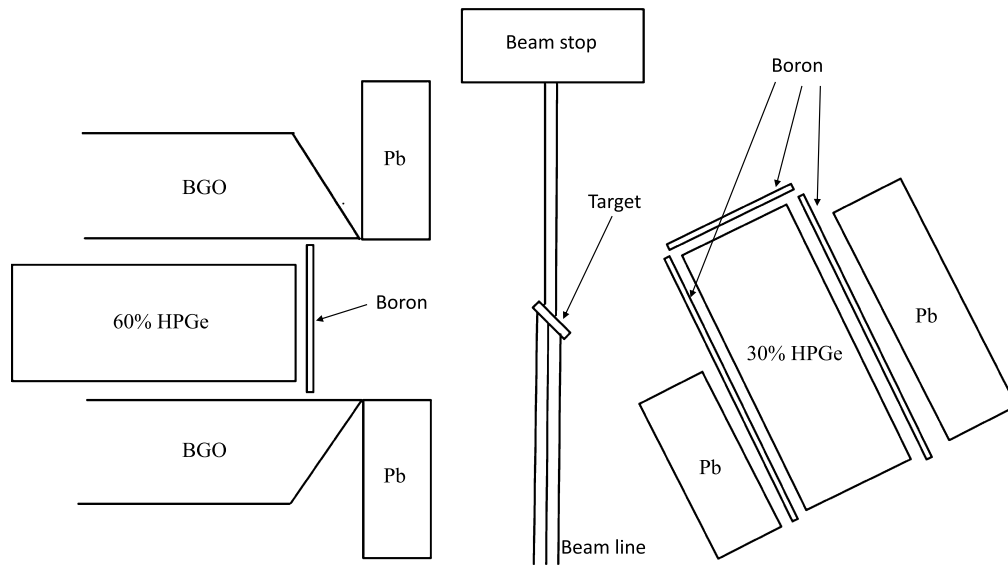
Fig. 1. Sketch of the experimental setup.

get (the ^{35}Cl(n,γ)^{36}Cl reaction) [47]. For the 30% detector the efficiency curve was $\ln(\epsilon) = -1.124210 \cdot \ln(E_\gamma) - 2.01161 \cdot \ln(E_\gamma/1022) + 0.453523 \cdot \ln^2(E_\gamma/1022)$, and for the 60% detector it was $\ln(\epsilon) = -0.751695 \cdot \ln(E_\gamma) + 0.150324 \cdot \ln(E_\gamma/1022) - 0.177287 \cdot \ln^2(E_\gamma/1022)$ Manganese two gamma ray events were recorded for 105.6 h.

3. Result and discussion

Only a short description of the applied procedure to extract the cascade events and intensities is presented here. The detailed description can be found in Ref. [1].

The most important part of the collected spectrum of sums of amplitudes for coincident pulses (SACP) is shown in Fig. 2. The five marked peaks in Fig. 2 present the two-step cascade peaks of $^{56}_{25}$Mn for transitions from the neutron binding energy (7270.0(5) keV) to the ground state and to the first four excited states with the energies of 26.5, 110.4, 212.0 and 341.0 keV. In Table 1, the core information about these five cascade peaks is presented. The remaining unmarked peaks in the SACP spectrum correspond to background events (Fig. 2). They may come from recording of coincidences of the first with the third or fourth quantum of the multiple-step gamma ray cascades or from neutron interaction with surrounding materials. In Table 1, there is also information about part of the resolved intensity, that represents the fraction of the total intensity (% per decay) observed in the spectra $E_{\gamma,1} + E_{\gamma,2} = $ const in the form of pairs of intense energy-resolved peaks in Fig. 3 and Fig. 4. These cascades are observed in the form of pairs of standard peaks. Their intensity is given in column 4 of Table 2 in the form of $I_{\gamma\gamma}$. The concept of "part of resolved cascade intensity" is used in further analysis to determine the ratio of the sum of the intensity of only resolved peaks to the total sum of the intensities of all resolved and unresolved cascades. The total sum includes all cascades without exception, primary and secondary transitions that satisfy the rules of selection by multiplicity. The cascades to other spins and multipolarities are impossible to determine in this type of experiment.
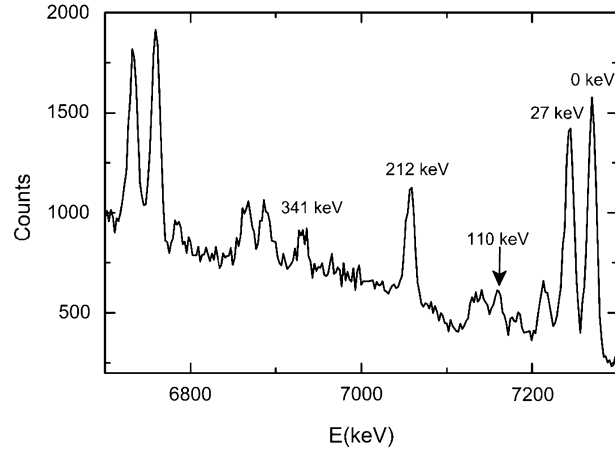
Fig. 2. Spectrum of sums of amplitudes for coincident pulses (SACP) at the radiative capture of thermal neutrons in ^{55}Mn nucleus. Peaks of the full capture of two quanta are labeled by energy of the final level of the resolved cascades.

Table 1
Information about the two-step cascades to the ground state and the first four excited states collected in the experiment. The spin values of the final levels were taken from [38].

Gamma ray cascade total energy (keV)	Final level (E_f) of the cascade (keV)	Spin of level E_f	Part of resolved cascade intensity	Full intensities % per decay
7270	0	3+	70(5)	17(3)
7243	26.5	2+	70(7)	13(3)
7160	110.4	1+	51(9)	5.0(10)
7058	212.0	4+	49(5)	16.0(20)
6929	341.0	3+	40(6)	6.0(10)
Sum of total			56(3)	57(5)

From collected SACP spectra the two-step-cascade (TSC) spectra were obtained. This was done for five energy-resolved amplitude peaks. The obtained TSC spectra represent the cascades from the initial state to the defined low-lying final levels of the $^{56}_{25}$Mn nucleus. The elimination of Compton background and random coincidences was done by gating on the region nearby the peaks of interest in Fig. 2. Figs. 3 and 4 show examples of the obtained TSC spectra for cascade total energies of 6929 and 7058 keV. The background in the two-step-cascade (TSC) spectra of mono-isotopic manganese is practically absent.

The mirror-symmetrical peaks [2] in the TSC spectra represent primary and secondary transitions of the investigated two-step gamma ray cascade. The peaks' positions correspond to the energies, $E_{\gamma,1}$ and $E_{\gamma,2}$, of primary and secondary quanta of the cascades. The relative intensity of each peak is proportional to its area. The criteria for selecting if the structure in the TSC spectrum is a peak is based on searching for the peak structures with non zero count across multiple channels, and then verifying the existence of the peak using the fitting procedure. All energy-resolved peaks are approximated by the Gauss function, and the background is approximated by a constant or a weakly varying linear function. The ratio of the area of all peaks to the sum of the spectrum gives the value of the proportion of resolved peaks detected in the experiment. The remainder is a continuum of the unresolved cascades.
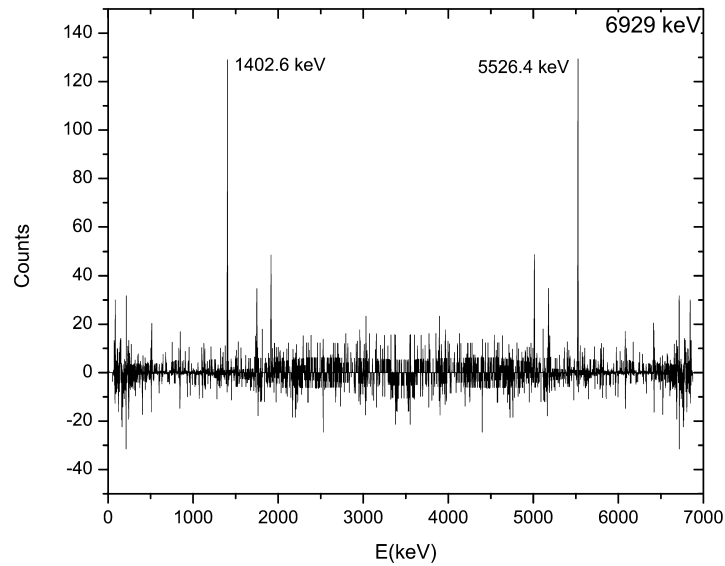
Fig. 3. Two step cascade (TSC) spectrum with the total energy of 6930 keV. The final level of the cascade is 340.957(6) keV (value taken from [38]). This spectrum represents the TSC spectrum with low number of cascades (8 pairs of gamma rays). The energies of the most intense pair of gamma rays are labeled.
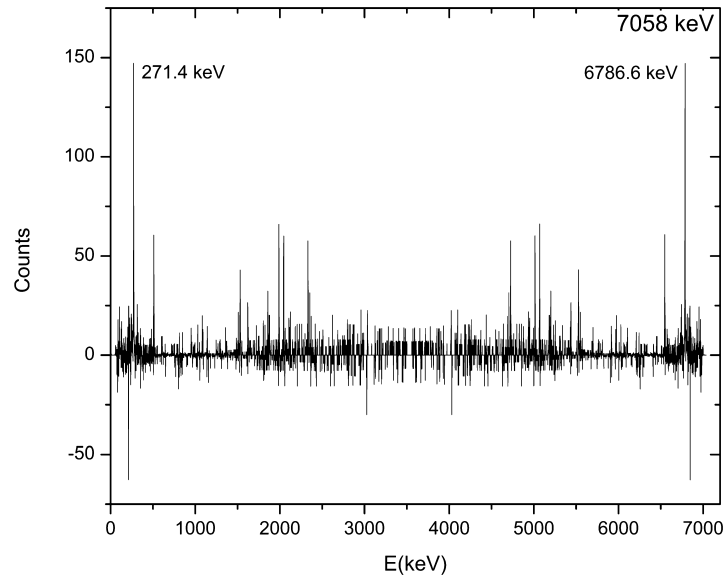
Fig. 4. Two step cascade (TSC) spectrum with the total energy of 7058 keV. The final level of the cascade is 212.004(5) keV (value taken from [38]). This spectrum represents the TSC spectrum with high number of cascades (22 pairs of gamma rays). The energies of the most intense pair of gamma rays are labeled.

Details of the method and the maximum likelihood function used to determine the energies of primary and secondary cascade transitions were presented in [1,4]. The intensities of 71 resolved cascades are determined from five TSC distributions. In all investigated cascades, primary tran-

sitions (except for 7 of them) have the higher energy in comparison with the energy of secondary quanta. All detected primary and secondary gamma ray transitions and their intensities as well as the energies of intermediate levels are presented in Table 2.

In order to compare the data of the cascade spectra (Figs. 3 and 4) with the experimental data for strongest primary transitions with $E_{\gamma,1}$=7058, 7160, 6929, 6784, 5527 and 5181 keV, the branching coefficients (Br) of their secondary transitions were obtained independently (using existing ENSDF data), which gave data of absolute intensity of the cascades for normalization of the data from Table 2.

The intensities of primary gamma transitions to individual low-lying levels i_1 are generally known. The product $i_1 \cdot Br$ is the absolute intensity of one of these cascades to the intermediate level. Then, from the proportion with three known values i_1 i_2, $i_1 \cdot Br$ and the total sum of the intensity of all transitions of the given stages $i_{\gamma\gamma} = 100\%$, we obtain the ratio $I_{\gamma\gamma} = i_1 \cdot Br \cdot i_1 i_2/100$. It is equal to the sum of $I_{\gamma\gamma}$ of all two-quantum cascades (resolved and unresolved energetically for the cascade with the corresponding finite level). The values of the total intensity $I_{\gamma\gamma}$ obtained in such a way (Table 1), which include both the resolved cascades and unresolved cascade continuum with sub-threshold intensity, show that, for the investigated nucleus, we have obtained in this experiment 57% of total intensity of all two-step cascades. At that, 56% of this intensity $I_{\gamma\gamma}$ falls to the share of the energy-resolved cascades (Table 2).

The data were compared with the existing ones in the ENSDF database [38]. From this comparison, 22 primary transitions that existed in the ENSDF data set were determined. 23 primary transitions, which are not included in the ENSDF library, can be therefore recommended as new data. 21 intermediate levels are identified in our experiment and already listed in the ENSDF database. However, for 24 levels observed in this study, there are no data in the ENSDF library yet. The difference between number of primary gamma rays and levels comes from the fact that in some cases, as is the case of gamma ray with energy (database value [38]) 5432.9 keV, that is identified as primary gamma-ray corresponding to experimental value of 5431.5 keV, gamma-rays exist in the database, but do not have a scheme position assigned to them, so the authors tentatively assigned the scheme position for a number of gamma rays as the primary gamma rays of the cascades. Same is the case for gamma ray with energies (database values [38]) 6019.2, 4324.1 and 3034.1 keV. In this work, we observed 32 secondary gamma ray transitions for which there is no information in the ENSDF database. 14 of these new observed secondary transitions come from the levels already in the ENSDF library, and 18 from levels determined for the first time in this work. Also, 11 secondary gamma rays observed in this study are listed in the ENSDF database, but do not have an assigned position in the decay scheme. In this paper we assigned the decay scheme positions for gamma rays with energies (database values [38]) of 1140.4, 2147.3, 2437.8, 2582.0, 2864.4, 2832.9, 2740.3, 2937.6, 3135.6, 4127.7 and 4024.5 keV.

The comparison of determined energies of levels and gamma rays with the ones from the ENSDF database shows an average deviation of about 1.5 keV. For levels and gamma rays where the deviation was larger than 2 keV, ENSDF values were in some cases assigned tentatively by the authors. This relatively large discrepancy can be explained by insufficient statistics in the present TSC spectra, as well as by the keV/Ch difference between the two detectors during measurement, which can cause uncertainty in the determination of the energy.

The level scheme of $^{56}_{25}$Mn obtained in this work is presented in Figs. 5 and 6.

Spin of the neutron capture level is determined by the ground state spin of the capturing nuclei $\pm$ the 1/2 spin of the neutron. This state decays primarily via dipole transition, predominantly of electric multipolarity. As the compound-state of $^{55}_{25}$Mn is $5/2^-$, after a capture of a thermal neutron primary gamma ray transitions can be emitted from the decay of levels with spins 2^- or

Table 2

Comparison of the experimental data with the ENSDF database. $E_{\gamma,1}$ and $E_{\gamma,2}$ are the energies of the first and second quanta of the cascade, respectively, E_i is the energy of the intermediate level and E_f are the final levels of the two step gamma ray cascade. $I_{\gamma\gamma}$ is the intensity of the cascade (per 100 decays) observed in the experiment. The experimental uncertainty of $E_{\gamma,2}$ has the same absolute values as for $E_{\gamma,1}$ (listed in the table). Values in bold are values for which there is no data in the ENSDF library.

Present work				ENSDF			
$E_{\gamma,1}$ (keV)	$E_{\gamma,2}$ (keV)	E_i (keV)	$I_{\gamma\gamma}$	E_f (keV)	$E_{\gamma,1}$ (keV)	$E_{\gamma,2}$ (keV)	E_i (keV)
7160.6(3)	82.9	109.0(6)	4.8(6)	26.516(3)	7159.7(2)	83.8990(15)	110.428(3)
7058.80(21)	211.20	211.2(5)	9.2(8)	g.s.	7057.8(2)	212.017(6)	212.004(5)
7053.1(13)	106.5	216.9(14)	0.9(4)	110.428(3)	–	104.6234(20)	215.057(3)
6925.1(12)	344.9	344.9(13)	0.10(5)	g.s.	6928.7(2)	340.990(25)	340.957(6)
6929.9(6)	313.6	340.1(8)	1.3(4)	26.516(3)	6928.7(2)	314.395(10)	340.957(6)
6786.6(7)	271.4	483.4(9)	1.3(4)	212.004(5)	6783.3(2)	271.175(9)	486.251(8)
6786.6(17)	142.4	483.4(18)	0.22(15)	340.957(6)	6783.3(2)	145.320(20)	486.251(8)
6733.0(8)	**510.5**	**537.0(9)**	0.55(17)	26.516(3)	–	–	–
6699.7(27)	229.3	**570.3(27)**	0.15(17)	340.957(6)	–	229.867(7)	–
6101.8(12)	1141.7	1168.2(13)	0.25(16)	26.516(3)	6103.9(2)	1140.4(10)	1166.54(21)
6101.8(9)	**1057.8**	1168.2(10)	0.16(5)	110.428(3)	6103.9(2)	–	1166.54(21)
6101.8(14)	**956.2**	1168.2(15)	0.09(4)	212.004(5)	6103.9(2)	–	1166.54(21)
6021.8(20)	**1221.7**	**1248.2(21)**	0.08(6)	26.516(3)	6019.2(8)	–	–
5919.4(15)	**1324.1**	1350.6(16)	0.18(11)	26.516(3)	5920.5(2)	–	1349.95(21)
5916.7(13)	**1141.3**	**1353.3(14)**	0.08(4)	212.004(5)	–	–	–
5789.8(27)	**1453.7**	**1480.2(27))**	0.09(8)	26.516(3)	–	–	–
5759.7(4)	**1510.3**	1510.3(6)	0.79(14)	g.s.	5760.9(2)	–	1509.55(21)
5759.7(13)	**1298.3**	1510.3(14)	0.07(3)	212.004(5)	5760.9(2)	–	1509.55(21)
5759.7(17)	1169.3	1510.3(18)	0.034(24)	340.957(6)	5760.9(2)	1169.71(13)	1509.55(21)
5547.5(10)	**1510.5**	**1722.5(11)**	0.10(4)	212.004(5)	–	–	–
5526.4(13)	1717.1	1743.6(14)	0.12(8)	26.516(3)	5527.4(2)	1716.63(14)	1744.3(10)
5526.4(5)	**1531.6**	1743.6(7)	0.46(8)	212.004(5)	5527.4(2)	–	1744.3(10)
5526.4(6)	1402.6	1743.6(8)	0.82(24)	340.957(6)	5527.4(2)	1401.7(10)	1744.3(10)
5438.7(12)	**1720.9**	1831.3(13)	0.07(3)	110.428(3)	5437.0(2)	–	1833.67(21)
5438.7(16)	**1619.3**	1831.3(17)	0.08(5)	212.004(5)	5437.0(2)	–	1833.67(21)
5431.5(24)	**1626.5**	**1838.5(25)**	0.10(7)	212.004(5)	5432.9(2)	–	–
5313.6(16)	**1956.4**	**1956.4(17)**	0.07(5)	g.s.	–	–	–
5270.3(11)	**1889.3**	**1999.7(12)**	0.17(7)	110.428(3)	–	–	–
5250.8(16)	2019.2	2019.2(17)	0.13(8)	g.s.	–	2016.5(2)	2016.39(15)
5201(3)	2042.5	**2069(3)**	0.12(12)	26.516(3)	–	2044.7(2)	–
5197.8(14)	**1961.8**	2072.2(15)	0.08(4)	110.428(3)	5199.1(2)	–	2071.39(15)
5197.8(11)	**1860.2**	2072.2(12)	0.17(9)	212.004(5)	5199.1(2)	–	2071.39(15)
5182.7(11)	2060.8	**2087.3(12)**	0.46(23)	26.516(3)	–	2063.2(2)	–
5180.6(7)	2089.7	2089.7(9)	0.54(10)	g.s.	5181.6(2)	2090.4(2)	2089.38(15)
5180.6(17)	1877.7	2089.7(18)	0.18(9)	212.004(5)	5181.6(2)	1876.2(10)	2089.38(15)
5180.6(7)	1748.7	2089.7(9)	0.49(14)	340.957(6)	5181.6(2)	1747.0(10)	2089.38(15)
5064.4(13)	2179.1	2205.6(14)	0.40(20)	26.516(3)	–	2176.6(2)	2202.73(15)
5064.4(16)	**1993.6**	2205.6(17)	0.22(12)	212.004(5)	–	–	2202.73(15)
5030.8(23)	**2128.8**	2239.2(24)	0.07(5)	110.428(3)	–	–	2235.14(21)
5013.5(9)	2044.5	2256.5(10)	0.26(13)	212.004(5)	5015.0(2)	2044.7(2)	2255.24(15)
5013.5(5)	1915.5	2256.5(7)	0.5(11)	340.957(6)	5015.0(2)	1915.2(10)	2255.24(15)
4950.9(12)	2292.6	2319.1(13)	0.31(14)	26.516(3)	4949.4(2)	2294.8(2)	2321.15(10)
4950.9(14)	2208.7	2319.1(15)	0.12(7)	110.428(3)	4949.4(2)	2211.3(2)	2321.15(10)
4907.4(11)	2252.2	2362.6(12)	0.12(7)	110.428(3)	4907.9(2)	2254.8(2)	2362.62(21)
4907.4(11)	2150.6	2362.6(12)	0.054(22)	212.004(5)	4907.9(2)	2147.3(2)	2362.62(21)

Table 2 (*continued*)

Present work				ENSDF			
$E_{\gamma,1}$ (keV)	$E_{\gamma,2}$ (keV)	E_i (keV)	$I_{\gamma\gamma}$	E_f (keV)	$E_{\gamma,1}$ (keV)	$E_{\gamma,2}$ (keV)	E_i (keV)
4831.9(13)	2438.1	2438.1(14)	0.23(11)	g.s.	4829.7(2)	2437.8(2)	2441.27(15)
4831.9(25)	2327.7	2438.1(25)	0.10(7)	110.428(3)	4829.7(2)	2331.2(2)	2441.27(15)
4730.2(14)	**2539.8**	**2539.0(15)**	0.14(10)	g.s.	–	–	–
4726.3(5)	2331.7	2543.7(7)	0.64(12)	212.004(5)	4725.0(2)	2331.2(2)	2545.65(20)
4659(3)	2584	**2611(3)**	0.17(26)	26.516(3)	–	2582.0(2)	–
4551.1(19)	**2506.9**	2718.9(20)	0.07(5)	212.004(5)	4550.6(2)	–	2719.96(21)
4379.0(14)	2864.5	2891.0(15)	0.15(11)	26.516(3)	4381.0(2)	2864.4(2)	2889.57(21)
4341.3(16)	**2716.7**	**2928.7(17)**	0.09(5)	212.004(5)	–	–	–
4325.1(22)	2834.5	**2944.9(23)**	0.05(4)	110.428(3)	4324.1(2)	2832.9(2)	–
4317.7(20)	2740.3	2952.3(21)	0.06(5)	212.004(5)	4319.5(2)	2740.3(8)	2951.07(21)
4263.3(16)	3006.9	**3006.9(17)**	0.17(10)	g.s.	–	3003.4(2)	–
4263.3(23)	2794.9	**3006.9(24)**	0.06(4)	212.004(5)	–	–	–
4224.5(16)	3045.5	3045.5(17)	0.19(10)	g.s.	4223.5(2)	3047.5(2)	3047.34(15)
4224.5(14)	2935.1	3045.5(15)	0.09(5)	110.428(3)	4223.5(2)	2937.6(8)	3047.34(15)
4134.8(22)	3135.2	**3135.2(23)**	0.16(10)	g.s.	–	3135.6(2)	–
3879(4)	**3391**	**3391(4)**	0.07(9)	g.s.	–	–	–
3871.6(14)	3057.4	3398.4(15)	0.09(5)	340.957(6)	3873.0(2)	3058.2(2)	3397.61
3751.1(13)	**3408.5**	3518.9(14)	0.22(10)	110.428(3)	3752.3(2)	–	3518.32(21)
3592.8(14)	**3465.2**	**3677.2(15)**	0.12(6)	212.004(5)	–	–	–
3035.0(11)	4124.6	**4235.0(12)**	0.20(7)	110.428(3)	3034.1(2)	4127.7(8)	–
3035.0(20)	4023.0	**4235.0(21)**	0.13(9)	212.004(5)	3034.1(2)	4024.5(10)	–
3035.0(17)	**3894.0**	**4235.0(18)**	0.13(7)	340.957(6)	3034.1(2)	–	–
2959.5(14)	**4200.1**	**4310.5(15)**	0.06(3)	110.428(3)	–	–	–
2959(5)	**4098**	**4311(5)**	0.05(6)	212.004(5)	–	–	–
2588(3)	**4571**	**4682(3)**	0.08(10)	110.428(3)	–	–	–
2179.7(9)	**4878.3**	**5090.3(10)**	0.12(4)	212.004(5)	–	–	–

3^-, exciting the levels with spins from J=1 to J=4. Cross section for the neutron resonance with a spin of 2^- is 8.36 b, for spin 3^- this cross section is 3.57 b, and for boundary resonance with cross section of 1.39 b, the spin is unknown [22]. Spin interval for the nuclear levels that are excited by secondary transitions of the cascade is from J=0 to J=5. Such limitation on the possible values of spins is due to decay of excited nucleus by mainly dipole E1- and M1-transitions, at least, if cascade energy is larger than 6930 MeV. Cascades of less total energy with ΔJ=3 were not observed in our experiment. A contribution of quadrupole gamma ray transitions to the total gamma ray spectrum is negligible.

Insufficient resolution of HPGe-detectors did not allow to uncouple the two-step cascades to doublets of final levels 212.026/215.128 keV and 335.529/340.989 keV. But small shift of average of total-energy sum of these doublets (7058 and 6934 keV) give us the reason to think that cascades to the final levels with the energies of 212 and 340 keV and corresponded to them spins 4^+ and 3^+ are dominated in the decay scheme.

4. Conclusion

In this paper, new spectroscopic information was obtained for $^{56}_{25}$Mn by investigating two-step gamma ray cascades following thermal-neutron capture on $^{55}_{25}$Mn. The level scheme and gamma ray transitions for the $^{56}_{25}$Mn nucleus were obtained. The data show good agreement with the ones from the ENDSF library. 24 new levels were observed with 23 new primary and 32 secondary
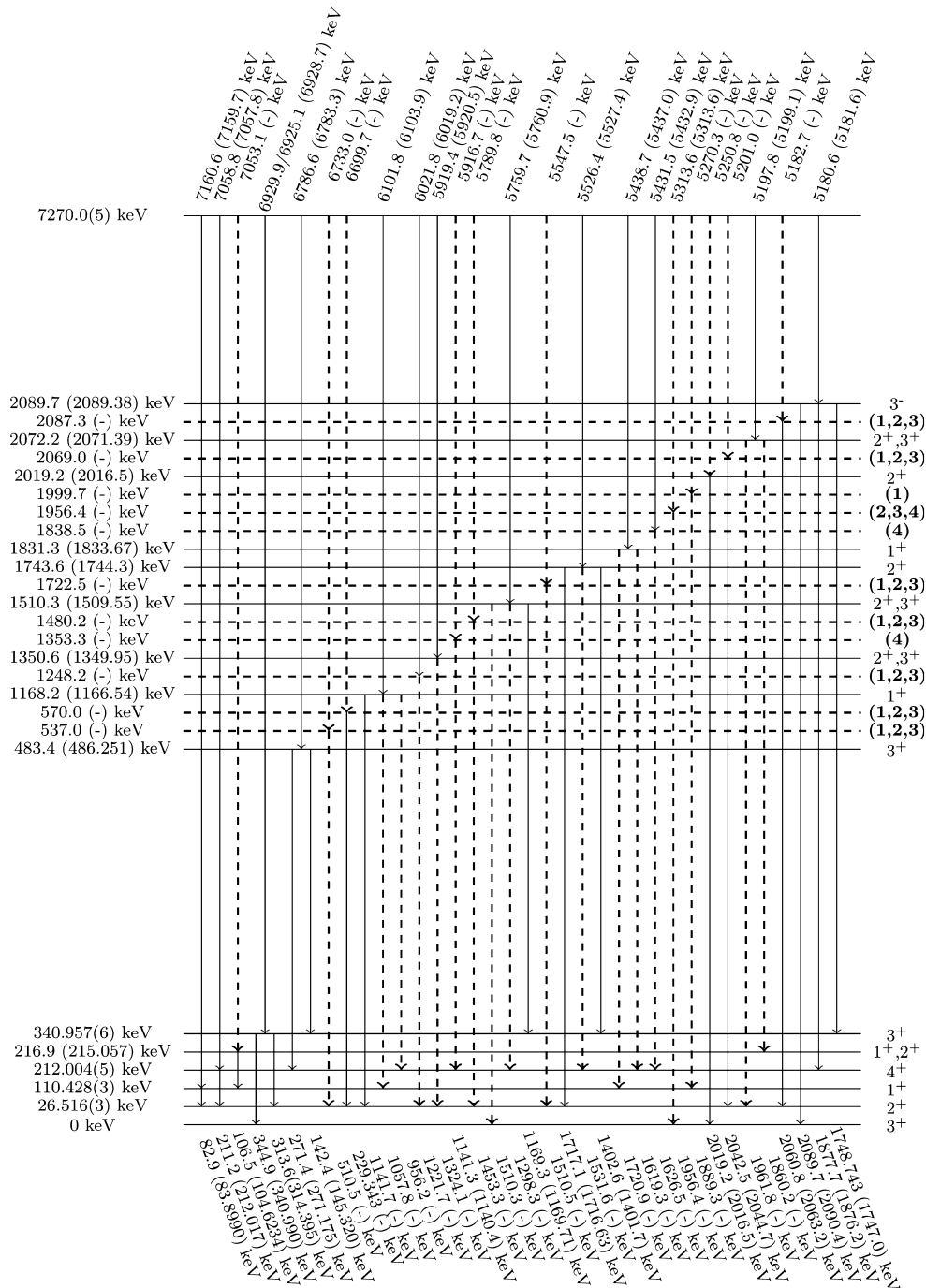
Fig. 5. Experimental level scheme of $^{56}_{25}$Mn with intermediate level energies up to 2100 keV. Dashed lines – levels and gamma rays not found in the ENSDF library; bold spin values – values suggested by the authors for the levels without spin information in the ENSDF library. All energy values, except the energy values for the first 4 low-lying levels are given in the form: Experimental value(ENSDF value).

Fig. 6. Experimental level scheme of $^{56}_{25}$Mn with intermediate level energies from 2200 to 5100 keV. Dashed lines – levels and gamma rays not found in the ENSDF library; bold spin values – values suggested by the authors for the levels without spin information in the ENSDF library. All energy values, except the energy values for the first 4 low-lying levels are given in the form: Experimental value(ENSDF value).
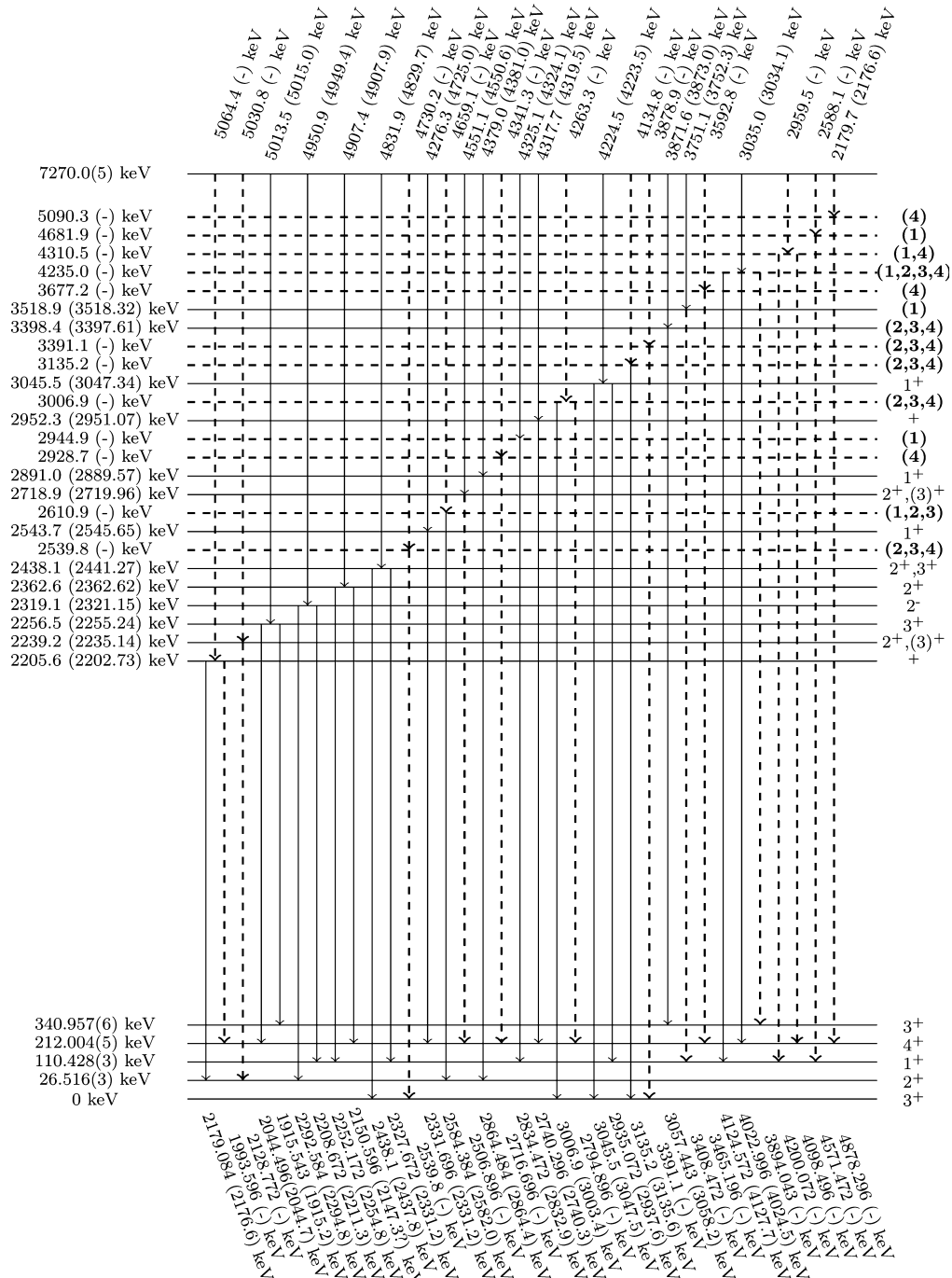
gamma ray transitions in the energy range between 0.3 MeV and 7.1 MeV. These new results can be useful for future investigations of nuclear structure parameters such as the nuclear level density and radiative strength function.

Acknowledgement

References

[1] S. Boneva, E. Vasil'eva, Y.P. Popov, A. Sukhovoi, V. Khitrov, Two-quantum cascades of radiative neutron capture 1. Spectroscopy of excited states of complex nuclei in the neutron binding energy region, Sov. J. Part. Nucl. 22 (2) (1991) 232–248 (English Translation).

[2] Y.P. Popov, A. Sukhovoj, V. Khitrov, Y.S. Yazvitskij, Study on the γ decay of 165 Dy with the help of the (n, 2γ) reaction, Izv. Akad. Nauk SSSR, Ser. Fiz. 48 (5) (1984) 891–900.

[3] A. Sukhovoi, V. Khitrov, Method of improving the amplitude resolution of the spectra of gamma-transition cascades in the computer processing of encoded coincidence data, Instrum. Exp. Tech. 27 (5) (1985) 1071–1074.

[4] E. Vasilieva, A. Sukhovoj, V. Khitrov, Direct experimental estimate of parameters that determine the cascade gamma decay of compound states of heavy nuclei, Phys. At. Nucl. 64 (2) (2001) 153–168.

[5] R.W. Bauer, M. Deutsch, Nuclear orientation of Mn-56, Phys. Rev. 117 (2) (1960) 519.

[6] S. Du Toit, L. Bollinger, Lifetimes of energy levels in Al-28, Mn-56, Cu-64, Rh-104, and I-128 excited by slow neutron capture, Phys. Rev. 123 (2) (1961) 629.

[7] I. Estulin, A. Melioransky, L. Kalinkin, Transitions between low-lying excited states of Mn-54 and Ho-166, Nucl. Phys. 24 (1) (1961) 118–125.

[8] P. Carlos, H. Nifenecker, J. Fagot, J. Matuszek, Étude de cascades $\gamma—\gamma$ dans la capture thermique de neutrons par les isotopes 55Mn, 56Fe, 59Co, 199Hg, J. Phys. 25 (11) (1964) 957–960.

[9] L. Hughes, T. Kennett, W. Prestwich, A study of the 55Mn (n, γ) 56Mn reaction, Nucl. Phys. 80 (1) (1966) 131–144.

[10] D. Dorioman, M. Popa, M. Cristu, Gamma Rays from Thermal Neutron Capture in Manganese, Germanium, and Iridium Nuclei, Tech. Rep., Inst. of Atomic Physics, Bucharest, 1967.

[11] R. Alves, J. Kuchly, J. Julien, C. Samour, J. Morgenstern, Capture radiative partielle des neutrons de résonance dans le chlore, le manganèse, le fer, le cuivre, le thulium et le mercure, Nucl. Phys. A 135 (2) (1969) 241–280.

[12] J. Kopeckỳ, E. Warming, Circular polarization measurements with a Ge (Li) detector, Nucl. Phys. A 127 (2) (1969) 385–398.

[13] J. Mellema, H. Postma, Investigation of nuclear level spins of 56Mn by means of nuclear orientation, Nucl. Phys. A 154 (2) (1970) 385–406.

[14] V. Orphan, N.C. Rasmussen, T. Harper, Line and Continuum Gamma-Ray Yields from Thermal-Neutron Capture in 75 Elements, Tech. Rep., Gulf Energy And Environmental Systems INC San Diego CA, 1970.

[15] J. Boulter, W. Prestwich, Lifetimes of the 26 and 110 keV levels in 56Mn, Can. J. Phys. 49 (23) (1971) 2911–2916.

[16] P. Van Assche, H. Baader, H. Koch, B. Maier, U. Gruber, O. Schult, J. McGrory, J. Comfort, R. Rimawi, R. Chrien, et al., Energy levels of 56Mn, Nucl. Phys. A 160 (2) (1971) 367–384.

[17] F. Stecher-Rasmussen, K. Abrahams, J. Kopecky, W. Ratynski, Circular polarization of neutron-capture gamma-rays from Mn, Ni, Ga and W, Nucl. Phys. A 1 (1972) 250.

[18] H. Börner, O. Schult, Resonance neutron capture in 55Mn and levels in 56Mn, Z. Naturforsch. A 29 (3) (1974) 385–388.

[19] A. Colenbrander, T. Kennett, An investigation of the reaction 55Mn (n, γ) 56Mn, Can. J. Phys. 53 (3) (1975) 236–250.

[20] P. Delheij, K. Abrahams, W. Huiskamp, H. Postma, The 55Mn (n, γ) 56Mn reaction studied with polarized neutrons and polarized manganese nuclei, Nucl. Phys. A 341 (1) (1980) 45–55.

[21] M. Islam, T. Kennett, S. Kerr, W. Prestwich, A self-consistent set of neutron separation energies, Can. J. Phys. 58 (2) (1980) 168–173.

[22] S. Mughabghab, Neutron Cross Sections: Neutron Resonance Parameters and Thermal Cross Sections, Part A: Z=1-60, vol. 1, Elsevier, 2012.

[23] R. Macklin, Resonance neutron capture by manganese below 2.5 keV, Nucl. Sci. Eng. 89 (4) (1985) 362–365.

[24] A. Wapstra, G. Audi, The 1983 atomic mass evaluation: (i). atomic mass table, Nucl. Phys. A 432 (1) (1985) 1–54.

[25] B. Dropesky, A. Schardt, T. Shull, Note on the decay of the new nucleide Cr-56, Nucl. Phys. 16 (2) (1960) 357–359.

[26] A.M. Nathan, J.W. Olness, E.K. Warburton, J.B. McGrory, Yrast decay schemes from heavy ion + ^{48}Ca fusion-evaporation reactions. i. $^{54-56}$Mn, ^{56}Cr, and $^{52-53}$V, Phys. Rev. C 16 (1977) 192–214, https://doi.org/10.1103/PhysRevC.16.192.

[27] T. Caldwell, D. Pullen, T. Mulligan, O. Hansen, (tau, p) reactions on Cr. ii. 54 Cr (tau, p), 56 Mn, Tech. Rep., Univ. of Pennsylvania, Philadelphia, 1971.

[28] U. Fister, R. Jahn, P. von Neumann-Cosel, P. Schenk, T. Trelle, D. Wenzel, U. Wienands, Stretched proton-neutron configurations in fp-shell nuclei:(i). experimental results of the (α, d) reaction, Nucl. Phys. A 569 (3) (1994) 421–440.

[29] J. Green, A. Smith, W. Buechner, M. Mazari, Excited states in Mn 56, Phys. Rev. 108 (3) (1957) 841.

[30] J. Bjerregaard, P. Dahl, O. Hansen, G. Sidenius, Energy levels from (p, p'),(d, p) and (d, α) reactions on the stable isotopes between Sc-45 and Ni-58, Nucl. Phys. 51 (1964) 641–666.

[31] J.R. Comfort, Nuclear structure of manganese-56, Phys. Rev. 177 (4) (1969) 1573.

[32] A. Garcia, A. Lopez, F. Senent, The 55Mn (d, p) 56Mn reaction, An. Fis. 67 (1971) 181.

[33] D.F. Measday, T.J. Stocki, γ rays from muon capture in natural Ca, Fe, and Ni, Phys. Rev. C 73 (4) (2006) 045501.

[34] F. Ajzenberg-Selove, R.E. Brown, E.R. Flynn, J.W. Sunier, (t,^{3}He) reactions on ^{56}Fe, ^{58}Fe, and ^{58}Ni, Phys. Rev. C 31 (1985) 777–786, https://doi.org/10.1103/PhysRevC.31.777.

[35] N. Anantaraman, S.M. Austin, J. Winfield, Heavy ion reactions as probes for spin strength, Nucl. Phys. A 482 (1–2) (1988) 331–342.

[36] S. Albergo, S. Costa, R. Potenza, J. Romanski, C. Tuvé, L. Jarczyk, B. Kamys, A. Magiera, A. Strzalkowski, R. Barna, V. D'Amico, D. De Pasquale, G. Mannino, Elastic transfer in the ^{11}B+^{12}C system in the c.m. energy range 5–40 MeV, Phys. Rev. C 43 (1991) 2704–2710, https://doi.org/10.1103/PhysRevC.43.2704.

[37] H. Kelleter, D. Bachner, B. Schmidt, W. Seliger, Level investigation by means of the (d, α) reaction (ii). 52Mn and 56Mn, Nucl. Phys. A 183 (3) (1972) 509–522.

[38] H. Junde, H. Su, Y. Dong, Nuclear data sheets for A=56, Nucl. Data Sheets 112 (6) (2011) 1513–1645.

[39] V. Khitrov, A. Sukhovoj, New technique for a simultaneous estimation of the level density and radiative strength functions of dipole transitions at $E_{ex}<B_n$-0.5 MeV, arXiv preprint, arXiv:nucl-ex/0110017.

[40] A. Sukhovoj, L. Mitsyna, N. Jovancevic, Overall picture of the cascade gamma decay of neutron resonances within a modified practical model, Phys. At. Nucl. 79 (3) (2016) 313–325.

[41] D. Vu, A. Sukhovoj, L. Mitsyna, S. Zeinalov, N. Jovancevic, D. Knezevic, M. Krmar, A. Dragic, Representation of radiative strength functions within a practical model of cascade gamma decay, Phys. At. Nucl. 80 (2) (2017) 237–250.

[42] A. Sukhovoj, New model of the cascade gamma decay of neutron resonances for practitioners: basic concepts and attainable precision, Phys. At. Nucl. 78 (2) (2015) 230–245.

[43] A.M. Sukhovoj, L.V. Mitsyna, The next-generation practical model of the cascade gamma-decay of neutron resonance and expected parameters for an arbitrary nucleus, in: Proceedings, 22nd International Seminar on Interaction of Neutrons with Nuclei: Fundamental Interactions and Neutrons, Nuclear Structure, Ultracold Neutrons, Related Topics (ISINN 22), Dubna, Russia, May 27–30, 2014, 2015.

[44] S. Boneva, V. Khitrov, A. Sukhovoj, A. Vojnov, Excitation study of high-lying states of differently shaped heavy nuclei by the method of two-step cascades, Nucl. Phys. A 589 (2) (1995) 293–306.

[45] Z. Revay, PGAA: Prompt gamma and in-beam neutron activation analysis facility, J. Large-Scale Res. Fac. JLSRF 1 (2015) 20.

[46] Z. Révay, P. Kudějová, K. Kleszcz, S. Söllradl, C. Genreith, In-beam activation analysis facility at MLZ, Garching, Nucl. Instrum. Methods Phys. Res., Sect. A, Accel. Spectrom. Detect. Assoc. Equip. 799 (2015) 114–123.

[47] B. Krusche, K. Lieb, H. Daniel, T. Von Egidy, G. Barreau, H. Börner, R. Brissot, C. Hofmeyr, R. Rascher, Gamma ray energies and 36Cl level scheme from the reaction 35Cl (n, γ), Nucl. Phys. A 386 (2) (1982) 245–268.
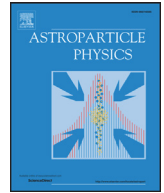
A novel method for atmospheric correction of cosmic-ray data based on principal component analysis

M. Savić, A. Dragić*, D. Maletić, N. Veselinović, R. Banjanac, D. Joković, V. Udovičić

Institute of Physics, University of Belgrade, Pregrevica 118, Zemun 11080, Serbia

A B S T R A C T

A new method for atmospheric correction of cosmic ray data is designed. It's fully empirical, based on the principal component analysis. The method requires knowledge of the pressure and the temperature profile of the atmosphere. It's applicable to all muon detectors. The method is tested on muon data from two detectors in Belgrade cosmic ray station, one located on the ground level and the other at the depth of 25 mwe. Correction reduces variance by 64.5% in ground level detector data and 38.1% in underground data. At the same time, the amplitude of the annual variation is reduced by 86.0% at ground level and 54.9% underground. With the same data sets the presented method performs better than the integral correction method.

© 2019 Elsevier B.V. All rights reserved.

1. Introduction

Count rates of ground based or underground cosmic-ray (CR) muon detectors are affected by atmospheric parameters (air pressure and temperature at different heights). The proper description of atmospheric effects is necessary for understanding primary CR variations, originating outside of the atmosphere.

Early studies in CR temporal variations [1,2] revealed the existence of a variation caused by the change of air pressure, the so called "barometric effect". With the increase in pressure the atmosphere represents thicker absorber, resulting in reduced number of muons reaching the ground level. Therefore, muon flux is expected to be anti-correlated with atmospheric pressure.

Observed negative correlation between muon flux and atmospheric temperature, the so called "negative temperature effect", has been explained by Blackett [3] to be a consequence of muon decay. During warm periods the atmosphere is expanded and the main layer of muon production (∼100 mb) is higher, resulting in longer muon path and lower surviving probability to the ground level. Low energy muons are more affected, while the flux of high energy muons, capable of penetrating great depth, does not suffer. At deep underground experiments another type of temperature effect, "positive temperature effect" is pronounced [4]. Development of nuclear emulsions capable of detecting energetic charged particles lead to discovery of charged pions in CRs and $\pi - \mu$ decay [5–7]. The positive temperature effect is interpreted as a conse-

quence of latter process [8,9]. Pions created in the interactions of primary CR particles with the atmospheric nuclei can decay into muons or interact with air nuclei. Higher temperature in the production layer means lower air density and consequently, lower interaction probability and higher muon production.

In most cases linear regression is sufficient to account for the barometric effect. The temperature effects are treated by empirical and theoretical methods. In addition to the barometric coefficient β, **the method of effective level of generation** [8] introduces two empirical parameters: α_H to encounter for muon intensity variations δI_μ correlated with the change of the height of generation level δH (negative effect) and α_T for the changes of the temperature of this level (positive temperature effect).

$$\delta I_\mu = \beta \delta p + \alpha_H \delta H + \alpha_T \delta T \qquad (1)$$

Duperier method has been successfully used in many studies for the atmospheric corrections of muon data ([10–15] etc.).

It's been argued [16,17] that for correct temperature correction of muon detectors count rate the vertical temperature profile of the entire atmosphere needs to be known. In the so called **integral method** the muon intensity variations caused by the temperature are described by the equation:

$$\frac{\delta I_\mu}{I_\mu} = \int_0^{h_0} W_T(h)\delta T(h)dh \qquad (2)$$

where $\delta T(h)$ is the variation of temperature at isobaric level h with respect to the referent value and $W_T(h)$ is the temperature coefficient density. The coefficients are calculated theoretically and the best known calculations are given in references [18,19].

---

* Corresponding author.
  E-mail address: dragic@ipb.ac.rs (A. Dragić).

The **mass-average temperature method** [20] is a variant of the integral method, based on the assumption of small changes of the temperature coefficient density $W_T(h)$ with the atmospheric depth h allowing its average value $\overline{W}_T$ to be put in front of the integral in the Eq. (2) and on determination of the mass-averaged temperature T_m:

$$\frac{\delta I_\mu}{I_\mu} = \overline{W}_T(h) \int_0^{h_0} \delta T(h) dh = \overline{W}_T(h) \cdot \delta T_m \qquad (3)$$

The method was used in numerous studies ([21–23] to name a few).

Another form of the integral method is **the effective temperature method** [24]. By introducing the temperature coefficient α_T:

$$\alpha_T = \int_0^{h_0} W_T(h) dh$$

the Eq. (2) can be normalized as:

$$\frac{\delta I_\mu}{I_\mu} = \int_0^{h_0} W_T(h) dh \cdot \frac{\int_0^{h_0} W_T(h) \delta T(h) dh}{\int_0^{h_0} W_T(h) dh} = \alpha_T \cdot \delta T_{eff} \qquad (4)$$

where the effective temperature T_{eff} is defined as:

$$T_{eff} = \frac{\int_0^{h_0} W_T(h) T(h) dh}{\int_0^{h_0} W_T(h) dh}$$

The latter method is popular with the underground muon telescopes [25,26].

Different methods of atmospheric correction might be compared on the basis of several criteria. One is requirement of the lowest variance of corrected data. Since the most prominent temperature effect on CR time series is seasonal variation, another criterion is the smallest residual amplitude of seasonal variation after correction is applied. The latter does not take into account possible genuine seasonal variation of non-atmospheric origin.

Early studies comparing Dupierier's empirical and Dorman's theoretical methods ([27] and references therein) found similar accuracy of two methods, with essentially the same corrections at sea level, but with the integral method overestimating the temperature effect.

A more recent study [28] compared different methods of atmospheric correction for data from Nagoya and Tibet supertelescopes, as well as Yakutsk, Moscow and Novosibirsk telescopes. They found the mass-averaged temperature method to practically coincide with the integral method. On the other hand, the effective level of generation method for Nagoya shows discrepancy from the integral method in winter time, being able to eliminate only 50% of the temperature effect. Even with the integral method in the case of Tibet muon telescope the removal of temperature effect is achieved with the density of temperature coefficients 3 times higher than calculated ones. The precise origin of disagreement is unknown.

The method of the effective level of generation takes care of key physical causes of the temperature effect. However, it does not make optimal use of the temperature data. Also, the assumption of a single level of main muon production is a simplification. Detailed CORSIKA simulation of the shower development in the atmosphere reveals the actual distribution of the muon generation heights (see Fig. 1).

Different implementations of the integral method exist, employing different approximations, choice of parameters, models of the atmosphere, whether kaon contribution is taken into account, leading to differences in calculated density temperature coefficients (see for instance discussion in [29]). As already mentioned, on the case of Tibet telescope [28] theoretical calculations do not fully correspond to the local experimental conditions and the origin of disagreement is difficult to trace.

The effective temperature method lacks universality, since it works best with the data from deep underground detectors.

Here we propose a new method for atmospheric corrections. It's fully empirical, makes use of the available temperature data through entire atmosphere and it's applicable to arbitrary detector irrespective to energy sensitivity and is simple to implement. The method is based on the principal component analysis, thus reducing dimensionality of the problem, exploiting correlations between atmospheric variables and ensuring mutual independence of correction parameters. The price is loss of clear physical interpretation of these parameters, since the pressure and the temperature at different levels are treated on equal footing.

2. Method description

2.1. Meteorological data

Set of variables that enter principal component decomposition consists of atmospheric temperature profile for the given location as well as locally measured atmospheric pressure. Meteorological balloon soundings for Belgrade are not done frequently enough to be used for suggested analysis. As a consequence, modeled temperatures were used instead. However, there were enough balloon sounding data for testing consistency of the modeled temperatures.

There are several weather and global climate numerical models available today. Here, Global Forecast System [30] data was used. GFS is a weather forecast model, developed by National Centers for Environmental Prediction [31], which is able to predict large number of atmospheric and land-soil parameters. Apart from forecast data, GFS also provides retrospective data produced taking into account most recent measurements by a world wide array of meteorological stations. Retrospective data are produced four times a day at 00:00, 06:00, 12:00 and 18:00 UTC. Data with finer temporal resolution are obtained by cubic spline interpolation. Temperatures for the following 25 isobaric levels (in mb) were used for initial analysis: 10, 20, 30, 50, 70, 100, 150, 200, 250, 300, 350, 400, 450, 500, 550, 600, 650, 700, 750, 800, 850, 900, 925, 975, 1000. Horizontal spatial resolution for modeled data is 0.5 degrees, so coordinates closest to the experiment location (latitude 44.86, longitude 20.39), were selected with this precision. Before any further analysis was done, GFS modeled temperature profiles were compared to local meteorological balloon soundings for Belgrade, where balloon data was available. Fig. 2 shows profile of differences between modeled and measured values for different isobaric levels. Disagreement was found between measured and modeled temperature at the lowest level. As a result, it was decided not to use temperature data for isobaric level of 1000 mb in further analysis. Ground temperature data measured by local meteorological stations was used for lowest layer instead. Similar problem with the GFS data was reported before by [28] who found 5° C deviation in the summer time near ground level at Yakutsk location.

Atmospheric pressure and ground level temperature from the Republic Hydro-meteorological Service of Serbia was used to compose unique local pressure and temperature time series.

2.2. Cosmic-ray data

The analysis is performed on data from Belgrade muon detectors. The Belgrade cosmic-ray station, together with the present detector arrangement is described in details elsewhere [32]. Two muon detectors are located in the laboratory, one at the ground level and the other at the depth of 25 mwe. Data are recorded on the event-by event basis and can be integrated into the time series with the arbitrary time resolution. For most purposes hourly data are used. Muon detectors are sensitive to primary cosmic rays
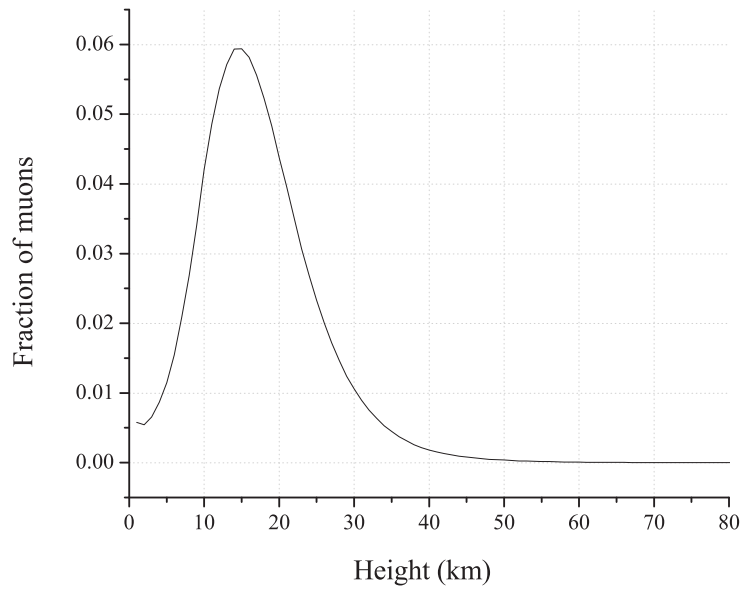
Fig. 1. Distribution of muon generation at different heights in the atmosphere, according to CORSIKA simulation.
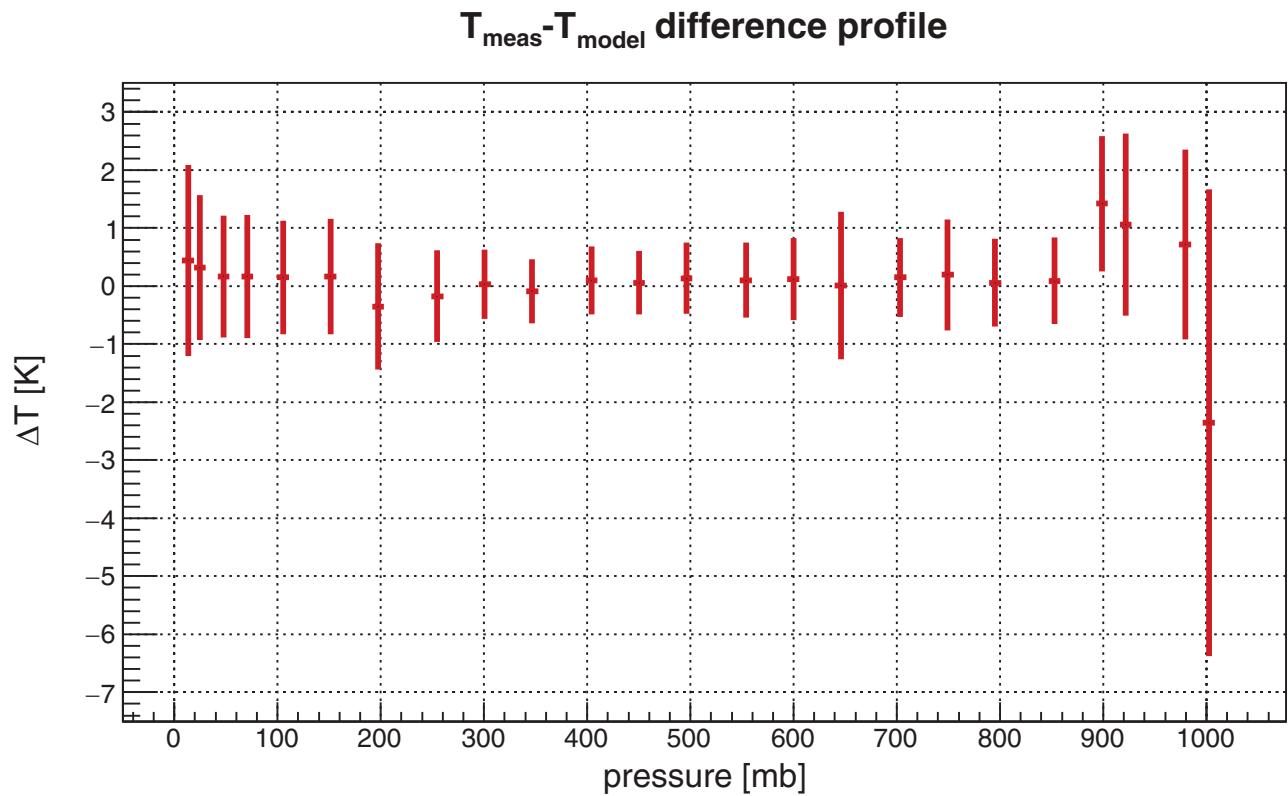
Fig. 2. Distribution of differences between measured temperatures and modeled by GFS.

of 59 GeV median energy in the case of ground level detector and 137 GeV for underground detector.

2.3. Principal component decomposition

Principal component analysis is a convenient and widely used data reduction method when dealing with strongly correlated data. It transforms the original set of variables into a set of uncorrelated variables (called principal components (PC)). The principal components are ordered according to decreasing variance. In our case, there are 26 input variables: 24 modeled temperatures (isobaric level 1000 mb temperature excluded), locally measured ground level temperature and local atmospheric pressure. Initial variables were centered and normalized before
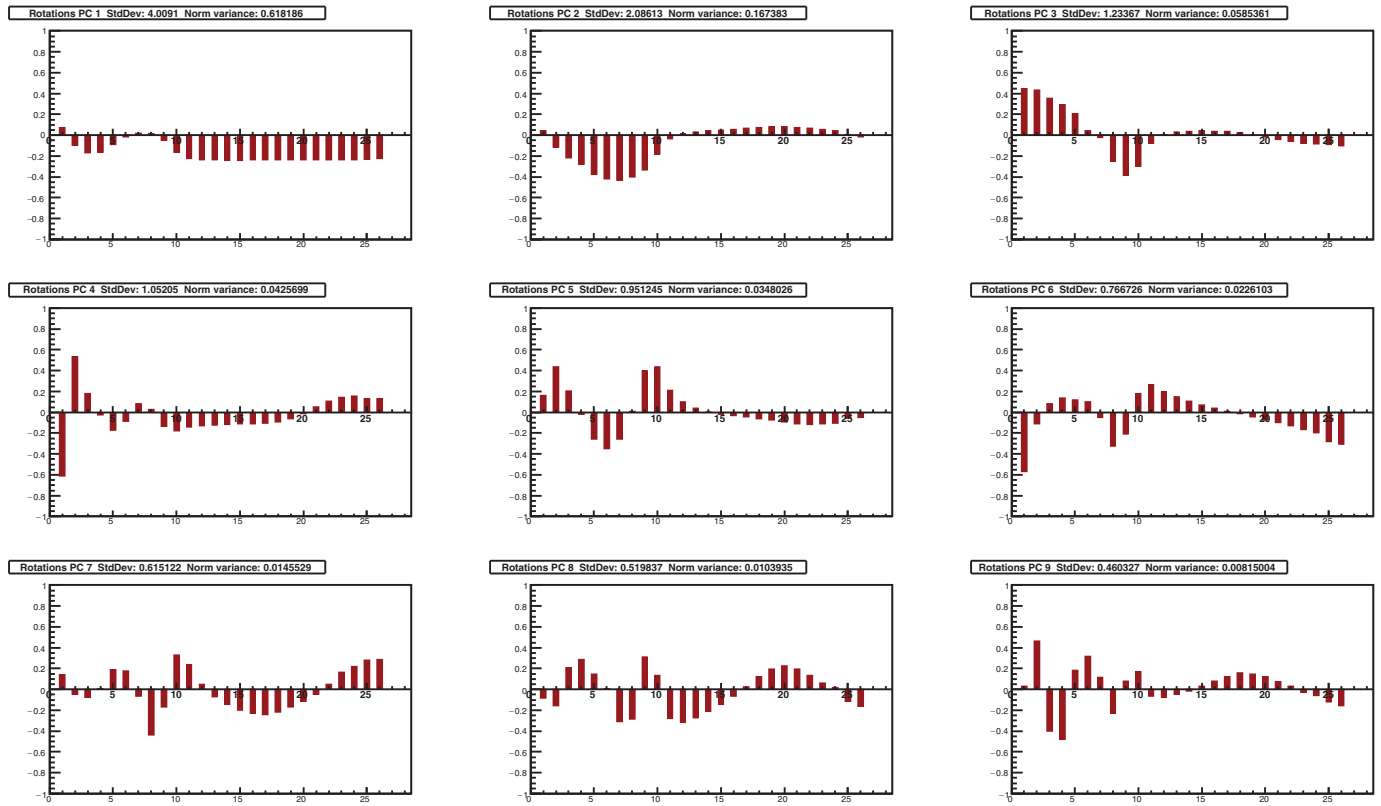
Fig. 3. Composition of nine principal components with largest variance (in decreasing order). Input variables are displayed on *X*-axis: 1 being pressure, 2 temperature of 10 mb isobaric level, 26 being local ground level temperature. *Y*-axis represents rotations.

decomposition. After decomposition, a new set of 26 principal components was obtained. Decomposition should not be regarded as universal, but it should be redone for every location and period under study.

One year was selected as a suitable time period for the analysis, in order to reduce possible seasonal bias, due to atmospheric temperature annual variation. Additional criteria were quality and consistency of muon data. Taking this into account, final time interval selected for analysis was from 01.06.2010 to 31.05. 2011.

Fig. 3 shows composition plots for the first nine principal components, that account for 98% of total variance. *X*-axis represents input atmospheric variables, first being atmospheric pressure, followed by 10 mb layer temperature, last being ground level local temperature. *Y*-axis represents decomposition rotations for a given principal component. Interesting features observed on these plots are that first two principal components depend almost exclusively on temperature. The first one is mostly combination of temperatures in the troposphere (isobaric levels 250–1000 mb) with almost equal weights. The second eigenvector accounts for significant variance of temperatures in higher atmospheric levels (10–250 mb), with the strongest contribution centered in the tropopause. Components 3 to 6 have mixed p-T composition. The correlation of atmospheric pressure and temperature at different heights is not surprising. The diurnal and semi-diurnal oscillations of pressure are attributed to the warming of the upper atmosphere by the Sun [33]. This correlation makes it impossible to define a single barometric parameter in PCA based method of atmospheric corrections. It's worth mentioning that Dorman [34] recognizes three different barometric effects: absorption, decay and genera-

tion effect. It also indicates that empirical methods with separated pressure and temperature corrections might lead to overcorrection.

The values of the eigenvectors for these first nine components are also given in Table 1.

Fig. 4 shows plot of proportion of variance as well as plot of cumulative variance for obtained principal components. Corresponding numerical values are given in Table 2.

Usually, only a first few principal components (containing high fraction of total variance) are of practical interest. There are various different methods and rules for choosing how many PCs to retain in the analysis, none completely free of subjectivity (see for example a thorough discussion in [35]). A rule based on cumulative percentage of total variation usually recommends to retain PCs responsible for 70–90% of total variation. When one or two components are dominant, higher value (95%) is appropriate. In our case it would mean keeping first 6 PCs. According to Kaisser's rule only PCs with the eigenvalue $\lambda > 1$ should be retained. Jolliffe [35] suggested 0.7 as correct level, exceeded by six of our PCs. Another rule proposes to retain components with the eigenvalue above mean, a condition satisfied by first seven of our PCs. Another popular model is broken stick, but in application to our problem is too restrictive, leading to only two relevant PCs. The scree graph or log-eigenvalue diagram don't provide clean cut with our set of PCs.

To test the meaningfulness of potentially relevant PCs, the time series from PC data are constructed and tested whether they are distinguishable from white noise. The procedure is often done when principal component analysis is applied to atmospheric physics problems [36]. The time series with hourly resolution for the first three PCs are plotted on Fig. 5.

Table 1
Definition of first nine principal components.

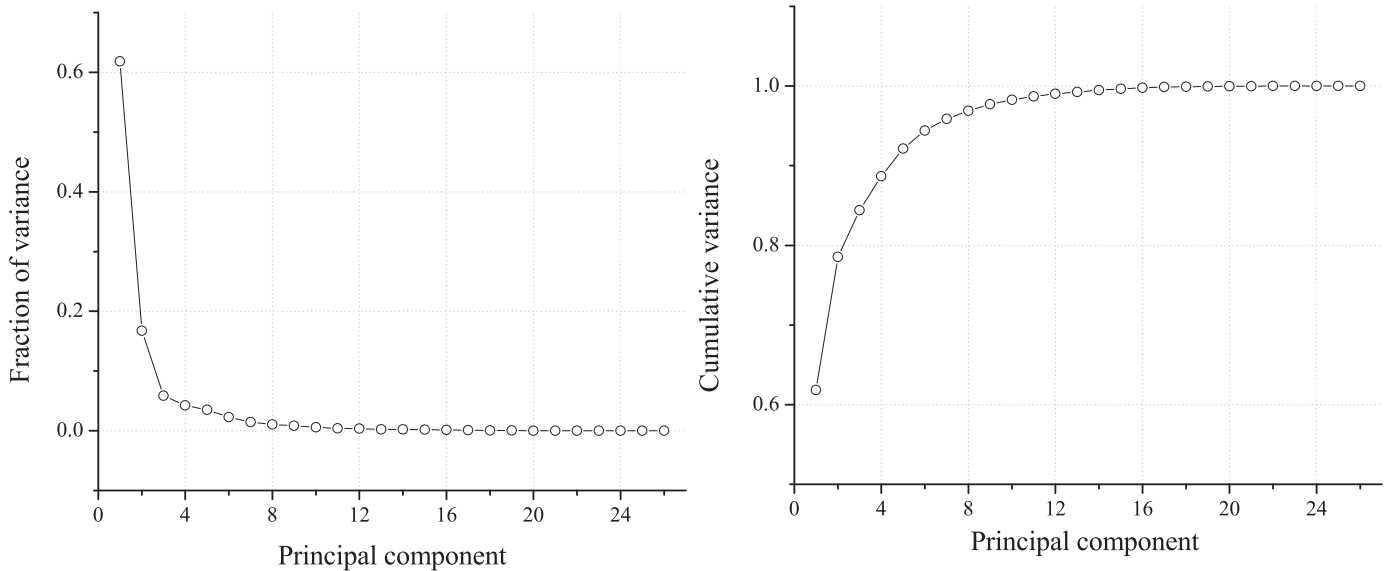| Variables	Principal components								
	PC1	PC2	PC3	PC4	PC5	PC6	PC7	PC8	PC9
p	0.07699	0.04117	0.44694	−0.61285	0.16301	−0.57121	0.14028	−0.08106	0.03443
$T(10)$	−0.0947	−0.11603	0.43488	0.5344	0.43741	−0.11036	−0.04499	−0.15825	0.46469
$T(20)$	−0.16947	−0.21766	0.35754	0.18029	0.20527	0.08546	−0.07719	0.20635	−0.40309
$T(30)$	−0.16476	−0.27825	0.29593	−0.02505	−0.02204	0.14134	0.00634	0.28574	−0.47812
$T(50)$	−0.09124	−0.37682	0.20969	−0.17322	−0.25798	0.12084	0.19349	0.14645	0.18493
$T(70)$	−0.01483	−0.42304	0.04507	−0.08651	−0.3472	0.09965	0.18155	0.01024	0.31886
$T(100)$	0.02192	−0.43132	−0.02451	0.08228	−0.25692	−0.04937	−0.06464	−0.3103	0.1183
$T(150)$	0.01487	−0.40127	−0.24673	0.03037	0.012	−0.32566	−0.43658	−0.28393	−0.23316
$T(200)$	−0.04737	−0.33404	−0.38636	−0.13563	0.40141	−0.2069	−0.16852	0.31181	0.07995
$T(250)$	−0.16218	−0.17984	−0.29739	−0.18123	0.43708	0.18013	0.32866	0.13662	0.17389
$T(300)$	−0.22473	−0.03266	−0.07561	−0.14073	0.21179	0.26504	0.23807	−0.27931	−0.06785
$T(350)$	−0.2369	0.01439	0.00488	−0.12991	0.0998	0.1988	0.05306	−0.31612	−0.0771
$T(400)$	−0.23956	0.03362	0.02958	−0.12159	0.04075	0.14932	−0.06959	−0.27189	−0.04852
$T(450)$	−0.24028	0.04271	0.0402	−0.11503	0.00384	0.10744	−0.14772	−0.21165	−0.01823
$T(500)$	−0.24005	0.04935	0.0428	−0.11304	−0.02187	0.07218	−0.19893	−0.14512	0.03068
$T(550)$	−0.23958	0.05695	0.03965	−0.11295	−0.03254	0.0388	−0.23263	−0.06843	0.08056
$T(600)$	−0.23881	0.06549	0.03681	−0.10649	−0.04369	0.01102	−0.24562	0.02401	0.12499
$T(650)$	−0.23854	0.07279	0.0236	−0.09184	−0.06132	−0.01542	−0.21788	0.12597	0.15977
$T(700)$	−0.23835	0.0801	0.00429	−0.06052	−0.07601	−0.04668	−0.16785	0.19559	0.14932
$T(750)$	−0.23842	0.08071	−0.01837	−0.01332	−0.09245	−0.07308	−0.11295	0.22563	0.12401
$T(800)$	−0.23814	0.07557	−0.03907	0.05036	−0.10989	−0.09943	−0.04696	0.19596	0.07735
$T(850)$	−0.23701	0.0675	−0.06202	0.1081	−0.11988	−0.12745	0.04989	0.13672	0.0304
$T(900)$	−0.23535	0.05462	−0.07977	0.14776	−0.11454	−0.16955	0.16551	0.06204	−0.02952
$T(925)$	−0.23414	0.04606	−0.08313	0.15641	−0.10257	−0.19925	0.21877	0.01715	−0.05804
$T(975)$	−0.23108	0.00789	−0.08827	0.13022	−0.05888	−0.28046	0.284	−0.11523	−0.12249
$T(1000)$	−0.22494	−0.01582	−0.10092	0.13401	−0.04977	−0.30749	0.28553	−0.16516	−0.15908

Fig. 4. Proportion of variance (left) and cumulative proportion of variance (right) for all 26 principal components.
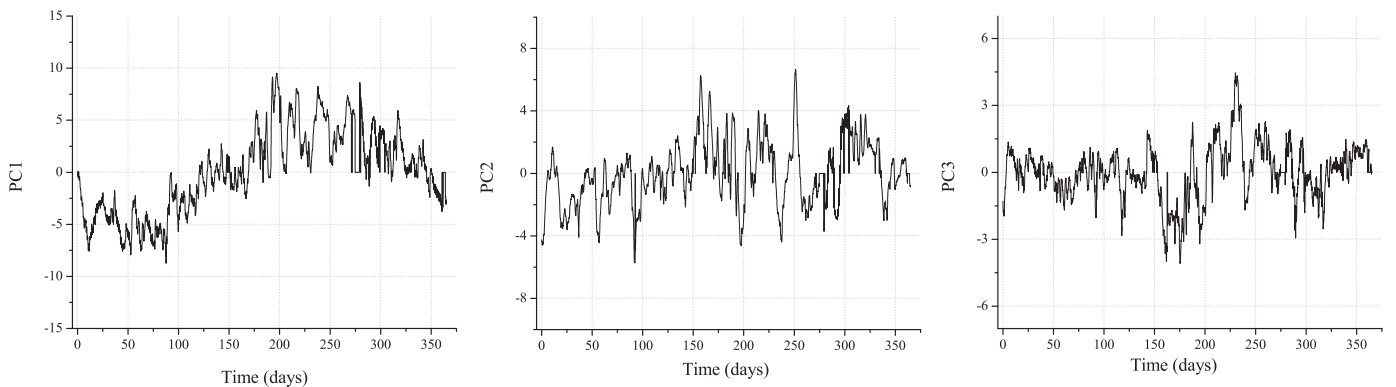
Fig. 5. Time series of the first 3 PCs.

Table 2
Variance (individual and cumulative) for all 26 PCs.

Principal component	Eigenvalue	Percentage of variance	Cumulative variance (%)
1	4.0091	0.618186	0.618186
2	2.08613	0.167383	0.785569
3	1.23367	0.0585361	0.844105
4	1.05205	0.0425699	0.886675
5	0.951245	0.0348026	0.921478
6	0.766726	0.0226103	0.944088
7	0.615122	0.0145529	0.958641
8	0.519837	0.0103935	0.969034
9	0.460327	0.00815004	0.977184
10	0.382006	0.00561263	0.982797
11	0.32832	0.00414592	0.986943
12	0.294489	0.00333553	0.990278
13	0.247876	0.00236317	0.992642
14	0.239462	0.00220546	0.994847
15	0.206157	0.00163465	0.996482
16	0.184453	0.00130857	0.99779
17	0.144657	8.04834E−4	0.998595
18	0.119676	5.5086E−4	0.999146
19	0.0938189	3.38538E−4	0.999485
20	0.0739496	2.10328E−4	0.999695
21	0.0586253	1.32189E−4	0.999827
22	0.0414996	6.62391E−5	0.999893
23	0.0338811	4.41511E−5	0.999937
24	0.0281359	3.04472E−5	0.999968
25	0.0219102	1.84637E−5	0.999986
26	0.0188263	1.36319E−5	1
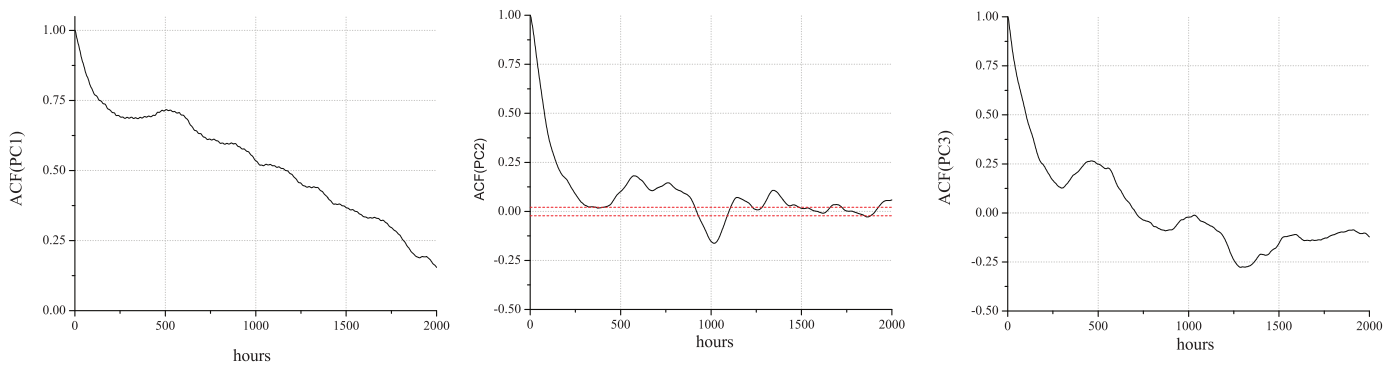
Fig. 6. Autocorrelation function of the first 3 PCs. Time lag is given in hours. In the case of PC2, 95% significance level is indicated by dashed red line. (For interpretation of the references to color in this figure legend, the reader is referred to the web version of this article.)
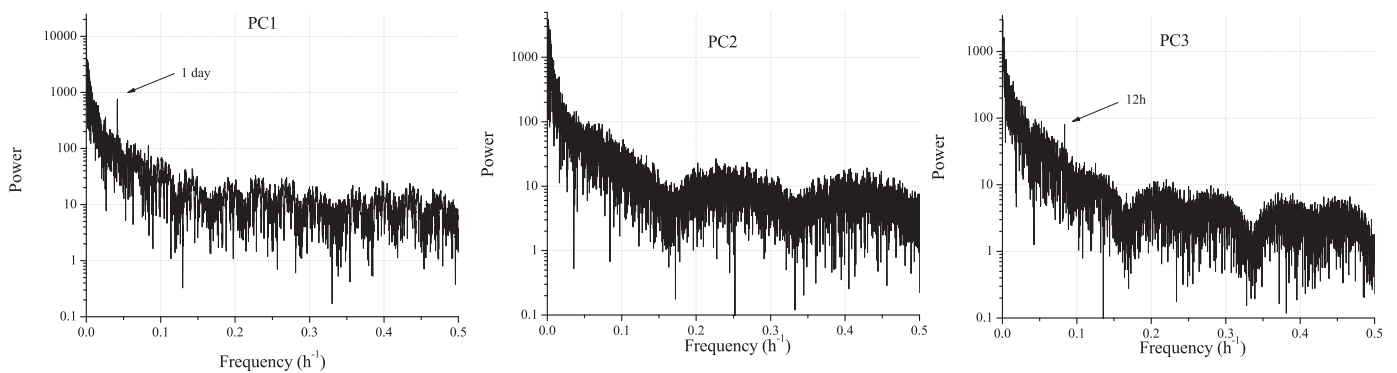
Fig. 7. Spectral analysis of time series of the first 3 PCs.
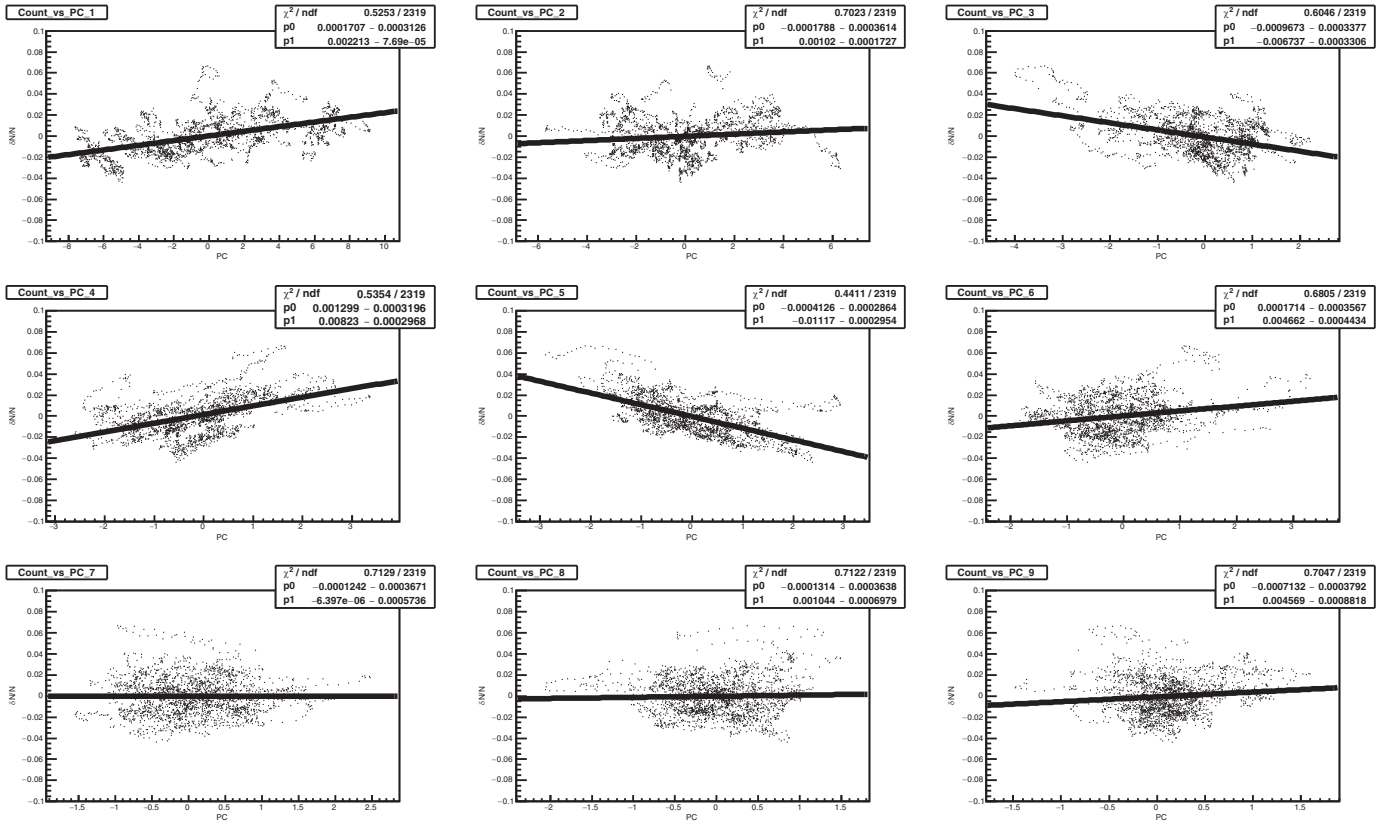
Fig. 8. Muon count dependence on principal components for the first nine principal components (GLL).
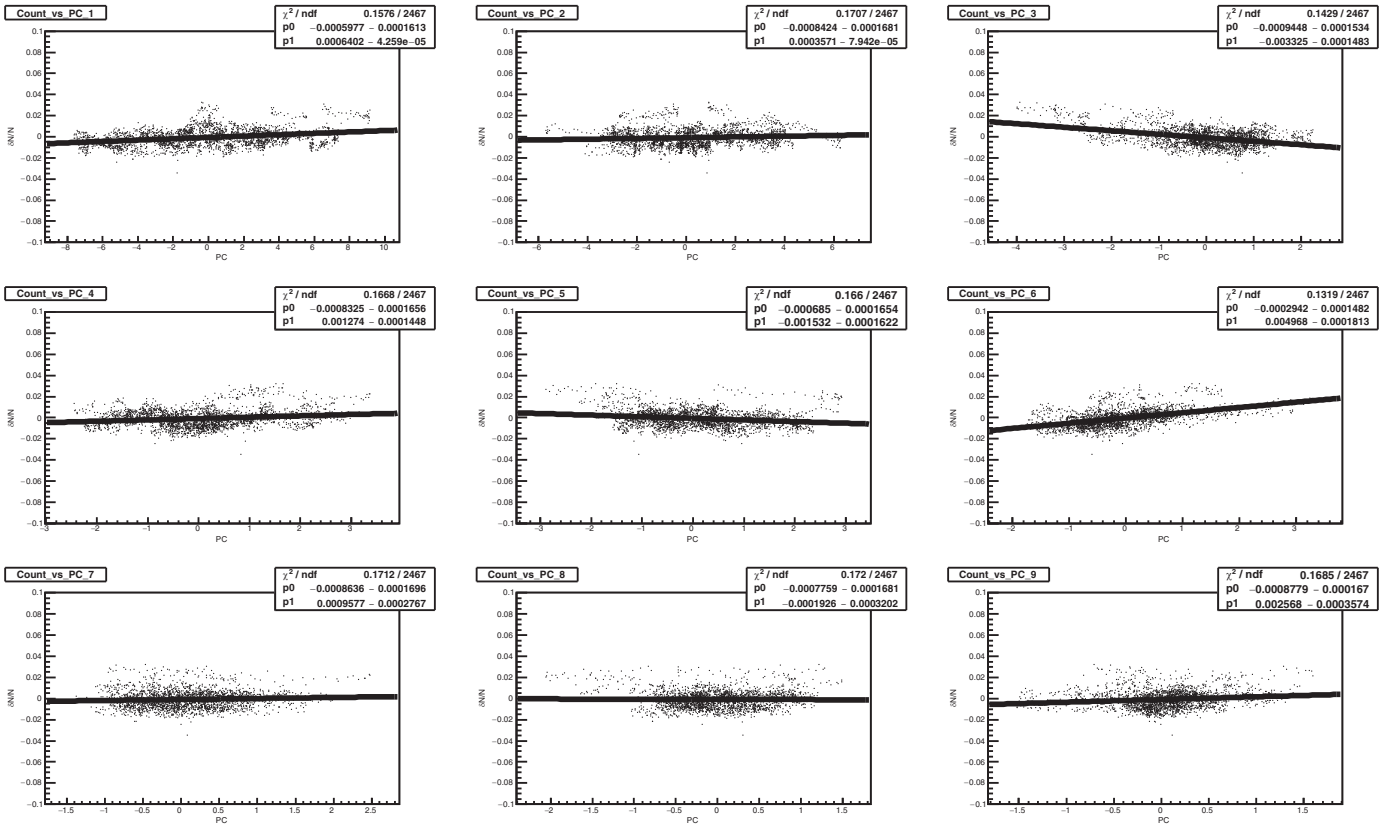
Fig. 9. Muon count dependence on principal components for the first nine principal components (UL).

The subsequent temperature and pressure measurements are highly correlated, as evident from autocorrelation function plot for selected PCs (Fig. 6).

The spectral analysis of the PC time series reveals, for PCs with the strong pressure component, semi-diurnal periodicity in addition to diurnal (Fig. 7).

Since our purpose is the regression of muon data with principal components, selecting the components with significantly high variance is not the main issue. It is more important to identify PCs with high correlation with CR data. Components with relatively low variance, can have high predictive power.

2.4. Correlation of principal components with CR muon count rate and correction of muon data

Scatter plot of muon count rate vs. PCs, together with the linear fit for the first nine principal components are shown on Fig. 8 (GLL) and Fig. 9 (UL). In the analysis hourly summed muon counts and principal component values for the respective hour were used. To minimize the effect of geomagnetic disturbances, only data for International Quiet Days were taken into account. The International Quiet Days are the days with minimum geomagnetic activity for each month. The selection of quiet days is deduced from K_p index. In our analysis 5 quietest days for each month are considered. The values of correlation coefficients are listed in Table 3.

Principal components PC1, PC3, PC4, PC5 and PC6 have been identified as ones with significant contribution to the muon flux variation. Interestingly enough, the PC2, responsible for 16.7% variance of the meteorological data has very little effect on muon flux, at neither ground nor underground level. Ground level muon flux variation is more affected by the first principal component, depending chiefly on the temperature in the troposphere. The finding agrees with usual negative temperature effect. The other PCs are difficult to compare with traditional correction parameters. Yet, the effect of PC3, that is composed more from upper atmosphere temperatures and hence could be loosely associated with positive temperature effect, is more pronounced for the underground muon flux. Fourth and fifth principal components with strong pressure contribution affect more ground level muon flux. On the other hand, PC6, also the one with high pressure component, has more pronounced influence on underground muon flux.

Gradients obtained from the fits for the significant principal components 1, 3, 4, 5 and 6 were then used to calculate the PCA corrected muon count according to the formula:

$$N_\mu^{(corr)} = N_\mu - <N_\mu> \sum_i k_i PC_i, \quad i = 1, 3, 4, 5, 6 \tag{5}$$

where $N_\mu^{(corr)}$ corr is the corrected muon count, N_μ is the raw muon count, $<N_\mu>$ is the mean count for the whole period, k_i are the gradients and PC_i are the corresponding principal components. Resulting corrected muon count time series are plotted on Figs. 10 (GLL) and 11 (UL) along with raw and pressure only corrected time series. Pressure corrected time series are produced for reference. Barometric coefficient was determined by applying linear regression to the same data set used for PCA. Data was previously corrected for temperature effect using integral method, as in Ref. [37]. Pressure corrected and PCA corrected time series are fitted with sine function with annual period in order to illustrate how PCA correction affects yearly variation induced by temperature effect.

PCA based atmospheric corrections remove 64.5% of total variance in GLL time series and 38.1% in UL time series. Pressure corrected CR time series exhibit annual variation, a consequence of

Table 3
Correlation coefficients between principal components and muon count rate in the ground level laboratory (GLL) and underground laboratory (UL).

PC	1	2	3	4	5	6	7	8	9	10	11	12	13	14	15	16	17	18	19	20	21	22	23	24	25	26
GLL	0.43	0.01	−0.37	0.48	−0.55	0.30	−0.01	0.03	−0.01	0.06	0.00	−0.04	0.00	0.01	0.02	−0.01	0.00	−0.01	−0.01	0.03	−0.03	0.00	0.02	−0.01	0.04	0.02
UL	0.26	0.02	−0.48	0.21	−0.19	0.52	0.02	0.04	0.07	0.04	0.01	−0.04	−0.07	0.06	−0.02	−0.05	0.04	0.04	−0.02	0.00	0.00	0.01	0.00	−0.03	0.01	0.01

Fig. 10. Raw (upper panel), pressure corrected (middle panel), pressure+temperature corrected with PCA method (3rd panel from the top) and pressure+temperature corrected with integral method (lower panel) normalized muon count rate for GLL. The sine function with one year period is fitted to the data.

the temperature effect. The performance of the temperature correction may be tested by comparing the amplitude of the annual variation before and after correction. With presented method the amplitude of the annual variation is reduced by 86% (54.9%) in the case of GLL (UL) with respect to the pressure only corrected time series.

To further test the new method, the atmospheric correction of GLL data are performed by the integral method. The correction resulted in 56.25% of variance reduction and 68.1% of reduction of the amplitude of the annual wave. At least in the case of our CR data set the new method performs somewhat better than the integral method.

3. Conclusion

The principal component analysis is successfully used to construct a new empirical method for the atmospheric corrections of CR muon data. The method is equally applicable to all muon detectors, irrespective to location: ground level, shallow or deep underground. It requires knowledge of the atmospheric pressure and temperatures along the entire atmosphere, which is nowadays available in databases such as GFS. The method is suitable for the near real-time correction, with the delay defined by the availability of the atmospheric data (one day in the case of present GFS data). When applied to Belgrade muon data from two detectors
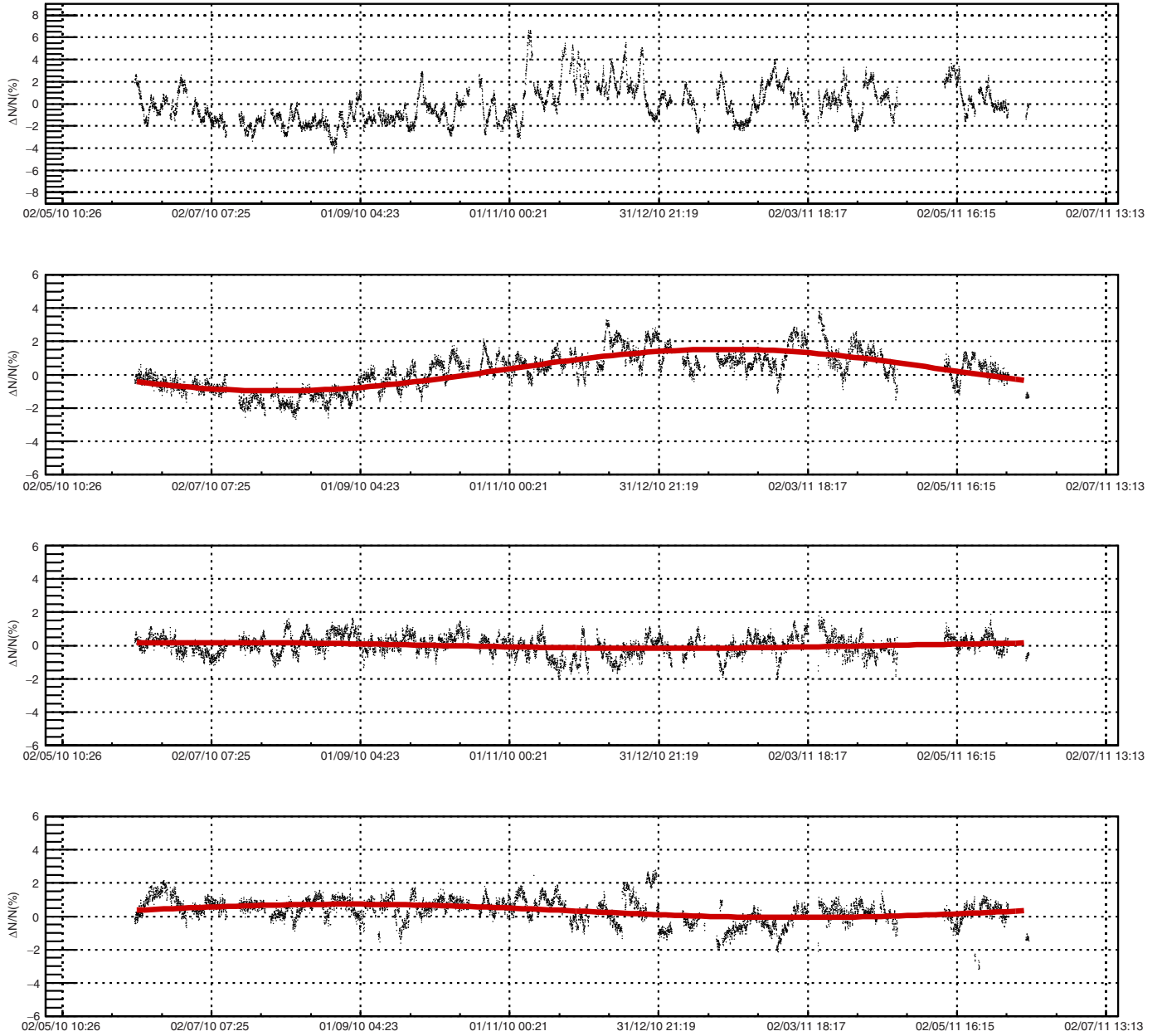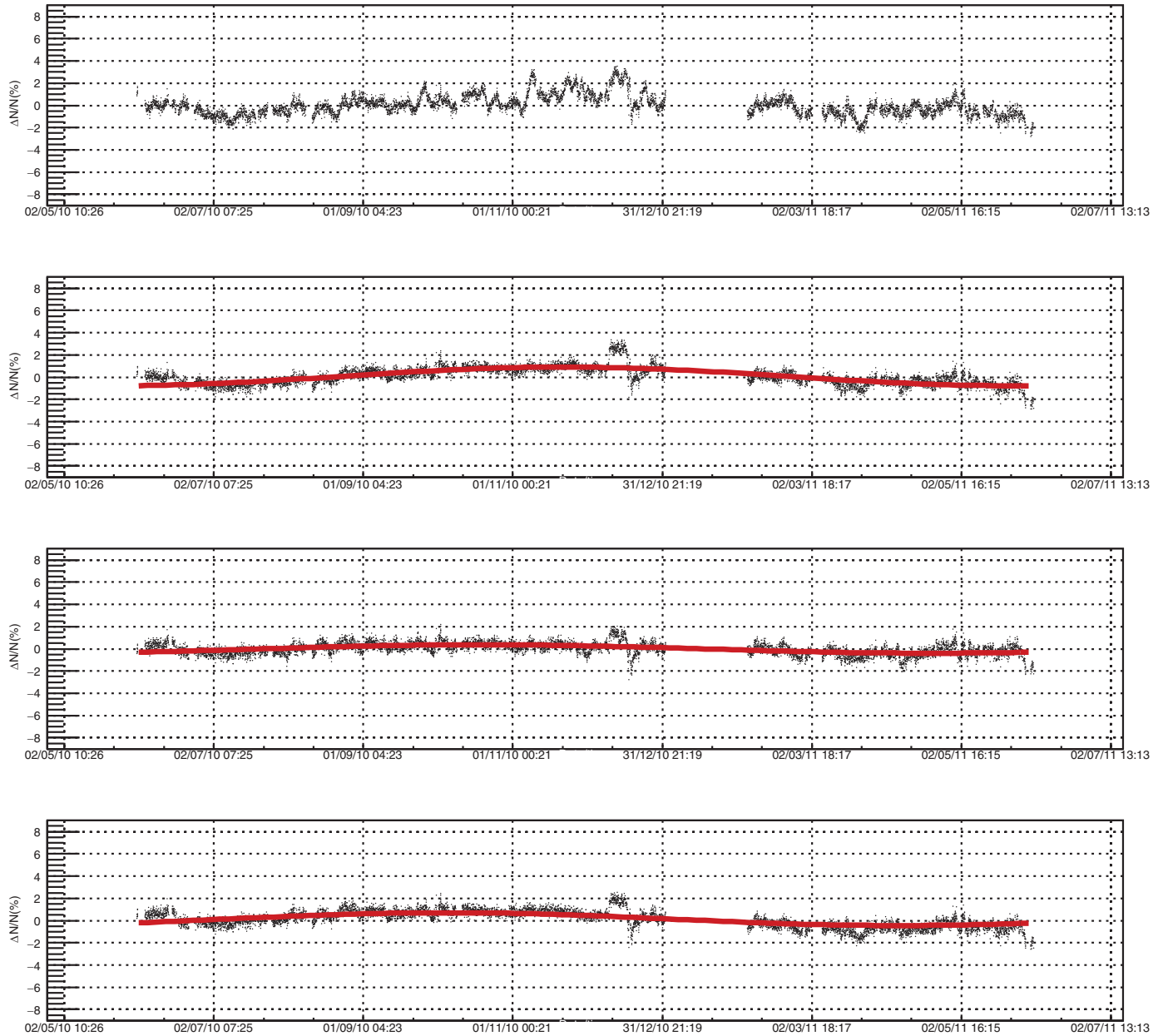
Fig. 11. Raw (upper panel), pressure corrected (middle panel), pressure+temperature corrected with PCA method (3rd panel from the top) and pressure+temperature corrected with integral method (lower panel) normalized muon count rate for UL. The sine function with one year period is fitted to the data.

(ground level and at 25 mwe), the method requires correction to five parameters, determined from linear regression. With the same CR dataset, the present method yields results superior to the integral method in terms of variance reduction and reduction of the annual variation. The new method is also suitable for temperature corrections of the neutron monitor data, which is seldom done in practice.

Acknowledgments

References

[1] L. Myssowsky, L. Tuwim, Unregelmäßige intensitätsschwankungen der höhenstrahlung in geringer seehöhe, Zeitsch. Phys. 39 (2–3) (1926) 146–150.

[2] E. Steinke, Über schwankungen und barometereffekt der kosmischen ultrastrahlung im meeresniveau, Zeitsch. Phys. 64 (1–2) (1930) 48–63.

[3] P.M. Blackett, On the instability of the barytron and the temperature effect of cosmic rays, Phys. Rev. 54 (11) (1938) 973.

[4] M. Forro, Temperature effect of cosmic radiation at 1000-m water equivalent depth, Phys. Rev. 72 (9) (1947) 868.

[5] C.M.G. Lattes, G.P. Occhialini, C.F. Powell, Observations on the tracks of slow mesons in photographic emulsions, Nature 160 (4067) (1947) 486.

[6] C.M.G. Lattes, H. Muirhead, G.P. Occhialini, C.F. Powell, Processes involving charged mesons, Nature 159 (4047) (1947) 694.

[7] G. Occhialini, C. Powell, Nuclear disintegrations produced by slow charged particles of small mass, Nature 159 (4032) (1947) 186.

[8] A. Duperier, The meson intensity at the surface of the earth and the temperature at the production level, Proc. Phys. Soc. Lond. Sect. A 62 (11) (1949) 684.

[9] A. Duperier, Temperature of the upper atmosphere and meson production, Nature 167 (4243) (1951) 312.

[10] C. Baker, D. Hall, J. Humble, M. Duldig, Atmospheric correction analysis for the Mawson muon telescopes, in: International Cosmic Ray Conference, 3, 1993, p. 753.

[11] A. Maghrabi, M. Almutayri, Atmospheric effect on cosmic ray muons at high cut-off rigidity station, Adv. Astron. 2016 (2016).

[12] C.R. Braga, A. Dal Lago, T. Kuwabara, N.J. Schuch, K. Munakata, Temperature effect correction for the cosmic ray muon data observed at the Brazilian Southern Space Observatory in São Martinho da Serra, J. Phys. 409 (2013) 012138 IOP Publishing..

[13] G.C. Castagnoli, M. Dodero, Temperature effect of the muon component underground and pion attenuation length, Il Nuovo Cimento B (1965–1970) 51 (2) (1967) 525–534.

[14] A. Fenton, R. Jacklyn, R. Taylor, Cosmic ray observations at 42 m we underground at hobart, tasmania, Il Nuovo Cimento (1955–1965) 22 (2) (1961) 285–295.

[15] M. Zazyan, M. Ganeva, M. Berkova, V. Yanke, R. Hippler, Atmospheric effect corrections of mustang data, J. Space Weather Space Clim. 5 (2015) A6.

[16] L. Dorman, The temperature effect of the hard component of cosmic rays, Doklady Akad. Nauk SSSR 95 (1954).

[17] E. Feinberg, On the nature of cosmic ray barometric and temperature effects, DAN SSSR 53 (5) (1946) 421–424.

[18] L.I. Dorman, Cosmic ray variations, Technical Report, Foreign Technology Div Wright-Patterson AFB OHIO, 1957.

[19] K. Maeda, M. Wada, Atmospheric temperature effect upon the cosmic-ray intensity at sea level, J. Sci. Res. Inst. 48 (1954).

[20] V. Dvornikov, Y.Y. Krest'yannikov, A. Sergeev, Determination of the variation of average-mass temperature of the atmosphere by data of cosmic ray intensity, Geomag. Aeron. 16 (1976) 923–925.

[21] V. Yanchukovsky, G.Y. Filimonov, R. Hisamov, Atmospheric variations in muon intensity for different zenith angles, Bull. Russ. Acad. Sci. 71 (7) (2007) 1038–1040.

[22] R. De Mendonça, C. Braga, E. Echer, A. Dal Lago, K. Munakata, T. Kuwabara, M. Kozai, C. Kato, M. Rockenbach, N. Schuch, et al., The temperature effect in secondary cosmic rays (muons) observed at the ground: analysis of the Global MUON Detector Network data, Astrophys. J. 830 (2) (2016) 88.

[23] A. Dmitrieva, I. Astapov, A. Kovylyaeva, D. Pankova, Temperature effect correction for muon flux at the earth surface: estimation of the accuracy of different methods, J. Phys. 409 (2013) 012130. IOP Publishing.

[24] P.H. Barrett, L.M. Bollinger, G. Cocconi, Y. Eisenberg, K. Greisen, Interpretation of cosmic-ray measurements far underground, Rev. Mod. Phys. 24 (3) (1952) 133.

[25] S. Tilav, P. Desiati, T. Kuwabara, D. Rocco, F. Rothmaier, M. Simmons, H. Wissing, et al., Atmospheric variations as observed by IceCube, arXiv:1001.0776 (2010).

[26] P. Adamson, C. Andreopoulos, K. Arms, R. Armstrong, D. Auty, D. Ayres, C. Backhouse, J. Barnett, G. Barr, W. Barrett, et al., Observation of muon intensity variations by season with the Minos far detector, Phys. Rev. D 81 (1) (2010) 012001.

[27] H. Carmichael, M. Bercovitch, J.F. Steljes, Introduction of meteorological corrections into meson monitor data, Tellus 19 (1) (1967) 143–160, doi:10.1111/j.2153-3490.1967.tb01468.x.

[28] M.D. Berkova, A.V. Belov, E.A. Eroshenko, V.G. Yanke, Temperature effect of the muon component and practical questions for considering it in real time, Bull. Russ. Acad. Sci. 75 (6) (2011) 820–824, doi:10.3103/S1062873811060086.

[29] A. Dmitrieva, R. Kokoulin, A. Petrukhin, D. Timashkov, Corrections for temperature effect for ground-based muon hodoscopes, Astropart. Phys. 34 (6) (2011) 401–411, doi:10.1016/j.astropartphys.2010.10.013.

[30] Global forecast system (GFS), https://www.ncdc.noaa.gov/data-access/modeldata/model-datasets/global-forcast-system-gfs.

[31] National centers for environmental prediction (NCEP), http://www.ncep.noaa.gov/.

[32] A. Dragić, V. Udovičić, R. Banjanac, D. Joković, D. Maletić, N. Veselinović, M. Savić, J. Puzović, I.V. Aničin, The new setup in the Belgrade low-level and cosmic-ray laboratory, Nucl. Technol. Radiat. Protect. 26 (3) (2011) 181–192.

[33] B. Haurwitz, The diurnal surface-pressure oscillation, Arch. Meteorol. Geophys. Bioklimatol. Ser. A 14 (4) (1965) 361–379, doi:10.1007/BF02253483.

[34] L.I. Dorman, Cosmic Rays in the Earth's Atmosphere and Underground, Springer Netherlands, 2004, doi:10.1007/978-1-4020-2113-8.

[35] I. Jolliffe, Principal Component Analysis, Springer-Verlag, 2002, doi:10.1007/b98835.

[36] R.W. Preisendorfer, D.M. Curtis, Principal component analysis in meteorology and oceanography, Elsevier, Amsterdam, 1988.

[37] M. Savić, D. Maletić, D. Joković, N. Veselinović, R. Banjanac, V. Udovičić, A. Dragić, Pressure and temperature effect corrections of atmospheric muon data in the belgrade cosmic-ray station, J. Phys. Conf. Ser. 632 (1) (2015) 012059.

Lattice design and expected performance of the Muon Ionization Cooling Experiment demonstration of ionization cooling

M. Bogomilov,[1] R. Tsenov,[1] G. Vankova-Kirilova,[1] Y. Song,[2] J. Tang,[2] Z. Li,[3] R. Bertoni,[4] M. Bonesini,[4] F. Chignoli,[4] R. Mazza,[4] V. Palladino,[5] A. de Bari,[6] G. Cecchet,[6] D. Orestano,[7] L. Tortora,[7] Y. Kuno,[8] S. Ishimoto,[9] F. Filthaut,[10] D. Jokovic,[11] D. Maletic,[11] M. Savic,[11] O. M. Hansen,[12] S. Ramberger,[12] M. Vretenar,[12] R. Asfandiyarov,[13] A. Blondel,[13] F. Drielsma,[13] Y. Karadzhov,[13] G. Charnley,[14] N. Collomb,[14] K. Dumbell,[14] A. Gallagher,[14] A. Grant,[14] S. Griffiths,[14] T. Hartnett,[14] B. Martlew,[14] A. Moss,[14] A. Muir,[14] I. Mullacrane,[14] A. Oates,[14] P. Owens,[14] G. Stokes,[14] P. Warburton,[14] C. White,[14] D. Adams,[15] R. J. Anderson,[15] P. Barclay,[15] V. Bayliss,[15] J. Boehm,[15] T. W. Bradshaw,[15] M. Courthold,[15] V. Francis,[15] L. Fry,[15] T. Hayler,[15] M. Hills,[15] A. Lintern,[15] C. Macwaters,[15] A. Nichols,[15] R. Preece,[15] S. Ricciardi,[15] C. Rogers,[15] T. Stanley,[15] J. Tarrant,[15] M. Tucker,[15] A. Wilson,[15] S. Watson,[16] R. Bayes,[17] J. C. Nugent,[17] F. J. P. Soler,[17] R. Gamet,[18] G. Barber,[19] V. J. Blackmore,[19] D. Colling,[19] A. Dobbs,[19] P. Dornan,[19] C. Hunt,[19] A. Kurup,[19] J.-B. Lagrange,[19,*] K. Long,[19] J. Martyniak,[19] S. Middleton,[19] J. Pasternak,[19] M. A. Uchida,[19] J. H. Cobb,[20] W. Lau,[20] C. N. Booth,[21] P. Hodgson,[21] J. Langlands,[21] E. Overton,[21] M. Robinson,[21] P. J. Smith,[21] S. Wilbur,[21] A. J. Dick,[22] K. Ronald,[22] C. G. Whyte,[22] A. R. Young,[22] S. Boyd,[23] P. Franchini,[23] J. R. Greis,[23] C. Pidcott,[23] I. Taylor,[23] R. B. S. Gardener,[24] P. Kyberd,[24] J. J. Nebrensky,[24] M. Palmer,[25] H. Witte,[25] A. D. Bross,[26] D. Bowring,[26] A. Liu,[26] D. Neuffer,[26] M. Popovic,[26] P. Rubinov,[26] A. DeMello,[27] S. Gourlay,[27] D. Li,[27] S. Prestemon,[27] S. Virostek,[27] B. Freemire,[28] P. Hanlet,[28] D. M. Kaplan,[28] T. A. Mohayai,[28] D. Rajaram,[28] P. Snopok,[28] V. Suezaki,[28] Y. Torun,[28] Y. Onel,[29] L. M. Cremaldi,[30] D. A. Sanders,[30] D. J. Summers,[30] G. G. Hanson,[31] and C. Heidt[31]

(The MICE collaboration)

[1]*Department of Atomic Physics, St. Kliment Ohridski University of Sofia, Sofia 1164, Bulgaria*
[2]*Institute of High Energy Physics, Chinese Academy of Sciences, Beijing 100039, China*
[3]*Sichuan University, Sichuan Sheng 610000, China*
[4]*Sezione INFN Milano Bicocca, Dipartimento di Fisica G. Occhialini, Milano 20126, Italy*
[5]*Sezione INFN Napoli and Dipartimento di Fisica, Università Federico II,
Complesso Universitario di Monte S. Angelo, Napoli 80126, Italy*
[6]*Sezione INFN Pavia and Dipartimento di Fisica, Pavia 27100, Italy*
[7]*INFN Sezione di Roma Tre and Dipartimento di Matematica e Fisica,
Università Roma Tre, 00146 Roma, Italy*
[8]*Osaka University, Graduate School of Science, Department of Physics,
Toyonaka, Osaka 565-0871, Japan*
[9]*High Energy Accelerator Research Organization (KEK), Institute of Particle and Nuclear Studies,
Tsukuba 305-0801, Ibaraki, Japan*
[10]*Nikhef, Amsterdam, The Netherlands and Radboud University, Nijmegen 1098, The Netherlands*
[11]*Institute of Physics, University of Belgrade, Belgrade 11080, Serbia*
[12]*CERN, Geneva 1217, Switzerland*
[13]*DPNC, Section de Physique, Université de Genève, Geneva 1205, Switzerland*
[14]*STFC Daresbury Laboratory, Daresbury, Cheshire WA4 4AD, United Kingdom*
[15]*STFC Rutherford Appleton Laboratory, Harwell Oxford, Didcot OX11 0QX, United Kingdom*
[16]*STFC Rutherford UK Astronomy Technology Centre, Royal Observatory,
Edinburgh, Blackford Hill, Edinburgh EH9 3HJ, United Kingdom*
[17]*School of Physics and Astronomy, Kelvin Building, The University of Glasgow,
Glasgow G12 8SU, United Kingdom*
[18]*Department of Physics, University of Liverpool, Liverpool L69 7ZE, United Kingdom*
[19]*Department of Physics, Blackett Laboratory, Imperial College London,
London SW7 2BB, United Kingdom*
[20]*Department of Physics, University of Oxford, Denys Wilkinson Building,
Oxford OX1 3PJ, United Kingdom*
[21]*Department of Physics and Astronomy, University of Sheffield, Sheffield S10 2TN, United Kingdom*
[22]*SUPA and the Department of Physics, University of Strathclyde, Glasgow G1 1XQ, United Kingdom
and Cockroft Institute, United Kingdom*
[23]*Department of Physics, University of Warwick, Coventry CV4 7AL, United Kingdom*
[24]*Brunel University, Uxbridge UB8 3PH, United Kingdom*
[25]*Brookhaven National Laboratory, New York NY 11967, USA*
[26]*Fermilab, Batavia, Illinois 60510, USA*

[27]*Lawrence Berkeley National Laboratory, Berkeley, California 94720, USA*
[28]*Illinois Institute of Technology, Chicago, Illinois 60616, USA*
[29]*Department of Physics and Astronomy, University of Iowa, Iowa City, Iowa 52242, USA*
[30]*University of Mississippi, Oxford, Mississippi 38677, USA*
[31]*University of California, Riverside, California 92521, USA*

Muon beams of low emittance provide the basis for the intense, well-characterized neutrino beams necessary to elucidate the physics of flavor at a neutrino factory and to provide lepton-antilepton collisions at energies of up to several TeV at a muon collider. The international Muon Ionization Cooling Experiment (MICE) aims to demonstrate ionization cooling, the technique by which it is proposed to reduce the phase-space volume occupied by the muon beam at such facilities. In an ionization-cooling channel, the muon beam passes through a material in which it loses energy. The energy lost is then replaced using rf cavities. The combined effect of energy loss and reacceleration is to reduce the transverse emittance of the beam (transverse cooling). A major revision of the scope of the project was carried out over the summer of 2014. The revised experiment can deliver a demonstration of ionization cooling. The design of the cooling demonstration experiment will be described together with its predicted cooling performance.

I. INTRODUCTION

Stored muon beams have been proposed as the source of neutrinos at a neutrino factory [1,2] and as the means to deliver multi-TeV lepton-antilepton collisions at a muon collider [3,4]. In such facilities the muon beam is produced from the decay of pions generated by a high-power proton beam striking a target. The tertiary muon beam occupies a large volume in phase space. To optimize the muon yield while maintaining a suitably small aperture in the muon-acceleration system requires that the muon beam be "cooled" (i.e., its phase-space volume reduced) prior to acceleration. A muon is short-lived, decaying with a lifetime of 2.2 μs in its rest frame. Therefore, beam manipulation at low energy (≤ 1 GeV) must be carried out rapidly. Four cooling techniques are in use at particle accelerators: synchrotron-radiation cooling [5]; laser cooling [6–8]; stochastic cooling [9]; and electron cooling [10]. Synchrotron-radiation cooling is observed only in electron or positron beams, owing to the relatively low mass of the electron. Laser cooling is limited to certain ions and atomic beams. Stochastic cooling times are dependent on the bandwidth of the stochastic-cooling system relative to the frequency spread of the particle beam. The electron-cooling time is limited by the available electron density and the electron-beam energy and emittance. Typical cooling times are between seconds and hours, long compared with the muon lifetime. Ionization cooling proceeds by passing a muon beam through a material, the absorber, in which it

loses energy through ionization, and subsequently restoring the lost energy in accelerating cavities. Transverse and longitudinal momentum are lost in equal proportions in the absorber, while the cavities restore only the momentum component parallel to the beam axis. The net effect of the energy-loss/reacceleration process is to decrease the ratio of transverse to longitudinal momentum, thereby decreasing the transverse emittance of the beam. In an ionization-cooling channel the cooling time is short enough to allow the muon beam to be cooled efficiently with modest decay losses. Ionization cooling is therefore the technique by which it is proposed to cool muon beams [11–13]. This technique has never been demonstrated experimentally and such a demonstration is essential for the development of future high-brightness muon accelerators.

The international Muon Ionization Cooling Experiment (MICE) collaboration proposes a two-part process to perform a full demonstration of transverse ionization cooling. First, the "Step IV" configuration [14] will be used to study the material and beam properties that determine the performance of an ionization-cooling lattice. Second, a study of transverse-emittance reduction in a cooling cell that includes accelerating cavities will be performed.

The cooling performance of an ionization-cooling cell depends on the emittance and momentum of the initial beam, on the properties of the absorber material and on the transverse betatron function ($\beta_\perp$) at the absorber. These factors will be studied using the Step IV configuration. Once this has been done, "sustainable" ionization cooling must be demonstrated. This requires restoring energy lost by the muons as they pass through the absorber using rf cavities. The experimental configuration with which the MICE collaboration originally proposed to study ionization cooling was presented in [15]. This configuration was revised to accelerate the timetable on which a demonstration of ionization cooling could be delivered and to reduce

*[*]j.lagrange@imperial.ac.uk

cost. This paper describes the revised lattice proposed by the MICE collaboration for the demonstration of ionization cooling and presents its performance.

II. COOLING IN NEUTRINO FACTORIES AND MUON COLLIDERS

At production, muons occupy a large volume of phase space. The emittance of the initial muon beam must be reduced before the beam is accelerated. A neutrino factory [16] requires the transverse emittance to be reduced from 15–20 mm to 2–5 mm. A muon collider [17] requires the muon beam to be cooled in all six phase-space dimensions; to achieve the desired luminosity requires an emittance of ~0.025 mm in the transverse plane and ~70 mm in the longitudinal direction [18,19].

Ionization cooling is achieved by passing a muon beam through a material with low atomic number (Z), in which it loses energy by ionization, and subsequently accelerating the beam. The rate of change of the normalized transverse emittance, $\varepsilon_\perp$, is given approximately by [12,20,21]:

$$\frac{d\varepsilon_\perp}{dz} \simeq -\frac{\varepsilon_\perp}{\beta^2 E_\mu}\left\langle\frac{dE}{dz}\right\rangle + \frac{\beta_\perp(13.6\ \text{MeV}/c)^2}{2\beta^3 E_\mu m_\mu X_0}; \quad (1)$$

where z is the longitudinal coordinate, βc is the muon velocity, E_μ the energy, $\left\langle\frac{dE}{dz}\right\rangle$ the mean rate of energy loss per unit path-length, m_μ the mass of the muon, X_0 the radiation length of the absorber and $\beta_\perp$ the transverse betatron function at the absorber. The first term of this equation describes "cooling" by ionization energy loss and the second describes "heating" by multiple Coulomb scattering. Equation (1) implies that the equilibrium emittance, for which $\frac{d\varepsilon_\perp}{dz} = 0$, and the asymptotic value of $\frac{d\varepsilon_\perp}{dz}$ for large emittance are functions of muon-beam energy.

In order to have good performance in an ionization-cooling channel, $\beta_\perp$ needs to be minimized and $X_0\left\langle\frac{dE}{dz}\right\rangle$

maximised. The betatron function at the absorber is minimized using a suitable magnetic focusing channel (typically solenoidal) [22,23] and $X_0\left\langle\frac{dE}{dz}\right\rangle$ is maximized using a low-Z absorber such as liquid hydrogen (LH_2) or lithium hydride (LiH) [24].

III. THE MUON IONIZATION COOLING EXPERIMENT

The muons for MICE come from the decay of pions produced at an internal target dipping directly into the circulating proton beam in the ISIS synchrotron at the Rutherford Appleton Laboratory (RAL) [25,26]. A beam line of 9 quadrupoles, 2 dipoles and a superconducting "decay solenoid" collects and transports the momentum-selected beam into the experiment [27]. The small fraction of pions that remain in the beam may be rejected during analysis using the time-of-flight hodoscopes and Cherenkov counters that are installed in the beam line upstream of the experiment [28]. A diffuser is installed at the upstream end of the experiment to vary the initial emittance of the beam. Ionization cooling depends on momentum through β, E_μ and $\left\langle\frac{dE}{dz}\right\rangle$ as shown in Eq. (1). It is therefore proposed that the performance of the cell be measured for momenta in the range 140 MeV/c to 240 MeV/c [15].

A. The configuration of the ionization-cooling experiment

The configuration proposed for the demonstration of ionization cooling is shown in Fig. 1. It contains a cooling cell sandwiched between two spectrometer-solenoid modules. The cooling cell is composed of two 201 MHz cavities, one primary (65 mm) and two secondary (32.5 mm) LiH absorbers placed between two superconducting "focus-coil" (FC) modules. Each FC has two separate windings that can be operated either with the same or in opposed polarity.
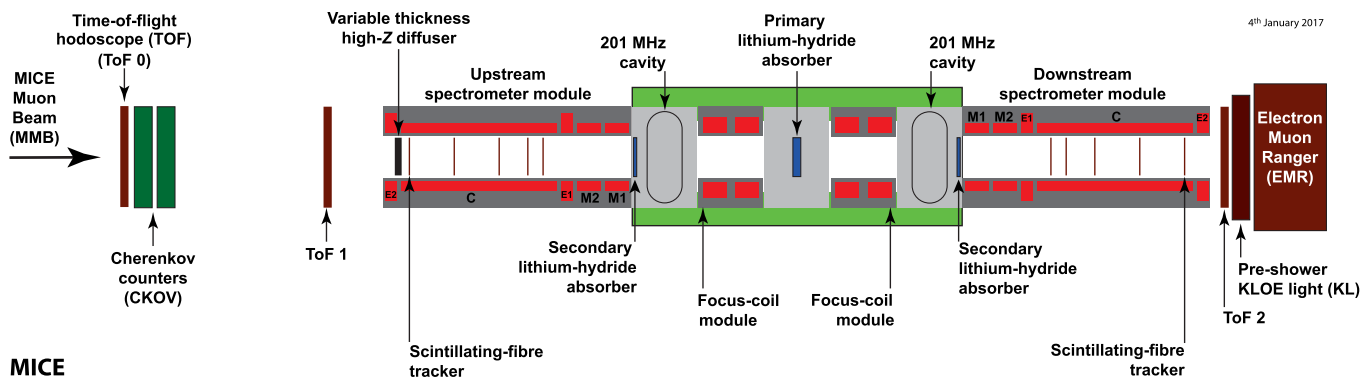
FIG. 1. Layout of the lattice configuration for the cooling demonstration. The red rectangles represent the solenoids. The individual coils in the spectrometer solenoids are labeled E1, C, E2, M1 and M2. The ovals represent the rf cavities and the blue rectangles the absorbers. The various detectors (time-of-flight hodoscopes [29,30], Cerenkov counters [31], scintillating-fibre trackers [32], KLOE Light (KL) calorimeter [27,33], electron muon ranger [34]) used to characterize the beam are also represented. The green-shaded box indicates the cooling cell.

The emittance is measured upstream and downstream of the cooling cell using scintillating-fiber tracking detectors [32] immersed in the uniform 4 T magnetic field provided by three superconducting coils (E1, C, E2). The trackers are used to reconstruct the trajectories of individual muons at the entrance and exit of the cooling cell. The reconstructed tracks are combined with information from instrumentation upstream and downstream of the spectrometer modules to measure the muon-beam emittance at the upstream and downstream tracker reference planes. The instrumentation upstream and downstream of the spectrometer modules serves to select a pure sample of muons. Time-of-flight hodoscopes are used to determine the time at which the muon crosses the rf cavities. The spectrometer-solenoid magnets also contain two superconducting "matching" coils (M1, M2) that are used to match the optics between the uniform field region and the neighboring FC.

The secondary LiH absorbers (SAs) are introduced between the cavities and the trackers to minimize the exposure of the trackers to "dark-current" electrons originating from the rf cavities. Experiments at the MuCool Test Area (MTA) at Fermilab [35] have observed that the rate of direct x-ray production from the rf cavities can be managed to ensure it does not damage the trackers [36]. The SAs are introduced to minimize the exposure of the trackers to energetic dark-current electrons that could produce background hits. The SAs are positioned between the trackers and the cavities such that they can be removed to study the empty channel. The SAs increase the net transverse-cooling effect since the betatron functions at these locations are small.

Retractable lead radiation shutters will be installed on rails between the spectrometer solenoids and the rf modules to protect the trackers against dark-current induced radiation during cavity conditioning. The SAs will be mounted on a rail system similar to that which will be used for the lead shutters and will be located between the cavities and the lead shutters. Both mechanisms will be moved using linear piezo-electric motors that operate in vacuum and magnetic field. The design of both the radiation shutter and the movable SA inside the vacuum chamber is shown in Fig. 2.

The rf cavities are 201 MHz "pillbox" resonators, 430 mm in length, operating in the TM_{010} mode with large diameter apertures to accommodate the high emittance beam. The apertures are covered by thin (0.38 mm) beryllium windows to define the limits for the accelerating rf fields whilst minimizing the scattering of muons. The cavity is excited by two magnetic-loop couplers on opposite sides of the cavity. At the particle rate expected in MICE there is no beam-loading of the rf fields. An effective peak field of 10.3 MV/m is expected for a drive power of 1.6 MW to each cavity. This estimate was used to define the gradient in the simulations described below.

The original configuration of the MICE cooling cell described in [15] was composed of three focus-coil modules, each of which housed a liquid-hydrogen absorber, and two,
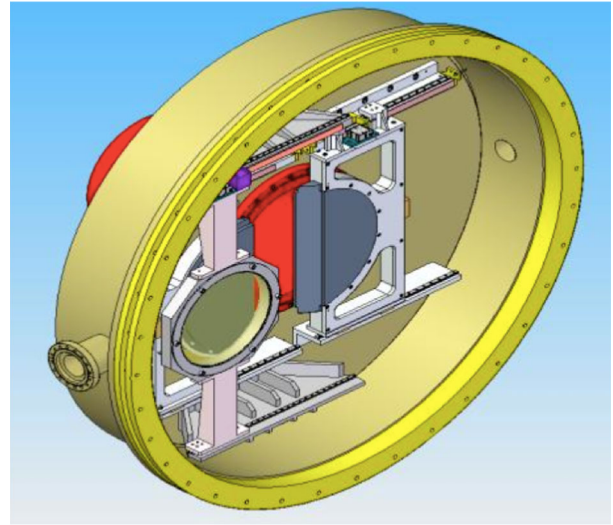

FIG. 2.   Design of the movable frame for the secondary absorber (front) and the lead radiation shutter (back). The half discs of the lead shutter (grey) can be seen together with the rails (white) inside the vacuum chamber (yellow).

four-cavity, linac modules. Each linac module incorporated a large, superconducting "coupling coil" to transport the beam. The configuration described in this paper was developed to simplify the lattice described in [15] such that the coupling coils are not required and acceleration is provided by two single-cavity modules. The revision of the magnetic lattice substantially reduces the technical risks associated with the implementation of the experiment since all of the superconducting solenoids required to transport and focus the beam have been commissioned on the beam line. Further, by reducing the number of cavities from eight to two and reconfiguring the rf-power-distribution system the cost of implementing the experiment has been reduced and the timetable on which the experiment can be mounted has been advanced. The present configuration was optimized to maximize its cooling performance as described in Sec. IV. The performance of the optimized lattice, though reduced compared to that described in [15], is sufficient for the principle of ionization-cooling to be demonstrated (see Sec. VI).

IV. LATTICE DESIGN

A. Design parameters

The lattice has been optimized to maximize the reduction in transverse emittance. The optimum is obtained by matching the betatron function to a small value in the central absorber while minimizing its maximum values in the FC modules; limiting the size of the betatron function in the FCs helps to reduce the influence of nonlinear terms in the magnetic-field expansion. The matching accounts for the change in energy of the muons as they pass through the cooling cell by adjusting currents in the upstream and

downstream FCs and in the matching coils in the spectrometer solenoids independently while maintaining the field in the tracking volumes at 4 T. In this configuration, it is also possible to keep the betatron function relatively small at the position of the secondary absorbers whilst maintaining an acceptable beam size at the position of the cavities.

Chromatic aberrations caused by the large momentum spread of the beam (∼5% rms) lead to a chromatic mismatch of the beam in the downstream solenoid unless the phase advance across the cooling cell (i.e., the rate of rotation of the phase-space ellipse) is chosen appropriately. The phase advance of the cell is obtained by integrating the inverse of the beta-function along the beam axis from the reference plane in the upstream spectrometer-solenoid to the reference plane in the downstream spectrometer-solenoid. Such a mismatch reduces the effective transverse-emittance reduction through the chromatic decoherence that results from the superposition of beam evolutions for the different betatron frequencies that result from the range of momenta in the beam. For beams with a large input emittance, spherical aberrations may lead to phase-space filamentation. The chromatic and spherical aberrations were studied by tracking samples of muons through the lattice using the "MICE Analysis User Software" (MAUS, see Sec. V). The betatron-function and emittance evolution of a 200 MeV/c beam with the
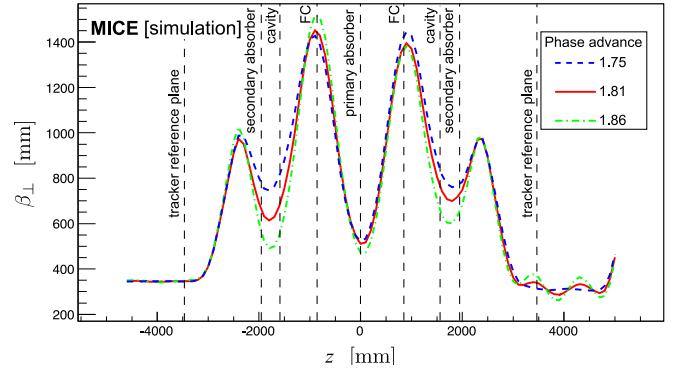

FIG. 3. Transverse 4D beta-function versus longitudinal coordinate z in the cooling-demonstration lattice for 200 MeV/c settings with a phase advance of $2\pi \times 1.75$ (dashed blue line), $2\pi \times 1.81$ (solid red line) and $2\pi \times 1.86$ (dot-dashed green line). The vertical dashed lines with labels show the positions of the tracker reference planes and the centers of the absorbers, rf cavities, and focus coil modules.

initial parameters given in Table I are shown, for different phase advances, in Figs. 3 and 4, respectively. The phase advance of $2\pi \times 1.81$ showed the largest transverse-emittance reduction and was therefore chosen. The lattice parameters for this phase advance are presented in Table II.

The currents that produce the optimum magnetic lattice were obtained using the procedure described above for three momentum settings: 140 MeV/c, 200 MeV/c, and 240 MeV/c. The magnetic field on axis for each of these settings is shown in Fig. 5. The fields in the downstream FC and spectrometer are opposite to those in the upstream FC and spectrometer, the field changing sign at the primary absorber. Such a field flip is required in an ionization cooling channel to reduce the build-up of canonical angular momentum [37]. The currents required to produce the magnetic fields shown in Fig. 5 are listed in Table III. All currents are within the proven limits of operation for the

TABLE I. General parameters of the initial beam conditions used in the simulations.

Parameter	Value
Particle	muon μ^+
Number of particles	10000
Longitudinal position [mm]	−4612.1
Central energy (140 MeV/c settings) [MeV]	175.4
Central energy (200 MeV/c settings) [MeV]	228.0
Central energy (240 MeV/c settings) [MeV]	262.2
Transverse Gaussian distribution:	
$\alpha_\perp$	0
$\beta_\perp$ (140 MeV/c settings) [mm]	233.5
$\varepsilon_\perp$ (140 MeV/c settings) [mm]	4.2
$\beta_\perp$ (200 MeV/c settings) [mm]	339.0
$\varepsilon_\perp$ (200 MeV/c settings) [mm]	6.0
$\beta_\perp$ (240 MeV/c settings) [mm]	400.3
$\varepsilon_\perp$ (240 MeV/c settings) [mm]	7.2
Longitudinal Gaussian distribution:	
Longitudinal emittance [mm]	20
Longitudinal β [ns]	11
Longitudinal α	−0.7
rms momentum spread (140 MeV/c settings)	4.8%
rms time spread (140 MeV/c settings) [ns]	0.40
rms momentum spread (200 MeV/c settings)	4.0%
rms time spread (200 MeV/c settings) [ns]	0.34
rms momentum spread (240 MeV/c settings)	3.6%
rms time spread (240 MeV/c settings) [ns]	0.31

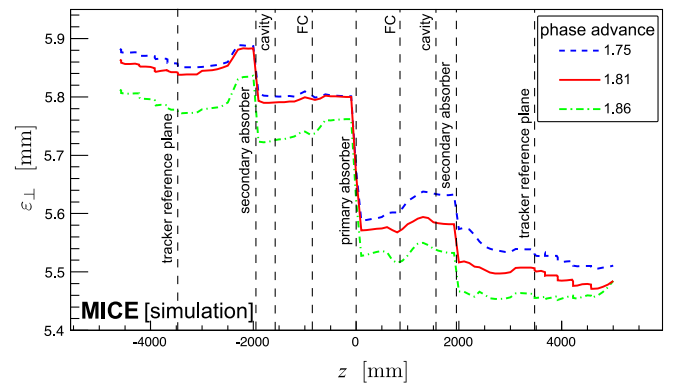FIG. 4. 4D emittance evolution in the cooling-demonstration lattice for 200 MeV/c settings with a phase advance of $2\pi \times 1.75$ (dashed blue line), $2\pi \times 1.81$ (solid red line) and $2\pi \times 1.86$ (dot-dashed green line). The vertical dashed lines with labels show the positions of the tracker reference planes and the centers of the absorbers, rf cavities, and focus coil modules.

TABLE II. Parameters of the cooling-demonstration lattice. $L_{SS \to FC}$ is the distance between the center of the spectrometer solenoid and the center of the neighboring FC, $L_{FC \to FC}$ the distance between the centers of the FCs, and $L_{RF \, module \to FC}$ the distance between the rf module and the neighboring FC.

Parameter	Value
Length $L_{SS \to FC}$ [mm]	2607.5
Length $L_{FC \to FC}$ [mm]	1678.8
Length $L_{rf \, module \to FC}$ [mm]	784.0
rf Gradient [MV/m]	10.3
Number of rf cavities	2
Number of primary absorbers	1
Number of secondary absorbers	2

individual coil windings. The magnetic forces acting on the coils have been analyzed and were found to be acceptable. Configurations in which there is no field flip can also be considered.

Figure 6 shows matched betatron functions versus longitudinal position for beams of different initial momentum. These betatron functions are constrained, within the fiducial-volume of the trackers, by the requirements on the Courant-Snyder parameters $\alpha_\perp = 0$ and $\beta_\perp = \frac{2 p_z}{e B_z}$ (where p_z is the mean longitudinal momentum of the beam, e the elementary charge and B_z the longitudinal component of the magnetic field). A small betatron-function "waist" in the central absorber is achieved. Betatron-function values at relevant positions in the different configurations are summarized in Table IV.

V. SIMULATION

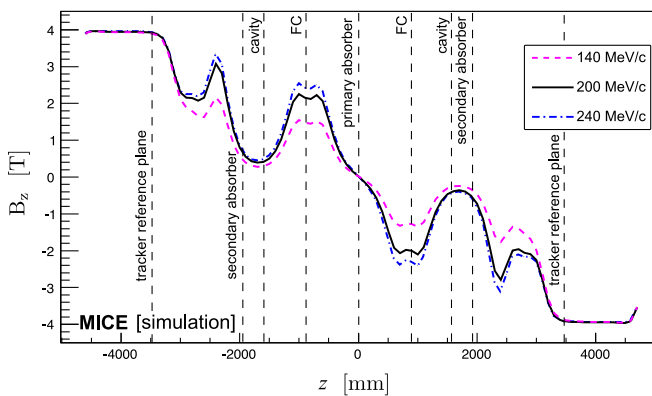Simulations to evaluate the performance of the lattice have been performed using the official MICE simulation

TABLE III. Coil currents used for 140 MeV/c, 200 MeV/c, and 240 MeV/c lattice settings.

Coil	140 MeV/c Lattice [A]	200 MeV/c Lattice [A]	240 MeV/c Lattice [A]
Upstream E2	+253.00	+253.00	+253.00
Upstream C	+274.00	+274.00	+274.00
Upstream E1	+234.00	+234.00	+234.00
Upstream M2	+126.48	+155.37	+163.50
Upstream M1	+175.89	+258.42	+280.72
Upstream FC-coil 1	+54.14	+79.35	+89.77
Upstream FC-coil 2	+54.14	+79.35	+89.77
Downstream FC-coil 1	−47.32	−74.10	−85.35
Downstream FC-coil 2	−47.32	−74.10	−85.35
Downstream M1	−140.43	−231.60	−261.71
Downstream M2	−100.12	−149.15	−159.21
Downstream E1	−234.00	−234.00	−234.00
Downstream C	−274.00	−274.00	−274.00
Downstream E2	−253.00	−253.00	−253.00

and reconstruction software MAUS (MICE Analysis User Software) [38]. In addition to simulation, MAUS also provides a framework for data analysis. MAUS is used for offline analysis and to provide fast real-time detector reconstruction and data visualisation during MICE running. MAUS uses GEANT4 [39,40] for beam propagation and the simulation of detector response. ROOT [41] is used for data visualisation and for data storage.

Particle tracking has been performed for several configurations. The parameters of the initial beam configurations used for the simulations are summarized in Table I.

FIG. 5. Magnetic field B_z on-axis versus the longitudinal coordinate z for the cooling-demonstration lattice design for 200 MeV/c (solid black line), 140 MeV/c (dashed purple line), and 240 MeV/c (dot-dashed blue line) settings. The vertical dashed lines with labels show the positions of the tracker reference planes and the centres of the absorbers, rf cavities, and focus coil modules.
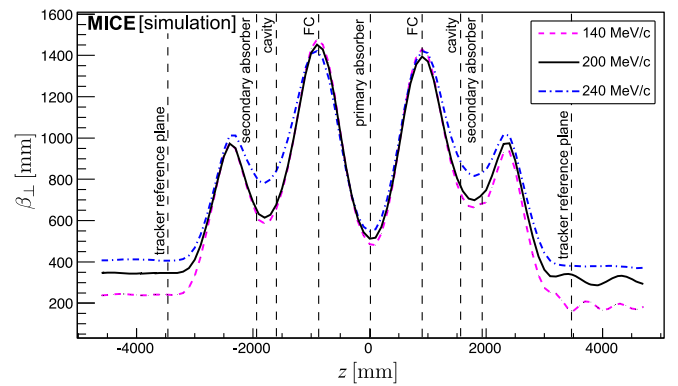

FIG. 6. $\beta_\perp$ versus the longitudinal coordinate z for 200 MeV/c (solid black line), 140 MeV/c (dashed purple line) and 240 MeV/c (dot-dashed blue line) in the cooling-demonstration lattice. The vertical dashed lines with labels show the positions of the tracker reference planes and the centers of the absorbers, rf cavities, and focus coil modules.

TABLE IV.   Beta-function values at relevant positions for an initial beam at 140 MeV/c, 200 MeV/c, and 240 MeV/c in the cooling-demonstration lattice design.

Parameter	Value for 140 MeV/c	Value for 200 MeV/c	Value for 240 MeV/c
$\beta_\perp$ at primary absorber [mm]	480	512	545
$\beta_\perp$ at upstream secondary absorber [mm]	660	710	840
$\beta_\perp$ at downstream secondary absorber [mm]	680	740	850
$\beta_{\perp\,max}$ at FC [mm]	1480	1450	1430

The simulation of the beam starts at a point between the diffuser and the first plane of the tracker. The beam is generated by a randomizing algorithm with a fixed seed. The number of particles launched for each simulation is a compromise between the statistical uncertainty required ($\approx 1\%$) and computing time. Each cavity is simulated by a TM_{010} ideal cylindrical pillbox with a peak effective gradient matched to that expected for the real cavities. The reference particle is used to set the phase of the cavities so that it is accelerated "on crest." The initial distributions defined in Table I are centred on the reference particle in both time and momentum. Table V lists the acceptance criteria applied to all analyses presented here. Trajectories that fail to meet the acceptance criteria are removed from the analysis.

The normalized transverse emittance is calculated by taking the fourth root of the determinant of the four-dimensional phase-space covariance matrix [20,21]. The MICE collaboration plans to take data such that the statistical uncertainty on the relative change in emittance for a particular setting is 1%. The MICE instrumentation was designed such that the systematic uncertainty related to the reconstruction of particle trajectories would contribute at the $\sim 0.3\%$ level to the overall systematic uncertainty [15]; such uncertainties would thus be negligible.

VI. PERFORMANCE

Figure 7 shows the evolution of the mean energy of a muon beam as it traverses the lattice. Beams with initial normalised transverse emittance $\varepsilon_\perp = 4.2$ mm,

TABLE V.   Acceptance criteria for analysis.

Parameter	Acceptance condition
Particle	muon μ^+
Transmission: pass through two planes	$z = -4600$ mm and $z = 5000$ mm
Radius at $z = -4600$ mm	≤ 150.0 mm
Radius at $z = 5000$ mm	≤ 150.0 mm

$\varepsilon_\perp = 6$ mm, and $\varepsilon_\perp = 7.2$ mm for initial muon beam momenta of 140 MeV/c, 200 MeV/c, and 240 MeV/c respectively are shown. The initial normalized transverse emittance is chosen such that the geometrical emittance of the three beams is the same. A 200 MeV/c muon passing through two 32.5 mm thick secondary LiH absorbers and one 65 mm thick primary LiH absorber loses an energy of 18.9 MeV. Including losses in the scintillating-fiber
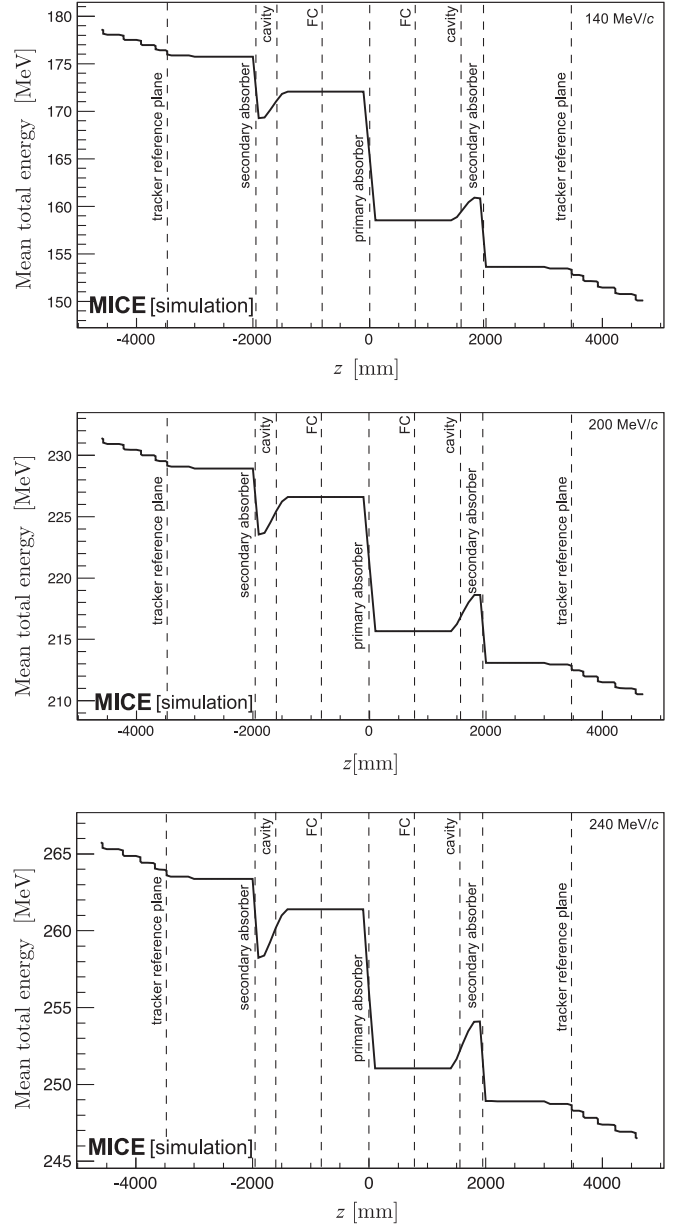
FIG. 7.   Mean energy of the beam versus longitudinal coordinate (z) in the cooling-demonstration lattice. Top: the 140 MeV/c configuration for initial emittance $\varepsilon_\perp = 4.2$ mm. Middle: the 200 MeV/c configuration for initial emittance $\varepsilon_\perp = 6$ mm. Bottom: the 240 MeV/c configuration for initial emittance $\varepsilon_\perp = 7.2$ mm. The vertical dashed lines with labels show the positions of the tracker reference planes, and the centers of the absorbers, rf cavities, and focus coil modules.

trackers and windows, this increases to 24.3 MeV. The accelerating gradient that can be achieved in each of the two cavities is constrained by the available rf power and is insufficient to replace all the lost energy. Therefore, a comparison of beam energy with and without acceleration is required. With acceleration an energy

deficit of $\langle \Delta E \rangle = 19$ MeV will be observed. This measurable difference will be used to extrapolate the measured cooling effect to that which would pertain if all the lost energy were restored.

The evolution of normalized transverse emittance across the lattice is shown in Fig. 8. The beam is subject to nonlinear effects in regions of high $\beta_\perp$, which cause the normalized transverse emittance to grow, especially in the 140 MeV/c configuration. This phenomenon can be seen in three different regions of the lattice: a moderate increase in emittance is observed at $z \approx -2500$ mm and $z \approx 1000$ mm while a larger increase is observed at $z \approx 3000$ mm. The nonlinear effects are mainly chromatic in origin, since they are greatly lessened when the initial momentum spread is reduced. This is illustrated for the 140 MeV/c case for which the evolution of normalized emittance for beams with an rms momentum spread of 6.7 MeV/c and 2.5 MeV/c are shown. Nonetheless, in all cases a reduction in emittance is observed between the upstream and downstream trackers ($z = \pm 3473$ mm). The lattice is predicted to achieve an emittance reduction between the tracker reference planes of $\approx 8.1\%$, $\approx 5.8\%$ and $\approx 4.0\%$ in the 140 MeV/c, 200 MeV/c, and 240 MeV/c cases, respectively. A reduction as large as $\approx 10\%$ can be reached in the 140 MeV/c configuration with an rms momentum spread of 1.4%.

The transmission of the cooling-demonstration lattice for beams of mean momentum 140 MeV/c, 200 MeV/c, and 240 MeV/c is shown in Fig. 9. Transmission is computed as the ratio of the number of particles that satisfy the acceptance criteria observed downstream of the cooling cell divided by the number that enter the cell. This accounts
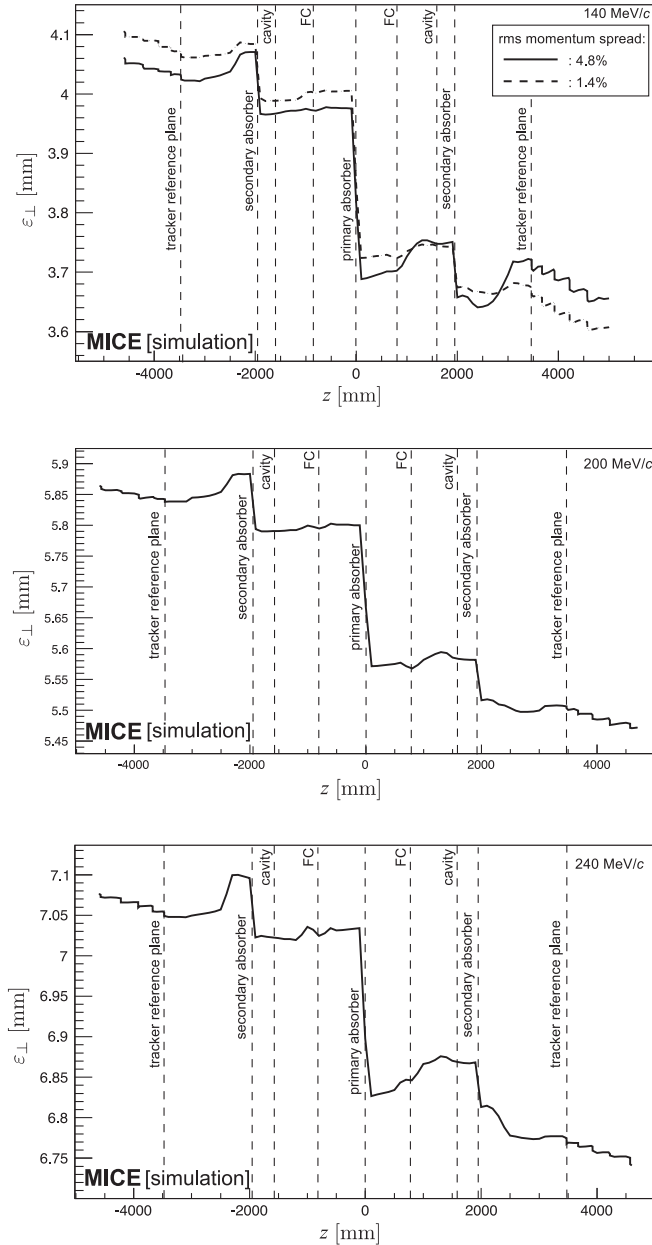
FIG. 8. Emittance variation versus the longitudinal coordinate (z) for the cooling-demonstration lattice design. Top: 140 MeV/c beam with initial $\varepsilon_\perp = 4.2$ mm with an rms momentum spread of 6.7 MeV/c (rms spread 4.8%, solid line) and 2.5 MeV/c (rms spread 1.8%, dashed line). Middle: 200 MeV/c beam with initial $\varepsilon_\perp = 6$ mm (rms spread 4.0%). Bottom: 240 MeV/c beam with initial $\varepsilon_\perp = 7.2$ mm (rms spread 3.6%). The vertical dashed lines with labels show the positions of the tracker reference planes, and the centers of the absorbers, rf cavities, and focus coil modules.
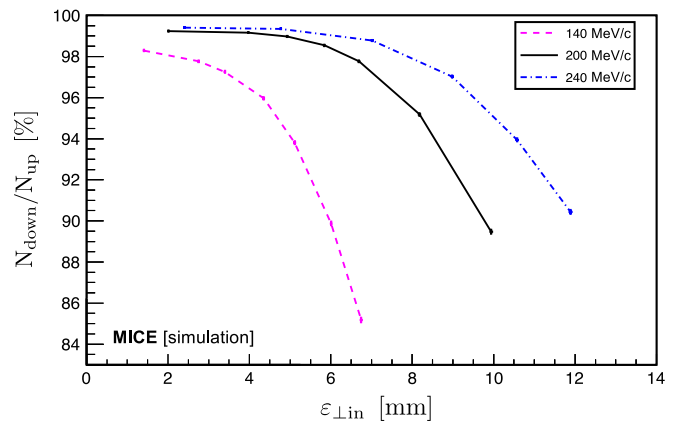
FIG. 9. Transmission (defined as the ratio of good muons observed downstream of the cooling cell, N_{down}, to those observed upstream, N_{up}) in percent versus initial emittance ($\varepsilon_{\perp\text{in}}$) for the cooling-demonstration lattice. The transmission of the 140 MeV/c, 200 MeV/c, and 240 MeV/c lattices are shown as the purple-dashed, solid black, and dot-dashed blue lines respectively. The error bars indicate the statistical precision that would be achieved using a sample of 100,000 muons.

for decay losses and implies that, in the absence of scraping or acceptance losses, the maximum transmission for beams of mean momentum 140 MeV/c, 200 MeV/c, and 240 MeV/c is 98.9%, 99.2%, and 99.5%, respectively. The lattice delivers transmission close to the maximum for 200 MeV/c and 240 MeV/c beams with input emittance below ≈ 5 mm and ≈ 7 mm, respectively. For beams of larger input emittance, the transmission gradually decreases with increasing initial emittance due to the scraping of high amplitude muons. The beam is subject to chromatic effects in regions of high $\beta_\perp$, which causes nonlinear emittance growth and limits the transmission. The behavior of the transmission for the various beam energies results from the different geometrical emittance values of the beam for the same initial normalised emittance and the energy dependence of the energy loss and scattering in the material through which the beam passes.

The fractional change in normalized transverse emittance with respect to the input emittance for beams of mean momentum 140 MeV/c, 200 MeV/c, and 240 MeV/c is shown in Fig. 10. The different values of the equilibrium emittance and the asymptote at large emittance for each momentum are clearly visible in Fig. 10. A maximum cooling effect of 15%, 8%, and 6% can be observed for beams with 140 MeV/c, 200 MeV/c, and 240 MeV/c, respectively.

The performance of the configuration proposed here is comparable to that described in [15]. In the "Step V" configuration, that incorporated two liquid-hydrogen absorbers each placed within a focus-coil module capable of providing a value $\beta_\perp$ smaller than that which can be achieved with the present lattice, the maximum cooling effect with an input momentum and emittance of 200 MeV/c and 10 mm respectively, was $\sim 10\%$. Figures 9 and 10 show the statistical uncertainties that will result from the reconstruction of a sample of 100,000 muons [42] with the configuration proposed in this paper. The instrumentation was specified to ensure that no single source of systematic uncertainty would contribute more than one third of the statistical uncertainty on the fractional change in emittance [15]. All of the instrumentation has been commissioned on the beam-line and performs to specification. The emittance-change evolution presented in Fig. 10 can therefore be measured with high significance.

VII. CONCLUSION

An experiment by which to demonstrate ionization cooling has been described that is predicted by simulations to exhibit cooling over a range of momentum. The demonstration is performed using lithium-hydride absorbers and with acceleration provided by two 201 MHz cavities. The equipment necessary to mount the experiment is either in hand (the superconducting magnets and instrumentation), or at an advanced stage of preparation. The configuration of the demonstration of ionization cooling has been shown to deliver the performance required for the detailed study of the ionization-cooling technique.

The demonstration of ionization cooling is essential to the future development of muon-based facilities that would provide the intense, well characterized low-emittance muon beams required to elucidate the physics of flavor at a neutrino factory or to deliver multi-TeV lepton-antilepton collisions at a muon collider. The successful completion of the MICE programme would therefore herald the establishment of a new technique for particle physics.

FIG. 10. Fractional change in emittance versus initial emittance ($\varepsilon_{\perp \text{in}}$) for the cooling-demonstration lattice design measured at the tracker reference planes. The fractional change in emittance of the 140 MeV/c, 200 MeV/c, and 240 MeV/c lattices are shown as the purple-dashed, solid black, and dot-dashed blue lines, respectively. The error bars indicate the statistical precision that would be achieved using a sample of 100,000 muons.

[1] S. Geer, Neutrino beams from muon storage rings: Characteristics and physics potential, Phys. Rev. D **57**, 6989 (1998).

[2] M. Apollonio *et al.*, Oscillation Physics with a Neutrino Factory, arXiv:hep-ph/0210192.

[3] D. V. Neuffer and R. B. Palmer, A high-energy high-luminosity μ^+-μ^- collider in *Proceedings of the Fourth European Particle Accelerator Conference EPAC 94, London, England* (World Scientific, River Edge, NJ, 1994), p. 52.

[4] R. B. Palmer, Muon colliders, Rev. Accel. Sci. Techol. **07**, 137 (2014).

[5] S. Y. Lee, *Accelerator Physics*, 3rd ed., edited by S. Y. Lee (World Scientific, Singapore, 2012).

[6] S. Schröder *et al.*, First laser cooling of relativistic ions in a storage ring, Phys. Rev. Lett. **64**, 2901 (1990).

[7] J. S. Hangst, M. Kristensen, J. S. Nielsen, O. Poulsen, J. P. Schiffer, and P. Shi, Laser cooling of a stored ion beam to 1 mK, Phys. Rev. Lett. **67**, 1238 (1991).

[8] P. J. Channell, Laser cooling of heavy ion beams, J. Appl. Phys. **52**, 3791 (1981).

[9] J. Marriner, Stochastic cooling overview, Nucl. Instrum. Methods Phys. Res., Sect. A **532**, 11 (2004).

[10] V. V. Parkhomchuk and A. N. Skrinsky, Electron cooling: 35 years of development, Phys. Usp. **43**, 433 (2000).

[11] A. N. Skrinsky and V. V. Parkhomchuk, Cooling methods for beams of charged particles, Fiz. Elem. Chastits At. Yadra **12**, 557 (1981) [Sov. J. Part. Nucl. **12**, 223 (1981)].

[12] D. Neuffer, Principles and applications of muon cooling, in *Proceedings, 12th International Conference on High-Energy Accelerators, HEACC 1983: Fermilab, Batavia, 1983*, Vol. C830811 (Fermi National Accelerator Laboratory, Batavia, 1983), p. 481–484.

[13] D. Neuffer, Principles and applications of muon cooling, Part. Accel. **14**, 75 (1983).

[14] D. Rajaram and V. C. Palladino, The status of MICE Step IV, in *Proceedings, 6th International Particle Accelerator Conference (IPAC 2015): Richmond, Virginia, USA, 2015* (JACoW, Geneva, 2015), p. 4000.

[15] MICE Collaboration, MICE: An International Muon Ionization Cooling Experiment, http://mice.iit.edu/micenotes/public/pdf/MICE0021/MICE0021.pdf (2003), MICE Note 21.

[16] M. Apollonio *et al.* (ISS Accelerator Working Group Collaboration), Accelerator design concept for future neutrino facilities, J. Instrum. **4**, P07001 (2009).

[17] C. M. Ankenbrandt *et al.*, Status of muon collider research and development and future plans, Phys. Rev. ST Accel. Beams **2**, 081001 (1999).

[18] M. M. Alsharoa *et al.* (Neutrino Factory and Muon Collider Collaboration), Recent progress in neutrino factory and muon collider research within the Muon collaboration, Phys. Rev. ST Accel. Beams **6**, 081001 (2003).

[19] R. B. Palmer, J. S. Berg, R. C. Fernow, J. C. Gallardo, H. G. Kirk, Y. Alexahin, D. Neuffer, S. A. Kahn, and D. Summers, A complete scheme of ionization cooling for a muon collider, in *Proceedings of the 22nd Particle Accelerator Conference, PAC-2007, Albuquerque, NM* (IEEE, New York, 2007), p. 3193.

[20] G. Penn and J. S. Wurtele, Beam Envelope Equations for Cooling of Muons in Solenoid Fields, Phys. Rev. Lett. **85**, 764 (2000).

[21] C. Rogers, Ph.D. dissertation, Imperial College of London, 2008.

[22] D. Stratakis and R. B. Palmer, Rectilinear six-dimensional ionization cooling channel for a muon collider: A theoretical and numerical study, Phys. Rev. ST Accel. Beams **18**, 031003 (2015).

[23] D. Neuffer, H. Sayed, T. Hart, and D. Summers, Final Cooling for a High-Energy High-Luminosity Lepton Collider, arXiv:1612.08960.

[24] A. V. Tollestrup and J. Monroe, Fermi National Accelerator Laboratory Technical Report No. FERMILAB-MUCOOL-176, 2000.

[25] C. N. Booth *et al.*, The design, construction and performance of the MICE target, J. Instrum. **8**, P03006 (2013).

[26] C. N. Booth *et al.*, The design and performance of an improved target for MICE, J. Instrum. **11**, P05006 (2016).

[27] M. Bogomilov *et al.* (MICE Collaboration), The MICE Muon Beam on ISIS and the beam-line instrumentation of the Muon Ionization Cooling Experiment, J. Instrum. **7**, P05009 (2012).

[28] D. Adams *et al.* (MICE Collaboration), Characterisation of the muon beams for the Muon Ionisation Cooling Experiment, Eur. Phys. J. C **73**, 2582 (2013).

[29] R. Bertoni *et al.*, The design and commissioning of the MICE upstream time-of-flight system, Nucl. Instrum. Methods Phys. Res., Sect. A **615**, 14 (2010).

[30] R. Bertoni, M. Bonesini, A. de Bari, G. Cecchet, Y. Karadzhov, and R. Mazza, The construction of the MICE TOF2 detector, http://mice.iit.edu/micenotes/public/pdf/MICE0286/MICE0286.pdf (2010).

[31] L. Cremaldi, D. A. Sanders, P. Sonnek, D. J. Summers, and J. Reidy, Jr., A Cherenkov radiation detector with high density aerogels, IEEE Trans. Nucl. Sci. **56**, 1475 (2009).

[32] M. Ellis *et al.*, The design, construction and performance of the MICE scintillating fibre trackers, Nucl. Instrum. Methods Phys. Res., Sect. A **659**, 136 (2011).

[33] F. Ambrosino *et al.*, Calibration and performances of the KLOE calorimeter, Nucl. Instrum. Methods Phys. Res., Sect. A **598**, 239 (2009).

[34] R. Asfandiyarov *et al.*, The design and construction of the MICE Electron-Muon Ranger, J. Instrum. **11**, T10007 (2016).

[35] M. Leonova *et al.*, MICE cavity installation and commissioning/operation at MTA, in *Proceedings, 6th International Particle Accelerator Conference (IPAC 2015): Richmond, Virginia, USA, 2015* (JACoW, Geneva, 2015), p. 3342–3344.

[36] Y. Torun *et al.*, Final commissioning of the MICE RF module prototype with production couplers, in *Proceedings, 7th International Particle Accelerator Conference (IPAC 2016): Busan, Korea, 2016* (JACoW, Geneva, 2016), p. 474.

[37] R. C. Fernow and R. B. Palmer, Solenoidal ionization cooling lattices, Phys. Rev. ST Accel. Beams **10**, 064001 (2007).

[38] C. D. Tunnell and C. T. Rogers, MAUS: MICE Analysis User Software, in *Proceedings of the 2nd International Particle Accelerator Conference, San Sebastián, Spain* (EPS-AG, Spain, 2011), p. 850.

[39] S. Agostinelli *et al.* (GEANT4 Collaboration), GEANT4: A simulation toolkit, Nucl. Instrum. Methods Phys. Res., Sect. A **506**, 250 (2003).

[40] J. Allison *et al.*, Geant4 developments and applications, IEEE Trans. Nucl. Sci. **53**, 270 (2006).

[41] R. Brun and F. Rademakers, ROOT: An object oriented data analysis framework, Nucl. Instrum. Methods Phys. Res., Sect. A **389**, 81 (1997).

[42] C. Hunt, Ph.D. dissertation, Imperial College of London, 2017.

CrossMark

ORIGINAL PAPER

Forecasting hourly particulate matter concentrations based on the advanced multivariate methods

M. Perišić[1] · D. Maletić[1] · S. S. Stojić[2] · S. Rajšić[1] · A. Stojić[1]

Abstract In this study, several multivariate methods were used for forecasting hourly PM_{10} concentrations at four locations based on SO_2 and meteorological data from the previous period. According to the results, boosted decision trees and multi-layer perceptrons yielded the best predictions. The forecasting performances were similar for all examined locations, despite the additional PM_{10} spatio-temporal analysis showed that the sites were affected by different emission sources, topographic and microclimatic conditions. The best prediction of PM_{10} concentrations was obtained for industrial sites, probably due to the simplicity and regularity of dominant pollutant emissions on a daily basis. Conversely, somewhat weaker forecast accuracy was achieved at urban canyon avenue, which can be attributed to the specific urban morphology and most diverse emission sources. In conclusion to this, the integration of advanced multivariate methods in air quality forecasting systems could enhance accuracy and provide the basis for efficient decision-making in environmental regulatory management.

Introduction

Over the last century, changes in emission sources, methane concentrations and climate have affected atmospheric composition and led to the significant increase in the levels of particulate matter (PM) and gaseous pollutants, particularly in developing countries (Fang et al. 2013). According to recent estimates, about 3.5 million cardiopulmonary deaths annually and globally can be attributed to exposure to anthropogenic $PM_{2.5}$, and the projections are that this number could double by 2050 (Lelieveld et al. 2015). In addition to stringent abatement measures, the accurate and reliable prediction of air pollutant episodes and establishment of an early public warning system is of vital importance for the increase in life expectancy and reduction of health care expenditures.

Despite the fact that significant progress has been made through integration of different scientific approaches, modeling of air pollution data remains a challenge, due to complexity and non-linear nature of atmospheric phenomena and processes (Pai et al. 2013). The variety of techniques and tools described in the literature for air quality forecasting covers simple empirical approaches, statistical approaches including artificial neural networks and fuzzy logic methods, and physically-based approaches including deterministic methods and ensemble and probabilistic methods (Zhang et al. 2012). The deterministic approach mostly refers to meteorological and chemical transport models, such as sophisticated Community Air Quality Modelling System (CMAQ) for prediction of air quality index at locations with no real-time measurements.

✉ M. Perišić
   mirjana.perisic@ipb.ac.rs

1 Institute of Physics Belgrade, University of Belgrade, Pregrevica 118, 11080 Belgrade, Serbia

2 Singidunum University, Danijelova 32, 11010 Belgrade, Serbia

🕊 Springer

The chemical transport models were first used in Germany for air quality forecasting purposes, and soon many other developed countries became aware of the benefits of such implementation and launched the centralized air quality forecasting systems based on different tools, from simple empirical to online-coupled meteorology and chemistry models. While deterministic models don't require a large quantity of observational data, they do demand sufficient knowledge and understanding of pollutant emission sources, transport and atmospheric reactions and transformations under the planetary boundary layer (Feng et al. 2015). Since crucial knowledge in this area is often limited and some processes are too complex to be presented within a model, deterministic models are computationally expensive and time-consuming for routine predictions and often employ approximations and simplifications that lead to strong biases and inaccuracy, thus making the forecasts useless for timely management of critical situations (Cobourn 2010; Russo and Soares 2014).

Over the last decade, the parametric or non-parametric statistical approaches have been proposed as a more economical alternative for discovering the underlying site-specific dependencies between pollutant concentrations and potential predictors (Feng et al. 2015). The most commonly examined were artificial neural networks, based on artificial neurons or nodes capable of learning relationships between the routinely-measured pollutant data and selected predictors through embedded functions and data from the previous period (Fernando et al. 2012). Unlike deterministic models, artificial neural networks provide more accurate air quality forecasts, whereas their major disadvantages are associated with "black box" nature and poor generalization performance (Moustris et al. 2013). Furthermore, both statistical and deterministic approaches show satisfactory or good performance in forecasting concentrations closer to average values, whereas the prediction of extreme pollution events is more challenging.

As summarized by Zhang et al. (2012), the integration of advanced statistical methods in future air quality forecasting systems could considerably reduce forecasting biases and further enhance accuracy. In our previous study, MVA methods were successfully applied for forecasting the contributions of industry and vehicle exhaust to volatile organic compound (VOC) levels in the urban area, with smallest relative forecast error of only 6% (Stojić et al. 2015a). In this study, we compared the performance of twelve advanced multivariate (MVA) methods for PM_{10} forecasting relying on meteorological data and SO_2 concentrations. The analysis was based on a multi-year dataset collected at four different locations, affected by traffic or industry emissions. The herein employed MVA classification and regression methods belong to the supervised learning algorithms designed within Toolkit for Multivariate Analysis (TMVA; Hoecker et al. 2007) within the ROOT framework (Brun and Rademakers 1997), for extracting the maximum available information from the extensive data in high-energy physics.

Materials and methods

The analyzed dataset comprising 5-year (2011–2015) hourly concentrations of PM_{10}, SO_2 and meteorological data (atmospheric pressure, temperature, humidity, wind speed and direction), was obtained from the automatic monitoring stations within the Institute of Public Health network, at four different sites (Fig. 1, Supplementary Material). In the urban area, mostly affected by vehicle-exhaust emissions, measurements were conducted at the Institute of Public Health and New Belgrade, the sites characterized as being urban canyon avenue (UCA) and urban boulevard (UB), respectively, due to their topographic configuration. In the area influenced by emissions from fossil fuel burning for industry and heating operations, the data were collected in Obrenovac and Grabovac, the sites corresponding to urban industry (UI) and rural industry (RI), respectively. The measurements at industrial sites were incomplete due to severe floods that affected the area in 2014. The concentrations of PM_{10} and SO_2 were measured by means of referent beta-ray attenuation (Thermo FH 62-IR) sampler and referent sampling device Horiba APSA 360, respectively. The meteorological data were obtained by using Lufft WS500-UMB Smart Weather Sensor. The accuracy and precision of detection methods are provided in Stojic et al. (2016).

The analyses of daily, weekly, seasonal and annual dynamics, trend (Pretty 2015) and periodicity were performed by means of Openair (Carslaw and Ropkins 2012) and Lomb (Ruf 1999) packages within the Statistical Software Environment R (Team 2012). The relationships between pollutant concentrations and wind characteristics were investigated by the use of bivariate polar plot and bivariate cluster analyses within the Openair package. The contribution of local emission sources, background and transport to the observed PM_{10} pollution was analyzed using the 72-h air mass back trajectories and trajectory sector analysis (TSA) as described in Stojić et al. (2016).

The following MVA methods were used for PM_{10} forecasting: Boosted decision trees (BDT, BDTG, BDTMitFisher), Artificial Neural Network Multilayer

Perceptron (MLP), MLP with Bayesian Extension (MLPBNN), Support Vector Machine (SVM), k-nearest neighbor (KNN), Linear Discriminant (LD), Boosted Fisher Discriminant (BoostedFisher), Multidimensional Probability Density Estimator Range Search Method (PDERS), Predictive Learning via Rule Ensembles (Rule-Fit) and Function Discriminant Analysis (FDA). All methods were used for both classification and regression. The five-year dataset was divided into two equal subsets, each consisting of PM_{10} concentrations and input data (meteorological and SO_2). One subset was used for method trainings, either to differentiate between high and low importance indicators for PM_{10} concentrations (classification), or to determine an approximation of the underlying functional behavior defining PM_{10} concentrations (regression). The other subset was utilized for method performance testing.

Results and discussion

Previous studies aimed at investigating the origin and spatio-temporal distribution of different pollutant species converge on the conclusion that poor air quality presents an important health risk factor in Belgrade area (Perišic et al. 2015; Stojić et al. 2015b). In the previous years, the mean annual PM_{10} concentrations in Belgrade area were in the range from 39.74 to 62.32 μg m^3, whereas the exceedances of the proposed air quality guideline value of 50 μg m^3 were registered during 20.5–42.2% of total number of days (Stanišić Stojić et al. 2016).

Specifics of measurement sites

In order to examine the MVA forecasting performances, PM_{10} observational data from four measurement sites affected by different emission sources were collected and analyzed (Fig. 1, Supplementary Material). The two locations defined as urban were affected by traffic emissions throughout the year. However, specific microclimatic conditions associated with contrasting urban morphology between UCA and UB plays an important role in spatial distribution of particles. The presence of tall buildings along both sides of the canyon avenue induces a complex wind flow that does not enhance the pollutant dispersion due to terrain configuration, but it facilitates suspension, particularly fine PM fraction (Vardoulakis et al. 2003). Furthermore, frequent congestions in the canyon avenue compared to free flowing traffic in the wide boulevard contributed to higher PM_{10} concentrations at UCA

throughout the year, with the exception of winter season, when the air quality at UB was additionally affected by fuel burning from the neighboring heating plant.

The herein presented industrial locations were affected either by fuel burning emissions only (RI), or by emissions from both industrial activities and vehicle exhaust (UI). Within the range of 15–20 km in NW/N and SE/S direction around the two industrial sites, the strong emission sources including three thermal power plants, four open-pit mines of high-sulfur lignite and several coal ash disposal sites are located.

As can be seen, the highest mean PM_{10} concentration for the entire period was registered at UI (Table 1, Supplementary Material), which was partly driven by extreme pollutant loadings in 2012 (Fig. 2, Supplementary Material). It should be noted that the PM_{10} variations at two industrial locations exhibited similar pattern, only with less significant deviations at rural site, which points to the prevalence of the same emission sources.

Daily mean PM_{10} exceedances (>50 μg m^{-3}) were commonly observed, whereas the episodes of extreme pollutant levels were registered only at UI (Fig. 3, Supplementary Material). The winter PM_{10} concentrations were considerably higher at all examined locations, which can be partly attributed to heating operations, but also to lower planetary boundary layer (PBL) height in winter season. Unsurprisingly, the lowest PM_{10} levels for the entire period were observed at rural site, particularly during spring and summer season, with the values of 29.15 and 32.09 μg m^{-3} being registered, respectively. Conversely, the highest concentrations in warm season were measured at UCA, the only site predominately affected by traffic. The differences between the summer and winter concentrations were relatively small at UCA and RI, whereas the inter-seasonal variations at two other sites exposed to the emissions from two strong sources were almost two times higher.

In Fig. 4, Supplementary Material, daily, weekly and seasonal PM_{10} variations are displayed. Accordingly, the lowest concentrations were registered in May and June, probably due to intense precipitations. The particle resuspension processes and atmospheric photochemical reactions in dry summer months starting from July, led to the rising pollutant levels, particularly at industrial sites in the vicinity of ash disposals. The accumulation of particles during working days was followed by a significant decrease at the weekend at two locations dominated by vehicle exhaust emissions, whereas the weekday/weekend difference was not observed at UI and RI sites. As regards diurnal PM_{10} variations, the same pattern was detected at all locations: daytime levels tended to be low with the exception of

morning and afternoon rush hours, whereas the pronounced increase in nighttime concentrations could be attributed to stable atmospheric conditions and shallow PBL.

According to bivariate and cluster analysis, the average contributions of the surrounding emission sources were dominant at all locations (Fig. 1), particularly at UCA (59.5 μg m^{-3}), due to limited pollutant dispersion, and UI (73.1 μg m^{-3}), which has been directly exposed to emissions from the thermal plant which produces more than 50% of electricity for the Serbian market. The UCA is located in the central city area and thus, the polluted air masses were observed to come from all directions, whereas at UB, the impact of heating plant emissions from S and intersections with intensive traffic coming from E can be noted. In the case of industrial locations, local sources appeared to be particularly significant during the heating season, whereas in spring and summer, both UI and RI were affected by emissions from ash disposals and lignite mining sites in NW/N and SE/S. The dynamics of cluster contributions on a daily, weekly and seasonal basis are shown in Fig. 5, Supplementary Material. As can be seen, local emissions, corresponding to cluster 4 at industrial sites, exhibited extremely regular daily variations, which suggests the prominent role of anthropogenic sources. The rush hour peaks were noticeable only in the variations of locally-emitted PM$_{10}$ concentrations at UCA (cluster 4), since the site has been dominated by traffic emissions.

The analysis was also performed to determine the impact of local emissions, transported pollution and background on the air quality at examined locations. According to TSA results, the estimated share of background was highest at rural site (48%), whereas the contribution of local production was the most significant factor (43%) for PM$_{10}$ concentrations at UI, as previously shown by bivariate and cluster analysis.

Upon the presented analysis, we have reached the conclusion that the selected locations are substantially different in terms of air quality and factors closely associated with it, including micro-climatic conditions, topographic features and proximity of strong sources. This was considered a prerequisite for examining the dependency between the efficiency of MVA methods for air quality forecasting and site characteristics.

Classification MVA methods

As previously mentioned, the 5-year dataset, including PM$_{10}$ and SO$_2$ concentrations, and meteorological data, was divided into two subsets equal in size, used for training and testing of MVA methods, respectively. In order to account for seasonal, *i.e.* weekday/weekend variations, two new variables were introduced for classification purposes: Yearreal is a quotient of the ordinal number of a day and total number of days per year, while Weekreal represents
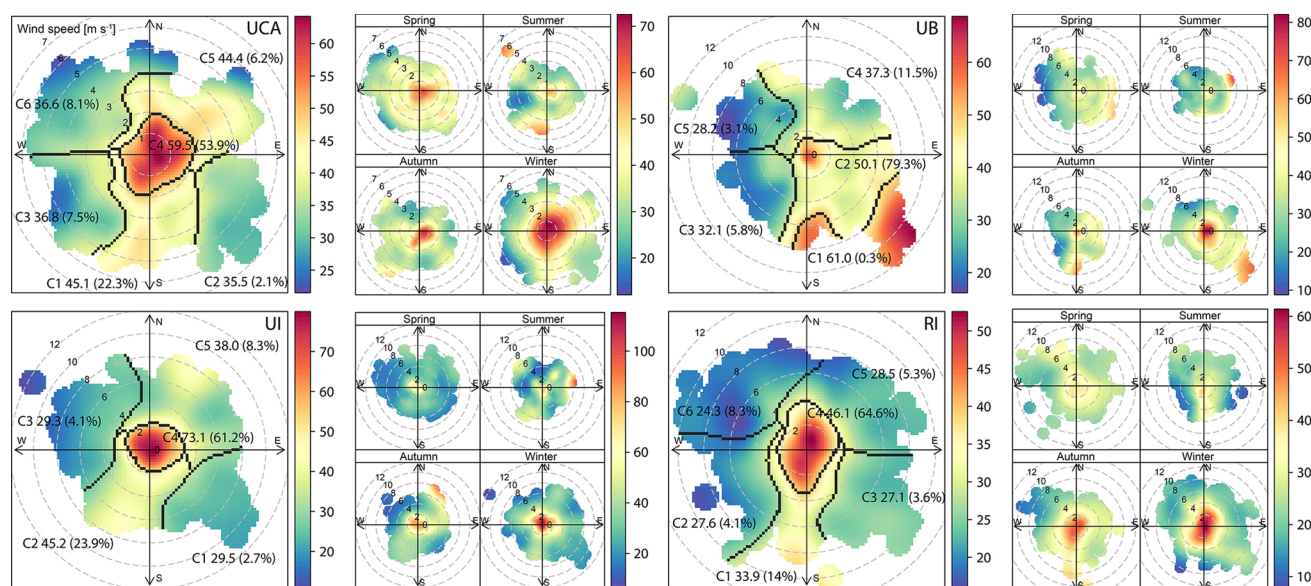

Fig. 1 The relationship between PM$_{10}$ concentrations and wind characteristics: bivariate cluster plot [frequency (%) and average contributions (μg m^{-3})] for the entire period (*left*) and seasonal variations (μg m^{-3}) (*right*)

the quotient of the ordinal number of a day and number 7. Correlation and mutual information of input variables and the observed PM_{10} mass concentrations for all sampling sites are presented in Table 1.

For the purposes of classification, the PM_{10} levels above 50 µg m^{-3} are considered to require the increased level of caution, whereas those exceeding 100 µg m^{-3} are considered extremely high—alarm triggering values, both of which are chosen as arbitrary limits. The estimation of classification method performances by using the Receiver Operating Characteristic (ROC) curve is presented in

Fig. 2. The highest separation between background and predicted PM_{10} concentrations was observed when PM_{10} classifier value of 100 µg m^{-3} was taken into account (Fig. 3), whereas somewhat poorer results were obtained for 50 µg m^{-3}, which suggests that including additional meteorological or pollutant variables as input data might further enhance classification performance.

The comparison of the results by evaluating signal and background efficiencies revealed that certain MVA methods are capable of classifying the PM_{10} levels which are considered to require a high degree of caution (Table 2, left). The results showed that BDTG and MLP exhibit the best results for all examined locations. Signal and background separation was most efficiently performed for RI and UB, and to a somewhat lower extent for UCA.

Regression MVA methods

Regression MVA methods were applied to interpret the relationships between pollutant concentrations and the examined input data. Similar to classification methods, BDTG and MLP exhibited the most satisfying performances with absolute and relative errors presented in Table 2, right. The MVA method performance was best for PM_{10} loadings at industrial sites, around 25%, while the forecast quality could be clearly seen at RI location, Fig. 4. It can be assumed that more accurate air quality forecasts can be

Table 1 Correlation (C) and mutual information (MI) of input variables (P, pressure; T, temperature; Rh, relative humidity; ws, wind speed; Yearreal, day of year; Weekreal, day of week) and measured PM_{10} concentrations at all sampling sites

Variable	UCA		UB		UI		RI	
	C	MI	C	MI	C	MI	C	MI
P	0.18	1.31	0.26	0.97	0.20	1.49	0.29	1.26
T	0.21	1.40	0.30	1.21	0.28	1.69	0.22	1.39
Rh	0.24	1.47	0.24	1.29	0.22	1.86	0.19	1.60
ws	0.29	1.39	0.25	0.82	0.26	1.57	0.32	1.18
SO_2	0.25	1.63	0.09	1.39	0.20	1.87	0.32	1.59
Yearreal	0.04	1.49	0.05	1.31	0.09	1.86	0.12	1.53
Weekreal	0.02	0.12	0.03	0.11	0.02	0.18	0.02	0.14

Fig. 2 ROC curves for MVA classification methods with PM_{10} classifier value of 100 µg m^{-3} (*left*) and 50 µg m^{-3} (*right*) for all sampling sites
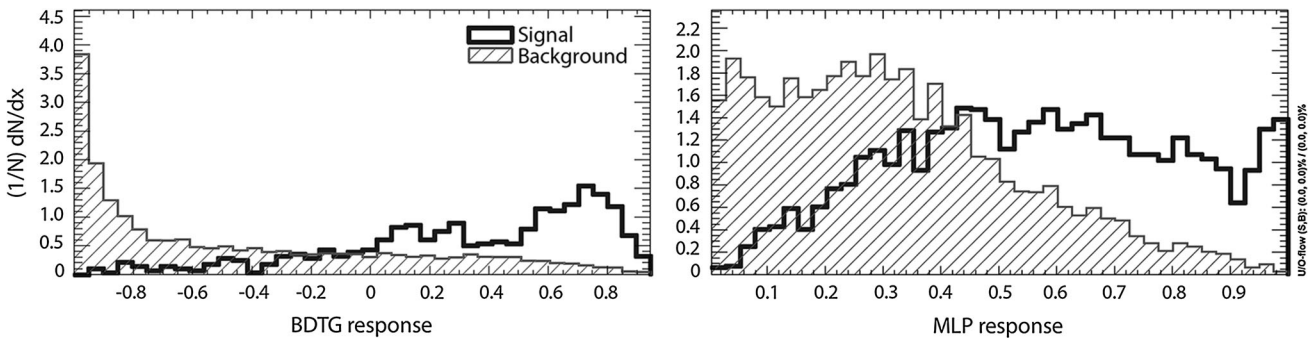
Fig. 3 MVA classification method response for PM_{10} classifier value of 100 µg m^{-3} (*left*) and 50 µg m^{-3} (*right*) for UCA site

Table 2 The comparison of best performing methods for ROC, separation and significance values for all measurement sites (left) and absolute ($\mu g\ m^{-3}$) and relative (%) errors of the best performing regression methods (right)

Sampling site	Method	Classification			Regression	
		ROC	Separation	Significance	Absolute error	Relative error
UCA	BDTG	0.806	0.282	0.883	17.2	29.6
	MLP	0.772	0.226	0.755	21.8	37.5
UB	BDTG	0.868	0.408	1.12	13.9	26.8
	MLP	0.841	0.352	1.015	17.4	33.5
UI	BDTG	0.855	0.379	1.059	15.6	24.6
	MLP	0.826	0.323	0.956	24.0	37.9
RI	BDTG	0.867	0.412	1.172	10.6	25.2
	MLP	0.837	0.345	0.962	15.1	36.0
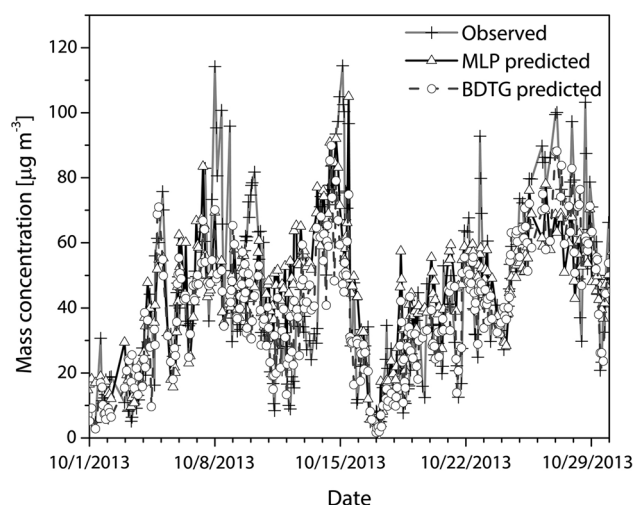
Fig. 4 The comparison of time series of the observed and best performing MVA-predicted PM_{10} concentrations ($\mu g\ m^{-3}$) at RI site

achieved at the locations such as RI, which are affected by less significant number of emission sources. Furthermore, the simplicity and regularity of dominant pollutant emissions on a daily, weekly and seasonal basis, as registered at UI location, as well as minor deviations from the commonly observed pollutant loadings, which is particularly evident for air quality forecasting at rural site, are probably the additional factors associated with forecast accuracy.

Conversely, the weakest MVA method performance was derived for PM_{10} concentrations at UCA, probably because the urban morphology of the canyon avenue represents the additional factor modifying the pollutant levels in a less predictable manner. Furthermore, the emission sources in the central city zone are diverse and primarily refer to traffic congestions and intense atmospheric reactions that take place in stagnant conditions of the canyon street. Moreover, they also relate to local fireboxes in residential area where lignite is burned

Fig. 5 The comparison of the observed and best performing MVA-predicted PM_{10} mass concentrations ($\mu g\ m^{-3}$)

during autumn and winter season and local manufactures that are associated with pollutant emissions highly variable in time and intensity.

As can be seen in Fig. 5, the PM_{10} time series evaluated by means of MVA regression methods correlated very well with the observed concentrations at all samp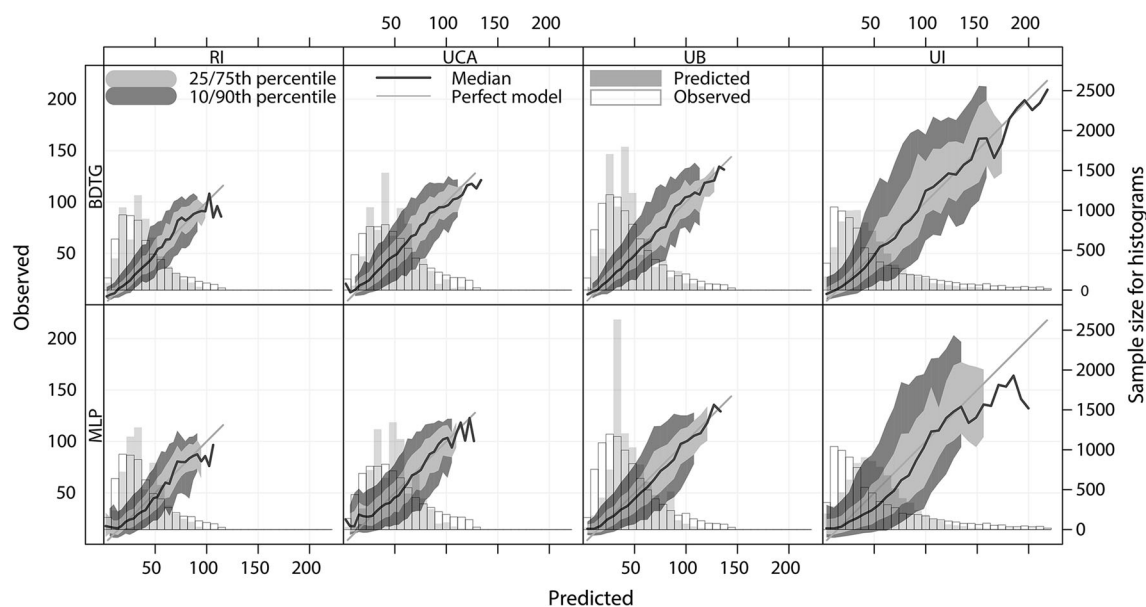ling sites. Mutual information obtained for BDTG-predicted and the observed PM_{10} mass concentrations were 0.71, 0.7. 0.65 and 0.64 for RI, UB, UCA and UI, respectively. This suggests that significant input variables were used for the forecasting process. In addition, it could be noted that their distributions are relatively well.

Although the other MVA methods employed in the present study generated similar results when being used for classification, they generated the significant PM_{10} forecast errors when being used for regression, at least based on the observed input variables. The herein presented errors are mostly in compliance with the findings of our previous study, aimed at forecasting the contributions from traffic and industry to the observed VOC concentrations in the urban area, which suggests that both PM and VOC, as important air quality indicators, can be predicted using the MVA methods.

Conclusion

In this study, the performances of MVA methods for forecasting PM_{10} concentrations and prediction of related health-damaging events were evaluated on the basis of datasets from traffic- and industry-affected locations with substantial differences in air quality, which has also been verified through additional analyses. The results of both classification and regression methods were rather promising, particularly considering the fact that the presented forecast accuracy referred to hourly concentrations. The quality of the prediction might be partly dependent on microclimatic conditions, topographic characteristics, presence of strong emission sources and other site characteristics, as well as on the input data. All that implies that the selection of additional or different variables could enhance the method forecasting performances. The importance of accurate air quality forecasts as part of the management system is reflected in the potential applications, including health alerts for susceptible categories, operational planning, as well as amendment of pollutant time-series and reduction of regular monitoring expenditures.

References

Brun R, Rademakers F (1997) ROOT—an object oriented data analysis framework. Nucl Instrum Methods A 389:81–86

Carslaw DC, Ropkins K (2012) Openair-an R package for air quality data analysis. Environ Model Softw 27:52–61

Cobourn WG (2010) An enhanced $PM_{2.5}$ air quality forecast model based on nonlinear regression and back-trajectory concentrations. Atmos Environ 44:3015–3023

Fang Y, Mauzerall DL, Liu J, Fiore AM, Horowitz LW (2013) Impacts of 21st century climate change on global air pollution-related premature mortality. Clim Change 121:239–253

Feng X, Li Q, Zhu Y, Hou J, Jin L, Wang J (2015) Artificial neural networks forecasting of $PM_{2.5}$ pollution using air mass trajectory based geographic model and wavelet transformation. Atmos Environ 107:118–128

Fernando HJS, Mammarella MC, Grandoni G, Fedele P, Di Marco R, Dimitrova R, Hyde P (2012) Forecasting PM_{10} in metropolitan areas: efficacy of neural networks. Environ Pollut 163:62–67

Hoecker A, Speckmayer P, Stelzer J, Therhaag J, Von Toerne E, Voss H, Backes M, Carli T, Cohen O, Christov A, Dannheim D, Danilowski K, Henrot-Versille S, Jachowski M, Kraszewski K, Krasznahorkay A, Kruk M, Mahalalel Y, Ospanov R, Prudent X, Robert A, Schouten D, Tegenfeldt F, Voigt A, Voss K, Wolter M, Zemla A (2007) TMVA users guide—toolkit for multivariate data analysis, PoSACAT 040. http://arxiv.org/abs/physics/0703039. Accessed 14 June 2015

Lelieveld J, Evans JS, Fnais M, Giannadaki D, Pozzer A (2015) The contribution of outdoor air pollution sources to premature mortality on a global scale. Nature 525:367–371

Moustris KP, Larissi IK, Nastos PT, Koukouletsos KV, Paliatsos AG (2013) Development and application of artificial neural network modeling in forecasting PM_{10} levels in a Mediterranean city. Water Air Soil Pollut 224:1–11

Pai TY, Hanaki K, Chiou RJ (2013) Forecasting hourly roadside particulate matter in Taipei County of Taiwan based on first-order and one-variable grey model. CLEAN Soil Air Water 41:737–742

Perišić M, Stojić A, Stojić SS, Šoštarić A, Mijić Z, Rajšić S (2015) Estimation of required PM_{10} emission source reduction on the basis of a 10-year period data. Air Qual Atmos Health 8:379–389

Pretty R (2015) TheilSen {openair} tests for trends using Theil–Sen estimates. http://www.inside-r.org/packages/cran/openair/docs/TheilSen. Accessed 12 Dec 2015

Ruf T (1999) The Lomb-Scargle periodogram in biological rhythm research: analysis of incomplete and unequally spaced time-series. Biol Rhythm Res 30:178–201

Russo A, Soares AO (2014) Hybrid model for urban air pollution forecasting: a stochastic spatio-temporal approach. Math Geosci 46:75–93

Stanišić Stojić S, Stanišić N, Stojić A, Šoštarić A (2016) Single and combined effects of air pollutants on circulatory and respiratory system-related mortality in Belgrade, Serbia. J Toxicol Environ Health A 79:17–27

Stojić A, Maletić D, Stojić SS, Mijić Z, Šoštarić A (2015a) Forecasting of VOC emissions from traffic and industry using classification and regression multivariate methods. Sci Total Environ 521:19–26

Stojić A, Stojić SS, Mijić Z, Šoštarić A, Rajšić S (2015b) Spatio-temporal distribution of VOC emissions in urban area based on receptor modeling. Atmos Environ 106:71–79

Stojić A, Stanišić Stojić S, Reljin I, Čabarkapa M, Šoštarić A, Perišić M, Mijić Z (2016) Comprehensive analysis of PM_{10} in Belgrade urban area on the basis of long term measurements. Environ Sci Pollut Res. doi:10.1007/s11356-016-6266-4

Team RC (2012) R: a language and environment for statistical computing. http://cran.case.edu/web/packages/dplR/vignettes/timeseries-dplR.pdf. Accessed 10 June 2015

Vardoulakis S, Fisher BE, Pericleous K, Gonzalez-Flesca N (2003) Modelling air quality in street canyons: a review. Atmos Environ 37:155–182

Zhang Y, Bocquet M, Mallet V, Seigneur C, Baklanov A (2012) Real-time air quality forecasting, part I: history, techniques, and current status. Atmos Environ 60:632–655

D. M. Maletić, *et al.*, Multivariate Analysis of Two-Year Radon Continuous ...
Nuclear Technology & Radiation Protection: Year 2023, Vol. 38, No. 4, pp. 000-000

1

MULTIVARIATE ANALYSIS OF TWO-YEAR RADON CONTINUOUS MONITORING IN GROUND LEVEL LABORATORY IN THE INSTITUTE OF PHYSICS BELGRADE

by

Dimitrije M. MALETIĆ [1], *Radomir M. BANJANAC* [1], *Dejan R. JOKOVIĆ* [1], *Aleksandar L. DRAGIĆ* [1], *Nikola B. VESELINOVIĆ* [1], *Mihailo R. SAVIĆ* [1], *Zoran MIJIĆ* [1], *Vladimir I. UDOVIČIĆ* [1*], *Svetlana ŽIVKOVIĆ-RADETA* [2], *and Jelena V. UDOVIČIĆ* [2]

[1] Institute of Physics Belgrade, National Institute of the Republic of Serbia,
University of Belgrade, Belgrade, Serbia
[2] Faculty of Applied Ecology Futura, Belgrade Metropolitan University, Belgrade, Serbia

Multivariate classification and regression analysis of multiple meteorological variables and indoor radon activity concentration in Ground Level Laboratory in the Institute of Physics Belgrade, was performed and discussed. Meteorological variables used in this analysis were from radon active device, nearby meteorological station and finally from Global Data Assimilation System. Single variate analysis has identified variables with greatest value of Pearson's correlation coefficient with radon activity concentration and also, variables with greatest separation of events with increased radon activity concentration (200 Bqm^{-3}) and of events with radon level below this value. This initial analysis is showing the expected behavior of radon concentration with meteorological variables, with emphasis on data periods with or without air conditioning and with emphasis on indoor water vapor pressure, which was, in our previous research, identified as important variable in analysis of radon variability. This single variate analysis, including all data, proved that Global Data Assimilation System data could be used as a good enough approximate replacement for meteorological data from nearby meteorological station for multivariate analysis. Variable importance of Boosted Decision Trees with Gradient boosting multivariate analysis method are shown for all three periods and most important variables were discussed. Multivariate analysis regression analysis gave good results, and can be useful to better tune the multivariate analysis methods.

Key words: continuous radon monitoring, multivariate analysis, Global Data Assimilation System, meteorological station

INTRODUCTION

Primarily, radon problem presents a health hazard [1]. The research of the dynamics of radon in various environments, living or working places, is of great importance in terms of protection against ionizing radiation and in designing of measures for its reduction. In the low-background laboratory for Nuclear Physics extensive research on various radon fields has been done in the past, especially radon monitoring in the special designed low-background underground and ground level laboratory, with the aim of investigating the rare nuclear processes [2]. Besides radon monitoring in the laboratory, we work on several research topics regarding radon: using multivariate classification and regression methods, as developed for data analysis in high-energy physics [3], to study connection of climate variables and variations of radon concentrations, modelling of the indoor radon behaviour and national indoor radon mapping [4], taking interest in similar indoor radon mapping analysis in Montenegro [5], or by research of radon variability in a single dwelling [6], using advanced analysis tools, or performing continuous measurements in multi-store building [7] or laboratory space [8]. Indoor radon variability depends on many variables. Soil content, and building characteristics are very important. In case of researching of indoor radon variability, meteorological effects become the most important ones. With recent experiences with lowering the limits of indoor radon level, both in dwellings and working places, and the demand for decrease of public radon exposure, the need for more detailed knowledge on radon variability is increasing. Besides a possibility for improvement of mitigation

2

D. M. Maletić, *et al*., Multivariate Analysis of Two-Year Radon Continuous ...
Nuclear Technology & Radiation Protection: Year 2023, Vol. 38, No. 4, pp. 000-000

techniques, we could look into creating online warning pages, like we already have, for example, for UV radiation. These online warning pages, with information on radon concentration variations, could be interesting to people living in dwellings or working spaces with previously known radon problem, or dwellings with radon activity concentration close to 200 Bqm^{-3} limit. These online warnings, could indicate a call for some temporary measures like starting of increased ventilation or reducing exposure. Local radon warning pages could be based on local meteorological station, but for larger regions, meteorological modeled data like Global Data Assimilation System (GDAS) could be used. In this paper we were looking into the possibility of using GDAS data in prediction of indoor radon variability, by jointly looking into GDAS and nearby meteorological station, and compare the results.

DATA PREPARATION AND SELECTION

The radon continuous monitoring in ground level laboratory was performed with active device RadonEye Plus2 with time sampling of one hour. The device recorded variables: Rn-activity, indoor temperature and indoor humidity. The radon the measurement was done from November 2020 to November 2022. After looking into indoor temperature data, we decided to do three analysis, one with using all the data samples (whole period of measurement's), second using only data when air conditioning (AC) was operating, and third sample used for analysis was for periods when air conditioning was OFF (noAC).

Meteorological station located in Institute of Physics Belgrade yard, and maintained by Environmental Physics Laboratory [8], has being recording variables at 5 minute interval, and hourly values are used for this analysis. Variables are named by adding prefix outside; outside-cloudbase, outside-dew point, outside-humidity, outside-temp, outside-pressure and outside-rain.

The US National Centers for Environmental Prediction (NCEP) runs a series of computer analyses and forecasts operationally. One of the operational systems is the GDAS. At National Oceanic and Atmospheric Administration's (NOAA) Air Resources Laboratory (ARL), NCEP model output is used for air quality transport and dispersion modeling. The ARL archives GDAS output which contains basic fields, such as the temperature, pressure and humidity. Those GDAS data are very interesting since they are widely used by weather forecast groups worldwide, and our idea is that if we could use this freely accessed and frequently updated database, we could improve forecasting of some kind of *relative* indoor radon concentrations, and indicate by result of automatic online MVA regression analysis when to expect increased indoor radon concentrations based on meteo-

rological variables. Because MVA methods are rather robust, and we wanted to see which, if any of GDAS variables are suited for our purpose, we included most of variables in our analysis. The GDAS1 data is available for integer values of latitude and longitude, so, for all variables', each data point was firstly 2-D linearly interpolated using variables' values on four integer latitudes and longitudes, surrounding latitude and longitude of our laboratory. The GDAS1 data is available for every three hours, so linear interpolation of each variable's data point was made in order that we can use hourly data. The GDAS1 variables used in our analysis can be identified as ones with prefix GDAS1; GDAS1-CAPE (convective available potential energy), GDAS1-CINH (convective inhibition), GDAS1-CPP6 (accumulated convective precipitation), GDAS1-CRAI (categorical rain), GDAS1-DSWF (downward short wave radiation flux), GDAS1-HCLD (high cloud cover), GDAS1-LCLD (low cloud cover), GDAS1-LHTF (latent heat net flux at surface), GDAS1-LIB4 (best 4-layer lifted index), GDAS1-LISD (standard lifted index), GDAS1-MCLD (middle cloud cover), GDAS1-PBLH (planetary boundary layer height), GDAS1-PRSS (pressure at surface), GDAS1-RH2M (relative humidity at 2m AGL), GDAS1-SHGT (geopotential height), GDAS1-SHTF (sensible heat net flux at surface), GDAS1-SOLM (volumetric soil moisture content), GDAS1-T02M (temperature at 2m AGL), GDAS1-TCLD (total cloud cover), GDAS1-TMPS (temperature at surface), GDAS1-TPP6 (accumulated precipitation), GDAS1-mofi-e (momentum flux intensity), GDAS1-mofd-e (momentum flux direction). In this analysis using GDAS data, we also could indicate if variables measured by local meteorological station do not differ too much from GDAS modeled and interpolated ones, that GDAS variables could be used in this kind of MVA analysis.

We included previously found interesting variable in radon research [5] and that is water vapor pressure in outdoor and indoor air, as well as the difference of the two. In order to calculate the water vapor pressure in air, we need to calculate the value of the saturation water vapor pressure

$$es(T) = 0.6108 \, e^{\frac{17.27 \, T}{T + 237.3}} \qquad (1)$$

In addition, the slope of the relationship between the saturation water vapor pressure (es [kPa]) and the air temperature T [°C], is given in [9, 10], so including the slope, we get new formula for the saturation water vapor pressure

$$es(T) = \frac{4098 \, 0.6108 \, e^{\frac{17.27 \, T}{T + 237.3}}}{(T + 237.3)^2} \qquad (2)$$

and since the formula used to calculate the relative humidity is

D. M. Maletić, *et al.*, Multivariate Analysis of Two-Year Radon Continuous ...
Nuclear Technology & Radiation Protection: Year 2023, Vol. 38, No. 4, pp. 000-000

3

Figure 1. The Rn activity indoor (a) and vapor pressure difference of outdoor and indoor (b). Note that with much greater outdoor water vapor pressure than indoor, comes influx of radon-free water vapor, and that results in significant decrease of indoor Rn activity
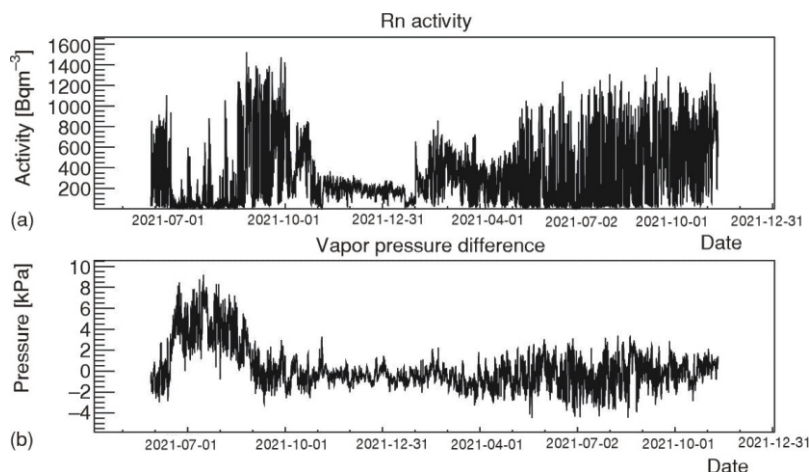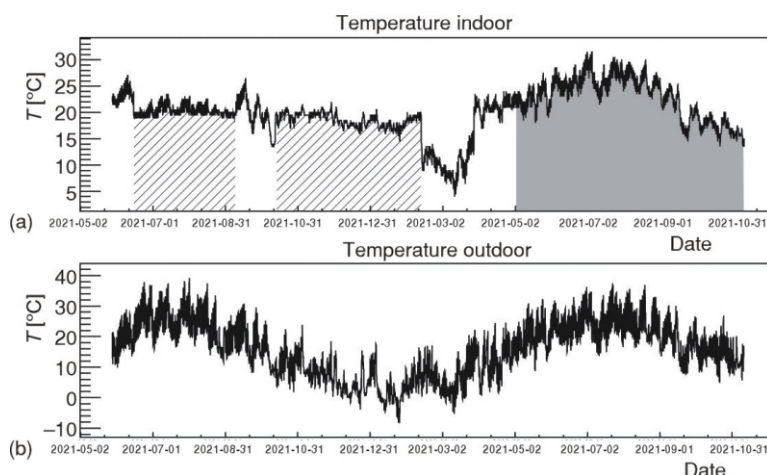

Figure 2. Indoor temperature (a) and outdoor temperature (b) is shown. Indoor temperature which was used for analysis when air conditioning (AC) was on, is indicated in two line pattern areas, while gray shaded interval indicates period when air conditioning was off (noAC)

$$RH = \frac{\text{vapor pressure}}{es(T)} \qquad (3)$$

we get the formula to calculate the vapor pressure in air

$$\text{vapor pressure}(T, RH) = RH \cdot \frac{4098 \cdot 0.6108 \cdot e^{\frac{17.27\,T}{T+237.3}}}{(T+237.3)^2} \qquad (4)$$

Using this formula, we calculate four variables: indoor-vapor-press (vapor pressure from indoor-temperature and indoor-humidity data), outside-vapor-press (vapor pressure from outdoor outside-humidity, outside-temp data), diff-vapor-press (vapor pressure difference of outdoor and indoor) and gdas1-vapor-press (vapor pressure from GDAS1-T02M, GDAS1-RH2M data). On the bottom of fig. 1 the vapor pressure difference is shown, and it can be clearly seen that if the outer vapor pressure is much higher than the indoor vapor pressure, the indoor radon activity is lower fig. 1(a).

Out of two years of data taking, after merging all the data together to form a single hourly event with all the variables measured at that time, the number of useful hourly events was 12654. Table 1 shows the number of hourly events used for each of the three periods

Table 1. Summary table of number of hourly events used for specific part of analysis

	noAC	AC	All period
Signal training	1343	912	3428
Signal testing	1343	912	3428
Signal training and testing	2686	1824	6856
Background training	942	1531	2899
Background testing	942	1531	2899
Background training and testing	1884	3062	5798

of analysis, which were split, firstly into signal and background events, where signal events are those for which Rn activity is more than 200 Bqm^{-3}, and background is less than that value, and then each set was split once more, into training and testing sample to be used in MVA analysis. Table 1 also shows the number of events used, and split, in periods with air condition operation on (AC), line pattern area on fig. 2(a), and air conditioning off (noAC) gray on fig. 2(a).

Before performing the multivariate (MVA) analysis, we have looked into single variable analysis, and the best way to see if variables could be useful for analysis is if they have, firstly, the greatest correlation with radon activity (concentration), and, secondly, which variable profiles for high Rn activity (signal) and low (background) data sam-

4

D. M. Maletić, *et al.*, Multivariate Analysis of Two-Year Radon Continuous ...
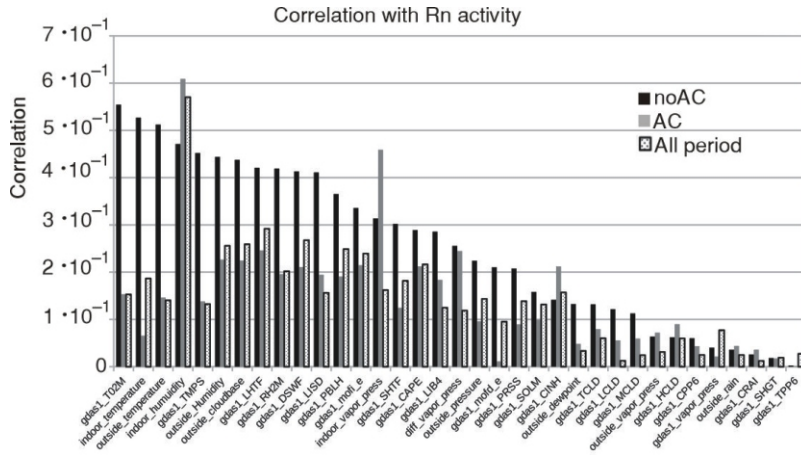Nuclear Technology & Radiation Protection: Year 2023, Vol. 38, No. 4, pp. 000-000

Figure 3. The modulus of Pearson's correlation coefficients of radon activity with each of variables used in the analysis is shown. Note the decreasing of correlation with temperature variables, and increasing with humidity variables, when air conditioning (AC) was turned on
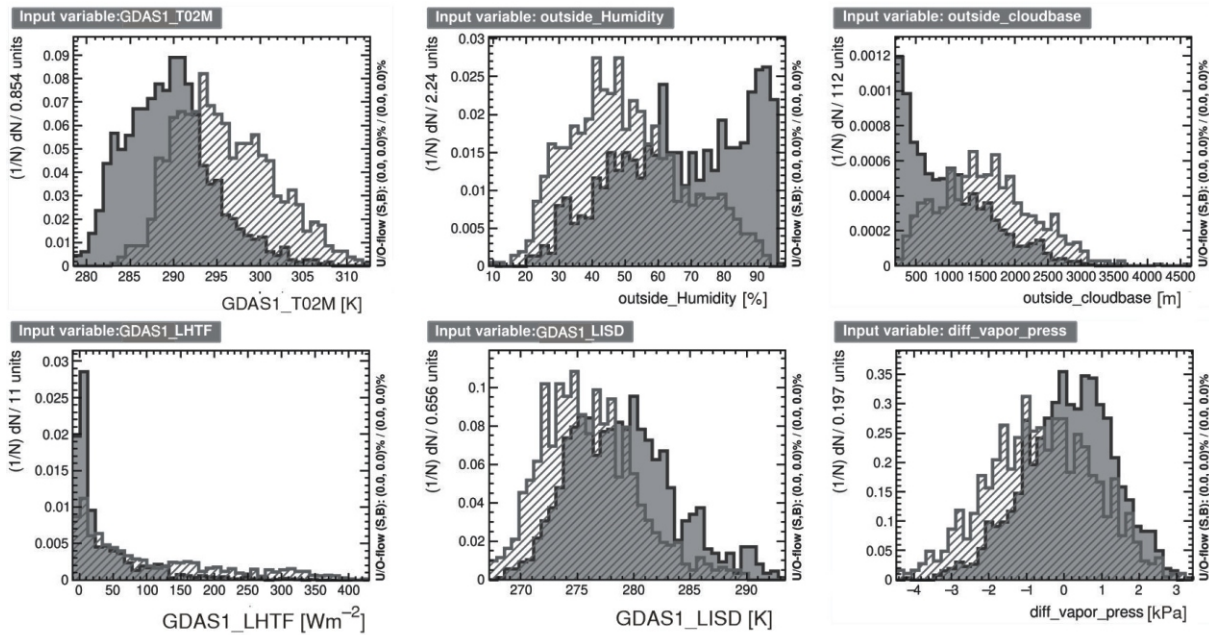

Figure 4. For some variables there is a significant separation of distributions of variables' values for events with low and events with high radon activity. Variables shown are: temperature at height of 2 m above the ground (GDAS1-TO2M), outside relative air humidity, measure of lowest visible part of the cloud (cloudbase), latent heat net flux at the surface (LHTF), standard lifted index (LISD) and the difference of water vapor pressure from indoor and outdoor

ples, have smallest overlap, meaning that they have greatest separation of high and low Rn activity samples. So, firstly, we are looking into modulus of Pearson's correlation coefficients for each of the variables used in this analysis with radon activity, fig. 3. Since the greatest variation of radon activity should give the best insight into correlation with variables, we are firstly looking into data with air condition off (noAC). To the variables with greatest modulus of Pearson's correlation coefficients with Rn activity (noAC) are temperature variables from all three sources of data GDAS, radonometar and meteorological station (GDAS1-T02M, indoor-temperature, outside-temperature, GDAS1-TMPS), than humidity (indoor-humidity, outside-humidity), outside-cloudbase, followed with GDAS variables: GDAS1-LHTF (latent heat net flux on surface) and GDAS1-DSWF (downward short wave radiation flux) and GDAS1-RH2M (relative humidity at height of 2 m), followed by indoor-vapor-pressure. When air conditioning is turned on, there is a change in correlation, where tempera-

ture variables correlations are decreasing, and there is an increase in correlation of humidity variables like indoor-humidity and indoor-vapor-pressure. We observe this change since temperature is now holding at approximately the same level by air conditioning, and any variation of radon activity we see does not come from approximately constant temperature. We noticed the similarity in modulus of Pearson's correlation coefficients of outside-T02M and outside-temperature with Rn activity of 55.4 % and 51.2 %, respectively, for noAC data, and 15.3 % and 14.6 %, respectively, for AC data. Also, outside-humidity and gdas1-RH2M with 44.4 % and 41.9 %, respectively, for noAC and 22.7 % and 19.6 % for AC data. When looking into pressure data, outside-pressure and GDAS1-PRSS have modulus of Pearson's correlation coefficients of 22.4 % and 20.8 %, respectively, for noAC data and 9.6 % and 9.0 % for AC data.

When looking into separation of variables for signal and background samples, fig. 4 shows selected variables, where separation can be seen with naked
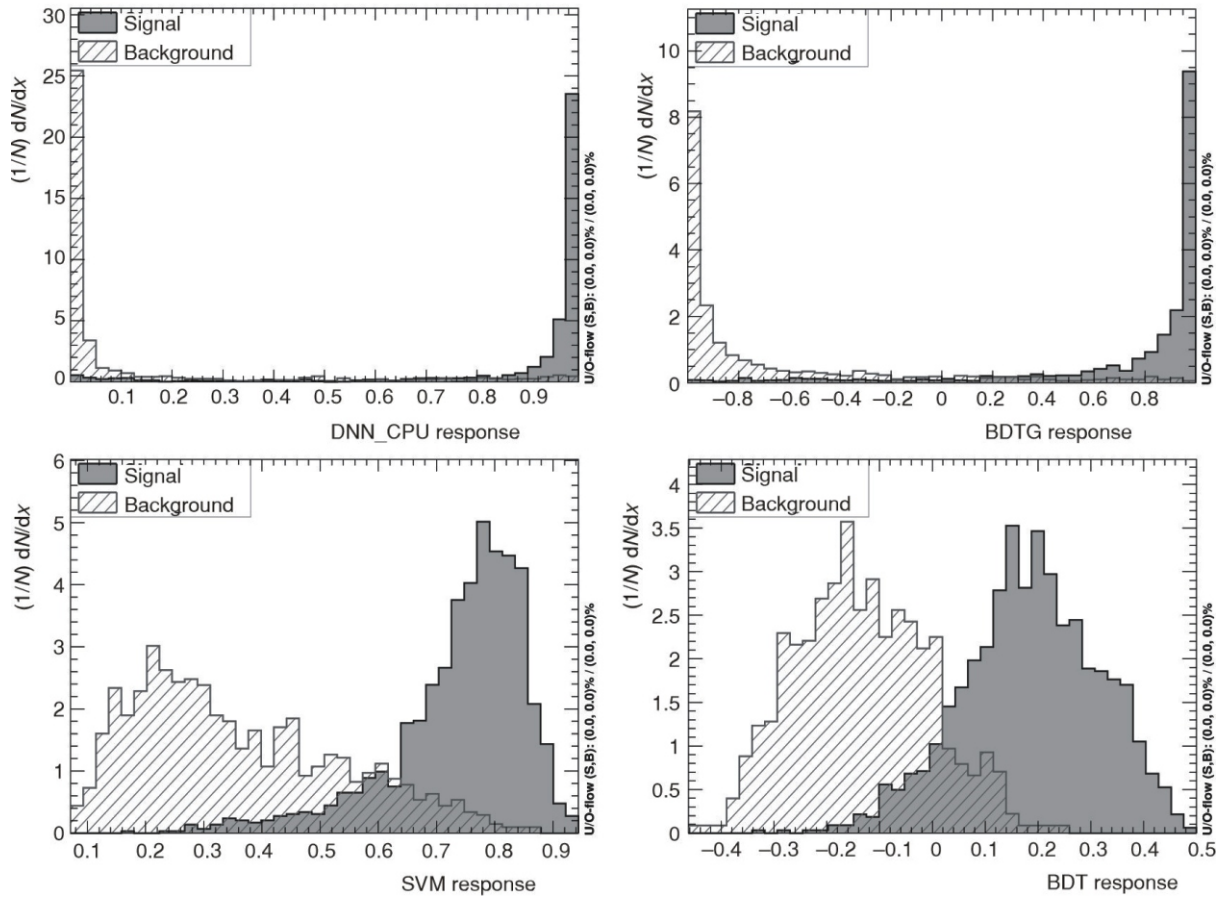
Figure 5. Separation of events with low and high Rn activity by each variable

eye, and also, separations of high and low Rn activity for different variables can be roughly compared. But, we want to have more precise insight into separation, and for all three samples AC, noAC and samples of whole measurement period. This is shown in fig. 5 where we can see that for noAC, temperature variables have most significant separation values, as was the case with modulus of Pearson's correlation coefficients with Rn activity on fig. 3. With air conditioning turned on, the variables of humidity and vapor pressure gain in separation value, while indoor temperature is decreasing its separation value. Notice that the change is not so pronounced as was the case with correlation variables. Again, we noticed the similarity separation values of outside-T02M and outside-temperature 29.1 % and 24.1 %, respectively, for noAC data, and 26.0 % and 20.8 %, respectively, for AC data. Also, outside-humidity and GDAS1-RH2M with 19.8 % and 19.5 %, respectively, for noAC and 8.8 % and 9.6 % for AC data. When looking into pressure data, outside-pressure and GDAS1-PRSS have separation values of 12.7 % and 9.7 %, respectively, for noAC data and 5.5 % and 4.6 % for AC data.

MULTIVARIATE CLASSIFICATION ANALYSIS

Toolkit for multivariate analysis (TMVA) [11] implemented in ROOT [12] framework for data analysis, has many of multivariate methods and tools implemented, which are frequently used for data analysis, as in High energy physics, also by data scientists in general. We will not get into details of wide spread of multivariate methods available, which can be found in TMVA manual [11]. The usage of those multivariate methods in TMVA is rather standardized. What is advantageous in using TMVA is that we could compare many of multivariate methods using the same training and testing sample. Also, the TMVA was used in many analyses, and is constantly under development, with many new methods implemented. The TMVA offers comparison of methods developed for other frameworks, like methods developed in py, or R, or modern

methods like Deep and Convolutional Neural Networks, which is best to be run in multi-thread mode or on CPU or on GPU (graphical cards).

In MVA analysis, the data sample consists of events. Event is composed of data measured/recorded at the same time for each input variable. We can run MVA as Classification, Classification with category, and Regression. The MVA Classification is done when sample is divided into two samples (classes); signal and background. The MVA methods are trained to make the same classification using events they have not seen before, and their performance in classification is measured. Second MVA analysis is done as regression analysis. It is similar to classification, in the sense that the number of classes into which initial sample is divided is much bigger, and the value of classifier is not only 1 (signal) and 0 (background) but has much more values in between. Classification with category was not used, as the maximum performance of Classification is obtained when no other categorical values besides 1 (signal) and 0 (background) are used. Future performance tests could include categories like; very high, high, medium, low and very low radon concentrations.

When a sample is prepared, MVA classification needs some time to complete the training process for each of MVA methods selected for comparison. Besides training, the sample of same number of events is used for evaluation, or testing, where MVA method is tested on samples not seen before (not used for training). The performance of some MVA method is expressed only using testing/evaluation sample.

The fig. 6 shows the response of best performing MVA methods, in analysis of noAC data, to events with low and high Rn activity, or signal and background. We can see, in fig. 7, that by looking into Receiver Operating Characteristic (ROC) curve comparison of all selected multivariate methods, that several methods have very good performances and also, very close performances. It is very good to have several methodologically very different multivariate methods performing in similar way, since this gives us confidence that classification is applicable. To illustrate this point, we can say that, very generally speaking, ANN

Figure 6. Response of MVA methods to events with low and high Rn activity
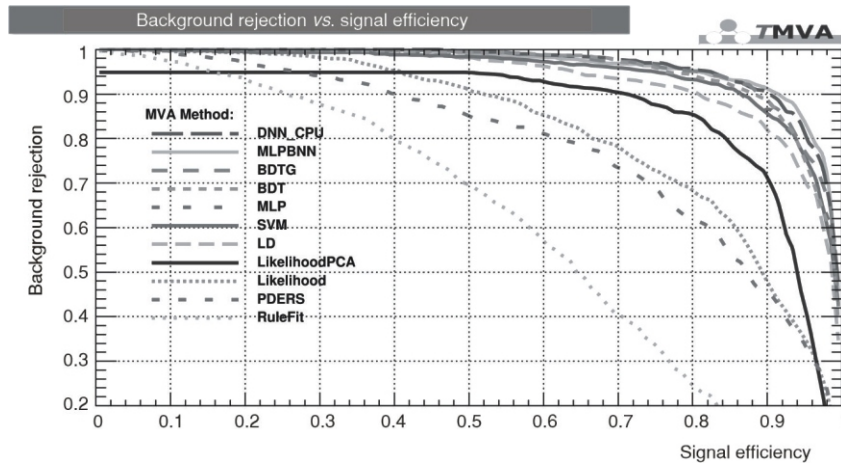

Figure 7. The ROC curve for MVA methods for the time interval where air conditioning was off (noAC)

are based on convolution of selected function to the resulting multivariate functional dependence, while Boosted Decision Trees are based on multidimensional space (cube) cuts, for approximation of multivariate functional dependence, and it is very good that both have very good performances in MVA classification.

The comparison of ROC curve integrals for best performing methods, for MVA classification analysis for all three intervals; noAC, AC and all-period analysis

is shown at fig. 8. For five best performing methods, DNN-CPU (Deep Neural Network), MLPBNN (Multi-Layer Perceptron Bayesian regulator Neural Network), BDTG (Boosted Decision Trees with Gradient boosting), BDT (Boosted Decision Trees), and MLP (Multi-Layer Perceptron – an ANN), results are very similar, and also for all the three intervals, which is very important in sense that while variables' correlation with Rn activity vary greatly, this is easily overcome in MVA methods, adding very important property of ro-

Figure 8. Value of the ROC integral for MVA methods for the selected time intervals, AC and noAC, and for whole time interval

Figure 9. Variable importance for MVA method BDTG for time intervals, AC and noAC, and for the whole time interval

bustness in variable selection. We should note that all the mentioned methods are ANN or DBT based multivariate methods.

The resulting trained multivariate methods are now ready to be included into some web applications, or used in variables' analysis. In web applications, Radon alarm could be constructed, when based on input variables, there is a great probability of increased indoor radon activity. For example, some places where it is known from previous measurements, like from participation in large indoor radon survey, that dwelling or working space has a problem with increased indoor radon concentration, some measures like increased ventilation or longer brakes from work, could be made. In variables' analysis, the simplification of MVA approximation of underlying multivariable function dependence could be made, not only with classification, but more effectively with regression methods.

The MVA methods which are trained and tested using full set of variables and all available data are ready to be used in some application. But, we can continue our work and try to modify something in our analysis chain to see if we can get better performance or method which uses lower number of input variables, without big loss in performance. We can make different selection of training data sets, like truncation of outlier

data, we can change the number of input variables, or change parameters specific for each MVA method. For this purpose, it could be very useful to look into variable importance for specific MVA method, in order to look into the influence of variables on MVA decision. To show why this is useful we pay attention on Pearson's correlation coefficients of input variables and radon concentrations and notice that there could be several variables with high correlation coefficient with radon concentration, but highly inter-correlated with each other, which results in no gain in MVA method performance if we add several variables which are inter-correlated. So, we can exclude variables if their exclusion does not lower the MVA method performance. We choose to look into importance of variables on BDTG classification, for all time intervals. Again, we start with noAC intervals, where indoor radon activity was highest, and indoor temperature was not regulated. We start with two GDAS variables, GDAS1-SHTF (sensible heat net flux at surface) and GDAS1-SOLM (volumetric soil moisture content), followed by indoor-humidity and diff-vapor-pressure, and GDAS1-T02M at position 6, with some other variables similarly important as gdas momentum flux direction and gdas cloud cover variables.

When comparing data from meteorological station and gdas data, we cannot compare them in, for example, multivariate importance, since if one variable is chosen to be used in MVA training, similar variable in, for example Pearson's correlation coefficients or separation of variable for increased and for low Rn activity value, do not have power to make discrimination. Comparison can only be used when each variable is observed separately in a single variable analysis. Also, similar situation can happen with preparation of variables, where resulting variables are, de-correlated, and first variable is significant for further analysis but other, very similar variable before de-correlation, remains with negligible significance for further analysis.

THE MVA REGRESSION

Regression analysis often fails if there is not a strong dependence of target variable, in our case Rn activity, on input variables. Reasoning is the following: Classification analysis has only two outputs, either it is signal (1) or background (0), but in case of regression, there are many more values between 0 and 1, and much more dependence, or events is needed to get positive results here. We ran MVA regression for three time intervals, noAC, AC and all-period. The BDTG and DNN-CPU show good prediction results after MVA regression training procedure, as a result of RMS of deviations of true and evaluated value of Rn activity are satisfyingly small, as is shown in fig. 10. The fig. 11 shows this in more detail for BDTG in noAC regression analysis, where the distribution of deviations is shown for each event in the testing sample.

CONCLUSIONS

Single variate analysis of correlations of each of meteorological variable with indoor radon activity and Multivariate classification and regression analysis of all meteorological variables and radon activity was performed and discussed. Meteorological variables used in this analysis were from radonometar device, then from a nearby meteorological station and finally from GDAS data. Single variate analysis has identified variables with greatest value of modulus of Pearson's correlation coefficient with Rn activity, and also variables with greatest separation of events with
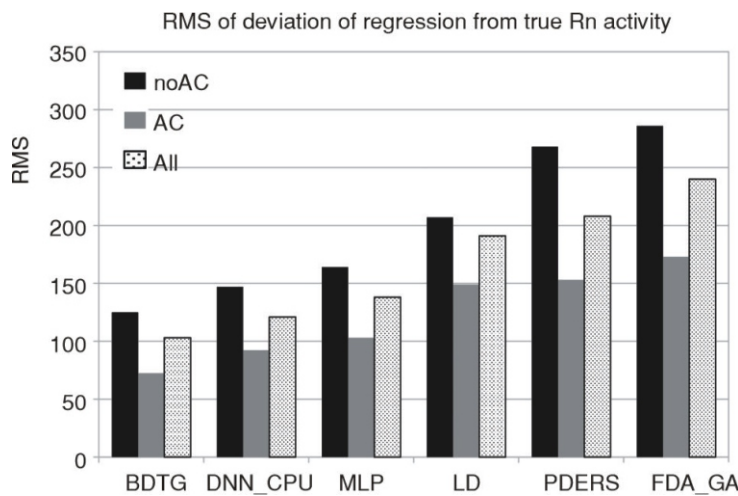

Figure 10. The RMS of deviations of regressions from true value for selected time intervals, AC and noAC, and for the whole time interval, for several MVA regression methods
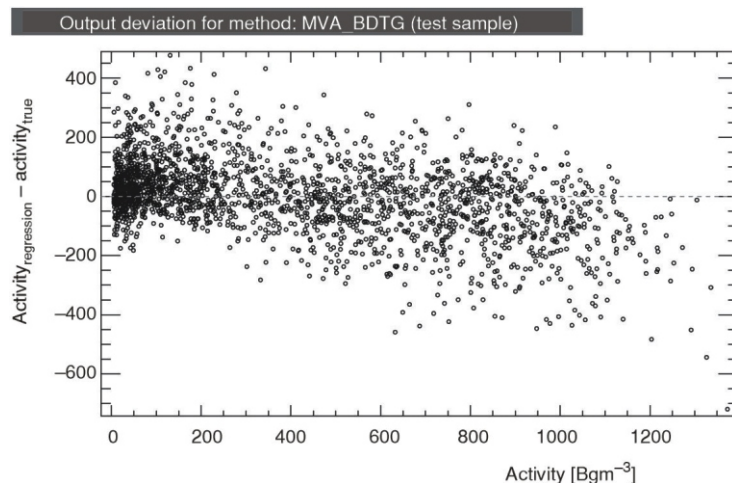

Figure 11. Deviation of regression from true value for noAC period and BDTG MVA method

D. M. Maletić, *et al*., Multivariate Analysis of Two-Year Radon Continuous ...
Nuclear Technology & Radiation Protection: Year 2023, Vol. 38, No. 4, pp. 000-000

9

increased Rn activity (200 Bqm^{-3}) and of events with Rn activity below this value. This initial analysis and looking into variables were showing the expected behavior of Rn concentration with meteorological variables, with emphasis on data periods with or without air conditioning, and also with emphasis on previously found variable of indoor water vapor pressure. This single variate analysis and observing all the data proved also useful for conclusion that GDAS data could be used as a good enough approximate replacement for meteorological data from the nearby meteorological station for MVA analysis. The MVA classification analysis found several very well performing MVA methods which can be used in web application or for further detailed analysis of specific input variables. Variable importance of BDTG MVA method was shown for all three periods, and most important variables were discussed. Finally, MVA regression analysis gave also good results, and more quality measurements in this rarely accessed ground level laboratory would be useful to better tune the MVA methods, and do more detailed analysis.

ACKNOWLEDGMENT

AUTHORS' CONTRIBUTIONS

The original idea and draft were carried out by D. M. Maletić. The data provided by R. M. Banjanac, V. I. Udovičić and Z. Mijić. Statistical analysis was done by D. M. Maletić, D. R. Joković and A. L. Dragić. N. B. Veselinović, M. R. Savić, S. Živković-Radeta and J. V. Udovičić worked on data preparation and selection. All the authors analyzed and discussed the results and reviewed the manuscript.

REFERENCES

[1]   ***, WHO Handbook on Indoor Radon: A Public Health Perspective, World Health Organization, Switzerland, 94, 2009

[2]   Dragić, A., *et al*., The New Set-Up in the Belgrade Low-Level and Cosmic-Ray Laboratory, *Nucl Technol Radiat, 26* (2011), 3, pp. 181-192

[3]   Maletić, D., *et al*., Comparison of Multivariate Classification and Regression Methods for the Indoor Radon Measurements, *Nucl Technol Radiat, 29* (2014), 1, pp. 17-23

[4]   Eremić-Savković, M., *et al.*, Results of the First National Indoor Radon Survey Performed in Serbia, *Journal of Radiological Protection, 40* (2020), 2, pp. N22-N30

[5]   Vukotić, P., *et al*., Influence of Climate, Building, and Residential Factors on Radon Levels in Ground-Floor Dwellings in Montenegro, *Nucl Technol Radiat, 36* (2021), 1, pp. 74-84

[6]   Udovičić, V., *et al*., Multiyear Indoor Radon Variability in a Family House – a Case Study in Serbia, *Nucl Technol Radiat, 33* (2018), 2, pp. 174-179

[7]   Udovičić, V., *et al*., Radon Variability Due to Floor Level in Two Typical Residential Buildings in Serbia, *Nukleonika, 65* (2020), 2, pp. 121-125

[8]   Maletić, D., *et al*., Correlative and Multivariate Analysis of Increased Radon Concentration in Underground Laboratory, *Radiation Protection Dosimetry, 162* (2014), 1-2, pp. 148-151

[9]   Tetens, O., About Some Meteorological Terms (original: Über Einige Meteorologische Begriffe.) *Z. Geophys, 6* (1930) pp. 297-309

[10] Murray, W., On the Computation of Saturation Vapor Pressure, *J. Applied Meteorology, 6* (1967), pp. 203-204

[11] Hoecker, A., *et al*, TMVA – Toolkit for Multivariate Data Analysis. *PoS ACAT, 40* (2009), p. 12

[12] Brun, R., Rademakers, F., ROOT – An Object Oriented Data Analysis Framework, *Nucl. Inst. & Meth. in Phys. Res. A, 389* (1997), pp. 81-86

10

D. M. Maletić, *et al*., Multivariate Analysis of Two-Year Radon Continuous ...
Nuclear Technology & Radiation Protection: Year 2023, Vol. 38, No. 4, pp. 000-000

**Димитрије М. МАЛЕТИЋ, Радомир М. БАЊАНАЦ, Дејан Р. ЈОКОВИЋ,
Александар Л. ДРАГИЋ, Никола Б. ВЕСЕЛИНОВИЋ, Михаило Р. САВИЋ, Зоран МИЈИЋ,
Владимир И. УДОВИЧИЋ Светлана ЖИВКОВИЋ-РАДЕТА, Јелена В. УДОВИЧИЋ**

МУЛТИВАРИЈАНТНА АНАЛИЗА ДВОГОДИШЊЕГ КОНТИНУАЛНОГ МОНИТОРИНГА РАДОНА У НАДЗЕМНОЈ ЛАБОРАТОРИЈИ У ИНСТИТУТУ ЗА ФИЗИКУ У БЕОГРАДУ

Приказана је мултиваријантна класификациона и регресиона анализа односа метеоролошких варијабли и концентрације радона у затвореној и ретко приступачној приземној лабораторији Института за физику Београд. Податке о метеоролошким варијаблама и концентрацији радона, коришћене у овој анализи, добијамо из активног уређаја за краткорочна мереЊа концентрације радона у затвореном простору, ближње метеоролошке станице и из података Глобалног система асимилације података. Једно-варијантном анализом идентификоване су варијабле са највећом вредношћу модула Пирсоновог коефицијента корелације са концентрацијом радона, као и варијабле са највећом моћи раздвајања догађаја са повећаном концентрацијом радона више од (200 Bqm⁻³) и догађаја са нижом концентрацијом од ове вредности. Ова почетна анализа и сагледавање варијабли показују очекивану везу концентрације радона и метеоролошких варијабли, са нагласком на анализу података из различитих временских интервала, када је у лабораторији радила и када није радила климатизација, као и са нагласком на варијаблу разлика унутрашњег и спољњег притиска водене паре. Ова једно-вариантна анализа доводи до закључка да се подаци Глобалног система асимилације података могу користити као довољно добра приближна замена за метеоролошке податке из ближње метеоролошке станице за мултиваријантну анализу. Мултиваријантном класификационом анализом пронађено је неколико веома добрих мулти-варијантних метода које се могу користити у некој веб апликацији или за даљу детаљну анализу специфичних улазних варијабли. Приказана је важност варијабли за мултиваријантни метод стабла одлучивања за сва три периода мерења, а разматране су и најважније варијабле. Коначно, мултиваријантна регресиона анализа је такође дала добре резултате, што може да буде корисно при оптимизацији класификационих мултиваријантних метода.

Кључне речи: континуирани радон мониторинг, мултиваријантна анализа, Глобални систем асимилације података, метеоролошка станица

DE GRUYTER
OPEN

The use of multivariate analysis of the radon variability in the underground laboratory and indoor environment

Jelena Filipović,
Dimitrije Maletić,
Vladimir Udovičić,
Radomir Banjanac,
Dejan Joković,
Mihailo Savić,
Nikola Veselinović

Abstract. The paper presents results of multivariate analysis of variations of radon concentrations in the shallow underground laboratory and a family house, depending on meteorological variables only. All available multivariate classification and regression methods, developed for data analysis in high-energy physics and implemented in the toolkit for multivariate analysis (TMVA) software package in ROOT, are used in the analysis. The result of multivariate regression analysis is a mapped functional behaviour of variations of radon concentration depending on meteorological variables only, which can be used for the evaluation of radon concentration, as well as to help with modelling of variation of radon concentration. The results of analysis of the radon concentration variations in the underground laboratory and real indoor environment, using multivariate methods, demonstrated the potential usefulness of these methods. Multivariate analysis showed that there is a potentially considerable prediction power of variations of indoor radon concentrations based on the knowledge of meteorological variables only. In addition, the online system using the resulting mapped functional behaviour for underground laboratory in the Institute of Physics Belgrade is implemented, and the resulting evaluation of radon concentrations are presented in this paper.

Key words: multivariate analysis • radon variability

J. Filipović, D. Maletić, V. Udovičić✉, R. Banjanac,
D. Joković, M. Savić, N. Veselinović
Institute of Physics Belgrade,
University of Belgrade,
118 Pregrevica Str., 11080 Belgrade, Serbia,
E-mail: udovicic@ipb.ac.rs

Introduction

The research of the dynamics of radon in various environments, especially indoors, is of great importance in terms of protection against ionizing radiation and in designing of measures for its reduction. Research of radioactive emanations (of radon (^{222}Rn) and thoron (^{220}Rn)) are in the domain of radiation physics, but since a few decades ago, subject of radioactive emanation involves many other scientific disciplines, thus giving a multidisciplinary character to this research. Published results and development of many models to describe the behaviour of indoor radon indicate the complexity of this research, especially with models for the prediction of the variability of radon, simply because the variability depends on large number of variables. Large number of factors (such as local geology, permeability of soil, building materials used to build the buildings as well as the habits of people) impact the variation of radon, and therefore, it is important to study their correlation. In this paper, the results of correlative analysis of indoor radon and meteorological variables are presented. Furthermore, the results of multivariate classification and regression analysis is presented. More details of this study can be found in [1].

Indoor radon variation depends significantly on large number of factors, which include the local ge-

ology, soil permeability, building materials, lifestyle characteristics and meteorological variables. In order to analyse the dependence of radon variation on multiple variables, multivariate analysis needs to be used.

The demand for detailed analyses of large amount of data in high-energy physics resulted in wide and intense development and usage of multivariate methods. Many of multivariate methods and algorithms for classification and regression are already integrated into the analysis framework ROOT [2], more specifically, into the toolkit for multivariate analysis (TMVA [3]). Multivariate analysis toolkit is used to create, test and apply all available classifiers and regression multivariate methods implemented in the TMVA in order to find methods that are the most appropriate and yield maximum information on the dependence of indoor radon concentrations on the multitude of meteorological variables. Classification methods are used to find out if it is possible to classify radon concentrations into low and high concentrations, using arbitrary cut value for radon concentrations. Regression methods are used as a next step with a goal to find out which regression method can, if any, on the basis of input meteorological variables only, give an output that would satisfactorily close match the observed variations of radon concentrations. The output of usage of multivariate regression analysis methods is mapped functional behaviour, which can be used to evaluate the measurements of radon concentrations using input meteorological variables only. The prediction of radon concentrations can be an output of mapped function when the prediction of input meteorological variables exists.

Short-term radon measurements in laboratory and real environment

Depending on the integrated measurement time, methods of measurement of radon concentrations in air may be divided into long-term and short-term ones. For the measurements of radon concentration presented in this paper, the SN1029 radon monitor (manufactured by the Sun Nuclear Corporation, NRSB approval-code 31822) has been used as active, short-term measurement device. The device consists of two diffused junction photodiodes as a radon detector and is furnished with sensors for temperature, barometric pressure and relative humidity. The user can set the measurement intervals from 30 min to 24 h. It was set to record simultaneously the radon concentration, temperature, atmospheric pressure and relative humidity.

For the purposes of determining the best multivariate methods to use in the analysis, the results are obtained using radon monitor are from measurements in two locations, the Low-Background Laboratory for Nuclear Physics in the Institute of Physics in Belgrade and in a family house.

The underground Low-Background Laboratory for Nuclear Physics is selected for measurement and analysis because routine measurements in this labo-

ratory require low levels of radon concentration with minimum temporal variations. Low-background laboratory is located on the right bank of the river Danube in the Belgrade borough of Zemun, on the grounds of the Institute of Physics. The ground level portion of the laboratory, at 75 m above sea level, is situated at the foot of a vertical loess cliff, about 10 m high. The underground part of the laboratory, useful area of 45 m^2, is dug into the foot of the cliff. Underground laboratory is surrounded with 30-cm thick concrete wall. The overburden of the underground laboratory is thus about 12 m of loess soil. Significant efforts are being made to contain the low radon concentration within the laboratory. The underground laboratory is completely lined with a hermetically sealed, 1-mm thick aluminium foil. The ventilation system maintains the overpressure of 2 mbar, so as to prevent radon diffusion from the soil. Fresh air entering the laboratory is passed through a two-stage filtering system. The first stage is a mechanical filter for dust removal. The second one is a battery of coarse and fine charcoal active filters. The concentration of radon is kept at an average value of about 10 Bq/m^3.

In the Low-Background Laboratory for Nuclear Physics, radon concentrations were measured in period from 2008 to 2011 and continued later on periodically about a couple of months each year. Measurements of meteorological variables used in the analysis were recorded since 2008 and are taken from the meteorological station located 4 km from the laboratory. Measurements of radon concentrations, room temperature, atmospheric pressure and relative humidity inside the laboratory were obtained using radon monitor. The results obtained from the measurements of radon concentrations and their influence on gamma and cosmic ray measurements in the laboratory were published in several articles in international scientific journals [4–6].

The family house selected for the measurements and analysis of variations of radon concentrations is a typical house in Belgrade residential areas, with requirement of existence of cellar. House is built on limestone soil. Radon measurements were carried out in the living room of the family house, which is built of standard materials (brick, concrete, mortar) and isolated with styrofoam. During the period of measurements (spring–summer), the house was naturally ventilated and air conditioning was used in heating mode at the beginning of the measurement period. During the winter period measurements, the electrical heating was used in addition to air conditioning. Measured radon concentrations, room temperature, atmospheric pressure and relative humidity inside the house were obtained using radon monitor. Values of meteorological variables in measurement period were obtained from an automatic meteorological station located 400 m from the house in which the measurement was performed. We used the following meteorological variables: external air temperature, pressure and humidity, solar radiation, wind speed at a height of 10 m above ground, precipitation, evaporation and temperature and humidity of the soil at a depth of 10, 20, 30 and 50 cm.

Correlation and regression analysis of the results

All multivariate methods implemented in the TMVA are used in our search. All multivariate methods in TMVA belong to the family of 'supervised learning' algorithms [1]. All methods make use of training events, for which the desired output is known, to determine the mapping function that either describes a decision boundary (classification) or an approximation of the underlying functional behaviour defining the target value (regression). Every MVA methods see the same training and test data. The two best performing multivariate methods for our purposes are boosted decision trees (BDT) and artificial neural networks (ANN).

The determination of correlation coefficients between measured radon concentration and meteorological variables serves as a good tool for identifying the variables with strongest correlation, which are not excluded from the analysis later on. Also, correlation coefficient tables gives a good overview of input data and their intercorrelations. In Fig. 1, the correlation matrix of linear correlation coefficients as an overview of intercorrelations of measured radon concentration and all input meteorological variables are shown for underground laboratory. The input variables in case of analysis of underground laboratory are atmospheric pressure, temperature and humidity in laboratory (P_{rm}, T_{rm}, H_{rm}) and outdoor (P, T, H) and differences in measured values of pressure ($P - P_{rm}$), temperature ($T - T_{rm}$) and humidity ($H - H_{rm}$) in laboratory and outdoor. Input meteorological variables in case of family house are the same as the list of measured meteorological variables from nearby meteorological station, with the addition of differences in temperature ($T - T_{rm}$) and humidity ($H - H_{rm}$) from indoor and outdoor values, where indoor measurements results were obtained using radon monitor.

Multivariate methods within the package TMVA in ROOT can search for best multivariate approximation of functional behaviour for the classification function of radon concentration depending on meteorological variables. In the analysis, several mul-

Fig. 2. ROC curve for all multivariate methods in case of house measurements.

tivariate methods were tested, and best performed method was BDT. This can be seen by presenting the receiver operating characteristics (ROC) curve for all tested multivariate methods in case of house measurements (Fig. 2). The BDT method has the highest value of integrated ROC function.

BDT has proven to be the most effective method for the classification of radon concentrations in case of data obtained from the house as well as those obtained from measurements in the Low-Background Laboratory for Nuclear Physics.

The next step in the analysis is the regression analysis, which is the way of finding a mapped function behaviour of dependence of radon concentrations and meteorological input variables. The regression analysis was done using the TMVA packages, already used in classification analysis, and for the same set of measured radon concentration and meteorological variables in underground laboratory and a family house in Serbia. Multivariate method BDT was found to be the best suited for regression analysis also, as was the case in classification analysis.

The data of measured radon concentration in house and BDT evaluated values, using only the values of meteorological variables, without the knowledge of measured values (i.e. in the testing set of multivariate analysis), is presented for comparison in Fig. 3.

One of the possible application of having resulting mapped function, given by multivariate regression analysis, is to have prediction of radon concentration values (evaluated) based on meteorological variables alone. The online application of the regression multivariate analysis can be imple-

Linear correlation coefficients in %

Radon	17	4	25	14	5	1	13	5	-14	100
H-H_mm	-81	13	-73	-94	10	79	-94	-8	100	-14
P-P_mm	9	-15	13	1	15			100	-8	5
T-T_mm	80	-14	77	99	-14	-68	100		-94	13
H	-43	3	-18	-65	3	100	-68		79	1
P	-4	95	-12	-13	100	3	-14	15	10	5
T	86	-13	80	100	-13	-65	99	1	-94	14
H_mm	84	-17	100	80	-12	-18	77	13	-73	25
P_mm	-7	100	-17	-13	95	3	-14	-15	13	4
T_mm	100	-7	84	86	-4	-43	80	9	-81	17
	T_mm	P_mm	H_mm	T	P	H	T-T_mm	P-P_mm	H-H_m	Radon

Fig. 1. Correlation matrix with linear correlation coefficients as an overview of radon and meteorological variables intercorrelations in case of the Low-Background Laboratory for Nuclear Physics.
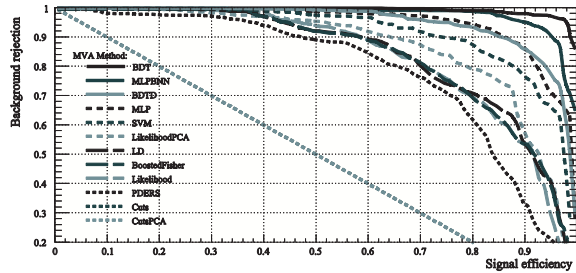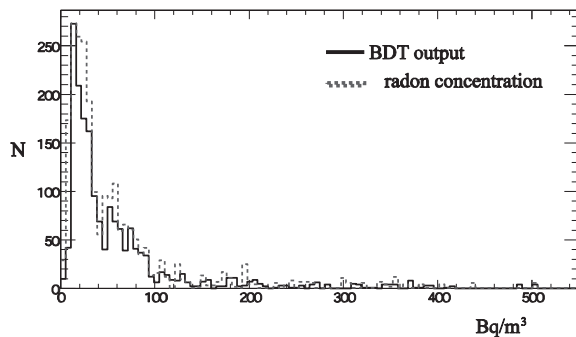

Fig. 3. BDT evaluated (predicted) values of radon concentrations based on meteorological variables using regression analysis within TMVA packages in house (left) and measured values (right).
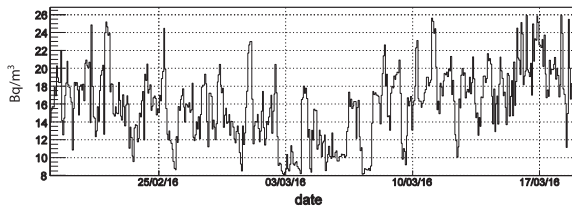
Fig. 4. BDT evaluated (predicted) values of radon concentration, based on meteorological variables alone of underground laboratory posted online and updated daily.

mented, as the one posted online for evaluation (and prediction) based on meteorological variables alone (Fig. 4).

Limitation of multivariate methods

As the multivariate methods used in the analysis are 'supervised learning' algorithms, the performance of the main result of multivariate analysis, the resulting mapped functional behaviour, depends on learning process. Limitation of multivariate analysis in the analysis of radon dependence on meteorological variables are coming from small number of measurements used in learning process, unlike the great number of measurements in high-energy physics experiments. As the next logical step in multivariate analysis presented in this paper should be inclusion of variables such as local geology, permeability of soil, building materials used to build the buildings as well as the habits of people, the requirement for efficient multivariate analysis is to have many measurements in many different houses. Many measurements would help to get good mapped functional behaviour, as opposed to possible existence of theoretical modelling that is independent on number of measurements. In this sense, if the number of measurements is not great, multivariate analysis can be used only as hell to indicate which variables are more important to be used in theoretical modelling, for comparison of mapped and modelled functions, and modelled function test. Another important limitation of multivariate analysis is that no 'straightforward' interpretation of mapped functional behaviour is possible, or simply, the mapped function is a 'black box'. This comes from the fact that the error minimization in learning algorithms, while mapping the functional behaviour, is an important part in learning process.

Conclusions

The paper presents the results of multivariate analysis of variations of radon concentrations in the shallow underground laboratory and a family house, depending on meteorological variables only. This test of multivariate methods, implemented in the

TMVA software package, applied to the analysis of the radon concentration variations connection with meteorological variables in underground laboratory (with ventilation system turned on and off) and typical house in Serbia, demonstrated the potential usefulness of these methods. It appears that the method can be used for the prediction of the radon concentrations, on the basis of predicted meteorological variables. The next step in multivariate analysis presented in this paper should be inclusion of variables such as local geology, permeability of soil, building materials used to build the buildings as well as the habits of people. The requirement for efficient multivariate analysis is to have many measurements in many different houses, which makes multivariate method very useful only when having many measurement, for instance, during radon mapping campaigns. Many measurements would help to get good mapped functional behaviour, as opposed to possible existence of theoretical modelling that is independent on number of measurements. Generally, multivariate analysis can be used to help indicate which variables are more important to be used in theoretical modelling, furthermore, for comparison of mapped and modelled functions, and modelled function test.

Another usage of the results of classification multivariate analysis presented in this paper is the implementation of online warning system for possible increased radon concentration in family houses based on meteorological variables only.

References

1. Maletić, D., Udovičić, V., Banjanac, R., Joković, D., Dragić, A., Veselinović, N., & Filipović, J. (2014). Comparison of multivariate classification and regression methods for indoor radon measurements. *Nucl. Technol. Radiat. Prot*., *29*, 17–23.
2. Hoecker, A., Speckmayer, P., Stelzer, J., Therhaag, J., Von Toerne, E., & Voss, H. (2007). TMVA – Toolkit for Multivariate Data Analysis. *PoS ACAT 040*. arXiv:physics/070303.
3. Brun, R., & Rademakers, F. (1997). ROOT – An Object Oriented Data Analysis Framework. *Nucl. Instrum. Methods Phys. Res. Sect. A-Accel. Spectrom. Dect. Assoc. Equip*. *389*(1/2), 81–86.
4. Udovičić, V., Grabež, B., Dragić, A., Banjanac, R., Joković, D., Panić, B., Joksimović, D., Puzović, J., & Aničin, I. (2009). Radon problem in an underground low-level laboratory. *Radiat. Meas*., *44*, 1009–1012.
5. Udovičić, V., Aničin, I., Joković, D., Dragić, A., Banjanac, R., Grabež, B., & Veselinović, N. (2011). Radon time-series analysis in the Underground Low-Level Laboratory in Belgrade, Serbia. *Radiat. Prot. Dosim*., *145*(2/3), 155–158.
6. Banjanac, R., Udovičić, V., Dragić, A., Joković, D., Maletić, D., Veselinović, N., & Grabež, B. (2013). Daily variations of gamma-ray background and radon concentration. *Rom. J. Phys*., *58*(Suppl.), S14–S21.

Forbush decrease events associated with coronal mass ejections: Classification using machine learning

M.R. Savić [ID]**, N.B. Veselinović, A.L. Dragić, D.M. Maletić, R.M. Banjanac, D.R. Joković, D.Knežević, M.Travar and V.I. Udovičić**

Institute of Physics Belgrade, University of Belgrade, Pregrevica 118, 11080 Belgrade, Serbia (E-mail: msavic@ipb.ac.rs)

Abstract. In presented work we further explore previously indicated possibility of the existence of two classes of Forbush decrease events, established by the prior analysis of the correlation between the shape of energetic proton fluence spectra and Forbush decrease properties. In an attempt to increase statistical robustness of the analysis and potentially reduce the uncertainties, we have developed an alternative classification procedure that employs machine learning and utilizes space weather parameters as input variables. Based on the overall performance, efficiency and flexibility of different machine learning methods we selected the best performing algorithm and established the optimal boundary value of Forbush decrease intensity to be used for class separation. A subset of good input variables was selected based on their predictive power.

Key words: cosmic rays – Forbush decrease – coronal mass ejection – solar energetic particles

1. Introduction

The dynamic activity of the Sun's coronal magnetic field can give rise to complex space weather events. These events may include solar flares (SFs), coronal mass ejections (CMEs), their interplanetary counterparts known as interplanetary coronal mass ejections (ICMEs), the emission of solar energetic particles (SEPs), and similar phenomena (Kahler, 1992; Yashiro & Gopalswamy, 2008; Gopalswamy, 2022).

One such complex event can produce a number of effects in the heliosphere, one of which is the acceleration of solar wind particles. There is a distinction between particles accelerated by a SF in the lower Sun's atmosphere and those accelerated locally by the CME shock. The later are often referred to as energetic storm particles (ESPs) (Desai & Giacalone, 2016).

Additionally, the passage of a CME can affect the primary cosmic rays (CRs) potentially resulting in a sudden drop in the observed CR flux, followed by a

recovery phase that takes place over the several following days. This effect is known as a Forbush decrease (FD) and can be observed by Earth-based CR detectors.

A previous study of the relationship between transient modulations in the fluxes of energetic protons and cosmic rays (measured near and at Earth respectively) indicated an existence of two classes of FD events (Savić et al., 2023). The main objective of this work is to expand this analysis and investigate whether a specific set of space weather (SW) parameters can be successfully used as input parameters for classification. The proposed procedure would aim to separate FD events into classes as indicated by the aforementioned analysis, while increasing the statistical significance and potentially the reliability of the analysis. Additional positive outcome of a successful classification would be the selection of a subset of SW parameters that prove to be good input variables. These variables could then be further used for the prediction of FD magnitudes utilizing some regression algorithm.

2. Motivation

As simultaneous ESP and FD events are very likely a consequence of the passage of an ICME, a relationship between them was assumed. To establish this possible connection, correlation of characteristics of proton fluence spectra and FD parameters was investigated (as described in more detail in Savić et al. (2023)).

The proton fluence spectra were calculated from in situ measurements at L1 by SOHO/ERNE instrument (Torsti et al., 1995), and fitted by a double-power law, as shown for one selected event on Figure 1.

Exponents obtained from these fits were used to parameterize the spectra shape, and some degree of correlation between these exponents and FD magnitudes was established. However, this analysis also indicated a possible existence of two classes of FD events, as illustrated in Figure 2. The plot shows the dependence of the FD magnitude corrected for the magnetospheric effect on one of the proton fluence spectra exponents. The green oval indicates a supposed class of events that exhibit a stronger correlation between these two variables, while the red oval indicates a class of events where this correlation is apparently weaker. One possible way to define the boundary between these two classes could be by introducing a cut on the intensity of the event.

Due to relatively low statistics of events where proton fluence can be reliably determined, one idea for extending this analysis is to try and utilize other space weather parameters in order to increase statistics and more strongly establish the assumed existence of two classes of FD events.
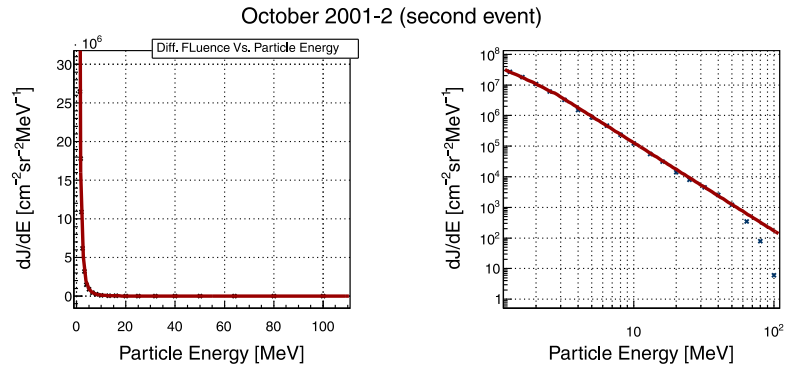
Figure 1. Proton fluence spectra at L1 for one event during October 2001, in linear (left) and logarithmic scale (right).
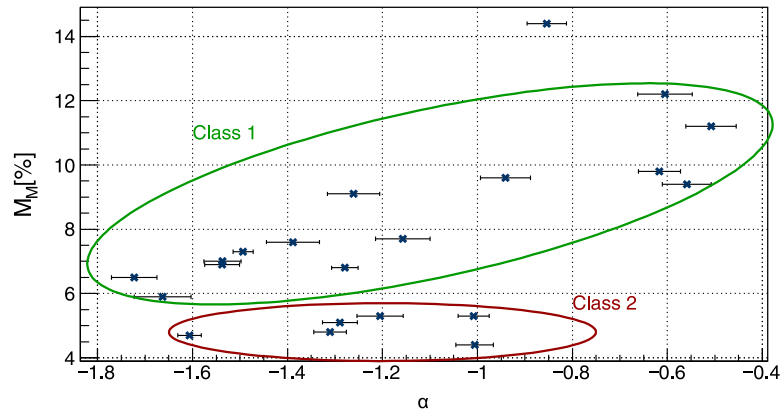

Figure 2. The dependence of the FD magnitude corrected for the magnetospheric effect (M_M) on one of the exponents used to parameterize the proton fluence spectra (α). Two assumed classes of FD events are indicated by the green and red ovals.

3. Methods and Results

IZMIRAN catalogue of Forbush effects (IZMIRAN, 2016) was used as the source of SW related data, as it contains an extensive list of FD events and associated SW parameters. The parameters selected from the IZMIRAN catalogue to be used in the analysis presented here fall into several cathegories: parameters describing the source (Otype, Stype) or the characteristics of the CME (Vmean, CMEwidth); solar wind parameters (Vmax, KTmax, KTmin); parameters describing interplanetary or geomagnetic field (Bzmin, Kpmax, Apmax, Dstmin); and parameters related to the associated solar flare (Xmagn, Sdur, SSN).

Several machine-learning-based classification methods implemented in the TMVA analysis network (Hoecker et al., 2007) were employed in order to establish the optimal FD magnitude for the separation of two classes (boundary criteria mentioned in Section 2), as well as to determine the optimal classification algorithm. Comparing the efficiency of various methods available in the TMVA (shown of Figure 3), it was found that the optimal separation between two classes is achieved with FD magnitude cut set to 6%, as separation efficiency seems to drop-off beyond that for most methods. Support vector machine (SVM) (Cortes & Vapnik, 1995) was identified as the overall best-performing algorithm.
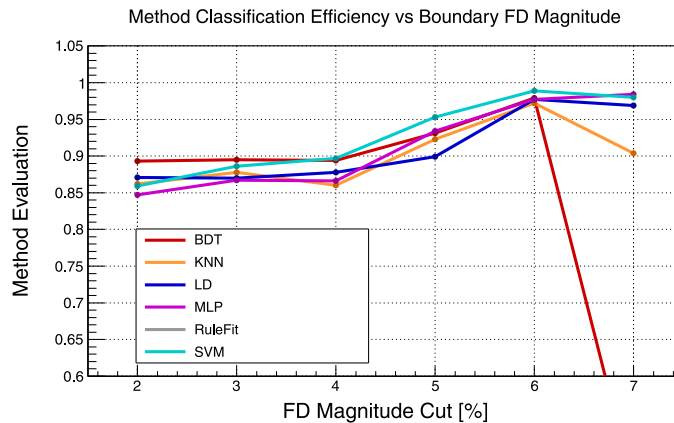
Figure 3. Comparison of the classification efficiency of various TMVA methods dependence on the FD magnitude cut used for class separation.

SVM implementation in the scikit-learn package (Pedregosa et al., 2011) was utilized to identify which of the SW parameters could reliably classify FD events. Third-degree polynomial kernel was found to have the most flexible and efficient performance.
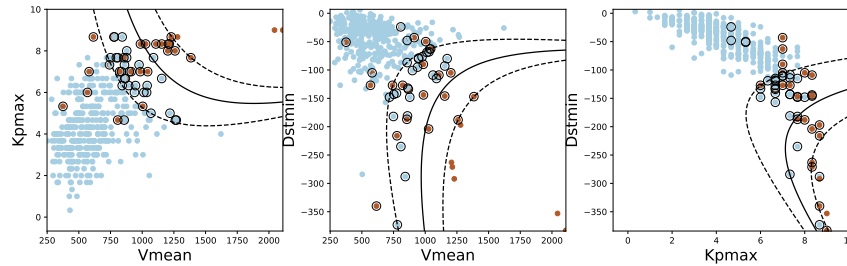
Figure 4. Example of SVM classification using some of SW parameters (mean CME velocity, maximum Kp index and minimal Dst index over the event's duration) that proved to be good input variables for FD classification.

Obtained results appear to confirm the assumption regarding the existence of two classes of FD events. Furthermore, a subset of SW parameters that provide a more reliable classification of FD events was determined. These include mean CME velocity (Vmean) and geomagnetic indices (Kpmax, Apmax, Dstmin), with a possible inclusion of the solar wind speed (Vmax) and minimal hourly component of the interplanetary magnetic field (Bzmin). Decision boundaries between some pairs of mentioned good input variables are showed on Figure 4. Other SW variables proved to be less well suited for classification (as illustrated in Figure 5, for KTmin and KTmax).
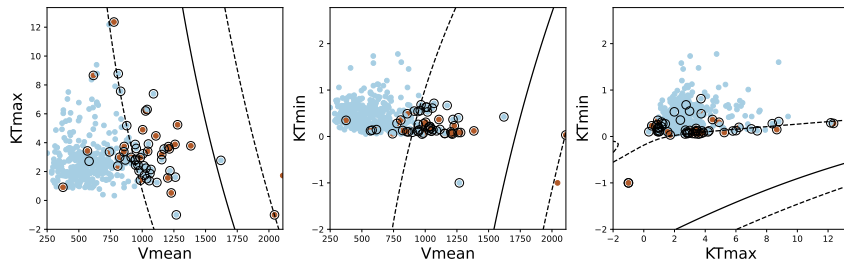
Figure 5. Example of SVM classification using some of SW parameters (KTmax, KTmin) that proved to be less well suited input variables for FD classification.

The identified good variables could prove useful in a potential future extension of the analysis. More specifically, they could serve as an input for a regression procedure that would potentially allow the prediction of FD magnitudes.

This prediction would provide either estimates of FD magnitude as measured by Earth-based detectors or, more importantly, estimates of FD magnitudes corrected for the magnetospheric effect.

4. Conclusions

The potential existence of two classes of FD events was investigated. To increase statistical robustness and reduce uncertainties, the analysis was expanded to include a wider set of various space weather parameters. Machine learning techniques were employed in an attempt to separate FD events into two assumed classes, using a number of selected SW parameters as input variables. We compared the efficiency of different machine learning algorithms, and established the optimal boundary value of FD intensity to be used for class separation. The SVM algorithm was selected for the analysis based on its overall performance, efficiency and flexibility, and used to select a subset of space weather variables to be used for reliable classification of FD events. This subset of good variables variables could prove useful for a future extension of the analysis, where they would provide an input for a regression procedure used to predict FD magnitudes.

References

Cortes, C. & Vapnik, V., Support Vector Networks. 1995, *Machine Learning*, **20**, 273

Desai, M. & Giacalone, J., Large gradual solar energetic particle events. 2016, *Living Reviews in Solar Physics*, **13**, 3, DOI: 10.1007/s41116-016-0002-5

Gopalswamy, N., The Sun and Space Weather. 2022, *Atmosphere*, **13**, DOI: 10.3390/atmos13111781

Hoecker, A., Speckmayer, P., Stelzer, J., et al., TMVA - Toolkit for Multivariate Data Analysis. 2007, *arXiv e-prints*, physics/0703039, DOI: 10.48550/arXiv.physics/0703039

IZMIRAN. 2016, Space weather prediction center (IZMIRAN), http://spaceweather.izmiran.ru/eng/index.html

Kahler, S. W., Solar flares and coronal mass ejections. 1992, *Annual Review of Astron and Astrophys*, **30**, 113, DOI: 10.1146/annurev.aa.30.090192.000553

Pedregosa, F., Varoquaux, G., Gramfort, A., et al., Scikit-learn: Machine Learning in Python. 2011, *Journal of Machine Learning Research*, **12**, 2825

Savić, M., Veselinović, N., Dragić, A., et al., New insights from cross-correlation studies between solar activity indices and cosmic-ray flux during Forbush decrease events. 2023, *Advances in Space Research*, **71**, 2006, DOI: 10.1016/j.asr.2022.09.057

Torsti, J., Valtonen, E., Lumme, M., et al., Energetic Particle Experiment ERNE. 1995, *Solar Physics*, **162**, 505, DOI: 10.1007/BF00733438

Yashiro, S. & Gopalswamy, N., Statistical relationship between solar flares and coronal mass ejections. 2008, *Proceedings of the International Astronomical Union*, **4**, DOI: 10.1017/S1743921309029342

MUON ACCELERATORS FOR PARTICLE PHYSICS — MUON

Performance of the MICE diagnostic system

The MICE collaboration

M. Bogomilov,[a] R. Tsenov,[a] G. Vankova-Kirilova,[a] Y.P. Song,[b] J.Y. Tang,[b] Z.H. Li,[c]
R. Bertoni,[d] M. Bonesini,[d] F. Chignoli,[d] R. Mazza,[d] V. Palladino,[e] A. de Bari,[f] D. Orestano,[g]
L. Tortora,[g] Y. Kuno,[h] H. Sakamoto,[h,1] A. Sato,[h] S. Ishimoto,[i] M. Chung,[j] C.K. Sung,[j]
F. Filthaut,[k,2] M. Fedorov,[l] D. Jokovic,[m] D. Maletic,[m] M. Savic,[m] N. Jovancevic,[n] J. Nikolov,[n]
M. Vretenar,[o] S. Ramberger,[o] R. Asfandiyarov,[p] A. Blondel,[p] F. Drielsma,[p,3] Y. Karadzhov,[p]
G. Charnley,[q] N. Collomb,[q] K. Dumbell,[q] A. Gallagher,[q] A. Grant,[q] S. Griffiths,[q] T. Hartnett,[q]
B. Martlew,[q] A. Moss,[q] A. Muir,[q] I. Mullacrane,[q] A. Oates,[q] P. Owens,[q] G. Stokes,[q]
P. Warburton,[q] C. White,[q] D. Adams,[r] V. Bayliss,[r] J. Boehm,[r] T.W. Bradshaw,[r] C. Brown,[r,4]
M. Courthold,[r] J. Govans,[r] M. Hills,[r] J.-B. Lagrange,[r] C. Macwaters,[r] A. Nichols,[r]
R. Preece,[r] S. Ricciardi,[r] C. Rogers,[r] T. Stanley,[r] J. Tarrant,[r] M. Tucker,[r] S. Watson,[r,5]
A. Wilson,[r] R. Bayes,[s,6] J.C. Nugent,[s] F.J.P. Soler,[s] R. Gamet,[t] P. Cooke,[t] V.J. Blackmore,[u]
D. Colling,[u] A. Dobbs,[u,7] P. Dornan,[u] P. Franchini,[u,*] C. Hunt,[u,8] P.B. Jurj,[u] A. Kurup,[u]
K. Long,[u] J. Martyniak,[u] S. Middleton,[u,9] J. Pasternak,[u] M.A. Uchida,[u,10] J.H. Cobb,[v]
C.N. Booth,[w] P. Hodgson,[w] J. Langlands,[w] E. Overton,[w,11] V. Pec,[w] P.J. Smith,[w]
S. Wilbur,[w] G.T. Chatzitheodoridis,[x,12,13] A.J. Dick,[x,13] K. Ronald,[x,13] C.G. Whyte,[x,13]
A.R. Young,[x,13] S. Boyd,[y] J.R. Greis,[y,14] T. Lord,[y] C. Pidcott,[y,15] I. Taylor,[y,16] M. Ellis,[z,17]

[1]Current address: RIKEN 2-1 Hirosawa, Wako, Saitama, Japan.
[2]Also at Radboud University, Houtlaan 4, Nijmegen, Netherlands.
[3]Current address: SLAC National Accelerator Laboratory, 2575 Sand Hill Road, Menlo Park, CA, U.S.A.
[4]Also at College of Engineering, Design and Physical Sciences, Brunel University, Kingston Lane, Uxbridge, U.K.
[5]Current address: ATC, Royal Observatory Edinburgh, Blackford Hill, Edinburgh, U.K.
[6]Current address: Laurentian University, 935 Ramsey Lake Road, Sudbury, ON, Canada.
[7]Current address: OPERA Simulation Software, Network House, Langford Locks, Kidlington, U.K.
[8]Current address: CERN, Esplanade des Particules 1, Geneva, Switzerland.
[9]Current address: School of Physics and Astronomy, University of Manchester, Oxford Road, Manchester, U.K.
[10]Current address: Rutherford Building, Cavendish Laboratory, JJ Thomson Avenue, Cambridge, U.K.
[11]Current address: Arm, City Gate, 8 St Mary's Gate, Sheffield, U.K.
[12]Also at School of Physics and Astronomy, Kelvin Building, University of Glasgow, Glasgow, U.K.
[13]Also at Cockcroft Institute, Daresbury Laboratory, Sci-Tech Daresbury, Keckwick Ln, Daresbury, Warrington, U.K.
[14]Current address: TNG Technology Consulting, Beta-Strasse 13A, Unterföhring, Germany.
[15]Current address: Department of Physics and Astronomy, University of Sheffield, Hounsfield Rd, Sheffield, U.K.
[16]Current address: Defence Science and Technology Laboratory, Porton Down, Salisbury, U.K.
[17]Current address: Macquarie Group, 50 Martin Place, Sydney, Australia.

R.B.S. Gardener,[z,18] **P. Kyberd,**[z] **J.J. Nebrensky,**[z] **M. Palmer,**[aa] **H. Witte,**[aa] **D. Adey,**[ab,19]
A.D. Bross,[ab] **D. Bowring,**[ab] **P. Hanlet,**[ab] **A. Liu,**[ab,20] **D. Neuffer,**[ab] **M. Popovic,**[ab]
P. Rubinov,[ab] **A. DeMello,**[ac] **S. Gourlay,**[ac] **A. Lambert,**[ac] **D. Li,**[ac] **T. Luo,**[ac] **S. Prestemon,**[ac]
S. Virostek,[ac] **B. Freemire,**[ad,20] **D.M. Kaplan,**[ad] **T.A. Mohayai,**[ad,21] **D. Rajaram,**[ad,22]
P. Snopok,[ad] **Y. Torun,**[ad] **L.M. Cremaldi,**[ae] **D.A. Sanders,**[ae] **D.J. Summers,**[ae,23]
L.R. Coney,[af,24] **G.G. Hanson**[af] **and C. Heidt**[af,25]

[a] *Department of Atomic Physics, St. Kliment Ohridski University of Sofia,*
5 James Bourchier Blvd, Sofia, Bulgaria

[b] *Institute of High Energy Physics, Chinese Academy of Sciences,*
19 Yuquan Rd, Shijingshan District, Beijing, China

[c] *Sichuan University, 252 Shuncheng St, Chengdu, China*

[d] *Sezione INFN Milano Bicocca and Dipartimento di Fisica G. Occhialini,*
Piazza della Scienza 3, Milano, Italy

[e] *Sezione INFN Napoli and Dipartimento di Fisica, Università Federico II,*
Complesso Universitario di Monte S. Angelo, Via Cintia, Napoli, Italy

[f] *Sezione INFN Pavia and Dipartimento di Fisica, Università di Pavia, Via Agostino Bassi 6, Pavia, Italy*

[g] *Sezione INFN Roma Tre and Dipartimento di Matematica e Fisica, Università Roma Tre,*
Via della Vasca Navale 84, Roma, Italy

[h] *Osaka University, Graduate School of Science, Department of Physics,*
1-1 Machikaneyamacho, Toyonaka, Osaka, Japan

[i] *High Energy Accelerator Research Organization (KEK), Institute of Particle and Nuclear Studies,*
Tsukuba, Ibaraki, Japan

[j] *Department of Physics, UNIST, 50 UNIST-gil, Ulsan, South Korea*

[k] *Nikhef, Science Park 105, Amsterdam, Netherlands*

[l] *Radboud University, Houtlaan 4, Nijmegen, Netherlands*

[m] *Institute of Physics, University of Belgrade, Pregrevica 118, Belgrade, Serbia*

[n] *Faculty of Sciences, University of Novi Sad, Trg Dositeja Obradovića 3, Novi Sad, Serbia*

[o] *CERN, Esplanade des Particules 1, Geneva, Switzerland*

[p] *DPNC, Section de Physique, Université de Genève, 24 Quai Ernest-Ansermet, Geneva, Switzerland*

[q] *STFC Daresbury Laboratory, Keckwick Ln, Daresbury, Cheshire, U.K.*

[r] *STFC Rutherford Appleton Laboratory, Harwell Campus, Didcot, U.K.*

[s] *School of Physics and Astronomy, Kelvin Building, University of Glasgow, Glasgow, U.K.*

[t] *Department of Physics, University of Liverpool, Oxford St, Liverpool, U.K.*

[u] *Department of Physics, Blackett Laboratory, Imperial College London, Exhibition Road, London, U.K.*

[v] *Department of Physics, University of Oxford, Denys Wilkinson Building, Keble Rd, Oxford, U.K.*

[w] *Department of Physics and Astronomy, University of Sheffield, Hounsfield Rd, Sheffield, U.K.*

---

[18] Current address: Inawisdom, Columba House, Adastral park, Martlesham, Ipswich, U.K.

[19] Current address: Institute of High Energy Physics, Chinese Academy of Sciences, 19 Yuquan Rd, Shijingshan District, Bejing, China.

[20] Current address: Euclid Techlabs, 367 Remington Blvd, Bolingbrook, IL, U.S.A.

[21] Current address: Fermilab, Kirk Rd and Pine St, Batavia, IL, U.S.A.

[22] Current address: KLA, 2350 Green Rd, Ann Arbor, MI, U.S.A.

[23] Deceased.

[24] Current address: European Spallation Source ERIC, Partikelgatan 2, Lund, Sweden.

[25] Current address: Swish Analytics, Oakland, CA, U.S.A.

*Corresponding author.

^{x} *SUPA and the Department of Physics, University of Strathclyde, 107 Rottenrow, Glasgow, U.K.*

^{y} *Department of Physics, University of Warwick, Gibbet Hill Road, Coventry, U.K.*

^{z} *College of Engineering, Design and Physical Sciences, Brunel University,*
Kingston Lane, Uxbridge, U.K.

^{aa} *Brookhaven National Laboratory, 98 Rochester St, Upton, NY, U.S.A.*

^{ab} *Fermilab, Kirk Rd and Pine St, Batavia, IL, U.S.A.*

^{ac} *Lawrence Berkeley National Laboratory, 1 Cyclotron Rd, Berkeley, CA, U.S.A.*

^{ad} *Illinois Institute of Technology, 10 West 35th St, Chicago, IL, U.S.A.*

^{ae} *University of Mississippi, University Ave, Oxford, MS, U.S.A.*

^{af} *University of California, 900 University Ave, Riverside, CA, U.S.A.*

E-mail: p.franchini@imperial.ac.uk

Abstract: Muon beams of low emittance provide the basis for the intense, well-characterised neutrino beams of a neutrino factory and for multi-TeV lepton-antilepton collisions at a muon collider. The international Muon Ionization Cooling Experiment (MICE) has demonstrated the principle of ionization cooling, the technique by which it is proposed to reduce the phase-space volume occupied by the muon beam at such facilities. This paper documents the performance of the detectors used in MICE to measure the muon-beam parameters, and the physical properties of the liquid hydrogen energy absorber during running.

Contents

1   Introduction

Stored muon beams have been proposed as the basis of a facility capable of delivering lepton-antilepton collisions at very high energy [1, 2] and as the source of uniquely well-characterised neutrino beams [3–5]. In the majority of designs for such facilities the muons are produced from the decay of pions created when an intense proton beam strikes a target. The phase-space volume occupied by the tertiary muon beam must be reduced (cooled) before the beam is accelerated and subsequently injected into a storage ring. The times taken to cool the beam using techniques that are presently in use at particle accelerators (synchrotron-radiation cooling [6], laser cooling [7–9], stochastic cooling [10], electron cooling [11] and frictional cooling [12]) are long when compared with the lifetime of the muon. Ionization cooling [13, 14], in which a muon beam is passed through a material (the absorber) where it loses energy, and is then re-accelerated, occurs on a timescale short compared with the muon lifetime. Ionization cooling is therefore the only technique available to cool the muon beam at a neutrino factory or muon collider. The international Muon Ionization Cooling Experiment (MICE) provided the proof-of-principle demonstration of the ionization-cooling technique [15].

MICE operated at the ISIS Neutron and Muon Source at the STFC Rutherford Appleton Laboratory. The ISIS synchrotron accelerates pulses of protons to a kinetic energy of 800 MeV at 50 Hz. For MICE operation, a titanium target was dipped into the halo of the proton beam at 0.78 Hz. Pions created in the interaction of the beam and target were captured in a quadrupole triplet (see figure 1). A beam line composed of dipole, solenoid, and quadrupole magnets captured muons produced through pion decay and transported the resulting muon beam to the MICE apparatus. The

momentum of the muon beam was determined by the settings of the two dipole magnets D1 and D2. Beams having muon central momenta between 140 MeV/c and 240 MeV/c were used for ionisation cooling studies. The emittance of the beam injected into the experiment was tuned using a set of adjustable diffusers, some made of tungsten and some of brass. The cooling cell was composed of a liquid hydrogen or lithium hydride absorber placed inside a focus coil (FC) module, sandwiched between two scintillating-fibre trackers (TKU, TKD) placed in superconducting solenoids (SSU, SSD). Together, SSU, FC, and SSD formed the magnetic channel. The MICE coordinate system is such that the z-axis is coincident with the beam direction, the y-axis points vertically upwards, and the x-axis completes a right-handed coordinate system.
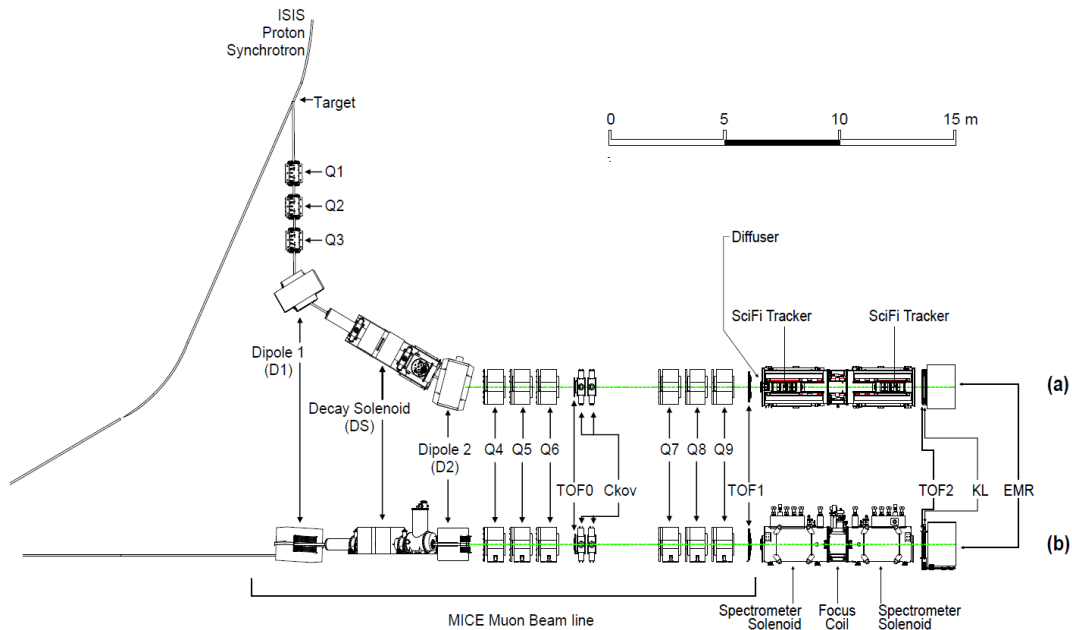
Figure 1. MICE, top (a) and side (b) views, showing the full beam line starting from the target position on the proton synchrotron with the quadrupoles and dipoles (Q1 to Q9, D1, D2), the Decay Solenoid, and instrumented magnetic channel elements (including the trackers upstream, TKU, and downstream, TKD, of the cooling channel, placed inside superconducting solenoids, respectively SSU and SSD) with all the other PID detectors (three TOF stations, two Ckov detectors, KL and the EMR). The cooling cell, defined to be the liquid hydrogen absorber vessel inside the focus coil (FC), is shown in figure 17.

MICE measured the passage of single particles through the apparatus which were aggregated into a beam offline. This paper documents the performance, during 2015-2017, of the instrumentation which was used to fully characterise the beam and its evolution along the magnetic channel, and quantifies the physical properties of the liquid hydrogen absorber. The beam instrumentation consisted of three time-of-flight detectors (TOF0, TOF1, TOF2) discussed in section 2, two threshold Cherenkov counters (CkovA, CkovB) discussed in section 3, a sampling calorimeter (KL) discussed in section 4, a tracking calorimeter (EMR) discussed in section 5, and the scintillating-fibre trackers discussed in section 6. The properties of the liquid hydrogen absorber are described in section 7.

2 Time-of-flight detectors

Three scintillator hodoscopes were used: to measure the time of flight (TOF) of the particles that made up the beam; to measure the transverse position at which the particle crossed each of the detectors; and to provide the trigger for the experiment. TOF0 and TOF1 [16–18] were placed upstream of the magnetic channel, while TOF2 [19] was located downstream of the channel, mounted in front of the KL pre-shower detector (see figure 1). At 240 MeV/c, the difference in the TOF for a muon and a pion between TOF0 and TOF1 was about 1.3 ns. The system was therefore designed to measure the TOF with a precision of 100 ps. This allowed the TOF between the first pair of TOF stations to be used to discriminate between pions, muons, and electrons, contained within the beam, with near 100% efficiency [20]. In addition, by assuming a mass hypothesis for each particle, the TOF measurement was used to infer the particle momentum. The TOF detectors, which operated smoothly during the running periods, were essential for all the measurements that were performed [15, 20–24].

Each TOF station was made of two planes of 1 inch thick scintillator bars oriented along the x and y directions. The bars of TOF0 (TOF1, TOF2) were made of Bricon BC-404 (BC-420) plastic scintillators. A simple fishtail light-guide was used to attach each end of each bar to Hamamatsu R4998 fast photomultiplier tubes (PMTs). Each PMT was enclosed in an assembly that included the voltage divider chain and a 1 mm thick μ-metal shield. For TOF1 and TOF2 an additional soft iron (ARMCO) local shield was also used [25, 26]. The shield was required to reduce the stray magnetic field within the PMT to a negligible level [18]. To increase the count-rate stability, active dividers were used. One TOF detector is illustrated in figure 2.
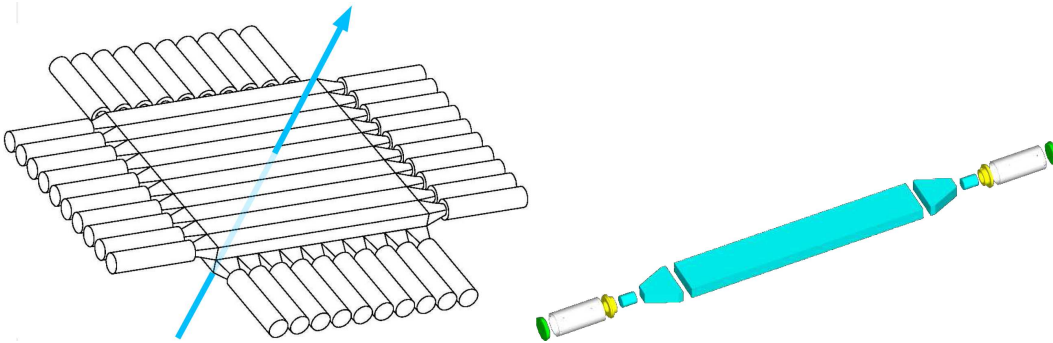

Figure 2. The structure of the time-of-flight detectors [16, 18] showing the horizontal and vertical layers of slabs (left) and an exploded view of each slab (right). The components of each slab are the central scintillator bar, two fishtail, clear plastic light-guides coupled to clear plastic matching pieces, and two PMTs. The beam direction is represented by the blue arrow perpendicular to the slabs.

The active areas of the three hodoscopes were 40×40 cm^2 (TOF0), 42×42 cm^2 (TOF1), and 60×60 cm^2 (TOF2). Each of the planes in TOF0 and TOF2 had 10 slabs while those in TOF1 had 7. A passive splitter was used to take the signal from each of the PMTs to a LeCroy 4115 leading-edge discriminator followed by a CAEN V1290 TDC for time measurement and to a CAEN V1724 FADC for pulse-height measurement. A local readout trigger was issued if the signals from each of the two PMTs on a single slab crossed a specific threshold and overlapped. TOF1 was used to trigger the readout of the experiment for most of the data taking.

Calibration. The intensity of the scintillation light produced when a particle crossed the plastic scintillator rose rapidly before decaying with a characteristic time of 1.8 ns. The scintillation light travelled from the particle-crossing point to each end of the scintillator slab. The light's travel time depended on the distance of the particle crossing from the PMT. The propagation speed of the light pulse along the slabs was determined to be 13.5 cm/ns.

The local readout-trigger signal was distributed to all TDC boards and was used as the reference time. The time between a particle hit in a TOF slab and the time when the trigger was generated varied with the position of the hit along the slab. As a consequence, the reference time had an offset dependent on the crossing position, an effect referred to as the readout-trigger signal delay. To compensate for this, the final time measurement in each station was an average of the times recorded for each channel above threshold.

Further delay was introduced by the signal-transit time of each PMT and of the cable that led the signal to the readout electronics. These signal-transit times were unique for each individual readout channel and were determined by dedicated measurements. The use of a linear, leading-edge discriminator led to a correlation between the total charge in the pulse and the time at which the discriminator fired. This correlation, referred to as the time-walk, introduced a systematic offset in the time recorded by the TDC that was dependent on the pulse height.

Precise determination of the TOF required a calibration procedure that allowed channel-by-channel variations in the response of the system to be accounted for. The calibration procedure described in [27] accounted for each of the effects identified above.

Reconstruction. A particle crossing a TOF station passed through two orthogonal slabs. Signals from each PMT were corrected for time-walk, readout-trigger signal delay, and the channel-specific delays. The slab-crossing time was taken to be the average of the corrected PMT times. Two slab signals were taken to have been produced by the passage of a particle if their slab-crossing times were within a 4 ns window. These two *matched* slabs were used to define a pixel of area given by the width of the slabs. The particle-crossing time was then determined as the average of the slab-crossing times and the approximate position of the particle crossing was refined using the PMT signals in the two orthogonal slabs.

Performance. The difference, Δt, between the slab-crossing times for *matched* slabs was used to determine the intrinsic time resolution, σ_t of the TOF system. The Δt resolution, $\sigma_{\Delta t}$, is given by $\sigma_{\Delta t} = 2\sigma_t$, assuming that the intrinsic resolution is the same in each of the planes that make up a particular TOF station. Figure 3 shows the distributions of Δt for TOF0, TOF1, and TOF2 for a representative set of data taken in 2017. The RMS width of the distributions are 114 ps, 126 ps, and 108 ps for TOF0, TOF1, and TOF2 respectively. The distributions are similar, and the RMS of each distribution is consistent with the measured intrinsic resolution of approximately 60 ps [18].

Figure 4 shows an example distribution of the measured TOF between TOF0 and TOF1. The TOF peaks characteristic of electrons, muons, and pions are clearly separated. The width of the electron peak is approximately 0.10 ns, consistent with the spread calculated from a naive quadrature addition of the timing resolution of the individual TOF stations.
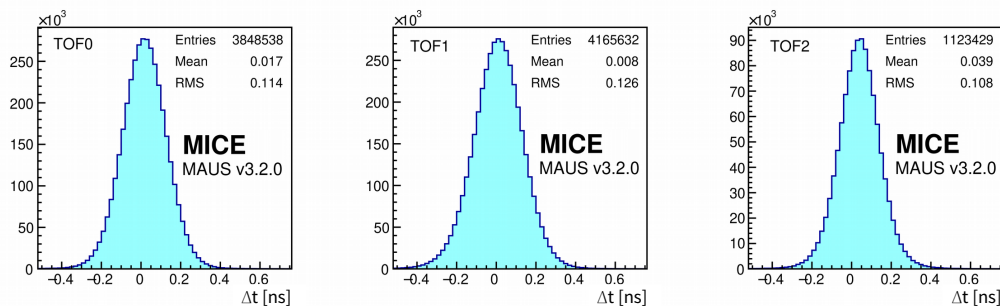
Figure 3. Slab Δt distributions. Total width of the distribution is due to the resolution of the individual channels and due to the offsets in their Δt distributions.
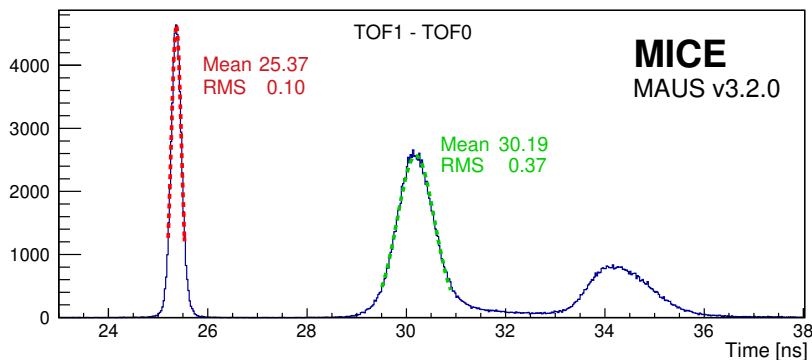

Figure 4. Time of flight between TOF0 and TOF1 after all corrections have been applied. The electron (left-most peak, shown in red), the muon (central peak, shown in green), and the pion (right-most peak, shown in blue) peaks are clearly separated.

3 Cherenkov detectors

The threshold Cherenkov counters were designed to distinguish muons from pions at particle momenta $\gtrsim 200\,\mathrm{MeV}/c$, where the precision of the time-of-flight measurement was not sufficient for conclusive identification. Two high-density silica aerogel Cherenkov detectors with refractive indices $n=1.07$ (CkovA) and $n=1.12$ (CkovB) were used [28]. The structure of the detectors is shown in figure 5. Light was collected in each counter by four eight-inch, UV-enhanced PMTs and recorded using CAEN V1731 FADCs [29]. The two detectors were placed directly one after the other in the beamline and located just after TOF0.

The refractive indices of CkovA and CkovB result in detection thresholds for muons of approximately 280 MeV/c and 210 MeV/c respectively. For pions, the thresholds are approximately 367 MeV/c (CkovA) and 276 MeV/c (CkovB). MICE was designed to operate using beams with a central momentum between 140 MeV/c and 240 MeV/c. The Cherenkov counters' thresholds were chosen to provide muon identification for beams of 210 MeV/c and above, while the TOFs provide muon identification for beam below 210 MeV/c. Unambiguous identification of particle species using the Cherenkovs exploited the momentum measurement provided by the trackers.
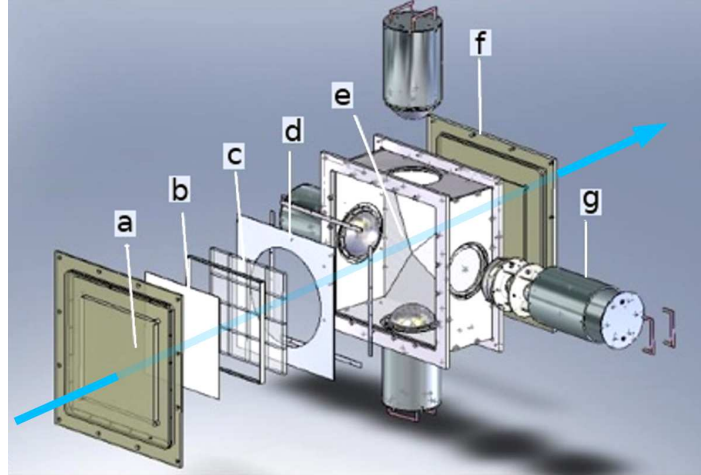
Figure 5. MICE aerogel Cherenkov counter: a) entrance window, b) mirror, c) aerogel mosaic, d) acetate window, e) GORE DRP reflector panel, f) exit window and g) eight-inch PMT in iron shield. The beam direction is represented by the blue arrow traversing the detector.

Performance. The performance of the detectors was determined using beams for which the momentum range was broad enough to observe the turn-on points and to allow the asymptotic light yields (as the particle velocity divided by the speed of light, β, approaches 1) to be obtained from fits to the data. The normalised photo-electron yields observed in CkovA and CkovB are plotted as a function of $\beta\gamma$ (where $\gamma = (1 - \beta^2)^{-\frac{1}{2}}$) in figure 6. The pedestal in the photo-tube response arising from background photons has been subtracted. The approximate turn-on points for CkovA and CkovB were found at $\beta\gamma \approx 2.6$ and ≈ 2.1 respectively, corresponding to refractive indices of $n \approx 1.07$ and ≈ 1.11 which are in broad agreement with the properties of the aerogel radiators.
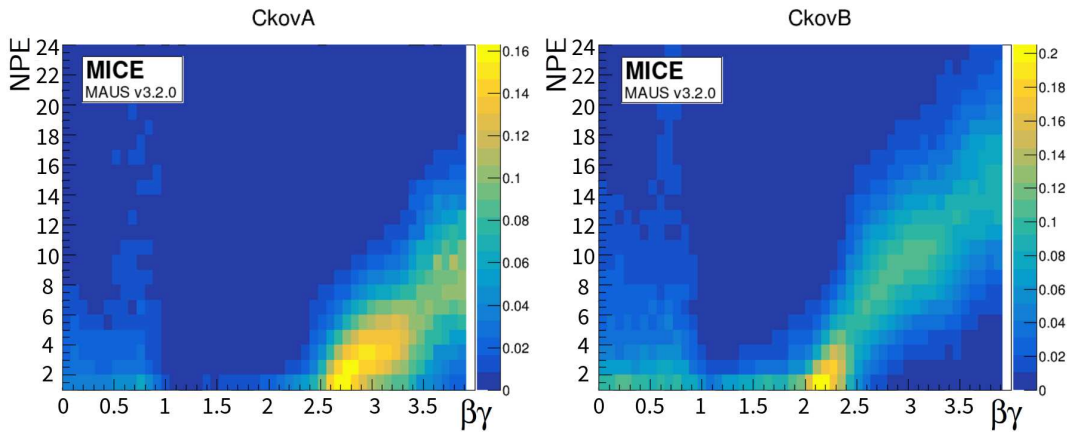
Figure 6. Photoelectron yields versus $\beta\gamma$ in CkovA and CkovB, where βc is the particle velocity and $\gamma = (1 - \beta^2)^{-\frac{1}{2}}$.
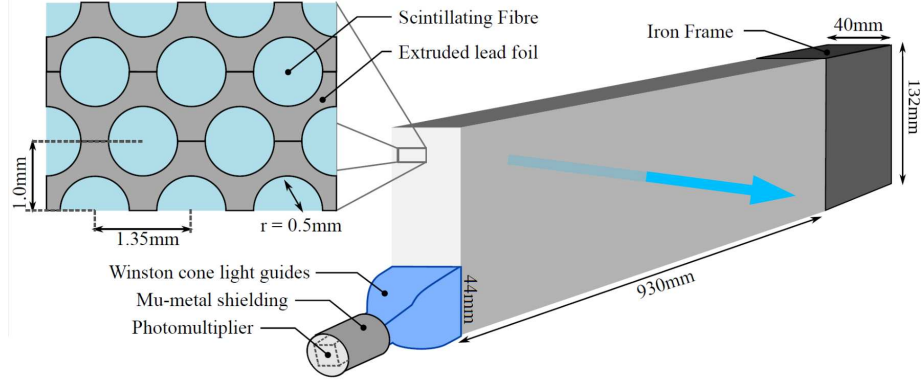
Figure 7. Single slab design of MICE KLOE-Light Calorimeter [31]; only one of the six PMT assemblies is shown. The beam direction is represented by the blue arrow traversing the slab.

4 KLOE-light calorimeter

The KLOE-Light (KL) pre-shower sampling calorimeter was composed of extruded lead foils in which scintillating fibres were placed. At normal incidence the thickness of the detector was 2.5 radiation lengths. The detector provided energy deposition and timing information and was used to distinguish muons from decay electrons [20]. The KL consisted of a series of layers of 1 mm diameter BICRON BCF-12 scintillating fibres embedded in an appropriately shaped lead sheets (see figure 7). Each fibre was separated by 1.35 mm from its neighbours within a layer and the distance between the centres of the fibres in adjacent layers was 0.98 mm. One layer was shifted by half the fibre pitch with respect to the next. The volume ratio of scintillator to lead was approximately 2:1, "lighter" than the ratio of 1:1 used in the similar calorimeter of the KLOE experiment [30]. Lead/scintillator layers were stacked into slabs, 132 mm in depth. A total of 7 slabs formed the whole detector, which had an active volume of 93 cm×93 cm×4 cm. Scintillation light was guided from each slab into a total of six PMTs (three at each end). Iron shields were fitted to each photomultiplier to mitigate the effect of stray magnetic fields. The signal from each PMT was sent to a shaping amplifier module that stretched the signal in time to match the sampling rate of the CAEN 1724 FADCs.

Performance. To study the response of the KL, the particle momentum was determined from the measured time-of-flight between TOF0 and TOF1. To compensate for the effect of attenuation the performance was evaluated in terms of the "ADC product" given by:

$$\text{ADC}_{\text{prod}} = \frac{2 \times \text{ADC}_{\text{left}} \times \text{ADC}_{\text{right}}}{(\text{ADC}_{\text{left}} + \text{ADC}_{\text{right}})} \; ; \qquad (4.1)$$

where ADC_{left} and $\text{ADC}_{\text{right}}$ are the signals from the two ends of a slab and the factor of 2 is present for normalisation. Data was taken with no field in the spectrometer solenoids or the focus coil at beam-momentum settings chosen to span the range of momenta used during MICE running. The resulting momentum distributions were centred at 140, 170, 200, 240, and 300 MeV/c. The response of the KL to muons and pions was observed to increase with beam momentum.
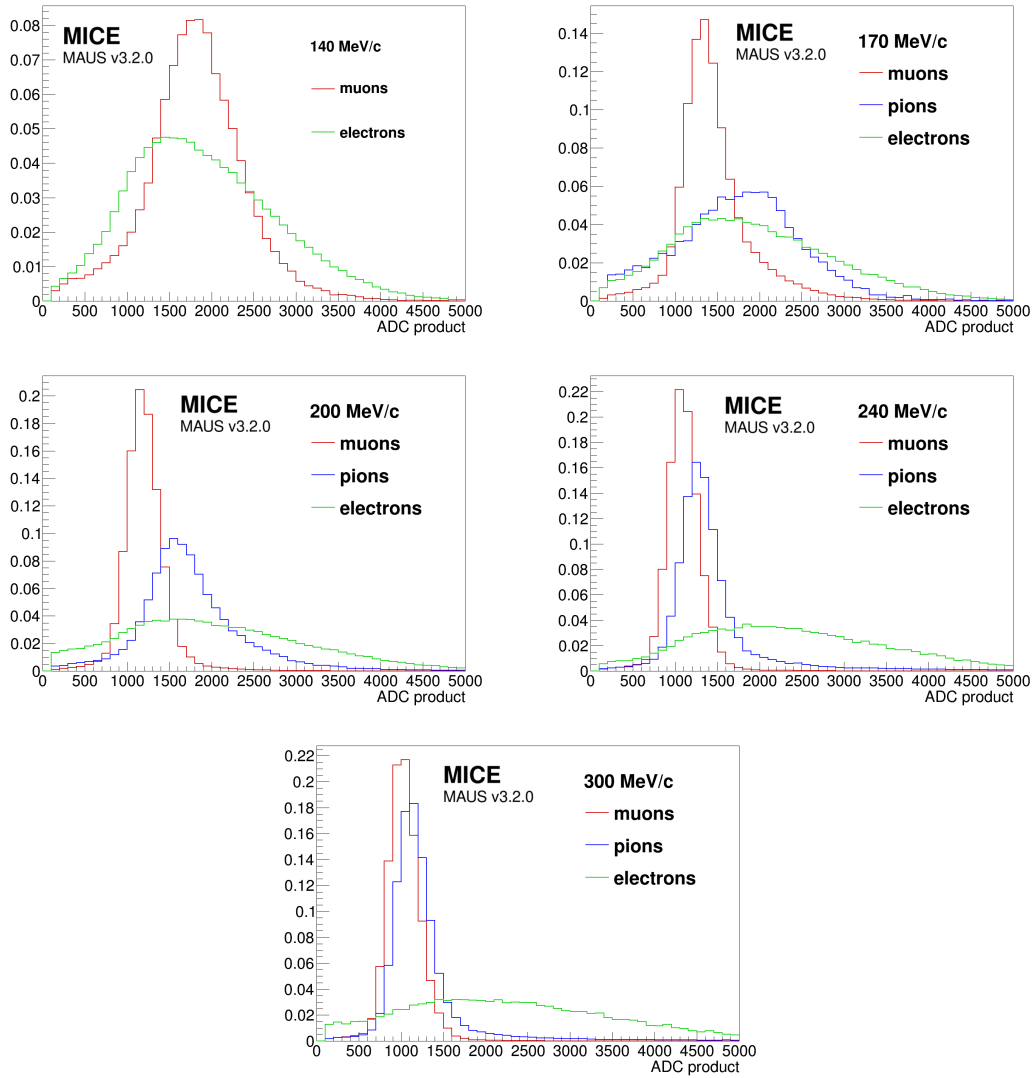
Figure 8. Comparison of ADC products of muons (red), pions (blue) and electrons (green) traversing the KL, at 140 MeV/c (top left), 170 MeV/c (top right), 200 MeV/c (middle left), 240 MeV/c (middle right) and 300 MeV/c (bottom).

Figure 8 presents a comparison of the response to muons, pions and electrons for various beam momentum settings. At high momentum, for example 300 MeV/c, the ADC product distributions for muons and pions are similar. At lower momentum the distributions become increasingly dissimilar, the pions having a broader distribution arising from hadronic interactions. The difference between the detector's response to pions and muons has been exploited to determine the pion contamination in the muon beams used for the MICE cooling measurements [20].

The ADC product distribution measured using a 300 MeV/c beam is compared to the MAUS [32] simulation of the detector response in figure 9. The simulation takes into account
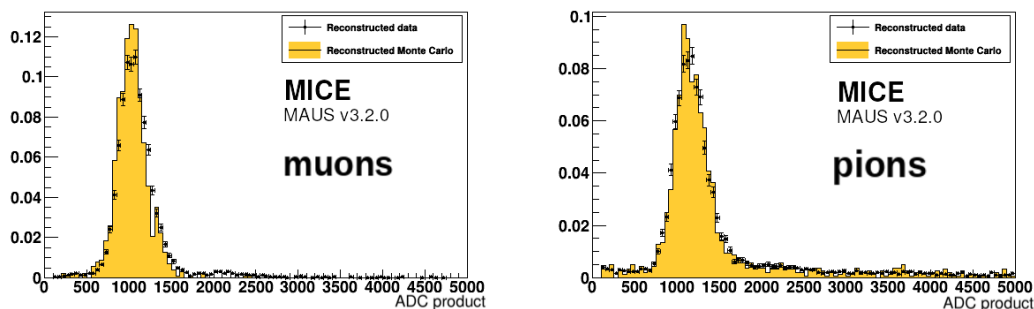
Figure 9. Comparison between data and Monte Carlo simulation of KL response to muons (left) and pions (right) at 300 MeV/c.

the light production distribution of the scintillating fibres, and the response of the PMTs for which the gain was approximately 2×10^6. The data is well described by the simulation.

5   Electron muon ranger

The EMR was a fully-active scintillator detector [33] with a granularity that allowed track reconstruction. The EMR consisted of extruded triangular scintillator bars arranged in planes. Each plane contained 59 bars and covered an area of $1.27 \, \text{m}^2$. Figure 10 shows the bar cross section and the arrangement of the bars in a plane. Triangular bars were chosen so that tracks moving parallel to the detector axis could not travel along the gaps between bars. Successive planes were mounted perpendicularly, so that hits in neighbouring planes defined a position. A single "X-Y module" was a pair of orthogonal planes. The scintillation light was collected using a wavelength shifting (WLS) fibre glued inside each bar. At each end, the WLS fibre was coupled to clear fibres that transported the light to a PMT. All the WLS fibres from one edge of a plane were read out using one single-anode PMT (SAPMT) so that an integrated charge measurement could be used to determine the energy deposited in the plane. The signals from the fibres emerging from the other edge of the plane were recorded individually using multi-anode PMTs (MAPMTs). The full detector was made up of 24 X-Y modules giving a total active volume of approximately $1 \, \text{m}^3$.

Measurements of the performance of the completed detector demonstrated an efficiency per plane of $99.73 \pm 0.02\%$ [33, 34]. The level of crosstalk was within acceptable values for the type of MAPMT used, with an average of $0.20 \pm 0.03\%$ between adjacent channels and a mean amplitude equivalent to $4.5 \pm 0.1\%$ of the primary signal. Only four dead bars were present.

The primary purpose of the EMR was to distinguish between a muon that crossed the entire magnetic channel and those which decayed in flight producing an electron. Muons and electrons exhibited distinct behaviours in the detector. A muon produced a single straight track before either stopping or exiting the scintillating volume. Electrons showered in the lead of the KL and created a broad cascade of secondary particles. Two main geometric variables, the "plane density" and the "shower spread", were used to differentiate them. The detector was capable of identifying electrons with an efficiency of 98.6%, providing a purity for the MICE beam that exceeds 99.8%.
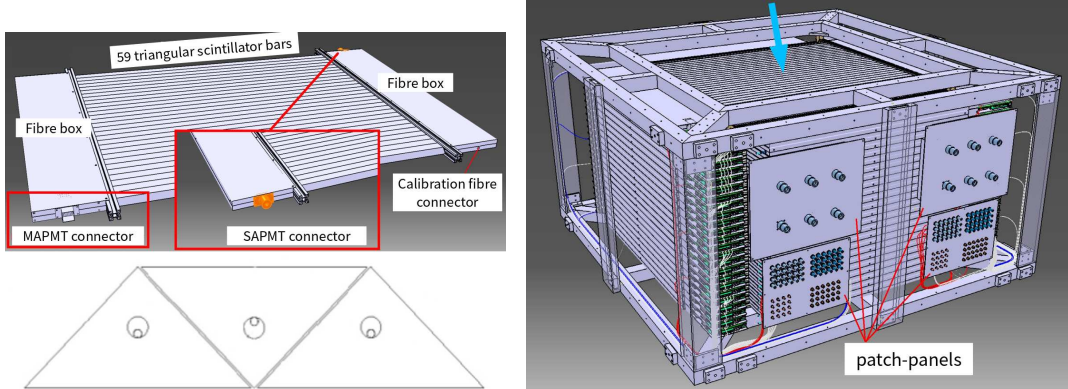
Figure 10. Drawing of one EMR plane (top left), cross section of the arrangement of 3 bars and their wavelength shifting fibres (bottom left) and drawing of the full detector and its supporting structure from a top perspective (right). The beam direction is represented by the blue arrow perpendicular to the detector.

The EMR also proved to be a powerful tool for the reconstruction of muon momenta in the range 100–280 MeV/c [23].

Performance. A full description of the detector and the reconstruction algorithms used may be found in reference [23]. Here the performance of the EMR detector over the course of the experiment is summarised.

To measure the performance of the EMR the MICE beamline was set to deliver a nominal momentum of 400 MeV/c. This maximised the muon transmission to the EMR and its range in the detector. In this configuration the beamline produced pions and muons in comparable quantities, as well as a smaller number of electrons. Time-of-flight between TOF1 and TOF2 was used to identify particle species and only particles compatible with the muon hypothesis were included in the analysis. Particles entering the muon sample had a momentum larger than 350 MeV/c at the upstream surface of TOF2 and were expected to cross both TOF2 and the KL and penetrate the EMR. 99.62 ± 0.03% of the particles entering TOF2 were observed to produce hits in the EMR. The small inefficiency may be attributed to pions in the muon sample that experienced hadronic interactions in the KL. If hits were produced in the detector, an (x, y) pair, defining a space point, was reconstructed 98.56 ± 0.06% of the time.

To evaluate the efficiency of the scintillator planes, only the muons that traversed the entire detector were used. Muons were selected which produced a hit in the most downstream plane. For these events a hit was expected in at least one bar in each plane on its path. The mode of the hit-multiplicity distribution per plane was one, in 3.26 ± 0.02% of cases a plane traversed by a muon did not produce a signal in the MAPMT, and the probability that the track was not observed in the SAPMT was 1.88 ± 0.01%.

Electron rejection. A broad range of beamline momentum settings was used to characterise the electron-rejection efficiency. Particle species were characterised upstream of the EMR using the time-of-flight between TOF1 and TOF2. For each momentum setting, a fit was carried out to determine the position of the muon and electron time-of-flight peaks and events were selected

accordingly to form muon and electron-template samples. Particles with a time-of-flight larger than the upper limit of the muon sample were either pions or slow muons and were rejected.

To distinguish the muon tracks from the electron-induced showers, two particle-identification variables were defined based on the distinct characteristics of the two particle species. The first is the plane density, ρ_p:

$$\rho_p = \frac{N_p}{Z_p + 1},\tag{5.1}$$

where N_p is the number of planes hit and Z_p the number of the most downstream plane [23]. A muon deposits energy in every plane it crosses until it stops, producing a plane density close to one. An electron shower contains photons that may produce hits deep inside the fiducial volume without leaving a trace on their path, reducing the plane density. The second variable is the normalised $\hat{\chi}^2$ of the fitted straight track given by

$$\hat{\chi}^2 = \frac{1}{N - 4} \sum_{i=1}^{N} \frac{\text{res}_{x,i}^2 + \text{res}_{y,i}^2}{\sigma_x^2 + \sigma_y^2};\tag{5.2}$$

where N is the number of space points (one per bar hit), $\text{res}_{q,i}$ the residual of the space point with respect to the track in the qz projection and σ_q the uncertainty on the space point in the qz projection, $q = x,\ y$ [35]. This quantity represents the transverse spread of the hits produced by the particle in the EMR. A muon produced a single track giving $\hat{\chi}^2$ close to one, while an electron shower produced a larger value. The two discriminating variables can be combined to form a statistical test on the particle hypothesis. Dense and narrow events will be tagged as muons while non-continuous and wide showers will not. The quality of this statistical test was characterised in terms of the fraction of the muon sample that is rejected, α, and the fraction of the electron sample that is selected, β.

The momentum of the particles was measured by the downstream tracker and this information used to determine the momentum dependence of the contamination and loss in the range 100–300 MeV/c. Figure 11 shows the loss, α, and the contamination, β, as a function of the momentum measured in TKD. α increases towards low muon momentum. This is due both to an increase in the decay probability between TOF2 and the EMR and a decrease in the number of muons that cross the KL to reach the EMR.

6 Tracking

The MICE instrumentation allowed individual particles to be tracked from TOF0 to the EMR, a distance of more than 15 m. High-resolution particle tracking was provided by two scintillating-fibre trackers (section 6.1). The precise relative alignment of the time-of-flight hodoscopes and the trackers was obtained by combining the measurements of both detector systems (section 6.2).

6.1 Trackers

The two high-precision scintillating-fibre trackers each had a sensitive volume that was 110 cm in length and 30 cm in diameter [36]. Each tracker was composed of five stations (labelled 1 to 5, with station 1 being closest to the cooling cell) held in position using a carbon-fibre space-frame. Adjacent stations were separated by different distances ranging from 20 cm to 35 cm. The
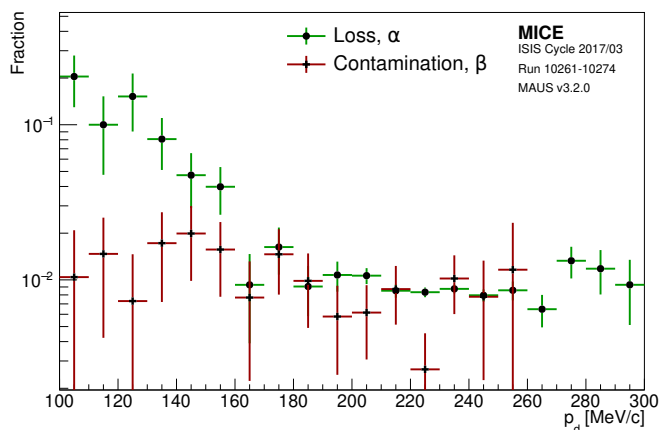
Figure 11. Percentage of electron contamination, β, and muon loss, α, for different ranges of momentum measured in the downstream tracker, p_d. The error bars are based on the statistical uncertainty in a bin, and the bin width set by the resolution of the measurement.

Figure 12. Photograph, with UV-filtered light, of one of the MICE trackers, showing the five stations. Each station has three doublet planes of scintillating fibres, each plane at 120° to the next (the central fibres of each plane can be seen as darker lines traversing the station).

separations were chosen to ensure that the azimuthal rotation of track position did not repeat from one station to the next. This property was exploited in the ambiguity-resolution phase of the pattern recognition. Each tracker was instrumented with an internal LED calibration system and four 3-axis Hall probes to monitor the field. A photograph of one of the trackers on the bed of the coordinate measuring machine used to verify the mechanical alignment of the stations is shown in figure 12.

Each tracker station consisted of three doublet layers of 350 µm scintillating fibres; these layers were arranged such that each was set at an angle of 120° with respect to the next. This arrangement ensured that there were no inactive regions between adjacent fibres. Fibres were grouped into one bundle of seven for each readout channel, to match the resolution to that imposed by multiple scattering and reduce the overall number of readout channels. This resulted in a spatial resolution per doublet layer of 470 µm and a measured light yield of approximately 10 photo-electrons [36].

The light from the seven scintillating fibres was coupled into a single clear fibre which took it to a visible light photon counter (VLPC) [37]. The signals from the VLPCs were digitised using electronics developed by the D0 collaboration [38].

Reconstruction.   The reconstruction software for the trackers is described in [39]. Each of the 15 doublet layers provided 214 readout channels. Calibration data taken without beam was used to determine the pedestal and the gain of each channel. These calibrations were used to correct the number of photoelectrons (NPE) corresponding to the signal recorded by the tracker electronics. The first step in the reconstruction was to record the unique channel number associated with each NPE value in a "digit". Digit profiles were used to identify hot or dead channels which were masked from the reconstruction to reduce the rate of ambiguities that had to be resolved in the pattern recognition and to ensure the accuracy of the calibration. The reconstruction proceeded to create "spacepoints" from the intersection of digits in adjacent doublet layers. Spacepoints were constructed from clusters from all three planes (a triplet spacepoint) or from any two out of the three planes (a doublet spacepoint). The pattern-recognition algorithm searched for spacepoints from neighbouring stations that were consistent with the helical trajectory of a charged particle in the solenoidal field. In the final stage of the tracker reconstruction the track parameters were estimated using a Kalman filter.

Noise.   Digits above a certain NPE threshold were admitted to the spacepoint-finding algorithm. Noise in the electronics arising from, for example, the thermal emission of electrons, could give rise to digits passing the threshold. Any digit not caused by the passage of a charged particle was classified as noise. To isolate noise from signal during beam-on data collection, events containing a track which included a spacepoint in each of the five tracker stations were selected. All digits corresponding to the track were removed from the total set of digits and the remainder were considered to be noise. The average noise rate per channel per event was then calculated as the total number of digits above the NPE threshold divided by the number of active channels and the number of events in the sample. The result of this calculation was that, for an NPE threshold of 2, the fraction of digits arising from noise was 0.18% in the upstream tracker and 0.06% in the downstream tracker.

Track-finding efficiency.   The track-finding efficiency was determined using a sample of events for which the time-of-flight determined from hits in TOF1 and TOF2 was consistent with passage of a muon. This requirement ensured that the particle had been transmitted successfully through the magnetic channel, crossing both trackers. The track-finding efficiency was defined to be the number of events in which a track was successfully reconstructed divided by the total number of events in the sample. The results of the efficiency analysis are tabulated in table 1 for a range of nominal beam momentum and emittance settings. The track-finding efficiency obtained in this way averaged over beam conditions was 98.70% for the upstream tracker and 98.93% for the downstream tracker. The spacepoint-finding efficiency, defined as the number of spacepoints found divided by the number of space points expected, was also determined. The spacepoint-finding efficiency is summarised for a range of beam conditions in table 2.

The efficiency of the trackers over the data taking period was evaluated by selecting events with a measured time-of-flight between TOF1 and TOF2 consistent with the passage of a muon. Events were required to contain at least one hit within the fiducial volume of the tracker. An event was added to the numerator of the efficiency calculation if it contained a single space point in each of

Table 1. The track finding efficiency for the upstream and downstream trackers for 140 MeV/c and 200 MeV/c beams, and for 3, 6 and 10 mm nominal emittances.

Momentum	Emittance	Upstream tracks found	Downstream tracks found
200 MeV/c	3 mm	98.38%	99.19%
200 MeV/c	6 mm	99.42%	96.07%
140 MeV/c	6 mm	98.37%	99.16%
140 MeV/c	10 mm	98.47%	98.93%
Average		98.70%	98.21%

Table 2. The spacepoint-finding efficiency, in the presence of a track, for the upstream and downstream trackers for 140 MeV/c and 200 MeV/c beams, and for 3, 6 and 10 mm nominal emittances.

Momentum	Emittance	Upstream spacepoints found	Downstream spacepoints found
200 MeV/c	3 mm	98.04%	97.41%
200 MeV/c	6 mm	99.41%	94.63%
140 MeV/c	6 mm	97.99%	99.16%
140 MeV/c	10 mm	98.07%	97.44%
Average		98.44%	97.01%

the five tracker stations. The evolution of the tracking efficiency in the upstream and downstream trackers is shown in figure 13. The efficiency is shown separately for data taken in the presence of a magnetic field ("helical") and with the solenoids turned off ("straight"). The data shows that the efficiency was generally greater than 99.0%. Water vapour ingress to the cold end of the VLPC cassettes caused the loss of channels and contributed to a reduction in the tracking efficiency. This was recovered by warming and drying the VLPCs.

Track-fit performance. Monte Carlo simulation with realistic field, beam conditions and detector geometry was used to estimate the performance of the track fit. A beam centred at 140 MeV/c with 10 mm nominal emittance, representing a typical data set, was used for the study. Results are presented in figure 14 for the upstream tracker and figure 15 for the downstream tracker. The resolution in the total momentum and transverse momentum is observed to be ~ 1.1 MeV/c independent of momentum in the range 120 MeV/c to 160 MeV/c. The small bias in the transverse and the total momentum did not give rise to significant effects in the analysis and was considered in systematic error studies.

6.2 Beam-based detector alignment

A beam-based alignment algorithm was developed to improve the resolution on the position of the scintillating-fibre trackers relative to the time-of-flight hodoscopes. The starting point for the beam-based alignment was the geometrical survey of the detectors in the MICE Hall which was performed using laser geodesy. Survey monuments on the TOF frames were surveyed with respect
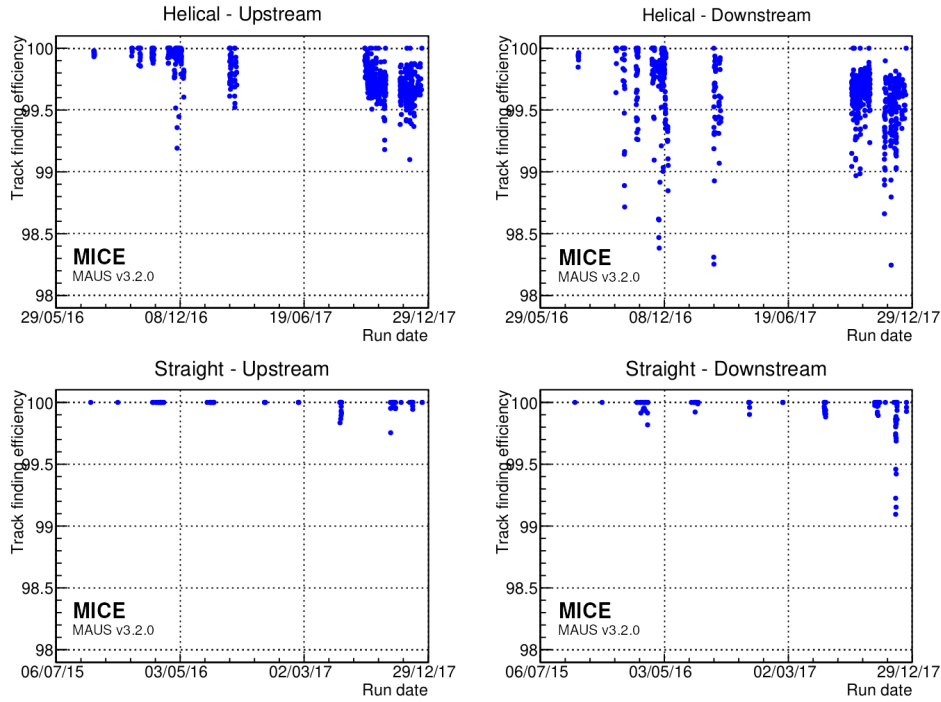
Figure 13. Evolution of the straight and helical track finding efficiencies over time for: the upstream (left); and downstream (right) trackers during the key periods of data taking since 2015. Each dot represents a single data taking run between 10 minutes and 3 hours long.

to the MICE Hall survey network. The trackers had been dowelled in position in the bores of the spectrometer solenoids. The dowels were used to locate each tracker precisely with respect to the axis of the warm bore of its solenoid. The position of the trackers along the beam line was inferred from the measurement of survey monuments mounted on the spectrometer-solenoid cryostats outer jackets. The beam-based alignment was used to determine the azimuthal orientation of the trackers with a resolution of $6\,\mathrm{mrad}/\sqrt{N}$ and their position transverse to the beamline with a resolution of $20\,\mathrm{mm}/\sqrt{N}$, where N is the number of tracks used in the analysis [40].

Analysis method. The position of each tracker in the MICE Hall coordinate system was described using the location of its centre and a set of three angles corresponding to rotation about the x axis (α), the y axis (β) and the z axis (ϕ). The rotation of the tracker about the z axis has a negligible effect on the alignment since ϕ was determined precisely at installation. An initial estimate for the position of each tracker along the beamline had been inferred from the survey. The surveyed location of the TOFs was used as the reference for the tracker alignment. The line that joins the centre of TOF1 with the centre of TOF2 was chosen as the reference axis. A deviation from this axis was considered to be due to misalignment of the trackers. The alignment could not be determined on a single-particle basis due to multiple Coulomb scattering in the absorber and other material present on the beamline. Therefore, the mean residuals in position (x and y) and angle (α and β) of the trackers with respect to the TOF1-TOF2 axis were evaluated to determine the alignment constants.
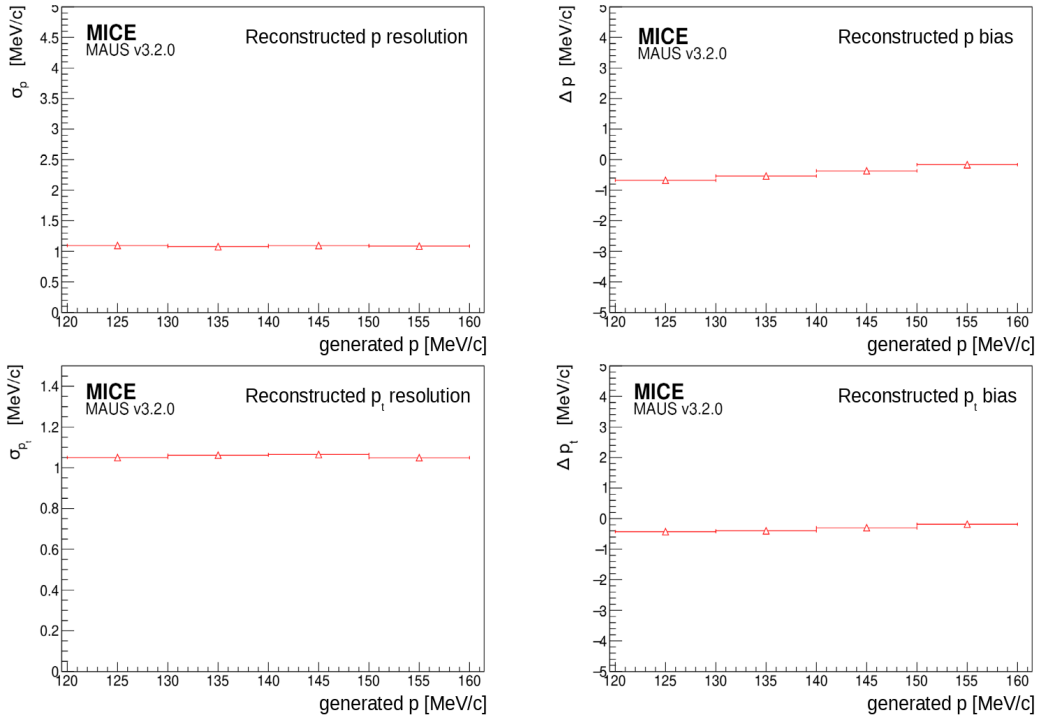
Figure 14. Momentum reconstruction resolution (left) and bias (right) for the total momentum (top) and transverse momentum component (bottom) in the upstream tracker.

Each TOF provided a single spacepoint in the Hall coordinate system. In Hall coordinates, on average, the track reconstructed between TOF1 and TOF2 should agree with the track reconstructed in each tracker, i.e. the mean residuals in x, y, α, and β should be zero. Applying this reasoning to the unknown offset and angles leads to a system of equations for the four unknown constants [40]. The measurement of four residual distributions per tracker yields the alignment constants. The main source of bias was the scattering in the material between TOF1 and TOF2. If the beam was not perfectly centred, particles preferentially scraped out on one side of the magnet bore, anisotropically truncating the tail of the residual distribution. A fiducial cut was applied to the upstream sample in order to remove this effect.

Data were recorded with the superconducting magnets turned off. High momentum beams were used to reduce the RMS scattering angle and to maximise transmission. Each data set was processed independently. Figure 16 shows the alignment parameters determined for each run during a specific data taking period. The measurements are in good agreement with one another and show no significant discrepancy: an agreement between the independent fits guaranteed an unbiased measurement of the alignment constants. The constant-fit χ^2/ndf was close to unity for each fit, indicating that there were no additional sources of significant uncertainty. The optimal parameters are summarised in table 3.
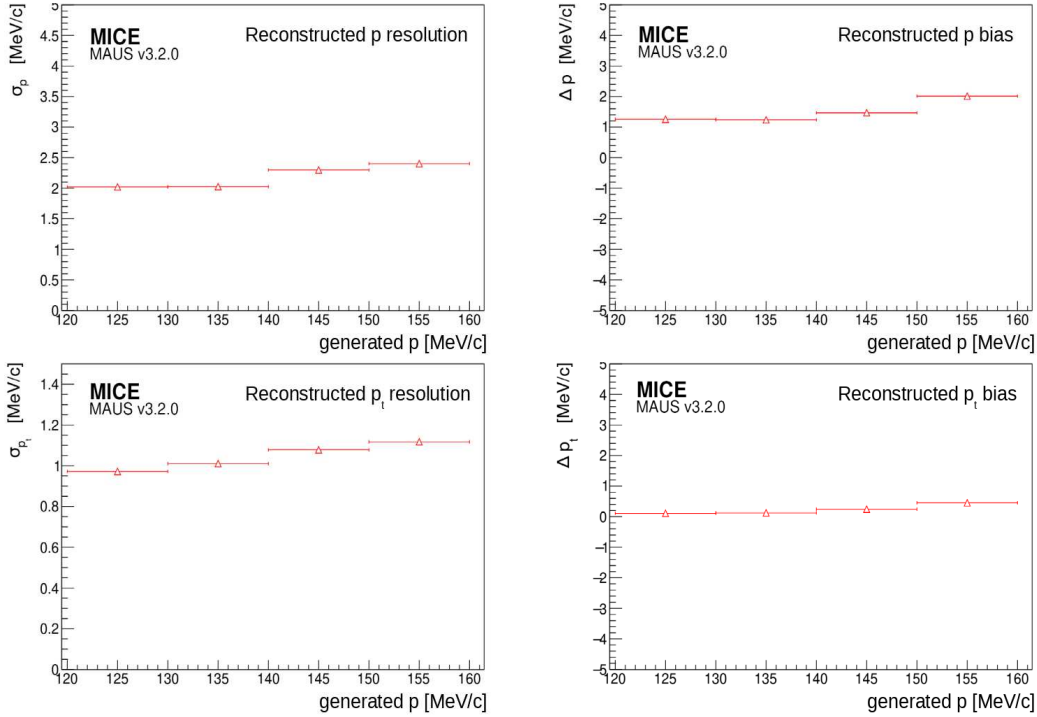
Figure 15. Momentum reconstruction resolution (left) and bias (right) for the total momentum (top) and transverse momentum component (bottom) in the downstream tracker.

Table 3. Optimal alignment constants measured in the high-momentum straight-track data acquired during May 2017 (summarised from figure 16).

	x [mm]	**y [mm]**	α **[mrad]**	β **[mrad]**
TKU	-0.032 ± 0.094	-1.538 ± 0.095	3.382 ± 0.030	0.412 ± 0.029
TKD	-2.958 ± 0.095	2.921 ± 0.096	-0.036 ± 0.030	1.333 ± 0.030

7   Liquid hydrogen absorber

The accurate characterisation of the properties of the liquid hydrogen absorber was a critically-important contribution to the study of ionisation cooling. The instrumentation used for this purpose and its performance are presented in this section.

The absorber vessel consisted of a cylindrical aluminium body sealed with two thin aluminium end windows, as shown in figure 17. The absorber vessel contained 22 l of liquid. The body of the absorber had an inner diameter of 300 mm and the end flanges were separated by a distance of 230 mm. The vessel was surrounded by a second pair of safety windows. The length along the central axis, between the two domes of the end windows, was 350 mm [41].

Variation of the density of liquid hydrogen due to varying temperature and pressure. The energy lost by a muon travelling through the liquid hydrogen absorber depends on the path length and
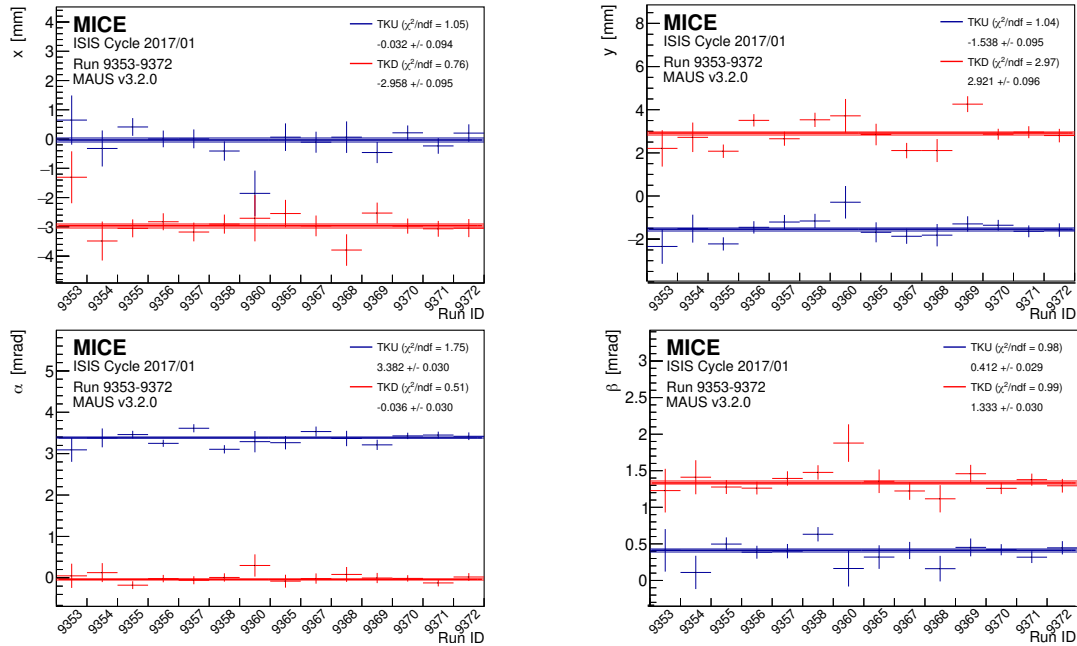
Figure 16. Consistency of the alignment algorithm results for upstream (blue) and downstream (red) trackers across runs acquired during the 2017/01 ISIS user cycle. The quantities x, y, α, and β are defined in the text.
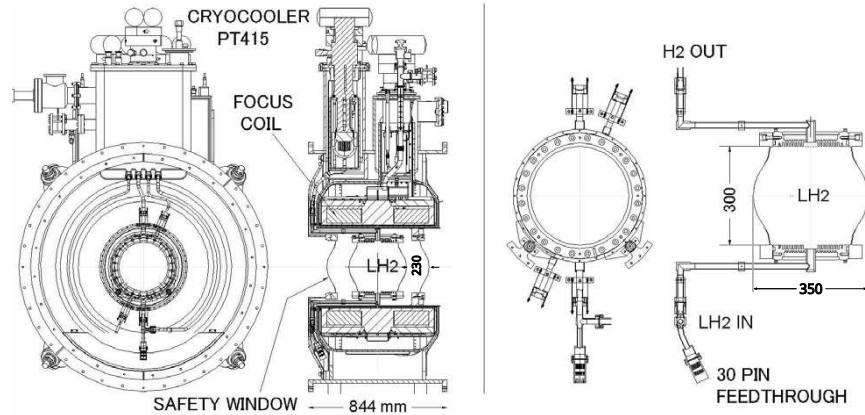

Figure 17. Left panel: drawing of the focus coil (FC) module showing the principal components. Right panel: detail of the liquid hydrogen absorber vessel [41].

on the density of the liquid hydrogen. The density of liquid hydrogen is a function of temperature and pressure. The temperature of the vessel was measured by eight LakeShore Cernox 1050 SD sensors, but with the values truncated for storage at a granularity of 0.1 K. Four of the sensors were used solely as temperature sensors, while the other four were also used as level sensors to ensure the liquid hydrogen reached the top of the vessel. The sensors were arranged in pairs, with two mechanically clamped at the top of the vessel, two at a polar angle of 45° to vertical from the top of the vessel, two at a polar angle of 45° to the bottom of the vessel, and a final two at the bottom of the vessel.

Cooldown and liquefaction were completed slowly over eight days at a pressure of 1105 mbar after which the vessel's pressure was lowered to 1085 mbar [41]. The vessel then remained in this steady state during the 21 day period of data taking, after which the vessel was vented. For the venting process, the cryocooler used to liquefy hydrogen was switched off and heaters were switched on to deliver a nominal power of 50 W to the absorber vessel. This resulted in an increase in pressure to 1505 mbar until the temperature stabilised at the boiling point. A rapid increase in temperature was observed once all the liquid hydrogen had boiled off.

The temperature sensors had a typical accuracy of ± 9 mK and a long-term stability of ± 12 mK at 20 K. The magnetic-field dependent temperature error, $\Delta T/T$, at 2.5 T is 0.04%, equivalent to ± 8 mK at 20 K [42]. These uncertainties were quoted by the manufacturer of the sensors. Magnetic fields caused reversible calibration shifts on the temperature measurements. To reduce the uncertainty in the liquid hydrogen density a calibration procedure was devised that used the boiling point, as observed during the venting process. A correction to the observed temperature reading was obtained by applying a cut-off correction, a correction for the effect of the magnetic field based on the current in the focus coil and its polarity, a correction for the non-linearity of the sensors, and a boiling point scaling factor [43].

The boiling point of hydrogen at 1085 mbar is 20.511 K. The sensors had a total uncertainty of 17 mK (9 mK accuracy, 12 mK stability, 8 mK magnetic). The deviation from the non-linearity of the sensors [42] added, on average, 0.03 K to the uncertainty. The temperature scaling and magnet-current correction factors also had an associated uncertainty as they were derived based on the 0.1 K resolution of the retrieved, truncated, values. For example, a calibrated sensor at boiling temperature and 1505 mbar should read 21.692 K, but we can only retrieve a value of 21.65 K (21.6 K truncated plus 0.05 K cut-off correction [43]) i.e. off by 0.042 K. The pressure sensors had an uncertainty of ± 5 mbar which equated to ± 0.016 K during steady state. The pressure uncertainty (± 5 mbar) added another uncertainty to the temperature calibration constants of ± 0.014 K. Collectively, all these uncertainties summed in quadrature to 0.2 K for each sensor.

While in the steady state condition the liquid hydrogen was close to the boiling temperature of liquid parahydrogen [43] (density of 70.53 kg/m^3): the average temperature of the eight sensors was (20.51 ± 0.07) K at 1085 mbar (figure 18) allowing us to determine the uncertainty in the density over this period as 0.08 kg/m^3.

Contraction of the absorber vessel due to cooling. The absorber was cooled from room temperature to the operating temperature of the experiment (20.51 K), contracting the vessel. The linear contraction of Al-6061 as it is cooled from 293 K is given by:

$$\alpha = -4.1277 \times 10^{-3}T - 3.0389 \times 10^{-6}T^2 + 8.7696 \times 10^{-8}T^3 - 9.9821 \times 10^{-11}T^4 \qquad (7.1)$$

where T is the operating temperature [44]. The equation is the result of a fit to data collated by the National Institute of Standards and Technology (NIST) and has an associated curve fit error of 4%. At the MICE operating temperature, this corresponds to a linear contraction of the vessel along each plane of 0.415%. As a result the length of the bore contracted by (1.45 ± 0.05) mm. The vessel was suspended within the warm bore of the focus coil and was therefore free to contract in each plane without restriction.
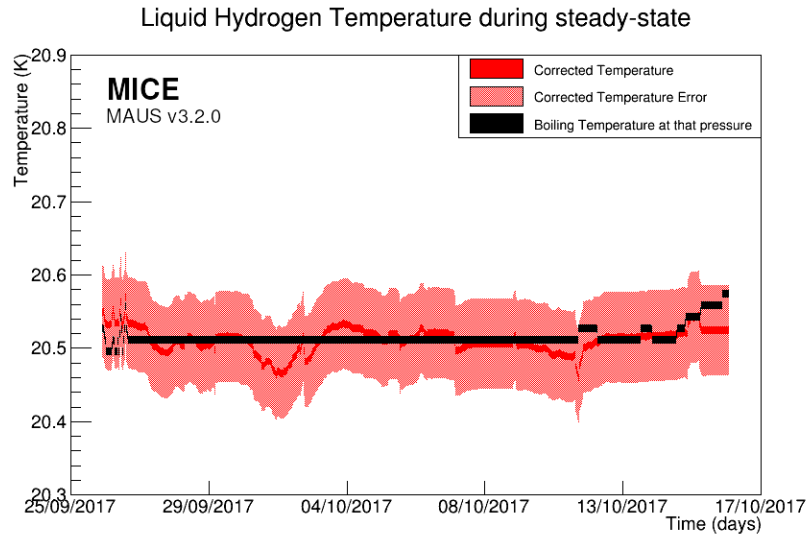
Figure 18. Average liquid hydrogen temperature recorded by the sensors during the steady state period. After applying all the correction factors the temperature remains at or close to the boiling point temperature.

Deflection of absorber vessel windows due to internal pressure.   To minimise energy loss and Coulomb scattering by the absorber vessel, the window thickness was minimised. The liquid hydrogen circuit was pressurised above atmospheric pressure to prevent air ingress [41, 45]. The vessel was designed to withstand at least 2500 mbar internally. The internal pressure was limited by the 1.5 bar relief valve to atmosphere, whilst the vessel was surrounded by vacuum.

The pressure at which the absorber operated resulted in deflection of the absorber windows. These deflections were modelled using ANSYS [46], and the uncertainty in the window deflection derived from this model was 20%. The model showed a linear dependence of the window deflection on pressure up to 2 Bar when the windows begin to yield. The pressure sensors were accurate to ± 5 mbar (0.25% of 2 Bar). At (1085 ± 5) mbar, the typical MICE operating pressure, this corresponded to a deflection of (0.5374 ± 0.1076) mm (model uncertainty) ± 0.0022 mm (sensor uncertainty) at the centre of the absorber window.

Variation of the absorber vessel window thicknesses.   On its passage through the absorber a muon would lose energy in the aluminium of the pair of hydrogen-containment windows, the two aluminium safety windows, and the liquid hydrogen itself. At the centre of the absorber, the total amount of aluminium the muon beam passed through was (785 ± 13) μm, producing a variance of 1.68%. However, as the windows were thin, the effects on energy loss were negligible. A 200 MeV/c muon passing along the central axis of an empty absorber lost 0.345 MeV, introducing a 0.006 MeV uncertainty on energy loss.

Total systematic uncertainty on energy loss.   The principal contributions to the systematic uncertainty on energy loss in the liquid hydrogen absorber are: the uncertainty in the contraction of the absorber vessel, the uncertainty in the deflection of the hydrogen-containment windows due to internal pressure, and the uncertainty in the variation of the window thickness. The impact of the

contraction of vessel and the deflection of the windows resulted in a reduction of the length of the vessel on axis of (0.4 ± 0.2) mm. The change in the combined thicknesses of the absorber windows on axis is 13 µm. The average temperature during the steady state period of the experiment when the pressure remained constant at (1085 ± 5) mbar is (20.51 ± 0.07) K corresponding to a liquid hydrogen density of (70.53 ± 0.08) kg/m^3.

During the MICE data taking, muon beams with nominal momenta of 140, 170, 200 and 240 MeV/c were used. The energy loss and its uncertainty were calculated. The calculation used a central bore length of (349.6 ± 0.2) mm, a total window thickness of (0.785 ± 0.013) mm and a liquid hydrogen density of (70.53 ± 0.08) kg/m^3. For a 140 MeV/c muon this corresponds to an energy loss of (10.88 ± 0.02) MeV, while for a 200 MeV/c muon particle this corresponds to an energy loss of (10.44 ± 0.02) MeV. For a muon travelling along the centre axis of the absorber the systematic uncertainty in the energy loss is 0.2%.

8 Summary and conclusions

A complete set of particle detectors has permitted the full characterisation and study of the evolution of the phase space of a muon beam through a section of a cooling channel in the presence of liquid hydrogen and lithium hydride absorbers, leading to the first measurement of ionization cooling. The PID performance of the detectors is summarised in table 4 and table 5 and is fully compatible with the specification of the apparatus [47].

Table 4. Summary of the performance of the MICE PID detectors.

Detector	Characteristic	Performance
Time-of-Flight	time resolution	0.10 ns
KLOE-Light	muon PID efficiency	99%
Electron Muon Ranger	electron PID efficiency	98.6%

Table 5. Summary of the MICE PID detector performance for different beam settings.

	KL efficiency			EMR efficiency		Track finding efficiency					
						3 mm		6 mm		10 mm	
Momentum	electrons	muons	pions	electrons	muons	US	DS	US	DS	US	DS
140 MeV/c	95%	97%	n.a.	98%	35%			98%	99%	98%	99%
170 MeV/c	95%	99%	89%	99%	99%						
200 MeV/c	94%	99%	95%	100%	99%	99%	96%	99%	96%		
240 MeV/c	96%	99%	97%	99%	99%						
300 MeV/c	95%	99%	98%	n.a.	99%						

All the different elements of the MICE instrumentation have been used to characterise the beam and the measurement of the cooling performance for a different variety of beam momenta, emittance, and absorbers. The measurement of the physical properties of the liquid hydrogen

absorber have been fully described here. The experiment has thus demonstrated a technique critical for a muon collider and a neutrino factory and brings those facilities one step closer.

Acknowledgments

References

[1] D.V. Neuffer and R.B. Palmer, *A high-energy high-luminosity μ^+-μ^- collider*, *Conf. Proc. C* **940627** (1995) 52.

[2] R.B. Palmer, *Muon colliders*, *Rev. Accel. Sci. Tech.* **7** (2014) 137.

[3] S. Geer, *Neutrino beams from muon storage rings: characteristics and physics potential*, *Phys. Rev. D* **57** (1998) 6989 [*Erratum ibid.* **59** (1999) 039903] [`hep-ph/9712290`].

[4] ISS Physics Working Group collaboration, *Physics at a future neutrino factory and super-beam facility*, *Rept. Prog. Phys.* **72** (2009) 106201 [`arXiv:0710.4947`].

[5] M. Apollonio et al., *Oscillation physics with a neutrino factory*, `hep-ph/0210192`.

[6] S.Y. Lee, *Accelerator physics*, third edition, World Scientific, Singapore (2012).

[7] S. Schröder et al., *First laser cooling of relativistic ions in a storage ring*, *Phys. Rev. Lett.* **64** (1990) 2901.

[8] J.S. Hangst, M. Kristensen, J.S. Nielsen, O. Poulsen, J.P. Schiffer and P. Shi, *Laser cooling of a stored ion beam to* 1 *mK*, *Phys. Rev. Lett.* **67** (1991) 1238.

[9] P.J. Channell, *Laser cooling of heavy-ion beams*, *J. Appl. Phys.* **52** (1981) 3791.

[10] J. Marriner, *Stochastic cooling overview*, *Nucl. Instrum. Meth. A* **532** (2004) 11 [`physics/0308044`].

[11] V.V. Parkhomchuk and A.N. Skrinsky, *Electron cooling:* 35 *years of development*, *Phys. Usp.* **43** (2000) 433 [*Usp. Fiz. Nauk* **170** (2000) 473].

[12] A. Antognini et al., *Demonstration of muon-beam transverse phase-space compression*, *Phys. Rev. Lett.* **125** (2020) 164802 [`arXiv:2003.11986`].

[13] A.N. Skrinsky and V.V. Parkhomchuk, *Cooling methods for beams of charged particles* (in Russian), *Sov. J. Part. Nucl.* **12** (1981) 223 [*Fiz. Elem. Chast. Atom. Yadra* **12** (1981) 557].

[14] D. Neuffer, *Principles and applications of muon cooling*, *Part. Accel.* **14** (1983) 75.

[15] MICE collaboration, *Demonstration of cooling by the Muon Ionization Cooling Experiment*, *Nature* **578** (2020) 53 [`arXiv:1907.08562`].

[16] M. Bonesini, *The design of MICE TOF*0 *detector*, MICE note 145, (2006), accessed 14 May 2021.

[17] R. Bertoni et al., *The construction and laboratory tests for MICE TOF0/1 detectors*, MICE note 241, (2008), accessed 14 May 2021.

[18] MICE collaboration, *The design and commissioning of the MICE upstream time-of-flight system*, *Nucl. Instrum. Meth. A* **615** (2010) 14 [arXiv:1001.4426].

[19] R. Bertoni et al., *The construction of the MICE TOF2 detector*, MICE note 286, (2010), accessed 14 May 2021.

[20] MICE collaboration, *Pion contamination in the MICE muon beam*, 2016 *JINST* **11** P03001 [arXiv:1511.00556].

[21] MICE collaboration, *The MICE muon beam on ISIS and the beam-line instrumentation of the Muon Ionization Cooling Experiment*, 2012 *JINST* **7** P05009 [arXiv:1203.4089].

[22] MICE collaboration, *Characterisation of the muon beams for the Muon Ionisation Cooling Experiment*, *Eur. Phys. J. C* **73** (2013) 2582 [arXiv:1306.1509].

[23] MICE collaboration, *Electron-muon ranger: performance in the MICE muon beam*, 2015 *JINST* **10** P12012 [arXiv:1510.08306].

[24] MICE collaboration, *First particle-by-particle measurement of emittance in the Muon Ionization Cooling Experiment*, *Eur. Phys. J. C* **79** (2019) 257 [arXiv:1810.13224].

[25] M. Bonesini, R. Bertoni, A. de Bari and M. Rossella, *Behaviour in magnetic fields of fast conventional and fine-mesh photomultipliers*, *Nucl. Instrum. Meth. A* **693** (2012) 130 [arXiv:1207.4909].

[26] M. Bonesini et al., *The TOF1 local shielding*, MICE note 455, (2015), accessed 14 May 2021.

[27] Y. Karadzhov et al., *TOF detectors time calibration*, MICE note 251, (2009), accessed 14 May 2021.

[28] L. Cremaldi, D.A. Sanders, P. Sonnek, D.J. Summers and J. Reidy Jr, *A Cherenkov radiation detector with high density aerogels*, *IEEE Trans. Nucl. Sci.* **56** (2009) 1475 [arXiv:0905.3411].

[29] L. Cremaldi et al., *Progress on Cherenkov reconstruction in MICE*, MICE note 473, (2015), accessed 14 May 2021.

[30] F. Ambrosino et al., *Calibration and performances of the KLOE calorimeter*, *Nucl. Instrum. Meth. A* **598** (2009) 239.

[31] E. Overton, *Studies and developments within the Muon Ionisation Cooling Experiment*, Ph.D. thesis, Sheffield U., Sheffield, U.K. (2014).

[32] R. Asfandiyarov et al., *MAUS: the MICE Analysis User Software*, 2019 *JINST* **14** T04005 [arXiv:1812.02674].

[33] R. Asfandiyarov et al., *The design and construction of the MICE electron-muon ranger*, 2016 *JINST* **11** T10007 [arXiv:1607.04955].

[34] F. Drielsma, *Electron-muon ranger: hardware characterization*, master's thesis, Geneva U., Geneva, Switzerland (2014) [arXiv:1710.06946].

[35] F. Drielsma, *Measurement of the increase in phase space density of a muon beam through ionization cooling*, Ph.D. thesis, Geneva U., Geneva, Switzerland (2018)

[36] M. Ellis et al., *The design, construction and performance of the MICE scintillating fibre trackers*, *Nucl. Instrum. Meth. A* **659** (2011) 136 [arXiv:1005.3491].

[37] M. Petroff and M. Stapelbroek, *Photon-counting solid-state photomultiplier*, *IEEE Trans. Nucl. Sci.* **36** (1989) 158.

[38] D0 collaboration, *The upgraded D0 detector*, *Nucl. Instrum. Meth. A* **565** (2006) 463 [physics/0507191].

[39] A. Dobbs et al., *The reconstruction software for the MICE scintillating fibre trackers*, 2016 *JINST* **11** T12001 [arXiv:1610.05161].

[40] F. Drielsma, *Beam-based detector alignment in the MICE muon beam line*, arXiv:1805.06623.

[41] MICE collaboration, *The liquid-hydrogen absorber for MICE*, 2018 *JINST* **13** T09008 [arXiv:1807.03019].

[42] *Temperature measurement and control catalog*, https://www.lakeshore.com/docs/default-source/product-downloads/lakeshoretc_l.pdf, accessed 2 October 2018.

[43] C. Brown et al., *Systematic uncertainties in the liquid hydrogen absorber*, MICE note 524, (2018), accessed 14 May 2021.

[44] G. Hardin, *Aluminum* 6061-*T*6 *(UNS AA*96061*)*, https://www.nist.gov/mml/acmd/aluminum-6061-t6-uns-aa96061, accessed 3 October 2018.

[45] S. Ishimoto, S. Suzuki, M. Yoshida, M.A. Green, Y. Kuno and W. Lau, *Liquid hydrogen absorber for MICE*, *Conf. Proc. C* **100523** (2010) 421.

[46] M. Green et al., *Does one know the properties of a MICE solid or liquid absorber to better than* 0.3 *percent?*, MICE note 155, (2006), accessed 14 May 2021.

[47] MICE collaboration, *Proposal to the Rutherford Appleton Lab: an international Muon Ionization Cooling Experiment (MICE)*, MICE note 21, (2003), accessed 14 May 2021.

[48] D. Britton et al., *GridPP: the U.K. grid for particle physics*, *Phil. Trans. Roy. Soc. A* **367** (2009) 2447.

[49] MICE collaboration, *Source code of MAUS — the MICE Analysis User Software*, 10.17633/rd.brunel.8337542.v2, (2019).

THE EUROPEAN
PHYSICAL JOURNAL D

Regular Article - Plasma Physics

Correlation analysis of solar energetic particles and secondary cosmic ray flux

Nikola Veselinović[a], Mihailo Savić, Aleksandar Dragić, Dimitrije Maletić, Radomir Banjanac, Dejan Joković, David Knežević, and Vladimir Udovičić

Institute of Physics Belgrade, University of Belgrade, Pregrevica 118, Belgrade 11080, Serbia

Abstract. Galactic cosmic rays entering heliosphere are modulated by interplanetary magnetic field which is carried away from the Sun by the solar wind. Cosmic rays are additionally modulated by coronal mass ejections and shock waves, which can produce Forbush decrease, a transient decrease in the observed galactic cosmic ray intensity. Measurements of magnetic field and plasma parameters in near-Earth space detect regularly coronal mass ejections, so it is important to understand the correlation between near-Earth particles fluxes associated with these coronal mass ejections and Forbush decreases. By combining in situ measurements of solar energetic particles with ground-based observations by the Belgrade muon detector, we analysed the dynamics of the variation of galactic cosmic rays. Correlation between variations of the flux of the cosmic rays and average in situ particle fluxes was investigated during Forbush decreases. Correlation exhibited dependence on the energy of solar wind particles, but also on cut-off rigidities of cosmic rays detected on the ground. The goal of cross-correlation analysis is to help in better understanding of how coronal mass ejections affect space weather as well as the effects they have on primary cosmic ray variations as detected by ground-based cosmic ray detectors.

1 Introduction

Space weather has been widely used as a term to define impact of the Sun, heliosphere and geomagnetic field on our biosphere and our technological systems. Understanding space weather is a matter of both scientific interest and practical importance as its impact could potentially be hazardous to our civilisation. Cosmic ray (CR) observations can also be used to study space weather. Primary (or galactic) CRs are high-energy nuclei (mainly protons) that originate from outside of our solar system. Their flux and energy range is covering several tens of orders of magnitude (flux from 10^{-28} up to 10^4 (m^2 sr sec eV/nucleon)$^{-1}$ and energy range up to 10^{21} eV [10]). As charged particles, CRs are sensitive to magnetic field, so often it is more convenient to use geomagnetic rigidity instead of energy to characterise primary CRs. Geomagnetic rigidity is defined as $R = B\rho = pq$, where B is the magnetic field, ρ is the gyroradius of the particle due to this field, p is the particle momentum and q is its charge [14]. As they traverse interplanetary space, galactic CRs interact with helio-

spheric magnetic field. The heliosphere is the region of space around the Sun dominated by the solar wind and the interplanetary magnetic field (IMF). The solar wind is a stream of supersonic plasma blowing outward from the Sun. IMF represents solar magnetic field carried by highly conducting solar wind plasma. Interaction of CRs with this large-scale field modulates CRs flux intensity measured on Earth, which is nested deep inside the heliosphere. Interaction with the heliosphere causes gradient and curvature drift motion of CRs and scattering by the magnetic irregularities embedded in the solar wind [19]. Variations in the solar magnetic field directly affect the heliosphere, most prominent being the solar cycle variation with a period of about 11 years. Solar cycle affects activity of the Sun which is visible in varying number of sunspots, solar flares (SFs) and coronal mass ejections (CMEs). Coronal mass ejection is an extreme solar activity event, followed by significant release of charged particles and accompanying magnetic field from solar corona. Intensity of measured CRs flux anticorrelates with the activity of the Sun, with lower intensity during maximum of the solar cycle and higher intensity during minimum of solar activity.

One of the transient phenomena of this interaction is the Forbush decrease (FD), which represents a rapid depression in CR flux. It is usually characterised by a sudden decrease reaching minimum within one day, followed by a subsequent gradual recovery phase, which

[a] e-mail: veselinovic@ipb.ac.rs (corresponding author)

can last for several days. Typical causes of FD are transient interplanetary events related to interplanetary coronal mass ejections (ICMEs). If the speed of the ICME is greater than fast magnetosonic wave speed in the solar wind reference frame, ambient solar wind plasma will be compressed. The shock can be formed, which is driven ahead of ICME and can cause enhancement of IMF. FD can also be formed due to corotating interaction regions between different solar wind streams with different speed [2]. In this paper, we will only focus on ICME induced FDs, of which we will study four cases.

Correlation between parameters characterising FDs (like magnitude of the decrease, duration, one-step or two-step FDs, etc.) and solar wind parameters has been studied for some time. There is reasonable evidence for correlation between FD magnitude and amplitude of magnetic field enhancement B, velocity of CME, maximum solar wind velocities and other parameters as shown in [7,22]. Also, profile of FDs is modelled and compared with CME magnetic structure, starting from the simple force-free flux rope with circular cross section, but it can deviate from this ideal concept. FD magnitude is explained with cumulative effect of diffusion of CRs through the turbulent sheath region [3,11]. FD is also energy dependent, where amplitude of decrease is typically around several percent. Higher-rigidity CRs only weakly interact with magnetic disturbances, so no significant change of the flux can be expected for CRs with rigidity of several dozen GV [9]. In order to detect FD at any location, larger statistics are needed for CRs of lower energy. CRs also interact with geomagnetic field which imposes the minimal rigidity CRs must have in order to reach Earth's surface. This geomagnetic cut-off rigidity depends on geomagnetic latitude. It is smaller at the poles and increases with latitude, with some exceptions due to deviation of Earth's magnetic field from the magnetic dipole model (i.e., South Atlantic anomaly [4]).

Primary CRs arriving at Earth interact with atoms and molecules in Earth's atmosphere. CRs with energy above $300-400$ MeV/nucleon generate showers of secondary particles. These secondary CRs consist of electrons and photons (electromagnetic component) and harder, in terms of energy, nuclear component of the cascade. Nuclear component, at the bottom of the atmosphere, is composed mainly of muons, protons, neutrons and neutrinos. Secondary CRs can be observed with detectors in the atmosphere (balloon probes), on the ground or even underground. High-energy muons can penetrate deep underground and can be an important component of the background in experiments requiring high sensitivity (dark matter search, proton decay, etc.).

There is a well-known correlation between parameters of solar wind plasma and CR flux, and the goal of this paper is to extend the study of FDs, specifically its magnitude and time evolution, to wider range of parameters of the heliosphere measured routinely with satellites. We concentrate our study on previously scarcely used parameters of the solar wind, particularly flux of

charged particles of different energies. These particles are the source of inhomogeneity in the IMF, so the goal is to try and find distinguishing characteristics of FDs, like magnitude of decrease and FD profile that can be related to the satellite proton flux data, and examine their potential correlation with other space weather parameters. This additional information can be useful in finding explicit connection between parameters of solar wind and CR flux and can lead to better understanding of these complex processes.

2 CR data

In order to provide higher count rate, detector on Earth has to be omnidirectional and to detect integral flux over different range of energies. For the last seventy years secondary CRs are measured using standard ground-based neutron monitors (NMs) [6]. There is a worldwide network of NMs (http://www01.nmdb.eu/) that measures flux of secondary CRs originated from primary CRs with rigidity range approximately between 1 GV and 20 GV. Every node of the worldwide network of ground stations has its unique cut-off rigidity depending on its geomagnetic coordinates and height. The other type of widely used ground-based CR detectors are muon monitors. Muon monitors are sensitive to primary CRs of higher rigidity and complement NMs measurements [26]. Worldwide network of these muon stations is still rudimentary, but it can provide insight into flux variation of primary CRs with energies higher than CRs detected by NMs. Since both NMs and muon detectors are energy-integrating detectors and use entire atmosphere above it as a moderator, it is not trivial to relate count rate of these detectors to the flux or energy spectrum of primary CRs at the top of the atmosphere. One needs to know the response of a detector to a unit flux of CRs with the given energy, the so-called detector yield function. Yield functions can be calculated either theoretically, using a numerical simulation of the nucleonic cascade caused by energetic cosmic rays in the Earth's atmosphere, e.g., [8], or semi-empirically, for example based on a latitudinal survey [16].

As flux of secondary cosmic rays is also sensitive to varying properties of the atmosphere through which these CRs propagate, it is necessary to conduct flux correction of the measured flux for atmospheric parameters, where atmospheric pressure correction is the most important. In addition to atmospheric pressure, CR muons are sensitive to temperature variations in the atmosphere, starting from the top of the atmosphere all the way to the ground level. There are several procedures for corrections of these effects which are regularly used. Most commonly used are the integral method and the method of effective level of generation, but some novel techniques have also been introduced in recent years [25]. Correction for these atmospheric parameters is necessary in order to increase detector sensitivity to

Table 1 Properties of primary CR flux related to muons detected at Belgrade CR station

Detector	Muon flux $1/(m^2 s)$	$E_{0.05}$ (GeV)	E_{med} (GeV)	$E_{0.95}$ (GeV)	Cut-off rigidity (GV)
GLL	137(6)	11	59(2)	915	5.3
UL	45(2)	31	137(5)	1811	12

variations of primary CRs flux and more precisely study the influence of solar modulation on galactic CRs.

Belgrade CR station started collecting data with the current experimental set-up in 2009. The station consists of two separate detector units: one placed on ground level (GLL) and the other in shallow underground (UL), both utilising the same experimental set-up. Such configuration provides opportunity to monitor muon fluxes in two different energy ranges with all other external parameters (such as atmospheric parameters, geomagnetic location and experimental set-up) being the same. Underground part of the station detects muons originated from primary CRs with higher energy because of the layer of soil overburden (13 m of loess) which absorbs lower-energy muons. Details of the detector systems at the Belgrade CRs station as well as calculated response functions are presented in [29]. The station is situated at the Laboratory for Nuclear Physics at the Institute of Physics Belgrade, Serbia. The altitude of the station is 78 m above sea level. Its geographic coordinates are: $44°51'$ N and $20°23'$ E, with geomagnetic latitude of $39°32'$ N. Sensitivity of Belgrade CR detectors to galactic CRs is given in Table 1, where primary CRs with the energy below $E_{0.05}$ (and above $E_{0.95}$) contribute with 5% to the count rate of the corresponding detector, and E_{med} is median energy based on simulation. In preparation for the analysis, detected muon count rates are corrected for efficiency, as well as for barometric and atmospheric temperature effects. Temperature effect correction is done using integral method [24].

3 Satellite data

In recent years, satellites provide new direct measurements of primary CRs flux in the heliosphere and the geomagnetic field. Also, detectors mounted on spacecraft allow us to probe even further, as Voyager recently crossed heliospheric boundary and for the first time galactic CRs flux was measured outside the heliosphere. The problem with such measurements is limitation to the size of the detectors, due to constraints of the construction of the satellites. In order to have valid statistics and good resolution, only low-energy particle flux can be measured. These low-energy particles are sensitive to geomagnetic field, which can introduce additional perturbation. Also, measurements of low-energy CRs can be masked by the increased flux of low-energy solar energetic particles (SEPs) in the MeV energy range. FDs detected by ground-based detectors are measured in energy range several orders of magnitude higher than the energy range available to satellites measurements. (NMs detect flux that originate from ~ 10 GeV, single muon detectors higher than that up to ~ 100 GeV, while solar weather satellite measurements range up to several 100 MeV.) SEP occurrence is sporadic and depends on which part of the solar cycle we are in, so long-term studies with stable data quality are necessary if we are to study solar modulation of CRs. Such long-term measurements have been performed with various spacecrafts during the last four decades. Data measured on different interplanetary locations are then used for modelling of the heliosphere, which is important for understanding and forecasting space weather. This is a relatively new and dynamic field that is still expanding. More in situ measurements that can be catalogued [17] and compared with data from ground based stations will improve our understanding of near space environment.

In this paper, we use proton data from ERNE (Energetic and Relativistic Nuclei and Electron experiment) detector at the SOHO (Solar and Heliospheric Observatory) (https://omniweb.gsfc.nasa.gov/ftpbrowser/flux_spectr_m.html), which has been performing measurements in Lagrangian point L1 for the last quarter of a century described in [13] and references therein. Experiments that collects in situ particles data are ERNE and COSTEP (Comprehensive SupraThermal and Energetic Particle analyser), where data are combined to meet requirements of the mission. ERNE detector provides proton flux data in relatively large energy range (1.6 to 131 MeV) separated in several energy channels ($1.3-1.6, 1.6-2.0, 2.0-2.5, 2.5-3.2, 3.2-4.0, 4.0-5.0, 5.0-6.4, 6.4-8.0, 8.0-10, 10-13, 13-16, 16-20, 20-25, 25-32, 32-40, 40-50, 50-64, 64-80, 80-100, 100-130$ MeV) . Measurements are taken with two different detectors: LED (low-energy detector) covers lower-energy and HED (high-energy detector) which covers higher-energy channels [28]. Satellites, including SOHO, also measure in situ parameters of the space environment and gather data about magnetic field, solar wind and concentration and flux of various types of particles on the location. Satellite data relevant to heliospheric studies are, among other places, available at GSFC/Space Physics Data Facility, in the form of low- and high-resolution OMNI data (https://spdf.gsfc.nasa.gov/pub/data/omni/low_res_omni/). In this study, we used the low-resolution OMNI data that contain hourly data for the solar wind magnetic field and plasma parameters, energetic proton fluxes, and geomagnetic and solar activity indices for different regions in proximity to Earth [12].

4 Four prominent FD events during rising phase of solar cycle 24

Previous (24th) solar cycle started in December 2008 and ended in November 2019 (as available from Sunspot Index and Long-term Solar Observations database http://www.sidc.be/silso/node/167). It had an unusually weak maximum, with smoothed maximum international sunspot number of 116. For comparison, in cycles 22 and 23 this number was 214 and 180, respectively (as available from Sunspot Index and Long-term Solar Observations database http://sidc.be/silso/home). Same period was also characterised by smaller number of FDs, especially ones with larger amplitudes.

There were fifteen strong FDs (with magnitude of decrease larger than 5% for particles with 10 GV rigidity) recorded in the rising phase of solar cycle 24, however in this study we will limit our analysis to four events detected by the Belgrade Cosmic Ray Station (http://www.cosmic.ipb.ac.rs/). Other prominent FDs that occurred in this period have not being detected by either GLL or UL detector due to discontinuity of operation, so they have been omitted from this study. All four events followed ejections from an active region on the Sun, accompanied by a solar flare with interplanetary shock wave and sudden storm commencing (SSC), and disturbance in the geomagnetic field. All of these FDs were seen by the NM detector network as well.

First significant FD of solar cycle 24 was recorded on 18 February 2011 and has been caused by a CME heading directly towards Earth [20]. It has been detected by most ground stations around the world. Its morphology is influenced by the interaction of two CMEs, first slower and the second faster (with respective speeds of 390 km/s and 1020 km/s), that occurred a day apart [27]. Geomagnetic activity has been relatively weak due to orientation of the magnetic field of the ejecta [21].

Second event was observed on 7 March 2012. It included an X-class flare (X5.4), that occurred in NOAA AR 11429 with an intense halo CME, followed by several smaller flares and another partial CME. It caused one of the strongest FDs of the last solar cycle. Observed solar activity was also related to the intense geomagnetic storm that followed [15].

A strong SF (X1.6) was detected by several spacecrafts during 10 September 2014, originating from active region NOAA AR 2158. Based on the SOHO coronagraph images, this flare was associated with a CME that was aimed towards Earth, where it arrived on September 12. This activity resulted in a major geomagnetic storm, one of the strongest in 2014.

In the second half of June 2015, solar activity was very intense, since a number of CMEs and flares were produced from the powerful AR 12371, which dominated solar activity during that period [23]. The impact of these CMEs on the Earth's magnetosphere resulted in a moderate to severe G4-class geomagnetic storm that occurred on the summer solstice. The result was a very interesting and unusual modulation galactic CRs flux, which appeared as a series of FDs.

For the study of FD events and their relationship with IMF and geomagnetic disturbances, researchers from IZMIRAN (Pushkov Institute of Terrestrial Magnetism, Ionosphere and Radio Wave Propagation, Russian Academy of Sciences) created an FD database (http://spaceweather.izmiran.ru/eng/dbs.html) which contains various FD parameters, as well as their relationship with heliospheric and geomagnetic parameters covering several solar cycles [1]. Properties of the four selected FDs, taken from the IZMIRAN database, are given in Table 2.

5 Data analysis

In order to establish the usability of SOHO SEP flux data in the study of CR variations, we will first analyse how muon count rate time series compare with some of the IMF parameters more commonly used in the analysis of solar activity-induced CR variations. To this end, we compare hourly muon count rates (measured by Belgrade muon station and corrected for atmospheric effects) with time series for selected parameters from OMNI database. To give more weight to this qualitative analysis, we concentrate only on periods of extreme solar activity, in particular periods of the occurrence of four FD events described in Sect. 4. We then examine the relationship between measured muon count rates and the SOHO/ERNE SEP flux data and analyse any discerning features in comparison with the ones observed in OMNI data time series. The period selected for this analysis is approximately one solar rotation of 27 days. All probes at L1 are about an hour upstream of the magnetosphere so all their data are interspersed with data from spacecraft close to Earth (e.g., IMP 8). In order to compute hourly averages "at Earth" this time shift has to be taken into account (https://omniweb.gsfc.nasa.gov/html/ow_data.html).

Next, we investigate the short-term correlation between SEP flux and muon count rate data during time periods of four selected FDs. Muon time series for this procedure were selected for times where average muon flux was significantly lower than the background level. Background level was determined from moving averages for hourly count rates 10 days before the event. We then perform correlative analysis between SOHO SEP flux data and muon count rates for a period of one year (from 01.06.2010 to 31.05.2011), in order to establish the long-term relationship. For further insight, we also look into the correlation between these variables during the periods of reduced geomagnetic activity (International Quiet Days) and increased geomagnetic activity (International Disturbed Days).

Finally, we look in greater detail into SOHO SEP flux time series. In order to perform more quantitative analysis, time-integrated flux is calculated for SEP data for different SOHO energy bins and for the duration of selected FD events. In order to provide a parameter for characterisation for different FD events, calculated integral flux is plotted as a function of proton energy and

Table 2 Selected FD and interplanetary disturbance parameters (taken from IZMIRAN database)

Parameter	FD 1	FD 2	FD 3	FD 4	Parameter comment
Date of FD	18.2.2011.	8.3.2012.	12.9.2014.	22.6.2015.	
Date of parent solar event	15.2.2011.	7.3.2012.	10.9.2014.	21.6.2015.	
AR number	1158	11429	2158	12371	NOAA active region
V_{meanC}	584	1198	906	1040	The average ICME velocity between the Sun and the Earth, calculated using the time of the beginning of the associated CME observations (in km/s)
V_{max}	691	737	730	742	Maximal hourly solar wind speed in the event (in km/s)
B_{max}	31	23.1	31.7	37.7	Maximal hourly IMF strength in the event (in nT)
B_{zmin}	− 5.5	− 16.1	− 9.5	− 26.3	Minimal hourly Bz component of the IMF in the event (in nT)
R_{bulk}	72.25	146.2	131.35	171.25	An estimate of the maximum proton rigidity (in GV) that can be reflected by the total magnetic field, integrated from the event onset to the FD minimum
Magn	5.2	11.7	8.5	8.4	FD magnitude for particles with 10 GV rigidity, calculated as maximal range CRs density variations in the event, obtained by GSM from NM network data (in %)
MagnM	4.7	13.1	6.9	10.4	FD magnitude for particles with 10 GV rigidity, corrected on magnetospheric effect with Dst-index (in %)
TminM	7	20	9	11	Time from the FD onset to minimum, calculated from the data corrected for magnetospheric effect
Kp_{max}	5	8	6.33	8.33	Maximal Kp-index in the event
Ap_{max}	48	207	94	236	Maximal 3-hour Ap-index in the event
Dst_{min}	− 30	− 143	− 75	− 204	Minimal Dst-index in the event (in nT)
Flare class	X2.2	X5.4	X1.6	M2.6	Associated X-ray flare data
SSN	85	97	126	56	Number of sunspot at the FD onset day

fitted with a power function. Dependence of magnitude for selected FDs on the exponents obtained from fitted distributions is then analysed.

6 Results and discussion

Comparison between time series of selected IMF parameters from OMNI database and muon count rate time series during the periods of four selected FD events is shown in Fig. 1. Observed anticorrelation between muon count rates and proton flux and temperature, as well as with the overall IMF magnetic field and detected plasma speed, is in agreement with previously stated evidence in the literature [30].

Similar comparison between muon count rate time series and selected channels of SOHO/ERNE proton flux data for the same time intervals is shown in Fig.
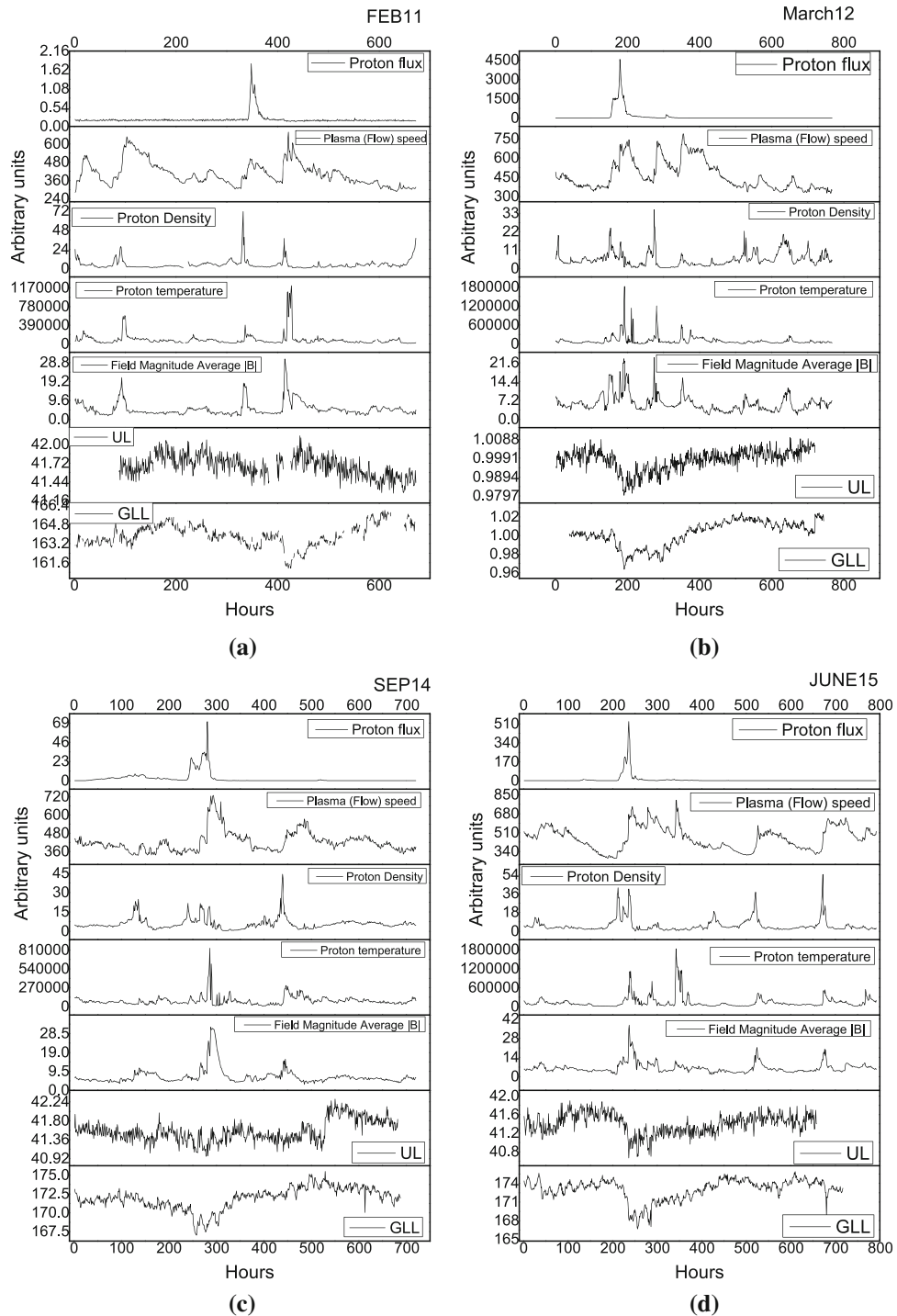
Fig. 1 Time series for particle and plasma parameters (taken from OMNI database) in the time interval of approximately one month around the occurrence of four selected FD events: **a** February 2011 (start of time interval on 1 February), **b** March 2012 (start of time interval on 1 March), **c** September 2014 (start of time interval on 1 September) and **d** June 2015 (start of time interval on 13 June)

2. For the sake of clarity, we chose three energy channels (1.6−2 MeV, 16−20 MeV, 100−130 MeV), approximately one order of magnitude apart, where first channel is measured with LED and the other two with HED detector on SOHO/ERNE instrument. In case of the

February 2011 event, there is an observable time lag (≈55 h) between the increase of measured proton flux at low-energy channels (1.6−2 MeV and 16−20 MeV energy channels) and the beginning of FD recorded at ground station. This time lag is also present between
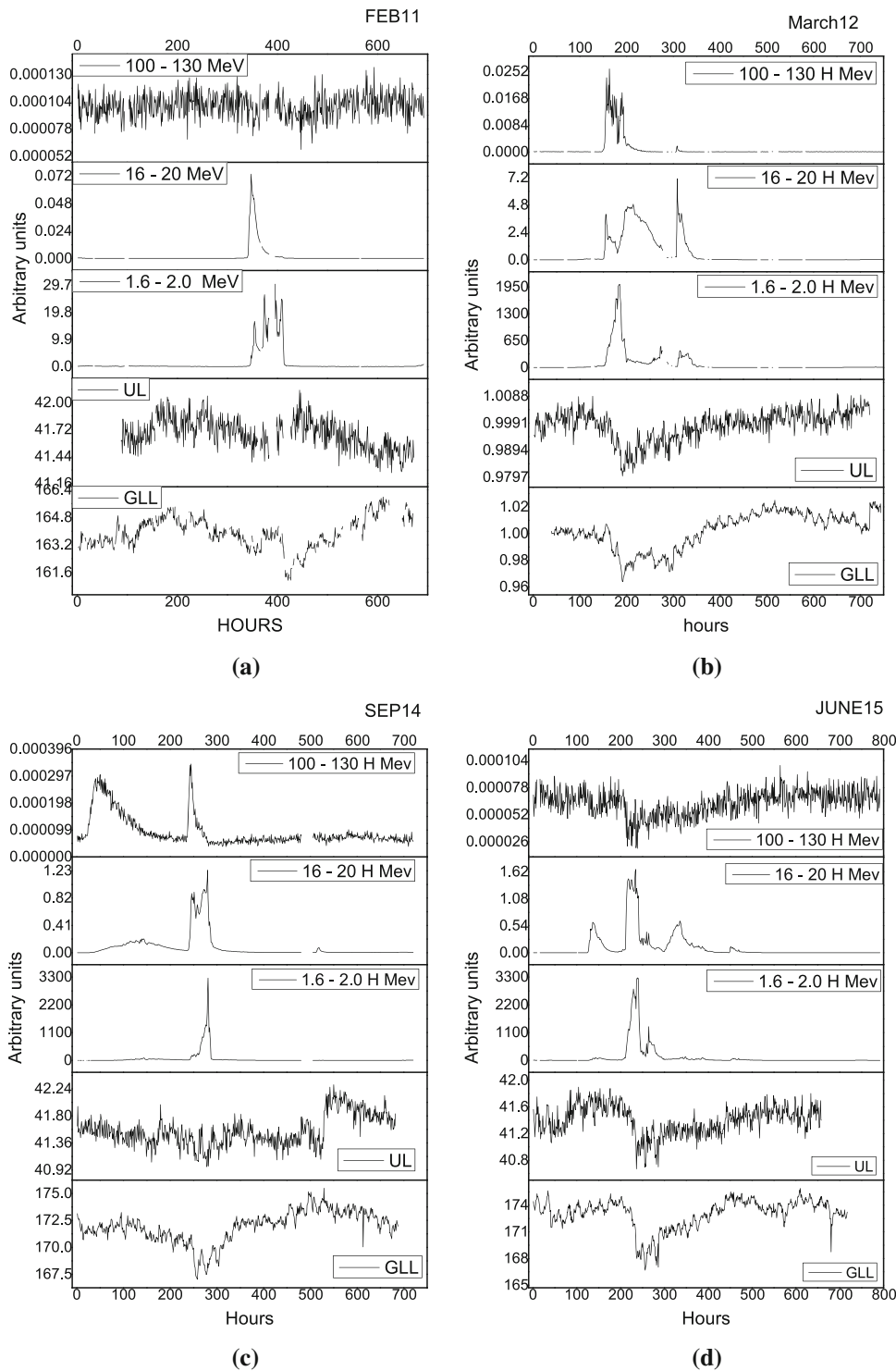
Fig. 2 Hourly time series for different proton channels from SOHO/ERNE and two muon detectors at Belgrade CR station, in the time interval of approximately one month around the occurrence of four selected FD events: **a**)February (start of time interval on 1 February) 2011, **b** March 2012 (start of time interval on 1 March), **c** September 2014 (start of time interval on 1 September) and **d** June 2015 (start of time interval on 13 June)

OMNI proton flux data and ground station measurements for this FD alone. FD is a complex modulation of CR flux that depends on a lot of parameters, like magnitude of magnetic field and its components,

speed of solar wind and CMEs (with CME average speed ≈ 490 km/s), most of which are listed in Table 2. Parameter values for all four ICMEs are mostly comparable, but one difference that stands out is the discrep-

(a)

(b)
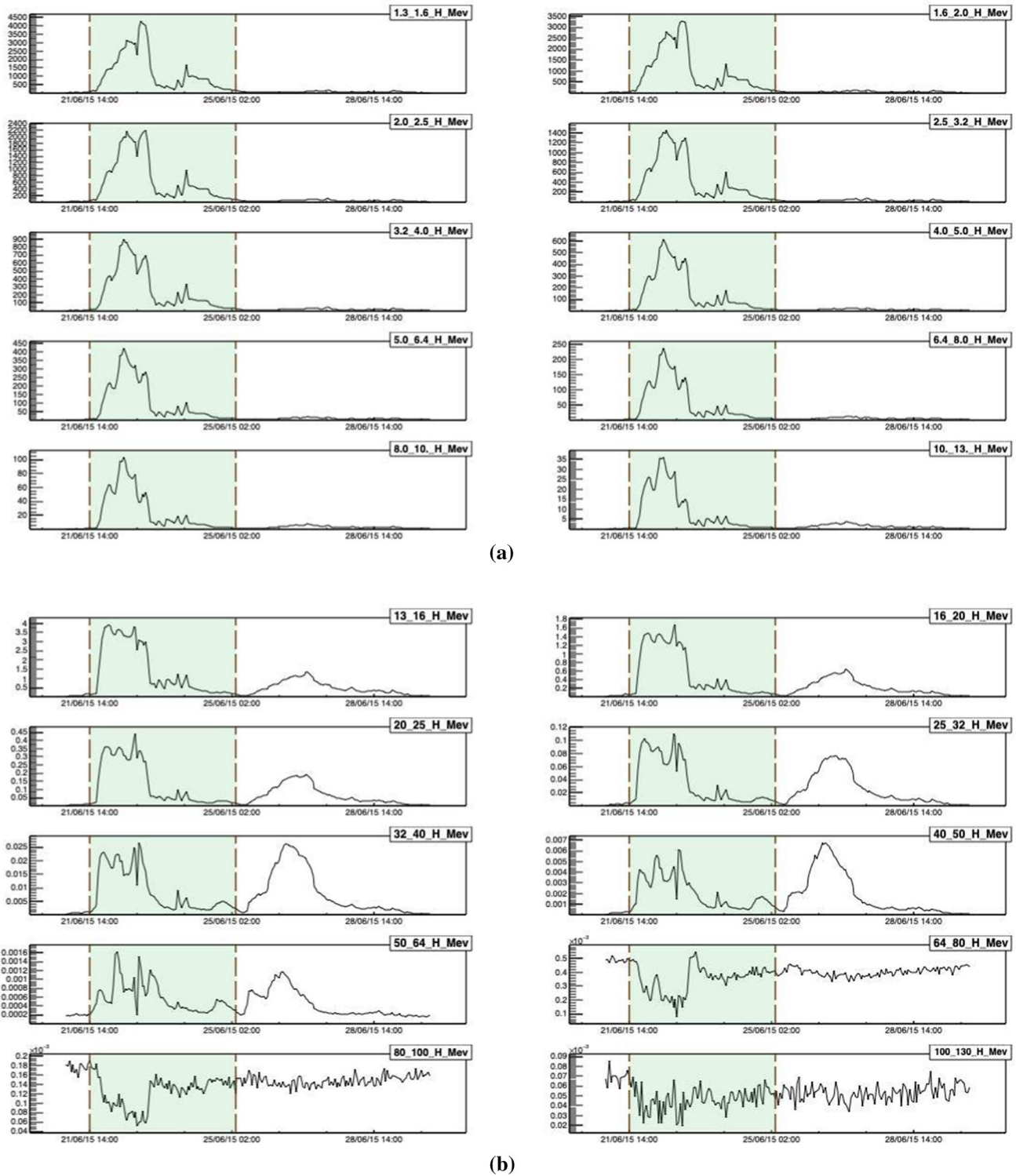
Fig. 3 Differential SEP fluxes during extreme solar event in June 2015, measured by SOHO/ERNE proton channels. Vertical dashed lines indicate the time for the start and the end of interval used to calculate the integral flux

ancy in average CME velocity (584 km/s from Table 2.) for the FD of February 2011, which can possibly explain the observed time lag for this particular FD.

Based on the observed time lag and other coincident features, we can establish good agreement between SOHO low-energy channel data and OMNI data time series. As for high-energy channels, SEP time series in 100−130 MeV energy range for February 2011 and June 2015 events appear to correlate with muon count rate measurements on the ground. One possible explanation

Table 3 Statistical correlation between Belgrade CR station and SOHO/ERNE measurements during the periods of four selected FD events

FD	Energy range (MeV)	GLL		UL	
		Pearson coefficient	P value	Pearson coefficient	P value
FEB 11	1.6–2.0 H	− 0.10877	0.01	− 0.05285	0.2
	16–20 H	− 0.18384	2×10^{-5}	− 0.10732	0.01
	100–130 H	0.24204	$< 10^{-6}$	− 0.13212	0.02
MAR 12	1.6–2.0 H	− 0.48477	$< 10^{-6}$	− 0.43994	$< 10^{-6}$
	16–20 H	− 0.72033	$< 10^{-6}$	− 0.68221	$< 10^{-6}$
	100–130 H	− 0.29172	$< 10^{-6}$	− 0.27822	$< 10^{-6}$
SEP 14	1.6–2.0 H	− 0.2839	$< 10^{-6}$	− 0.48052	$< 10^{-6}$
	16–20 H	− 0.37814	$< 10^{-6}$	− 0.63735	$< 10^{-6}$
	100–130 H	− 0.04951	0.007	− 0.10466	0.2
JUN 15	1.6–2.0 H	− 0.3921	$< 10^{-6}$	− 0.27531	$< 10^{-6}$
	16–20 H	− 0.31229	$< 10^{-6}$	− 0.17113	$< 10^{-6}$
	100–130 H	0.48588	$< 10^{-6}$	0.39296	$< 10^{-6}$

could be that in addition to SEP these energy channels are also populated by very low-energy CRs.

We can further investigate this assumption by looking more closely into SOHO SEP flux time series for one of the two weaker FD events. We have selected June 2015 event, as time series for higher-energy channels appear to be slightly more informative. Figure 3 shows proton flux series for all energy channels measured by SOHO/ERNE detector. From these plots, it is apparent that proton fluxes for energies larger than 64 MeV exhibit different dynamic relative to fluxes of lower energies, and seem to be in anticorrelation with them. This indeed supports the assumption these channels are populated by low-energy CR.

Another way we can illustrate this observation more quantitatively is by performing correlative analysis. Firstly, we will look into short-term correlations between proton flux and muon count rate time series during four selected FD evens. Correlation between respective time series was found using Pearson correlation coefficient. For significance two-tailed test is used. Correlation coefficient and its significance level between ground station and in situ measurement from SOHO/ERNE instrument is given in Table 3.

Due to higher energy of the primary CRs detected in UL, the correlation between SEPs and measured flux in UL is smaller than correlation between SEPs and flux measured in GLL. The greatest anticorrelation (i.e., between GLL and UL data and $16-20$ MeV protons ≈ -0.7) is observed for the strongest ICME (and corresponding FD) of March 2012, and this anticorrelation is observed in all energy channels. However, for lower-intensity events of June 2015 and February 2011, correlations between detected CR flux in GLL and highest energy channel ($100-130$ MeV) are mostly positive. These observations further confirm the assumption about high-energy channels being populated by low-energy CR, which is especially evident in case of low-intensity FD events.

Table 4 Pearson correlation coefficient for the correlation between CR flux detected at Belgrade CR station (GLL detector) and flux of protons of different energies detected with SOHO/ERNE detector, for the period of one year (from June 2010 May 2011)

	GLL	
	Pearson coefficient	P value
H 1.3–1.6 MeV	− 0.02	0.13
H 1.6–2.0 MeV	− 0.02	0.16
H 2.0–2.5 MeV	− 0.02	0.20
H 2.5–3.2 MeV	− 0.01	0.27
H 3.2–4.0 MeV	− 0.01	0.36
H 4.0–5.0 MeV	− 0.01	0.57
H 5.0–6.4 MeV	< 0.01	0.75
H 6.4–8.0 MeV	< 0.01	1.00
H 8.0–10 MeV	< 0.01	0.78
H 10–13 MeV	0.01	0.57
H 13–16 MeV	0.01	0.41
H 16–20 MeV	0.01	0.31
H 20–25 MeV	0.01	0.26
H 25–32 MeV	0.01	0.24
H 32–40 MeV	0.01	0.27
H 40–50 MeV	0.01	0.46
H 50–64 MeV	< 0.01	0.80
H 64–80 MeV	0.05	< 0.01
H 80–100 MeV	0.12	< 0.01
H 100–130 MeV	0.07	< 0.01

Similar results, with even greater correlation between the entire time profile for flux measured with NMs and solar wind speed and magnetic field during ICME, are reported for stronger FDs during solar cycle 23 [5].

Next, we will analyse long-term correlations between SOHO proton flux and measured muon count rates. Pearson coefficients for this correlation over a period of one year (from June 2010 May 2011), when activity of the Sun was low at the commencement of the 11-years cycle, are presented in Table 4. Here we see very

Table 5 Pearson correlation coefficient for the correlation between CR flux detected at Belgrade CR station (GLL detector) and flux of protons of different energies detected with SOHO/ERNE detector, during international geomagnetically quiet and disturbed days for the period of one year (from June 2010 May 2011)

	GLL Quiet days		GLL Disturbed days	
	Pearson coefficient	P value	Pearson coefficient	P value
H 1.3–1.6 MeV	0.01	0.61	− 0.05	0.13
H 1.6–2.0 MeV	0.01	0.80	− 0.05	0.14
H 2.0–2.5 MeV	0.02	0.30	− 0.05	0.13
H 2.5–3.2 MeV	0.03	0.11	− 0.05	0.12
H 3.2–4.0 MeV	0.04	0.04	− 0.05	0.10
H 4.0–5.0 MeV	0.05	0.02	− 0.06	0.08
H 5.0–6.4 MeV	0.05	0.01	− 0.06	0.07
H 6.4–8.0 MeV	0.06	0.01	− 0.06	0.06
H 8.0–10 MeV	0.06	0.01	− 0.06	0.06
H 10–13 MeV	0.06	0.01	− 0.06	0.07
H 13–16 MeV	0.06	< 0.01	− 0.06	0.08
H 16–20 MeV	0.06	< 0.01	− 0.05	0.10
H 20–25 MeV	0.06	< 0.01	− 0.05	0.12
H 25–32 MeV	0.06	< 0.01	− 0.05	0.15
H 32–40 MeV	0.06	< 0.01	− 0.04	0.20
H 40–50 MeV	0.06	< 0.01	− 0.02	0.57
H 50–64 MeV	0.07	< 0.01	0.07	0.03
H 64–80 MeV	0.25	< 0.01	0.08	0.02
H 80–100 MeV	0.38	< 0.01	0.11	< 0.01
H 100–130 MeV	0.15	< 0.01	0.09	0.01

little correlation between CR and proton fluxes in all but the highest energy channels (above 64 MeV).

Table 5 shows the same correlation analysis if only data for 10 geomagnetically quietest or 5 geomagnetically most disturbed days of each month (http://isgi. unistra.fr/events_qdays.php) are used. The fact that we observe a significant increase of positive correlation coefficients in the case of geomagnetically quiet days, further corroborates the assumption about the mixed nature of particles that populate higher-energy channels. Consequentially, care should be taken how data from these channels are treated in analysis.

To provide further quantitative support for the use of SOHO SEP flux measurements in the analysis of FD events, we will calculate integral proton flux in all energy channels for the four selected FDs. Integration intervals are selected to include the period of increased proton flux that corresponds to a particular FD, but not to extend the interval to include potential follow-up structures that cannot be associated with the event. One such selection for all energy channels, for June 2015 event, is indicated by dashed lines in Fig. 3. In Fig. 4, we show thusly calculated integral flux as a function of particle energy (where lower boundary values from SOHO SEP energy bins are taken), using both linear and log scale for clarity.

One feature that can be noticed from plots in Fig. 4 is that integral flux drops off is more steeply in February 2011 than for others studied FDs, where a change in the trend between high-energy and low-energy range can be observed. FD that occurred in March 2012 was the longest and the most intensive of the four. Steepness of

the integral flux for this FD shows relatively more populated proton channels with higher energies compared to weaker FD. This is in agreement with strongest modulation of CRs flux during this FD. There is a discontinuity in the integral flux between proton energy channel $13-16$ MeV and $16-20$ MeV due to different acquisition method from different instruments, and possibly because of degradation of the detectors on board the spacecraft [13] and saturation of the instrument due to high intensity of solar protons [18].

One simple way to characterise relative abundance of SEP particles of different energies for a given event would be to fit described integral flux distribution with a power function, where (in a simple approximation) larger exponent would indicate greater relative abundance of lower-energy particles, while smaller exponent would point to greater relative abundance of higher-energy particles. Distributions were fitted with a power function given by the formula $I(E) = a * E^b$ (where I is the integral flux and E is particle energy), resulting fits represented by red lines in Fig. 4, while values for the exponents of power function fits are represented in Table 6.

If SOHO protons flux measurements are to be proved useful in the analysis of FD events, SEP flux characteristics should correlate with some of the FD and interplanetary disturbance parameters. To test this, we have analysed dependence of different FD parameters on the exponent of the integral proton flux power distribution (labelled b in the formula in previous paragraph). We have found some correlation for most tested parameters, most striking being one between the magnitude
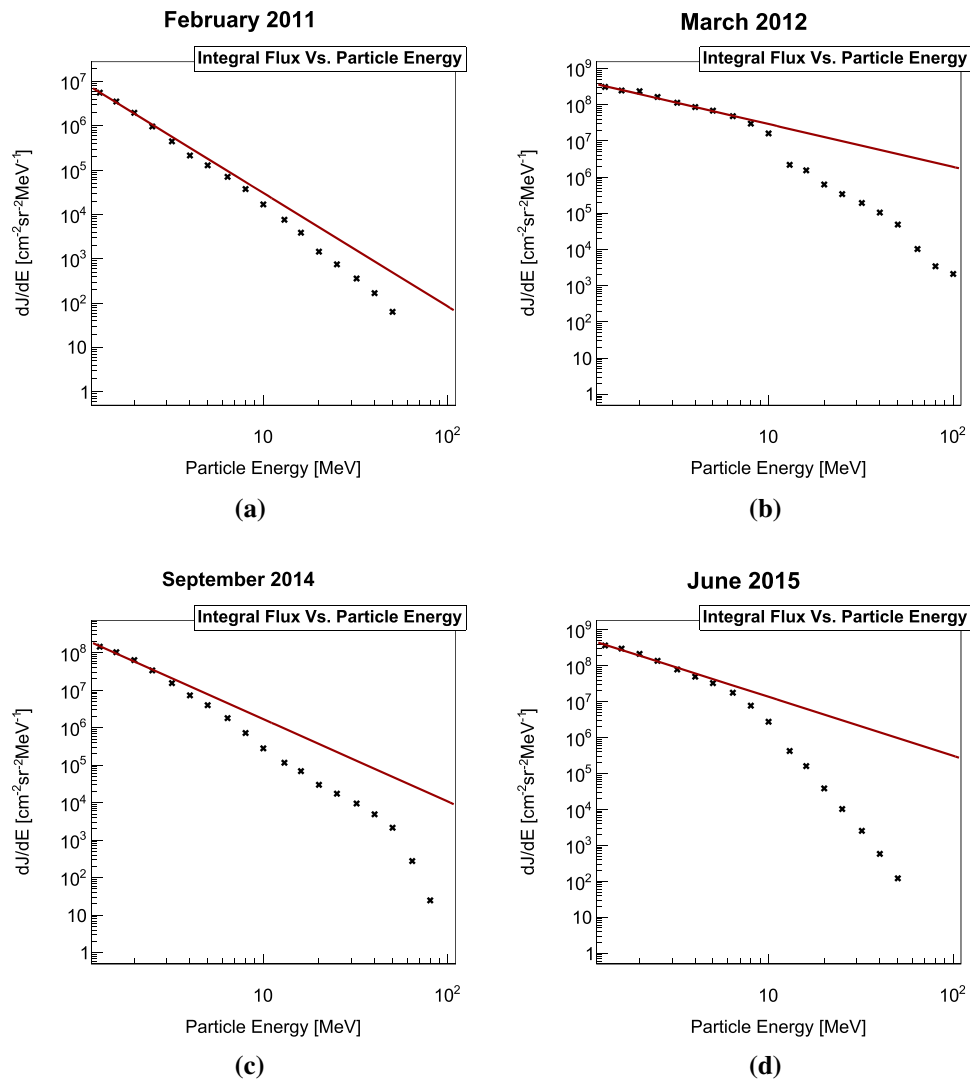
Fig. 4 Time-integrated flux of differential SEP fluxes during the four selected FD events: **a** February 2011, **b** March 2012, **c** September 2014 and **d** June 2015, in linear and logarithmic scale. Power function fits are represented by red lines

Table 6 Exponent values of power function fits of integral proton flux distributions

FD	Power function exponent values
FEB 2011	− 2.56
MAR 2012	− 1.18
SEP 2014	− 2.20
JUN 2015	− 1.64

of FD for particles with $10\,\text{GV}$ rigidity (corrected for magnetospheric effect) and the exponent of the integral flux. This dependence (strictly for illustrative purposes fitted with linear fit) is shown in Fig. 5.

Observed strong dependence is potentially a very good indicator that SOHO SEP flux measurements can be a valid source of data to be used in the analysis of

interplanetary disturbances and their interaction with cosmic rays.

7 Conclusions

Analysing strong aperiodic variations of cosmic ray flux, such as Forbush decreases, allows us to study violent processes that occur on the Sun, and corresponding perturbations in the heliosphere, using Earth-based detectors. In addition to cosmic ray flux and magnetic field data commonly used to study such events, we have extended analysis to include proton flux measurements, obtained using spacecraft mounted detectors. Based on the analysis of four selected Forbush decrease events, we have found SOHO/ERNE proton flux measurements to be consistent with solar plasma parameters, as well as with observations by the ground-based muon detectors.
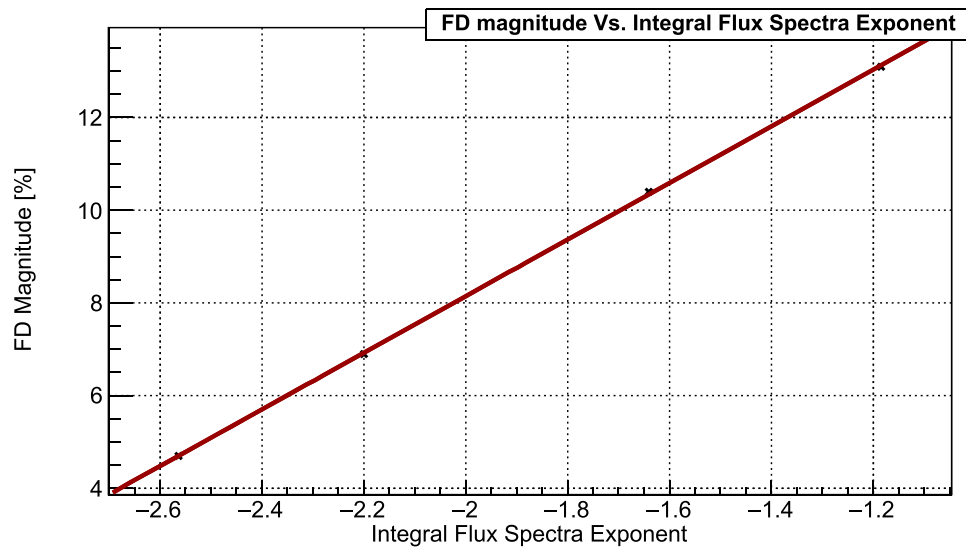
Fig. 5 Dependence of FD magnitude, corrected for magnetospheric effect with Dst-index for particles with 10 GV rigidity, on the power exponent of the integral SEP flux, four selected FD events: **a** February 2011, **b** March 2012, **c** September 2014 and **d** June 2015. Linear fit (for illustrative purposes) is indicated by the red line

We have concluded that during Forbush decrease events lower-proton-energy channels are dominated by SEP particles, while in higher-energy channels there is a contribution of low-energy cosmic rays, especially apparent during less intense events. We have found a clear correlation between Forbush decrease magnitude (corrected for magnetospheric effect with Dst-index for particles with 10 GV rigidity) and power exponent of the integral flux of SOHO/ERNE measurements. This result gives grounds to further pursue the analysis of heliospheric proton flux data, as it may yield additional valuable information. Such information can potentially help us to classify and study in greater detail the dynamics of interaction of cosmic rays in the heliosphere.

Data Availability Statement "This manuscript has data included as electronic supplementary material".

References

1. A.A. Abunin, M.A. Abunina, A.V. Belov, S.P. Gaidash, E.A. Eroshenko, I.I. Pryamushkina, L.A. Trefilova, E.I. Gamza, J. Phys. Conf. Ser. **1181**, 012062 (2019). https://doi.org/10.1088/1742-6596/1181/1/012062

2. K.P. Arunbabu, H.M. Antia, S.R. Dugad, S.K. Gupta, Y. Hayashi, S. Kawakami, P.K. Mohanty, T. Nonaka, A. Oshima, P. Subramanian, A and A **555**, A139 (2013). https://doi.org/10.1051/0004-6361/201220830

3. K.P. Arunbabu, H.M. Antia, S.R. Dugad, S.K. Gupta, Y. Hayashi, S. Kawakami, P.K. Mohanty, A. Oshima, P. Subramanian, A and A **580**, A41 (2015). https://doi.org/10.1051/0004-6361/201425115

4. C.R.A. Augusto, V. Kopenkin, C.E. Navia, K.H. Tsui, H. Shigueoka, A.C. Fauth, E. Kemp, E.J.T. Manganote, M.A. Leigui de Oliveira, P. Miranda, R. Ticona, A. Velarde, ApJ **759**, 143 (2012). https://doi.org/10.1088/0004-637X/759/2/143

5. A. Bhaskar, G. Vichare, K.P. Arunbabu et al., Astrophys. Space Sci. **361**, 242 (2016). https://doi.org/10.1007/s10509-016-2827-8

6. V. Belov, SpaceSci. Rev. **93**(1), 79–105 (2000). https://doi.org/10.1023/A:1026584109817

7. H.V. Cane, Space Sci. Rev. **93**, 55–77 (2000). https://doi.org/10.1023/A:1026532125747

8. J.M. Clem, L.I. Dorman, Space Sci. Rev. **93**, 335–359 (2000). https://doi.org/10.1023/A:1026508915269

9. E.S. Comedi, A.S. Elias, B.S. Zossi, S. Bruno, JASTP **211**, 105475 (2020). https://doi.org/10.1016/j.jastp.2020.105475

10. M. Duldig, Science **314**(5798), 429–430 (2006). https://doi.org/10.1126/science.1134046

11. M. Dumbović, B. Vršnak, J. Guo et al., Sol. Phys. **295**, 104 (2020). https://doi.org/10.1007/s11207-020-01671-7

12. J.H. King, N.E. Papitashvili, J. Geophys. Res. **110**, A02104 (2005). https://doi.org/10.1029/2004JA010649

13. P. Kühl, B. Heber, R. Gómez-Herrero, O. Malandraki, A. Posner, H. Sierks, J. Space Weather Space Clim. (2020). https://doi.org/10.1051/swsc/2020056

14. S.Y. Lee, *Accelerator Physics*, 2nd edn. (World Scientific, Singapore, 2004)

15. M. Livada, H. Mavromichalaki, C. Plainaki, Astrophys. Space Sci. **363**, 8 (2018). https://doi.org/10.1007/s10509-017-3230-9

16. R.A. Caballero-Lopez, H. Moraal, JGR Space Phys. **117**, A12 (2012). https://doi.org/10.1029/2012JA017794

17. R. Miteva, S.W. Samwel, M.V. Costa-Duarte, JASTP (2018). https://doi.org/10.1016/j.jastp.2017.05.003

18. R. Miteva, D. Danov, in *Proceedings of the tenth Workshop 'Solar Influences on the Magnetosphere, Ionosphere and Atmosphere', Primorsko, Bulgaria*, ed. by K. Georgieva, B. Kirov, D. Danov, 2018. https://doi.org/10.31401/WS.2018.proc

19. H. Moraal, Space Sci. Rev. **176**, 299–319 (2013). https://doi.org/10.1007/s11214-011-9819-3

20. S.Y. Oh, Y. Yi, A Sol. Phys. **280**, 197–204 (2012). https://doi.org/10.1007/s11207-012-0053-2

21. A. Papaioannou, A. Belov, H. Mavromichalaki et al., J. Phys. Conf. Ser. **409**, 012202 (2013). https://doi.org/10.1088/1742-6596/409/1/012202

22. A. Papaioannou, M. Belov, E. Abunina, A. Eroshenko, A. Abunin, S. Anastasiadis, Patsourakos, H. Mavromichalaki, ApJ **890**, 101 (2020). https://doi.org/10.3847/1538-4357/ab6bd1

23. E. Samara, A. Smponias, I. Lytrosyngounis et al., Sol. Phys. **293**, 67 (2018). https://doi.org/10.1007/s11207-018-1290-9

24. M. Savic, A. Dragic, N. Veselinovic et al., *XXV ECRS 2016 Proceedings—eConf C16-09-04.3*, e-Print: 1701.00164 [physics.ins-det], arXiv:1701.00164v1

25. M. Savić, A. Dragić, D. Maletić et al., Astropart. Phys. (2019). https://doi.org/10.1016/j.astropartphys.2019.01.006

26. M. Savić, N. Veselinović, A. Dragić et al., ASR **63**, 4 (2019). https://doi.org/10.1016/j.asr.2018.09.034. ISSN 0273-1177

27. M. Temmer, A.M. Veronig, V. Peinhart, B. Vršnak, ApJ **785**, 85 (2014). https://doi.org/10.1088/0004-637X/785/2/85

28. J. Torsti, E. Valtonen, M. Lumme et al., Sol. Phys. **162**, 505–531 (1995). https://doi.org/10.1007/BF00733438

29. N. Veselinović, A. Dragić, M. Savić, D. Maletić, D. Joković, R. Banjanac, V. Udovičić, NIM A **875**, 1 (2017). https://doi.org/10.1016/j.nima.2017.09.008. ISSN 0168-9002

30. L.-L. Zhao, H. Zhang, ApJ **827**, 13 (2016). https://doi.org/10.3847/0004-637X

MULTIVARIATE ANALYSIS OF TWO-YEAR RADON CONTINUOUS MONITORING IN GROUND LEVEL LABORATORY IN THE INSTITUTE OF PHYSICS BELGRADE

by

Dimitrije M. MALETIĆ [1], Radomir M. BANJANAC [1], Dejan R. JOKOVIĆ [1], Aleksandar L. DRAGIĆ [1], Nikola B. VESELINOVIĆ [1], Mihailo R. SAVIĆ [1], Zoran R. MIJIĆ [1], Vladimir I. UDOVIČIĆ [1*], Svetlana D. ŽIVKOVIĆ-RADETA [2], and Jelena V. UDOVIČIĆ [2]

[1] Institute of Physics Belgrade, National Institute of the Republic of Serbia,
University of Belgrade, Belgrade, Serbia
[2] Faculty of Applied Ecology Futura, Belgrade Metropolitan University, Belgrade, Serbia

Multivariate classification and regression analysis of multiple meteorological variables and indoor radon activity concentration in Ground Level Laboratory in the Institute of Physics Belgrade, was performed and discussed. Meteorological variables used in this analysis were from radon active device, nearby meteorological station and finally from Global Data Assimilation System. Single variate analysis has identified variables with greatest value of Pearson's correlation coefficient with radon activity concentration and also, variables with greatest separation of events with increased radon activity concentration of over 200 Bqm^{-3} and of events with radon level below this value. This initial analysis is showing the expected behavior of radon concentration with meteorological variables, with emphasis on data periods with or without air conditioning and with emphasis on indoor water vapor pressure, which was, in our previous research, identified as important variable in analysis of radon variability. This single variate analysis, including all data, proved that Global Data Assimilation System data could be used as a good enough approximate replacement for meteorological data from nearby meteorological station for multivariate analysis. Variable importance of Boosted Decision Trees with Gradient boosting multivariate analysis method are shown for all three periods and most important variables were discussed. Multivariate regression analysis gave good results, and can be useful to better tune the multivariate analysis methods.

Key words: continuous radon monitoring, multivariate analysis, Global Data Assimilation System, meteorological station

INTRODUCTION

Primarily, radon problem presents a health hazard [1]. The research of the dynamics of radon in various environments, living or working places, is of great importance in terms of protection against ionizing radiation and in designing of measures for its reduction. In the Low-Background Laboratory for Nuclear Physics extensive research on various radon fields has been done in the past, especially radon monitoring in the special designed low-background underground and ground level laboratory, with the aim of investigating the rare nuclear processes [2]. Besides radon monitoring in the laboratory, we work on several research topics regarding radon: using multivariate classification and regression methods, as developed for data analysis

in high-energy physics [3], to study connection of climate variables and variations of radon concentrations, modelling of the indoor radon behaviour and national indoor radon mapping [4], taking interest in similar indoor radon mapping analysis in Montenegro [5], or by research of radon variability in a single dwelling [6], using advanced analysis tools, or performing continuous measurements in multi-store building [7] or laboratory space [8]. Indoor radon variability depends on many variables. Soil content, and building characteristics are very important. In case of researching of indoor radon variability, meteorological effects become the most important ones. With recent experiences with lowering the limits of indoor radon level, both in dwellings and working places, and the demand for decrease of public radon exposure, the need for more detailed knowledge on radon variability is increasing. Besides a possibility for improvement of mitigation

---

274

D. M. Maletić, *et al*., Multivariate Analysis of Two-Year Radon Continuous ...
Nuclear Technology & Radiation Protection: Year 2023, Vol. 38, No. 4, pp. 273-282

techniques, we could look into creating online warning pages, like we already have, for example, for UV radiation. These online warning pages, with information on radon concentration variations, could be interesting to people living in dwellings or working spaces with previously known radon problem, or dwellings with radon activity concentration close to 200 Bqm^{-3} limit. These online warnings, could indicate a call for some temporary measures like starting of increased ventilation or reducing exposure. Local radon warning pages could be based on local meteorological station, but for larger regions, meteorological modeled data like Global Data Assimilation System (GDAS) could be used. In this paper we were looking into the possibility of using GDAS data in prediction of indoor radon variability, by jointly looking into GDAS and nearby meteorological station, and compare the results.

DATA PREPARATION AND SELECTION

The radon continuous monitoring in ground level laboratory was performed with active device RadonEye Plus2 with time sampling of one hour. The device recorded variables: Rn-activity, indoor temperature and indoor humidity. The radon the measurement was done from November 2020 to November 2022. After looking into indoor temperature data, we decided to do three analysis, one with using all the data samples (whole period of measurement's), second using only data when air conditioning (AC) was operating, and third sample used for analysis was for periods when air conditioning was OFF (noAC).

Meteorological station located in Institute of Physics Belgrade yard, and maintained by Environmental Physics Laboratory [8], has being recording variables at 5 minute interval, and hourly values are used for this analysis. Variables are named by adding prefix outside; outside-cloudbase, outside-dew point, outside-humidity, outside-temp, outside-pressure and outside-rain.

The US National Centers for Environmental Prediction (NCEP) runs a series of computer analyses and forecasts operationally. One of the operational systems is the GDAS. At National Oceanic and Atmospheric Administration's (NOAA) Air Resources Laboratory (ARL), NCEP model output is used for air quality transport and dispersion modeling. The ARL archives GDAS output which contains basic fields, such as the temperature, pressure and humidity. Those GDAS data are very interesting since they are widely used by weather forecast groups worldwide, and our idea is that if we could use this freely accessed and frequently updated database, we could improve forecasting of some kind of *relative* indoor radon concentrations, and indicate by result of automatic online MVA regression analysis when to expect increased indoor radon concentrations based on meteo-

rological variables. Because MVA methods are rather robust, and we wanted to see which, if any of GDAS variables are suited for our purpose, we included most of variables in our analysis. The GDAS1 data is available for integer values of latitude and longitude, so, for all variables', each data point was firstly 2-D linearly interpolated using variables' values on four integer latitudes and longitudes, surrounding latitude and longitude of our laboratory. The GDAS1 data is available for every three hours, so linear interpolation of each variable's data point was made in order that we can use hourly data. The GDAS1 variables used in our analysis can be identified as ones with prefix GDAS1; GDAS1-CAPE (convective available potential energy), GDAS1-CINH (convective inhibition), GDAS1-CPP6 (accumulated convective precipitation), GDAS1-CRAI (categorical rain), GDAS1-DSWF (downward short wave radiation flux), GDAS1-HCLD (high cloud cover), GDAS1-LCLD (low cloud cover), GDAS1-LHTF (latent heat net flux at surface), GDAS1-LIB4 (best 4-layer lifted index), GDAS1-LISD (standard lifted index), GDAS1-MCLD (middle cloud cover), GDAS1-PBLH (planetary boundary layer height), GDAS1-PRSS (pressure at surface), GDAS1-RH2M (relative humidity at 2m AGL), GDAS1-SHGT (geopotential height), GDAS1-SHTF (sensible heat net flux at surface), GDAS1-SOLM (volumetric soil moisture content), GDAS1-T02M (temperature at 2m AGL), GDAS1-TCLD (total cloud cover), GDAS1-TMPS (temperature at surface), GDAS1-TPP6 (accumulated precipitation), GDAS1-mofi-e (momentum flux intensity), GDAS1-mofd-e (momentum flux direction). In this analysis using GDAS data, we also could indicate if variables measured by local meteorological station do not differ too much from GDAS modeled and interpolated ones, that GDAS variables could be used in this kind of MVA analysis.

We included previously found interesting variable in radon research [6] and that is water vapor pressure in outdoor and indoor air, as well as the difference of the two. In order to calculate the water vapor pressure in air, we need to calculate the value of the saturation water vapor pressure

$$\mathrm{es}(T) = 0.6108 \cdot \mathrm{e}^{\frac{17.27 \cdot T}{T+237.3}} \qquad (1)$$

In addition, the slope of the relationship between the saturation water vapor pressure (es [kPa]) and the air temperature T [°C], is given in [9, 10], so including the slope, we get new formula for the saturation water vapor pressure

$$es(T) = \frac{4098 \cdot \left(0.6108 \cdot \mathrm{e}^{\frac{17.27 \cdot T}{T+237.3}}\right)}{(T+237.3)^2} \qquad (2)$$

and since the formula used to calculate the relative humidity is

Figure 1. The Rn activity indoor (a) and vapor pressure difference of outdoor and indoor (b). Note that with much greater outdoor water vapor pressure than indoor, comes influx of radon-free water vapor, and that results in significant decrease of indoor Rn activity
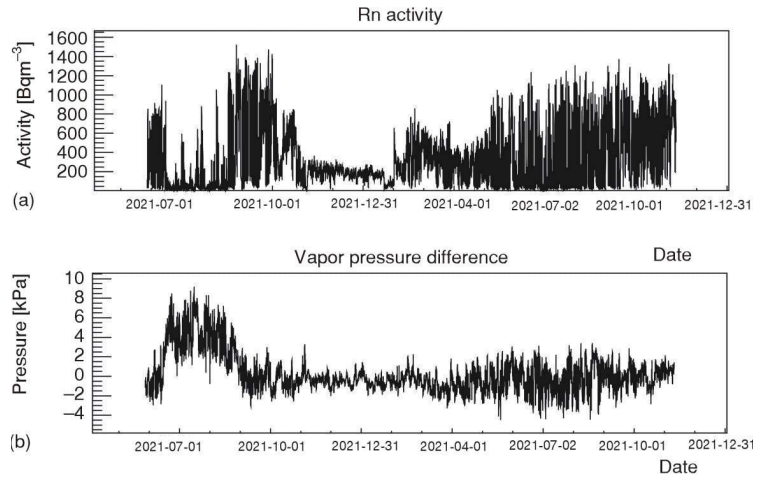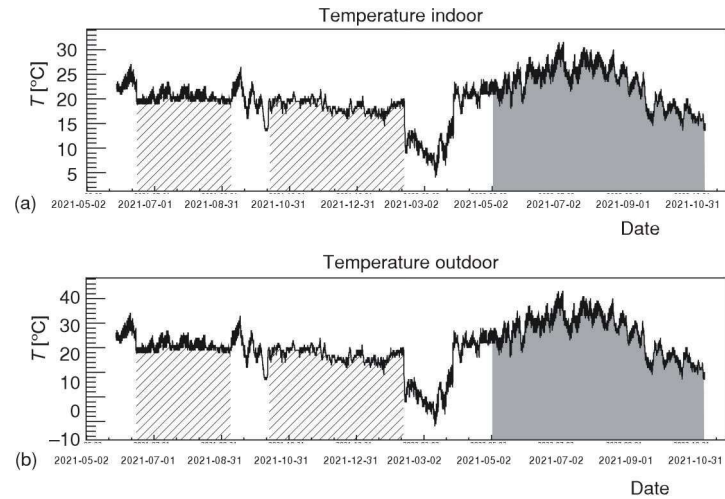

Figure 2. Indoor temperature (a) and outdoor temperature (b) is shown. Indoor temperature which was used for analysis when air conditioning (AC) was on, is indicated in two line pattern areas, while gray shaded interval indicates period when air conditioning was off (noAC)

$$RH = \frac{\text{vapor pressure}}{\text{es}(T)} \qquad (3)$$

we get the formula to calculate the vapor pressure in air

$$\text{vapor pressure}(T, RH) = RH \cdot$$
$$4098 \cdot \frac{\left(0.6108 \cdot e^{\frac{17.27 \cdot T}{T + 237.3}} \right)}{(T + 237.3)^2} \qquad (4)$$

Using this formula, we calculate four variables: indoor-vapor-press (vapor pressure from indoor-temperature and indoor-humidity data), outside-vapor-press (vapor pressure from outdoor outside-humidity, outside-temp data), diff-vapor-press (vapor pressure difference of outdoor and indoor) and gdas1-vapor-press (vapor pressure from GDAS1-T02M, GDAS1-RH2M data). On the bottom of fig. 1 the vapor pressure difference is shown, and it can be clearly seen that if the outer vapor pressure is much higher than the indoor vapor pressure, the indoor radon activity is lower fig. 1(a).

Out of two years of data taking, after merging all the data together to form a single hourly event with all the variables measured at that time, the number of useful hourly events was 12654. Table 1 shows the num-

Table 1. Summary table of number of hourly events used for specific part of analysis

	noAC	AC	All period
Signal training	1343	912	3428
Signal testing	1343	912	3428
Signal training and testing	2686	1824	6856
Background training	942	1531	2899
Background testing	942	1531	2899
Background training and testing	1884	3062	5798

ber of hourly events used for each of the three periods of analysis, which were split, firstly into signal and background events, where signal events are those for which Rn activity is more than 200 Bqm^{-3}, and background is less than that value, and then each set was split once more, into training and testing sample to be used in MVA analysis. Table 1 also shows the number of events used, and split, in periods with air condition operation on (AC), line pattern area on fig. 2(a), and air conditioning off (noAC) gray on fig. 2(a).

Before performing the multivariate (MVA) analysis, we have looked into single variable analysis, and the best way to see if variables could be useful for analysis is if they have, firstly, the greatest correlation with radon activity (concentration), and, secondly, which variable profiles for

276

D. M. Maletić, *et al.*, Multivariate Analysis of Two-Year Radon Continuous ...
Nuclear Technology & Radiation Protection: Year 2023, Vol. 38, No. 4, pp. 273-282
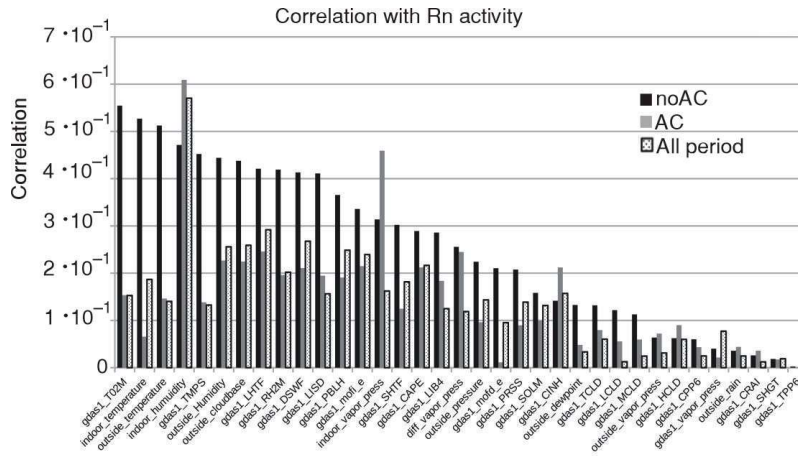
Figure 3. The modulus of Pearson's correlation coefficients of radon activity with each of variables used in the analysis is shown. Note the decreasing of correlation with temperature variables, and increasing with humidity variables, when air conditioning (AC) was turned on
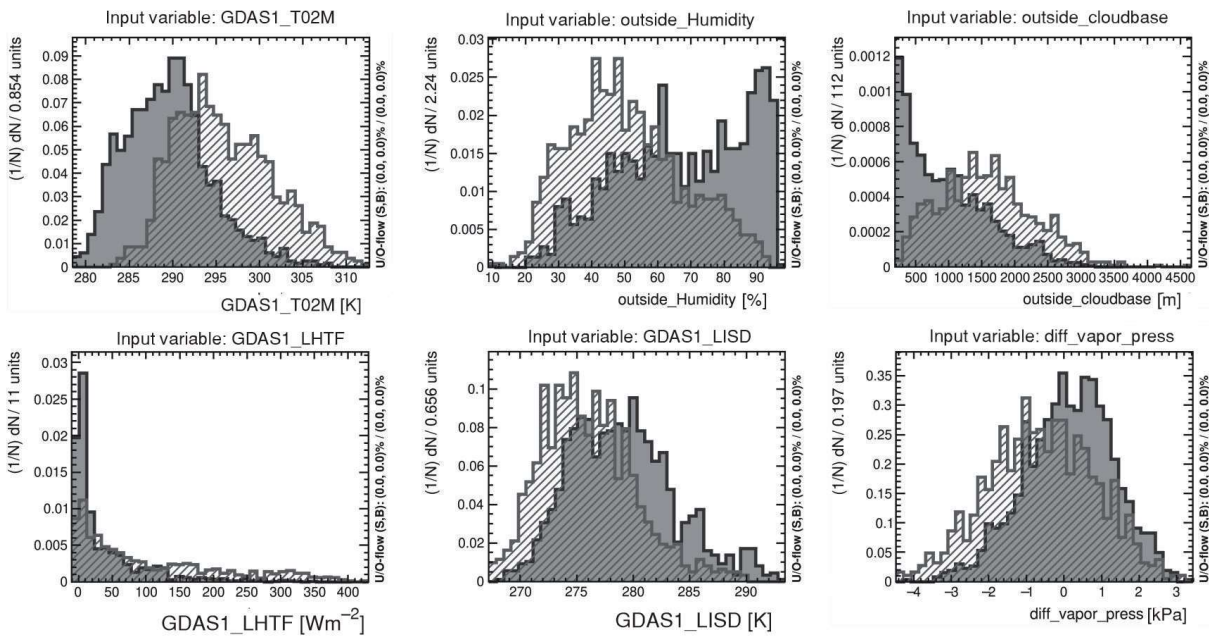

Figure 4. For some variables there is a significant separation of distributions of variables' values for events with low and events with high radon activity. Variables shown are: temperature at height of 2 m above the ground (GDAS1-TO2M), outside relative air humidity, measure of lowest visible part of the cloud (cloudbase), latent heat net flux at the surface (LHTF), standard lifted index (LISD) and the difference of water vapor pressure from indoor and outdoor

high Rn activity (signal) and low (background) data samples, have smallest overlap, meaning that they have greatest separation of high and low Rn activity samples. So, firstly, we are looking into modulus of Pearson's correlation coefficients for each of the variables used in this analysis with radon activity, fig. 3. Since the greatest variation of radon activity should give the best insight into correlation with variables, we are firstly looking into data with air condition off (noAC). To the variables with greatest modulus of Pearson's correlation coefficients with Rn activity (noAC) are temperature variables from all three sources of data GDAS, radonometar and meteorological station (GDAS1-T02M, indoor-temperature, outside-temperature, GDAS1-TMPS), than humidity (indoor-humidity, outside-humidity), outside-cloudbase, followed with GDAS variables: GDAS1-LHTF (latent heat net flux on surface) and GDAS1-DSWF (downward short wave radiation flux) and GDAS1-RH2M (relative humidity at height of 2 m), followed by indoor-vapor-pressure. When air conditioning

is turned on, there is a change in correlation, where temperature variables correlations are decreasing, and there is an increase in correlation of humidity variables like indoor-humidity and indoor-vapor-pressure. We observe this change since temperature is now holding at approximately the same level by air conditioning, and any variation of radon activity we see does not come from approximately constant temperature. We noticed the similarity in modulus of Pearson's correlation coefficients of outside-T02M and outside-temperature with Rn activity of 55.4 % and 51.2 %, respectively, for noAC data, and 15.3 % and 14.6 %, respectively, for AC data. Also, outside-humidity and gdas1-RH2M with 44.4 % and 41.9 %, respectively, for noAC and 22.7 % and 19.6 % for AC data. When looking into pressure data, outside-pressure and GDAS1-PRSS have modulus of Pearson's correlation coefficients of 22.4 % and 20.8 %, respectively, for noAC data and 9.6 % and 9.0 % for AC data.

When looking into separation of variables for signal and background samples, fig. 4 shows selected
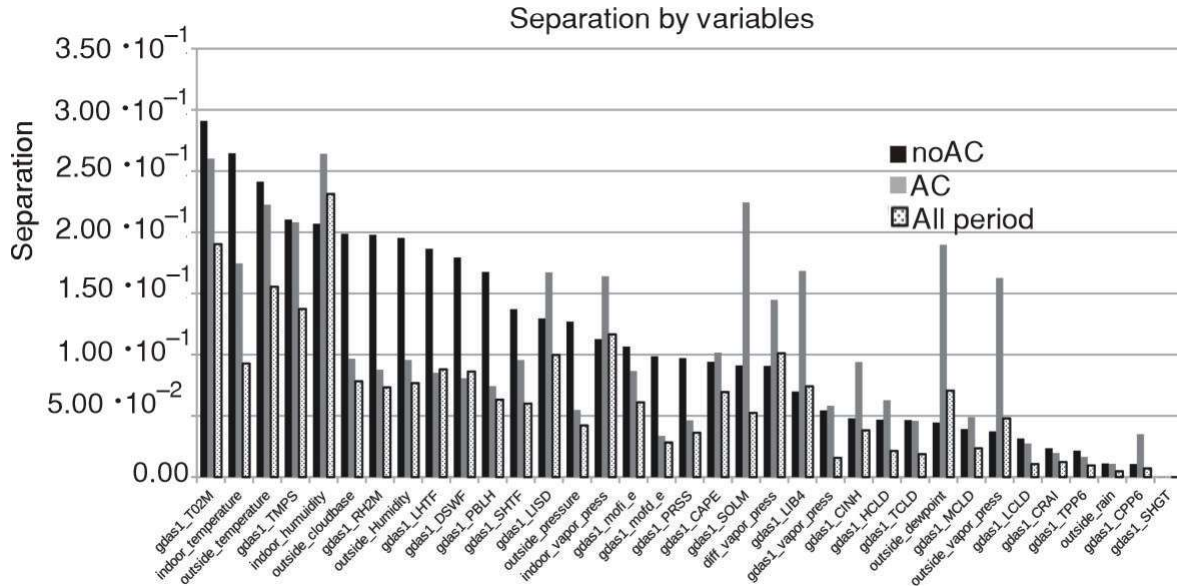
D. M. Maletić, *et al*., Multivariate Analysis of Two-Year Radon Continuous ...
Nuclear Technology & Radiation Protection: Year 2023, Vol. 38, No. 4, pp. 273-282

277

Figure 5. Separation of events with low and high Rn activity by each variable

variables, where separation can be seen with naked eye, and also, separations of high and low Rn activity for different variables can be roughly compared. But, we want to have more precise insight into separation, and for all three samples AC, noAC and samples of whole measurement period. This is shown in fig. 5 where we can see that for noAC, temperature variables have most significant separation values, as was the case with modulus of Pearson's correlation coefficients with Rn activity on fig. 3. With air conditioning turned on, the variables of humidity and vapor pressure gain in separation value, while indoor temperature is decreasing its separation value. Notice that the change is not so pronounced as was the case with correlation variables. Again, we noticed the similarity separation values of outside-T02M and outside-temperature 29.1 % and 24.1 %, respectively, for noAC data, and 26.0 % and 20.8 %, respectively, for AC data. Also, outside-humidity and GDAS1-RH2M with 19.8 % and 19.5 %, respectively, for noAC and 8.8 % and 9.6 % for AC data. When looking into pressure data, outside-pressure and GDAS1-PRSS have separation values of 12.7 % and 9.7 %, respectively, for noAC data and 5.5 % and 4.6 % for AC data.

**MULTIVARIATE
CLASSIFICATION ANALYSIS**

Toolkit for multivariate analysis (TMVA) [11] implemented in ROOT [12] framework for data analysis, has many of multivariate methods and tools implemented, which are frequently used for data analysis, as in High energy physics, also by data scientists in general. We will not get into details of wide spread of multivariate methods available, which can be found in

TMVA manual [11]. The usage of those multivariate methods in TMVA is rather standardized. What is advantageous in using TMVA is that we could compare many of multivariate methods using the same training and testing sample. Also, the TMVA was used in many analyses, and is constantly under development, with many new methods implemented. The TMVA offers comparison of methods developed for other frameworks, like methods developed in programming langnages Python, or R, or modern methods like Deep and Convolutional Neural Networks, which is best to be run in multi-thread mode or on CPU or on GPU (graphical cards).

In MVA analysis, the data sample consists of events. Event is composed of data measured/recorded at the same time for each input variable. We can run MVA as Classification, Classification with category, and Regression. The MVA Classification is done when sample is divided into two samples (classes); signal and background. The MVA methods are trained to make the same classification using events they have not seen before, and their performance in classification is measured. Second MVA analysis is done as regression analysis. It is similar to classification, in the sense that the number of classes into which initial sample is divided is much bigger, and the value of classifier is not only 1 (signal) and 0 (background) but has much more values in between. Classification with category was not used, as the maximum performance of Classification is obtained when no other categorical values besides 1 (signal) and 0 (background) are used. Future performance tests could include categories like; very high, high, medium, low and very low radon concentrations.

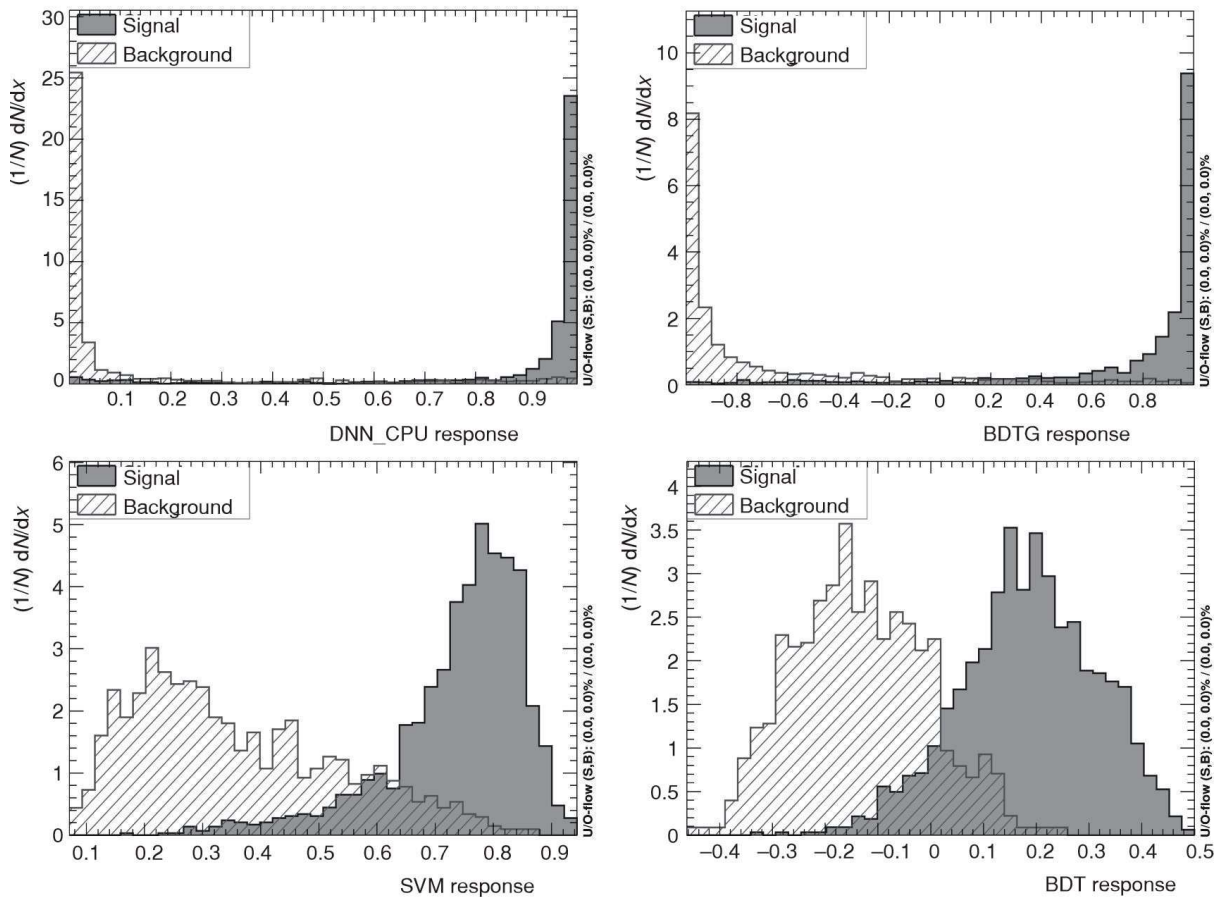When a sample is prepared, MVA classification needs some time to complete the training process for

278

D. M. Maletić, *et al.*, Multivariate Analysis of Two-Year Radon Continuous ...
Nuclear Technology & Radiation Protection: Year 2023, Vol. 38, No. 4, pp. 273-282

Figure 6. Response of MVA methods to events with low and high Rn activity
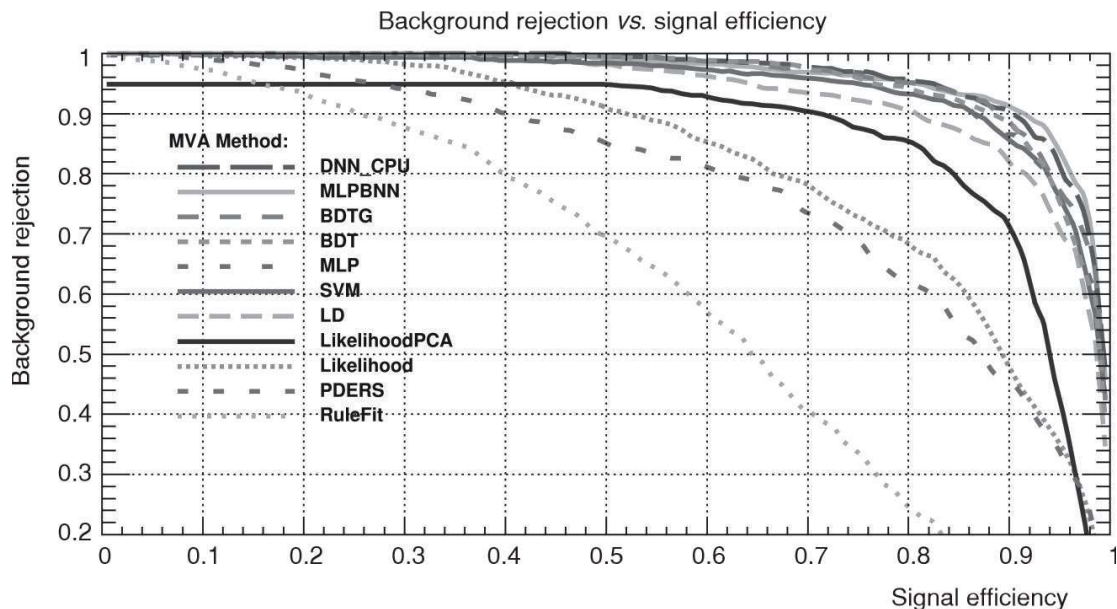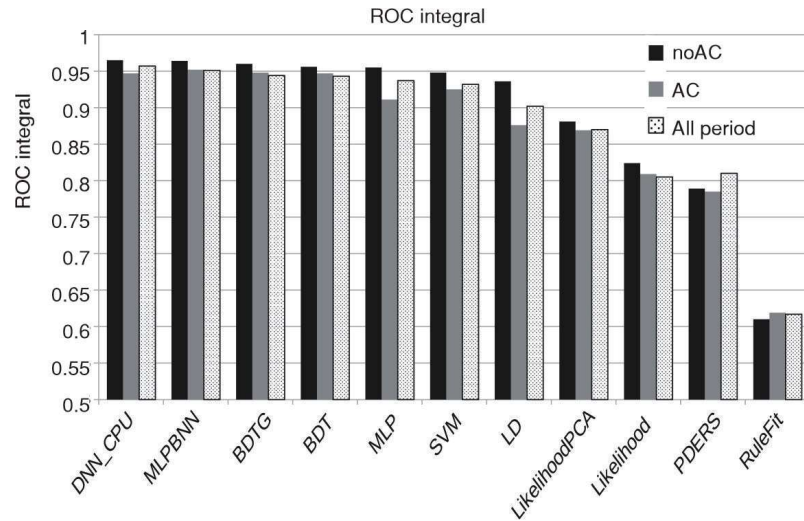

Figure 7. The ROC curve for MVA methods for the time interval where air conditioning was off (noAC)

each of MVA methods selected for comparison. Besides training, the sample of same number of events is used for evaluation, or testing, where MVA method is tested on samples not seen before (not used for training). The performance of some MVA method is expressed only using testing/evaluation sample.

The fig. 6 shows the response of best performing MVA methods, in analysis of noAC data, to events with low and high Rn activity, or signal and background. We can see, in fig. 7, that by looking into Receiver Operating Characteristic (ROC) curve comparison of all selected multivariate methods, that several

D. M. Maletić, *et al*., Multivariate Analysis of Two-Year Radon Continuous ...
Nuclear Technology & Radiation Protection: Year 2023, Vol. 38, No. 4, pp. 273-282

279

Figure 8. Value of the ROC integral for MVA methods for the selected time intervals, AC and noAC, and for whole time interval

methods have very good performances and also, very close performances. It is very good to have several methodologically very different multivariate methods performing in similar way, since this gives us confidence that classification is applicable. To illustrate this point, we can say that, very generally speaking, ANN are based on convolution of selected function to the resulting multivariate functional dependence, while Boosted Decision Trees are based on multidimensional space (cube) cuts, for approximation of multivariate functional dependence, and it is very good that both have very good performances in MVA classification.

The comparison of ROC curve integrals for best performing methods, for MVA classification analysis for all three intervals; noAC, AC and all-period analysis is shown at fig. 8. For five best performing methods, DNN-CPU (Deep Neural Network), MLPBNN (Multi-Layer Perceptron Bayesian regulator Neural Network), BDTG (Boosted Decision Trees with Gradient boosting), BDT (Boosted Decision Trees), and MLP (Multi-Layer Perceptron – an ANN), results are very similar, and also for all the three intervals, which is very important in sense that while variables' correlation with Rn activity vary greatly, this is easily overcome in MVA methods, adding very important property of robustness in variable selection. We should note that all the mentioned methods are ANN or DBT based multivariate methods.

The resulting trained multivariate methods are now ready to be included into some web applications, or used in variables' analysis. In web applications, Radon alarm could be constructed, when based on input variables, there is a great probability of increased indoor radon activity. For example, some places where it is known from previous measurements, like from participation in large indoor radon survey, that dwelling or working space has a problem with increased indoor radon concentration, some measures like increased ventilation or longer brakes from work, could be made. In variables' analysis, the simplification of MVA approximation of

underlying multivariable function dependence could be made, not only with classification, but more effectively with regression methods.

The MVA methods which are trained and tested using full set of variables and all available data are ready to be used in some application. But, we can continue our work and try to modify something in our analysis chain to see if we can get better performance or method which uses lower number of input variables, without big loss in performance. We can make different selection of training data sets, like truncation of outlier data, we can change the number of input variables, or change parameters specific for each MVA method. For this purpose, it could be very useful to look into variable importance for specific MVA method, for example for BDTG in fig. 9, in order to look into the influence of variables on MVA decision. To show why this is useful we pay attention on Pearson's correlation coefficients of input variables and radon concentrations and notice that there could be several variables with high correlation coefficient with radon concentration, but highly inter-correlated with each other, which results in no gain in MVA method performance if we add several variables which are inter-correlated. So, we can exclude variables if their exclusion does not lower the MVA method performance. We choose to look into importance of variables on BDTG classification, for all time intervals. Again, we start with noAC intervals, where indoor radon activity was highest, and indoor temperature was not regulated. We start with two GDAS variables, GDAS1-SHTF (sensible heat net flux at surface) and GDAS1-SOLM (volumetric soil moisture content), followed by indoor-humidity and diff-vapor-pressure, and GDAS1-T02M at position 6, with some other variables similarly important as gdas momentum flux direction and gdas cloud cover variables.

When comparing data from meteorological station and gdas data, we cannot compare them in, for example, multivariate importance, since if one variable is chosen to be used in MVA training, similar variable in, for example Pearson's correlation coefficients or
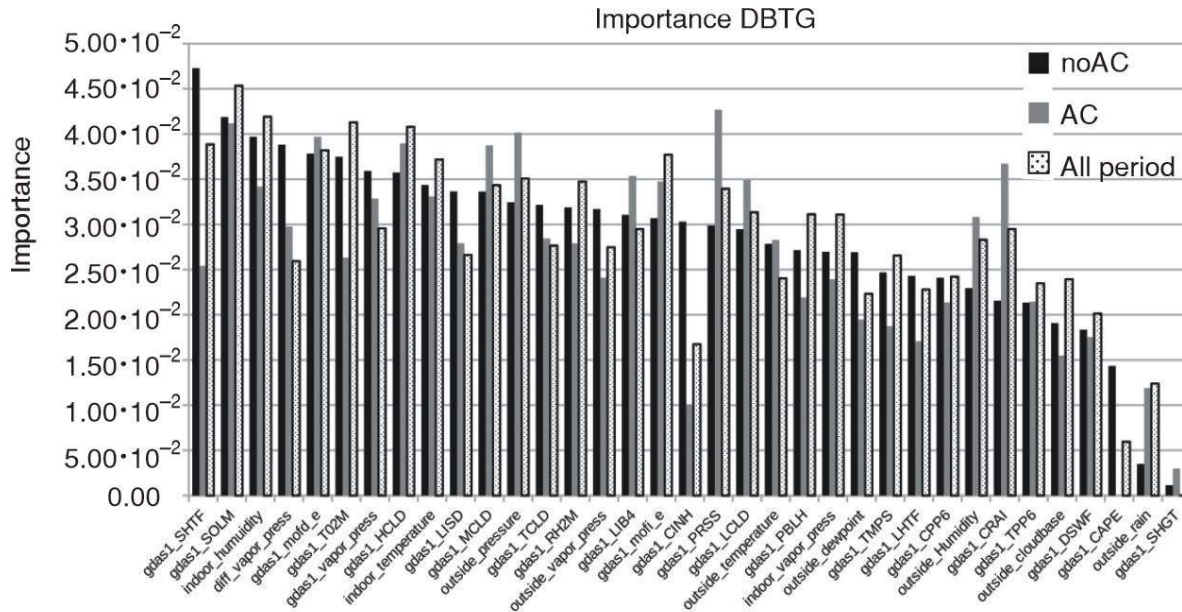
280

D. M. Maletić, *et al.*, Multivariate Analysis of Two-Year Radon Continuous ...
Nuclear Technology & Radiation Protection: Year 2023, Vol. 38, No. 4, pp. 273-282

Figure 9. Variable importance for MVA method BDTG for time intervals, AC and noAC, and for the whole time interval

separation of variable for increased and for low Rn activity value, do not have power to make discrimination. Comparison can only be used when each variable is observed separately in a single variable analysis. Also, similar situation can happen with preparation of variables, where resulting variables are, de-correlated, and first variable is significant for further analysis but other, very similar variable before de-correlation, remains with negligible significance for further analysis.

THE MVA REGRESSION

Regression analysis often fails if there is not a strong dependence of target variable, in our case Rn activity, on input variables. Reasoning is the following: Classification analysis has only two outputs, either it is signal (1) or background (0), but in case of regression,

there are many more values between 0 and 1, and much more dependence, or events is needed to get positive results here. We ran MVA regression for three time intervals, noAC, AC and all-period. The BDTG and DNN-CPU show good prediction results after MVA regression training procedure, as a result of RMS of deviations of true and evaluated value of Rn activity are satisfyingly small, as is shown in fig. 10. The fig. 11 shows this in more detail for BDTG in noAC regression analysis, where the distribution of deviations is shown for each event in the testing sample.

CONCLUSIONS

Single variate analysis of correlations of each of meteorological variable with indoor radon activity and Multivariate classification and regression analysis of all meteorological variables and radon activity was per-

Figure 10. The RMS of deviations of regressions from true value for selected time intervals, AC and noAC, and for the whole time interval, for several MVA regression methods
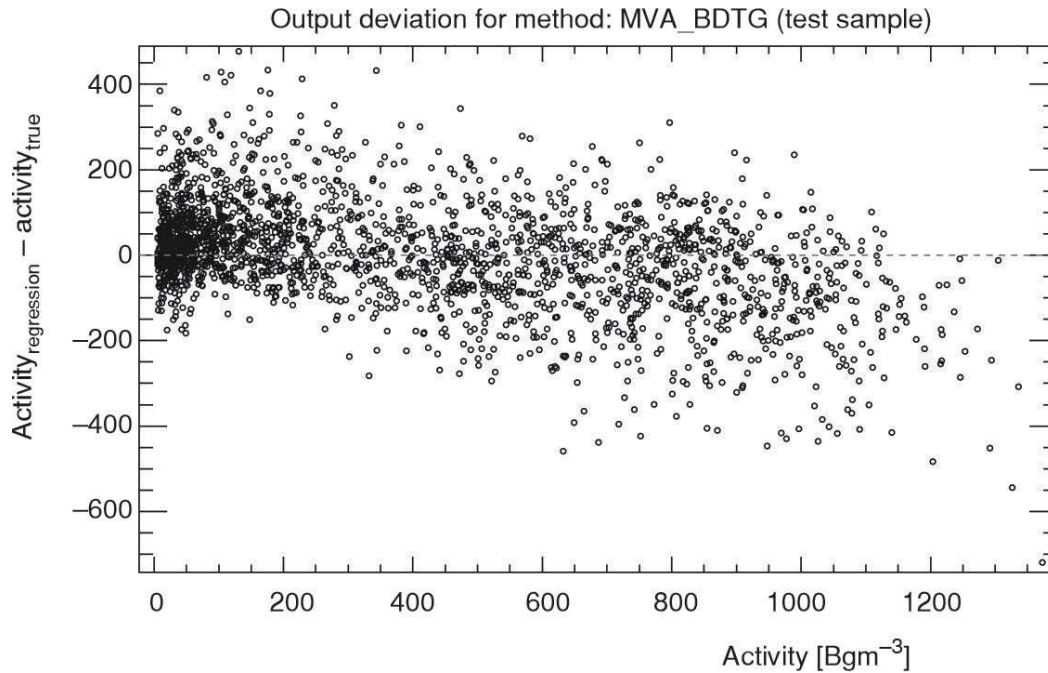
Figure 11. Deviation of regression from true value for noAC period and BDTG MVA method

formed and discussed. Meteorological variables used in this analysis were from radonometar device, then from a nearby meteorological station and finally from GDAS data. Single variate analysis has identified variables with greatest value of modulus of Pearson's correlation coefficient with Rn activity, and also variables with greatest separation of events with increased Rn activity of over 200 Bqm^{-3} and of events with Rn activity below this value. This initial analysis and looking into variables were showing the expected behavior of Rn concentration with meteorological variables, with emphasis on data periods with or without air conditioning, and also with emphasis on previously found variable of indoor water vapor pressure. This single variate analysis and observing all the data proved also useful for conclusion that GDAS data could be used as a good enough approximate replacement for meteorological data from the nearby meteorological station for MVA analysis. The MVA classification analysis found several very well performing MVA methods which can be used in web application or for further detailed analysis of specific input variables. Variable importance of BDTG MVA method was shown for all three periods, and most important variables were discussed. Finally, MVA regression analysis gave also good results, and more quality measurements in this rarely accessed ground level laboratory would be useful to better tune the MVA methods, and do more detailed analysis.

ACKNOWLEDGMENT

AUTHORS' CONTRIBUTIONS

The original idea and draft were carried out by D. M. Maletić. The data provided by R. M. Banjanac, V. I. Udovičić and Z. Mijić. Statistical analysis was done by D. M. Maletić, D. R. Joković and A. L. Dragić. N. B. Veselinović, M. R. Savić, S. Živković-Radeta and J. V. Udovičić worked on data preparation and selection. All the authors analyzed and discussed the results and reviewed the manuscript.

REFERENCES

[1]   ***, WHO Handbook on Indoor Radon: A Public Health Perspective, World Health Organization, Switzerland, 94, 2009

[2]   Dragić, A., *et al.*, The New Set-Up in the Belgrade Low-Level and Cosmic-Ray Laboratory, *Nucl Technol Radiat, 26* (2011), 3, pp. 181-192

[3]   Maletić, D., *et al.*, Comparison of Multivariate Classification and Regression Methods for the Indoor Radon Measurements, *Nucl Technol Radiat, 29* (2014), 1, pp. 17-23

[4]   Eremić-Savković, M., *et al.*, Results of the First National Indoor Radon Survey Performed in Serbia, *Journal of Radiological Protection, 40* (2020), 2, pp. N22-N30

[5] Vukotić, P., *et al.*, Influence of Climate, Building, and Residential Factors on Radon Levels in Ground-Floor Dwellings in Montenegro, *Nucl Technol Radiat, 36* (2021), 1, pp. 74-84

[6] Udovičić, V., *et al.*, Multiyear Indoor Radon Variability in a Family House – a Case Study in Serbia, *Nucl Technol Radiat, 33* (2018), 2, pp. 174-179

[7] Udovičić, V., *et al.*, Radon Variability Due to Floor Level in Two Typical Residential Buildings in Serbia, *Nukleonika, 65* (2020), 2, pp. 121-125

[8] Maletić, D., *et al.*, Correlative and Multivariate Analysis of Increased Radon Concentration in Underground Laboratory, *Radiation Protection Dosimetry, 162* (2014), 1-2, pp. 148-151

[9] Tetens, O., About Some Meteorological Terms (original: Über Einige Meteorologische Begriffe.) *Z. Geophys, 6* (1930) pp. 297-309

[10] Murray, W., On the Computation of Saturation Vapor Pressure, *J. Applied Meteorology, 6* (1967), pp. 203-204

[11] Hoecker, A., *et al*, TMVA – Toolkit for Multivariate Data Analysis. *PoS ACAT, 40* (2009), p. 12

[12] Brun, R., Rademakers, F., ROOT – An Object Oriented Data Analysis Framework, *Nucl. Inst. & Meth. in Phys. Res. A, 389* (1997), pp. 81-86

Димитрије М. МАЛЕТИЋ, Радомир М. БАЊАНАЦ, Дејан Р. JOKOВИЋ, Александар Л. ДРАГИЋ, Никола Б. ВЕСЕЛИНОВИЋ, Михаило Р. САВИЋ, Зоран Р. МИЈИЋ, Владимир И. УДОВИЧИЋ Светлана Д. ЖИВКОВИЋ-РАДЕТА, Jeлена В. УДОВИЧИЋ

МУЛТИВАРИЈАНТНА АНАЛИЗА ДВОГОДИШЊЕГ КОНТИНУАЛНОГ МОНИТОРИНГА РАДОНА У НАДЗЕМНОЈ ЛАБОРАТОРИЈИ У ИНСТИТУТУ ЗА ФИЗИКУ У БЕОГРАДУ

Приказана је мултиваријантна класификациона и регресиона анализа односа метео-ролошких варијабли и концентрације радона у затвореној и ретко приступачној приземној лабораторији Института за физику Београд. Податке о метеоролошким варијаблама и кон-центрацији радона, коришћене у овој анализи, добијамо из активног уређаја за краткорочна мерења концентрације радона у затвореном простору, оближње метеоролошке станице и из података Глобалног система асимилације података. Једно-варијантном анализом идентификоване су варијабле са највећом вредношћу модула Пирсоновог коефицијента корелације са концентрацијом радона, као и варијабле са највећом моћи раздвајања догађаја са повећаном концентрацијом радона више од (200 Bqm⁻³) и догађаја са нижом концентрацијом од ове вредности. Ова почетна анализа и сагледавање варијабли показују очекивану везу концентрације радона и метеоролошких варијабли, са нагласком на анализу података из различитих временских интервала, када је у лабораторији радила и када није радила климатизација, као и са нагласком на варијаблу разлика унутрашњег и спољашег притиска водене паре. Ова једно-вариантна анализа доводи до закључка да се подаци Глобалног система асимилације података могу користити као довољно добра приближна замена за метеоролошке податке из оближње метеоролошке станице за мултиваријантну анализу. Мултиваријантном класификационом анализом пронађено је неколико веома добрих мулти-варијантних метода које се могу користити у некој веб апликацији или за даљу детаљну анализу специфичних улазних варијабли. Приказана је важност варијабли за мултиваријантни метод стабла одлучивања за сва три периода мерења, а разматране су и најважније варијабле. Коначно, мултиваријантна регресиона анализа је такође дала добре резултате, што може да буде корисно при оптимизацији класификационих мултиваријантних метода.

Кључне речи: континуирани радон мониторинг, мултиваријантна анализа, Глобални систем асимилације података, метеоролошка станица

sciendo

Radon variability due to floor level in two typical residential buildings in Serbia

Vladimir Udovicic (ORCID),
Nikola Veselinovic,
Dimitrije Maletic,
Radomir Banjanac,
Aleksandar Dragic,
Dejan Jokovic,
Mihailo Savic,
David Knezevic,
Maja Eremic Savkovic

Abstract. It is well known that one of the factors that influence the indoor radon variability is the floor level of the buildings. Considering the fact that the main source of indoor radon is radon in soil gas, it is expected that the radon concentration decreases at higher floors. Thus at higher floors the dominant source of radon is originating from building materials, and in some cases there may be deviations from the generally established regularity. In such sense, we chose one freestanding single-family house with loft and other 16-floor high-rise residential building for this study. The indoor radon measurements were performed by two methods: passive and active. We used passive devices based on track-etched detectors: Radtrak^2 Radonova. For the short-term indoor radon measurements, we used two active devices: SN1029 and SN1030 (manufactured by Sun Nuclear Corporation). The first device was fixed in the living room at the ground level and the second was moved through the floors of the residential building. Every measuring cycle at the specified floor lasted seven days with the sampling time of 2 h. The results show two different indoor radon behaviours regarding radon variability due to floor level. In the single-family house with loft we registered intense difference between radon concentration in the ground level and loft, while in the high-rise residential building the radon level was almost the same at all floors, and hence we may conclude that radon originated mainly from building materials.

Keywords: Radon variability • Time series

V. Udovicic✉, N. Veselinovic, D. Maletic, R. Banjanac, A. Dragic, D. Jokovic, M. Savic, D. Knezevic
Institute of Physics Belgrade
University of Belgrade
Pregrevica 118 St., 11080 Belgrade, Serbia
E-mail: udovicic@ipb.ac.rs

M. Eremic Savkovic
Serbian Radiation and Nuclear Safety and Security Directorate
Masarikova 5 St., 11000 Belgrade, Serbia

Introduction

Radon sources in the buildings are primarily from soil, building materials and water. Considering the nature of the occurrence and all the sources, the concentration of radon is higher in the ground-floor rooms compared with that in the higher floors of the dwellings in apartments. In the literature one can find a lot of papers dealing with the influence of various factors, including the floor levels, on the radon concentration and variability. In one group of the articles, investigation of the indoor radon concentration distribution due to floor levels of the buildings is the part of the data analysis which was drawn from the national or regional radon surveys [1–6] and others are dedicated to these specific studies [7–11]. In the case of the big buildings with a several number of floors a deviation from the general regularity can be observed, since the dominant source of indoor radon at higher floors is building materials. On the other hand, the radon variability due to floor level, especially in big cities with a much higher number of high-rise buildings and population density compared with rural environments, may have an impact on the assessments of the effective dose from radon exposure at the national level. Usually, the indoor radon map represents the arithmetic mean value of indoor radon concentration on the ground floor, and thus it is not

representative of the radon exposure to all citizens since most people do not live on the ground floor. So, it is necessary to convert indoor radon map to a dose map. One of the examples is presented as a plan to develop models that allow correction from ground-floor dwellings to the real situation, accounting data from the national buildings database [12]. In Serbia, national typology of residential buildings is based on the results from the monography "National typology of residential buildings of Serbia" by a group of authors from the Faculty of Architecture [13]. There are six types of the residential buildings in Serbia: two for family housing – freestanding single-family house and single-family house in a row and four types for multifamily housing – freestanding residential building and residential building (lamella) (apartment block with repeated multiple lamellar cores and separate entrances), residential building in a row, and high-rise residential building. Distribution of buildings by type at the national level shows that 97% of all residential buildings are family housing. Also, for all defined types of buildings, number of floors ranges from one to eight above the ground level. Freestanding family houses are mostly ground floor (37%) or ground floor with loft in use (26%), while there is a very low representation of houses that have more than two floors (5%), with average floor level of family buildings of 1.4 [13]. In such sense, we chose one freestanding single-family house with loft with well-known radon characteristics [14] and one 16-floor high-rise residential building for this study.

Materials and methods

Two housing units were selected, one from the family housing group and one high-rise residential building from the collective housing group. The family house has a characteristic construction style in which the house has been built for several years with constant upgrading, which can potentially be a source of radon entry into such houses. The house has a basement and is made of standard materials (brick block, concrete, plaster). Finally, insulation was made using 5-cm thick styrofoam. Long-term measurements of radon concentrations have been carried out in this house by various methods, and several scientific papers have been published so far [14–16].

From the group of residential buildings for collective housing, we chose high-rise building in New Belgrade. It was built in the 1960s as block type. The soliter has a basement, while on the ground floor there are outlets and business premises. The apartments are located in the first floor upward. The soliter has 16 floors. One of the important parameters in the selection of building in municipality New Belgrade is the fact that this municipality is the most populated in Serbia.

The long-term radon measurements were performed with passive device Radtrak^2 Radonova based on CR-39 track detector. The detectors were exposed for three months from March to June. In the high-rise building, passive radon detectors were deployed at some of the floors in one or several apartments. Time series of measured radon concentrations in the studied residential buildings were obtained using two active devices: SN1029 with the following characteristics declared by the manufacturer – the measurement ranging from $1 \ Bq \cdot m^{-3}$ to $99.99 \ kBq \cdot m^{-3}$, accuracy equal to ±25%, sensitivity of 0.16 counts/h/$Bq \cdot m^{-3}$ and SN1030 with the following characteristics – the measurement ranging from $1 \ Bq \cdot m^{-3}$ to $99.99 \ kBq \cdot m^{-3}$, accuracy equal to ±20%, sensitivity of 0.4 counts/h/$Bq \cdot m^{-3}$. SN1029 device were calibrated at the accredited metrological Lab (SUJCHBO Kamenna, Czech Republic) in 2015 and model SN1030 were calibrated by the manufacturer in 2017. The both instruments participated in 2018 NRPI Intercomparisons of radon gas continuous monitors and also, SN1029 device participated in 2015 NRPI Intercomparisons of radon gas measurement devices at SURO v.v.i. Institute, Prague, Czech Republic within the IAEA Technical Cooperation Projects RER 9153 and RER 9127, with excellent results. These are measuring devices of simple construction and practical application. It is a counter with the addition of a sensor for measuring meteorological parameters. The operator can adjust the time sequences from 0.5 h to 24 h. One measurement cycle can take 1000 h or a total of 720 time sequences (the number of successive measurements, i.e. points in a time series). The devices were set to operate in a 2-h time sequence. One was fixed in the downstairs living room and the other was fixed in repositioning floors in apartment buildings. Each measurement cycle on a given floor lasted seven days.
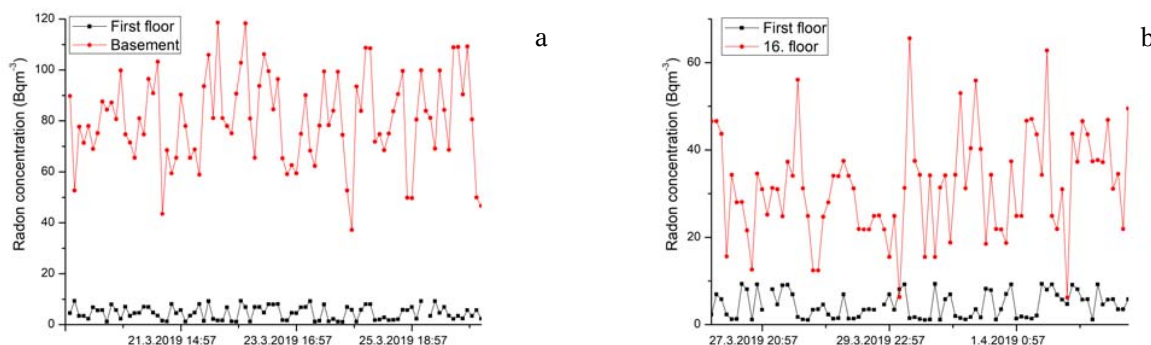

Fig. 1. The time series of the radon concentrations at the first floor vs. basement (a) and 16th floor (b) in the big residential building.
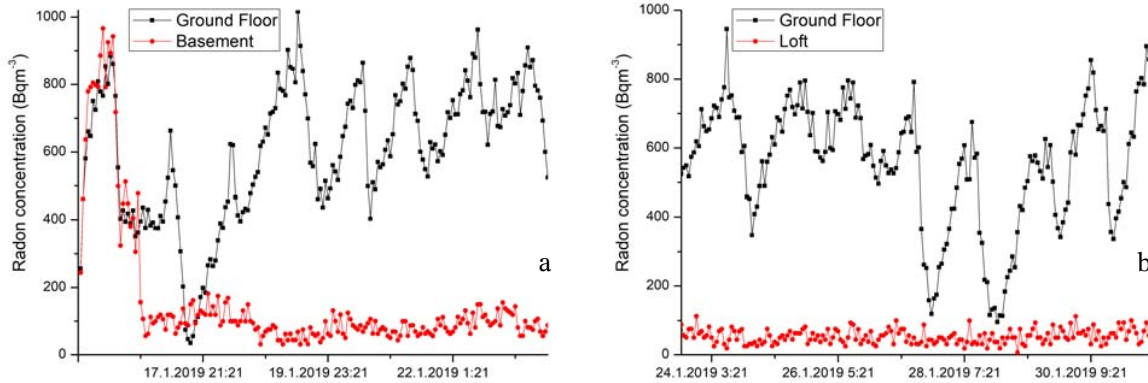
Fig. 2. The time series of the radon concentrations at the first floor vs. basement (a) and loft (b) in the single-family house.

Table 1. Results of indoor radon measurements in the high-rise residential building using passive (Radtrak[2] Radonova) and active radon devices

Floor level	Radon concentration/ Passive device (Radtrak[2]) [Bq·m⁻³]	Average radon concentration per floor level (Radtrak[2]) [Bq·m⁻³]	Arithmetic mean (standard deviation) radon concentration over measuring cycle [Bq·m⁻³]
Basement	52 ± 10 69 ± 12 38 ± 10 55 ± 10	53.5	81(17)
1	<10 14 ± 8	14	5(3)
2	17 ± 8	17	24(9)
3			25(10)
4	21 ± 8 20 ± 8	20.5	26(11)
5	11 ± 8 27 ± 10	19	
6	22 ± 8 12 ± 8 17 ± 8	17	
7	23 ± 8	23	25(10)
8	22 ± 8	22	
9	15 ± 8 16 ± 8 22 ± 8	17.7	24(10)
10	20 ± 8 15 ± 8	17.5	
11	16 ± 8	16	
12	<10	<10	
14	20 ± 8 17 ± 8	18.5	29(9)
15	15 ± 8 16 ± 8	15.5	
16	31 ± 8	31	32(12)
Overall mean	24	21.6	30

Results and discussions

Figure 1 shows the illustrative examples that show radon time series from high-rise building, and Fig. 2 originates from the observed single-family house.

The arithmetic mean radon concentrations obtained from long- and short-term measurements are shown in Tables 1 and 2 for high-rise building and single-family house with loft, respectively.

In the family house, it is possible to notice marked variations in radon concentration with 1-day periodicity. Also interesting is the ratio of radon concentration on the ground floor to the basement of the house, which is the opposite of the usual situation in houses with a basement. This inverse behaviour can be explained by the fact that the basement does not cover the whole ground floor but a smaller part of it. The rest of the ground floor is covered by a concrete slab as a substrate, but cracks and poor joint with the walls are potential sources of elevated radon. Also, the differences in the results between two methods, passive and active devices, are due to the fact that presented radon values are measured in different seasons. With high-rise residential building, the situation is the opposite and it can be considered from the first floor that the dominant source of radon is the building material. There may even be a slight increase in the mean radon concentration on the higher floors. Also, the results show very low radon level on the first floor (well below the outdoor values) in the apartment. In such sense, we performed test intercomparison radon measurements for two active devices SN1029 and SN1030 in well-defined and controlled radon atmosphere (radon concentration below 30 Bq·m⁻³) in the Underground Low-background Laboratory in the Institute of Physics Belgrade [17, 18]. Additional testing includes the same place and time of the measurements but different sampling time set to 1, 2, 4, 8 and 12 h. The results are shown in Table 3.

In the above performed measurements, both devices show significant differences in the low-level radon range, which may originate from individual instruments characteristics presented in the "Materials and methods" section.

Table 2. Results of indoor radon measurements in the single-family house with loft using passive (Radtrak² Radonova) and active radon devices

Floor level	Radon concentration/Passive device (Radtrak²) [Bq·m⁻³]	Arithmetic mean (standard deviation) radon concentration over measuring cycle [Bq·m⁻³]
Basement		160(202)
Ground level	330 ± 50	579(194)
Loft	18 ± 8	53(21)

Table 3. Test intercomparison indoor radon measurements with active radon devices SN1029 and SN1030

	Arithmetic mean (standard deviation) radon concentration over measuring cycle [Bq·m⁻³]				
Sampling time [h]	1	2	4	8	12
SN1029	28(12)	28(11)	27(7)	23(6)	32(14)
SN1030	12(6)	14(7)	10(3)	12(5)	14(6)

Conclusions

The results show that the radon behaviour in two different residential buildings is diametrically opposite. In the single-family house with loft we registered intense difference between radon concentration in the ground level and loft, while in the high-rise residential building the radon level was almost the same at all floors and hence we may conclude that radon originated mainly from building materials. However, the results from the high-rise building can be predicted on the basis of work of a group of authors who have determined the internal exposure from construction material used in Serbia which originates from the exhalation of radon and thoron [19] and the study presented in this article [10]. We can expect similar results in any other multistorey buildings in Serbia. In the future work, we will focus on the additional radon measurements in the typical residential buildings from other types of houses.

ORCID

V. Udovicic http://orcid.org/0000-0002-7839-1537

References

1. Bochicchio, F., Campos-Venuti, G., Piermattei, S., Nuccetelli, C., Risica, S., Tommasino, L., Torri, G., Magnoni, M., Agnesod, G., Sgorbati, G., Bonomi, M., Minach, L., Trotti, F., Malisan, M. R., Maggiolo, S., Gaidolfi, L., Giannardi, C., Rongoni, A., Lombardi, M., Cherubini, G., D'Ostilio, S., Cristofaro, C., Pugliese, M., Martucci, V., Crispino, A., Cuzzocrea, P., Sansone Santamaria, A., & Cappai, M. (2005). Annual average and seasonal variations of residential radon concentration for all the Italian Regions. *Radiat. Meas*., *40*, 686–694.

2. Friedmann, H. (2005). Final results of the Austrian Radon Project. *Health Phys*., *89*(4), 339–348.

3. Du, L., Prasauskas, T., Leivo, V., Turunen, M., Pekkonen, M., Kiviste, M., Aaltonen, A., Martuzevicius, D., & Haverinen-Shaughnessy, U. (2015). Assessment of indoor environmental quality in existing multi-family buildings in North-East Europe. *Environ. Int*., *79*, 74–84.

4. Cucoş (Dinu), A., Cosma, C., Dicu, T., Begy, R., Moldovan, M., Papp, B., Niţă, D., Burghele, B., & Sainz, C. (2012). Thorough investigations on indoor radon in Băiţa radon-prone area (Romania). *Sci. Total Environ*., *431*, 78–83.

5. Yarmoshenko, I., Vasilyev, A., Malinovsky, G., Bossew, P., Žunić, Z. S., Onischenko, A., & Zhukovsky, M. (2016). Variance of indoor radon concentration: Major influencing factors. *Sci. Total Environ*., *541*, 155–160.

6. Kropat, G., Bochud, F., Jaboyedoff, M., Laedermann, J. P, Murith, C., Palacios, M., & Baechler, S. (2014). Major influencing factors of indoor radon concentrations in Switzerland. *J. Environ. Radioact*., *129*, 7–22.

7. Borgoni, R., De Francesco, D., De Bartolo, D., & Tzavidis, N. (2014). Hierarchical modeling of indoor radon concentration: how much do geology and building factors matter? *J. Environ. Radioact*., *138*, 227–237.

8. Xie, D., Liao, M., & Kearfott, K. J. (2015). Influence of environmental factors on indoor radon concentration levels in the basement and ground floor of a building – A case study. *Radiat. Meas*., *82*, 52–58.

9. Man, C. K., & Yeung, H. S. (1999). Modeling and measuring the indoor radon concentrations in high-rise buildings in Hong Kong. *Appl. Radiat. Isot*., *50*, 1131–1135.

10. Vukotić, P., Zekić, R., Antović, N. M., & Andjelić, T. (2019). Radon concentrations in multi-story buildings in Montenegro. *Nucl. Technol. Radiat. Prot*., *34*, 165–174.

11. Lorenzo-González, M., Ruano-Ravina, A., Peón, J., Piñeiro, M., & Barros-Dios, J. M. (2017). Residential radon in Galicia: a cross-sectional study in a radon-prone area. *J. Radiol. Prot*., *37*(3), 728–741.

12. Elío, J., Cinelli, G., Bossew, P., Gutiérrez-Villanueva, J. L., Tollefsen, T., De Cort, M., Nogarotto, A., & Braga, R. (2019). The first version of the Pan-European Indoor Radon Map. *Nat. Hazards Earth Syst. Sci*., *19*, 2451–2464.

13. Jovanović Popović, M., Ignjatović, D., Radivojević, A., Rajčić, A., Ćuković Ignjatović, N., Đukanović, Lj., & Nedić, M. (2013). *National typology of residential*

buildings in Serbia. Belgrade: Faculty of Architecture University of Belgrade.

14. Udovičić, V., Maletić, D., Banjanac, R., Joković, D., Dragić, A., Veselinović, N., Živanović, J., Savić, M., & Forkapić, S. (2018). Multiyear indoor radon variability in a family house–A case study in Serbia. *Nucl. Technol. Radiat. Prot*., *33*(2), 174–179.

15. Maletić, D., Udovičić, V., Banjanac, R., Joković, D., Dragić, A., Veselinović, N., & Filipović, J. (2014). Comparison of multivariate classification and regression methods for indoor radon measurements. *Nucl. Technol. Radiat. Prot*., *29*, 17–23.

16. Filipović, J., Maletić, D., Udovičić, V., Banjanac, R., Joković, D., Savić, M., & Veselinović, N. (2016). The use of multivariate analysis of the radon variability in the underground laboratory and indoor environment. *Nukleonika*, *61*(3), 357–360. DOI: 10.1515/nuka-2016-0059.

17. Udovičić, V., Aničin, I., Joković, D., Dragić, A., Banjanac, R., Grabež, B., & Veselinović, N. (2011). Radon time-series analysis in the Underground Low-level Laboratory in Belgrade, Serbia. *Radiat. Prot. Dosim*., *145*(2/3), 155–158.

18. Udovičić, V., Filipović, J., Dragić, A., Banjanac, R., Joković, D., Maletić, D., Grabež, B., & Veselinović, N. (2014). Daily and seasonal radon variability in the underground low-background laboratory in Belgrade, Serbia. *Radiat. Prot. Dosim*., *160*(1/3), 62–64.

19. Ujić, P., Čeliković, I., Kandić, A., Vukanac, I., Đurašević, M., Dragosavac, D., & Žunić, Z. S. (2010). Internal exposure from building materials exhaling ^{222}Rn and ^{220}Rn as compared to external exposure due to their natural radioactivity content. *Appl. Radiat. Isot*., *68*, 201–206.

MAUS: the MICE analysis user software

R. Asfandiyarov,[a] **R. Bayes,**[b] **V. Blackmore,**[c] **M. Bogomilov,**[d] **D. Colling,**[c] **A.J. Dobbs,**[c]
F. Drielsma,[a] **M. Drews,**[h] **M. Ellis,**[c] **M. Fedorov,**[e] **P. Franchini,**[f] **R. Gardener,**[g] **J.R. Greis,**[f]
P.M. Hanlet,[h] **C. Heidt,**[i] **C. Hunt,**[c] **G. Kafka,**[h] **Y. Karadzhov,**[a] **A. Kurup,**[c] **P. Kyberd,**[g]
M. Littlefield,[g] **A. Liu,**[j] **K. Long,**[c,n] **D. Maletic,**[k] **J. Martyniak,**[c] **S. Middleton,**[c] **T. Mohayai,**[h,j]
J.J. Nebrensky,[g] **J.C. Nugent,**[b] **E. Overton,**[l] **V. Pec,**[l] **C.E. Pidcott,**[f] **D. Rajaram,**[h,1]
M. Rayner,[m] **I.D. Reid,**[g] **C.T. Rogers,**[n] **E. Santos,**[c] **M. Savic,**[k] **I. Taylor,**[f] **Y. Torun,**[h]
C.D. Tunnell,[m] **M.A. Uchida,**[c] **V. Verguilov,**[a] **K. Walaron,**[b] **M. Winter**[h] **and S. Wilbur**[l]

[a] *DPNC, section de Physique, Université de Genève, Geneva, Switzerland*

[b] *School of Physics and Astronomy, Kelvin Building, The University of Glasgow, Glasgow, U.K.*

[c] *Department of Physics, Blackett Laboratory, Imperial College London, London, U.K.*

[d] *Department of Atomic Physics, St. Kliment Ohridski University of Sofia, Sofia, Bulgaria*

[e] *Radboud University of Nijmegen, Netherlands*

[f] *Department of Physics, University of Warwick, Coventry, U.K.*

[g] *Brunel University, Uxbridge, U.K.*

[h] *Physics Department, Illinois Institute of Technology, Chicago, IL, U.S.A.*

[i] *University of California, Riverside, CA, U.S.A.*

[j] *Fermilab, Batavia, IL, U.S.A.*

[k] *Institute of Physics, University of Belgrade, Serbia*

[l] *Department of Physics and Astronomy, University of Sheffield, Sheffield, U.K.*

[m] *Department of Physics, University of Oxford, Denys Wilkinson Building, Oxford, U.K.*

[n] *STFC Rutherford Appleton Laboratory, Harwell Oxford, Didcot, U.K.*

E-mail: durga@fnal.gov

ABSTRACT: The Muon Ionization Cooling Experiment (MICE) collaboration has developed the MICE Analysis User Software (MAUS) to simulate and analyze experimental data. It serves as the primary codebase for the experiment, providing for offline batch simulation and reconstruction as well as online data quality checks. The software provides both traditional particle-physics functionalities such as track reconstruction and particle identification, and accelerator physics functions, such as calculating transfer matrices and emittances. The code design is object orientated, but has a top-level structure based on the Map-Reduce model. This allows for parallelization to support live data reconstruction during data-taking operations. MAUS allows users to develop in

---

[1]Corresponding author.

https://doi.org/10.1088/1748-0221/14/04/T04005

either Python or C++ and provides APIs for both. Various software engineering practices from industry are also used to ensure correct and maintainable code, including style, unit and integration tests, continuous integration and load testing, code reviews, and distributed version control. The software framework and the simulation and reconstruction capabilities are described.

Contents

1 Introduction

1.1 The MICE experiment

The Muon Ionization Cooling Experiment (MICE) sited at the STFC Rutherford Appleton Laboratory (RAL) has delivered the first demonstration of muon ionization cooling [1] — the reduction of the phase-space of muon beams. Muon-beam cooling is essential for future facilities based on

muon acceleration, such as the Neutrino Factory or Muon Collider [2, 3]. The experiment was designed to be built and operated in a staged manner. In the first stage, the muon beamline was commissioned [4] and characterized [5]. A schematic diagram of the configuration used to study the factors that determine the performance of an ionization-cooling channel is shown in figure 1. The MICE experiment was operated such that muons passed through the experiment one at a time. The experiment included instrumentation to identify particle species (the particle-identification detectors, PID) [6–11] and to measure the phase-space coordinates of each muon. An ensemble of muons that was representative of the muon beam was then assembled using the measured coordinates. The techniques used to reconstruct the ensemble properties of the beam are described in [12] and the first observation of the ionization-cooling of a muon beam is presented in [1].

The configuration shown in figure 1 was used to study the factors that determine the performance of an ionization-cooling channel and to observe for the first time the reduction in transverse emittance of a muon beam.

The MICE Muon Beam line is described in detail in [4]. There are 5 different detector systems present on the beamline: time-of-flight (TOF) scintillators [6], threshold Cherenkov (Ckov) counters [13], scintillating-fiber trackers [14], a sampling calorimeter (KL) [8, 9], and the Electron Muon Ranger (EMR) — a totally active scintillating calorimeter [10, 11]. The TOF, Ckov, KL and EMR detectors are used for particle identification (PID), and the scintillating-fiber trackers are used to measure position and momentum. The TOF detector system consists of three detector stations, TOF0, TOF1 and TOF2, each composed of two orthogonal layers of scintillator bars. The TOF system determines PID via the time-of-flight between the stations. Each station also provides a low-resolution image of the beam profile. The Ckov system consists of two aerogel threshold Cherenkov stations, CkovA and CkovB. The KL and EMR detectors, the former using scintillating fibers embedded in lead sheets, and the latter scintillating bars, form the downstream calorimeter system.

The tracker system consists of two scintillating-fiber detectors, one upstream of the MICE cooling cell, the other downstream, in order to measure the change in emittance across the cooling cell. Each detector consists of 5 stations, each station having 3 fiber planes, allowing precision measurement of momentum and position to be made on a particle-by-particle basis.
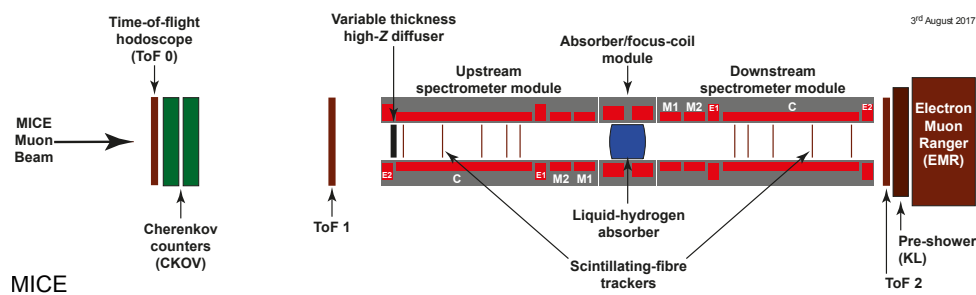

Figure 1. Schematic diagram of the MICE experiment.The red rectangles represent the coils of the spectrometer solenoids and focus-coil module. The individual coils of the spectrometer solenoids are labelled E1, C, E2, M1 and M2. The various detectors (time-of-flight hodoscopes (TOF0, TOF1) [6], Cherenkov counters [13], scintillating-fiber trackers [14], KLOE-Light (KL) calorimeter [7, 8], and Electron Muon Ranger (EMR) [10, 11]) are also represented.

1.2 Software requirements

The MICE software must serve both the accelerator-physics and the particle-physics needs of the experiment. Traditional particle-physics functionality includes reconstructing particle tracks, identifying them, and simulating the response from various detectors, while the accelerator-physics aspect includes the calculation of transfer matrices and Twiss parameters and propagating the beam envelopes. All of these items require a detailed description of the beamline, the geometries of the detectors, and the magnetic fields, as well as functionality to simulate the various detectors and reconstruct the detector outputs. MICE aims to measure the change in emittance to 1%, which imposes requirements on the performance of the track reconstruction, particle identification and measurements of scattering widths. In addition, the computational performance of the software was also important in order to ensure that the software can reconstruct data with sufficient speed to support live online monitoring of the experiment.

2 MAUS

The MICE Analysis User Software (MAUS) is the collaboration's simulation, reconstruction, and analysis software framework. MAUS provides a Monte Carlo (MC) simulation of the experiment, reconstruction of tracks and identification of particles from simulations and real data, and provides monitoring and diagnostics while running the experiment.

Installation is performed via a set of shell scripts with SCons [15] as the tool for constructing and building the software libraries and executables. The codebase is maintained with GNU Bazaar [16], a distributed version control system, and is hosted on Launchpad [17], a website that provides functionalities to host and maintain the software repository. MAUS has a number of dependencies on standard packages such as Python, ROOT [18] and Geant4 [19] which are built as "third party" external libraries during the installation process. The officially supported platform is Scientific Linux 6 [20] though developers have successfully built on CentOS [21], Fedora [22], and Ubuntu [23] distributions.

Each of the MICE detector systems, described in section 1.1, is represented within MAUS. Their data structures are described in section 2.2 and their simulation and reconstruction algorithms in sections 3 and 4. MAUS also provides "global" reconstruction routines, which combine data from individual detector systems to identify particle species by the likelihood method and perform a global track fit. These algorithms are also described in section 4.

2.1 Code design

MAUS is written in a mixture of Python and C++. C++ is used for complex or low-level algorithms where processing time is important, while Python is used for simple or high-level algorithms where development time is a more stringent requirement. Developers are allowed to write in either Python or C++ and Python bindings to C++ are handled through internal abstractions. In practice, all the reconstruction modules are written in C++ but support is provided for legacy modules written in Python.

MAUS has an Application Programming Interface (API) that provides a framework on which developers can hang individual routines. The MAUS API provides MAUS developers with a well-defined environment for developing reconstruction code, while allowing independent development of the back-end and code-sharing of common elements, such as error handling.

The MAUS data processing model is inspired by the Map-Reduce framework [24], which forms the core of the API design. Map-Reduce, illustrated in figure 2 is a useful model for parallelizing data processing on a large scale. A *map* process takes a single object as an input, transforms it, and returns a new object as the output (in the case of MAUS this input object is the *spill* class, see section 2.2).

A module is the basic building block of the MAUS API framework. Four types of module exist within MAUS:

1. **Inputters** generate input data either by reading data from files or over a network, or by generating an input beam;

2. **Mappers** modify the input data, for example by reconstructing signals from detectors, or tracking particles to generate MC hits;

3. **Reducers** collate the mapped data and provide functionality that requires access to the entire data set; and

4. **Outputters** save the data either by streaming over a network or writing to disk.
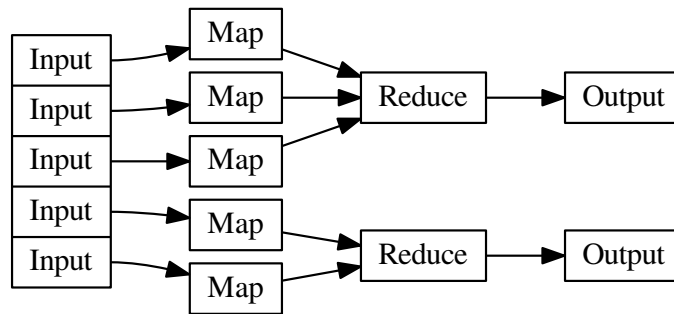
Figure 2. A Map-Reduce framework.

Each module type follows a common, extensible, object-orientated class hierarchy, shown for the case of the *map* and *reduce* modules in figure 3.

There are some objects that sit outside the scope of this modular framework but are nevertheless required by several of the modules. For instance, the detector geometries, magnetic fields, and calibrations are required by the reconstruction and simulation modules, and objects such as the electronics-cabling maps are required in order to unpack data from the data acquisition (DAQ) source, and error handling functionality is required by all of the modules. All these objects are accessed through a static singleton *globals* class.

MAUS has two execution concepts. A *job* refers to a single execution of the code, while a *run* refers to the processing of data for a DAQ run or MC run. A job may contain many runs. Since data are typically accessed from a single source and written to a single destination, *inputters* and *outputters* are initialized and destroyed at the beginning and end of a job. On the other hand, *mappers*
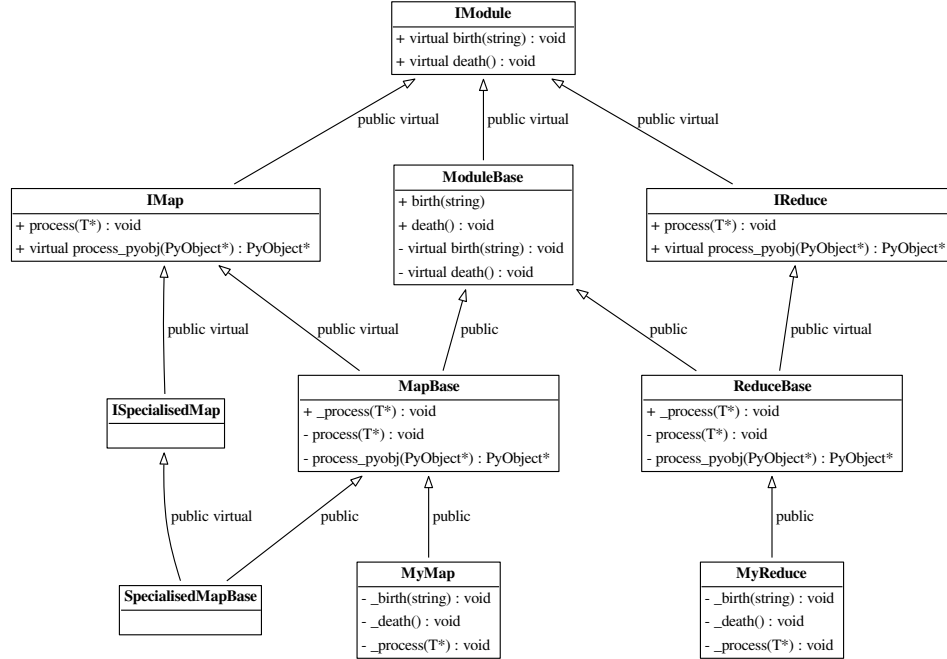
IModule

+ virtual birth(string) : void

+ virtual death() : void

public virtual   public virtual   public virtual

IMap

+ process(T*) : void

+ virtual process_pyobj(PyObject*) : PyObject*

ModuleBase

+ birth(string)

+ death() : void

- virtual birth(string) : void

- virtual death() : void

IReduce

+ process(T*) : void

+ virtual process_pyobj(PyObject*) : PyObject*

public virtual   public virtual   public   public   public virtual

ISpecialisedMap

MapBase

+ _process(T*) : void

- process(T*) : void

- process_pyobj(PyObject*) : PyObject*

ReduceBase

+ _process(T*) : void

- process(T*) : void

- process_pyobj(PyObject*) : PyObject*

public virtual   public   public   public

SpecialisedMapBase

MyMap

- _birth(string) : void

- _death() : void

- _process(T*) : void

MyReduce

- _birth(string) : void

- _death() : void

- _process(T*) : void

Figure 3. The MAUS API class hierarchy for Map and Reduce modules. The input and output modules follow related designs. *T* represents a templated argument. "+" indicates the introduction of a virtual void method, defining an interface, while "-" indicates that a class implements that method, fulfilling that aspect of the interface. The *process_pyobj* functions are the main entry points for Python applications, and *process* the entry points for C++ applications. The framework can be extended as many times as necessary, as exemplified by the "SpecialisedMap" classes.

and *reducers* are initialized at the beginning of a run in order to allow run-specific information such as electronics cabling maps, fields, calibrations and geometries to be loaded.

The principal data type in MAUS, which is passed from module to module, is the *spill*. A single spill corresponds to data from the particle burst associated with a dip of the MICE target [4]. A spill lasts up to ∼ 3 ms and contains several DAQ triggers. Data from a given trigger define a single MICE *event*. In the language of the Input-Map-Reduce-Output framework, an *Input* module creates an instance of spill data, a *Map* module processes the spill (simulating, reconstructing, etc.), a *Reduce* module acts on a collection of spills when all the *mappers* finish, and finally an *Output* module records the data to a given file format.

Modules can exchange spill data either as C++ pointers or JSON [25] objects. In Python, the data format can be changed by using a converter module, and in C++ *mappers* are templated to a MAUS data type and an API handles any necessary conversion to that type (see figure 3).

Data contained within the MAUS data structure (see section 2.2) can be saved to permanent storage in one of two formats. The default data format is a ROOT [18] binary and the secondary format is JSON. ROOT is a standard high-energy physics analysis package, distributed with MAUS, through which many of the analyses on MICE are performed. Each spill is stored as a single entry in a ROOT TTree object. JSON is an ASCII data-tree format. Specific JSON parsers are available — for example, the Python *json* library, and the C++ *JsonCpp* [26] parser come prepackaged with MAUS.

In addition to storing the output from the *map* modules, MAUS is also capable of storing the data produced by *reducer* modules using a special *Image* class. This class is used by *reducers* to store images of monitoring histograms, efficiency plots, etc. *Image* data may only be saved in JSON format.

2.2 Data structure

2.2.1 Physics data

At the top of the MAUS data structure is the spill class which contains all the data from the simulation, raw real data and the reconstructed data. The spill is passed between modules and written to permanent storage. The data within a spill is organized into arrays of three possible event types: an *MCEvent* contains data representing the simulation of a single particle traversing the experiment and the simulated detector responses; a *DAQEvent* corresponds to the real data for a single trigger; and a *ReconEvent* corresponds to the data reconstructed for a single particle event (arising either from a Monte Carlo(MC) particle or a real data trigger). These different branches of the MAUS data structure are shown diagrammatically in figures 4–9.

The sub-structure of the MC event class is shown in figure 5. The class is subdivided into events containing detector hits (energy deposited, position, momentum) for each of the MICE detectors (see section 1.1). The event also contains information about the primary particle that created the hits in the detectors.

The sub-structure of the reconstruction event class is shown in figure 6. The class is subdivided into events representing each of the MICE detectors, together with the data from the trigger, and data for the global event reconstruction. Each detector class and the global-reconstruction class has several further layers of reconstruction data. This is shown in figures 7–9.
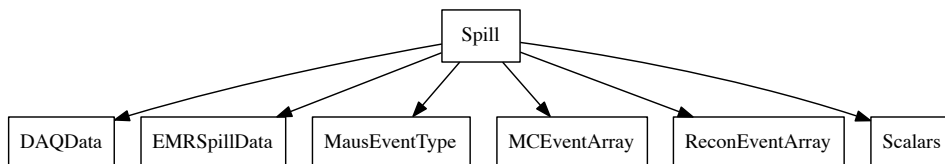
Figure 4. The MAUS output structure for a spill event. The label in each box is the name of the C++ class.
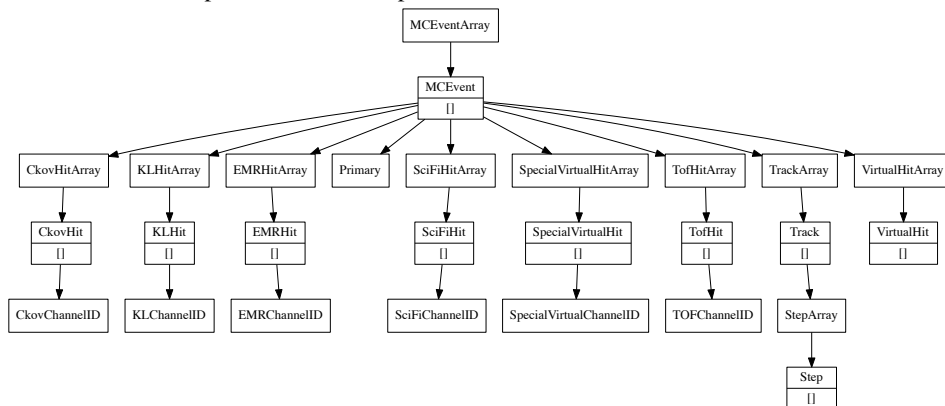
Figure 5. The MAUS data structure for MC events. The label in each box is the name of the C++ class and [] indicates that child objects are array items.
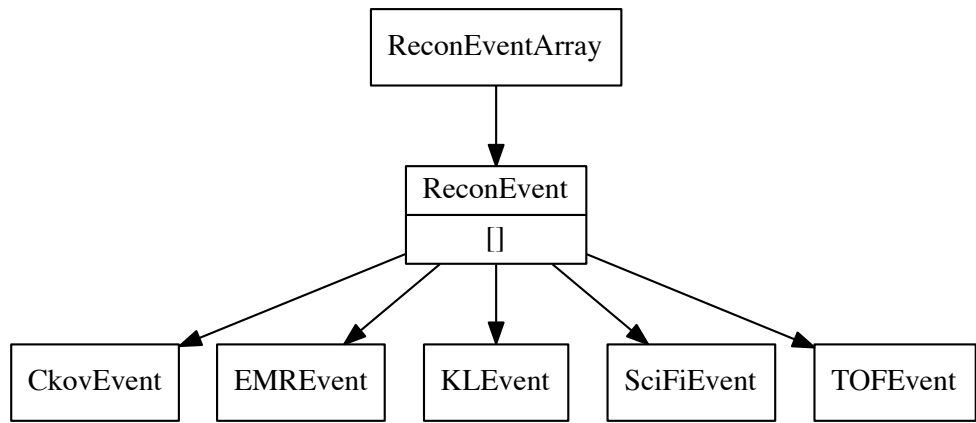
Figure 6. The MAUS data structure for reconstructed events. The label in each box is the name of the C++ class.
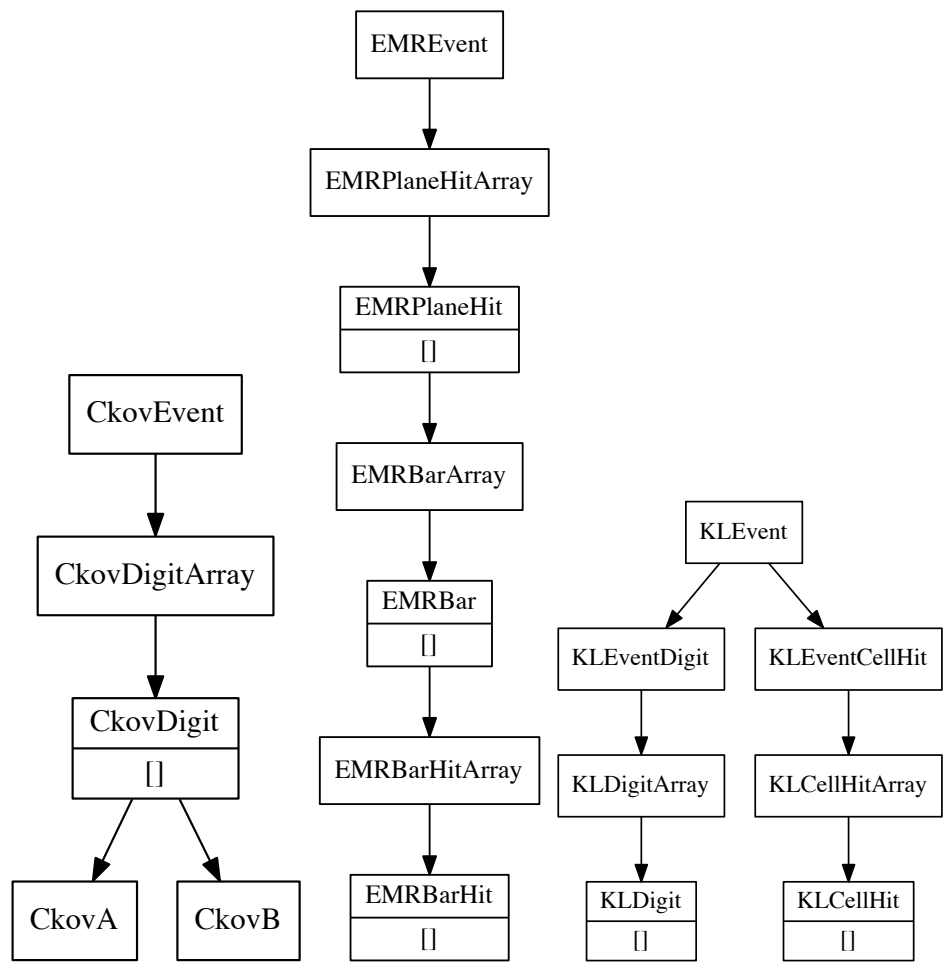

Figure 7. The MAUS data structure for CKOV (left), EMR (middle) and KL (right) reconstructed events. The label in each box is the name of the C++ class [] indicates that child objects are array items.
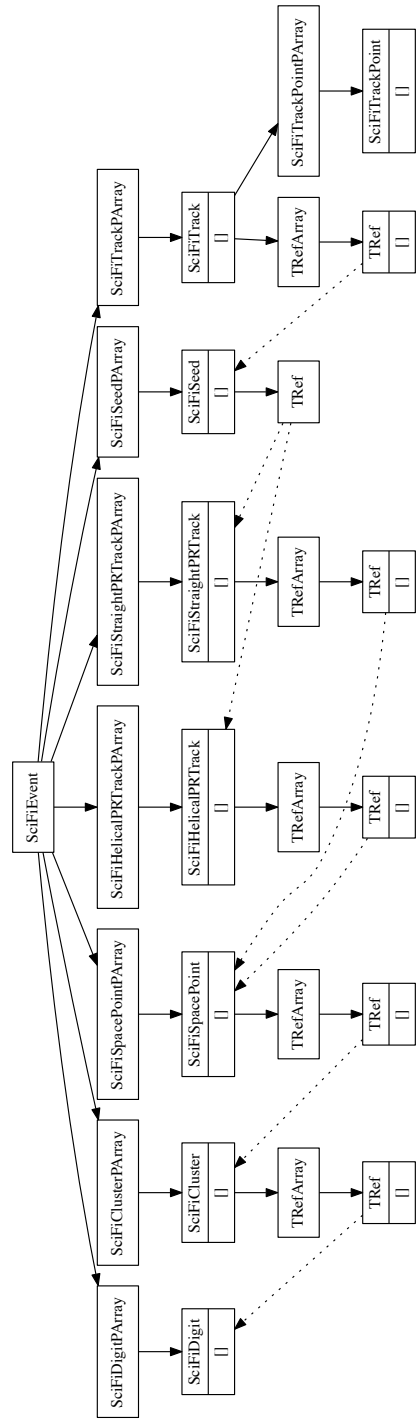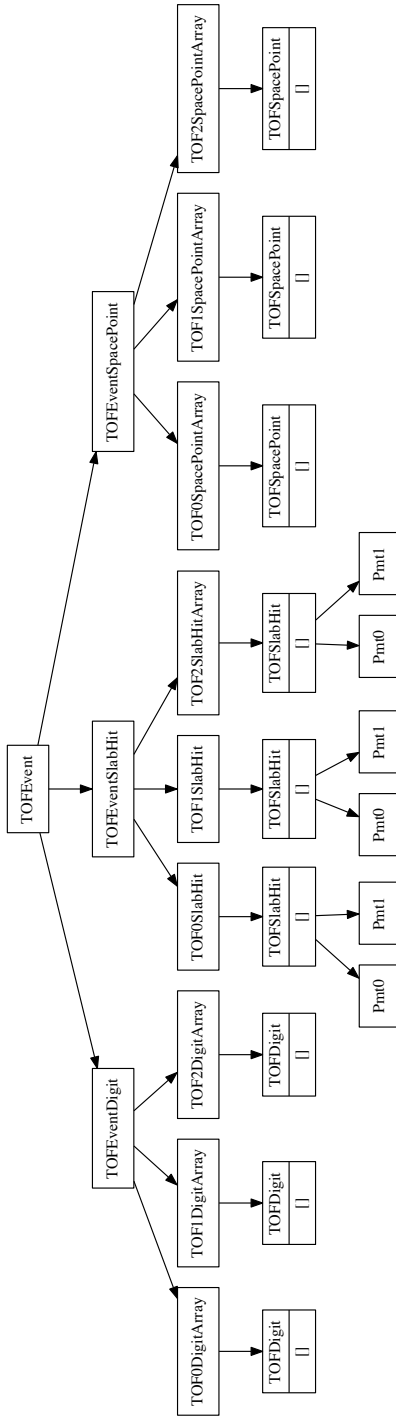
Figure 8. The MAUS data structure for the tracker. The label in each box is the name of the C++ class and [] indicates that child objects are array items.

Figure 9. The MAUS data structure for the TOFs. The label in each box is the name of the C++ class and []
indicates that child objects are array items.

2.2.2 Top level data organization

In addition to the spill data, MAUS also contains structures for storing supplementary information for each run and job. These are referred to as *JobHeader* and *JobFooter*, and *RunHeader* and *RunFooter*. The *JobHeader* and *JobFooter* represent data, such as the MAUS release version, associated with the start and end of a job, and the *RunHeader* and *RunFooter* represent data, such as the geometry and calibrations associated with a run, associated with the start and end of a run. These are saved to the output along with the spill.

In order to interface with ROOT, particularly in order to save data in the ROOT format, thin wrappers for each of the top level classes, and a templated base class, were introduced. This allows the ROOT TTree, in which the output data is stored (see section 2.2.1), to be given a single memory address to read from. The wrapper for Spill is called *Data*, while for each of RunHeader, RunFooter, JobHeader and JobFooter, the respective wrapper class is just given the original class name with "Data" appended, e.g., *RunHeaderData*. The base class for each of the wrappers is called *MAUSEvent*. The class hierarchy is illustrated in figure 10.
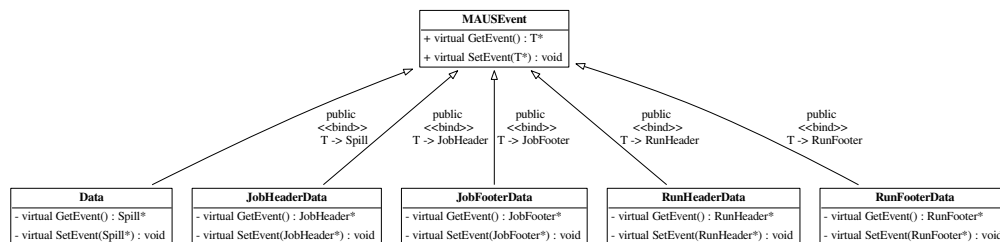
Figure 10. Class hierarchy for the wrappers and base class of the top-level classes of the MAUS data structure.

2.3 Data flow

The MAUS data-flow, showing the reconstruction chain for data originating from MC or real data, is depicted in figure 11. Each item in the diagram is implemented as an individual module. The data flow is grouped into three principal areas: the simulation data flow used to generate digits (electronics signals) from particle tracking; the real data flow used to generate digits from real detector data; and the reconstruction data flow which illustrates how digits are built into higher level objects and converted to parameters of interest. The reconstruction data flow is the same for digits from real data and simulation. In the case of real data, separate input modules are provided to read either directly from the DAQ, or from archived data stored on disk. A *reducer* module for each detector provides functionality to create summary histograms.

2.4 Testing

MAUS has a set of tests at the unit level and the integration level, together with code-style tests for both Python and C++. Unit tests are implemented to test a single function, while integration tests operate on a complete workflow. Unit tests check that each function operates as intended
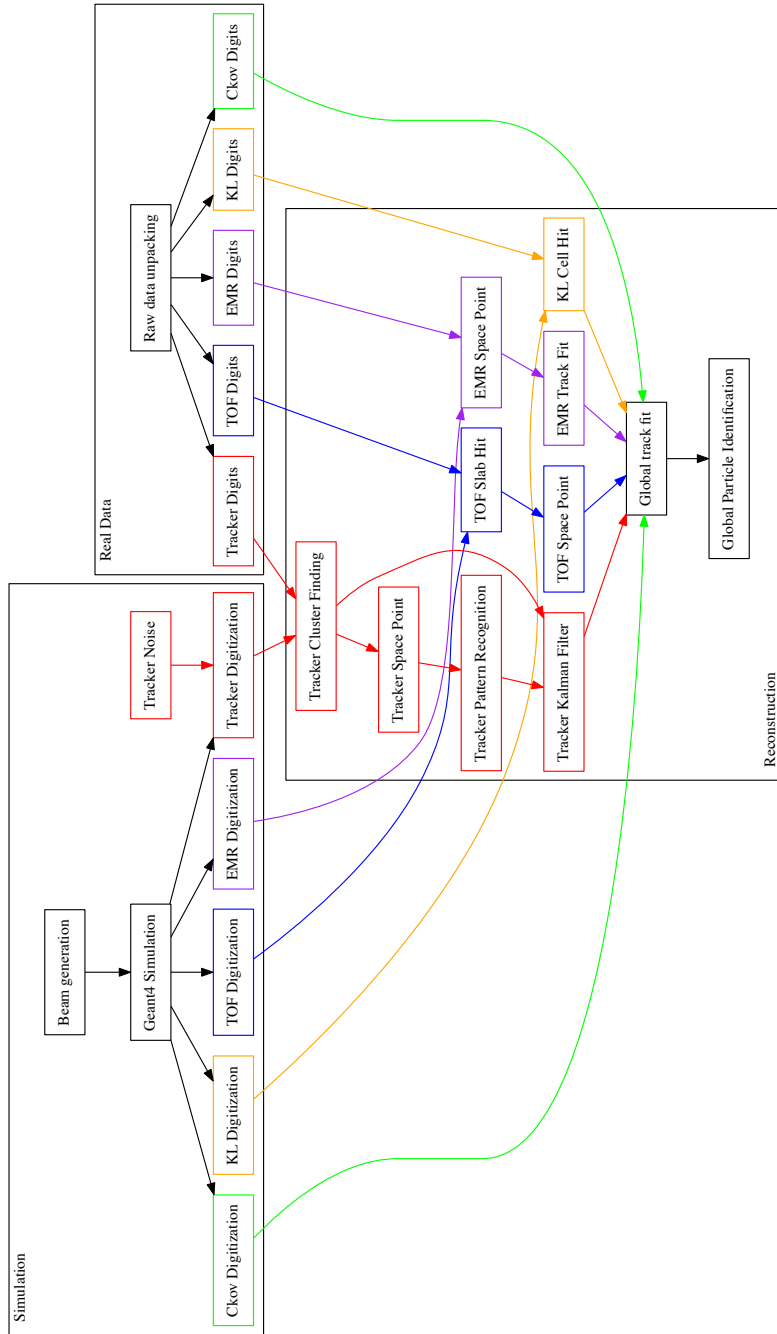
Figure 11. Data flow for the MAUS project. The data flow is color-coded by detector: Ckov — green, EMR — purple, KL — orange, TOF — blue, Tracker — red.

by the developer. Tests are run automatically for every version committed to the repository and results show that a high level of code coverage has been achieved. Integration tests allow the overall performance of the code to be checked against specifications. The MAUS team provides unit test coverage that executes 70–80 % of the total code base. This level of coverage typically results in a code that performs the major workflows without any problems.

The MAUS codebase is built and tested using a Jenkins [27] continuous integration environment deployed on a cluster of servers. Builds and tests of the development branch are automatically triggered when there is a change to the codebase. Developers are asked to perform a build and test on a personal branch of the codebase using the test server before requesting a merge with the development trunk. This enables the MAUS team to make frequent clean releases. Typically MAUS works on a 4–8 week major-release cycle.

3 Monte Carlo

The Monte Carlo simulation of MICE encompasses beam generation, geometrical description of detectors and fields, tracking of particles through detectors and digitization of the detectors' response to particle interactions.

3.1 Beam generation

Several options are provided to generate an incident beam. Routines are provided to sample particles from a multivariate Gaussian distribution or generate ensembles of identical particles (pencil beams). In addition, it is possible to produce time distributions that are either rectangular or triangular in time to give a simplistic representation of the MICE time distribution. Parameters, controlled by data-cards, are available to control random seed generation, relative weighting of particle species and the transverse-to-longitudinal coupling in the beam. MAUS also allows the generation of a polarized beam.

Beam particles can also be read in from an external file created by G4Beamline [28] — a particle-tracking simulation program based on Geant4, or ICOOL [29] — a simulation program that was developed to study the ionization cooling of muon beams, as well as files in user-defined formats. In order to generate beams which are more realistic taking into account the geometry and fields of the actual MICE beamline, we use G4Beamline to model the MICE beamline from the target to a point upstream of the second quad triplet (upstream of Q4). The beamline settings, e.g., magnetic field strengths and number of particles to generate, are controlled through data-cards. The magnetic field strengths have been tuned to produce beams that are reasonably accurate descriptions of the real beam. Scripts to install G4beamline are shipped with MAUS.

Once the beam is generated, the tracking and interactions of particles as they traverse the rest of the beamline and the MICE detectors are performed using Geant4.

3.2 Geant4

A drawing of the MICE Muon Beam line [4] is shown in figure 12. It consists of a quadrupole triplet (Q123) that captures pions produced when the MICE target intersects the ISIS proton beam, a pion-momentum-selection dipole (D1), a superconducting solenoid (DS) to focus and transport the particles to a second dipole (D2) that is used to select the muon-beam momentum, and a transport

channel composed of a further two quadrupole triplets (Q456 and Q789). As described in the next section, the positions and apertures of the beamline magnets were surveyed and are reproduced in the geometry along with windows and materials in the path of the muon beams. The Geant4 simulation within MAUS starts 1 m downstream of the second beamline dipole magnet D2. Geant4 bindings are encoded in the Simulation module. Geant4 groups particles by run, event and track. A Geant4 run maps to a MICE spill; a Geant4 event maps to a single inbound particle from the beamline; and a Geant4 track corresponds to a single particle in the experiment.
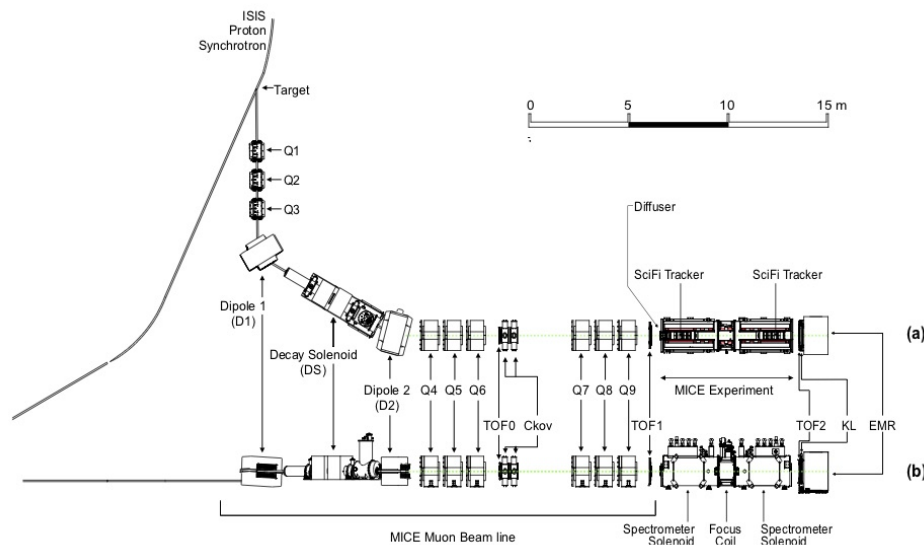
Figure 12. (a) Top and (b) side views of the MICE Muon Beamline, its instrumentation, and the experimental configuration. A titanium target dipped into the ISIS proton synchrotron and the resultant spill of particles was captured with a quadrupole triplet (Q1–3) and transported through momentum-selecting dipoles (D1, D2). The quadrupole triplets (Q4–6, Q7–9) transported particles to the upstream spectrometer module. The time-of-flight of particles, measured between TOF0 and TOF1, was used for particle identification.

Geant4 provides a variety of reference physics processes to model the interactions of particles with matter. The default process in MAUS is "*QGSP_BERT*" which causes Geant4 to model hadron interactions using a Bertini cascade model up to 10 GeV/c [30]. MAUS provides methods to set up the Geant4 physical processes through user-controlled data-cards. Finally, MAUS provides routines to extract particle data from the Geant4 tracks at user-defined locations.

3.3 Geometry

MAUS uses an online Configuration Database to store all of its geometries. These geometries have been extracted from CAD drawings which are updated based on the most recent surveys and technical drawings available. The CAD drawings are translated to a geometry-specific subset of XML, the Geometry Description Markup Language (GDML) [31] prior to being recorded in the configuration database through the use of the FastRAD [32] commercial software package.

The GDML formatted description contains the beamline elements and the positions of the detector survey points. Beam-line elements are described using tessellated solids to define the

shapes of the physical volumes. The detectors themselves are described using an independently generated set of GDML files using Geant4 standard volumes. An additional XML file is appended to the geometry description that assigns magnetic fields and associates the detectors to their locations in the GDML files. This file is initially written by the geometry maintainers and formatted to contain run-specific information during download.

The GDML files can be read via a number of libraries in Geant4 and ROOT for the purpose of independent validation. The files are in turn translated into the MAUS-readable geometry files either by accessing directly the data using a python extension or through the use of EXtensible Stylesheet Language Transformations (XSLT) [33].

3.4 Tracking, field maps and beam optics

MAUS tracking is performed using Geant4. By default, MAUS uses 4th order Runge-Kutta (RK4) for tracking, although other routines are available. RK4 has been shown to have very good precision relative to the MICE detector resolutions, even for step sizes of several cm.

In a solenoid focussing lattice a cylindrically symmetric beam can be described by the 4D RMS beam emittance ε_N and optical parameters $\beta_\perp$ and $\beta'_\perp$, its derivative with respect to z. $\beta_\perp$ is related to the variance of the position of particles x by [34]:

$$\beta_\perp = \frac{p_z \text{Var}(x)}{\varepsilon_N mc}; \tag{3.1}$$

where m is the particle mass, c is the speed of light, and p_z is the beam longitudinal momentum. In the approximation that particles travel near to the solenoid axis, transport of the beam envelope can be performed by integration of the differential equation:

$$2\beta_\perp \beta''_\perp - (\beta'_\perp)^2 + 4\beta_\perp^2 \kappa^2 - 4(1 + \mathcal{L})^2 = 0. \tag{3.2}$$

Transport of individual particles can be performed using numerical integration of the Lorentz force law. Alternately transport can be performed by calculating a transfer map $\mathbf{M}$ defined by:

$$\vec{u}_{ds} = \mathbf{M}\vec{u}_{us}; \tag{3.3}$$

where $\vec{u}_{us}$ and $\vec{u}_{ds}$ are the upstream and downstream transverse phase space vectors $\vec{u} = (x, p_x, y, p_y)$. MAUS can calculate the transfer map at arbitrary order by transporting a handful of particles and fitting to a multidimensional polynomial in $\vec{u}$.

Electromagnetic field maps are implemented in a series of overlapping regions. The world volume is divided into a number of voxels, and the field maps that impinge on each voxel is stored in a list. At each tracking step, MAUS iterates over the list of fields that impinge on the voxels within which the particle is stepping. For each field map, MAUS transforms to the local coordinate system of the field map, and calculates the field. The field values are transformed back into the global coordinate system, summed, and passed to Geant4. The voxelization enables the simulation of long accelerators without a performance penalty.

Numerous field types have been implemented within the MAUS framework. Solenoid fields can be calculated numerically from cylindrically symmetric 2D field maps, by taking derivatives of an on-axis solenoidal field or by using the sum of fields from a set of cylindrical current sheets.

The use of field maps enables the realistic reproduction of the MICE apparatus, while a derivatives-based approach enables the exclusion of different terms in the higher order parts of the transfer map [35]. Multipole fields can be calculated from a 3D field map, or by taking derivatives from the usual multipole expansion formulae. Linear, quadratic and cubic interpolation routines have been implemented for field maps. Pillbox fields can be calculated by using the Bessel functions appropriate for a TM010 cavity or by reading a cylindrically symmetric field map.

The transport algorithms have been compared with each other and experimental data and show agreement at linear order [36] in $\vec{u}$. Work is ongoing to study the effect of aberrations in the optics, indicated by non-linear terms in the transfer map relationship. These aberrations can cause distortion of the beam leading to emittance growth, which has been observed in the tails of the MICE beam. The tracking in MAUS has been benchmarked against ICOOL, G4Beamline, and MaryLie [37], demonstrating good agreement. The routines have been used to model a number of beamlines and rings, including a neutrino factory front-end [38].

3.5 Detector response and digitization

The modeling of the detector response and electronics enables MAUS to provide data used to test reconstruction algorithms and estimate the uncertainties introduced by detectors and their readout.

The interaction of particles in materials is modeled using Geant4. For each detector, a "sensitive detector" class processes Geant4 hits in active detector volumes and stores hit information such as the volume that was hit, the energy deposited and the time of the hit. Each detector's digitization routine then simulates the response of the electronics to these hits, modeling processes such as the photo-electron yield from a scintillator bar, attenuation in light guides and the pulse shape in the electronics. The data structure of the outputs from the digitizers are designed to match the output from the unpacking of real data from the DAQ.

4 Reconstruction

The reconstruction chain takes as its input either digitized hits from the MC or DAQ digits from real data. Regardless, the detector reconstruction algorithms, by requirement and design, operate the same way on both MC and real data.

4.1 Time of flight

There are three time-of-flight detectors in MICE which serve to distinguish particle type. The detectors are made of plastic scintillator and in each station there are orthogonal x and y planes with 7 or 10 slabs in each plane.

Each Geant4 hit in the TOF is associated with a physical scintillator slab. The energy deposited by a hit is first converted to units of photo-electrons. The photo-electron yield from a hit accounts for the light attenuation corresponding to the distance of the hit from the photomultiplier tube (PMT) and is then smeared by the photo-electron resolution. The yields from all hits in a given slab are then summed and the resultant yield is converted to ADC counts.

The time of the hit in the slab is propagated to the PMTs at either end of the slab. The propagated time is then smeared by the PMT's time resolution and converted to TDC counts. Calibration

corrections based on real data are then added to the TDC values so that, at the reconstruction stage, they can be corrected just as is done with real data.

The reconstruction proceeds in two main steps. First, the slab-hit-reconstruction takes individual PMT digits and associates them to reconstruct the hit in the slab. If there are multiple hits associated with a PMT, the hit which is earliest in time is taken to be the real hit. Then, if both PMTs on a slab have fired, the slab is considered to have a valid hit. The TDC values are converted to time and the hit time and charge associated with the slab hit are taken to be the average of the two PMT times and charges respectively. In addition, the product of the PMT charges is also calculated and stored. Secondly, individual slab hits are used to form space-points. A space-point in the TOF is a combination of x and y slab hits. All combinations of x and y slab hits in a given station are treated as space-point candidates. Calibration corrections, stored in the Configurations Database, are applied to these hit times and if the reconstructed space-point is consistent with the resolution of the detector, the combination is said to be a valid space-point. The TOF has been shown to provide good time resolutions at the 60 ps level [6].
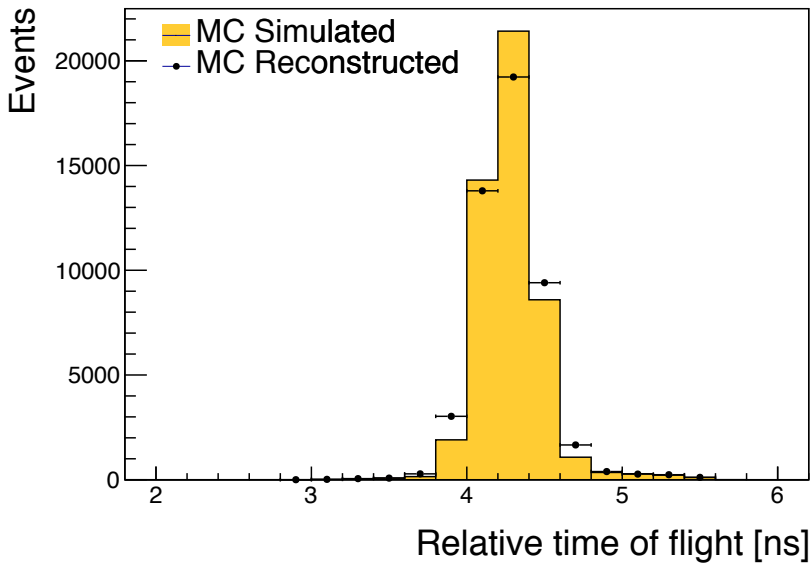
Figure 13. Relative time of flight between TOF0 and TOF1. The yellow histogram represents true MC events and the solid markers represent the same sample reconstructed with MAUS.

4.2 Scintillating-fiber trackers

The scintillating-fiber trackers are the central piece of the reconstruction. As mentioned in section 1.1, there are two trackers, one upsteam and the other downstream of an absorber, situated within solenoidal magnetic fields. The trackers measure the emittance before and after particles pass through the absorber.

The tracker software algorithms and performance are described in detail in [39]. Digits are the most basic unit fed into the main reconstruction module, each digit representing a signal from one channel. Digits from adjacent channels are assumed to come from the same particle and are grouped to form clusters. Clusters from channels which intersect each other, in at least two planes from the
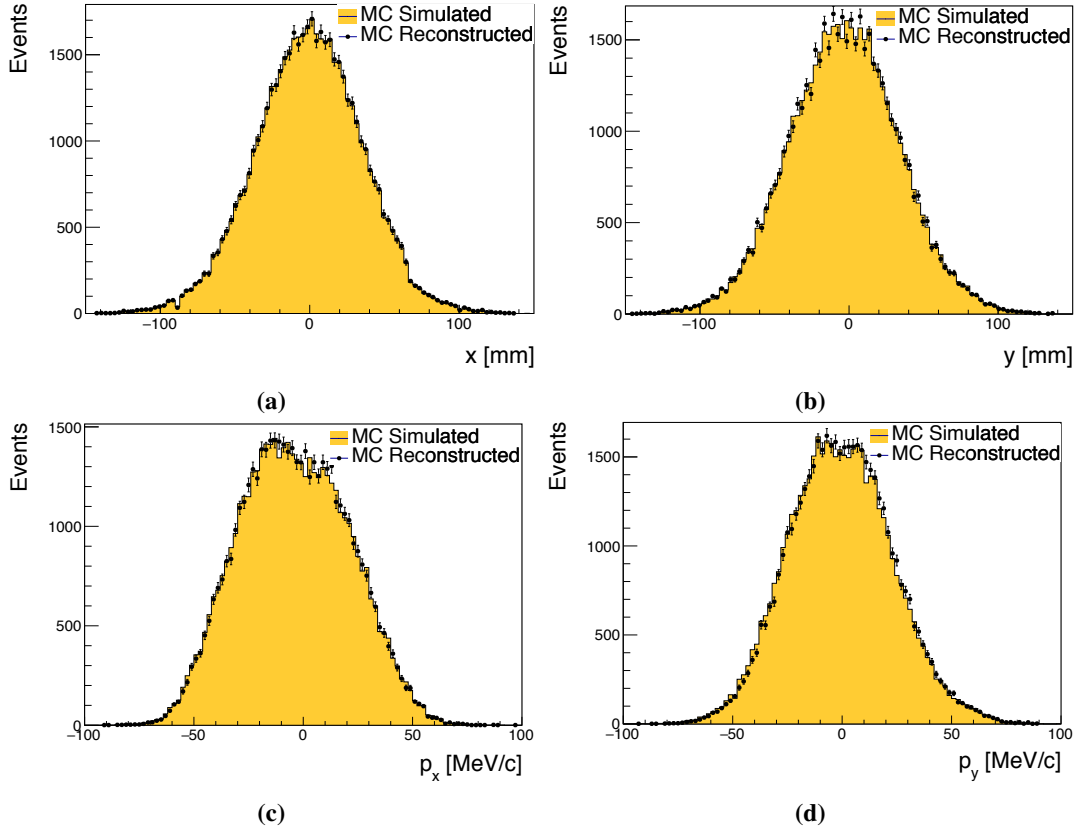
Figure 14. Position and momentum distributions of muons reconstructed at upstream tracker station nearest to the absorber: a) x, b) y, c) p_x, d) p_y. The yellow histograms represent true MC simulations, and the markers represent the MC sample reconstructed using MAUS.

same station, are used to form space-points, giving x and y positions where a particle intersected a station. Once space-points have been found, they are associated with individual tracks through pattern recognition (PR), giving straight or helical PR tracks. These tracks, and the space-points associated with them, are then sent to the final track fit. To avoid biases that may come from space-point reconstruction, the Kalman filter uses only reconstructed clusters as input.

4.3 KL calorimeter

Hit-level reconstruction of the KL is implemented in MAUS. Individual PMT hits are unpacked from the DAQ or simulated from MC and the reconstruction associates them to identify the slabs that were hit and calculates the charge and charge-product corresponding to each slab hit. The KL has been used successfully to estimate the pion contamination in the MICE muon beamline [9].

4.4 Electron-muon ranger

Hit-level reconstruction of the EMR is implemented in MAUS. The integrated ADC count and time over threshold are calculated for each bar that was hit. The EMR reconstructs a wide range of

variables that can be used for particle identification and momentum reconstruction. The software and performance of the EMR are described in detail in [10].

4.5 Cherenkov

The CKOV reconstruction takes the raw flash-ADC data, subtracts pedestals, calculates the charge and applies calibrations to determine the photo-electron yield.

4.6 Global reconstruction

The aim of the Global Reconstruction is to take the reconstructed outputs from individual detectors and tie them together to form a global track. A likelihood for each particle hypothesis is also calculated.

4.6.1 Global track matching

Global track matching is performed by collating particle hits (TOFs 0, 1 and 2, KL, Ckovs) and tracks (Trackers and EMR) from each detector using their individual reconstruction and combining them using a RK4 method to propagate particles between these detectors. The tracking is performed outwards from the cooling channel — i.e., from the upstream tracker to the TOF0 detector, and from the downstream tracker to the EMR detector. Track points are matched to form tracks using an RK4 method. Initially this is done independently for the upstream and downstream sections (i.e., either side of the absorber). As the trackers provide the most accurate position reconstruction, they are used as starting points for track matching, propagating hits outwards into the other detectors and then comparing the propagated position to the measured hit in the detector. The acceptance criterion for a hit belonging to a track is an agreement within the detector's resolution with an additional allowance for multiple scattering. Track matching is currently performed for all TOFs, KL and EMR.

The RK4 propagation requires the mass and charge of the particle to be known. Hence, it is necessary to perform track matching using a hypothesis for each particle type (muons, pions, and electrons). Tracks for all possible PID hypotheses are then passed to the Global PID algorithms.

4.6.2 Global PID

Global particle identification in MICE typically requires the combination of several detectors. The time-of-flight between TOF detectors can be used to calculate velocity, which is compared with the momentum measured in the trackers to identify the particle type. For all events but those with very low transverse momentum (p_t), charge can be determined from the direction of helical motion in the trackers. Additional information can be obtained from the CKOV, KL and EMR detectors. The global particle identification framework is designed to tie this disparate information into a set of hypotheses of particle types, with an estimate of the likelihood of each hypothesis.

The Global PID in MAUS uses a log-likelihood method to identify the particle species of a global track. It is based upon a framework of PID variables. Simulated tracks are used to produce probability density functions (PDFs) of the PID variables. These are then compared with the PID variables for tracks in real data to obtain a set of likelihoods for the PIDs of the track.

The input to the Global PID is several potential tracks from global track matching. During the track matching stage, each of these tracks was matched for a specific particle hypothesis. The Global PID then takes each track and determines the most likely PID following a series of steps:

1. Each track is copied into an intermediate track;

2. For each potential PID hypothesis *p*, the log-likelihood is calculated using the PID variables;

3. The track is assigned an object containing the log-likelihood for each hypothesis; and

4. From the log-likelhoods, the confidence level, C.L., for a track having a PID *p* is calculated and the PID is set to the hypothesis with the best C.L.

4.7 Online reconstruction

During data taking, it is essential to visualize a detector's performance and have diagnostic tools to identify and debug unexpected behavior. This is accomplished through summary histograms of high and low-level quantities from detectors. The implementation is through a custom multi-threaded application based on a producer-consumer pattern with thread-safe FIFO buffers. Raw data produced by the DAQ are streamed through a network and consumed by individual detector *mappers* described in section 3. The reconstructed outputs produced by the *mappers*, are in turn consumed by the *reducers*. The *mappers* and *reducers* are distributed among the threads to balance the load. Finally, outputs from the *reducers* are written as histogram images. Though the framework for the online reconstruction is based on parallelized processing of spills, the reconstruction modules are the same as those used for offline processing. A lightweight tool based on Django [40] provides live web-based visualization of the histogram images as and when they are created. Typical data rates during experimental operations were ∼ 300 MB/s. The average event rate varied, depending on the configuration of the beamline, with the maximum instantaneous rate being ∼ 150 kHz. MAUS performance matched the data rates and online reconstruction happened virtually "live" with the reconstructed outputs available instantly allowing collaborators to monitor the quality of the data being acquired.

5 Summary

The MICE collaboration has developed the MAUS software suite to simulate the muon beamline, simulate the MICE detectors, and reconstruct both simulated and real data. The software also provides global track-matching and particle-identification capabilities. Simplified programming interfaces and testing environments enable productive development. MAUS has been successfully used to reconstruct data online during data collection. In addition, MAUS is routinely used to perform reconstruction of the entire MICE data volume on batch production systems. MICE has collected ∼ 15 TB of raw data and a full reconstruction of the data is performed with each released version of MAUS. The batch systems are also used to perform compute-intensive simulations with various configurations of the beamline and the cooling channel.

Acknowledgments

References

[1] MICE collaboration, *First Demonstration of Ionization Cooling in MICE*, in *Proceedings of the International Particle Accelerator Conference*, Vancouver, Canada, 29 April–May 4 2018, pp. 5035–5040.

[2] IDS-NF collaboration, *International design study for the neutrino factory: Interim design report*, 2011.

[3] S. Geer, *Muon Colliders and Neutrino Factories*, *Annu. Rev. Nucl. Part. Sci.* **59** (2009) 345.

[4] MICE collaboration, *The MICE Muon Beam on ISIS and the beam-line instrumentation of the Muon Ionization Cooling Experiment*, 2012 *JINST* **7** P05009 [arXiv:1203.4089].

[5] MICE collaboration, *Characterisation of the muon beams for the Muon Ionisation Cooling Experiment*, *Eur. Phys. J.* **C 73** (2013) 2582 [arXiv:1306.1509].

[6] MICE collaboration, *The design and commissioning of the MICE upstream time-of-flight system*, *Nucl. Instrum. Meth.* **A 615** (2010) 14 [arXiv:1001.4426].

[7] KLOE collaboration, *The KLOE electromagnetic calorimeter*, *Nucl. Instrum. Meth.* **A 494** (2002) 326.

[8] F. Ambrosino et al., *Calibration and performances of the KLOE calorimeter*, *Nucl. Instrum. Meth.* **A 598** (2009) 239.

[9] MICE collaboration, *Pion Contamination in the MICE Muon Beam*, 2016 *JINST* **11** P03001 [arXiv:1511.00556].

[10] MICE collaboration, *Electron-Muon Ranger: performance in the MICE Muon Beam*, 2015 *JINST* **10** P12012 [arXiv:1510.08306].

[11] R. Asfandiyarov et al., *The design and construction of the MICE Electron-Muon Ranger*, 2016 *JINST* **11** T10007 [arXiv:1607.04955].

[12] MICE collaboration, *First particle-by-particle measurement of emittance in the Muon Ionization Cooling Experiment*, *Eur. Phys. J.* **C 79** (2019) 257 [arXiv:1810.13224].

[13] L. Cremaldi, D.A. Sanders, P. Sonnek, D.J. Summers and J. Reidy, Jr, *A Cherenkov Radiation Detector with High Density Aerogels*, *IEEE Trans. Nucl. Sci.* **56** (2009) 1475 [arXiv:0905.3411].

[14] M. Ellis et al., *The Design, construction and performance of the MICE scintillating fibre trackers*, *Nucl. Instrum. Meth.* **A 659** (2011) 136 [arXiv:1005.3491].

[15] https://scons.org.

[16] https://bazaar.canonical.com.

[17] https://launchpad.net.

[18] R. Brun and F. Rademakers, *ROOT: An object oriented data analysis framework*, *Nucl. Instrum. Meth.* **A 389** (1997) 81.

[19] GEANT4 collaboration, *GEANT4: A Simulation toolkit*, *Nucl. Instrum. Meth.* **A 506** (2003) 250.

[20] https://scientificlinux.org.

[21] https://centos.org.

[22] https://getfedora.org.

[23] https://ubuntu.com.

[24] J. Dean and S. Ghemawat, *MapReduce: Simplified data processing on large clusters*, in *Proceedings of OSDI04*, San Francisco, CA, U.S.A., 2004, pp. 137–150.

[25] https://json.org.

[26] https://github.com/open-source-parsers/jsoncpp.

[27] https://jenkins-ci.org.

[28] T.J. Roberts and D.M. Kaplan, *G4BeamLine programme for matter dominated beamlines*, in *Proceddings of the Particle Accelerator Conference*, Albuquerque, NM, U.S.A., 25–29 June 2007, pp. 3468–3470.

[29] R.C. Fernow, *Icool: A simulation code for ionization cooling of muon beams*, in *Proceedings of the Particle Accelerator Conference*, New York, NY, U.S.A., 27 March–2 April 1999, pp. 3020–3022.

[30] J. Apostolakis et al., *Geometry and physics of the geant4 toolkit for high and medium energy applications*, *Radiat. Phys. Chem.* **78** (2009) 859.

[31] R. Chytracek, J. McCormick, W. Pokorski and G. Santin, *Geometry description markup language for physics simulation and analysis applications.*, *IEEE Trans. Nucl. Sci.* **53** (2006) 2892.

[32] https://fastrad.net.

[33] https://www.w3.org/standards/xml/transformation.

[34] G. Penn and J.S. Wurtele, *Beam envelope equations for cooling of muons in solenoid fields*, *Phys. Rev. Lett.* **85** (2000) 764.

[35] R. Ryne and C. Rogers, *Nonlinear effects in the MICE step iv lattice*, MICE-NOTE-461, 2015.

[36] S.C. Middleton, *Characterisation of the MICE experiment*, Ph.D. Thesis, Imperial College London (2018).

[37] R.D. Ryne et al., *Recent progress on the MARYLIE/IMPACT beam dynamics code*, in *Proceedings of the 9th International Computational Accelerator Physics Conference*, Chamonix, France, 2–6 October 2006, pp. 157–159.

[38] C.T. Rogers, D. Stratakis, G. Prior, S. Gilardoni, D. Neuffer, P. Snopok et al., *Muon front end for the neutrino factory*, *Phys. Rev. ST Accel. Beams* **16** (2013) 040104.

[39] A. Dobbs, C. Hunt, K. Long, E. Santos, M.A. Uchida, P. Kyberd et al., *The reconstruction software for the MICE scintillating fibre trackers*, 2016 *JINST* **11** T12001 [arXiv:1610.05161].

[40] https://www.djangoproject.com.

[41] https://www.gridpp.ac.uk.

174

V. I. Udovičić, *et al*.: Multiyear Indoor Radon Variability in a Family House – ...
Nuclear Technology & Radiation Protection: Year 2018, Vol. 33, No. 2, pp. 174-179

MULTIYEAR INDOOR RADON VARIABILITY IN A FAMILY HOUSE – A CASE STUDY IN SERBIA

by

Vladimir I. UDOVIČIĆ [1*], Dimitrije M. MALETIĆ [1], Radomir M. BANJANAC [1], Dejan R. JOKOVIĆ [1], Aleksandar L. DRAGIĆ [1], Nikola B. VESELINOVIĆ [1], Jelena Z. ŽIVANOVIĆ [1], Mihailo R. SAVIĆ [1], and Sofija M. FORKAPIĆ [2]

[1]Institute of Physics, University of Belgrade, Belgrade, Serbia
[2]Department of Physics, Faculty of Science, University of Novi Sad, Novi Sad, Serbia

The indoor radon behavior has complex dynamics due to the influence of the large number of different parameters: the state of indoor atmosphere (temperature, pressure, and relative humidity), aerosol concentration, the exchange rate between indoor and outdoor air, construction materials, and living habits. As a result, indoor radon concentration shows variation, with the usual periodicity of one day and one year. It is well-known that seasonal variation of the radon concentration exists. It is particularly interesting to investigate indoor radon variation at the same measuring location and time period, each year, due to estimation of individual annual dose from radon exposure. The long-term indoor radon measurements, in a typical family house in Serbia, were performed. Measurements were taken during 2014, 2015, and 2016, in February and July, each year. The following measuring techniques were used: active and charcoal canisters methods. Analysis of the obtained results, using multivariate analysis methods, is presented.

Key words: radon variability, multivariate regression analysis, multi-seasonal radon
measurements, indoor radon

INTRODUCTION

The research of the dynamics of radon in various environments, especially indoors, is of great importance in terms of protection against ionizing radiation and in designing of measures for its reduction. Published results and development of many models to describe the behavior of indoor radon, indicates the complexity of this research, especially with models for prediction of the variability of radon [1-3]. This is because the variability of radon depends on a large number of variables such as local geology, permeability of soil, building materials used for the buildings, the state of the indoor atmosphere (temperature, pressure and relative humidity), aerosol concentration, the exchange rate between indoor and outdoor air, construction materials, as well as the living habits of people. It is known that the indoor radon concentration variation has periodicity of one day and one year. It is also well-known that the seasonal variation of the radon concentration exists. This is why it is particularly interesting to investigate indoor radon variation at the same measuring location and time period, year after

year, in order to estimate the individual annual dose from radon exposure. In that sense, we performed long-term indoor radon measurements in a typical family house in Serbia. Measurements were taken during the 2014, 2015, and 2016, in February and July, each year. We used the following measuring techniques: active and charcoal canisters methods. The detailed analysis of the obtained results using multivariate analysis (MVA) methods is presented in this paper.

First, MVA methods were tested on the radon variability studies in the Underground Low Background Laboratory in the Institute of Physics, Belgrade [4, 5]. Several climate variables: air temperature, pressure, and humidity were considered. Further advance was made by using all the publicly available climate variables monitored by nearby automatic meteorological station. In order to analyze the dependence of radon variation on multiple variables, multivariate analysis needs to be used. The goal was to find an appropriate method, out of the wide spectrum of multivariate analysis methods that are developed for the analysis of data from high-energy physics experiments, to analyze the measurements of variations of radon concentrations in indoor spaces. Previous

---

* Corresponding author; e-mail: udovicic@ipb.ac.rs

V. I. Udovičić, *et al.*: Multiyear Indoor Radon Variability in a Family House – ...
Nuclear Technology & Radiation Protection: Year 2018, Vol. 33, No. 2, pp. 174-179

175

analysis were done using the maximum of 18 climate parameters and use and comparison of 8 different multivariate methods. In this paper the number of variables is reduced to the most important ones and new derived variables, like vapor pressure, simple modeled solar irradiance and simple modeled precipitation, which were introduced in the multivariate analysis.

INDOOR RADON MEASUREMENTS METHODS

Depending on the integrated measurement time, methods of measurement of the indoor radon concentrations may be divided into long-term and short-term ones. The device for the performed short-term radon measurements is SN1029 radon monitor (manufactured by the Sun Nuclear Corporation, NRSB approval-code 31822) with the following characteristics: the measurement range from 1 Bqm^{-3} to 99.99 $kBqm^{-3}$, accuracy equal to +25 %, sensitivity of 0.16 counts hour per Bqm^{-3}. The device consists of two diffused junction photodiodes as the radon detector which is furnished with sensors for temperature, barometric pressure, and relative humidity. The sampling time was set to 2 h. The method for Charcoal Canister used is: EERF Standard Operating Procedures for Radon-222 Measurement Using Charcoal Canisters [6], also used by major laboratories which conduct radon measurements in Serbia [7]. Exposure time of the charcoal canisters was 48 h. The connection between short term and long term measurements has attracted some interest previously [8].

The family house, selected for the measurements and analysis of variations of radon concentrations, is a typical house in Belgrade residential areas, with requirement of existence of cellar. House is built on limestone soil. Radon measurements were carried out in the living room of the family house, which is built of standard materials (brick, concrete, mortar) and isolated with styrofoam. During the period of measurements (winter-summer 2014, 2015, and 2016), the house was naturally ventilated and air conditioning was used in heating mode at the beginning of the measurement period. During the winter period measurements, the electrical heating was used in addition to air conditioning. Measured radon concentrations, room temperature ($T\_$id), atmospheric pressure ($P\_$id) and relative humidity ($H\_$id) inside the house, were obtained using radon monitor. Values of meteorological variables, in the measurement period, were obtained from an automatic meteorological station, located near the house in which the measurement was performed. We used the following meteorological variables: external air temperature (T), also at height of 5cm, pressure (P) and humidity (H), solar irradiation, wind speed, precipitation, temperature of the soil at depths of 10 cm, 20 cm and 50 cm. The natural ventilation routine was not monitored. Since the ventilation is of

crucial importance for the level of radon indoors [9], Multivariate regression analysis was used mainly for winter periods.

MULTIVARIATE REGRESSION ANALYSIS

In many fields of physics, especially in high-energy physics, there is the demand for detailed analyses of a large amount of data. For this purpose, the data analysis environment ROOT [10], is developed. ROOT is modular scientific software framework, which provides all the functionalities needed to deal with big data processing, statistical analysis, visualization and storage. A specific functionality gives the developed Toolkit for Multivariate Analysis (TMVA) [11]. The TMVA provides an environment for the processing, parallel evaluation and application of multivariate regression techniques.

TMVA is used to create, test and apply all available regression multivariate methods, implemented in ROOT, in order to find methods which are the most appropriate and yield maximum information on the dependence of indoor radon concentrations on the multitude of meteorological variables. Regression methods are used to find out which regression method can, if any, on the basis of input meteorological variables only, give an output that would satisfactorily close match the observed variations of radon concentrations. The output of usage of multivariate regression analysis methods has mapped functional behavior, which can be used to evaluate the measurements of radon concentrations using input meteorological variables only. All the methods make use of training events, for which the desired output is known and is used for training of Multivariate regression methods, and test events, which are used to test the MVA methods outputs.

RESULTS

Measurements were performed during February and July in 2014, 2015, and 2016 using radon monitor and charcoal canister measurements. The descriptive results are summarized in tab. 1. The measurements using radon monitor and charcoal canisters are in good agreement.

Previous work done by researchers from the Low Background Laboratory, Institute of Physics, Belgrade, using the MVA analysis in search of connections between radon concentration and meteorological variables, included only one period of measurement, February or July 2014 [4]. Now the MVA analysis is using all the measured data February/July 2014-2016. New variables introduced in MVA analysis are modeled solar irradiance, modeled precipitation and vapor
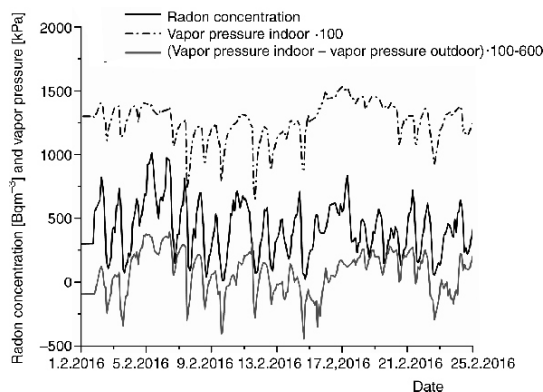
176

V. I. Udovičić, *et al.*: Multiyear Indoor Radon Variability in a Family House – ...
Nuclear Technology & Radiation Protection: Year 2018, Vol. 33, No. 2, pp. 174-179

Table 1. Descriptive results of February and July 2014, 2015, and 2016 measurements, using radon monitor and charcoal canisters (only in February)

Results of measurements	2014		2015		2016	
	Feb.	July	Feb.	July	Feb.	July
Minimal radon activity using radon monitor [Bqm^{-3}]	15	0	28	0	12	3
Maximal radon activity using radon monitor [Bqm^{-3}]	1000	286	915	88	1013	262
Median radon activity using radon monitor [Bqm^{-3}]	418	25	524	22	412	28
Arithmetic mean of radon activity using radon monitor (standard deviation) [Bqm^{-3}]	402 (216)	40 (41)	508 (207)	27 (18)	423 (214)	39 (32)
Room temperature using radon monitor (standard deviation) [°C]	20.4 (0.8)	24.7 (0.9)	21.2 (0.6)	24.9 (0.8)	22.3 (0.6)	24.6 (0.8)
Relative humidity using radon monitor (standard deviation) [%]	67.4 (5.7)	67.8 (4.8)	68.2 (4.8)	51.5 (4.7)	64.0 (6.4)	58.9 (7.5)
Radon activity using charcoal canister (standard deviation) [Bqm^{-3}]	432 (10)	/	518 (6)	/	407 (5)	/
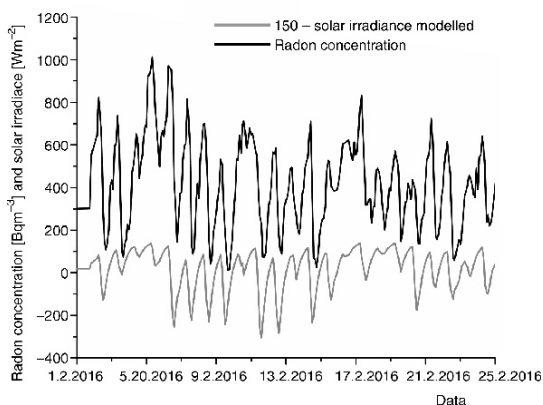
Figure 1. Modeled solar irradiance in comparison with measured radon concentration during February 2016

Figure 2. Vapor pressure in comparison with measured radon concentration during February 2016

pressure. In order to make use of intensity of solar irradiance during the whole day and night, the solar irradiance is modeled so that it includes 80 % of solar irradiance value from the previous measurement (previous hour) with addition of solar irradiance value for the actual hour of measurement (fig. 1). The value of 80 % is chosen so that the modeled solar irradiation has the best correlation with the radon measurements. Similar model of precipitation was used in this analysis. The next new variable is vapor pressure. The vapor pressure variable is calculated using the slope s(T), of the relationship between saturation vapor pressure and air temperature and is given by [12, 13], so that the vapor pressure equals relative humidity times saturation vapor pressure, fig. 2.

Before the start of training of Multivariate regression methods using TMVA toolkit in ROOT, the description of input meteorological variables is performed, mainly by looking into inter-correlations of input variables and their connections with the measured radon concentrations. The MVA is using all the measured data. Table 2 presents the meteorological variables and their module value of correlation with the measured radon concentrations (target), which is indicative in finding linear dependence of radon mea-

surements and input variables. The second column in tab. 2 presents us with correlation ration values which indicate if there are some functional dependence (not only linear) between input variables and radon concentration, and the last column presents the mutual information which indicates if there is a non-functional dependence of input variables and radon measurements [11].

From tab. 2 it can be noticed that linear correlated values are not the only ones which can be used in MVA analysis, for example variable solar irradiance has high mutual information with the radon measurements.

In the data preparation for MVA training the whole dataset is consisting of many events. An event includes time of measurement, radon measurement and meteorological variables. The dataset is randomly split in two halves, one half of the events will be used for training of multivariate regression methods, and the other half of events for testing of methods, mainly to compare the measured and MVA evaluated values for radon concentration.

It turns out that the methods best suited for our purpose is the Boosted Decision Trees (BDT) method. This means that BDT gives the smallest difference be-

Table 2. Input variable rank and values for correlation, correlation ratio and mutual information, all with the measured radon concentrations (target) for February and July 2014-2016 measurements

Variable	Correlation with target		Correlation ratio		Mutual information	
	Rank	Value	Rank	Value	Rank	Value
Soil temperature depth 20 cm [°C]	1	0.87	1	0.60	13	1.48
Soil temperature depth 50 cm [°C]	2	0.86	2	0.57	14	1.31
Soil temperature depth 10 cm [°C]	3	0.82	3	0.54	9	1.84
Temperature outdoor [°C]	4	0.82	5	0.53	8	1.85
Vapor indoor – vapor od [mbar]	5	0.81	9	0.41	11	1.73
Temperature od – temperature id [°C]	6	0.80	4	0.53	6	1.92
Temperature height 5 cm [°C]	7	0.77	8	0.48	7	1.91
Vapor od [mbar]	8	0.76	10	0.41	5	1.92
Temperature id [°C]	9	0.75	7	0.49	17	1.16
Solar irradiance [Wm^{-2}]	10	0.61	6	0.50	2	2.23
Humidity indoor [%]	11	0.45	11	0.26	1	2.26
Humidity outdoor [%]	12	0.31	13	0.20	10	1.76
Air pressure outdoor [mbar]	13	0.27	17	0.07	12	1.55
Wind speed [ms^{-1}]	14	0.22	16	0.01	16	1.28
Air pressure indoor [mbar]	15	0.17	18	0.04	15	1.31
Humidity od – Humidity id [%]	16	0.10	14	0.19	4	2.11
Precipitation [Lm^{-2}]	17	0.01	15	0.19	18	1.13
Vapor indoor [mbar]	18	0.002	12	0.02	3	2.17

tween the measured radon concentration from test sample and the evaluation of value of radon concentration using input variables only. This can be seen in fig. 3, which shows the distribution of BDT and BDTG regression method outputs (evaluated values) in comparison with the measured radon concentration during February 2016.

Since TMVA has 12 different regression methods implemented, only some of those will give useful results when evaluating the radon concentration measurements. Table 4 summaries the results of MVA analysis. It shows the MVA methods RMS of difference of evaluated and measured radon concentration. Also, tab. 4 shows the mutual information of measured and MVA evaluated radon concentration. Besides
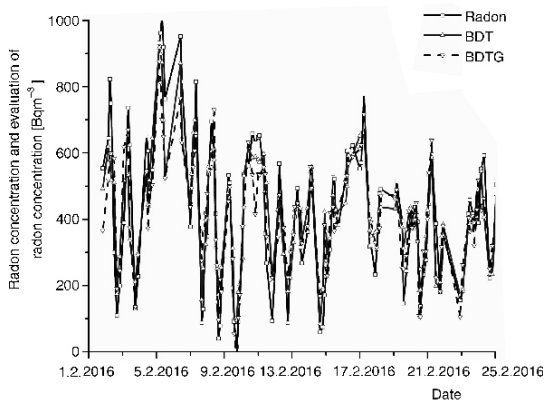
BDT, the Multi-Layer Perceptron (MLP) [10], an implementation of Artificial Neural Network multi variate method, also gives good results.

The MVA regression analysis results in mapped functional behavior and, as opposed to possible existence of theoretical modeling, which is independent of the number of measurements, MVA depends on the number of events. More events, the better mapped function we get as a result. In this sense, if the number of measurements is not great, multivariate analysis can be used only as help, to indicate which variables are more important to be used in theoretical modeling, for comparison of mapped and modeled functions, and modeled function test.

CONCLUSION

Indoor radon variation at one location in the same periods (February and July), was investigated for three years. Long-term indoor radon measurements show intense seasonal variation. The results obtained with different measuring methods are in good agreement. The radon behavior in the house is almost the same and shows good reproducibility year by year. The small variations in the year by year dynamics are originated mostly from the variations in meteorological variables during winter seasons and mostly due to ventilation habits during summer season. Ventilation habits were not monitored nor taken into account in MVA regression analysis. The preliminary results using multivariate analysis methods in TMVA are shown. Main output of Multivariate regression analy-

Figure 3. Comparison of MVA evaluated radon concentration and measured one from the test sample of events during February 2016

178

V. I. Udovičić, *et al.*: Multiyear Indoor Radon Variability in a Family House – ...
Nuclear Technology & Radiation Protection: Year 2018, Vol. 33, No. 2, pp. 174-179

Table 3. Input variable correlation with the measured radon concentrations for February and July 2016

Correlation with target			
February 2016		July 2016	
Variable	Value	Variable	Value
Vapor id-vapor od [mbar]	0.58	Soil temperature depth 20 cm [°C]	0.46
Humidity id [%]	0.54	Soil temperature depth 50 cm [°C]	0.42
Vapor id [mbar]	0.52	Solar irradiance	0.32
Solar irradiance [Wm^{-2}]	0.48	Temperature id [°C]	0.30
Temperature od – temperature id [°C]	0.46	Soil temperature depth 10 cm [°C]	0.24
Temperature [°C]	0.44	Temperature od [°C]	0.21
Soil temperature depth 10 cm [°C]	0.43	Humidity od [%]	0.20
Soil temperature depth 20 cm [°C]	0.42	Humidity id [%]	0.19
Humidity [%]	0.38	Air pressure [mbar]	0.17
Temperature height 5 cm [°C]	0.32	Precipitation [Lm^{-2}]	0.17
Temperature id [°C]	0.29	Temperature od – temperature id [°C]	0.16
Air pressure od [mbar]	0.23	Air pressure_id [mbar]	0.16
Air pressure id [mbar]	0.21	Humidity od – humidity id [%]	0.14
Soil temperature depth 50 cm [°C]	0.20	Wind speed [ms^{-2}]	0.13
Precipitation [Lm^{-2}]	0.19	Temperature height 5 cm [°C]	0.12
Humidity od – humidity id [%]	0.15	Vapor id [mbar]	0.06
Vapor od [mbar]	0.08	Vapor od [mbar]	0.03
Wind speed [ms^{-1}]	0.05	Vapor id – vapor od [mbar]	0.02

Table 4. RMS of MVA method's evaluation error and mutual information; February/July 2014-2016

MVA method	RMS [Bqm^{-3}]	Mutual information
BDT	85.5	1.477
BDTG	92.1	1.614
MLP	101	1.401

sis is the initial version of *mapped* function of radon concentration dependence on multitude of meteorological variables. Simplification of MVA methods can be made by choosing only the most important input variables and exclude the other variables.

AUTHORS' CONTRIBUTIONS

The idea for this paper came as a result of discussions of V. I. Udovičić, R. M. Banjanac, D. R. Joković, A. L. Dragić, and D. M. Maletić. Gathering climate data and MVA analysis was done by D. M. Maletić and V. I. Udovičić. Performed indoor radon measurements were done by V. I. Udovičić and S. M. Forkapić. Writing of the paper was done by D. M. Maletić and V. I. Udovičić. A. L. Dragić gave idea about using MVA methods in cosmic and radon measurements. N. B. Veselinović and M. R. Savić analyzed and validated climate data. J. Z. Živanović helped with MVA analysis. D. R. Joković helped with data analysis and paper technical preparation.

REFERENCES

[1] Collignan, B., *et al.*, Development of a Methodology to Characterize Radon Entry in Dwellings, *Building and Environment, 57* (2012), Nov., pp. 176-183

[2] Li, F., Baixeras, C., The RAGENA Dynamic Model of Radon Generation, Entry and Accumulation Indoors, *Science of the Total Environment, 307* (2003), 1-3, pp. 55-69

[3] Jelle, B. P., *et al.*, Development of a Model for Radon Concentration in Indoor Air, *Science of the Total Environment, 416* (2012), Jan., pp. 343-350

[4] Maletić, D., *et al.*, Comparison of Multivariate Classification and Regression Methods for Indoor Radon Measurements, *Nucl Technol Radiat, 29* (2014), 1, pp. 17-23

[5] Udovičić, V., *et al.*, Radon Problem in an Underground Low-Level Laboratory, *Radiation Measurements, 44* (2009), 9-10, pp. 1009-1012

[6] ***, EPA 520/5-87-005, Gray D.J, Windham S.T, United States Environmental Protection Agency, Montgomery, 1987

[7] Živanović, M. Z., *et al.*, Radon Measurements with Charcoal Canisters, *Nucl Technol Radiat, 31* (2016), 1, pp. 65-72

[8] Stojanovska, Z., *et al.*, Prediction of Long-Term Indoor Radon Concentrations Based on Short-Term Measurements, *Nucl Technol Radiat, 32* (2017), 1, pp. 77-84

[9] Nikolić, M. D., *et al.*, Modelling Radiation Exposure in Homes from Siporex Blocks by Using Exhalation Rates of Radon, *Nucl Technol Radiat, 30* (2015), 4, pp. 301-305

[10] Brun, R., Rademakers, F., ROOT – An Object Oriented Data Analysis Framework, *Nucl. Inst. Meth. in Phys. Res., A 389* (1997), 1-2, pp. 81-86

[11] Hoecker, A., *et al.*, TMVA – Toolkit for Multivariate Data Analysis, PoS ACAT 040, arXiv:physics/070 303, 2007

[12] Murray, F. W., On the Computation of Saturation Vapor Pressure, *J. Applied Meteorology, 6* (1967), 1, pp. 203-204

[13] Tetens, O., About Some Meteorological Aspects (in German), *Z. Geophys, 6* (1930), pp. 207-309

**Владимир И. УДОВИЧИЋ, Димитрије М. МАЛЕТИЋ, Радомир М. БАЊАНАЦ,
Дејан Р. ЈОКОВИЋ, Александар Л. ДРАГИЋ, Никола Б. ВЕСЕЛИНОВИЋ,
Јелена З. ЖИВАНОВИЋ, Михаило Р. САВИЋ, Софија М. ФОРКАПИЋ**

СТУДИЈА СЛУЧАЈА ВИШЕГОДИШЊЕ ВАРИЈАБИЛНОСТИ РАДОНА У ПОРОДИЧНОЈ КУЋИ У СРБИЈИ

Понашање радона у затвореном простору има сложену динамику због утицаја великог броја различитих параметара који утичу на његову варијабилност: метеоролошких (температура, притисак и релативна влажност), концентрације аеросола, брзине размене између унутрашњег и спољашњег ваздуха, грађевинских материјала и животних навика. Као резултат, концентрација радона у затвореним просторијама показује варијацију, уз стандардну периодичност од једног дана и једне године. Годишња варијабилност је добро позната сезонска варијација концентрације радона. Посебно је интересантно пратити вишегодишње варијације концентрације радона на истој мерној локацији и временском периоду, пре свега због процене индивидуалних годишњих доза од изложености радону. У типичној породичној кући у Србији извршена су дуготрајна мерења радона у дневном боравку. Мерења су рађена током 2014, 2015, и 2016. године, у фебруару и јулу, сваке године. Коришћене су следеће мерне технике: активна и метода коришћења угљених канистера. Добијени резултати анализирани су коришћењем мултиваријантне регресионе анализе.

Кључне речи: варијабилност радона, мултиваријантна регресиона анализа, радон у затвореним просторијама, вишегодишње мерење радона

DE GRUYTER
OPEN

First steps towards national radon action plan in Serbia

Vladimir Udovičić,
Dimitrije Maletić,
Maja Eremić Savković,
Gordana Pantelić,
Predrag Ujić,
Igor Čeliković,
Sofija Forkapić,
Dragoslav Nikezić,
Vladimir M. Marković,
Vesna Arsić,
Jovana Ilić

Abstract. Radon problem has a special attention in many countries in the world and the most of them have established national radon programmes. The radon issues in Serbia have not been approached in a systematic and organized way. Currently, there are many research groups and institutions working in radon field, and it is a good basis to integrate all these activities into a comprehensive national programme to define the strategic objectives and action plan for the next few years. Also, Serbia as a candidate for membership in the EU is obliged to harmonize its legislation, including the field of radiation protection in which the radon issues has an important role. In this report, a brief history of radon research, present status and plans for the future activity on radon issues in Serbia are presented. Regarding the long-term plans, the establishment and implementation of the Radon Action Plan with the primary goal of raising awareness about the harmful effects of public exposure to radon and implementing a set of measures for its reduction. In that sense, the synergy between the national, regional and local organizations responsible for public health and radiation protection must be achieved.

Key words: radon • action plan • survey

V. Udovičić✉, D. Maletić
Institute of Physics Belgrade,
University of Belgrade,
118 Pregrevica Str., 11080 Belgrade, Serbia,
E-mail: udovicic@ipb.ac.rs

M. Eremić Savković
Serbian Radiation Protection and Nuclear Safety Agency,
Belgrade, Serbia

G. Pantelić, P. Ujić, I. Čeliković
Vinča Institute of Nuclear Sciences,
University of Belgrade,
Belgrade, Serbia

S. Forkapić
Department of Physics,
Faculty of Science,
University of Novi Sad,
Novi Sad, Serbia

D. Nikezić, V. M. Marković
Faculty of Science,
University of Kragujevac,
Kragujevac, Serbia

V. Arsić, J. Ilić
Serbian Institute of Occupational Health
"Dr Dragomir Karajović",
Belgrade, Serbia

Introduction

Radon is a noble, naturally occurring radioactive gas. Radon contribute to almost 50% of the overall high-effective annual dose to the population received from all sources of natural radioactivity. Harmful effects of radon has been proven in a large number of epidemiological studies [1]. The latest recommendation of the International Atomic Energy Agency (IAEA) [2] and Directive EC [3] relating to the field of radiation protection, radon problem got more space and importance because the World Health Organization (WHO) has identified radon as the second biggest cause of cancer lung [4]. In addition, radon is included in the ranks of major pollutants of indoor air [5]. Current knowledge about the mechanisms by which radon is harmful to human health are reflected primarily in harmful, radioactive radon progeny fact. In fact, radon progenies are attached to the aerosol particles from the air and such radioactive particles enter the body through inhalation. These radioactive aerosols deposited in the lungs emit alpha radiation. The harmful activity can be seen in disorders of the cellular structure of DNA, causing the development of cancer cells. Consequently, radon problem has been addressed seriously, and in a number of countries, national radon programme is established, which is basically a multidisciplinary nature and requires the involve-

ment of a large number of experts, researchers involved in radiation physics, geo sciences, chemistry, biology to specialist in various fields of medicine. In that sense, the group of radon professionals decide to start working on establishing and developing national radon programme in Serbia. In this paper, a brief history of radon research, present status and plans for the future activity on radon issues in Serbia are presented.

International framework

The regulations related to the exposure of the population to radon and its progenies are different worldwide. Based on the researches and a large number of epidemiological studies done in the recent past, the new standards and recommendations have to be incorporated into the national legislation regarding radon issues. Basically, a new approach to the radon issue is to introduce the concept of the reference level (not as strict boundaries between safe and dangerous concentrations of radon, but the annual average indoor radon concentration above which it is necessary to take measures to reduce radon). It differs from action level (the radon concentration above which, if it is found that the measured concentration is greater than defined, gives recommendations to take measures for its reduction). The new concept is incorporated in two new documents. One is developed at the International Atomic Energy Agency (IAEA) [2]. In this new BSS (international Basic Safety Standards), radon is placed in several topics, but the most important is requirements of 50 (Requirement 50: Public exposure because of radon indoors). It defines the reference level, in dwellings of high occupational factors, which must not exceed 300 Bq·m^{-3}. Assuming equilibrium factor for radon 0.4 and the annual occupational factors of 7000 h, the reference level of 300 Bq·m^{-3} corresponds to an annual effective dose of 10 mSv, with dose conversion factor (DCF) of 7.5 mSv per WLM (working level month). The request 52 (Requirement 52: Exposure in workplaces) defines the reference level for radon in workplaces of 1000 Bq·m^{-3}. As the occupation factor for 2000 h with the same factor to balance radon of 0.4 leads to the same effective annual dose of 10 mSv. Important conclusions are based on the collected data and performed radon risk maps, the country has to decide and implement adequate control of the indoor radon, to inform the public and other stakeholders and, finally, to establish and implement Radon Action Plan (RAP).

The second document is EU Directive 2013/59 [3]. In the article 74: Indoor exposure to radon, writes the similar as in the new BSS, accept that the reference level shall not exceed 300 Bq·m^{-3} for the all indoor environment, living and workplaces. Article 103 defines RAP to be developing in member states: The action plan shall take into account the issues set out in Annex XVIII and be updated on a regular basis. Annex XVIII defined 14 items to consider in preparing the national RAP. In the case of Serbia, the first steps towards RAP are described in the next section.

National radon action plan in Serbia

Serbia did not have a systematic approach to the radon problem. In this sense, there were individual initiatives and research activities dealing with radon:

University of Novi Sad, Faculty of Science, Department of Physics, Chair of Nuclear Physics, Novi Sad

Radon mapping of Autonomous Province of Vojvodina [6], long-term and short-term measurements of radon concentration in soil, water and air using passive devices, active device RAD7, exhalation and diffusion measurements [7], charcoal canisters with gamma spectrometric analysis [8].

University of Belgrade, Vinča Institute of Nuclear Sciences, ECE Lab Belgrade

Department for Nuclear and Plasma Physics

Mapping radon and thoron throughout south-eastern Serbia, Kosovo and Metohija parts of western Serbia [9, 10] by using different passive devices; electrochemical etch track detectors in a specially designed and built in laboratory [11]; developing method for radon and thoron exhalation from building material [12]; radon measurement campaigns in the schools and houses in the Sokobanja municipality [13].

Radiation and Environmental Protection Department

Active charcoal detectors are used for testing the concentration of radon in dwellings. The method of measurement is based on radon adsorption on coal and measurement of gamma radiation of radon daughters according to US EPA protocol. Based on this EPA procedure and national and international intercomparison, the laboratory developed a set of procedures for charcoal detector exposure and measurement [14, 15].

University of Belgrade, Institute of Physics Belgrade, Low-Background Laboratory for Nuclear Physics

Radon monitoring in the underground low-background laboratory with the passive and active devices [16]; radon laboratory for chemical etching of the track detectors and automatic counting of the tracks by optical microscopy [17]; modelling of the indoor radon behaviour [18].

Institute of Occupational Health of Serbia "Dr Dragomir Karajović", Center for Radiological Protection, Belgrade

Radon measurements using charcoal canisters with gamma spectrometric analysis, radon monitoring in

schools and kindergartens in the city of Belgrade from 1991 [19] and radon measurements campaigns in schools and kindergartens in Belgrade from 2010 [20].

University of Kragujevac, Faculty of Science Kragujevac, Institute of Physics

Radon measurement using passive devices with chemical treatment of the track detectors and automatic scanning of the developed detectors; modelling of the behaviour of indoor radon [21]; dosimetric modelling of the effects of the inhalation of radon and its progeny in the lung [22].

Based on the great experience of research related to radon, the group of radon professionals organized Radon Forum in May 2014 and made a decision to start work on RAP in Serbia. The responsibility for the establishment and implementation of RAP is on national regulatory body: Serbian Radiation Protection and Nuclear Safety Agency (SRPNA). We started with Internet radon forum (www.cosmic.ipb. ac.rs/radon_forum), which provides an opportunity for radon professionals in Serbia to meet and discuss radon activities and plans. Also, SRPNA formed a 'radon working group' that will manage RAP. The organization chart of the institutions involved in RAP is shown in Fig. 1.

Short-term plans (to the end of 2015) include
– carrying out initial representative national indoor radon survey for this purpose,
– developing communication strategy (first basic information leaflet on radon to accompany the measurement explaining the purpose of the measurement, Internet site: http://cosmic.ipb.ac.rs/radon/index.html; public relation; etc.).

First national indoor radon survey in Serbia

As a first step in RAP, it is the national radon survey in Serbia planned to be done in 2015. In the cooperation with IAEA, SRPNA through radon working group made the design of the first national radon survey in Serbia. It is well known that regarding the objective of the indoor radon survey, there are two types of survey:
– population-weighted survey by measuring indoor radon levels in randomly selected homes (to estimate the distribution of radon public exposures),
– geographically based survey where homes are randomly selected to obtain a minimum density of measurements per area unit chosen, e.g., a grid square, an administrative unit (to identify radon prone areas, radon map).

Every radon survey needs to check the representativeness (e.g. compare certain parameters in the actual sample with corresponding values in the last census). A carefully designed survey can, in principle, meet the requirements and objectives of both the types of surveys. In the case of Serbia, we choose a stratified (target population is partitioned into separated groups – STRATA) sampling design. We defined STRATA according to the administrative divisions of Serbia into districts.

In principle, our design model can be described as follows:
– SRPNA, in cooperation with the IAEA through the national project SRB9003 – Enhancing the Regulatory Infrastructure and Legislative System,
– Expert mission on National Radon Trial Survey and Raising Awareness of Key Stakeholders held in SRPNA, Belgrade, 2–4 February 2015,
– Equipment: Leasing of 6000 track-etched indoor radon detectors; the distribution of detectors across the Serbian territory should be the responsibility of SRPNA,

and relevant ministries began with the national programme for indoor radon measurements in dwellings and flats in Serbia. The aim of this programme is to determine the radiological exposure risk to radon in residential areas because of the inhalation of this gas as well as to locate areas in Serbia with high concentrations, areas with high radon potential. Within the working group on radon, the division of
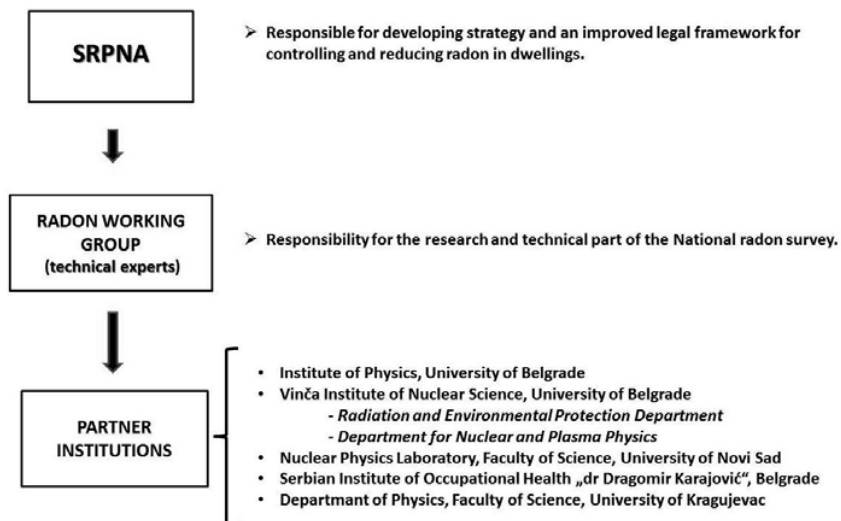

Fig. 1. Organization chart of the institutions involved in RAP.

responsibilities of individual institutions in a given set of administrative regions was established. All owners of houses and apartments (who wish to participate in the project), with the aim of determining the concentration of radon, filled predefined questionnaire on the Web site dedicated to radon in Serbia (http://cosmic.ipb.ac.rs/radon/index.html). In this way, they expressed interest to participate in the project. In total, 6000 detectors have been distributed during October 2015 and will be exposed in houses and apartments for six months (till April 2016). Afterwards, the detectors will be sent to an authorized laboratory to be processed, and consequently, we should get data for the first national map radon risk in Serbia. The measurement results will be presented to the owners of houses and apartments that are used for the measurement. Based on these results, in cases where radon concentration exceeds current intervention level of 200 Bq·m^{-3} for new developments or 400 Bq·m^{-3} for existing facilities, the whole set of measures that could result in a reduction of the radon concentrations and thus reduce the risk of getting lung cancer will be recommended. Additionally, all data collected for the whole of Serbia will enable the determination of the national reference level for radon. During the realization of the national programme for indoor radon measurements, we plan to perform communication strategy (first basic information leaflet on radon to accompany the measurement explaining the purpose of the measurement, internet site, public relation, public education, etc.).

Conclusions

World Health Organization declared radon as the second most important cause of getting lung cancer. Radon problem being addressed seriously, and in a number of countries, there are established national radon programme. Serbia started work on RAP in 2014, with the first step of preparing, and performed the national indoor radon survey in Serbia, planned to be done in 2015. The responsibility for the establishment and implementation of RAP is on national regulatory body: Serbian Radiation Protection and Nuclear Safety Agency. The results of national radon survey serves to evaluate the existing exposure situation and to define the next steps in establishing and developing RAP in Serbia**.** Also, the Serbian experience in efforts to have systematic approach to the radon issues, described in this paper, may be useful to the other countries who wish to establish their own RAP.

References

1. Darby, S., Hill, D., Auvinen, A., Barros-Dios, J. M., Baysson, H., Bochicchio, F., Deo, H., Falk, R., Forastiere, F., Hakama, M., Heid, I., Kreienbrock, L., Kreuzer, M., Lagarde, F., Mäkeläinen, I., Muirhead, C., Oberaigner, W., Pershagen, G., Ruano-Ravina, A., Ruosteenoja, E., Schaffrath Rosario, A., Tirmarche, M., Tomáscaronek, L., Whitley, E., Wichmann, H.-E., & Doll, R. (2005). Radon in homes and risk of lung cancer: collaborative analysis of individual data from 13 European case-control studies. *Brit. Med. J.*, *330*, 223–227.

2. International Atomic Energy Agency. (2011). *Radiation protection and safety of radiation sources: International basic safety standards Interim edition. General safety requirements Part 3*. Vienna: IAEA. Retrieved from http://www-pub.iaea.org/MTCD/publications/PDF/p1531interim_web.pdf.

3. Council of the European Union. (2014). *Council Directive 2013/59/EURATOM of 5 December 2013 laying down basic safety standards for protection against the dangers arising from exposure to ionising radiation, and repealing Directives 89/618/Euratom, 90/641/Euratom, 96/29/Euratom, 97/43/Euratom and 2003/122/Euratom*. (Official Journal of the European Union 2014; L13). Retrieved from http://www.srbatom.gov.rs/srbatom/doc/eu-direktive/2013%2059%20eng.pdf.

4. World Health Organization. (2009). *WHO handbook on indoor radon: a public health perspective*. Retrieved from http://www.who.int/ionizing_radiation/env/radon/en/index1.html.

5. World Health Organization. (2010). *WHO guidelines for indoor air quality: selected pollutants*. Retrieved from http://www.who.int/indoorair/publications/9789289002134/en/index.html.

6. Forkapić, S., Bikit, I., Slivka, J., Čonkić, Lj., Vesković, M., Todorović, N., Varga, E., Mrđa, D., & Hulber, E. (2006). Indoor radon in rural dwellings of the South-Pannonian region. *Radiat. Prot. Dosim.*, *123*(3), 378–383.

7. Nikolov, J., Todorovic, N., Bikit, I., Petrovic Pantic, T., Forkapic, S., Mrda, D., & Bikit, K. (2014). Radon in thermal waters in South-East part of Serbia. *Radiat. Prot. Dosim.*, *160*(1/3), 239–243.

8. Todorović, N., Bikit, I., Vesković, M., Krmar, M., Mrda, D., Forkapić, S., Hansman, J., Nikolov, J., & Bikit, K. (2014). Radioactivity in the indoor building environment in Serbia. *Radiat. Prot. Dosim.*, *158*(2), 208–215.

9. Žunić, Z. S., Yarmoshenko, I. V., Veselinović, N., Zhukovsky, M. V., Ujić, P., Čeliković, I., Mc Laughlin, J. P., Simopoulos, S. E., Birovljev, A., Fujimoto, K., Paridaens, J., Trotti, F., Tokonami, S., Olko, P., Kozak, K., Bochicchio, F., Ramola, R., Mietelski, J. W., Jakupi, B., Milić, G., Ciotoli, G., Kelleher, K., Budzanowski, M., Sahoo, S. K., Vanmarcke, H., & Waligorski, M. P. R. (2009). Identification and assessment of elevated exposure to natural radiation in Balkan region (Serbia). *Radioprotection*, *44*, 919–925.

10. Žunić, Z. S., Janik, M., Tokonami, S., Veselinović, N., Yarmoshenko, I. V., Zhukovsky, M., Ishikawa, T., Ramola, R. C., Ciotoli, G., Jovanović, P., Kozak, K., Mazur, J., Celiković, I., Ujić, P., Onischenko, A., Sahoo, S. K., & Bochicchio, F. (2009). Field experience with soil gas mapping using Japanese passive radon/thoron discriminative detectors for comparing high and low radiation areas in Serbia (Balkan region). *J. Radiat. Res.*, *50*(4), 355–361.

11. Zunic, Z. S., Ujić, P., Nađđerđ, L., Yarmoshenko, I. V., Radanović, S. B., Komatina Petrović, S., Čeliković, I., Komatina, M., & Bossew, P. (2014). High variability of indoor radon concentrations in uraniferous bedrock areas in the Balkan region. *Appl. Radiat. Isot.*, *94*, 328–337.

12. Ujic, P., Čeliković, I., Kandić, A., & Žunić, Z. (2008). Development of method for radon/thoron exhalation measurement. *Radiat. Meas.*, *43*(8), 1396–1401.

13. Bochicchio, F., Žunić, Z. S., Carpentieri, C., Antignani, S., Venoso, G., Carelli, V., Cordedda, C., Veselinović, N., Tollefsen, T., & Bossew, P. (2014). Radon in indoor air of primary schools: a systematic survey to evaluate factors affecting radon concentration levels and their variability. *Indoor Air*, *24*, 315–326.

14. Pantelić, G., Živanović, M., Eremić Savković, M., & Forkapić, S. (2013). Radon concentration intercomparison in Serbia. In Ž. Knežević, M. Majer, & I. Krajcar-Bronić (Eds.), *Proceedings of the Ninth Symposium of the Croatian Radiation Protection Association, 10–12. April 2013, Krk, Croatia* (pp. 193–198). Zagreb: CRPA.

15. Pantelić, G., Eremić Savković, M., Živanović, M., Nikolić, J., Rajačić, M., & Todorović, D. (2014). Uncertainty evaluation in radon concentration measurement using charcoal canister. *Appl. Radiat. Isot.*, *87*, 452–455.

16. Udovičić, V., Aničin, I., Joković, D., Dragić, A., Banjanac, R., Grabež, B., & Veselinović, N. (2011). Radon time-series analysis in the Underground Low-Level Laboratory in Belgrade, Serbia. *Radiat. Prot. Dosim.*, *145*(2/3), 155–158.

17. Banjanac, R., Dragić, A., Grabež, B., Joković, D., Markushev, D., Panić, B., Udovičić, V., & Aničin, I. (2006). Indoor radon measurements by nuclear track detectors: Applications in secondary schools. *Facta Universitatis*, *4*, 93–100.

18. Maletić, D., Udovičić, V., Banjanac, R., Joković, D., Dragić, A., Veselinović, N., & Filipović, J. (2014). Comparison of multivariate classification and regression methods for indoor radon measurements. *Nucl. Technol. Radiat. Prot.*, *29*, 17–23.

19. Eremić-Savković, M., Pantelić, G., Tanasković, I., Vuletić, V., & Javorina, Lj. (2002). Concentration of radon in apartments on the territory of Belgrade in period 1997–2001. *Arch. Toxicol. Kinet. Xenobiot. Metab.*, *10*(1/2), 195–197.

20. Arsić, V., Ilić, J., Bogojević, S., Tanasković, I., Eremić-Savković, M., & Javorina, Lj. (2014). Assessment of the effective radon dose, measured in schools and kindergartens in Belgrade during 2012 and 2013. In Proceedings of Second East European Radon Symposium (SEERAS), May 27–30, 2014, Niš, Serbia (pp. 17–20).

21. Stevanovic, N., Markovic, V., & Nikezic, D. (2010). Relationship between deposition and attachment rates in Jacobi room model. *J. Environ. Radioact.*, *101*(5), 349–352.

22. Jovanovic, B., Nikezic, D., & Stevanovic, N. (2011). Applied mathematical modeling for calculating the probability of the cell killing per hit in the human lung. *J. Radioanal. Nucl. Chem.*, *290*(3), 607–613.

DE GRUYTER
OPEN

The use of multivariate analysis of the radon variability in the underground laboratory and indoor environment

Jelena Filipović,
Dimitrije Maletić,
Vladimir Udovičić,
Radomir Banjanac,
Dejan Joković,
Mihailo Savić,
Nikola Veselinović

Abstract. The paper presents results of multivariate analysis of variations of radon concentrations in the shallow underground laboratory and a family house, depending on meteorological variables only. All available multivariate classification and regression methods, developed for data analysis in high-energy physics and implemented in the toolkit for multivariate analysis (TMVA) software package in ROOT, are used in the analysis. The result of multivariate regression analysis is a mapped functional behaviour of variations of radon concentration depending on meteorological variables only, which can be used for the evaluation of radon concentration, as well as to help with modelling of variation of radon concentration. The results of analysis of the radon concentration variations in the underground laboratory and real indoor environment, using multivariate methods, demonstrated the potential usefulness of these methods. Multivariate analysis showed that there is a potentially considerable prediction power of variations of indoor radon concentrations based on the knowledge of meteorological variables only. In addition, the online system using the resulting mapped functional behaviour for underground laboratory in the Institute of Physics Belgrade is implemented, and the resulting evaluation of radon concentrations are presented in this paper.

Key words: multivariate analysis • radon variability

J. Filipović, D. Maletić, V. Udovičić✉, R. Banjanac,
D. Joković, M. Savić, N. Veselinović
Institute of Physics Belgrade,
University of Belgrade,
118 Pregrevica Str., 11080 Belgrade, Serbia,
E-mail: udovicic@ipb.ac.rs

Introduction

The research of the dynamics of radon in various environments, especially indoors, is of great importance in terms of protection against ionizing radiation and in designing of measures for its reduction. Research of radioactive emanations (of radon (^{222}Rn) and thoron (^{220}Rn)) are in the domain of radiation physics, but since a few decades ago, subject of radioactive emanation involves many other scientific disciplines, thus giving a multidisciplinary character to this research. Published results and development of many models to describe the behaviour of indoor radon indicate the complexity of this research, especially with models for the prediction of the variability of radon, simply because the variability depends on large number of variables. Large number of factors (such as local geology, permeability of soil, building materials used to build the buildings as well as the habits of people) impact the variation of radon, and therefore, it is important to study their correlation. In this paper, the results of correlative analysis of indoor radon and meteorological variables are presented. Furthermore, the results of multivariate classification and regression analysis is presented. More details of this study can be found in [1].

Indoor radon variation depends significantly on large number of factors, which include the local ge-

ology, soil permeability, building materials, lifestyle characteristics and meteorological variables. In order to analyse the dependence of radon variation on multiple variables, multivariate analysis needs to be used.

The demand for detailed analyses of large amount of data in high-energy physics resulted in wide and intense development and usage of multivariate methods. Many of multivariate methods and algorithms for classification and regression are already integrated into the analysis framework ROOT [2], more specifically, into the toolkit for multivariate analysis (TMVA [3]). Multivariate analysis toolkit is used to create, test and apply all available classifiers and regression multivariate methods implemented in the TMVA in order to find methods that are the most appropriate and yield maximum information on the dependence of indoor radon concentrations on the multitude of meteorological variables. Classification methods are used to find out if it is possible to classify radon concentrations into low and high concentrations, using arbitrary cut value for radon concentrations. Regression methods are used as a next step with a goal to find out which regression method can, if any, on the basis of input meteorological variables only, give an output that would satisfactorily close match the observed variations of radon concentrations. The output of usage of multivariate regression analysis methods is mapped functional behaviour, which can be used to evaluate the measurements of radon concentrations using input meteorological variables only. The prediction of radon concentrations can be an output of mapped function when the prediction of input meteorological variables exists.

Short-term radon measurements in laboratory and real environment

Depending on the integrated measurement time, methods of measurement of radon concentrations in air may be divided into long-term and short-term ones. For the measurements of radon concentration presented in this paper, the SN1029 radon monitor (manufactured by the Sun Nuclear Corporation, NRSB approval-code 31822) has been used as active, short-term measurement device. The device consists of two diffused junction photodiodes as a radon detector and is furnished with sensors for temperature, barometric pressure and relative humidity. The user can set the measurement intervals from 30 min to 24 h. It was set to record simultaneously the radon concentration, temperature, atmospheric pressure and relative humidity.

For the purposes of determining the best multivariate methods to use in the analysis, the results are obtained using radon monitor are from measurements in two locations, the Low-Background Laboratory for Nuclear Physics in the Institute of Physics in Belgrade and in a family house.

The underground Low-Background Laboratory for Nuclear Physics is selected for measurement and analysis because routine measurements in this laboratory require low levels of radon concentration with minimum temporal variations. Low-background laboratory is located on the right bank of the river Danube in the Belgrade borough of Zemun, on the grounds of the Institute of Physics. The ground level portion of the laboratory, at 75 m above sea level, is situated at the foot of a vertical loess cliff, about 10 m high. The underground part of the laboratory, useful area of 45 m², is dug into the foot of the cliff. Underground laboratory is surrounded with 30-cm thick concrete wall. The overburden of the underground laboratory is thus about 12 m of loess soil. Significant efforts are being made to contain the low radon concentration within the laboratory. The underground laboratory is completely lined with a hermetically sealed, 1-mm thick aluminium foil. The ventilation system maintains the overpressure of 2 mbar, so as to prevent radon diffusion from the soil. Fresh air entering the laboratory is passed through a two-stage filtering system. The first stage is a mechanical filter for dust removal. The second one is a battery of coarse and fine charcoal active filters. The concentration of radon is kept at an average value of about 10 Bq/m³.

In the Low-Background Laboratory for Nuclear Physics, radon concentrations were measured in period from 2008 to 2011 and continued later on periodically about a couple of months each year. Measurements of meteorological variables used in the analysis were recorded since 2008 and are taken from the meteorological station located 4 km from the laboratory. Measurements of radon concentrations, room temperature, atmospheric pressure and relative humidity inside the laboratory were obtained using radon monitor. The results obtained from the measurements of radon concentrations and their influence on gamma and cosmic ray measurements in the laboratory were published in several articles in international scientific journals [4–6].

The family house selected for the measurements and analysis of variations of radon concentrations is a typical house in Belgrade residential areas, with requirement of existence of cellar. House is built on limestone soil. Radon measurements were carried out in the living room of the family house, which is built of standard materials (brick, concrete, mortar) and isolated with styrofoam. During the period of measurements (spring–summer), the house was naturally ventilated and air conditioning was used in heating mode at the beginning of the measurement period. During the winter period measurements, the electrical heating was used in addition to air conditioning. Measured radon concentrations, room temperature, atmospheric pressure and relative humidity inside the house were obtained using radon monitor. Values of meteorological variables in measurement period were obtained from an automatic meteorological station located 400 m from the house in which the measurement was performed. We used the following meteorological variables: external air temperature, pressure and humidity, solar radiation, wind speed at a height of 10 m above ground, precipitation, evaporation and temperature and humidity of the soil at a depth of 10, 20, 30 and 50 cm.

Correlation and regression analysis of the results

All multivariate methods implemented in the TMVA are used in our search. All multivariate methods in TMVA belong to the family of 'supervised learning' algorithms [1]. All methods make use of training events, for which the desired output is known, to determine the mapping function that either describes a decision boundary (classification) or an approximation of the underlying functional behaviour defining the target value (regression). Every MVA methods see the same training and test data. The two best performing multivariate methods for our purposes are boosted decision trees (BDT) and artificial neural networks (ANN).

The determination of correlation coefficients between measured radon concentration and meteorological variables serves as a good tool for identifying the variables with strongest correlation, which are not excluded from the analysis later on. Also, correlation coefficient tables gives a good overview of input data and their intercorrelations. In Fig. 1, the correlation matrix of linear correlation coefficients as an overview of intercorrelations of measured radon concentration and all input meteorological variables are shown for underground laboratory. The input variables in case of analysis of underground laboratory are atmospheric pressure, temperature and humidity in laboratory (P_{rm}, T_{rm}, H_{rm}) and outdoor (P, T, H) and differences in measured values of pressure ($P - P_{rm}$), temperature ($T - T_{rm}$) and humidity ($H - H_{rm}$) in laboratory and outdoor. Input meteorological variables in case of family house are the same as the list of measured meteorological variables from nearby meteorological station, with the addition of differences in temperature ($T - T_{rm}$) and humidity ($H - H_{rm}$) from indoor and outdoor values, where indoor measurements results were obtained using radon monitor.

Multivariate methods within the package TMVA in ROOT can search for best multivariate approximation of functional behaviour for the classification function of radon concentration depending on meteorological variables. In the analysis, several mul-

Fig. 2. ROC curve for all multivariate methods in case of house measurements.

tivariate methods were tested, and best performed method was BDT. This can be seen by presenting the receiver operating characteristics (ROC) curve for all tested multivariate methods in case of house measurements (Fig. 2). The BDT method has the highest value of integrated ROC function.

BDT has proven to be the most effective method for the classification of radon concentrations in case of data obtained from the house as well as those obtained from measurements in the Low-Background Laboratory for Nuclear Physics.

The next step in the analysis is the regression analysis, which is the way of finding a mapped function behaviour of dependence of radon concentrations and meteorological input variables. The regression analysis was done using the TMVA packages, already used in classification analysis, and for the same set of measured radon concentration and meteorological variables in underground laboratory and a family house in Serbia. Multivariate method BDT was found to be the best suited for regression analysis also, as was the case in classification analysis.

The data of measured radon concentration in house and BDT evaluated values, using only the values of meteorological variables, without the knowledge of measured values (i.e. in the testing set of multivariate analysis), is presented for comparison in Fig. 3.

One of the possible application of having resulting mapped function, given by multivariate regression analysis, is to have prediction of radon concentration values (evaluated) based on meteorological variables alone. The online application of the regression multivariate analysis can be imple-
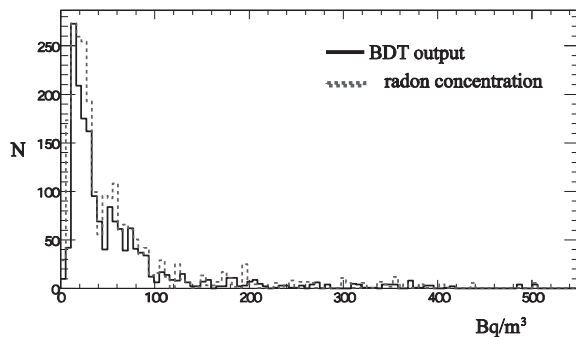
Linear correlation coefficients in %

	T_mm	P_mm	H_mm	T	P	H	$T\text{-}T\_mm$	$P\text{-}P\_mm$	$H\text{-}H\_m$	Radon
Radon	17	4	25	14	5	1	13	5	-14	100
H-H_mm	-81	13	-73	-94	10	79	-94	-8	100	-14
P-P_mm	9	-15	13	1	15			100	-8	5
T-T_mm	80	-14	77	99	-14	-68	100		-94	13
H	-43	3	-18	-65	3	100	-68		79	1
P	-4	95	-12	-13	100	3	-14	15	10	5
T	86	-13	80	100	-13	-65	99	1	-94	14
H_mm	84	-17	100	80	-12	-18	77	13	-73	25
P_mm	-7	100	-17	-13	95	3	-14	-15	13	4
T_mm	100	-7	84	86	-4	-43	80	9	-81	17

Fig. 1. Correlation matrix with linear correlation coefficients as an overview of radon and meteorological variables intercorrelations in case of the Low-Background Laboratory for Nuclear Physics.

Fig. 3. BDT evaluated (predicted) values of radon concentrations based on meteorological variables using regression analysis within TMVA packages in house (left) and measured values (right).
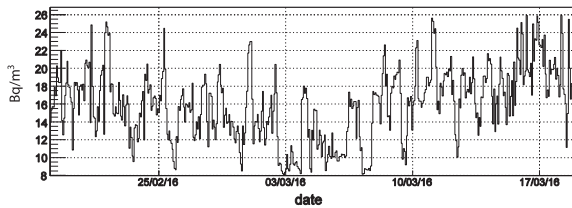
Fig. 4. BDT evaluated (predicted) values of radon concentration, based on meteorological variables alone of underground laboratory posted online and updated daily.

mented, as the one posted online for evaluation (and prediction) based on meteorological variables alone (Fig. 4).

Limitation of multivariate methods

As the multivariate methods used in the analysis are 'supervised learning' algorithms, the performance of the main result of multivariate analysis, the resulting mapped functional behaviour, depends on learning process. Limitation of multivariate analysis in the analysis of radon dependence on meteorological variables are coming from small number of measurements used in learning process, unlike the great number of measurements in high--energy physics experiments. As the next logical step in multivariate analysis presented in this paper should be inclusion of variables such as local geology, permeability of soil, building materials used to build the buildings as well as the habits of people, the requirement for efficient multivariate analysis is to have many measurements in many different houses. Many measurements would help to get good mapped functional behaviour, as opposed to possible existence of theoretical modelling that is independent on number of measurements. In this sense, if the number of measurements is not great, multivariate analysis can be used only as hell to indicate which variables are more important to be used in theoretical modelling, for comparison of mapped and modelled functions, and modelled function test. Another important limitation of multivariate analysis is that no 'straightforward' interpretation of mapped functional behaviour is possible, or simply, the mapped function is a 'black box'. This comes from the fact that the error minimization in learning algorithms, while mapping the functional behaviour, is an important part in learning process.

Conclusions

The paper presents the results of multivariate analysis of variations of radon concentrations in the shallow underground laboratory and a family house, depending on meteorological variables only. This test of multivariate methods, implemented in the

TMVA software package, applied to the analysis of the radon concentration variations connection with meteorological variables in underground laboratory (with ventilation system turned on and off) and typical house in Serbia, demonstrated the potential usefulness of these methods. It appears that the method can be used for the prediction of the radon concentrations, on the basis of predicted meteorological variables. The next step in multivariate analysis presented in this paper should be inclusion of variables such as local geology, permeability of soil, building materials used to build the buildings as well as the habits of people. The requirement for efficient multivariate analysis is to have many measurements in many different houses, which makes multivariate method very useful only when having many measurement, for instance, during radon mapping campaigns. Many measurements would help to get good mapped functional behaviour, as opposed to possible existence of theoretical modelling that is independent on number of measurements. Generally, multivariate analysis can be used to help indicate which variables are more important to be used in theoretical modelling, furthermore, for comparison of mapped and modelled functions, and modelled function test.

Another usage of the results of classification multivariate analysis presented in this paper is the implementation of online warning system for possible increased radon concentration in family houses based on meteorological variables only.

References

1. Maletić, D., Udovičić, V., Banjanac, R., Joković, D., Dragić, A., Veselinović, N., & Filipović, J. (2014). Comparison of multivariate classification and regression methods for indoor radon measurements. *Nucl. Technol. Radiat. Prot*., *29*, 17–23.
2. Hoecker, A., Speckmayer, P., Stelzer, J., Therhaag, J., Von Toerne, E., & Voss, H. (2007). TMVA – Toolkit for Multivariate Data Analysis. *PoS ACAT 040*. arXiv:physics/070303.
3. Brun, R., & Rademakers, F. (1997). ROOT – An Object Oriented Data Analysis Framework. *Nucl. Instrum. Methods Phys. Res. Sect. A-Accel. Spectrom. Dect. Assoc. Equip*. *389*(1/2), 81–86.
4. Udovičić, V., Grabež, B., Dragić, A., Banjanac, R., Joković, D., Panić, B., Joksimović, D., Puzović, J., & Aničin, I. (2009). Radon problem in an underground low-level laboratory. *Radiat. Meas*., *44*, 1009–1012.
5. Udovičić, V., Aničin, I., Joković, D., Dragić, A., Banjanac, R., Grabež, B., & Veselinović, N. (2011). Radon time-series analysis in the Underground Low-Level Laboratory in Belgrade, Serbia. *Radiat. Prot. Dosim*., *145*(2/3), 155–158.
6. Banjanac, R., Udovičić, V., Dragić, A., Joković, D., Maletić, D., Veselinović, N., & Grabež, B. (2013). Daily variations of gamma-ray background and radon concentration. *Rom. J. Phys*., *58*(Suppl.), S14–S21.

Analyzing solar activity with Belgrade muon station: case study of 2021 November 4th Forbush decrease

N.B. Veselinović [iD]**, M.B. Savić, D.M. Maletić, A.L. Dragić, R.M. Banjanac, D.R. Joković, D. Knežević, M. Travar and V.I. Udovičić**

Institute of Physics Belgrade, University of Belgrade, Pregrevica 118, 11080 Belgrade, Serbia, (E-mail: veselinovic@ipb.ac.rs)

Abstract. The first significant Forbush decrease of the solar cycle 25 was recorded on November 4th, 2021. The Forbush decrease was observed with numerous ground based cosmic rays stations including Belgrade cosmic rays muons' station. Series of coronal mass ejections during October 28–November 4 2021. produce conditions for this Forbush decrease. We discuss here the variation of cosmic rays' flux detected with ground-based detectors and connection with conditions, measured in-situ, in interplanetary space around Earth, flux of solar wind protons measured with SOHO probe to assess implication for solar-terrestrial coupling processes.

Key words: Cosmic rays – Forbush decrease – Space weather – muon detector

1. Introduction

One of the methods of researching solar-terrestrial coupling processes is observing the response of the flux of cosmic rays (CR) to various types of disturbances (or drivers) in the heliosphere. Transient phenomena detected in CR flux due to modulation in the heliosphere is the Forbush decrease: a sudden drop in CR flux followed by a gradual return to the previous level. It occurs as CR interact with irregularities in the interplanetary magnetic field (IMF), usually connected with the emission of coronal plasma known as a coronal mass ejection (CME) and its interplanetary counterpart (ICME) (Yermolaev et al., 2021). In recent decades, space probes have measured IMF parameters in-situ as well as particle flux. The detected particles can be fast-moving particles, known as solar energetic particles (SEPs), related to violent eruptions from the Sun that can cause a sudden increase in measured CR flux at the surface - a ground level enhancement (GLE). The other particles detected with probes, aside from solar wind particles and SEPs, are energetic storm particles (ESP) accelerated locally by shocks driven by fast ICMEs (Desai & Giacalone, 2016) and low-energy CR

(Veselinović et al., 2021). It has been shown (Koldobskiy et al., 2019; Savić et al., 2023; Kolarski et al., 2023) that parameters measured in-situ correlate with the magnitude and time evolution of FD. The end of October and the beginning of November 2021 marked extreme activity with a strong X-class solar flare (CIT), accompanied by the first Ground Level Enhancement (GLE) event in this cycle on October 28th, measured by several ground stations (Papaioannou, A. et al., 2022). There were several typical CMEs during this period. Most pronounced were two halo CMEs on October 28th and November 2nd. The second halo CME, due to its speed, caught up with previous ICMEs and produced a CME-CME interaction (Li et al., 2022).These disturbances created additional modulation of CR, producing the first strong FD in the present solar cycle, detected by multiple ground stations around the globe (Chilingarian et al., 2022).

The present case-study combines in-situ measurements of solar wind parameters and proton flux in near-Earth space with measurements on the ground to analyze how these parameters affect parameters of the FD detected on November 4th, 2021.

2. Ground level cosmic ray observations

The most widely method of detecting CR use detectors that are part of the worldwide network of Neutron Monitors (NM) (https://www.nmdb.eu/nest/). One of the other species of these secondary CR that can be detected and used for monitoring primary CR are muons.

2.1. Belgrade muon detector

The ground level Belgrade muon station (GLL) is a part of the Low-Background Laboratory for Nuclear Physics at the Institute of Physics, Belgrade, Serbia. The energy range of the observed primary CR extends and complements the energy ranges detected by the NM network, but is still sensitive to CR modulation of the heliosphere. Details of the experimental setup, as well as the calculated response function of the detectors, are presented in (Veselinović et al., 2017).

2.2. Ground level data analysis

Both NM and muon detectors measure integral flux over different energy ranges, so the median energy of the detected primary CR is used in the analysis of the measured data. Another property of the detector system is Cut-off rigidity, the minimal magnetic rigidity that the CR must have in order to penetrate the IMF and geomagnetic field. To determine the amplitude of the FD for each station, which differs in median energy and asymptotic direction, a baseline was established using the average hourly count rate during mid-October 2021 when solar activity was low. For this study, we utilized 1-hour time series of CR flux detected at 17 NM stations and GLL data (Table 1).

Table 1. Cut-off rigidity (R_c) and median energy (E_m) of primary CR for several stations.

Stations	R_c (GV)	E_m (GeV)	Stations	R_c (GV)	E_m (GeV)
Belgrade	5.3	63	Kerguelen	1.14	10.4
Athens	8.53	17.8	Oulu	0.8	10.3
Guadalajara	6.95	15.4	Apatity	0.65	10.3
Baksan	5.6	13.7	Norilsk	0.63	10.3
Jungfraujoch	4.5	12.6	Tixie Bay	0.5	10.2
Lomnicky stít	3.84	12	Fort Smith	0.3	10.2
Dourbes	3.18	11.5	Inuvik	0.3	10.2
Kiel	2.36	11	S. Pole bare	0.1	10.1
Yakutsk	1.65	10.6	S. Pole	0.1	10.1

Median energy for NM was found using formula given in Li et al. (2023) and median energy for GLL was found using Monte Carlo method of CR transport. Dependence of FD amplitude on CR median energy is given by power law (Cane, 2000)

$$\frac{\Delta N}{N} = E^{-a} \tag{1}$$

Here N is CR flux, E is median energy and a is power exponent that depends on heliospheric conditions.

A scatter plot of the selected event is given (Figure 1) plotted in log-log scale and it show clear median rigidity dependence of the amplitude of FD.

Steeper spectrum during this event shows greater modulation of primary CR. If GLL data is included in the plot, the power exponent is not so large so that can be interpreted as stronger modulation of the lower energy CR due to CME-CME interaction. Linear regression is performed to found power indices correspond to November 2021 event. Power index for NM only is 1.23±0.22 and for NM and GLL power index is 0.62±0.10. This is, in general, in good agreement with some previous studies (Lingri et al. (2016) and references within).

3. Relation to in-situ measured data

In this study we used measured in-situ parameters relevant for heliospheric studies which are available at GSFC/Space Physics Data Facility, in the form of 1-hour resolution OMNI data (https://spdf.gsfc.nasa.gov/pub/data/omni/lowresomni/). Also we used proton flux date gathered by SOHO probe with two detectors, ERNE and EPHIN, onboard SOHO probe (Torsti et al., 2000; Kühl & Heber, 2019) at Lagrange point 1 in vicinity of Earth. Comparison between 1-hour time series of selected parameters of IMF from OMNI data and
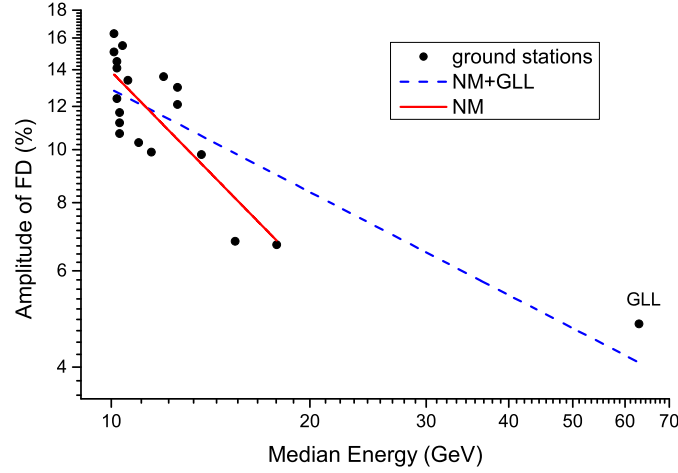
Figure 1. Rigidity spectrum of FD from November 4th 2021. Points represent the amplitude of the Forbush decrease as seen by 18 NMs and Belgrade GLL muon station.

relative detected CR flux of NM with low cut-off rigidity at South Pole and Belgrade muon detector and similar comparison for the same time interval between CR flux detected with two ground level detectors and selected channels of SOHO/ERNE and SOHO/EPHIN proton flux data is shown in Figure 2.

The discrepancies between time series of CR flux detected with ground stations and parameters of the IMF shows that CR was influenced by complex interactions in the heliosphere where low energy proton flux detected in-situ with detectors on board SOHO does not contribute substantially either to condition in heliosphere or CR flux. Increase of SEP flux, apparent in all detected proton flux from SOHO/ERNE and SOHO/EPHIN, produce GLE event detected with NM with low cut-off rigidity. Shape of detected FD on different stations varied, as expected due to difference cut-off rigidity, median energy, detector design, and sensitivity.

Correlation between respective time series was found using Pearson correlation coefficient using 2-tail test for significance is given at Table 2.

As expected correlation of CR flux is greater for NM detector at South Pole due to lower energy of detected CR which are more sensitive to disturbances of IMF. Inverse correlation of average magnetic field and solar wind plasma speed with CR flux is expected due to scattering of CR on turbulent magnetic field that produce a decrease in detected CR flux. The lack of correlation between proton fluxes and higher energy CR flux detected with GLL shown that monitor only some of the proton energy channel is not sufficient to model FD over range of CR energies during complex event with CME-CME interaction. Modeling of
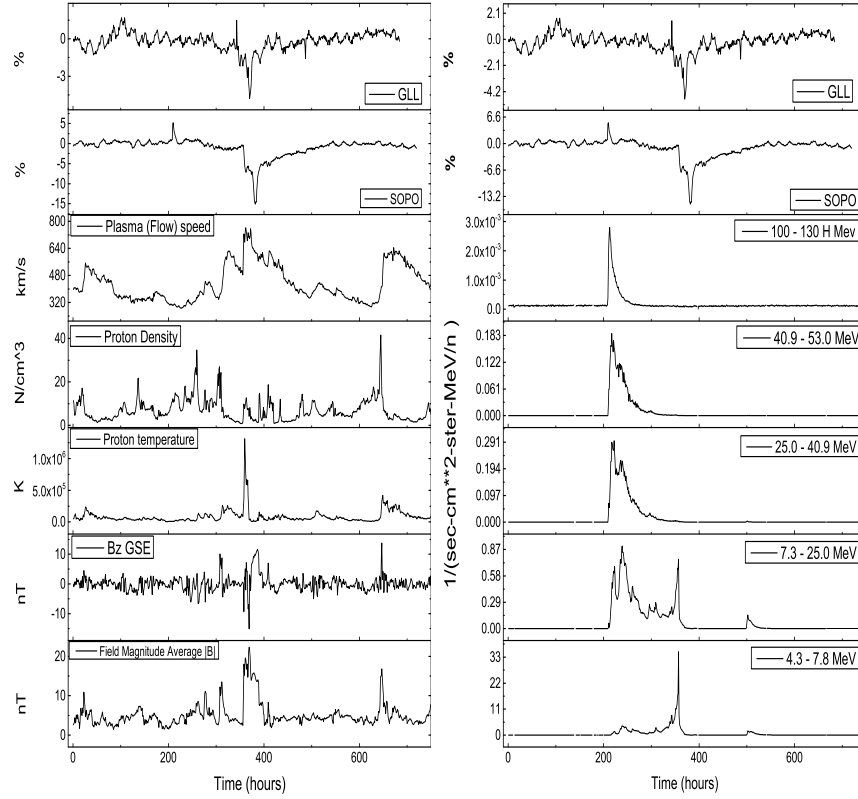
Figure 2. Left: Time series for plasma parameters (taken from OMNI database) and cosmic ray flux (measured at South Pole NM and GLL) from October 20th until November 20th, 2021. Right: Hourly time series for different proton energy channels from SOHO/ERNE and SOHO/EPHIN and two CR detectors time series for the same period.

this complicated shock-associated ICME disturbance where multiple shocks and transient flows merged is challenging and other studies (Zhao & Zhang, 2016; Werner et al., 2019) showed similar complex dependence of CR flux on different parameters of the IMF condition.

4. Summary

In this work we studied the FD occurred in November 4th, 2021, using data from Belgrade muon station and other multiple sources. Increased solar activity at the begging of the November 2021 had a measurable effect on CR, observed as a

Table 2. Pearson correlation coefficients for the correlation between CR flux detected at Belgrade CR station (GLL), at South pole (SOPO), flux of protons of different energies from SOHO/ERNE and SOHO/EPHIN and plasma parameters (from OMNI database) for the period from October 20$^{\text{th}}$ until November 20$^{\text{th}}$, 2021.

	SOPO		GLL	
	Pearson Corr.	p-value	Pearson Corr.	p-value
SOPO	1		0.52	$<10^{-5}$
GLL	0.52	$<10^{-5}$	1	
|B| Average	-0.55	$<10^{-5}$	-0.48	$<10^{-5}$
Bz	-0.4	$<10^{-5}$	-0.15	$<10^{-4}$
Proton temperature	-0.18	$<10^{-5}$	-0.23	$<10^{-5}$
Proton Density	0.23	$<10^{-5}$	0.14	$<10^{-4}$
Plasma (Flow) speed	-0.61	$<10^{-5}$	-0.53	$<10^{-5}$
7.3-25.0 MeV p	0.17	$<10^{-5}$	-0.12	0.002
4.3-7.8 MeV p	0.01	0.67	-0.29	$<10^{-5}$
25.0-40.9 MeV p	0.21	$<10^{-5}$	0.02	0.5
40.9-53.0 MeV p	0.21	$<10^{-5}$	0.03	0.45
80-100 H Mev p	0.22	$<10^{-5}$	0.03	0.37

decrease in measured flux by all relevant CR stations. Energy range of affected primary CR was wide enough so effect was detected by neutron monitors but also muon detectors. Rapid decrease was detected with CR detectors around the world and it was one of the consequence, along with the strong G3-class geomagnetic storm, auroras and GLE event, of series of overlapping CMEs. We showed that based on measured amplitude of FD of the range of ground station that higher energy CR was less affected with heliospheric disturbance. Cross correlations between time series of CR flux and IMF and solar wind characteristics during these strongly disturbed heliospheric conditions were presented. Lack of strong correlation is also apparent for higher energy CR flux time series and time series of the heliospheric parameters and proton flux of certain energy ranges. This proves that, in order to better understand solar-terrestrial coupling processes, particularly its effect for higher energy particles requires more data from various sources and various probes and this analysis can be done in the future.

References

Cane, H. V., Coronal Mass Ejections and Forbush Decreases. 2000, *Space Science Reviews*, **93**, 55, DOI: 10.1023/A:1026532125747

Chilingarian, A., Hovsepyan, G., Martoyan, H., et al. 2022, Forbush decrease observed by SEVAN particle detector network on November 4, 2021

Desai, M. & Giacalone, J., Large gradual solar energetic particle events. 2016, *Living Reviews in Solar Physics*, **13**, 3, DOI: 10.1007/s41116-016-0002-5

Kühl, P. & Heber, B., Revising More Than 20 Years of EPHIN Ion Flux Data-A New Data Product for Space Weather Applications. 2019, *Space Weather*, **17**, 84, DOI: https://doi.org/10.1029/2018SW002114

Kolarski, A., Veselinović, N., Srećković, V. A., et al., Impacts of Extreme Space Weather Events on September 6th, 2017 on Ionosphere and Primary Cosmic Rays. 2023, *Remote Sensing*, **15**, DOI: 10.3390/rs15051403

Koldobskiy, S. A., Bindi, V., Corti, C., Kovaltsov, G. A., & Usoskin, I. G., Validation of the Neutron Monitor Yield Function Using Data From AMS-02 Experiment, 2011-2017. 2019, *Journal of Geophysical Research: Space Physics*, **124**, 2367, DOI: https://doi.org/10.1029/2018JA026340

Li, W.-h. et al., A study of Forbush Decreases effects with DAMPE experiment. 2023, *PoS*, **ICRC2023**, 1311, DOI: 10.22323/1.444.1311

Li, X., Wang, Y., Guo, J., & Lyu, S., Solar Energetic Particles Produced during Two Fast Coronal Mass Ejections. 2022, *The Astrophysical Journal Letters*, **928**, L6, DOI: 10.3847/2041-8213/ac5b72

Lingri, D., Mavromichalaki, H., Belov, A., et al., Solar Activity Parameters and Associated Forbush Decreases During the Minimum Between Cycles 23 and 24 and the Ascending Phase of Cycle 24. 2016, *Solar Physics*, **291**, 1025, DOI: 10.1007/s11207-016-0863-8

Papaioannou, A., Kouloumvakos, A., Mishev, A., et al., The first ground-level enhancement of solar cycle 25 on 28 October 2021. 2022, *A&A*, **660**, L5, DOI: 10.1051/0004-6361/202142855

Savić, M., Veselinović, N., Dragić, A., et al., New insights from cross-correlation studies between solar activity indices and cosmic-ray flux during Forbush decrease events. 2023, *Advances in Space Research*, **71**, 2006, DOI: https://doi.org/10.1016/j.asr.2022.09.057, recent progress in the physics of the Sun and heliosphere

Torsti, J., Mäkelä, P., Teittinen, M., & Laivola, J., SOHO/Energetic and Relativistic Nucleon and Electron Experiment Measurements of Energetic H, He, O, and Fe Fluxes during the 1997 November 6 Solar Event. 2000, *The Astrophysical Journal*, **544**, 1169, DOI: 10.1086/317219

Veselinović, N., Dragić, A., Savić, M., et al., An underground laboratory as a facility for studies of cosmic-ray solar modulation. 2017, *Nuclear Instruments and Methods in Physics Research Section A: Accelerators, Spectrometers, Detectors and Associated Equipment*, **875**, 10, DOI: https://doi.org/10.1016/j.nima.2017.09.008

Veselinović, N., Savić, M., Dragić , A., et al., Correlation analysis of solar energetic particles and secondary cosmic ray flux. 2021, *The European Physical Journal D*, **75**, 173, DOI: 10.1140/epjd/s10053-021-00172-x

Werner, A. L. E., Yordanova, E., Dimmock, A. P., & Temmer, M., Modeling the Multiple CME Interaction Event on 6–9 September 2017 with WSA-ENLIL+Cone. 2019, *Space Weather*, **17**, 357, DOI: https://doi.org/10.1029/2018SW001993

Yermolaev, Y. I., Lodkina, I. G., Dremukhina, L. A., Yermolaev, M. Y., & Khokhlachev, A. A., What Solar-Terrestrial Link Researchers Should Know about Interplanetary Drivers. 2021, *Universe*, **7**, DOI: 10.3390/universe7050138

Zhao, L.-L. & Zhang, H., Transient galactic cosmic-ray modulation during solar cycle 24: A comparative study of two prominent Forbush decrease events. 2016, *The Astrophysical Journal*, **827**, 13, DOI: 10.3847/0004-637X/827/1/13

MEASUREMENT OF PHASE SPACE DENSITY EVOLUTION IN MICE

F. Drielsma[*], Université de Genève, Geneva, Switzerland

D. Maletic[†], Institute of Physics Belgrade, Belgrade, Serbia

Abstract

The Muon Ionization Cooling Experiment (MICE) collaboration will demonstrate the feasibility of ionization cooling, the technique by which it is proposed to cool the muon beam at a future neutrino factory or muon collider. The position and momentum reconstruction of individual muons in the MICE trackers allows for the development of alternative figures of merit in addition to beam emittance. Contraction of the phase space volume occupied by a fraction of the sample, or equivalently the increase in phase space density at its core, is an unequivocal cooling signature. Single-particle amplitude and nonparametric statistics provide reliable methods to estimate the phase space density function. These techniques are robust to transmission losses and non-linearities, making them optimally suited to perform a quantitative cooling measurement in MICE.

INTRODUCTION

Future facilities such as the Muon Collider and the Neutrino Factory will require high intensity and low emittance stored muon beams [1, 2]. Muons are produced as tertiary particles ($p + N \rightarrow \pi + X$, $\pi \rightarrow \mu + \nu$) inheriting a large emittance from the isotropic decay of the pions. For efficient acceleration, the phase space volume of these beams must be reduced significantly, i.e. "cooled", to fit within the acceptance of a storage ring or accelerator beam pipe. Due to the short muon lifetime, ionization cooling is the only practical and efficient technique to cool muon beams [3, 4]. Each muon in the beam loses momentum in all dimensions through ionization energy loss in an absorbing material, reducing the RMS emittance and increasing its phase space density. Subsequent acceleration though radio frequency cavities restores longitudinal energy, resulting in a beam with reduced transverse emittance. A factor of close to 10^6 in reduced 6D emittance has been achieved in simulation with a 970 m long channel [5]. The rate of change in normalized transverse RMS emittance, ϵ_N, is given by the ionization cooling equation [3]:

$$\frac{d\varepsilon_N}{ds} \simeq -\frac{\varepsilon_N}{\beta^2 E_\mu} \left| \frac{dE_\mu}{ds} \right| + \frac{\beta_\perp (13.6\,\text{MeV})^2}{2\beta^3 E_\mu m_\mu c^2 X_0}, \qquad (1)$$

where βc is the muon velocity, $|dE/ds|$ is the average rate of energy loss, E_μ and $m\mu$ are the muon energy and mass, $\beta_\perp$ is the transverse betatron function and X_0 is the radiation length of the absorber material. The first term on the right can be referred to as the "cooling" term driven by energy loss, while the second term is the "heating term" that uses the PDG approximation for the multiple Coulomb scattering.

---

[*] francois.drielsma@unige.ch

[†] Speaker

MICE [6] is currently taking data in the Step IV configuration in order to make detailed measurements of the scattering, energy loss [7] and phase space evolution at different momenta and channel configurations, with lithium hydride and liquid hydrogen absorbers. A schematic drawing of MICE Step IV is shown in Figure 1. MICE consists of two scintillating fiber trackers upstream and downstream of the absorber in strong solenoid fields to accurately reconstruct the position and the momentum of individual muons selected in a series of particle identification detectors, including 3 time-of-flight hodoscopes (ToF0/1/2), 2 threshold Cherenkov counters, a pre-shower calorimeter (KL) and a fully active tracker-calorimeter (EMR) [8–11].

COOLING CHANNEL

The two spectrometer solenoid modules each generate a region of uniform 3 T field in which diagnostic trackers are situated and a matching region that transports the beam from the solenoid to the focus coil module. The focus coil module, positioned between the solenoids, provides additional focusing to increase the angular divergence of the beam at the absorber, improving the amount of emittance reduction that can be achieved. The magnetic field model is shown in Figure 2. The absorber was a single 65 mm thickness lithium hydride disk. Lithium hydride was chosen as an absorber material as it provides less multiple Coulomb scattering for a given energy loss.

In this paper the evolution of phase space density is reported for a single configuration of the cooling apparatus. Results from one transfer line configuration are reported, with the accumulated muon sample having a nominal emittance of 6 mm at momenta around 140 MeV/c in the upstream spectrometer solenoid, denoted as '6–140'.

As MICE measures each particle event individually, it is possible to select a particle ensemble from the collection of measured tracks. This enables the study of momentum spread and transverse beam parameters on the cooling. In this analysis, muons have been selected with:

- longitudinal momentum in the range 135 to 145 MeV/c;

- time-of-flight between TOF0 and TOF1 consistent with muons in this momentum range; and

- a single, good quality track formed in the upstream diagnostics.

In order to study the evolution of the phase space density through the whole cooling channel and across the absorber, a realistic simulation of the setting of interest was produced. The betatron function of the selected muon ensemble is shown for the Monte Carlo (MC) simulation, the
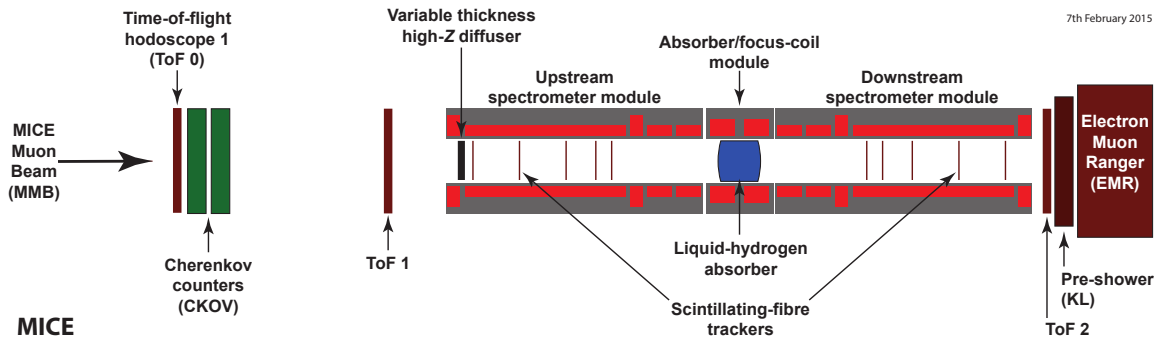
Figure 1: Layout of the MICE Step IV configuration, its absorber module, tracking spectrometers and PID detectors.
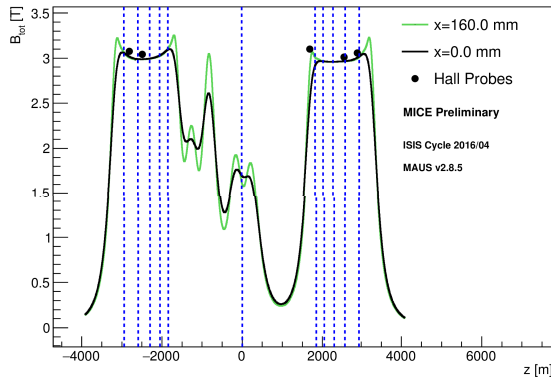

Figure 2: Modelled magnetic field for the configuration on the axis and with 160 mm horizontal displacement from the axis. Hall probes, situated 160 mm from the beam axis, show a 2 % discrepancy with the model. Dashed lines show position of the tracker stations and absorber (at $z = 0$).

reconstructed MC and the data for the '6–140' setting in Figure 3. The graph shows a large growth of the beam size in the downstream section due to the absence of the downstream match coils in this configuration. The simulation closely reproduces the function measured in the data.
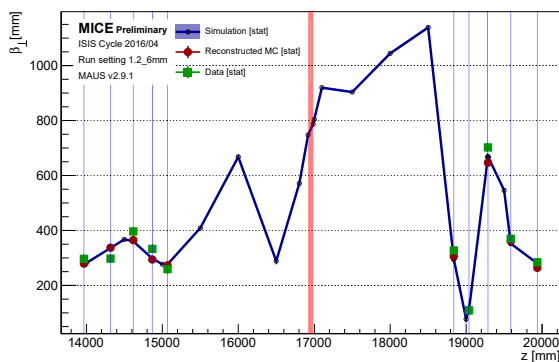
Figure 3: Beta function profile in the MC truth (blue line), reconstructed MC (red circles) and data (green squares).

PHASE SPACE DENSITY EVOLUTION

Emittance

The transverse normalized RMS emittance is the most common cooling figure of merit and is defined as

$$\epsilon_N = \frac{1}{m_\mu} |\Sigma|^{\frac{1}{4}}, \qquad (2)$$

with m_μ the muon mass and $|\Sigma|$ the determinant of the 4D transverse phase space covariance matrix, i.e. $\Sigma_{ij} = \langle ij \rangle - \langle i \rangle \langle j \rangle$ with $i, j \in [x, p_x, y, p_y]$. For a Gaussian beam, this quantity is directly related to the volume of the $1\,\sigma$ RMS ellipse, V_{RMS}, through $\epsilon_N = \sqrt{2V_{RMS}}/(m\pi)$.

In a fully transmitted beam, emittance reduction is a clean signature of the contraction of transverse phase space volume. For a partially scraped beam, as shown for the '6–140' setting in Figure 4, the emittance evolution exhibits apparent emittance reduction in the downstream section due to the loss of the tails of the distribution. It also experiences significant apparent growth in the downstream tracker due to high field gradient, causing filamentation in the beam.
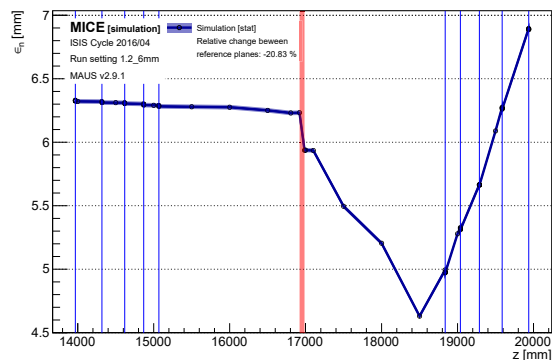
Figure 4: Normalized transverse RMS emittance evolution through the MICE cooling channel.

An alternative to RMS emittance is to study the evolution of the density distribution of the ensemble, as it allows for the selection of a defined and identical fraction of phase space upstream and downstream of the absorber.

Amplitude

The 4D amplitude of a particle with phase space vector $\mathbf{v} = (x, p_x, y, p_y)$ is given by

$$A_\perp = \epsilon_N (\mathbf{v} - \boldsymbol{\mu})^T \Sigma^{-1} (\mathbf{v} - \boldsymbol{\mu}). \qquad (3)$$

with $\boldsymbol{\mu} = (\langle x \rangle, \langle p_x \rangle, \langle y \rangle, \langle p_y \rangle)$, the beam centroid. In order to prevent the tails of the distribution from skewing the core, only those events with amplitude less than $A_\perp$ have been included in the calculation of $\boldsymbol{\mu}$ and Σ for a given event. The high amplitude particles are iteratively removed from the sample first as they are calculated.

The distribution of muons is represented in Figure 5 in the tracker station that is furthest downstream in the (x, p_x) projection. The color of the points in the scatter plot represents the amplitude of the particle at that position. The distribution exhibits a clear Gaussian core of low amplitudes, while the tails are easily identified as high amplitude points.
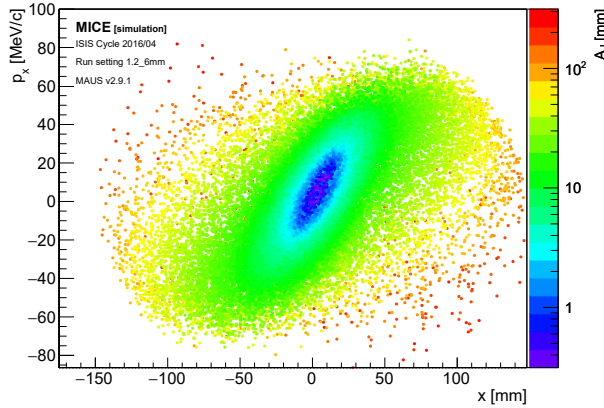
Figure 5: Scatter plot of the particles in the tracker station that is furthest downstream in the (x, p_x) projection. The color scale represents the individual particle amplitudes.

The amplitude of a particle in a Gaussian beam is related to its local density through

$$\rho(\mathbf{v}) = \frac{1}{4\pi^2 m^2 \epsilon_N^2} \exp \left[-\frac{A_\perp}{2\epsilon_N} \right]. \qquad (4)$$

A low amplitude sample corresponds to the high density core of the beam.

Subemittance

The α-subemittance, e_α, is defined as the RMS emittance of the core fraction α of the parent beam. For a truncated 4D Gaussian beam of covariance S, it satisfies

$$\frac{e_\alpha}{\epsilon_N} = \frac{|S|^{\frac{1}{4}}}{|\Sigma|^{\frac{1}{4}}} = \frac{1}{2\alpha} \gamma \left(3, Q_{\chi_4^2}(\alpha)/2 \right), \qquad (5)$$

with $\gamma(\cdot, \cdot)$ the lower incomplete gamma function and $Q_{\chi_4^2}(\cdot)$, the 4-degrees-of-freedom χ^2 distribution quantiles.

If an identical fraction α of the input beam is selected upstream and downstream, i.e. the same amount of particles, the measured subemittance change is identical to the normalized RMS emittance change. The evolution of the 9 %-subemittance is represented in Figure 6. The choice of 9 % is natural in four dimensions as it represents the fraction contained within the 4D RMS ellipsoid of a 4-variate Gaussian. This quantity exhibits a clean cooling signal across the absorber that is unaltered by transmission losses and nonlinearities. The only trade-off is that the relative statistical error on α-subemittance grows as $\alpha^{-\frac{1}{2}}$. The estimated relative emittance change with this technique is -7.54 ± 1.25 %, compatible with predictions.
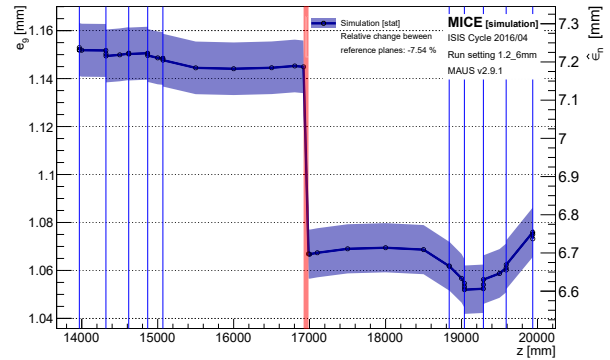

Figure 6: 9 %-subemittance evolution through the MICE cooling channel.

Fractional Emittance

The α-fractional emittance, ϵ_α, is defined as the phase space volume occupied by the core fraction α of the parent beam. For a truncated 4D Gaussian beam, it satisfies

$$\epsilon_\alpha = \frac{1}{2} m^2 \pi^2 \epsilon_N^2 Q_{\chi_4^2}^2(\alpha). \qquad (6)$$

This volume scales as function of α only and is proportional to the square of the normalized emittance. For a relative emittance change $\delta = \Delta \epsilon_N / \epsilon_N^{up}$, one yields

$$\frac{\Delta \epsilon_\alpha}{\epsilon_\alpha^{up}} = \delta(2 + \delta) \simeq 2 \frac{\Delta \epsilon_N}{\epsilon_N^{up}}. \qquad (7)$$

The last approximation holds for small fractional changes. The volume of a fraction α of the beam is reconstructed by taking the convex hull of the selected ensemble [12]. Figure 7 shows the evolution of the 9 %-fractional emittance. The estimated relative emittance change with this technique is -7.85 ± 1.08 %.

Nonparametric Density Estimation

Nonparametric statistics are not based on parameterized families of probability distributions. Unlike parametric density estimation, such as amplitude, nonparametric statistics
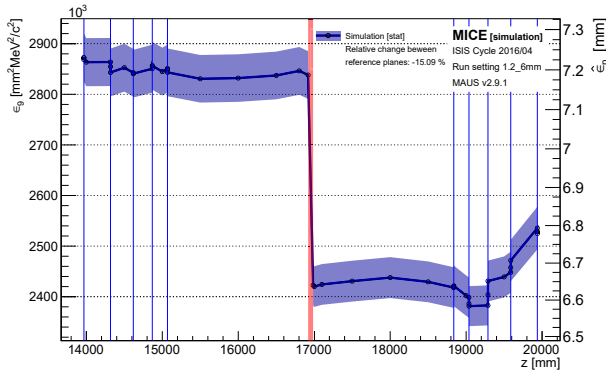
Figure 7: 9 %-fractional emittance evolution through the MICE cooling channel.

make no assumptions about the probability distributions of the variables being assessed.

There are many classes of estimators that have been developed in the last century. Three of them have been considered in this study: optimally binned histograms, k-Nearest Neighbors (kNN) and Tessellation Density Estimators (TDEs) [13–16]. Systematic studies showed that the kNN method is the most efficient and robust technique in four dimensions. For a given phase space vector $\mathbf{v} = (x, p_x, y, p_y)$, find the k nearest points in the input cloud, calculate the distance to the kth nearest neighbor, R_k, and evaluate the density as

$$\rho(\mathbf{v}) = \frac{k}{\mathcal{V}_k} = \frac{k\Gamma\left(\frac{d}{2} + 1\right)}{\pi^{\frac{d}{2}} R_k^d}, \tag{8}$$

with d the dimension of the space, V_k the volume of the d-ball of radius R_k and $\Gamma(\cdot)$ is the gamma function. The choice of parameter $k = \sqrt{N}$ has been shown to be quasi-optimal in general [17] and is used in the following. This estimator is applied to the sample in the tracker station that is furthest downstream and is represented in the (x, p_x) projection for $(y, p_y) = (0, 0)$ in Figure 8.
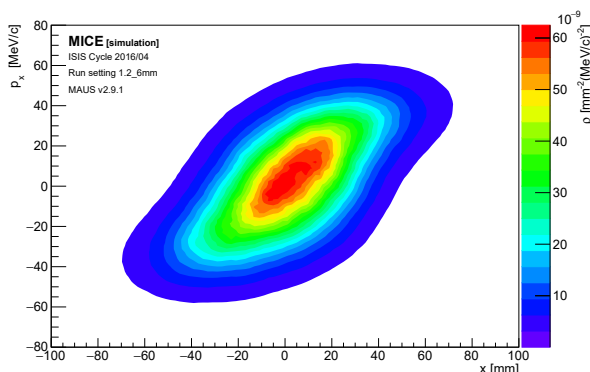
Figure 8: k-Nearest Neighbors estimate of the phase space density in the (x, p_x) projection for $(y, p_y) = (0, 0)$ in the tracker station that is furthest downstream.

This method removes any underlying assumption about a Gaussian core and allows to reconstruct generalized probability contours. The volume of the α-contour is the α-fractional emittance, as defined above. An MC method is used to reconstruct the volume of a contour: select the densest fraction α of the input points and record the level of the lowest point, ρ_α. Sample N random points uniformly distributed inside a box that encompasses the contour and record the amount, N_α, that have a density above the level, i.e. $\rho > \rho_\alpha$. The volume of the contour is simply $\epsilon_\alpha = N_\alpha V_{box}/N$, with V_{box} the volume of the 4-box. The 9 %-contour volume evolution is represented in Figure 9. The estimated relative emittance change with this technique is -7.97 ± 1.63 %.
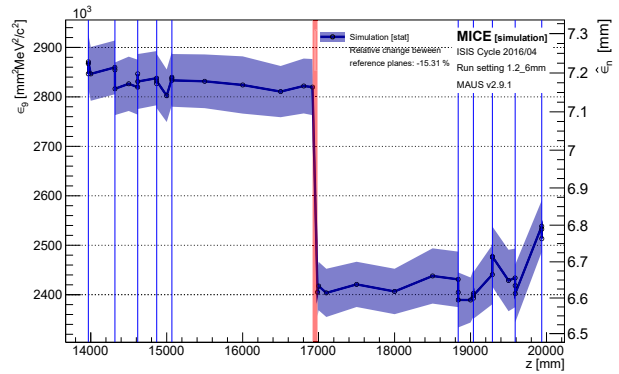
Figure 9: 9 %-contour volume evolution through the MICE cooling channel.

CONCLUSION

While the traditional normalized RMS emittance measurement is vulnerable to transmission losses and non-linearities in the particle ensemble, density estimation techniques provide the most viable option to recover quantitative cooling measurements. Amplitude-based techniques – subemittance and fractional emittance – rely on a well known quantity to select and study an identical fraction of the beam upstream and downstream of the absorber. Nonparametric density estimators allow to go one step further in removing any assumption on the underlying distribution. Both approaches yield compelling results when applied to a poorly transmitted and highly non-linear beams in a realistic simulation of one of the MICE cooling channel settings.

ACKNOWLEDGEMENT

REFERENCES

[1] IDS-NF Collaboration, M. Apollonio *et al.*, "International Design Study for the Neutrino Factory", *Nucl. Phys. Proc. Suppl.* 229-232 (2012) 515–515

[2] Neutrino Factory and Muon Collider Collaboration, M. Alsharoa, *et al.*, "Recent progress in neutrino factory and muon collider research within the Muon collaboration", *Phys. Rev. ST Accel. Beams* 6 (2003) 081001

[3] D. Neuffer, "Principles and Applications of Muon Cooling", *Part. Accel.* 14 (1983) 75–90.

[4] V. Parkhomchuck and A. Skrinsky, "Cooling Methods for Charged Particle Beams", *Rev. Accel. Sci. Tech.* 1 no. 1 (2008) 237

[5] D. Stratakis and R. Palmer, "Rectilinear six-dimensional ionization cooling channel for a muon collider: A theoretical and numerical study" *Phy. Rev. ST Accel. Beams* 18 (2015) 031003

[6] MICE Collaboration, "MICE: An International Muon Ionization Cooling Experiment", MICE Note 21 (2003). http://mice.iit.edu/micenotes/public/pdf/MICE0021/MICE0021.pdf.

[7] F. Drielsma, "Results from MICE Step IV", in *Proceedings of "The 2017 European Physical Society Conference on High Energy Physics"* PoS(EPS-HEP2017)534

[8] C. Heidt, "The tracker systems for the muon ionization cooling experiment", *Nucl. Instr. Meth.*, vol. 718 (2014), 560–562.

[9] U. Braver *et al.*, "MICE: the Muon Ionization Cooling Experiment. Step I: First Measurement of Emittance with Particle Physics Detectors", https://arxiv.org/abs/1110.1813.

[10] D. Adams *et al.*, "Pion contamination in the MICE muon beam", *JINST* 11 (2016) P03001

[11] D. Adams *et al.*, "Electron-muon ranger: performance in the MICE muon beam", *JINST* 10 (2015) P12012

[12] C.B. Barber, D.P. Dobkin, and H.T. Huhdanpaa, "The Quickhull algorithm for convex hulls", *ACM Trans. on Mathematical Software*, 22(4) (1996) 469-483, http://www.qhull.org.

[13] D.W. Hogg, "Data analysis recipes: Choosing the binning for a histogram", https://arxiv.org/pdf/0807.4820

[14] Y.P. Mack and M. Rosenblatt, "Multivariate k-nearest neighbor density estimates", *Journal of Multivariate Analysis* Volume 9, Issue 1 (1979), 1–15

[15] M. Browne, "A geometric approach to non-parametric density estimation", *Pattern Recognition* 40(1) (2007), 134–140

[16] M. Browne, "Regularized tessellation density estimation with bootstrap aggregation and complexity penalization", *Pattern Recognition* 45(4) (2012), 1531–1539

[17] D.O. Loftsgaarden and C.P. Quesenberry, "A nonparametric estimate of a multivariate density function", *The Annals of Mathematical Statistics* Vol. 36, No. 3 (1965), 1049–1051

OFFLINE SOFTWARE AND COMPUTING FOR THE SPD EXPERIMENT

V. Andreev[1], A. Belova[2], A. Galoyan[2], S. Gerassimov[1], G. Golovanov[2], P. Goncharov[2], A. Gribowsky[2], D. Maletic[3], A. Maltsev[2], A. Nikolskaya[4], D. Oleynik[2], G. Ososkov[2], A. Petrosyan[2], E. Rezvaya[2], E. Shchavelev[4], A.Tkachenko[2], V. Uzhinsky[2], A. Verkheev[2], A. Zhemchugov[2,a]

[1] *P.N. Lebedev Physical Institute of the Russian Academy of Sciences, 53 Leninskiy Prospekt,119991, Moscow, Russia*

[2] *Joint Institute for Nuclear Research, 6 Joliot-Curie, Dubna, Moscow region, 141980 Russia*

[3] *Institute of Physics Belgrade, Pregrevica 118, Belgrade, Serbia*

[3] *Saint Petersburg State University, 7-9 Universitetskaya emb., Saint Petersburg, 199034, Russia*

E-mail: [a] zhemchugov@jinr.ru

The SPD (Spin Physics Detector) is a planned spin physics experiment in the second interaction point of the NICA collider that is under construction at JINR. The main goal of the experiment is the test of basic of the QCD via the study of the polarized structure of the nucleon and spin-related phenomena in the collision of longitudinally and transversely polarized protons and deuterons at the center-of-mass energy up to 27 GeV and luminosity up to 10^{32} **1/(cm**^{2} s). The data rate at the maximum design luminosity is expected to reach 0.2 Tbit/s. Current approaches to SPD computing and offline software will be presented. The plan of the computing and software R&D in the scope of the SPD TDR preparation will be discussed.

Keywords: NICA, SPD, high throughput computing, distributed computing, offline software

Vladimir Andreev, Anna Belova, Aida Galoyan, Sergey Gerassimov, Georgy Golovanov, Pavel Goncharov, Alexander Gribowsky, Dimitrije Maletic, Andrey Maltsev, Anastasiya Nikolskaya, Danila Oleynik, Gennady Ososkov, Artem Petrosyan, Ekaterina Rezvaya, Egor Shchavelev, Artur Tkachenko, Vladimir Uzhinsky, Alexander Verkheev, Alexey Zhemchugov

1. Introduction

The SPD (Spin Physics Detector) is a planned spin physics experiment in the second interaction point of the NICA collider that is under construction at JINR. The main goal of the experiment is the test of basic of the QCD via the study of polarized structure of nucleon and spin-related phenomena in the collision of longitudinally and transversely polarized protons and deuterons at the center-of-mass energy up to 27 GeV and luminosity up to 10^{32} cm^{-2} s^{-1}. Transverse Momentum-Dependent partonic distributions (TMD PDFs) for gluons is the main goal of the experiment. They will be accessed in such hard processes as the production of the open charm, charmonia and prompt photons. The SPD detector is planned as a universal 4π spectrometer based on modern technologies. It will include such subsystems as a silicon vertex detector, a straw tube-based main tracker, a time-of-flight system, an electromagnetic calorimeter and a muon identification system. A total number of the detector channels in SPD is about 500 000, with the major part coming from the vertex detector. Assuming that all sub-detectors are in operation, the raw data flow was estimated as 10–20 GB/s. This poses a significant challenge both to the DAQ system and to the offline computing system and data processing software. Taking into account recent advances in the computing hardware and software, the investment in the research and development necessary to deploy software to acquire, manage, process, and analyze the data recorded is required along with the physics program elaboration and the detector design.

2. SPD computing model

Expected event rate of the SPD experiment is about 3 MHz (*pp* collisions at $\sqrt{s}$ = 27 GeV and 10^{32} cm^{-2}s^{-1} design luminosity). This is equivalent to the raw data rate of 20 GB/s or 200 PB/year, assuming the detector duty cycle is 0.3, while the signal-to-background ratio is expected to be in order of 10^{-5}. Taking into account the bunch crossing rate of 12.5 MHz, one may conclude that pile-up probability cannot be neglected.

The key challenge of the SPD Computing Model is the fact, that no simple selection of physics events is possible at the hardware level, because the trigger decision would depend on measurement of momentum and vertex position, which requires tracking. Moreover, the free-running DAQ provides a continuous data stream, which requires a sophisticated unscrambling prior building individual events. That is the reason why any reliable hardware-based trigger system turns out to be over-complicated and the computing system will have to cope with the full amount of data supplied by the DAQ system. This makes a medium-scale setup of SPD a large-scale data factory.

The continuous data reduction is a key point in the SPD computing. While simple operations like noise removal can be done yet by DAQ, it is an online filter that is aimed at fast partial reconstruction of events and data selection, thus being a kind of a software trigger. The goal of the online filter is to decrease the data rate at least by a factor of 50 so that the annual upgrowth of data including the simulated samples stays within 10 PB. Then, data are transferred to the Tier-1 facility, where full reconstruction takes place and the data is stored permanently. Two reconstruction cycles are foreseen. The first cycle includes reconstruction of some fraction of each run necessary to study the detector performance and derive calibration constants, followed by the second cycle of reconstruction of full data sample for physics analysis. The data analysis and Monte-Carlo simulation will likely run at the remote computing centers (Tier-2s). Given the large data volume, a thorough optimization of the event model and performance of reconstruction and simulation algorithms are necessary.

Taking into account recent advances in the computing hardware and software, the investment in the research and development necessary to deploy software to acquire, manage, process, and analyze the data recorded is required along with the physics program elaboration and the detector design. While the core elements of the SPD computing system and offline software now exist as prototypes, the system as a whole with capabilities such as described above is in the conceptual design stage and information will be added as it is developed.

3. Online filter

The SPD online filter facility will be a high-throughput system which will include heterogeneous computing platforms similar to many high-performance computing clusters. The computing nodes will be equipped with hardware acceleration. The software framework will provide the necessary abstraction so that common code can deliver the selected functionality on different platforms.

The main goal of the online filter is a fast reconstruction of the SPD events and suppression of the background ones at least by a factor of 50. This requires fast tracking and fast clustering in the electromagnetic calorimeter, followed by reconstruction of event from a sequence of time slices and an event selection (software trigger). Several consecutive time slices shall be considered, tracker data unpacked and given for a fast tracking. The result of the fast track reconstruction is the number of tracks, an estimate of their momentum and an estimate of primary vertex (to distinguish between tracks belonging to different collisions). Using this outcome, the online filter should combine information from the time slices into events and add a trigger mark. The events shall be separated in several data streams using the trigger mark and an individual prescale factor for each stream is applied.

One of the most important aspects of this chain is the recognition of particle tracks. Traditional tracking algorithms, such as the combinatorial Kalman filter, are inherently sequential, which makes them rather slow and hard to parallelize on modern high-performance architectures (graphics processors). As a result, they do not scale well with the expected increase in the detector occupancy during the SPD data taking. This is especially important for the online event filter, which should be able to cope with the extremely high data rates and to fulfill the significant data reduction based on partial event reconstruction "on the fly". The parallel resources like multicore CPU and GPU farms will likely be used as a computing platform, which requires the algorithms, capable of the effective parallelization, to be developed, as well as the overall cluster simulation and optimization.

Machine learning algorithms are well suited for multi-track recognition problems because of their ability to reveal effective representations of multidimensional data through learning and to model complex dynamics through computationally regular transformations, that scale linearly with the size of input data and are easily distributed across computing nodes. Moreover, these algorithms are based on the linear algebra operations and can be parallelized well using standard ML packages. This approach has already been applied successfully to recognize tracks in the BM@N experiment at JINR and in the BESIII experiment at IHEP CAS in China [1, 2]. In the course of the project an algorithm, based on recurrent neural networks of deep learning, will be developed to search for and reconstruct tracks of elementary particles in SPD data from the silicon vertex detector and the straw tube-based main tracker. The same approach will be applied to the clustering in the SPD electromagnetic calorimeter, and fast π^0 reconstruction. The caution is necessary, though, to avoid possible bias due to an inadequacy of the training data to the real ones, including possible machine background and the detector noise. A dedicated workflow that includes continuous learning and re-learning of neuron network, deployment of new versions of network and the continuous monitoring of the performance of the neural networks used in the online filter is necessary and needs to be elaborated.

Besides the high-level event filtering and corresponding data reduction, the online filter will provide input for the run monitoring by the shift team and the data quality assessment, as well as local polarimetry.

4. Computing system

The projected rate and amount of data produced by SPD prescribe to use high throughput computing solutions for the processing of collected data. It is the experience of a decade of the LHC computing that already developed a set of technologies mature enough for the building of distributed high-throughput computing systems for the experiments in high energy physics.

The 'online' part of computing systems for the SPD experiment, namely the online filter described above, is an integral part of experimental facilities, connected with the 'offline' part using a high throughput backbone network. The entry point to 'offline' facilities is a high capacity storage system, connected with 'online facility' through a multilink high-speed network. Data from high capacity storage at the Meshcheryakov Laboratory of Information Technologies will be copied to the tape-based mass storage system for long-term storage. At the same time, data from high capacity storage will be processed on different computing facilities as at JINR as in other collaborative institutions.

The hierarchy of offline processing facilities can be introduced:

- Tier 1 level facilities should provide high capacity long-term storage which will have enough capacity to store a full copy of primary data and a significant amount of important derived data;

- Tier 2 level facility should provide (transient) storage with capacity that will be enough for storing of data associated with a period of data taking;

- optional Tier 3 level are opportunistic resources, that can be used to cope with a pile-up of processing during some period of time or for special analysis.

Offline data processing resources are heterogeneous as on hardware architecture level so by technologies and at JINR site it includes batch processing computing farms, high-performance (supercomputer) facilities, and cloud resources. A set of middleware services will be required to have unified access to different resources.

Computing systems for NICA at JINR are naturally distributed. Experimental facilities and main data processing facilities placed across two JINR sites and, inter alia, managed by different teams. That causes some heterogeneity not only on hardware systems but also on the level of basic software: different OSs, different batch systems etc. Taking into account the distributed nature and heterogeneity of the existing infrastructure, and expected data volumes, the experimental data processing system must be based on a set of low-level services that have proven their reliability and performance. It is necessary to develop a high-level orchestrating system that will manage the low-level services. The main task of that system will be to provide efficient, highly automated multi-step data processing following the experimental data processing chain.

The Unified Resource Management System is a IT ecosystem composed from the set of subsystem and services which should:

- unify the access to the data and compute resources in a heterogeneous distributed environment;

- automate most of the operations related to massive data processing;

- avoid duplication of basic functionality, through sharing of systems across different users (if it possible);

- as a result - reduce operational cost, increase the efficiency of usage of resources;

- transparent accounting of usage of resources.

Many distributed computing tools have already been developed for the LHC experiments and can be re-used in SPD. For the task management one can use PANDA [3] or DIRAC [4] frameworks. For the distributed data management RUCIO [5] package has been developed. For the massive data transfer FTS [6] can be used. Evaluation of these tools for the SPD experiment and their implementation within the SPD Unified Resource Management System is planned in scope of the TDR preparation.

5. Offline software

Offline software is a toolkit for event reconstruction, Monte-Carlo simulation and data analysis. Linux is chosen as a base operating system.

Currently, the offline software of the SPD experiment – SpdRoot – is derived from the FairRoot software [7] and it is capable of Monte Carlo simulation, event reconstruction, data analysis and visualization. The SPD detector description is flexible and based on the ROOT geometry package. Proton-proton collisions are simulated using a multipurpose generator Pythia8 [8]. Deuteron-deuteron collisions are simulated using a modern implementation of the FRITIOF model [9, 10], while UrQMD [11, 12] generator is used to simulate nucleus-nucleus interactions. Transportation of secondary particles through the material and the magnetic field of the SPD setup and the simulation of detector response is provided by Geant4 toolkit [13, 14, 15]. Track fitting is carried out on the base of GenFit toolkit [16, 17] while the KFparticle package [18] is used to reconstruct secondary vertices. The central database is going to be established to keep and distribute run information, slow control data and calibration constants.

Recent developments in computing hardware resulted in the rapid increase in potential processing capacity from increases in the core count of CPUs and wide CPU registers. Alternative processing architectures have become more commonplace. These range from the multi-core architecture based on x86_64 compatible cores to numerous alternatives such as other CPU architectures (ARM, PowerPC) and special co-processors/accelerators: (GPUs, FPGA, etc). For GPUs, for instance, the processing model is very different, allowing a much greater fraction of the die to be dedicated to arithmetic calculations, but at a price in programming difficulty and memory handling for the developer that tends to be specific to each processor generation. Further developments may even see the use of FPGAs for more general-purpose tasks.

The effective use of these computing resources may provide a significant improvement in offline data processing. However, the offline software should be capable to do it by taking advantage of concurrent programming techniques, such as vectorization and thread-based programming. Currently, the SPD software framework, SpdRoot, cannot use these techniques effectively. The studies of the concurrent-capable software frameworks (e.g. ALFA [19], Key4Hep [20]) are needed to provide input for the proper choice of the offline software for Day-1 of the SPD detector operation, as well as a dedicated R&D effort to find proper solutions for the development of efficient cross-platform code.

A git-based infrastructure for the SPD software development already established at JINR [21].

4. Conclusion

The expected SPD data rate of 0.2 Tbit/s at the maximum design luminosity poses a significant challenge to the DAQ system, to the online event filter, and to the offline computing system and data processing software. Fast event reconstruction based on deep learning algorithms, distributed computing, and extensive use of concurrent programming techniques, such as vectorization and thread-based programming, are the key points in the SPD data processing paradigm. Taking into account recent advances in computing hardware and software, the investment in the research and development necessary to deploy software to acquire, manage, process, and analyze the data recorded is required along with the physics program elaboration and the detector design.

References

[1]   D. Baranov, S. Mitsyn, P. Goncharov, G. Ososkov, The Particle Track Reconstruction based on deep neural networks // EPJ Web Conf. 214 (2019) 06018

[2]   G. Ososkov, et al., Tracking on the BESIII CGEM inner detector using deep learning // Computer Research and Modeling 10 (20) 1–24

[3]   F. B. Megino, et al., PanDA: Evolution and Recent Trends in LHC Computing // Procedia Comput. Sci. 66 (2015) 439–447

[4]   F. Stagni, A. Tsaregorodtsev, L. Arrabito, A. Sailer, T. Hara, X. Zhang, DIRAC in Large Particle Physics Experiments // J. Phys. Conf. Ser. 898 (9) (2017) 092020

[5]   M. Barisits, T. Beermann, F. Berghaus, et al., Rucio: Scientific data management // Comput. Softw. Big Sci. 3 (2019) 11

[6]   A. Frohner, J.-P. Baud, R. M. Garcia Rioja, G. Grosdidier, R. Mollon, D. Smith, P. Tedesco, Data management in EGEE // J. Phys. Conf. Ser. 219 (2010) 062012

[7]   M. Al-Turany, D. Bertini, R. Karabowicz, D. Kresan, P. Malzacher, T. Stockmanns, F. Uhlig, The FairRoot framework // J. Phys. Conf. Ser. 396 (2012) 022001

[8]   T. Sjöstrand, S. Ask, J. R. Christiansen, R. Corke, N. Desai, P. Ilten, S. Mrenna, S. Prestel, C. O. Rasmussen, P. Z. Skands, An introduction to PYTHIA 8.2 // Comput. Phys. Commun. 191 (2015) 159–177

[9]   B. Andersson, G. Gustafson, B. Nilsson-Almqvist, A Model for Low p(t) Hadronic Reactions, with Generalizations to Hadron - Nucleus and Nucleus-Nucleus Collisions // Nucl. Phys. B 281 (1987) 289–309

[10] B. Nilsson-Almqvist, E. Stenlund, Interactions Between Hadrons and Nuclei: The Lund Monte Carlo, Fritiof Version 1.6 // Comput. Phys. Commun. 43 (1987) 387

[11] S. Bass, et al., Microscopic models for ultrarelativistic heavy ion collisions // Prog. Part. Nucl. Phys. 41 (1998) 255–369.

[12] M. Bleicher, et al., Relativistic hadron hadron collisions in the ultrarelativistic quantum molecular dynamics model // J. Phys. G 25 (1999) 1859–1896

[13] S. Agostinelli, et al., GEANT4–a simulation toolkit // Nucl. Instrum. Meth. A 506 (2003) 250–303

[14] J. Allison, et al., Geant4 developments and applications // IEEE Trans. Nucl. Sci. 53 (2006) 270

[15] J. Allison, et al., Recent developments in Geant4 // Nucl. Instrum. Meth. A 835 (2016) 186–225

[16] J. Rauch, T. Schlüter, GENFIT — a Generic Track-Fitting Toolkit // J. Phys. Conf. Ser. 608 (1) (2015) 012042

[17] GenFit: https://github.com/GenFit/GenFit

[18] S. Gorbunov, I. Kisel, Reconstruction of decayed particles based on the Kalman filter // Tech. Rep. CBM-SOFT-note-2007-003, CBM Collaboration (2007)

[19] M. Al-Turany, et al., ALFA: The new ALICE-FAIR software framework, J. Phys. Conf. Ser. 664 (7) (2015) 072001

[20] Key4hep software: // https://key4hep.github.io/key4hep-doc/index.html

[21] JINR git SPD software: https://git.jinr.ru/nica/spdroot

BACKGROUND SPECTRUM CHARACTERISTICS OF THE HPGE DETECTOR LONG-TERM MEASUREMENT IN THE BELGRADE LOW-BACKGROUND LABORATORY

Radomir Banjanac, Vladimir Udovičić, Dejan Joković, Dimitrije Maletić, Nikola Veselinović, Mihailo Savić, Aleksandar Dragić, Ivan Aničin

Institute of Physics, Belgrade, Serbia

Abstract. *The Belgrade low-level background laboratory, built in 1997, is shallow (25 m.w.e) underground space (45m²) which is constantly ventilated with fresh air against radon. The muon intensity (about 3.5 times less than at ground level), radon concentration (suppressed to averaged value of 15 Bqm⁻³), as well as gamma-ray background are monitoring for more than eight years. After long-term measurement using the radiopure HPGe detector with 35% relative efficiency, the measured data includes radionuclide concentration of detector surroundings, estimation of background time variation due to radon and cosmic-rays as well as MDA values for typical samples of water matrix. The detailed characteristics of gamma-ray background spectra are here presented.*

Key words : *Underground laboratory, Low-level background, long-term gamma-ray measurement*

1. INTRODUCTION

Various experiments which strive for the detection of very rare events require the lowest possible background radiation which can be achieved only in a deep underground laboratory. Some of recent the most interesting are double beta-decay experiments, [1] and dark matter searches, [2]. In any applied measurements of low activities, a goal that is pursued by all gamma spectroscopist is to lower the minimum detectable activity (MDA) of their detection system obtaining more statistical evidence in less time.

But, any long and even short-term gamma-ray background measurement is subject to certain temporal variations due to time variability of two prominent contributors to background, cosmic-rays and radon. The most of the low background laboratories that deal with low activity measurements have developed routine measurements of background. The duration of these measurements may be from one day to even a month and they are designed to produce results with sufficiently low statistical errors for the envisaged measurements. These measurements yield only average values of the background, what in principle may lead to systematic errors in later measurements, especially of NORM samples.

The averaged values of the background, gamma lines and continuum, nuclide concentrations or MDA presenting a "personal card" of used detector system for certain samples in any low-level background laboratory, [3]. Here is attempt to present our low-level background laboratory in a similar way. First of all, the detailed description of the laboratories and used detector system are described.

2. DESCRIPTION OF THE LABORATORIES AND EQUIPMENT

The Belgrade underground low-level laboratory (UL), built in 1997 and located on the right bank of the river Danube in the Belgrade borough of Zemun, on the grounds of the Institute of Physics. The overburden of the UL is about 12 meters of loess soil, equivalent to 25 meters of water. It is equipped with ventilation system which provides low radon concentration of 15(5) Bq/m³. The "passive" shield consists of 1 mm thick aluminum foil which completely covers all the wall surfaces inside the laboratory, including floor and ceiling. As the active radon shield the laboratory is continuously ventilated with fresh air, filtered through one rough filter for dust elimination followed by active charcoal filters for radon adsorption. The UL has an area of 45m² and volume of 135m³ what required the rate of air inlet adjusted to 800m³/h. This huge amount of fresh air contributes to greater temperature variations and the long-term mean value of temperature inside the UL is 19(4)°C. The rate of air outlet (700m³/h) was adjusted to get an overpressure of about 200 Pa over the atmospheric pressure, what prevents radon diffusion through eventual imperfections in the aluminum layer. Relative humidity is controlled by a dehumidifier device, what provides that the relative humidity in the underground laboratory does not exceed 60%. The muon intensity (which is about 3.5 times less than at ground level), radon concentration and gamma-ray background are monitoring for more than eight years. Comparative background study is performing in the GLL (at ground level) which is equipped with a Ge detector (13% relative efficiency and not intrinsically low-radioactivity level, named SGe) and a big plastic scintillator (1m², named BPS) in veto position. The GLL is air-conditioned (average radon concentration of

50(30) Bq/m³) has an area of 30m² and volume of 75m³. The Fig. 1 presents veto arrangement of the HPGe detector (BGe, in 12cm lead shield) and big plastic scintillator, inside the UL.
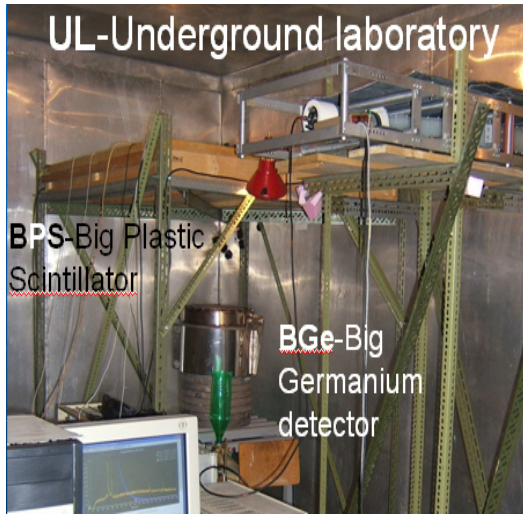

Fig. 1 Veto arrangement of the HPGe detector (BGe) and big plastic scintillator inside the UL

3. DESCRIPTION OF DETECTOR SYSTEMS IN THE UL

The low-level background detector system in the UL includes an intrinsically low-radioactivity level p-type Ge detector (35% relative efficiency, named BGe) and another plastic veto scintillator (1m², named BPS) situated coaxially above the BGe detector. The BGe is a GEM30 model (made by ORTEC) in LB-GEM-SV cryostat configuration with magnesium end cap. The energy resolution at 1332.5keV, measured by analog data acquisition system, is 1.72keV, 0.65keV at 122keV as well as the Peak to Compton ratio at 1332.5keV has value of 68. The cylindrical lead shielding of the BGe, with a wall thickness of 120 mm and an overall weight of about 900kg, was cast locally out of scratch plumbing retrieved after the demolition of some old housing. Radon monitoring inside the laboratories was performed by radon monitor, model RM1029 manufactured by Sun Nuclear Corporation. The device consists of two diffused junction photodiodes as a radon detector, and is furnished with sensors for temperature, pressure and relative humidity. A pair of plastic scintillator detectors is used for CR muon measurements at both laboratories. One of them is a larger (100cmx100cmx5cm) detector (BPS), equipped with four PMT directly coupled to the corners beveled at 45°, made by Amcrys-H, Kharkov, Ukraine. The other, a smaller 50cmx23cmx5cm plastic scintillator detector, with a single PMT looking at its longest side via a Perspex light guide tapering to the diameter of a PMT, made by JINR, Dubna, Russia, and assembled locally. The smaller detector may serve as a check of stability of the muon time series obtained from the larger detector, which is important for long term measurements. Two flash analog to digital converters (FADC), made by C.A.E.N (type N1728B), which sample at 10 ns intervals into 214 channels were used

to analyze spectra from Ge detectors as well as corresponding BPS. User-friendly software was developed to analyze the C.A.E.N data with the possibility to choose the integration time for further time-series analysis that corresponds to integration time of the radon monitor. The performances of digital acquisition system as well as software developed for analysis were described in detail, [4].

4. THE RESULTS OF BACKGROUND MEASUREMENTS IN THE UL

Additional to intrinsically low-radioactivity level of the BGe itself, environmental radioactivity is low, too. The UL was built from low activity concrete about 12 Bq/kg of U-238 and Th-232, and of 23 Bq/kg and 30 Bq/kq of surrounding soil, respectively. Radioactivity of aluminum wall-lining is negligible. Pb-210 activity of used lead shield of 30Bq/kg is measured. After long-term cosmic-ray, [5], radon concentration, [6] and gamma-ray background measurements, no significant long-term time variations of gamma background was found, [7]. After several years of almost continuously background measurements, the integral background rate in the region from 40keV to 2700keV has mean value of about 0.5 cps. The lines of Co-60 are absent in the background spectrum, while the line of Cs-137 with the rate of 1×10^{-4} cps starts to appear significantly only if the measurement time approaches one month. Fukushima activities, though strongly presented in our inlet air filters samples, did not enter the background at observable levels, in spite of the great quantities of air that we pump into the UL to maintain the overpressure, and it seems that the double air filtering and double buffer door system, along with stringent radiation hygiene measures, is capable of keeping the UL clean in cases of global accidental contaminations. No signatures of environmental neutrons, neither slow nor fast, are present in direct background spectra.

The Fig. 2 shows a characteristic shape of background spectrum obtained in the UL after about 6 months of measuring, with distinctive Pb X-ray lines at the beginning of the spectrum, annihilation line, and lines from ^{40}K and ^{208}Tl (2614.5keV) at the end of the spectrum with a lot of post-radon lines between them.
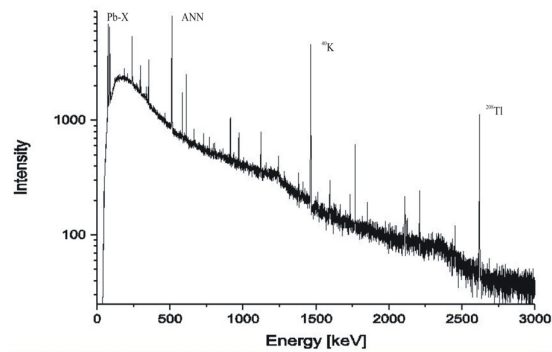

Fig. 2 Background spectrum of the HPGe detector (BGe) inside the UL after about 6 months of measuring

The table 1 in the third column presents gamma-ray background values of typical spectrum measured in

the UL using the BGe in direct (no veto) mode. The measurement time was about 6 months.

Table 1 The background characteristics of the BGe inside the UL

Line/ region (keV)	Radionuclide/ series/ nuclear reaction	Intensity $(10^{-3}\,s^{-1})$	MDA (mBq) for 100ks Water matrix
40-2700	-	500	-
46.5	Pb-210/U-238	0.38(11)	1500
53.2	U-234	-	9400
63.3	Th-234	-	700
72.8	Pb-X-$K_{\alpha2}$	3.1(1)	-
75	Pb-X-$K_{\alpha1}$	6.2(1)	-
84.9	Pb-X-$K_{\beta1}$	4.2(1)	-
87.3	Pb-X-$K_{\beta2}$	1.49(6)	-
92.5	Th-234	-	100
143.8	U-235	-	20
163.4	U-235	-	110
200.3	U-235	-	100
238.6	Pb-212/Th-232	0.83(4)	40
242	Pb-214/U-238	0.20(2)	-
295.2	Pb-214/U-238	0.71(4)	40
338.3	Ac-228/Th-232	0.15(2)	-
351.9	Pb-214/U-238	1.26(5)	30
477.6	Be-7	-	40
510.8+511	Tl-208/Th-232/ANN	7.0(1)	-
583.2	Tl-208/Th-232	0.30(3)	56
609.2	Bi-214/U-238	1.08(5)	60
661.7	Cs-137	0.10(5)	9
727.3	Bi-212	-	200
803.3	Pb-206 (n,n^l) Pb-206	0.11(2)	-
911.2	Ac-228/Th-232	0.25(2)	110
969	Ac-228/Th-232	0.11(2)	80
1001	Pa-234m	-	1300
1120.4	Bi-214/U-238	0.28(3)	-
1173.2	Co-60	-	19
1332.5	Co-60	-	11
1238.1	Bi-214/U-238	0.09(2)	-
1460.8	K-40	3.27(9)	850
1764.6	Bi-214/U-238	0.49(3)	230
2103.7	2614.5SE/Tl-208	0.13(2)	-
2204.2	Bi-214/U-238	0.15(2)	-
2614.5	Tl-208/Th-232	1.05(5)	-

The fourth column of the same table presents minimum detectable activity (MDA) calculated for predicted measurement time of 100000 seconds (approximately one day) for cylindrical sample (volume of 120cm³) situated on the top of the detector. Efficiency calibration was obtained by GEANT4 simulation toolkit as well as experimentally using appropriate standard. The difference between the two efficiency calibration curves is less than 5% for sample of water matrix, which MDA is here presented. MDA values are calculated as MDA=L_D/(t x Eff x p), where the L_D=2.71+4.65$B^{1/2}$ is detection limit. B is background at the energy of gamma-ray line with absolute detection efficiency Eff and emission probability p. If the predicted measurement time t is valued in seconds then MDA values have Bq unit. The obtained MDA values are presented for water matrix cylindrical samples in bottles with volume of 120cm³.

With the BPS currently positioned rather high over the detector top, at a vertical distance of 60cm from the top of the lead castle, in order to allow for the placing of voluminous sources in front of the vertically oriented detector, the off-line reduction of this integral count by the CR veto condition is only about 18%. Up to a factor of two might be gained if the veto detector were to be positioned at the closest possible distance over the BGe detector. This configuration requires some changes of the lead shield including introducing a sliding lead lid. Such a new shielding and veto configuration would be additionally reduce gamma-ray background up to the same factor that corresponds to factor of reduction expected for cosmic rays.

We do not insist on the lowering of statistical errors which depend on background levels solely and are difficult to reduce further with available means, but rather emphasize its stability due to the low and controlled radon concentration in the laboratory. This is essential, especially in NORM measurements, and makes our system virtually free of systematic errors as compared to systems which operate in environments where radon is not controlled. In that systems the reduction of post-radon background activities is achieved by flushing the detector cavity with liquid nitrogen vapor, where the transient regimes during sample changes and possible deposition of radon progenies may introduce systematic uncertainties which are difficult to estimate.

REFERENCES

1. W.G. Kang, *et al.*, "Ultra-low gamma-ray measurement system for neutrinoless double beta decay", Appl. Radiat. Isot. (2013), vol. 81, pp. 290–293.
2. G. Angloher, *et al.*, "Results from 730 kg days of the CRESST-II Dark Matter search", Eur. Phys. J. (2012), vol. C72, pp. 1971
3. L. Dragounová and P. Rulík, "Low level activity determination by means of gamma spectrometry with respect to the natural background fluctuation", Appl. Radiat. Isot. (2013), vol. 81, pp. 123–127
4. A. Dragić *et al.*, "The new set-up in the Belgrade low-level and cosmic-ray laboratory", Nucl. Techn. Radiat. Prot. (2011), vol. 26/3, pp. 181-192
5. A. Dragić *et al.*, "Variations of CR-muon intensity in the declining phase of the 23rd solar cycle in ground and shallow underground data", 29th International Cosmic Ray Conference, Pune (2005), vol. 1, pp. 249-252
6. V. Udovičić *et al.*, "Daily and seasonal radon variability in the underground low-background laboratory in Belgrade, Serbia", Radiation Protection Dosimetry (2014), vol. 160, Issue 1-3, pp. 62-64
7. R. Banjanac *et al.*, "Variations of gamma-ray background in the Belgrade shallow underground low-level laboratory", Applied Radiation and Isotopes, (2014), vol. 87, pp. 70-72

CORRELATIVE AND PERIODOGRAM ANALYSIS OF DEPENDENCE OF CONTINUOUS GAMMA SPECTRUM IN THE SHALLOW UNDERGROUND LABORATORY ON COSMIC RAY AND CLIMATE VARIABLES

Dimitrije Maletić, Radomir Banjanac, Dejan Joković, Vladimir Udovičić, Aleksandar Dragić, Mihailo Savić, Nikola Veselinović

Institute of Physics University of Belgrade, Serbia

Abstract. The continuous gamma spectrum, Cosmic ray intensity and climate variables; atmospheric pressure, air temperature and humidity were continually measured in the Underground laboratory of Low Background Laboratory in the Institute of Physics Belgrade. Same three climate variables for outside air were obtained from nearby meteorological station. The obtained gamma spectrum, measured using HPGe detector, is split into three energy ranges, low, intermediate and high ending with energy of 4.4 MeV. For each of the energy intervals periodogram and correlative analysis of dependence of continuous gamma spectrum on cosmic ray intensity and climate variables is performed. Periodogram analysis is done using Lomb-Scargle periodograms. The difference of linear correlation coefficients are shown and discussed, as well as the differences in resulting periodograms.

Key words: gamma spectroscopy, surface air, underground laboratory, correlative analysis, periodogram analysis.

1. INTRODUCTION

The low-level and cosmic-ray laboratory in the Low-Background laboratory for Nuclear Physics in the Institute of Physics Belgrade is dedicated to the measurements of low activities and to the studies of the muon and electromagnetic components of cosmic rays at the ground level and at the shallow depth under-ground, and in particular to the detailed studies of the signatures of these radiations in HPGe spectrometers situated shallow underground. The ground level part of the laboratory (GLL), at 75 m above sea level, is situated at the foot of the vertical loess cliff, which is about 10 meters high. The underground part of the laboratory (UL), of the useful area of 45 m², is dug into the foot of the cliff and is accessible from the GLL via the 10 meters long horizontal corridor, which serves also as a pressure buffer for a slight overpressure in the UL (Fig.1). The overburden of the UL is about 12m of loess soil, equivalent to 25 meters of water. [1]

In the UL laboratory the gamma spectrum is recorded using HPGe detector and fast ADC unit made by CAEN, and analysed using software developed in our laboratory. Besides HPGe measurements the air pressure, temperature and humidity were recorded in UL also. Values for temperature, pressure and humidity of outside air was taken from publicly available web site. The time period from which the

measurements were used in this analysis is from beginning of December 2009 till end of April 2010.
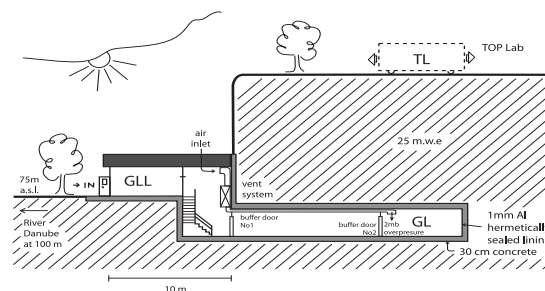
Figure 1. Cross-section of the low-level and CR laboratory at IOP, Belgrade, 44°49'N, 20°28'E, vertical rigidity cut off 5.3 GV.

Continuous Cosmic rays' (CR) spectrum measure-ments by means of a pair of small plastic scintillators [(50x25x5)cm] started in the GLL and UL back in 2002 and lasted for about 5 years. It agrees to the spectrum of relatively shallow underground laboratories worldwide [2]. These measurements yielded the precise values of the integral CR muon flux at the ground level and underground level laboratory, at the location of Belgrade [3]. Different analyses of the time series of these measurements have also been performed [4, 5]. Since the UL is completely lined with the hermetically sealed 1 mm thick aluminum lining, and the ventilation system keeps the overpressure of 2 mbars of doubly filtered air, the concentration of radon is kept at the low average value of about 10 Bq/m³.

Measurements and analysis of periodicy of gamma-rays in underground laboratory had been reported [6-7], and also for Radon measurements and periodicity [8-9] including advanced Multivariate Analysis tecniques [10-11].

Most recent research done in our laboratory [12] addresses the question of determination of origin of low energy gamma-rays detected by HPGe detector, which are coming either from environmental radiation or from CR. In this paper the correlative analysis is used to address the same question of composition of low-energy gamma-rays spectrum, thus giving us the new approach to the research done in [12].

The correlative analysis in this paper was done using Toolkit for Multivariate Analysis TMVA[13] package as part of the ROOT[14] software, widely used in analysis, especially for High Energy Physics experiments. The TMVA was used for analysis extensively in our laboratory, and it was the natural choice to use the software for correlative analysis also. Lomb-Scargle periodograms were produced using software developed in Low-Background laboratory.

2. EXPERIMENTAL SETUP

In the UL 35% efficiency radiopure HPGe detector, made by ORTEC, is used. The HPGe is sourounded by 12 cm thick cylindrical lead castle. Cosmic ray setup consists of a single [(100x100x5)cm] plastic scintillator detector equipped with four PMTs directly coupled to the corners beveled at 45°, made by Amcrys-H of Kharkov, Ukraine. The signals from HPGe detector and plastic scintillators give output to fast ADC unit with four independent inputs each, made by CAEN, of the type N1728B. CAEN units are versatile instruments capable of working in the so-called energy histogram mode, when they perform like digital spectrometers, or/and in the oscillogram mode, when they perform like digital storage oscilloscopes. In both modes they sample at 10 ns intervals, into 2^{14} channels. The full voltage range is ±1.1V.

CAEN units are capable of operating in the list mode, when every analyzed event is fully recorded by the time of its occurrence over the set triggering level, and its amplitude, in the same PC, which controls their workings. This enables to off-line coincide the events at all four inputs, prompt as well as arbitrarily delayed, with the time resolution of 10 ns, as well as to analyze the time series not only of all single inputs, but also of arbitrary coincidences, with any integration period from 10 ns up. The flexible software that performs all these off-line analyses is user-friendly and is entirely homemade.

The preamplifier outputs of the PMTs of detectors are paired diagonally, the whole detector thus engaging the two inputs of the CAEN unit. The signals from these inputs are later off-line coincided and their amplitudes added, to produce the singles spectra of these detectors. Offline coincidence allows that the high intensity but uninteresting low energy portion of the background spectrum of this detector (up to some 3 MeV), which is mostly due to environmental radiations, is practically completely suppressed, leaving only the high energy-loss events due to CR muons and EM showers that peak at about 10 MeV, as shown in Figure 2.

Since event of HPGe gamma spectrum and Cosmic rays consists of time-stamp and the amplitude, off-line analysis is used to create time series of arbitrary time window with selection of specific part of gamma spectrum as well as the time series of Cosmic ray flux in UL (Figure 3.). This enables that whole gamma spectrum can be divided into energy ranges, and analyze each energy range separately. The spectrum separation is done on channel numbers, and after the energy calibration, the energy ranges used in our analysis are 180-440 keV, 620-1330 keV and 1800-4440 keV. The full gamma spectrum is recorded in range of 180-6670 keV. The part of gamma spectrum of the HPGe is shown in Figure 4.
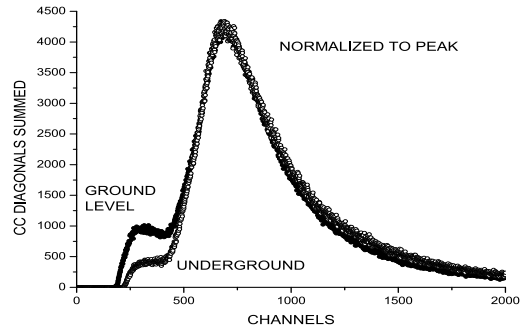

Fig. 2. The sum spectra of two diagonals of big plastic detectors in the UL and GLL .
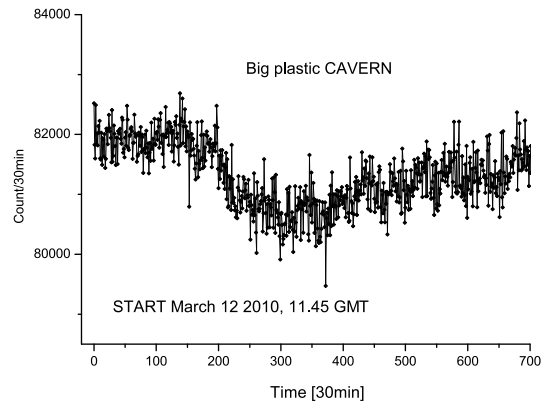

Fig. 3. The time series of the CR muon count of the big plastic detector in the UL.
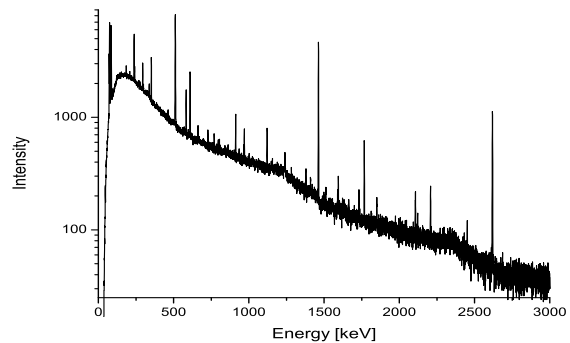

Figure 4. Gamma spectrum of the HPGe detector in 12cm lead castle in the Underground laboratory.

The analysis starts with correlation analysis. The software for correlative analysis is a part of TMVA package. Hourly time series of variables, atmospheric pressure P, temperature T, and humidity H for UL (P_R, T_R, H_R), and outside (P,T,H) are used, Cosmic ray time series (CR) as well as T (DT) and H (DH) difference of UL and outside values make the number of nine input variables. The table summarizing the linear correlation coefficients is shown in Table 1. We can see correlation between each input variable and HPGe gamma spectrum for full energy range in Table 1 also.

	HPGe	T	P	H	T_R	P_R	H_R	CR	DT	DH
DH	-10	69	-9	-86	57	-22	51	-25	-64	100
DT	7	-98	7	60	-30	10	-24	42	100	-64
CR	-14	-42	-65	36	-14	-52	13	100	42	-25
H_R	-2	30	-44	-1	42	-59	100	13	-24	51
P_R	14	-13	80	-8	-22	100	-59	-52	10	-22
T_R	1	43	-16	-41	100	-22	42	-14	-30	57
H	10	-63	-15	100	-41	-8	-1	36	60	-86
P	11	-9	100	-15	-16	80	-44	-65	7	-9
T	-6	100	-9	-63	43	-13	30	-42	-98	69
HPGe	100	-6	11	10	1	14	-2	-14	7	-10

Table 1. Summary table of linear correlation coefficient for all 9 input variables' 1 hour time series and 1 hour time series of HPGe gamma spectrum for full energy range.

Correlation analysis was done also for three mentioned energy ranges, the Table 2. summarizes the results.

	180-6670 keV	180-440 keV	620-1330 keV	1780-4440 keV
T	-0.070	-0.045	-0.041	-0.096
P	**+0.111**	**+0.124**	**+0.033**	**+0.010**
H	+0.106	+0.056	+0.047	+0.101
T_{UG}	+0.013	-0.029	+0.014	-0.012
P_{UG}	+0.149	+0.111	+0.091	+0.061
H_{UG}	-0.029	-0.068	-0.030	+0.028
CR	**-0.140**	**-0.179**	**-0.030**	**+0.036**
T_{UG}-T	+0.076	+0.043	+0.046	+0.100
H_{UG}-H	-0.105	-0.083	-0.055	-0.072

Table 2. Linear correlation coefficients in % for full and three narrower energy ranges.

All the correlation of HPGe gamma spectrum hourly time series and input variables are not significant. The biggest correlation coefficient with HPGe time series is pressure time series measured underground followed by Cosmic ray time series. It is interesting to notice the change of correlation coefficients with HPGe for atmospheric pressure and Cosmic rays time series. While pressure correlation coefficients tend to drop going towards higher gamma energies, Cosmic rays' correlation coefficients are increasing from negative sign to positive one. This observation is in agreement with the fact that the Cosmic rays are contributing

more to the the gamma spectrum of higher energies, as it was shown in [12]. Since Cosmic rays and pressure are anti-correlated with correlation coefficient of -65%, as can be seen in Table 1, increase in atmospheric pressure will give negative correlation coefficient of HPGe and Cosmic rays' time series. This can be explained by having in mind that Cosmic rays are contributing insignificantly to gamma spectrum on lower energies [12] behaving like constant in low energy range, while increase in pressure increases the air density, thus more gamma scattering events are contributing to low energy gamma spectrum.

In the periodogram analysis the Lomb-Scargle periodograms were produced for atmospheric variables P, T, H and HPGe gamma spectrum. The periodograms show only daily periodicity of T, H time series as shown on figures 5 and 6. The P periodogram on Figure 7. Shows expected daily and mid-daily periodicity. It is noticeable that the periodogram for P has lowest spectral powers, which means that periodicity of P is less noticeable. Also, the unexpected 1/3 day periodicity is with low spectral power. The periodogram analysis showed that there is no significant periodicity in HPGe gamma spectrum time series, as shown on Figure 8.
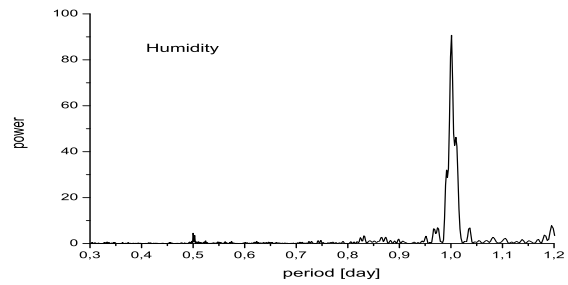

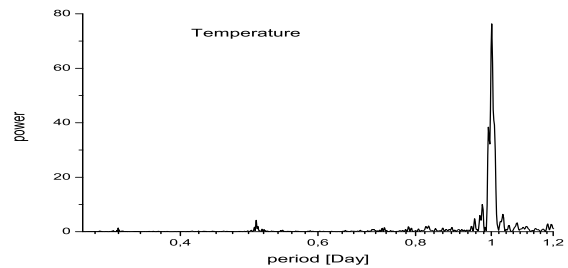Figure 5. Lomb-Scargle periodogram of air humidity.

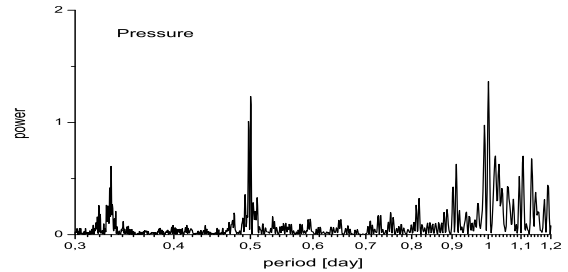Figure 6. Lomb-Scargle periodogram of air temperature.

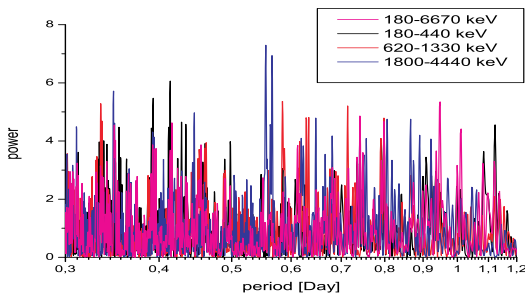Figure 7. Lomb-Scargle periodogram of air pressure.

Figure 8. Lomb-Scargle periodogram of full and three different energy range HPGe gamma spectrum time series.

CONCLUSION

In the Underground laboratory of Low Background Laboratory in the Institute of Physics Belgrade the continuous HPGe gamma spectrum, Cosmic ray intensity and climate variables were continually measured in the period from beginning of December 2009 till the end of April 2010. The HPGe gamma spectrum is split into three energy ranges, low, intermediate and high. For each of the energy intervals periodogram and correlative analysis of dependence of continuous gamma spectrum on cosmic ray intensity time series and climate variables time series is performed. Periodogram analysis is done using Lomb-Scargle periodograms. The correlation coefficient between air pressure and Cosmic rays is -65%. The correlation coefficients between HPGe gamma spectrum and input variables are not significant. The decrease of values of correlation coefficients of gamma spectrum and air pressure is present. The increase of values of correlation coefficients of gamma spectrum and Cosmic rays is present also. Increase in atmospheric pressure is resulting in negative correlation coefficient between HPGe and Cosmic rays' time series for low energy gamma spectrum. The more significant contribution of Cosmic rays in high energy gamma spectrum, as opposite to insignificant contribution of Cosmic rays to low energy gamma spectrum is evident. Lomb-Scargle periodograms showed daily periodicity for air temperature and humidity, and additional mid-daily periodicity for air pressure. There is no noticeable periodicity for each of energy ranges of gamma spectrum.

REFERENCES

1. Dragic Aleksandar, Udovicic Vladimir I, Banjanac Radomir M, Jokovic Dejan R, Maletic Dimitrije M, Veselinovic Nikola B, Savic Mihailo, Puzovic Jovan M, Anicin Ivan V "The New Set-Up in the Belgrade Low-Level and Cosmic-Ray Laboratory", NUCLEAR TECHNOLOGY & RADIATION PROTECTION, vol. 26, br. 3, pp. 181-192, 2011

2. S. Niese, "Underground laboratories for low-level radioactivity measurements", Analysis of Environmental Radionuclides, Ed. P.Povinec, Elsevier, Amsterdam, pp.209-239, 2008

3. A.Dragić, D.Joković, R.Banjanac, V.Udovičić, B.Panić, J.Puzović and I.Aničin, "Measurement of cosmic ray muon flux in the Belgrade ground level and underground laboratories", Nucl. Instr. and Meth. in Phys. Res. A591 , pp. 470 − 475, 2008

4. A. Dragić, R. Banjanac, V. Udovičić, D. Joković, I. Aničin and J. Puzović, "Comparative study of power spectra of ground and shallow underground muon data", Int. Journal of Modern Physics A, Vol. 20 pp. 6953-6955, 2005

5. A. Dragić, R. Banjanac, V. Udovičić, D. Joković, J. Puzović, I. Aničin, "Periodic Variations of CR Muon Intensity in the Period 2002-2004", Proc. 21st European Cosmic Ray Symposium, Košice, Slovakia, pp.368-373, 2008.

6. Banjanac Radomir M, Udovicic Vladimir I, Dragic Aleksandar, Jokovic Dejan R, Maletic Dimitrije M, Veselinovic Nikola B, Grabez Bojana S "Daily Variations of Gamma-Ray Background and Radon Concentration", ROMANIAN JOURNAL OF PHYSICS, vol. 58, br. , pp. S14-S21, 2013

7. Banjanac Radomir M, Dragic Aleksandar, Udovicic Vladimir I, Jokovic Dejan R, Maletic Dimitrije M, Veselinovic Nikola B, Savic Mihailo "Variations of gamma-ray background in the Belgrade shallow underground low-level laboratory", APPLIED RADIATION AND ISOTOPES, vol. 87, br. , pp. 70-72, 2014

8. V. Udovičić, B. Grabež, A. Dragić, R. Banjanac, D. Joković, B. Panić, D. Joksimović, J. Puzović, I. Aničin, "Radon problem in an underground low-level laboratory", Radiation Measurements 44 pp. 1009-1012. 2009

9. V. Udovičić, I. Aničin, D. Joković, A. Dragić, R. Banjanac, B. Grabež, N. Veselinović, "Radon Time-series Analysis in the Underground Low-level Laboratory in Belgrade, Serbia", Radiation Protection Dosimetry 145 (2-3) pp. 155-158, 2011

10. Maletic Dimitrije M, Udovicic Vladimir I, Banjanac Radomir M, Jokovic Dejan R, Dragic Aleksandar L, Veselinovic Nikola B, Filipovic Jelena Z "Comparison of Multivariate Classification and Regression Methods for the Indoor Radon Measurements", NUCLEAR TECHNOLOGY & RADIATION PROTECTION, vol. 29, br. 1, pp. 17-23 (2014)

11. Maletic Dimitrije M, Udovicic Vladimir I, Banjanac Radomir M, Jokovic Dejan R, Dragic Aleksandar L, Veselinovic Nikola B, Filipovic Jelena Z "Correlative and Multivariate Analysis of Increased Radon Concentration in Underground Laboratory", RADIATION PROTECTION DOSIMETRY, vol. 162, br. 1-2, pp. 148-151, 2014

12. Banjanac Radomir M, Maletic Dimitrije M, Jokovic Dejan R, Veselinovic Nikola B, Dragic Aleksandar, Udovicic Vladimir I, Anicin Ivan V "On the omnipresent background gamma radiation of the continuous spectrum", NUCLEAR INSTRUMENTS & METHODS IN PHYSICS RESEARCH SECTION A, vol. 745, br. , str. 7-11, 2014.

13. R. Brun and F. Rademakers, "ROOT - An Object Oriented Data Analysis Framework", Nucl. Inst. Meth. in Phys. Res. A 389, 81, 1997

14. A. Hoecker, P. Speckmayer, J. Stelzer, J. Therhaag, E. von Toerne, and H. Voss, "TMVA - Toolkit for Multivariate Data Analysis", PoS ACAT 040 (2007), arXiv:physics/070303

50

Pressure and temperature effect corrections of atmospheric muon data in the Belgrade cosmic-ray station

M Savić, D Maletić, D Joković, N Veselinović, R Banjanac, V Udovičić, A Dragić

Institute of Physics, University of Belgrade

Pregrevica 118, 11080 Belgrade, Serbia

E-mail: yokovic@ipb.ac.rs

Abstract. We present results of continuous monitoring of the cosmic-ray muon intensity at the ground and shallow underground level at the Belgrade cosmic-ray station. The cosmic-ray muon measurements have been performed since 2002, by means of plastic scintillation detectors. The scintillator counts are corrected for atmospheric pressure for the whole period of measurements and, as well, for vertical temperature profile for the period of the last six years. The results are compared with other correction methods available. One-hour time series of the cosmic-ray muon intensity at the ground level are checked for correlation with European neutron monitors, with emphasis on occasional extreme solar events, e.g. Forbush decreases.

1. Introduction

The Belgrade cosmic-ray station, situated in the Low-level Laboratory for Nuclear Physics at Institute of Physics, Belgrade, have been continuously measuring the cosmic-ray intensity since 2002. The station is at near-sea level at the altitude of 78 m a.s.l.; its geomagnetic latitude is 39° 32' N and geomagnetic vertical cut-off rigidity is 5.3 GV. It consists of two parts: the ground level lab (GLL) and the underground lab (UL); the UL is located at a depth of 12 metres below the surface, i.e. 25 metre water equivalent. At this depth practically only the muonic component is present. The cosmic-ray muon measurements are performed by means of plastic scintillation detectors, a pair of which is, along with instrumentation modules for data acquisition, placed in both the GLL and the UL. The set-up is quiet flexible, as the scintillators could be arranged in different ways, which allows conducting different experiments. The analyses of the measurements yielded some results on variations of the cosmic-ray muon intensity and on precise values of the integral muon flux at the ground level and at the depth of 25 m.w.e. [1,2,3,4].

2. Experimental set-up

The experimental set-up in both the GLL and the UL consists of a large plastic scintillation detector (rectangular shape, 100cm x 100cm x 5cm) and a data acquisition system (DAQ). The scintillator is polystyrene based UPS-89, with four 2-inch photomultiplier tubes attached to its corners, so that each PM tube looks at the rectangle diagonal. Preamplifier signals from two PM tubes looking at the same diagonal are summed in one output signal, thus two output signals are led to the DAQ from each scintillator.

The summed signals from the PM tubes on the same diagonal of the detectors are stored and digitized by the DAQ, which is based on 4-channel flash analog-to-digital converters (FADC), made by CAEN (type N1728B), with 100 MHz sampling frequency. The FADCs are capable of operating in

the event-list mode, when every analyzed event is fully recorded by the time of its occurrence and its amplitude. This enables the correlation of events, both prompt and arbitrarily delayed, at all four inputs with the time resolution of 10 ns. Single and coincident data can be organized into time series within any desired integration period. The FADCs can also be synchronized with each other for the additional coinciding of the events in the GLL and the UL.

   For both the GLL and the UL detector, two input channels on the corresponding FADC are reserved for events recorded by each of detector's diagonals. The cosmic-ray events recorded by a single diagonal are drown in the background. Coinciding of the prompt events from two diagonals within a narrow time window gives the resulting experimental spectrum of the plastic scintillator, which is the energy deposit (ΔE) spectrum of the cosmic-ray particles (figure 1). Interpretation of the experimental spectra and their features as well as their calibration have been done using Geant4 based Monte Carlo simulation [4,5]. The spectra peak at ~11 MeV and have the instrumental thresholds at ~4 MeV. Comparing the spectra of the GLL detector and the UL detector one can notice the obvious difference in their shape, especially in the low-energy part below ~6 MeV. This difference points to the contribution of the cosmic-ray electrons and gammas (electromagnetic component) to the ΔE spectra at the ground level, which is absent in case of the underground detector.
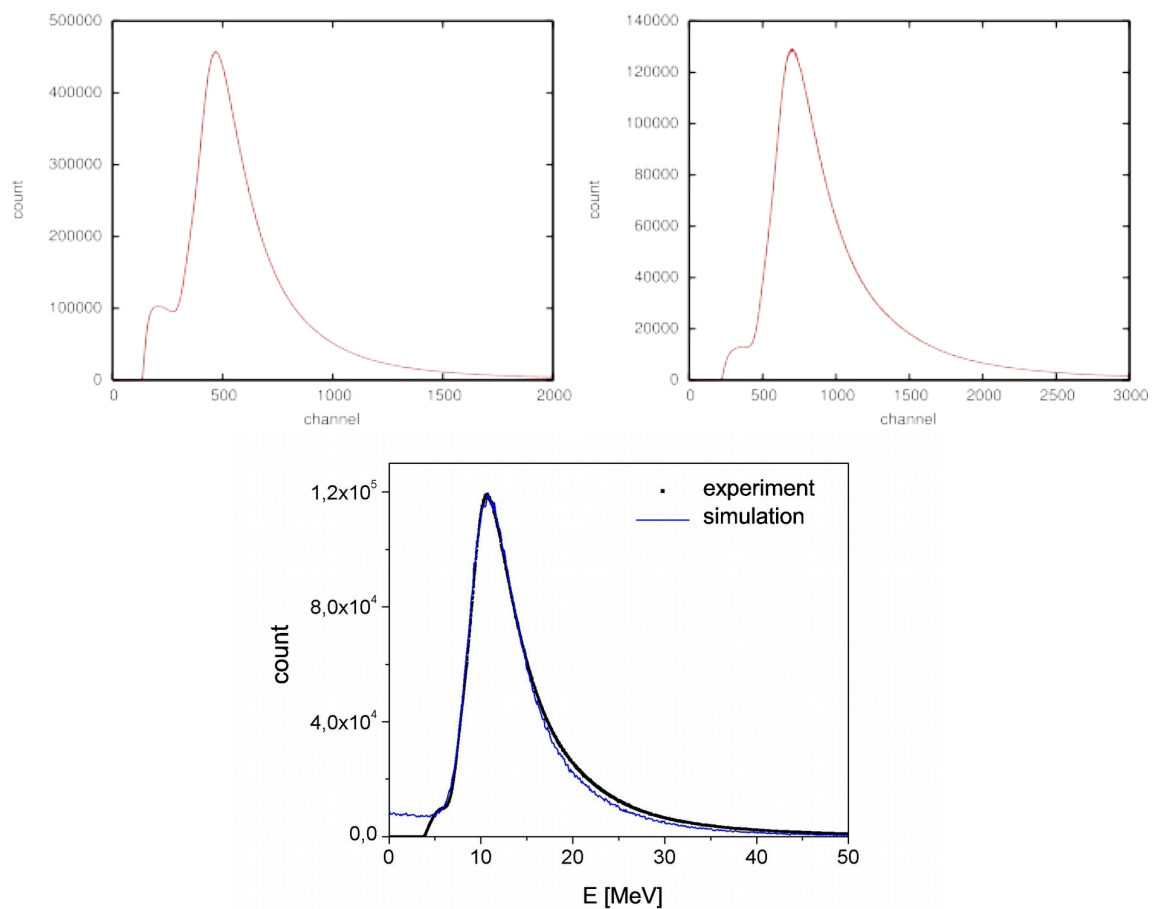
Figure 1. The cosmic-ray ΔE spectra of the GLL detector (top left) and the UL detector (top right). Experimental and simulated ΔE spectra of the UL detector (bottom).

3. Results and discussion

The cosmic-ray intensity data are automatically processed, using a web-based "robot" developed for this purpose, and published online at www.cosmic.ipb.ac.rs/muon_station. The online available data are raw scintillator counts in time series with resolution of 5 min or 1 h. Time series of the raw data are corrected for pressure and temperature effect; pressure corrections have been done for the whole data taking period and temperature effect corrections have been done for the the time period of the last six years.

3.1. Efficiency corrections

The first data corrections are related to detector assembly efficiency. As mentioned, the instrumental thresholds cut the spectra at ~3 MeV. However, the thresholds may vary, thus changing the initial spectrum and resulting in fluctuations of the integral spectrum count. Related to this, the necessary correction has been done by means of constant fraction discriminator (CFD) function (figure 2); with use of the CFD cut the spectrum fluctuations decreased significantly. The CFD is based on cut on chosen height as a percentage of peak height where the spectrum is cut. The simulation tells us that, for the underground detector, ~6% of muon events is also cut (figure 1).
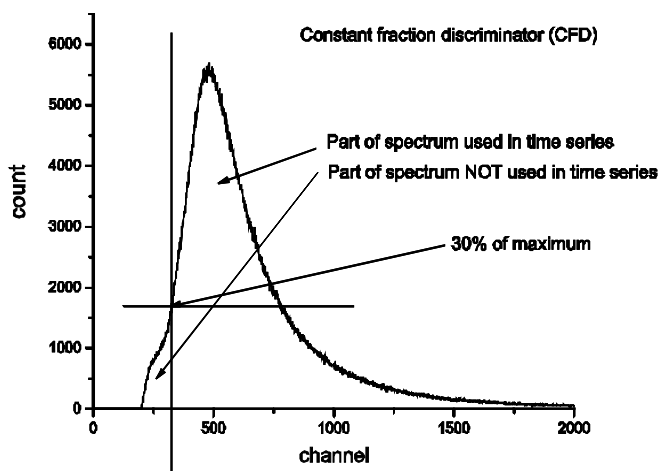
Figure 2. Constant fraction discriminator (CFD) applied in efficiency corrections. The obtained truncated spectrum is used for calculating time series.

The next step in the efficiency corrections is a correction of 5-min count values that are clearly lower than a mean 5-min count in surrounding time intervals. This undershoot comes at the beginning/end of runs, where events are not collected for all 5 min of measurement. The last and smallest correction is a correction of fluctuations of spectrum due to fluctuation in amplification which influence the cut on diagonals and efficiency of coincidence of two diagonals. We found that the CFD cut is proportional to efficiency of coincidence.

3.2. Corrections for atmospheric pressure and for temperature

Significant part of variation of cosmic ray muon component intensity can be attributed to meteorological effects. Here, two main contributors are barometric and temperature effect [6].

Barometric effect is caused by variation of the atmospheric mass above the detector. These pressure corrections are done by finding the linear regression coefficient, using only International Quiet Days, i.e. time series data from periods with more or less constant intensity of galactic cosmic rays, for creation of the distribution of scintillator counts vs. atmospheric pressure. Atmospheric pressure data are available due to on-site continuous measurement.
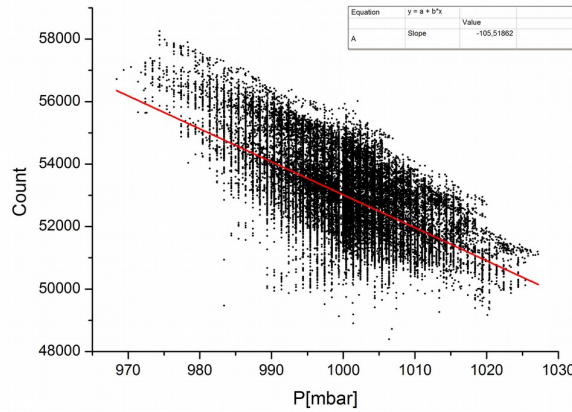
Figure 3. Dependence of 5-min counts on atmospheric pressure.

The temperature effect is related to the variation of the atmospheric temperature profile. The effect is two-fold, as it affects pion decay (positive contribution) as well as muon ionization losses and possible decay (negative contribution). To correct for these effects, integral correction method was applied [6,7]. The variation of the muon intensity due to temperature variations is calculated by using the formula:

$$\delta I_T = \int_0^{h_0} \alpha(h) \cdot \delta T(h) \cdot dh$$

where δI_T is the variation of the muon intensity due to the temperature effect, $\delta T(h)$ is the variation of the atmospheric temperature, which is calculated in reference to the mean temperature value for a given time period (denoted by index M): $\delta T(h) = T_M(h) - T(h)$, where h is atmospheric depth. Temperature coefficient densities $\alpha(h)$ are calculated according to [6].

Available meteorological models make it possible to have hourly atmospheric temperature profiles for 17 standard isobaric levels at the geographic position of the Belgrade muon station, necessary for application of formula shown above. The procedure used here is as described in [7]. Temperature profiles have been obtained from ftp://cr0.izmiran.rssi.ru/COSRAY!/FTP_METEO/blgd_Th/, courtesy of IZMIRAN laboratory.

3.3. Time series of the cosmic-ray intensity

In Figure 4 the count rate time series is shown for all corrections. First, the corrected count rate for efficiency corrected data is shown. Also, the atmospheric pressure and combined atmospheric pressure and temperature corrections time series of count rates are shown.

One-hour time series of the cosmic-ray muon intensity at the ground level are checked for correlation with European neutron monitors (NM), with emphasis on occasional extreme solar events, e.g. Forbush decreases.

In Figure 5 the comparison of time series of pressure corrected and pressure and temperature corrected count rates for the Belgrade muon station and Jungfraujoch, Rome, Baksan and Oulu neutron monitors is presented for Forbush candidate in March 2012. The count rates of neutron monitors are shifted to be close to each-other for visibility. The count rate for the Belgrade station is shown in percentages with additional shift down for visibility. The count rate drop for the neutron monitors is clearly more pronounced than for Belgrade muon monitor.
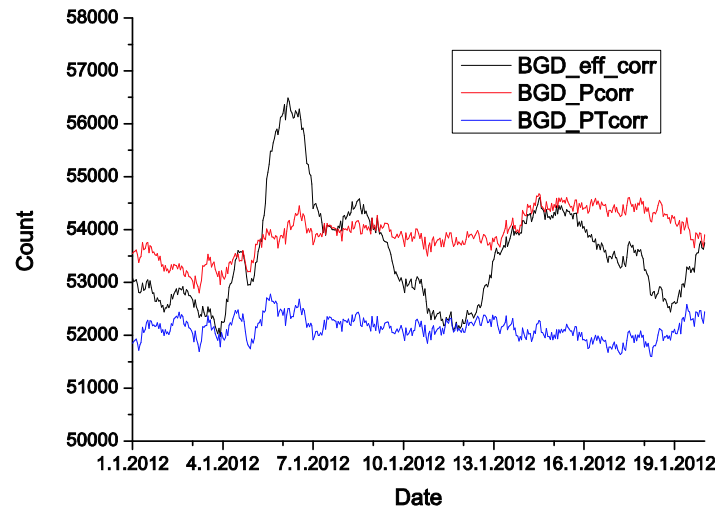
Figure 4. Time series of efficiency corrected, pressure corrected and pressure and temperature corrected counts.
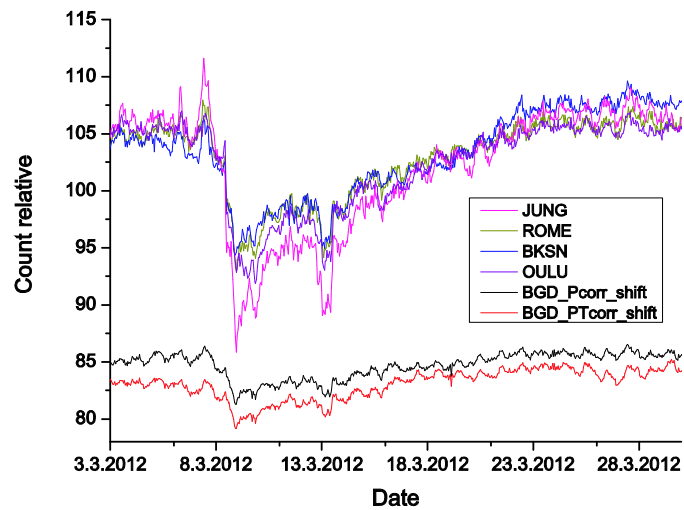
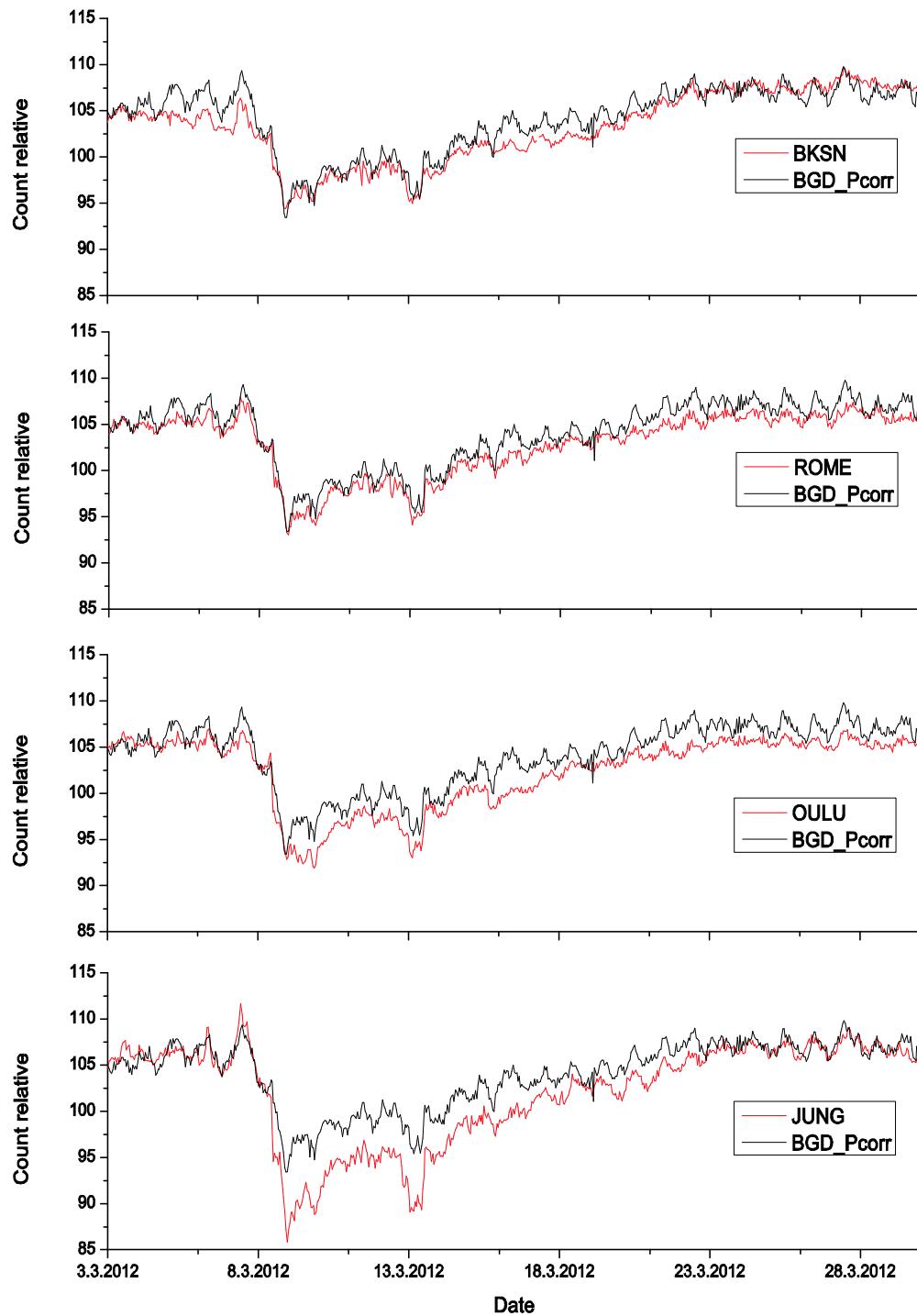Figure 5. Comparison of time series of pressure corrected and pressure and temperature corrected count rates for the Belgrade muon monitor station and neutron monitors. Count rates are shifted for comparison.

In Figure 6 the comparison of time series of pressure corrected count rates for the Belgrade muon station Jungfraujoch, Rome, Baksan and Oulu neutron monitors is presented. The count rates of neutron monitors are shifted to be close to each-other for visibility. The count rate for Belgrade station is scaled in the way that the drop in count rate is similar to most of the stations (except Jungfraujoch, which is at high altitude). The visual comparison shows the good correlation of the count rates of Belgrade muon monitor and neutron monitors, previously noticed using correlative analyses of count rates. The pressure corrected count rates from Belgrade muon monitor is only dataset used for visual comparison, since neutron monitor data are also only pressure corrected. This was also observed previously using correlative analyses of count rates.

Figure 6. Comparison of time series of pressure corrected count rates for the Belgrade muon monitor station and neutron monitors. Count rates are shifted and scaled for comparison.

4. Conclusions

The results of continuous monitoring of the cosmic-ray muon intensity at the ground and shallow underground level at the Belgrade cosmic-ray station are presented. The scintillator counts are corrected for atmospheric pressure for the whole period of measurements and, as well, for vertical temperature profile for the period of the last six years. The results are compared with other correction methods available and showed excellent agreement. One-hour time series of the cosmic-ray muon intensity at the ground level are checked for correlation with European neutron monitors, with emphasis on occasional extreme solar events, e.g. Forbush decreases. As a result of correlative analysis, the Forbush candidate in March 2012 is the best choice to be used for visual comparison presented in this work. The comparison showed high correlation of the Belgrade muon monitor with neutron monitors, especially geographically closer neutron monitors such as Rome NM. In some specific time periods, like during the Forbush candidate in March 2012, we showed that our muon measurement system has sensitivity comparable to European neutron monitors in this period, but still not as efficient as NM with better geographical position (at high altitude), e.g. Jungfraujoch in the Swiss Alps.

5. Acknowledgements

6. References

[1]   Dragić A, Banjanac R, Udovičić V, Joković D, Aničin I and Puzović J 2005 *Int. J. Mod. Phys.* A **20** 6953
[2]   Dragić A, Banjanac R, Udovičić V, Joković D, Puzović J and Aničin I 2008 *Proc. 21st European Cosmic Ray Symposium (Košice, Slovakia)* p 368
[3]   Dragić A, Banjanac R, Udovičić V, Joković D, Aničin I and Puzović J 2009 *Proc. 31st Int. Cosmic Ray Conf. (Lodz, Poland)*
[4]   Dragić A, Joković D, Banjanac R, Udovičić V, Panić B, Puzović J and Aničin I 2008 *Nucl. Instrum. Meth.* A **591** 470
[5]   Joković D, Dragić A, Udovičić V, Banjanac R, Puzović J and Aničin I 2009 *Appl. Radiat. Isot.* **67** 719
[6]   Dorman L.I. 2004 *Cosmic Rays in the Earth's Atmosphere and Underground* (Berlin: Springer)
[7]   Berkova M, Belov A, Eroshenko E and Yanke V 2012 *Astrophys. Space Sci. Trans.* **8** 41

Cosmic Rays Muon Flux Measurements at Belgrade Shallow Underground Laboratory

N. Veselinović [a], A. Dragić, D. Maletić, D. Joković, M. Savić, R. Banjanac, V. Udovičić, I. Aničin

Institute of Physics, University of Belgrade, Pregrevica 118, Belgrade, Serbia

[a] Corresponding author: veselinovic@ipb.ac.rs

Abstract. The Belgrade underground laboratory is a shallow underground one, at 25 meters of water equivalent. It is dedicated to low-background spectroscopy and cosmic rays measurement. Its uniqueness is that it is composed of two parts, one above ground, the other bellow with identical sets of detectors and analyzing electronics thus creating opportunity to monitor simultaneously muon flux and ambient radiation. We investigate the possibility of utilizing measurements at the shallow depth for the study of muons, processes to which these muons are sensitive and processes induced by cosmic rays muons. For this purpose a series of simulations of muon generation and propagation is done, based on the CORSIKA air shower simulation package and GEANT4. Results show good agreement with other laboratories and cosmic rays stations.

Belgrade Cosmic Rays Station

Cosmic rays are energetic particles from outer space that continuously bombard Earth atmosphere, causing creation of secondary showers made of elementary particles. For last hundred years, after Hess' discoveries, cosmic rays (CR) has been studied at almost every location accessible to research, from deep underground to above atmosphere [1]. Low-level and cosmic-ray lab in Belgrade is dedicated to the measurement of low activities and CR muon component. One of the objectives is also intersection of these two fields, namely, muon–induced background in gamma spectroscopy. Belgrade lab is relatively shallow underground laboratory [2] located at the right bank of river Danube on the ground of Institute of Physics in Belgrade. It is located at near-sea level at the altitude of 78 m a.s.l. and its geographic position is 44° 51' N and longitude 20° 23' E with geomagnetic latitude 39° 32' N and geomagnetic vertical cut-off rigidity 5.3 GV. The lab has two portions, ground level portion (GL) is situated at the foot of the vertical loess cliff. Other portion, the underground level (UL) is dug into the foot of the cliff and is accessible from the GL via horizontal corridor as can be seen at Fig.1. Working area of UL has three niches for independent experiments.
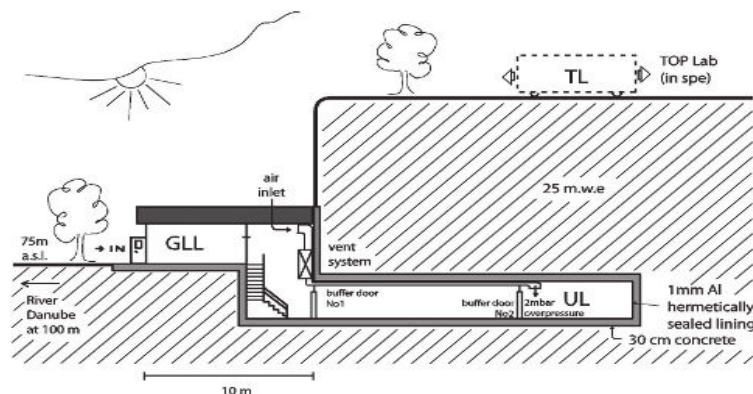

FIGURE 1. Scheme of low-level and CR laboratory at Institute of Physics, Belgrade

The overburden of the UL is about 12 meters of loess soil, which is equivalent to 25 meters of water. The walls are made of 30 cm thick reinforced concrete and covered with the hermetically sealed Al lining 1 mm thick, to

prevent the radon from the soil to diffuse into the laboratory. The low-level laboratory is equipped with an air ventilation system which keeps 2 mbar overpressure in the UL, in order to minimize radon diffusion through eventual imperfections in the Al lining.

Experimental Set-up

The equipment of the lab consists of two identical set of detectors and analyzing electronics. One set is situated in the GL and other in the UL. Each set is composed of gamma spectrometer and muon detectors. For muon measurements a pair of plastic scintillator detectors is used. One of the detectors is small, 50 cm x 23 cm x 5 cm plastic scintillator detector, with a single PMT looking at its longest side via a Perspex light guide tapering to the diameter of a PMT, made by JINR, Dubna, Russia, and assembled locally. The other, larger one has dimensions of 100 cm x 100 cm x 5 cm, equipped with four PMT directly coupled to the corners beveled at 45°,made by Amcrys-H, Kharkov, Ukraine. The smaller detector may serve as a check of stability of the muon time series obtained from the larger detector, which is important for long term measurements. It can also be used (in coincidence with the larger detector) for measurements of the lateral spread of particles in CR showers and decoherence. Plastic scintillation detectors are also employed for active shielding of gamma spectrometers. In the UL, a 35% efficiency radio-pure p-type HPGe detector, made by ORTEC, 12 cm thick cylindrical lead castle is deployed around the detector. One of the set-ups is presented at Fig.2. Another HPGe detector, of 10% efficiency, is placed in GL.

FIGURE 2. Detectors in the underground laboratory. Large scintillator detector is placed above HPGe and small scintillator can change position.

Data acquisition system is identical both in UL and GL and it has two flash analog to digital converter (FADC), one in each laboratory, made by CAEN (type N1728B). These are versatile instruments, capable of working in two modes, energy histogram mode when performing as digital spectrometers or, in the oscillogram mode, when they perform as digital storage oscilloscopes. In both modes, they sample at 10 ns intervals into 2^{14} channels in four independent inputs. The full voltage range is ±1.1 V. They are capable of operating in the list mode, when every analyzed event is fully recorded by the time of its occurrence and its amplitude. This enables the correlation of events, both prompt and arbitrarily delayed, at all four in puts with the time resolution of 10 ns. Single and coincident data can be organized into time series within any integration period from 10 ns up. The two N1728B units are synchronized, enabling coincidence/correlation of the events recorded in both of them. The flexible software encompassing all above said off-line analyses is user-friendly and entirely homemade. The preamplifier outputs of the PMT of the larger detectors are paired diagonally. Signals from these paired inputs are later coincided off-line and their amplitudes added to produce the single spectra. This procedure suppress low-energy portion of the background spectrum (up to some 3 MeV), mostly environmental radiation, leaving only high-energy loss events due to CR muons and EM showers that peak at about 10 MeV, shown at Fig 3. The output of the PMT of the smaller detector is fed to the third input of FADC. [3]
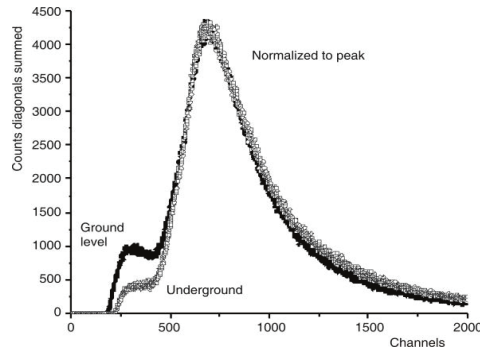
FIGURE 3. The sum spectra of two diagonals of the large plastic detectors in the UL and GLL. For comparison, the spectra are normalized for the peaks to coincide. Channel 650 corresponds to the muon energy loss of 10 MeV.

Simulation and Results

The experimental set-up is rather flexible, thus allowing different studies of the muon and electromagnetic components of cosmic rays at the ground level and at the shallow depth underground. The cosmic-ray muon flux in the underground laboratory has been determined from data taken from November 2008 till June 2013 (there were some small gaps in recording data during this period). These measurements yielded the precise values of the integral cosmic ray muon flux at the location of Belgrade. Measured muon flux is: 137(6) $m^{-2}s^{-1}$ at the ground level and 45(2) $m^{-2}s^{-1}$ at the underground level [4]. Different analyses of time series of these measurements have also been performed. Interpretation and calibration of the experimental spectra has been done using Monte Carlo simulation packages CORSIKA and Geant4 [5, 6]. CORSIKA simulates extensive air showers generated by the primary cosmic-rays in interactions with air nuclei at the top of the atmosphere. It gives spectra of the secondary cosmic-rays at the preferred observation level. These secondary particles, their energy and momentum direction distribution, obtained by CORSIKA, are then used as an input for the Geant4 based simulation of the detectors. In this simulation, particles first traverse through soil and infrastructure of the UL lab before hitting the detector. Then the response of the plastic scintillation detectors is simulated. For the UL scintillators, the simulated spectra are shown in Fig. 4.[7]

They agree very well with the experimental ones, except in the low-energy part where the ambiental gamma radiation is mostly present and where the cuts are applied. We also used these simulation packages to simulate different experimental set-ups and to obtain information about lower cut-of energy of primary cosmic rays at our site and for single muons and muons in coincidence. Energy of the primary particles from which detected muons originate increases for UL compared to GL but also for muons in coincidence compared with single detected muons.
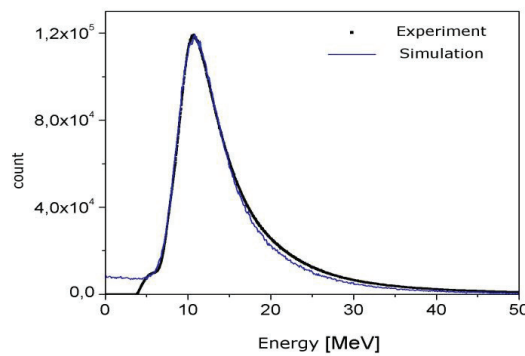

FIGURE 4. Experimental vs simulated spectrum of large plastic scintillator detector at UL

These measurements allow us to study fluctuations in muon flux intensity during the rising phase of Solar Cycle 24 and to make five-minutes or one-hour time series of the flux. The scintillator counts are corrected for atmospheric pressure for the whole period of measurements and, as well, for vertical temperature profile for the period of last six years. The results are compared with other correction methods available. One-hour time series of the cosmic ray muon intensity at the ground level are checked for correlation with European neutron monitors (NM), with emphasis on occasional extreme solar events, e.g. Forbush decreases (FD) in order to investigate claims of influence of cosmic-rays on cloud formation and climate [8,9] In some specific time periods, like during the FD in March 2012, we showed that our muon measurement system has sensitivity comparable to European neutron monitors in this period, but still not as efficient as NM with better geographical position (at high altitude), e.g. Jungfraujoch in the Swiss Alps.These results are presented at Fig. 5. Due to fact that muons detected underground originate from primary particles with energy around and above the limit for solar modulation time series from UL are less sensitive to these Solar events.

FIGURE 5. Time series for March 2012 recorded at NM at Jungfraujoch compared to time series obtained at Belgrade cosmic-rays station

References

[1] L.I. Dorman, *Cosmic-rays in the Earth's Atmosphere and Underground*, Kluwer, Dordrecht, 2004.

[2] S. Niese, *Underground laboratories for low-level radioactivity measurements*. Analysis of Environmental Radionuclides, 209-240, (2008) P.P. Povinec, ed.,Elsevier, Amsterdam.

[3] A.Dragić, V.Udovičić, R.Banjanac, D.Joković, D.Maletić, N.Veselinović, M.Savić, J.Puzović, I.Aničin, *The new set-up in the Belgrade low-level and cosmic-ray laboratory*, Nucl. Technol. Radiat. 26 (2011) 181-192

[4] A. Dragić, D. Joković, R. Banjanac, V. Udovičić, B. Panić, J. Puzović, I. Aničin, *Measurement of cosmic ray muon flux in the Belgrade ground level and underground laboratories*, Nuclear Instruments and Methods in Physics Research A 591 (2008) 470-475.

[5] D. Heck, *CORSIKA: a Monte Carlo code to simulate extensive air showers*, Report FZKA 6019, Forschungszentrum Karlsruhe, 1998.

[6] S. Agostinelli et al., *the Geant4 collaboration*, Nucl. Instrum. and Meth. A 506 (2003) 250-303

[7] A.Dragić, R. Banjanac, V. Udovičić, D. Joković, J.Puzović, I Aničin, I., *Periodic Variations of CR Muon Intensity in the Period 2002-2004* Proceedings of the 21st European cosmic-ray Symposium, Košice, Slovakia (2008) 368-373.

[8] A.Dragić, I.Aničin, R.Banjanac, V.Udovičić, D.Joković, D.Maletić, J.Puzović, *Forbush decreases - clouds relation in the neutron monitor era,* Astrophys. Space Sci. Trans. 7 (2011) 315-318.

[9] H. Svensmark, *Cosmoclimatology: a new theory emerges*, Astron. Geophys. 48 (2007) 1.18-1.24.

New empirical methods for correction of meteorological effects on cosmic ray muons

M. Savić,[a,*] **A. Dragić,**[a] **D. Maletić,**[a] **N. Veselinović,**[a] **D. Joković,**[a] **R. Banjanac,**[a] **V. Udovičić**[a] **and D. Knežević**[a]

[a] *Institute of Physics Belgrade,*
Pregrevica 118, 11080 Belgrade, Serbia
E-mail: msavic@ipb.ac.rs

Flux of muon component of secondary cosmic rays is affected by varying conditions in the atmosphere. Dominant effects are barometric and temperature effect, which reflect variations of atmospheric pressure and atmospheric temperature respectively. Precise modelling and correction for these meteorological effects significantly increases sensitivity of Earth-based muon detectors to variations of primary cosmic ray flux. We are presenting two recently developed empirical methods for correction of meteorological effects on cosmic ray muons. First method is based on principal component analysis, while second employs multivariate analysis using machine learning techniques. Both methods are applied for correction of barometric and temperature effects, but can easily be generalised to take more atmospheric parameters into account. We apply these corrections to muon count rates measured by Belgrade cosmic ray station and study their effect on sensitivity of detection of periodic and aperiodic flux variations of primary cosmic rays. Comparison with the most widely used method for correction of meteorological effects – integral method, as well as with neutron monitor data, demonstrates very high effectiveness of presented methods.

---

*Presenter

1. Introduction

Cosmic ray muons (hard component of secondary cosmic rays) are affected by variations of atmospheric parameters as they propagate toward Earth. There are a number of meteorological effects that affect cosmic ray muon flux, most prominent being the *barometric (pressure) effect* and the *temperature effect*, which depend on atmospheric pressure and atmospheric temperature respectively. Apart from fundamental, precise modelling of these effects also has practical importance, as it allows for correction that significantly increases the sensitivity of ground based muon monitors to variations of primary cosmic rays.

A number of methods for correction of barometric and temperature effect have been developed over the years. Some (i.e. method of effective level of generation [1]) are empirical in nature, while others (most notably integral method) rely on the theory of meteorological effects, developed by Dorman [2] among others. All these methods are at least in some part approximative, but for all intents and purposes we have decided to use the integral method as a reference in our analysis, as it gives the most complete treatment of the problem.

The idea behind the work presented here is to try and develop a new, easy to use empirical method, less approximative in nature, compare it to the reference integral method, and investigate whether a more precise model of meteorological effects can be constructed, and possibly some additional information extracted. In order to most completely treat the meteorological effects, both atmospheric pressure and full atmospheric temperature profile need to be taken into account. For analysis that involves that many potentially highly correlated input variables, we have decided to employ modern techniques used for decorrelation and dimensionality reduction, and introduce two new methods for modelling and correction of meteorological effects - *PCA method* based on principal component analysis (PCA), and *MVA method* based on multivariate analysis (MVA) via use of machine learning. Though these two are somewhat similar in nature, a more "hands on" approach of the PCA method can offer a somewhat different insight than the more "blackbox" machine learning approach.

2. Data

2.1 CR data

Muon count rates used in this analysis were measured in the Ground Level Laboratory (GLL) of the Low Background Laboratory for Nuclear Physics, at the Institute of Physics Belgrade [3]. More detailed description of the laboratory and current detector system can be found in some of our previous work [4]. Muon count rates can have arbitrary time resolution but five-minute and hour sums were used in the analysis. For quality and consistency of data reasons, and to remove potential biases due to annual variation, data for a period of one year (from 01.06.2010 to 31.05.2011) were selected.

2.2 Meteo data

This analysis requires information about both atmospheric pressure and vertical atmospheric temperature profile. Data about atmospheric pressure is readily available from the Republic Hydrometeorological Servis of Serbia. As for the vertical temperature profile data, temperatures for 24
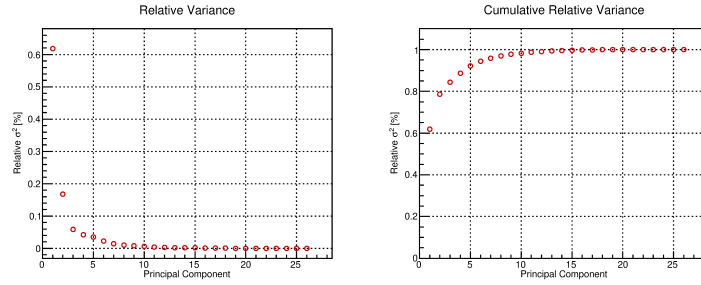
2

Figure 1: Relative variance (left) and cumulative relative variance (right) for all 26 principal components.

isobaric levels modelled by the Global Forecast System (GFS) [5] were used, starting from the top layer of the atmosphere (10 mb), to the level just above ground level (975 mb). For the above ground layer, locally measured temperature was used as the model was performing poorly there. More details about the preparation of meteorological data is available elsewhere [7].

3. Methodology

3.1 PCA method

Principal component analysis is a well established technique for dimensionality reduction of complex problems that involve large number of correlated variables, and as such very well suited for application to our problem. Using principal component decomposition we have transformed the initial set of correlated meteorological variables (locally measured atmospheric pressure, 24 modelled temperatures, and locally measured ground temperature) to a set of 26 uncorrelated principal components.

Using a series of tests typically used in such analysis (cumulative percentage rule, modified Kaisser's rule, mean eigenvalue rule, ...), we have determined that the first six components (responsible for close to 95% of total variance, as seen on Figure 1) are significant. Composition of the these components is shown on Figure 2, where variables on the x-axis are atmospheric pressure followed by atmospheric temperatures, starting from the top layer of the atmosphere.

Correlative analysis of muon count rate and significant principal components showed practically no correlation between measured muon count rate and the second principal component, further reducing the set of principal components to five. This is an interesting results as this component, mainly composed of lower stratosphere and upper troposphere temperatures, is responsible for close to 17% of total variation of meteorological variables.

Finally, we have determined the muon count rate corrected for meteorological effects according to formula:

$$N_\mu^{(corr)} = N_\mu - \langle N_\mu \rangle \sum_i k_i PC_i, \quad i = 1, 3, 4, 5, 6 \tag{1}$$

where $N_\mu^{(corr)}$ is corrected, N_μ measured and $\langle N_\mu \rangle$ mean muon count rate, while k_i, that correspond to principal components PC_i, are coefficients determined by linear regression, as shown on Figure 3. Full analysis and results are presented in more detail in our other work [8].
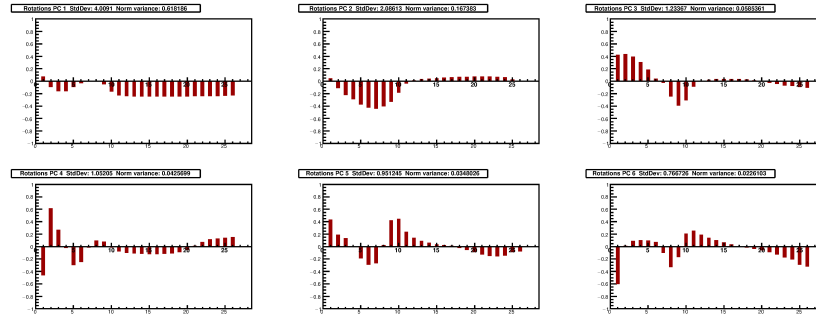
Figure 2: Composition for six most significant principal components. Meteorological variables are on the x-axis, first one being atmospheric pressure, followed by atmospheric temperatures (starting with the top layer of the atmosphere and ending with the ground level).
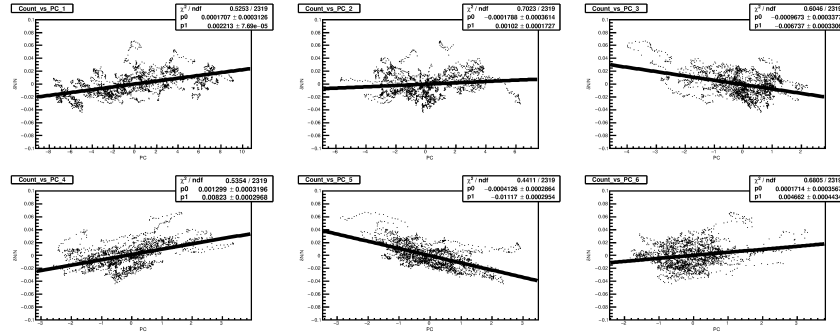

Figure 3: Muon count rate dependence on principal components for six most significant components, distributions fitted with linear function.

3.2 MVA method

Multivariate analysis utilising machine learning techniques can be a powerful tool for modelling of highly correlated systems. We have tested a number of algorithms implemented in Toolkit for Multivariate Data Analysis (TMVA), which has been successfully used for classification and regression problems in particle physics. For us, regression application is of greater interest, as the idea is to train and test multivariate algorithms on a subset of data (for geomagnetically quiet days), where most of the variation can be attributed to atmospheric effects, using meteorological variables as input and muon count rate as the target value. Trained algorithms can be then used on a full data set to predict the muon count rate (which would ideally depend only on meteorological parameters), and corrected muon count rate can be calculated using the formula:

$$N_\mu^{(corr)} = \Delta N_\mu + \langle N_\mu \rangle, \quad \Delta N_\mu = N_\mu^{(mod)} - N_\mu, \tag{2}$$

where $N_\mu^{(corr)}$ is corrected, N_μ measured, $N_\mu^{(mod)}$ modelled, and $\langle N_\mu \rangle$ is mean muon count rate.

Minimal average quadratic deviation of modelled from measured value was the only criterion used for optimisation of algorithm parameters in the training phase, so a series of tests have been
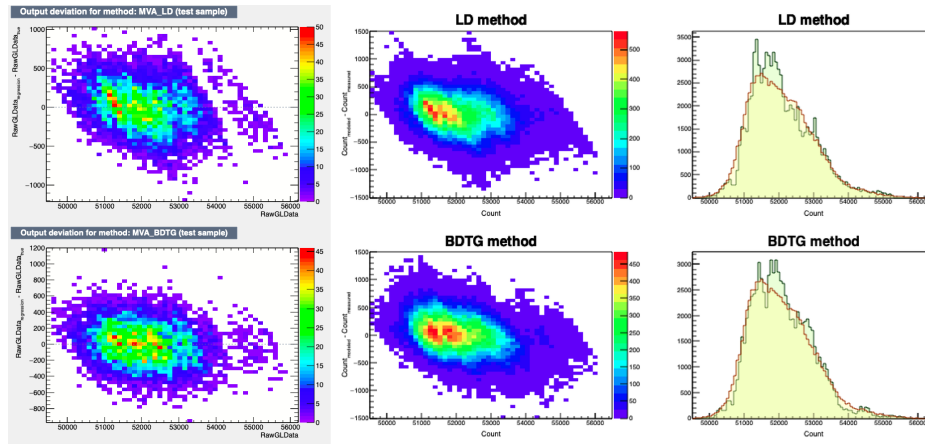
Figure 4: Modelled count rate and its deviation from measured count rate as a function of measured count rate for LD (top) and BDTG (bottom) algorithms. Deviation distributions for test data set are on left, for the full data set are in the middle, while distributions of modelled count rate (compared with the measured one) are on the right.
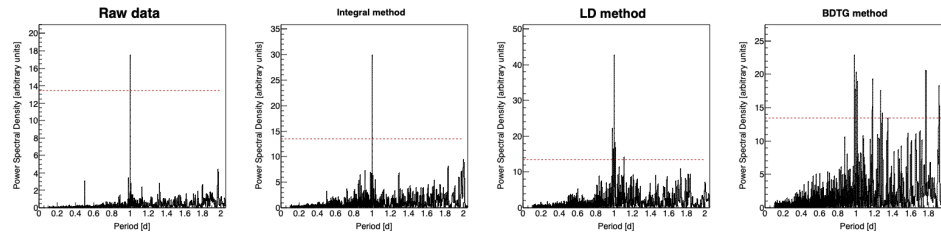

Figure 5: Power spectra for periods in the interval [0, 2] days, for measured data (far left), and data corrected using integral (central left), LD (central right) and BDTG (far right) methods.

devised in order to investigate the consistency of application of trained algorithms and minimise the possibility of artificial features being introduced.

Some of the tests included comparison of distributions of residual deviation of modelled from measured data for the test and full data set, or looking for anomalous features in distributions of modelled count in comparison with measured count distribution (both types of distributions for selected algorithms shown in Figure 4.

Based on these tests, the best performing algorithm proved to be LD (Linear Discriminant method), which is closely related to PCA approach. The second best potential candidate was BDTG (Gradient Boosted Decision Tree method), but there are probably some limits to its applicability, as indicated by spectral analysis (Figure 5). From the remaining tested methods, algorithms based on probability density techniques performed more poorly, which was not that surprising as the problem analysed here involves highly linear dependencies, but poor performance of methods based on neural networks was not expected, and possibly some improvement can be made there.
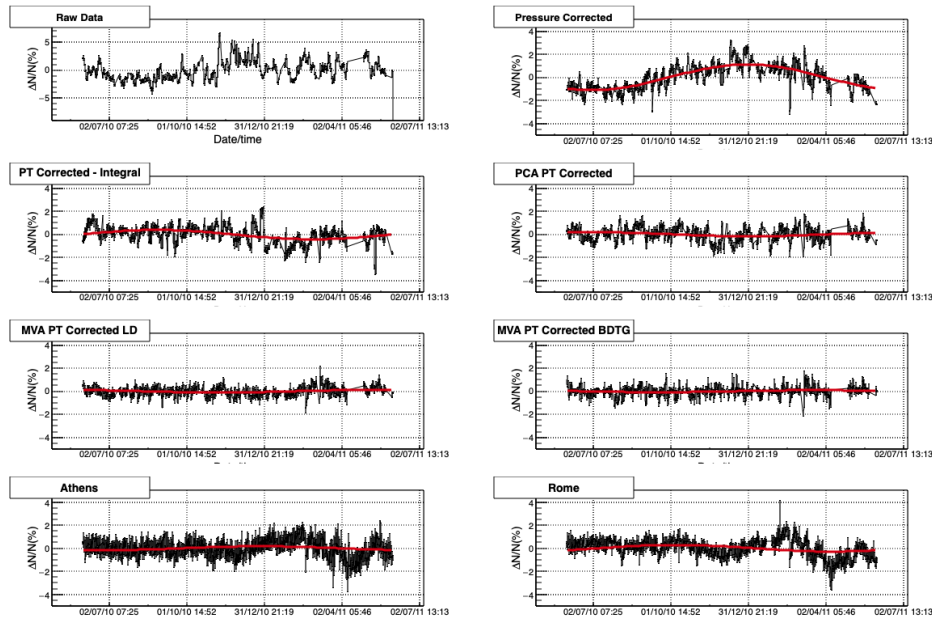
Figure 6: Muon count rate time series and reference neutron monitor data for the period of one year (01.06.2010-31.05.2011), fitted with sine function with a period of one year.

4. Results

4.1 Effect of corrections on periodic CR variations

One way to assess the performance of different methods for correction of meteorological effects could be to compare the efficiency with which they remove the annual variation due to temperature variation. In order to determine this variation, we have fitted pressure corrected data with a sine function, with a period of one year. Amplitude determined from such fit is then used as an estimate of magnitude of the annual variation. The same procedure was used to determine the residual annual variation after the correction via use of different methods (Figure 6). As neutron monitor count rates are usually considered to negligibly depend on atmospheric temperature (at least in the first approximation), we can treat their time series the same way in order to estimate the expected annual variation magnitude.

Table 1 shows amplitudes for the annual variation calculated based on plots in Figure 6, as well as reduction in annual variation relative to pressure corrected data. As can be seen, values for PCA and LD methods are closer to the estimates based on the neutron monitor data than the integral method value, while for BDTG method the value is somewhat smaller.

4.2 Effect of corrections on aperiodic CR variations

To study the effect of corrections on aperiodic variations we have selected the most intense Forbush decrease event in the one year period used for the analysis. For the event that occurred on 18.02.2011, we determined the amplitude of decrease for data corrected via different methods and reference neutron monitors, using procedure suggested by Barbashina et al. [9] (as shown on

Method/ Neutron monitor	P corr.	Integral	PCA	LD	BDTG	Athens	Rome
Annual amplitude [%]	1.11(9)	0.40(3)	0.18(5)	0.11(3)	0.086(9)	0.17(5)	0.29(1)
Relative reduction [% of P corrected]	-	64(10)	84(28)	90(30)	92(30)	-	-

Table 1: Amplitude and reduction of the amplitude of annual variation relative to pressure corrected data (P corr.) for pressure and temperature corrected data (using integral and selected multivariate methods). Athens and Rome neutron monitor data also included for reference
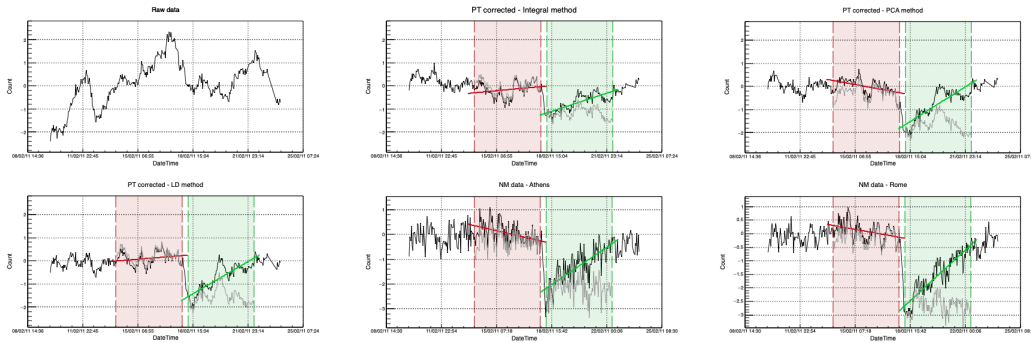
Figure 7: Muon count rate time series and reference neutron monitor data for the period around the Forbush decrease event of 18.02.2011. Highlighted intervals are used for detrending and calculation of decrease amplitude.

Method/ Neutron monitor	Integral	PCA	LD	BDTG	Athens	Rome
FD amplitude [%]	1.38(14)	1.52(21)	1.96(18)	1.10(13)	1.97(15)	2.68(15)
Relative FD amplitude	4.31(44)	4.90(66)	7.09(65)	4.78(56)	5.30(40)	8.65(48)

Table 2: Amplitudes and relative amplitudes for the Forbush decrease event of 18.02.2011 for pressure and temperature corrected muon data and reference neutron monitors

Figure 7). Additionally, as a measure of sensitivity to such events, we have introduced amplitude calculated relative to standard deviation of count rates leading up to the event.

Values for thusly calculated amplitudes and relative amplitudes are shown in Table 2. LD algorithm has values comparable to neutron monitor values, but that is at least in part due to somewhat larger calculated amplitude. This is most likely a feature pertaining to the specific event, as preliminary results for other events outside the interval used in this work show values closer to expected.

7

5. Conclusions

Two new methods for correction of meteorological effects on cosmic ray muons are introduced. Both are fully empirical, require knowledge about the atmospheric pressure and atmospheric temperature profile and can be applied to any muon monitor. The effect on reduction of the annual variation of CR data, as well as the effect on sensitivity of FD event detection was compared to the integral method and reference neutron monitor data. Their effectiveness was comparable or possibly better than for the integral method, allowing for the possibility that a part of meteorological effects is not taken into account by theory.

References

[1] A Duperier, "The Meson Intensity at the Surface of the Earth and the Temperature at the Production Level", in Proceedings of the Physical Society. Section A, volume 62, number 11, pages 684, year 1949, doi: 10.1088/0370-1298/62/11/302

[2] Dorman, L. I., "On the temperature effect of the hard component of cosmic rays", in Reports of Academy of Sciences of USSR (DAN SSSR), volume 95, issue 1, pages 49 - 52, year 1954b

[3] Low Background Laboratory for Nuclear Physics, url: http://www.cosmic.ipb.ac.rs/

[4] Dragic Aleksandar, Udovicic Vladimir, Banjanac Radomir, Jokovic Dejan, Maletic Dimitrije, Veselinovic Nikola, Savic Mihailo, Puzovic Jovan, Anicin Ivan, "The New Set-Up in the Belgrade Low-Level and Cosmic-Ray Laboratory", in NUCLEAR TECHNOLOGY AND RADIATION PROTECTION, volume 26, number 3, pages 181-192, year 2011, doi: 10.2298/NTRP1103181D

[5] GFS, url: https://www.ncdc.noaa.gov/data-access/model-data/model-datasets/global-forcast-system-gfs

[6] Berkova M., Belov A., Eroshenko E., Yanke Victor, "Temperature effect of muon component and practical questions of how to take into account in real time", in Astrophysics and Space Sciences Transactions, year 2012, pages 41-44, volume 8, doi: 10.5194/astra-8-41-2012

[7] Savic Mihailo, Dragic Aleksandar, Veselinovic Nikola, Udovicic Vladimir, Banjanac Radomir, Jokovic Dejan, Maletic Dimitrije, "Effect of pressure and temperature corrections on muon flux variability at ground level and underground", in "25th European Cosmic Ray Symposium", Torino, Italy, eprint: 1701.00164, year 2016

[8] Savic Mihailo, Dragic Aleksandar, Maletic Dimitrije, Veselinovic Nikola, Banjanac Radomir, Jokovic Dejan, Udovicic Vladimir, "A novel method for atmospheric correction of cosmic-ray data based on principal component analysis", in ASTROPARTICLE PHYSICS, volume 109, pages 1-11, year 2019, doi: 10.1016/j.astropartphys.2019.01.006

[9] Barbashina N., Dmitrieva Anna, Kompaniets K., Petrukhin A., Timashkov D., Shutenko V., Yakovleva Elena, Yashin, Igor, "Specific features of studying Forbush decreases in the muon flux", in Bulletin of The Russian Academy of Sciences: Physics, year 2009, pages 343-346, volume 73, doi: 10.3103/S1062873809030198

6.3 From motivation through the national radon survey to European indoor radon map

Vladimir Udovičić[1], Dimitrije Maletić[1], Maja Eremić Savković[2], Sofija Forkapić[3]

[1] Institute of Physics Belgrade, University of Belgrade, Belgrade, Serbia

[2] Serbian Radiation Protection and Nuclear Safety Agency, Belgrade, Serbia

[3] Department of Physics, Faculty of Science, University of Novi Sad, Novi Sad, Serbia

E-mail: udovicic@ipb.ac.rs

By 2014, radon issues were treated in Serbia through the scientific research projects. Among radon professionals, there was always the desire to create a radon risk map first of all. In 2014, with a certain amount of lucky circumstances, there was a chance that the radon problem would be raised to the national level. In that sense, Serbia has started to work on the national radon action plan (RAP), and in 2014 made its decision to perform the first national indoor radon survey. The responsibility for the establishment RAP and make indoor radon map in Serbia is on national regulatory body in the field of radiation protection: Serbian Radiation Protection and Nuclear Safety Agency (SRPNA). The project was supported by the IAEA through the technical cooperation programme. In this work, the planning and execution of the survey, including sampling design of the first national indoor radon survey are described in detail. Also, the results from national indoor radon survey and indoor radon mapping based on GPS coordinates was transformed to square map by creating a 10 km x 10 km squares where the starting point (0,0) is the center of Belgrade - Slavia Square are presented. To complete our work, we prepare data from the first Serbian indoor radon survey together with the data from indoor radon survey of Vojvodina, north province of Republic of Serbia performed during 2002-2005, and send to European Indoor Radon Map Group in JRC, Ispra, Italy.

AN OVERVIEW OF THE RADON RESEARCH IN THE INSTITUTE OF PHYSICS BELGRADE

Vladimir Udovičić, Dimitrije Maletić, Aleksandar Dragić,
Radomir Banjanac, Dejan Joković, Mihailo Savić and Nikola Veselinović
Institute of Physics, University of Belgrade, Belgrade, Serbia
udovicic@ipb.ac.rs

INTRODUCTION

Radon studies in the Institute of Physics Belgrade last a few decades. The first project related to radon was searching for connection between radon variability in soil and water and seismic activity in Montenegro [1]. After that, in the Low-Background Laboratory for Nuclear Physics, Institute of Physics Belgrade, the new research topics of rare nuclear processes was in the scientific focus. There was the need to build up the laboratory space to accomplish this type of research. In the 1997, underground low-background laboratory was built in, with the aim of investigating the rare nuclear processes. In the laboratory of this type, the influence of radon on the natural background radioactivity is dominant and there is an imperative that radon levels must be as low as it possible, with minimal time variation. In that sense, continuous radon monitoring became the mandatory activity. This paper presents the results of many years of radon monitoring in the underground low-background laboratory in the Institute of Physics Belgrade.

Besides radon monitoring in the laboratory, we work on several research topics regarding radon: using multivariate classification and regression methods, as developed for data analysis in high-energy physics and implemented in the TMVA software package, to study connection of climate variables and variations of radon concentrations, modelling of the indoor radon behaviour and radon mapping. All these research activities are presented in this work in more details.

RADON MONITORING IN THE UNDERGROUND LOW-BACKGROUND LABORATORY

The Low-Background Laboratory for Nuclear Physics at the Institute of Physics in Belgrade is a shallow underground laboratory (Figure 1). The laboratory was built in the loamy loess cliff on the bank of the river Danube with the overburden of 12 m of soil. It has an active area of about 60 m^2.

The walls, the floor and the ceiling of the laboratory are built of reinforced concrete of 30 cm thickness. From the measurements of the absolute flux of cosmic-ray muons in the underground as well as in the ground level laboratory [2] it was estimated that the equivalent depth of the laboratory is about 25 m.w.e. (a shielding thickness of the overburden soil expressed as water equivalent thickness). Description of the laboratory is presented in more detail elsewhere [3].
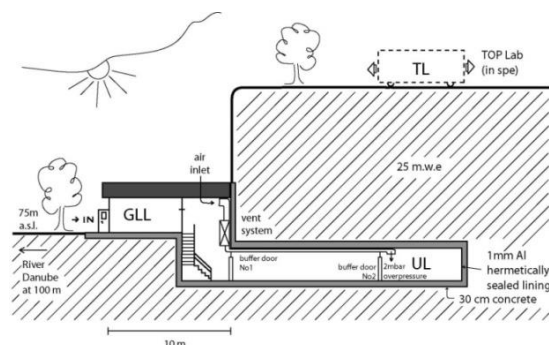

Figure 1. Cross-section of the underground low-background laboratory at the Institute of Physics Belgrade.

The system for the reduction of radon concentration in the laboratory consists of three stages. First, the active area of the laboratory is completely lined up with aluminium foil of 1 mm thickness, which is hermetically sealed with a silicon sealant to minimize the diffusion of radon from surrounding soil and concrete used for construction. The second one is the ventilation system. The laboratory is continuously ventilated with fresh air, filtered through one rough filter for dust elimination followed by the battery of coarse and fine charcoal active filters. The inlet of air is outside of the laboratory, at the height of 2.5 m above the ground. Finally, the parameters of the ventilation system are adjusted so as to result in an overpressure of about 2 mbar over the atmospheric pressure, which further prevents radon diffusion through eventual imperfections in the aluminium layer.

The device for the performed short-term radon measurements is SN1029 radon monitor (manufactured by the Sun Nuclear Corporation, NRSB approval code 31822) with the following characteristics: the measurement range from 1 Bq m^{-3} to 99.99 kBq m^{-3}, accuracy equal to ±25 %, sensitivity of 0.16 counts hour per Bq m^{-3}. With these characteristics, SN1029 radon monitor is defined as a high-sensitivity passive instrument

344

for the short-term radon measurements and it is an optimal solution for radon monitoring in the underground laboratory.

The radon data from radon monitor device SN1029 for the period of 3 years are spectrally analysed. The Lomb-Scargle periodogram analysis method has been used in spectral analysis of radon time series. The obtained periodogram show two periodicity, on the 1 day and 1 year [4]. Mean radon value is 13.8 Bq m^{-3} with standard deviation of 9.9 Bq m^{-3} over the 3 years of continuos measurements with daily and sesonal variability [5]. It has been shown that the radon behaviour in the underground low-level laboratory in Belgrade has the similar characteristics as in the other underground environment (caves, mines, boreholes and so on), because it has the same source and the places are completely surrounded with the soil.

MVA METHODS AND MODELLING OF THE INDOOR RADON BEHAVIOUR

The demand for detailed analyses of large amount of data in high-energy physics resulted in wide and intense development and usage of multivariate methods. Many of multivariate methods and algorithms for classification and regression are already integrated into the analysis frame work ROOT, more specifically, into the toolkit for multivariate analysis (TMVA). We use these multivariate methods to create, test and apply all available classifiers and regression methods implemented in the TMVA in order to find the method that would be the most appropriate and yield maximum information on the dependence of indoor radon concentrations on the multitude of climate variables. The first step is to calculate and rank the correlation coefficients between all the variables involved, what will help in setting up and testing the framework for running the various multivariate methods contained in the TMVA. Although these correlation rankings will later be superseded by method specific variable rankings, they are useful at the beginning of the analysis. The next step is to use and compare the multivariate methods in order to find out which one is best suited for classification (division) of radon concentrations into what would be considered acceptable and what would be considered increased concentration in indoor spaces. Main aim is to find out which method can, if any, on the basis of input climate variables only, give an output that would satisfactorily close match the observed variations of radon concentrations. Towards this aim, this work were tested in a many specific cases (underground low-background laboratory and other indoor environment) to

comprise the multitude of possible representative situations that occur in real life.

The test of multivariate methods, implemented in the TMVA software package, applied to the analysis of the radon concentration variations connection with climate variables in different indoor spaces demonstrated the potential usefulness of these methods. It appears that the method can be used with sufficient accuracy (around 15 %) for prediction of the radon concentrations. All the obtained results were published in several research articles [6-8].

RADON MAPPING IN SERBIA

In the last three years, we were involved in the establishing national radon action plan (RAP) and performed first national indoor radon survey as a leading institution in the technical support of the project. The responsibility for the establishment and implementation of RAP is on national regulatory body: Serbian Radiation Protection and Nuclear Safety Agency (SRPNA). As a first step in RAP, it was the national indoor radon survey in Serbia performed during 2015-2016. The project was supported by IAEA through the national project: SRB9003 - Enhancing the Regulatory Infrastructure and Legislative System, with two components:
- Expert mission on „National Radon Trial Survey and Raising Awareness of Key Stakeholders„ held in SRPNA, Belgrade, 2 - 4 February 2015.
- Equipment: Leasing of 6000 track-etched indoor radon detectors; the distribution of detectors across the Serbian territory was the responsibility of SRPNA.

Also, during the realization of the national programme for indoor radon measurements, Institute of Physics Belgrade and other research institutions involved in the project together with the SRPNA, performed good communication strategy (first basic information leaflet on radon to accompany the measurement explaining the purpose of the measurement, internet site, public relation, public education...) which led to high survey efficiency (about 90 %), together with very hard field work. In total 6000 detectors have been distributed during October 2015 and exposed in houses and apartments for six months (till April 2016). Afterwards, the detectors were collected and sent to an authorized laboratory (Landauer Nordic AB) to be processed and consequently, we got data for the first national indoor radon survey. The preliminary results and radon map was presented at the 8th Conference of Protection against Radon at Home and at Work, 12 - 14 September 2016, Prague, Czech Republic [9].

Acknowledgements

REFERENCES

[1] Antanasijević R, Milošević I. Correlation between the concentration of 222-Rn at the Earth's surface and in waters with seismic activities. Nucl. Tracks Radiat. Meas. 1990;17:79.

[2] Dragić A, Joković D, Banjanac R, Udovičić V, Panić B, Puzović J, Aničin I. Measurement of cosmic ray muon flux in the Belgrade ground level and underground laboratories. Nucl. Instr. Meth. Phys. Res. 2008;A591:470–475.

[3] Dragić A, Udovičić V, Banjanac R, Joković D, Maletić D, Veselinović N, Savić M, Puzović J, Aničin I. The new set-up in the Belgrade low-level and cosmic-ray laboratory. Nucl. Technol. Radiat. Protect. 2011; 26(3):181–192.

[4] Udovičić V, Aničin I, Joković D, Dragić A, Banjanac R, Grabež B, Veselinović N. Radon time-series analysis in the underground low-level laboratory in Belgrade, Serbia. Radiat. Prot. Dosim. 2011;145:155–158.

[5] Udovičić V, Filipović J, Dragić A, Banjanac R, Joković D, Maletić D, Grabež B, Veselinović N. Daily and seasonal radon variability in the underground low-background laboratory in Belgrade, Serbia. Radiat. Prot. Dosim. 2014;160(1-3):62-64.

[6] Maletić D, Udovičić V, Banjanac R, Joković D, Dragić A, Veselinović N, Filipović J. Comparison of multivariate classification and regression methods for the indoor radon measurements. Nucl. Technol. Radiat. Prot. 2014; 29(1): 17–23.

[7] Maletić D, Udovičić V, Banjanac R, Joković D, Dragić A, Veselinović N, Filipović J. Correlative and multivariate analysis of increased radon concentration in underground laboratory. Radiat. Prot. Dosim. 2014;162:148-151.

[8] Filipović J, Maletić D, Udovičić V, Banjanac R, Joković D, Savić M, Veselinović N. The use of multivariate analysis of the radon variability in the underground laboratory and indoor environment. Nukleonika 2016; 61(3):357-360.

[9] Udovičić V, Maletić D, Eremić Savković M, Pantelić G, Ujić P, Čeliković I, Forkapić S, Nikezić D, Marković V, Arsić V, Ilić J, Nilsson P. Preliminary results of the first national indoor radon survey in Serbia. In: Book of Abstracts of 8th Conference of Protection against Radon at Home and at Work, September 12-14, 2016; Prague, Czech Republic.

Utilization of a shallow underground laboratory for studies of the energy dependent CR solar modulation

N.Veselinović A. Dragić, M. Savić, D. Maletić, D. Joković, R. Banjanac, V. Udovičić,

Institute of physics, University of Belgrade, Serbia

The aim of the paper is to investigate possibility of utilizing a shallow underground laboratory for the study of energy dependent solar modulation process and to find an optimum detector configuration sensitive to primaries of widest possible energy range for a given site. The laboratory ought to be equipped with single muon detectors at ground level and underground as well as the underground detector array for registration of multi-muon events of different multiplicities. The response function of these detectors to primary cosmic-rays is determined from Monte Carlo simulation of muon generation and propagation through the atmosphere and soil, based on Corsika and GEANT4 simulation packages. The simulation predictions in terms of flux ratio, lateral distribution, response functions and energy dependencies are tested experimentally and feasibility of proposed setup in Belgrade underground laboratory is discussed. .

1. INTRODUCTION

Cosmic rays (CR) are energetic particles, arriving at the Earth from space after interaction with the heliosphere. The interaction of these, primary CRs, with the atmosphere leads to production of a cascade (shower) of secondary particles: hadrons, electrons and photons, muons, neutrinos. CR research has been undertaken at almost every location accessible to humans – from the outer space to deep underground [1].

At the low energy part of the spectrum, lower than 100 GeV, CRs are affected by the solar magnetic field. Modulation effects are energy dependent and have been studied extensively by the neutron monitors, sensitive up to about 10 GeV. Muon detectors at the ground level are sensitive to higher energy primaries [2], and the muons detected underground correspond to even higher energies. The possibility to further extend the sensitivity to higher energies with the detection of multi-muon events underground is the intriguing one. The idea was exploited with the EMMA underground array [3]. For a shallow underground laboratory, exceeding the energy region of solar modulation would open the possibility to study CR flux variations of galactic origin.

2. BELGRADE CR STATION

The Belgrade cosmic-ray station is situated at the Laboratory for Nuclear Physics at the Institute of Physics. Its geographic position is: latitude 44° 51' N and longitude 20° 23' E, altitude of 78 m a.s.l., with geomagnetic latitude 39° 32' N and geomagnetic vertical cut-off rigidity 5.3 GV. It is composed of two sections, the underground lab (UL) with useful area of 45 m^2, dug at the 12-meter shallow depth (equivalent to 25 m.w.e) and the ground level lab (GLL). At UL depth, practically, only the muonic component of the atmospheric shower is present.

The cosmic-ray muon measurements in Belgrade CR station are performed by means of the plastic scintillation detectors, placed both in the GLL and in the UL. With the previous set-ups, monitoring is continuous from 2002.

Measured cosmic-ray intensity data were thoroughly analysed, yielding some results on the variations of the cosmic-ray intensity [4,5,6].

Time series (pressure and temperature corrected) of these measurements can be accessed online at http://cosmic.ipb.ac.rs/muon_station/index.html.

In addition to single muon detectors, a small-scale test setup for multi-muon events is installed underground. It consists from three scintillators: one large detector (100cm x 100cm x 5cm) and two small detectors (50cm x 23cm x 5cm) which are placed horizontally on their largest sides. Their mutual position is adaptable. The data acquisition system is based on fast 4-channel flash analog-to-digital converters (FADC), made by CAEN (type N1728B), with 100 MHz sampling frequency. The events are recorded in the list mode. For each event from every input channel the timing and amplitude are saved, together with auxiliary information such as the result of pile-up inspection routine. From this list a time series of single or coincident events could be constructed. The experimental set-up is sketched in Figure 1.
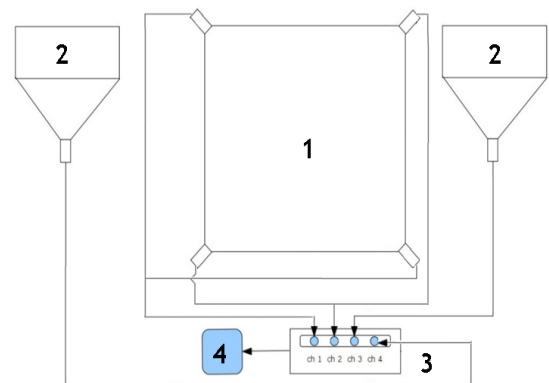

Figure 1 : Sketch of the experimental set-up for the cosmic-ray measurements:
1) Large scintillation detector, 2) small scintillation detectors, 3) flash analog-to-digital Converter (FADC), 4) experiment control and data storage computer

With simultaneous operation of several detector systems, as described, a single facility with the same rigidity cut-off would be used for investigation of solar modulation at different energies. Further integration with the Neutron Monitors data would be beneficial [7, 8, 9].

3. SIMULATION DETAILS AND RESULTS

Simulation of the CR shower dynamics up to the doorstep of GLL and UL has been done using Monte Carlo simulation packages CORSIKA and Geant4 [10, 11]. The cosmic-ray muon spatial and momentum distribution at 78m a.s.l. is of our interest. The output of CORSIKA at ground level is used as the input for Geant4 based simulation of particle transport through the soil and simulation of detector response. For this purpose soil analysis is done beforehand. The mean density is found to be (2.0±0.1) g/cm3 and soil type is loess with the assumed composition of Al2O3 20%, CaO 10% and SiO2 70%. For the simulation of underground detector system only those muons with energy sufficient enough to survive passage through soil are taken into consideration (Figure 2).
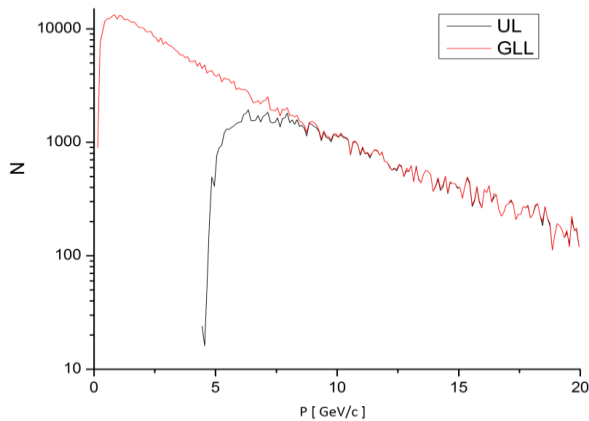
Figure 2: Surface momentum distribution for muons at GLL and muons reaching UL at Belgrade CR station based on GEANT4 and CORSIKA

At lower energies, protons make ~85% of CR, so primary particles used in the simulation were protons. The number of muons reaching UL is not linearly proportional to energy of the primary particle, especially for energies lower than 200 GeV which is energy range of interest, as showed in Figure 3.This correspond to similar work done elsewhere [12]. Probability that a registered event corresponds to a primary particle of certain energy is inferred from the simulation for every detection system:
- Single muon detector at ground level
- Single muon detector underground
- Two-fold muon coincidences underground
- Muon coincidences of higher multiplicity
For these response functions, simulation use 23 million primary protons with energy range from 5 GeV to 10^{16} eV

with zenith angle between (0°, 70°) and with power law energy spectrum with the exponent -2.7.
Shift toward higher energies is evident for transition from GL to UL and to the events of higher multiplicities.
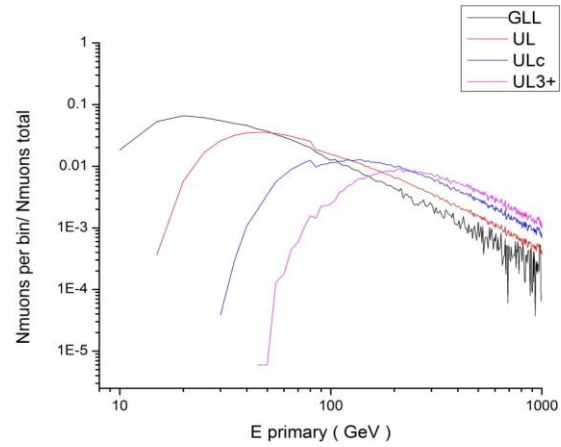

Figure 3: Differential response functions of muon detectors in GLL and UL based on simulation for: single muons at ground level (GLL), underground level (UL), coincident muons at underground level (ULc) and triple and higher multiplicity coincident muons at underground level (UL3+) normalized to total number of muons respectively.

For all relevant quantities of the muon flux is given at Table 1. Equivalent depth was found using ratios of integral fluxes of muons at different shallow depth [13].

Table 1: Properties of the flux of the primary particles at Belgrade CR station based on simulation for: ground level (GLL), underground level (UL), coincident muons at underground level (ULc) and triple and more coincident muons at underground level (UL3+).

Primary protons	**GLL**	**UL**	**ULc**	**UL3+**
Energy cut-off	5 GeV	12.3±0.7 GeV	30±4 GeV	55±14 GeV
Equivalent depth	0 m.w.e. GLL Belgrade	25 m.w.e.	40 m.w.e.	66 m.w.e.
Peak energy	20 GeV	45 GeV	125 GeV	200 GeV
Median energy	62 GeV	122±5 GeV	296 ± 8 GeV	458±18 GeV

Cut-off energy at the ground level is due to geomagnetic cut-off rigidity at Belgrade CR station. For the

underground level, the 25 m.w.e. of soil overburden is the cause of the higher cut-off underground. All the relevant quantities: cut-off, peak and median energies are higher underground and for the events with higher multiplicity. This, in principle, creates a possibility to investigate the CR flux and its variations at different energies of primaries, exceeding the energies relevant to neutron monitors, the most frequently used instrument for study of the low energy side of the CR spectrum. This vindicates the aim of the simulation to investigate possibility of utilizing a shallow underground laboratory for the study of energy dependent solar modulation process and to find an optimum detector configuration sensitive to primaries of different energy range for a given site.

4. DISCUSION ON FEASIBILITY

It is needed, however, to address the questions of reliability of simulation. On the graph 3, the discontinuity at energy of 80 GeV of primary protons is visible, especially muon in UL and muons in UL in coincidence. CORSIKA, by default, uses GHEISHA 2002d particle generator to calculate the elastic and inelastic cross-sections of hadrons below 80 GeV in air and their interaction and particle collisions and for higher energies QGSJET 01C routine is used. Also it is important to know whether sufficient statistics of multi-muon events could be achieved in the limited laboratory space. For this purpose, the flux of single muons is measured at ground level and underground, the rate of double coincidences as a function of detector distance is simulated also. In addition, the rates of double and triple coincidences are also measured for several detector arrangements.

The muon flux is calculated, from simulation, by finding ratio between the number of muons reaching depth of UL (for single and muons in coincidence) and numbers of muons generated from CORSIKA at the surface and multiplying by experimentally measured value of integrated muon surface flux which is 137(6) muons per $m^2 s$ [14]. The experimental value of integrated flux, compared with number of muons from simulation, is also used to find physical time needed to generate same number of muons at the site as the simulation.

Absolute muon fluxes measured at the site for surface and shallow underground is well reproduced by the simulation (Table 2).

Table 2: Ratio of muon fluxes at Belgrade CR station based on measurements and simulation for: ground level (GLL), underground level (UL), coincident muons at underground level (ULc) and triple and more coincident muons at underground level (UL3+)

Muon flux ratio	Measured GLL/UL	Simulation GLL/UL	Simulation UL/ULc	Simulation UL/UL3+
	3.17(8)	3.06(3)	1.86(4)	2.68(6)

Recently with new detector arrangement, the scintillators in Belgrade CR station measured coincident events and triple coincident events at two distances of the detectors: 1.5m and 6m, in UL part of the laboratory. Number of coincidences per unit area of the detector, based on simulation for these distances is 80 and 66 muon coincidences per m^2 per day respectively. Experimental values are higher for closer (~350 coincidences a day) and ~60 coincidences per day for farther arrangement. The ratio of single/coincidence events underground is well reproduced for greater distance of the detector. At shorter distances the measured ratio is higher than predicted by simulation, further study will show is it due to contribution from local EM showers and knock-on electrons. Numbers of measured triple coincidences at same distances are the order of magnitude smaller.

When upgraded, the detector arrangements will cover the whole area of the UL with muon detectors it should provide, based on the simulation, approximately 61k coincidences per day thus allowing to observe ~ 1.2% fluctuation of the CR flux with 3σ certainty originated from Solar modulation (e.g. Forbush decreases) thus allowing possibility to study solar modulation on three different energy ranges of the primary particles and at higher energies then regular energies detected with NM. To prevent miss-identification of muons, additional methods of sorting muons is needed (lead shielding, hodoscopes...) or to measure only coincidences that occur on reliable distances between detectors, larger then 6m, allowing observation of higher fluctuations (~2.5%) with same certainty.

In principle, larger shallow depth laboratories [15] can be used to investigate solar modulation and extreme solar events on different energies of primary particles, using rate of detected muons on different detectors in coincidence but present small detection area at Belgrade CR station can also give some valuable insight.

5. CONCLUSION

The possibility of utilizing a shallow underground laboratory for the study of energy dependent solar modulation of CR is investigated, by means of computer simulation based on CORSIKA and GEANT packages, combined with the experiment. On the experimental part, the muon flux is measured at ground level and underground at the depth of 25 mwe. In the present feasibility study, the flexible test setup for detection of multiple muons is installed underground in an attempt to achieve sensitivity to higher energy primaries. The rates of double and triple coincidences are measured for several detector distances. The simulation revealed the response functions of each experimental setup. The experimental fluxes are compared with those arising from simulation (Table 2). For single muons, the experimental ratio of

fluxes GLL/UL agrees with the simulated one. The experimental ratio of single/coincident events underground is well reproduced by simulation if the detector distance is greater than 6m. At shorter distances the measured ratio is higher than predicted by simulation, mainly due to contribution from local EM showers and knock-on electrons. When upgraded, the detector arrangements will cover almost the entire area of the UL with muons detectors resulting in expected approximately 61k coincidence per day. One day of measurements will be sufficient to observe ~ 1.2% fluctuation of the flux at 3σ significance for CRs with several hundred GeV of energy. Together with the single muon measurements at GLL and UL we will have simultaneous measurements centered on three different energies, under the same atmospheric and geomagnetic conditions. Any difference in time series behavior could be attributed to energy dependent response to the forcing. The rate of triple coincidences is too low to be effectively exploited in our conditions.

Acknowledgments

References

[1]   L.I. Dorman, Cosmic-rays in the Earth's Atmosphere and Underground, Kluwer, Dordrecht, (2004)

[2]   I. Braun, J. Engler, J.R. Hörandel, J. Milke, Forbush decreases and solar events seen in the 10 - 20GeV energy range by the Karlsruhe Muon Telescope, ADVANCES IN SPACE RESEARCH 43(4):480-488, (2008)

[3]   Kalliokoski ,L. Bezrukov, T. Enqvist, H. Fynbo, L. Inzhechik, P.J. Jones, J. Joutsenvaara, J. Karjalainen, P. Kuusiniemi, K. Loo, B. Lubsandorzhiev, V. Petkov, T. Räihä, J. Sarkamo, M. Slupecki, W.H. Trzaska, A. Virkajärvi, Can EMMA solve the puzzle of the knee?, Progress in Particle and Nuclear Physics 66, 468-472, (2011)

[4]   A.Dragić, V.Udovičić, R.Banjanac, D.Joković, D.Maletić, N.Veselinović, M.Savić, J.Puzović, I.Aničin, The new set-up in the Belgrade low-level and cosmic-ray laboratory, Nucl. Technol. Radiat. 26, 181-192 , (2011)

[5] A.Dragić, R.Banjanac, V.Udovičić, D.Joković, J.Puzović, I.Aničin, Periodic Variations of CR Muon Intensity in the Period 2002-2004 , Proceedings of the 21st European cosmic-ray Symposium, Košice, Slovakia ,368-373, (2008)

[6]   N. Veselinović, A. Dragić, D. Maletić, D. Joković, M. Savić, R. Banjanac ,V. Udovičić and I. Aničin, Cosmic rays muon flux measurements at Belgrade shallow underground laboratory, AIP Conf. Proc. 1645, 421 (2015); http://dx.doi.org/10.1063/1.4909614

[7]   S.N.Karpov ,Z.M. Karpova, A.B. Chernyaev, Multiplicity, yield and response functions for Baksan EAS-arrays and Muon Detector in comparison with similar functions of Neutron Monitors, Proceedings of the 29th International Cosmic Ray Conference, Pune, India, (2005)

[8]   D. Maurin, A. Cheminet, L. Derome, A. Ghelfi, G Hubert, Neutron Monitors and muon detectors for solar modulation studies: Interstellar flux, yield function, and assessment of critical parameters in count rate calculations, Advances in Space Research **55 (1)** 363 (2015)

[9]   J.M. Clem and L.I. Dorman, Neutron monitor response functions, Space Science Reviews, Volume 93, Issue 1, pp 335-359,(2000)

[10]   D. Heck et al., CORSIKA: a Monte Carlo code to simulate extensive air showers, Report FZKA 6019, Forschungszentrum Karlsruhe, (1998)

[11]   S. Agostinelli et al., the Geant4 collaboration, Nucl. Instrum. Meth. A 506, 250-303, (2003)

[12]   A. Bogdanov, A. Dmitrieva, R. Kokoulin, A. Petrukhin, D. Timashkov, E. Yakovleva, Coupling functions for primary cosmic rays and ground-level muons at various zenith angles, Proceedings of the 21st European Cosmic Ray Symposium, pp341-346L, (2008)

[13]   N. Bogdanova, M. G. Gavrilov, V. N. Kornoukhov, A. S. Starostin, Cosmic muon flux at shallow depths underground, Phys.Atom.Nucl. 69 , 1293-1298, (2006)

[14]   A. Dragić et al., Measurement of cosmic ray muon flux in the Belgrade ground level and underground laboratories,Nucl. Instrum. Meth. A 591, 470-475, (2008)

[15]   F. Suarez for the Pierre Auger Collaboration, The AMIGA muon detectors of the Pierre Auger Observatory: overview and status, 33rd international cosmic ray conference,   (2013)

Effect of pressure and temperature corrections on muon flux variability at ground level and underground

M. Savic, A. Dragic, N. Veselinovic, V. Udovicic, R. Banjanac, D. Jokovic, D. Maletic

Institute of Physics, Belgrade, Pregrevica 118, Serbia

In Low Background Laboratory at Institute of Physics Belgrade, plastic scintillators are used to continuously monitor flux of the muon component of secondary cosmic rays. Measurements are performed on the surface as well as underground (25 m.w.e depth). Temperature effect on muon component of secondary cosmic rays is well known and several methods to correct for it are already developed and widely used. Here, we apply integral method to calculate correction coefficients and use GFS (Global Forecast System) model to obtain atmospheric temperature profiles. Atmospheric corrections reduce variance of muon flux and lead to improved sensitivity to transient cosmic ray variations. Influence of corrections on correlation with neutron monitor data is discussed.

Belgrade Low Background Laboratory (LBL) is located at Institute of Physics, Belgrade and consists of two interconnected spaces, a ground level laboratory (GLL) and a shallow underground one (UL) [Fig. 1]. GLL is at 75 meters above sea level while UL is dug under a 10 meter cliff and has a 12 meters of loess soil overburden (25 meters of water equivalent) [1]. Geographic latitude for the site is 44.86 and longitude is 20.39 while geomagnetic rigidity cutoff is 5.3 GV.
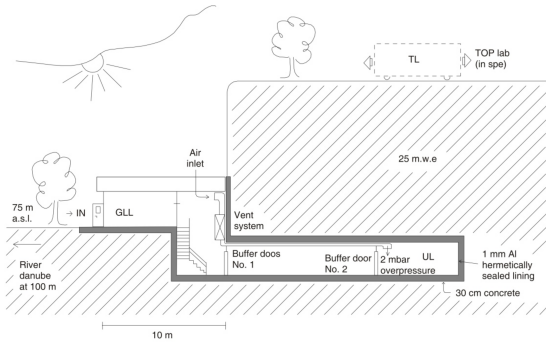
FIG. 1: Layout of the Low Background Laboratory.

Experimental setup consists of two identical sets of detectors and read out electronics, one situated in GLL and the other in UL. Each setup utilizes a plastic scintillator detector with dimensions 100cm x 100cm x 5cm (Amcrys-H, Kharkov, Ukraine) equipped with 4 PMTs (Hammamatsu R1306) directly coupled to the corners [Fig. 2]. Flash ADC (CAEN type N1728B) with 10ns sampling are used for read out [1].

Preamplifier outputs of two diagonally opposing PMTs are summed and fed to a single FADC input thus engaging two inputs of the FADC for two such diagonal pairings. Signals recorded by the two inputs are coincided in offline analysis, resulting in coincidence spectrum which is then used to determine the integral count [Fig. 3]. This procedure almost completely eliminates low-energy environmental background leaving only events induced by cosmic ray muons and muon related EM showers [1].
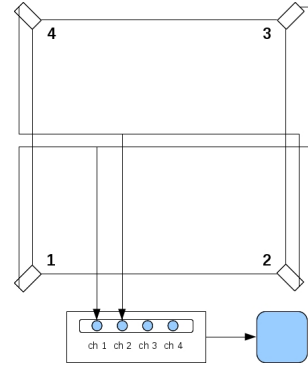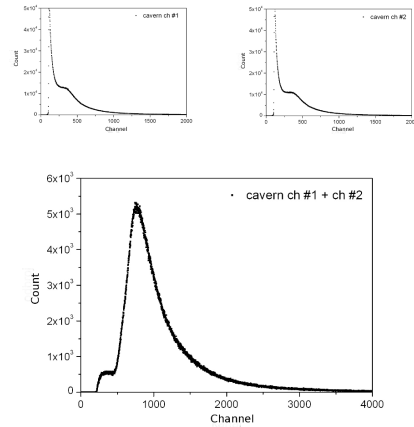

FIG. 2: Experimental setup scheme.

FIG. 3: Single summed diagonal and coincidence spectra.

I. SIGNIFICANCE OF METEOROLOGICAL EFFECTS

Meteorological effects on muon component of secondary cosmic rays are well known, with pressure and temperature effect being most dominant [2]. Correcting for these effects noticeably increases data usefulness, especially increasing sensitivity to periodic and aperiodic variations of non-atmospheric origin (vari-

ations of primary cosmic rays, different heliospheric processes, etc.)

In Belgrade Low Background Laboratory continual measurements utilizing described setup started in April of 2008 for the GLL and in November of 2008 for the UL, and with some interruptions are still ongoing. Base time resolution for integrated count is 5 minutes but time resolution of 1 hour is also often used in analysis. Link to Belgrade cosmic ray station can be found on the following address: http://www.cosmic.ipb.ac.rs/.

FIG. 4: Yearly values for barometric coefficient for GLL and UL.

A. Pressure effect

Barometric effect is defined by the following equation:

$$\left(\frac{\delta I}{I}\right)_P = \beta \cdot \delta P \qquad (1)$$

where $\frac{\delta I}{I}$ is the normalized variation of muon flux intensity, β is barometric coefficient and δP is pressure variation. Pressure variation is calculated as $\delta P = P - P_B$, where P is current pressure and P_B is base pressure value [4].

Since no in situ pressure measurement was performed prior to 2015, current pressure values have mostly been acquired from official meteorological measurements performed by Republic Hydrometeorological Service of Serbia as well as from Belgrade airport meteorological measurements. In all, data from 5 different stations were used. All pressure data was normalized to Belgrade main meteorological station. Stations were sorted according to geographical proximity and consistence of data. Unique pressure time series was composed by using data from the first station with available pressure entries for a given hour. Linear interpolation was then performed and pressure values were sampled with 5 minute step. Normalized variation of muon flux intensity vs. pressure variation was plotted for each year. Only data for the 5 geomagnetically most quiet days of each month were taken into account (selected from International Quiet Days list). Barometric coefficient for each year was determined from linear fits of these plots [Fig. 4].

B. Temperature effect

Temperature effect on hard muons is well known [2] and there are several methods developed to describe and correct for it. Method we used was integral method, where normalized variation of muon flux dependence on temperature variation is described as:
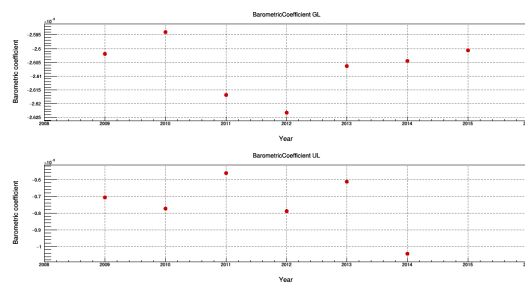
$$\left(\frac{\delta I}{I}\right)_T = \int_0^{h_0} \alpha(h) \cdot \delta T(h) \cdot dh \qquad (2)$$

$\alpha(h)$ being temperature coefficient density and temperature variation calculated as $\delta T = T - T_B$, where T is current temperature and T_B is base temperature value [3].

To correct for temperature effect using formula above it is necessary to have most complete information about atmospheric temperature profile for a given geographical location as well as to know temperature coefficient density function. Temperature profile measurements performed by local meteorological service are not done on consistent basis but more detailed information is available from meteorological models. One such model is GFS (Global Forecast System) that, among other data, provides temperatures for 25 isobaric levels for a given geographical location with latitude/longitude precision of 0.5 degrees [3].
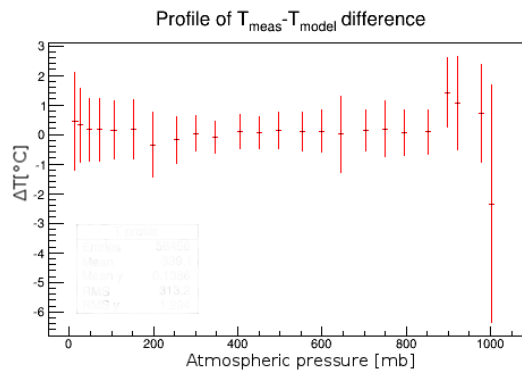

FIG. 5: Distribution of difference between modelled temperatures and temperatures measured by meteorological balloons above Belgrade (where such data was available).

Measured and modelled values seem to be in fairly good agreement [Fig. 5] except for the lowest isobaric level. That is why for this level temperature from local meteorological stations was used, treated in the same manner as described for local pressure data . Time

resolution for modelled temperatures is 6 hours so interpolation was performed using cubic spline [3] and temperature values were sampled in 5 minute steps.

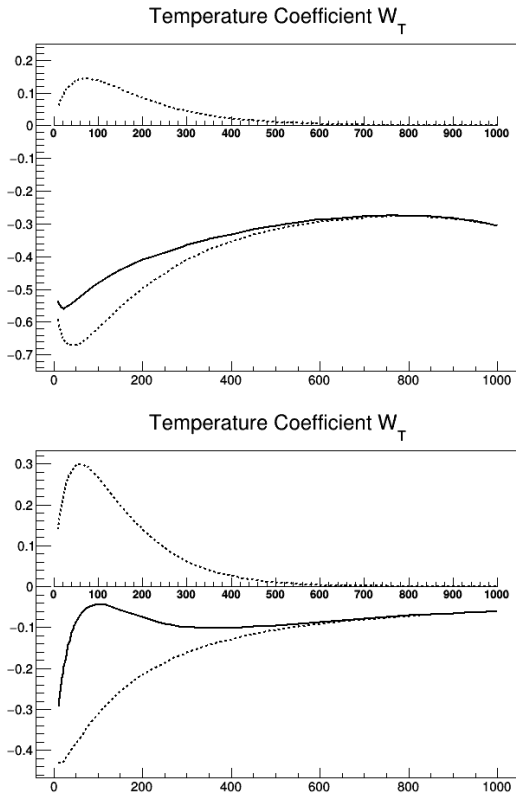Temperature density functions [Fig. 6] are calculated according to procedure described in [2].
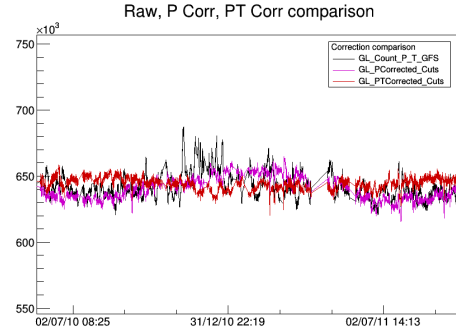

FIG. 7: GLL raw (black), pressure corrected (magenta) and PT corrected (red) muon count time series for a selected period.
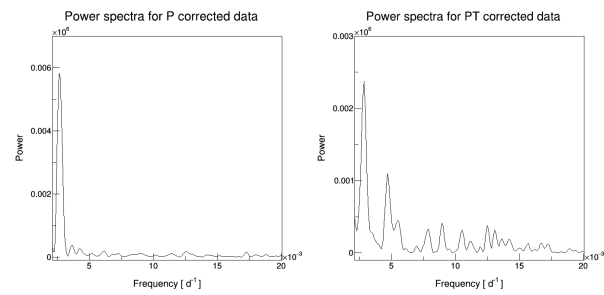

FIG. 8: Power spectra for pressure corrected and temperature and pressure corrected data.

FIG. 6: Temperature coefficient density functions for ground level (above) and depth 25 m.w.e. (below).

II. RESULTS

A. PT corrected time series

It would seem that pressure correction successfully removes aperiodic pressure induced fluctuations while temperature correction most significantly affects annual variation induced by atmospheric temperature variations [Fig. 7].

B. Spectral analysis

Spectral analysis can give us more insight into effect of temperature correction on annual variation of muon count (presented for GLL data in [Fig. 8])

After temperature correction, peak related to annual periodicity in power spectrum appears to be significantly reduced relative to nearby peaks.

C. Neutron monitor correlation

Possible validation for correction procedure would be agreement of pressure/temperature corrected muon count time series with neutron monitor data. BAK-SAN neutron monitor was selected as a possible reference [Fig. 9].

III. CONCLUSIONS

Corrections for temperature and pressure effect are essential for muon data gathered at Belgrade LBL. Atmospheric temperature profile for Belgrade seems to be adequately modeled by GFS. Temperature correction utilizing integral method seems to give acceptable results (while quality can still be further improved). Also, other methods could be applied and results compared. Muon flux data after pressure and temperature corrections has increased sensitivity to periodic and aperiodic effects of non-atmospheric origin. Preliminary comparison with neutron monitor data supports this claim with more detailed correlation analysis to follow in the future.
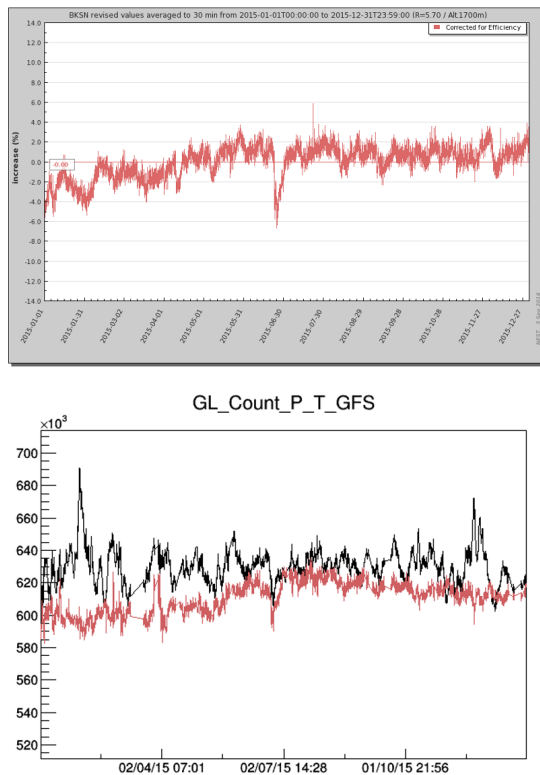
FIG. 9: BAKSAN neutron monitor (above) and GLL raw and pressure/temperature corrected data (below in red) comparison for year 2015.

V. REFERENCES

[1] The new set-up in the Belgrade low-level and cosmic-ray laboratory Nucl. Technol. Radiat. 26 (2011) 181-192. A.Dragic at all
[2] Dorman, Cosmic Rays in the Earths Atmosphere and Underground
[3] M. Berkova , A. Belov, E. Eroshenko, and V. Yanke, Temperature effect of muon component and practical questions of how to take into account in real time, Astrophys. Space Sci. Trans., 8, 41-44, 2012
[4] R. R. S. De Mendona, J. -P. Raulin, E. Echer, V. S. Makhmutov, and G. Fernandez, Analysis of atmospheric pressure and temperature effects on cosmic ray measurements. JOURNAL OF GEOPHYSICAL RESEARCH: SPACE PHYSICS, VOL. 118, 14031409, doi:10.1029/2012JA018026, 2013

PREDICTABILITY OF LEAD-210 IN SURFACE AIR BASED ON MULTIVARIATE ANALYSIS

Jelena Ajtić [1,*], Dimitrije Maletić [2], Đorđe Stratimirović [3,*], Suzana Blesić [4,*], Jelena Nikolić [5], Vladimir Đurđević [6], and Dragana Todorović [5]

[1] University of Belgrade, Faculty of Veterinary Medicine, Belgrade, Serbia
[*] Institute for Research and Advancement in Complex Systems, Belgrade, Serbia
[2] University of Belgrade, Institute of Physics, Belgrade, Serbia
[3] University of Belgrade, Faculty of Dental Medicine, Belgrade, Serbia
[4] University of Belgrade, Institute of Medical Research, Belgrade, Serbia
[5] University of Belgrade, Vinča Institute of Nuclear Sciences, Belgrade, Serbia
[6] University of Belgrade, Faculty of Physics, Institute of Meteorology, Belgrade, Serbia

Abstract. *Dependence of the lead-210 activity concentration in surface air on meteorological variables and teleconnection indices is investigated using multivariate analysis, which gives the Boosted Decision Trees method as the most suitable for variable analysis. A mapped functional behaviour of the lead-210 activity concentration is further obtained, and used to test predictability of lead-210 in surface air. The results show an agreement between the predicted and measured values. The temporal evolution of the measured activities is satisfactorily matched by the prediction. The largest qualitative differences are obtained for winter months.*

Key words: *lead-210, surface air, meteorological variables, teleconnection indices, multivariate analysis, wavelet transform analysis*

1. INTRODUCTION

Lead-210 is a naturally occurring radionuclide with a half-life of 22.23 years. The main source of ^{210}Pb in surface air is its radioactive parent radon-222 that emanates from the soil. After formation, ^{210}Pb attaches to aerosols whose fate is governed by atmospheric circulation and removal processes.

A number of studies that looked into the ^{210}Pb activity concentrations at different measuring sites have shown a uniform radionuclide distribution, both in the vertical and horizontal. For example, [1] showed no significant variations in the ^{210}Pb activity concentration at three locations over distance of approximately 200 km, and still noted a case in which the ^{210}Pb activity concentration rapidly changed due to a passage of a cold front. Similarly, [2] investigated differences in the ^{210}Pb activity concentration between two measurement sites at a distance of 12 km in the horizontal and of 800 m in the vertical. Their results also showed that over longer periods of time, the radionuclide was well mixed within the atmosphere. Further, [3] found good correlation between the ^{210}Pb activity concentrations across two sites 100 km apart, which were influenced by different local conditions, including different prevalent winds.

On the other hand, the vertical profile of the ^{210}Pb activity concentration in the atmosphere has been shown to reflect the fact that the radionuclide source is in the lowermost layer - surface air masses are richer in ^{210}Pb than air masses from higher altitudes, with the sharpest decrease in activity concentration between the ground and an altitude of 3 km [4, 5]. Further, the ^{210}Pb activity concentration is higher in continental air masses than in air masses originating over a body of water [2, 6, 7], which results in the radionuclide activity concentration variations in the horizontal, and also explains temporal differences in a location under influence of interchangeable winds of either continental or maritime origin [2].

The above mentioned studies, however, did not include an analysis of ^{210}Pb relation with large-scale atmospheric circulation. The North Atlantic Oscillation (NAO) index is one of the most commonly used teleconnection indices to describe a large-scale circulation pattern over the North Atlantic Ocean and surrounding land masses [8]. The two oscillation phases of NAO induce changes in large-scale circulation patterns [9], which further reflect on local weather conditions especially over eastern North America and across Europe, including Serbia [10]. The Polar/Eurasia pattern [8] is another teleconnection that has an impact on weather in Europe [11]. Further, the East Atlantic/Western Russia pattern [8] influences the amount of precipitation in southeast part of Europe [12], and can thus be a contributing factor in the amount of ^{210}Pb in surface air.

In contrast to a very limited number of studies looking into an influence of large-scale atmospheric transport on the ^{210}Pb activity concentrations, a link between local meteorological variables and the radionuclide activities has been extensively investigated [7, 13, 14, 15]. For example, to name only a few: [16] showed a strong positive relationship between the ^{210}Pb deposition and precipitation; [17] found a positive correlation of ^{210}Pb activity concentration with temperature, and negative correlation with precipitation, relative humidity and wind speed; [14] showed that washout is the most significant mechanism of ^{210}Pb removal from the atmosphere.

The goal of our analysis is to combine meteorological data and large-scale atmospheric transport patterns (quantified by teleconnection indices) and treat the ^{210}Pb concentration in surface air as a result of their interplay. Different statistical tools are employed to achieve this. On one hand, a set of multivariate methods incorporated in the Toolkit for Multivariate Analysis (TMVA) [18] is used. It is complemented by a wavelet transform spectral analysis [19]. A mapped functional behaviour which is obtained in the analysis is then used to test predictability of the ^{210}Pb activity concentration in surface air.

2. DATASETS

In Belgrade, Serbia, at the Vinča Institute of Nuclear Sciences, continual measurements of the ^{210}Pb activity concentrations in surface air started in 1985. The monthly mean activity concentrations in composite aerosol samples were determined on High Purity Germanium detectors by standard gamma spectrometry. The activity concentrations of ^{210}Pb were determined using the gamma energy of 46.5 keV. A detailed description of the measurement procedure is given in [15].

The meteorological daily data: minimum, maximum and mean temperature, atmospheric pressure, relative humidity, precipitation, sunshine hours and cloud cover data for Belgrade, were obtained from the European Climate Assessment & Dataset (ECA&D) [20] and the Republic Hydrometeorological Service of Serbia. In addition, a temperature variable, which does not have a local character, was included to investigate the extent to which the local meteorological variables influence the ^{210}Pb activity concentration in the air. The chosen variable was the Northern Hemispheric mean monthly temperature anomaly over land calculated from historical temperature records (http://www.cru.uea.ac.uk/cru/data/temperature/CRUTEM4-nh.dat visited on 10 March 2015). The temperature anomaly was derived as a deviation from a reference temperature value which, in this data set, was taken as the mean over a reference period 1961–1990. More details on the temperature anomaly calculations can be found in [21, 22].

The data for eight teleconnection indices of large-scale atmospheric circulation: North Atlantic Oscillation (NAO), East Atlantic (EA), East Atlantic/Western Russia, Scandinavia (SCAND), Polar/ Eurasia, Western Pacific (WP), East Pacific-North Pacific (EP-NP), and Pacific/North American (PNA) were obtained from the data archive of the United States National Oceanic and Atmospheric Administration's Climate Prediction Center (http://www.cpc.ncep.noaa.gov/data/teledoc/telecontents.shtml visited on 18 October 2013). A description of the procedure used to identify the Northern Hemisphere teleconnection patterns and indices is given in [8]. The monthly values of teleconnection indices since 1950 were available.

The temporal resolution of the input variables differed: the ^{210}Pb activity concentrations and the teleconnection indices, apart from NAO, were available as monthly mean values. This resolution implied a total number of data points that was insufficient for MVA which inherently requires a large number of points to determine the mapped behaviour. To overcome this drawback, an interpolation of the monthly measurements was performed using Fast Fourier Transform smoothing on monthly data (Fig. 1).
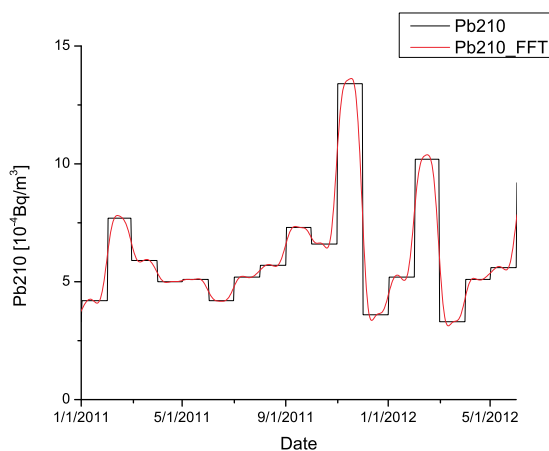

Fig. 1 Fast Fourier Transform of the monthly ^{210}Pb activity concentrations in surface air. The Fast Fourier Transform curve gives interpolated daily ^{210}Pb values which were used in the MVA classification and regression analysis.

3. CALCULATIONS

3.1. Multivariate Analysis

Many multivariate methods and algorithms for classification and regression are integrated in the analysis framework ROOT [23], and the Toolkit for Multivariate Analysis (TMVA) [18]. Multivariate analysis is used to create, test and apply all available classifiers and regression methods to single out one method that is the most appropriate and yields maximum information on the dependence of an investigated variable on a multitude of input variables. Thus, in TMVA there is no need to choose *a priori* a method for the data classification and regression – all of the techniques incorporated in TMVA are tested and the most suitable one is chosen for further analysis.

The TMVA package includes various techniques, such as multi-dimensional likelihood estimation, linear and nonlinear discriminant analysis, artificial neural networks, support vector machine, and boosted/bagged decision trees. All the techniques in TMVA belong to the family of "supervised learning" algorithms. They make use of training events, for which the desired output is known, to determine the mapping function that either describes a decision boundary (classification) or an approximation of the underlying functional behaviour defining the target value (regression). All MVA methods see the same training and test data.

The multivariate methods are compared within the procedure in order to find one which, on the basis of input variables, gives a result satisfactorily close to the observed values of the output variable. More details on calculation procedure are given in [24].

In our analysis, the output variable was the activity concentration of ^{210}Pb in surface air, while the input variables were the nine meteorological variables, one derived variable, and eight teleconnection indices, adding to 18 input variables in total. A multivariate method that gave the best regression results in our study was the Boosted Decision Trees method.

3.1.1. Boosted Decision Trees

Boosted Decision Trees (BDT) is a method in which a decision is reached through a majority vote on a result of several decision trees. A decision tree consists of successive decision nodes which are used to categorise the events in a sample, while BDT represents a forest of such decision trees. The (final) classification for an event is based on a majority vote of the classifications done by each tree in the forest, which ultimately leads to a loss of the straightforward interpretation in a decision tree. More detailed information on training in BDT can be found in [24].

An importance of an input variable is measured by a "variable rank". In BDT, this measure is derived by counting the number of times a specific variable is used to split decision tree nodes, and then weighting each split occurrence by the separation gain-squared it achieved and by the number of events in the node [18].

3.2. Wavelet Transform Analysis

Wavelet transform (WT) is a standard analytical tool in investigation of time series with nonstationarities at different frequencies [19]. In WT analysis, a calculated global wavelet power spectrum (which corresponds to Fourier power spectrum) is smooth and can therefore be used to estimate characteristic periods in the data sets. To detect these characteristic periods, a standard peak analysis was performed by searching the maximum and saddle (for hidden peaks) points in the global wavelet power spectra of the ^{210}Pb activities.

4. Results and Discussion

The WT analysis showed a number of characteristic periods in the ^{210}Pb activity concentration in surface air (Fig. 2). The periods are given by the time coordinates of the local maxima in the ^{210}Pb activity concentration power spectrum. Three short characteristic periods were found, with a seasonal one (at 2.6 months) most pronounced. The annual cycle (at 11.8 months) was also evident, as well as a longer period of approximately three years (at 36.5 months). Apart from the annual cycle [2, 14, 15], the other ^{210}Pb periodicities have not been studied in detail.
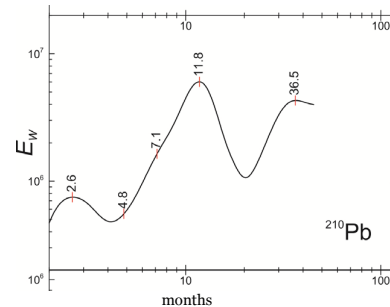

Fig. 2 Power spectrum of the ^{210}Pb activity concentration in surface air. Positions of the maximum and saddle points are marked with the assigned values of characteristic time in months.

To allow for the prominent annual cycle in the ^{210}Pb activity concentration in surface air, another input variable, called MonthDay, was introduced in the analysis. The MonthDay variable is purely mathematical – its values represent a sum of the month number (1 to 12) and the day number in a month divided by the total number of days in the given month. For example, a MonthDay value for 10 January is 1+10/31. This variable has an annual cycle and thus serves as a proxy of any contributing variable which is not specified in the analysis but also exhibits an annual cycle.

Prior to the multivariate analysis, the Pearson's linear correlation coefficients for the input variables and ^{210}Pb activity concentrations were calculated (Tab. 1) using the monthly means. The strongest correlation was found with temperature anomaly. However, that correlation was not significant at the 0.05 level. Statistically significant linear correlation was obtained only for atmospheric pressure and three teleconnection indices: EP-NP, East Atlantic/Western Russia, and Polar/Eurasia.

The calculated correlation coefficients describe the measure of linear correlation between the ^{210}Pb activity concentrations and the input variables. However, apart from linear, other types of dependance between variables could exist. Each method incorporated in the MVA gives its own ranking (as one of the results), which does not necessarily coincide with a ranking of another method, or with the order given by the linear correlation coefficients.

Table 1. Pearson's linear correlation coefficients (r) of the input variables and the ^{210}Pb activity concentration in surface air, and the BDT variable ranking. The correlation coefficients significant at the 0.05 level are given in bold.

Variable	r	BDT rank
Temperature anomaly	-0.47	1
Precipitation	-0.22	18
Atmospheric pressure	**+0.21**	15
EP-NP	**+0.19**	6
Cloud cover	-0.16	17
East Atlantic/Western Russia	**+0.14**	8
Polar/Eurasia	**+0.12**	7
NAO	+0.10	4
SCAND	+0.08	9
Mean temperature	-0.08	11
Minimum temperature	-0.08	12
Maximum temperature	-0.07	14
Relative humidity	+0.07	16
Sunshine hours	-0.07	13
PNA	+0.04	5
WP	+0.03	3
EA	+0.008	10
MonthDay value	N/A	2

4.1. Regression Analysis

A result of MVA regression method training is an approximation of the underlying functional behaviour that defines the dependence of the target value, the ^{210}Pb activity concentrations in our analysis, on the input variables. This set of calculations was based on the measurements performed during the training period, which was from 1985 to 2010 in our case. Predictability of the ^{210}Pb activity concentration in surface air was tested in the ensuing calculations, in which the measurements for 2011 and 2012 were used.

The analysis indicated that the best regression method, in which the output values (evaluated, or predicted, ^{210}Pb activity concentrations) were closest to the measured concentrations, was BDT. In an ensemble of multivariate methods, the average quadratic deviation between the evaluated and measured values was the least for BDT (Fig. 3). The BDT output deviation from the measurements over the training period was close to zero for the majority of data points (Fig. 4), which confirmed the good quality of the regression method.
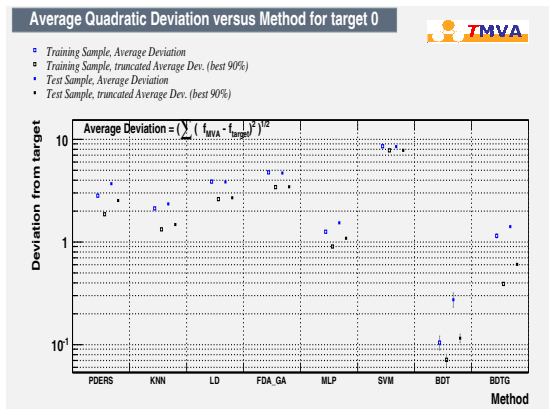

Fig. 3 Average quadratic deviation for multivariate regression methods. The deviation was the least for BDT.
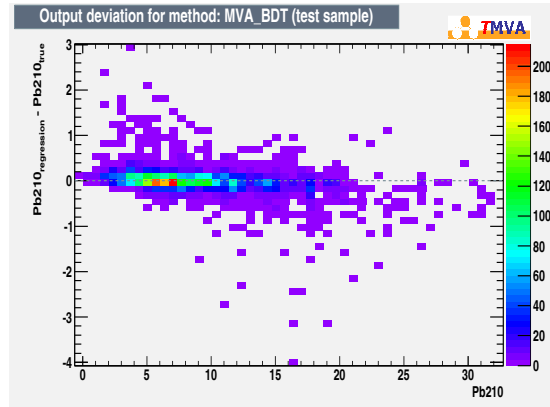
Fig. 4 Difference between the BDT evaluated and the measured ^{210}Pb activity concentrations. The colour bar on the right gives the number of data points.

One of the results given by the BDT method is a variable ranking (Table 1). Apart from temperature anomaly (rank 1), all other meteorological variables were ranked as less important than the teleconnection indices. The influence of the large-scale circulation is not well understood, but the local ^{210}Pb activity concentration could be significantly influenced by mesoscale and synoptic scale variations in atmospheric pressure (as quantified by the teleconnection indices). The local variations in atmospheric pressure, on the other hand, could play a minor role (low BDT rank in Table 1).

Similarly, a high rank obtained for temperature anomaly (Table 1) may imply that the ^{210}Pb activity concentration in surface air is to a certain extent insensitive to relatively fast variations in local temperature.

The high rank of the MonthDay variable could indicate an existence of another contributing factor with a strong annual cycle.

4.2. ^{210}Pb activity concentration prediction

The final step in our analysis was an evaluation of the ^{210}Pb activity concentration outside the training period for which the mapped functional behaviour was obtained. In other words, the input variables for 2011 and the first half of 2012 were used to calculate the output variable which was then compared to the measured ^{210}Pb activity concentration over that period (Fig. 5).

The standard deviation of all the absolute and relative differences between the BDT evaluated and measured ^{210}Pb values were $0.64 \cdot 10^{-4}$ Bq/m^3 and 0.12, respectively.

The temporal evolution of the ^{210}Pb activity concentration was satisfactorily captured by the regression method (Fig. 5). However, the regression was not able to quantitatively predict the observed values in winter periods, when the radionuclide activity concentration reached maximum values. Thus, during January and February 2011, the evaluated values were conspicuously higher than the measured ones, while in November and December of the same year, the evaluation first underestimated and then overestimated the ^{210}Pb

activity concentration. It can, however, be argued that the sum of the predicted ²¹⁰Pb activity concentrations for these two months matched the sum of the measured values. Furthermore, a local maximum seen in February 2012 was satisfactorily reproduced by the method.
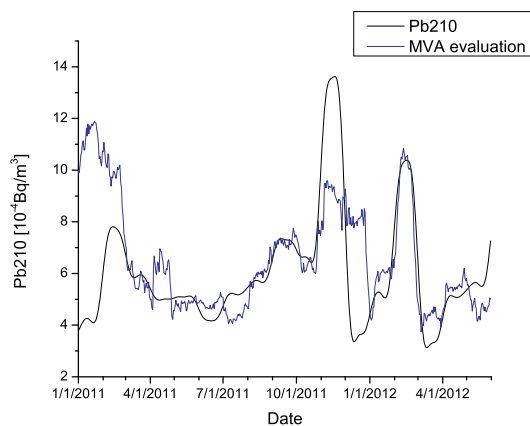

Fig. 5 ²¹⁰Pb activity concentration measured in surface air (black line) and evaluated by MVA (blue line) during 2011 and the first half of 2012.

The above results may indicate that in winter some additional processes play a key role in the ²¹⁰Pb activity concentration in surface air. Emanation of radon-222, the parent radionuclide, could be affected by soil conditions, such as snow cover, soil temperature and moisture, and it could thus induce changes in the ²¹⁰Pb source abundance. Future choice of input variables should include some soil parameters in an attempt to increase the accuracy of the ²¹⁰Pb prediction in winter months.

Further assessments and refinements of the prediction should also address the limitation given by the temporal resolution of the measured ²¹⁰Pb activity concentration in the air. The interpolation of the monthly data performed to obtain daily values (Fig. 1) could give rise to spurious relations between the ²¹⁰Pb activity concentration and input variables, which could reflect on the mapped functional behaviour, and in turn, on the prediction of ²¹⁰Pb in surface air. A possible way to check the validity of our method is to run the prediction using only the measured monthly values, while still employing the daily data in the training period. However, a preferred approach to our method refinement would be to use a more comprehensive database with the measured ²¹⁰Pb activity concentration of higher temporal resolution.

5. CONCLUSIONS

The dependence of the ²¹⁰Pb activity concentration in surface air on different meteorological variables and indices of large-scale circulation was investigated using multivariate analysis.

Boosted Decision Trees was singled out as the best regression method with the least average quadratic deviation between the evaluated and measured activity concentrations. The importance variable ranking given by the BDT method implied a greater influence of large-scale transport than of local meteorological variables.

The prediction of the ²¹⁰Pb activity concentrations showed an agreement with the measurements, except in winter months when the largest differences were obtained.

REFERENCES

1. T. Abe, T. Kosako and K. Komura, "Relationship between variations of ⁷Be, ²¹⁰Pb and ²¹²Pb concentrations and sub-regional atmospheric transport: Simultaneous observation at distant locations", J. Environ. Radioact., vol. 101, pp. 113-121, 2010.
2. L. Bourcier, O. Masson, P. Laj, J. M. Pichon, P. Paulat, E. Freney and K. Sellegri, "Comparative trends and seasonal variation of ⁷Be, ²¹⁰Pb and ¹³⁷Cs at two altitude sites in the central part of France", J. Environ. Radioact., vol. 102, pp. 294-301, 2011.
3. R. L. Lozano, M. A. Hernández-Ceballos, J. F. Rodrigo, E. G. San Miguel, M. Casas-Ruiz, Eason, R. García-Tenorio and J. P. Bolívar, "Mesoscale behavior of ⁷Be and ²¹⁰Pb in superficial air along the gulf of Cadiz (south of the Iberian Peninsula)", Atmos. Environ., vol. 80, pp. 75-84, 2013.
4. L. Kownacka, Z. Jaworowski and M. Suplinska, "Vertical distribution and flows of lead and natural radionuclides in the atmosphere", Sci. Total Environ., vol. 91, pp. 199-221, 1990.
5. J. Braziewicz, L. Kownacka, U. Majewska and A. Korman, "Elemental concentrations in tropospheric and lower stratospheric air in a Northeastern region of Poland", Atmos. Environ., vol. 38, pp. 1989-1996, 2004.
6. F. P. Carvalho, "Origins and concentrations of ²²²Rn, ²¹⁰Pb, ²¹⁰Bi and ²¹⁰Po in the surface air at Lisbon, Portugal, at the Atlantic edge of the European continental landmass", Atmos. Environ., vol. 29, pp. 1809-1819, August 1995.
7. A. S. Likuku, "Factors influencing ambient concentrations of ²¹⁰Pb and ⁷Be over the city of Edinburgh (55.9°N, 03.2°W)", J. Environ. Radioact., vol. 87, pp. 289-304, 2006.
8. A. G. Barnston and R. E. Livezey, "Classification, seasonality and persistence of low-frequency atmospheric circulation patterns", Mon. Wea. Rev., vol. 115, pp. 1083-1126, June 1987.
9. J. W. Hurrell, "Decadal trends in the North Atlantic Oscillation: regional temperatures and precipitation", Science, vol. 269, pp. 676-679, August 1995.

321

Cosmic Rays and Their Connection to Space Weather and Earth's Climate

Mihailo Savić[1*], Nikola Veselinović[1], Aleksandar Dragić[1], Dimitrije Maletić[1], Dejan Joković[1], Radomir Banjanac[1], Vladimir Udovičić[1], David Knežević[1] and Miloš Travar[1]

[1]Institute of Physics Belgrade, Pregrevica 118, Belgrade, Serbia

*Correspondence: Mihailo Savić, msavic@ipb.ac.rs

Abstract: Cosmic rays have been studied for over a century. In addition to investigating their fundamental properties, such as origin, composition, and acceleration mechanisms, some of the most important studies in the field involve the interaction of cosmic rays within the heliosphere, near-Earth space, and the immediate Earth's environment. These areas have been of particular interest in recent years.

One such type of study focuses on the modulation of cosmic rays by the solar magnetic field and the geomagnetic field in the heliosphere and Earth's magnetosphere, respectively. Among other things, the study of these modulations allows for the indirect observation of solar events, which produce characteristic signatures in the interplanetary magnetic field.

Another interesting aspect of cosmic ray physics involves the interactions of secondary cosmic rays, primarily the muon component, within Earth's atmosphere. Precise models of these interactions allow for corrections for atmospheric effects to be made to the muon flux, increasing the sensitivity of Earth-based detectors. Additionally, these models can enable inverse

diagnostics of the atmosphere, potentially providing an additional technique for atmospheric sounding.

Thus, precise monitoring of cosmic ray variations can serve as a proxy for measuring solar activity and variations in Earth's atmosphere. This can be invaluable in situations where direct measurements are not available and can provide significant contributions to the study of space weather and Earth's climate.

ASYMMETRY IN EXPERIMENTS TESTING CPT IN ORTHO-Ps DECAYS

Nevenka Antović[1], Sergey Andrukhovich[2]

1 Faculty of Natural Sciences and Mathematics, University of Montenegro, Podgorica, Montenegro
2 Institute of Physics, Academy of Sciences, Minsk, Belarus

In this paper we consider *asymmetry* in the CPT test experiments performed using polarized ortho-positronium atom decay. Ortho-positronium, a triplet state of Ps, annihilates dominantly into three gamma rays with the continuous energy spectrum in the range (0-511) keV. In searching for decays of ortho-Ps which violate CPT symmetry, the correlation $S*k_1xk_2$ was tested, where S is the ortho-Ps spin, and k_1, k_2 are momenta of the two most energetic annihilation photons ($E_{g1}>E_{g2}>E_{g3}$). The experimental tests consisted in comparing the number of asymmetric decays of polarized ortho-Ps in two identical reflection-symmetric geometries, and the angular correlation coefficient was calculated from the *asymmetry* (A). Using our previous results, as well as results of the other researchers, we particularly discuss the tests carried out at the three and seven-detector system (A=0.0017±0.0017 and A=0.0008±0.00091, respectively), together with their measuring errors.

A SEPARATION PROCEDURE FOR THE DETERMINATION OF NEPTUNIUM AND PLUTONIUM ISOTOPES BY EXTRACTION CHROMATOGRAPHY

Jana Strišovská, Dušan Galanda, Silvia Dulanská, Jozef Kuruc

Department of Nuclear Chemistry, Faculty of Natural Sciences, Comenius University, Bratislava, Slovakia

The subject of this study was to develop, respectively modify and implement these analytical methods for the determination of long-lived radionuclides, namely ^{237}Np and ^{241}Pu in environmental samples. We examined the separation of Np from Pu and from other interfering radionuclides, such as U, Am and Th. A separation procedure was developed for the determination of Pu isotopes (^{238}Pu, ^{239,240}Pu and ^{241}Pu) and ^{237}Np using co-precipitation and separation of radionuclides by using extraction chromatography and commercially available sorbents TEVA® resin and TRU resin supplied by Eichrom Technologies, LLC. ^{239}Np a ^{237}Np were selectively captured on the sorbent TEVA® resin in oxidation state IV. TRU resin was used for purification of plutonium fraction from interfering americium radionuclide. ^{242}Pu and ^{239}Np radionuclides as tracers have been used to monitor the radiochemical yields of separation. Before every radiochemical separation tracer radionuclide ^{239}Np was obtained by separation from the parent radionuclide ^{243}Am, which is in radioactive equilibrium to ^{239}Np. Radionuclides ^{242}Pu, ^{238}Pu, ^{239,240}Pu and ^{237}Np were determined by alpha-spectrometry by using low background semiconductor detector with silicon surface barrier (Alpha 576a-ORTEC, 919, USA), ^{241}Pu was determined by liquid scintillation spectrometry (Tri-Carb 2900 TR, PerkinElmer, USA) and gamma-spectrometric system (Gamma-spectrometer ORTEC with HPGe detector ORTEC, USA) was used to determine activity of tracer ^{239}Np. Sources for alpha-spectrometric counting were prepared by co-precipitation with Nd carrier and hydrofluoric acid. The method was applied to determine plutonium and neptunium radionuclides in reference materials IAEA-375 and IAEA-414, as well as in samples of contaminated soils from the area of Nuclear power plant AI Jaslovské Bohunice which is stored temporarily before disposal.

ISSUES OF SYNERGY AND ANTAGONISM OF RADIATION AND CHEMICAL FACTORS

Yuriy Kutlakhmedov, Svitlana Pchelovska, Anastasia Salivon, Ludmila Tonkal

Institute of Cell Biology and Genetic Engineering, Kyiv, Ukraine

An important task of modern radiobiology, radioecology and general ecology is the study of the effects caused by the combination of the various stress factors impact on living organisms and the processes of restoration and adaptation to stressful influences. In polluted environments, it is important to know the features of the joint impact of various harmful factors on organisms, their interactions with each other.

The phenomenon of synergies in the interaction of different stressors in nature - it is a topical issue that attracts the attention of many biologists, radiobiology, ecologists.

To assess the effect of exposure to radiation alone, and in combination with the introduction into the medium of toxic metals salts on the state of the model plant ecosystem (aquatic plant culture), we proposed to use a sensitive indicator - radiocapacity factor. The radiocapacity of ecosystem, as mentioned above, is defined as the limit of radionuclides deposit in the ecosystem and its components, which can occur above oppression, suppression and destruction of the ecosystem biota. Radiocapacity factor is calculated as a percentage of radionuclide tracer (for example- 137Cs) in the components of ecosystem.

For example, for water culture of maize plants, when the observation time is large, it is possible to calculate and estimate a radiocapacity factor of biota and water as follows: ($a12$ – tracer absorption rate, a_{21} – the outflow velocity of tracer): $Fb \approx a12/(a21+ a12)$; $Fw \approx a21/(a21+ a12)$. The formula for radiocapacity factor comparing these equations can be obtained: $a12/a21 = Fb/Fw = (1- Fw)/Fw = Z$ (denoted by the parameter- Z).

We performed a quantitative analysis of the role of systems recovery and adaptation to the effects of the interaction of various factors, through their influence on the parameters radiocapacity water culture of maize plants. The effects are not additive (synergistic) with different modes of action of the combined stressors. In general, the -n pollutants that act on the ecosystem, the formula for estimating synergy through radiocapacity parameters is as follows:

$Sn = (Z \Sigma \cdot Z n -1) / (\Pi Zi)$, where $Z \Sigma$ – the parameter of relationship Fb / Fw, while the action to biota of the ecosystem - n factors, $Zn -1$ – setting Fb / Fw for control $(n -1)$ - degree, ΠZi - the product of parameters Fb/Fw subject to action individual factors of -n. Thus, we have a model of assessment of the combined effects of several pollutants on the ecosystem, introduced the necessary parameters to assess synergies and formulas are based on experimental data.

DIFFERENT POTENTIAL SYSTEMATIC UNCERTAINTIES INVOLVED IN ^{210}PB DATING METHOD

Robert-Csaba Begy[1], Edina Reizer[1], Alida Timar Gabor[1], Ferenc Forray[2]

1 Babes Bolyai University, Faculty of Environmental Sciences and Engineering, Cluj Napoca, Romania
2 Babes Bolyai University, Faculty of Biology and Geology, Cluj Napoca, Romania

The ^{210}Pb dating method is widely used for determining the ages of young sediments (0-200 y). In order to apply this method, measurements have to be made to determine the activity levels of ^{210}Pb consisting of two components: the supported ^{210}Pb (generated in situ from ^{226}Ra) and the unsupported ^{210}Pb (deposited via airborne fallout).

The aim of this study is to analyze two potential error sources associated with the ^{210}Pb measurements dating method, namely the effect of the silicates found in the sediments and the variation of the mass attenuation in concordance with the sediment depth. In order to achieve this, sediment cores were taken form lakes having different genesis. Sediments were collected from three lakes situated in the Rodnei Mountains National Park (Buhaiescu, Stiol and TaulMuced Lake), one from the Ciomadu Mountains (St. Anna Lake, being situated in a volcano crater) and one from the Danube Delta (Iacob lake, formed between the Sulina an Chilia branches).

The total ^{210}Pb content of the sediments was determined via ^{210}Po, which is the alpha particle emitting progeny of the ^{210}Pb (E_α= 5.31 MeV, $T_{1/2}$ = 138,37 ± 0,002 d). The method employs chemical separation using HNO_3, HCl, H_2O_2 and optionally HF.

^{209}Po tracer was used for determining the chemical yield and ascorbic acid was added to eliminate interferrents (Fe^{3+}). Spontaneous deposition was made onto high nickel content stainless steel discs. Measuremnts were then carried out using an alpha spectrometer containing detectors.

Results show, that if the acidic digestion is carried out without the use of HF, the ages of the sediment layers tend to appear 1-19% younger because of the silicate content. The leaching in teflon dishes can cause contaminations of up to 20-30%. The highest value measured (30%) is attributed to the Iacob Lake, explainable by the fact that the lake gathers its supply form a large catchment area.

Implications of the Temperature Effect Analysis Using Simulated Secondary Cosmic Muon Data

Savić, M.R.,[1] **Veselinović, N.B.,**[1] **Dragić, A.L.,**[1] **Maletić, D.M.,**[1] **Joković, D.R.,**[1] **Banjanac, R.M.,**[1] **Knežević, D.,**[1] **Travar, M.**[1] **and Udovičić, V.I.**[1]

[1]Institute of Physics Belgrade, Pregrevica 118, 11080 Belgrade, Serbia
E-mail: msavic@ipb.ac.rs

As it propagates through the atmosphere, the muon component of secondary cosmic rays is influenced by variations in atmospheric parameters. The two most significant atmospheric effects affecting the muon flux detected at ground level are the barometric effect, due to changes in atmospheric pressure, and the temperature effect, caused by fluctuations in atmospheric temperature.

To enhance the sensitivity of ground-based muon detectors to cosmic ray variations of non-atmospheric origin, these effects must be corrected, with the temperature effect being more complex to model. The most well-established method for correcting the temperature effect is the integral method, based on the theory of atmospheric effects (Dorman 2004). However, as it is not so straightforward to implement, several empirical methods have been developed over the years, including the effective level of generation method (Duperier 1949), the mass-averaged temperature method (Dvornikov et al. 1976), as well as more recent approaches based on principal component analysis (Savić et al. 2019) and machine learning applications (Savić et al. 2021).

Each theoretical and empirical approach has its advantages and limitations, and directly comparing the effectiveness of these methods with real measured data is not necessarily simple. One way to address this is to test model performance on simulated data, where atmospheric variation is the only source of flux change. Preliminary results from data simulated with the CORSIKA package (Heck et al. 1998) provide a clearer picture of the strengths and limitations of these methods. Specifically, the results suggest that the integral method may lead to overcorrections if applied too directly, an issue that hadn't been that obvious before.

References

Dorman, L., Cosmic Rays in the Earth's Atmosphere and Underground. 10.1007/978-1-4020-2113-8. (2004).

Duperier A., The meson intensity at the surface of the earth and the temperature at the production level, Proceedings of the Physical Society. Section A 62 (11) (1949) 684.

V. Dvornikov, Y. Y. Krest'yannikov, A. Sergeev, Determination of the variation of average-mass temperature of the atmosphere by data of cosmic ray intensity., Geomagnetism and aeronomy 16 (1976) 923–925.

M. Savić, A. Dragić, D. Maletić, N. Veselinović, R. Banjanac et al., A novel method for atmospheric correction of cosmic-ray data based on principal component analysis, Astropart.Phys. 109 (2019), 1-11.

Savić, M., Maletić, D., Dragić, A., Veselinović, N., Joković, D., Banjanac, R., et al. (2021). Modeling meteorological effects on cosmic ray muons utilizing multivariate analysis. Space Weather, 19, e2020SW002712.

Heck, D.; Knapp, J.; Capdevielle, J. N.; Schatz, G.; Thouw, T., CORSIKA: a Monte Carlo code to simulate extensive air showers. Forschungszentrum Karlsruhe GmbH, Karlsruhe (Germany)., Feb 1998, V + 90 p., TIB Hannover, D-30167 Hannover (Germany).

THE IMPACT OF GASEOUS POLLUTANTS ON PARTICULATE MATTER DISTRIBUTION

Svetlana Stanisic[2], Mirjana Perisic[1,2], Andreja Stojic[1,2*], Andrej Sostaric[3], Dusan Vudragovic[1], Dimitrije Maletic[1], Gordana Jovanovic[1,2]

[1]Institute of Physics Belgrade, National Institute of the Republic of Serbia, University of Belgrade, 118 Pregrevica Street, 11000, Belgrade, Serbia

[2]Singidunum University, 32 Danijelova Street, Belgrade, 11000, Serbia

[3]Institute of Public Health Belgrade, 54 Despota Stefana Street, 11000, Belgrade, Serbia

*Corresponding author e-mail: andreja.stojic@ipb.ac.rs

Abstract

In this study, we used eXtreme Gradient Boosting machine learning and SHapley Additive exPlanations (SHAP) explainable artificial intelligence methods to examine the relationships between PM_{10} and other air pollutant concentrations in the urban area of Belgrade. The data was provided by the Institute of Public Health Belgrade, Serbia. As shown, the most significant relative impact of benzene levels (50%) on the increase of PM_{10} concentrations up to several tens of µg m^{-3} was recorded at the occasions when benzene concentrations exceeded 5 µg m^{-3} and the concentrations of NO_2 were low (combustion of fossil fuels). The same effect was less pronounced at higher NO_2 concentrations. Taking into consideration the relative impact of SO_2 on PM_{10} levels and the observed relationship between NO and PM_{10}, four dominant environment types that describe the PM level dynamics were distinguished. In the first-type environment, the decrease of PM_{10} levels noticed for SO_2 levels below 50 µg m^{-3} and the dominance of sources with a significant share of NO (> 120 µg m^{-3}) were attributed to traffic emissions. The ambiance recognized as type 2 with no effect on PM levels is characterized by low gaseous oxide concentrations. The third and the fourth type of environment are characterized by SO_2 values exceeding 50 µg m^{-3} and their significant impact on the increase of PM_{10} concentrations.

Keywords

particulate matter, inorganic gaseous pollutants, explainable artificial intelligence

Acknowledgement
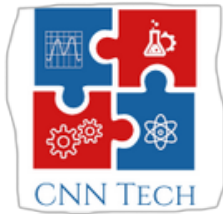
SPATIO-TEMPORAL ANALYSIS OF MOBILITY PATTERNS IN THE CITY OF BELGRADE

Nikola Stupar[1], Ana Vranic[1], Andreja Stojic[1,2], Gordana Vukovic[1,2], Dusan Vudragovic[1], Dimitrije Maletic[1], Marija Mitrovic Dankulov[1*]

[1] Institute of Physics Belgrade, University of Belgrade, Pregrevica 118, 11080 Belgrade, Serbia

[2]Singidunum University, 32 Danijelova Street, Belgrade, 11000, Serbia

*Corresponding author e-mail: mitrovic@ipb.ac.rs

Abstract

Information about human mobility is essential for sustainable development planning. It is crucial for urban and transportation planning and the role of mobility in reducing contributions of human activities in air pollution and fighting climate change. While *human* mobility patterns are typically stable over space and time, they can dramatically change due to critical events, such as earthquakes and epidemics. We still lack a detailed description and understanding of how these critical events influence mobility patterns. In this work, we combine artificial intelligence tools with tools and methods from complex network theory to study human mobility patterns in the City of Belgrade during the COVID-19. We use data about mobility in the City of Belgrade between May 2020 and January 2021 from the Facebook Data for Good dataset. The City of Belgrade is divided into 201 cells with information on the mobility before and during the crises within and between the cells. The time resolution of the data is 8 hours. We use the k-mean clustering technique to cluster the data and find five clusters with different average mobility patterns. All mobility time series have trends and cycles, but they differ between clusters. While residential and suburban area clusters have the peaks of activity during the working days, clusters including central municipalities have the peak of activity during Saturday afternoon. Our results show that different city areas react differently to COVID19 information and that this aspect has to be considered in air pollution and crisis management planning.

Keywords

mobility patterns, time series analysis, k-means clustering

Acknowledgement
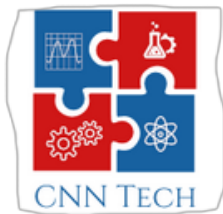
THE POTENTIAL FOR FORECASTING THE PARTICULATE MATTER LEVELS IN COMPLEX URBAN ENVIRONMENT

Mirjana Perisic [1,2], Andreja Stojic[1,2*], Gordana Jovanovic[1,2], Andrej Sostaric[3], Dimitrije Maletic[1], Dusan Vudragovic[1], Svetlana Stanisic[2]

[1]Institute of Physics Belgrade, National Institute of the Republic of Serbia, University of Belgrade, 118 Pregrevica Street, 11000, Belgrade, Serbia

[2]Singidunum University, 32 Danijelova Street, Belgrade, 11000, Serbia

[3]Institute of Public Health Belgrade, 54 Despota Stefana Street, 11000, Belgrade, Serbia

*Corresponding author e-mail: andreja.stojic@ipb.ac.rs

Abstract

In this study, we employed regression analysis by means of machine learning eXtreme Gradient Boosting method for estimating the relationships between particulate matter (PM_{10}) concentrations and a number of parameters including benzene, inorganic gaseous pollutants (SO_2, NO, NO_2, NOx), Global Data Assimilation System-modeled (GDAS1) meteorological parameters, as well as daily and weekend PM variations in Belgrade, Serbia. The data was provided by the Institute of Public Health Belgrade, Serbia. The successful and reliable predictions were provided with relative errors in the range from approx. 19% to 26% and correlation coefficients higher than 0.95. The lowest relative error and the highest correlation coefficient were obtained for monitoring station of rural/industrial type located in Ovca, while the highest difference between modeled and measured values were detected at urban-type monitoring stations Novi Beograd and Institute of Public Health Belgrade, both of which are exposed to traffic emissions. The modeling results were not satisfying for rural/industrial monitoring station located in Veliki Crljeni (relative error>30%, corr. coefficient<0,8), which implies that the dynamic of PM_{10} emissions at the selected monitoring site were not governed by the available data on pollutant concentrations and meteorological parameters.

Keywords

Particulate matter, air pollution forecast, machine learning

Acknowledgement

A29

RADON VARIABILITY DUE TO FLOOR LEVEL IN THE TWO TYPICAL RESIDENTIAL BUILDINGS IN SERBIA

Vladimir Udovičić [1], Nikola Veselinovic[1], Dimitrije Maletic[1], Radomir Banjanac[1], Aleksandar Dragic[1], Dejan Jokovic[1], Mihailo Savic[1], David Knezevic[1], Maja Eremic Savkovic[2]

[1] *Institute of Physics Belgrade, University of Belgrade, Belgrade, Serbia*

[2] *Serbian Radiation and Nuclear Safety and Security Directorate, Belgrade, Serbia*

E-mail: udovicic@ipb.ac.rs

It is well known that one of the factors that influences the indoor radon variability is the floor level of the buildings. Considering the fact that the main source of indoor radon is radon in soil gas, it is expected that the radon concentration decreases at higher floors. Thus, at higher floors the dominant source of radon is originating from building materials and in some cases there may be deviations from the generally established regularity. On the other hand, the radon variability due to floor level, especially in big cities with a much higher number of high-rise buildings and population density compared with rural environments, may have an impact on the assessments of collective dose from radon.

According to the national typology [1], there are six types of residential buildings in Serbia; two for family housing: Freestanding single-family house and single-family house in a row, and four for multi-family housing: Freestanding residential building, residential building - lamela (apartment block with repeated multiple – lamellar – cores and separate entrances), residential building in a row and high-rise residential building. Distribution of buildings by type at national level shows that 97.23% of all residential buildings are family housing. Also, for all defined types of buildings number of floors ranges from one to eight above the ground level. Freestanding family houses are mostly ground floor (37%) or ground floor with loft in use (26%), while there is a very low representation of houses that have more than two floors (5%), with average height of family buildings of 1.4. In that sense, we chose one freestanding single-family house with loft with well-known radon characteristics [2] and one sixteenth floor high-rise residential building for this study.

The indoor radon measurements are performed with two active devices. One was fixed in the living room at the ground level and the second one was moved through the floors of the residential building. Every measuring cycle at the specified floor lasted seven days with the sampling time of the two hours. In this work, the analysis of the obtained results is shown in details.

Ref.

[1] Jovanović Popović M., Ignjatović D., Radivojević A., Rajčić A., Ćuković Ignjatović N., Đukanović Lj. & Nedić M. (2013), National Typology of Residential Buildings in Serbia, Faculty of Architecture University of Belgrade, Belgrade (2013), ISBN 978-86-7924-102-3.

[2] Udovičić V., Maletić D., Banjanac R., Joković D., Dragić A., Veselinović N., Živanović J., Savić M., Forkapić S. Multiyear Indoor Radon Variability in a Family House – a Case Study in Serbia, Nuclear Technology and Radiation Protection Vol. XXXIII, No. 2 (2018), pp. 174-179.

DISTRIBUCIJA KONCENTRACIJE RADONA PO SPRATNOSTI STAMBENIH ZGRADA

Vladimir UDOVIČIĆ[1], Dimitrije MALETIĆ[1], Aleksandar DRAGIĆ[1], Radomir BANJANAC[1], Dejan JOKOVIĆ[1], Nikola VESELINOVIĆ[1], Mihailo SAVIĆ[1], David KNEŽEVIĆ[1] i Maja EREMIĆ-SAVKOVIĆ[2]

1) *Institut za fiziku u Beogradu, Institut od nacionalnog značaja za Republiku Srbiju, Beograd, Srbija, udovicic@ipb.ac.rs, maletic@ipb.ac.rs, dragic@ipb.ac.rs, banjanac@ipb.ac.rs, yokovic@ipb.ac.rs, veselinovic@ipb.ac.rs, msavic@ipb.ac.rs, davidk@ipb.ac.rs*

2) *Direktorat za radijacionu i nuklearnu sigurnost i bezbednost Srbije, Beograd, Srbija, eremic.savkovic@srbatom.gov.rs*

SADRŽAJ

Dobro je poznato da je jedan od faktora koji utiče na varijabilnost radona u zatvorenom prostoru spratnost stambenih zgrada. Imajući u vidu činjenicu da glavni izvor radona u zatvorenim prostorijama potiče iz zemljišta, očekuje se smanjenje koncentracije radona na višim spratovima. Na višim spratovima dominantan izvor radona potiče od građevinskog materijala, a u nekim slučajevima može doći do odstupanja od ove opšte utvrđene pravilnosti. S druge strane, varijabilnost radona zbog spratnosti, posebno u velikim gradovima, sa mnogo većim brojem visokih zgrada i gustinom naseljenosti u poređenju sa ruralnim sredinama, može uticati na procenu kolektivne doze koja potiče od radona. U tom smislu, a u svrhu naših istraživanja, izabrali smo jednu tipičnu porodičnu kuću sa potkrovljem i jedan šesnaestospratni soliter. Merenje koncentracije radona u odabranim stambenim objektima izvršeno je sa dva aktivna uređaja. Jedan je bio fiksiran u dnevnoj sobi u prizemlju, a drugi je menjao poziciju po spratovima u stambenim zgradama. Svaki merni ciklus na datom spratu trajao je sedam dana uz vreme uzorkovanja od dva sata. U ovom radu detaljno je urađena analiza dobijenih rezultata.

1. Uvod

Izvori radona u stambenim i poslovnim zgradama su, pre svega iz zemljišta, građevinskog materijala i vode. S obzirom na prirodu nastanka i svih pomenutih izvora, koncentracija radona je veša u prizemnim prostorijama u odnosu na stanove na višim spratovima stambenih objekata. U literaturi se može pronaši dosta radova koji se bave uticajem raznih faktora na nivo i varijabilnost radona u zatvorenim prostorijama, pa između ostalih i uticajem spratnosti [1-4]. U slučaju velikih stambenih objekata sa vešim brojem spratova, može se uočiti odstupanje od opšte pravilnosti, jer je na višim spratovima dominantan izvor radona građevinski materijal, te se mogu uočiti povešane koncentracije radona u odnosu na situaciju na nižim spratovima. U tom smislu, urađena su merenja radona u dva tipična stambena objekta. Izbor zgrada je baziran na rezultatatima iz monografije „Nacionalna tipologija stambenih zgrada Srbije— grupe autora sa Arhitektonskog fakulteta [5]. S obzirom na specifiţnosti gradnje u Srbiji, broj

NATIONAL PROGRAMME FOR THE CONTROL OF PUBLIC EXPOSURE TO RADON IN SERBIA

10 authors, including:

Vladimir Udovičić
Institute of Physics Belgrade
75 PUBLICATIONS **482** CITATIONS

SEE PROFILE

Dimitrije M Maletić
Institute of Physics Belgrade
149 PUBLICATIONS **9,576** CITATIONS

SEE PROFILE

Gordana Pantelic
University of Belgrade
70 PUBLICATIONS **503** CITATIONS

SEE PROFILE

Predrag Ujić
Vinča Institute of Nuclear Sciences
94 PUBLICATIONS **907** CITATIONS

SEE PROFILE

NACIONALNI PROGRAM KONTROLE IZLOŽENOSTI STANOVNIŠTVA RADONU U SRBIJI

V. Udovičić[*], D. Maletić[*], M. Eremić Savković[**], G. Pantelić[***], P. Ujić[***], I. Čeliković[***], S. Forkapić[****], D. Nikezić[*****], V. M. Marković[*****], V. Arsić[******]

Institut za fiziku Beograd, Univerzitet u Beogradu, Beograd, Srbija[*]
Agencija za zaštitu od jonizujućih zračenja i nuklearnu sigurnost Srbije, Beograd Srbija[**]
Institut za nuklearne nauke Vinča, Univerzitet u Beogradu, Beograd, Srbija[***]
Prirodno-matematički fakultet, Univerzitet u Novom Sadu, Novi Sad, Srbija[****]
Prirodno-matematički fakultet, Univerzitet u Kragujevcu, Kragujevac, Srbija [*****]
Institut za medicinu rada Srbije " Dr Dragomir Karajović", Beograd, Srbija[******]

Rezime. *Rizici po zdravlje ljudi izloženih jonizujućim zračenjem su dobro poznati. U tom smislu, doprinos radona ukupnom izlaganju stanovništva je najveći i predstavlja najvažniji izvor jonizujućih zračenja među onima koji su prirodnog porekla. Veliki broj zemalja u svetu posvećuje posebnu pažnju problemu radona i u većini su uspostavljeni nacionalni programi za radon. U ovom radu su predstavljeni prvi koraci u razvoju nacionalnog akcionog plana za radon u Srbiji. Implementacija efikasnog nacionalnog akcionog plana za radon ima za cilj zaštitu i smanjenje rizika izloženosti stanovništva radonu u zatvorenim prostorijama. Ovaj akcioni plan zahteva rad mnogih nacionalnih agencija, institucija i drugih zainteresovanih strana, uključuju i nacionalne, regionalne i lokalne organizacije odgovorne za javno zdravlje i zaštitu od zračenja. Na početku, projektovanje i realizacija prve nacionalne prospekcije radona u boravišnim prostorijama u Srbiji je od presudnog značaja. Predloženi dizajn je predstavljen u ovom radu.*

Ključne reči: *radon, akcioni plan, prospekcija*

NATIONAL PROGRAMME FOR THE CONTROL OF PUBLIC EXPOSURE TO RADON IN SERBIA

V. Udovičić[*], D. Maletić[*], M. Eremić Savković[**], G. Pantelić[***], P. Ujić[***], S. Forkapić[****], D. Nikezić[*****], N. Stevanović[*****], V. M. Marković[*****], V. Arsić[******]

Institute of Physics Belgrade, University of Belgrade, Belgrade, Serbia[*]
Serbian Radiation Protection and Nuclear Safety Agency, Belgrade, Serbia[**]
Vinča Institute of Nuclear Sciences, University of Belgrade, Belgrade, Serbia[***]
Faculty of Science, University of Novi Sad, Novi Sad, Serbia[****]
Faculty of Science, University of Kragujevac, Kragujevac, Serbia[*****]
Serbian Institute of Occupational Health "Dr Dragomir Karajović", Belgrade, Serbia[******]

Abstract. *The risks to human health exposed by ionizing radiation are well known. In that sense, radon contribution to the overall public exposure is the greatest and represents the most important source of ionizing radiation among those that are of natural origin. The large number of the countries in the world pays special attention to the radon problem and the most of them have established national radon programmes. In this report, the efforts and first steps in developing radon action plan in Serbia, are presented. The implementation of an effective radon action plan is aimed at protecting the public against indoor radon exposures. This action plan requires input from many national agencies, institutions and other stakeholders, also include the national, regional and local organizations responsible for public health and radiation protection. At the beginning, design and realization of the first national indoor radon survey are of the crucial importance. The proposed design is presented in this work.*

Key words: *radon, action plan, survey*

Introduction. Radon is a nobel, natural occurring gas. Radon is formed as a product of the natural radioactive series of ^{238}U in the soil and relatively easily reaches the earth's surface and penetrates into the housing and accumulate in enclosed spaces. Above all, it is a radioactive gas, and thus is a factor that has an adverse effect on the health of the population. Also, source of indoor radon is in construction material. Radon contribute to almost 50% of the overall high effective annual dose to the population receives from all sources of natural radioactivity. Harmful effects of radon has been proven in a large number of epidemiological studies (1). World Health Organisation declared radon as the second most important cause of getting lung cancer (2). In addition, radon is included in the ranks of major pollutants of indoor air (3). Current knowledge about the mechanisms by which radon is harmful to human health are reflected primarily in harmful, radioactive radon progeny fact. In fact, radon progeny are attached to the aerosol particles from the air and such radioactive particles enter the body through inhalation. These radioactive aerosols deposited in the lungs, emitting alpha radiation. The harmful activity can be seen in disorders of the cellular structure of DNA, causing the development of cancer cells. Consequently, radon problem being addressed seriously and in a number of countries there are established national radon programme, which is basically a multidisciplinary nature and require the involvement of a large number of experts, researchers involved in radiation physics, geo sciences, chemistry, biology to specialist in various fields of medicine.

New safety standards and regulations related to radon. The regulations related to the exposure of the population to radon and its progeny are different worldwide. Based on the researches and a large number of epidemiological studies done in a recent past, the new standards and recommendations have to be incorporated into the national legislation relgarding radon issues. Basically, a new approach to the radon issue is to introduce the concept of the reference level (not as strict boundaries between safe and dangerous concentrations of radon, but the annual average indoor radon concentration above which it is necessary to take measures to reduce radon). It differs from action level (the radon concentration above which, if it is found that the measured concentration greater than defined, gives recommendations to take measures

for its reduction). The new concept is incorporated in two new documents. One is developed at the International Atomic Energy Agency (IAEA) (4). In this new BSS (International Basic Safety Standards) radon is mentioned in several places, but the most important: requirements of 50 (Requirement 50: Public exposure due to radon indoors). It defines the reference level, in dwellings of high occupational factors, which must not exceed 300 Bqm^{-3}. Assuming equilibrium factor for radon 0.4 and the annual occupational factors than 7000 hours, the reference level of 300 Bqm^{-3} corresponds to an annual effective dose of 10 mSv. The request 52 (Requirement 52: Exposure in workplaces) defines the reference level for radon in workplaces of 1000 Bqm^{-3}. Since the occupation factor for 2000 hours with the same factor to balance radon of 0.4 leads to the same effective annual dose of 10 mSv. Important conclusions are: countries to consider if control of radon is necessary, information on radon levels to be collected, information on exposure due to radon and health risks to be provided to the public and other interested parties, where radon levels are of concern for public health, a radon action plan to be established.

The second document is EU Directive 2013/59 (5). In the article 74: Indoor exposure to radon, writes:

- Member States shall establish national reference levels for indoor radon concentrations. The reference levels for the annual average activity concentration in air shall not be higher than 300 Bq/m3.
- Member States shall ensure that local and national information is made available on indoor radon exposure and the associated health risks, on the importance of performing radon measurements and on the technical means available for reducing existing radon concentrations.

Article 103 defines Radon Action Plan (RAP) to be developing in member states:

Member States shall establish a national action plan addressing long-term risks from radon exposures in dwellings, buildings with public access and workplaces for any source of radon ingress, whether from soil, building materials or water. The action plan shall take into account the issues set out in Annex XVIII and be updated on a regular basis. Annex XVIII defined 14 items to consider in preparing the national radon action plan.

Developing national radon action plan in Serbia. Serbia did not have a systematic approach to the radon problem. In this sense, there were individual initiatives and research activities dealing with radon:

- University of Novi Sad, Faculty of Science, Department of Physics, Chair of Nuclear Physics, Novi Sad:

Radon Mapping of Autonomous Province of Vojvodina (6), Long-term and Short-term measurements of radon concentration in soil, water and air using passive devices, active device RAD7, exhalation and difusion measurements (7), charcoal canisters with gamma spectrometric analysis (8).

- University of Belgrade, Vinča Institute of Nuclear Sciences, ECE Lab Belgrade:

Department for Nuclear and Plasma Physics: Mapping radon and thoron throughout south-eastern Serbia, Kosovo and Metohija parts of western Serbia using different passive devices, electro-chemical etch track detectors in a specially designed and built in laboratory (9),

developing method for radon and thoron exhalation from building material (10), radon measurement campaigns in the schools and houses in the Sokobanja municipality (11).

Radiation and Environmental Protection Department: Active charcoal detectors are used for testing the concentration of radon in dwellings. The method of measurement is based on radon adsorption on coal and measurement of gamma radiation of radon daughters according to US EPA protocol. Based on this EPA procedure and national and international intercomparison, the laboratory developed a set of procedures for charcoal detector exposure and measurement (12),(13).

- University of Belgrade, Institute of Physics Belgrade, Low-Background Laboratory for Nuclear Physics:

Radon monitoring in the underground low-background laboratory with the passive and active devices (14), radon laboratory for chemical etching of the track detectors and automatic counting of the tracs by optical microscopy (15), modeling of the indoor radon behavior (16).

- Institute of Occupational Health of Serbia "Dr Dragomir Karajović", Center for Radiological Protection, Belgrade:

Radon measurements using charcoal canisters with gamma spectrometric analysis, radon monitoring in schools and kindergartens in the city of Belgrade from 1991 (17) and radon measurements campaigns in schools and kindergartens in Belgrade from 2010 (18).

- University of Kragujevac, Faculty of Science Kragujevac, Institute of Physics:

Radon measurement using of passive devices with chemical treatment of the track detectors and automatic scanning of the developed detectors, modeling of the behavior of indoor radon (19), dosimetric modeling of the effects of the inhalation of radon and its progeny in the lung (20).

Based on the great experience of research related to radon, the group of radon professionals organized Radon Forum, in the May 2014 and made a decision to start work on RAP in Serbia. The responsibility for the establishment and implementation of RAP is on national regulatory body: Serbian Radiation Protection and Nuclear Safety Agency (SRPNA). We started with internet radon forum (www.cosmic.ipb.ac.rs/radon_forum) which provides an opportunity for radon professionals in Serbia to meet and discuss radon activities and plans. Also, SRPNA formed a "radon working group" that will manage RAP. The organization chart of the institutions involved in RAP is shown in Figure 1.

Figure 1. *Organization chart of the institutions involved in RAP.*

Short-term plans (to the end of 2015) include:

- Development measurement protocol for long-term measurements for the purpose of radon survey.

- Carry out initial representative national indoor radon survey for this purpose.

- Developing communication strategy (first basic information leaflet on radon to accompany the measurement explaining the purpose of the measurement, internet site: http://cosmic.ipb.ac.rs/radon/index.html, public relation…).

Design of the first national radon survey in Serbia. As a first step in RAP, it is the national radon survey in Serbia, planned to be done in 2015. In the cooperation with IAEA, SRPNA through radon working group made the design of the first national radon survey in Serbia. It is well known that, regarding the objective of the indoor radon survey there are two types of survey:

- **population-weighted survey** by measuring indoor radon levels in randomly selected homes (to estimate the distribution of radon public exposures)
- **geographically based survey** where homes are randomly selected to obtain a minimum density of measurements per area unit chosen, e.g. a grid square, an administrative unit... (to identify radon prone areas, radon map)

Every radon survey needs to check the representativeness (e.g. compare certain parameters in the actual sample with corresponding values in the last census). A carefully designed survey can, in principle, meet the requirements and objectives of both types of surveys. In the case of Serbia, we choose a stratified (target population is partitioned into separated groups - STRATA) sampling design. We defined STRATA according to the administrative divisions of Serbia into districts.

In principle, our design model can be described as follows: To cover all districts, the detectors will be distributed to local physics teachers in high schools, who further distributed them among their pupils. Teachers will recommended pupils to place CR39 diffusion chambers in living rooms and bedrooms where they spend a lot of time. The phases of the survey will be:

- Web questionnaire − teacher send them to pupils who wish to participate in the project. This may be used as a tool for selection of measuring place.
- Performed communication strategy (first basic information leaflet on radon to accompany the measurement explaining the purpose of the measurement, internet site, public relation, public education...)
- The questionnaire.

The crucial stakeholder in the radon survey will be the Ministry of Education, Science and Technological Development, offering the logistic in communication with school administration in specific districts (Figure 2).
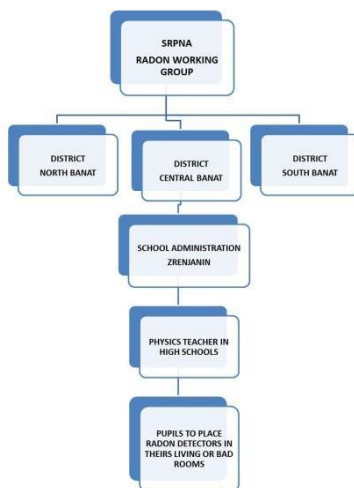

Figure 2. *Organization chart of the first national radon survey in Serbia.*

Finally, the results of national radon survey serves to evaluate the existing exposure situation and to define the RAP in Serbia**.**

Conclusions

World Health Organisation declared radon as the second most important cause of getting lung cancer. Radon problem being addressed seriously and in a number of countries there are established national radon programme. Serbia started work on radon action plan (RAP) in 2014. The responsibility for the establishment and implementation of RAP is on national regulatory body: Serbian Radiation Protection and Nuclear Safety Agency. The first step in RAP is the national radon survey in Serbia, planned to be done in 2015. The results of national radon survey serves to evaluate the existing exposure situation and to define the RAP in Serbia**.**

References

1. Darby, S., Hill, D., Auvinen, A., et al., 2005. *Radon in homes and risk of lung cancer: collaborative analysis of individual data from 13 European case-control studies*. Brit. Med. J. 330, 223-227.
2. *WHO handbook on indoor radon: a public health perspective.* (2009), www.who.int/ionizing_radiation/env/radon/en/index1.html

3. *WHO guidelines for indoor air quality: selected pollutants.* (2010), http://www.who.int/indoorair/publications/9789289002134/en/index.html

4. *Radiation Protection and Safety of Radiation Sources: International Basic Safety Standards* INTERIM EDITION, General Safety Requirements Part 3 (2011) http://www-pub.iaea.org/MTCD/publications/PDF/p1531interim_web.pdf

5. *Council Directive 2013/59/EURATOM of 5 December 2013 laying down basic safety standards for protection against the dangers arising from exposure to ionising radiation, and repealing Directives 89/618/Euratom, 90/641/Euratom, 96/29/Euratom, 97/43/Euratom and 2003/122/Euratom*. Official Journal of the European Union 2014; L13., http://www.srbatom.gov.rs/srbatom/doc/eu-direktive/2013%2059%20eng.pdf

6. S.Forkapić, I.Bikit, J.Slivka, Lj.Čonkić, M.Vesković, N.Todorović, E.Varga, D.Mrđa and E.Hulber: *Indoor radon in rural dwellings of the South-Pannonian region*, Radiation Protection Dosimetry, Vo 123, Issue 3, pp 378-383 (2006)

7. Jovana Nikolov, Natasa Todorovic, Istvan Bikit, Tanja Petrovic, Pantic, Sofija Forkapic, Dusan Mrda and Kristina Bikit: *Radon in Thermalwaters in South-East Part of Serbia*, Radiation Protection Dosimetry Vol.160, No.1-3, pp.239-243 (2014)

8. Todorović, N., Bikit, I., Vesković, M., Krmar, M., Mrda, D., Forkapić, S., Hansman, J., Nikolov, J., Bikit, K.: *Radioactivity in the indoor building environment in Serbia*, Radiation Protection Dosimetry, Volume 158, Issue 2, pp 208-215 (2014)

9. Zunic et al., *High variability of indoor radon concentrations in uraniferous bedrock areas in the Balkan region*, Applied radiation and isotopes, vol. 94, pp. 328-337 (2014)

10. Ujic et al., *Development of method for radon/thoron exhalation measurement*, Radiation Measurements, vol. 43(8), pp. 1396-1401 (2008)

11. F. Bochicchio, Z. S. Žunić, C. Carpentieri, S. Antignani, G. Venoso, V. Carelli, C. Cordedda, N. Veselinović, T. Tollefsen, P. Bossew. *Radon in indoor air of primary schools: a systematic survey to evaluate factors affecting radon concentration levels and their variability*, Indoor Air 24, (2014) pp. 315–326.

12. Pantelić G, Živanović M, Eremić SavkovićM, Forkapić S. *Radon concentration intercomparison in Serbia, Proceedings of the ninth symposium of the Croatian Radiation Protection Association*; Eds. Ž. Knežević, M. Majer, I. Krajcar-Bronić, 10-12. April 2013. Krk, Croatia, ISBN 978-953-96133-8-7, CRPA Zagreb, 2013, 193-198

13. G. Pantelić, M. Eremić Savković, M. Živanović, J. Nikolić, M. Rajačić, D. Todorović, *Uncertainty evaluation in radon concentration measurement using charcoal canister*, Applied Radiation and Isotopes, 87, 2014, 452-455

14. Udovičić V., Aničin I., Joković D., Dragić A., Banjanac R., Grabež B., Veselinović N., *Radon Time-series Analysis in the Underground Low-level Laboratory in Belgrade, Serbia*. Radiation Protection Dosimetry 145 (2-3), pp:155-158 (2011)

15. R. Banjanac, A. Dragić, B. Grabež, D. Joković, D. Markushev, B. Panić, V. Udovičić, I. Aničin, *Indoor Radon Measurements by Nuclear Track Detectors: Applications in Secondary Schools*. Facta Universitatis 4, pp. 93-100 (2006)

16. Dimitrije M. MALETIĆ, Vladimir I. UDOVIČIĆ, Radomir M. BANJANAC, Dejan R. JOKOVIĆ, Aleksandar L. DRAGIĆ, Nikola B. VESELINOVIĆ, and Jelena Z. FILIPOVIĆ, *Comparison of Multivariate Classification and Regression Methods for the Indoor Radon Measurements*, Nuclear Technology and Radiation Protection Vol. XXIX, No. 1, pp.17-23 (2014)

17. Eremić-Savković M, Pantelić G, Tanasković I, Vuletić V, Javorina Lj,*Concentration of radon in apartments on the territory of Belgrade in period 1997-2001*, Archives of toxicology, kinetics and xenobiotic metabolism, Vol.10, No. 1-2, Belgrade, pp.195-197 (2002)

18. V. Arsić, J. Ilić, S. Bogojević, I.Tanasković, M. Eremić-Savković, Lj. Javorina, *Assessment of the Effective Radon Dose, Measured in Schools and Kindergartens in Belgrade During 2012 and 2013*, Proceedings of Second East European Radon Symposium (SEERAS), Niš Serbia, May 27 – 30 2014, pp. 17-20

19. Stevanovic, N., Markovic V., Nikezic D. *Relationship between deposition and attachment rates in Jacobi room model.* Journal of Environmental Radioactivity, Vol.101(5), pp. 349-352 (2010)

20. Jovanovic B., Nikezic D., Stevanovic N. *Applied mathematical modeling for calculating the probability of the cell killing per hit in the human lung.* Journal of radioanalytical and nuclear chemistry, Volume: 290(3), pp: 607-613 (2011)

PROCENA TEMPERATURSKOG PROFILA ATMOSFERE NA OSNOVU DETEKTOVANOG FLUKSA KOSMIČKIH MIONA

Mihailo SAVIĆ, Vladimir UDOVIČIĆ, Dimitrije MALETIĆ, Aleksandar DRAGIĆ, Radomir BANJANAC, Dejan JOKOVIĆ, Nikola VESELINOVIĆ i David KNEŽEVIĆ

Institut za fiziku u Beogradu, Institut od nacionalnog značaja za Republiku Srbiju, Beograd, Srbija, msavic@ipb.ac.rs

SADRŽAJ

Uticaj atmosferskih parametara na intenzitet mionske komponente sekundarnog kosmičkog zračenja dobro je poznat. Dominantan doprinos varijaciji fluksa kosmičkih miona usled atmosferskih parametara daju dva meteorološka efekta - barometarski (usled varijacije atmosferskog pritiska) i temperaturski (usled varijacije temperature atmosfere). Postoji više teorijskih i empirijskih modela koji dobro opisuju ove zavisnosti. Obično se na osnovu ovih modela vrši korekcija kako bi se eliminisala varijacija fluksa kosmičkih miona atmosferskog porekla.

Obrnuto, osetljivost mionskih detektora na varijacije atmosferskih parametara može se iskoristiti da se na osnovu poznatih parametara modela i poznatog odbroja kosmičkih miona odredi temperatura različitih nivoa atmosfere. U ovom radu ćemo demonstrirati ovaj pristup na osnovu podataka merenih mionskim monitorima Niskofonske laboratorije za nukelarnu fiziku Instituta za fiziku u Beogradu i primenom empirijskog modela meteoroloških efekata, zasnovanog na tehnici dekompozicije na osnovne komponente.

1. Uvod

Intenzitet pljuskova sekundarnog kosmičkog zračenja zavisi od atmosferskih meteoroloških parametara. To se naročito odnosi na mionsku komponentu sekundarnog kosmičkog zračenja. Dva efekta dominantno utiču na fluks sekundarnih miona: barometarski koji opisuje antikorelaciju fluksa kosmičkih miona sa atmosferskim pritiskom [1] i temperaturski koji se odnosi na uticaj varijacije atmosferske temperature na detektovani intenzitet miona [2].

Osim fundamentalnog, detaljno poznavanje meteoroloških efekata ima značaj u proceduri korekcije na date efekte, čime se povećava osetljivost zemaljskih detektora kosmičkog zračenja na varijacije neatmosferskog porekla. Alternativno, dobar model meteoroloških efekata bi u principu omogućio predviđanje atmosferskih parametara na osnovu merenja fluksa miona. Ovo je potencijalno značajno za određivanje temperatura pojedinih slojeva atmosfere u slučaju da su druge metode nedostupne.

Postoji više predloženih metoda za predikciju atmosferskih meteoroloških parametara na osnovu merenja intenziteta kosmičkog zračenja zemaljskim detektorima. Mogu se bazirati na merenju različitih komponenti fluksa kosmičkih miona [3, 4], simultanom merenju neutronske i mionske komponente [5] ili upotrebi mionskog teleskopa sposobnim da meri ugaonu distribuciju intenziteta [6]. Sve pomenute metode karakteriše relativna kompleksnost eksperimentalne postavke i analize. Takođe, zajedničko svim pomenutim metodama je da se u proceduri određivanja atmosferskih temperatura oslanjaju na teorijski izračunate koeficijente za opisivanje zavisnosti inenziteta miona od temperaturskog profila atmosfere. Ovaj pristup ima određenih ograničenja usled nužno aproksimativnog karaktera i neprilagođenosti konkretnom